

# **Geosynthetics Conference 2023 Proceedings**

Edited by:

Melissa Beauregard, Ph.D., P.E.

Stephan Gale, P.E., D.GE, F. ASCE

Copyright © 2023 Advanced Textiles Association

All rights reserved. Published by Advanced Textiles Association

ISBN: 978-0-935803-24-2

# Table of Contents

Foreword .....	V
----------------	---

## Applications of Fabricated Geosynthetics – Organized by FGI

<a href="#">Carbon Footprint Calculator</a> .....	1-8
<a href="#">Case Study: Lake Forest Reservoir Relining &amp; Floating Cover</a> .....	9-18
<a href="#">Payment Bases in Liner Projects</a> .....	19-24
<a href="#">Performance Comparison of Evapotranspiration and Engineered Turf Covers</a> .....	25-32
<a href="#">Protection of Geofoam using High Strength, Chemically Resistant Geomembranes</a> .....	33-42
<a href="#">PVC Geomembranes in Agricultural Uses</a> .....	43-50

## Case Histories

<a href="#">Five Geotextile Tube Projects Review for Survivability and Performance after Decades in Challenging Environments</a> .....	51-62
<a href="#">Lessons Learned from Three Failures</a> .....	63-69
<a href="#">Lining A Highly Irregular Vertical Wall with Polyurea/Conductive Geotextile Geomembrane</a> .....	70-74
<a href="#">Mitigation of Cracks in Flexible Pavements with Expansive Subgrade Using Geosynthetics: A Case Study in Austin, Texas</a> .....	75-83
<a href="#">Reinforced Soil Embankment for Rockfall Protection - Case History</a> .....	84-89
<a href="#">The Use of Geotextile Tubes as The Containment Dyke for The Construction of Davao Coastal Highway, Philippines</a> .....	90-99

## Electric Leak Location

<a href="#">Comparative Analysis of Electrical Leak Location Methods on Exposed Geomembranes</a> .....	100-112
<a href="#">Development of a Conductive Textile and Its Uses in Electrical Leak Location (ELL) Survey of Geosynthetic Containment Systems</a> .....	113-118
<a href="#">Increasing the Sensitivity of the Dipole Method: A Case Study</a> .....	119-130
<a href="#">The Effect of Cover Material Conductivity on Dipole Method Testing</a> .....	131-142

## Exposed Geosynthetic Performance – Organized by GSI

<a href="#">Engineered Turf Landfill Closure: How Long Will It Last?</a> .....	143-151
<a href="#">Evaluation of the UV Exposure of Polymeric Geomembranes Using Geographic and Climate Data</a> .....	152-161
<a href="#">Exposed Geomembrane Cover Performance at Polk County Landfill in Florida</a> .....	162-167
<a href="#">Exposed NPNW GT Exposed Npnw GT Performance at a Large Surface Impoundment for Nearly One Year</a> .....	168-174

## Fabricated Geosynthetics for Water Retention Projects – Organized by FGI

<a href="#">Best Practices for Design and Installation of Geosynthetic Floating Covers</a> .....	175-187
--	---------

<a href="#"><u>Chambers Dam Reservoir Remediation: Case Study</u></a> .....	188-192
<a href="#"><u>Netherlands Motorway Underpass Case Study</u></a> .....	193-198
<a href="#"><u>New Developments in PVC-EIAs for Potable Water Containment Applications</u></a> .....	199-206
<a href="#"><u>Operation and Maintenance Guideline for Water Reservoirs</u></a> .....	207-217
<b>Geosynthetic Properties and Laboratory Testing</b>	
<a href="#"><u>An Evaluation of Soil-Geogrid Interaction Models</u></a> .....	218-230
<a href="#"><u>Hydraulic Conductivity of Lighter Bentonite-Polymer Geosynthetic Clay Liners</u></a> .....	231-238
<a href="#"><u>Long-term Hydraulic Conductivity of Bentonite-Polymer Geosynthetic Clay Liner to Coal Combustion Product Leachates</u></a> .....	239-247
<a href="#"><u>Quantification of Suction-driven Flow of Enhanced Lateral Drainage Geotextiles</u></a> .....	248-258
<a href="#"><u>White Polyethylene Geomembrane: Forensic and Laboratory Evidence for Superior Durability</u></a> .....	259-269
<b>Geosynthetic Wettability and Performance</b>	
<a href="#"><u>Contact Angle Determination of a Wicking Geotextile Composed of Both Hydrophilic and Hydrophobic Materials</u></a> .....	270-276
<a href="#"><u>Efficacy of Nonwoven Based Geosynthetic Drainage Product for Pore Pressure Reduction in Moderately Fine Soils or Tailings</u></a> .....	277-287
<a href="#"><u>Experimental Investigation on the Effect of Fines Content on the Drainage Performance of Wicking and Non-wicking Geotextiles</u></a> .....	288-296
<a href="#"><u>Hydrophobizing Treatment in Saline Soil: Conditions and Mechanisms</u></a> .....	297-304
<a href="#"><u>Investigation of Moisture Reduction in Sandy Soil Using Geotextiles</u></a> .....	305-314
<b>Geosynthetics in Roadways</b>	
<a href="#"><u>Effect of Tensile Strength Development in Stabilization Geogrids on Bearing Capacity in Pavements and Railway Application</u></a> .....	315-323
<a href="#"><u>Evaluation of Geosynthetic-reinforced Asphalt Milling Characteristics and Suitability as Pavement Base Course</u></a> .....	324-335
<a href="#"><u>Local Stiffness Enhancement by Multi-Axial Geogrid Stabilization Evaluated Through Shear Wave Measurement</u></a> .....	336-347
<a href="#"><u>Role of Geosynthetics in Improving Freeze-Thaw Resistance of Bases - A Literature Survey</u></a> .....	348-359
<a href="#"><u>Role of High-Modulus Geogrids in Improving Base Layer Properties</u></a> .....	360-370
<b>Hydraulic and Coastal Applications 1</b>	
<a href="#"><u>25m3 Geotextile Bags and Geotextile Tubes Used to Protect a 42" Pipeline Against Scouring, 30M Deep on the Seabed, Covenas, Colombia, S.a</u></a> .....	371-377
<a href="#"><u>Dredging Works and Geotextile Tube Applications for The Construction of Deep C Industrial Zones, Vietnam</u></a> .....	378-387
<a href="#"><u>Investigation of Geotextile Integrity Subjected to Vertical Drains Installation</u></a> .....	388-397

<a href="#"><u>Use of Treated Soft Soil as Infill Material in Geotextile Tubes</u></a> .....	398-410
<b>Hydraulic and Coastal Applications 2</b>	
<a href="#"><u>Effectively Utilizing a Nature-Based HPTRM Solution for Municipal Drainage Channels</u></a> .....	411-420
<a href="#"><u>Hydraulic Roughness Testing of Geosynthetics</u></a> .....	421-432
<a href="#"><u>Installation of Geotextile Tubes as Perimeter Bund in Mega-Reclamation Project at Penang, Malaysia</u></a> .....	433-443
<a href="#"><u>Shoreline Protection in Kerala Coastline (India) And Use of Geosynthetics</u></a> .....	444-456
<b>Innovative Solutions 1</b>	
<a href="#"><u>Emerging Uses of Geosynthetic Floating Covers in the Energy Sector</u></a> .....	457-465
<a href="#"><u>Feasibility Evaluation of Lightweight Aggregate to Improve Performance of Load Transfer Platforms in Geosynthetic-reinforced Embankments</u></a> .....	466-478
<a href="#"><u>Geogrid-Reinforced Timber Pile Supported Modular Block Retaining Wall</u></a> .....	479-489
<a href="#"><u>Polymeric Alloy Geocell Reinforced Design for a Heavily Loaded Gravel Pad with Restricted Fill Thickness</u></a> .....	490-501
<b>Innovative Solutions 2</b>	
<a href="#"><u>Decentralized Stormwater Runoff Treatment with Active Geocomposites</u></a> .....	502-508
<a href="#"><u>Evolution in Geosynthetics Starts with Utilizing Data Technology</u></a> .....	509-515
<a href="#"><u>New Geotextile Quarry By-Product Geocomposite System for Permanent Road Foundation</u></a> .....	516-527
<a href="#"><u>Simplified Model for Analysis of Piled Embankment Considering Multi-Interaction Arching and Subsoil Consolidation</u></a> .....	528-538
<b>Landfill Covers and Liner Systems</b>	
<a href="#"><u>Environmental, Social, and Governance (ESG) Offerings of an Engineered Turf Final Cover System</u></a> .....	539-548
<a href="#"><u>Hydraulic Conductivity of Bentonite-Polymer Composite Geosynthetic Clay Liners Under Elevated Temperature and Extreme pH</u></a> .....	549-560
<a href="#"><u>Practical Aspects of Exposed Geomembrane Cap (EGC) Design and Construction</u></a> .....	561-571
<a href="#"><u>Remediation of a Former Quarry and Permanent Containment of Buried Toxic Materials</u></a> .....	572-582
<b>Mining Applications</b>	
<a href="#"><u>High Performance Geomembranes in Aggressive Mining Applications</u></a> .....	583-591
<a href="#"><u>Initial Stress Condition and the Hydraulic Conductivity of BPC Geosynthetic Clay Liners for Acidic Heap Leach Solutions</u></a> .....	592-603
<a href="#"><u>Sustainable Practices with Geosynthetics in Mining: Review of Select Case Studies</u></a> .....	604-613
<b>Recent Advances in MSE Walls Analysis, Design and Performance</b>	
<a href="#"><u>Effect of Spread Footing Loads on Stability of Geosynthetic-Reinforced Retaining Walls</u></a> .....	614-621



<a href="#"><u>Migrating From the Simplified Method to the Stiffness Method for Internal Stability Design of Mse Walls</u></a> .....	622-633
<a href="#"><u>New Closed-Form Analytical Solutions for Total Reinforcement Force in a GRS Retaining Wall at the Limit State</u></a> .....	634-643
<b>Walls, Slopes, and Embankments</b>	
<a href="#"><u>Applications of Geosynthetics for Building Passive Protective Structures against Rockfall, Debris Flows and Snow Avalanches</u></a> .....	644-653
<a href="#"><u>Design of True Abutments of Mechanically Stabilized Soil Walls under high seismicity in Guatemala City</u></a> .....	654-662
<a href="#"><u>Embankment Reinforcement Using the World’s Strongest Geogrid – Florianopolis Ring Road, Brazil</u></a> .....	663-671
<a href="#"><u>Impact of Primary Geogrids Spacing and Secondary Geogrids on Geosynthetic Reinforced Soil-Integrated bridge Systems (GRS-IBS) and Lateral Earth Pressure</u></a> .....	672-683

## Foreword to Technical Paper Sessions

The Geosynthetics 2023 Conference is once again being held in-person on February 5-8, 2023, in Kansas City, MO. The conference is being co-located with the International Erosion Control Association (IECA) Annual Conference and Expo. The Geosynthetics 2023 conference is hosted by the Geosynthetic Materials Association (GMA), a division of Advanced Textiles Association (ATA), and supported by the North American chapter of the International Geosynthetics Society under the auspices of the International Geosynthetics Society.

The conference proceedings consist of 70 technical papers presented in 16 technical sessions during the 4-day conference. These papers represent the forefront of geosynthetics in research, engineering applications, and testing to advance the resilience, durability, and protection of our infrastructure, not only here in North America, but worldwide. Paper topics include research, testing, and case histories involving: landfill covers and liners, the role of geosynthetics in sustainability and resiliency, geosynthetics in pavements and roadways, geosynthetics in shoreline and coastal protection, geosynthetics in mining, geosynthetics used to resolve landslides and in levees over soft ground, geosynthetics for bridge abutments, walls and oversteepened slopes, and geosynthetics for ground improvement. Each paper was peer-reviewed by a minimum of two independent reviewers.

The Technical Co-Chairs sincerely appreciate and thank the Conference Organizing committee, led by Committee Chair Prof. Jie Han, the Technical Program committee, authors, session chairs, and reviewers who contributed their valuable time and effort, resulting in the production of these proceedings.

In addition to the technical sessions, the conference program included a welcome keynote session, 5 panel and round-table discussions, 4 workshops, 9 special sessions, 8 short courses, and the Koerner Award Lecture by Dr. JP Giroud – live from France, all of which focused on an impressive variety of current topics on geosynthetics engineering and education.

The Technical Co-Chairs also thank the efforts of these other contributors: the Koerner Lecturer, plenary speakers, panel and round-table discussion chairs, and ATA members for organizing and contributing to the outreach and interaction on important topics within the geosynthetics community.

Lastly, Technical Co-Chairs thank Ms. Barbara J. Connett and Ms. Megan M. Firl of ATA for their experience and commitment in planning and organizing a successful conference. This conference would not have been possible without their dedication and guidance.

*Melissa Beauregard, Ph.D., P.E.*

*Stephan Gale, P.E., D.GE, F. ASCE*

Co-Chairs, Technical Program Committee

# Carbon Footprint Calculator

Timothy D. Stark, Ph.D., P.E.<sup>1</sup>

<sup>1</sup> University of Illinois at Urbana-Champaign, 205 N. Mathews Ave., Urbana, IL 61801; e-mail: [tstark@illinois.edu](mailto:tstark@illinois.edu).

## ABSTRACT

This paper describes a carbon footprint calculator for a containment system consisting of low hydraulic conductivity compacted soil, a geomembrane (GM), or a geosynthetics clay liner (GCL). In particular, the main objective of this paper is to compare the carbon footprint (or equivalent greenhouse gas emissions, in kg of CO<sub>2</sub> equivalents per hectare) for a 0.6 m thick compacted soil liner (CSL), GM and GCL. The analysis shows the largest single component of the carbon footprint calculation for these barrier options is transportation of the material to the project site. For a one-hectare (2.5 acres) cell or containment area, over 550 truckloads of fine-grained soil are required to construct a 0.6 m thick CSL compared to only 3.2 truckloads to transport a GM or GCL from the nearest factory or distributor (assumed 1,610 km (~1,000 miles) away). These factors are incorporated in a user-friendly calculator/spreadsheet that engineers, owners, and contractors can use to compare the installed carbon footprint of a proposed containment system. This paper describes the carbon footprint calculator and provides an example of how to optimize the geosynthetics design, purchase, and bidding to minimize environmental impact.

## INTRODUCTION

Geosynthetics are playing an important role in environmental, mining, potable water, energy development, waste containment, and other infrastructure applications. This paper presents a calculator/spreadsheet for estimating the carbon footprint for a containment system that can be used for these applications. The calculator is based on the analyses presented in Athanassopoulos and Vamos (2011) and yields estimates of the carbon footprint (or equivalent greenhouse gas emissions, in kg of CO<sub>2</sub> equivalents per hectare) for a 0.6 m thick compacted soil liner (CSL), GM, and GCL. If a single composite liner system is desired, the carbon footprint of the GM footprint can be added to a CSL or GCL to estimate the carbon footprint for the single composite liner system.

The calculator estimates the carbon footprint for each of the following barrier materials:

- 0.6-meter thick compacted soil liner with a saturated hydraulic conductivity of  $1 \times 10^{-7}$  cm/sec,
- 1.5-mm thick high-density polyethylene (HDPE) geomembrane, and
- Geosynthetic Clay Liner (GCL).

## COMPACTED SOIL LINER

A CSL was the first barrier material used for containment applications. Initially containment systems could consist of only a CSL without a geomembrane. In some states a CSL still can be used for a bottom liner system of a waste containment facility as well as the cover system after waste placement ceases. Most state regulatory requirements call for a CSL with a minimum thickness of 0.6 meters, with a maximum saturated hydraulic conductivity of  $1 \times 10^{-7}$  cm/sec. Off-site borrow sources of fine-grained soil, i.e., clay and/or silt soils, are often required to construct a low hydraulic conductivity CSL. Significant upfront investigation is necessary to properly characterize the extent and the quality of the borrow soil before constructing a CSL. In addition, testing and compaction control during CSL construction is required to ensure proper thickness and a maximum hydraulic conductivity of  $1 \times 10^{-7}$  cm/sec.

Emissions associated with pre- and post-construction investigations and characterization of the borrow source and completed CSL are not included in the carbon footprint analysis. Only the carbon footprint estimated for the construction of the CSL are estimated by the calculator described below. In addition, emissions are only considered for excavating soil and bentonite from the borrow sources, but it is assumed that bentonite is not added to the excavated soil to reduce the hydraulic conductivity of the CSL, which commonly occurs. The following emission factor from U.S. EPA report EPA 430-K-08-004 (USEPA, 2008a) and EPA 430-R-08-006 (USEPA, 2008b) for diesel equipment of 2.71 kg of CO<sub>2</sub> per liter of diesel fuel consumed is used in the calculations (Athanasopoulos and Vamos, 2011).

It is assumed the fine-grained soil is excavated at the borrow source using standard construction equipment and placed in dump trucks with a capacity of 15 cubic meters. A compaction factor of 1.38 (Athanasopoulos and Vamos, 2011), is assumed so over 550 truckloads of fine-grained soil is needed to construct a one-hectare CSL with a thickness of 0.6 meters. Some states require a thicker CSL than 0.6 meters, which can be modified in the calculator.

The distance from the borrow source to the CSL construction site varies so this is a user input in the calculator. In the example shown below, a distance of 17 km (10 miles) is assumed for the distance from the borrow source to the CSL location. This transportation distance is a large component of the overall carbon emissions so users can vary this distance to assess the overall impact on the calculated carbon footprint.

Daniel and Koerner (2007) recommend that the subgrade on which a CSL is constructed should provide adequate support for compaction and be free from mass movements. For this analysis, subgrade preparation is assumed to only consist of grading to meet elevations in the grading plan using a bulldozer and a grader. If additional effort is needed to prepare the subgrade, and carbon footprint induced by this additional effort should be added to the value estimated by the calculator.

The CSL is constructed in lifts or layers with a lift thickness of 0.15- to 0.2 meters. Each lift is subjected to a number of passes of a sheepsfoot compaction roller to knead the soil, break up soil chunks and clods, and create a homogeneous CSL free of cracks, voids, and/or large pores to reduce hydraulic conductivity (Daniel and Koerner, 2007). Water is added to the borrow soil to

produce a moisture content that is wet of the optimum compaction moisture content and yields a saturated hydraulic conductivity less than  $1 \times 10^{-7}$  cm/sec. The surface of the final lift is compacted with a smooth-drum roller to yield a smooth surface of the CSL for waste placement or placement of an overlying geomembrane.

Daniel and Koerner (2007) suggest the typical installation rate for a CSL is 0.25 hectares per day (0.6 acres per day), which is assumed in the calculator. This corresponds to placement of 2,000 cubic meters (~2,000 cubic yards) of compacted soil per day during periods of good weather (Athanasopoulos and Vamos, 2011). After the CSL is completed, tested, and certified, it is covered with waste, a GM, GCL, or both to create a barrier system.

## GEOMEMBRANE

Until 1996 when the design criteria/requirements of Subpart D (RCRA, 1988) became effective, a CSL was the only barrier material required for a municipal solid waste (MSW) landfill. The relevant design requirements of Subpart D are available in sections §§ 258.40-258.42 (<https://www.ecfr.gov/current/title-40/chapter-I/subchapter-I/part-258>). Under §§258.40(b), the minimum requirements for a single composite liner system for a MSW landfill consists of:

“two components; the upper component must consist of a minimum 30-mil flexible membrane liner (FML), and the lower component must consist of at least a two-foot (0.6 m) layer of compacted soil with a hydraulic conductivity of no more than  $1 \times 10^{-7}$  cm/sec. FML components consisting of high density polyethylene (HDPE) shall be at least 60-mil thick. The FML component must be installed in direct and uniform contact with the compacted soil component.”

A geomembrane was added to the 0.6 m of compacted soil in 1996 because of the results of laboratory hydraulic conductivity tests conducted by Brown et al. (1980, 1983, and 1984) on various CSLs. Brown et al. (1980, 1983, and 1984) show that some contaminants caused micro and macro cracking of the CSL that could lead to increased leakage and contaminant transport through the CSL. This resulted in the U.S. Environmental Protection Agency (USEPA) requiring an FML or GM to be placed over the CSL to create a composite liner system so contaminants could only reach the CSL if there was a defect in the GM. Of course, this is only true if the geomembrane is in intimate contact, i.e., “in direct and uniform contact”, with the underlying CSL. As a result, it is important to minimize/eliminate geomembrane wrinkles so leakage cannot reach a greater area of the CSL than the area of the GM defect. The following emission factor from Hammond and Jones (2008) for HDPE geomembrane manufacturing is used in the calculator: 1.6 tonnes CO<sub>2</sub> per tonne of HDPE resin from Athanasopoulos and Vamos (2011).

## GCLs

GCLs are also factory-manufactured and consist of a thin (~0.7 mm thick) layer of sodium bentonite clay sandwiched between two geotextiles. A GCL typically exhibits a laboratory saturated hydraulic conductivity of  $5 \times 10^{-9}$  cm/sec or about 100 times less than a CSL. Due to the

lower cost and easier installation, GCLs frequently replace or reduce the thickness of a CSL used in waste containment applications. For example, Ohio requires a 1.5 m (5 ft) thick CSL, which can be reduced to 1.0 m (3 ft) thick with inclusion of a GCL.

Sodium bentonite is a clay mineral formed through the aqueous deposition and weathering of volcanic ash in the Benton Sea (Athanassopoulos and Vamos, 2011). Much of the worldwide sodium bentonite supply lies within the United States in Wyoming and South Dakota (Trauger, 1994). The typical mining sequence of bentonite involves excavation of a series of pits about 0.5 to 1.0 hectares in area and 5 to 10 meters deep. Once excavated from the pit, the bentonite clay is transported in dump trucks to a processing plant that is assumed to be less than 30 km away. The processed clay is applied to a carrier geotextile at a rate of about 4.3 kg/square meters and then a cover nonwoven geotextile is applied over the bentonite. The geotextiles are purchased from an outside manufacturer, located in northern Georgia, approximately 2,760 km (1,700 miles) away, which adds to the carbon footprint for manufacturing of a GCL. The three layers are then passed through a needle-punching loom, where fibers from the nonwoven cover geotextile are pushed through the bentonite layer and underlying woven or nonwoven carrier geotextile.

The finished reinforced GCL is rolled up into rolls containing 209 square meters that can be transported to a project site using trucks. This study assumes that the distance from the GCL production plant is located in Wyoming, i.e., location of the Benton Sea, to the example project site is 1,610 km (1,000 miles). Each truck can hold up to 17 rolls, or 3,555 square meters of GCL for estimating purposes. Using a waste factor of 1.15 (for GCL overlap and scrap), it is estimated that 3.24 truckloads of GCL are needed to line a one-hectare area in the example below (Athanassopoulos and Vamos, 2011).

## **CARBON CALCULATOR**

This section of the paper describes the calculator/spreadsheet that can be used to estimate the carbon footprint created by constructing/manufacturing a CSL, GM, GCL, and/or a single composite liner system by combining a GM with a CSL and/or a GCL. The carbon footprint calculator/spreadsheet can be downloaded for free using the following link and distributed to colleagues: <https://www.fabricatedgeomembrane.com/protected/pond-liner-calculator>.

Following the analysis of Athanassopoulos and Vamos (2011), the calculator includes direct emissions (Scope 1), indirect emissions (Scope 2), and other indirect emissions (Scope 3) if practical using the World Resources Institute (WRI, 2004) guideline. The greenhouse gases (GHGs) included in the calculation are carbon dioxide, methane, and nitrous oxide. Each of these gases contributes differently to climate change and is assigned a Global Warming Potential (GWP) in the calculator. Carbon dioxide has a GWP of unity (1.0) in accordance with WRI (2004). To include the contributions of methane and nitrous oxide to the overall carbon impact, the mass of methane and nitrous oxide emissions are multiplied by their respective GWP factors and then added to the mass emissions of CO<sub>2</sub> to calculate a “carbon dioxide equivalent” mass emission (Athanassopoulos and Vamos, 2011). The GWP factors for methane (CH<sub>4</sub>) and nitrous oxide (N<sub>2</sub>O) were estimated to be 21.0 and 310.0, respectively, from USEPA (2010). As a result, the mass of carbon dioxide equivalents (CO<sub>2eq</sub>) is calculated as follows in the calculator:

$$\text{CO}_{2\text{eq}} = \text{kg CO}_2 + (21.0 \times \text{kg CH}_4) + (310.0 \times \text{kg N}_2\text{O}) \quad (1)$$

Additional details and supporting references for the calculations are presented in Athanassopoulos and Vamos (2011). The excluded sources of emissions include: development of diesel fuel, development of the soil and bentonite borrow sources, disposal of wastes from the manufacturing processes, employees commuting to the manufacturing plant and project site, and other materials placed above the CSL, GCL, or GM to complete the containment system.

The carbon footprint calculator is divided into two (2) main parts or steps: (1) Input Parameters and General Summary (see **Figure 1**) and (2) Detailed information and calculations on the CSL (see **Figure 2**), GM (see **Figure 3**), and GCL (see **Figure 4**) carbon equivalents. **Figure 1** presents a screenshot of Step One (1) in the carbon footprint calculator, which summarizes the input information (total pond volume and total area to be lined) and the results of the calculations.

The example involves a one-hectare (2.5 acres) area or cell as shown in **Figure 1** and was taken from Athanassopoulos and Vamos (2011) to verify the calculator. The analysis assumes a landfill site located 1,610 km (~1,000 miles) from the GCL and GM manufacturing plants and only 16 km (~10 miles) from the fine-grained soil borrow source used for the CSL. The Step 1 results show the carbon footprints of the CSL, GCL, and GM are: 139,099.6 kg, 95,809.7 kg, and 102,799.6 kg, respectively. These results show the CSL produces a 31% and 26% larger carbon footprint than a GCL and GM, respectively.

The largest single component of the overall carbon footprint for all of the barrier options is transportation to the project site, i.e., 92,527 kg for the CSL and 41,894 kg for the GCL and GM. The carbon footprint for the transportation of the borrow material to the project site corresponds to 67% of the total carbon footprint for the CSL. Conversely, the carbon footprint for the transportation of the GCL and GM to the project site corresponds to 44% and 41%, respectively, of the total carbon footprint. This assumes that the GCL and GM manufacturing plants are located 1,610 km (1,000 miles) from the project site, which may be farther than most sites. Athanassopoulos and Vamos (2011) show the CSL option produces a lower carbon footprint than the GCL option if the borrow source is within approximately 9 km (5.5 miles) of the project site and the GCL manufacturing plant is still located 1,610 km (1,000 miles) from the project site.



1	Carbon Footprint Calculation- June, 2022				
2	By: Timothy D. Stark, Ph.D., P.E., D.GE, F.ASCE				
3	Fabricated Geomembrane Institute				
4	University of Illinois at Urbana-Champaign				
5					
6					
7					
8	Total volume of the pond	0.0	Gallons		
9	Total area	1	Hectares		
10					
11					
12					
13	Total Carbon Footprint of Compacted Soil Liner	139,099.6	Kg		
14	Total Carbon Footprint of GCL	95,809.7	Kg		
15	Total Carbon Footprint of Geomembrane	102,799.6	Kg		
16					
17					

**Figure 1: Step One input parameters and general calculations in carbon footprint calculator for a CSL, GM, and GCL.**

Carbon Footprint Calculator for Different Materials					
STEP TWO (Detailed Information)					
Input Parameters: Carbon Footprint Per Hectare					
Compacted Soil Liner	Excavate Soil at Borrow Source	=	2,656	Kg	CAT 329 Excavator, operating 40 hours/ha. Assume 24.5 Liters/hr diesel consumption.
	Haul soil to Job Site	=	93,527	Kg	Assume site is 16 km from borrow source, and 552 truckloads (each carrying 15 m3 of soil) are needed to cover 1 hectare.
	Subgrade preparation:	/	/	/	
	Rough Grading	=	1,741	Kg	CAT D6 dozer, operating 25 hours/ha. Assume 25.7 Liters/hr diesel consumption.
	Fine Grading	=	1,565	Kg	CAT 160 Grader, operating 25 hours/ha. Assume 23.1 Liters/hr diesel consumption.
	Construct Compacted Soil Liner:	/	/	/	
	CAT D6 Bulldozer	=	2,786	Kg	Operating 40 hours/ha. Assume 42 Liters/hr diesel consumption.
	CAT 815 sheepsfoot compactor	=	4,553	Kg	Operating 40 hours/ha. Assume 42 Liters/hr diesel consumption.
	10,000-gallon water truck	=	1,518	Kg	Operating 40 hours/ha. Assume 14 Liters/hr diesel consumption.
	CAT 815 smooth drum compactor	=	4,553	Kg	Operating 40 hours/ha. Assume 14 Liters/hr diesel consumption.
	Labor	=	197	Kg	Everyone produces about 4.68Kg Carbon per day. Crew size and work days for compacted soil liner will be 6 people working for
	Cover Soil	=	26,004	Kg	

**Figure 2: Step Two calculated carbon footprint in kg of CO2 equivalents per hectare for a CSL.**

Carbon Footprint Calculator for Different Materials					
STEP TWO (Detailed Information)					
GCL - CETCO TR-278	Mine Bentonite	=	391	Kg	Assumes 43.45 metric tons of bentonite per hectare lined area.
	Haul to Processing Plant	=	280	Kg	Emission factor (2.71kg CO2e / liter diesel)
	In-Plant Processing	=	2,126	Kg	Emission factor (2.71kg CO2e / liter diesel)
	Geotextiles:	/	/	/	
	Woven Manufacture	=	3,416	Kg	
	Transport to GCL	=	1,454	Kg	
	Nonwoven Manufacture	=	6,210	Kg	
	Transport to GCL	=	5,269	Kg	
	Transport GCL to Job Site	=	41,894	Kg	Assume site is 1,610 km away, with 160-km origination and return trip.
	Unload GCL	=	949	Kg	CAT TL355 Telehandler, operating 25 hours/ha. Assume 14 Liters/hr diesel consumption.
	Subgrade preparation:	/	/	/	
	Rough Grading	=	1,741	Kg	CAT D6 dozer, operating 25 hours/ha. Assume 25.7 Liters/hr diesel consumption.
	Fine Grading	=	1,565	Kg	
	Rolling	=	2,846	Kg	CAT 815 Compactor (smooth drum), operating 25 hours/ha. Assume 42 Liters/hr diesel consumption.
	Deploy GCL	=	1,660	Kg	CAT 329 Excavator, operating 25 hours/ha. Assume 24.5 Liters/hr diesel consumption.
	Labor	=	5	Kg	Everyone produces about 4.68Kg Carbon per day. Crew size and work days for GM will be 1 people working for one day.
	Cover Soil	=	26,004	Kg	

**Figure 3: Step Two calculated carbon footprint in kg of CO2 equivalents per hectare for a GCL.**



Carbon Footprint Calculator for Different Materials				
STEP TWO (Detailed Information)				
60 mil HDPE Geomembrane	Producing	=	25,944	Kg
	Transport Geomembrane to Job Site	=	41,894	Kg
	Unload Geomembrane	=	343	Kg
	Subgrade preparation:	/	/	/
	Rough Grading	=	1,741	Kg
	Fine Grading	=	1,565	Kg
	Rolling	=	2,846	Kg
	Deploy Geomembrane	=	1,660	Kg
	Cover Soil	=	26,004	Kg
	Labor	=	197	Kg

**Figure 4: Step Two calculated carbon footprint in kg of CO<sub>2</sub> equivalents per hectare for a GM.**

## SUMMARY

A carbon footprint calculator is described herein that can be used to compare the carbon footprint, i.e., kg of CO<sub>2</sub>, generated for installation of a CSL, GCL, and GM. The calculator uses the analysis developed by Athanassopoulos and Vamos (2011). The results show the CSL will produce a 31% and 26% larger carbon footprint than a GCL and a GM, respectively. The largest single component of the overall carbon footprint for all options is transportation to the project site, i.e., 92,527 kg for the CSL and 41,894 kg for the GCL and GM. The carbon footprint for the transportation of the CSL borrow material to the project site corresponds to 67% of the total carbon footprint for a CSL so minimizing this distance is important. Conversely, the carbon footprint for the transportation of the GCL and GM to the project site corresponds to 44% and 41%, respectively, of the total carbon footprint, which is assumed to be 1,610 km (1,000 miles). The carbon footprint for a single composite liner system can be estimated by combining a GM with a CSL and/or a GCL.

## REFERENCES

Athanassopoulos, C. and Vamos R.J., (2011). "Carbon Footprint Comparison of GCLs and Compacted Clay Liners." Proceedings of 24th Annual Geosynthetic Research Institute (GRI) Conference: Optimizing Sustainability Using Geosynthetics, Dallas, TX, March 16, <https://geosynthetic-institute.org/publications.htm>.

Brown, K.W. and Anderson, D.C. (1980). "Effect of Organic Chemicals on Clay Liner Permeability: A Review of Literature. In Disposal of Hazardous Waste," Proceedings of Sixth Annual Research Symposium, EPA - 600/19 -80 -010, Chicago, Illinois, March 17 - 20.

Brown, K.W., Green, J., and Thomas, J. (1983). "The Influence of Selected Organic Liquids on the Permeability of Clay Liners. Land Disposal of Hazardous Waste," Proceedings of Ninth Annual Research Symposium, EPA - 600/19 - 83 - 018, Ft. Mitchell, Kentucky, May 2 - 4.

Brown, K.W., Thomas, J.C., and Green, J.W. (1984). "Permeability of Compacted Soils to Solvents Mixtures and Petroleum Products in Land Disposal of Hazardous Waste," Proceedings of the Tenth Annual Research Symposium, EPA - 60019 - 84 - 007, Ft. Mitchell, Kentucky, April 3 - 5.

Daniel, D.E. and R.M. Koerner (2007), Waste Containment Facilities: Guidance for Construction Quality Assurance and Construction Quality Control of Liner and Cover Systems.

Hammond, G. and C. Jones (2008), "Inventory of Carbon and Energy," Institution of Civil Engineers (ICE), Version 1.6a.

Resource Conservation and Recovery Act (RCRA), (1988). Code of Federal Regulations (CFR) parts 239 through 282, CHAPTER 4 SUBPART D DESIGN CRITERIA  
<https://archive.epa.gov/epawaste/nonhaz/municipal/web/pdf/subpartd.pdf>.

Trauger, R.J. (1994). "The Structure, Properties, and Analysis of Bentonite in Geosynthetic Clay Liners," Proceedings of the 8th GRI Conference: Geosynthetic Resins, Formulations, and Manufacturing, Geosynthetic Research Institute, Drexel University, Philadelphia, PA, pp. 185-198.

USEPA (2008a), "Climate Leaders: Direct Emissions from Mobile Combustion Sources," Office of Air and Radiation, EPA-430-R-08-004  
<http://large.stanford.edu/courses/2013/ph240/cabrera2/docs/epa-430-k-08-004.pdf>.

USEPA (2008b), "Climate Leaders: Optional Emissions from Commuting Business and Travel Product Transport," Office of Air and Radiation, EPA-430-R-08-006  
<https://nepis.epa.gov/Exe/ZyNET.exe/P1001177.TXT?ZyActionD=ZyDocument&Client=EPA&Index=2006+Thru+2010&Docs=&Query=&Time=&EndTime=&SearchMethod=1&TocRestrict=n&Toc=&TocEntry=&QField=&QFieldYear=&QFieldMonth=&QFieldDay=&IntQFieldOp=0&ExtQFieldOp=0&XmlQuery=&File=D%3A%5Czyfiles%5CIndex%20Data%5C06thru10%5CTxt%5C00000003%5CP1001177.txt&User=ANONYMOUS&Password=anonymous&SortMethod=h%7C-&MaximumDocuments=1&FuzzyDegree=0&ImageQuality=r75g8/r75g8/x150y150g16/i425&Display=hpfr&DefSeekPage=x&SearchBack=ZyActionL&Back=ZyActionS&BackDesc=Results%20page&MaximumPages=1&ZyEntry=1&SeekPage=x&ZyPURL>.

USEPA (2010), "Mandatory Reporting of Greenhouse Gas Emissions", Code of Federal Regulations, Title 40, Part 98.

WRI (2004), "GHG Protocol-A Corporate Accounting and Reporting Standard, Revised Edition". World Resources Institute.

## Case Study: Lake Forest Reservoir Relining & Floating Cover

**Brian Fraser, MBA<sup>1</sup>, Douglas Hilts, P.E.<sup>2</sup>, Robert Emmons<sup>3</sup>**

<sup>1</sup>Layfield Canada, Edmonton, AB, Canada; e-mail: [brian.fraser@layfieldgroup.com](mailto:brian.fraser@layfieldgroup.com)

<sup>2</sup>Hilts Consulting Group, Yorba Linda, CA USA; email: [doug.hcg@HiltsConsulting.com](mailto:doug.hcg@HiltsConsulting.com)

<sup>3</sup>Layfield USA, Kent, WA, USA; email: [robert.emmons@layfieldgroup.com](mailto:robert.emmons@layfieldgroup.com)

### ABSTRACT

This paper highlights a very challenging geosynthetic floating cover project for the Seattle Public Utilities Forest Park Reservoir. The reservoir was first built in 1962 as an open top concrete lined 60-million-gallon containment facility for potable water storage. The reservoir perimeter has a vertical concrete parapet wall with a 2:1 interior reservoir side slope. In 2002, the owner constructed a 28-foot high (8.5 meter) vertical divider wall partitioning the reservoir into two operating cells. The existing geomembrane liner and floating cover material installed in 2002 were showing signs of aging and degradation and required replacement. The new geomembrane liner required a watertight mechanical attachment at the bottom of the parapet wall and extended to the top of the divider wall. The floating cover was anchored mechanically to the top of the perimeter parapet wall and divider wall. The vertical divider wall created specific design and installation challenges for the replacement floating cover and liner. This paper highlights the design challenges and the custom prefabrication and installation techniques needed for the geosynthetic liner and floating cover. In addition, a custom fabricated double trough system was designed and installed to handle the tensioning loads of the floating cover resulting from the vertical divider wall. The paper also addresses the importance of the material selection process and the challenges for geosynthetic materials used in floating cover applications resulting from multiple factors including chemical disinfectants, UV exposure, and the need for material flexibility and folds.

### INTRODUCTION

The Lake Forest reservoir as shown in Figure 1 was originally built in 1962 as an open-air drinking water reservoir with concrete lining on the reservoir floor and side slopes. In 2002, the reservoir underwent multiple modifications and improvements which included a 28-foot high vertical cast-in-place reinforced concrete center divider wall and the installation of a geomembrane liner and floating cover. With the divider wall the reservoir was separated into two independent operating cells; each approximately 288 feet wide by 671 feet long by 24 feet deep (87.8 m x 204.5 m x 7.3 m). The reservoir operates as a potable drinking water storage facility and provides emergency water supply. A 45 mil reinforced polypropylene geomembrane liner and floating cover were installed in 2002 and were experiencing problems that required replacement.

In May 2021, phase 1 of construction began on the new replacement geomembrane liner and floating cover system for the east cell of the Lake Forest reservoir and was completed in September

2021. Phase 2 included the installation of a new geomembrane liner and floating cover system on the west cell. This construction was completed September 2022.



**Figure 1. Aerial view of the completed east cell (left side) completed in 2021 and west cell (right side) reservoir under construction in July 2022**

## PROJECT CHALLENGES

The construction challenges included developing required design changes on the floating cover and installation methods to address the mechanical attachment requirements for both the 28-foot high vertical divider wall and the perimeter concrete parapet wall. To address the vertical wall configuration and shape of the reservoir, the design engineer selected a weighted tension cover system. This system uses a series of designed troughs in conjunction with surface floats and ballast weights to supply the required cover tensioning, buoyancy in the floating cover, and create rainwater collection troughs to drain surface water adjacent to the vertical divider wall. To handle the additional material slack developed in the floating cover from the 28-foot high vertical divider wall during the different reservoir operating levels, a special double trough system was designed and installed. The installation of this required large custom size panels be fabricated in the factory. These panels then needed to be lifted onto the vertical wall on site to be vertically welded together.



The joining of the panels required 3-inch (7.62 cm) wide field seams. The perimeter parapet wall required each panel to be lifted above the parapet wall for deployment of the factory produced panels and anchorage to the top of the perimeter wall. The geomembrane liner was anchored at the base of the perimeter wall and the floating cover was anchored to the top of the perimeter wall. The mechanical attachment consisted of stainless steel concrete anchors and stainless steel batten bars with rubber gasket material. The welding on site was done primarily by thermal wedge and performed in compliance with the Geosynthetics Research Institute GM 19 standards and engineers specified field factory and seam strength requirements.

The weight tensioned floating cover system in both reservoir cells also required various additional appurtenances including access hatches, air vents, access stairways, double material over existing concrete stairs on slope, and a pump surface water removal system. Figure 2 below shows the installation of the divider wall trough system on the west cell. Figure 3 shows the east cell wall trough system in application at close to full operating level of the reservoir.



**Figure 2. Installation underway of double trough system on 28-foot divider wall on west cell**



**Figure 3. East Cell divider wall trough in full service**

The rainwater removal system was designed for a 10-year, 24-hour duration and 25-year, 24-hour duration storm event. The number and size of the rainwater removal system pumps was based on a 48-hour and 72-hour removal capacity. Each cell has five submersible sump pumps housed in perforated aluminum sump cans located in the rainwater collection troughs. The surface water is pumped to the top of reservoir perimeter and discharge into pipes located outboard of the perimeter parapet wall. Figure 4 shows one of the aluminum sump cans located in the east reservoir cell. Figures 5 – 10 show additional installation and inflating testing performed during phase 2 on the west cell.



**Figure 4 – Rainwater Removal System**

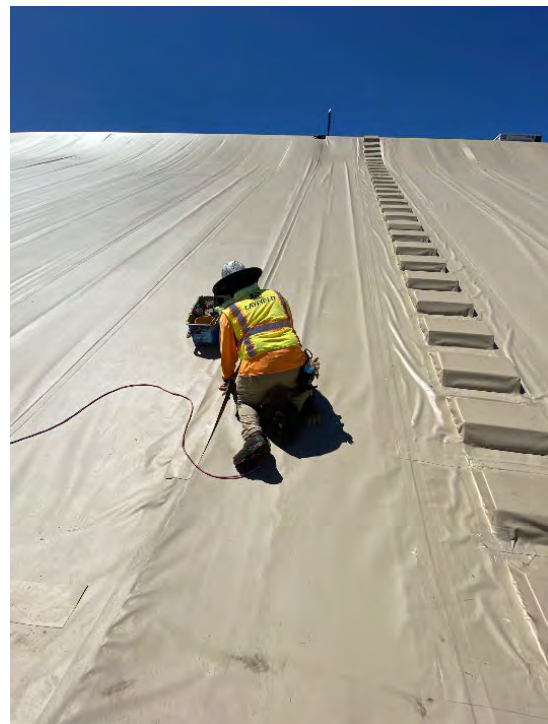


**Figure 5 and 6. Crews installing fabricated entry stairways and welding floating cover seams**



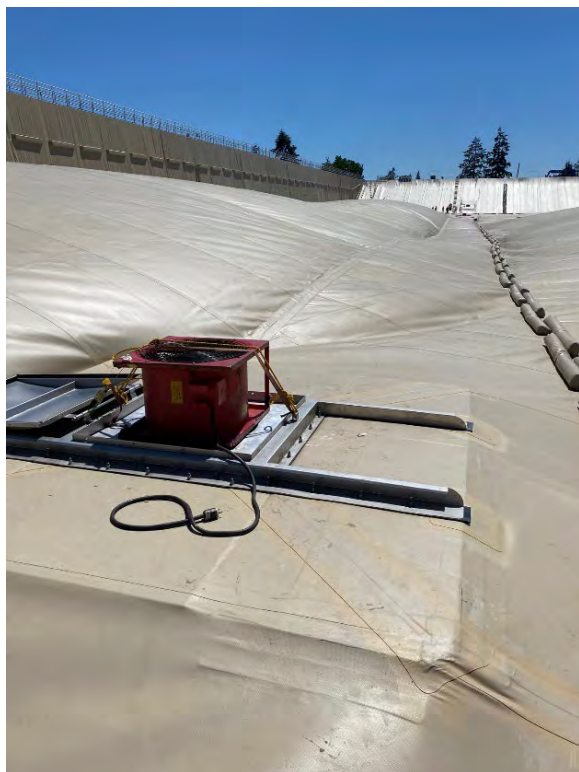


**Figure 7 and 8. Inflation via access hatch and west cell cover undergoing inflation inspection**



**Figure 9. East cell trough & floats in service**





**Figure 10 Floating cover mechanical anchorage at parapet wall**

## **GEOMEMBRANE FABRICATION**

The Lake Forest reservoir required substantial prefabrication of the geomembrane liner, floating cover, and appurtenances. The project required approximately 850,000 ft<sup>2</sup> (79,000 m<sup>2</sup>) of prefabricated geomembrane panels. This included a large amount of custom size fabricated panels to address the divider wall and various curves and slopes of the reservoir. In total the project required close to 120 days of equivalent plant fabrication time. The prefabrication of the geomembrane liner, cover and components resulted in substantial reduction in the amount of required field welding, construction time and installation cost. This was also important considering the highly inclement weather conditions typically experienced in the Seattle and Puget Sound region of Western Washington. Figure 11 shows a plant technician in Lakeside, CA welding the CSPE liner.

There are many recognized performance advantages of using factory fabricated panels for geomembrane liners and floating covers. The constant and favorable factory-controlled environmental conditions yield higher quality, better seams between individual geomembrane rolls, than field fabricated geomembranes and fewer opportunities for damage by field activities and personnel. The Fabricated Geomembrane Industries (Stark et al. (2020) has previously compared factory and field welded thermal geomembrane seams for a large off-stream water reservoir project. This comparison showed that factory welded seams exhibit higher seam peel and shear strengths, less variability, and more consistency than field welded thermal seams. The compiled test results showed that factory seams are about 10% stronger than field seams. Factory fabrication can typically result in about 75% less field seams on a project.

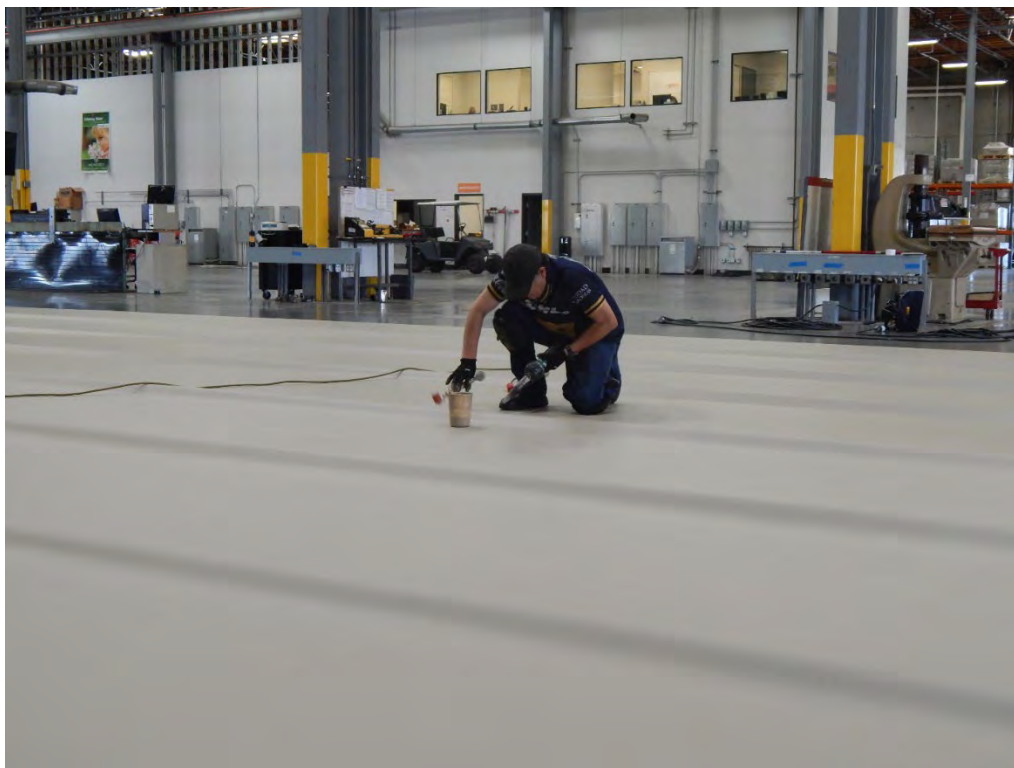
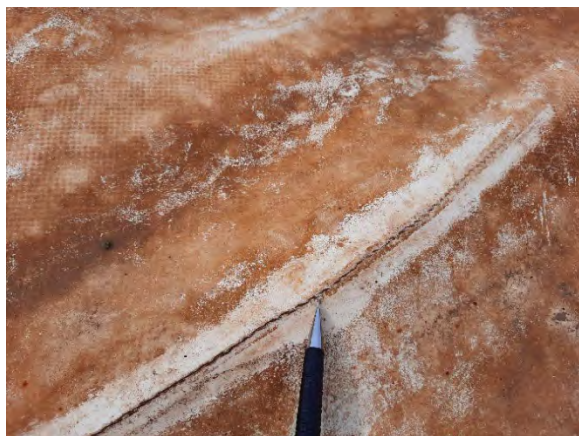


**Figure 11. Factory fabrication of CSPE panels in Lakeside CA plant**

## **MATERIAL SELECTION**

The material selection process was an important factor for the geomembrane liner and floating cover portion of the project. The current reinforced polypropylene (RPP) material had demonstrated signs of fatigue and premature degradation at approximately 16 years in service. This included various cracks located around folds and creases as per Figures 12 and 13 below. Also, the extent of damage on the geomembrane liner material could not be determined until the reservoir was taken out of service and the floating cover system was fully removed. The type of cracking in the material folds is often associated with multiple factors including prolonged UV exposure, continuous exposure to chlorine used for potable water disinfection, and stress concentrations at upstanding folds resulting from hydrostatic pressure. Chemicals used for disinfectants in municipal water treatment include chlorine and chloramines and can function as accelerators in breaking down or leaching out the protective antioxidant packages of certain geomembranes resulting in environmental stress cracking and premature material failure (Mills 2011).



**Figures 12 & 13. Surface cracks found in the RPP liner material folds and creases**

After a detailed review process and consideration of available materials, the owner selected chlorosulfonated polyethylene (CSPE) for the replacement geomembrane material. CSPE is a highly flexible geomembrane which has been on the market for over 50 years with a long established history of proven performance in municipal water containment applications using chlorine and other disinfectants. The CSPE geomembrane material is also noted to have excellent UV resistance and backed by a 30 year weathering warranty.

## CONCLUSION

The relining and cover replacement of the Lake Forest project incorporated many of the current best practices outlined in the AWWA Manual M25, *Flexible Membrane Covers and Linings for Potable-Water Reservoirs*. As the owner required a 30-year service life for the liner and cover, the material selection of the CSPE material with its 50 year proven record in potable water reservoir was an important decision. The project also incorporated an important weighted tensioned floating cover design including strategically located custom troughs designed to manage the water service levels and center divider wall. Factory prefabrication of the materials and appurtenances was essential ensuring high quality as well as reduced installation risk and costs. With the integration of a site specific operations and maintenance program including regular planned inspections, all stakeholders involved are confident that the new Lake Forest reservoir liner and floating cover system will perform very well and achieve its expected 30-year service life.

## REFERENCES

- AWWA M25 Manual of Water Supply Practices, *Flexible Membrane Covers and Linings for Potable-Water Reservoirs*, 3<sup>rd</sup> Edition, American Water Works Association, Denver, CO, USA
- GSI GRI GM 19 Standard Specification. Seam Strength and Related Properties of Thermally Bonded Homogeneous Polyolefin Geomembranes/Barriers, Geosynthetic Institute, Folsom, Pennsylvania, USA
- Mills, A. (2011) The effects of chlorine on very low-density thermoplastic olefins, *Geofrontiers*

2011, IFAI, Dallas, TX, USA

Stark, T.D., Hernandez, M.A., and Rohe, D.S., (2020). "Geomembrane Factory and Field Thermally Welded Geomembrane Seams Comparison," *Geotextiles and Geomembranes Journal*, 48(4), August 2020, 454-467, <https://doi.org/10.1016/j.geotexmem.2020.02.004>.

## Payment Bases in Liner Projects

Duff Simbeck<sup>1</sup>

<sup>1</sup>Simbeck and Associates, Inc., 38256 Highway 160, Mancos, CO 81328. E-mail:

[duff@simbeckliners.com](mailto:duff@simbeckliners.com)

### ABSTRACT

This technical/legal analysis will discuss payment bases for geosynthetic projects. Accurate drawings, thorough design details, clear Specifications are essential to prepare budgets, advertise and evaluate bid packages. Lump Sum and Unit Price bid bases are pretty familiar, but what do they include (Work Scope) and what does “fair payment” constitute for all parties – once construction starts and progress and final payment requests go up the chain for approval? Does gross quantity include more than overlap, wastage, and slope gain? This paper will describe fundamentals and a few pitfalls of payment bases, with an array of situations to elicit discussion. Contracts are often vague and inconsistent on payment terms. Communication, clarity, accountability and proper documentation can be built into a Project to minimize the chance of Owners, Engineers, and Contractors falling into contentious change order territory – or even litigation.

### INTRODUCTION

Payment bases in liner contracts resemble a mine-field. Imagine the headache of a \$5M dollar project going smoothly --under budget, on schedule, high quality work -- but ending with disputes over final payment terms. One expects that bid documents and contracts all work together to facilitate agreeable working relationships. Communications -- written and verbal -- are never perfect, however, and fighting over the money remains an unpleasant consequence on too many jobs.

### DEFINITIONS

“Lump Sum” means Plans and Specifications are clear enough that all bidders can work up the gross quantities needed – then back into a net payment amount *provided nothing changes*. “Stipulated Sum” is synonymous, with an emphasis on the stipulated scope of work. In other words, a certain lump sum figure would be paid upon performance of a definite list of items—refined by Exclusions and Inclusions. Some stipulated sum contracts pay Lump Sum on certain items, others Unit price. Those hybrids often include restrictions on Subs and Suppliers ever communicating directly with the Engineer, or clauses like *All Engineer decisions are final*.

“Unit Price” contracts depend upon verifiable and equitable quantities in accordance with drawings and other bid documents. If more is needed – or sometimes lesser amounts are required -- an agreed unit cost has been established between the parties. Adjustments can therefore be reasonably made, covering ideally consequential costs as well, like freight or restock charges.

“Cost Plus” allows for fair expense and mark-up, plus adjustments as work scope evolves. If a second liner shipment is requested, for instance, actual cost is easy enough to submit, with an agreed-upon percentage for profit. Other payment bases exist -- such as Design-Build and



Indefinite Quantity/Indefinite Schedule -- but they are variants or hybrids of the foregoing. In essence, parties spell out the scope and agree to move forward in partnership. Bad actors may be deterred with some accountability steps so everyone can limit disputes.

The rules of engagement are set down by an Owner and its agents, sometimes funding agencies and regulators behind them. When a Design Engineer hands off to a Construction Engineer, do they confer on design features? Hopefully, all parties are open to improvements at submittal and later stages. Consistency, communication and accountability are three fundamentals to follow as geosynthetic projects move from conception to completion.

Consider three real-world examples of where the basic payment terms get mis-construed: A land-fill expansion in 2018 goes out with a Bid Form expressing Unit Price basis for all the bid items. However, in the course of construction it becomes clear the Engineer is only approving pay requests on a Lump Sum basis. Once the final deployment area gets lined, a serious quantity over-run becomes clear. Finger pointing goes on for months. Ultimately the Owner/Operator over-ruled their Engineer-- and final payments release.

Waste-water lagoons in 2020 are built and lined by an inexperienced Construction Management firm that handled subcontracts in dubious ways: Unit Price pay requests to the Owner, Lump Sum arrangement with Installer, Cost-Plus or time and materials with the dirt-mover. They were unapologetic about *managing the project as they saw fit* but the lack of consistency led to an unhappy Owner and funding agencies, Subs that compromised on final payments, reputation loss and minimal profit to the General Contractor.

An industrial waste cap in 2010 is awarded to a diligent, qualified, specialty construction outfit – then the Owner trimmed the Scope of Work without telling anyone. “We’re in charge and only paying what we decide.” Re-stocking of materials (at a hefty charge: 30% shipped back) left everyone from Supplier to field techs regretting they ever got involved. This one represents a private cap where the corporation was used to controlling every aspect of their project.

The fatal flaw in those projects was that bid documents did not match the contract terms. How do payments for liner work turn awry, in this imperfect world with mostly well-meaning people? For starters, Unit Price and Lump Sum don’t mean what they appear if the Specifications don’t detail everything about payment bases. Specifically:

- a. Is the scale accurate and consistent on all the plan drawings? Often one designer preps the grading plan and another works up the liner sections.
- b. Will payment be issued for gross quantity of liner delivered (with fair markup so suppliers can be fully paid despite retainage)? Who keeps leftover materials?
- c. Do progress payments exclude overlaps, wastage on corners and roll ends, accessory work?
- d. Does bid quantity exclude slope gain (see diagram B), for just a two-dimensional coverage area from survey points rather than true, three-dimensional net covered area?
- e. Will final pay quantity include buried geosynthetics in anchor trenches (see slope lined cell below where 40% of the required membrane in trenches top and bottom are not part of the net payment area)?
- f. If a final survey determines pay quantities, who conducts it --and using which method?
- g. How promptly do Subs and Suppliers get their money after release to the Prime?
- h. Are Change Orders acknowledged by Inspector or an Owner’s representative? “Pay if paid” provisions may need balanced by a change order involving all parties involved.



Figure 1. Slopes only liner, trenches top and bottom represent 40% of total liner needed

Here is an example of how the anchor trench + final survey ambiguity was caught pre-bid, in a 2022 Addendum: helping estimators to calculate gross versus net liner area:

*Question:* “How will payment quantity of geosynthetics be measured. Will it be 3D area, including material buried in anchor trench and runouts for future tie-in zones?”

*Answer:* Measurement of the geosynthetics will be based on 3D survey. Details C and D on Drawing 6 have callouts for survey points which will be used for the measurement. The anchor trench line item (No. 004) is separate from the geosynthetics line items (Nos. 005 and 006), and therefore, the material placed in anchor trench shall be incidental.”

## CASE STUDIES

Four years ago, a liner crew began a multi-layer installation at an industrial holding pond in the Rocky Mountains. Quantities were calculated off Not For Construction drawings – before the dikes were built – then revised three months later with the issuance of Final Construction Drawings. Contractors inked a subcontract in July, noting an extra \$50,000 worth of materials would be needed per latest survey. The Prime contractor, after delivery of the necessary geosynthetics, refused to pay until a Unit Price subcontract change was accepted -- offering assurances all would work out when the final survey proved net quantities. Specifications read as follows (prior to bid, well before Final Drawings):

**Contractor and Sub will be paid for lined area of approximately 72,000 SY (TBD).**

The Prime contract set out the following vague payment base:

*Contract Price:* The total of all Contractor costs, fees, expenses and profit payable to Contractor for performance of the Work as specified shall be as set forth in Exhibit B, Schedule of Compensation: Geosynthetics (4 bid items) shall be paid upon completion at 72,000 SY bid quantity (Neat Line Estimates) as per final measured quantity at completion of the project. Survey shall be taken by an independent 3<sup>rd</sup> party surveyor.

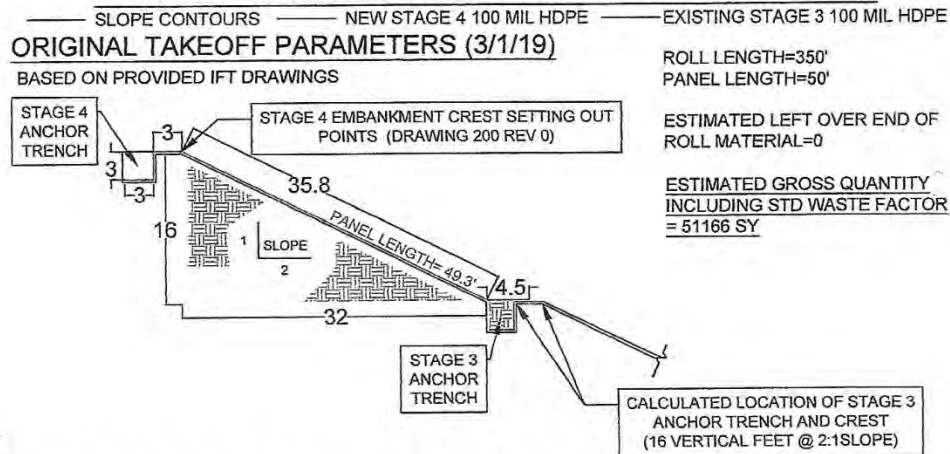
The Subcontract initially read:

*\$900,000 Lump Sum payment for approximately 78,000 SY with a final survey to allow adjustment based on changes in the course of construction.*

Once summer and fall delays pushed liner work into the winter months, the Contractor refused to divulge when payments would release, and blamed the Installer for slow progress. The Owner and Engineers sat on the sidelines and wouldn't blow a whistle or even host a meeting. Playing fast and loose with payment terms set everyone up for a multi-million-dollar dispute. No final survey ever took place.

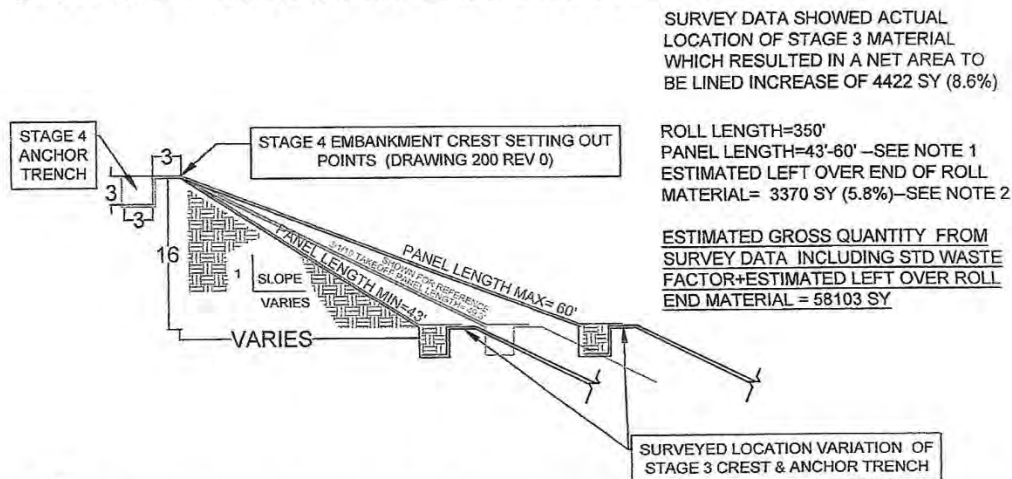


## 100 MIL HDPE QUANTITY REVISIONS



### REVISED TAKEOFF PARAMETERS POST SURVEY (6/18/19)

SURVEY SHOWED 2 FACTORS WHICH HAD A SIGNIFICANT EFFECT ON THE GROSS QUANTITIES REQUIRED



**NOTE:**

- 1) HORIZONTAL SEAMS ON SLOPES ARE NOT PERMITTED THEREFORE ANY ROLL END MATERIAL SHORTER THAN THE LENGTH OF SLOPE RUN INCLUDING REQUIRED ANCHOR TRENCH AND MINIMUM 3' RUN OUT FROM TOE OF SLOPE WILL BE LEFT OVER MATERIAL

Figure 2. Calculating gross liner quantity for a given, net pay quantity, when site conditions are shifting

To further emphasize the importance of bid documents corresponding to Contracts --and ultimately payments -- consider 30 lined cells at a Fish Hatchery. Last summer and fall (2022) the Installer placed 45 mil liner over existing (reworked) lagoons. Even experienced dirt-moving operators face a challenge removing old liner, regrading lagoons, re-digging anchor trenches. Sure enough, the first three cells in July proved ten feet wider in one direction (wasteful with pre-fabricated panels). The final dozen cells proved eight feet narrower. Scale was off in the initial drawings and the Engineer made it clear he needed proof to authorize payments beyond bid form quantity. The Installer therefore went extra miles to document (and sign off) actual quantities for every one of those 30 cells, with supplemental material ordered to arrive before completion. Every progress payment thus became incredibly complex. The Owner's Rep came to understand FMLs don't follow the same QA/QC steps as roll goods; that pipe boots are a different work item from batten attachment to concrete pads; that polyethylene

liner requires backfill of trenches in the coolest part of the next day, plus minimal compaction and traffic to avoid pulling liner upslope into the trenches.

The Installer worked there with a very professional Contractor, whose sludge removal and dirt quantities were tied to final lined area, regardless of the unrelated quantities involved. He was already behind eight weeks and “under water” from flooding in the region, yet the Engineer insisted on paying strictly off the shifting quantity of liner amounts.

## CONCLUSION

Over the years we see twists and turns made extra difficult by overlooking a few standard procedures. First, it's critical to establish a thorough sequence of communication (all parties included) from bid documents to submittals, to shipment and delivery, CQA, progress payments, then final walk-through and/or survey. If the contracts are not clear, meeting notes must address payment bases. Don't leave payment base out of your pre-bid, pre-con and weekly meetings – assuming the General Contractor will “handle those details.” The biggest problem in communication is the illusion that it has taken place (Oscar Wilde).

Secondly, decide and stay consistent with the payment structure that's outlined in Plans and Specs. Not a “foolish consistency,” of course: when work items shift, adjust equitably. If a Contractor is allowed to mix and match how progress billings are handled, that's a sign everyone is no longer on the same page. [Engineers, Inspectors and Regulators are not always equipped to detect such red flags. They are the ones, however, under the gun to resolve significant money issues before close-out]. If Specifications and Prime contract call out Cost-Plus compensation, never allow subcontracts based on other terms. That violates flow-down principals and sets a stage for winners and losers.

Thirdly, approve payments based on what unambiguous bid documents called out, plus document and inform all parties impacted when pay items revise in the course of construction. Addenda often clarify pay terms before bid opening. Partial bids get accepted all the time, yielding award to Contractors who missed items, gathers submittal packets from two different installers, jockeys for concessions before the suppliers and subcontractors line up on a construction schedule. That chaos results in unfair bid practices and --over the long run -- projects tend to run over budget or beneath industry standard quality. Accountability among all parties improves the chances of a successful project close-out.

Payment bases represent one aspect where it's not too difficult to minimize the potential for confusion, rancor, costly surprises and (sometimes) recourse to dispute resolution which can be as long running and contentious as full-on litigation. Engineers, Regulators, General and Specialty contractors all make communication mistakes, but with money on the line it's hard to admit one's share of the equation and work toward a fair and equitable resolution. Consistency and accountability sound like no brainers, but they are not as common in actual contracts and pay requests as they could be. We estimate 30% of geosynthetic jobs suffer from incomplete or ambiguous payment terms. Only half of them rectify in the course of bidding, installation and billing. Roughly 15% remain to resolve at project completion. How you manage jobs matters. It's not micro-managing to make sure every participant works under the same set of rules.

## Performance Comparison of Evapotranspiration and Engineered Turf Covers

**Md Jobair Bin Alam, Ph.D., P.E., M. ASCE<sup>1</sup> Maalvika Aggarwal<sup>2</sup> and  
Ram L. Ray, Ph.D., P.E., M. ASCE, ACUE<sup>3</sup>**

<sup>1</sup>Prairie View A&M University, PO Box 519, MS 2510, TX 77446; e-mail: [mdalam@pvamu.edu](mailto:mdalam@pvamu.edu)

<sup>2</sup>Prairie View A&M University, PO Box 519, MS 2510, TX 77446; e-mail: [aggarwal@pvamu.edu](mailto:aggarwal@pvamu.edu)

<sup>3</sup>Prairie View A&M University, PO Box 519, MS 2510, TX 77446; e-mail: [raray@pvamu.edu](mailto:raray@pvamu.edu)

### ABSTRACT

Controlling the moisture intrusion into landfill final covers and limiting water drainage into the waste mass is one of the challenging tasks for engineers and solid waste professionals. Compared to traditional clay cover and evapotranspiration (ET) cover, the performance of engineered turf cover is very limited in the literature. This technical paper will discuss the sub-soil moisture variation of two different types of landfill final cover systems: (1) ET cover and (2) engineered turf cover under identical atmospheric conditions. Both the pilot-scale test sections were constructed side-by-side and were instrumented identically with state-of-art sensors to measure volumetric moisture content (VMC) and soil suction. A weather station was also installed at the site to measure the climatic parameters. The ET cover was constructed with compacted clayey soil seeded with local grass. The engineered turf cover included compacted clay overlain by the engineered turf. The engineered turf consisted of structured LLDPE geomembrane overlain by synthetic turf (comprised of polyethylene fibers tufted through a double layer of woven polypropylene geotextiles) and sand infill. Based on the field investigation, the analysis showed that the soil under the engineered turf had a negligible change in soil moisture and suction. In contrast, the ET cover soil underwent noticeable moisture variation. The preliminary findings from this study showed better efficiency of the engineered turf cover in the humid subtropical climate as a barrier to moisture intrusion into the underlying cover soil.

### INTRODUCTION

Evapotranspiration (ET) covers, also known as Water Balance covers, are increasingly being considered for the final closure of landfills for their enhanced performance compared to the conventional cover system. ET cover system uses the water store-release principle to reduce the water percolation into the waste mass. The basic principle of this type of cover is to store precipitation during rainfall events and discharge it into the environment during the dry period through surface evaporation and plant transpiration (Benson et al. 2002; Albright et al. 2004). Therefore, soil and plant become crucial components of the ET cover system, where soil acts as the storage media for water and plants invigorates the evapotranspiration process. It offers a natural approach to the final closure of waste facilities. It is also a cost-effective solution for waste containment (Benson and Bareither, 2012). Most importantly, the performance of ET covers enhances with time (Albright et al. 2004; Hauser, 2009).

However, the performance of ET covers largely depends on site-specific factors (e.g., climatic conditions, availability of suitable soil, etc.). Soil hydraulic properties strongly influence the field hydrology of ET covers. As-built hydraulic properties of soil are degraded due to post-construction processes such as insect and animal burrowing, freeze-thaw cycling, wet-dry cycling,

and plant root growth and death. These natural processes significantly alter the soil's hydraulic characteristics and influence cover hydrology (Alam et al. 2019; Suter et al. 1993; Benson and Othman, 1993). Hence, over time, the changed hydraulic properties (which is in-service hydraulic properties) of ET cover soils, such as hydraulic conductivity and the soil-water characteristic curve (SWCC), significantly affect the percolation rate (Khire et al. 1997; Ogorzalek et al. 2008; Bohnhoff et al. 2009). Another concern of ET cover is that while promoting the storage capacity of the soil, the less compaction effort of the cover soil can cause significant erosion. Additionally, under the local climatological condition (especially in the humid climate), ET cover design may require increased cover thickness to improve storage capacity. The increased design thickness of the cover may appear unattainable from the construction and financial perspectives. Alam et al. (2021) presented a study on the effect of precipitation on cover thickness and storage capacity. Therefore, though ET covers offer better solutions than conventional covers, there are still uncertainties that limit the use of ET covers, especially in humid climates.

Alternative to the conventional and ET cover systems for landfill closure has been proposed and used across the country for years. Engineered turf cover, or synthetic turf, has recently been adopted as an alternative final cover system for landfill closure in many states of the US. Synthetic turf consists of two separate geosynthetics. The lower geosynthetic material is typically an LLDPE geomembrane liner, and the upper component is a geotextile integrated with synthetic grass-like fibers. Engineered turf may have potential advantages over the traditional cover, and ET covers, such as reduced installation, operation, and maintenance costs, reduced depth of soil foundation layer above the waste mass, thereby gaining additional airspace for MSW, and controlled moisture movement into the waste, eventually controlled/no percolation. Though engineered turf has been accepted in many states of the US, there are very limited available data to compare the performance of engineered turf cover with ET cover derived from field demonstration. Since the moisture movement characteristics of the foundation soil layer under the turf cover have not been fully investigated and compared to that of ET cover, hence, the objective of this study was to investigate the moisture variation of the cover soil of ET cover and engineered turf cover under the identical climatic condition. To pursue the objective, two test sections (one as ET cover and the other as turf cover) of dimensions  $3\text{ m} \times 3\text{ m} \times 1.22\text{ m}$  were constructed side-by-side at the demonstration farm of Prairie View A&M University. The construction of the test sections was followed by instrumentation to measure the climatic parameters, soil moisture content, and suction.

## CONSTRUCTION OF TEST SECTION

Two large-scale test sections of dimensions  $3\text{ m} \times 3\text{ m}$  (10 ft.  $\times$  10 ft.) and 1.22 m (4 ft.) deep were constructed side by side as shown in Figure 1. The existing subgrade where the test sections were constructed mainly consists of fine-grained soil. One test section was constructed as ET cover using native vegetation, and the other was constructed as engineered turf. The side-by-side construction of the test sections was designed so that every test section undergoes identical weather conditions. After excavating the test pit, the subgrade of each test section was overlain by a 6-mil impermeable plastic sheet. The plastic sheet was also placed along the sidewall of the excavation and extended to almost 0.6 m (runout length) along the top surface to ensure that intra-section moisture flow does not occur. The bottom of the pit was constructed at a 2% slope to allow water to flow toward the sloping end under gravitational action. At the sloping end, a sand strip was placed. Details of the sand strip are provided in the instrumentation section. Coarse sand was used in the sand strip that had hydraulic conductivity of approximately  $1 \times 10^{-1}\text{ cm/sec}$  based on the



laboratory-measured constant head permeability test. The sand strip was required to prevent water accumulation at the bottom of the pit. It was hypothesized that the high contrast in the permeability of the coarse sand and the compacted backfilled fine-grained soil should potentially divert the water out of the test section after any heavy rainfall events.

After the placement of the plastic sheet, both the test sections were backfilled with the excavated fine-grained soil and compacted. During the excavation period, soil samples were collected from all the test sections. These collected samples were subjected to laboratory characterization. All the laboratory tests on the samples were conducted following the ASTM standard. Based on the laboratory investigation of the collected samples, the fine fractions of the samples were found more than 70%. The soil's liquid limit ( $w_L$ ) and plasticity index (IP) were found almost 52% and 27%, respectively. According to the Unified Soil Classification System (USCS), the soil was classified as high-plastic clay (CH). From the Standard Compaction Test results, the optimum moisture content (OMC) and maximum dry density ( $\gamma_{d(max)}$ ) were found around in the range of 15 to 16.5%, and 16.7 to 17.3 kN/m<sup>3</sup>, respectively.

A few days after the backfilling, extensive instrumentation was implemented at both the test pits to monitor the soil parameters (soil moisture and suction) and climatic factors (precipitation). The instrumentation detail is provided in the following section. Immediately after the instrumentation and smoothing of the top surface, a structured LLDPE geomembrane (Figure 2a) was placed over the turf cover, which was overlain by synthetic turf. The synthetic turf (Figure 2b) was comprised of polyethylene fibers tufted through a double layer of woven polypropylene geotextiles and sand-infill. The top surface of the other test section (ET cover) was strewn with local grass seed.



**Figure 1. Construction activities.**



**Figure 2. (a) Textured geomembrane layer (b) engineered turf.**

## INSTRUMENTATION

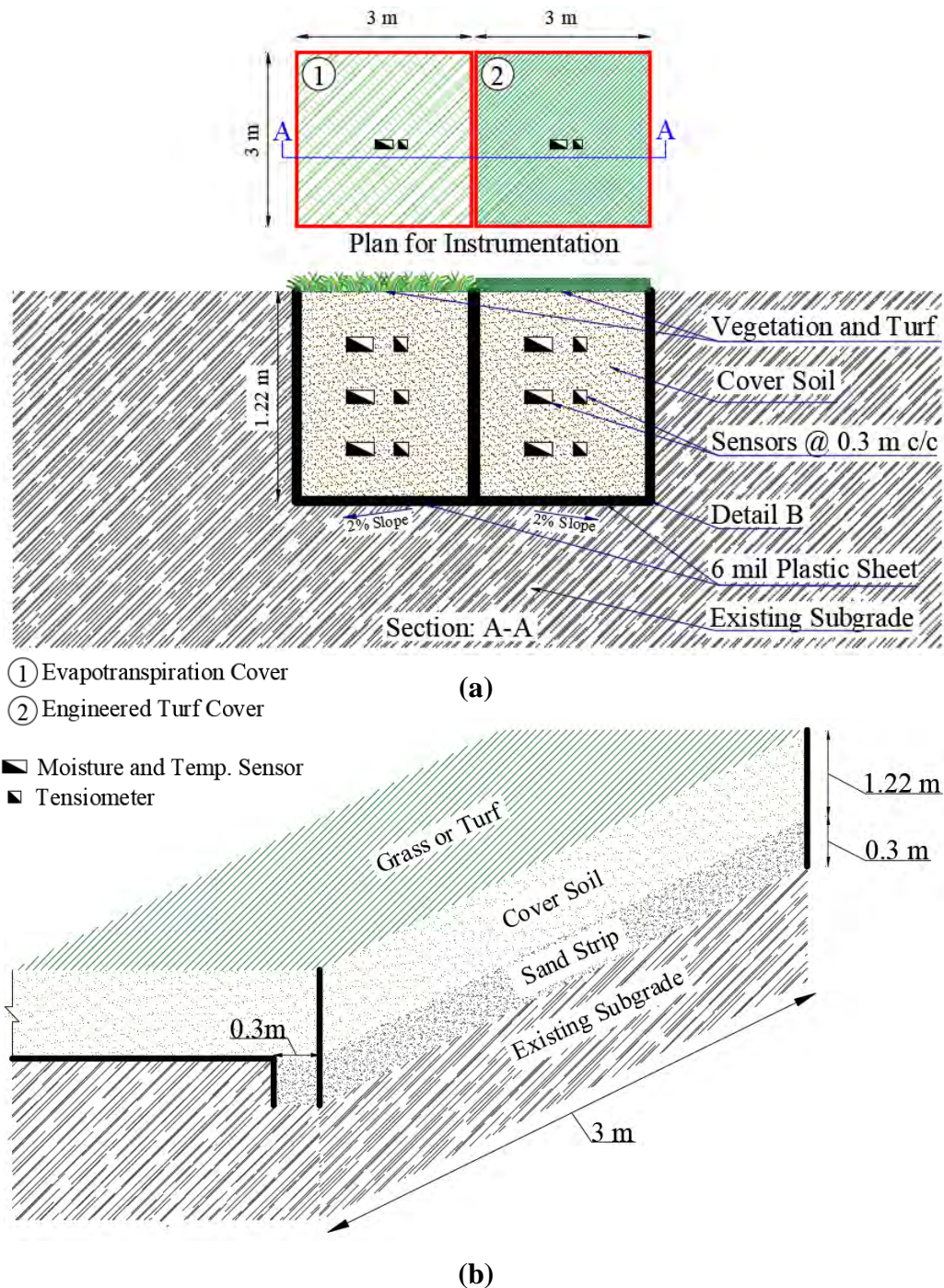
Multiple moisture sensors and tensiometers were installed at varying depths to closely monitor soil moisture and negative pore-water pressure (suction) in the field test sections. The plan and section of the instrumentation are shown in Figure 3(a). Moisture sensors were installed at 0.3 m (1 ft.) intervals, as shown in Figure 3(a). Changes in the negative pore water pressure in the soil are associated with variations in moisture content. So, tensiometers were installed in the test sections at identical depths along with the moisture sensors (Figure 3a). Both the test sections were instrumented similarly to compare the performance of the two cover types. The sensors installed at the test pits had an automatic data logging system. The data loggers were adjusted to record and store data every 5 minutes. A weather station was installed to evaluate soil moisture and suction changes in response to precipitation at the site. The weather station also had an automatic data recording and storing facility. Similar to the data logging cycle (every 5 minutes) of the sensors installed in the pits, the data logger of the weather station was also set to record and store data every 5 minutes. The weather station records precipitation, air temperature, relative humidity, wind speed and direction, vapor pressure, and solar radiation. However, in this paper, the changes in soil parameters were only evaluated in response to precipitation.

Figure 3(b) shows the schematic of the sand strip. Towards the sloping end (2% slope), a 0.3 m × 0.3 m (1 ft. × 1 ft.) trench was excavated to construct the longitudinal sand strip. Coarse sand was placed along the entire length of the trench. After the sand placement, it facilitated the anchoring of the 6-mil plastic sheet at the inner wall of the trench.

## RESULTS AND ANALYSIS

The time series analysis of the field monitoring results is presented in Figure 4. It is to be noted that the results from the engineered turf cover and ET cover are denoted by T and V, respectively, as can be seen from the figure legends. It is observed from Figure 4(a) that variation in VMC in the ET cover is more significant than in the engineered turf cover. The initial VMCs (inception of data monitoring) of the soil under the engineered turf at three different depths were different, and the VMC profile remained almost flat. At 0.3 m (1 ft.) depth, the VMC profile was nearly 0.21 m<sup>3</sup>/m<sup>3</sup>. The VMC profile at 0.6 m (2 ft.) depth had a slightly increasing trend after May 13, 2022.

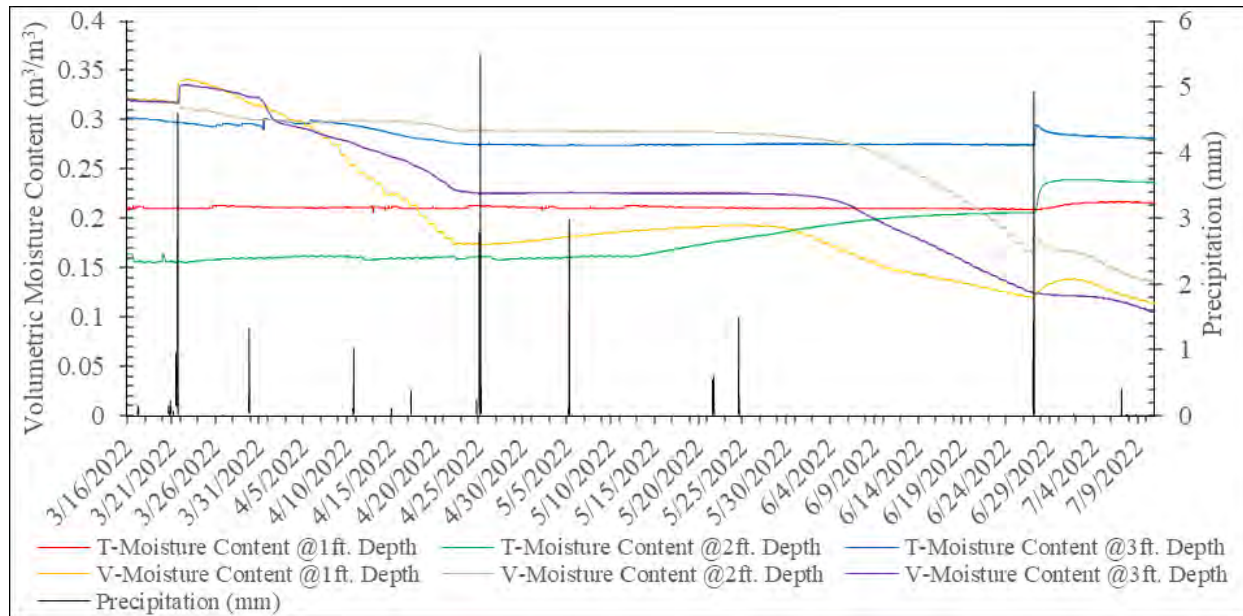




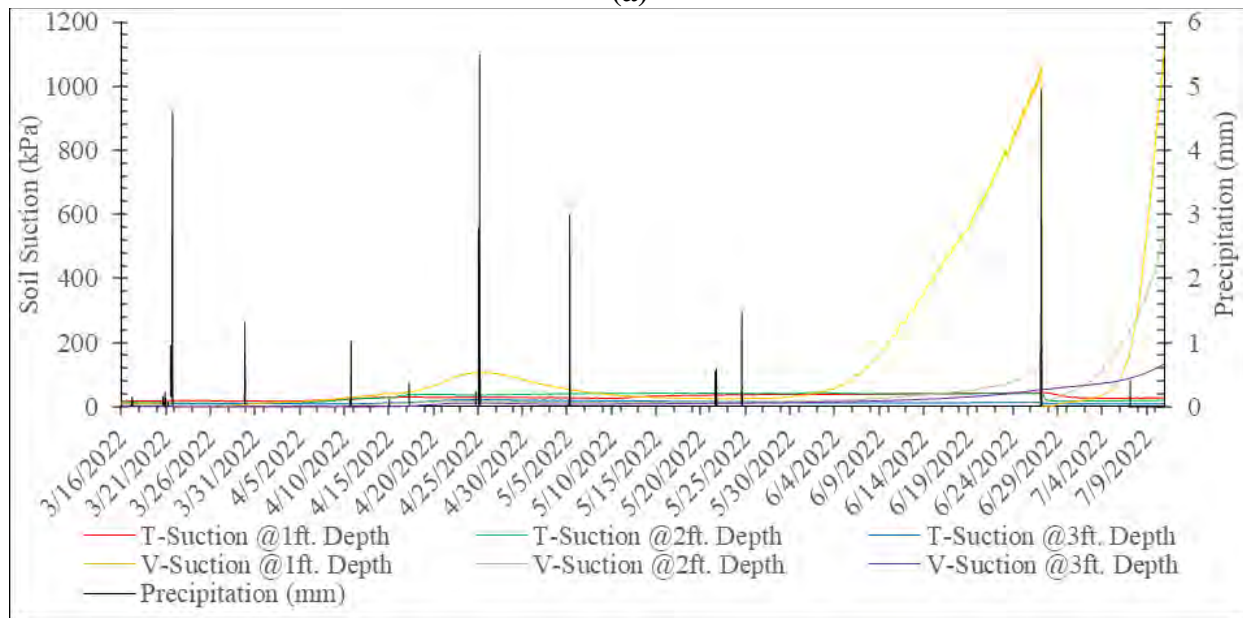
**Figure 3. (a) Instrumentation plan and section (b) Detail-B.**

Another point to notice in Figure 4(a) is that there is a sudden rise in VMC (not a sharp rise) at 0.6 (2 ft.) and 0.9 m (3 ft.) depths after the rainfall events (on June 27, 2022). Apparently, it appeared that VMC's rise at those depths is due to the precipitation events. However, there is no rise at 0.3 m depth. The site was investigated for any possible damage to the turf, which could lead to the development of a preferential flow path. But no damage was observed on the turf. As there is no sudden rise in the VMC at 0.3 m depth, it is implied that the sudden rise in VMC at 0.6 and 0.9 m depths is not due to the direct contribution of the precipitation. This could be theorized that

the rise in those depths could be due to the developed suction gradients. This could also be the outcome of lateral moisture flow toward the sensor tip at those depths. However, with long-term continued monitoring, more insights could be gained into this phenomenon. Overall, the changes in moisture content at all depths are very negligible.



(a)



(b)

**Figure 4. Time series analysis (a) volumetric moisture content (VMC) (b) suction.**

Contrary to the turf cover, the VMC profiles for the ET cover are not flat in all three depths. There is a significant fluctuation of VMC profiles, as can be seen in Figure 4(a), especially at 0.3 m depth. After the initial rise of moisture content ( $0.33 \text{ m}^3/\text{m}^3$  on March 22, 2022), a gradually decreasing trend was observed at all depths until April 25, 2022, when few precipitation events were recorded. Though there were no sharp spikes of moisture increments after the rainfall events,



the VMC profile turned to a flat orientation to almost  $0.18 \text{ m}^3/\text{m}^3$  of VMC. After May 30, the soil moisture again started to decrease (decreased to  $0.128 \text{ m}^3/\text{m}^3$ ) until June 27. On June 27, though there were few rainfall events (low intensity and low duration), the decreasing trend of VMC continued. It is to be noted that the ambient temperature during that one month was almost  $86^\circ\text{F}$  to  $100^\circ\text{F}$ . So, the rate of evapotranspiration was higher during that time. The change (decrease) in soil moisture at 0.3 m depth was prominent compared to the other two depths. This could further be understood from the time series analysis of soil suction data at different depths, as shown in Figure 4(b). It was observed that the suction at 0.3 m depth started to increase exponentially after June 04. The suction value peaked at almost 1041 kPa on June 27. Then it dropped suddenly to almost 0 after the rainfall event on June 27. The suction value started to rise again and reached almost 1082 kPa in just two weeks, as shown in Figure 4(b). It indicates that the soil is under high evapotranspiration demand and drying faster in the ambient summer temperature. However, the increase in soil suction at 0.6 m and 0.9 m depths was not as prominent as at depth 0.3 m. On the other hand, the soil suction under the turf varied from 10 to 35 kPa in that identical atmosphere. So based on the comparative spatial and temporal profiles of VMC and suction of both the test sections' soil, it can reasonably be inferred that the soil under the turf is somewhat in moisture equilibrium condition. Here, moisture equilibrium refers to the soil's negligible gaining or losing of moisture. However, long-term performance monitoring is required to fully understand this phenomenon.

In addition to the time series analysis, basic statistical analysis was conducted on the monitoring data to further understand the moisture variation perception of the two covers. The relative standard deviation (RSD) of the moisture content data gathered (34573 data) for the soil of ET cover and turf cover is presented in Table 1. The RSD is the measure of the deviation of a set of numbers distributed around the mean. The RSD of the turf soil at different depths ranged from 0.91% to 9.12%, indicating the data are tightly clustered around the mean value, especially at 0.3 m depth. On the other hand, the RSD values for the ET cover soil are 33.5%, 20.4%, and 29.2%, at depths of 0.3 m, 0.6 m, and 0.9 m, respectively. Therefore, the moisture content data for ET cover are more spread out from the mean as compared to the turf cover. The simple statistical analysis presented here implies the significant variation of moisture in the ET cover soil compared to the soil under the engineered turf.

**Table 1. Relative Standard Deviation (RSD) of the monitored VMC data.**

Depth (m)	Relative Standard Deviation (RSD)	
	Engineered Turf Cover	ET Cover
0.3	0.91	33.49
0.6	9.12	20.35
0.9	3.24	29.23

## CONCLUSION

Moisture content and soil suction variation obtained from the field instrumentation of two different final cover types have been presented in this study. The sub-soil moisture variation under the engineered turf was considerably less than the ET cover. The ET cover soil underwent a considerable increase in soil suction, especially at shallow depths (0.3 m) as the soil dried because of favorable ambient conditions such as high temperature, solar radiation, etc. The suction profile at all three depths under the engineered turf showed negligible variation under identical ambient

environmental conditions. As such the cover soil under the turf was in a moisture equilibrium state compared to the ET cover. Although this paper presents the short-term monitoring results, the engineered turf cover seemed to be an effective barrier to precipitation based on the field instrumentation results. However, both the covers shall be continued to monitor for three more years or more. Overall, the preliminary monitoring data obtained from this study showed some encouraging results of engineered turf regarding sub-soil moisture variation under the turf.

## ACKNOWLEDGEMENT

The authors gratefully acknowledge the funding provided for this research by the National Science Foundation (NSF), grant number #2101081. The authors also acknowledge Watershed Geosynthetics LLC. for providing materials, technical expertise, and support to install the engineered turf and for being a part of the project reviewer.

## REFERENCES

- Albright, W. H., Benson, C. H., Gee, G. W., Roesler, A. C., Abichou, T., Apiwantragoon, P. & Rock, S. A. (2004). Field water balance of landfill final covers. *J. of Environmental Quality*, 33(6): 2317-2332.
- Alam, M. J. B. & Hossain, M. S. (2019, March). Evaluation of post-construction changes in soil hydraulic properties through field instrumentation and in situ testing. In *Geo-Congress 2019: Geotechnical Materials, Modeling, and Testing* (pp. 722-732). Reston, VA: American Society of Civil Engineers.
- Alam, M. J. B., Ahmed, A., Hossain, M. S., & Rahman, N. (2021). Estimation of percolation of water balance cover using field-scale unsaturated soil parameter. In *MATEC Web of Conferences* (Vol. 337, p. 04005). EDP Sciences.
- Benson, C. H., Albright, W. H., Roesler, A. C. & Abichou, T. (2002). Evaluation of final cover performance: field data from the alternative cover assessment program (ACAP). *Proc. Waste Management*, 2: 1-15.
- Benson, C. H. & Bareither, C. A. (2012). Designing water balance covers for sustainable waste containment: Transitioning state of the art to state of the practice. *Geotechnical Engineering State of the Art and Practice*, 1-33.
- Benson, C. H. and Othman, M. A. (1993). Hydraulic conductivity of compacted clay frozen and thawed *in situ*. *J. Geotech. Engrg.*, 119(2), 276-294.
- Bohnhoff, C., Ogorzalek, A., Benson, C., Shackelford, C. and Apiwantragoon, P. (2009). Field Data and Water-Balance Predictions for a Monolithic Cover in a Semiarid Climate. *J. Geotech. Geoenviron. Eng.*, 135(3), 333-348.
- Hauser, V.L. (2009). *Evapotranspiration Covers for Landfills and Waste Sites*. CRC Press, Boca Raton, FL.
- Khire, M., Benson, C. and Bosscher, P. (1997). Water Balance Modeling of Earthen Landfill Covers. *J. Geotech. Geoenviron. Eng.*, 123(8), 744-754.
- Ogorzalek, A. S., Bohnhoff, G. L., Shackelford, C. D., Benson, C. H. & Apiwantragoon, P. (2008). Comparison of field data and water-balance predictions for a capillary barrier cover. *Journal of geotechnical and geoenvironmental engineering*, 134(4), 470-486.
- Suter, G.W., R.J. Luxmoore, and E.D. Smith. (1993). Compacted soil barriers at abandoned landfills will fail in the long term. *Journal of Environmental Quality*, Vol. 22, 217-226.

## Protection of Geofoam using High Strength, Chemically Resistant Geomembranes

William D. Shehane, P.E.<sup>1</sup>, Tina Oliver<sup>2</sup>, and Felon R. Wilson, P.E.<sup>3</sup>

<sup>1</sup>Seaman Corporation, 1000 Venture Blvd. Wooster, OH 44691 USA; e-mail: [bshehane@seamancorp.com](mailto:bshehane@seamancorp.com)

<sup>2</sup>Seaman Corporation, 1000 Venture Blvd. Wooster, OH 44691 USA; e-mail: [toliver@seamancorp.com](mailto:toliver@seamancorp.com)

<sup>3</sup>Consultant, 1000 Venture Blvd. Wooster, OH 44691 USA; e-mail: [fwilson@seamancorp.com](mailto:fwilson@seamancorp.com)

### ABSTRACT

Background and state of the art use of geomembranes to protect Geofoam are presented. The rationale for the need and application of the Geofoam in Engineered applications is reviewed. The extreme lightweight properties of Geofoam pose unique considerations for construction. Further, the chemical nature of the Geofoam itself presents special considerations in that it must be protected from petroleum hydrocarbons and many organic compounds. Typical layouts of geomembranes installed to maintain the integrity of the Geofoam in these installations are discussed. Essential properties for geomembrane performance in Geofoam protective applications are presented and reviewed along with a discussion of current industry specifications. Two non-transportation infrastructure applications utilizing high strength, hydrocarbon resistance geomembranes for Geofoam protection are presented along with installation details.

### INTRODUCTION

Expanded Polystyrene or Expanded Polystyrene Foam (EPS) is used in a variety of industries to deliver many end products. Many applications are for thermal or acoustic insulation and for packaging. Examples include, foam cups, packing peanuts and white foam core boards. The first well-documented use of these materials in infrastructure, was in the 1970's in Norway, and the use has grown world-wide. EPS Geofoam (Geofoam) blocks, used in conjunction with chemically resistant geomembranes have seen increased acceptance in transportation and infrastructure applications.

Expanded Polystyrene Geofoam (EPG or Geofoam) is manufactured in a slightly different manner than conventional Styrofoam, utilizing a polystyrene polymer. The material is a thermoplastic and can be shaped and remolded repeatedly. Heat and pressure during the polymerization process are varied to produced different densities of Geofoam. Table 1 is a typical set of published properties for Geofoam blocks. Note the very low densities in relation to soils at typically  $1.7 \text{ t/m}^3$  ( $110 \text{ lb/ft}^3$ ).

**Table 1. Typical Geofoam Properties**  
**Source: Geofoam.org**

<b>ASTM D6817 Physical Property Requirements of EPS Geofoam</b>							
Density, min. kg/m <sup>3</sup> (lb/ft <sup>3</sup> )	11.2 (0.70)	14.4 (0.90)	18.4 (1.15)	21.6 (1.35)	28.8 (1.80)	38.4 (2.40)	45.7 (2.85)
Compressive Resistance, min., kPa (psi) at 1%	15 (2.2)	25 (3.6)	40 (5.8)	50 (7.3)	75 (10.9)	103 (15.0)	128 (18.6)
Flexural Strength, min., kPa (psi)	69 (10.0)	172 (25.0)	207 (30.0)	240 (35.0)	345 (50.0)	414 (60.0)	517 (75.0)
Oxygen, min., volume %	24.0	24.0	24.0	24.0	24.0	24.0	24.0

Compressive strengths at 15 kPa (2.2 psi) to 128 kPa (18.6 psi) at 1% strain provide sufficient strength for most applications. However, load distribution, sometimes in the form of a slab is needed. Some sources also quote compressive strengths at strains of 5% and 10%, but it is generally agreed that the material has elastic properties within the 1% strain level so most designs work within that amount of strain. Acceptable short-term deflection and limited long-term creep deformation is reported to then occur.

Other Geofoam properties include:

- Chemical Resistance – Good resistance to many inorganics but poor resistance to alcohols, organic solvents, hydrocarbons and petroleum.
- Fire – Geofoam is readily combustible.
- UV – Geofoam is not UV resistant, and some sources recommend not more than 1 day of UV exposure.
- Wind, Buoyancy – The light weight and low density make Geofoam a floatable, readily moveable material.
- Water Absorption – The structure of the Styrene compound, coupled with the closed cell physical structure of the molded Geofoam make it not prone to water absorption.

The lack of resistance to contact with many carbon-based compounds dictates the need for protection from spills or from adjacent contaminated soils.

## APPLICATION CONSIDERATIONS

Geofoam is widely gaining acceptance as a lightweight fill material. It finds application as an alternative to compacted earthen fill when it improves subsurface stability and/or there are factors making the fill more difficult or expensive to place such as:

- Tight working conditions such as adjacent to angular surfaces.
- Difficult to place areas such as bridge abutments.
- Subsurface conditions requiring extensive improvement to carry load from compacted overburden.
- Absorption of active earth pressure when used against a wall.
- Adjacent to structures when compaction from vibration is undesirable.
- Inability or high cost to acquire select backfill materials.

Reported applications for Geofoam include:

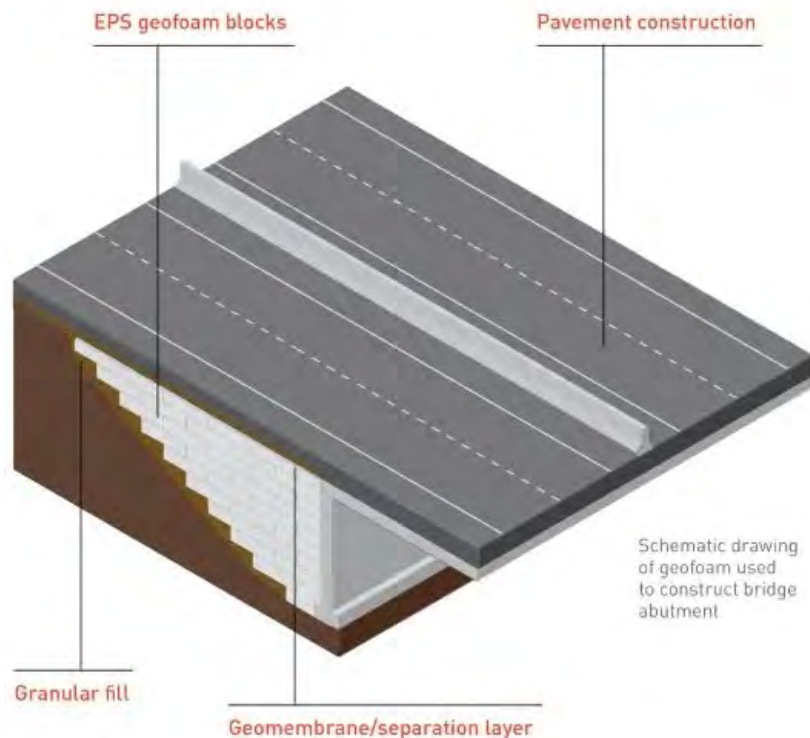
- Bridge abutments
- Retaining structures
- Soil stabilization
- Built-up slopes
- Embankments
- Stadium seating
- Berms and land forming
- Plaza decks

Figure 1 is an image of a backfilling application which simply illustrates the use of Geofoam. In this transportation use, rather than import and compact earthen fill, the Geofoam is used to raise the working surface. Figure 2 is a typical diagram of a bridge abutment layout using Geofoam. Again, the blocks provide cost and time savings by replacing natural materials. Many of the applications to date in North America have been bridge and highway related.



**Figure 1. Typical Geofoam Application. Source: EPS Alliance**





**Figure 2. Typical Bridge Abutment schematic using Geofoam protected with a Geomembrane. Source: PolymoldingLLC.com**

Figure 3 illustrates placement of geofoam blocks in an active construction project. Often used in applications that include rough terrain, heavy equipment and other challenging working conditions, the protective petroleum resistance geomembrane must demonstrate superior performance in specific physical properties.



**Figure 3. Placement of Geofoam on project site. I75 Toledo OH USA**



## ROLE AND PERFORMANCE OF GEOMEMBRANES TO PROTECT GEOFOAM

Geofoam is manufactured and designed as a structural fill. It is not designed to resist contact with all substances. Inherent in transportation are hydrocarbon fuels and other chemicals which can be spilled or leaked. Additionally, over 90% of the roads in the U.S are paved with petroleum-based asphalt. Geofoam is itself a hydrocarbon and is miscible with other hydrocarbons. In other words, Geofoam dissolves in contact with many hydrocarbons, losing its ability to function as a lightweight fill. Consequently, it must be protected to withstand certain compounds, primarily organics and hydrocarbons. Properly selected, designed, and installed geomembranes provide the protection needed for the Geofoam.

The normal layout is to place the Geofoam on a prefabricated geomembrane and then when the Geofoam installation is complete, the geomembrane is configured to completely encapsulate the Geofoam. Any hydrocarbons, other chemicals, or water are shed off the geomembrane. Figures 4 - 8 illustrate Geofoam being installed over the placed Reinforced Ethylene Copolymer geomembrane. Figures 4-7 are highway bridge abutment applications.



Geomembrane to  
encapsulate the  
geofoam

**Figures 4 and 5. Geomembrane to encapsulate Geofoam. I5 Construction, LaMirada CA USA**



**Figure 6. Geomembrane over Geofoam edges. I75 Toledo OH USA**



**Figure 7. Geomembrane completion over Geofoam. Norfolk VA USA**



**Figure 8. Geomembrane over Geofoam in Railway application. Salt Lake City UT USA. Source: University of Utah**

## **GEOMEMBRANE SPECIFICATION DEVELOPMENT**

The protective geomembrane is expected to perform under these conditions:

- Construction site activity
- Puncture resistance from placement and from long term use.
- Abrasion to withstand installation activity in often tight and rough construction sites
- Resistance to spilled hydrocarbons including most fuels such as gasoline, diesel, etc.
- Resistance to water, various organic compounds, and aggregates.
- Tensile strength of sheet and seams to withstand placement and shear loading from adjacent backfill.
- Bending and wrapping at 90° angles under various temperatures.

While all these properties are essential for a geomembrane to protect Geofoam, there are two common themes:

1. Survivability
2. Chemical Resistance

Neither is exclusive as the system will not function without both. Some construction site activity has shown that films made with an internal hydrocarbon resistant layer exhibit excellent hydrocarbon resistance but are plagued with damage from normal site activity. Hydraulic equivalent permeabilities differences of  $10^{-11}$  vs.  $10^{-13}$  cm/sec are irrelevant when one small puncture can transmit 0.1 l/day (0.03 g/day). Heavily reinforced, chemically resistant geomembranes are the primary choice in these applications, meeting the criteria listed above.

**Geomembrane specifications.** Most specifications to date have been written by State DOT's. The specs for the most part carry a theme centered around the Survivability and Chemical resistance properties. As gasoline resistance is considered a benchmark, some designate the geomembranes as Gasoline Resistant Geomembranes (GRG), which is helpful but does ignore other chemical resistance properties needed. Some of the specs specifically call out geomembrane (or polymer) types, some of which are not recommended by their manufacturers for contact with hydrocarbons. There exists a gap in the current state of the art in understanding of the total geomembrane system requirements and needs to focus on the essential properties:

- Yield Tensile
- Shear and Dead Load Seam Strength
- Puncture Resistance
- Hydrocarbon, Organic vapor transmission and liquid compatibility – long term, proven

New highway and road construction, temporary road construction, bridge abutments, retaining walls, railway track systems and airfield pavements all must consider the potential of exposure to hydrocarbons. Looking at the performance demands for a geomembrane in a Geofoam protection application, there are two common themes in these requirements: Survivability & Hydrocarbon resistance.

## BEYOND TRANSPORTATION

While most Geofoam applications in infrastructure have been transportation related to date, there are increasing uses of the material in other areas. Two notable, high profile, projects are the Detroit Waterfront Plaza and the Argo Drain stormwater infiltration facility, both utilizing the XR-5 Ethylene CoPolymer geomembrane. Brief descriptions of each follow.

**Detroit Waterfront Plaza.** A renovation of the downtown Detroit waterfront was a \$0.5 billion project that included construction of the GM Plaza, between the GM Renaissance Center and a concrete seawall along the Detroit River. It was a tight area. The entire area had to be raised over 4 m (13 ft) and minimize lateral pressures due to soil conditions and the close proximity of the Windsor, Ontario tunnel. The designers specified a 24 Kg/m<sup>3</sup> (1.5 lb/ft<sup>3</sup>) Geofoam in lieu of normal earthen fill. Subsidence had occurred in the area and there were concerns about what had



been deposited there in the past. Therefore, the geomembrane needed broad chemical resistance in addition to robust physical properties. A total of 4,700 sm (50,000 sf) of geomembrane was placed only over the Geofoam, or in some sections over a top sand layer, and then perimeter anchored. Due to the elevation of the Geofoam relative to river level, other liquid intrusion was not a concern. Figures 9 through 12 (sourced from Environmental Protection Inc.) illustrate the construction.



**Figure 9. Geofoam with adjacent planters and knee wall construction.**



**Figure 10. Geomembrane Installation over Geofoam.**



**Figure 11. Geomembrane deployed over Geofoam.**



**Figure 12. Completed GM Plaza.**

**Argo Drain.** In Los Angeles, an initiative called “Proposition O” containing 41 projects designed to protect water quality, provide flood protection and increase water conservation, habitat protection and open space. One of these projects, the \$37 million Argo Drain Sub-Basin facility, was designed to help comply with the Santa Monica Bay Beaches Total Maximum Daily Load Requirement by capturing, treating, and retaining stormwater.

Captured stormwater goes through Primary treatment and then is released into a storage tank for infiltration. Consulting Engineers, AECOM and Geosyntec Consultants, designed the tank for both storage and infiltration, as the tank has an open bottom. To get maximum infiltration, vibration caused by compaction adjacent to the tank was undesirable. Geosyntec Consultants offered an alternative: The use of Expanded Polystyrene Geofoam adjacent to the tank instead of

compacted fill. Geofoam provided a lightweight solution to the need for backfill. The Argo Drain site was subject to concern about in situ hydrocarbons and is located in a methane buffer zone. To alleviate the concern, a hydrocarbon- and methane-resistant geomembrane was specified to encapsulate the geofoam for long-term protection. The 8.2 m (27 ft) deep tank required over 0.4 ha (1 acre) of geomembrane liner which was placed against the tank outside perimeter then, the Geofoam was installed in large blocks which, for stability, were tapered in size. Subsequently, the geomembrane was brought up the outside of the Geofoam blocks and a perimeter field weld was performed at the top of the Geofoam block.

Figures 13 through 17 illustrate the tank, Geofoam and geomembrane installation. These figures are sourced from Project Management Construction Services and/or EC Applications.



**Figure 13. Infiltration Tank Construction.**



**Figure 14. Geofoam Installation.**  
**Note Geomembrane behind and under Geofoam.**



**Figure 15. Geomembrane Installation over Geofoam with top closure seam.**



**Figure 16. Argo Drain Infiltration Tank Completed Installation.**

## CONCLUSIONS

Geofoam is a growing and valuable tool to consider in many types of infrastructure projects. To protect it chemically, a chemically resistance geomembrane must be employed as a fluid barrier. Additionally, the geomembrane itself must exhibit a high level of survivability to maintain it's ability to serve as a barrier, and not be damaged or compromised by construction activity and long-term stresses on the site.

Current specifications in the industry do not adequately describe the two major concerns (chemical resistance and survivability) and designers should properly address these issues when specifying geomembranes to protect Geofoam.

## REFERENCES

- www.argodrain.com.  
www.atlasmoldedproducts.com.  
Bartlett, Steven F., Ph.D., P.E., Fabricated Geomembranes for EPS Geofoam Applications, University of Utah.  
www.EPSalliance.com.  
State of California, Cal Trans Geotechnical Specifications, Section 19-13 EPS Geofoam Blocks.  
State of California, Cal Trans Geotechnical Specifications, Section 96-1.02T Gasoline Resistant Geomembranes.  
Giroud, R.P.; Bonaparte, R.; "Leakage through Liners Constructed with Geomembranes—Part II. Composite Liners"; Geotextiles and Geomembranes 8 (1989) 71-111.  
Koerner, Robert M., *Designing with Geosynthetics*, 6<sup>th</sup> Edition, 518-524 and 806-834.  
www.Geofoam.org.  
www.Geofoamintl.org.  
Rohe, Fred P., "Geomembrane Installation over Structural Foam Fill", Environmental Protection Inc., <https://www.geomembrane.com/case-studies/development/geomembrane-installation-over-structural-foam-fill.html>.  
State of New York, Guidelines for Design and Construction of Expanded Polystyrene Fill as a Lightweight Soil Replacement, Geotechnical Engineering Manual, GEM-24, Revision #1  
www.PolymoldingLLC.com.  
Wilson, Felon R., P.E., "In Search of the Impermeable Geomembrane White Paper", Seaman Corporation, 22 April 2021, <https://www.xrgeomembranes.com/blog/in-search-of-impermeable-geomembrane>.



## **PVC Geomembranes in Agricultural Uses**

**Meldau, Adolpho Engineer,<sup>1</sup> Duarte, Jucieli Engineer<sup>2</sup>**

<sup>1</sup> Cipatex® Group Cerquillo, São Paulo , Brazil. Av. 1º de Maio, 1341  
[adolpho.meldau@cipatex.com.br](mailto:adolpho.meldau@cipatex.com.br)

<sup>2</sup> Cipatex® Group Cerquillo, São Paulo , Brazil. Av. 1º de Maio, 1341  
[jucieli.silva@cipatex.com.br](mailto:jucieli.silva@cipatex.com.br)

### **ABSTRACT**

Geomembranes have shown a considerable increase in the variety of their applications in recent years, such as in mining works, the environment, tunnels, agriculture, etc. The purpose of this work is to delve into the use of geomembranes in one of the fields that has been gaining prominence, fish farming. Currently, Brazil is one of the pioneers in the agricultural sector, due to the wide variety of production, and the sector of fish farming in water depths created in terrestrial areas is one of the most outstanding. The production of farmed fish in the country was 841,000 tons in 2021 (tilapia, native fish, and others), which represented an increase of 4.7% compared to 2020, with Nile tilapia accounting for 63.5% of the total. production and growth from 2020 to 2021 was 9.8%, more than double the average overall fish production growth. Nile tilapia is present in all Brazilian states and is one of the most resistant fish to be raised in culture, with an ideal temperature for development in the range of 25-30°C.

### **INTRODUCTION**

The creation of fish in culture can be done by different production systems, however, the objective of the present work is to create fish in tanks and ponds lined with geomembranes. One of the advantages presented by the use of geomembranes is in the manufacture of tanks and ponds of the most varied sizes, being this in the most varied places, including urban regions. Many of these productions use a low volume of water, since they allow its reuse through the filtering process. It can be subdivided into armed tanks that do not require soil excavation and ponds; the geomembranes can be prefabricated with the necessary dimensions for the application, which makes the installation very feasible. Geomembranes that are used in tanks are normally pre-made or made in a factory and then shipped to the project site.

The constructions are normally designed considering the available space, the budget to be used and the quantity (production that is intended). In the case of ponds, construction with the use of geomembranes practically does not differ in any way from the construction of ponds for other uses, which allows an installer accustomed to the use of geomembranes to find no difficulty in operating in this market.

## **DEFINITION OF GEOMEMBRANE COLOR**

One of the important factors for the quality and productivity of the fish is the level of stress that it is submitted, and this level is influenced by the color of the geomembrane used to produce the ponds. In Brazil, agriculture tanks are manufactured in most cases with black or blue geomembranes, with the predominant black color, due to the lower level of stress generated, reducing the agitation and sudden movement of the fish.

## **GENERAL INFORMATION**

Among the aspects that can influence the quality and development of fish are the depth of the pond, water pH, temperature and production capacity per m<sup>3</sup>. These conditions may vary according to the species: this information is not part of the scope of the present work, but they are fundamental in the elaboration of a project; as an example, we can comment on the creation of Nile tilapia, which needs an average pH in the range of 7.2, height of the water layer with a depth of one meter, average temperature of 25°C, average cycle is 4 to 6 months for the fish to reach an average size for commercialization and an average production of 15 to 35kg/m<sup>3</sup>

An important fact is water filtration, which can be through phytoremediation, decantation or similar processes, the main factor to be controlled is the ammonia index, which in high concentrations can cause contamination and death of fish.

The cleaning system is one of the most important points, as any accumulation of dirt can contaminate the entire creation, often the cleaning outlet nozzle is central, as in Figure 1, which demonstrates the drainage system for cleaning.



**Figure 1: Drainage system for cleaning**

To assist in the oxygen index of the water, the producers use aerators, (Ex: for 500 m<sup>2</sup> of tank an aerator of 0.5 cv is used on average) that also bring benefits in the ammonia index, when used weekly.

## **MATERIALS AND ACCESSORIES**

These sections discuss the materials and accessories that are needed to construct tank liner systems for agricultural applications.

### **SUSPENDED TANKS**

Suspended tanks are usually made of galvanized sheets or masonry (in this case, preferably in concrete blocks). Among the most used materials for the production of masonry tanks are concrete, cement and reinforced mortar, in some cases the bottom is finished in soil, with only the sides coated. This type of tank is generally used for high density production with high water turnover. A relevant information about the shape of the tank is that some species adapt better in circular tanks, since this shape simulates the movement of water with great similarity to the natural habitat of fish.

In Figure 2, we have an example of an excavated tank, which we can see that was molded with concrete blocks and coated with PVC geomembrane, which helps in the movement of fish and water, consequently, increasing the oxygen level.



**Figure 2: Suspended tank**

Figure 3 shows an example of a suspended tank produced with galvanized sheet, which has excellent mechanical strength and can be moved to another location.





**Figure 3: Suspended galvanized sheet tank**

## **EXCAVATED TANKS**

The construction of excavated tanks complies with the general rules of construction of tanks for other purposes, and there is the possibility of checking the slope of the site to reduce costs with earth moving.

Although the construction techniques of excavated tanks are well known, as mentioned in the geomembrane installation recommendations manual issued by the installation manufacturer, the following best installation practice is important:

The surface to be coated must be flat, continuous and free from all rocks and stones, sticks, roots, sharp objects or debris of any kind that could damage the geomembrane. The surface must be firm, and stable. There should be no standing water, mud, snow and moisture - in this case, geomembrane placement will be allowed. It is also important to check for underground water or the possibility of gas appearing - in both cases, the placement of drains is essential. A 100% visual inspection of the open area should be done.

Being circular, square or rectangular, the excavated ponds are the closest to the natural conditions in which the fish are born, grow and develop, which is beneficial for production. In Figure 4, we have an example of the shape of the tanks, which is configured according to the needs of the project.

As mentioned before, the tanks can have formats that suit the needs of the producer. Figures 5 and 6 represent the rectangular and circular tanks, coated with PVC geomembrane.



**Figure 4: Shape of the excavated tank**



**Figure 5: Circular tank coated with PVC geomembrane**



**Figure 6: Rectangular tank coated with PVC geomembrane**



## **SYSTEM COVERAGE**

The ideal is to make plastic greenhouses to maintain a constant temperature in the breeding sites and we noticed that these greenhouses are more efficient than metal sheet roofs, because the latter do not allow heat to pass through.

## **GEOMEMBRANE PROPERTIES**

One of the main properties of geomembranes in this area is their flexibility and conformability, in relation to supports, whether suspended or ground tanks. Another great property is the ability to produce panels, and many times, depending on the dimensions, they already leave the factory in the exact necessary size, without the need for welding in the field.

## **CONCLUSION**

Among the systems for raising fish in captivity, suspended tanks and ponds lined with geomembranes (here in this case, we comment on the use of PVC geomembrane) show that, in addition to having excellent cost-effectiveness, that is, they are cheap, quick to install and easy to maintain, making it a great solution for raising fish in captivity. It is important to emphasize that the information contained in this document, for the most part, was obtained from the experience of one manufacturer.

## **REFERENCES**

- ANIMAL, Vaccinar Nutrição et al. WHAT ARE THE BEST TYPES OF TANKS FOR FISH FARMING? Nutrition and Animal Health. Sao Paulo, p. 1-2. June 20 2022. Available at: <https://nutricaoesaudeanimal.com.br/tanques-para-piscicultura/>. Accessed on: 20 jun. 2022
- CIPATEX, Group. CIPATEX INSTALLATION MANUAL. Cipatex Group. Cerquilho, p. 1-8. 01 feb. 2022
- FERREIRA, Adriana et al. Construction of ponds: family fish farming. Embrapa. Sao Paulo, 01 Jan. 2012. p. 1-6. Available at: <https://www.embrapa.br/pesca-e-aquicultura/busca-de-publicacoes/-/publicacao/946441/construcao-de-viveiros-piscicultura-familiar>. Accessed on: 20 jun. 2022
- MEDEIROS, Francisco et al (org.). Yearbook 2022: br fish of psiculture. Brazilian fish Sao Paulo, 01 Feb. 2022. p. 1-79. Available at: <https://www.peixebr.com.br/anuario2022/>. Access on: 15 Mar. 2022



## **Five Geotextile Tube Projects Review for Survivability and Performance after Decades in Challenging Environments**

**Thomas Stephens<sup>1</sup>, Nathalia Castro<sup>2</sup>**

<sup>1</sup>Solmax, USA; [tstephens@solmax.com](mailto:tstephens@solmax.com)

<sup>2</sup>Solmax, USA; [ncastro@solmax.com](mailto:ncastro@solmax.com)

### **ABSTRACT**

Engineers, agencies, and owners have been asking the question, “How long will a geotextile tube survive and perform in severe environments?”. This paper will help answer that question by reviewing five geotextile tube projects and review their design, their installation, and their survival and performance over the past 30 years. The first two projects have been in service since 1993; one in the Mississippi River and one along the US Atlantic Ocean shoreline. The third project was installed in Galveston Bay along the Intercoastal Waterway in 2008. In the fourth project, the geotextile tubes are part of the foundation of a container port in Brazil installed in 2011 and the fifth project, completed in 2012, presents the geotextile tubes in combination with a woven geotextile wrapped face retaining wall being used to rebuild and protect a shoreline in Punta Hermosa, Peru. All projects have been monitored for survivability and all are performing as designed.

### **UNDERWATER RIVER CONTROL STRUCTURES - MISSISSIPPI RIVER RED EYE CROSSING, BATON ROUGE, LOUISIANA**

The Mississippi River is one of the most important transportation corridors in the United States carrying approximate 460 million metric tons annually. Below the port of Baton Rouge, Louisiana the US Army COE maintains a depth of 13.7m (45 FT.) to accommodate ocean going ships. Annual dredging operations at numbers of locations are required to maintain this depth. One problematic section Red Eye Crossing, 15 km (9.3 miles) south of Baton Rouge, is where the river widens depositing millions of cubic meters of sediment annually. This required the COE to station a barge permanently at this site to dredge the channel. In 1993 the New Orleans COE district engineering office proposed installing underwater “soft” dikes constructed of sand filled geotextile bags and geotextile container to constrict the width of the Mississippi from 1,200 meters (4,000 ft.) to 600 meters (2,000 ft). By constricting the width in this wide section, the flow increased, thus “self-dredging” the channel reducing the maintenance cost by \$7.5 million per year. Because this area of the river was used as station barges traveling up-river against the bank during transportation stoppage events, traditional rock structures were not recommended that would damage the bottom of barges during the lower water seasons.

Starting in fall of 1993 and completing the project 80 days later. A 12 ft wide and 13 ft deep bin split hull bottom dump barge was used to deploy the 360 containers, which volumes varied from 80 to 550 cy. The barge bin was filled to a depth of about 4-ft. The geotextile container was constructed to fit the dimensions of the barge depending on its position in the dike prism. Container lengths varied from about 12.2 to 35m (40 to 115 ft) and the circumference was maintained at 13.7m (45 ft.). 38,000 geotextile bags with a volume of 3 m<sup>3</sup> (4 yd<sup>3</sup>) each were deployed to construct six underwater soft dikes. The river depths of deployment ranged from 9.2m

to 12.2m (30 ft. to 40 ft.). The geotextile used to fabricate the containers had the following specification: ultimate tensile strength in machine and cross machine direction of 70 kN/m (400lb/in), seam strength of 44 kN/m (250 lb/in) and AOS (Apparent Opening Size) of #30 sieve. The original estimate was that the structures would last 30 years before needing to be replaced. However, after 30 years, the geotextile “soft dikes” are still functioning as designed saving the US Army COE an estimated \$225 million/USD in 1994 dredging cost dollars. Figure 1 shows a Google Earth image from back in 2014 (Fowler et al 1995). Figure 2 shows the current Mississippi river navigation map (Missouri Bend - Red Eye Crossing), which takes into consideration the presence of the six dikes.



**Figure 1. 2014 Google Earth Image of six underwater geotextile soft dikes**



**Figure 2. Current Mississippi river navigation map**

## **SAND DUNE CORE – ATLANTIC CITY, NEW JERSEY**

Alexander Boardman, a railroad conductor, conceived the idea of constructing a boardwalk as a means of keeping sand out of the railroad cars, hotels, and businesses that were starting to be constructed along the beachfront property of Atlantic City, New Jersey. The city used its tax revenues to build a 2.4m (8.0 ft) wide by 1.6 km (1.0 mile) long temporary wooden walkway that was 30 cm (1.0 ft) above the top of the sand dune. It could be dismantled during the winter when tourist departed for home. The original structure ran from the town to the beach and then parallel to the beach. This first section was opened on June 26, 1870. Since that time until the early 1990's, Atlantic City population and popularity grew until The Boardwalk expanded to 12.2m wide and to run from Caspian Avenue at the north end to Fredericksburg Avenue on the south end for 10.7 km (6.7 miles).

Over the years, the beach fronting Atlantic City and in some places including the natural sand dune were totally eroded exposing the hotels and businesses to damage during Atlantic storm events. In 1992, the Philadelphia office of the US Army COE proposed installing a 9.1m (30 ft.) circumference x 1.5m (5.0 ft.) high x 30m (100 ft.) long geotextile tube filled with sand as the core of the sand dune the entire length of Atlantic City.

The geotextile tube installation started in November 1993 (Figure 3) and was completed in February 1994. Where the sand dune was in place, it was opened-up and the geotextile tube

installed. Where the sand dune was eroded, the geotextile tube was installed at the same elevation as the tubes inside the dune. Sand was pumped from the beach shoreline in front of the sand dune to fill the tubes to the 1.5m height. After the filling of all geotextile tubes was completed, sand was imported to cover the geotextile core and establish a natural appearing sand dune. The geotextile tube was constructed of a 70 kN/m x 70 kN/m UV stable polypropylene woven geotextile with an elongation of <20% in both directions (Table 1). Less than two years after installation, Atlantic City was hit by a hurricane in the fall of 1995 that created a lot of wave attack that caused a tremendous amount of shoreline erosion. In Fig. 7 you will note the erosion in front of the geotextile tube sand dune core, but the erosion was stopped at that point. After the storm passed, the maintenance crew recovered the geotextile tube and reestablished vegetation (Figure 4). There was no damage to The Boardwalk of property behind the sand dune. Even though the top of the geotextile tube has been uncovered by wind erosion, the core is still visible and performing as designed (Figure 5).

Over the past 30 years since the Atlantic City geotextile tube sand dune core was installed the structure has survived more than 62 tropical storms, hurricanes, and nor'easters combined that have impacted Atlantic City and the surrounding shoreline area. However, the original geotextile tube structure is still intact and performing as designed. The most severe test occurred in 2012 when Hurricane Sandy impacted the shoreline with a 2.7m (8.6 ft.) storm surge. During the storm the geotextile tube core of the sand dune was not overtopped. There was some sand erosion in front, but there was no undermining of the structure. A recent examination of the site revealed the same results. Figure 6 and Figure 7 show images that were taken in December 2019. The keys to this longevity and performance of this geotextile tube structure are the UV resistance and strength of the woven geotextile, plus the maintenance of the sand dune after storms uncover the core.

**Table 1: Atlantic City Geotextile Tube Physical Properties**

Mechanical Properties	Test Method	Unit	Minimum Average Roll Value	
			MD	CD
Tensile Strength (at ultimate)	ASTM D4595	lbs/ft (kN/m)	4800 (70.0)	4800 (70.0)
Wide Width Tensile Elongation	ASTM D4595	%	8	4
CBR Puncture Strength	ASTM D6241	lbs (N)	2000 (8900)	
			Minimum Roll Value	
Flow Rate	ASTM D4491	gal/min/ft <sup>2</sup> (l/min/m <sup>2</sup> )	30 (1222)	
			Maximum Opening Size	
Apparent Opening Size (AOS)	ASTM D4751	U.S. Sieve (mm)	30 (0.60)	
			Minimum Test Value	
Pore Size 0 <sub>95</sub> <sup>1</sup>	ASTM D6767	microns	555	
Pore Size 0 <sub>50</sub> <sup>1</sup>	ASTM D6767	microns	340	
Factory Sewn Seam	ASTM D4884	lbs/ft (kN/m)	3000 (43.8)	
UV Resistance (at 500 hours)	ASTM D4355	% strength retained	80	

<sup>1</sup> Based on Third Party Testing

Physical Properties	Test Method	Unit	Typical Value
Mass/Unit Area	ASTM D5261	oz/yd <sup>2</sup> (g/m <sup>2</sup> )	11.0 (373)
Thickness	ASTM D5199	mils (mm)	45 (1.1)





**Figure 3. During 1993 installation**



**Figure 4. After vegetation**



**Figure 5. Erosion stopped by geotextile tube sand dune core**



**Figure 6. 2019 Geotextile tube**



**Figure 7. 2019 Note sand erosion**

## **DREDGE SPOIL CONTAINMENT ISLAND – CHOCOLATE BAY, GALVESTON, TEXAS**

The Intracoastal Waterway (ICW) is a 3,000-mile (4,800 km) inland waterway along the Atlantic and Gulf of Mexico coasts of the United States, running from Massachusetts southward along the Atlantic Seaboard and around the southern tip of Florida,



then following the Gulf Coast to Brownsville, Texas. Some sections of the waterway consist of natural inlets, saltwater rivers, bays, and sounds, while others are artificial canals. It provides a navigable route along its length without many of the hazards of travel on the open sea. Today, federal law provides for the waterway to be maintained at a minimum depth of 3.7m (12 ft.) x 30.5m (100 ft.) width for most of its length. To have this consistent depth and width, maintenance dredging is required in many sections. One such section is in West Galveston Bay, Texas where the waterway crosses a natural inlet know as Chocolate Bay. This section of the waterway was completed in 1949 and has had maintenance dredging performed approximately every five years. Originally, there were upland dredge disposal sites available in the area (Figure 8). However, by 2004 all available upland sites in the area were full of dredge spoils. Therefore, the Galveston US Army COE proposed an innovative solution to build a near shore dredge disposal site that would create a wetlands area. The scope of the wetland's creation project required installing 3,000 meters (9,800 ft.) of 9.1m (30 ft.) circumference by 61m (200 ft.) long geotextile tube units to create a 1.5 meter (5.0 ft.) high perimeter dike to contain more than 2.5 million m<sup>3</sup> (3.25 million yd<sup>3</sup>) of dredge material taken from the waterway. The unique feature of this design was the geotextile tubes would be filled with the dredge material taken from the waterway thus creating a beneficial use for approximately 50,000 m<sup>3</sup> (65,000 yd<sup>3</sup>) of dredge spoils.

The geotextile tube units were fabricated from a highly UV stabilized woven polypropylene geotextile with a 78.8 x 109.4 kN/m (450 x 625 lb./in.) tensile strength. The O<sub>50</sub> pore size was 135 micron and the O<sub>95</sub> pore size was 305 microns. With this large range of pore size, a polymer would be required to agglomerate the fine dredged particles to be retained in the geotextile tube. Table 2 shows the woven geotextile mechanical, hydraulic, and physical properties. However, the contractor chose to line the geotextile tube with a non-woven geotextile with a smaller pore size. Construction started in December 2005 and continued into 2006. Figure 9 shows the project completed and Figures 10 and 11 show the project during construction phase.



**Figure 8. 2005 - Upland disposal site before**



**Figure 9. 2006 - Completed disposal site**

**Table 2. Chocolate Bay geotextile tube mechanical, hydraulic, and physical properties**

Mechanical Properties	Test Method	Unit	Minimum Average Roll Value	
			MD	CD
Wide Width Tensile Strength (at ultimate)	ASTM D4595	lbs/in (kN/m)	450 (78.8)	625 (109.4)
Wide Width Tensile Elongation	ASTM D4595	%	20 (max.)	20 (max.)
Factory Seam Strength	ASTM D4884	lbs/in (kN/m)	400 (70)	
CBR Puncture Strength	ASTM D6241	lbs (N)	2000 (8900)	
			Maximum Opening Size	
Apparent Opening Size (AOS)	ASTM D4751	U.S. Sieve (mm)	40 (0.425)	
			Minimum Roll Value	
Water Flow Rate	ASTM D4491	gpm/ft <sup>2</sup> (l/min/m <sup>2</sup> )	20 (813)	
			Minimum Test Value	
UV Resistance (% strength retained after 500 hrs)	ASTM D4355	%	80	
Filtration Properties	Test Method	Unit	Typical Value	
Pore Size Distribution (O <sub>90</sub> )	ASTM D6767	micron	135	
Pore Size Distribution (O <sub>95</sub> )	ASTM D6767	micron	305	
Physical Properties	Test Method	Unit	Typical Value	
Mass/Unit Area	ASTM D5261	oz/yd <sup>2</sup> (g/m <sup>2</sup> )	16.4 (556)	
Thickness	ASTM D5199	mils (mm)	70 (1.8)	



**Figure 10. Construction starting**



**Figure 11. Continuing into 2006**

The geotextile tube perimeter dike was completed in late 2006 and has been receiving maintenance dredging spoils since that time. As can be viewed in Fig. 12, the nearshore dredge disposal site is beginning to fill up with dredge spoils. As it fills up, it is becoming a newly created wetlands for a wildlife habitat. In addition, the new wetland is acting as an erosion protection to the original shoreline that was experiencing erosion due the large volume of barge traffic in the waterway and because of the number of storms that routinely impact the coast. Since the construction was completed in 2006, 32 named tropical storms and hurricanes have hit the Texas Gulf Coast and impacted the site with storm surges and wave attack. The strength of the woven geotextile and its UV protection properties have contributed to the performance of the structure over the past 16 years. In this location the most severe test occurred in 2008 when Hurricane Ike directly passed over the site with a 2.4m (8 ft.) storm surge. During the storm surge the geotextile tube structure was overtopped. However, there was no damage to or undermining of the structure.



**Figure 12. 2020 Chocolate Bay near shore dredge spoil site becoming wetland habitat**

## **OCEAN CONTAINER PORT – SANTOS, SP, BRAZIL**

Embraport (Empresa Brasileira de Terminal Portuarios S.A.) is one of the largest multiple use private ports of Brasil and its construction started in 2011 in Santos, Sao Paulo, Brazil by one of most relevant Brazilian construction and engineering companies. The construction challenges were multifaceted. However, two were the most challenging. First, more 50% of the footprint of the project was located at sea level in a tidal marsh. Second, more than 600,000 m<sup>3</sup> (785,000 yd<sup>3</sup>) of contaminated sediments were required to be dredged from in front of the port site to create the depth for container ships, and to create the depth for the port entry channel. There was no upland disposal site for the dredged material other than on the existing footprint. If this area was used, the remaining site footprint would make the project financially not feasible. Therefore, the Brazilian contractor chose to adopt geotextile tube containment and dewatering technology to solve these two most construction challenges.

The solution was to construct an earthen dike around the perimeter of the project that was in the tidal marsh and pump the area dry. Next, geotextile dewatering tubes would be placed to contain and dewater more than 600,000 m<sup>3</sup> (785,000 yd<sup>3</sup>) of dredged material. This contained and dewatered volume will replace the same volume of imported select fill. Over the entire geotextile tube fill, a 1.0m (3.2 ft.) thick layer gravel will be placed followed by 20 cm (8 in.) thick concrete pavers. This will be the final surface on top of which 5 layers of shipping containers can be stacked (Stephens et al 2013). Figure 13 shows a cross section with the final elevations for each phase of the project, including the 5 ton/m<sup>2</sup> surcharge to accelerate the settlements. Designed to support a maximum load of 91tons (weight equivalent to the 5 layers of shipping containers stacked) or 185.7 ton/m<sup>2</sup> distributed to a 70cm x 70cm area, the foundation had to be geotechnically studied considering two verifications: the maximum vertical stresses applied to the pavement considering the presence of the reinforcement of the woven geotextile of the geotextile tubes and bearing capacity against puncture of the deep subgrade layer, which was improved with the presence of the high strength woven geotextile encapsulating and dewatering the dredged sediments. Figures 14 and 15 show the schematics for both verifications.

Construction on the port began in 2011 by constructing the perimeter dike as detailed in Figure 16. Next, three cells were created behind the perimeter dike in which 36.5m cir. x 91m long (120 ft. cir. x 300 ft. long) high strength woven geotextile containment and dewatering tubes were placed and filled with the contaminated dredged material (Figure 17). The geotextile tube units



were fabricated from a highly UV stabilized woven polypropylene geotextile with a 78.8 x 109.4 kN/m (450 x 625 lb./in.) tensile strength. The O<sub>50</sub> pore size was 135 micron and the O<sub>95</sub> pore size was 305 microns. The effluent draining from the dewatering tubes during the construction phase would be captured, treated and released back into the Bay of Santos. Finally, the geotextile tubes filled to 2.5m (8.2 ft.) were covered over and the final pavement was added (Figure 18). The project was completed in 2013 and opened for business saving the client more than \$60 million/USD in construction cost by using geotextile tubes versus importing select fill material and reducing the project execution time. The project has been in continuous operation since opening and has handled more than 12 million TEU's (twenty-foot equivalent container units). Figure 19 shows a photo that was taken in July 2022. The current Embraport configuration is at total capacity and has operated for 10 years without any interruption due to the strength of the pavement and underlying filled geotextile tubes containing the dewatered fill material that supports the heavy traffic and container loads stacked five layers high.

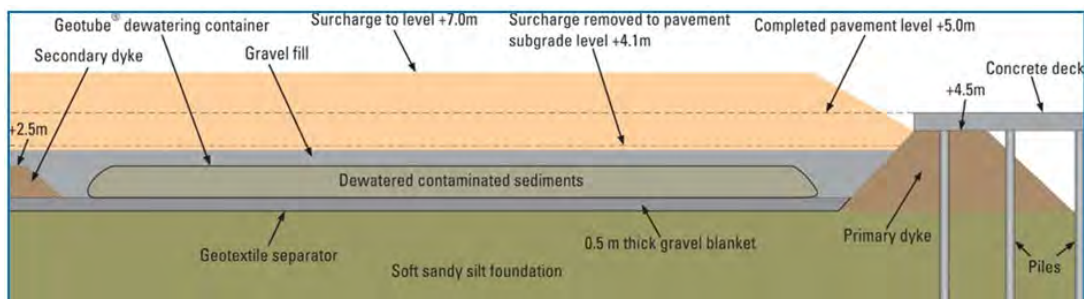


**Figure 13. Embraport designed cross section**

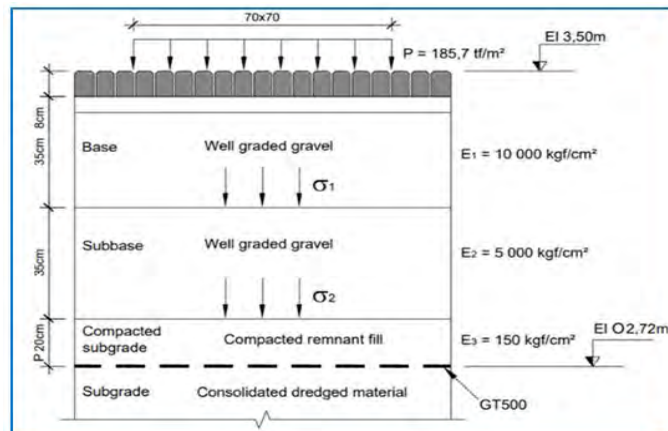


**Figure 14. Verification of the maximum stress applied to foundation**



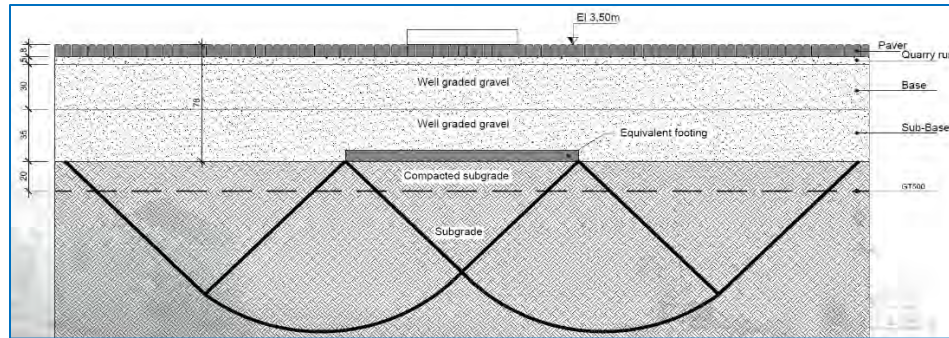


**Figure 15. Verification of bearing capacity of the foundation**



**Figure 16. Partially constructed perimeter dike**

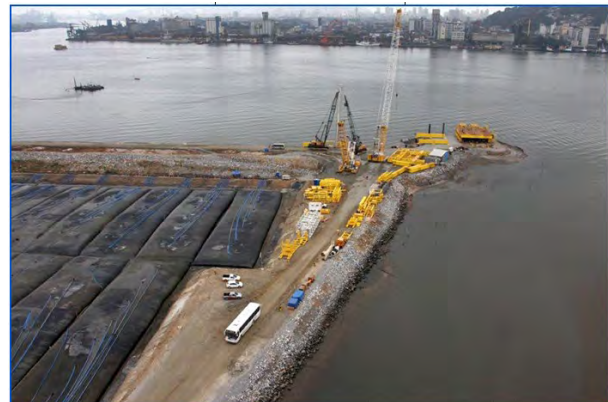


**Figure 17. Geotextile tubes containing and dewatering the dredged sediments from the Bay of Santos**



**Figure 18. Covering the geotextile tube containers**

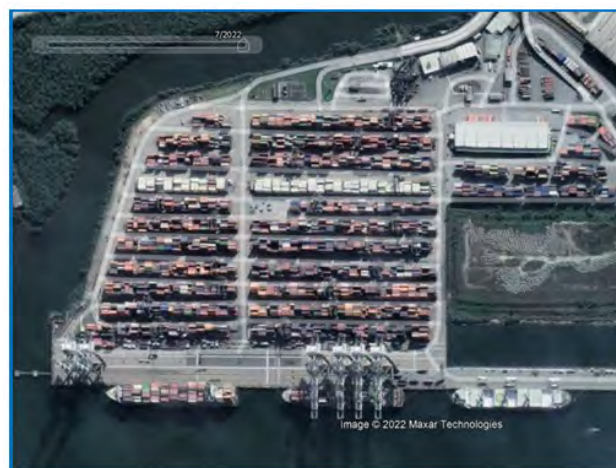


**Figure 19. In 2022 - Embraport 10 years after construction.**

## SEA WALL REVETMENT – PUNTA HERMOSA, PERU

Punta Hermosa is a seaside town with a population of approximately 23,000 located on the Peruvian coast of the Pacific Ocean 42 km (26 miles) south of Lima. The draw are the beaches but there are many homes and businesses built on the bluffs above the shoreline in many areas. Over the years the toe of the bluff has eroded. One location had significant erosion due to the many storm events impacting the coast of Peru as can be seen in Figure 20. The Punta Hermosa city engineers issued an RFP (Request For Proposal) from local engineers and one firm proposed a geosynthetic solution of geotextile tubes and a wrapped face retaining wall. The proposal was accepted due to the emergency requiring immediate protection for the residences and businesses located at the top of the bluff in danger of collapsing into the ocean (Figure 21). The design included installation of two high strength woven geotextile tube layers fabricated from a 200 kN/m x 200 kN/m (1,142 lb.in.) high tenacity woven geotextile followed by a vertical woven geotextile (70 kN x 70 kN) wrapped face wall the same geotextile referenced in Table 1. The total structure height ranged from 7 to 8m (23 to 26 ft.). Figure 22 shows the designed typical cross section. The construction starting in April 2012 was challenging, but the project was completed in two months saving more than ten residences and businesses. See Figure 23 for the construction details. In 2016, a concrete walkway was added of the top of the geotextile tube and wrapped face wall. The structure after 10 years is still performing and protecting the homes and businesses.

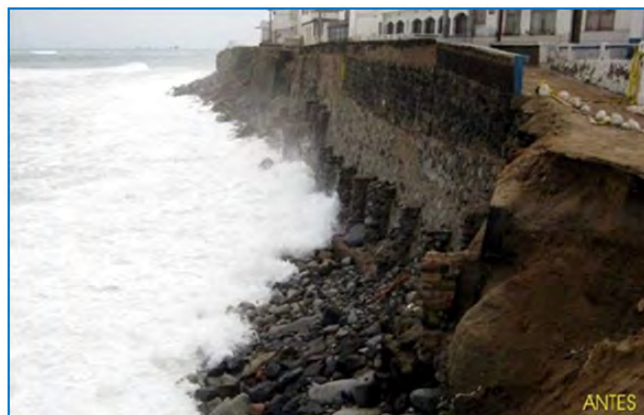


**Figure 20. Punta Hermosa Bluff Erosion**

**Table 3. Punta Hermosa Geotextile Mechanical and Physical Properties**

Mechanical Properties	Test Method	Unit	Minimum Average Roll Value	
			MD	CD
Wide Width Tensile Strength (at ultimate)	ASTM D4595	lbs/in (kN/m)	1142 (200)	1142 (200)
Wide Width Tensile Elongation	ASTM D4595	%	20 (max.)	20 (max.)
Factory Seam Strength	ASTM D4884	lbs/in (kN/m)	913 (160)	
CBR Puncture Strength	ASTM D6241	lbs (kN)	4000 (17.8) <sup>1</sup>	
UV Resistance (% strength retained after 500 hrs)	ASTM D4355	%	85	
Hydraulic Properties	Test Method	Unit	Minimum Average Roll Value	
			30 (0.60)	
			20 (815)	
			0.35	
Physical Properties	Test Method	Unit	Typical Value <sup>1</sup>	
			33 (1119)	





Figure 21. Collapsing shoreline required immediate protection

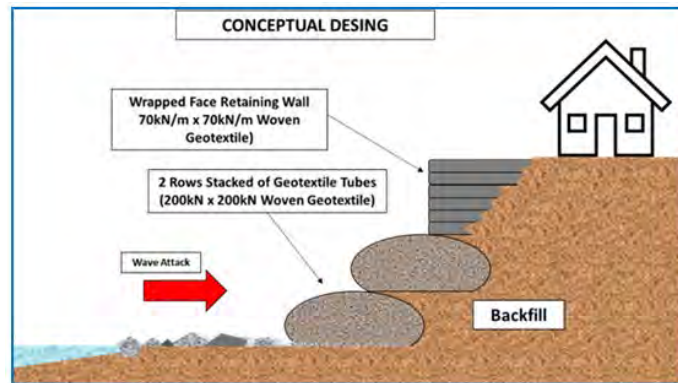


Figure 22. Project typical cross section.



Figure 23. Punta Hermosa erosion protection project construction sequence

In spite of being located in a seismic active zone, the geotextile tube and wrapped face retaining wall has remained stable without experiencing any liquefaction damage. Also there has been no damage due to the continuous wave attack.

## CONCLUSION

For the past 30 years geotextile tubes structures have been installed in many applications around the world ranging from very large commercial projects protecting billions of dollars of property to small projects protecting family homes and businesses. In all the case histories highlighted above in this paper, the environments were harsh and conditions that the geotextile tubes were subjected to were severe. The functioning of the geotextile tubes in each of the five projects provides irrefutable documented evidence of survivability and performance after decades in these challenging environments. These are just a few examples of many projects installed around the world where geosynthetic products present a sustainable life expectancy providing robustness, real performance, and viability over extended periods of time.

## REFERENCES

- Fowler, J., Toups, D., Duarte, F., and Gilbert, P. (1995). Geotextile contained dredged material, Red Eye Crossing, Baton Rouge, LA, Proceedings, Western Dredging Association 16<sup>th</sup> Technical Conference, 28<sup>th</sup> Annual Texas A&M Dredging Seminar, University of Wisconsin Sea Grant Dredging Workshop, May 23-24, 1995, Minneapolis, MN.
- Stephens, T., Melo, L. C. Q. C. (2013), Beneficial Use of Dredged Contaminated Sediments Using Geotextile Tube Technology at a Container Port in Santos, Brazil, *Geosynthetics 2013*, Long Beach, California, April 1-4.



## **Lessons Learned from Three Failures**

**R. D. Holtz, PE, PhD, D.GE, Dist.M.ASCE<sup>1</sup>**

<sup>1</sup>University of Washington (Emeritus), Seattle; holtz@uw.edu

### **ABSTRACT**

Three failures involving geosynthetics are described. The first is a geosynthetic-reinforced steep slope in Taiwan that failed twice, the first during construction and the second due to a major earthquake. The second case involved an approximately 19m tiered modular-faced geosynthetic-reinforced wall that failed shortly after completion. Multiple factors were involved in this catastrophe. The third failure was an unusual application: a silt curtain, that failed very soon after installation. As is true of most failures, all had multiple causes, but only this one, the silt curtain, was due to the incorrect selection of the geosynthetic. Each case is described in some detail, with observations about each failure, post-failure investigations of the soils and geosynthetics involved, and other factors that may have influenced the failures. Finally, valuable lessons learned from each case are given.

Note: These cases were presented orally at the GeoAmericas 2020 conference in Brazil, but it was never published.

### **CASE 1: STEEP GRS SLOPE IN TAIWAN**

Because geosynthetic reinforced soil (GRS) structures have generally performed quite well under seismic conditions, this failure offered a rare opportunity to investigate the performance of a full-scale GRS structure after a major earthquake. Important features of this failure include:

- ~80m high steep cut slope with a 40m high geogrid GRS zone designed to stabilize the cut (Figures 1 and 2)
- First failure occurred during construction
- Second failure was due to the Chi-Chi magnitude 7.3 earthquake (Figures 1 and 2)
- The site was ~20km from the epicenter; peak ground acceleration > 0.5g
- The ~40m GRS zone used on-site lateritic soil as backfill (not free draining)
- No drainage system behind the reinforced section.

Based on field observations, several factors probably contributed to the failure. Among them were separation between adjacent geogrid layers, geogrids pulling out of backfill, and collapse of the wrapped face. Reinforcement layer spacing was about 1m, which may have been too large. The backfill in the reinforced section was poorly compacted.

Material properties were determined by laboratory tests on samples of soils and geosynthetics. Two types of geogrids were used, and their design tensile strengths were 60 and 104kN/m, or much lower than the wide width ultimate tensile strengths we found. The designers

used combined reduction factors for installation damage, and chemical and biological degradation of 3 to 4, which is common practice for GRS in Taiwan.



**Figure 1. Photo of the failed slope.**

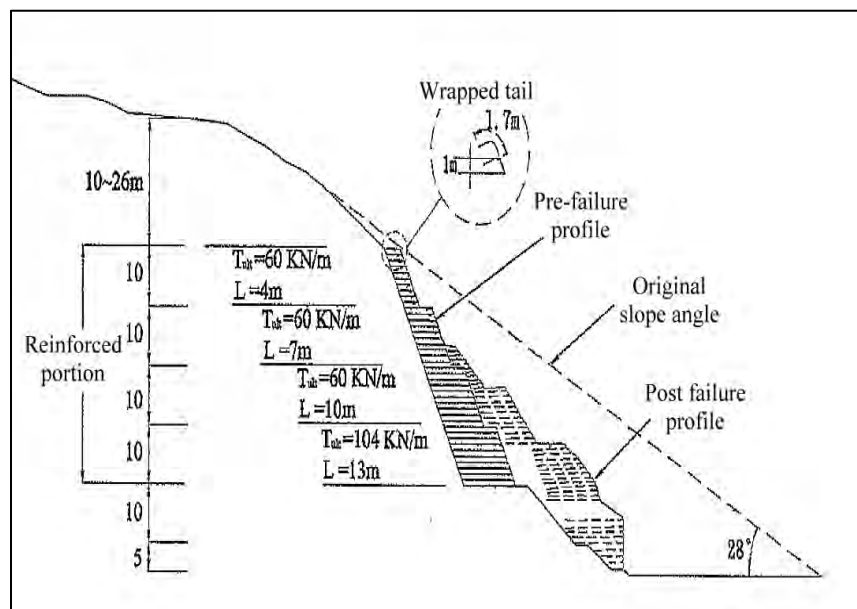


**Figure 2. Cross-sectional view of the original slope and the failed GRS section. The small insert shows a detail of the wrapped face.**

Conclusions and important lessons learned from these investigations include:

- The steep (~2V:1H) slope was under-reinforced.
- Geogrid embedded lengths were too short for an 40m high GRS structure
- Vertical 1m grid spacing also contributed to the observed face instability
- Butt joints or small overlap of geogrids perpendicular to the face was insufficient to prevent separation and failure of the face
- Poor compaction of backfill in failed section
- No drainage system behind reinforced fill section (in a semi-tropical climate?)
- Observed slump-type failure mode is similar to those observed in shaking table model tests and FEM analyses
- Even with poor backfill compaction, an under-reinforced design, and after being subjected to very strong EQ shaking, the failure was a slump-type rather than a catastrophic landslide.

## **CASE 2: ~19m TIERED MODULAR-FACE GRS WALL**

An approximately 19m high GRS modular block faced wall, with five tiers, failed shortly after it was completed. The wall supported a large parking area in front of the entrance of the store. The owner, a big box nationally known chain store, insisted on shrubbery and other plants on the tiers that required a watering system of 50mm plastic pipes. This watering system later turned out to be defective and did not have an automatic system shut-off valve. Excessive water flow in the tiers undoubtedly contributed to the face instability. Backfill in reinforced and retained zones was obtained from grading of nearby hillsides but unfortunately it was not free draining. Later a slow-moving, deep-seated global failure occurred due to high GWT caused by leaks in 250 and 400mm water mains, and by problems with a 0.9m storm drain. The wall is shown in Figure 3 a few days after the failure.



**Figure 3. The failure shown several days later.**

There were many factors that contributed to the failures; all provide important lessons for engineers involved in GRS design and construction.

1. Owner insisted, over objections of the geotechnical engineers, to use local backfill in the reinforced zone—it was not free draining!
2. Local backfill materials were poorly sorted; contained zones of large particles as well as fine-grained soils.
3. Compaction of the backfill was questionable; test pits found several zones of loosely compacted materials.
4. Inadequate internal drainage.
5. Leaks in the irrigation system (50mm pipes) in face tiers.
6. The modular facing panel/counterfort system was very sensitive to water; the counterforts pulled out before any other mode of failure.
7. The face panels also were not positively connected to the geogrids.
8. Continuous leakage of large water mains (250 and 400mm) and by problems with a 0.9m storm drain in the backfill caused temporary high groundwater in the area of a deep-seated failure
9. Contractor did not comply with construction plans
10. Lack of coordination between owner and civil and geotechnical engineers
11. Poor coordination between prime contractor and subcontractors

It's sad, but this failure could easily have been prevented or avoided.

### **CASE 3: TURBIDITY CURTAIN TO CONTAIN CONTAMINATED SEDIMENTS**

This case is the only one of the three that was due to the incorrect selection of the geosynthetic. The site was located at the end of long salt-water fjord with large tidal fluctuations in Puget Sound, Washington. The site was undergoing remediation of an abandoned wood treatment (creosote) plant that left contaminants, mostly NAPLs, in the subsoils that had migrated into the groundwater and then into the nearshore sediments. Remediation involved dredging and on-site disposal of 31,000m<sup>3</sup> of contaminated sediments, and then capping the disposal site. Key features are shown in Figure 4



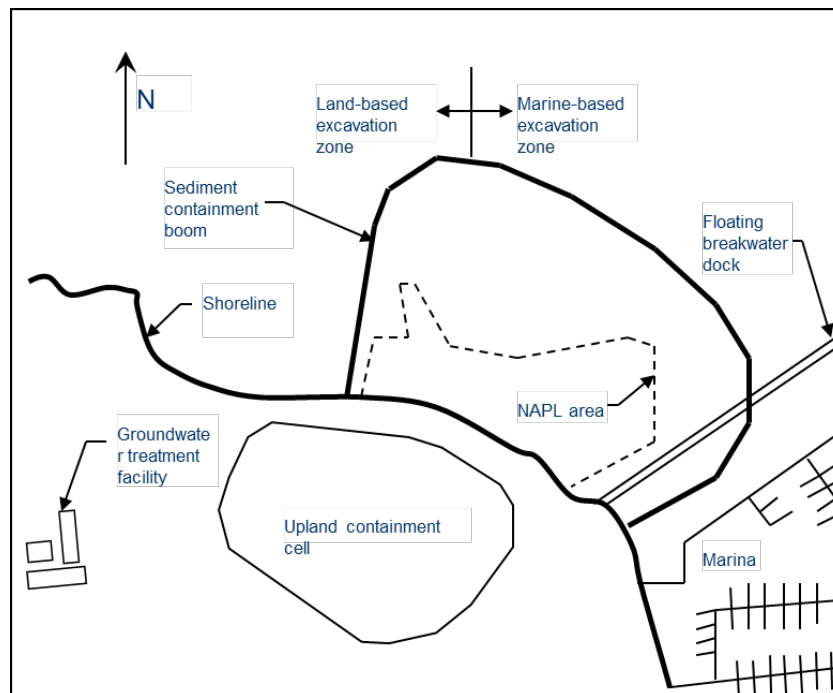


**Figure 4. Plan view of site showing dredging and containment areas; not to scale (Carscadden, 2002)**

To prevent the migration of contaminated sediments into an adjacent waterway during construction, a turbidity containment boom supporting a geotextile curtain was deployed (Figure 5). The boom supplier selected a 540g/m<sup>2</sup> polypropylene needlepunched staple filament nonwoven geotextile for the curtain component of the containment system. Also shown in Figure 5 is how the curtain is anchored to the seafloor with concrete blocks.

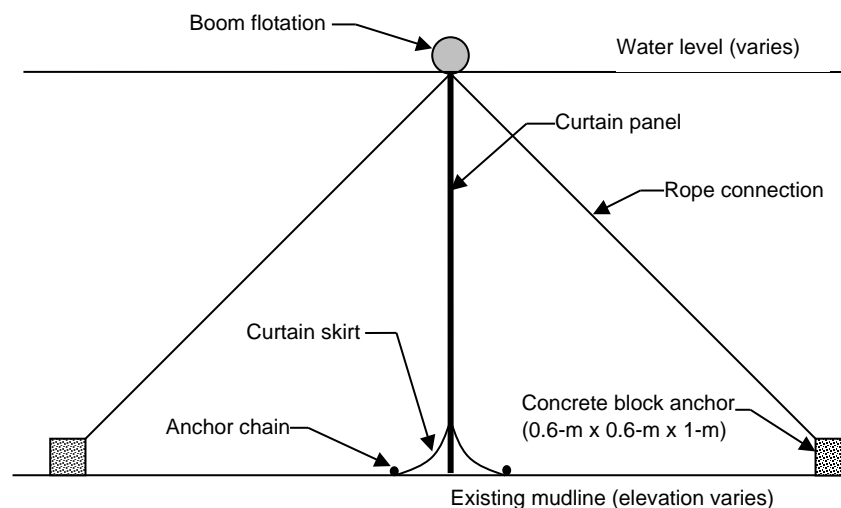


**Figure 5. Typical section of containment boom, curtain, and anchor system.**

Unfortunately, only a few hours after completing the deployment, the curtain billowed out with the outgoing tide, and flow was diverted over the boom. Later, divers found large tears in the curtain. The boom supplier suggested that the float be temporarily weighted down so that large “windows” could be cut into the curtain.

So, why did it fail? First, the designers assumed a tidal fluctuation of 6.4-m with half the geotextile openings clogged (i.e.,  $FS = 2$ ) and they used the manufacturer’s value of the permittivity  $\psi = 0.7 \text{ sec}^{-1}$ . Second, the failure must have occurred because the geosynthetic had clogged and was unable to endure the high pressures imposed by the high tide. That is why it failed in tension. Thus, we focused our investigation on the strength and hydraulic properties of the geotextile. We were able to obtain both virgin as well as deployed samples of the geotextile, so we could test for their wide-width strength (ASTM D 4595) and hydraulic properties, specifically permittivity and clogging potential (ASTM D 4491). Interestingly the deployed material was noticeably contaminated with reddish-brown organic or biological materials. The difference in the odor between the deployed and virgin samples was very strong!

Test results indicated negligible differences in strength and stress-strain behavior, but about an order of magnitude reduction in permittivity for the deployed material as compared to the virgin material. These results are shown in Figure 6. Also shown are the designer’s choices of permittivity.

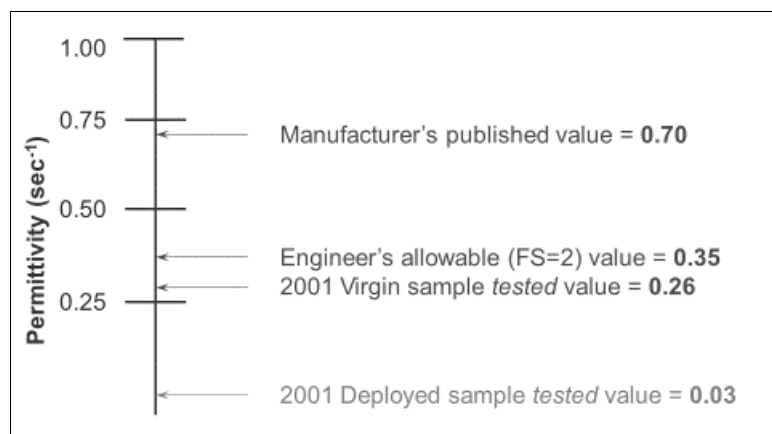


**Figure 6. Comparison of permittivity results; mean values of our laboratory tests are shown.**

As with the other cases, several factors contributed to the failure of the curtain. This was a critical application, an approximately \$0.5 million containment system, with severe hydraulic conditions, tidal fluctuations greater than 6m, and *no* laboratory tests were done. Designers did not consider possible clogging of the geotextile, nor any consequences of possible clogging and poor flow through it, even though they were certainly aware of the high tides at the site.

Had the designers followed the FHWA (Holtz, et al., 2008) Filter Design Procedure recommendation to use a  $FS \geq 10$  for critical and severe conditions *and* to do laboratory tests on the candidate geotextiles, the design might have worked. See Fig. 6. At least the tearing of the geotextile may not have occurred. Of course, with successive high tides, two per day, clogging may have accelerated the effect of repeated high tensile stresses on the geotextile, and failure may have occurred later on anyway.

So what would have been a more suitable geotextile for this curtain? A very strong slit-film with wide openings or a woven monofilament may have provided the necessary permittivity and tensile strength. Obviously, a laboratory testing program is warranted for such a critical application.

## **CONCLUSIONS...FOR ALL THREE CASES**

Hindsight is always perfect; however, all three failures could have been avoided by correct design, correct soil and geosynthetic properties, and by using common sense.

And by now it should be obvious that owners, designers, civil engineers, geotechnical specialists, contractors, and material suppliers all need to work together as a team and not as adversaries, if failures such as these are to be avoided.

## **ACKNOWLEDGEMENTS:**

Taiwan coauthors and colleagues: Steve Kramer, University of Washington, Wayne Hsieh, National Pingtung University of Science and Technology, A-B Huang, National Chiao-Tung University, Wei Lee, Taiwan Construction Research Institute,

Prescott GRS wall: Dan Steussy, Opterra, inc., San Diego

Turbidity curtain: Mike Harney, Shannon & Wilson, Seattle; Reid Carscadden, Integral Consulting, Seattle

## **BIBLIOGRAPHY**

Harney, M. D. and Holtz, R. D. (2005) "Case History: Failure of the Geotextile Turbidity Curtain", *Proceedings of the NAGS2005/GRI-19 Cooperative Conference*, Las Vegas, Nevada (CD-ROM).

Holtz, R. D., Christopher, B. R., and Berg, R. R. (2008) *Geosynthetic Design and Construction Guidelines*, U.S. Federal Highway Administration, National Highway Institute, Washington, D. C., Publication No. FHWA-NHI-07-092, 592 pp.

Holtz, R. D., Kramer, S. L., Hsieh, C. W., Huang, A. B., and Lee, W. F. (2001) "Failure Analysis of an 80 m High Geogrid Reinforced Wall in Taiwan", *Proceedings of the 15th International Conference on Soil Mechanics and Geotechnical Engineering*, Istanbul, Turkey, Volume 2, pp 1159-1162.

Luft, R. (2012) "Lowe's of Prescott, AZ, 6 April 2012", Final Report, SGH Project 077372, 191 pp + appendices.

Steussy, D. K. (2012) "Geotechnical Investigation of Retaining Wall Failures, Lowe's HIW, inc. v. Thomas James

Civil Design Group. et al.", Report by Opterra, Inc., San Diego, CA, 190pp.

Steussy, D. K. (2012) "Kleinfelder Mediation Presentation, Lowe's HIW, Inc. v. Thomas James Civil Design Group, et al.," (109 Powerpoint slides)

## **Lining A Highly Irregular Vertical Wall with Polyurea/Conductive Geotextile Geomembrane**

**Dave Martin, P. Eng.<sup>1</sup> and Rohit Sati, M.Sc., MBA<sup>2</sup>**

<sup>1</sup>Quantum Technical Services Ltd, 15 Riel Dr. St. Albert, AB, Canada T8N 3Z2;  
[dmartin@quantumchemical.com](mailto:dmartin@quantumchemical.com)

<sup>2</sup>Layfield Group, 17720 – 129 Ave NW, Edmonton, AB, Canada T5V 0C4  
[Rohit.Sati@layfieldgroup.com](mailto:Rohit.Sati@layfieldgroup.com)

### **ABSTRACT**

Vertical walls for a fire water containment pond were cut into bedrock and covered with shotcrete. The shotcrete was anchored into the bedrock at roughly 1m intervals. This created a highly uneven surface both on the macro level (with large bulges in the shotcrete at the anchor points), and at the micro level (with smaller dimples in the surface). A conductive geotextile was hung down the vertical walls, and anchored in place with mechanical connections. A spray applied fast set polyurea was applied over the geotextile to create a composite liner. Once filled the pond was over 9 m deep and the water pressure forced the liner to completely conform to the convoluted shape of the wall. The polyurea/geotextile composite liner was able to stretch over and into both the large scale and small scale irregularities in the subgrade. The conductive geotextile allowed spark testing of the composite liner before the pond was filled and after initial filling when the pond was drained. Spark testing was able to demonstrate that the composite liner provided an effective water barrier in this application.

### **INTRODUCTION**

Lining a highly irregular subgrade presents challenges to the containment designer both from a standpoint of conforming to the substrate under pressure, and anchoring effectively to the substrate to avoid large scale movement of the liner during the construction and service phases of the ponds life. Often a floating liner design is chosen, consisting of a geotextile backing and spray applied polyurea lining system. The advantages of a floating liner design include the ease of anchoring the system to the substrate in a water tight fashion. The geotextile alone can be mechanically attached to the substrate at regular intervals, and then the geotextile and anchors are sealed with the application of polyurea. A pre-sprayed composite of polyurea and geotextile can also be mechanically attached to the substrate, with additional polyurea added to cover the anchor points and make them water tight. Fast set aromatic based polyureas are available that possess great toughness and elongation capabilities on their own. The elastic capabilities of polyurea (the ability to elongate without “yielding”, or being damaged) are reduced somewhat when a composite of polyurea on geotextile is made. It is important when designing a polyurea floating liner to test the physical capabilities of the particular polyurea/geotextile combination to be used.



## CONSTRUCTION

The design uses a floating polyurea geomembrane (the finished liner is shown in Figure 1), attached to an irregular and uneven shotcrete wall. This style of liner involves mechanically attaching the geotextile to the wall at individual points and spraying over the textile and attachment hardware with polyurea. The use of a floating polyurea geomembrane to seal uneven, irregular concrete is routinely done in industry (Leonard, 2014).

The conductive geotextile consists of a conductive layer which is needle-punched into a nonwoven geotextile. This provides a conductive surface to facilitate spark testing, and a nonwoven geotextile surface (the white surface visible in Figures 2 and 3). Nonwoven geotextile is routinely used to create composite liners with polyurea, as it has a 3 dimensional felt like structure which absorbs a small amount of a fast set polyurea creating a true composite system.

The geotextile was hung vertically on the walls prior to coating, and was mechanically tacked in place using 1.5" nail attachments. An additional layer of black nonwoven geotextile was hung between the shotcrete and the conductive geotextile primarily to protect the composite liner from the rough subgrade. The vertical walls are made of porous and uneven shotcrete put in place on bedrock. A drain system exists between the shotcrete and the bedrock.



**Figure 1. The Finished Floating Liner**

## INSTALLATION OF THE POLYUREA

The geotextile was deployed and attached to the wall in sections. An effort was made to coat the geotextile with polyurea in a timely fashion, and not leave it exposed to the elements. As each section of polyurea was applied, a spark test was done to detect any voids in the polyurea. Polyurea has a recoat window, typically 24 hours in length. Fresh polyurea can be applied to polyurea that is within its recoat window and it will adhere quite well without any additional surface preparation. The application of the polyurea involved seaming the sections of conductive geotextile together as they hung vertically on the wall. An effort was made to install the polyurea in a continuous fashion, ensuring each section was joined to the previous one within the recoat window. This was not always possible due to weather interruptions. When sections needed to be joined outside of the recoat window a surface preparation method of abrasion and priming was used for the aged polyurea.



**Figure 2. Applying Polyurea to the Conductive Geotextile**





**Figure 3. Conforming the Geotextile into A Corner**

The finished floating liner faced several challenges upon filling the pond. The anchoring of the conductive geotextile to the subgrade created stress concentrations around the anchor points. The areas between the anchor points involved bridging and spanning between the large bulges in the shotcrete. The composite liner would have to stretch over these large scale bulges and stress concentration points and conform tightly to the subgrade under the head pressure of the filled pond. On a small scale the subgrade was deeply dimpled and rough, under the head pressure of 9 m of water the composite liner would have to stretch and conform on a small scale to these dimples. The pond was filled and drained within the span of 30 days, and visual inspection of the composite liner after the filling/emptying cycle confirmed the composite liner selected for the walls of this project was able to substantially meet these challenges. A second round of spark testing after the pond was emptied did show some thinning and possible pinholes had developed around some of the anchor points, and these areas were touched up with additional polyurea.

## CONCLUSION

A floating liner design, consisting of a polyurea/geotextile combination, which is mechanically attached at regular intervals over the subgrade is a strong design option when faced with an irregular or damaged subgrade. In this case a highly irregular and challenging vertical subgrade was lined with a floating polyurea/geotextile liner in such a way that allowed the installation to be spark tested to detect any flaws in the completed system.

## REFERENCES

Leonard, K. (2014) Polyurea “Loose” Liners: A Floating fix for Cracked Concrete Secondary Containment, Journal of Protective Coatings & Linings (February).

<http://www.paintsquare.com/archive/?fuseaction=viewarticleid=5227>

(link requires a subscription)



## Mitigation of Cracks in Flexible Pavements with Expansive Subgrade Using Geosynthetics: A Case Study in Austin, Texas

Natalia S. Correia, Ph.D.,<sup>1</sup> V. Vinay Kumar, Ph.D.,<sup>2</sup> and  
Jorge G. Zornberg, Ph.D., P.E.<sup>3</sup>

<sup>1</sup>Civil Engineering Department, Federal University of Sao Carlos, Sao Paulo, Brazil; e-mail: [ncorreia@ufscar.br](mailto:ncorreia@ufscar.br)

<sup>2</sup>Department of Civil, Architectural, and Environmental Engineering, The University of Texas at Austin, Austin, TX; e-mail: [vinay.vasanth@utexas.edu](mailto:vinay.vasanth@utexas.edu)

<sup>3</sup>Department of Civil, Architectural, and Environmental Engineering, The University of Texas at Austin, Austin, TX; e-mail: [zornberg@mail.utexas.edu](mailto:zornberg@mail.utexas.edu)

### ABSTRACT

Geosynthetics have been effective in minimizing the detrimental effects of expansive soil subgrades on the performance of flexible pavements. This study presents a case history on the use of geosynthetic reinforcement to minimize cracks in a flexible pavement with an expansive soil subgrade in an urban roadway in Austin, Texas. The crack mitigation techniques included use of a fiberglass geogrid reinforcement at the interface of pre-existing asphalt layer and the overlay. Specifically, the geogrid was placed directly over the severely cracked surface, after cleaning dirt, dust and other deleterious material, and a trackless tack was then applied prior to the installation of the asphalt overlay. The test sections with and without geogrid reinforcement was monitored for over a period of 8 years and it was observed that the longitudinal edge cracks reappeared along the unreinforced section. While, the geosynthetic reinforced sections did not show any signs of crack development during the monitoring period. Overall, the field monitoring program demonstrated that the use of geosynthetic reinforcements could significantly help in mitigating the longitudinal cracks associated with volumetric changes in flexible pavements built over an expansive soil subgrade.

### INTRODUCTION

Globally, expansive soils create serious engineering problems and economic losses in several countries. In the U.S., the Department of Agriculture estimates that 50% of the households are constructed on expansive soils. The U.S. Department of Agriculture (USDA) estimates that 50 percent of the houses in the U.S. are constructed over expansive soils, and the American Society of Civil Engineers (ASCE) estimates that one-quarter of all homes in the U.S. are affected by the volumetric changes associated with the expansive soil (Virginia Department of Mines, Minerals and Energy, 2021). According to ASCE, historically, expansive soils account for more home-related damage each year than floods, tornadoes, and hurricanes combined. A similar situation happens in China, where expansive soils are responsible for an economic loss of about 15 billion US dollars every year (Wang, et al. 2016). On the other hand, it is estimated that 20% of the surface soils in Australia are expansive and six out of their eight largest cities have large expansive soil deposits posing them serious problems (Delaney et al, 2005). Specifically, in the case of lightweight structures, such as pavements, where there is no construction load above the expansive soil layer to compensate clay swelling, the high volumetric changes due to the seasonal moisture

fluctuations affects the stability and performance of pavement layers resulting in undulations and cracks. According to Zornberg et al. (2010), these ground movements are observed in the form of heave during wet season and shrinkage during dry season. A pavement section built over an expansive soil subgrade may have a compromised quality and performance life. Specifically, the load bearing capacity, fatigue performance, roadway serviceability and safety may be compromised. Problems involving the appearance of longitudinal cracking on pavements over expansive subgrade have been reported (Luo and Prozzi, 2010; Mezhoud et al. 2016; Zornberg and Roodi, 2021).

Several techniques that mitigate the cracking in flexible pavements have been evaluated. Traditionally, the problems associated with flexible pavements built over expansive soil subgrades have been addressed by completely replacing these soils or by stabilization techniques (Zornberg, 2010). Among them, excavation and replacement, pre-watering, chemical or mechanical modification using lime or cement stabilization and moisture barriers are the most common and economic alternatives. The construction of flexible pavements over expansive subgrades treated with lime has been the most common alternative in regions such as central Texas. However, situations of compromised performance due to the appearance of longitudinal cracks over lime-treated subgrades are also common. Figure 1 presents an example of a typical scenario of longitudinal cracks in flexible pavement with lime-treated expansive soil subgrades in Taylor, Texas. As shown in the figure, the longitudinal cracks initiated from expansive subgrades, subsequently propagated into the asphalt surface through the 10% lime-treated base layer.



**Figure 1. Examples of longitudinal cracks from expansive subgrades, in Taylor, Texas.**

On the other hand, geosynthetic reinforcements have been effective in minimizing the detrimental effects of expansive soil subgrades on the performance of flexible pavements, mainly on the mitigation of longitudinal cracks (Gupta 2009, Zornberg et.al 2008). Comprehensive laboratory and field investigations have been conducted to evaluate the ability of geosynthetic reinforcements stabilizing the expansive subgrade and enhancing the flexible pavement performance. Dessouky et al. (2015), conducted a field study involving 14 years of performance and condition monitoring of various treatment techniques and reported that geogrid reinforcement

combined with lime-treatment of expansive subgrade was an effective repair at areas with low to moderate plasticity subgrade soil. While, Roodi and Zornberg (2020) conducted an extensive field study in Texas (9 years of wet and dry season cycles) and reported that the geosynthetics restricted the development of longitudinal cracks in low volume roadways built over an expansive clay subgrade that is subjected to high environmental loads. In addition, they reported that the performance improvement expected from the implementation of geosynthetic stabilization in roadways founded on expansive clays may be due to the stiffness of the soil-geosynthetic composite. On the other hand, Zornberg and Roodi (2021) suggested that the crack mitigation techniques for roads founded over expansive clays should avoid approaches that lead to stiff performance (e.g. lime stabilization of subbase layers) and focus instead on approaches leading to comparatively ductile responses, such as the use of geosynthetics. Shumbusho et al. (2021) suggested that a geogrid layer in a reinforced pavement section can reduce surface differential shrinking and swelling deformation resulting from underlying expansive soils by a factor of 2 and 3 respectively in comparison to unreinforced section.

Overall, existing literature studies highlights that the use of geosynthetics was found to effectively minimize the detrimental effects of expansive soil subgrades on flexible pavement performance. This study presents a case history on the use of geosynthetics to minimize longitudinal cracks from expansive soil subgrade in Austin, Texas. Specifically, the case history involves an urban roadway (Ferguson Lane in Austin, Texas) built on an expansive subgrade soil that is subjected to heavy passenger traffic and 8 years of wet and dry season cycles.

## CASE STUDY: AUSTIN, TEXAS

### Background:

The experimental test section is a small portion of an urban roadway with heavy traffic, which is located on the east portion of Austin, Texas, and to the east of Interstate Highway I-35. Specifically, the experimental section was a small portion of the roadway along Ferguson Lane, between Cameron Road (west) and Brown Lane (east) measuring about 220 m in length. The cross-section of the pre-existing pavement structure comprised of an expansive soil subgrade, 250 mm-thick granular base, and 75 mm thick asphalt layers. The subgrade soil up to a depth of 2 m under the roadway has been mapped as Houston Black clay, per USDA web soil survey. Figure 2 presents a google map view of the location of the experimental section under Houston Black soil.

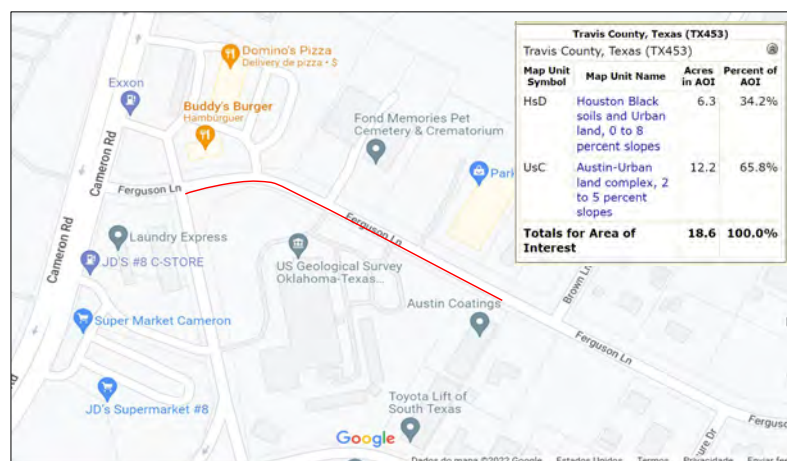


**Figure 2. Google Map View of Experimental section Location in Austin, Texas.**



Houston Black is a high plasticity clayey soil that possess high volumetric changes (shrink-swell behavior) associated with their moisture content variation. In order to understand expansive soil properties, the soil was tested at the University of Texas at Austin. The primary characterization of subgrade soil included Atterberg limits and Centrifuge swelling for Potential Vertical Rise (PVR) determination, per TEX-6048B. Based on the laboratory evaluation, it was determined that the Houston Black soil had a liquid limit, plastic limit, and plasticity index of 75%, 21% and 54% respectively, per ASTM D 4318, indicating great potential for swelling upon wetting. The PVR of subgrade soil (Houston Black) was determined by conducting centrifuge test on undisturbed samples at three different effective stresses (5g, 25g, 200g). Specifically, the swell and effective stresses were determined to calculate the PVR i.e., swell multiplied by the thickness of the soil layer, which was determined to be 3.8 inches and suggests a high potential for swelling in presence of moisture.

The asphalt surface along the Ferguson Lane had developed distresses in the form of longitudinal cracks, alligator cracks and undulations/rut along the wheel paths as shown in Fig. 3. The Austin city transport authority proposed to rehabilitate the roadway to restore the serviceability to road users and the rehabilitation process is discussed in the following section.



**Figure 3. Distresses in the Pre-existing Roadway: April 2014.**

### **Roadway Rehabilitation:**

The roadway rehabilitation along Ferguson Lane involved placing and compacting 75 mm thick Type-C dense-graded asphalt overlay on the pre-existing asphalt surface, similar to any other



traditional roadway rehabilitation technique. However, geosynthetic reinforcements were installed on the pre-existing asphalt surface, in portions that had severe cracks (e.g., alligator, longitudinal, and transverse), as an alternate and efficient solution against the base course reinforcement. Specifically, the west bound lane along the Ferguson Lane had a geosynthetic reinforcement below the overlay (reinforced section), while the east bound lane did not have any geosynthetic reinforcement below the overlay (unreinforced section).

The geosynthetic reinforcement adopted in the study was a biaxial geogrid made up of fiberglass strands that were coated with an elastomeric polymer and had a pressure sensitive adhesive backing to enhance their bonding with adjacent asphalt layers. The biaxial geogrid had an ultimate tensile strength of 100 kN/m at a strain of 3%, per ASTM D6637. The geogrid was placed directly on the pre-existing asphalt surface after removing dirt, dust, and other deleterious material. It is important to note that the pre-existing asphalt was not repaired i.e., neither milled nor levelled or any tack applied prior to the installation of geogrid. Figure 4 presents the treatment comprising the use of a geogrid reinforcement directly over alligator cracks and longitudinal edge cracks that were not treated. A polymer modified emulsion was then applied as a tack coat at a rate of 0.15 gal/yd<sup>2</sup> on the geosynthetic reinforcement.



**Figure 4. Installation of geogrid reinforcement at Ferguson Lane in April 2014.**

This trackless tack emulsion is applied hot and would cool down in less than 20 seconds, helping the truck pass over the geogrid without damaging the geosynthetic installation.

Subsequently, a 75 mm-thick dense graded asphalt (TY-C) was placed at a temperature of 122 °C and compacted. As the tackless tack emulsion is heat-activated, it allows a better bonding between interlayers when hot asphalt is placed over it. Figure 5 presents the cooled tack coat and the compaction and final overview of the geosynthetic-reinforced asphalt overlay section.



**Figure 5. Final paving work at the geosynthetic-reinforced section.**

#### **Evaluation of Experimental Sections (2014-2022):**

The experimental sections were evaluated in May 2022, after about 8 years of rehabilitation, to investigate the condition of unreinforced and geosynthetic-reinforced sections. The evaluation of experimental sections included visual examinations to identify the possible locations and types of distresses in both, unreinforced and geosynthetic-reinforced sections. Figure 6 shows the pavement surface conditions of the experimental sections during the visual examination survey conducted in 2022. As shown in the figure, the visual evaluation revealed that the longitudinal cracks reflected onto the asphalt overlays in the unreinforced section, while the geosynthetic reinforcements were effective in minimizing the reflection of such cracks from the pre-existing roadway. As shown in the figure, specifically, the longitudinal cracks existed on the pavement edges before pavement rehabilitation reflected in the unreinforced section. On the other hand, longitudinal edge cracks in the reinforced section did not reflect to the new surface suggesting that the geosynthetic reinforcement minimized the reflective cracks and any fresh longitudinal cracks from the expansive subgrade. This observation is particularly similar to the findings from Zornberg and Roodi (2021), in which environmental longitudinal cracks were found to be significantly lower in geosynthetic-stabilized sections than in control sections.





**Figure 6. Road conditions during 2022 survey.**

In addition, Figure 6 also revealed that some transverse cracks, roughly perpendicular to the centerline of the pavement, were observed in the unreinforced and geosynthetic-reinforced sections. However, it is important to note that these cracks are maybe caused due to the thermal expansion and contraction of the asphalt layer as a result of temperature variations. On the other hand, geosynthetic reinforcements were effective in resisting the reflection of severe alligator cracks for a duration of 8 years. Figure 7 shows a closer view of the edge cracks and the deteriorated surface condition in the unreinforced section, while the surface condition of geosynthetic-reinforced section looks much better in comparison.



**Figure 7. View of road condition of a geogrid-reinforced section (left) and control section (right) showing edge cracks in the unreinforced section.**

Overall, geosynthetic reinforcement installed below the asphalt overlays were effective in resisting the reflection of longitudinal and alligator cracks from the pre-existing asphalt surface into the asphalt overlay effectively for a period of 8 years. The evaluation of experimental (unreinforced and reinforced) sections shall be continued to quantify the effectiveness of geosynthetic reinforcement against the reflection of cracks from pre-existing roadway.

## CONCLUSIONS

This study presents a case history on the use of geosynthetic reinforcement to minimize cracks from expansive soil subgrade in an urban roadway in Austin, Texas. After 8 years, an investigation of the experimental sections showed the benefits of the geogrid reinforcement inclusion in the deteriorated pavement structure, mitigating cracks and pavement distresses. On the other hand, longitudinal cracks reflected around the edges of the asphalt overlay in the unreinforced section. Geogrid inclusion also highlighted their capability to resist the reflection of severe alligator cracks effectively for a duration of 8 years without any asphalt surface treatments prior to the geosynthetic installation (e.g. milling, level up).

Unlike other case studies evaluated and reported in the literature, this case study highlights the effectiveness of geogrid reinforcement installed below the asphalt overlay in minimizing cracks associated with expansive subgrade soil. This case study also highlights the inclusion of geosynthetic reinforcement below the asphalt overlay may be a viable solution for mitigating cracks and other pavement distresses associated with expansive subgrade soils. It is also worth noting that the above-mentioned findings were based on the observations from one site and may need additional evaluations before directly correlating the results to similar situations from a different location. This also points the need for continued evaluation of the experimental sections for the design of geosynthetic-reinforced pavements over expansive subgrades against reflective cracks and other pavement distresses.

## REFERENCES

- ASTM D4318-17e1 (2018). Standard Test Methods for Liquid Limit, Plastic Limit, and Plasticity Index of Soils, American Society for Testing and Materials.
- Delaney, M, Li, J and Fityus, S. (2005). Field monitoring of Expansive soil behavior in the Newcastle-Hunter region. *Journal of Australian Geomechanics*, vol. 40, no. 2, p. 12.
- Dessouky, S. H., Oh, J. Ilias, M., Lee, S. I., Park, D. (2015). Investigation of Various Pavement Repairs in Low-Volume Roads over Expansive Soil, *Journal of Performance of Constructed Facilities*, Volume 29 Issue 6, December 2015
- Gupta, R. (2009). "A study of geosynthetic reinforced flexible pavement system, PhD. Dissertation." University of Texas, Austin, TX.
- Luo, R., Prozzi, J. A. (2010). Development of Longitudinal Cracks on Pavement over Shrinking Expansive Subgrade, *Road Materials and Pavement Design*, Volume: 11, 4, pp 807-832
- Mezhoud, S., Clastres ,P., Houari, H., Belachia, M. (2016). Forensic Investigation of Causes of Premature Longitudinal Cracking in a Newly Constructed Highway with a Composite Pavement System, *Journal of Performance of Constructed Facilities*, 31, 2, 2016.
- Roodi, G. H. and Zornberg, J. G. (2021). Use of geosynthetics to mitigate problems associated with expansive clay subgrades, *Geosynthetics International*, 2021, 28, No. 3



- Roodi, G. H., J. R. Phillips, and J. G. Zornberg. (2016). Evaluation of vertical deflections in geosynthetic reinforced pavements constructed on expansive subgrades. In Proc., *3rd Pan-American Conf. on Geosynthetics*, 1970–1987. St. Paul, MN: Industrial Fabrics Association International.
- Shumbusho, R.; Ghataora, G. S.; Burrow, M. P. N.; Rwabuhungu, D. R. (2021). The Use of Geogrids in Mitigating Pavement Defects on Roads Built over Expansive Soils. *Rwanda Journal of Engineering, Science, Technology and Environment*, Volume 4, Issue 1, June 2021
- Texas Department of Transportation. 2019. “TEX-6048B: Swelling Characterization of Natural and Chemically Stabilized Clays using Centrifuge Technology”. Austin: Texas Department of Transportation.
- Virginia Department of Mines, Minerals and Energy (2021). Division of Geology and Mineral Resources. Expansive Soils and Frost Heaves.
- Wang, J. X. (2016). Expansive Soils and Practice in Foundation Engineering, in Presentation delivered at the 2016 Louisiana Transportation Conference, Baton Rouge, Louisiana, 03 March 2016. Available from: [\\_Property\\_Risk\\_Assessment\\_for\\_Expansive\\_Soils\\_in\\_Louisiana. https://www.researchgate.net/publication/355747695](https://www.researchgate.net/publication/355747695) [accessed Jul 12 2022].
- Zornberg, J. G. and Gupta, R. (2010). Geosynthetics in pavements: North American contributions. *Proceedings of the 9th International Conference on Geosynthetics* (pp. 379-400). Guarujá, Brazil.
- Zornberg, J. G. and Roodi, G. H. (2020). Long-Term Field Evaluation of a Geosynthetic-Stabilized Roadway Founded on Expansive Clays. *J. Geotech. Geoenviron. Eng.*, ASCE, 2020, 146(4): 05020001
- Zornberg, J. G., J. A. Prozzi, R. Gupta, R. Luo, J. S. McCartney, J. A. Z. Ferreira, and C. Nogueira. (2008). *Validating mechanisms in geosynthetic reinforced pavements*. FHWA/TX-08/0-4829-1. Austin, TX: Texas DOT.
- Zornberg, J. G., J. A. Z. Ferreira, R. Gupta, R. V. Joshi, and G. H. Roodi. (2012). *Geosynthetic-reinforced unbound base courses: Quantification of the reinforcement benefits*. FHWA/TX-10/5-4829-1. Austin, TX: Texas DOT.

## **Reinforced soil embankment for rockfall protection - Case History**

**Marianna Ferrara, M. Sc.,<sup>1</sup> Stefano Rignanese, M. Sc.<sup>2</sup>**

<sup>1</sup>Officine Maccaferri S.p.A., Zola Predosa, BO, Italy, e-mail: [m.ferrara@maccaferri.com](mailto:m.ferrara@maccaferri.com)

<sup>2</sup>Officine Maccaferri S.p.A., Zola Predosa, BO, Italy, e-mail: [s.rignanese@maccaferri.com](mailto:s.rignanese@maccaferri.com)

### **ABSTRACT**

Geohazards mitigation measures can broadly be classified in the following categories: land use plans, enforcement of building codes and good construction practice, early warning systems, construction of physical protection barriers, network of escape routes and "safe" places, community preparedness and awareness building. Physical barriers such as catch fences, drapery systems and reinforced embankments are widely used for rockfall mitigation solutions. Rockfall protection embankments are elevated massive, reinforced structures designed to protect urban and transportation infrastructure from hydro-geologic hazards, landslides, rockfalls, avalanches, etc. Their effectiveness is based on the combination of the damping characteristics of the soil and the tensile resistance of the reinforcements. This paper will focus on the use of geogrids as reinforcement elements of rockfall protection embankments and it will present a recent case history.

### **INTRODUCTION**

Rockfall protection embankments are passive systems, both in civil and in mining applications, used to protect roads, urban areas, quarry plants or workers when surface stabilization systems cannot be installed (e.g., for very wide slopes) or where interception of falling rocks is not possible due to the whole slope being inaccessible.

These high energy impact systems can accommodate extreme rockfall impacts (potentially up to 20,000kJ) and divert potential debris flows. Unlike rockfall catch fences, rockfall embankments can sustain multiple impacts and rockfall events without the need for repair. Additionally, rockfall protection embankments are built using reinforced soil, enabling the use of in-situ soils. A variety of face finishes are available, including a vegetated embankment facing, which reduces the environmental and visual impact of the system.

### **REINFORCED SOIL STRUCTURES CONSIDERATIONS**

The design of a rockfall protection embankments should take into consideration the following aspects for it to work effectively:

- the embankment height shall be sufficient to intercept the rock trajectories.
- the area directly upslope of the embankment must provide sufficient space to accumulate fallen rocks.
- the embankment must have sufficient thickness and density to prevent the rocks from penetrating the embankment.

Therefore, a successful design should result in energy absorption capacity, trajectory interception, and optimization of the structure and its related costs.

The rockfall embankments are made as ordinary reinforced soil structures (RSS). From a geotechnical point of view RSSs are composed of soil and reinforcing elements which help to distribute tensile stresses. These reinforcements are usually geogrids placed horizontally during the installation of the structure and wrapped at the edges of the embankment to enclose the layers of soil. In this way, the stresses on the RSS, due loads increase, are absorbed by the tensile strength of the reinforcements which are mobilized through the friction with the soil. At the same time, the compacted soil can resist to the compression stresses linked to vertical loads. The most important advantages associated with reinforced soil embankments, are listed below:

- the foundation surface is reduced because the face inclination increases from 30°-40° (soil embankments) to 65°-90° (reinforced soil structures).
- the amount of soil necessary to build the reinforced embankment is around 2-2.5 times less than the volume used for normal soil embankment.
- the risk that a boulder overcomes the embankment after the impact is reduced because of the high inclination of the mountain side facing, as shown in Figure 1.

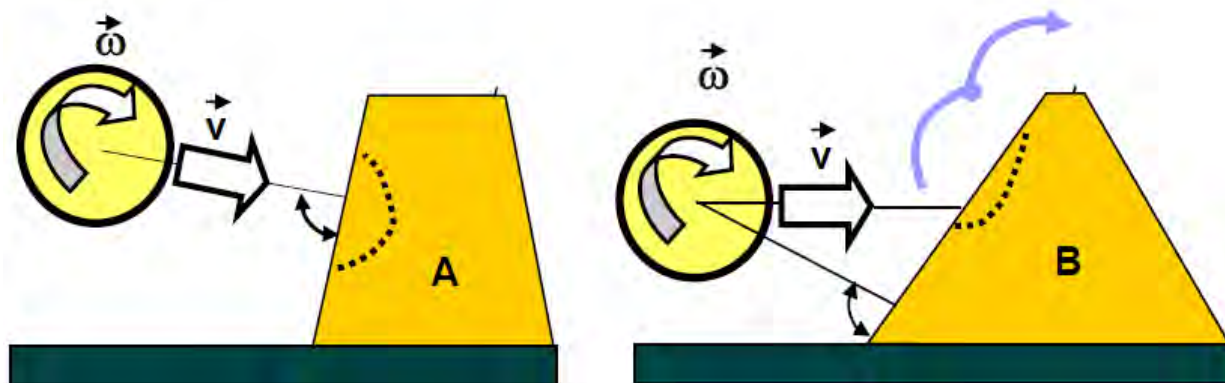


**Figure 1. The block has not enough rotational energy to overcome the embankment because reinforced embankments have 65°-90° mountain side face inclination.**

An example of a reinforced soil structure used as a protection against rockfalls, and landslides is shown in Figure 2.



**Figure 2. Example of rockfall protection embankment.**

The structure in the picture above is composed by:

- Prefabricated units of double twisted wire mesh (8×10 type) as facing system. Each unit is lined with an erosion control blanket and stiffened with a welded mesh panel. The inclined face is guaranteed by two pre-formed steel braces which can be used to vary the slope angle. The inclined front face and the erosion control blanket are designed to facilitate the establishment of natural vegetation on the units.
- Polymeric reinforcement elements. These geogrids are manufactured from high tenacity, multifilament polyester yarns aligned and co-extruded with LLDPE (Linear Low-Density Polyethylene).

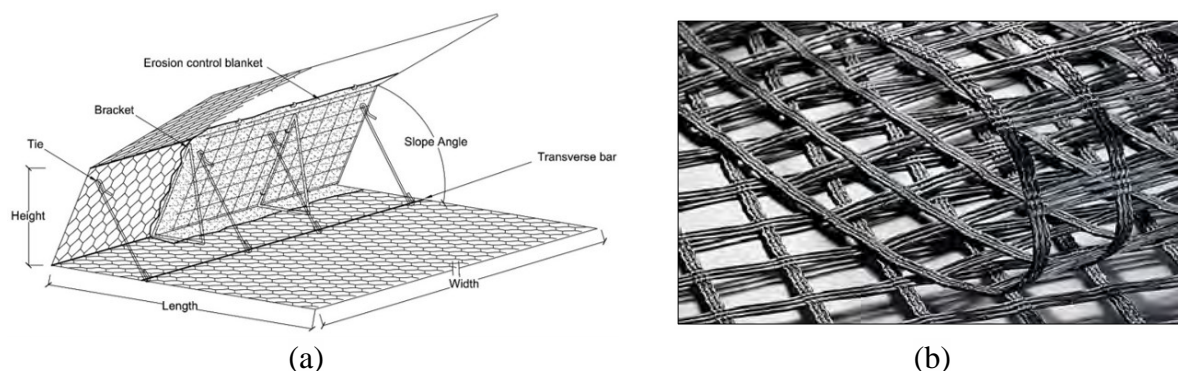


**Figure 3. Elements of a typical rockfall protection embankment: a) prefabricated face units, b) geogrids.**

Among the numerous studies conducted on the matter, a numerical analysis based on Finite Element Method (FEM) was used to model the embankment, simulate the impact of a block and predict its effect on the structure (Figure 4)

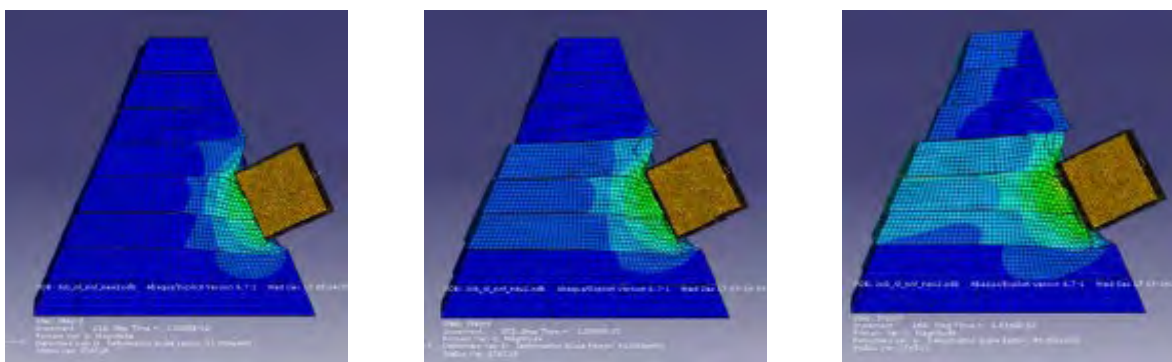


**Figure 4. Simulation of a block impacting a rockfall protection embankment using FEM.**

F.E.M. modelling results showed that the impact consequences are limited only on the layers directly involved in the impact, as also observed in full-scale tests. It is also possible to observe that the kinetic energy of the block is dissipated in 3 different ways at the time of the impact:

- The majority of this energy is dissipated because of the creation of a void on the mountain side: plastic dissipation.
- The rest of the kinetic energy is dissipated because of the deformation on the downslope side of the layers involved in the impact: friction dissipation.
- A negligible amount is dissipated because of the settlement of the grains of the soil in the impacted surface: elastic dissipation.



Moreover, it is possible to define the relationship between the impact energy and the volume of the crater made by the block on the embankment. This connection is tightly linked to the type of reinforcement used, which defines a linear coefficient ( $k$ ) of a curve shown in Figure 5.

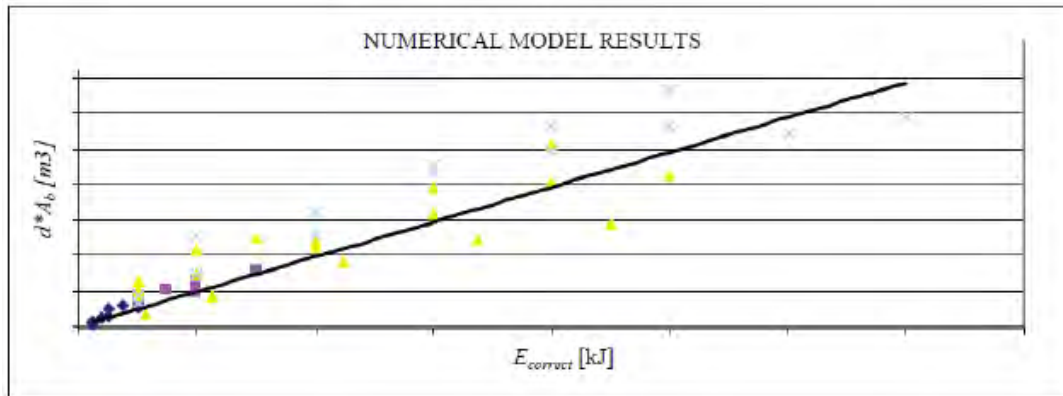


**Figure 5. Linear relationship between energy and crater volume (Politecnico di Torino and Officine Maccaferri research, 2009).**

$$A \times d = k \times E_{correct} \quad [1]$$

where:

- $A$  = block area [ $\text{m}^2$ ].
- $d$  = displacement of the block into the embankment [ $\text{m}$ ].
- $k$  = coefficient function of the reinforcement (inclination of the curve above).
- $E_{correct}$  = block kinetic energy corrected considering the plastic dissipation [ $\text{kJ}$ ].

Finally, numerical analyses confirmed that the blocks are not able to pass over the embankment, the only critical situation is when the impact is at the top of the embankment.

## CASE HISTORY – PLAN CHECROIT EMBANKMENT

The detachment from Mont Chétif of a tabular prism of approx.  $1,000 \text{ m}^3$  in volume caused the landslide that reached Plan Checrouit ski area in Courmayeur, Italy in February 2020. The violent landslide reached and destroyed a children ski school and some ski slopes of this touristic area during high season. After the assessment of the damages and the confirmation of no injuries, the area was closed to allow further analysis of the damages and possible solutions. The final intervention had a total cost of approx. 4.5 million euros and included a massive rockfall embankment.

The maximum high of the embankment is 8 m with a face inclination of  $80^\circ$  and a total length of 250 m. Double twisted wire mesh units were used as facing elements with 0.8 m vertical spacing and high strength PET geogrids were used as reinforcement every 1.6 m. The use of geogrid with 80 kN/m tensile strength allowed to build an almost vertical slope on the mountain side and a reduced foundation footprint, as shown in Figure 6.

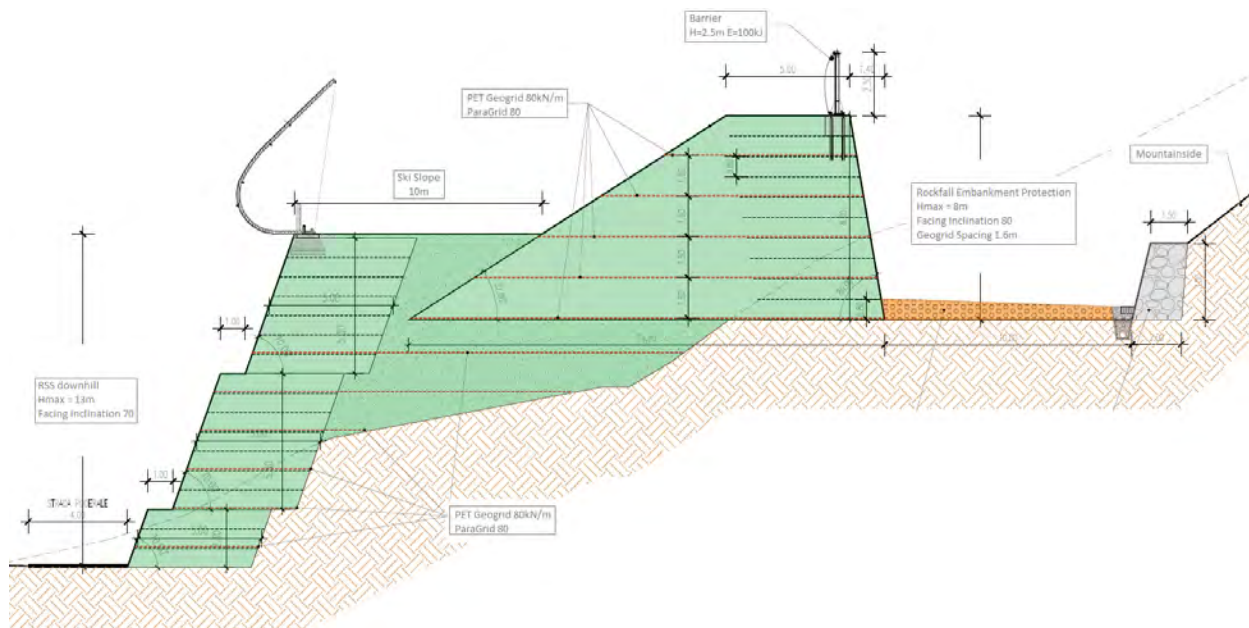


**Figure 6. Typical cross-section of the project**

The design of the rockfall protection embankment considered a block with a volume of 300 m<sup>3</sup> and an estimated energy of 12,000 kJ. The following aspects were checked:

- Penetration of the block through the embankment
- Overtopping of the embankment by post-impact projectile fragments
- Overtopping of the embankment by rolling blocks
- Collapse of the embankment due to geometrical deformation after the impact

The design input data were defined after a thorough analysis of site conditions and various simulations of possible future rockfall events. These studies led to the identification of the most critical aspect of the design: the block penetration.

The main function of the embankment is to stop the loads by the dissipation of kinetic energy. The impact of a boulder on the embankment generates a localized punching effect; its print is mainly associated with permanent deformations and a negligible elastic component. Therefore it's essential to ensure a sufficient volume of soil to be deformed without failures on the downhill side during the impact. The compressive strength with free lateral expansion must be calculated considering the cohesion and friction angle of the soil improved by the presence of geogrids. Subsequently the print size left by the block impact is calculated to evaluate the total width of the rockfall protection embankment.

An additional RSS was design to recreate the ski slope impacted by the landslide, it was built downhill using the same components of the rockfall protection embankment and in-situ soil. Both RSSs were designed following European standards to check the internal and external structure stability in static and dynamic conditions.

## CONCLUSIONS

Reinforced embankments for rockfall protection are a reliable solution mainly because they allow high energy level resistance and multiple impacts with low maintenance investment. Usually, massive structures have to be built to resist penetration, deformation or overtopping of big blocks and landslides. A soil embankment with these characteristics tends to have a big footprint and huge

amount of soil. The use of geosynthetic reinforcement like high strength PET geogrids gives the possibility to create steeper slopes and smaller footprint foundation in comparison with traditional soil structure. This is an advantage also in terms of costs and installation time because in-situ soil can be used, and the total volume of the embankment is reduced.

## REFERENCES

- Barrett, R. K. and White, J. L.: Rockfall prediction and control, in: Proceedings of National Symposium on Highway and Railway Slope Maintenance, Association of Engineering Geologists, Chicago, U.S.A, 23-40, 1991.
- Bertrand, D., Nicot, F., Gotteland, P., and Lambert, S.: Modelling a geo-composite cell using discrete analysis, *Computers and Geotechnics*, 32 (8), 564-577, 2005.
- Burroughs, D.K., Henson, H.H., and Jiang, S.S.: Full scale geotextile rock barrier wall testing, analysis and prediction, in: Proceedings of Geosynthetics 1993, Vancouver, Canada, 30 March- 1 April 1993, 959-970, 1993.
- Carotti, A., Peila, D., Castiglia, C., and Rimoldi, P.: Mathematical modelling of geogrid reinforced embankments subject to high energy rock impact, in: Proceedings of Eurogeo, II European Geosynthetics Conference and Exhibition, Bologna, Italy, 15- 18 October 2000, 305-310, 2000.
- ETAG 027 - Guideline Falling Rock Protection Kits, EOTA, January 2008.
- Oggeri C., Peila D., Ronco C., 2008 – Numerical analysis of embankments behaviour done with reinforced soil – Preliminary report – contract of research between DITAG Politecnico di Torino and Maccaferri SPA (in Italian).
- Oggeri, C., Peila, D., and Recalcatti, P.: Rilevati paramassi, in: Proceedings of Convegno su Bonifica di versanti rocciosi per la protezione del territorio, Trento, Italy, 11-12 March 2004, 191-232, 2004.
- Pasqualotto, M., Hugonin, B., and Vagliasindi, B.: Rilevati in terra rinforzata a protezione dalla caduta massi in Val di Rhemes (AO), *GEAM*, 114 (1), 55-67, 2005.
- Peila D., Castiglia C., Oggeri C., Guasti G., Recalcatti P. & Sassudelli F., 2000. Full scale tests on geogrid reinforced embankments for rockfall protection, II European Geosynthetics Conference and Exhibition, 1, Bologna. pp. 317-322.
- Peila D., Oggeri C., Castiglia C., Recalcatti P. & Rimoldi P. 2002. Testing and Modelling geogrid reinforced soil embankments to high energy rock impacts, *Geosynthetics - 7<sup>th</sup> I.C.G.*, Delmas, Gourc & Girard (eds), Swets & Zeitlinger, Nice, pp. 133-136.
- Peila, D., Oggeri, C., and Castiglia, C.: Ground reinforced embankments for rockfall protection: design and evaluation of full scale tests, *Landslides Investigations and Mitigation*, 4 (3), 255-265, 2007.

## **The Use of Geotextile Tubes as The Containment Dyke For The Construction Of Davao Coastal Highway, Philippines**

**T. Renato<sup>1</sup>, L.K. Lim<sup>2</sup>, L. Kenneth<sup>3</sup>, and M.H. Woo<sup>4</sup>**

<sup>1</sup>TenCate Geosynthetics Asia, Philippines; e-mail: r.tolentino@solmax.com

<sup>2</sup>TenCate Geosynthetics Asia, Malaysia; e-mail: lk.lim@solmax.com

<sup>3</sup>Arizona Geosynthetics Inc., Philippines; e-mail: kennethlaguitao@gmail.com

<sup>4</sup>TenCate Geosynthetics Asia, Malaysia; e-mail: mh.woo@solmax.com

### **ABSTRACT**

With the unwavering growth of economic and population of Davao City, traffic congestion has become a major issue within the domestic part of the city with road users so dependable on vehicular transportations. This Davao City Coastal Road Project will serve as a bypass road, a coastal shore protection and breakwater that protects the city from wave actions, water surges and shore erosion. During the last surge in 2020, many residents in nearby subdivisions were thankful of this project as they were spared from the surge effect. The Coastal Road required sections along the coast to be reclaimed to provide a sturdy working platform for the new road alignment. The dyke structure used for the Coastal Road new alignment was designed using three types of different geosynthetics products: geotextile engineering tube, high strength polypropylene woven mattress and nonwoven continuous filament polypropylene geotextile. Each of these geosynthetics product serve their very own function in building up to the final dyke system. The high strength polypropylene woven mattress was installed to act as a basal reinforcement for the dyke structure. The geotextile engineering tube units were then hydraulically infilled with sand-slurry to a filled height of 2m and stacked into two layers to form the mass gravity structure. A layer of nonwoven geotextiles was then cover over the geotextile tubes to serve as a protection layer prior to the placement of Class I and Class II rocks that were also put in place with hexapods, seawall and wave deflector to reduce the intensity of wave actions which is prevalent in the area during “Amihan” season. This project has shown that converting conventional hard engineering method to the use of geosynthetics has greatly help reducing the cost of material, logistic and labour which as well affects the carbon emission to be reduced.

### **INTRODUCTION**

Traffic volume in Davao City has been increasing due to its growth of its population and economic activities. To aid this problem, there is a need to distribute vehicular traffic outside the downtown area. In the inland part of the city, many people depend on road-based public transportation services such as jeepneys, tricycles, taxi, and buses which cause severe traffic congestion. Hence, the idea of the construction of coastal road was proposed to divert private vehicles from passing the downtown/población area if it has no purpose within the vicinity of the area. With this development, vehicular traffic on roads within the city proper will loosen up thereby making it more convenient to the riding public.

Apart from being an infrastructure landmark, it will also serve as a tourism destination as esplanades will be developed at strategic location where parks, playgrounds, outdoor theater and botanical gardens shall be constructed. The Davao City Coastal Highway is approximately 18.59



kilometers long with a total estimated cost of Php 19.818 billion by which the alignment starts at Bago Aplaya and end at R. Castillo Street.

Due to the crowded area along the shoreline of the Davao City, the development is faced with 2 options; extrude and relocate all the inhabitants along the shoreline which may induce additional compensations and local political conflicts; or build outwards from the shoreline which requires land reclamation. Eventually, a 26m width of land reclamation along the shoreline was adopted to make this mega project a success. The reclamation will be completed using dyke system to contain the hydraulic fill. Instead of conventional rock core followed by secondary and first armor layers, the rock core were replaced with geotextile tube units along the stretch of dyke. Hexapods concrete units were placed in front of dyke system for additional protection against storm surge. Figure 1 shows the dyke design for one of the cross-sections along the project stretch with hexapods protection.

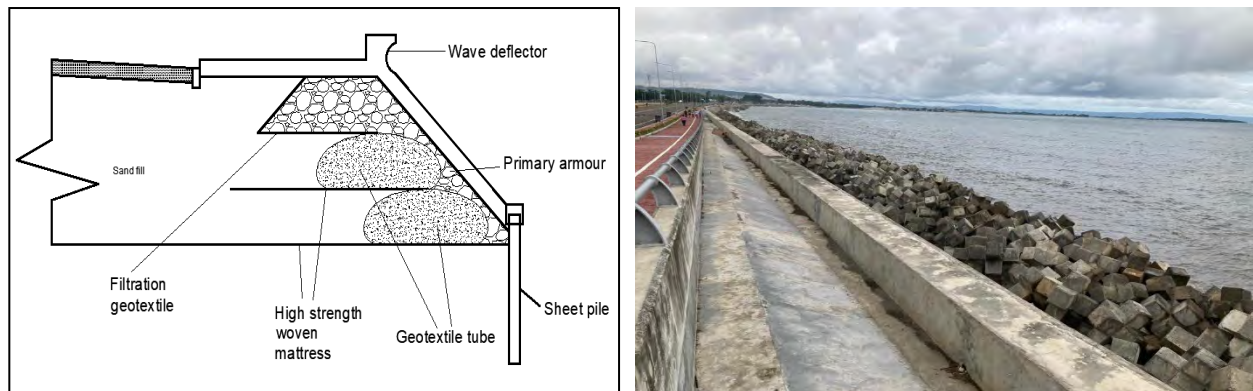


**Figure 1. Proposed dyke system using geotextile tube units as core with hexapods protection.**

## **SITE INVESTIGATIONS**

In this technical paper we will only evaluate the soil investigation report carried out at Talomo Salakot section. A total of eleven (11) nos. of boreholes were carried out prior to the commencement of work where undisturbed soil samples and Standard Penetration Test (SPT) were conducted at an interval of 1.5m. The retrieved samples will be tested on several tests i.e. Atterberg's limit, moisture content and particle size distribution to determine it's characteristics. The borehole subsoil profile is shown as in Figure 2.

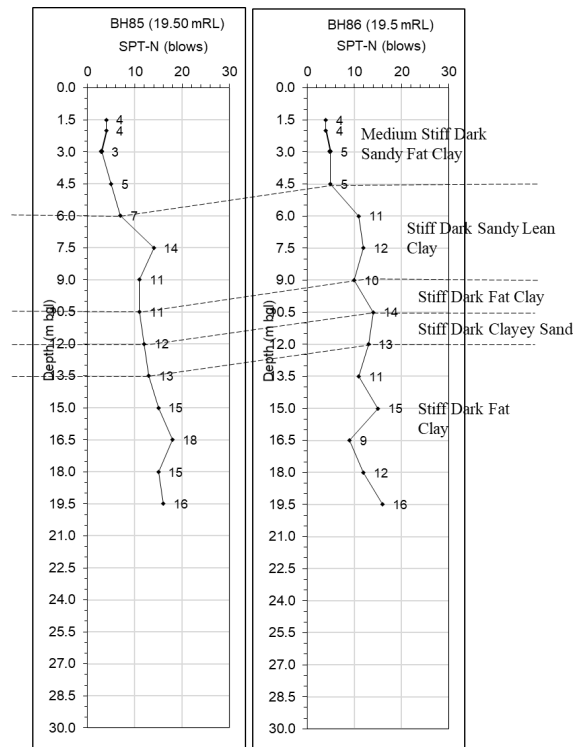


**Figure 2. Subsoil profile obtained from borehole BH85 & BH86**

The first 5.5m consists of a soft to medium stiff dark sandy fat clay with SPT-N values of 4 – 5 blows. The next layer at 5.5m to 8.5m depth is a stiff dark sandy lean clay and dark clayey sand with SPT-N values ranging from 11 – 12. This layer is then underlain by 11.55 meters of stiff dark fat clay with sand with SPT-N values ranging from 10 – 16 blows, with an intermediate 1.5m meters layer between the depth of 11.5m – 13.0m consisting of stiff dark clayey sand of 13 blows of SPT-N values.

## GEOTEXTILE TUBE TECHNOLOGY

As cited in GRI Test Method GT11: Standard Practice for “Installation of Geotextile Tubes used as Coastal and Riverine Structures”, geotextile tube can be defined as “a large tube (greater than 2.3m in circumference) fabricated from high strength, woven geotextile, in lengths greater than 6.1m”. Most of the time, mixture of slurry with sand and water are used to hydraulically filled geotextile tubes, although there were other fill materials used as well.

Geotextile tubes are supplied with closure seams around the tube. Fill ports are provided at certain intervals securely sewn at the top of the tube where it will be the main mechanism to allow the geotextile tube to be filled. The procedure to fill the tube commence by only utilizing the fill ports at both ends with any remaining intermediate ports closed. With one end attached to the pump discharge pipe and the other end left open, this allows the slurry to flow throughout the whole length of the tube as the open end will relief and discharge the water pressure. As the slurry flows through, the sand will be gradually deposited as the pressure drops. The process can be visualized as in Figure 3. After filling completes, all the port will be closed and attached to the tube to prevent the sleeve movement due to external forces.

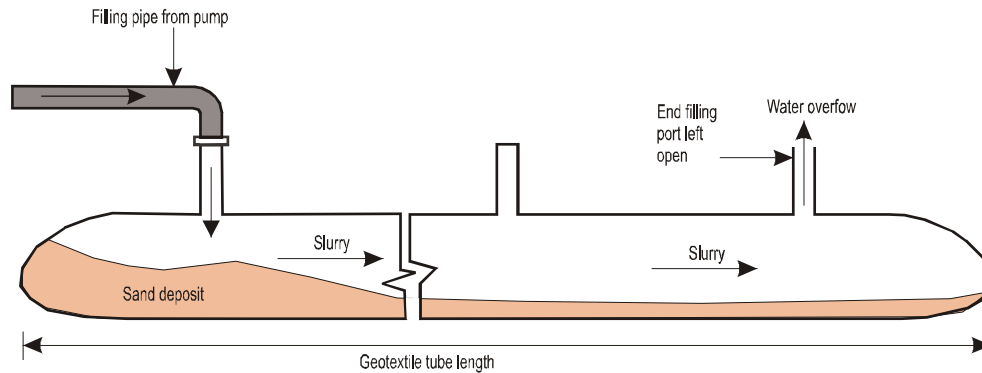


**Figure 3. Schematic of geotextile tube filling with sand slurry**

## DESIGN AND STABILITY ANALYSIS

According to Yee (2002), the design of geotextile tubes will need to be checked against the following requirements.

**Internal stability.** The fabric of the geotextile tube should be able to resist the stresses generated during the filling and placement operation. The geotextile fabric should be adequately permeable to prevent excessive pressure to build up but in unison avoid unnecessary loss of fines during the filling process.

**External stability.** The geotextile tube should be able to withstand against sliding, overturning, bearing and global slip failure when subjected to lateral forces as in Figure 4. Waves and currents should be put into consideration as well to validate that the geotextile tube is hydraulically stable against these forces.

**Durability.** The geotextile tube should be able to survive, withstand and perform its function throughout the required design lifespan.

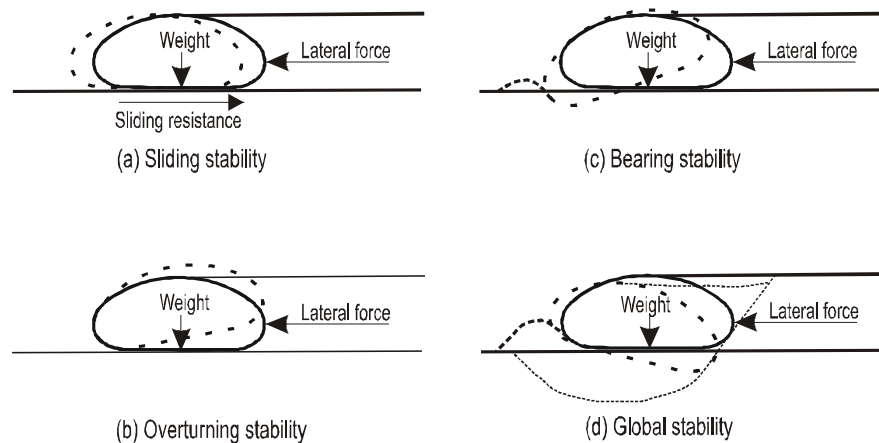


**Figure 4. Geotechnical stability check**

To simulate the pressures generated on the tube, TUBEWIN, a geotextile tube simulator is used to provide the output parameters. The spreadsheet program requires input of the geotextile tube filling height, tube circumference, infill slurry density, and certain other parameters in order to perform the output runs. Crucial parameters such as stresses around the geotextile tube can be derived to ensure that the material strength can sustain the stresses generated after the geotextile tube is completely filled. An example of the program output of the geotextile tube used in the project is shown in Figure 5.

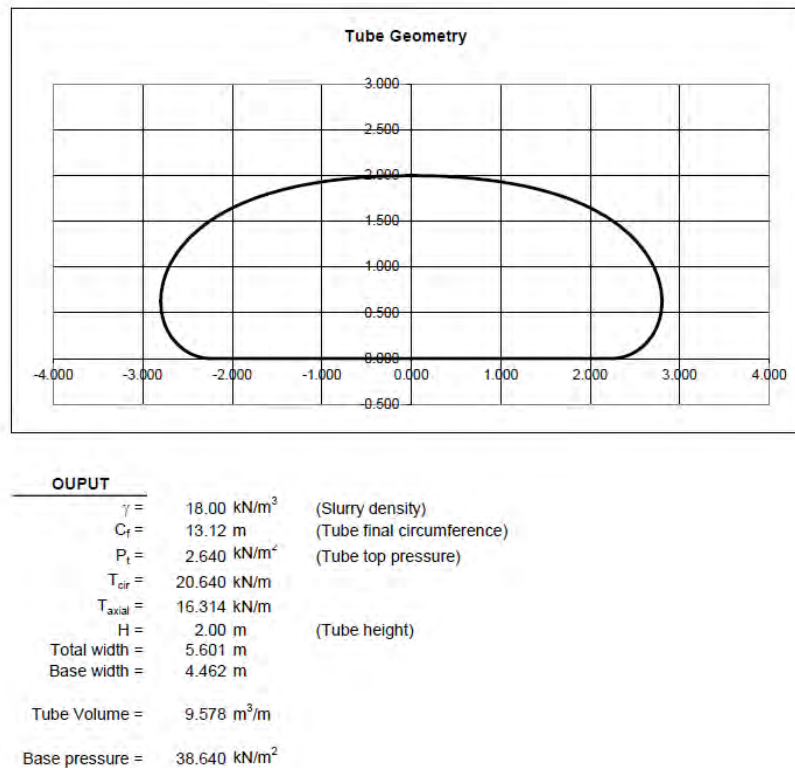


**Figure 5. TUBEWIN program output analysis**

In the design stage, the generated pressure will be subjected to a global safety factor of 4 to account for environmental factors, external forces, construction damage, seam efficiency, creep, etc. From the generated program output, the ultimate circumference tensile stresses and axial tensile stresses after applying the safety factor is determined to be 82.56 kN/m and 65.26kN/m respectively. With this, the geotextile tube with a tensile strength of 130 kN/m in both warp and weft and a seam strength of 90 kN/m were required. In Figure 6, the stress-strain curve for the fabric used to fabricate the geotextile tube is shown and the plot was obtained from a laboratory testing certified by Geosynthetic Accreditation Institute – Laboratory Accreditation Program (GAI-LAP). As shown in the plot, the tensile strength of 130 kN/m were achieved in both the warp and weft direction where the initial two graphs represented. The seam strength using 6 lines Lap seam was also tested and meets the 90 kN/m requirement where the later graph represented.



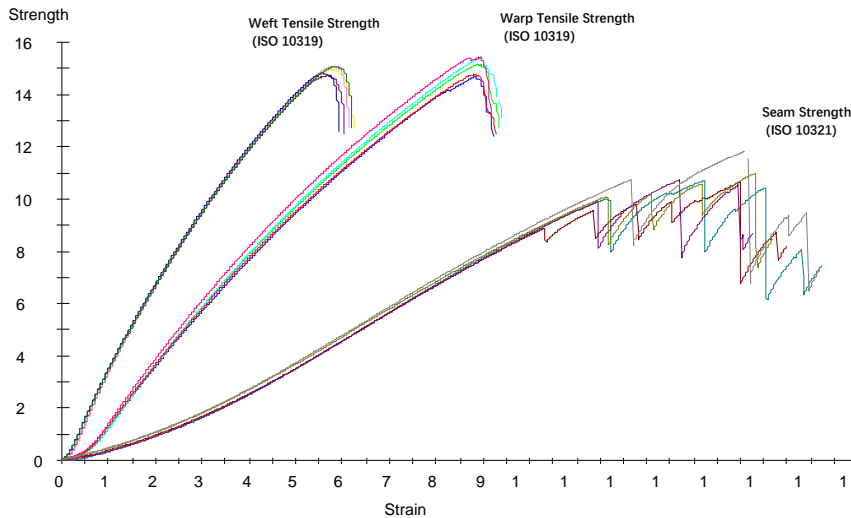


**Figure 6. Stress-Strain Curve for Fabric & Seam in Warp and Weft Direction**

## CONSTRUCTION METHODOLOGY

**High strength polypropylene woven mattress.** High strength polypropylene woven mattress with a tensile strength of 120 kN/m (wrap and weft direction) was used along the stretch of the shore reclamation as a basal reinforcement. The high strength polypropylene woven mattress helps to stabilize the soft soils and reduce differential settlement on the embankment as the reclamation progresses.

**Geotextile tube.** For the Davao Coastal Road, a few layers of stacked geotextile tubes are used to build up the reclamation dyke system. During the filling operation, to hold the tube in position and to ensure the geotextile tube is in its intended shape when it is filled to the required height, the straps provided around the geotextile tube are attached to a standing A-frame structure. The A-frame structure can stand on itself and at the same time temporarily withstand the weight of the geotextile tube during the filling process as shown in Figure 7.



**Figure 7. A-frame structure to hold the geotextile tube during filling operation**

The geotextile tubes are filled using the conventional method of slurry pump where slurry pump inlet is attached to the first inlet port as in Figure 8. Subsequent intermediate inlet ports are all closed except for the last inlet port which will be left open for water pressure relief and discharged as mentioned earlier.



**Figure 8. Filling of geotextile tube using slurry pump method**

**Sand for geotextile tube filling.** To maximize the construction rate, sand used for infill material is directly obtained from the project vicinity. Particle Size Distribution test was conducted on the sand samples to check its suitability to be used for filling of the geotextile tube. The test result is shown as in Figure 9. The sand used should be within the fineness range without the risk of the fine particles piping through the geotextile tube fabric when subjected to dynamic hydraulic load.

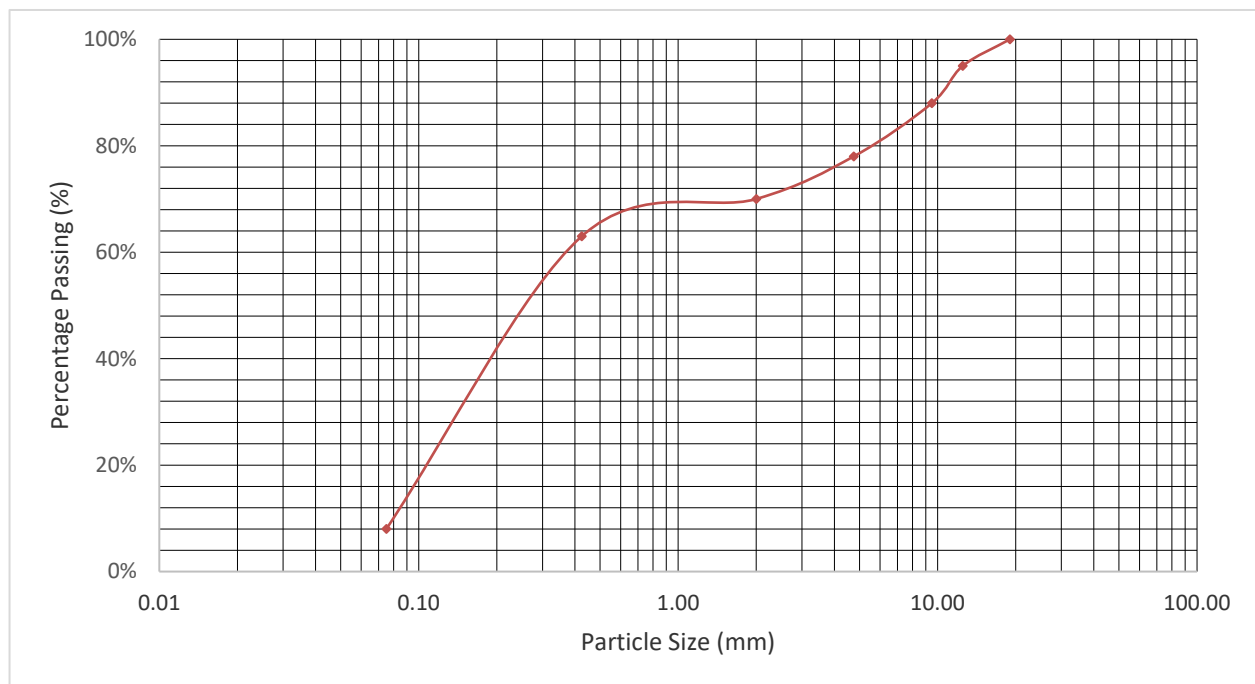


**Figure 9. Sand particle size distribution curve**

At certain locations along the stretch of the project the sand to be used for filling the geotextile tube contains large quantity of pebbles and small rocks fractures which will potentially damage the pump impeller used for the sand slurry pumping. Therefore, the filling operation of geotextile tube using the slurry pumps are found not feasible. Due to this, the contractor adopted the hopper system where funnels are attached to the filling ports on the tube and sand are then poured through the funnel into the tubes. At the same time, water will be continuously pumped through the tube to facilitate the deposit of the sand in the geotextile tube providing a more uniform fill. This filling method is as shown in Figure 10.

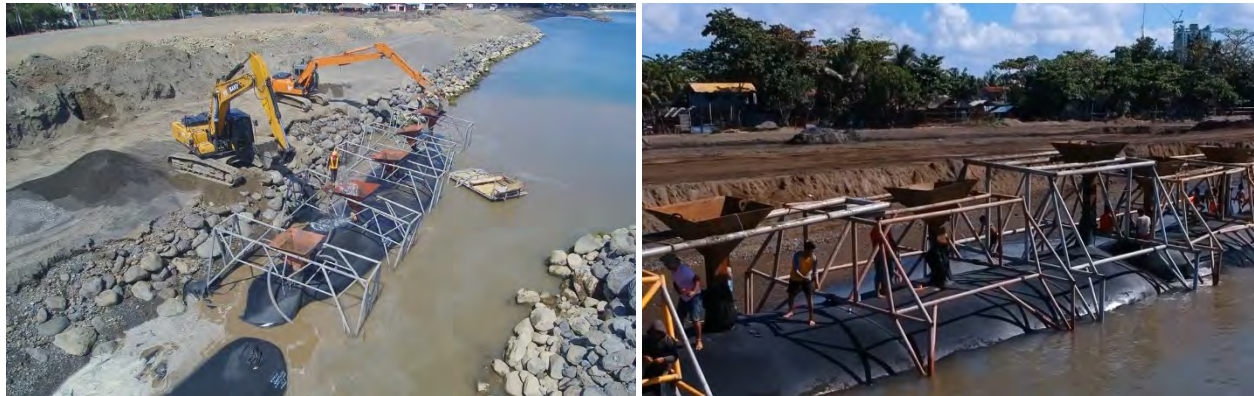


**Figure 10. Filling of geotextile tube using the hopper method**

**Filtration geotextile and sheet piles scour protection.** Upon the completion of the initial level of reclamation, a filtration geotextile is used to layer in between the reclamation layers. The filtration geotextile used is a combination of 2 layers needle-punched non-woven geotextile with a layer of coarse fiber with large opening pore as a protection layer and a layer of thin fiber with smaller opening pore as a filter layer. The coarse fiber layer functions as a protective outer layer while at the same time allowing fine soil particles to pipe through the layer reducing the risk of clogging. This protective layer is more resistant to potential installation and ultraviolet (UV) damage. The thin fiber layer performs as a filter layer with high water permeability to provide sufficient retention capacity for internal soil without the potential of clogging. Through this filtration geotextile, the goal of providing a protective and filtration layer can be achieved using a single filtration geotextile layer. To prevent scouring at the toe of the geotextile tube structure, a layer of sheet piles was installed to an embedded depth of 6m as given in Figure 11.



**Figure 11. Installation of sheet piles for toe protection and geotextile protection layer**



## CONCLUSION

Through this mega project, it has showcased how the use of geosynthetic solutions can bring significant benefits to the environment as well as the construction timeline. Over the course of the project, a functional system using the combination of geosynthetics was properly designed against the external and environmental forces. At the early stage of the reclamation, high strength polypropylene woven mattress was used to provide a stable base to act as a basal reinforcement. The use of geotextile tubes act as a main mass-gravity structure to form the reclamation dyke. In between the tube layers, filtration geotextiles were used to prevent soil from piping internally but at the same time provide adequate permeability for water to drain through to reduce water pressure.

In terms of material, the geotextile tubes have replaced the need of rock armor core which significantly reduced the need of extra use of boulders. This directly affects the amount of logistic, labor, cost and time generated as filling the geotextile tubes requires minimum supervision and machineries. Through these resources' reduction, the carbon footprint generated was significantly reduced which helps the local community as carbon footprint reduction is a subject that every country in the world is trying to address.

To date, the completion of Davao Coastal Highway has successfully served its purpose to curb traffic congestion within Davao downtown and additionally, the coastal highway provides opportunity for tourism and economic growth with esplanades provided at strategic locations with entertainment and leisure premises generated next to it (Figure 12). With the opening of the Davao City Coastal Road to pedestrians, many Davao City residents flocked to esplanades/boardwalks, spending their time biking, walking, and doing other recreational activities. This project has provided the solution as an alternative route to Pan-Philippine Highway in the southern part of the city. It will also serve as diversion road for inter-provincial and regional transport movements.



**Figure 12. Overview of completed coastal road project**



## REFERENCES

- Bezuijen, A. and Vastenburg, E. W. (2013). *Geosystems: Design Rules and Applications*, 1st ed., CRC Press, Boca Raton, FL, USA.
- Lawson, C.R. (2006). *Geotextile containment for hydraulic and environmental engineering*, Proceedings of the Eighth International Conference on Geosynthetics, Yokohama, Japan, Vol. 1.
- Lim, L.K., Chew, S.H., Wee, S.H. and Lau, U.C. (2018). Bioengineering Approach for Shoreline Protection using Geosynthetics: A Malaysian Experience, *International Conference of Geosynthetics '18*, International Geosynthetics Society, Seoul, South Korea: 3-4.
- Yee, T.W. (2002). Construction of underwater dykes using geotextile containment systems, *Proceedings of the Seventh International Conference on Geosynthetics*, Nice, France.
- GRI Test Method GT11: Standard Practice for “International of Geotextile Tubes used as Coastal and Riverine Structures”, Folsom, PA, USA.

## **Comparative Analysis Electrical Leak Location Methods on Exposed Geomembranes**

**Carl Charpentier,<sup>1</sup> Abigail Gilson-Beck,<sup>2</sup>  
and Matthew Kemnitz.<sup>3</sup>**

<sup>1</sup>Groupe Alphard, Montréal (Québec) H2T 1X9 Canada; e-mail: [ccharpentier@alphard.com](mailto:ccharpentier@alphard.com)

<sup>2</sup>TRI Environmental, Inc. Austin, TX; e-mail: [abeck@tri-env.com](mailto:abeck@tri-env.com)

<sup>3</sup>Leak Location Services, Inc, San Antonio, TX 78249; e-mail: [mattk@llsi.com](mailto:mattk@llsi.com)

### **ABSTRACT**

When referring to Electrical Leak Location testing (ELL), the geosynthetics community is focusing a lot on the dipole method due to its capacity to detect leaks through various materials and site conditions.

Different types of leaks, following placement of the cover material, can be impressive in size. That said, the ELL methods used on exposed geomembranes do not necessarily work automatically with the desired sensitivity to all situations. Site conditions play a critical role regarding any ELL method's capacity to reliably locate defects in geomembranes.

All aspects of the project design and conditions should be considered to select the optimal ELL method on an exposed geomembrane. Certain factors influencing the effectiveness of ELL methods on exposed geomembranes include type and thickness of the geomembrane, electrical conductivity of the geomembrane's underlying layer (e.g., subgrade), the presence of puddles and/or dirt, slope angles, poor contact between the geomembrane and the underlying layer (e.g., wrinkles), leak detection path length (e.g., repair patches), and weather conditions.

In the following sections, results from detection sensitivity trials, in different conditions, using small-scale test pads, will be detailed to demonstrate the capabilities and limitations of the ELL methods on various exposed geomembranes. Also, each author will share field experiences drawn from the past decades to illustrate the importance of selecting the optimal method for any given project. Comparing method-specific capabilities and limitations, in various conditions, empowers engineers and owners to better define the methods to use on exposed geomembranes. Safety hazards are a growing concern amongst project owners and will be addressed as well.

### **HISTORY**

Leak location surveys began in 1981 when the Southwest Research Institute was under contract with the U.S. Environmental Protection Agency. Development was in progress and testing was performed on a lined installation at the Southwest Research Institute facility in San Antonio, Texas. In 1985 or so, the methods being invented were patented and used commercially. Glen Darilek and Daren Laine purchased the rights to the electrical leak location method and started a Texan Corporation named Leak Location Services, Inc. (LLSI), in June 1992.

Meanwhile in France, in the early 1990s, Thierry Jacquelin developed a geoelectrical method, used on exposed geomembranes, for domestic waste landfills, now known as the water puddle method. He was then working for a company called Solmers and is now CEO of Groupe Alphard inc.

Vladimir Nosko (Sensor) invented various electrical leak location methods in parallel with the United States. Sensor went ahead and introduced the arc testing technology to the United States at a 2013 trade show and the arc testing ASTM standards were authored shortly after by Abigail Gilson.

Abigail Gilson was trained by the Solmer's leak location crew, with Carl Charpentier, in 2004. In an effort to spread the testing technology, Gilson and mechatronics engineer Jared Hamilton (Mechaconsulting) teamed up with TRI Environmental to develop their ELL testing equipment. The resulting GPS-based data acquisition system, in tandem with the recently published ASTM D8265 Standard Practice (authored by Gilson), is currently the only standardized way to provide zero-leak verification.

These 3 authors represent over 50 years of field experience pertaining to various ELL methods and equipment types. The statements shown herein are reflections of their views and feelings based on their own experiences. It should be noted that different ELL technologies could change or void those statements when referring to survey speed, ease of use, efficiency, etc. The paper's authors have used their own technology and tested various methods and available brands of equipments but they have certainly not tried all equipment developed worldwide.

Currently, there are many leak location survey companies worldwide performing one or more of the multiple ASTM methods now available (see ASTM D6747 for an updated and comprehensive guide summarizing all geoelectrical methods). Most of those companies developed their own ELL equipment and keep improving and developing to push the quality and efficiency of leak location methods forward.

## INTRODUCTION

Electrical leak location surveys on geomembranes have been used commercially for almost three decades. The electrical leak location method is a powerful tool used to detect electrical paths through holes in a geomembrane. Leak location surveys are conducted on bare geomembranes, geomembranes covered with soil, and geomembranes covered with water. Industry standards have been developed for all major electrical methods.

A voltage is applied to an electrode placed in the soil or in the water covering the liner and to an electrode placed in the leak detection zone for double-lined systems or connected to earth ground for single-lined systems. Because the geomembrane liner is an electrical insulator (including HDPE, LLDPE, PVC, and Bituminous types), current will only flow through leaks in the liner. The electrical current then produces localized high-density areas near the holes.

Optimal leak detection sensitivity depends not only on the proper performance of the survey itself, but on good preparation prior to testing and on the liner system's design. Performing a leak location survey on a geomembrane-lined impoundment, before it goes into service, has many benefits: the site being tested is usually cleaner with fewer items inside the cell causing interference or grounding.

Performing a leak location survey while the geomembrane's installation process is ongoing is also an efficient way to repair defects located on the spot, giving the installers direction for the remaining areas. Project design and preparation should consider these tips to help increase leak detection sensitivity, geosynthetic installation improvement and low cost repairs.

Leak location surveys on bare liners are important. Since there is nothing above the liner, the testing apparatus and the hole are in direct contact. Unlike a covered geomembrane, the current must travel through the cover material before it can go through the hole making contact with the conductive media under the geomembrane. At this stage of the construction, multiple defects being

created at the seam, panel, or patches can easily be detected and repaired. Because of how efficient bare liner surveys are, they should not delay or hinder the installation process. To obtain a completely unbiased leak survey, it is highly recommended to hire a third-party specialized in ELL.

All available ASTM-based bare geomembrane methods are discussed herein for comparison, for the way they can be affected by different materials, for the way they can be used adequately, and to know when certain methods are not as effective.

**Water Puddle.** The Water Puddle Test detects electrical current flowing through a hole in the geomembrane liner using a small amount of water which is temporarily placed in contact with the liner using a squeegee. One power supply output is connected to an earth ground or a conducting layer under the geomembrane and the second output is connected to the squeegee through an electronic leak detection unit. When the water in the leak contacts the earth ground or the conducting layer, a circuit is completed and the electrical current increases. The electronic leak detector unit converts the increase in the current to an audible tone indicating the presence of a leak.

The advantages of this method are:

- \* the method demonstrates a tolerance to puddles or dirt without needing to be flooded with water;
- \* the setup time and survey rate are fast;
- \* the weight of the equipment is typically heavier than high-voltage methods and it helps ensure good contact with the subgrade (push down wrinkles);
- \* the leaks can be repaired immediately without needing to remove the cover material;
- \* the method can be applied as construction progresses on large projects, to allow overlying layers to be installed and installation quality problems to be remedied.

The method can easily detect leaks as small as 1 mm (sometimes less). The method is described in detail in ASTM Standard D6747 and standard procedures for this method are specified in ASTM standard D7002.

**Water Lance.** The Water Lance Test detects electrical current flowing through a hole in the geomembrane liner using a stream of water. One power supply output is connected to the earth ground or a conducting layer under the geomembrane and the second output is connected to the probe through an electronic leak detection unit. When the water in the leak contacts the earth ground or the conducting layer, a circuit is completed and the electrical current increases. This method is typically used on slopes but can be used on flat surfaces as well.

The advantages of this method are:

- \* the geomembrane does not need to be (completely) flooded with water;
- \* the setup time and survey rate are fast;
- \* the leaks can be repaired immediately;



- \* the method can be applied as construction progresses on large projects, to allow overlying layers to be installed and installation quality problems to be remedied.

The disadvantage is:

- \* the testing rate is much slower than the water puddle method.

The method can easily detect leaks as small as 0.04 inches. The method is described in more detail in ASTM Standard D6747 and standard procedures for this method are specified in ASTM standard D7703.

**Arc Test.** The Arc Test detects electrical current flowing through a hole in the geomembrane liner. One output is connected to the earth ground and the second output is connected to the arc tester. A wand or brush is guided over the top of the liner and when an electrical connection is made a visible spark is observed and an audible alarm can be heard to signify a hole in the liner.

The advantages of this method are:

- \* the method does not require water;
- \* the setup time and survey rate are fast;
- \* the leaks can be repaired immediately;
- \* the method can be applied as construction progresses on large projects, to allow overlying layers to be installed and installation quality problems to be remedied.

The disadvantages are:

- \* there can be no ponding water and the geomembrane needs to be relatively clean;
- \* the testing rate is much slower than the water puddle method;
- \* if the geomembrane never leaked before the test, or if there wasn't enough time for humidity to build up under the geomembrane, leak signals can be masked on repair patches and other tortuous paths to ground. In other words, a dry patch with a relatively long distance between a defect in the extrusion and the initial leak will not spark, and therefore won't generate any leak signal.

The method can easily detect leaks at least as small as 0.04 inches. The method is described in more detail in ASTM Standard D6747, and standard procedures for this method are specified in ASTM standard D7953.

**Spark Test.** The Spark Test detects electrical current flowing through a hole in the geomembrane liner using conductive-backed geomembranes. The Spark test uses a high voltage to charge a capacitor formed by the conductive-backed geomembrane and a coupling pad. A conductive wand or brass brush is guided over the top of the liner. The area is surveyed, and leaks are found when the capacitor discharges through a leak. Leaks are detected when an audible alarm is triggered, and the leak can be seen when a spark occurs at the leak location.

The advantages of this method are:

- \* this method does not require water;
- \* the setup time and survey rate are fast;
- \* the leaks can be repaired immediately;
- \* on large projects, the method can be applied as construction progresses to allow overlying layers to be installed and installation quality problems to be remedied.

The disadvantages are:

- \* there can be no ponding water and the geomembrane has to be relatively clean;
- \* works only on bare, conductive-backed geomembranes;
- \* improperly exposed seams can present issues;
- \* the testing rate is much slower than the water puddle method.

The method can easily detect leaks at least as small as 0.04 inches. The method is described in more detail in ASTM Standard D6747, and standard procedures for this method are specified in ASTM standard D7240.

## AVAILABLE MATERIALS TO SUPPORT ELL TESTING

**Natural Materials.** As explained in the previous section, all electrical leak location methods require an electrically conductive pathway to ensure current can reach the electrode. Typically, all types of soil and compacted clay are sufficiently conductive to ensure sufficient leak signals. ELL can even be performed on an exposed geomembrane laid directly onto concrete, provided the concrete is not too dry.

Also, there are the following cases where the material under the lining is not conductive enough:

Bad subgrade:

Natural or residual materials with very low electrical conductivity. Experience has shown that volcanic rock tends to be very dry and not sufficiently conductive to allow for ELL. Similarly, mining waste materials with residues stripped out of the rock may not be sufficiently conductive for ELL.

Non-conductive layer:

Most green-roof designs include a thick plastic drainage layer that will retain moisture while expelling excess liquid. This kind of product can prevent ELL if no additional conductive medium is added during the project's design phase. Similarly, concrete reservoirs are often constructed with two layers of insulating Styrofoam installed between the concrete and the geomembrane to improve frost resistance, preventing effective ELL.

Double-lined systems:

A classic example of a double-lined system is a drainage geocomposite installed between two geomembrane layers. Without the addition of a conductive medium between the two geomembranes, the whole system should be considered as a single geomembrane layer (i.e., only defects that pass through all layers can be found by ELL, and probably only if the defects through the multiple layers occur at the same location).

Frozen subgrade:

Ice does not conduct electricity because it does not have free mobile ions to freely flow through it to conduct electricity. Therefore, when ambient temperatures are lower than 0 °C, there is a fair chance that water going through a defect in an exposed geomembrane will get in contact with the subgrade, but electricity will not make it to the return electrode placed outside of the site.

**Conductive Geotextiles.** Puncture resistant geotextiles are often featured in the design of impervious systems. Replacing puncture resistant layers with conductive geotextiles, to facilitate ELL, does not significantly impact the overall project budget. While many types and brands of conductive geotextiles are available, the following three have consistently been shown to work well with ELL:

Conductive mesh fixed on geotextile or between two sheets of geotextile:

This type of geotextile has a conductive core made of stainless-steel wires and nylon mesh and benefits greatly from the durability of its conductive core, which can maintain its conductivity for many years even in wet environments.

Its main limitation is the delayed response time when applying water-based methods.

The water will take time to soak into the material and make contact with the conductive core depending on the thickness of the top geotextile layer and the position of the leak in relation to the 5 cm x 5 cm conductive mesh.

Conductive sheet bonded to a geotextile:

An electrically conductive sheet is typically made of aluminum, carbon black plastic, or graphene. Its main benefits are the instant response time, even for water-based ELL methods, and its installation simplicity. A downside specific to the aluminum is that it can easily deteriorate during storage or installation.

Silver-coated geotextile:

The silver-coated geotextile provides a durable and easy-to-install alternative to aluminum, although it is significantly more expensive.

While each of these conductive geotextiles have their own installation methods, continuity between individual panels on the whole geomembrane surface is essential for ELL. Proper knowledge of the requirements is crucial. The leak location crew will not be on-site until part of the geomembrane installation is completed thus no adjustments can be carried out to the conductive geomembrane underneath.

Another important factor is the type of geomembrane to be installed on top of the geotextile layer. In one case study, the installation of a sheet of textured liner risked damaging the aluminum geotextile layer installed on the subgrade. To reduce the risk of damage, the geotextile layer was installed face down and then tested to ensure the reverse side of the aluminum was conductive enough to allow for ELL. In all cases, manufacturer specifications for installation should be requested and followed, and available quality control procedures should be implemented to ensure continuity between panels.

**Conductive-Backed HDPE.** Another method of ensuring adequate conductivity is to use conductive-backed HDPE liners. These were originally developed by Gundle Lining Construction Corporation in Houston, Texas, in 1994, and are now manufactured and sold internationally by a variety of geomembrane manufacturers. A standard conductive-backed HDPE liner consists of a layer of coextruded geomembrane with an HDPE core and a high carbon-black content HDPE conductive coating applied to one side. They are available in colored (white) and textured models. HDPE conductive-backed geomembranes allow the use of the spark test method (ASTM D7420). If any other ELL methods are employed, there are several details about conductive-backed liner installation that need to be considered that are not issues on other types of geomembranes.

An electrical conductivity break in the double-fusion seam is important. Theoretically, the bottom part of each panel is conductive, and might cross the seam and create false-positive signals along each weld.

It is imperative to break the electrical connection through the wedge seam, and this can be achieved easily by using a custom wedge welder with an added pin scratching the conductive layer just deep enough to guarantee flap isolation.

The overlap flap of fusion seams installed in anchor trenches on the periphery of the site will act as a ground for all panels to which they are connected, and this grounding effect will be registered as a leak by the arc test and water-based methods. To prevent this grounding effect, panel seams should be entirely grinded before entering the trench to ensure isolation from external ground.

Once all flaps are isolated from the subgrade and external ground, they are still conductive which can complicate things when in contact with a leak somewhere along its length. If a leak with a puddle of water is in contact with a flap, the operator could be 60 m away, touch the flap, and get a leak signal. Nothing can prevent this but being aware of the phenomenon can prevent wasting time.

All ELL methods besides spark-testing require the whole process to be connected as one conductive layer. A basic conductive liner installation will not have any contact between panels, which would require a current-return connection on every panel. To achieve global connectivity, the installer needs to put pieces of conductive geomembrane with the conductive face pointing up. The frequency of these bridges is found in manufacturers' recommendations, typically about 20 m apart. The spark-test method does not need the extra step since the connection with the conductive part of the geomembrane is achieved by electrical capacitance and a conductive neoprene pad, one panel at a time, as described in section 2.

Installation details, specific to conductive liners, are similar to those used for connecting panels together, but are used for repairs and patches. When applying a large patch (> than 2 m), the neoprene pad can be installed on one side, the other half can be surveyed, and vice-versa. On smaller repairs, the center of its location should be cut in a circular shape, and a piece of conductive liner should be inserted under the installed geomembrane, with the conductive face pointing up. This way, a defect on the side of a patch will carry electricity toward the middle giving access to



the rest of the conductive installation, finally reaching the return electrode, and generating a leak signal.

The main advantage of good quality conductive-backed HDPE liners is that no additional geosynthetic material is required to ensure conductivity (provided the guidelines outlined above are closely followed). Another significant advantage is that the liner's conductive element will remain molded to the liner despite deformation or wrinkles, increasing the chances of detecting defects in the liner. Wrinkles should be avoided during installation as they allow leachate to flow beneath the geomembrane preventing close contact between the rigid probe and the surface of the geomembrane. When using heavier ELL equipment (i.e., for the water puddle method) it is possible to flatten wrinkles, but this requires additional effort from the ELL operator.

Conductive geotextiles and geomembranes facilitate ELL by providing a dependable conductive medium where conductivity is unreliable (bad subgrade materials) or entirely lacking (double-lined systems).

When a geomembrane layer is installed on natural ground with good electrical conductivity, there is no benefit to installing conductive geomembranes other than facilitating the location of leaks on wrinkles or other poor contact scenarios.

## **METHOD COMPARISON**

When comparing available ELL methods, the focus is usually on leak detection sensitivity. Leak detection “sensitivity testing” is part of every bare geomembrane’s survey methodology. This terminology is slowly being changed through the ASTM revision process to “functionality testing” because the procedures outlined by the standardized methodologies are much more demonstrative of functionality over a known leak, of a particular size, and all methods must at least demonstrate this minimum level of “sensitivity” (a 1 mm diameter hole). All bare geomembrane methodologies exhibit the same level of “sensitivity” if conditions are good for a specific leak. However, holes much smaller than 1 mm are only typically found with high-voltage methods.

Just because a method can detect a leak does not mean it will detect every leak. The conditions required for detection can be slightly different depending on the method. Leak diameter is not the greatest factor in method sensitivity, but rather conditions around the leak(s). It should be noted that every bare geomembrane method standardized by ASTM allows alternative methods to be used if warranted by site conditions and if mutually agreed upon. This is because site conditions will sometimes dictate which method(s) will be most effective. Puddles of water, dirt, wrinkles in the geomembrane, and the distance to ground from the leak, all factor into method functionality. Learning the particularities of each methodology is necessary for determining the most effective method(s).

It is most useful to group the testing methodologies into two categories; the high voltage-based testing methodologies (Arc and Spark Testing) and the water-based testing methodologies (Water Puddle and Water Lance Testing), since each of these categories contains two methods that share similar testing characteristics, while being intrinsically different (low voltage through water or high voltage (approximately 1,000 x higher), channeled through air).

The water-based methodologies are much more forgiving of partially wet and dirty survey areas. It is also easier to make sure a survey area has been thoroughly tested with the water-based methods. The main drawback of the water-based methods is that they require a low point in the survey area where the applied water can collect and maintain isolation from ground. A second drawback is that they are less effective on slopes, especially vertical walls, since the water relies

on the force of gravity to travel through a leak. Holes, such as knife slices, are also difficult to get water to travel through. It is also an additional burden that the water-based methods require the application of water, which might be expensive, and must be conveyed via a series of hoses, requiring additional effort and labor. However, the speed of the water puddle method is much faster than the high-voltage testing methods.

The high voltage-based methods are preferred for areas such as slopes, where it is difficult to get water to flow through a small hole.

The furthest distance from the high-voltage testing probe to the underlying conductive surface is site-, material-, and climate-specific, but tends to be approximately 3 cm.

It is recommended that a wand no longer than 1 m be used as a probe, since a longer probe is very difficult to control, and it is difficult to maintain intimate contact with the geomembrane surface over areas where the geomembrane is not completely flat. Losing intimate contact with the geomembrane surface can cause leaks to remain undetected. This size probe results in a survey speed of approximately 1-1.5 acres per day, per operator, but will be slower on steep slopes that cannot be traversed without assistance. The spark testing method requires that the conductive neoprene pad be placed on the geomembrane being tested for leaks. Certain repair patches are quite small and cannot accommodate both the neoprene grounding pad and the testing wand. Additionally, the Spark Testing method cannot test in a fusion-welded seam vicinity due to the false positives caused by the conductive back side of the overlap. If the geomembrane is dirty, and especially if it is wet, arc testing should not be performed; false positive signals occur wherever water is present and false negative signals occur when sediments cover a hole.

The water-based methods work perfectly if water easily flows through the hole and is effectively isolated from ground. On slopes steeper than 3H:1V, applied water tends to flow down the geomembrane surface rather than through a small hole like a pinhole or knife slice. The arc testing method works much better on slope holes, and especially vertical walls. If a leak has a tortuous path, for example on an extrusion weld that is part of a repair patch, where the distance from the leak to underlying subgrade is greater than 3 cm, which it practically always is, arc testing may not be effective. If there is sufficient moisture in the underlying subgrade and there is sufficient time for humidity to develop inside the repair patch, or if condensation exists on the underside of the repair patch, the arc tester will work appropriately. Arc testing is therefore unreliable on repair patches or other tortuous leak paths. The water-based methods, especially when applied slowly and with pressure, can reliably locate leaks on the extrusion welds of repair patches.

Geomembrane trampolining will be an issue for all methods when a conductive-backed geomembrane is not used. Geomembrane wrinkles can often be worked out as the water-based methods are applied, but the arc testing will not be effective on wrinkles exceeding the arc testing leak detection distance. This is because the arc tester glides across the geomembrane and if an operator holds a wrinkle down with his/her foot while trying to test that location with the arc tester, the operator will likely receive an unpleasant shock. Therefore, this is not typically done, especially while testing HDPE since the wrinkles are quite stiff.

Geomembranes are not perfect electrical insulators, and the various types of geomembranes have different values for electrical resistivity. HDPE is generally the most electrically resistive type of geomembrane, with EPDM generally the most electrically conductive type of geomembrane. The high-voltage methods will exhibit false positive signals on geomembranes that are not electrically resistive enough. The resistivity of a geomembrane will be a function of its material properties and the thickness of the geomembrane. Additionally, if a

subgrade is hyper conductive, this could result in more false positive signals on thinner geomembranes. The water-based methods can be used for more electrically conductive geomembranes because the applied voltage can be decreased. The high-voltage methods require the electrons to travel through the air, which requires a few thousand volts.

Since the water-based methods use water to carry the voltage, they can employ very low voltage. Geomembranes tend to be non ohmic materials, where the resistivity increases with decreasing applied voltage.

## **FIELD EXPERIENCES**

To evaluate the arc tester's ability to detect a leak in the extrusion weld of a repair patch, two identical repair patches were created using a conductive-backed geomembrane for only one of the patches. The repair patches measured roughly 16 square inches. An intentional breach was created in each patch through the extrusion weld by creating the weld across a wire, and then pulling the wire out while the extrudate was still warm. The arc tester was applied to each patch. It easily detected the leak on the repair patch that was made from conductive-backed geomembrane. The leak on the other repair patch was not positively detected. Approximately six months later, this exercise was repeated over the same two repair patches. The leaks in both patches were easily detected. This shows that with humidity building up inside the patch over time, leaks such as this can be detected, but newly installed repair patches cannot be reliably tested with the arc tester.

Another example of repair patch testing occurred at a site where a leak was detected by the vacuum test at the end of the "Tee" bead of a repair patch. This was immediately after installation of the patch. The arc tester was applied to the patch and the leak was not detected. The water puddle method was then applied. The leak was not detected right away, but after a few seconds, adding water and pressure, the leak was detected.

Integrating a conductive-backed geomembrane into the site design allows the use of the spark test method but does not remove any of the technical survey challenges. Despite being easy to connect and having light equipment, spark testing is the most complicated of the exposed geomembrane ELL methods. Avoiding false positives while guaranteeing an exhaustive survey requires precise settings and regular readjustments as the survey progresses. Unlike the water-based methods, both high-voltage methods are very sensitive to moisture and dirt on the surface of the geomembrane. Finally, all other exposed geomembrane ELL methods have binary results: either a leak signal is detected, or it is not, as long as the applied water is isolated from ground (even if the water puddle method can have certain sensitivity adjustments within a water puddle). By contrast, available spark test equipment requires the setting of an alarm threshold based on system discharge estimates, and even the accidental movement of the neoprene pad can trigger a discharge that will trigger the alarm.

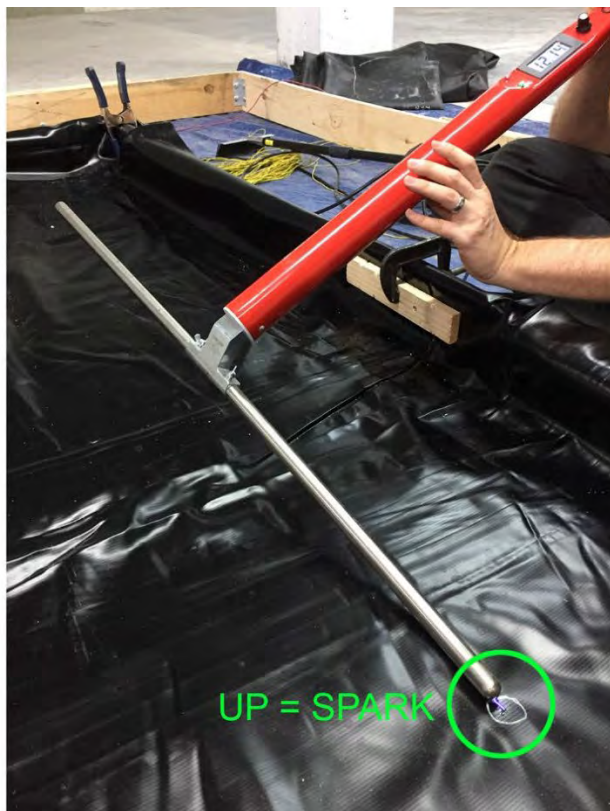
Third party surveys are also important as their focus is ELL. A specialized technician with experience will fully understand what needs to be done in order to achieve an optimal survey. In certain cases, installers were witnessed carrying out their own spark testing on freshly pulled geomembranes BEFORE any seams and repairs were completed. Other installers on a different job were using spark testing equipment without a neoprene pad, with a small 20-foot wire directly plugged onto an isolated flap, trying to convince the client they could do the entire pond with that kind of equipment.

Arc Testing on very thin and less electrically resistive geomembranes exposed shocking behaviors. The liner was made of PVC with a 0.75 mm thickness (30 mils), and the arc tester was



set to approximately 30,000V (typical). Many small arcs were visible on the probe, running along the geomembrane. These surface arcs did not damage the liner, besides a very subtle polishing. The problem was that no “strong arcs” were produced through actual holes in the geomembrane.

Lifting the probe up in the air and going near a leak worked, big strong arcs were visible, and an audio alarm was triggered, but nothing was happening when the probe was flat. Lab tests were conducted, and this behavior did not happen on 1.5 mm thick HDPE geomembranes and did not happen if the thickness of the PVC geomembrane was doubled with a hole going through both layers. This would mean that below a certain thickness (to be determined), arc testing would simply not work on this type of PVC.



## SAFETY HAZARDS

Like any field job, ELL operators need to exercise caution while working. The most common risks are tripping, slipping, or falling when crossing slopes with ELL equipment (probes, hoses, etc.). Textured and bituminous liners offer the most stability and grip for ELL operators. On smooth membranes, a 3 to 1 gradient slope represents a significant challenge, and anything steeper will require a harness and additional operators, reducing the pace of the survey. The addition of a geotextile strip or a rope ladder can also help in performing surveys on slopes, but again, significantly reducing the pace of the survey.

Dehydration is also a risk for ELL operators, particularly when using the puddle method, due to the weight of the equipment and hose. Good hydration is key and having an additional laborer to aid in carrying the hose reduces the amount of effort required.



It should also be noted that high-voltage ELL methods create sparks that can shock the operators.

We are not aware of any injuries arising from arc and spark ELL testing, but certain equipment brands will regularly “spark” the operators. Additionally, when using the spark test method, the geomembrane acts as an electrical capacitor that will discharge and shock the operator if the conductive side of the liner is touched. As the high-voltage ELL methods rely on the generation of sparks, they are forbidden for use on oil and gas facilities, or anywhere with explosive gases present, such as landfill caps. Low-voltage methods such as the water puddle method typically use power sources below 50V.

## CONCLUSION

If bare geomembrane ELL testing is used for a project, the first things to consider are the construction materials and the liner system design. Bare geomembrane testing cannot be performed in certain configurations, such as the double-lined system, without a conductive layer between both geomembranes. Different materials must be specified to enable bare geomembrane testing. If a conductive-backed geomembrane is used, its installation will dictate which method(s) may be appropriate.

Every bare geomembrane method has advantages and limitations. Project design and site conditions must be factored into the method selection. Every method works with suitable conditions, which typically only ELL practitioners are intimately familiar with. For this reason, project specifications should not be rigid and method selection should be done by ELL practitioners. The 1 mm pinhole leak detection criteria for bare geomembrane methods makes them all technically equivalent. A rigid method specification can result in ineffective or inefficient testing.

Specifying the most suitable method for a project is a balancing act between effectiveness and practicality. It is best to anticipate all possible site conditions when specifying ELL as part of a project. For wet climates, high-voltage methods might not be effective. Certain site conditions, such as the degree of moisture inside a repair patch, cannot be known. It is therefore conservative to employ methods that work more reliably on whatever is being tested. The methods should also be used in combination whenever warranted. For example, for pond configurations, the water puddle method should be used on the floor, which is more prone to wrinkles, dirt, and puddles from rain events. The arc testing method should be used on side slopes that are too steep to safely walk on in the presence of water, and where applied water is prone to run down the surface rather than through holes. Bad repair patches or any opening with a tortuous path to ground should always be tested with the water-based methods. Large survey areas cannot be practically tested by a third party using the arc testing or water lance methods due to the slow speed of these methods. Sites that cannot supply construction water may be forced to use the arc testing method regardless. Safety should also be considered anywhere that explosive gases may exist.

However, each ELL practitioner has slightly different capabilities and methods, so an expert ELL practitioner should always be relied upon for method selection.

The effectiveness of bare geomembrane testing is completely reliant on the equipment operator's skill and care. These methods are typically performed in blazing heat or on extreme side slopes, which are physically exhausting. The quality of the survey execution can therefore be compromised.

Bare geomembrane surveys should be performed with care, without being rushed, and only if the operator is physically rested. This can be tricky with rigorous construction schedules. Even with all the skill and experience in the world, bare geomembrane testing is prone to human error. It is helpful to provide oversight for these methods to identify when method execution is being compromised by poor operator practice.

## REFERENCES

- ASTM D 6747. Standard Guide for Selection of Techniques for Electrical Leak Location of Leaks in Geomembranes, American Society for Testing and Materials, West Conshohocken, Pennsylvania, USA.
- Beck. A. (2016). Best Practices for Groundwater Protection, GeoAmericas 2016.
- Beck, A. (2015). Available Technologies to Approach Zero Leaks, Geosynthetics 2015 Conference Proceedings, Portland, Oregon, February 15-18, 2015.
- Beck. A. (2014). Designing to minimize geomembrane leakage, Geosynthetics Magazine, August/September Issue.
- Darilek, G.T. and Laine, D.L. (1999), Performance-based specification of electrical leak location surveys for geomembrane liners, Geosynthetics '99, Boston, Massachusetts, USA, April 1999, pp. 645-650.
- Darilek, G.T. and Laine, D.L., (2010). Leak Location Surveys, The Past, The Present, The potential, GSI Annual Meeting 2010.
- Forget, B. et al., (2005). Lessons Learned from 10 Years of Leak Detection Surveys on Geomembranes, Sardinia Symposium, Sardinia, Italy.
- Touze Foltz. N. (2002). Méthodes de détection et de localisation de défauts dans les géomembranes. Ingénieries, E A T, 2002, pp. 17-25.

## **Development of a Conductive Textile and Its Uses in Electrical Leak Location (ELL) Survey of Geosynthetic Containment Systems**

**Rohit Sati, M.Sc.<sup>1</sup>**

<sup>1</sup>Layfield Group, 17720 129 avenue Edmonton; e-mail: [rohit.sati@lafieldgroup.com](mailto:rohit.sati@lafieldgroup.com)

### **ABSTRACT**

Electric Leak Location (ELL) surveys have proven to be a reliable method to evaluate construction integrity of containment systems. The challenge often encountered with this method is providing a consistent conductive layer beneath the geomembrane to facilitate an effective survey. Factors affecting a consistent conductive layer include: a non-conductive subgrade, inconsistent seams with conductive sheet, multi-layer containment systems with non-conductive intermediate layers, spray applied liners, and several others. This paper details the development and testing of a unique conductive composite of nonwoven geotextile and a thin conductive film to overcome these issues by providing a consistent conductive layer that can be used under any non-conductive sheet, or between geomembranes where drainage layers may be present. Multiple scenarios replicating the cases noted above were simulated and tested and are featured in this paper. The author found that testing sensitivity of the exposed/bare ELL methods was extremely reliable when using the new material and the equipment could find holes less than 1mm in diameter. Testing sensitivity was proven to be effective, and holes were successfully detected at applied test voltage between 15-35 kV.

### **INTRODUCTION**

The Electrical Leak Location method is a sensitive technique that accurately locates leaks in geomembrane liners in landfills or other impoundments. This field-proven method has located many leaks not previously found using conventional methods. Leak location surveys are effective for both exposed and backfilled geomembranes. ELL testing on single lined systems is very effective where the geomembrane is in direct contact with a conductive soil subgrade such as compacted clay, a GCL, or other fine-grained native soil. If the subgrade is not conductive (frozen, poorly graded gravel, or too dry), a conductive medium is required to perform the ELL testing.

In double lined systems, the ELL testing can be challenging due to absence of a conductive medium under the primary geomembrane. However, the ELL testing can be performed with flooding the interstitial space or by using a conductive geomembrane. Both these methods come with challenges. Flooding of the interstitial space requires water to be hauled to site, it takes a while to flood the space between primary and secondary geomembrane depending on the size of the containment. The other challenge is to remove this water prior to putting the pond in service. Polyethylene (PE) geomembranes that are created using co-extrusion technology can be made conductive by adding carbon black in the outer layer. In recent discussions with 3rd party ELL contractors, it was mentioned that the potential issue with a conductive PE geomembrane is the isolation of bonded seams, the seams must be isolated to ensure efficient ELL testing. The conductive squeeze out from seams must be grinded and every seam isolated prior to ELL testing. This can be both labour intensive and costly in large projects. Just one non-isolated seam can show

up as a large leak during the ELL testing and can impact the efficiency and accuracy of the survey. For both single and double lined ponds one method is to lay a conductive geotextile.

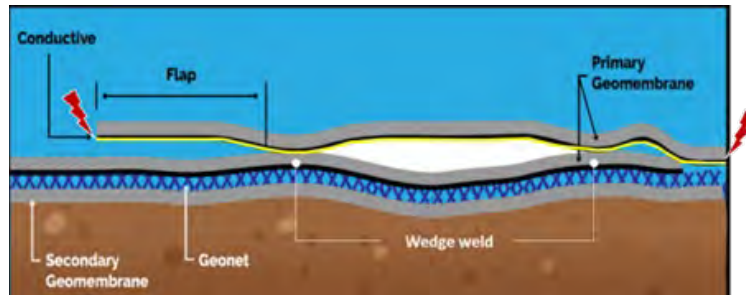


**Figure 1. Schematic of spark testing on a conductive liner.**

Conductive geotextile is easy to deploy and does not require isolation of seams. This white paper presents the development of conductive geotextile and case studies of installation and testing of conductive geotextile in the field using Electrical leak location techniques.

## DEVELOPMENT OF A CONDUCTIVE TEXTILE COMPOSITE

Electrical conductivity is a material property that indicates the amount of electrical current a material can carry or how an electrical current can move within a substance. For a material to conduct it needs to receive and transmit electrical signals, Geosynthetics are planar materials hence the surface resistivity can be used to measure and identify their electrical behavior.

Most geomembrane and geotextiles are insulators meaning they cannot move electrical current. Since a conductive layer was needed the first phase of this project was to investigate existing conductive textiles. Our initial search results showed a variety of smart textiles which were conductive and flexible. The use of these materials was limited to high performance clothing. Containment applications are mostly industrial, and the costs of smart textiles made them unfit for large environmental applications. We then reached out to staple(short) fiber manufacturers that were supplying to non-woven geotextile manufacturers. A quote was obtained from a manufacturer of conductive fiber non-woven geotextile which was a blend of conductive fibers and regular staple fibers, the price was about 5 times more expensive compared to regular grade non-woven geotextile and the surface resistivity tested using a multimeter showed higher resistance meaning less conductivity. Other options researched included a narrow width foil based non-woven. Traditional nonwoven geotextile is 14.5' wide but the foil-based fabric was only 6 ft wide and had to be sewn to maintain conductivity across the seams.

Our primary idea was to use a conductive film and to needle punch it with the non-woven fiber web making a composite conductive. One of the challenges we faced was extruding a very thin film with conductive properties and laminating/needle punching it to the non-woven fiber web. After many deliberations, we made some samples of different thicknesses and tested them for surface resistivity. The results showed good conductive properties at a 3-mil thickness. Our next step was to mimic the spark testing in a field setting. The spark trials were successful, and the technicians were able to spark test a leak through geomembrane. Picture 2 show a standard non-



woven on the floor, followed by a 3-mil conductive film and a geomembrane placed on top and arc tested.



**Figure 2. Arc testing on a 3-mil conductive film.**

Next phase of the project involved needle punching the conductive film to a non-woven matrix. The composite material was re-tested to ensure electrical conductivity. The needle punching process perforated the film which resulted in holes in the conductive film making the composite permeable. The needle punching was primarily done to create a bond between the conductive film and nonwoven geotextile. We performed some physical tests on the conductive textile composite which yielded good results showing good mechanical properties. Water flow tests were performed using the ASTM D4491 which is the standard test method for water permeability of geotextiles by permittivity.

**Table 1. Tested properties**

Property	ASTM Test Method	Typical Values
Weight	D5261	6 oz/yd <sup>2</sup> 200 gsm
Tensile	D4632	100 lbs 445 N
Elongation	D4632	50%
Trapezoidal Tear	D4533	50 lbs 222 N
CBR Puncture	D6241	340 lbs 1500 N
AOS	D4751	70 sieve 212 microns
Water Flow	D4491	20 gal/min.ft <sup>2</sup> 810 l/min.m <sup>2</sup>
Surface resistivity	D4496	<5000 ohm/sq

### Salient features of a conductive geotextile:

1. Provides a uniform conductive medium under any non-conductive barrier.
2. Does not require water for ELL testing.
3. One layer of conductive textile provide both conductivity and protection functions.
3. 15' wide sheet for faster deployment.
4. Compatible with electrical leak location methods.

### RECENT CASE STUDIES

This section provides recent projects that used conductive textile in various containment applications.

**Secondary Containment Tank Farm (2020-2022).** An environmentally sensitive project in western Canada required secondary containment to contain the potential release of hydrocarbons from existing and new above ground storage tanks. The design of the secondary containment system included concrete walls built around the secondary containment facility.

A secondary containment liner system was chosen to be an integral part of the concrete wall. Due to the complexity of installation a spray applied liner was selected to overcome challenges with multiple penetrations on the concrete wall. A non-woven geotextile is a preferred substrate to be sprayed with polyurea (PU), the geotextile was attached to the concrete wall and sprayed with the polyurea to create a containment system. During the design phase, it was decided to perform electrical leak location survey on the spray on liner.

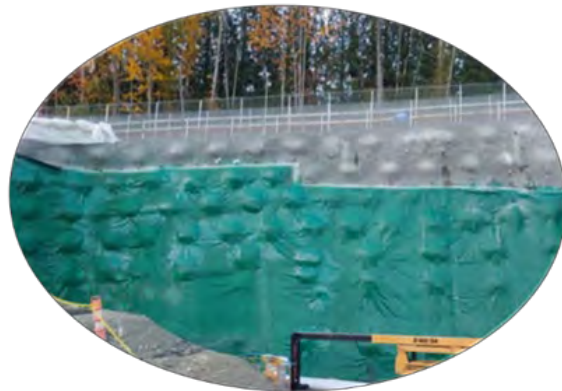


**Figure 3. Spray applied PU liner on earthen berms and vertical wall lined with conductive textile.**

However, with a standard non-woven geotextile it was not practical to conduct this survey as the standard non-woven does not have conductive properties. The conductive textile supplier proposed spraying directly on the conductive textile. After initial trials it was approved by the

engineer for use as a substrate material. The electrical leak location testing was found to be very effective and holes up to 1mm were found by the lining contractor.

**Aboveground Synthetically lined Tank- Double lined system (2021).** A liner contractor was awarded supply and installation of a 150' diameter and 32' high above ground synthetically lined system (AWSS). An 80 mil thick HDPE primary and secondary geomembrane were selected to line the steel walls and bottom of the tank. The wastewater contained a variety of organic and inorganic compounds. As part of the project scope, liner installer was asked by the facility owner to perform ELL testing on the primary geomembrane. The containment system required a conductive medium between the primary and secondary geomembrane. ELL testing was performed on the primary geomembrane using the newly developed conductive textile.

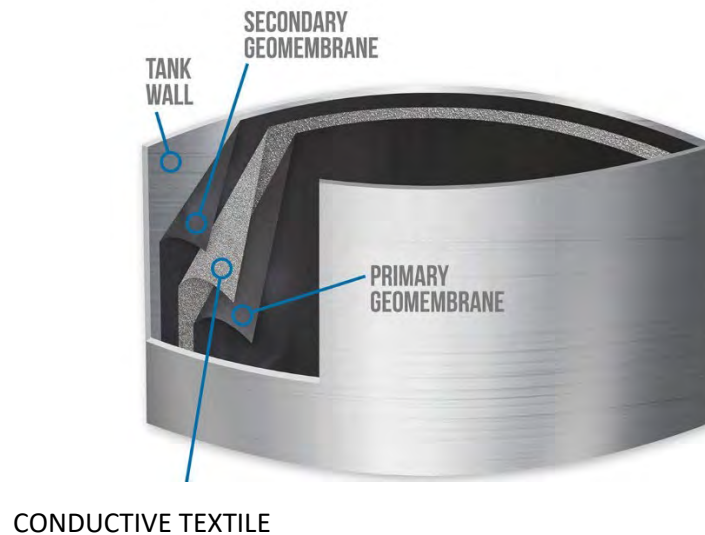


**Fig 4. Schematic of aboveground tank lined with geosynthetics**

During ELL testing, one defect (puncture) was detected in the primary geomembrane liner of the tank. The defect was located on the wall area of the tank, approximately 15 feet up from the tank's floor and 1 foot from the welded seam

**Wastewater Treatment Facility (2022).** Originally constructed in 1960, the Humber treatment plant is Toronto's second-largest wastewater treatment plant and services approximately 680,000 residents with an annual capacity of 473,000m<sup>3</sup>. The facility underwent extensive upgrades to improve air quality and odor issues which included the addition of biofilters to clean the emissions from the plants. During a recent inspection at the plant, it was determined the biofilter media has reached its end of life and required change out. During the removal of the biofilter media and tank clean-out, it was decided to improve the integrity of the containment and install a geomembrane lining system within the tank as an added level of protection against any leakage which may occur in the concrete tank. The concrete biofilter tank was lined by the installation team with a continuous layer of conductive textile. Seams were overlapped to create a continuous conductive

surface. Following the installation of the conductive textile, a flexible geomembrane was installed. Geomembrane seams and penetrations were fusion welded and liner was mechanically attached at the top of the tank using a typical mechanical attachment consisting of an SS316 1/4"x2" bar & gasket. All conductive elements were isolated prior electric leak survey. Arc method (ASTM D7953) was chosen for performing the ELL survey.



**Figure 5. Technician performing arc testing on the primary liner**

## CONCLUSION

The development of conductive textile can largely benefit non-conductive geomembranes that do not contain a conductive backing. All type of polymeric non-conductive barriers like PVC, EIA, Elvoloy's, Propylene's and CSPE can be tested using this new innovative conductive textile. This new technological innovation will benefit the overall construction quality assurance and will lower the risk of a leakage in both primary and secondary containment systems. The various case studies presented in this paper shows the diverse range of applications this product can be used and tested. The next step for the author is to try and laminate this material on a geonet so it can be used as a conductive geocomposite suited for ELL testing of the primary geomembrane in a double lined application.



## Increasing the Sensitivity of the Dipole Method: A Case Study

Abigail Gilson-Beck, P.E.,<sup>1</sup>  
Richard Thiel, P.E.,<sup>2</sup>

<sup>1</sup>TRI Environmental, Inc. Austin, TX; e-mail: [abeck@tri-env.com](mailto:abeck@tri-env.com)

<sup>2</sup>Thiel Engineering, Inc. Oregon House, CA; e-mail: [richard@rthiel.com](mailto:richard@rthiel.com)

### ABSTRACT

Dipole method sensitivity for electric leak location (ELL) surveys on geomembranes is primarily a function of site conditions. Poor site conditions can completely preclude the functionality of the method. A common misconception introduced by the ASTM D7007 standard practice for dipole method surveys is that increasing the measurement density of a survey will increase the method sensitivity. This has led to engineers to specify measurement density in project specifications for dipole method surveys. In fact, increasing the measurement density increases the survey resolution, but not the sensitivity. The most significant way to increase sensitivity through survey instrumentation is to increase the dipole spacing (Gilson-Beck, 2021). However, if site conditions are poor, no instrument adjustments or procedures can be implemented to cause the method to be effective. The most common cause of poor survey sensitivity is poor isolation along the perimeter of the survey area. This case study details a site where multiple surveys were performed on various phases of the project, with sensitivity continually decreasing with an increasingly dirty perimeter isolation gap. On the final testing event for the project, when sensitivity had completely deteriorated, a novel method of isolating the cover material using a leaf blower was used. Drying the perimeter isolation gap with the leaf blower drastically restored survey area sensitivity. Dipole method specifications should therefore focus on enforceable requirements for proper site isolation and specify the use of the largest practical dipole spacing in order to realize maximum method sensitivity rather than prescribing a minimum measurement density.

### INTRODUCTION

The term “sensitivity” when it comes to Electrical Leak Location (ELL) methods is not simple to define. Some factors in method success do not increase the method sensitivity as it is defined in a strictly technical sense, but they can increase the chances of finding a leak. For example, good method procedures do not increase survey area sensitivity, but they can increase the chances of finding a leak through, for example, good data management. For the purposes of this paper, sensitivity is defined as the ability to detect small differences in voltage responses where defects exist in non-conductive (insulating) geomembranes for purposes of locating leaks present in a survey area. The main subject of this paper is to discuss methods for improving dipole method sensitivity.

Another concept that will be discussed in this paper, but which is not the subject of this paper, is ‘functionality testing’. The term ‘functionality testing’ has largely replaced the confusing terms of ‘sensitivity testing’ and/or ‘leak detection distance testing’ that have been used in the ASTM standard guides and practices. Since the latter two terms are misleading, the

term ‘functionality testing’ is used throughout this paper to describe procedures used to check for method functionality and survey area conduciveness to testing.

Nine factors influencing method sensitivity are described in depth below in order of descending magnitude of effect. This order is a rough approximation based on two decades of field experience. For each factor, the relationship to other factors is discussed as well as whether and how the relevant ASTM standards address consideration of the factor. ASTM D7007-16 and D8265-21 are referenced. Future revisions of these standards should be checked for the continued validity of the statements made here.

**#1 Survey Area Isolation.** Without survey area isolation, none of the subsequent factors in sensitivity matter; the method will not work. Method sensitivity has a direct correlation with degree of survey area isolation and the method effectiveness will range from 0% (no leaks detectable) to 100% (every leak detectable). More highly electrically conductive cover material exacerbates isolation issues. Even with excellent perimeter isolation, existing leaks in the lining system can affect survey area isolation to some degree, with larger holes having a larger effect. If extensive damage to the liner is limited to a few specific areas (e.g. one or two locations), the damaged location(s) will be easy to detect, although initial functionality testing on a smaller leak may have indicated “poor sensitivity”. Once the damage is repaired or removed from its connection to the cover material, sensitivity should increase and it warrants repeating the method if a higher level of sensitivity is desired. This consideration is dependent on whether small holes were detectable before the larger damage was uncovered. If damage to the liner is extensive in area (e.g. breaches occurring in many places), the method can have difficulty locating any of the damage, depending on how large the damaged area(s) are relative to the survey area. In this situation increased localized measurement density might assist in pinpointing the locations of some of the more significant defects, and once those are repaired then the survey will become more and more sensitive, allowing the location of the smaller defects. In an extreme case, no discrete damage locations are detectable and site response current measurements will reveal that the liner is not able to inhibit current flow and the liner should be replaced.

Survey area isolation issues are identifiable by the level of site response current with applied voltage. A well isolated soil-covered survey area should generally not go above 100 mA with an applied voltage of up to 500 V. A poorly isolated survey area will often exceed 300 mA (DC current limit for human safety) at a lower applied voltage.

As of the writing of this paper, only D8265-21 requires reporting issues with survey area isolation as part of the final report, however D7007 will likely require it in future revisions. Only ASTM D 8265-21 requires that the site response current and applied voltage be reported with every survey area condition (i.e. before test, after test, with leak(s) present, without leak(s) present), however D7007 will likely require it in future revisions. ASTM D8265-21 also requires that issues with site conditions including isolation be reported before commencing testing and that the issue(s) be ameliorated if possible before testing begins.

**#2 Cover material and underlying substrate material electrical conductivity.** A minimum level of electrical conductivity is required for the method to be effective. If either the cover material above the geomembrane, or the underlying conductive layer below the geomembrane, is not electrically conductive enough, the method will not work. However, it is very rare for either the cover material (which can be irrigated) or the underlying layer to be insufficiently conductive, as most earthen materials only require a couple of percent of moisture content. However, issues have

been noted with insufficient electrical conductivity with some encapsulated geosynthetic clay liners (GCL) when installed as the sole conductive layer between two geomembranes (Beck et. al., 2008).

The electrical conductivity of the cover material affects the voltage drop distribution in the vicinity of a leak. A more conductive material exhibits smaller voltage drops, resulting in a smaller leak signal, since it is based on measured voltage through a distance of cover material (Gilson-Beck et. al., 2023). Conversely, a less conductive material provides a larger leak signal, translating directly in increased sensitivity (Cen, 2020). Therefore, there is a range of electrical conductivity that is conducive to ELL testing, with a minimum under which the testing will not work and an upper limit that causes leak signals to be so weak that they are difficult to detect. This means that the voltage drop is so small that it cannot practically be measured, especially in the presence of “background” oscillations in voltage. There is no maximum conductivity for the underlying substrate, since that layer is simply a return path for the electrical signal. Earthen materials become more electrically conductive with increasing moisture content.

Both ASTM D7007-16 and D8265-21 require reporting issues with the detectability of an actual or artificial leak (whose signal must be able to travel through both the cover material and the underlying conductive layer) as part of final reporting requirements. ASTM D8265-21 also requires that issues with site conditions related to material conductivity be reported before commencing testing, in order to provide the opportunity to improve site conditions before the test begins.

**#3 Moisture Content of Material(s) Overlying Geomembrane.** Although moisture content of the cover material is an essential component of cover material electrical conductivity as described in #2, this third factor addresses the adequate moisture required to ensure electrical contact at the leak location(s). If a small leak (too small for cover material to fill the void created by the breached geomembrane) is not wet, it will likely evade detection. Additionally, many containment facilities include cushion geotextiles or geocomposite drainage layers over the geomembrane. These plastic materials will not conduct the electrical signal(s) unless they are adequately moist. Additionally, they will tend to bridge small holes and prevent fines from bridging the air gap through the hole. This site condition will not typically be documented by the dipole method, since an artificial leak is most commonly used and the dipole method practitioner is allowed to ensure ideal contact between the artificial leak and the overlying materials. This is obviously not an issue for water-covered geomembranes. It should be noted that functionality testing using an actual leak is detailed in ASTM D7909-21a, which can more realistically gauge moisture directly above a leak.

Only ASTM D8265-21 requires reporting the condition of the material directly above the geomembrane. This requirement is slated for a future publication of ASTM D7007-16.

**#4 Dipole Instrument Spacing.** The distance between the two measurement points on the dipole determines how many voltage drops are captured by a dipole measurement, with a larger spacing between points capturing a larger magnitude voltage drop and therefore increased leak detection sensitivity. With all other factors being equal, a threefold increase in dipole spacing from one meter to three meters increases signal magnitude by over 300% (Gilson-Beck, 2021). The increase in signal strength as a function of dipole spacing is actually nonlinear, and tends to stabilize after the dipole spacing exceeds the spacing appropriate for the survey area geometry (Cen, 2020). Of course, there are practical limitations to increasing the dipole spacing. Dipoles measuring over three meters long become physically difficult to handle.

The best practice for dipole method surveys is to take measurements throughout the survey area in a grid pattern, spaced the same distance as the dipole instrument. When a larger dipole is used, it is a common misconception that the survey resolution is compromised, especially in the case of multiple leaks that might be spaced closer to each other than the measurement grid spacing. Multiple leaks are revealed during the pinpointing process, when the largest signal between measurement acquisition locations is excavated, then the surrounding area rechecked for additional signals. Pinpointing always uses a much greater measurement density than the bulk survey as well as multiple directions, to locate the exact position(s) of the leaks. This process must be repeated until the entire area encompassing the area of anomalous readings has been restored to background voltage values.

Both ASTM D7007-16 and D8265-21 require reporting the dipole spacing as part of final reporting requirements. Neither standard practice controls dipole instrument spacing, since the spacing used should also take into consideration the survey area size and geometry. For very small survey areas, a large dipole simply will not be able to acquire enough measurements to be meaningful. However, ASTM D8265-21 standardizes sensitivity between various dipole sizes by requiring that the distance between measurement points be no greater than the dipole spacing as detailed in the next section.

**#5 Dipole Method Procedures.** Survey procedures are strictly defined here as data acquisition methodologies including measurement density and data analysis methodology, even though many other parameters could be listed here, as well, all with minimal effects, assuming that an ASTM based standard practice is being adhered to. Due to the variability in the treatment of measurement density by the ASTM standard practices, this variable is considered the most significant factor in this category.

Leak detection “sensitivity” is shown to be approximately the same for a one meter dipole at a one meter by one meter measurement grid spacing as for a three meter dipole at a three meter by three meter measurement grid spacing (Gilson-Beck, 2021). Dipole spacing must therefore be taken into account when considering measurement density. Using a grid measurement spacing less than the dipole spacing will simply improve survey resolution, not sensitivity. If the grid measurement spacing is greater than the dipole spacing, then increasing the measurement density will increase the sensitivity as defined for this paper. It therefore depends on which ASTM standard practice is being used whether measurement density can be used to increase method “sensitivity”.

ASTM D8265-21 requires that the measurement grid spacing be no larger than the dipole spacing. This standardizes the detection sensitivity across all different dipole sizes, so an increase in measurement density will not affect method sensitivity since the prescribed measurement density sufficiently encompasses the survey area. ASTM D7007-16 allows for a larger measurement grid spacing than the dipole spacing upon demonstration of sufficient detection of an actual or artificial leak, which allows for skipping data acquisition locations throughout the survey area. This could result in undetected leaks, especially if the existing leaks are much smaller or drier than the actual or artificial leak used for the demonstration of sensitivity.

Two main data presentation methods for purposes of data analysis exist for soil-covered surveys: two dimensional and three dimensional. Two dimensional presentations consist of plotting voltage values on the Y-axis along the dipole transect (distance) representing the X-axis of a graph. Three dimensional presentations consist of plotting the survey area on the X and Y-axis of a map, with the voltage values shown as the Z-axis. In this manner the voltage values can be contoured, similar to a topographical map, with voltage values rather than surface elevations.



Plotting voltage values on a map not only shows the magnitude of a leak signal, but also the shape as it propagates through the cover material. Low magnitude leak signals are often recognized due to their shape in plan view, whereas the signal magnitude might be lost in the background voltage values when plotted on two-dimensional transect lines. Thus, the analysis of dipole survey data is significantly improved, and more easily understood, when presented in a three-dimensional format compared to a two-dimensional format. Additionally, voltage maps show the geographical relationship between different features. Since each feature will be more highly affected by other features near it, it is useful know, for example, if an artificial leak was installed near a perimeter isolation issue. The requirement to plot data acquisition locations on a voltage map is an additional quality control measure to ensure that the survey area was completely covered and that no data are missing. GPS-based data acquisition has shown that locational referencing of data points using GPS techniques is far quicker and less prone to errors than other methods. In addition, GPS-based data acquisition makes it possible to define non-square edges of the survey area and obtain extra data points, since the data acquisition is not constrained to linear string lines.

ASTM D8265-21 requires data analysis by way of voltage maps (three-dimensional analysis), with data acquisition locations plotted on the map(s). ASTM D7007-16 does not prescribe a data analysis method, but cites two and three dimensional analysis as the most common methods. Neither standard requires GPS-based data acquisition.

**#6 Dipole Instrument Design.** The dipole itself must be designed so that the only point of contact of the voltage measuring apparatus is at the measurement location. The measurement location must be electrically isolated from the rest of the structure that holds the measurement probes in place. Otherwise, current can short circuit the voltmeter. The physical design and materials used to construct the probes to measure voltage at the surface of the survey area are important to the success of the survey. The materials that they are comprised of may exchange electrons with the cover material. Copper sulfate reference electrodes are generally used, but even these can generate a voltage offset of up to 5 mV. These types of probes must be cleaned and/or tested frequently to assure that they are providing clean voltage readings. The voltmeter itself should have a high internal resistance for a most accurate reading.

ASTM D8265-21 requires that the dipole measurement probes be non-reactive with the cover material and that the internal resistance of the voltmeter used be at least 1 giga-ohm. ASTM D7007-16 does not address instrument design.

**#7 Cover Material Chemistry.** Although mineralogy affects the electrical conductivity of the cover material, this point goes beyond that. Electrons flow between different particles of biologically or chemically reactive cover material. The electron movement will be measured by the dipole as a voltage differential. If the voltage differentials are large enough, they can obscure leak signals.

Neither ASTM D8265-21 nor D7007-16 address this, but this is usually only an issue with active (in use) containment facilities. The dipole method is usually performed on recently constructed containment facilities with chemically and biologically inert cover material. However, for survey areas with dissimilar cover materials, for example a leachate collection trench ‘window’ composed of gravel while the remainder of the cover material is fine-grained, a voltage gradient is sometimes measured when the dipole instrument has one foot on each of the different materials (e.g. crossing the trench perpendicular to length of trench). Anomalies characteristic of leak signals

caused by the dissimilar materials require additional measurements parallel to the anomalous feature to rule out or confirm the presence of a leak.

**#8 Survey Direction.** The optimal transect direction for detecting a leak depends on where a leak is located in relation to the a) limits of the survey area, b) the current injector, c) other leaks, and d) perimeter isolation issues. It is impossible to know where a leak might be located, so the survey direction is typically arbitrarily chosen and validated by functionality testing. Also, leaks are difficult to detect if a dipole approaches a leak but does not move past it to acquire data on the other side of it. Leaks along the edge of the survey area that runs perpendicular to the direction chosen for the survey are therefore subject to being missed.

ASTM D8265-21 requires that data be acquired parallel to every edge of the survey area. ASTM D7007-16 does not require that data be acquired parallel to every edge of the survey area.

**#9 Cover Material Thickness.** The further away from a leak voltage measurements are made, the smaller the leak signal will be. This also applies to cover material thickness. The dipole method was developed for relatively thin cover material and is not purported to work for a “deep fill” configuration. ASTM D6747-21 defines a “deep soil fill” configuration as greater than 3 meters in depth. A common rule of thumb is that the cover material thickness should be no greater than the dipole spacing. Increasing the cover material within the “deep fill” limit as defined by ASTM D6747 will have a greater effect if a smaller dipole instrument is used. It will have a nominal effect with a larger dipole instrument.

ASTM D8265-21 states that thickness should be minimized and should not exceed approximately 3 meters (i.e. largest dipole size commonly used). ASTM D7007-16 states that if the cover material thickness exceeds 600 m, then a larger artificial leak than 6.4 mm should be used, but no maximum thickness is recommended.

## BACKGROUND

The case study detailed here is a 11-hectare double-lined landfill expansion cell located in Visalia, CA with the following cross section, from top to bottom: 0.6m silty soil operations layer, primary geocomposite drainage layer, 60 mil HDPE geomembrane, GCL, 0.3m silty soil separation layer, secondary geocomposite drainage layer, secondary 60 mil HDPE geomembrane, and 0.2m prepared silty subgrade. The secondary geomembrane was tested using the dipole method after placement of the 0.3m silty soil separation layer. The primary geomembrane was tested while bare using the water puddle method (ASTM D7002) and again after the 0.6m silty soil operations layer placement using the dipole method. Because of the project size and sequencing, the covered secondary geomembrane was tested in three separate campaigns, and the primary geomembrane was tested in four separate campaigns. Only the covered geomembrane testing is discussed herein.

The case study detailed here used the same survey procedures (ASTM D8265-21) and survey instrumentation for every testing event. A three-meter dipole was used with a measurement density spacing of three meters by three meters. The only testing parameter that varied from test to test was the degree of survey area perimeter isolation, since no leaks were found during the surveys that could have affected method sensitivity. The cover materials were profusely sprayed with water during excavation and placement, and on their surface during each testing event, and the same standardized functionality verification with a 6.4 mm diameter artificial leak was used each time.

During each survey, the relevant upper soil layer being surveyed (i.e. the 0.3m separation layer for the secondary liner system, and the 0.6m operations layer for the primary liner system) was stopped short of connecting with the perimeter of the new cell to provide electrical isolation. On three sides of the rectangular cell the perimeter consisted of a permanent anchor trench, and on one side the perimeter consisted of a tie-in to a previous cell. At the base of the unconnected gap between the new soil layers and the other side of the perimeter one could visibly see the exposed geocomposite drainage layer over the geomembrane. Electrical isolation was maintained by keeping the exposed geocomposite and geomembrane in this gap relatively clean and dry (Figure 1).

The method of electrically isolating access roads to maintain survey area truck access for spray-irrigating the cover soil material was to use a geomembrane flap. The flap was placed across the isolation trench and extended up through the access road soils to create an exposed edge, as shown in Figure 2. Such a flap, if used, is best welded to a rubsheet, which in turn should be welded continuously all around to the containment geomembrane, so that the flap weld does not adversely affect the containment geomembrane.

## RESULTS

Functionality testing results generated from the seven sequential survey campaigns are shown in Table 1 (three portions for the secondary liner system, and four portions for the primary liner system) in the general order that the testing was performed. Functionality of the survey methodology is evaluated based on the detectability of an artificial leak. The detectability of an artificial leak can be quantified by measuring the voltage when the front dipole probe is directly over the artificial leak and again when the back dipole probe is directly over the artificial leak. For the artificial leak to be considered detectable, the first measurement should be strongly negative and the second measurement should be strongly positive. Other measurements are made at offsets to the artificial leak during functionality testing, but to simplify the reporting of detectability between the various testing events for the purposes of this paper, only these two measurements are reported here. Additionally, a “detectability” column was generated of the difference between the two measured voltages. A positive value indicates that the artificial leak was detectable, with increasingly positive values showing an increased level of sensitivity. A negative value indicates that the artificial leak was not detectable.

Testing Event	Description of Dipole Location During Measurement	Measured Value (V)	Detectability
Secondary (1 <sup>st</sup> Portion)	Front Foot On 1/8" Artificial Leak	-5.397	+10.907
	Back Foot On 1/8" Artificial Leak	+5.510	
Secondary (2 <sup>nd</sup> Portion)	Front Foot On 1/4" Artificial Leak	-0.532	+1.576
	Back Foot On 1/4" Artificial Leak	+1.044	
Secondary (3 <sup>rd</sup> Portion)	Front Foot On 1/4" Artificial Leak	-0.016	+0.084
	Back Foot On 1/4" Artificial Leak	+0.068	
Primary (1 <sup>st</sup> Portion)	Front Foot On 1/4" Artificial Leak	-0.589	+1.134
	Back Foot On 1/4" Artificial Leak	+0.545	
Primary (2 <sup>nd</sup> Portion)	Front Foot On 1/4" Artificial Leak	-0.184	+0.228
	Back Foot On 1/4" Artificial Leak	+0.044	
Primary (3 <sup>rd</sup> Portion)	Front Foot On 1/4" Artificial Leak	+0.253	+0.128
	Back Foot On 1/4" Artificial Leak	+0.381	
Primary (4 <sup>th</sup> Portion)	Front Foot On 1/4" Artificial Leak	+0.215	-0.007
	Back Foot On 1/4" Artificial Leak	+0.208	

**Table 1. Functionality Testing Results for Seven Sequential Survey Campaigns.**

As shown in Table 1, the detectability of the artificial leak declined with each testing event of the secondary geomembrane as the perimeter isolation gap grew increasingly dirty during the course of construction. The detectability increased when the primary geomembrane started to be tested, which was the beginning of a new survey area since the primary geomembrane isolation gaps would have been newly installed for that layer. However, the same pattern of decreasing detectability was noted with each successive testing campaign in the primary liner system as was noted with the secondary liner system. In both cases, by the time the 3<sup>rd</sup> portion of the surveys were conducted for each layer, the results of the dipole measurements showed that the artificial leak was weakly detectable.

The 3<sup>rd</sup> portion of the primary liner system campaign showed particularly troubling voltage readings in that both of the functionality measurements had positive values. Without the negative voltage value with the front dipole foot over the artificial leak, the artificial leak is not strongly detectable. After reviewing these results, the perimeter isolation gap was inspected and the isolation improved before beginning the testing. A location along the perimeter immediately adjacent to the location of the artificial leak exhibited a strong signal due to the isolation issues shown in Figure 1. This location was determined to be the cause of the isolation issues upon analysis of the voltage mapping. This type of perimeter isolation issue is very typical of landfill expansions. Also it is noteworthy that the silty/clayey soils comprising the upper soil layers at this site are much more electrically conductive than clean sand and gravel layers that might be used for the drainage and operations layers at other sites, and this increased conductivity exacerbates the isolation issues.





**Figure 1. Perimeter Isolation Issue at Access Road Location Causing Primary Survey Portion 3 Sensitivity Issues Before Cleaning (Left) and After Cleaning (Right).**

For the fourth portion of the covered primary geomembrane testing, the initial functionality testing results shown in Table 1 indicated that the artificial leak was not detectable at all. The slight difference between the voltage readings was likely caused by measurement error, since the first number was slightly higher than the second number. During this final testing event, the entire survey area was complete, and thus the condition of the entire perimeter was influencing the sensitivity. It had rained significantly a few days before the final testing campaign, causing shallow flooding of the materials in the isolation gaps. After the rain event, the geocomposite under the isolation flap at the access road (Figure 2) was saturated, along with the entire bottom layer of geotextile throughout the isolation gap. At other sites, cutting the geocomposite and peeling it back has been used as a solution to increase sensitivity when the geocomposite is saturated. Since the survey area was bounded on three sides by anchor trenches, it was not acceptable to the engineer to cut the geocomposite.





**Figure 2. Method of Electrically Isolating Access Roads**

The entire perimeter isolation gap was then further cleaned and all of the access roads, such as the one shown in Figure 2, were completely removed. Functionality testing was repeated without any significant improvement. The second author was the approving engineer for this project and insisted that the 1/4" artificial leak be detectable before commencing the survey. He suggested the use of a high-powered leaf blower, directed at the geocomposite, proceeding along the entire isolation gap very slowly in order to thoroughly dry out the moisture trapped by the geotextile on the underside, and it would also tend to blow out any loose soil in the gap area. The backpack leaf blower that was used is shown in use in Figure 3.

Functionality testing was repeated after use of the leaf blower and the artificial leak was strongly detectable, as shown in Table 2.

Testing Event	Description of Dipole Location During Measurement	Measured Value (V)	Detectability
Primary (4 <sup>th</sup> Portion), After Leaf Blower	Front Foot On 1/4" Artificial Leak	-2.683	+6.507
	Back Foot On 1/4" Artificial Leak	+3.824	



**Table 2. Functionality Testing Results After Application of Leaf Blower.**



**Figure 3. Backpack Leaf Blower Used to Dry out the Geocomposite in the Perimeter Isolation Gap.**

## CONCLUSIONS

It is clear from the results of the testing sequence on this project that survey area isolation is the single most critical factor in the effectiveness of dipole electrical leak location testing. Since moisture has a direct correlation on electrical conductivity, a focus on drying out the material(s) in the isolation gap rather than completely removing them proved extremely effective on the installed geocomposite. The use of the backpack blower provided a low-cost, speedy and highly effective fix for the perimeter isolation issue encountered in this instance. This method is recommended for the toolbox of any leak location purveyor when conducting a dipole method survey over soils.

Project specifications with the intention of maximizing method sensitivity should focus on site isolation as an enforceable requirement and should be considered as part of the design documents and specifications. Decisions related to dipole spacing should generally be left to the judgement of an experienced leak location specialist, but it is recommended that the measurement

density not exceed the dipole spacing. Given that increased sensitivity is typically achieved with a greater dipole spacing (up to reasonable limits), and that increased dipole spacing typically results in quicker and less expensive surveys, there are strong arguments to consider using a dipole spacing on the order of 3m with a corresponding measurement density of 3m by 3m for practical production surveys, allowing that increased measurement densities are useful for evaluating anomalous signals and pinpointing leaks.

Plotting dipole survey data in a three-dimensional format that shows contours of voltage readings, as recommended in the Standard Practice of ASTM D8265-21, provides improved data interpretation that is also more understandable to the client and regulators. Although the georeferencing data required for presentation in this format can be acquired by traditional stringline grid techniques, the advent of GPS technology provides a very expedient, cost-effective, reliable, and more flexible means to perform this task.

## REFERENCES

- ASTM D 6747. Standard Guide for Selection of Techniques for Electrical Leak Location of Leaks in Geomembranes, *ASTM International*, West Conshohocken, Pennsylvania, USA.
- ASTM D 7002. Standard Practice for Electrical Leak Location on Exposed Geomembranes Using the Water Puddle Method, *ASTM International*, West Conshohocken, Pennsylvania, USA.
- ASTM D 7007. Standard Practices for Electrical Methods for Locating Leaks in Geomembranes Covered with Water or Earthen Materials, *ASTM International*, West Conshohocken, Pennsylvania, USA.
- ASTM D 7909. Standard Guide for Placement of Intentional Leaks During Electrical Leak Location Surveys of Geomembranes, *ASTM International*, West Conshohocken, Pennsylvania, USA.
- ASTM D 8265. Standard Practices for Electrical Methods for Mapping Leaks in Installed Geomembranes, *ASTM International*, West Conshohocken, Pennsylvania, USA.
- Beck, A., Kramer, E., Smith, M. (2008). Specifications for Moisture Content of GCL to Perform Electrical Leak Location Surveys. *EuroGeo4 Conference Proceedings*, Edinburgh, Scotland.
- Cen, W.J., Du, X.H., He, H.N., Yan, J. and Rahman, M.S. (2020). Laboratory testing and numerical modeling of geomembrane electrical leak detection surveys. *Geosynthetics International*, Vol. 27(5), pp. 490-502.
- Gilson-Beck, A. (2021). Dipole Measurement Density and Dipole Spacing for Electrical Leak Location. *Geosynthetics Conference 2021 Proceedings*, Virtual Conference, February 22-25.
- Gilson-Beck, A. and Corby, T. (2023). The Effect of Cover Material Conductivity on Dipole Method Testing. *Geosynthetics Conference 2023 Proceedings*, Kansas City, MO, USA, February 5-8.



## The Effect of Cover Material Conductivity on Dipole Method Testing

Abigail Gilson-Beck, M.S., P.E.<sup>1</sup>  
Tyler Corby<sup>2</sup>

<sup>1</sup>TRI Environmental, Inc. Austin, TX; e-mail: [abeck@tri-env.com](mailto:abeck@tri-env.com)

<sup>2</sup>TRI Environmental, Inc. Austin, TX; e-mail: [tcorby@tri-env.com](mailto:tcorby@tri-env.com)

### ABSTRACT

The success of dipole method testing relies on site conditions including cover material electrical conductivity, with testing issues reported when testing takes place in highly conductive solutions. The goal of this study was to provide a quantitative analysis of how cover material electrical conductivity affects dipole method testing, in particular signal strength over a given leak. For the dipole method, signal strength is determined by voltage measurements obtained by a dipole. For this study, a water-filled, bench-scale test cell containing one circular leak was constructed. Voltage values collected using the dipole method throughout the test cell were organized into voltage maps in order to observe leak signal strengths as a function of cover material conductivity. The conductivity of the cover material was increased by adding salt to the solution inside of the test cell. Five trials were run at increasing levels of electrical conductivity, from fresh tap water up to a saturated brine solution, considered to be highly conductive. The test cell current draw was measured for each trial. Results of the trials show that as electrical conductivity of the cover material increases, signal strength of a given leak decreases. Poor electrical contact conditions of either the current injector or current return electrode results in a decrease in leak signal strength. Weaker leak signals can be amplified by increasing the applied voltage. Additionally, any level of leak signal can be magnified through detection meter gain and/or increasing the contour interval of the data analysis mapping software. These results are put into a practical context, with recommendations for increasing dipole method leak detection sensitivity in highly conductive solutions.

### BACKGROUND/INTRODUCTION

Dipole method testing is by far the most widely used testing method for electrical leak location testing of covered geomembranes. The authors have noted from field experience that cover material conductivity factors into leak signal size and strength. Although cover material conductivity is not measured directly onsite, it is indirectly measured through the site response current at an applied voltage of the testing circuit. It has been noted that at higher cover material conductivity, leak signals are more difficult to detect. In order to study in more detail what this phenomenon looks like when all other factors remain the same and only the cover material conductivity changes, a test cell was created in order to provide a highly controlled environment for measuring this phenomenon.

Analytical models have been created to calculate the effect of signal strength on various dipole method testing parameters (Cen, et. al., 2020 and Lugli and Mahler, 2016). Analytical methods have reported that the applied voltage increases leak signal strength and that signal strength decreases with increasing cover material conductivity (Cen et. al. 2020). However, these studies have not shown how this increase or decrease in signal strength is measured by the dipole method and dipole method voltage maps, since it was not the main focus of the research. Also, although helpful, there are some testing details that a computer model cannot predict, such as the reaction between the solution in the testing area and the electrodes used for testing as well as the current injector and return electrodes used. Electrical current can chemically interact with the elements of a testing circuit in unpredictable ways. This is why it is useful to study this phenomenon using commonly used tools for dipole method testing on an actual test cell.

The test cell was designed to show what a leak signal looks like through dipole measurements and voltage mapping, primarily as the conductivity of the cover material changes, but also by changing the applied voltage. It is the Authors' hope that in understanding the phenomenon more thoroughly, that these variables can be more successfully controlled for large-scale field testing applications.

## **BENCH-SCALE TESTING**

Water was chosen as the cover material for a bench-scale testing apparatus since the cover material conductivity can easily be changed by adding ions to the solution. Additionally, water-covered surveys yield less measurement error because the contact between the dipole probes and the cover material is excellent in water as opposed to on the surface of soil. An electrically insulated box was placed inside of a larger water-filled container. To simulate a lining system failure, a hole was drilled into the box. The box was then filled with solution of various, measured electrical conductivities. The area inside of the box is referred to as the "test cell" and the space in between the box and the container is referred to as the "leak detection layer". Placing electrodes inside of both the test cell and the leak detection layer allowed for electrical current flow via the hole in the box. A pair of submersible reference electrodes was used for data acquisition of the voltage potential using the dipole method throughout the test cell. The electrical conductivity of the solution in the test cell was changed in between testing events using various amounts of common water softening salt.

The electrically-insulative box and test cell measured 20" x 60". After filling the box to a specified depth, metal L-brackets were fastened to opposing sides of the box's 20" sides, above the water level. A common 2x4 rested on top of the L-brackets. At a spacing of 3" on center, holes matching the diameter of the submersible reference electrodes (~1.0 in.) were drilled into the top of the 2x4. The 2x4 was then used as a measurement spacing template for data acquisition as the reference electrodes could be held in the same position for each data point. The 2x4 was moved along the L-bracket for each row of data. Each data set included twelve

data acquisition points in the Y-direction and six data acquisition points in the X-direction for a total of 72 voltage measurements. A 0.125" diameter hole was drilled into the box at the location called out as "leak" in Figure 1. A diagram of the test cell is provided as Figure 1.

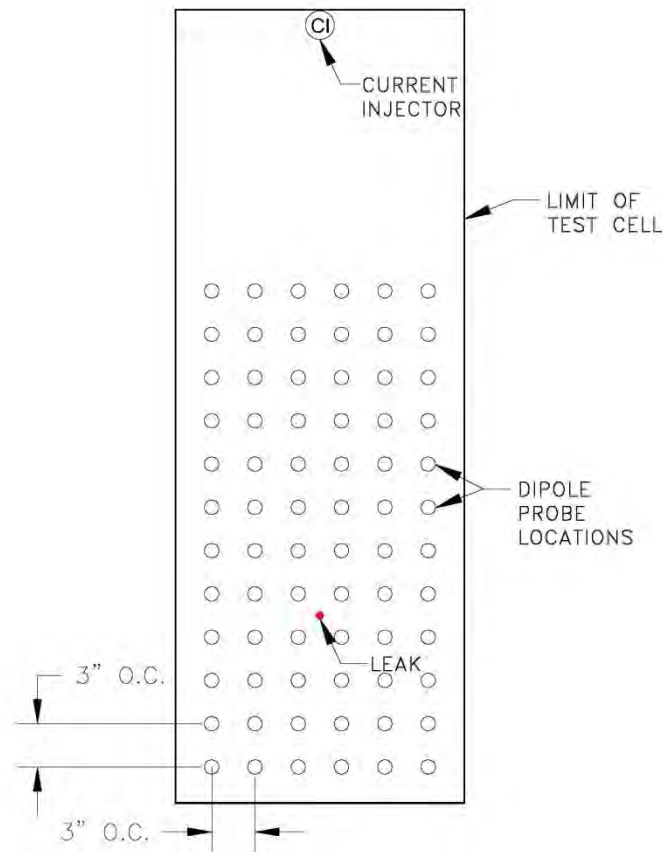


**Figure 1. Diagram of Bench-Scale Test Cell**

A direct-current power supply was used to apply an electrical potential across the test cell box. Great care was taken to mitigate chemical reactions between the electrodes and the cover material. Electrodes designed to be non-reactive with brine were therefore used as the current injector and current return electrodes of the power supply. The current injector electrode was placed in the far side of the test cell, away from the data acquisition area, whereas the current return electrode was placed in the leak detection layer. The first test cell design included a conductive geotextile connected to a simple stainless steel current return electrode, in order to keep the stainless steel electrode out of the solution, since stainless steel is known to react with brine. However, the conductive geotextile appeared to breakdown once subjected to a high current level. As a result, all trials were repeated without the conductive geotextile, with a non-reactive electrode touching the solution in the leak detection layer directly. One result obtained

while using the conductive geotextile is reported here to show how the breakdown of the geotextile affected the signal strength and it is also used as an example of weak signal strength.

Voltage measurements obtained throughout the testing area were organized and mapped using the “surfer” program by Golden Software. An “Omegaette” Microprocessor Based Water Test meter (PHH-7000 Series) was used to measure the solution electrical conductivity.

**Table 1. Descriptions of Trials.**

<b>Trial</b>	<b>Description</b>	<b>Electrical Conductivity (Siemens)</b>	<b>Applied Voltage (Volts)</b>
1	Tap Water	0.000075	50
1B	Tap Water	0.000075	200
1C	Tap Water	0.000075	500
2	Target Conductivity between 0.001 and 0.002 Siemens (slightly salty tap water)	0.0016	50
3	Trial 4 Solution diluted ~50/50 with tap water	0.0066	50
4	Conductivity just under maximum conductivity reading of meter	0.0168	50
5	Saturated Brine Solution	N/A (over limit of meter)	50

**Leak Signal Measurements.** In addition to the voltage mapping performed, measurements were taken directly over the leak. Measurements directly over the leak will yield the highest leak signal, which is calculated by finding the difference between the voltage reading when the front dipole electrode is directly over the leak (Dipole Position 1) and the voltage reading when the back dipole electrode is directly over the leak (Dipole Position 2). Three measurements were taken for each dipole position and then averaged in order to smooth out slight measurement errors. Signal strength was calculated as the difference between the measured values at the two positions. Signal measurements were taken at the same applied voltage with increasing electrical conductivity of the cover material.

## RESULTS

The results of the trials are detailed below in groups in order to show a comparison between the trials with a single changing variable. The colors used for the dipole method voltage maps are indicative of positive and negative values. Negative values change from red to blue to black with increasing magnitude and positive values change from green to yellow to white with increasing magnitude.



**Increasing cover material conductivity.** The measured leak signal decreased with increasing cover material conductivity as shown in Figures 2, 3 and 4 and Table 2. It was noted during the trials that the response current was not always behaving according to Ohm's law. It was also noted that very slight adjustments to the circuit (e.g. tightening connections) changed the response current and, correspondingly, the leak signal strength. In order to correct for these slight variables between trials, the measured current draw was used to normalize the signal strengths, which resulted in the significantly higher coefficient of determination shown on Figure 4. The current response of each trial is shown in Table 2.

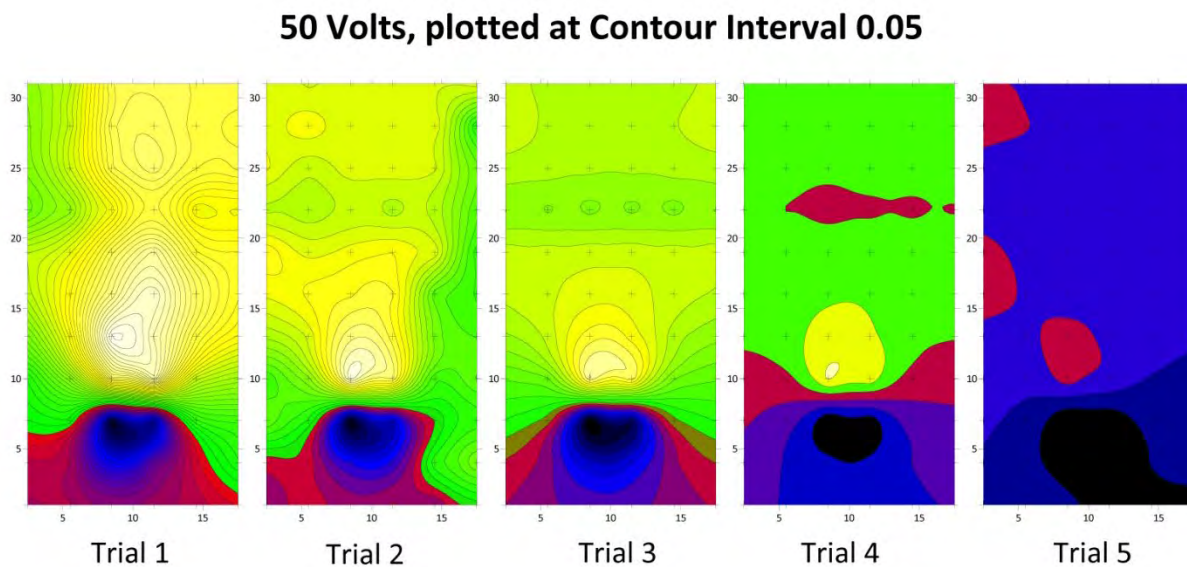


**Figure 2. Leak Signal as Electrical Conductivity of Cover Material Increases**

**Table 2. Leak Signal as a Function of Cover Material Conductivity at an Applied Voltage of 50 V.**

<b>Trial</b>	<b>Dipole Position 1 (Volts)</b>	<b>Dipole Position 2 (Volts)</b>	<b>Signal Strength (Volts)</b>	<b>Current Response (mA)</b>
1	-1.04	2.42	3.46	0.23
2	-1.09	1.28	2.37	3.58
3	-0.78	0.99	1.77	11.83
4	-0.73	0.65	1.38	22
5	-0.25	0.16	0.40	75

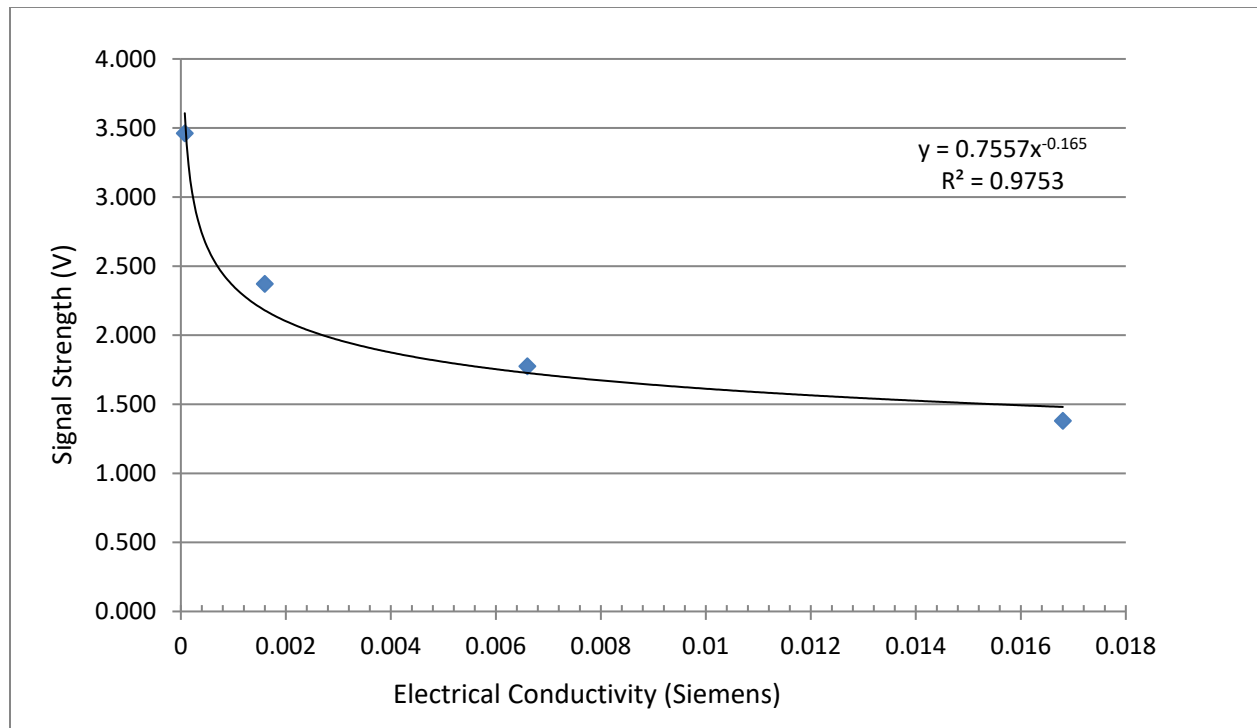


**Figure 3. Leak Signal Strength as a Function of Cover Material Conductivity**

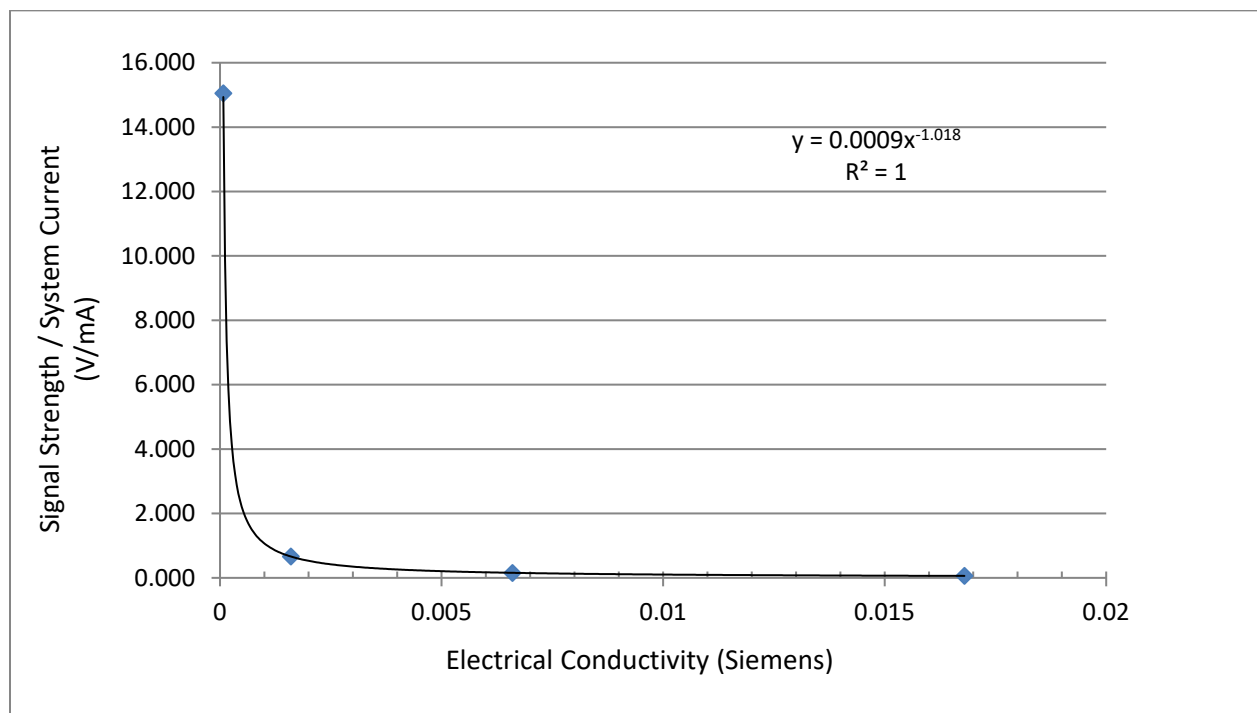


**Figure 4. Leak Signal Strength Corrected for Current Response as a Function of Cover Material Conductivity**

**Applied Voltage.** Increasing the applied voltage directly increased the signal strength, as shown in Figures 5 and 6 and Table 3. The current draw did not increase directly proportionally with the increase in applied voltage. This is likely due to more circuit losses at a higher applied voltage. This exercise was also performed on the Trial 4 conductivity solution, but the resulting extreme increase in current draw caused the system to become too unstable for repeatable voltage and current measurements, so the results are not shown here. However, the same trend applies to any solution conductivity as long as the higher current flow does not cause chemical reactions or component breakdown.

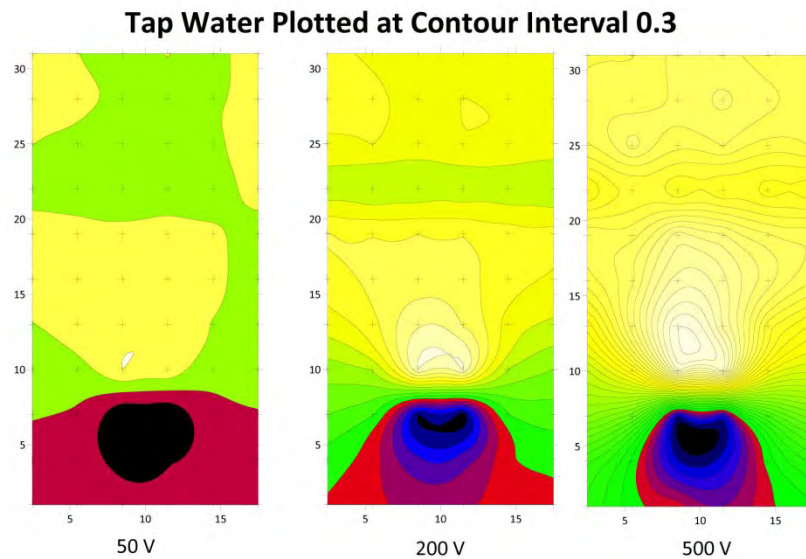


**Figure 5. Voltage Plot of Leak Signal with Increasing Applied Voltage**

**Table 3. Leak Signal as a Function of Increasing Applied Voltage.**

<b>Trial</b>	<b>Dipole Position 1 (Volts)</b>	<b>Dipole Position 2 (Volts)</b>	<b>Signal Strength (Volts)</b>	<b>Current Response (mA)</b>
1	-1.26	1.55	2.82	0.5
1B	-3.51	5.27	8.79	1.5
1C	-7.29	17.9	25.2	1.9

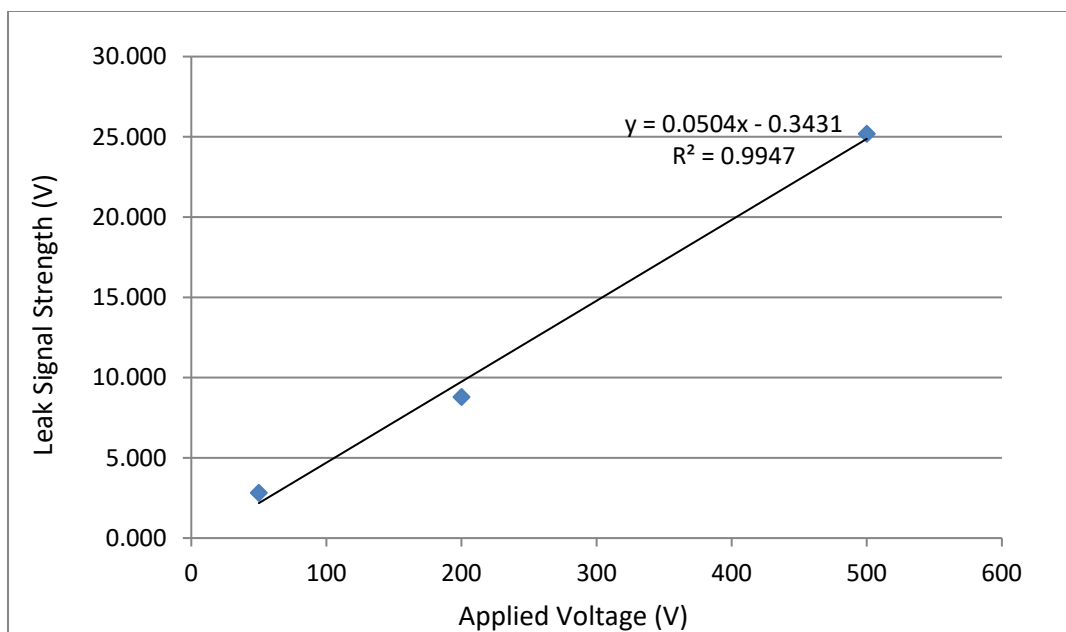


**Figure 6. Leak Signal as a Function of Increasing Applied Voltage**

**Data Analysis.** The detectability of a leak signal in the field is usually dependent on the positive/negative voltage pattern, whose visibility is enhanced through color coding the voltage measurements as positive or negative values. However, some weak signals have been observed that do not exhibit positive/negative values, but they do retain the same leak pattern of high voltage peak above lower voltage dip separated by closely spaced contour lines. Two 50 volt trials are shown in Figure 7, one of tap water and one of the Trial 4 conductivity with the poor geotextile ground. When plotted at the same contour interval with the same positive/negative color coding, the high conductivity trial is much more difficult to detect than the tap water trial. However, when the contour interval is changed inside of the mapping software and the color coding is changed to black and white (low to high voltage with no distinguishing between positive and negative voltage values), then the signal strengths look equally detectable.



## 50 Volts

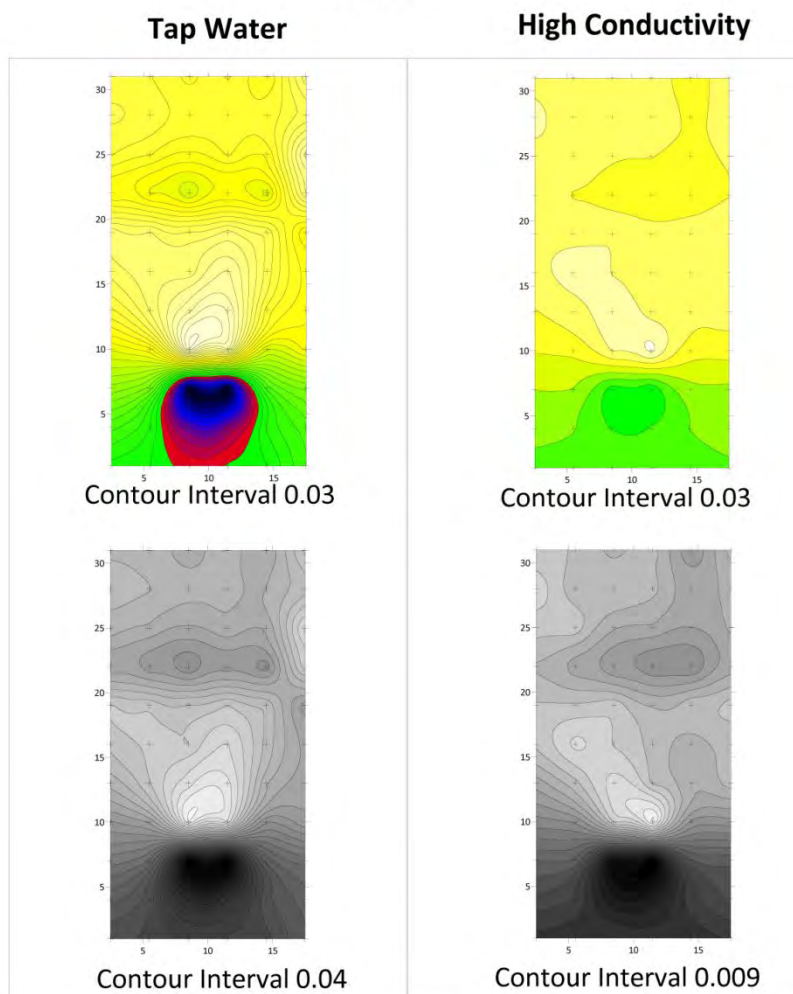


**Figure 7. Leak Signal Detectability Amplified by Data Analysis Method**

**Grounding Issues.** The Trial 4 conductivity results are shown with two different grounds in Figure 8. The map on the left is shown with the conductive geotextile ground after it had been subjected to a high current and the map on the right was created using all of the same testing parameters, but with the non-reactive electrode ground placed directly in the water of the leak detection layer rather than attached to the conductive geotextile.

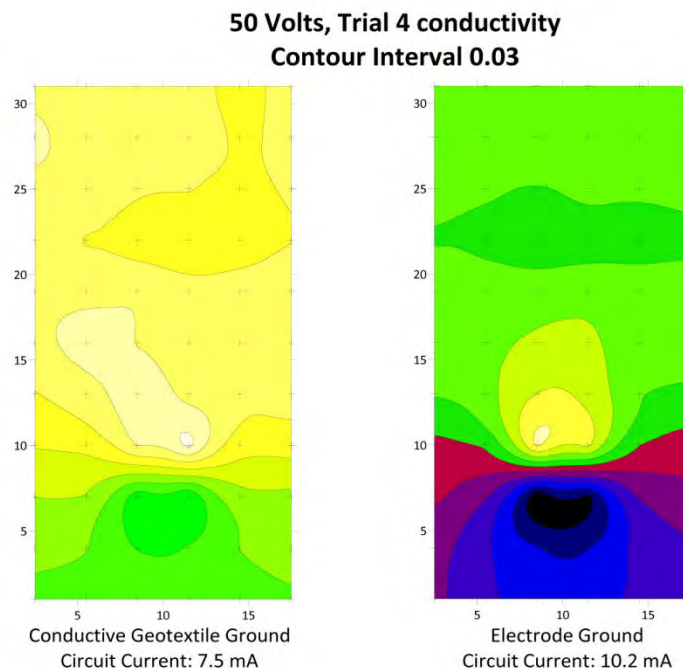


**Figure 8. Leak Signal as Affected by Electrode Contact**

## CONCLUSIONS AND DISCUSSION

As cover material conductivity increases, response current increases and leak signal decreases. Intuitively, one would expect more voltage drops to be measurable with an increase in circuit current, but that is not the case. During field testing, leak signal strength can be increased by increasing the contacts of the circuit (e.g. wetting the current injector), which results in higher current flow and a larger leak signal. However, when current flow is increased by increasing the cover material conductivity, the leak signal gets smaller. Energy is dissipated with impedance through a system. This impedance is measured by a dipole as voltage drops. In the case of water, the water can be heated or the molecules in the water can become disassociated. Interestingly, the medium must be conductive enough to allow current flow, but not so conductive so that the voltage drops cannot practically be measured. Some sites do not fall inside of this “goldilocks” zone, so what can be done for those sites?

Surveying highly conductive soils has been reported as an “unsolved” problem (Garcia and Lara, 2013). Using a dipole with a larger spacing will help with this problem, since the larger the dipole spacing, the longer distance of cover material it is measuring, which will result in a higher measured voltage value (Cen et. al, 2020 and Gilson-Beck, 2021). Applying a “gain” on the detector meter can also help magnify small signals, but only to a point, since magnifying the voltage will increase both the signal and the noise of the system. The type of data analysis shown in Figure 7 can be very effective for highly conductive solution surveys, but again only to a point, since specifying a smaller contour interval magnifies the noise as well as the signals. Therefore,

one part of the solution is to obtain very clean data by using measurement electrodes that are not reactive with the cover material.

One reliable way to increase the signal strength is to increase the applied voltage. As reported by Cen et. al., the leak signal strength increases approximately linearly with increasing applied voltage. However, increasing the voltage will increase the site response current proportionately in accordance with Ohm's law. Leak location surveys in highly conductive solutions are known to be conducted at a lethal current level (Garcia and Lara, 2013). In the Author's experience, highly conductive solutions regularly require a current draw that is unsafe for humans, which is anything higher than 300 mA DC. This should therefore be addressed as a safety consideration.

One common symptom of poor detectability due to highly conductive cover material is that the leak signal does not produce the typical negative/positive polarity. The solution to this could be a reduction in contour interval along with changing the color scheme to avoid "color blindness", as shown in Figure 7. In this example, the data reviewer's attention is focused on the signal trend of the characteristic drop and peak, rather than looking for the positive/negative polarity typical of highly detectable leak signals. However, small signals have a high potential to be masked by background noise, which tends to be higher when measurements are taken through drier and more granular material such as gravel. Making sure that the survey area is moist all the way to the surface where measurements are taken will help reduce measurement noise. Dipole probe design and internal resistance of the detection voltmeter also factors into measurement error, which is why the more recently published standard practice for the dipole method addresses this (ASTM D8265).

Conductive geosynthetic products are emerging in the marketplace. To date, there is only one organization that is attempting to create a standard for such products (ASTM D7852). However, currently, this standard lacks any detailed requirements for how the products should be tested for functionality. In particular, they should be evaluated for their current carrying capacity, both in bulk and at contact points with any applied electrodes. The Authors do not know of any manufacturer of conductive geosynthetics products that provides any specifications for electrode contact. Fires have been caused by too small of an electrode contact and/or too high of a current applied through "conductive" geosynthetic products. The conductive geotextile used as part of the original circuit of the test box functioned until subjected to approximately 10 mA. Even though the contact with the product was moved and improved after the breakdown in conductivity, it never behaved the same. This is a conductive geosynthetic design issue that must be addressed in product development as well as any standard practices.

## REFERENCES

ASTM D 7852. Standard Practices for Use of an Electrically Conductive Geotextile for Leak Location Surveys, *American Society for Testing and Materials*, West Conshohocken, Pennsylvania, USA.

- ASTM D 8265. Standard Practices for Electrical Methods for Mapping Leaks in Installed Geomembranes, *American Society for Testing and Materials*, West Conshohocken, Pennsylvania, USA.
- Cen, W.J., et. al. (2020). Laboratory testing and numerical modeling of geomembrane electrical leak detection surveys, *Geosynthetics International*, Volume 27, Issue 5, October, 2020, pp.490-502.
- Garcia, M. and Lara, A. (2013). Electrical Leak Detection Surveys for Brine Ponds in SQM, Chile, *Proceedings of IFAI Geosynthetics Conference*, Long Beach, CA, USA.
- Gilson, A. (2019). Electrical Leak Location Testing for Zero Leak Verification, *Proceedings of IFAI Geosynthetics Conference*, Houston, TX, USA.
- Gilson-Beck, A. (2021). Dipole Measurement Density and Dipole Spacing for Electrical Leak Location, *Proceedings of IFAI Geosynthetics Conference*, Virtual Meeting.
- Lugli, F. and Mahler, C.F. (2016), Analytical study of the performance of a geomembrane leak detection system, *Waste Management & Research*, Vol. 34(5) 482-486.



## Engineered Turf Landfill Closure: How Long Will It Last?

**Bryan Scholl, Ph.D., P.E.<sup>1</sup>, Ming Zhu, Ph.D., P.E.<sup>2</sup>, and Zehong Yuan, Ph.D., P.E.<sup>3</sup>**

<sup>1</sup>Watershed Geosynthetics, 11400 Atlantis Place, Suite 200, Alpharetta, GA 30022; e-mail: [bscholl@watershedgeo.com](mailto:bscholl@watershedgeo.com)

<sup>2</sup>Watershed Geosynthetics, 11400 Atlantis Place, Suite 200, Alpharetta, GA 30022; e-mail: [mzhu@watershedgeo.com](mailto:mzhu@watershedgeo.com)

<sup>3</sup>SGI Testing Services, 4405 International Blvd., Suite B117, Norcross, GA 30093; e-mail: [zyuan@sgilab.com](mailto:zyuan@sgilab.com)

### ABSTRACT

The engineered turf final cover system is an innovative landfill capping technology that addresses long-standing challenges of traditional soil covers. A traditional soil-geosynthetic cover requires large amounts of soil meeting specific properties, such as permeability, plasticity, particle size, and organic content to name a few. Soil is frequently unavailable in sufficient quantities and quality within an economical distance for the landfill closure. As a geosynthetic-based landfill closure system, the engineered turf final cover system provides engineers and site owners a more predictable solution to the persistent, long-standing challenges of traditional soil covers, such as soil erosion and final cover veneer slope instability. The engineered turf final cover system is presently installed in 35 states in the U.S. and has been utilized as a final landfill closure system for over ten years. Research and development have been conducted on the components of the engineered turf final cover system. This paper presents results from field and laboratory work to help answer the question: “How long will this engineered turf final cover system last?”

### INTRODUCTION

The United States Environmental Protection Agency (USEPA) recognizes four distinct classifications of landfill: (1) municipal solid waste (MSW), (2) hazardous waste, (3) industrial waste, including coal combustion residuals (CCRs) and construction and demolition (C&D) debris, and (4) polychlorinated biphenyls (PCB) (USEPA, 2022a). Even though USEPA does not maintain a comprehensive database of landfills, the Landfill Methane Outreach Program (LMOP) recognizes over 2,600 unique landfills (USEPA, 2022b). The majority of those are likely MSW landfills as they are the most associated with methane production. Including other landfill types, a reasonable conjecture is that there are more than 3,000 landfills in the United States. Clearly, there are a significant number of landfills planning for closure or already in the closure process. Solutions are needed to properly close these sites in an environmentally safe manner while minimizing risk to human health and the environment. When it comes to landfill covers, increased regulatory demands and challenges of traditional covers are driving landfill operators to use more innovative and better-performing solutions.

In response, ClosureTurf<sup>®</sup> (CT) was developed over ten years ago and has now been the final closure of choice for over 3,500 acres in 35 states in the U.S. CT is a patented three-component engineered turf final cover system. CT utilizes a structured geomembrane that serves as the hydraulic barrier, an engineered turf with polyethylene (PE) synthetic turf fibers tufted into

a double-layer woven polypropylene (PP) geotextile backing for protection of the underlying geomembrane, and a specified sand infill placed within the engineered turf for additional ultraviolet (UV) protection and ballast against wind uplift, as illustrated in Figure 1.

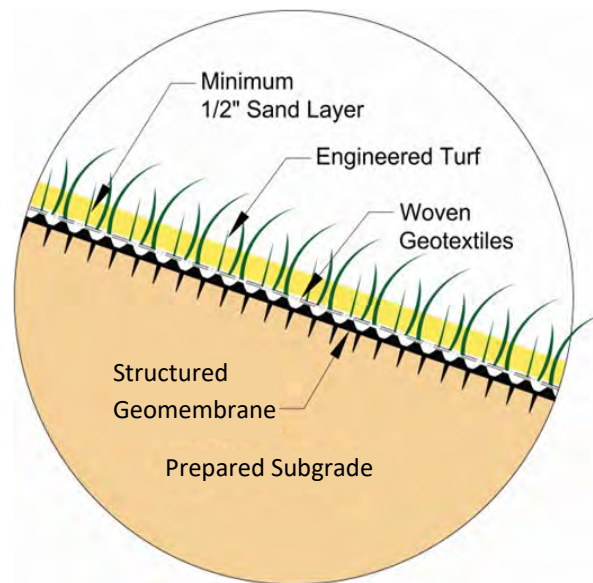


**Figure 1. Illustration of CT's three-component system**

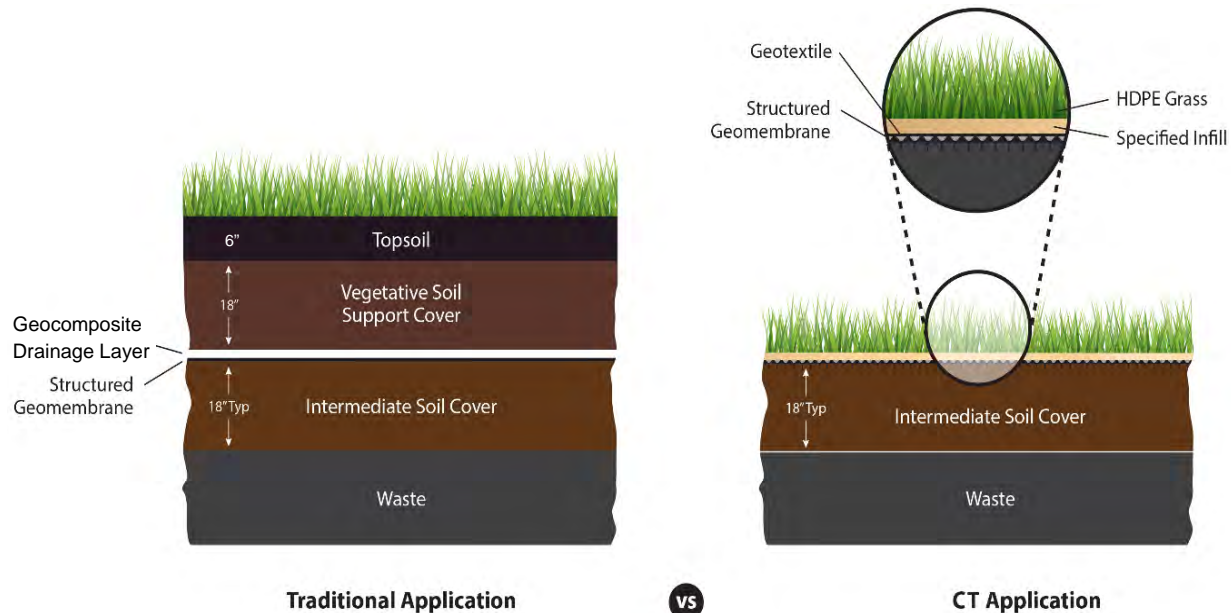


**Figure 2. Traditional vs. CT final cover cross section**

The traditional soil cover, which meets the USEPA Subtitle D landfill final cover requirements, is typically comprised of (from bottom to top) a geomembrane, a drainage layer which is usually a geocomposite, 18 inches of vegetative/protective soil cover, and 6 inches of topsoil. This

traditional cover is shown in Figure 2 side by side with the CT cover system. In terms of components, both the traditional and CT covers have a geomembrane. The traditional cover typically uses 24 inches (36 inches in some states) of soil cover to protect the underlying drainage layer and geomembrane. CT uses an engineered synthetic turf infilled with sand for the purpose of protecting the underlying geomembrane.

Stability of the final cover system is an important criterion. CT utilizes a structured geomembrane with a textured or spiked surface to achieve a high interface friction against a wide range of subgrade soil conditions. The high interface friction and elimination of the soil overburden significantly increases the final cover veneer stability, making it a preferred system for steep slope applications.

One of the CT structured geomembranes, Super Gripnet®, is a double-sided geomembrane that is comprised of upward-facing drainage studs and downward-facing friction spikes of two different styles. The studded side features consistent pattern and spacing, delivering internal drainage. These built-in studs eliminate the need for a separate drainage layer, providing cost savings in material usage and installation. The bottom-facing portion of the geomembrane uses spikes for a high-friction surface to deliver veneer stability. The friction spikes of the geomembrane are manufactured using a flat die-cast extrusion method, which provides high shear strength performance for closure applications. The geomembrane is manufactured with high-quality high-density polyethylene (HDPE) or linear low-density polyethylene (LLDPE), which offers large elongation at break providing resiliency in applications with a high potential for settlement.

As a landfill final closure system, CT offers predictable performance in the face of frequently less predictable environmental conditions. Unlike traditional closure systems that rely upon vegetation to meet regulatory requirements for erosion control, CT provides a solution that will perform regardless of drought or heavy precipitation. This predictability, along with excellent slope stability and reduced post-closure maintenance, provides the industry with another viable final closure option.

The remainder of the paper is focused on answering the question, “How long will it last?” that arises for CT. To address this question, published longevity data on geomembrane and geotextile are evaluated. Testing by independent laboratories has been performed on the CT cover system. To determine the anticipated longevity of the engineered turf fibers, samples were collected from multiple sites with CT installed as the closure system. In addition, accelerated natural exposure weathering testing has been independently conducted using the Fresnel Solar Collector method by Atlas Material Testing Solutions® in Arizona. Both the long-term field samples and accelerated natural weathering samples were then tested for retained tensile strength by an independent laboratory.

## LONGEVITY OF THREE COMPONENTS

To address the longevity question, each of the three CT components are examined and an estimated longevity determined for each component. Subsequently, the entire system can be assessed for anticipated longevity.

**Structured Geomembrane.** The structured geomembrane component, which serves as the hydraulic barrier for closure, is covered and protected by the engineered turf, which in turn is infilled with and protected by the specified sand infill. Since the CT geomembrane is covered, it

corresponds to the unexposed condition in the study on geomembrane lifetime by GSI (Koerner et al., 2011). Depending on in-service temperature, the GSI study predicts that the half-lives of an unexposed geomembrane are expected to be 446, 265, 166, 106, and 69 years, corresponding to constant service temperatures of 20 °C, 25 °C, 30 °C, 35 °C and 40 °C, respectively. The GSI study also recognizes that a 50% reduction in a specific property (e.g., tensile strength), which corresponds to the half-life, is an arbitrary standard and does not represent “end of life”. At the half-life, the material continues performing in place at a potentially decreased service level relative to new conditions. For the structured geomembrane of CT, even at the half-life, it is still serviceable with a remaining tensile strength much greater than the minimum required tensile strength due to the lack of overburden and minimal tensile stress in the geomembrane. Therefore, the geomembrane service life is anticipated to be much longer than the predicted half-life. A conclusion can be reasonably drawn based on the GSI study that the unexposed structured geomembrane component of CT is expected to have a service life of over 200 years under most climate conditions.

**Engineered Turf.** The second CT component is the engineered turf, which is buried with sand infill and protects the geomembrane from exposure. The engineered turf is comprised of a double-layer woven PP geotextile backing containing UV stabilizers, which are tufted with PE synthetic turf fibers. The function of the turf fibers is to hold the sand infill in place, which provides complete blockage of UV exposure of the geotextile backing. The turf fibers also provide partial blockage of UV through shading on the sand infill and geotextile backing. Gobla (2014) anticipates a design life of 100 years or more for most buried geotextile applications. The noted exceptions are extreme high or low pH and other strong chemical environments, which are unlikely for a CT system. Since the geotextile backing is covered with sand and the turf fibers lock the sand in place, the geotextile backing will remain covered and unexposed. Therefore, the geotextile backing of the engineered turf is expected to have a minimum service life of 100 years, provided that regular maintenance of the final cover system is performed according to the post-closure care plan.

The unburied portion of a turf fiber is the only geosynthetic component of CT that is directly exposed to UV radiation. A testing program has been carried out to evaluate the service life of the turf fibers, as detailed next in Section “Service Life Prediction of Turf Fibers”. The results indicate that the turf fibers are expected to have a service life of over 100 years, as well.

**Specified Sand Infill.** The third CT component is the specified sand infill. The sand infill is typically a locally sourced sand based on specified material properties and made of native rock material. Once the sand infill is applied and brushed into the turf fibers to a minimum ½ inch thickness, the upright, tightly spaced turf fibers hold the sand infill in place. Sand under normal exposed weathering conditions will not degrade appreciably for centuries.

## SERVICE LIFE PREDICTION OF TURF FIBERS

Research and development have been conducted on the engineered turf component of the CT. There are now CT installations that have been in the field for over ten years, making real-world performance data available. In addition, accelerated natural weathering has been undertaken at an independent weathering laboratory in Arizona. The accelerated weathering followed ASTM G90 “*Standard Practice for Performing Outdoor Accelerated Weathering Tests of Plastics Using*



*Concentrated Sunlight, Cycle 2*". Accelerated aging was accomplished with the Fresnel Solar Collector technology, which utilizes natural sunlight for accelerated weathering. Even though more costly, an accelerated natural method was chosen over fluorescent UV and Xenon arc acceleration methods because the natural sunlight is closer to actual installed conditions, eliminating a much-debated question of whether the simulated irradiance spectrum sufficiently duplicates the field conditions. Equivalent weathering time is determined by equating naturally occurring UV irradiance in MJ/m<sup>2</sup> to the measured UV irradiance on the sample in the laboratory. UV irradiance in the United States ranges from below 200 MJ/m<sup>2</sup> in the Northeast to maximum UV irradiance over 330 MJ/m<sup>2</sup> as at the weathering facility in Arizona. Figure 3 presents approximate UV irradiance across the United States and the CT sample locations and associated exposure years from the laboratory and field installations.

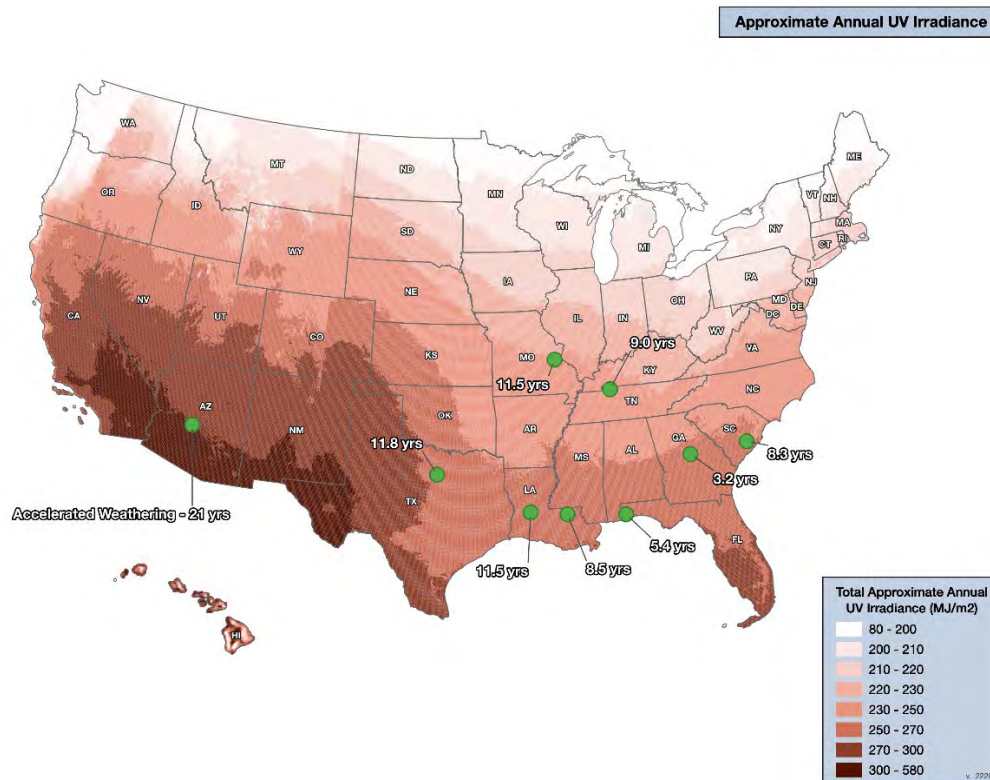


**Figure 3. Average UV irradiance and CT sample locations**

Note: The number of years after installation of field samples and the equivalent years of the accelerated weathering test specimens are shown on the map.

For laboratory accelerated weathering testing, test specimens were placed without sand infill to ensure the turf fiber was exposed and receiving the full rate of sunlight exposure. Control samples were maintained in a climate-controlled environment, while weathered samples were exposed to elevated sunlight levels with temperatures recorded for the duration of the test period. Test samples were exposed to elevated levels of natural sunlight using Fresnel Solar Collectors. Average annual total solar irradiance at the test site is approximately 7,500 MJ/m<sup>2</sup> (Sengupta et al., 2018). Average annual UV irradiance (295 – 385 nm) is 330 MJ/m<sup>2</sup>. At 7-, 14- and 21-year equivalent weathering durations, test samples were collected and sent for independent testing. A side-by-side comparison of weathered CT samples after 6,930 MJ/m<sup>2</sup> of radiant energy (equivalent

to 21 years of exposure) to control samples over a testing period of 2.95 years is presented in Figure 4.

Temperature was recorded at ten-minute intervals. The maximum recorded ambient temperature was 46.9 °C, and the average recorded ambient temperature was 23.1 °C for the year 2020. For the weathered samples, the maximum recorded temperature was 69.1 °C and the average recorded temperature was 27.3 °C for the same period. The thermocouple wire is visible on the weathered samples at the top of Figure 4.



**Figure 4. Laboratory weathered (top) at 21 years of equivalent exposure and control (bottom) engineered turf samples**

Field samples of engineered turf were collected during site visits with approval of site managers. Field control samples were obtained from material quality control (MQC) testing during installation or by exhuming engineered turf that had been continuously buried in an anchor trench. The samples were tested via a modified ASTM D2256 “*Test Method for Tensile Properties of Yarn Single Strand Method*”. The modifications are a result of short yarn lengths and therefore, a reduction in constant-rate-of-extension (CRE) cross head speed. Experiments were run at a rate of one gauge length/min to normalize results by exposed test specimen length. Representative photos of ASTM D2256 testing are presented in Figure 5.

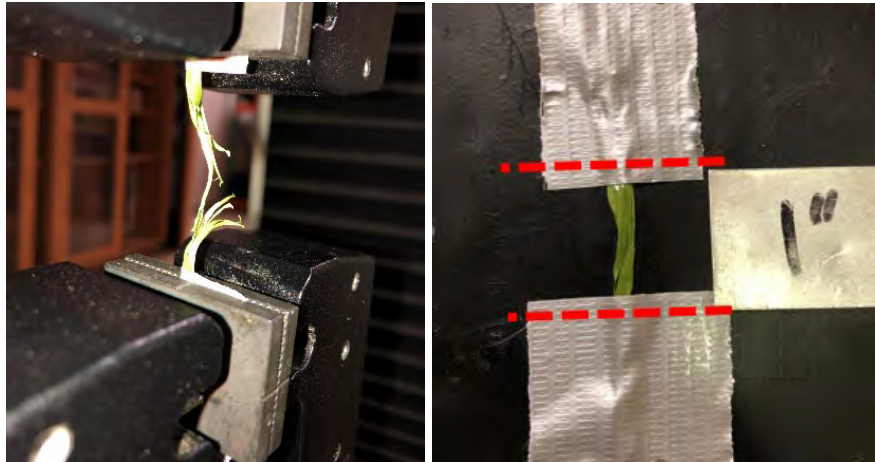


**Figure 5. Representative testing of engineered turf fibers per ASTM D2256 (modified)**

Ten weathered samples and ten control samples of the engineered turf fibers were tested for each field location and for each accelerated weathering duration. As previously stated, accelerated weathering durations were 7, 14 and 21 years of equivalent exposure. Field sample weathering exposure ranged from 2 to 11.5 years. An example of testing results is presented in Figure 6. The ultimate strength results of the ten samples were averaged and compared to the ultimate strength results of the control samples for a percent retained strength. Figure 7 presents retained strength results for accelerated and field weathered samples of the engineered turf fibers.

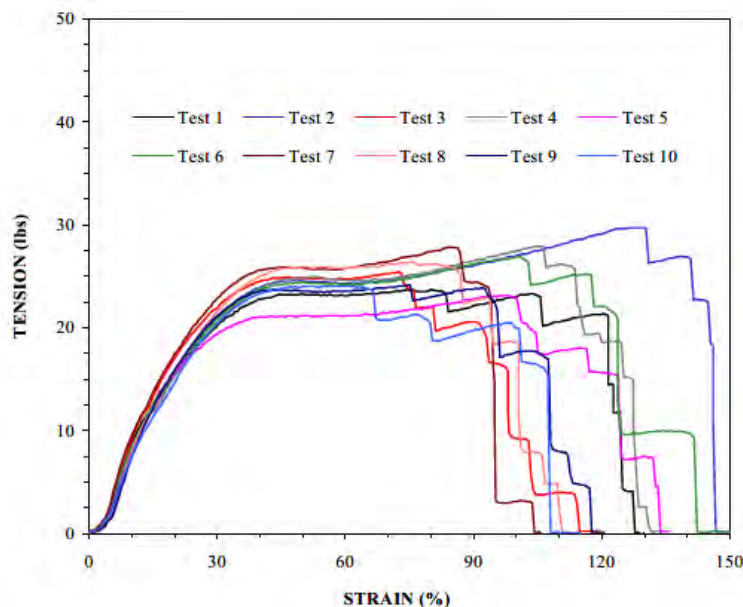


**Figure 6. Representative ultimate strength results of engineered turf fibers per ASTM D2256 (modified)**



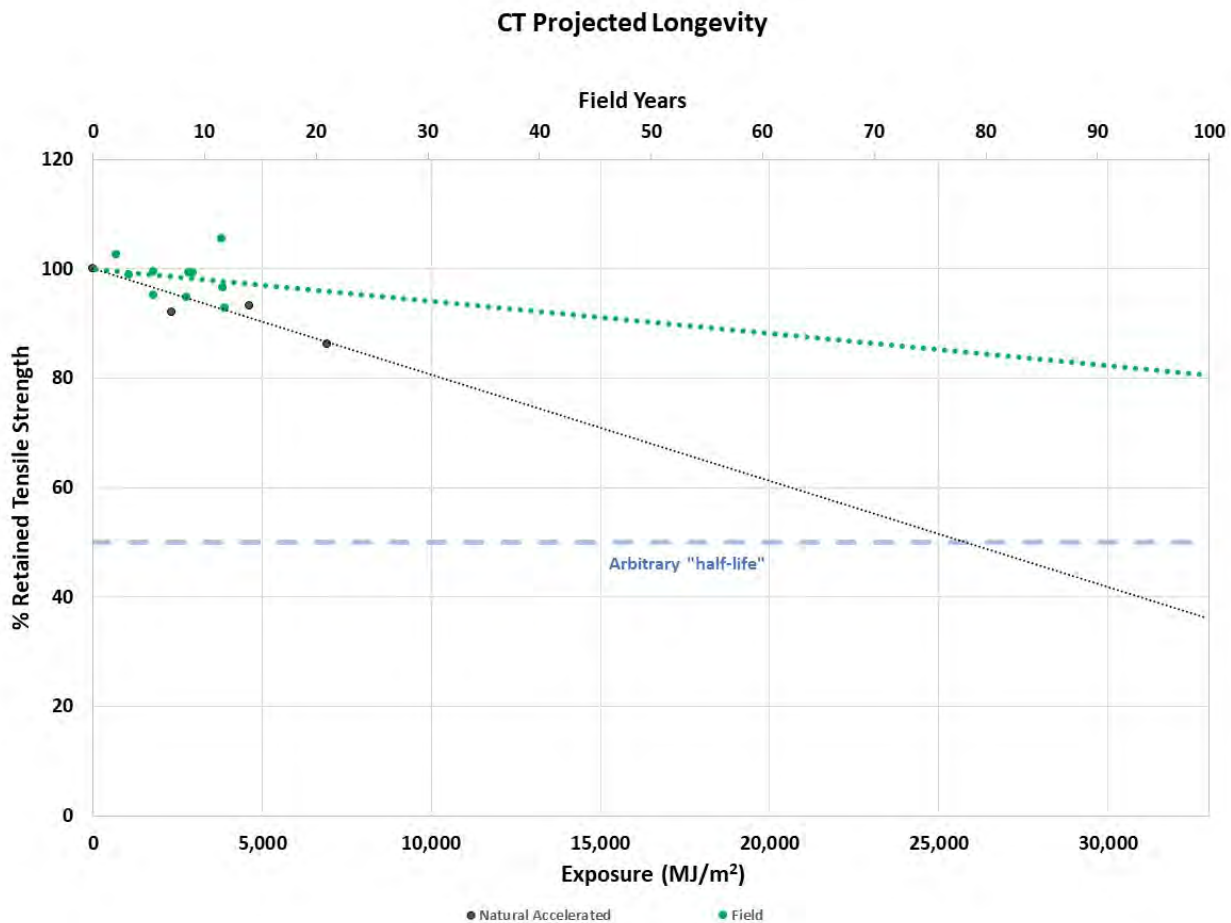


**Figure 7. Projected longevity of engineered turf fibers**

It can be seen that the accelerated natural weathering method more aggressively degrades the engineered turf fibers than field installations. The lack of sand infill and periodic unnaturally high temperatures of the accelerated natural weathering method provide conservative results in regard to evaluating long-term performance. Following accepted practice allowing extrapolation of one order of magnitude (ASCE, 1985; Jewell and Greenwood, 1988; Koerner, 1990), extrapolation of the more aggressive accelerated weathering test results indicates a half-life of approximately 75 years and a service life greater than 100 years considering a 25% retained tensile strength, at which the engineered turf fibers still perform in the field. Real turf fiber performance in the field thus far indicates a half-life more than 100 years and a much longer service life, as well. It should be noted that the data extrapolation was assumed to be linear. The projected service life will be longer, if the semi-log extrapolation method is used.

## SUMMARY

The engineered turf final cover system, ClosureTurf® (CT), has been the final closure method of choice for more than 10 years and over 3,500 acres. CT provides a predictable final closure system in the face of less predictable environmental conditions. CT is comprised of three components:



(1) a structured geomembrane performing as the hydraulic barrier for closure, (2) an engineered turf protecting the geomembrane from exposure, and (3) the specified sand infill providing an additional protection layer and ballast against wind uplift.

Longevity of a CT system depends on the longevity of individual components. The unexposed geomembrane has an anticipated service life of greater than 200 years, because the geomembrane is covered by the engineered turf and specified sand infill. The engineered turf geotextile backing has an expected service life greater than 100 years, provided it remains covered with the specified sand infill. The sand infill will not degrade appreciably from weathering for centuries. The most critical CT component with respect to longevity is the exposed engineered turf fibers forming the “grass” matrix that hold the sand infill in place.

A testing program was instituted to evaluate the service life of the engineered turf fibers. Field samples were collected from multiple sites and an accelerated natural weathering program undertaken at Atlas Material Testing Solutions® in Arizona using Fresnel Solar Collectors to obtain accelerated results equivalent to 21 years of UV exposure. A linear extrapolation of real-world field sample and accelerated natural weathering test results yields a projected service life greater than 100 years for the exposed engineered turf fibers.

How long will the engineered turf final cover system last? The answer is more than 100 years.

## REFERENCES

- American Society of Civil Engineers (ASCE) (1985). Structural Plastics Selection Manual, ASCE Manuals and Reports on Engineering Practice No. 66, *prepared by Task Committee on Properties of Selected Plastics Systems of the Structural Plastics Research Council of the Technical Council on Research of ASCE*, New York, NY, USA.
- Current Results (2022). <https://www.currentresults.com/Weather/US/average-annual-state-temperatures.php>, the webpage was accessed on October 13, 2022.
- Gobla, M.J. (2014). Design Standards No. 13 - Embankment Dams, Chapter 19: Geotextiles. *United States Department of Interior, Bureau of Reclamation*, Washington D.C., USA.
- Jewell, R.A. and Greenwood, J.H. (1988). Long-Term Strength and Safety in Steep Soil Slopes Reinforced by Polymer Materials. *Geotextiles and Geomembranes*, Vol.7, Nos. 1 and 3, pp. 81-118.
- Koerner, R.M. (1990). Determination of the Long-Term Design Strength of Stiff Geogrids, *GRI Standard Practice GG4(a)*, Folsom, PA, USA.
- Koerner, R.M., Hsuan, G.Y., and Koerner, G.R. (2011). Geomembrane Lifetime Prediction: Enexposed and Exposed Conditions. *GRI White Paper No.6*, Geosynthetic Institute, Folsom, PA, USA.
- Sengupta, M., Y. Xie, A. Lopez, A. Habte, G. Maclaurin, and J. Shelby (2018). *The National Solar Radiation Data Base (NSRDB)*. Renewable and Sustainable Energy Reviews. 89 (June): 51-60.
- United States Environmental Protection Agency (USEPA) (2022a). Landfills. <https://www.epa.gov/landfills>
- United States Environmental Protection Agency (USEPA) (2022b). Landfill Methane Outreach Program (LMOP), Project and Landfill Data by State. <https://www.epa.gov/lmop/project-and-landfill-data-state>.

## **Evaluation of geomembrane UV exposure using geographic and climate data**

**Beaumier, David, Eng. M.A.Sc.<sup>1</sup>, Fazli, Ali, Ph.D.<sup>2</sup>**

<sup>1</sup>SAGEOS/CTT Group, 3000 Boulle, St-Hyacinthe, QC, Canada; e-mail: dbeaumier@gcttg.com

<sup>2</sup>SAGEOS/CTT Group, 3000 Boulle, St-Hyacinthe, QC, Canada; e-mail: afazli@gcttg.com

### **ABSTRACT**

Several geomembrane applications involve long-term UV exposure conditions: covers, ponds, leach pads, dams, and canals. High-density polyethylene (HDPE) geomembranes are used in most of these applications. In HDPE geomembranes, UV degradation (photodegradation) induced by long-term exposure to UV or visible light results in discoloration, surface cracks, brittleness, and deterioration in mechanical properties. This paper aims to present specific data from weather stations for the evaluation of light intensity with climates. Weather station data, including irradiance, UV index, latitude, longitude, and altitude, are used to calculate the effective irradiance on HDPE geomembranes. In addition, the orientation to sunlight changes the level of radiant energy on the exposed geomembranes. A model using radiant energy is proposed for guidance to service life prediction of exposed geomembranes.

### **INTRODUCTION**

The exposure of geomembranes to weather conditions is a key issue in the assessment of their service lifetime. Among other conditions to be considered, the exposure to sunlight will cause the degradation of polymeric geomembranes. Artificial weathering through standardized test methods is often used for the assessment of geomembranes durability. For comparison to real-life, different approaches are suggested: correlation to field tests and correlation with site conditions. The decision for material selection is most often based on a comparison between materials in laboratory conditions, but sometimes unrealistic of field conditions.

Climatic data from weather stations are useful to some extent in the prediction of laboratory exposures to real-life conditions. One method uses equivalent radiant energy dosage. However, the sensitivity of polymers to ultraviolet (UV) light should be considered for modeling the photooxidation reaction. Correlations include numerous parameters resulting in insufficient data for prediction. Simplified methods for the prediction of polymeric geomembranes to natural aging are herein discussed and standardized exposure methods are compared with specific considerations for polyethylene (linear low-density polyethylene (LLDPE) or high-density polyethylene (HDPE)) geomembranes.

### **BACKGROUND**

Koerner et al. (2005) compared field exposure with accelerated laboratory exposures of different types of geomembranes. Acceleration factor was calculated with the cumulative radiation energy of the controlled wavelength of UV lamps, for both UVA fluorescent lamps and Xenon Arc lamps. Acceleration factors were estimated: 6.8 for the UVA fluorescent weatherometer, and 4.3 for the Xenon Arc weatherometer. Tian et al. (2019) evaluated the antioxidant depletion of exhumed HDPE geomembranes, after 12 years of site exposure. The most exposed samples from the

exposed south slope have shown 26% retention of standard oxidative induction time (OIT). Baroso et al. (2016) monitored an OIT depletion between 40 and 60% for 12-year exposure sites. Rowe et al. (2015) used high-pressure OIT (HP-OIT) measurements and standard OIT to monitor antioxidant depletion. The antioxidant depletion from an exposure of 16 years in Argentina (warm-hot climate) was measured to roughly less than 20% retention, but a minor number of samples failed mechanical and stress-cracking resistance per GRI-GM13 requirements. In a mild-cold climate (6 years, Kingston, Canada), the antioxidant depletion was found acceptable with full compliance to GRI-GM13.

Laboratory artificial weathering may be conducted through several apparatus types and procedures. The evaluation of geomembranes most often refers to Xenon arc weatherometers or UV-fluorescent weatherometers. In a review of lifetime prediction of geosynthetics, Hsuan et al (2008) referred to the following four standard methods: AASHTO M288, ASTM D4355, ASTM D7238, and EN 12224. The first two methods use a Xenon arc exposure whereas the latest two methods use a UV-fluorescent exposure, with specific UVA lamps. The source of light exposure is also related to lamp types or specific filters. The comparison of UV light spectra between artificial weathering and sunlight is shown in Figure 1. The Xenon arc lamps, from conditions of ASTM D4355, are quite closer to the light intensity of sunlight, perhaps, the UV-fluorescent exposure type is emphasizing the intensity of the UV light, which is of greatest interest for the assessment of polymer degradation for polymers degrading below 340 nm.

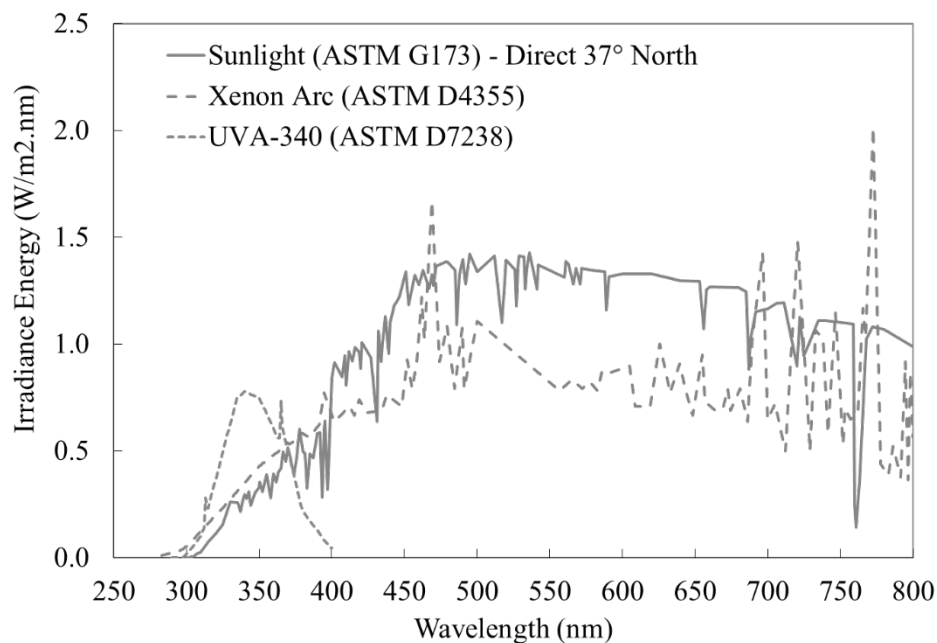


**Figure 1. Comparison of artificial UV-light spectra and sunlight.**

The source of light exposure will also affect the sensitivity of polymers to photodegradation. The sensitivity of polymers to UV light is related to their chemistry, hence, different polymers will not be affected in the same way by the same source of UV light. Atlas (2020) covered the chemistry of photooxidation degradation mechanisms. UV radiation will affect polymers differently because of the different chemical bonds and structures of polymers and hence their different UV sensitivity. For instance, polyethylene (PE) will progressively absorb UV light

below 300 nm, and polyethylene terephthalate (PET) will absorb UV light below 360 nm. Energy from the absorbed UV radiation will affect chemical bonding and result in chemical degradation.

The chemical bond dissociation is related to a specific wavelength using Plank's constant, resulting in a polymer activation spectrum. The proposed approach to the chemical UV degradation of polymers uses the evaluation of spectral sensitivity. Spectral sensitivity correlates the activation spectrum to the spectrum of the light source. Using the spectral sensitivity, an effective irradiance may be modeled with an Arrhenius-type equation. The UV activation wavelength of PE is about 290 nm, but its spectral sensitivity is in the range of 300 to 310 nm. Xingzhou (1997) provided measurements of photooxidation with light source wavelength. When the PE activation spectrum is correlated with lamp source irradiance energy, the effective irradiance (energy) is calculated. Figure 2 represents the sensitivity of PE with typical light sources in the artificial weathering of geomembranes.

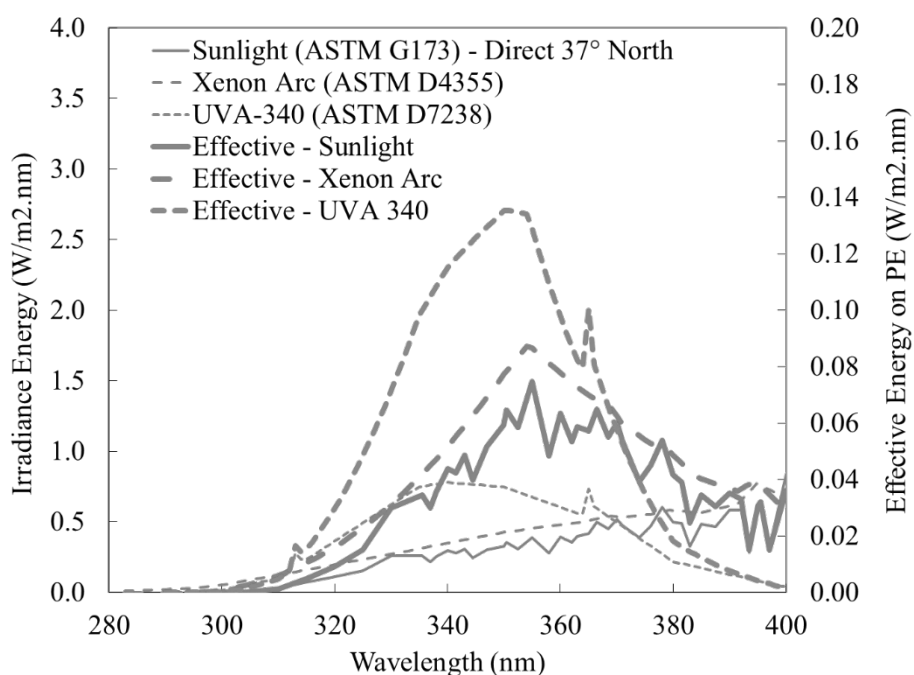


**Figure 2. Effective irradiance for the exposure of PE to artificial weathering.**

The World Ozone and Ultraviolet Data Centre (WOUDC) has developed a wide range of data on both UV radiations. UV radiations are available from different sites throughout the world and are likely well-documented in North America (Figure 3). Sunlight is composed of a range of irradiance energy, varying with wavelength (spectrum). Standard sunlight spectra are also documented in ASTM G173. These spectra are specific to conditions, i.e. latitude, orientation, year time, and day time. Data from WOUDC are more specific than models proposed by ASTM G173, perhaps, UV spectrum measurements are documented with a correlation of irradiance to wavelength, along with the most common meteorological data: UV index. The UV index is based on the erythral sensitivity of the skin, hence, a correlation to PE is suggested for an adequate light sensitivity evaluation of a polymer, not human skin.



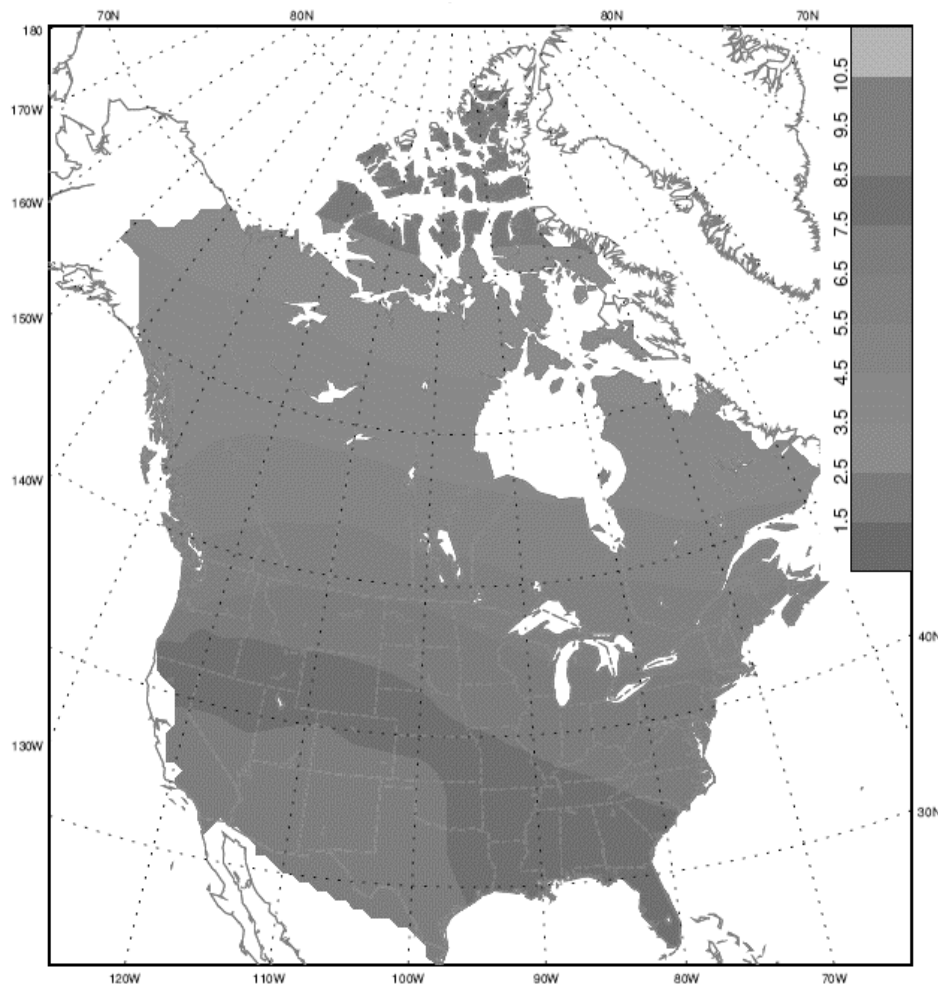


**Figure 3: Noon (11.00 am - 12.59 pm) mean UV index in July, 1980 - 1990  
(Source: WOUDC)**

## METHODOLOGY

A comparison of artificial weathering to service life is herein estimated from climatic data. A survey of different HDPE geomembranes is presented with exposure to UV-fluorescent (ASTM D7238). A generic designation of geomembranes is presented and the HP-OIT depletion is measured with exposure time, and it is projected to real-time sunlight exposure in given climate irradiance.

**Materials.** The exposure of geomembranes made of specific formulations is presented. Nominal characteristics are listed in Table 1. These data are used for benchmarking to correlate equivalency to natural exposure to sunlight. The projection of these measurements is figured for different climates, based on WOUDC data and its correlation to artificial UV exposure.

**Table 1. Designation of exposed HDPE geomembranes, and properties.**

Type	UV- loading	Extrusion process	Exposed surface	Exposed color	Thickness (mm)	Density (g/cm <sup>3</sup> )	OIT (min)	HP-OIT (min)
A	Std	Blown film	Smooth	Black	1.5	0.960	181	486
A1	Low	Blown film	Smooth	Black	1.5	-	130	1099
A2	High	Blown film	Smooth	Black	1.5	-	218	1476
B	Std	Flat die	Smooth	Black	1.5	0.947	-	1096
B	Std	Flat die	Textured	Black	1.5	0.947	-	1001
C	Std	Blown film	Smooth	Black	1.5	0.948	-	1827
C	Std	Blown film	Smooth	Black	2	0.948	-	2126
C	Std	Blown film	Textured	Black	1.5	0.947	-	2202
C	Std	Blown film	Textured	Black	2	0.947	-	1972
C	Std	Blown film	Textured	White	2	-	-	1744
C	Std	Blown film	Smooth	White	2	-	-	1680

**UVA Exposure.** The UV weathering of HDPE geomembranes was conducted per ASTM D7238. GRI-GM13 requires the antioxidant depletion measured by HP-OIT after exposure of 1600 hr, with a minimum HP-OIT retention of 50% from the unaged geomembrane. The procedure used UVA fluorescent lamps with the following exposure cycle conditions:

- 20 hr of light at a controlled irradiance of 0.78 W/m<sup>2</sup>.nm, and a temperature of 75°C;
- 4 hr condensation at 60°C, without light.

Specimens were repositioned and rotated weakly.

**High Pressure-Oxidative Induction Time (HP-OIT).** High pressure-oxidative induction time (HP-OIT) was measured accordingly with ASTM D5885. HP-OIT tests were conducted at 150°C and 3450 kPa oxygen pressure using a high-pressure differential calorimeter. The time to the onset of oxidation was measured from the exothermic reaction of PE oxidation. For evaluating UV additives, the preferred test method was ASTM D5885 (HP-OIT), to evaluate UV additives and tested at a lower temperature than OIT (Fay and King (1994)).

## RESULTS

The antioxidant depletion is reported in Figures 4 to 7. When expressed in terms of percent retained HP-OIT, the monitored geomembranes are in the range of 80% to 100% retained HP-OIT. Intermediate testing shows a progressive loss of additives and no complete depletion at the end of 1600 hr of UV exposure. The retained HP-OIT at the end of 1600 hr exposure is in the range of 80% to 100%. Longer exposures are needed to reach complete antioxidant depletion and obtain a prediction model of photooxidation with time.

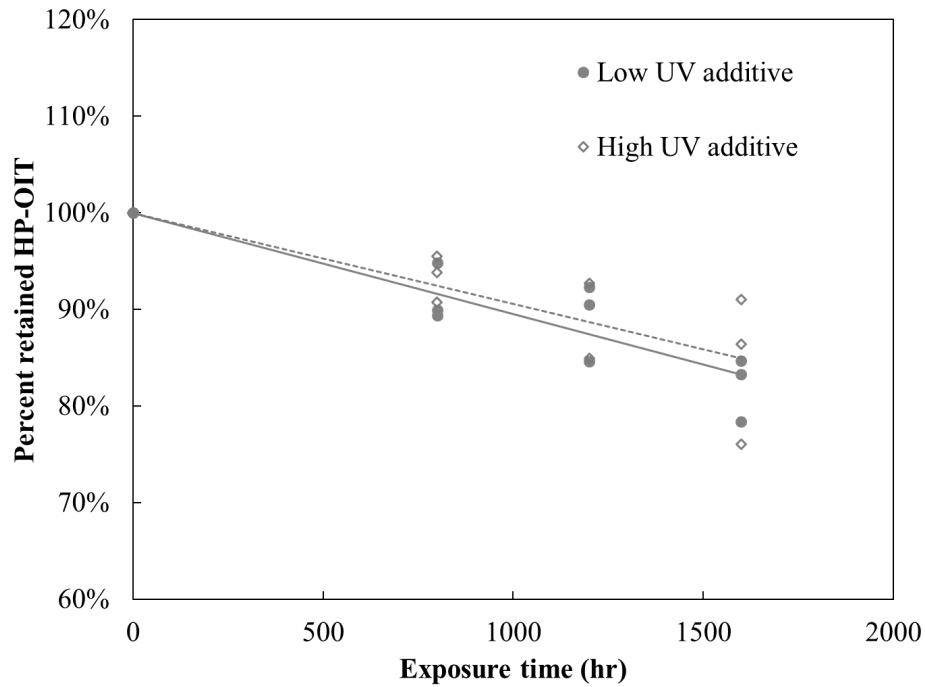


**Figure 4. Antioxidant depletion on 1.5mm-thick smooth HDPE geomembrane.**

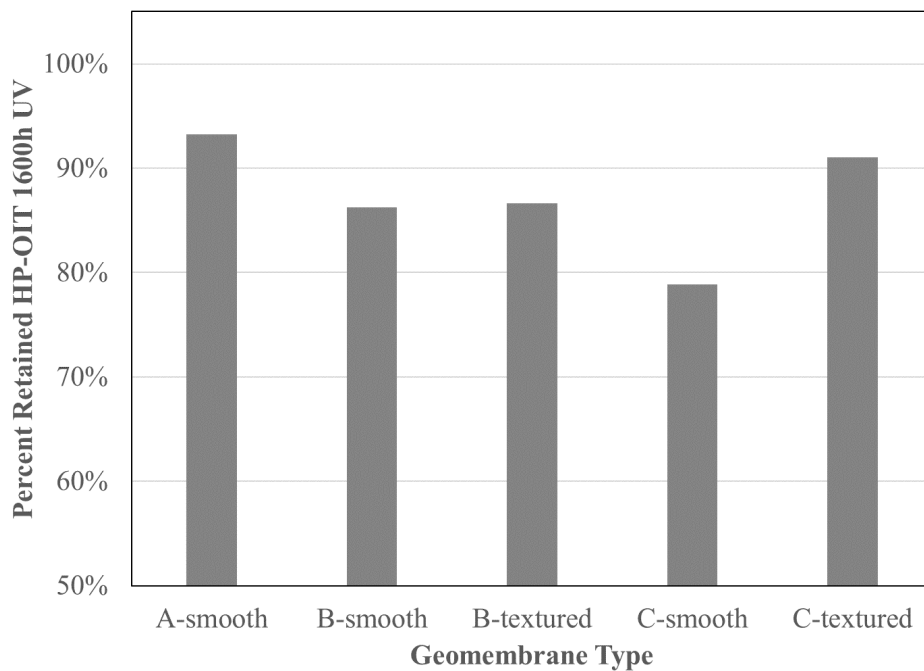


**Figure 5. Average retained HP-OIT on 1.5mm-thick HDPE geomembranes after 1600h UV exposure as per ASTM D7238.**

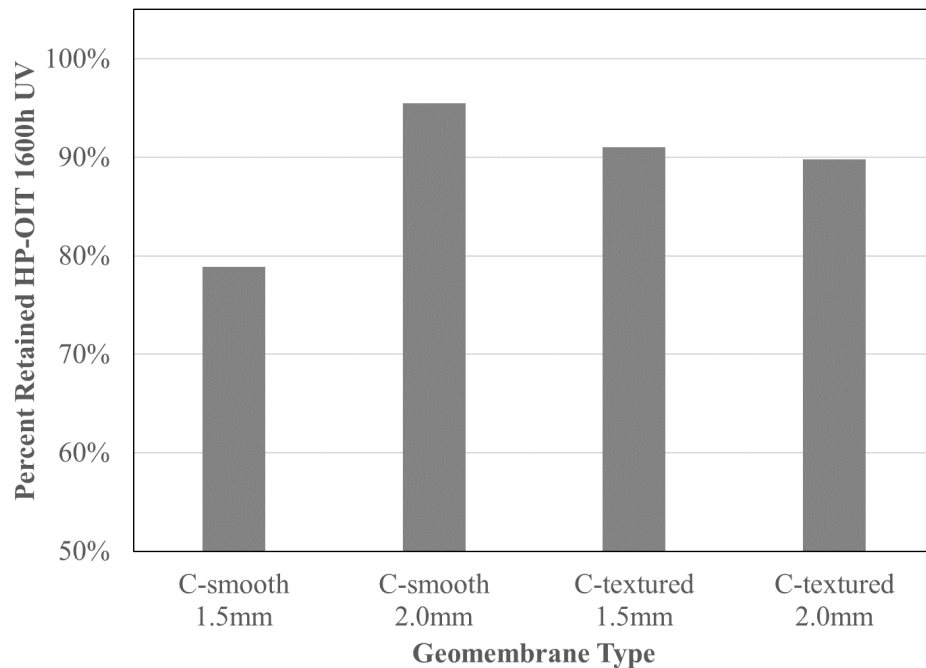


**Figure 6. Average retained HP-OIT on HDPE geomembranes after 1600h UV exposure, compared with thickness and surface finish.**

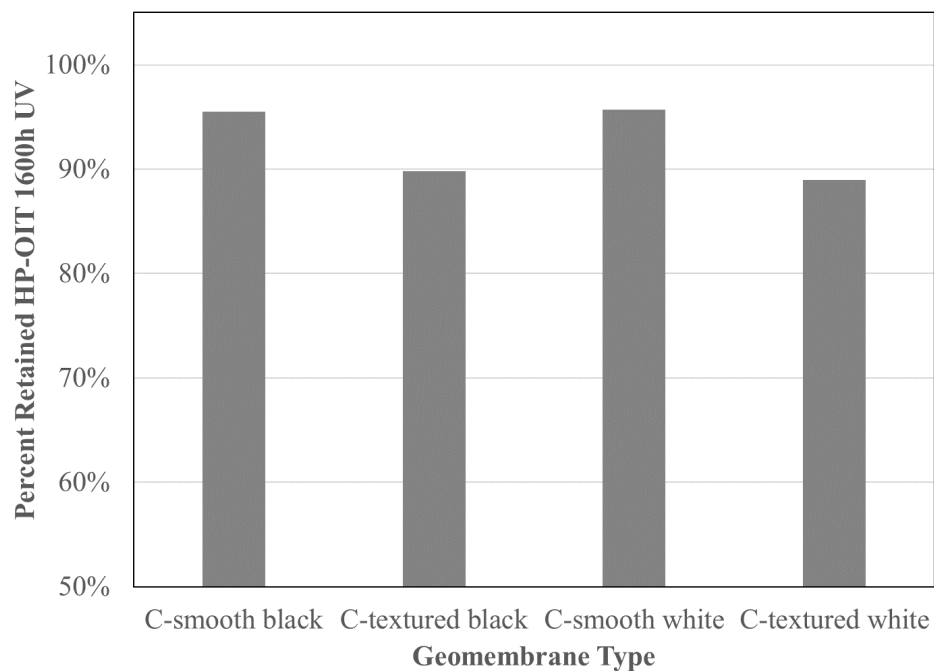


**Figure 7. 2mm-thick HDPE geomembranes after 1600h UV exposure, compared with color and surface finish.**



## DISCUSSION

**Correlation to natural sunlight.** The test irradiance of the UV exposure cycle as per ASTM D7238 is correlated with the effective energy on PE, but also with the UV index. When compared with a standard spectral distribution from ASTM G173, Direct 37° North, the acceleration factor (AF) from exposure as per ASTM D7238 is correlated with the daily average UV index.

$$AF = \frac{T_{UVI}}{T_{D7238}}$$

Where:  $T_{UVI}$  = Real-time exposure at a given UV index (hours);  $T_{D7238}$  = Laboratory exposure to ASTM D7238 light exposure time (hours). Figure 8 presents the model of the acceleration factor with UV index.

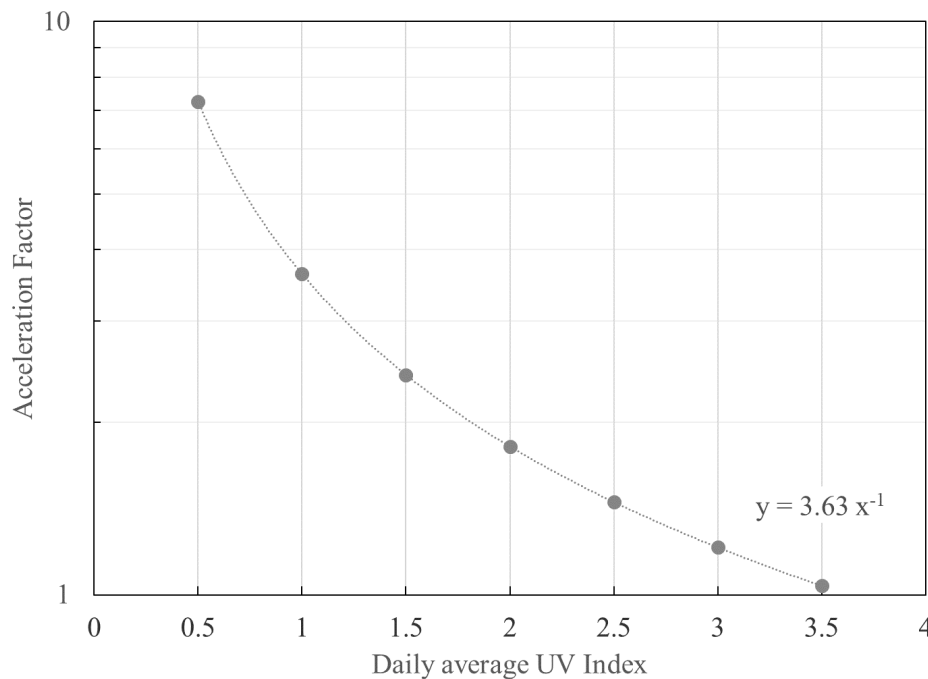


**Figure 8. Acceleration factor of UV exposure from ASTM D7238 to exposure to a daily average UV index sunlight condition.**

Data from WOUDC are compiled from the Toronto weather station. Monthly measurements from 2011 are used for the model. Figure 9 shows the UV index fluctuations throughout the year. In addition to the average UV index, the maximum UV index and the maximum UV index on a vertical wall facing South (VWFS) are compared. The VWFS correction is useful for consideration of exposure reduction with the Zenith angle. Considering the relation of the acceleration factor of accelerated aging to the sunlight intensity, the projection of geomembranes to real-life exposure should be estimated with vigilance. Table 2 compares the average UV index of two locations in North America: Toronto (ON, Canada, latitude = 43.78; longitude = -79.47; altitude = 198m) and the Everglades (FL, USA, latitude = 25.39; longitude = -80.68; height = 15m). The acceleration factor of artificial exposure of 1600 hr UVA light as per ASTM D7238 is correlated with the average UV index (UVI). The correlation to effective sunlight energy in regards to the activation of PE photodegradation shows a difference of 65% between

Toronto and the Everglades. Specific data on sunlight is thus critical to the durability assessment of geomembranes to sunlight. Overall, moderate acceleration factors are deducted from these calculations, resulting in a shorter projection of real life if compared to historical references (Koerner et al., 2005).

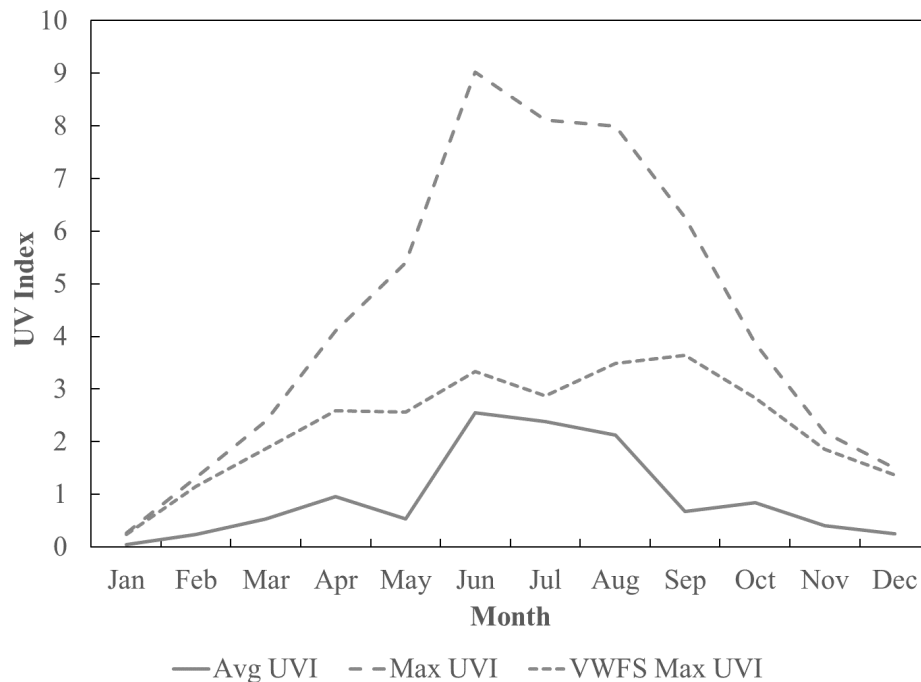


**Figure 9. Yearly sunlight in Toronto (2011), rated by UV index.**

**Table 2. Service lifetime equivalent to 1600h UVA light as per ASTM D7238**

	Toronto, ON	Everglades, FL
UVI (yearly avg.)	0.961	1.596
AF (D7238)	3.8	2.3
Eq. 1600h (months)	8.4	5.1

## CONCLUSION

A review of the testing of geomembrane in UV-exposed conditions was proposed. The exposure to UVA fluorescent lamps per ASTM D7238 was compared with several types of geomembranes. The projection to real-life exposure was done using UV index data. Correlations were developed with polyethylene sensitivity to UV light and photodegradation to obtain an empirical relation of the acceleration factor of artificial UV exposure to the UV index. Further developments on the evaluation of the photo-degradation of HDPE geomembranes are suggested with the following considerations: temperature, humidity, albedo, and slope angle.

## REFERENCES

- ASTM G173-03 (2020). Standard Tables for Reference Solar Spectral Irradiances : Direct Normal and Hemispherical on 37° Tilted Surface, *ASTM International*, West Conshohocken, Pennsylvania, USA.
- ASTM D7238-20. Standard Test Method for Effect of Exposure of Unreinforced Polyolefin Geomembrane Using Fluorescent UV Condensation Apparatus, *ASTM International*, West Conshohocken, Pennsylvania, USA.
- ASTM D5885/D5885-20. Standard Test Method for Oxidative Induction Time of Polyolefin Geosynthetics by High-Pressure Differential Scanning Calorimetry, *ASTM International*, West Conshohocken, Pennsylvania, USA.
- Atlas Material Testing Solutions (2020). *Photooxidation & Stabilization Mechanisms*, Atlas Online Seminar.
- Barroso, M., Lopes, M. G., Reis, A. (2016). Ageing HDPE geomembranes exposed to different climate conditions for 12 years, *EuroGeo6*, Ljubljana, Slovenia.
- Fay, J. J., and King R. E., (1994). “Antioxidants for Geosynthetic Resins and Applications”, *Geosynthetic Resins*, Formulations and Manufacturing, Edited by Hsuan, Y.G. and Koerner, R.M., GRI Conference Series, Published by IFAI, St Paul, MN., U.S.A., pp. 77-96.
- GRI - GM13 Standard Specification (2016). Standard Specification for “Test Methods, Test Properties, and Testing Frequency for High Density Polyethylene (HDPE) Smooth and Textured Geomembranes”, *Geosynthetic Institute*, Folsom, Pennsylvania, USA.
- Hare, E.W., Fioletov, V.E., Wardle, D.I., Carty, E.J. (2006). *Guide to the WMO/GAW World Ultraviolet Radiation Data Centre, Version 6.0*, Environment Canada.
- Hsuan, Y. G., Schroeder, H. F., Rowe, K., Müller, W., Greenwood, J., Cazzuffi, D., Koerner, R.M. (2008). Long-Term Performance and Lifetime Prediction of Geosynthetics, *EuroGeo4 Keynote Paper, European Geosynthetics Conference (EuroGeo4)*, Edinburgh, Scotland.
- Jablonka M., Beaumier D., Blond E. (2015). Long-term durability of polymeric water-resistive barriers, *10th Annual North American Passive House Conference*, Chicago, IL, USA.
- Koerner, R. M., Hsuan, Y. G., Koerner, G. R. (2005). *GRI White Paper #6 on Geomembrane Lifetime Prediction: Unexposed and Exposed Conditions*, *Geosynthetic Institute*, Folsom, Pennsylvania, USA.
- Rowe R. K., Ewais, A.M.R. (2015). Ageing of exposed geomembranes at locations with different climatological conditions, *Can. Geotech. J.*, 52: 326–343.
- Tian, K., Benson, C. H., Yesiller N., Hanson, J. (2019). Evaluation of a HDPE Geomembrane from a Composite Liner After 12 Years of Atmospheric Exposure, *Geosynthetics Conference 2019*, IFAI, Houston, Texas, USA.
- Xingzhou, H, (1997). Wavelength sensitivity of photo-oxidation of polyethylene, *Polymer Degradation and Stability*, 55 (1997):131-134.

## **Exposed Geomembrane Cover Performance at Polk County Landfill in Florida**

**George A. Reinhart, III, Ph.D., P.E.,<sup>1</sup> and George Koerner, Ph.D., P.E., CQA<sup>2</sup>**

<sup>1</sup>Jones Edmunds & Associates, Inc., Gainesville, FL 32641; email:

[greinhart@jonesedmunds.com](mailto:greinhart@jonesedmunds.com)

<sup>2</sup>Geosynthetic Institute, Folsom, PA 19033; email: [gsigeokoerner@gmail.com](mailto:gsigeokoerner@gmail.com)

### **ABSTRACT**

The days when geomembranes were constructed as only one thick monolithic layer are gone. They currently can be made of assorted colors, and have different conductivities, diffusion characteristics, etc., to meet client needs for various applications all over the world. This paper describes a case history of a new multi-layer geomembrane used as a municipal solid waste (MSW) cover in Polk County, Florida, that was designed by Jones Edmunds & Associates, Inc. and manufactured by Solmax (formerly GSE-Gundle).

### **INTRODUCTION**

In summer 2001, an exposed geomembrane cover (EGC) made of 1.5-mm (60-mil) high-density polyethylene (HDPE) green/black textured geomembrane was installed as a cover at the Polk County North Central Landfill (NCLF). The cover caps approximately 4 hectares (16 acres) on both flat and side sloped sections of the landfill.

Increasingly, over the past decade, geosynthetic caps have been used at sites where a “traditional” soil cover may be problematic. Site conditions such as steep slopes, sites with limited or no available “borrow” soils, bioreactor sites where large subsidence is anticipated and/or sites with erosion control issues are all good candidates for EGC. The Polk County site chose a green geomembrane as the capping system based on many of the above considerations.

Green was selected for its aesthetically pleasing appearance. This material had been previously installed at several sites in the southeastern portion of the USA (Hullings 2017) with good success. The geomembrane formulation was stabilized with titanium dioxide and an additive package containing a hindered amine light stabilizer. It also used a very select resin for long-term support of the green pigmentation.

In addition to the concern regarding life expectancy, wind uplift was a significant concern at the site. Polk County Landfill normally uses a vacuum gas extraction system to hold down the EGC. The system would not withstand a significant storm event when both high winds and loss of electrical power occur. To address this issue, vertical anchor trenches were installed in the cover, which is addressed in Case et. al., (2010), Hullings, (2017) and Thiel et.al., (2003).

### **LABORATORY INVESTIGATION**

Although all types of polymers react with oxygen causing gradual degradation, polyolefins (polypropylene and polyethylene) are generally considered to be the most susceptible to this phenomenon. Koerner, et al. (2005) presents the chemical mechanisms that are involved. In



addition, there are several ongoing investigations to assess geosynthetic oxidative behavior of HDPE at elevated temperatures. Obviously, the higher the temperature, the greater the rate of oxidative degradation. Caution should be exercised when incubating geosynthetics at extremely high temperatures, (polyethylene melts at 125°C.) These high temperatures should certainly be avoided so as not to influence the molecular structure of the HDPE. The highest recommended incubation temperature is a conservative value of 80°C.

Ultraviolet light is also an important cause of degradation to polyethylene. Energy from the sun is divided into three parts:

- Infrared, with wavelengths longer than 760 nm
- Visible, with wavelengths between 760 and 400 nm
- Ultraviolet or UV, with wavelengths shorter 400 nm

The UV region is particularly detrimental to polyethylene. Other factors that affect the UV degradation process of polymers are geographic location, temperature, cloud cover, wind, moisture, atmospheric pollution, and product orientation. Although difficult to assess, these factors should be considered for field lifetime prediction. Laboratory simulation is critical because it provides the base line degradation under completely controlled conditions such as radiation, temperature, and moisture.

Laboratory simulation of sunlight using artificial light sources (lamps) is generally compared with worst-case conditions or the “solar maximum condition.” The actual degradation is caused by light photons breaking the polymer’s chemical bonds. Each type of bond has a threshold wavelength for bond scission. We used UV fluorescent devices per ASTM D7238 for our experiments as shown in Figure 1.

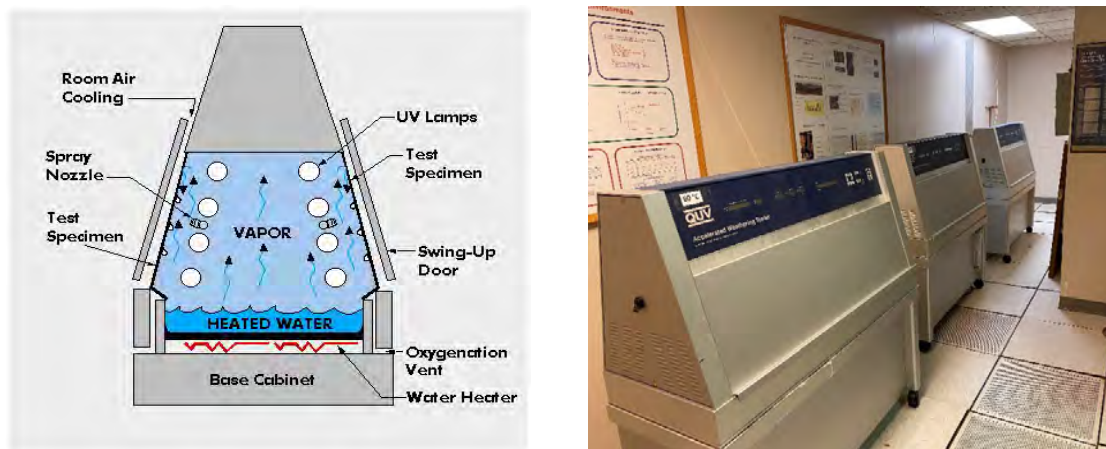
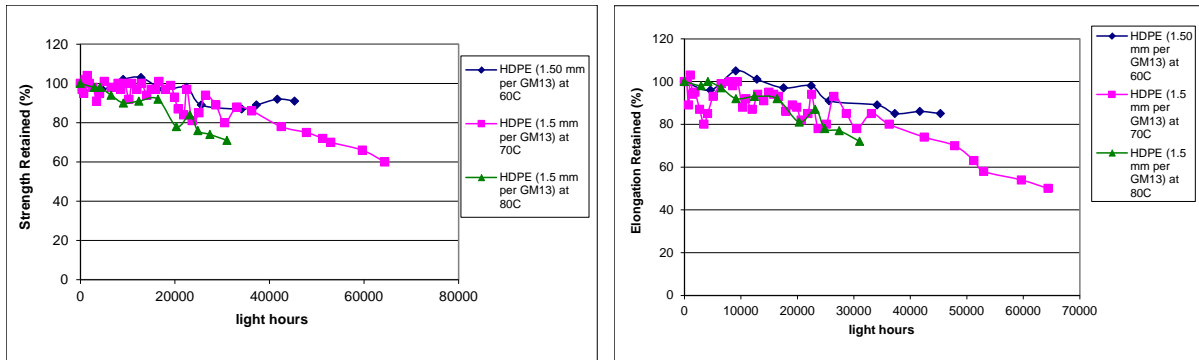
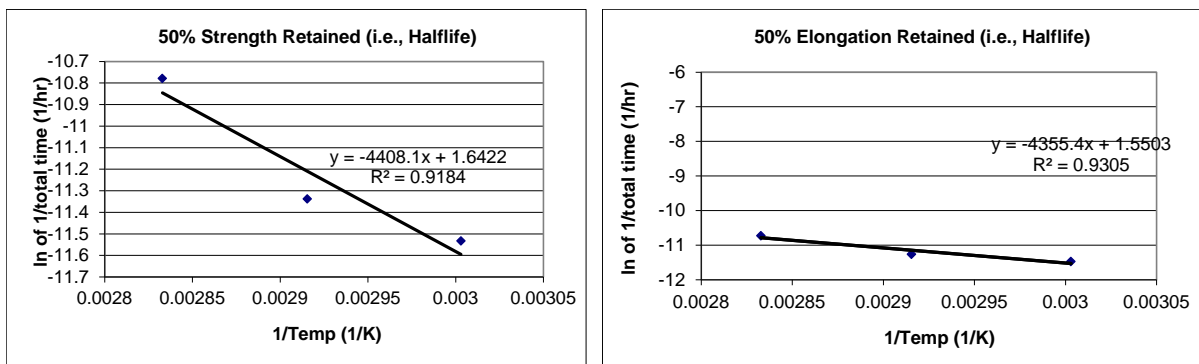


**Figure 1. UV Fluorescent Weathering Devices for Polymer Durability Incubation per ASTM D 7238**

Representative test coupons are incubated and removed at designated times, cut into tension test specimens, and evaluated for their retained strength and elongation. The results are then compared to the unexposed geosynthetic for percent retained values; see Koerner, et al. (2005) for further details. When plotted and extrapolated to lower temperatures, lifetime predictions in laboratory weathering devices can be obtained. Using this information as an extension to specific field locations can be generated albeit with some quite serious assumptions. Figure 2 (a-c) presents specific results for HDPE.



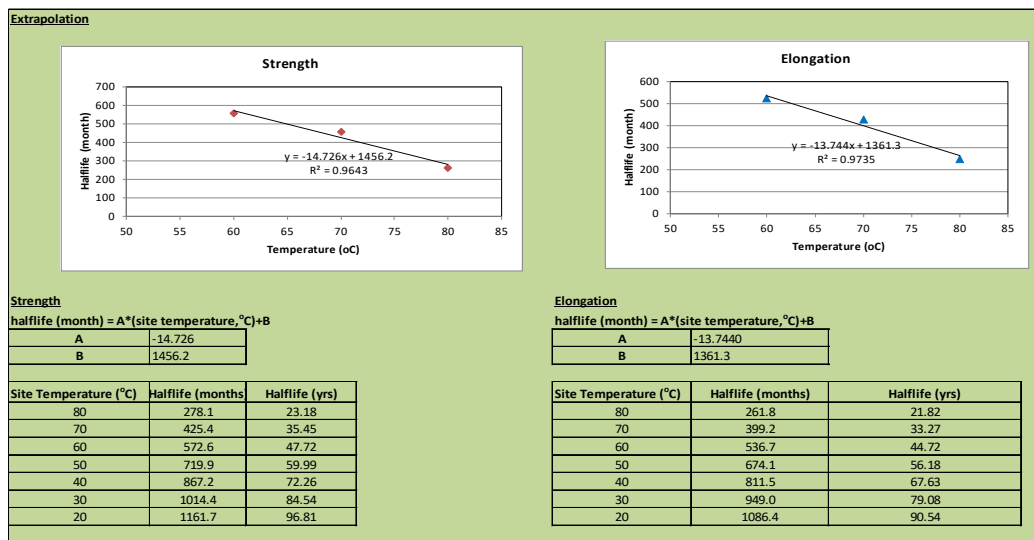
(a) Reduction in Strength and Elongation at 80, 70, and 60°C



Prediction		
Temperature	Lifetime (hours)	Lifetime (years)
80	48000	5.5
70	84000	9.6
60	102000	11.6
50	163548	18.7
40	252930	28.9
30	402582	46.0
20	661436	75.5

Prediction		
Temperature	Lifetime (hours)	Lifetime (years)
80	45600	5.2
70	78000	8.9
60	96000	11.0
50	151247	17.3
40	232684	26.6
30	368294	42.0
20	601500	68.7

(b) Half-Life Laboratory Predictions Down to 20°C



(c) Half-Life Field Predictions in Phoenix, Arizona, Down to 20°C

**Figure 2. (a – c) Data and Lifetime Predictions for 1.5-mm HDPE Geomembrane (Per GRI GM13 Specification) Using Fluorescent Ultraviolet Weather Devices per ASTM D7238**

## FIELD INVESTIGATION

Figure 3 shows a photograph of the sampling zone on the EGC at the Polk County NCLF. The location is near the crest of the south facing slope where stresses in the cover geomembrane are high. Figure 4 shows its decay curve with respect to time. Table 1 summarizes the test results of the EGC over 20 years and contrasts them with GRI GM13. The performance of the material is very good; the only property that is decreasing is HP-OIT.



**Figure 3. Sampling Zone at Polk County NCLF EGC**

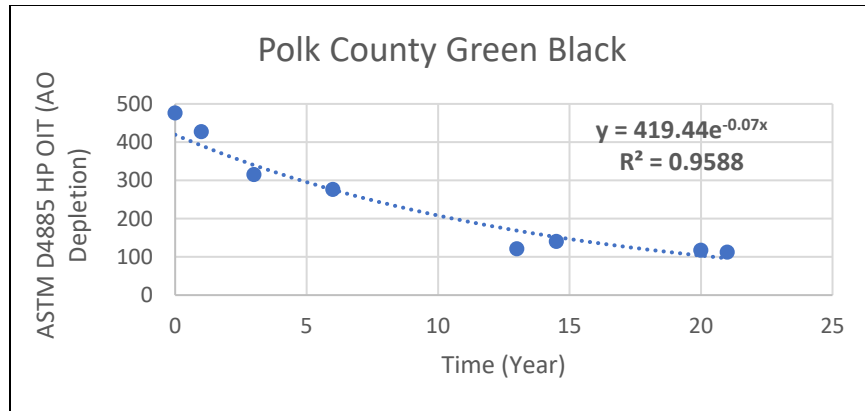


**Figure 4. HPOIT Depletion Over Time at Polk County EGC**

**Table 1. Summary of Polk County EGC Green DS Text 60 mil HDPE Results  
(Data from years 6, 13, and 14.5 were obtained from Ramsey, 2016)**

Property	Test Method	Units	GM13 Values	PC Spec	6 years	13 years	14.5 years	20 years
Core Thickness nominal -5%	D 5994	mil	<b>57</b>	-	-	-	-	60
Lowest individual for 8 of 10 values, nominal -10%		mil	<b>54</b>	-	-	-	-	58
Lowest individual for any of 10 values, nominal -15%		mil	<b>51</b>	-	-	-	-	54
Asperity Height Side "A" PGreen	D 7466	mil	<b>16</b>	-	-	-	-	16
Asperity Height Side "B" Black	D 7466	mil	<b>16</b>	-	-	-	-	24
Density	D792	g/cc	<b>0.94</b>	-	-	-	-	0.944
<b>Mechanical Properties</b>								
Tensile Properties, yield stress MD	D 6693 IV	lb/in.	<b>126</b>	130	178	194	193	183
Tensile Properties, break stress MD	D 6693 IV	lb/in.	<b>90</b>	90	187	192	161	149
Tensile Properties, yield elongation MD	D 6693 IV	%	<b>12</b>	13	18	18	18	17
Tensile Properties, break elongation MD	D 6693 IV	%	<b>100</b>	150	477	411	333	191
Tensile Properties, yield stress X-MD	D 6693 IV	lb/in.	<b>126</b>	130	183	210	198	183
Tensile Properties, break stress X-MD	D 6693 IV	lb/in.	<b>90</b>	90	150	159	147	133
Tensile Properties, yield elongation X-MD	D 6693 IV	%	<b>12</b>	13	18	17	17	16
Tensile Properties, break elongation X-MD	D 6693 IV	%	<b>100</b>	150	271	156	244	195
Tear Resistance MD	D 1004	lb	<b>42</b>	-	-	-	-	62
Tear Resistance X-MD	D 1004	lb	<b>42</b>	-	-	-	-	61
Puncture Resistance	D 4833	lb	<b>90</b>	-	-	-	-	168
<b>Chemical Finger Printing</b>								
Stress Crack Resistance X-MD	D 5397 (App.)	hr.	<b>500</b>	>500	>500	>500	>500	610*
Carbon Black Content	D4218	%	<b>2.0-3.0</b>	-	-	-	-	2.55
Carbon Black Dispersion	D 5596	NA	<b>1 or 2</b>	-	-	-	1.8	1.2
Oxidative Induction Time Standard OIT	D 3895	min.	<b>100</b>	125	38	10	9	7
Oxidative Induction Time High Pressure OIT	D 5885	min.	<b>400</b>	-	276	121	140	115
Oven Aging at 85°C	D 5721							
(a) Standard OIT retained after 90 days	D 3895	%	<b>55</b>	-	-	-	-	DNT
(b) High Pressure OIT retained after 90 days	D 5885	%	<b>80</b>	-	-	-	-	DNT
<b>UV Resistance</b>								
(a) Standard OIT retained after 1600 hrs. <b>Not Recommended</b>	D 3895	%	<b>NR</b>	-	-	-	-	DNT
(b) High Pressure OIT retained after 1600 hrs.	D 5885	%	<b>50</b>	-	-	-	-	DNT

\*Tested plaqued material from homogenized material after cryogenic grinding.



## SUMMARY AND CONCLUSIONS

This installation has been a highly successful demonstration of the benefits and performance of EGC systems. After a 20-year exposure period, not only is the geomembrane performing well but it has significantly exceeded performance expectations beyond its expected 10-year lifespan. The EGC has performed well over time with its material properties still more than that of GRI GM13 specification. Regular inspections have been conducted throughout the lifespan of the EGC. “Polk County EGC inspections” observed several areas requiring minor repairs; however, no significant EGC damage was identified. Most of the identified damage is minor mechanical damage near defects in extrusion-welds or around pipe boots that have seen excessive differential settlement.

Although it is not specifically related to lifespan, this site was subjected to three direct strikes by hurricanes in 2004. The site and cover performed very well throughout these extreme weather events. Polk County NCLF has experienced savings related to the EGC, including lower construction and maintenance costs and fewer compliance-related issues, which have contributed to the overall efficiency of landfill operations. It is gratifying that the results of this laboratory and field study incubation corroborate one another; they indicate that the geomembrane of an EGC can last for well over 20 years in extreme weather conditions.

## ACKNOWLEDGEMENTS

We sincerely thank all our sponsoring organizations that have supported GSI since our inception in 1986. Without them, GSI simply could not exist. This paper is part of ongoing research at the institute. The current member organizations and their company information are available at the institute’s website at [www.geosynthetic-institute.org/memberlist.htm](http://www.geosynthetic-institute.org/memberlist.htm). We are very grateful for their continued support.

## REFERENCES

- ASTM D 7238. Standard Test Method for Effect of Exposure of Unreinforced Polyolefin Geomembrane Using Fluorescent UV Condensation Apparatus, *ASTM International*, West Conshohocken, Pennsylvania, USA.
- Case, M.E., Koerner, G.R., Hsuan, Y.G. and Koerner, R.M. (2010). Case History of a 16-Year-Old Exposed HDPE Geomembrane Cover, *9th ICG*, Brazil (on CD).
- Koerner, R.M., Koerner, G.R. and Hsuan, Y.G. (2005). Lifetime Prediction of Exposed Geomembranes, *GRI-18 Conference Proceedings on Geosynthetics Research & Development In-progress at Geo-Frontiers Austin, TX*, GRI Publication, Folsom, Pennsylvania, USA, 2.18: 336-340.
- Hullings, D. (2017). The Benefits of Exposed Geomembrane Covers for Intermediate Applications at Landfills, *Geotechnical Frontiers 2017: Geotechnical Materials, Modeling and Testing*, ASCE, Orlando, Florida, USA, GSP 276: 251-258.
- Ramsey, B. (2016), 13-Year Study of Exposed Geomembrane Cover in Polk County, South Central Florida, *Geosynthetica* (online).
- Thiel, R., Purdy, S. and Yazdani, R. (2003). Case History of Exposed Geomembrane Cover for Bioreactor Landfill, *9th International Waste Management and Landfill Symposium*, Geosynthetica, Sardinia, Italy: Session D06.

## **Exposed NPNW GT Performance at a Large Surface Impoundment For Nearly One Year**

**Stephan Fourmont,<sup>1</sup> Silda Rivas,<sup>2</sup> George Koerner, Ph.D., P.E., CQA,<sup>3</sup>**

<sup>1</sup>Afitex-Textel Geosynthetics Inc., Boucherville, QC J4B 2X3 Canada; email:

[sfourmont@afitextexel.com](mailto:sfourmont@afitextexel.com)

<sup>2</sup>Alkegen, Ste-Marie, QC G6E 1V8, Canada; email:

[srivas@alkegen.com](mailto:srivas@alkegen.com)

<sup>3</sup>Geosynthetic Institute, 475 Kedron Avenue, Folsom, PA 19033; email:

[gsigeokoerner@gmail.com](mailto:gsigeokoerner@gmail.com)

### **ABSTRACT**

Exposed needle punched nonwoven (NPNW) Geotextiles are uncommon in Civil Engineering applications. Most specifications limit their exposure to a few weeks after installation due to the threat of UV degradation. This very unusual case history allowed us to evaluate an exposed NPNW geotextile over a long period of time (8 months). In addition, we performed laboratory UV exposure tests to counterpoint field versus lab performance and develop correlations between different methods of exposure.

### **INTRODUCTION**

The functional requirements of the geotextile in each application will determine the properties required, and any assessment of the products durability will be based on the degradation of these properties over a given time. There are several factors that will help to determine the durability of a geotextile; the physical structure of the fabric, the nature of the polymer used, the quality and consistency of the manufacturing process, and the environment in which the product is placed. It is essential that a geotextile performs effectively for the required duration of the design life. The project was supposed to have protective soil cover installed in three weeks. Instead, it was covered in eight (8) months. This was due to a miss calculation of the available soil from the borrow site.

### **LOCATION OF THE SITE**

Navigable waterways are essential to all inland transportation. Critical to this navigation is the maintenance of adequate depth or the waterway (which was originally regulated by the U.S. Congress in 1824!). The typical maintenance method to gain navigable depths is, and has been for centuries, that of dredging. Historically, dredge spoils have been placed in lined impoundments. This case history is a 105-ha dredge disposal site adjacent to the C & D Canal in the state of Maryland USA. The roughly triangular site was lined with a geomembrane and had a geotextile beneath and above the geomembrane. Strips of multi-linear drainage geocomposite DRAINTUBE were also placed to collect gas from the dredge spoils. This investigation concentrated on the upper geotextile used for puncture protection.



**Figure 1. Map showing location of the site**



**Figure 2. Aerial photograph of the site**

The site is operated by the U.S. Army Corps of Engineers (USACE) and is identified as the Pearce Creek Confined Disposal Facility, which receives dredge sediment from the Chesapeake and Delaware (C & D) Canal southern approach channels. The C & D canal is shown on the map in Figure 1 and the site location is identified by a star. Figure 2 shows an aerial view of the dredge disposal facility. This facility is in the Mid-Atlantic region of the USA just outside of Wilmington Delaware. The site's closest town is Elk Neck, Maryland, with a longitude and latitude of 39.4848° N, 75.9848° W.

Climate conditions include summers that are warm, humid, and wet; winters are very cold and snowy; and it is partly cloudy year-round. Over the course of the year, the temperature typically varies from 26°F to 86°F and is rarely falls below 13°F or above 93°F. The exposure test period was conducted in 2017, from January to August. This was advantageous because the solar radiation at the site was lower during the winter months. In addition, the containment facility was often covered with snow or water during the winter months.

## THE GEOTEXTILE

The geotextile used at this site was a 350 g/m<sup>2</sup> black needle-punched nonwoven made of polypropylene staple fibers. The geotextile was intended to serve as puncture protection for the underling geomembrane. Unexpectedly, the upper geotextile was left exposed to ultraviolet degradation for eight months prior to soil covering at the Pierce Creek dredge disposal facility. As a result of this miscalculation, this case history was made possible. Originally the geotextile conformed to the following minimum properties as they appear in Table 1.

**Table 1– Properties of Geotextile Used at Pearce Creek as Geomembrane Protection (or Cushioning) Materials**

Property	Test Method ASTM	Unit	Result	Unit	Result
Grab tensile strength	D4632	lb.	250	N	1112
Grab tensile elongation	D4632	%	50-105	%	50-105
Trap. tear strength	D4533	lb.	100	N	445
Puncture (CBR) strength	D6241	lb.	700	N	3114
UV resistance <sup>(1)</sup>	D7238	%	70	%	70

Notes: (1) Evaluation to be on 2.0-inch (50 mm) strip tensile specimens per ASTM D5035 after 500 lt. hrs. exposure.

The geotextiles are a non-woven needle-punched fabric manufactured from 100% short polypropylene fibers. The fibers size is 3-6 denier, length is 3-4 in. (76-102 mm). The rolls were 17.2 ft. (5.25m) width and 300 ft. (91.44 m) long.

## **FIELD INVESTIGATION**

The most important conditions affecting the seasonal variability of exposure conditions are the quantity and quality of sunlight, the amount of humidity, time of wetness, and the average maximum specimen temperature. Seasonal variability can vary greatly from year to year and must be accounted for in our test.

While laboratory weatherability and light stability tests are important for many geotextiles, the best way to test geotextiles is through natural exposure. Natural exposure testing has many advantages in that it is realistic, in-expensive, and easy to perform. However, most manufacturers do not have several years to wait to see if a “new and improved” product formulation is feasible.

Geotextile samples were taken in the field at the beginning of the project after 85 days of exposure and then finally after 252 days of exposure. A site photograph of the geotextile being deployed is shown in Figure 3. Figure 4 shows geotextile samples being taken at 85 days.



**Figure 3. Site photo of deployed geotextile**



**Figure 4. Photo of geotextile being sampled**

The results of the field study are shown in Figure 5. Although the data is sparse for this site during this time increment, (only three points), the half-life of the geotextile is 200 days via a linear regression of the data. We were pleasantly surprised by this finding.



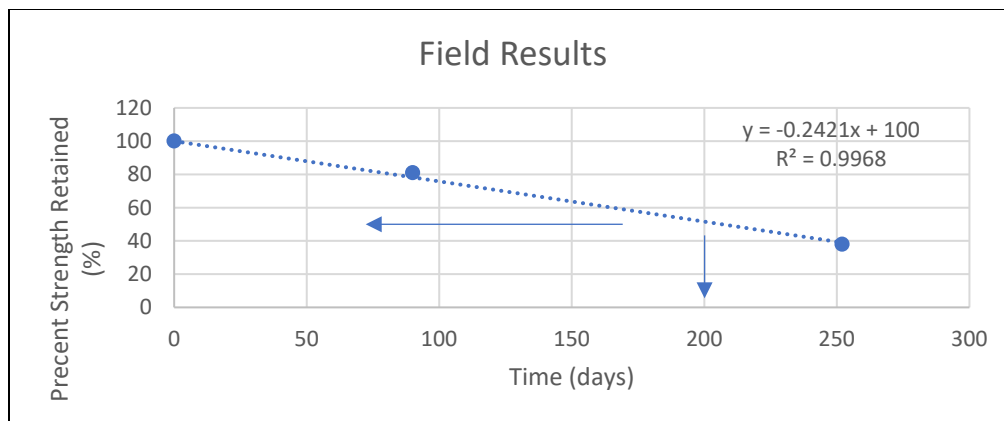


**Figure 5. Field results of percent strength retained versus time plot for the NPNW protection geotextile at the Pearce Creek Disposal Facility**

Figure 6 shows an aerial photograph of the completed project.



**Figure 6. Aerial photograph of the Pearce Creek Disposal Facility**

## LABORATORY INVESTIGATION

Durability issues with exposed geotextiles are caused by three factors: light, high temperature, and moisture. Any one of these factors may cause deterioration. Together, they often work synergistically to cause more damage than any one factor would cause alone.

Light spectral sensitivity varies for each polymer type. For durable materials, like geosynthetics, short-wave UV is the cause of most polymer degradation. The destructive effects of light exposure are typically accelerated when temperature is increased.

Although temperature alone does not affect the primary photochemical reaction, it does affect secondary reactions involving the by-products (Hsuan, Lord and Koerner 2002). A laboratory weathering test must therefore provide accurate control of temperature.

Moisture Dew, rain, and high humidity are the main causes of moisture damage. Objects stay wet outdoors for several hours each day (on average 8-12 hours daily) and condensation in the form of dew is responsible for most outdoor wetness. Dew is more damaging than rain because it remains on the material for a long time, allowing significant moisture absorption. Rain can cause thermal shock over the course of a hot summer day and can be rapidly dissipated by a sudden

shower. Mechanical erosion caused by the scrubbing action of rain can also degrade materials because it wears away the surface, continually exposing fresh material to the damaging effects of sunlight.

The xenon arc and UV accelerated weathering testers are the most commonly used accelerated testers. The equipment cross-sections are shown in Figures 7 and 8 respectively. GSI's UV exposure room is shown in the photograph of Figure 9.

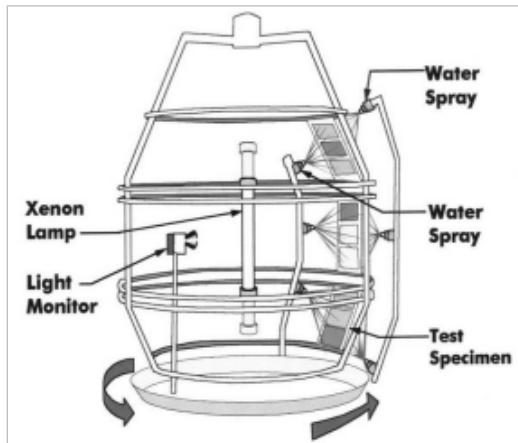


**Figure 7. Cross-section of Xenon Apparatus**

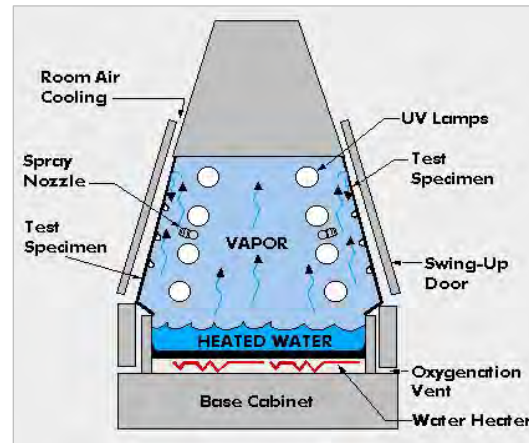


**Figure 8. Cross-section of UV accelerated weathering Apparatus**



**Figure 9. Photograph of the weathering durability lab at the Geosynthetic Institute (GSI). Note, four UV accelerated weathering apparatuses on the left and a single Xenon apparatus on the right**

Each apparatus reproduces light, temperature, and moisture in different ways. The xenon test chamber reproduces the entire spectrum of sunlight, including ultraviolet (UV), visible light, and infrared (IR). The xenon arc is essentially an attempt to replicate sunlight itself, from 295 nm - 800 nm. The UV weathering test chamber does not attempt to reproduce sunlight, just the damaging effects of sunlight that occur from wavelengths between 295 nm and 400 nm. It is based

on the concept that, for durable materials (geosynthetic polymers) exposed outdoors, short-wave UV causes the most weathering damage.

Which is the better way to test? There is no simple answer to this question. Depending on the application, either approach can be quite effective. Your choice of tester should depend on the product or material you are testing, the end-use application, the degradation mode with which you are concerned, and your budgetary restrictions, (UV accelerated weathering devices are much more economical to maintain and operate than Xenon devices).

The UV accelerated weathering tester is designed to reproduce the damaging effects of sunlight. We used UVA-340 lamps for this experiment and the procedure described by ASTM D7238 Test Method for Effect of Exposure of Unreinforced Polyolefin Geomembrane Using Fluorescent UV Condensation Apparatus. Control of irradiance was achieved with the Q-Lab Corporation SOLAR EYE feedback-loop system. The calibration of this UV accelerated weathering apparatus is traceable to the National Institute of Standards and Technology (NIST) for ISO 9000 compliance.

Xenon arc testers are considered to be the best simulation of full-spectrum sunlight because they produce energy in the UV, visible, and infrared regions. To simulate natural sunlight, the xenon arc spectrum must be filtered. The filters reduce unwanted radiation and/or heat. Two boron filters were used in our experiment as described in procedure ASTM D4355 Test Method for Deterioration of Geotextiles from Exposure to Ultraviolet Light and Water (Xenon-Arc Type Apparatus). The results of the laboratory study undertaken on the NPNW geotextile samples taken in the field at the beginning of the Pearce Creek Disposal facility project are shown in Figure 10.

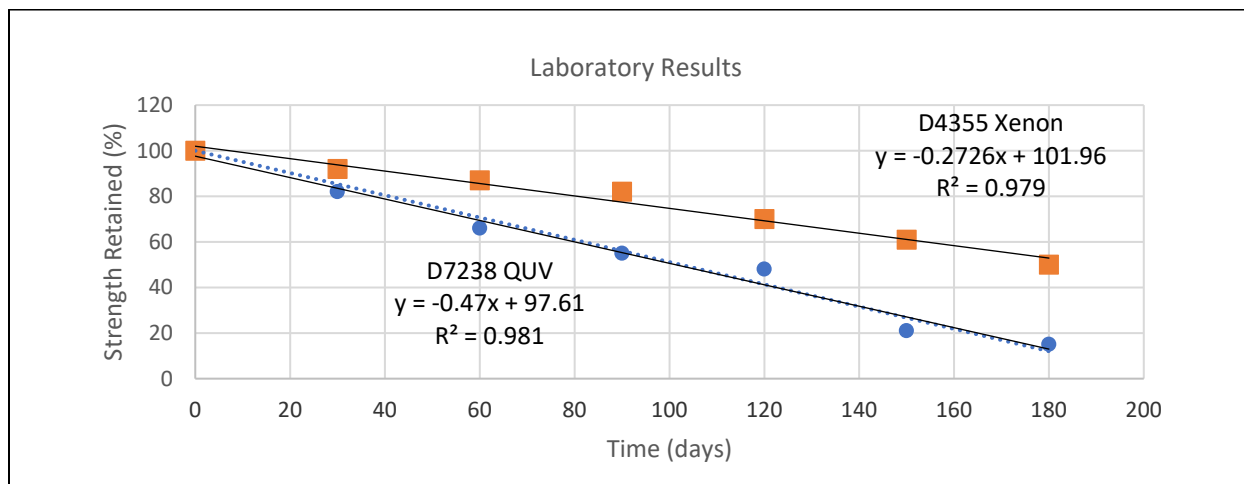


**Figure 10. Laboratory results of percent strength retained versus time plot for the NPNW protection geotextile at Pearce Creek Disposal facility. Note that both the ASTM D4355 Xenon and ASTM D7238 UV accelerated weathering results are shown on the same plot**

From these results we can determine the half-life for the NPNW geotextile from both the ASTM D4355 Xenon and ASTM D7238 UV accelerated weathering experiments. They are 175 and 100 days respectively. Again we were pleasantly surprised by these findings.

## SUMMARY AND CONCLUSIONS

Weathering testing is a tool to mitigate risks. This can be done when introducing new products, qualifying new vendors, or forensic work. Accelerated testing is used because market forces require rapid decisions, but the use of accelerated methods presents challenges. Our investigation had optimal conditions which incorporated a field case history to calibrate-normalize the findings.

A test program has the best ability to predict performance of materials used in a real-world application by combining outdoor and accelerated test results. The main objective of this work was to study the effect of aging by UV radiation on the tensile properties of a polypropylene-based non-woven geotextile and compare them to long term field exposure. The results obtained show that the mechanical properties, such as the tensile strength, held up better than anticipated for both the field and laboratory investigations. Half-lives for the three tests are as follows:

1. Field Exposure = 200 days
2. Xenon = 175 days
3. UV accelerated weathering = 100 days

It should be noted that most specifications suggest that geotextiles should have 70% strength retained after 500 hours (21 days) of exposure. This work shows that we are currently making NPNW polypropylene geotextiles that are less sensitive to ultraviolet radiation because of better antioxidant packages (HALS) and stabilizers. Hence, they will easily meet current durability specifications and have exceeded expectation.

## REFERENCES

- Seeger, S. and Muller, W. (1996), Requirements and Testing of Protective Layer Systems for Geomembranes, *Geotextiles and Geomembranes* 14 (7-8): 365-376
- Salman, A., Elias, V., Juran, I, and Pearce, E. (1997), Durability of geosynthetics based on accelerated laboratory testing, *Proceeding of Geosynthetics' 97*, IFAI, Long Beach, California, USA 1: 217-234.
- Koerner, R.M. (1989) *Durability and aging of geosynthetics*, Elsevier Science Publishers, New York, NY, USA
- Schroeder, H.F., Bahr, H., and Lorentz, E., and al, (2002) Resistance of polyolefin geosynthetics to oxidation: a new accelerated test working at elevated oxygen pressure, *7th International Conference on Geosynthetics*, IGS, Nice, France
- Mueller, W. and Jacob I. (2003). Oxidative Resistance of High-Density Polyethylene Geomembranes, *Polymer Degradation and Stability* 79 (1): 161-172
- Cooke, T.F. and Rebenfeld, L. (1988). Effect of Chemical Composition and Physical Structure of Geotextiles on their Durability, *Geotextiles and Geomembranes* 7 (1-2): 7-22
- Rowe, R.K. and Sangam, H.P. (2002). Durability of HDPE Geomembranes, *Geotextiles and Geomembranes* 20 (2): 77-95



## Best Practices for Design and Installation of Geosynthetic Floating Covers

Brian Fraser, MBA<sup>1</sup>, Douglas Hilts, P.E.<sup>2</sup>

<sup>1</sup>Layfield USA, San Diego, California; e-mail: brian.fraser@layfieldgroup.com

<sup>2</sup>Hilts Consulting Group, Yorba Linda, California; e-mail: Doug.hcg@HiltsConsulting.com

### ABSTRACT

As a result of a growing scarcity of freshwater around the world, reservoirs with geosynthetic floating covers are increasingly being used to retain, store, treat, protect, and distribute large volumes of water. This paper addresses the current best practices in designing and constructing geosynthetic floating covers for municipal potable water and wastewater treatment and storage. This includes important floating cover design requirements for proper floating cover tensioning, buoyancy, ballasting, wind-loads, geometry and the requirements of sumps, troughs, surface water removal and air venting systems requirements. The paper also addresses the lifecycle cost comparisons, economics and sustainability of floating covers as compared to other common structural methods of storing water including above ground tanks and underground concrete reservoirs. Finally, the paper addresses important material selection, testing, and maintenance requirements that help ensure longer-term performance of bottom liner system geomembranes and floating cover materials exposed to chemical disinfectants, UV light, weather, and other material application stresses related to the day-to-day operation of the floating cover.



**Figure 1. 350,000 ft<sup>2</sup> Floating Cover Eagle Rock Reservoir, CA USA**

## INTRODUCTION

Geosynthetic floating covers (see **Figure 1**) have been used since the late 1960's when the first CSPE floating covers were installed in Southern California for municipal water applications. Since then, floating covers have been used extensively in many regions of the world for the protection and storage of water. The demand for floating covers has increased because of regulatory requirements and an increased scarcity of fresh water in many regions of the world. Floating covers also provide one of the most economical methods of protecting and storing large volumes of water. The primary function of floating covers is to prevent dirt and debris from contaminating the water being stored and therefore maintaining water quality. Floating covers also provide an excellent method to control or eliminate evaporation control in reservoirs. Floating covers also lower the amount of disinfectants required helping to reduce treatment costs. There are a number of different floating cover systems used today for covering reservoirs as discussed below.

## APPLICATIONS & MARKETS

One of the main markets for floating covers is municipal water which includes municipal water districts and private water operators under the control and direction of government agencies. In municipal applications, floating covers are used for both potable water storage and wastewater treatment applications. For potable water applications, floating covers prevent dirt and debris from contaminating the water storage. Floating covers are also used for evaporation control. Properly designed and installed, floating covers can eliminate evaporation losses as a result of warmer air temperatures, wind, relative humidity, and large exposed water surface areas. In wastewater applications, insulated floating covers are often used in colder regions for biological secondary wastewater treatment of lagoons. In this application, modular insulated floating covers are used to insulate the surface of the water to maintain higher water temperatures which further enhances bioactivity for nitrification and associated reduction levels of biological oxygen demand, chemical oxygen demand, total suspended solids.

By eliminating UV light, floating covers also help reduce algae growth in the water. This is important to protect mechanical piping system, water quality and odor control.

In addition to municipal water markets, floating covers are increasingly being used in other markets including oil and gas, mining, agriculture, waste and airports for evaporation control, odor control, fluid dilution prevention, algae control, biogas containment and security of water. **Table 1** below lists the common applications of floating covers by water type (Gersh 2019).

Water Storage Type	Function
Potable Water	<ul style="list-style-type: none"> <li>• Eliminate evaporation</li> <li>• Eliminate algae growth</li> <li>• Reduce chlorine dosing &amp; costs</li> <li>• Protect from airborne contaminants</li> <li>• Protection for bird and wildlife contamination</li> <li>• Security of water source</li> </ul>
Raw Water	<ul style="list-style-type: none"> <li>• Eliminate evaporation (salinity increases)</li> <li>• Eliminate algae growth</li> <li>• Reduce chlorine dosing and costs</li> <li>• Protection from airborne contaminants</li> </ul>
Recycled Water	<ul style="list-style-type: none"> <li>• Eliminate evaporation</li> <li>• Eliminate algae growth</li> <li>• Reduce chemical dosing</li> <li>• Odor capture</li> </ul>
Wastewater	<ul style="list-style-type: none"> <li>• Odor capture</li> <li>• Biogas capture</li> <li>• Reduce algae growth</li> <li>• Reduce chlorine dosing</li> </ul>
Mineral Processing	<ul style="list-style-type: none"> <li>• Eliminate evaporation</li> <li>• Eliminate algae growth</li> <li>• Elimination of increased process water inventory with raining in storage pond</li> <li>• Protecting birds and wildlife</li> </ul>

**Table 1. Floating Cover by water storage applications (Gersh 2019)**

## ECONOMICS & SUSTAINABILITY

Floating covers provide one of the most economical methods of storing large volumes of water verses the use of above ground tanks or below grade reservoir with structural roof. For example, in 2009 an 18-acre, 244-million-gallon, (923 M liters) water reservoir designed with a RPP bottom liner geomembrane and CSPE geomembrane floating cover was completed for the Upper Chiquita Reservoir owned by the Santa Margarita Water District in Southern California, USA (Mills and Falk, 2013). The overall cost of the Upper Chiquita project including the construction of the earthen dam, installation of the geomembrane liner and floating cover was approximately \$53 million dollars and it took 1.5 years to complete. Based on the cost to construct the reservoir, the average price per gallon of water was \$0.22 USD.

In comparison, the Kelly Butte underground concrete reservoir in Portland, Oregon, USA was completed in 2016. The Kelly Butte project involved the replacement of two older 10-million-gallon (3.8 M liters) storage reservoirs, covered by a steel enclosure. These were replaced with a 25 million-gallon (113.6 M liters) underground concrete storage reservoirs with structural roof. The overall cost in the Kelly Butte project was approximately \$90 million and 4 years to complete. This works out to a cost of \$3.60 USD per gallon (Fraser and Lotufo, 2021).

A recent estimate for the supply and installation of a 4.2-million-gallon (19.1 M liters) welded steel tank system for water storage installed in Texas in 2020 was \$4,200,000. This converts to a construction cost of \$1.05 per gallon (B. Matchet, Spiess Construction, 2022).

Table 2 below compares the construction cost per gallon for the three project types. Providing the availability of land, floating covers and reservoirs are the most economical method of storing large quantities of water. In mid to large water storage applications, the cost of constructing a reservoir with a floating cover can be under 30% of the cost of a steel tank or underground concrete reservoir. This represents a major capital and lifecycle project costs savings for the owner.

Project Type	Size	Construction Cost per gal (USD)
Upper Chiquita Floating Cover & Earth Reservoir (2011)	244,000,000 gal	\$0.23 gal
Kelly Butte, Under Ground Concrete Reservoir (2016)	25,000,000 gal	\$3.60 gal
Texas, Above Ground Steel Water Tank (2020)	4,200,000 gal	\$1.05 gal

**Table 2. Comparison table of construction cost per gallon of water**

Another important benefit of properly design floating covers is their ability to control and eliminate evaporation losses. In hot arid regions, evaporation losses can be substantial and represent a significant cost to owners. As an example, a Texas Water Development Board report showed a maximum annual 2013 evaporation losses of 97.34” (246.8 cm). Figure 2 shows a lighter colored floating cover installed for an oil & gas company in West Texas in 2014 for evaporation control. (Fraser & Killian, 2015).



**Figure 2. Evaporation control floating cover, West Texas, USA**



Earth or concrete lined reservoirs with floating covers can also provide a sustainability advantage to owners and communities. Compared to structural steel and reinforced concrete tanks and below grade reservoirs with structural roofs, geomembrane floating covers provide a lower carbon footprint resulting in reduced greenhouse gases and CO<sub>2</sub> emissions into the environment. Geosynthetics including geomembranes provide a lower embodied carbon footprint versus many other traditional building materials including steel and reinforced concrete. A polyethylene geomembrane has an approximate calculated embodied carbon footprint of 1.7 – 2.0 Kg CO<sub>2</sub>/Kg (GSI White Paper #42).

## DESIGN CRITERIA

The long-term performance of floating covers requires the floating cover system to be properly designed by an experienced licensed engineer. A project specific engineered design is required for each project. One of the main floating cover systems is the weighted tensioned floating cover also referred to as a defined sump system (see Figures 3 and 4). This system uses a series of strategically located troughs to provide the required tensioning and buoyancy in the floating cover. The troughs are designed to take up the excess floating cover material and tension the floating cover throughout the reservoir fluctuating high and low operating levels. The tensioning is required to support surface loads on the floating cover including ponded rainwater, operations and maintenance personnel, and floating cover appurtenances. Weight tensioned systems use troughs consisting of surface floats and ballast weights. In standard shaped rectangular reservoirs, it is common to use either a central double wye or bottom of slope trough configuration. Irregular shaped reservoirs often require a custom trough configuration and design. The location of the troughs needs to be properly determined based on the expected operating levels and reservoir geometry including reservoir depth, corners, floor, ramps, intermediate benches, and curves within the reservoir. Weighted tensioned floating covers are scalable and can be used on small reservoirs up to very large size reservoirs.



**Figure 3. Defined sump cover in operation**



**Figure 4. Personnel on cover in full operation**

An alternative to the weight tensioned floating cover system is a mechanically tensioned floating cover. For mechanically tensioned floating covers, cables are attached to the floating cover that are connected to counter-weights and a pulley system to maintain the floating cover tensioning.

The components are housed in individual steel towers located around the perimeter of the reservoir. The steel cables are attached to the floating cover using a reinforced geomembrane strip located near the top perimeter slope of the floating cover as shown in Figures 5 and 6. Tensioned cable systems are normally best used on rectangular shaped reservoirs up to 250,000 ft<sup>2</sup> (23,235 sq m) in surface area.



**Figure 5. Tension cable and towers      Figure 6. Tensioned Cable System, Greely, CO**

The design of floating covers also requires a rainwater surface removal system. With weight tensioned floating covers, this is normally done with surface dewatering sump pumps in conjunction with the designed floating cover troughs. For mechanically tensioned floating covers, the rainwater removal system consists of a submersible pumps or gravity type drains installed on the floating cover. The rainwater removal system should be designed for two storms and removal rates:

- 1) 10 year storm, 24 hour rainfall intensity with capacity to remove rainwater 24 hours after the storm has passed, and
- 2) 25 year storm, 24 hour rainfall intensity with the capacity to remove rainwater 48 hours after the storm has passed.

Important design considerations involve understanding the geometry and capacity of the reservoir including size, shape, depth, slopes, and all interior hydraulic structures. Operating water levels need to be determined including standard freeboard, high and low water levels, and fluctuation intervals. Inlet and outlet pipe flow rates and their location need to be factored into the floating cover design.

Site conditions also need to be factored into the design including whether the reservoir is a concrete, asphalt, compacted earth, or geomembrane lined. For earth lined reservoirs, the subgrade needs to be properly compacted and prepared. Older concrete reservoirs often require restoration and repair work prior to relining with a geomembrane liner and floating cover. Groundwater levels in reservoirs also need to be determined to be acceptable to prevent geotechnical problems with the subgrade which can impact the liner and floating cover system.

Engineered loads need to be calculated for all associated dead and live loads on the floating cover including trough ballasting. Wind loads need to be factored into the design and potential additional wind ballasting.

The floating cover and geomembrane liner should be anchored continuously around the reservoir perimeter above the overflow operating water level plus applicable freeboard. Proper perimeter anchorage of the floating cover (and geomembrane liner) is required by means of either mechanical anchorage into a concrete curb or an earth backfilled anchor trench.

Various appurtenances are required on most floating cover systems. These include surface vents for release of any entrapped air or gases under the floating cover, access hatches, inflation hatches, dewater sump pumps, textured walkways, access steps, and ladders. These appurtenances need to be properly attached to the floating cover system by means of welding or mechanical attachment following standard geomembrane installation best practices.

A number of industry engineering design standards, guidelines, and reference materials are available for floating covers used for water reservoir applications as listed below.

- AWWA national, Manual M25, *Flexible Membrane Covers and Linings for Potable-Water Reservoirs*
- AWWA national, Standard D130, *Geomembrane Materials for Potable Water Applications*
- AWWA California - Nevada Section, *Reservoir Floating Cover Guidelines*
- ASCE Standard, *ASCE/SEI 7 Minimum Design Loads and Associated Criteria for Buildings and Other Structures*

## **MATERIAL SELECTION**

Material selection process is also an important part of the design process. This includes determining material required mechanical and endurance properties for all materials, including but not limited to, geosynthetics, concrete, metals, etc.

The material selection process in conjunction with a proper floating cover design and installation are the main factors required to ensure the required performance of the floating cover throughout its expected service life. In municipal potable water applications, several material types have been used over the years for floating covers. These include Chlorosulfonated polyethylene (CSPE), Reinforced polypropylene (RPP), PVC based Interpolymer alloy (EIA), Linear Low Density Polyethylene (LLDPE) and other specialty polyolefin alloy materials. The industry has experienced some inconsistency and performance problems with certain of these materials primarily in municipal potable and wastewater applications. For this reason, it is important for owners and engineers to carefully research their material selection. The material selection process should include ensuring the material has a well-established history of proven performance in the required application. This should be further backed by an acceptable longer term material weathering warranty from the geomembrane manufacturer.

Completing a site assessment and water analysis is an important part of the material selection process. This includes determining pH levels, disinfectant type and levels, other chemicals involved and water temperatures. Chemicals used for disinfectants in municipal water treatment include chlorine and chloramines and can function as accelerators in breaking down or leaching out the protective antioxidant packages of certain geomembranes resulting in environmental stress cracking and premature material failure (Mills 2011). Other related conditions include regions of high UV radiation, warmer ambient temperatures, cold temperatures and material folds and creases. These conditions have been known to further accelerate the degradation of certain geomembrane material as well as impact the floating cover performance.

In addition to flexibility, other important mechanical properties of the material should include tensile strength, elongation, tear, puncture, UV resistance and stress crack resistance. It is important that floating cover materials have the ability to retain key mechanical properties including tensile during the expected life of the floating cover. In potable water applications, the materials should have potable water certification including NSF 61 and meet other regional regulated requirements.

Additional independent material performance testing in more challenging or unknown project applications should be considered when choosing a geomembrane material. This can include accelerated chemical testing where material samples are immersed in higher temperature liquids and evaluated for various criteria including antioxidant retention levels, tensile strength losses and surface stress cracking. It is recommended that immersion testing be performed for periods of 60 – 180 days for best results. Further references for chemical immersion testing and related environmental stress crack testing include ASTM D5747, ASTM D1693 and the EPA Test Method 9090A.

The expected lifecycle of floating covers can vary by application and can range from 5 – 30 years. Based on the authors' experiences, Table 4 below shows a suggested service life expectancy by material type for floating covers used for municipal water storage applications. Note, this is an approximation only by general material polymer type and can vary by specific manufacturers product formulations. Another important factor for achieving longer term performance of the floating cover material is having a proper operations and maintenance plan during the life of the floating cover.

Suggested Service Life for Floating Cover Materials in Potable Water Applications	
Under 10 Years	Lightweight RPE, LLDPE (GM 17), PVC
10 – 20 Years	RPP, EIA-PVC, TPO's, PE Alloys
20 – 30 Years	CSPE

**Table 3. Projected service life of floating cover by material type**

## FLOATING COVER FABRICATION

Based on the need for floating cover materials to move and flex with changing water levels, the materials used for floating covers requires very good flexibility and the ability to be prefabricated into custom size panels in the factory.



Geomembrane roll stock materials are typically prefabricated into custom-sized panels based on specific size and configuration based on reservoir geometry and location within the reservoir. There are many performance advantages of using factory fabricated panels for floating covers. The constant and favorable factory-controlled environmental conditions yield higher quality, including, better seams between individual geomembrane rolls, than field fabricated geomembranes and fewer opportunities for damage by field activities and personnel. The Fabricated Geomembrane Industries (Stark et al. (2020) has previously compared factory and field welded thermal geomembrane seams for a large off-stream water reservoir project. This comparison showed that factory welded seams exhibit higher seam peel and shear strengths, less variability, and more consistency than field welded thermal seams. The compiled test results showed that factory seams are about 10% stronger than field seams. Factory fabrication can typically result in about 75% less field seams on a project.

In addition to the prefabrication of the floating cover panels, several of the floating cover components and appurtenances can be prefabricated further saving installation time and costs. These include trough float caps, trough ballast tubes, sand tubes, access hatch floats, vent floats, walkways, and access steps.

Testing of factory fabricated seams should be performed in accordance with ASTM D751, D7747, D7982 (reinforced geomembranes), D882, D6214, D6392 (unreinforced geomembranes), or other relevant test methods. Trial welds should be performed prior to starting any panel fabrication. The trial welds must pass all seam peel and shear strength requirements before any panel production starts. Welders should be prequalified prior to commencement of welding and retested at 4-hour intervals. It is recommended that all seams, and patches, be 100% air-lance tested per ASTM D4437. The results of all testing must be documented and available to the owner and/or project engineer of record. All factory testing should be fully documented and stored as part of the fabricators FQA procedures for further reference and submittal purposes.

## **INSTALLATION PRACTICES**

The installation of a floating cover is normally quite different than that of a standard geomembrane project. Floating covers by design require considerably more detailed installation work on the floating cover related to the various troughs, floats, ballast, hatches, vents, and other components not normally required on a standard geomembrane installation (see Figure 7). Floating covers also normally require the installation of highly flexible materials which are prefabricated into larger custom size panels. This can be particularly challenging for non-experienced installers resulting in installation cost overruns, potential quality problems, and sub-standard in-service performance.

Owners and engineers should establish a minimum amount of prior floating cover installation experience by material type as part of approving qualified floating cover fabricators and installers. An example of this would be requiring a minimum of 3 million ft<sup>2</sup> (278,709 m<sup>2</sup>) of similar reinforced geomembrane material fabrication and installation experience within the past 5-year period.

## Dry Installations

Most floating covers are installed in dry conditions whether as a part of a new floating cover installation or replacement floating cover. Working with larger prefabricated factory panels, the installer will require the correct material handling equipment for transporting and placement of fabricated panels. All factory panels are required to be labelled in the factory and installed in the proper sequence and location as per the approved project installation drawings. All field welded seam strength properties should be performed in accordance with the Geosynthetic Institute GM 19 A for non-reinforced and GM 19 B for reinforced (GRI GM 19) or meet the manufacturers or engineers field seaming specifications. Another information source is the Fabricated Geomembrane Institute (FGI) website for typical installation details and a geomembrane guide listing various manufactured materials and specifications. The International Association of Geosynthetic Installers (IAGI) also provides installation guidelines for fabricated geomembranes on their website. The following is a list of industry resources for installation of geomembranes and floating covers.

- Fabricated Geomembrane Institute (FGI) – [FabricatedGeomembrane.com](http://FabricatedGeomembrane.com)
  - Typical Installation Details
  - Geomembrane Guide
- Geosynthetic Institute (GSI) – [Geosynthetic-institute.org](http://Geosynthetic-institute.org)
  - GRI GM 19a & 19b Seam Strength and Related Properties of Thermally Bonded Homogeneous and Reinforced Polyolefin Geomembranes/Barrier
- International Association of Geosynthetic Installers (IAGI) – [iagi.org](http://iagi.org)
  - Geomembrane Installation Guidelines
- American Water Works Association (AWWA)
  - CA/NV Section, *Reservoir Floating Cover Guidelines*
  - Manual M25, *Flexible Membrane Covers and Liners for Potable Water Reservoirs*
  - Standard D130, *Geomembrane Materials for Potable Water Applications*

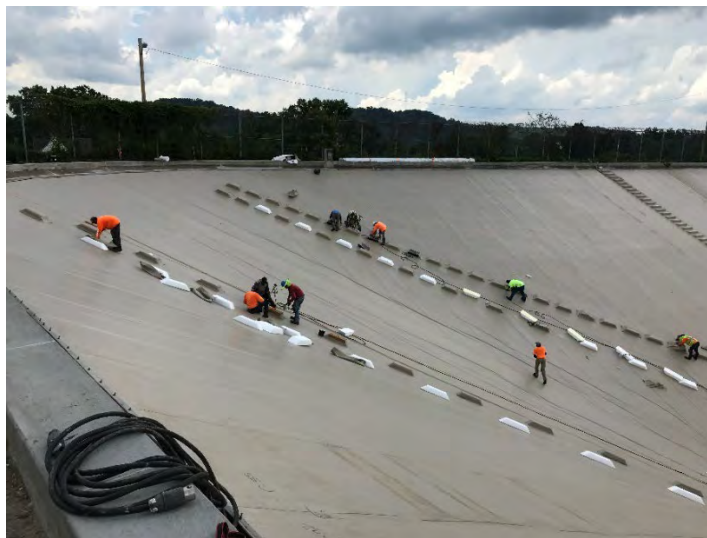


**Figure 7. Crew installing float and caps near Pittsburgh, PA.**

At the completion of the floating cover installation, the floating cover should undergo inflation testing prior to being put into operation. Inflation of floating covers includes inflating the floating cover using positive pressure. On larger floating covers, this often requires inflation testing by sections using inflation hatches and sand tubes for weights. When the floating cover is inflated, a technician will go under the floating cover with proper safety equipment to determine if they can see any light coming through the floating cover because of a tear, puncture, or welding problem. Any areas of concern are communicated with a technician above the floating cover who can then mark the point of concern for further investigation and repair.

## **WET INSTALLATIONS**

When reservoirs cannot be taken out of service or the water fully removed, the floating cover needs to be floated in place on top of the reservoir surface while it remains in service (see Figure 8). This is referred to as a wet installation and can be more challenging as compared to a dry installation. The installation requires a sufficient available space located at one end of the reservoir for staging, deployment and field fabrication of the factory supplied floating cover panels. Factory fabricated panels are deployed outside the reservoir in the width direction and pulled into place using heavy gauge ropes and equipment located on each side of the reservoir. Typical equipment for pulling the panels into place include forklifts, backhoes, or trucks. The first panel requires a special reinforced leading edge with additional structural support and floats built into it to prevent it from tearing or sinking while being pulled into place.

On larger projects, multiple prefabricated geomembrane panels may be required so the factory fabricated panels can be welded together on site and then floated into place. Additional surface floats and float caps can be fabricated on site prior to the panel being pulled into place. As each single panel is pulled into place, the last panel edge remaining on top of the deployment area is then welded to the first edge of next unrolled panel. This process of welding additional panels is required until all panels are installed ensuring complete coverage of the pond surface area. Similar to a dry installation, field welding should be performed in accordance with GRI GM 19.

The floating cover panels need to be installed in good weather conditions, which includes low wind conditions. The project owner and installer must verify satisfactory weather conditions before scheduling the installation. Once all the floating cover panels are pulled into place the floating cover needs to be immediately secured whether in an earth anchor trench or mechanically attached to a concrete curb. Temporary anchorage is recommended while the floating cover is being permanently anchored.

For further information on installing floated in wet floating cover systems, reference the FGI Guideline for Biogas Cover Systems.



**Figure 8. Floating cover being pulled into place with rope and reinforced leading edge.**

## **OPERATIONS & MAINTENANCE PLAN**

A well-defined, site-specific service inspection and repair program helps ensure long-term effectiveness of lined reservoirs and floating covers. Floating covers are well known to demonstrate longer term service life from regularly conducted inspection and maintenance. Documented inspections enable operators to detect and address various signs of potential damage or leakage and make required repairs. Without a proper documented operation and maintenance program in place, floating covers will over time develop problems associated with material tears, punctures and leaks resulting in potential premature failure of the material and floating cover.

While operators should regularly monitor the surface of the floating covers for site anomalies. These can include ponding water on top of the floating cover which could indicate a leak or rainwater pump malfunction or required tensioning adjustments to the floating cover. It is recommended that floating covers undergo regular inspection and maintenance in accordance with a prescribed operations and maintenance plan. This can include a surface inspection of the floating cover, rainwater removal pump maintenance, floating cover cleanings, and underwater inspections performed by divers or remote operating vehicles (ROVs) with cameras. Any tears, holes or areas of concern need to be fully documented before and after repair. For further information on operations and maintenance, reference American Water Works Association publications or the Fabricated Geomembrane Institute (FGI) Operation and Maintenance Guideline for Geosynthetic Lined Water Reservoirs.

## **SAFETY**

Proper safety practices are paramount on floating covers to avoid the risk of drowning or serious injuries from falls. Safety procedures should include properly designed walkways on the floating cover, ladders, and access ropes. Unexperienced personnel on top of the floating cover should avoid the trough and sump areas. A minimum of two experienced people with a communication system should be on site when working on or inspecting the floating cover. Other important safety equipment includes the mandatory use of lifejackets, proper footwear, ropes with attached floats, and a safety knife. Safety procedures and training programs are required for all personnel operating on or near the floating covers including operations staff and site visitors. A security fence should



be installed around the perimeter of the reservoir to prevent unapproved access, vandalism, and potential accidents.

## REFERENCES

- AWWA M25 Manual of Water Supply Practices. Flexible-Membrane Covers and Lining for Portable Water Reservoirs, 3<sup>rd</sup> Edition, *American Water Works Association*, Denver, CO, USA
- AWWA California-Nevada Section, Reservoir Floating Cover Guidelines (1999), American Water Works Association, Denver, CO, USA
- ASTM D5747 Standard Practice for tests to Evaluate Chemical Resistance of Geomembranes to Liquids, *ASTM International*, West Conshohocken, PA, USA
- FGI Guideline for Biogas Cover Systems (2022), Fabricated Geomembrane Institute, University of Illinois, Urbana, Champaign, Urbana, Illinois, USA
- FGI Guideline for Operation and Maintenance for Geosynthetic Lined Water Reservoirs (2022), Fabricated Geomembrane Institute, University of Illinois, Urbana, Champaign, Urbana, Illinois, USA
- Fraser, B., and Lotufo, D (2021), The Economics of Open Top Reservoirs and Floating Covers, *Geosynthetics 2021*, IFAI, Virtual
- Fraser, B., and Killian B (2015) Emerging Applications for Evaporation Control Covers, *Geosynthetics 2015*, Portland, OR, USA
- Gersch, A. (2019), A History of Geomembrane Floating Covers in Australia, *Geosynthetics 2019*, IFAI, Houston, TX, USA
- GSI GRI GM 19 Standard Specification. Seam Strength and Related Properties of Thermally Bonded Homogeneous Polyolefin Geomembranes/Barriers, Geosynthetic Institute, Folsom Pennsylvania, USA
- GSI White Paper #41 - Embodied Carbon Values for Different Plastics and Plastic Products, Koerner, Robert, Koerner George and Koerner Jamie (2019)
- IAGI Guidelines for Installation (2014), International Association of Geosynthetic Installers, Roxborough, Colorado, USA
- Mills, A. (2011) The effects of chlorine on very low-density thermoplastic olefins, *Geofrontiers 2011*, IFAI, Dallas, TX, USA
- Mills A., and Falk S (2013). Upper Chiquita Reservoir Floating Covers and Liner, *Geosynthetics 2013*, IFAI, Long Beach CA, USA
- Stark, T.D., Hernandez, M.A., and Rohe, D.S., (2020). "Geomembrane Factory and Field Thermally Welded Geomembrane Seams Comparison," *Geotextiles and Geomembranes Journal*, 48(4), August 2020, 454-467

## Chambers Dam Reservoir Remediation: Case Study

Patrick Elliott<sup>1</sup>

<sup>1</sup>Viaflex, 1062 Singing Hills Drive, Parker, CO 80138, E-mail: [Pat.Elliott@ravenind.com](mailto:Pat.Elliott@ravenind.com)

### ABSTRACT

This paper will discuss upgrading and re-lining an earthen raw water storage reservoir. The reservoir area was re-lined with a geosynthetic liner system to minimize leakage into the subgrade. The liner system consisted of fabricating and installing a scrim reinforced geomembrane with a heavy weight geotextile underlayment. In addition, 2,013 m (6,600 linear feet) of black color contrasting safety ladders were installed at various locations around the reservoir perimeter to allow for safe ingress and egress from the reservoir for operation and maintenance personnel along with the potential risk of trespassers or wildlife. The use of a scrim reinforced R-LLDPE geomembrane for the liner system reduced geomembrane slope creep and wrinkles at the slope toe, which are common for large reservoirs like this one. Furthermore, the use of intermittent soil berms across the reservoir floor prevented erosion and subgrade issues during rain events that occurred throughout the geomembrane deployment and installation process. Use of large, prefabricated geomembrane panels maximized daily geomembrane installation and shortened the overall installation time, which proved crucial to meeting owner deadlines and avoiding inclement Colorado weather in the fall/winter.

### INTRODUCTION

Phase II of the Chambers Reservoir project consists of upgrading an existing earthen raw water storage reservoir that was built in 2011 and experienced significant slope failures due to long steep side slopes, poor soil conditions, and a shallow groundwater level. The reservoir has a plan area of 170,302 square meters (1,833,120 square feet). It became apparent by 2018 that the earthen reservoir was not functioning properly and could no longer handle the shallow groundwater condition. It was critical that more water not be introduced into an already saturated subgrade, so it was decided to install a new synthetic lining system. This project was sent out for bid and awarded in 2019 and completed in 2020 (see **Figure 1**).



**Figure 1. Project overview with steep slopes.**

With the realization that the earthen reservoir could not handle the shallow groundwater condition, the 185, 806 square meters (2 million square ft) reservoir was re-designed with a synthetic lining system that would raise the floor level and provide more overburden to the underlying groundwater. An underdrain system to control the groundwater and prevent slope failures below the new synthetic lining system was also incorporated into the design because it was critical to control the flow of ground water and any reservoir leakage to reduce the saturation of soil in the side slopes to prevent future failures.

Raven Industries (RAVEN) worked closely with the owner, Arapahoe County Water and Wastewater Authority (ACWWA), and design engineer, AECOM, to determine the best geomembrane and lining system design for this application. In particular, it was important for the geomembrane to be able to be pre-fabricated into large panels in a controlled factory environment to reduce field seaming and testing, reduce installation time for budget and looming Colorado winter months that could dramatically affect the project cost and duration, and mitigate safety risks for the technicians by reducing the welding time on the long and steep interior side slopes. When dealing with unsupported geomembranes that have large thermal expansion and contraction, i.e., poor dimensional stability, large wrinkles can form especially along the slope toe. Therefore, a scrim reinforced linear low density polyethylene (R-LLDPE) geomembrane was chosen to improve dimensional stability, increase puncture resistance, limit wrinkles to provide intimate contact with the subgrade to limit leakage if a defect did develop. This dramatically reduced slope creep and wrinkling in the toe of the slope, which is the most vulnerable point of the geomembrane due to the extreme head pressure from the depth. It was important to the owner to use a tan color membrane (see **Figure 2**) for the following two reasons: (1) to reduce the water temperature and amount of evaporation in the hot, arid summer months and (2) to blend into the surrounding desert areas for aesthetic purposes in the highly populated area.



**Figure 2. Tan color reinforced geomembrane after installation**

Once site preparation began, all vegetation was removed, the reservoir ground floor was raised above the shallow groundwater level, and the side slopes were re-graded. A 16-ounce non-woven geotextile underlayment was installed on top of the prepared subgrade to protect the geomembrane from subgrade imperfections, while providing enough material thickness to move water and air laterally beneath the geomembrane. The geotextile transmissivity allowed water to move down side slopes and floor to the underdrain system if any groundwater seeped into the reservoir area or a geomembrane defect developed. The geotextile underlayment also allowed air to escape up slope to the perimeter vents, while applying protection to the geomembrane from the soft and rocky subgrade.

Several prefabricated apparatuses were installed to aid in design concerns. Vents were pre-manufactured and attached to the liner system around the perimeter above reservoir water level in the required freeboard

The project site is in a residential area and directly across the street from a local high school. This coupled with the steep side slopes, deep water depths, and potential for slippery conditions from moisture and ice/frost presented a high risk of curious trespassers or wildlife potentially falling into the reservoir. As a result, black safety ladders were installed at several locations around the reservoir perimeter to allow safe ingress and egress. These ladders have aggressive treads that allow someone to pull them self out of the water even in extremely cold/frozen conditions with heavy wet clothing (see **Figure 3**).

Ballast tubes for the inner sides of the earthen access ramp were utilized to reduce geomembrane bridging or trampolining. The flexible geomembrane used allowed intermittent soil berms to be installed across the reservoir floor to prevent erosion and subgrade issues during rain events that occurred throughout the geomembrane deployment and installation process. These berms also served as ballast by allowing water to remain across the reservoir floor during low reservoir usage or periods of draining for maintenance.





**Figure 3. Typical black safety ladder for reservoir ingress and egress**

Next, a 1.1 mm (45-mil) thick scrim reinforced linear low density polyethylene (LLDPE) geomembrane was installed on top of the non-woven geotextile. **Figure 4** shows the large panels being factory fabricated, which resulted in higher quality seams than field seams and dramatically reduced the amount of destructive seam sampling. The factory fabrication allowed for a rapid installation to avoid fall and winter inclement weather delays in Colorado.



**Figure 4. Large panels factory fabricated**

## **SUMMARY**

Factory fabrication allowed a large potable water reservoir to be quickly lined and placed back into service without experiencing a typical Colorado winter weather delay. Based on a number of design criteria, a synthetic lining system consisting of a cushion non-woven geotextile and 1.1 mm (45 mil) thick reinforced R-LLDPE geomembrane was selected. The R-LLDPE geomembrane was selected due to great dimensional stability, puncture resistance, cold temperature behavior, and ability to accommodate the steep side slopes. The non-woven geotextile served as a cushion layer to protect the geomembrane from subgrade imperfections, a means to convey groundwater seepage or reservoir leakage to the underdrain to improve side slope stability and lastly to allow any trapped gas or air to move up the side slopes to the perimeter vents. Use of large, prefabricated geomembrane panels maximized daily geomembrane installation and shortened the overall installation time, which proved crucial to meeting owner deadlines and avoiding inclement Colorado weather in the fall/winter.

## Netherlands Motorway Underpass Case Study

Dick van Regteren<sup>1</sup> and Charlie Angenent<sup>2</sup>

<sup>1</sup>Genap, Goorsestraat 1, 7041 GA, 's-Heerenberg, The Netherlands.

E-mail: [d.vanregteren@genap.nl](mailto:d.vanregteren@genap.nl)

<sup>2</sup>Genap, Goorsestraat 1, 7041 GA, 's-Heerenberg, The Netherlands.

E-mail: [c.angenent@genap.nl](mailto:c.angenent@genap.nl)

### ABSTRACT

This technical paper will discuss a case study of submerging geomembrane panels as to create a groundwater barrier for the access ramps of an underpass (tunnel) in the existing motorway in Raalte in The Netherlands. The normal way to build the underpass access ramps by pit dewatering, was not possible because of the high groundwater table and the major influx of groundwater that would cause to much discharge water. To build the access ramps the contractor has chosen to use the Geomembrane submerging technique to create the groundwater barrier. For this, two prefabricated geomembrane panels (see Figure 1) for each ramp are about 32,500 ft<sup>2</sup> and were unrolled and welded together on site to create a single panel of about 65,000 ft<sup>2</sup> for each tunnel access ramp. The groundwater barrier system consists of a 40mil thick PVC geomembrane underlain and overlain by a nonwoven geotextile that was prefabricated in five panels. After the underwater excavation of the tunnel ramp was complete, the single geomembrane panel was pulled across the water surface with ropes and winches and then submerged (sunk) to create the groundwater barrier system. After the geomembrane was pulled across the water body, the nonwoven geotextile was pulled across the water with rope hems and then submerged on top of the geomembrane to create the groundwater barrier system.

### INTRODUCTION

To create two road tunnels under an existing motorway in Raalte in the Netherlands, Genap submerged four prefabricated geomembrane panels to create a groundwater barrier along the tunnel ramps of the tunnels. The motorway could not be closed for more than 48 hours so the contractor had to tunnel under it. For each ramp, two geomembrane panels of 32.500 ft<sup>2</sup> were prefabricated (see Figure 1), unrolled and welded together on site to create a panel of 65.000 ft<sup>2</sup> to create the groundwater barrier. The groundwater barrier system consists of a 40mil thick PVC geomembrane underlain and overlain by a nonwoven geotextile of 90gram/ft<sup>2</sup> for protection.

After the underwater excavation of the ramp, the first layer of cushion geotextile was installed. The cushion geotextile layer was prefabricated in five panels because of the thickness of the material, unrolled on site and stitched together before pulling it across the water surface (see Figure 3). After submerging the geotextile, the PVC geomembrane was pulled across the water by winches and ropes (see Figure 4) and then submerged (sunk). Figure 2 shows the white underlying geotextile already installed before pulling the geomembrane across the water surface





**Figure 1. Prefabrication PVC geomembrane panels in production area**

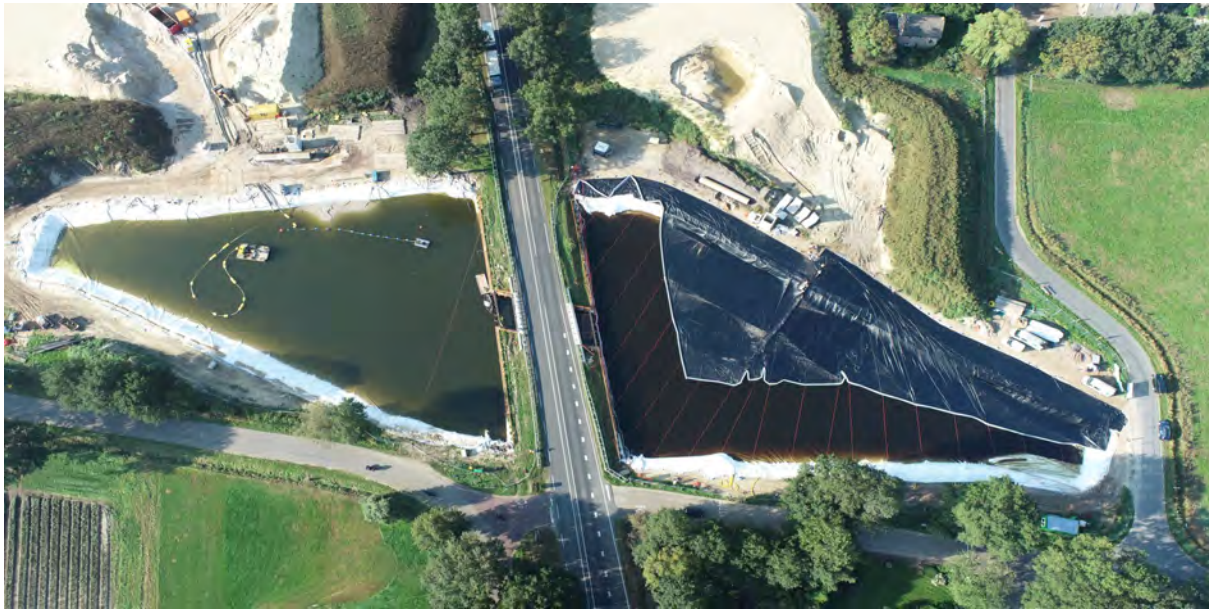


**Figure 2. Aerial view tunnel while pulling the geomembrane across the water surface**

After performing a geo-electric leak location survey that showed the geosynthetic construction was 100% watertight, the overlain layer of nonwoven geotextile was installed and the ramps were partially backfilled with ballast sand. The ramp area was then dewatered to permit construction of the ramps to the tunnel (see Figure 5). Figure 6 shows the tunnel open for traffic and the groundwater barrier system is maintaining a dry ramp. This project shows that a geosynthetic barrier system is effective, the groundwater barrier allowed the soil along the sides of the ramps to seeded to grass for a natural look (see Figure 7).



## LESSONS LEARNED

The immersion of geosynthetics is possible and has already proven itself in several projects. However, this technique is not known to many contractors, so coordination between different construction activities is of great importance and must be worked out before construction starts.

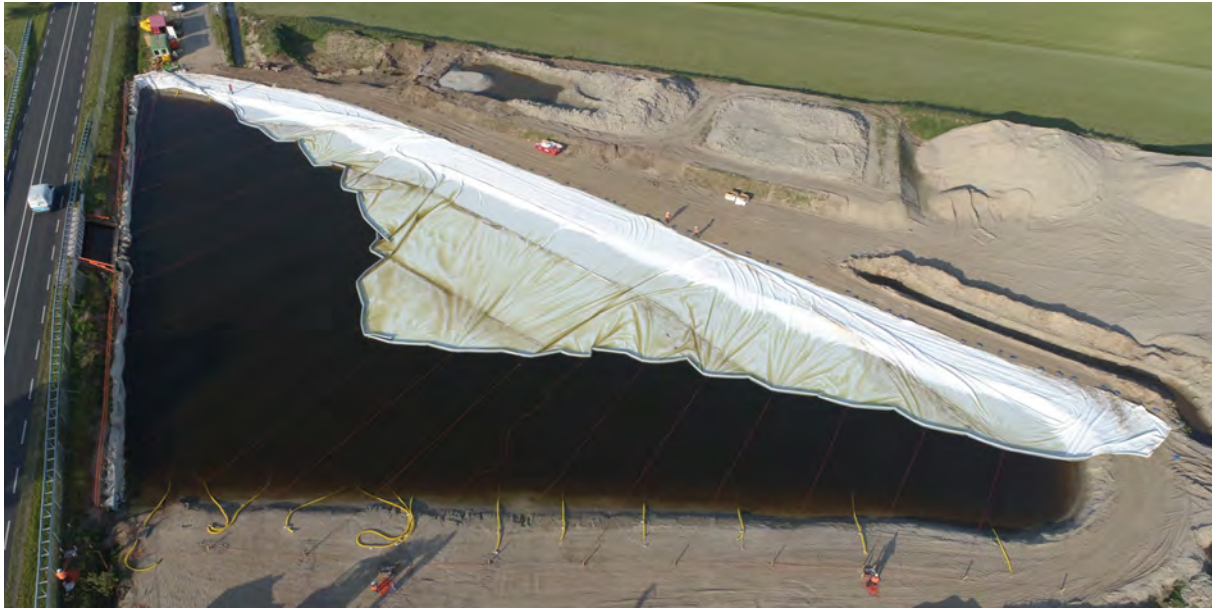


**Figure 3. Nonwoven geotextile being pulled across the water surface using ropes**



**Figure 4. Geomembrane being pulled across the water surface using ropes**



**Figure 5. Ramp after backfilling and dewatering**



**Figure 6. Aerial view showing tunnel ramps after project completion**





**Figure 7. Road view tunnel ramp after 6 months of use**



**Figure 8. Road arial view tunnel ramp after 6 months of use**

## CONCLUSION

Welding the individual rolls of geomembrane at the confined site (see Figure 2) was not possible because of the level of water tightness required, time available, and site access and logistical constraints. The use of prefabricated geomembrane panels also required in only one seam or weld being performed on site, which reduced construction time, cost, and equipment needed. In addition, the prefabricated panels were created in the exact shape of the ramps, which resulted in no waste generation on site.



## **New Developments in PVC-EIAs for Potable Water Containment Applications**

**J.P. Lens, Ph.D.,<sup>1</sup> Lance Reed,<sup>2</sup> and Ray Peebles<sup>3</sup>**

<sup>1</sup>Cooley Group, 350 Esten Ave., Pawtucket, RI 02860; e-mail: [lensj@cooleygroup.com](mailto:lensj@cooleygroup.com)

<sup>2</sup>Cooley Group, 350 Esten Ave., Pawtucket, RI 02860; e-mail: [ReedL@cooleygroup.com](mailto:ReedL@cooleygroup.com)

<sup>3</sup>Cooley Group 350 Esten Ave., Pawtucket, RI 02860; e-mail: [peeblesr@cooleygroup.com](mailto:peeblesr@cooleygroup.com)

### **ABSTRACT**

This paper highlights developments of new polyvinylchloride-ethylene interpolymer alloys (PVC-EIA) in liners and covers for potable water reservoirs. Resilient physical properties combined with excellent performance after extensive weathering and actual outdoor exposure show that these new PVC-EIA products have a designated service life of more than 30 years. Immersion into disinfectants used in potable water storage such as chlorine and chloramine, followed by Congo red thermal stability analysis, further proved that the new PVC-EIA materials outperform legacy PVC-EIA products as well as chlorosulfonated polyethylene (CSPE). Thus, innovation and material development yields new PVC-EIA materials that remove limitations of the use of current materials for future liners and covers in a wide-array of containment applications.

### **INTRODUCTION**

Floating covers and liners are now validated by decades of successful, global applications. Especially in the United States of America and Australia water authorities prefer geomembrane lined and covered earthen constructions over concrete and steel constructions because of a myriad of benefits across installation, environmental, and project cost criteria. Floating covers for water reservoirs obstruct sunlight, which prevents algae and reactive byproducts from interfering with water taste and odor, prevent the evaporation of water and disinfectants, and prevent dilution from precipitation. Furthermore, the use of geomembranes lowers the life cycle costs compared to concrete reservoirs and steel tanks. Typical project costs for a geomembrane lined and covered water reservoir can be up to four times lower than building concrete constructions. Finally, the carbon footprint of using geomembranes in water management applications is typically about 90% lower than for concrete constructions [Sangster].

The typical lifetime of geomembrane liners and covers is 20 years. The materials need to possess the right physical properties to withstand the rigors of installation, protect against rocks and vegetation, and resist tear (propagation) and strain on seams. Furthermore, the products need to tolerate extreme climate conditions ranging from exposure to sunlight and high desert temperatures to extreme arctic conditions. Also, the materials require excellent chemical resistance. Harsh chemicals, such as chlorine or chloramine, are typically used as disinfectants in potable water storage. These chemicals not only impact the integrity of polymers, but also lead to the breakdown of the additives used in the compounds to provide the required long-term heat and UV-stability. Potable water certifications are required to ensure the base materials and the included additives will not affect the safety, smell, or taste of the water.

The geomembranes that are used for liners and floating covers are typically made by applying a polymer coating on both sides of woven or knitted fabrics. Compared to unreinforced materials, fabrics provide improved mechanical properties (i.e., tensile strength, tear resistance, and puncture resistance). These fabrics are typically made from polyethylene terephthalate, nylon, or combinations of the two. With increasing performance (and costs), the polymers that are used for the coating are polyethylene, polypropylene, PVC, and CSPE. Although materials like thermoplastic polyurethane and polyvinylidene fluoride have been used as coating materials for containment solutions, they are typically only applied for the containment of *e.g.*, fuels, and, because of the high costs, are not used in potable water storage.

Of the materials that could be used in liners and covers for potable water storage, reinforced PVC is the most suitable. Reinforced PVC has strong dimensional stability and tensile strength, ensuring that the geomembrane conforms and/or elongates without breaking when subjected to an uneven subgrade or localized subgrade subsidence. Additionally, reinforced PVC's high puncture resistance will prevent damage when exposed to hydraulic pressure on the geomembrane over a rock or sharp protuberance. PVC performs well in both high and cold temperatures. It has excellent weathering and chemical resistance properties. Because of the extreme flexibility of reinforced PVC, the membranes can be prefabricated into large panels and folded for transport to the construction site thereby minimizing field seams. The material can be both thermally and dielectrically seam welded.

To render PVC with the desired flexibility for use in geomembranes, plasticizers are added to decrease the glass transition temperature ( $T_g$ ) from 80-100°C to 10-20°C. Traditionally, manufacturers used phthalates like di(2-ethylhexyl) phthalate (DEHP), the diester of phthalic acid and the branched-chain 2-ethylhexanol, to decrease the  $T_g$ . However, health concerns associated with these compounds led to the development of alternatives, replacing phthalic acid with terephthalic acid (dioctyl terephthalate, DOTP), or replacing the fatty acid chain with *e.g.*, nonyl alcohol (diisononyl phthalate, DINP). In food contact materials and medical applications, phthalic acid has mostly been replaced by saturated diacids (cyclohexane-1,2-dicarboxylic acid-diisononyl ester, DINCH). These liquid plasticizers that are compounded into the PVC matrix have relatively low molecular weights. Therefore, these plasticizers can slowly migrate out of the polymer matrix, contaminating the water and making the PVC brittle with the risk of cracks and other damages.

In the 1970s, DuPont developed ketone ethylene esters (KEE), high molecular weight polymers that are miscible with and plasticize PVC. The KEEs form an ethylene interpolymer alloy (EIA) with PVC and because of their high molecular weight, the KEEs do not migrate out of the polymer matrix. Thus, geomembranes made with these PVC-EIA materials will maintain their flexibility much longer and safely last longer than PVC materials using the traditional liquid plasticizers. The KEEs are terpolymers made from ethylene, carbon monoxide, and either vinyl acetate or n-butyl acrylate and are available in different molecular weights. They have been used in PVC compounds and have shown proven performance for geomembranes and single-ply roofing products for more than 30 years. Cooley worked together with DuPont to develop a high performance (HP) KEE polymer, specifically designed for use in PVC-EIA materials for potable water applications.

## PERFORMANCE ASSESSMENT OF PVC-EIA(HP) MATERIALS

Standard KEE grades from DuPont (now DOW) are widely used in PVC-EIAs. HP KEE grades have higher molecular weights than standard KEEs and were developed for applications that

require an even longer designated service life, such as single-ply commercial roofing applications. A special HP KEE was developed for geomembranes that addressed the presence of residual solvent that are undesirable for potable water applications. Combined with improving the strength of the fabric and using an advanced stabilization package, reinforced PVC-EIA(HP) geomembranes with a service life of more than 30 years are now available for potable water applications. The next paragraphs compare the PVC-EIA(HP) materials with typical industry PVC-EIA geomembranes.

### Physical properties

The physical properties of reinforced geomembranes are, besides by the type of polymer and the choice of plasticizer type and content, largely determined by the fabric or scrim. Typically, knitted fabrics are made from polyester fibers of 1,000D. To increase the strength of the fabric, heavier fibers of 1,300 or even 2,000D can be used. To further increase the strength of the fabrics, the picks (amount of fiber ends per inch) in each direction of the knitted fabric can be increased. Typical industrial PVC-EIA membranes use a 9x9, 1,000x1,300D knitted fabric. Reinforced PVC-EIA(HP) uses a 9x9, 2,000x2,000D knitted fiber to improve the physical properties compared to the typical industrial PVC-EIA materials (**Table 1**).

Using HP KEE instead of the regular KEE makes the geomembrane less stiff. Measured against ASTM D2097, the material can withstand 750,000 flex cycles at 23°C, which makes the material conform better to uneven subgrades and makes it easier to handle for detail work. The  $T_g$  of PVC-EIA(HP) materials with 25-35wt% of HP KEE is typically close to -30°C, where typical industrial PVC-KEE has a  $T_g$  of about -15-20°C. Thus, PVC-EIA(HP) materials can withstand

**Table 1. Typical properties of reinforced PVC-EIA and PVC-EIA(HP) geomembranes.**

Properties	Test Method	Typical specifications <sup>1</sup>	PVC-EIA (Industr Typical)	PVC-EIA(HP)
Thickness	D751	1.5 mm	1.5 mm	1.5 mm
Thickness – Lowest individual	D5199	-5%	-10%	-10%

Tensile strength – Grab test	D751A	> 1,100 N	1,500 x 1,500 N	2,000 x 2,000 N
Tensile elongation – Grab test	D751A	> 25%	25-30 x 25-30%	30 x 30%
Wide width – Tensile strength	D4885	20 kN/m	<i>No data</i>	50 kN/m
Tongue tear resistance	D751B	>165 N	110 – 130 N	580 N
Puncture resistance screwdriver	D751	>250 N	290 – 310 N	330 N
Abrasion resistance	D3389	>2,000 cycles	2,500 cycles	10,000 cycles
Seam peel adhesion	D7747 Meth A	> 100 N/25mm	70 – 100 N/25mm	110 N/25mm
Seam shear strength (grab)	D7749	> 900 N	900 N	1,200 N
Seam shear strength (strip)	D7747 Meth A	> 300 N/25mm	400 N/25mm	1,000 N/25mm

<sup>1</sup> Specifications vary per project.

The data for the typical industry PVC-EIA materials are the average of multiple samples obtained from water reservoir applications in the field from different suppliers.

200,000 flex cycles at -5°C and pass a -40°C bend test where typical industrial PVC-EIA fail the bend test at -30°C. Increasing HP KEE to over 35wt% results in diminishing returns as the incremental improved properties do not justify the additional costs.

The higher thermal stability of the HP KEE also guarantees higher service temperatures and a longer service life in hot environments. Although the use of HP KEE also contributes to an increased melt strength and impact strength of the PVC-EIA, most of the improved physical properties in Table 1, like the tensile and tear resistance, are provided by the stronger fabric using the 9x9, 2,000x2,000D fabric.

## Longevity

As discussed above, one of the advantages of using high molecular weight KEE materials is that they provide improved performance during outdoor exposure or contact with chemicals where low molecular weight, liquid plasticizers would migrate out of the geomembranes. The long-term performance of the PVC-EIA materials can further be enhanced by using relatively high concentrations of high-quality heat and UV stabilizers. To assess the performance against UV irradiation, samples were exposed in a UV chamber (ASTM G154: UVA 340nm (0.68 irradiance W/m<sup>2</sup>) 60°C 8:00 hrs - Cond. 50°C 4:00 hrs cycle), where 1,000hrs approximate about 1 year of outdoor exposure (**Figure 1**). The change in color (Delta E) is a measure of any chemical changes that occur on the surface because of the UV exposure. The higher concentration of UV stabilizers in the PVC-EIA(HP) material ensures that after more than 35,000hrs of exposure, the Delta E is still below 3, whereas the delta E for the regular PVC-EIA material was already higher than 4 after about 25,000hrs of exposure. At that time, the typical industrial PVC-EIA material also started to crack. In comparison, the PVC-EIA(HP) material still did not show any signs of cracking after 35,000hrs of exposure.



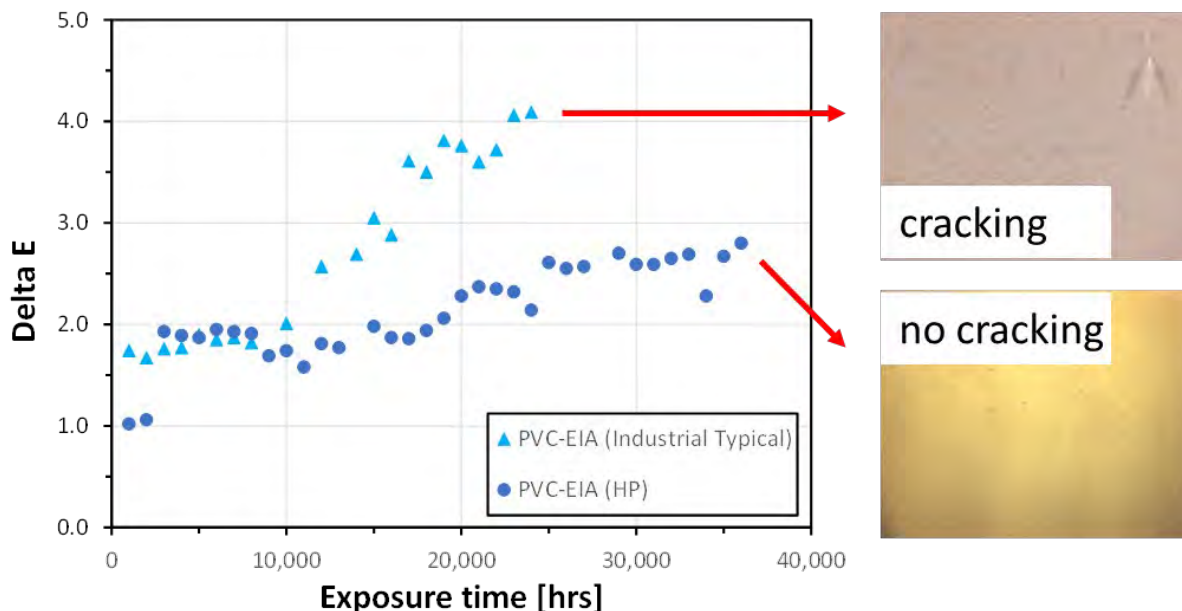


**Figure 1. Delta E of reinforced PVC-EIA and a PVC-EIA(HP) geomembranes as a function of UV exposure time.**

To compare the lab data with real-life applications, PVC-EIA(HP) was exposed to accelerated UV testing in Arizona for 57 months, accumulating approximately 73,014 kW-hr/m<sup>2</sup>. This is equivalent to ~47 years exposure in the Melbourne area (in 2019, Bureau of Meteorology estimated that the total irradiance in Melbourne was 1,538 kW-hr/m<sup>2</sup>). No cracks were observed on the material when viewed with a microscope under 7X magnification.

The resistance to the effects of a hot, dry environment was further evaluated in accordance with ASTM D5721 where materials were aged for 90 days at 85°C in an air circulating oven. Using a simple rate reaction model (reaction doubles with every 10°C change) this would be equivalent to about 16 years at 25°C. Properties like grab and tensile strength showed 99-100% retention after exposure. These data confirm the lab data that the PVC-EIA(HP) materials have a robust performance when exposed to sun and high temperatures.

### Chemical resistance

Exposure to chemicals may curtail the life of geomembranes, especially when low molecular weight plasticizers that migrate out of the polymer matrix are used. Thus, PVC-EIA materials have a much wider spectrum of chemical resistance than PVC materials containing liquid plasticizers and can be used as primary and secondary containment materials such as oils, gasoline, diesel, kerosene, and many other sensitive substances. Especially for potable water applications, the resistance against chlorine and chloramine is important. These chemicals are used as disinfectants. Typically, the maintenance dose for chlorine in potable water is about 2-5ppm and for major disinfection can be increased to 50 ppm.

To evaluate the chemical resistance of PVC-EIA, trial materials were immersed in water, deionized (DI) water, chloramine, and chlorine at 50°C for 120 days (**Figure 2**). Congo red induction times (CRIT, ISO 182-1:1990 (modified)) were determined by heating the PVC-EIA samples at 180°C. Upon consumption of all stabilizers, PVC will break down and HCl vapors will be released. These vapors change the color of a Congo red test. Thus, the higher the CRIT, the

more stable the PVC. The CRITs were measured before and after immersion. The higher loading of stabilizers in the PVC-EIA(HP) material is apparent from the initial CRIT time of 240 minutes

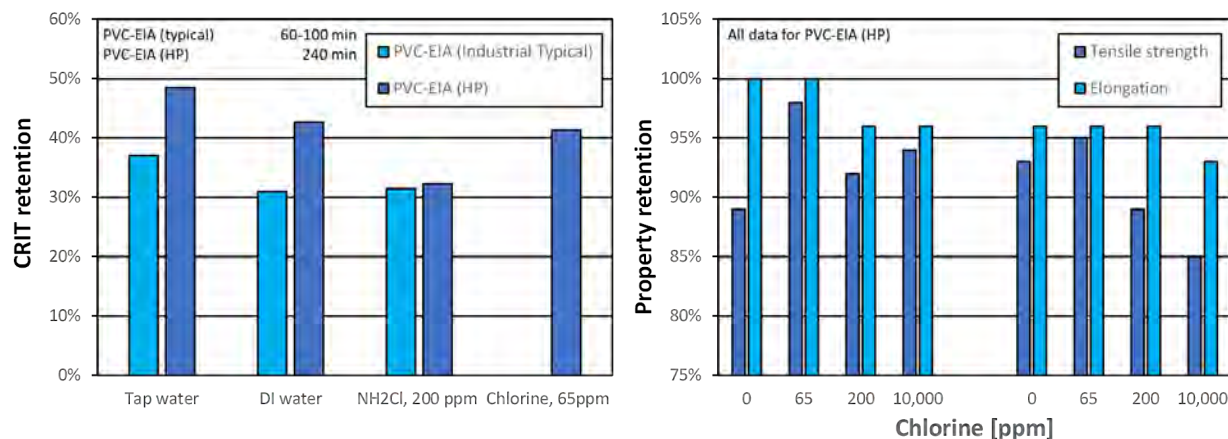


**Figure 2. Congo Red Induction Time (CRIT) and property retention after immersing reinforced PVC-EIA(HP) geomembranes in different media.**

compared to 60-100 minutes for typical industrial PVC-EIA. Upon immersion of the materials, the CRIT retention of the PVC-EIA(HP) materials is equal or higher than for the regular PVC-EIA materials.

The PVC-EIA(HP) materials were further exposed to increasing chlorine levels and the retention of physical properties was determined. The most significant changes occurred at elevated temperature and chlorine concentration. The changes in the physical properties are still within the noise of the test, indicating no significant change after extended immersion in high concentrations of chlorine. The data from Figure 2 further show that exposure to 65ppm of chlorine at 50°C for 120 days resulted in a reduction of about 60% in CRIT, but tensile properties were essentially unchanged. Thus, although the material contains a much lower content of stabilizers, which may affect the remaining lifetime of a material, the exposure does not necessarily impact the integrity of the material after that specific exposure.

When using PVC-EIA materials as floating covers for water reservoirs, instead of direct immersion in different media, the effects of exposure to vapors coming from chloramine or chlorine solutions may be more relevant. Thus, circular specimens were secured to the top of Mason jars half-filled with 2 ppm chlorine and 2 ppm chloramine solutions. The jars were heated to 50°C in a hot oil bath. Gases concentrated in the head space between liquid and specimen. The solutions were changed every 2-3 days throughout the test to ensure chlorine and chloramine concentrations remained stable (**Figure 3**). Again, the higher CRIT times of the PVC-EIA(HP) materials is clear but also upon exposure to chlorine and chloramine vapors for 120 days, the CRIT remains high, indicating the presence of higher level of stabilizers than the regular PVC-EIA materials. The tests also included samples of chlorosulfonated polyethylene (CSPE), another material that is frequently used for potable water reservoirs, and the different materials were visually compared to each other (**Figure 4**). Where the typical industrial PVC-EIA and the PVC-

EIA(HP) did not show any changes upon exposure to chloramine for up to 120 days, the CSPE materials showed the formation of bubbles and delamination after 60 days.

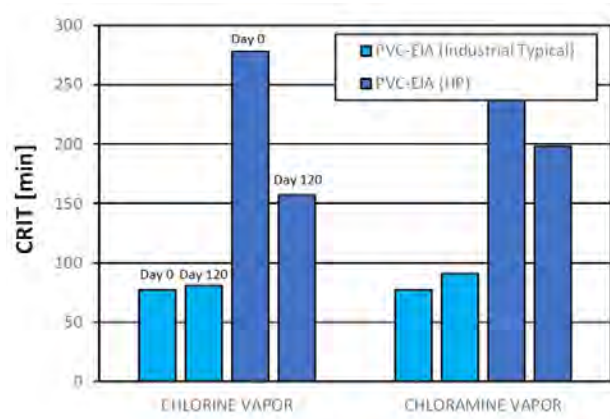


**Figure 3. CRIT after exposing materials to chlorine and chloramine vapors up to 120 days.**

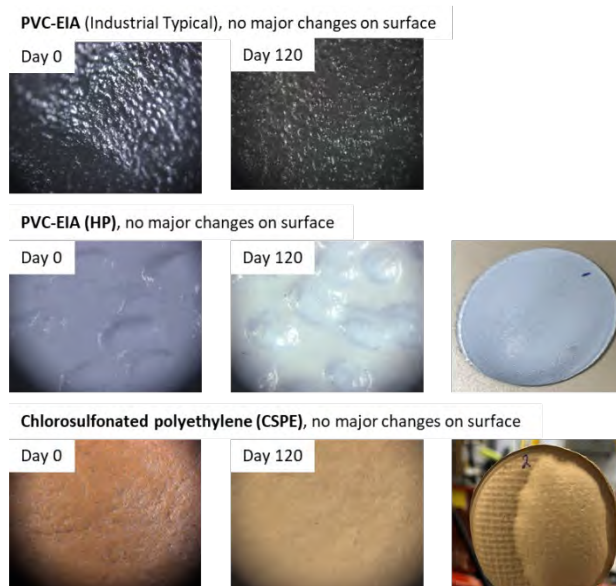


**Figure 4. Pictures of samples exposed to chloramine vapors up to 120 days.**

## CONCLUSION

New developments in the use of plasticizers, UV and heat stabilizers, and different type of fabrics in PVC-EIA(HP) geomembranes generate materials with improved physical properties (extra high

strength and low temperature flexibility), weathering performance, and chemical resistance. Furthermore, these materials are all qualified for safe use in potable water applications though *e.g.*, NSF standard 61 and AS/NZS 4020 certifications. Thus, reinforced PVC-EIA(HP) geomembranes are excellent materials of choice for liners and floating covers for potable water applications. Future requirements (*e.g.*, PFAS containment) will demand further product development and an industry-wide willingness to adopt new materials.

## REFERENCES

Sangster, T. (2022). The role of geosynthetics in combatting the effects of global warming, *GEOANZ #1, Advances in Geosynthetics 2022*, Brisbane, Australia.



## Operation and Maintenance Guideline for Water Reservoirs

Duff Simbeck<sup>1</sup>, Ronald K. Frobels<sup>2</sup>, Timothy D. Stark<sup>3</sup>, Prabeen Joshi<sup>4</sup>, and Matthew Kemnitz<sup>5</sup>

<sup>1</sup>Simbeck and Associates, 38256 Highway 160, Mancos, CO 81328. E-mail: [duff@simbeckliners.com](mailto:duff@simbeckliners.com)

<sup>2</sup>R.K. Frobels & Associates Consulting Engineers, PO Box 2633 Evergreen, CO 80437. E-mail: [geosynthetics@msn.com](mailto:geosynthetics@msn.com)

<sup>3</sup>Dept. of Civil and Environmental Engineering, University of Illinois Urbana-Champaign, 205 N. Mathews Ave., Urbana, IL 61801. E-mail: [tstark@illinois.edu](mailto:tstark@illinois.edu)

<sup>4</sup>Arcadis Construction Services, 121 Granton Drive, Suite 12, Richmond Hill, Ontario, Canada L4B 3N4. E-mail: [Prabeen.Joshi@arcadis.com](mailto:Prabeen.Joshi@arcadis.com)

<sup>5</sup>Leak Location Services, Inc, 16124 University Oak, San Antonio, TX 76249. E-mail: [matk@llsi.com](mailto:matk@llsi.com)

### ABSTRACT

This guideline recommends regular inspections and maintenance for geosynthetic-lined water reservoirs to increase service life of the liner system. A well-defined, site-specific inspection, and repair program can improve the long-term effectiveness of a water reservoir liner system. Documented inspections enable operators to monitor and address various signs of potential geomembrane and leakage – while minor and repairable. Without this well-defined operation, inspection, and maintenance program and its necessary documentation, geomembranes will develop signs that may become a potential for leakage of the stored water and eventual fail. Floating cover systems for water reservoirs, similarly, benefit from an inspection and maintenance program and are the subject of the next operation and maintenance guideline being prepared by the authors.

### INTRODUCTION

A geomembrane providing containment for a water reservoir is subject to many potential sources of stress over its operational lifetime, which can compromise the integrity of the geomembrane and thus the bottom liner system. Many of these post-installation stresses are created by environmental factors (wind, hail, ice, UV, etc.), operational conditions (water-level fluctuations, human/mechanical traffic), and wildlife – each of which have the potential to cause tears, punctures, and other damage to the geomembrane. Other sources of damage may include improper design and/or construction of the subgrade and/or installation of the geosynthetics, which are not addressed herein because the focus is on post-installation damage.

To prevent excessive damage from post-installation failures, visual inspection of the system should be made during first filling of the reservoir. Thereafter, it is recommended that regular quarterly inspections be performed (see **Table 1**) throughout the life of the reservoir. More frequent inspections may be needed based on frequency of operational activities and/or wildlife in the area. If failures in the geomembrane are observed or suspected, a more detailed inspection should be conducted by a geosynthetics consultant or the installer who may be able to provide a more in

depth analysis of the damage and suggest a suitable repair. The reservoir may need to be lowered to determine the full extent of observable damage and/or whether damage exists below the water surface. If defects are discovered, the causes should be determined and appropriate repairs made immediately by the installer or a repair contractor.

## **GEOMEMBRANE PROTECTION**

This section provides some best practices for protecting the geomembrane in water reservoir applications.

### **A. Ancillary Activities Beyond Geomembrane**

It is important to remember that damages to a geomembrane does not only occur while people are working within the reservoir. In fact, a lot of damage occurs while people are not working within the reservoir, e.g., environmental, wildlife, and other events. Damage also tends to occur from ancillary work surrounding the reservoir, e.g., during reservoir access road maintenance, fence installation, landscaping, mowing, and snow removal activities. The following suggestions may help minimize and expedite identification of damages caused by ancillary activities:

- Train all personnel working within close proximity to the reservoir on how easily the geosynthetics/geomembrane can be damaged and the implications of damage, even if minor.
- Train all personnel regularly working in the area on identification of common visual indicators of damage, many of which are illustrated pictorially below.
- Consider using video cameras, both for security and identification of damage with daily monitoring of captured images.

### **B. Activities On Geomembrane/Geosynthetics**

Proper equipment and geosynthetics protection protocols should be used at all times when performing inspections and maintenance work so the geomembrane and other geosynthetics are not damaged during the work. Specifically, to protect the geomembrane from damage the following equipment protocols should be followed:

- Sharp knives, objects, and/or tools should not be brought onto the deployed geomembrane panels unless absolutely required for the repair. When required, approved knives with retractable blades and other sharp tools should be used only by properly trained personnel and used in an approved manner that will not damage the geosynthetics. When not in use, these tools should be properly sheathed and secured to prevent damage to the geosynthetics/geomembrane.
- No heavy equipment should be used on the geosynthetics. Heavy equipment should be left at the top of slope (properly secured) and not on the geosynthetics. However, if the allowable electrical cord cannot reach the repair location from the top of slope, the generator(s) or other equipment should be placed on and properly secured to a pad and not directly on the installed geosynthetics.
- Do not use any sharp hooks, probes, or knives to check the integrity of the geomembrane seams.

- Do not park vehicles or place equipment, e.g., a pump or hose with hose clamps, directly on or immediately adjacent to the geomembrane or geosynthetics so hydrocarbon spills do not occur as shown in **Figure 1** below. Place a sacrificial geomembrane under the equipment or ATV so no hydrocarbon leakage occurs on the installed geosynthetics.
- Any repair tools should be used and set on rub sheet or a pad rather than directly on the geomembrane to prevent damage to the liner system.



**Figure 1. Hydrocarbon spills on geosynthetics for a water reservoir, which indicates driving too close to the geosynthetics.**

Other general protocols that should be followed to minimize the potential to damage to the geomembrane during inspection and maintenance activities include:

- Wear non-sharp boots and footwear.
- Remove rocks and any other objects from the bottom of your boots and footwear before walking on the geomembrane and geosynthetics.
- When low ground pressure equipment, such as ATVs, are needed on the geomembrane/geosynthetics, a rub sheet should be placed at the access point. Once the equipment is driven onto the rub sheet, it should be parked and secured. An inspection should be performed of the tires and any rocks or other objects must be removed from the tires before driving on the geomembrane.
- Smoking on the geomembrane is prohibited.

- No chemicals should be left on top of the geomembrane.
- Whenever solvents are used, they must be capped immediately after use and technicians should be wearing/using proper personal protection equipment (PPE). When not in use, solvents should be stored in their original packaging and in a protected location or at least on a rub sheet.
- Geomembrane welding personnel must be informed of the risks of using a solvent and use of appropriate PPE, such as gloves and masks, during the operation.

## RESERVOIR OPERATION

Reservoir operators should closely monitor and, if possible, control reservoir operating levels whenever ice has formed on or beneath the surface of a geomembrane. If ice has formed beneath the geomembrane, there may be a leak on the geomembrane and the geomembrane should be carefully inspected. Wide fluctuations in reservoir levels can result in ice damage to the surface of a geomembrane, particularly along sideslopes. As a result, a reservoir operating range not exceeding 0.3 m vertical is typically recommended during freezing weather conditions.

Complete inspections of the geomembrane and other geosynthetics should be performed at regular intervals to identify possible leaks, buildup of debris, separation of seams or patches, damage caused by vandalism and/or wildlife. Inspections should also check for proper operation of pumps and drains. A careful record of any required maintenance should be developed and preserved for future reference, monitoring, and inspections.

## INSPECTION INFORMATION

The inspector should record the following project information so it is readily available for future inspections:

- Job Name
- Date/Time of inspection
- Current site activity
- Material(s) inspected
- Inspector's contact information (i.e., Cell Phone Number, email)
- Date of inspection
- Date of last inspection
- Date of next inspection due
- Prior repairs that are visible or available in project documentation that should be provided to the inspector so they can properly inspect the prior repairs
- Electric Leak Location (ELL) Performed? Yes \_\_\_\_\_ No \_\_\_\_\_
- Recommend ELL be performed if conditions permit? Yes \_\_\_\_\_ No \_\_\_\_\_
- Inspector Name:
- Inspector Signature: \_\_\_\_\_



## GEOMEMBRANE INSPECTION

**Table 1** shows a sample inspection and maintenance checklist with frequency of inspections. The schedule is intended only as a guide. Site-specific written procedures should be developed by reservoir operators that reflect site-specific inspection locations and consideration. Factors such as climatic conditions, location of the geomembrane, age and condition of the geomembrane and other geosynthetics, type of geomembrane material/polymer, reservoir size, jurisdictional and regulatory agency requirements, available personnel, and other factors, should be considered when developing a site-specific inspection procedure and schedule. As a minimum, the intervals for inspection indicated in **Table 1** are recommended. An accompanying field checklist is presented in Appendix A of the full O&M Guideline, which is available at <https://www.fabricatedgeomembrane.com/protected/fgi-guidelines>, and can be completed during the visual inspection. The full guideline also presents photographs of common geomembrane damage, e.g., geomembrane tightness, wrinkles, decolorization, delamination, cracking, oxidation, and seam failure, to facilitate inspectors identifying geomembrane damage.

If geomembrane damage is observed during the inspection, the installer or a repair contractor should be contacted to inspect the area and possibly make repairs. The installer or repair contractor should document the location and type of repair completed and the inspection issue addressed so future inspections can focus on inspecting and monitoring the repair. Depending on the level of damage observed, an electric leak location survey, discussed below, may be needed to ensure the entire defect is identified. Regardless, it is recommended that an electric leak location be conducted every five years to minimize water loss.

The following list details some of the visual observations and inspections of the geomembrane that should be made during the periodic inspections:

- The perimeter and exposed portion of the bottom liner system should be inspected for vegetation. Vegetation can grow on or below the geomembrane due to the presence of water. For example, **Figure 2** shows vegetation growing under the geomembrane along the perimeter of the bottom liner system of a potable water reservoir. If present, this vegetation should be removed before it becomes large and creates a void under the geomembrane and the root system damages the geomembrane.
- All geomembrane panels or sheets should be inspected for punctures, tears, splits, and evidence of leakage. Where the integrity of the geomembrane is questioned, the installer or a repair contractor should be consulted.
- All subgrade should be traversed and inspected for rutting, excess settlement, softening, pooling water, or degradation beneath the geomembrane.
- All mechanical anchorage points should be visually inspected for pullout or leakage. Where pullout or leakage is detected, the cause of the failure should be determined before repairs are made. Repairs should be made by the installer or a qualified repair contractor.
- All bonding, e.g., caulk, mastic, adhesive, of the geomembrane to appurtenances, e.g., columns, pipe penetration, valves, and other components, should be visually inspected and re-bonded where necessary by the installer or a qualified repair contractor. Any damage identified should be photographed and documented (e.g., size, location, possible repair, etc.) to facilitate future inspections.

**Table 1. Inspection checklist for geosynthetic lined water reservoirs.**

		Weekly	Quarterly	Annually	Responsible Entity		
					Department Engineer	Dam Operator	Independent Dam Safety Engineer
External Embankment or Dam Periodic Inspections & Monitoring	Monitor Weather Forecasts	As Needed			✓	✓	
	Presence of vegetation growing on or under geomembrane – (see <b>Figure 2</b> )		✓		✓	✓	✓
	Erosion protection measures – vegetation, mats, and geotextiles		✓		✓	✓	✓
	Routine Inspections – sloughing, cracking, settlement, sinkholes		✓		✓	✓	✓
	Seepage Observations		✓		✓	✓	
	Regular Dam Safety		✓		✓	✓	
	Reservoir Level		✓		✓	✓	
	Formal Dam Safety		✓		✓	✓	✓
	Animal intrusion – deer, rodents		✓	✓	✓	✓	✓
Special Inspections	After Unusual Event	As Needed			✓	✓	✓
	If Unusual Conditions	As Needed			✓	✓	✓
Outlet Works Pipe	Internal Inspection	Every 5 years			✓		✓
		Weekly	Quarterly	Annually	Responsible Entity		

					Department Engineer	Dam Operator	Independent Dam Safety Engineer
Primary Geomembrane (GM) and Geosynthetics Inspection	Observe all GM seams and patches – identify any loose seams or extrusion welds; clean as needed for inspection		✓		✓		✓
	Observe exposed GM – (see <b>Figure 1</b> )		✓		✓		✓
	Observe GM tightness, which can cause cracking at batten strips, pipe boots, other attachments, etc.		✓		✓		✓
	Check all attachments and seals		✓		✓		✓
	Anchor trenches		✓		✓		✓
	Inlet and outlet diversion ditches		✓		✓		✓
	Damage to protective materials and/or GM		✓		✓		✓
	GM cracking or delamination		✓		✓		✓
	GM decolorization – oxidation		✓		✓		✓
	GM oxidation – color on hand wipe or chalky		✓		✓		✓
	GM wrinkles and folds		✓		✓		✓
	Material separation – cracking, exposed scrim, etc.		✓		✓		✓
	Check slopes and reservoir for subgrade softening and failures		✓		✓		✓
	Check slopes and reservoir for subgrade settlement and improper remedial measures		✓		✓		✓
	Check slopes & reservoir for geomembrane whales or bubbles		✓		✓		✓
		Weekly	Quarterly	Annually	Responsible Entity		

					Department Engineer	Dam Operator	Independent Dam Safety Engineer
Embankment/Dam Instrumentation  Electric Leak Location (ELL)	Check all instrumentation: piezometers in embankment, liquid level in pipes, sump indicators, surface monuments, flow meters (inflow and outflow)	As Needed or as required by dam safety	✓				✓
	If GM damage is observed, ELL may be needed						
	Conduct ELL every five years regardless of inspections to reduce water loss - tests 100% of lining area						



(a)



(b)

**Figure 2. Vegetation growing: (a) under geomembrane batten strip at top of reservoir sideslope and (b) around reservoir instrumentation within bottom liner system.**



## **ELECTRIC LEAK LOCATION**

Owners and operators should perform electric leak location surveys to maintain their liner system after installation. This can be done on a routine basis, e.g., every five years, or as damage or leakage becomes evident. The post installation surveys will extend the service of the liner system by identifying leaks at an early stage, which limits subgrade damage and leak size.

The electric leak location method is a powerful tool that can detect electrical paths through holes or leaks in a geomembrane. Many forms of the ELL method exist depending on the geosynthetics involved, i.e., presence of a conductive or non-conductive materials. ASTM D6747 presents a guide for selecting techniques for electrical detection of potential leak paths in a geomembrane that can assist people with assessing the different testing options and selecting the appropriate test.

In general, a voltage is applied to an electrode placed in earth ground outside the reservoir for a single-lined system and in the leak detection zone for a double-lined system placed and then the geomembrane is traversed with a current detection device. Because the geomembrane is an electrical insulator, electrical current will flow only through holes or leaks in the geomembrane. The electrical current produces localized anomalous areas of high current density at the defects or leaks. Electrical measurements are then made on the soil, in the water, or on a bare geomembrane to locate these points of current flow through the defects or leaks.

Areas where the geomembrane is not in intimate contact with the underlying subgrade should be documented and more thoroughly examined because they may limit the effectiveness of an ELL survey. This is due to ELL method not being able to work in areas with insulating features, such as, wrinkles filled with air (unless conductive geomembrane is used), geomembrane bridging over the subgrade, and other situations where the geomembrane is not in intimate contact with the subgrade. In most cases, these situations are addressed during installation but any area of exposed geomembrane will be subject to heat/cooling cycles and can develop wrinkles which will limit the effectiveness of the ELL method. Areas that will be ELL tested should have a thorough visual inspection performed, which may require cleaning of the geomembrane, which again must be done in a manner that does not damage or harm the geomembrane and other geosynthetics.

Electric leak location should be considered in the following situations:

- Immediately after geomembrane installation as part of the final construction quality assurance (CQA) and acceptance.
- As a part of a preventive maintenance schedule to test the geomembrane on a scheduled basis of every 2, 3, or 5 years depending on the project.
- As an integral part of locating damage due to a known leak in the system resulting in water loss.
- As a follow-up to a geomembrane repair or routine maintenance repair.

## **GEOMEMBRANE REPAIRS**

Geomembrane repairs should be performed by properly trained maintenance personnel using materials and methods recommended by the geomembrane manufacturer. Original project specifications and requirements should be considered by the inspector as part of the repair process. Repair work should not be attempted with the geomembrane in service if the repaired area can come into contact with the potable water during the procedure. Taste- and odor-causing chemicals may be used in making the repairs so extreme caution must be taken to ensure that any excess materials are thoroughly dissipated once repairs are completed.

Repairs along reservoir sidewalls can often be completed by temporarily lowering the operating reservoir level. Repair crews should carefully follow the geomembrane manufacturer's repair recommendations. An improperly repaired area will likely fail again so it is important to perform the first repair properly.

When performing any geomembrane repairs, it is important to recognize that incidental damages associated with the repair may occur, e.g., foot traffic, equipment traffic, and equipment operation. Therefore, it is recommended that prior to performing repairs a plan be implemented (in conjunction with proper safety protocols) to minimize the area subject to repair related traffic. Such pathways should be marked off with cones, sandbags (gently placed, not tossed), or other approved methods and all personnel directed to stay within these pathways. Thus, a post-repair visual inspection (and/or ELL) can remain focused on these particular work areas/access/egress pathways to reduce the area that must be inspected and tested.

## **SUMMARY**

If regular inspections of the geosynthetic bottom liner system for a water reservoir are performed and problems quickly addressed, field experience shows the geomembrane containment system will perform successfully for many decades. Once damaged, the bottom liner system/geomembrane can deteriorate rapidly. Repairing soon after damage detection can prevent more costly degradation, embankment and/or subgrade damage, and/or uncontrolled discharge.

For example, geomembranes used for freshwater containment applications date back to 1957 when the U.S. Bureau of Reclamation (USBR) installed a small experimental test section of a PVC geomembrane in an irrigation canal on the Shoshone Project in Wyoming (Hickey, 1969). The first PVC installation under construction specifications (604C-72) was on the Helena Valley Canal, Montana in 1968 (Geier and Morrison, 1968). Based on these early installations, the USBR concluded that buried geomembranes provide satisfactory service for seepage control in water retaining and conveying structures and are a viable alternative for areas not suitable for concrete or compacted earth linings (Morrison and Comer, 1995). Some of the USBR water canals are still operating successfully after over sixty years. As a result, if regular inspections of the geosynthetic bottom liner system are performed and problems quickly addressed, the geomembrane containment system will perform successfully for many decades and retain the valuable water.

## REFERENCES

Hickey, M. E. (1969). "Investigations of plastic films for canal linings," Research Report No. 19. A Water Resources Technical Publication. Bureau of Reclamation, Denver, Colorado, 1969.

Geier, F. H. and Morrison, W. R. (1968). "Buried asphalt membrane canal lining," Research Report #12. Water Resources Technical Publication. Bureau of Reclamation, Denver, CO, 1968.

Morrison, W. R. and Comer, A.I. (1993). "Use of Geomembranes in Bureau of Reclamation Canals, Reservoirs, and Dam Rehabilitation," U.S. Bureau of Reclamation, Report # REC-95-01, Denver, CO, December, 203 p.  
[https://www.usbr.gov/tsc/techreferences/hydraulics\\_lab/pubs/REC/REC-ERC-95-01.pdf](https://www.usbr.gov/tsc/techreferences/hydraulics_lab/pubs/REC/REC-ERC-95-01.pdf).

## An Evaluation of Soil-Geogrid Interaction Models

David Marx<sup>1</sup> and Jorge Zornberg, Ph.D., P.E.<sup>2</sup>

<sup>1</sup>The University of Texas at Austin, 301 E Dean Keeton St, Austin, Texas, 78703; e-mail: [dawie.marx@utexas.edu](mailto:dawie.marx@utexas.edu)

<sup>2</sup>The University of Texas at Austin, 301 E Dean Keeton St, Austin, Texas, 78703; e-mail: [zornberg@mail.utexas.edu](mailto:zornberg@mail.utexas.edu)

### ABSTRACT

Analytical models from literature for geogrid pullout resistance were reviewed in this study. The models were characterized as either grid-like or planar, rigid or non-rigid, and based on whether they predict the load displacement curve or only the ultimate pullout resistance. Seven of the models were reviewed in terms of their adequacy to capture soil-geogrid interaction. Three of these models are related to the FHWA model and four to the mechanistic model by Jewell et al. (1984). The sensitivity of these seven models to normal stress, embedded length, friction angle and transverse rib thickness is compared to experimental observations. For the mechanistic models, the plasticity solution for bearing resistance that best captured the sensitivity differed depending on the variable under consideration. The FHWA model with  $F^*\alpha$  a function of normal stress best represented the experimentally observed sensitivity of pullout resistance to the four variables considered. When using the default  $F^*\alpha$  values, the FHWA model was less sensitive to the input variables than the experimental results, i.e., the model was conservative.

### INTRODUCTION

Characterization of soil-geogrid interaction lies at the heart of designing with geogrids, whether for reinforcement or stabilization applications. Conventional geotechnical design procedures typically do not consider the interaction of individual geogrid ribs with particles of soil. Rather, the behaviour of the soil-geogrid composite is considered, e.g., the interface shear strength, the pull-out strength, or the coefficient of soil-geosynthetic interaction. However, modelling the contribution and behaviour of the individual ribs is useful when investigating the difference in performance of several geogrids in a soil type, or the difference in performance of a given geogrid in different soil types.

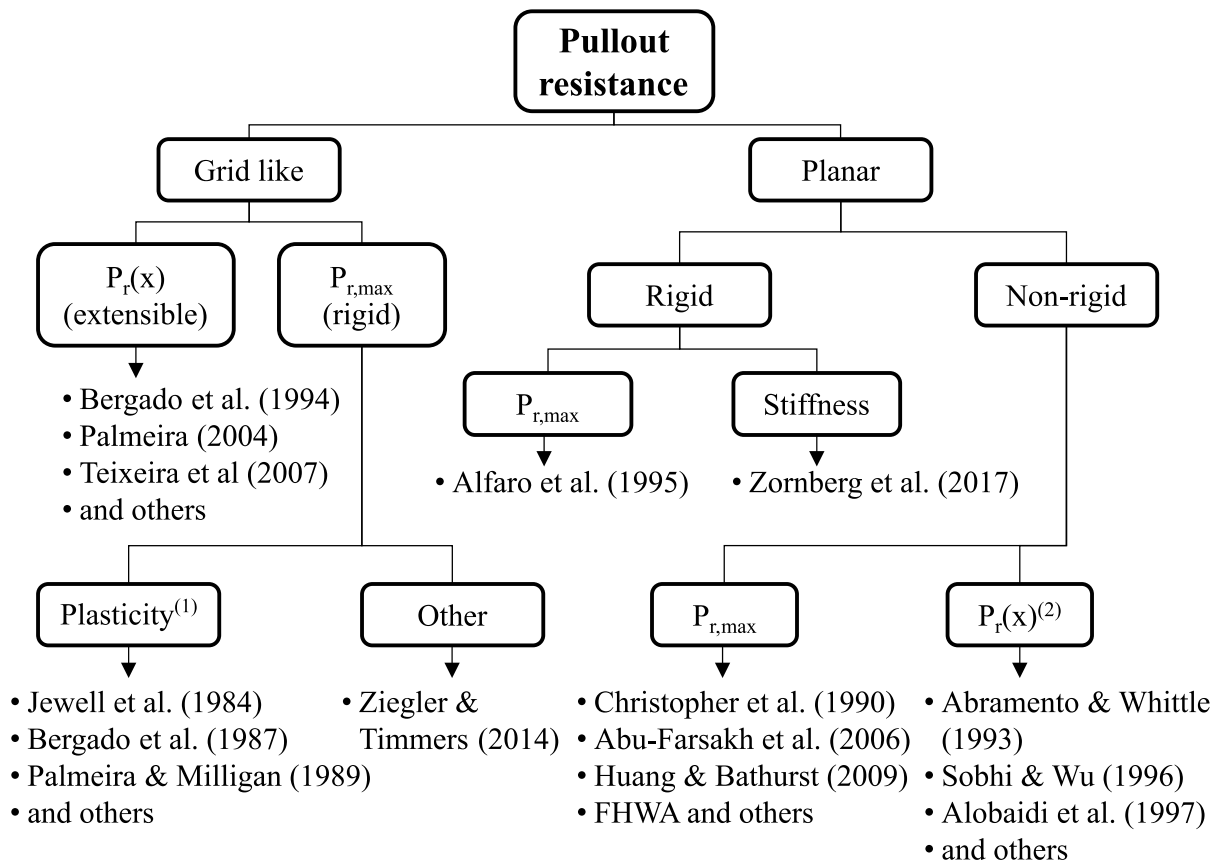
In this work, analytical models for soil-geogrid interaction during pull-out are discussed. A subset of these models is also compared to experimental results in terms of their sensitivity to a series of key variables.

### FOUR GROUPS OF MODELS IN LITERATURE

The prediction of geogrid pullout capacity has been thoroughly studied in literature. The models were developed either by considering the interaction of individual ribs with the soil or by calculating an average interaction factor across the geogrid. Thus, the models can be broadly categorized as either considering the geogrid as a grid-like inclusion or a planar inclusion. One can further distinguish between models that predict the full load-displacement curve ( $P_r(x)$ ) and those only concerned with the ultimate pullout capacity ( $P_{r,max}$ ). Finally, some models simplify the



geogrid to be a rigid body. A summary of the different types of analytical models is shown in Figure 1. This diagram is by no means exhaustive. Four of these groups of models are discussed in the following sections.



#### Notes

- 1) Can be simplified to a planar model
- 2) Mostly for geotextiles

**Figure 1. Classification of analytical models for pullout resistance.**

### Grid-like, ultimate strength (rigid), plasticity

One of the first analytical models for geogrid pullout resistance was presented by Jewell et al. in 1984. The pullout resistance ( $P_r$ ) is modelled as the sum of the frictional resistance along the surface of the geogrid ( $P_{R,F}$ ) and the bearing resistance of the individual transverse ribs ( $P_{R,B}$ ):

$$\begin{aligned}
 P_R &= P_{R,F} + P_{R,B} \\
 &= 2 \cdot \alpha_f L_e \sigma_n \tan \delta + A_b \cdot \frac{L_e}{S} \cdot \sigma_b
 \end{aligned} \quad (1)$$

where  $\alpha_f$  is the fraction solid area of the geogrid,  $L_e$  is the embedded length,  $\sigma_n$  is the normal stress acting on the geogrid,  $\delta$  is the soil-geogrid interface friction angle,  $A_b$  is the average area of a transverse rib,  $S$  is the spacing of the transverse ribs and  $\sigma_b$  is the bearing resistance of an individual transverse rib.

Jewell et al. (1994) combined the contribution of the frictional resistance and bearing resistance into a single interaction  $f_b$  as shown in Equation 2. A similar model that considered the frictional resistance of the transverse separate from that of the longitudinal ribs was presented by Koerner et al. in 1989.

$$P_r = 2L_e \sigma_n \tan \phi f_b \quad (2)$$

$$\text{where } f_b = \alpha_f \left( \frac{\tan \delta}{\tan \phi} \right) + \frac{\sigma_b}{\sigma_n} A_b \cdot \frac{1}{S} \cdot \frac{1}{2 \tan \phi} \quad (3)$$

The bearing resistance ( $\sigma_b$ ) for an individual transverse rib can be calculated from plasticity theory. Two solutions were presented by Jewell et al. (1984) for granular materials. The first ( $\sigma_{b,upper}$ , Equation 4) assumed the ribs to be a rotated horizontal footing and formed an upper bound to the experimental results. The second ( $\sigma_{b,lower}$ , Equation 5) assumed a punching failure, and was a lower bound to the experimental results. An alternative solution by Matsui et al. (1996), shown in Equation 6, falls between the two. For cohesive backfill, Bergado et al. (1987) assumed the ribs to be a deeply embedded strip footing when calculating the bearing resistance.

$$\sigma_{b,lower} = e^{\left(\frac{\pi}{2} + \phi\right) \tan \phi} \cdot \tan \left( \frac{\pi}{4} + \frac{\phi}{2} \right) \cdot \sigma_n \quad (4)$$

$$\sigma_{b,upper} = e^{\pi \tan \phi} \cdot \tan^2 \left( \frac{\pi}{4} + \frac{\phi}{2} \right) \cdot \sigma_n \quad (5)$$

$$\sigma_{b,Matsui} = \sigma_n e^{\pi \tan \phi} \tan \left( \frac{\pi}{4} + \frac{\phi}{2} \right) \left[ \cos \left( \frac{\pi}{4} - \frac{\phi}{2} \right) + (1 - \sin \phi) \sin \left( \frac{\pi}{4} - \frac{\phi}{2} \right) \right] \quad (6)$$

The models in Equations 1 to 6 are the only purely mechanistic models considered in this paper, that is only the results of unit cell tests are required to predict pullout capacity. All subsequent models include one or more coefficients calibrated in various forms of pullout tests.

Some authors (Palmeira and Milligan, 1989; Jewell, 1990; Bergado & Chai, 1994; Moraci & Gioffre, 2006; Cardille et al., 2017; and others), recommended minor adjustments to the model in Eq. 1 to better capture the effect of interference between transverse ribs. These adjustments are based on the experimental observation that interference occurs when  $S/t$  is less than 50 (Palmeira & Milligan, 1989).

The models discussed above all approximate the transverse ribs of the geogrid as footings that increases the pullout resistance by providing bearing resistance. In contrast, Ziegler & Timmers (2004) assumed that the transverse ribs cuts into the soil like a plough. The volume of soil mobilized by these transverse “ploughs” provides frictional resistance against the adjacent soil body, and this increases the pullout resistance of the composite.

### Planar, ultimate strength (non-rigid)

In 1990 Christopher et al. presented a model for ultimate pullout resistance of planar reinforcement:

$$P_r = F^* \cdot \alpha \cdot \sigma_v \cdot L_e \cdot C \quad (7)$$

where  $F^*$  is the pullout resistance factor,  $\alpha$  a scale correction factor and  $C$  a constant equal to 2 for geogrids.

The model in Equation 7 is in the same general form as that of Jewell et al. (1984) (see Equation 2). That is, pullout resistance is a function of normal stress, friction angle, length, and a

factor representing soil-geogrid interaction. Furthermore, in the absence of experimental data  $F^*$  can be calculated from contribution of the individual ribs as in the case of Jewell et al. (1984). However, in current practice  $F^*\alpha$  is either considered to be a single variable calculated from experimental data (Huang & Bathurst, 2009), or the default values in the FHWA design guide (Berg et al. 2009) is used:

$$F^* = \frac{2}{3} \tan \phi \text{ and } \alpha = 0.8 \text{ for geogrids} \quad (8)$$

In the original model by Christopher et al. (1990), the  $\alpha$  factor represented the extensibility of the geosynthetic and the strain softening behaviour of the backfill. Thus, the model is classified as non-rigid for this study.

Several authors have refined this model for specific use cases. Alfaro et al. (1995) separated the contribution of the purely frictional resistance to pullout (“2D interaction”) from the restrained dilatancy at the edges of the geogrid (“3D interaction”). The so-called “3D interaction” at the edge of the geogrid was back calculated from experimental data for each configuration. Abu-Farsakh et al. (2006) proposed a modification to calculate the scaling factors for cohesive soils.

Huang & Bathurst (2009) investigated the accuracy of the FHWA model for a database of 478 pullout tests. They proposed a non-linear model following earlier experimental studies that showed the non-linear relationship between normal stress and pullout resistance:

$$P_r = \beta (2\sigma_v L_e F^* \alpha)^{1+\kappa} \quad (9)$$

where  $\beta = 5.51$ ,  $1 + \kappa = 0.629$  and  $F^*\alpha$  is the default FHWA factors.

Similarly, Miyata & Bathurst (2012) proposed non-linear modifications to the Japanese model for pullout resistance.

### Grid-like, load-displacement (non-rigid)

The mechanistic models based on plasticity theory (Eq. 1 to 6) are limited in that it does not consider the extension of a geogrid during pullout. Furthermore, these models cannot predict the development of the pullout resistance with displacement. As an alternative, several authors developed incremental models (Palmeira, 2009) for pullout-displacement. These models have the following general form:

- 1) Assume a displacement and force at the front of the geogrid.
- 2) Calculate the bearing resistance mobilized at the first transverse rib due to the displacement, the extension of the first segment due to the applied force, and the frictional resistance of the first segment.
- 3) Calculate the bearing resistance, extension and frictional resistance for subsequent ribs based on the extension of the prior segments.
- 4) Iterate by adjusting the applied force until the force at  $L_e = 0$  is 0.

The models differ in their assumption regarding the development of rib bearing resistance with displacement, as well as the constitutive relationship assumed for the shear stress along the interface. For example, Bergado & Chai (1994) modelled the bearing resistance to increase hyperbolically with displacement. The relationship between shear stress and displacement was assumed to be elastic-perfectly plastic. Sieira et al. (2009) modelled the bearing resistance to

increase linearly with geogrid strain and the shear-stress to be hyperbolically related to displacement.

Alternatively, Palmeira (2004) and Teixeira et al. (2007) used the results of single transverse rib pull-out tests as input to the model. In addition, the model by Teixeira et al. (2007) requires experimentally measured frictional resistance of isolated longitudinal ribs. Thus, a significant limitation of this group of models is that they often require involved calibration coefficients.

### **Planar, load-displacement and stiffness (non-rigid)**

The interaction mechanism between geotextiles and soil is typically simpler than that between a geogrid and soil. Consequently, the development of tensile stress along a length of geotextile can be accurately modelled by considering the local equilibrium along the interface:

$$\frac{dT}{dx} = -2\tau \quad (10)$$

where  $dT$  is the change in unit tension over a length  $dx$  and  $\tau$  the interface shear stress between the geosynthetic and the soil.

Different assumptions have been made in the literature to solve the partial differential equation. Abramento & Whittle (1993) used shear lag analysis from the field of fibre reinforced composites. Other authors assumed the shear stress-displacement relationship to be elastic-perfectly plastic (Sobhi & Wu, 1996), bi-linear (Madhav et al., 1998), hyperbolic (Gurung et al., 1999; Perkins & Cuelho, 1999) or strain softening (Alobaidi et al., 1997). Furthermore, the stress-strain response of the geosynthetic can be modelled as linear elastic (e.g. Sobhi & Wu, 1996) or hyperbolic (e.g. Perkins & Cuelho, 1999).

Weerasekara & Wijewickreme (2010) considered the resistance contributed by the section of the soil that has strained post-peak separate from resistance where the shear stress is still developing. Pullout tests for design projects are typically done in unsaturated soils, consequently, Ghazavi & Bavandpouri (2022) explicitly considered the effect of matric suction when modelling the pullout resistance.

Even though these models are developed for geotextiles they can be used to analyse the distribution of stress and strain in a geogrid during pullout (e.g. Sugimoto & Alagiyawanna, 2003). In addition, Zornberg et al. (2017) solved Equation 10 to derive the stiffness of the soil-geosynthetic composite at small strain.

### **Summary of the available models**

Multiple analytical models have been developed to predict geogrid pullout capacity. These models range from simple empirical models to complex, iterative models that require calibration coefficients from non-conventional tests. The accuracy of the models typically increases with complexity. However, the complex models are not necessarily practical for conventional design or for use in sensitivity studies where multiple calibration coefficients would be required.

The mechanistic model by Jewell et al. (1984) and the semi-empirical FHWA models are simpler to implement but may not capture the complex mechanisms of soil-geogrid interaction. To investigate the validity of these simpler models, the sensitivity of the predicted pullout capacity to a series of key variables will be compared to experimentally measured sensitivity.



## SENSITIVITY ANALYSIS OF GEOGRID PULLOUT RESISTANCE

Several factors affect the ultimate resistance of a geogrids in a pullout test. Some of these relate to the experimental setup such as the length of the sleeve at the opening, the method of applying normal stress and the flexibility of the face (Farag & Acar, 1993; Sugimoto et al, 2001; Wang et al, 2017). Others relate to the boundary conditions imposed during the test, such as the magnitude of the normal stress and the displacement rate. Finally, the soil properties, geogrid properties and soil-geogrid interaction all contributed to the measured resistance.

To study the relevance of some of the analytical models discussed above, the sensitivity of these models to the tests variables was compared to pullout results reported in literature. Only the ultimate pullout resistance was considered for the analysis, and only two sets of models will be analysed: 1) the purely mechanistic model by Jewell et al. (1984) for a rigid geogrid and 2) the mostly empirical model by Christopher et al. (1990) that considers geogrid extensibility.

For the mechanistic model, the bearing resistance of the transverse ribs was calculated using the solution that forms a lower bound (Eq. 4), the one that forms an upper bound (Eq. 5) as well as the solution by Matsui et al. (1996) (Eq. 6) as recommended by Moraci & Gioffre (2006). For the empirical models the FHWA model with default values (Eq. 7), the FHWA model with an average  $F^*\alpha$ , the FHWA model with normal stress dependent  $F^*\alpha$  (Huang & Bathurst, 2009) and the non-linear model by Huang & Bathurst (2009) (Eq. 9) was considered. The second and third variations of the FHWA models were only implemented when tests were repeated at three or more different confining stresses.

The models and the experimental results were compared in terms of their sensitivity to normal stress ( $\sigma_n$ ), embedded length ( $L_e$ ), soil friction angle ( $\tan \phi$ ) and the average thickness of the transverse ribs ( $t_{avg}$ ). The sensitivity to  $t_{avg}$  was only calculated if the geometry of the different geogrids were otherwise the same. Only unitized, uniaxial geogrids were considered for this study. As such, the average thickness was also correlated to the ultimate strength of the geogrids.

Four sets of data from literature were selected for the sensitivity analysis for a total of 59 tests. A summary of the datasets is shown in Table 1. These datasets were selected as they all considered at least two of the variables of significance to this study in each test. The tests were all conducted at a displacement rate of 1 mm/min. The soil-geosynthetic interface friction angle was assumed to be  $\frac{1}{3}\phi$  (Cardille et al. 2017). For the tests by Lopes & Lopes (1999) only the residual friction angle was reported. The tests by Lopes & Lopes (1999) are also the only ones that cannot be considered dense.

The sensitivity ( $m$ ) of the models and the experimental results to the four variables was defined as the change in pullout resistance (predicted:  $P_r^*$  or measured:  $P_r$ ) for a change in the variable under consideration ( $\Delta X$ ):

$$m = \frac{\Delta P_r}{\Delta X} \text{ or } m^* = \frac{\Delta P_r^*}{\Delta X}$$

All variables were normalized using its minimum and maximum value in this dataset before calculating the sensitivity. Thus, if an increase in length from 0.4 m to 0.9 m results in an increase in  $P_r$  of 6 kN/m the sensitivity will be equivalent to when an increase in thickness of 0.005 m also results in an increase  $P_r$  of 6 kN/m.

**Table 1. Datasets analysed for the sensitivity analysis**

Source	Number of tests	Variables			
		Normal stress	Length	Soil type	Geogrid geometry
Lopes & Lopes (1999)	4	Yes	No	Two granular	Yes (2)
Abu-Farsakh et al. (2006)	10	Yes	No	One cohesive	Yes (3)
Moraci & Recalcati (2006)	36	Yes	Yes	One granular	Yes (3)
Abdi & Mirzaeifar (2017)	9	Yes	No	Three granular	No

Soil-geogrid interaction is a complex, non-linear problem. As such, the sensitivity to variable depends on the magnitude of change of the dependent variable. For example, increasing the length from 0.8 m to 1 m will not result in the same increase in  $P_r$  as increasing the length from 0.2 m to 0.4 m. Thus, the sensitivity was calculated for each available permutation in the experimental data, e.g.  $\Delta P_r^*$  for  $\sigma_n = 25$  to 50 kPa,  $\sigma_n = 25$  to 100 kPa, and  $\sigma_n = 50$  to 100 kPa.

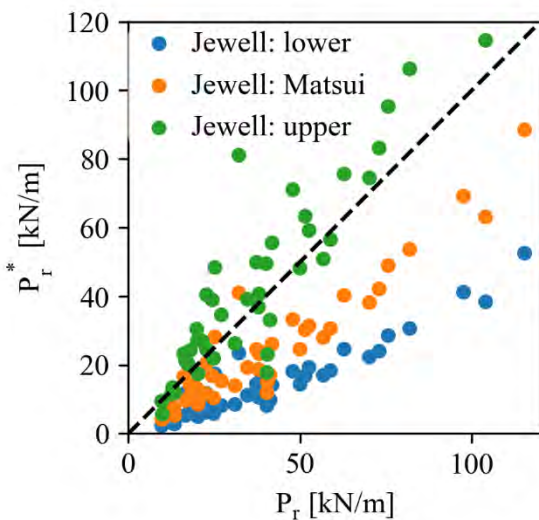
## RESULTS OF THE SENSITIVITY ANALYSIS

The objective of this work was not to evaluate the accuracy of the different models. However, the predicted values ( $P_r^*$ ) are compared to the measured values ( $P_r$ ) in Figure 2 as a reference. For this dataset, the upper bound solution for transverse rib bearing resistance (Eq. 5) best correlated with the measured pullout resistance. For the FHWA models, the most accurate model considered  $F^*\alpha$  as a variable of normal stress.

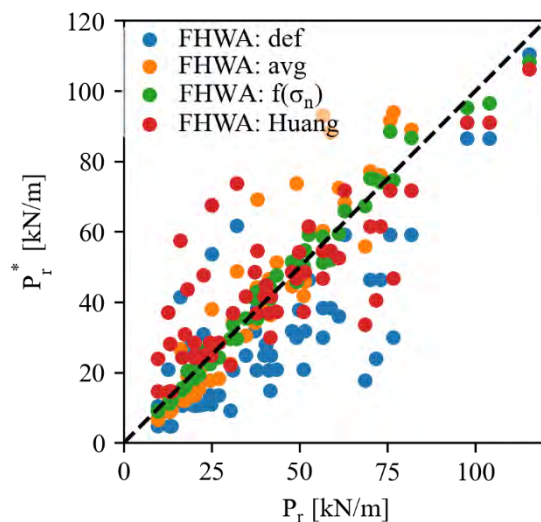
The sensitivity of the analytical models ( $\Delta P_r^*/\Delta X$ ) is shown as a function of the experimentally measured sensitivity ( $\Delta P_r/\Delta X$ ) in Figure 3 to Figure 6 for length, normal stress, friction angle and average rib thickness respectively. Values above the 1:1 line indicates that the models are more sensitive to the variables than measured experimentally, values below the 1:1 line indicates the inverse.

Figure 3b shows that all four of the FHWA models were for the most part as sensitive to a change in the embedded geogrid length ( $L_e$ ) as the experimental results. Similarly, the sensitivity of the mechanistic model with the Matsui et al. (1996) solution for bearing capacity agreed with the experimental results. However, the lower bound solution for rib bearing resistance results in a model that was less sensitive to  $L_e$  than the experimental results (see Figure 3a). In contrast, the upper bound solution for bearing resistance results in a model that is overly sensitive to  $L_e$ . The under- and oversensitivity of these two models is due to the non-linear effect of  $L_e$  in the models – by increasing  $L_e$  the frictional resistance increases, however, the number of bearing members also reduces.

It has been shown that  $P_r$  increases non-linearly with confining stress (Huang & Bathurst, 2009). The upper bound mechanistic model captured this trend as shown in Figure 4a. In contrast, the lower bound mechanistic model, and the one based on Matsui's solution, was less sensitive to  $\sigma_n$  than the experimental results. The error was the most significant for tests where a small change in  $\sigma_n$  resulted in a large difference in  $P_r$ .

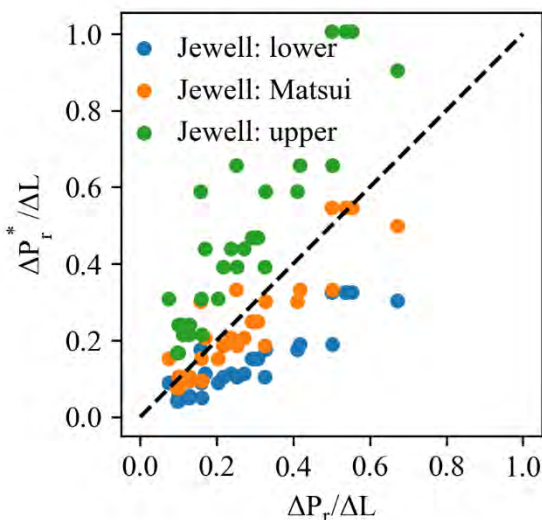


(a) Jewell et al. (1984) and related models

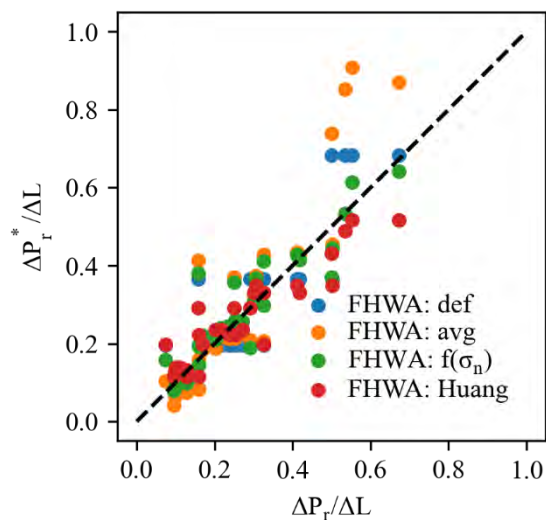


(b) FHWA and related models

**Figure 2. Modelled and predicted pullout resistance for two groups of models.**



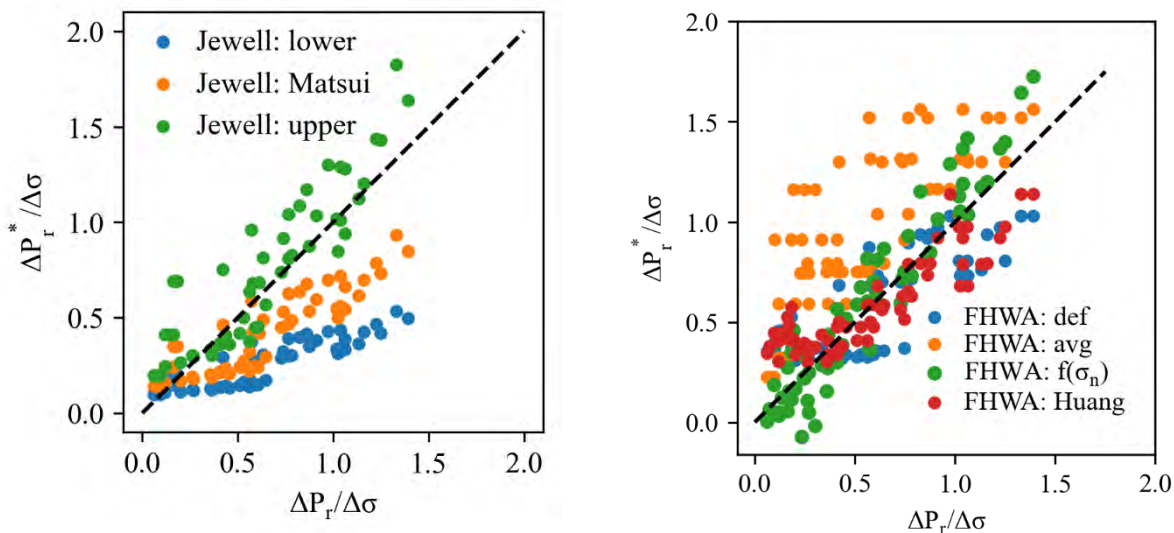
(a) Jewell et al. (1984) and related models



(b) FHWA and related models

**Figure 3. Comparison of modelled and measured sensitivity to embedded length for two groups of models.  $P_r$  and  $L_e$  is normalized between 0 and 1.**

As the relationship between  $P_r$  and  $\sigma_n$  is non-linear, an empirical model based on an average value of  $F^*\alpha$  will be oversensitive to a change in  $\sigma_n$ . The large scatter in the results for the average  $F^*\alpha$  model emphasizes the limitations of this approach. Both the default model and that by Huang & Bathurst (2009) varies from slightly oversensitive to slightly under sensitive. Finally, the stress dependent  $F^*\alpha$  model has the best match to the experimental results.



(a) Jewell et al. (1984) and related models

(b) FHWA and related models

**Figure 4. Comparison of modelled and measured sensitivity to normal stress for two groups of models.  $P_r$  and  $\sigma_n$  is normalized between 0 and 1.**

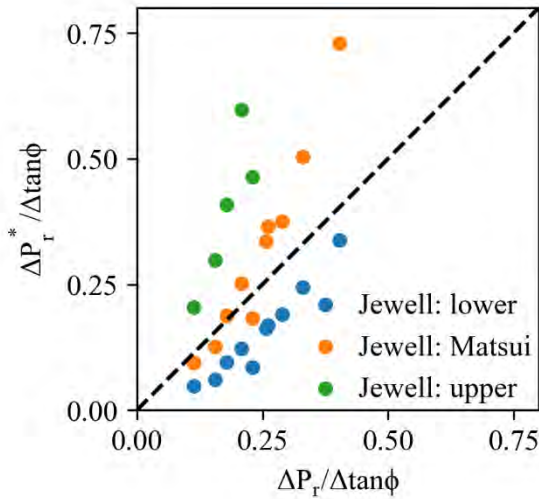
The datapoints available to investigate the sensitivity to friction angle is limited. However, for the available results both the upper bound mechanistic model and the Matsui's model were overly sensitive to a change in  $\tan \phi$  as shown in Figure 5a (some data points for the upper bound solution lies above the range of the y-axis). The difference between these models and the experimental results increased as  $\Delta P / \Delta \tan \phi$  increased. The lower bound solution was slightly less sensitive to a change in  $\tan \phi$ , with a consistent difference across  $\Delta P / \Delta \tan \phi$ . All the FHWA models shown in Figure 5 were a fair match to experimental data in terms of the sensitivity to  $\tan \phi$ .

In Figure 6a there is a cluster of points where  $\Delta P_r / \Delta t_N < 0$ . For these data points, increasing the thickness of the geogrid resulted in a decrease in pullout resistance. The points where  $\Delta P_r / \Delta t_{avg} < 0$  were limited to the comparison of two specific geogrids in the dataset. This behaviour may either have been due to experimental scatter, due to a more complex mechanism of interaction related to particle size, or due to a difference in the geogrids not related to  $t_{avg}$ .

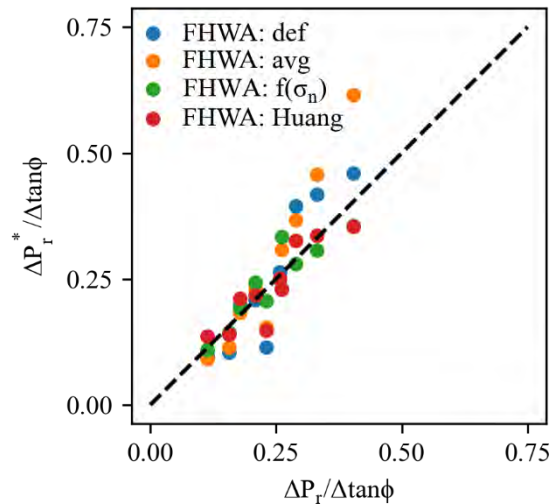
For the mechanistic models the lower bound model, as well as the one based on Matsui's mechanism, was less sensitive to a change in  $t_{avg}$  than the experimental results when  $\Delta P_r / \Delta t_N > 0$ . However, the upper bound model of Jewell et al. (1984) matched the experimental data's sensitivity to  $t_{avg}$  for  $\Delta P_r / \Delta t_N > 0$ .

None of the FHWA models explicitly considers the effect of transverse rib height on pullout resistance. Consequently, the default model and the one by Huang & Bathurst (2009) was insensitive to a change in geogrid as shown Figure 6b. By calibrating  $F^* \alpha$  to the experimental results, the effect of  $t_{avg}$  was implicitly considered in the other FHWA models and thus the models were a fair match to the experimental data where  $\Delta P_r / \Delta t_N > 0$ .



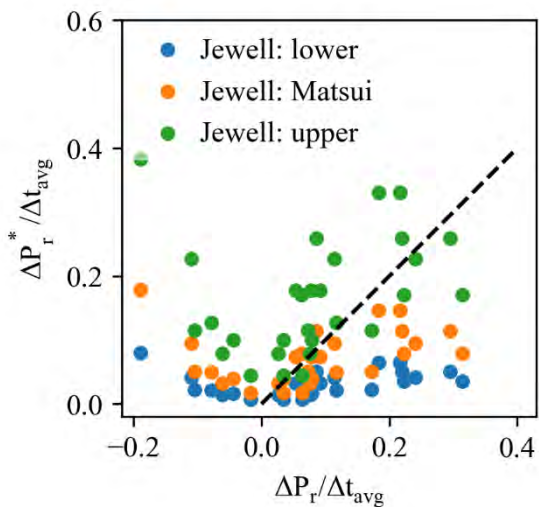


(a) Jewell et al. (1984) and related models

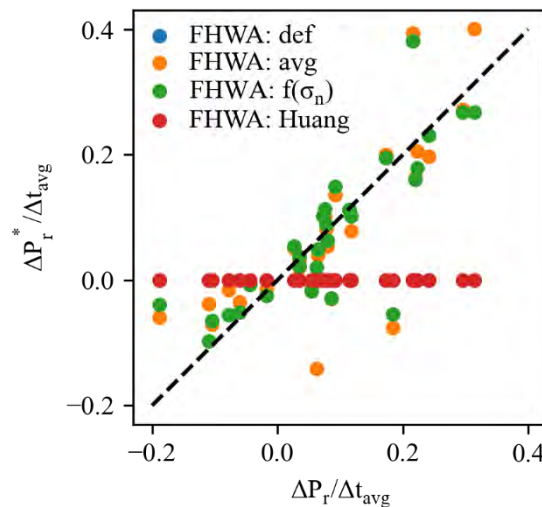


(b) FHWA and related models

**Figure 5. Comparison of modelled and measured sensitivity to friction angle for two groups of models.  $P_r$  and  $\tan \phi$  is normalized between 0 and 1.**



(a) Jewell et al. (1984) and related



(b) FHWA and related

**Figure 6. Comparison of modelled and measured sensitivity to average rib thickness for two groups of models.  $P_r$  and  $t_{avg}$  is normalized between 0 and 1.**

## SUMMARY

This work presented a summary of some of the analytical models that are available to predict the pullout resistance of geogrids. The models were categorized as grid like or planar, rigid or non-rigid and whether the full load-displacement curve or only the maximum pullout resistance is predicted.

Typically, the models that predict the full load-displacement curve are complex to implement and require non-conventional tests to determine the coefficients. These tests are not always practical for routine design or a sensitivity analysis to develop new products. Consequently, the adequacy of seven of the simpler models to capture the behaviour of the soil-geogrid interaction

mechanisms was evaluated using experimental data from literature. The sensitivity of the seven models to four different variables ( $L_e, \sigma_n, \tan \phi, t_{avg}$ ) was compared to the sensitivity of experimental results to those same variables. The study was limited to uniaxial, unitized geogrids.

The findings from the analysis of experimental data can be summarized as:

- The FHWA model with default coefficients, and related models, were all as sensitive to a change in embedded length as the experimental results. For models in the form of Jewell et al. (1984), using Matsui et al.'s (1996) mechanism for rib bearing resistance best captured the measured sensitivity to a change in embedded length.
- The FHWA model with  $F^*\alpha$  calibrated as the average of a series of tests at different normal stresses is oversensitive to a change in normal stress. The default FHWA model and the model by Huang & Bathurst (2009) adequately captured the sensitivity to a change in normal stress. So did using a stress-dependent  $F^*\alpha$ . For the mechanistic models, the upper bound solution for rib bearing resistance by Jewell et al. (1984) was found to be the most accurate.
- For the available data the FHWA models adequately matched the sensitivity of the experimental data to a change in friction angle. Both the upper bound solution for the Jewell et al. (1984) model and Matsui's solution were severely oversensitive to a change in friction angle.
- The relationship between pullout resistance and transverse rib height is complex. For some tests analysed the pullout resistance decreased for an increase in rib thickness. Only the two FHWA models calibrated to the tests data had some resemblance to the experimental sensitivity to transverse rib thickness.
- Of the seven simple models analysed the FHWA models with calibrated, stress dependent  $F^*\alpha$  values best captured the sensitivity of the experimental results to the variables considered. However, this model is also highly empirical, which reduces its relevance for investigating the mechanism of soil-geogrid interaction.
- The upper bound solution of Jewell et al. (1984) best predicted the pullout resistance of this dataset. However, the model fell short in terms of the sensitivity to friction angle and average transverse rib thickness.

## ACKNOWLEDGEMENTS

The financial assistance of Tensar International Corporation for this study is acknowledged by the authors. Opinions expressed and conclusions presented are solely those of the authors.

## REFERENCES

- Abdi, M.R. and Mirzaeifar, H. (2017). Experimental and PIV evaluation of grain size and distribution on soil-geogrid interactions in pullout test, *Soils and Foundations*, 57(6): 1045–1058.
- Abramanto, M. and Whittle, A.J. (1993). Shear-Lag Analysis of Planar Soil Reinforcement in Plane-Strain Compression, *Journal of Engineering Mechanics*, 119(2): 270–291.
- Abu-Farsakh, M.Y., Almohd, I. and Farrag, K. (2006). Comparison of Field and Laboratory Pullout Tests on Geosynthetics in Marginal Soils, *Transportation Research Record: Journal of the Transportation Research Board*, 1975: 124–136.

- Alfaro, M.C., Hayashi, S., Miura, N., Watanabe, K. (1995). Pullout Interaction Mechanism of Geogrid Strip Reinforcement, *Geosynthetics International*, 2(4): 679–698.
- Alobaidi, I.A., Hoare, D.J. and Ghataora, G.S. (1997) Load Transfer Mechanism in Pull-Out Tests', *Geosynthetics International*, 4(5): 509–521.
- Berg, R.R., Christopher, B.R. and Samtani, N.C. (2009) *Design and Construction of Mechanically Stabilized Earth Walls and Reinforced Soil Slopes - Volume 1*. FHWA-NHI-10-025. United States: Federal Highway Administration, p. 306.
- Bergado, D.T., Bukkanasuta, A. and Balasubramaniam, A.S. (1987). Laboratory pull-out tests using bamboo and polymer geogrids including a case study, *Geotextiles and Geomembranes*, 5(3): 153–189.
- Bergado, D.T. and Chai, J.-C. (1994). Pullout Force/Displacement Relationship of Extensible Grid Reinforcements, *Geotextiles and Geomembranes*, 13: 295–316.
- Cardile, G., Giofrè, D., Moraci, N., Calvarano, L.S (2017). Modelling interference between the geogrid bearing members under pullout loading conditions, *Geotextiles and Geomembranes*, 45(3): 169–177.
- Christopher, B.R., Gill, S., Giroud, J.P., Juran, I., Mitchell, J.K., Schlosser, F., Dunncliff, J. (1990) *Reinforced soil structures*. FHWA-RD-89-043. Washington, USA.: U.S. Department of Transportation Publication.
- Farrag, K. and Acar, Y.B. (1993) Pull-Out Resistance of Geogrid Reinforcements', *Geotextiles and Geomembranes*, 12: 133–159.
- Ghazavi, M. and Bavandpouri, O. (2022) Analytical solution for calculation of pull out force-deformation of geosynthetics reinforcing unsaturated soils, *Geotextiles and Geomembranes*, 50(2): 357–369.
- Gurung, N., Iwao, Y. and Madhav, M.R. (1999) Pullout test model for extensible reinforcement, *International Journal for Numerical and Analytical Methods in Geomechanics*, 23(12): 1337–1348.
- Huang, B. and Bathurst, R.J. (2009) Evaluation of Soil-Geogrid Pullout Models Using a Statistical Approach, *Geotechnical Testing Journal*, 32(6).
- Jewell, R.A., Milligan, G.W.E., Sarsby, R.W., Dubois, D. (1984) Interaction between soil and geogrids, in *Polymer Grid Reinforcement*. London: Thomas Telford Publishing: 18–30.
- Jewell, R.A. (1990) Reinforcement bond capacity, *Géotechnique*, 40(3), p. 6.
- Koerner, R.M., Wayne, M.H. and Carroll, R.G. (1989). *Analytic Behaviour of Geogrid Anchorage*, in Proceedings of Geosynthetics '89. San Diego, U.S.A.: IFAI.
- Lopes, M.J. and Lopes, M.L. (1999) Soil-Geosynthetic Interaction - Influence of Soil Particle Size and Geosynthetic Structure, *Geosynthetics International*, 6(4): 261–282.
- Madhav, M.R., Gurung, N. and Iwao, Y. (1998) A Theoretical Model for the Pull-Out Response of Geosynthetic Reinforcement, *Geosynthetics International*, 5(4): 399–424.
- Matsui, T., San, K.C., Nabeshima, Y., Amin, U.N. (1996) Bearing mechanism of steel reinforcement in pull-out test, in *Earth Reinforcement*. Rotterdam: Balkema.
- Miyata, Y. and Bathurst, R.J. (2012) Reliability analysis of soil-geogrid pullout models in Japan, *Soils and Foundations*, 52(4): 620–633.
- Moraci, N. and Gioffre, D. (2006) A simple method to evaluate the pullout resistance of extruded geogrids embedded in a compacted granular soil, *Geotextiles and Geomembranes*, 24(2): 116–128.
- Moraci, N. and Recalcatti, P. (2006) Factors affecting the pullout behaviour of extruded geogrids embedded in a compacted granular soil, *Geotextiles and Geomembranes*, 24(4): 220–242.

- Palmeira, E.M. (2004) Bearing force mobilisation in pull-out tests on geogrids, *Geotextiles and Geomembranes*, 22(6): 481–509.
- Palmeira, E.M. and Milligan, G.W.E. (1989) Scale and other factors affecting the results of pull-out tests of grids buried in sand, *Géotechnique*, 39(3): 511–524.
- Perkins, S.W. and Cuelho, E.V. (1999) Soil-Geosynthetic Interface Strength and Stiffness Relationships From Pullout Tests, *Geosynthetics International*, 6(5): 321–346.
- Sieira, A.C.C.F., Gerscovich, D.M.S. and Sayão, A.S.F.J. (2009) Displacement and load transfer mechanisms of geogrids under pullout condition, *Geotextiles and Geomembranes*, 27(4):
- Sobhi, S. and Wu, J.T.H. (1996) An Interface Pullout Formula for Extensible Sheet Reinforcement, *Geosynthetics International*, 3(5): 565–582.
- Sugimoto, M. and Alagiyawanna, A.M.N. (2003) Pullout Behavior of Geogrid by Test and Numerical Analysis, *Journal of Geotechnical and Geoenvironmental Engineering*, 129(4): 361–371.
- Sugimoto, M., Alagiyawanna, A.M.N. and Kadoguchi, K. (2001) Influence of rigid and flexible face on geogrid pullout tests, *Geotextiles and Geomembranes*, 19(5): 257–277.
- Teixeira, S.H.C., Bueno, B.S. and Zornberg, J.G. (2007) Pullout Resistance of Individual Longitudinal and Transverse Geogrid Ribs, *Journal of Geotechnical and Geoenvironmental Engineering*, 133(1): 37–50.
- Wang, Z., Jacobs, F. and Ziegler, M. (2014) Visualization of load transfer behaviour between geogrid and sand using PFC2D, *Geotextiles and Geomembranes*, 42(2): 83–90.
- Weerasekara, L. and Wijewickreme, D. (2010) An analytical method to predict the pullout response of geotextiles, *Geosynthetics International*, 17(4): 193–206.
- Ziegler, M. and Timmers, V. (2004) A new approach to design geogrid reinforcement, in *Proceedings of the 3rd European Geosynthetics Conference*.
- Zornberg, J.G., Roodi, G.H. and Gupta, R. (2017) Stiffness of Soil–Geosynthetic Composite under Small Displacements: I. Model Development, *Journal of Geotechnical and Geoenvironmental Engineering*, 143(10).



## Hydraulic Conductivity of Lighter Bentonite-Polymer Geosynthetic Clay Liners

Dong Li<sup>1</sup>, Kuo Tian, Ph.D.,<sup>2</sup> Reza Gorakhki, Ph.D.,<sup>3</sup> and Michael Donovan, Ph.D.<sup>4</sup>

<sup>1</sup>Department of Civil and Environmental Engineering, George Mason University, Fairfax, VA 22030, USA. E-mail: [dli8@gmu.edu](mailto:dli8@gmu.edu)

<sup>2</sup>Department of Civil, Environmental, and Infrastructure Engineering, George Mason University, Fairfax, VA 22030, USA. (Corresponding author). E-mail: [ktian@gmu.edu](mailto:ktian@gmu.edu)

<sup>3</sup>Minerals Technologies Inc, Arlington Heights, IL 60004, USA. E-mail: [reza.gorakhki@mineralstech.com](mailto:reza.gorakhki@mineralstech.com)

<sup>4</sup>Minerals Technologies Inc, Arlington Heights, IL 60004, USA. E-mail: [michael.donovan@mineralstech.com](mailto:michael.donovan@mineralstech.com)

### ABSTRACT

The objective of this study was to evaluate the hydraulic conductivity of lighter bentonite-polymer (B-P) geosynthetic clay liners (GCLs) permeated with single-species salt solutions. The lighter B-P GCL is produced with lower mass per unit area of sodium bentonite (Na-B) (e.g., 2.9 kg/m<sup>2</sup>) than that of regular GCL (e.g.,  $\geq 3.6$  kg/m<sup>2</sup>). Due to lower mass, the length of lighter GCL roll can be longer than that of regular GCL roll, which can reduce the transportation and installation costs. To mitigate the low mass per unit area on the chemical compatibility of regular GCL, polymer additives is mixed with Na-B. Hydraulic conductivity tests were conducted with lighter B-P GCL (polymer loading of 2.4%) to saline solutions at 20 kPa according to ASTM D6766. The saline solutions, including 50 mM NaCl, 25 mM Na<sub>2</sub>SO<sub>4</sub>, 7.5 mM MgCl<sub>2</sub>, and 7.5 mM MgSO<sub>4</sub> solutions, were selected to mimic dilute leachate from municipal solid waste landfill. The test results showed that lighter B-P GCL can maintain low hydraulic conductivity to these four single-species salt solutions (e.g.,  $1.2 \times 10^{-12}$  to  $1.1 \times 10^{-11}$  m/s). It illustrates that lighter GCL with polymer additives can maintain its chemical compatibility to dilute salt solutions.

**Keywords:** bentonite-polymer (B-P) composite, geosynthetic clay liners (GCLs), hydraulic conductivity, mass per unit area

### INTRODUCTION

Geosynthetic clay liners (GCLs) consist of a thin layer (5-10 mm) of sodium bentonite (Na-B) sandwiched between two geotextiles (Shackelford et al. 2000; Jo et al. 2001, 2005; Scalia et al. 2014; Chen et al., 2018, 2019; Rowe, 2020). The Na-B in GCLs is enriched in Na-montmorillonite (65 to 90%), which has large surface area, high cation exchange capacity, and high swelling potential (Shackelford et al. 2000; Jo et al. 2001, 2005). Osmotic swelling of montmorillonite yields a tortuous flow path for the permeant solution, consequently resulting in low hydraulic conductivity (e.g.,  $\leq 1.0 \times 10^{-10}$  m/s) (Kolstad et al., 2004; Tian et al., 2019; Li et al., 2021). Therefore, the GCLs have been widely used as hydraulic barrier in waste containment facilities such as landfills and surface impoundments (Chen et al., 2018, 2019; Tian et al., 2019; Li et al., 2021; Zainab et al., 2021; Wireko et al., 2022).

Decreasing mass of Na-B in GCLs leads to higher length of GCL roll than that of regular GCL roll, which can reduce the transportation and installation costs. However, the mass per unit area (MPUA) of Na-B GCLs may influence the hydraulic performance of Na-B GCLs (Von Maubeuge and Ehrenberg, 2014; Row et al., 2017; Salemi et al., 2018; Polat et al., 2021). Na-B GCLs preserve low hydraulic conductivity with lower MPUAs when water was used as the permeant solution. Von Maubeuge and Ehrenberg (2014) reported that the hydraulic conductivity of Na-B GCLs to water ranged from  $8.4 \times 10^{-12}$  to  $2.4 \times 10^{-11}$  m/s as the MPUA decreased from 8.0 to 3.0 kg/m<sup>2</sup>. However, MPUA had a significant effect on the hydraulic conductivity of Na-B GCLs when permeated with single-species salt solutions. For example, Polat et al. (2021) reported that the hydraulic conductivity of Na-B GCLs with MPUA of 5.0 kg/m<sup>2</sup> to 30 mM CaCl<sub>2</sub> solution was 16 times lower than that of Na-B GCLs with MPUA of 3.0 kg/m<sup>2</sup> (e.g.,  $8.3 \times 10^{-9}$  vs.  $1.3 \times 10^{-7}$  m/s).

High MPUA of GCLs may not be enough to guarantee low hydraulic conductivity when permeated with aggressive leachates. Lee et al. (2005) reported that hydraulic conductivity of Na-B GCLs with mass per unit area of 5.1 kg/m<sup>2</sup> was  $3.5 \times 10^{-9}$  m/s when permeated with 100 mM CaCl<sub>2</sub> solution. The Na-B GCLs can be modified by adding polymer additives to improve the chemical compatibility of GCLs, known as bentonite-polymer (B-P) GCLs (Scalia et al. 2014; Di Emidio et al. 2015; Chen et al. 2019; Tian et al., 2019; Li et al., 2021; Zainab et al., 2021; Wireko et al., 2022). B-P GCLs have been found to have high resistance to chemicals and lower hydraulic conductivity when permeated with aggressive leachates. Scalia et al. (2014) reported that B-P GCLs maintained low hydraulic conductivity for 5-500 mM CaCl<sub>2</sub> solutions, whereas Na-B GCLs had hydraulic conductivity at least three orders of magnitude higher (except for 5 mM CaCl<sub>2</sub> solution) when permeated with the same solutions.

The objective of this study was to evaluate the hydraulic performance of lighter bentonite-polymer (B-P) GCLs permeated with single-species salt solutions. One commercially available B-P GCL with polymer loading of 2.4% (B-P-2.4) and one sodium-bentonite (Na-B) GCL were tested in this study. The lighter B-P-2.4 GCL was produced with lower mass per unit area of sodium bentonite (Na-B) (e.g., 2.9 kg/m<sup>2</sup>) than that of regular GCL (e.g.,  $\geq 3.6$  kg/m<sup>2</sup>). Hydraulic conductivity tests were conducted in the flexible wall permeameter following the falling head method according to ASTM D6766. Tests were conducted with four single-species salt solutions, consisting of 50 mM NaCl, 25 mM Na<sub>2</sub>SO<sub>4</sub>, 7.5 mM MgCl<sub>2</sub>, and 7.5 mM MgSO<sub>4</sub> solutions to mimic dilute leachate from municipal solid waste landfill.

## MATERIALS AND METHODS

**Geosynthetic Clay Liners.** Two GCLs were used in this study, including one conventional Na-B and one B-P GCLs (e.g., B-P-2.4). The granule size distribution of the GCLs was determined by mechanical sieve analysis following ASTM D6913. All the GCLs had similar grain size distribution (medium to fine sand), as shown in Figure 1. Mass per unit area, thickness, and polymer loading of the GCLs is given in Table 1.

Polymer loading in B-P GCLs was determined following the loss on ignition (LOI) method adopted by Scalia et al. (2014). Polymer loading was determined by discounting the LOI of the conventional Na-B based on the assumption that the polymer burns completely.

The mass per unit area of GCLs was determined according to the ASTM D5993. The mass per unit area of B-P-2.4 GCL was 2.9 kg/m<sup>2</sup>, which was lower than that of Na-B GCLs used in this study (e.g., 4.0 kg/m<sup>2</sup>), and GCLs reported by previous studies (e.g., 3.6~6.8 kg/m<sup>2</sup>) (Scalia et al.,

2014; Chen et al., 2018, 2019; Tian et al., 2019; Li et al., 2021; Zainab et al., 2021; Wireko et al., 2022).

**Table 1. Mass per unit area, initial thickness and polymer loading of Na-B and B-P GCLs used in this study.**

GCL	Mass per unit area (kg/m <sup>2</sup> )	Thickness (mm)	Polymer loading (%)
Na-B	4.0	5.0	-
B-P-2.4	2.9	5.2	2.4

Note: Polymer loading is calculated based on loss on ignition as per ASTM D7348. Mass per unit area is measured as per ASTM D5993. “-” indicates not applicable. The numeric digits with B-P GCLs represent their polymer loading.

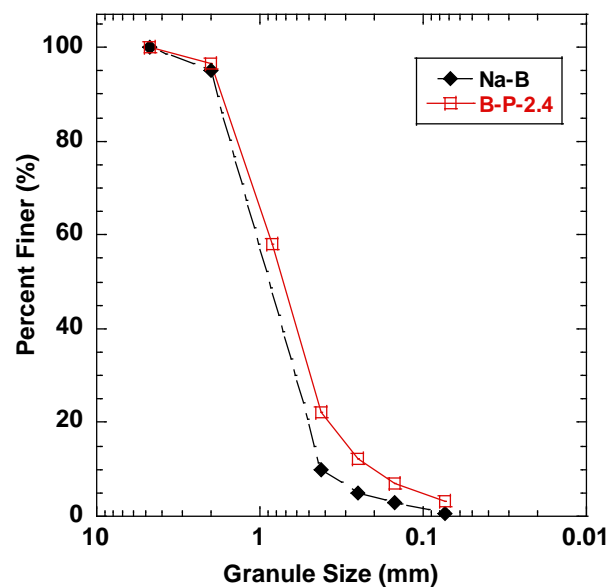


**Figure 1. Grain size distribution of Na-B and B-P GCLs used in this study.**

**Permeant Solutions.** Four single-species salt solutions, consisting of 50 mM NaCl, 25 mM Na<sub>2</sub>SO<sub>4</sub>, 7.5 mM MgCl<sub>2</sub>, and 7.5 mM MgSO<sub>4</sub> solutions were used in this study. The permeant solution was prepared by dissolving reagent-grade NaCl, Na<sub>2</sub>SO<sub>4</sub>, MgCl<sub>2</sub>, and MgSO<sub>4</sub> in Type II DI water as per ASTM D1193.

**Hydraulic Conductivity Test.** Hydraulic conductivity tests were conducted on 6-inches circular GCL specimens using flexible-wall permeameters according to ASTM D6766. All GCL specimens were first hydrated in the permeameter with the specific leachate at an effective confining stress of 20 kPa for 48 hours, and then were conducted hydraulic conductivity test. Fifty mL burettes were used to gather the influent liquid and the effluent was collected in 70 mL polyethylene bottles. The tests were continued until the hydraulic and chemical equilibrium was achieved in accordance with ASTM D6766.

Hydraulic equilibrium criteria require that three consecutive hydraulic conductivity values are within 25% of the mean and without temporal trend, and the ratio of inflow over outflow ( $Q_{out}/Q_{in}$ ) is within 0.75 and 1.25. The chemical equilibrium criteria require that the electric conductivity

(EC) of the effluent ( $EC_{out}$ ) are falling within  $1.0 \pm 10\%$  of the influent value ( $EC_{in}$ ), and the ratio of the pH of effluent ( $pH_{out}$ ) and influent ( $pH_{in}$ ) are within  $1.0 \pm 10$ .

**Swell Index Test.** Swell index of B-P-2.4 GCLs and Na-B GCL was measured using DI water and single-species salt solutions following the test method in accordance with ASTM D5890. The specimens were first crushed using a pastel and mortar such that 100% passes #100 sieve and at least 65% passes #200 sieve. The tests were conducted using 2 g of oven-dried specimens, added into a 100 mL graduated cylinder filled with 90 mL of solution (DI water and single-species salt solutions). The GCL specimen was added into the graduated cylinder with an increment of 0.1 g. After adding 2 g of specimen, the cylinder was filled to 100 mL with the solution (DI water and single-species salt solutions). The SI was measured as the volume of the swollen specimen in the graduated cylinder after 24 h (in mL/2 g).

## RESULTS AND DISCUSSION

The swell index of Na-B GCL and B-P-2.4 GCLs to DI water and single-species salt solutions are shown in Figure 2. The swell index of B-P-2.4 GCLs were higher than that of Na-B GCLs in same permanent solutions. The swell index of Na-B was 28.5 mL/2g in DI water, whereas B-P-2.4 GCL showed the swell index of 30.0 mL/2g in DI water. The swelling of bentonite and formation of polymer hydrogel were promoted when permeated with DI water (Tian et al., 2019).

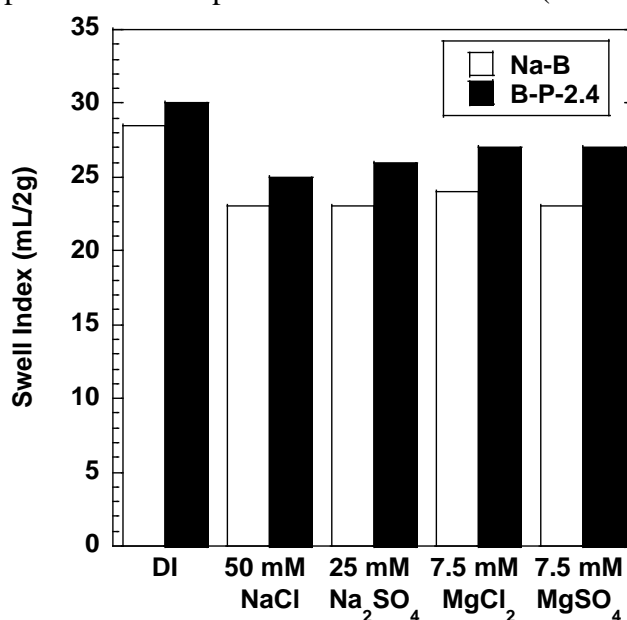


**Figure 2. Swell index of Na-B and B-P GCLs to DI water and single-species salt solutions.**

Temporal behavior of the B-P-2.4 permeated with 7.5 mM  $MgSO_4$  solution is shown in Figure 3. The hydraulic equilibrium was achieved at the PVF of 7 to 10, where the  $Q_{out}/Q_{in}$  was within  $1 \pm 25\%$  (Figure 3a). The chemical equilibrium reached around 15 PVF, i.e., both EC and pH of the effluent leveled off and fell within the  $1 \pm 10\%$  of the EC and pH in the influent (Figure 3b). Test of B-P-2.4 GCL to 7.5 mM  $MgSO_4$  solution was still ongoing to evaluate long-term hydraulic conductivity.



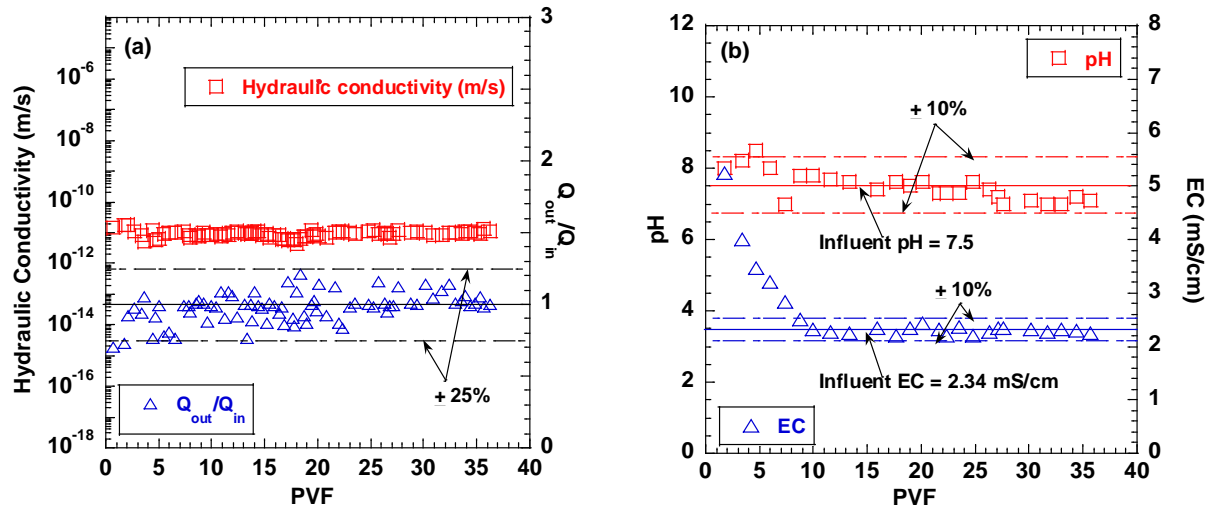


**Figure 3. Hydraulic conductivity, ratio of inflow to outflow ( $Q_{out}/Q_{in}$ ), pH, and EC from test on B-P-2.4 permeated to 7.5 mM  $MgSO_4$  solution.**

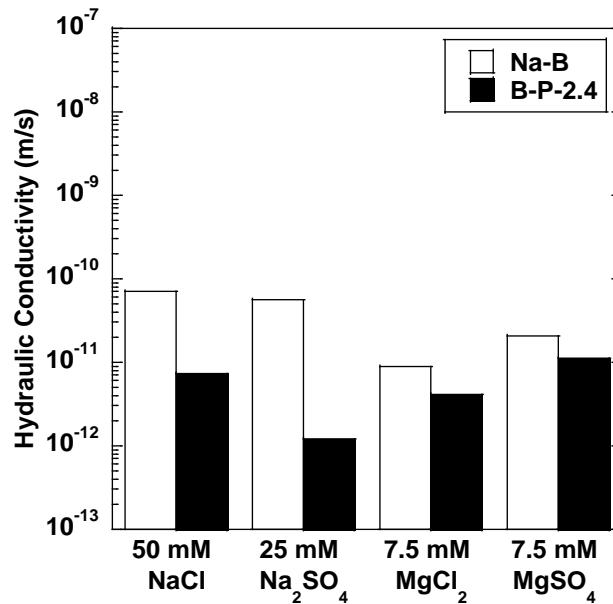


**Figure 4. Hydraulic conductivity of GCLs permeated with single-species salt solutions**

Hydraulic conductivity of Na-B and B-P-2.4 GCLs to four single-species salt solutions are shown in Figure 4. Hydraulic conductivity of Na-B GCLs ( $MPUA = 4.0 \text{ kg/m}^2$ ) to four single-species salt solutions were lower than  $10^{-10}$  m/s, ranging from  $8.9 \times 10^{-12}$  to  $7.2 \times 10^{-11}$  m/s. B-P-2.4 GCLs with lower mass per unit area showed lower hydraulic conductivity than that of Na-B GCLs when permeated with the same solution (e.g.,  $1.2 \times 10^{-12}$  to  $1.1 \times 10^{-11}$  m/s). For example, the hydraulic conductivity of B-P-2.4 GCLs ( $MPUA = 2.9 \text{ kg/m}^2$ ) was  $7.3 \times 10^{-12}$  m/s when permeated with 50 mM NaCl solution, which was one order of magnitude lower than that of Na-B GCL (e.g.,  $7.2 \times 10^{-11}$  m/s). The bentonite and polymer hydrogel function together to fill the pore space, which resulted in low hydraulic conductivity when permeated with dilute solutions

(Tian et al.,2019). It illustrates that Na-B GCL with low mass per unit area can maintain chemical compatibility to dilute salt solutions by adding polymer.

## CONCLUSION

Hydraulic conductivity of Na-B GCL (MPUA = 4.0 kg/m<sup>2</sup>) and B-P-2.4 GCL (MPUA = 2.9 kg/m<sup>2</sup>) were evaluated using 50 mM NaCl, 25 mM Na<sub>2</sub>SO<sub>4</sub>, 7.5 mM MgCl<sub>2</sub>, and 7.5 mM MgSO<sub>4</sub> solutions.

The following conclusions can be made based on the findings of the study:

1. All the Na-B (MPUA = 4.0 kg/m<sup>2</sup>) and B-P-2.4 (MPUA = 2.9 kg/m<sup>2</sup>) GCLs can maintain low hydraulic conductivity to four dilute single-species salt solutions.
2. The hydraulic conductivity of lighter B-P-2.4 GCLs (MPUA = 2.9 kg/m<sup>2</sup>) were lower than Na-B GCL (MPUA = 4.0 kg/m<sup>2</sup>) when permeated with the same solution. The chemical compatibility of Na-B GCLs with low mass per unit area can be improved by adding polymer additives.
3. The polymer modification of bentonite can possibly mitigate the low mass per unit area on the chemical compatibility of regular GCL, which can reduce manufacturing, transportation, and installation costs.

## ACKNOWLEDGEMENT

This material is based upon work supported by Minerals Technologies Inc. Any opinions, findings and conclusions in this material are those of the authors and do not necessarily reflect the views of Minerals Technologies Inc.

## REFERENCE

- ASTM D 1193. Standard Specification for Reagent Water, *ASTM International*, West Conshohocken, Pennsylvania, USA.
- ASTM D 5890. Standard test method for swell index of clay mineral component of geosynthetic clay liners, *ASTM International*, West Conshohocken, Pennsylvania, USA.
- ASTM D 5993. Standard Test Method for Measuring Mass per Unit of Geosynthetic Clay Liners, *ASTM International*, West Conshohocken, Pennsylvania, USA.
- ASTM D 6766. Standard Test Method for Evaluation of Hydraulic Properties of Geosynthetic Clay Liners Permeated with Potentially Incompatible Aqueous Solutions, *ASTM International*, West Conshohocken, Pennsylvania, USA.
- ASTM D 6913. Standard Test Methods for Particle-Size Distribution (Gradation) of Soils Using Sieve Analysis, *ASTM International*, West Conshohocken, Pennsylvania, USA.
- ASTM D 7348. Standard Test Methods for Loss on Ignition (LOI) of Solid Combustion Residues, *ASTM International*, West Conshohocken, Pennsylvania, USA.
- Chen, J. N., Benson, C. H. and Edil, T. B. (2018). Hydraulic conductivity of geosynthetic clay liners with sodium bentonite to coal combustion product leachates, *Journal of Geotechnical and Geoenvironmental Engineering*, (3): 04018008.
- Chen, J. N., Salihoglu, H., Benson, C., Likos, W. and Edil, T. (2019). Hydraulic Conductivity of Bentonite-Polymer Composite Geosynthetic Clay Liners Permeated with Coal Combustion Product Leachates, *Journal of Geotechnical and Geoenvironmental Engineering*, 145 (9): 04019038.

- Di Emidio, G., Mazziere, F., Verastegui-Flores, R. D., Van Impe, W. and Bezuijen, A. (2015). Polymer-treated bentonite clay for chemical-resistant geosynthetic clay liners. *Geosynthetics International*, 22(1): 125-137.
- Jo, H. Y., Katsumi, T., Benson, C. H. and Edil, T. B. (2001). Hydraulic conductivity and swelling of nonprehydrated GCLs permeated with single-species salt solutions, *Journal of Geotechnical and Geoenvironmental Engineering*, 127(7): 557-567.
- Jo, H. Y., Benson, C. H., Shackelford, C. D., Lee, J. M. and Edil, T. B. (2005). Long-term hydraulic conductivity of a geosynthetic clay liner permeated with inorganic salt solutions, *Journal of Geotechnical and Geoenvironmental Engineering*, 131(4): 405-417.
- Kolstad, D.C., Benson, C.H. and Edil, T.B. (2004). Hydraulic conductivity and swell of nonprehydrated geosynthetic clay liners permeated with multispecies inorganic solutions, *Journal of Geotechnical and Geoenvironmental Engineering*, 130(12): 1236-1249.
- Lee, J.M., Shackelford, C.D., Benson, C.H., Jo, H.Y. and Edil, T.B. (2005). Correlating index properties and hydraulic conductivity of geosynthetic clay liners. *Journal of Geotechnical and Geoenvironmental Engineering*, 131 (11): 1319-1329.
- Li, D., Zainab, B. and Tian, K. (2021). Effect of effective stress on hydraulic conductivity of bentonite-polymer geosynthetic clay liners to coal combustion product leachates, *Environmental Geotechnics*, [Doi.org/10.1680/jenge.21.00077](https://doi.org/10.1680/jenge.21.00077).
- Polat, F., Kul, T.Ö. and Ören, A.H. (2021). Influence of Mass Per Unit Area on the Hydraulic Conductivity of Geosynthetic Clay Liners (GCLs), *Avrupa Bilim ve Teknoloji Dergisi*, (28): 1269-1273.
- Rowe, R.K., Brachman, R.W., Hosney, M.S., Take, W.A. and Arnepalli, D.N. (2017). Insight into hydraulic conductivity testing of geosynthetic clay liners (GCLs) exhumed after 5 and 7 years in a cover, *Canadian Geotechnical Journal*, 54(8): 1118-1138.
- Rowe, R. K (2020). Geosynthetic clay liners: Perceptions and misconception, *Geotextiles and Geomembranes*, 48(2): 137-156.
- Salemi, N., Abtahi, S.M., Rowshanzamir, M. and Hejazi, S.M. (2018). Geosynthetic clay liners: effect of structural properties and additives on hydraulic performance and durability, *Environmental earth sciences*, 77(5): 1-13.
- Scalia IV, J., Benson, C. H., Bohnhoff, G. L., Edil, T. B. and Shackelford, C. D. (2014). Long-term hydraulic conductivity of a bentonite-polymer composite permeated with aggressive inorganic solutions, *Journal of Geotechnical and Geoenvironmental Engineering*, 140(3): 04013025.
- Shackelford, C. D., Benson, C. H., Katsumi, T., Edil, T. B. and Lin, L. (2000). Evaluating the hydraulic conductivity of GCLs permeated with non-standard liquids, *Geotextiles and Geomembranes*, 18(2): 133-161.
- Tian, K., Likos, W. J. and Benson, C. H. (2019). Polymer Elution and Hydraulic Conductivity of Bentonite-Polymer Composite Geosynthetic Clay Liners, *Journal of Geotechnical and Geoenvironmental Engineering*, 145(10): 04019071.
- Von Maubeuge, K.P. and Ehrenberg, H. (2014) Investigation of bentonite mass per unit area requirements for Geosynthetic Clay Liners, *In Proceedings of the 10th International Conference on Geosynthetics*, Berlin, Germany: 21-25.
- Wireko, C., Abichou, T., Tian, K., Zainab, B. and Zhang, Z. (2022). Effect of incineration ash leachates on the hydraulic conductivity of bentonite-polymer composite geosynthetic clay liners, *Waste Management*, 139: 25-38.

Zainab, B., Wireko, C., Dong, L., Tian, K. and Tarek., K. (2021). Hydraulic conductivity of bentonite-polymer geosynthetic clay liners to coal combustion product leachates, *Geotextiles and Geomembranes*, 49(5): 1129-1138.



## Long-term Hydraulic Conductivity of Bentonite-Polymer Geosynthetic Clay Liner to Coal Combustion Product Leachates

Hanrui Zhao,<sup>1</sup> Dong Li,<sup>2</sup> and Kuo Tian, Ph.D.<sup>3</sup>

<sup>1</sup>Dept. of Civil, Environmental, and Infrastructure Engineering, George Mason Univ., Fairfax, VA. Email: hzhao25@gmu.edu

<sup>2</sup>Dept. of Civil, Environmental, and Infrastructure Engineering, George Mason Univ., Fairfax, VA. Email: dli8@gmu.edu

<sup>3</sup>Dept. of Civil, Environmental, and Infrastructure Engineering, George Mason Univ., Fairfax, VA. Email: ktian@gmu.edu

### ABSTRACT

Hydraulic conductivity tests were conducted with one conventional geosynthetic clay liner (Na-B GCL) and four bentonite-polymer GCLs (B-P GCLs) to synthetic coal combustion product (CCP) leachate. B-P composite in GCL is created by dry-mixing bentonite and polymer. Two B-P GCLs consist of linear polymer whereas the other two have crosslinked polymer. The synthetic leachate was created by taking the geometric mean of leachate data collected from more than 130 CCP disposal facilities and impoundment ponds. The ionic strength of CCP leachate is 50 mM, and the relative abundance of monovalent and divalent cations (RMD) is  $0.1 \text{ M}^{1/2}$ . Hydraulic conductivity tests were conducted at 20 kPa according to ASTM D6766 and lasted 724 to 1321 days to evaluate long-term performance of B-P GCLs. Hydraulic conductivity of B-P GCLs ( $3.3 \times 10^{-11} \text{ m/s}$  to  $5.4 \times 10^{-12} \text{ m/s}$ ) was approximately 2-3 orders of magnitude lower than that of Na-B ( $4.9 \times 10^{-9} \text{ m/s}$ ) based on hydraulic and chemical equilibriums in accordance with ASTM D6766. The tests were continued to investigate long-term performance of B-P GCLs. The results illustrated that hydraulic conductivity of B-P GCLs showed an increasing trend after achieving chemical equilibrium, indicating polymer elution may affect long-term performance of B-P GCLs.

**Keywords:** Bentonite-polymer (B-P), Geosynthetic clay liners (GCLs), Hydraulic conductivity, Polymer elution, Long-term performance

### INTRODUCTION

Geosynthetic clay liners (Na-B GCL), consisting of a layer of sodium bentonite (Na-B) sandwiched by two layers of geotextiles, have been widely used in waste containment applications due to ease of installation and low hydraulic conductivity ( $K < 1 \times 10^{-10} \text{ m/s}$ ) (Rubl and Daniel, 1997; Shackelford et al., 2000; Kolstad et al., 2004a; Setz et al., 2017; Tian and Benson, 2017). The swelling of sodium bentonite within a GCL can reduce the intergranular pore size and narrow the flow path, resulting in a low hydraulic conductivity of GCL (Shackelford et al., 2000; Lee & Shackelford, 2005; Norris et al., 2021). However, aggressive leachate, e.g. coal combustion products (CCP) leachate, has a high ionic strength (e.g.,  $4685 \text{ mM} > I > 0.42 \text{ mM}$ ) and polyvalent cations (e.g.  $\text{Ca}^{2+}$ ,  $\text{Mg}^{2+}$ ), which suppresses swelling capability of Na-B, and leads to high hydraulic conductivity ( $K > 1.0 \times 10^{-10} \text{ m/s}$ ) (Ho et al., 2005; Benson et al., 2010; Chen et al.,

2018; 2019; Zainab et al., 2021). As a result, the hydraulic barrier performance of Na-B GCL cannot meet the requirements established by USEPA [80 Fed. Reg. 21301(October 14, 2015)].

Bentonite modified with polymer is used in GCL, denoted as bentonite-polymer GCL (B-P GCLs), to improve the chemical compatibility of GCL and mitigate the impact of aggressive leachate on the hydraulic conductivity of B-P GCLs (Tian et al., 2016; 2019; Tian and Benson, 2017; 2019; Chen et al., 2019; Zainab et al., 2021; Wireko et al., 2022). The hydraulic conductivity of the B-P GCL (with higher polymer loading  $>1.9$ ) can maintain a low hydraulic conductivity ( $K < 1 \times 10^{-10}$  m/s) when exposed to CCP leachate, which is 1 to 2 orders of magnitude lower than that of Na-B GCL (Chen et al., 2018; 2019). However, polymer elution from B-P GCLs has been observed during the GCL leachate permeation process (Scalia et al., 2014; Tian et al., 2016; 2019; Chen et al., 2019; Tian and Benson, 2019; Zainab et al., 2021; Wireko et al., 2022; Norris et al., 2022). Elution of polymer from the B-P GCL opens pores, leading to a large flow path during the permeation process, which results in higher hydraulic conductivities of B-P GCL (Chen et al., 2019; Tian et al., 2019). The hydraulic conductivities of GCLs to leachates is evaluated according to ASTM D6766 (ASTM 2020a), which defines the test termination by hydraulic and chemical equilibrium. The criteria commonly represent the long-term hydraulic conductivity of Na-B GCL, however, polymer elution from B-P GCLs is not listed as a criterion in ASTM D6766 (Scalia et al., 2014; Norris et al. 2022). These observations raise concerns over the long-term performance of B-P GCL to leachates as the application of BP GCLs is assumed to last for several decades as a landfill liner system (Chen et al., 2019; Norris et al., 2022), for example, CCP landfills of at least 60 years of operation and post-closure maintenance based on USEPA regulation [80 Fed. Reg. 21301(October 14, 2015)].

Testing to measure the hydraulic conductivity of B-P GCLs (up to 4 yrs) was performed to determine the effect of long-term polymer elution on hydraulic performance of B-P GCLs. One synthetic leachates were used that are chemically representative of CCP leachates. Four B-P GCLs with polymer loading ranging from 0.5 to 5.5% were used in this study, and one Na-B GCL was tested as a control.

## **MATERIALS AND METHOD**

### **Geosynthetic clay liners**

Five commercial GCLs were used in this study, including one conventional Na-B GCL and four B-P GCLs with different polymer loading and polymer type. The polymer loading in B-P GCL ranges from 0.5 to 5.5%. The GCLs were denoted as B-LP-0.5, B-LP-1.5, B-CP-3.4, B-CP-5.5. The LP represents liner polymer, and the CP means crosslinked polymer. The numeric digits in the GCL designation indicate the polymer loading of the GCLs in percent. Loss on ignition (LOI) was used to quantify polymer loading of BP GCLs based on ASTM D7348 (ASTM 2021).

### **Permeant solutions**

The synthetic leachate recipe was determined based on an analysis of leachate data collected from 130 CCP disposal unit located in the United State (Zainab et al., 2021; Li et al., 2022). One synthetic solution was created and used in this study: Low RMD (LRMD) leachate ( $I = 96$  mM,  $RMD = 0.005 \text{ M}^{1/2}$ ,  $R = 0.55$ ). Low RMD leachates were prepared with reagent-grade NaCl,  $\text{MgSO}_4$ , and  $\text{MgCl}_2 \cdot 6\text{H}_2\text{O}$  in Type II DI water. The Low RMD (LRMD) leachate was

created by taking the geometric mean of all the leachates collected from Flue Gas Desulfurization (FGD) gypsum disposal facilities, which represents the leachate with a high concentration of divalent cations.

### Hydraulic conductivity test

Hydraulic conductivity tests on GCLs to CCP leachate were conducted in a flexible wall permeameter using falling headwater and constant tailwater methods according to ASTM D6766 (ASTM 2020a). GCL samples were cut from commercially manufactured rolls with a diameter of 152 mm. Tests were conducted with falling head and constant tailwater method at an average hydraulic gradient of approximately 150 at 20 kPa confining stress. Termination criteria was followed ASTM 6766 requirements, in which the ratio of inflow to outflow volume must be within 0.75 and 1.25 for the last three consecutive flow measurements and chemical equilibrium requires the ratios of effluent-to-influent EC and pH fall within  $1 \pm 0.1$ . All tests were continued to observe the long-term performance of B-P GCLs when chemical equilibrium was achieved. Additionally, to evaluate the long-term cation exchange behavior of GCLs, major cation concentrations ( $\text{Na}^+$ ,  $\text{K}^+$ ,  $\text{Mg}^{2+}$ ) were tested by inductively coupled plasma optical emission spectrometry (ICP-OES) periodically following USEPA Method 6010B.

### Total Organic Carbon

Effluent from each of the B-P GCLs was analyzed periodically for total organic carbon (TOC) analysis to quantify the concentration of polymer eluted. Tests were conducted using a Shimadzu TOC-L analyzer and performed according to ASTM D4839 (ASTM 2017). A calibration solution was made in glucose. The first 20 PVF samples were diluted 25-fold to keep the carbon content within the range of standard calibration solutions.  $\text{CO}_2$  was generated from carbon by combusting the sample and was detected and analyzed in a nondispersive infrared (NDIR) gas analyzer. Then, the polymer concentration (mg/L) in the effluent was recorded.

## RESULTS AND DISCUSSION

The hydraulic conductivity when chemical equilibrium was achieved based on ASTM D6766 ( $K_{6766}$ ),  $\text{Mg}^{2+}_{\text{out}} / \text{Mg}^{2+}_{\text{in}}$  equilibrium ( $K_{\text{Mg}}$ ),  $\text{Na}^{+}_{\text{out}} / \text{Na}^{+}_{\text{in}}$  equilibrium ( $K_{\text{Na}}$ ), long-term hydraulic conductivity ( $K_L$ ), and the ratio  $K_{6766} / K_L$  of BP GCL are defined and summarized in Table 1.

### Temporary Hydraulic Performance

The temporal behavior of the B-CP-3.4 GCL permeated with LMRD leachate is shown in Figure 1. The chemical equilibrium and hydraulic equilibrium termination criteria per ASTM D6766 were achieved at approximately 18 PVF, with a hydraulic conductivity of  $7.0 \times 10^{-12}$  m/s. The hydraulic conductivity increased gradually during a long-term permeation process (247 PVF). To further research the effect of slow rate cation exchange on long-term hydraulic conductivity of Na-B GCL by ICP tests proposed by Ho et al., (2005). Based on ICP results, at approximately 59 PVF,  $\text{Mg}^{2+}_{\text{out}} / \text{Mg}^{2+}_{\text{in}}$  was within  $1 \pm 0.1$ , but  $\text{Na}^{+}_{\text{out}}$  was approximately one order higher than that

of  $\text{Na}^+_{\text{in}}$ . Additionally, the hydraulic conductivity of B-CP-3.4 GCL is  $6.5 \times 10^{-11}$  m/s. The  $\text{Na}^+_{\text{out}}/\text{Na}^+_{\text{in}}$  was within  $1 \pm 0.1$  of each other until 124 PVF, with a hydraulic conductivity of  $8.4 \times 10^{-11}$

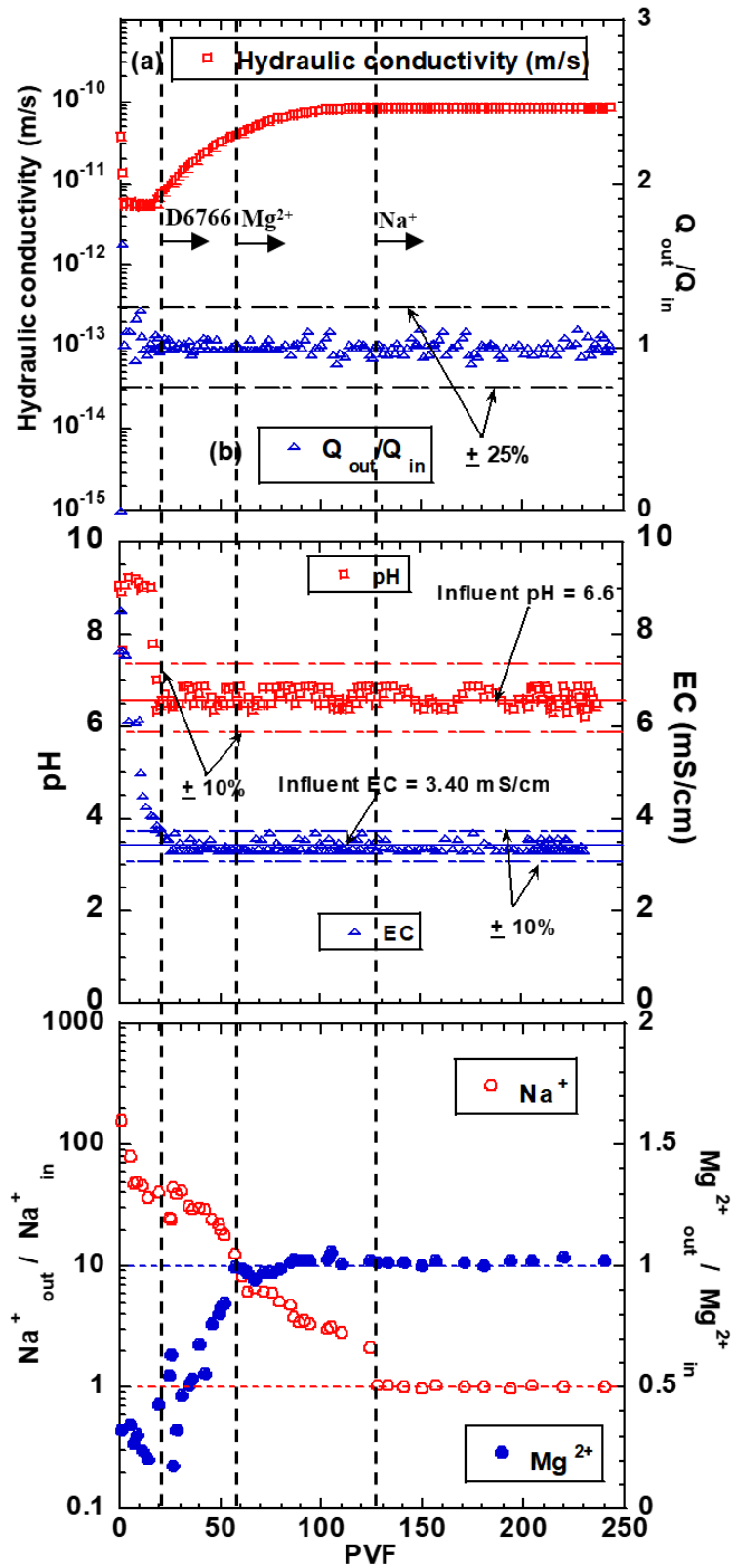




**Figure 1 Hydraulic conductivity, ratio of outflow to inflow ( $Q_{out}/Q_{in}$ ), pH, EC,  $Mg^{2+}_{out}/Mg^{2+}_{in}$ ,  $Na^{+}_{out}/Na^{+}_{in}$  from B-CP-3.4 permeated with LMRD**  
m/s. The test was continued until 247 PVF, and the hydraulic conductivity remained at  $8.4 \times 10^{-11}$  m/s. However, a different result was observed for B-LP-0.5 and B-LP-1.5 GCL permeated with LMRD. For example, the hydraulic conductivity of B-LP-1.5 to LMRD still increased from  $7.2 \times 10^{-11}$  m/s ( $Na^{+}_{out}/Na^{+}_{in} = 1.0 \pm 0.1$ ) to  $8.6 \times 10^{-11}$  m/s, indicating the effect of long-term polymer elution on hydraulic conductivity of B-LP GCLs.

## Hydraulic Conductivity

The hydraulic conductivities of GCLs were summarized in Table 1. The hydraulic conductivity ( $K_{6766}$ ) of the Na-B GCL was  $4.9 \times 10^{-9}$  m/s to LMRD leachates, whereas B-P GCLs maintained low hydraulic conductivities ( $K_{6766} < 1.0 \times 10^{-10}$  m/s) under the same permeation condition. In addition, the hydraulic conductivities of BP GCL increased after chemical equilibrium termination per ASTM D6766 was achieved ( $14.7 > K_L/K_{6766} > 3.3$ ), for example, hydraulic conductivity of B-LP-1.5 to LMRD was  $2.6 \times 10^{-11}$  m/s when chemical equilibrium was achieved and increase to  $8.6 \times 10^{-11}$  m/s for a long-term permeation process.

**Table 1 Hydraulic conductivity of B-P GCLs and Na-B GCL to LMRD leachate**

GCL	Permeation liquid	ASTM 6766		$Mg^{2+}_{out}/Mg^{2+}_{in}$		$Na^{+}_{out}/Na^{+}_{in}$		Long term		$K_L/K_{6766}$
		PVF	$K_{6766}$	PVF	$K_{Mg}$	PVF	$K_{Na}$	PVF	$K_L$	
Na-B	DI	-	-	-	-	-	-	12.8	$2.2 \times 10^{-11}$	-
Na-B	LRMD	7.3	$4.9 \times 10^{-9}$	-	-	-	-	7.3	$4.9 \times 10^{-9}$	-
LP-0.5	DI	-	-	-	-	-	-	5.6	$2.2 \times 10^{-11}$	-
LP-0.5	LRMD	18	$3.3 \times 10^{-11}$	60	$4.4 \times 10^{-11}$	96	$5.2 \times 10^{-11}$	399.4	$1.4 \times 10^{-10}$	4.2
LP-1.5	DI	-	-	-	-	-	-	10.8	$7.8 \times 10^{-12}$	-
LP-1.5	LRMD	20	$2.6 \times 10^{-11}$	40	$3.8 \times 10^{-11}$	96	$7.2 \times 10^{-11}$	147.5	$8.6 \times 10^{-11}$	3.3
CP-3.4	DI	-	-	-	-	-	-	6.5	$5.1 \times 10^{-12}$	-
CP-3.4	LRMD	19	$5.7 \times 10^{-12}$	59	$6.5 \times 10^{-11}$	124	$8.4 \times 10^{-11}$	261.6	$8.4 \times 10^{-11}$	14.7
CP-5.5	DI	-	-	-	-	-	-	15.8	$9.4 \times 10^{-12}$	-
CP-5.5	LRMD	17	$5.4 \times 10^{-12}$	74	$3.1 \times 10^{-11}$	-	-	103.5	$3.7 \times 10^{-11}$	6.9

The  $K_{6766}$ ,  $K_{Mg}$ ,  $K_{Na}$ ,  $K_L$  of B-P GCL to LMRD versus polymer loading are shown in Figure 2. The hydraulic conductivity ( $K_{6766}$ ) of BP GCL decreased as polymer loading increased per ASTM D6766, which was consistent with the observation that polymer clogging behavior controls the hydraulic performance of B-P GCL as proposed by Chen et al., (2019) and Tian et al. (2019). All hydraulic conductivities of B-P GCLs increased after chemical equilibrium was achieved. However, a different increase trend was observed for the LP and CP GCLs during the slow ionic exchange process. For example, the hydraulic conductivity of B-LP-0.5 to LMRD increased from  $3.3 \times 10^{-11}$  m/s ( $K_{6766}$ ) at chemical equilibrium to  $5.2 \times 10^{-11}$  m/s ( $K_{Na}$ ) at cation exchange completion and still increased to  $1.4 \times 10^{-10}$  m/s ( $K_L$ ) for a long term test, whereas the hydraulic conductivity of B-CP-3.4 to LMRD increased from  $5.7 \times 10^{-12}$  m/s ( $K_{6766}$ ) at chemical equilibrium to  $8.4 \times 10^{-11}$  m/s ( $K_{Na}$ ) at cation exchange completion, but maintained at  $8.4 \times 10^{-11}$  m/s ( $K_L$ ) for a long term test. The results indicate that the effect of polymer elution should be considered, and

polymer conformation is another factor controlling the long-term hydraulic performance of B-P GCLs.

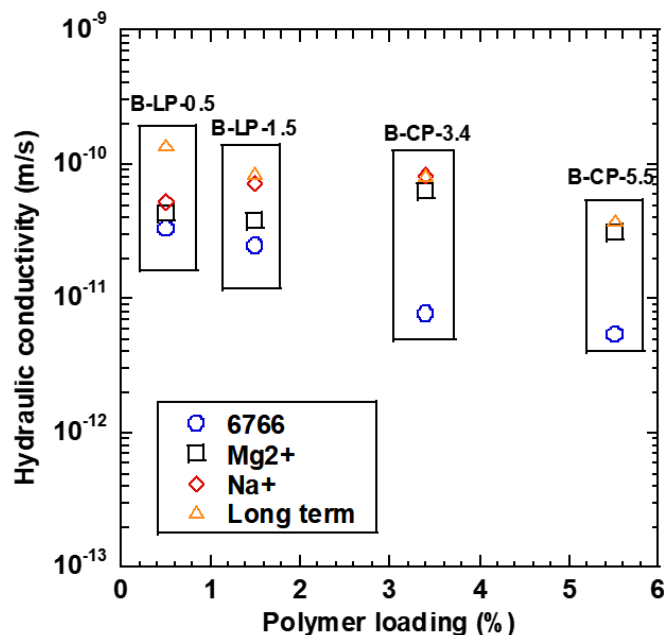


Figure 2 Hydraulic conductivity of B-P GCLs to LMRD leachate

### Polymer elution

Temporary polymer elution versus PVF of B-CP-3.4 to LMRD leachate is shown in Figure 3. Generally, the greatest polymer elution happened at the first few PVF and decreased as PVF increased, meanwhile, polymer elution still occurred during the long-term permeation. For example, approximately 550 mg/L TOC was measured at the first PVF and gradually decreased to 18 mg/L when chemical equilibrium was achieved (18 PVF), then 10 mg/L TOC was observed when cation exchange was completed (82 PVF). In addition, approximately 10 mg/L TOC still eluted from the GCL for a long-term test. The result indicates that polymer elution of B-P GCL might occur during the service life in a liner system.

Accumulate polymer elution versus hydraulic conductivity of B-LP-0.5 and B-LP-3.4 GCL to LMRD leachate is shown in Figure 4. Generally, polymer elution happened during permeation process. The effect of long-term polymer elution on hydraulic conductivity of BP with linear polymer and crosslink polymer was different after the ionic exchange was completed. For example, the hydraulic conductivity of B-LP-0.5 increased from  $5.2 \times 10^{-11}$  m/s( $K_{Na}$ ) to  $1.4 \times 10^{-11}$  m/s( $K_L$ ) as continuously polymer elution behavior. Comparatively, the hydraulic conductivity of B-CP-3.4 maintained in hydraulic conductivity of  $8.4 \times 10^{-11}$  m/s ( $K_{Na} = K_L$ ). The results indicated polymer type and polymer loading influence long-term hydraulic performance of BP GCLs should be considered.

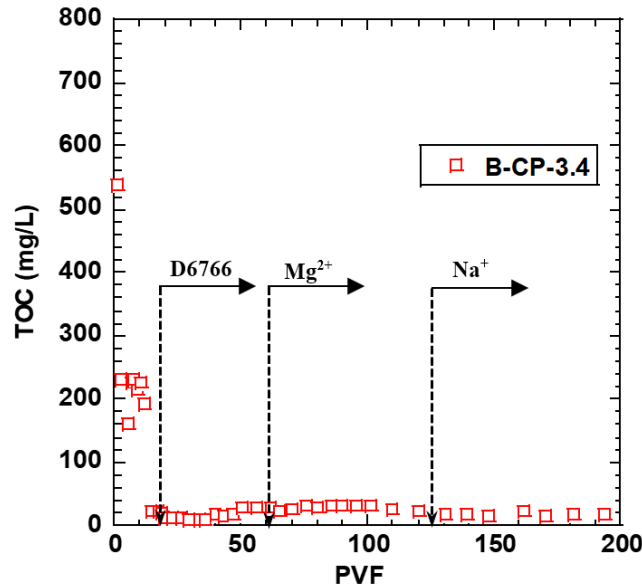


Figure 3 Temporary polymer elution versus PVF of B-CP-3.4 to LMRD leachate

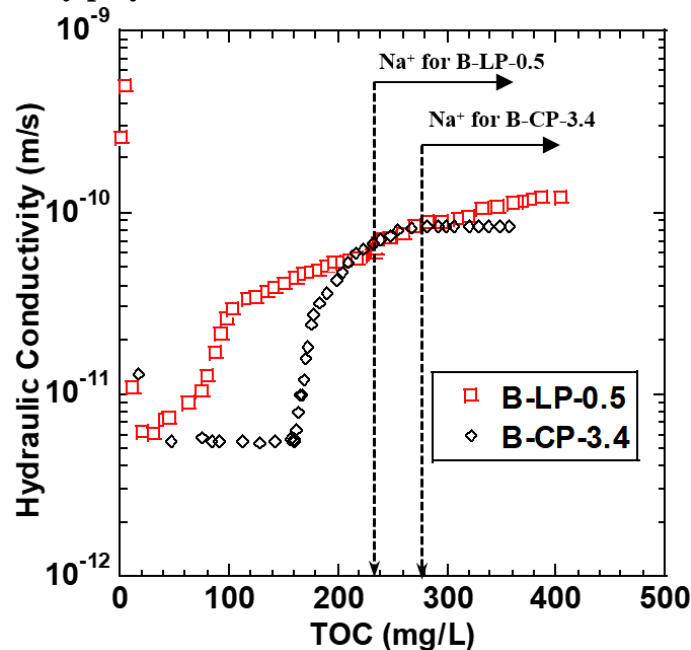


Figure 4 Accumulate polymer elution versus hydraulic conductivity of B-P GCL to LMRD leachate

## CONCLUSION

Long-term of hydraulic conductivity tests of B-P GCLs were conducted permeating with CCP leachate, and the effect of long-term polymer elution on the hydraulic performance of B-P GCL was investigated. The following conclusions can be made based on the findings of the study:

1. The hydraulic conductivity ( $K_{6766}$ ) of Na-B GCL was  $4.9 \times 10^{-9}$  m/s to LMRD leachate per ASTM D6766. However, B-P GCLs can maintain low hydraulic conductivity ( $3.3 \times 10^{-11}$  m/s to  $5.4 \times 10^{-12}$  m/s) under 20 kPa at hydraulic gradient of approximately 150

- per ASTM D6766. The hydraulic conductivity ( $K_{6766}$ ) of B-P GCLs decreased as polymer loading increased.
2. All BP GCL showed an increasing trend after chemical equilibrium was achieved. However, ICP testing was conducted to evaluate the effect of slow cation after chemical equilibrium was achieved. The hydraulic conductivities of B-LP-0.5 and B-LP-1.5 to LMRD increased as cation exchange was completed after a long-term process whereas B-LP-3.4 to LMRD maintained a constant hydraulic conductivity after cation exchange was completed.
  3. Polymer elution occurred during the whole permeation process of all B-P GCLs. LP GCLs and CP GCLs with different polymer loading showed a different increase trend of hydraulic conductivity as accumulated polymer elution occurred, indicating polymer loading and polymer conformation should be considered to evaluate the long-term hydraulic conductivity of B-P GCLs.

## REFERENCES

- [1]. ASTM D 6766. Standard Test Method for Evaluation of Hydraulic Properties of Geosynthetic Clay Liners Permeated with Potentially Incompatible Aqueous Solutions, *ASTM International*, West Conshohocken, Pennsylvania, USA.
- [2]. ASTM D 7348. Standard Test Methods for Loss on Ignition (LOI) of Solid Combustion Residues, *ASTM International*, West Conshohocken, Pennsylvania, USA.
- [3]. Chen, J. N., Benson, C. H., and Edil, T. B. (2018). Hydraulic Conductivity of Geosynthetic Clay Liners with Sodium Bentonite to Coal Combustion Product Leachates. *Journal of Geotechnical and Geoenvironmental Engineering*, 144(3), 04018008.
- [4]. Chen, J. N., Salihoglu, H., Benson, C. H., Likos, W. J. and Edil, T. B. (2019). Hydraulic Conductivity of Bentonite–Polymer Composite Geosynthetic Clay Liners Permeated with Coal Combustion Product Leachates. *Journal of Geotechnical and Geoenvironmental Engineering*, 145(9), 04019038.
- [5]. Jo, H. Y., Benson, C. H., Shackelford, C. D., Lee, J. M. and Edil, T. B. (2005). Long-term hydraulic conductivity of a geosynthetic clay liner permeated with inorganic salt solutions. *Journal of Geotechnical and Geoenvironmental Engineering*, 131(4), 405-417.
- [6]. Kolstad, D. C., Benson, C. H. and Edil, T. B. (2004). Hydraulic Conductivity and Swell of Nonprehydrated Geosynthetic Clay Liners Permeated with Multispecies Inorganic Solutions. *Journal of Geotechnical and Geoenvironmental Engineering*, 130(12), 1236–1249.
- [7]. Lee, J. M. and Shackelford, C. D. (2005). Impact of Bentonite Quality on Hydraulic Conductivity of Geosynthetic Clay Liners. *Journal of Geotechnical and Geoenvironmental Engineering*, 131(1), 64–77.
- [8]. Li, D., and Tian K. (2022). Effects of Prehydration on Hydraulic Conductivity of Bentonite-Polymer Geosynthetic Clay Liner to Coal Combustion Product Leachate. *Geo-Congress*, Charlotte, North Carolina, USA, 568-577.
- [9]. Norris, A., Aghazamani, N., Scalia, J. and Shackelford, C. D. (2022). Hydraulic Performance of Geosynthetic Clay Liners Comprising Anionic Polymer–Enhanced Bentonites. *Journal of Geotechnical and Geoenvironmental Engineering*, 148(6), 04022039.



- [10]. Norris, Anna (2021). Mechanisms of Interaction Between Bentonite and Anionic Polymers in Enhanced Geosynthetic Clay Liners. Diss. *Colorado State University*.
- [11]. Scalia, J., Benson, C. H., Bohnhoff, G. L., Edil, T. B. and Shackelford, C. D. (2014). Long-Term Hydraulic Conductivity of a Bentonite-Polymer Composite Permeated with Aggressive Inorganic Solutions. *Journal of Geotechnical and Geoenvironmental Engineering*, 140(3), 04013025.
- [12]. Setz, M. C., Tian, K., Benson, C. H. and Bradshaw, S. L. (2017). Effect of ammonium on the hydraulic conductivity of geosynthetic clay liners. *Geotextiles and Geomembranes*, 45(6), 665–673.
- [13]. Shackelford, C. D., Benson, C. H., Katsumi, T., Edil, T. B. and Lin, L. (2000a). Evaluating the hydraulic conductivity of GCLs permeated with non-standard liquids. *Geotextiles and Geomembranes*, 18(2-4), 133-161.
- [14]. Tian, K., Asce, A. M., Benson, C. H., Asce, F., Likos, W. J. and Asce, M. (2016). Hydraulic Conductivity of Geosynthetic Clay Liners to Low-Level Radioactive Waste Leachate. *Journal of Geotechnical and Geoenvironmental Engineering*, 142(8), 04016037.
- [15]. Tian, K. and Benson, C. H. (2017). Chemical Compatibility of Geosynthetic Clay Liners to Aggressive Bauxite Liquor. *Proceedings of 35th International ICSOBA Conference*, Hamburg, Germany, 281-288.
- [16]. Tian, K. and Benson, C. H. (2018). Containing bauxite liquor using bentonite-polymer composite geosynthetic clay liners. *The International Congress on Environmental Geotechnics*. Springer, Singapore, 672-678.
- [17]. Tian, K., Likos, W. J. and Benson, C. H. (2019). Polymer Elution and Hydraulic Conductivity of Bentonite–Polymer Composite Geosynthetic Clay Liners. *Journal of Geotechnical and Geoenvironmental Engineering*, 145(10), 04019071.
- [18]. Wireko, C., Abichou, T., Tian, K., Zainab, B. and Zhang, Z. (2022). Effect of incineration ash leachates on the hydraulic conductivity of bentonite-polymer composite geosynthetic clay liners. *Waste Management*, 139, 25-38.
- [19]. Zainab, B., Wireko, C., Li, D., Tian, K. and Abichou, T. (2021). Hydraulic conductivity of bentonite-polymer geosynthetic clay liners to coal combustion product leachates. *Geotextiles and Geomembranes*, 49(5), 1129-1138.

## Quantification of suction-driven flow of enhanced lateral drainage geotextiles

<sup>1</sup>Gino Sicha, M.S.,<sup>2</sup> Kangwei Chen, M.S.,<sup>3</sup> and  
Jorge Zornberg, P.h.D., P.E.<sup>3</sup>

<sup>1</sup>The University of Texas at Austin; e-mail: [gino.sicha@utexas.edu](mailto:gino.sicha@utexas.edu)

<sup>2</sup>Tongji University; e-mail: [kwchen@tongji.edu.cn](mailto:kwchen@tongji.edu.cn)

<sup>3</sup>The University of Texas at Austin; e-mail: [zornberg@mail.utexas.edu](mailto:zornberg@mail.utexas.edu)

### ABSTRACT

Advances in geosynthetics have led to the development of geotextiles with enhanced drainage capabilities to allow suction-driven in-plane drainage of geotechnical and transportation systems. Specifically, fibers that incorporate grooves in their cross-section, referred to as “wicking fibers”, have been developed to trigger enhanced drainage mechanisms. This paper presents the results of a theoretical and experimental evaluation of the in-plane flow of geotextiles with enhanced drainage capabilities conducted in isolation to assess the variables governing the flow magnitude. An analytical solution based on Lucas-Washburn’s law was derived to predict flow in geotextile with enhanced drainage capabilities specimens. Additionally, horizontal drainage tests were conducted to assess the in-plane drainage behavior of geotextiles while avoiding moisture losses due to evaporation. These tests involved geotextiles positioned horizontally along a leveled surface, with one end of the geotextile submerged in a water reservoir and the other end allowed to drain freely. The flow rate was determined by measuring the wetted length over time. The flow model developed as part of this study was found to be useful for explaining and predicting the behavior of in-plane drainage of geotextiles with enhanced drainage capabilities under a high relative humidity.

### INTRODUCTION

Geotextiles with enhanced drainage capabilities have been developed to facilitate drainage of soil layers that may be under unsaturated conditions and are placed in contact with the geotextile. While field and experimental evidence has been documented on the drainage capabilities of these new geosynthetic materials, quantification of the lateral drainage has been challenging as it depends on the laboratory conditions under which the geotextiles with enhanced drainage capabilities are tested. The present study focuses on the analytical prediction of spontaneous horizontal flow which consists of the generation of flow exerted only by the capillary force. External forces, such as pressure head, that could lead to a higher in plane-flow are not evaluated in this paper. The analytical prediction of spontaneous horizontal flow focuses particularly on geotextiles with enhanced drainage capabilities tested in isolation. Additionally, laboratory tests were performed to validate the analytical prediction of spontaneous horizontal flow.

### THEORETICAL PREDICTION OF SPONTANEOUS HORIZONTAL FLOW

The geotextiles with enhanced drainage capabilities evaluated in this study are made of nylon wicking fibers in the cross-machine direction. A schematic of cross-section of a wicking fiber is shown in Figure 1a. These nylon fibers are capable of transporting water through their grooves. The microscopic grooves allow water along their entire length since they are not enclosed. Thus,

they can be characterized as open micro-channels. Figure 1b shows an electron microscope view of one nylon fiber. In the product considered in this investigation, each yarn involves approximately 150 fibers, creating a preferential path for water to flow. An electron microscope view of a yarn cross-section is shown in Figure 1c.

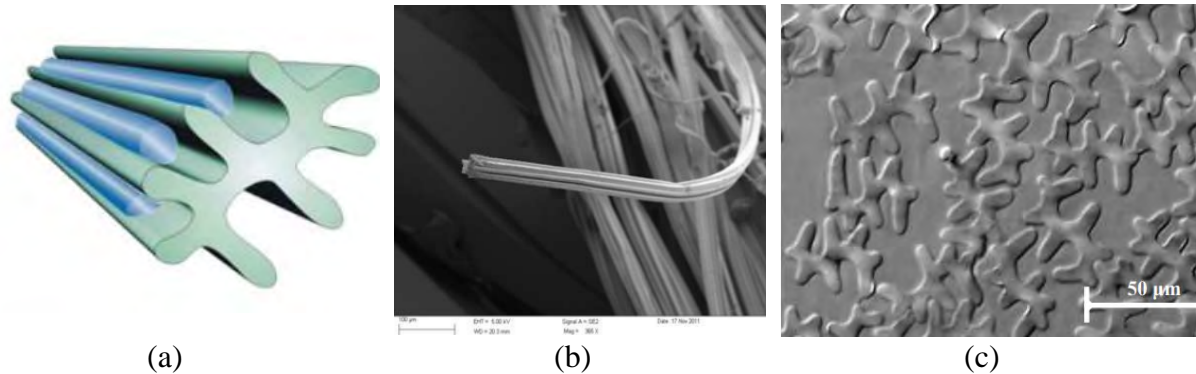


**Figure 1. Wicking fibers in geotextiles with enhanced drainage capabilities used in this study: (a) schematic of grooved cross-section of a nylon fiber; (b) electron microscope view of in nylon fiber; (c) electron microscope view of cross-section of wicking yarns (Azevedo,2016).**

To predict spontaneous horizontal capillary flow in geotextiles with enhanced drainage capabilities, the principle of flow in enclosed, cylindrical capillary tubes was studied based on a simplified model that follows Lucas-Washburn law (Berthier et al., 2019). Spontaneous capillary flow consists of the movement of a liquid in confined areas such as tubes with very small diameters. The liquid movement is triggered by the capillary force resulting from the intermolecular forces of the liquid and the liquid and the solid interaction. The intermolecular forces called “cohesive forces” are responsible for the bulk property of liquids and consists of the attractive forces between molecules of the same liquid. At the wetting front, the cohesive forces generate tension due to the liquid-air interaction which is called “surface tension” (De Gennes et al., 2002). On the other hand, the liquid-solid interactions identified in the technical literature as “adhesive forces” involve the attraction of the liquid to a solid (Berthier et al., 2019). At the wetting front, a concaved shape will be formed called “meniscus”. The concavity of the meniscus will depend on the relationship between cohesive and adhesive forces. The angle between the liquid and the solid at the meniscus is called contact angle (De Gennes et al., 2002). The principle of spontaneous horizontal capillary flow is presented in figure 2 showing the capillary forces generating water flow at the meniscus inclined by an angle  $\theta$  which corresponds to the contact angle. For the theoretical analysis presented in this paper, the spontaneous horizontal flow of water was studied along a circular capillary tube made of nylon.



**Figure 2. Principle of capillary pumping (based on Berthier and Brakke, 2012).**

The flow from a water reservoir into an initially dry capillary tube placed horizontally involves two different regimes (Berthier et al, 2019). First, when water starts flowing through a dry capillary tube the inertial regime occurs. In this regime, an external force such as the capillary force is applied to the liquid forcing the liquid to flow through the capillary tube. The liquid will initially resist to a change in velocity or acceleration. The resistance to the movement of the matter, which is the liquid in this case, is called inertial force (Cohen and Whitman, 1999). After the wetting front has been initially mobilized, the friction between the liquid molecules and the inner walls of the capillary tube is called “viscous force” will increase and will start to prevail, while the inertial forces become negligible. This regime is called the viscous regime. Figure 3 presents a schematic of the location of the different regimes during spontaneous capillary flow. Lucas (1918) and Washburn (1921) derived an analytical prediction of horizontal flow in circular capillary tubes based on the assumption that the inertial forces are negligible focusing on the viscous regime. In this paper, the prediction of spontaneous horizontal flow is based on the Lucas-Washburn law (De Gennes et al., 2002). An additional force that is opposed to the movement is the air resistance, but it is typically neglected (Berthier et al, 2019).

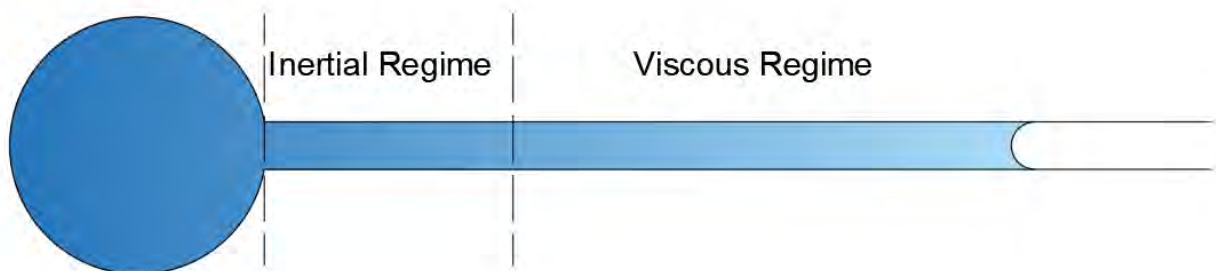


**Figure 3. Inertial and viscous regime zones identified along a capillary tube during evolution of capillary flow (based on Berthier et al. 2019).**



The driving force that causes the spontaneous driven flow in a capillary tube is called capillary force ( $F_c$ ). It is related to the density of the liquid, contact angle, and radius of the tube. The driving force is defined in equation (1).

$$F_c = 2\pi R\gamma \cos \theta \dots (1)$$

where:

$R$  is the radius of the capillary tube;

$\theta$  is the contact angle; and

$\gamma$  is the density of the fluid.

On the other hand, some forces resist the liquid movement. One such force, called inertial force, is negligible for this analysis, as previously stated, as the focus of this study is on the viscous regime zone of flow. Another such force, termed viscous force ( $F_v$ ), is obtained from the Poiseuille profile for laminar flow in a cylindrical tube (Berthier et al, 2019). It is implicitly assumed that the flow travels following smooth paths in layers (laminar flow) and that the viscosity of the liquid does not depend on the shear stress (Newtonian liquid). Additionally, the velocity of the flow changes within the radius of the tube due to the friction with the tube, moving slower at the vicinity of the cylinder walls and achieving its maximum velocity at the center of the tube. The velocity gradient the liquid in the tube ( $\frac{dv}{dr}$ ) and the resistance to movement between liquid layer paths called “dynamic or absolute viscosity” of the fluid ( $\eta$ ) are used to determine the average wall friction per unit surface defined as  $4\eta \frac{dv}{dr}$  (Berthier et al, 2019). This average wall friction per unit surface is defined along the total surface of the tube in contact with the liquid, which depends on the radius and wetted length of the tube ( $2\pi Rz$ ). This means that as flow progresses, the viscous forces increase as well (De Gennes et. al., 2002). The viscous force is defined in equation (2).

$$F_v = (2\pi Rz)4\eta \frac{dv}{dr} \dots (2)$$

The weight of the fluid ( $W$ ) is also a resistant force, which means that it is opposed to the movement of the flow. Nevertheless, it only considered when the flow is vertical, but is neglected when flow is horizontal. The general flow equation, including the inertial force and weight, is:

$$\frac{d(MV)}{dt} = F_c - F_v - W \dots (3)$$

As previously discussed, since the analysis focusses on the viscous regime, the inertial force of the fluid can be neglected in comparison to the viscous friction. Also, because the flow is horizontal, the weight of the fluid (gravity force) can be neglected. Thus, the flow equation can be simplified as follows:

$$F_c = F_v \dots (4)$$

Replacing equations (1) and (2) in equation (4):

$$2\pi R\gamma \cos \theta = (2\pi Rz)4\eta \frac{dv}{dr} \dots (5)$$

Thus:

$$\gamma \cos \theta \, dr = 4\eta z \, dv \, (6)$$

Since  $dv = \frac{dz}{dt}$ :

$$\frac{\gamma \cos \theta}{4\eta} dr = z \frac{dz}{dt} \dots (7)$$

$$\int_0^t \int_0^R \frac{\gamma \cos \theta}{4\eta} dr dt = \int_0^z z \, dz \dots (8)$$

Integrating:

$$\frac{\gamma R \cos \theta}{4\eta} t = \frac{z^2}{2} \dots (9)$$

Rearranging the variables:

$$z^2 = \frac{\gamma R \cos \theta}{2\eta} t \dots (10)$$

The following equation is known as Lucas-Washburn's law:

$$z = \sqrt{\frac{\gamma R \cos \theta}{2\eta}} \sqrt{t} \dots (11)$$

The Lucas-Washburn's law establishes that the distance of the advancing liquid front is directly proportional to the square root of time. This means that the liquid progresses quickly at the beginning of the flow process, and it later slows down. Since the fibers in geotextiles with enhanced drainage capabilities are not actually straight, a tortuosity factor was included in the flow prediction to account for this characteristic (Azevedo, 2016). Tortuosity is inversely proportional to the movement of flow. Thus, equation (11) was modified to incorporate the tortuosity of the fibers as shown next:

$$z(t) = \sqrt{\frac{\gamma R \cos \theta}{2\eta \tau^2}} \sqrt{t} \dots (12)$$

By getting the derivative of the previous equation, the velocity of the wetting front was determined as a function of time, as follows:

$$\frac{dz(t)}{dt} = v(t) = \sqrt{\frac{\gamma R \cos \theta}{4\eta\tau^2}} \frac{1}{\sqrt{t}} \dots (13)$$

To predict flow along the wetting front, Darcy's law can be used as follows:

$$Q = v(t)A = \pi R^2 \sqrt{\frac{\gamma R \cos \theta}{4\eta\tau^2}} \frac{1}{\sqrt{t}} \dots (14)$$

The velocity of the advancing liquid, in terms of the distance of the wetting front (wetted length), can also be obtained as follows:

$$v(z) = \frac{\gamma}{\eta} \frac{R}{4\tau^2 z(t)} \cos \theta \dots (15)$$

The velocity versus distance equation demonstrates that the velocity of a liquid in a horizontal capillary tube is inversely proportional to the length of the tube, indicating that the flow will slow as the liquid advances.

Based on the equations (12), (13), (14) and (15), a theoretical prediction of spontaneous horizontal flow was made. The actual values of the different variables adopted in this study to predict the wetting front in the wicking fibers are those shown in Table 1. It should be noted that the wicking fibers do not have a cylindric transversal section, which is the assumed shape in the adopted theory. Nevertheless, this paper assumes that flow through the grooves in the wicking fibers can be represented by the water flows through a cylindrical tube of a given equivalent diameter. Consequently, the inner diameter of the equivalent cylindrical tube was back calculated based on the experimental data presented later in this paper. The objective of using the theoretical model was to establish a theoretical framework to establish the flow through geotextiles with enhanced drainage capabilities as well as the relevant variables that govern such flow.

**Table 1. Variables used for theoretical prediction of horizontal flow.**

Symbols	Variables	Value
$\theta$	Contact angle	60°
$d$	Capillary tube diameter	3.5x10 <sup>-5</sup> m
$\eta$	Fluid viscosity	8.9x10 <sup>-4</sup> Pa.s
$\tau$	Tortuosity	1.2
$\gamma$	Surface tension	0.045 N/m

Note: The contact angle, tortuosity and surface tension were extracted from Azevedo (2016).

The results obtained from the theoretical evaluation of spontaneous horizontal flow are presented in Figure 4. The distance advanced by the wetting front away from the water reservoir in relation to time (Lucas-Washburn law) was predicted using equation (12) and plotted in Figure 4a. The liquid was predicted to advance rapidly initially and then decrease its velocity. This reduction in velocity over time is due to the increase of the viscous force over the length of the capillary tube model. The reduction of velocity can be explained mathematically as well since the distance of the wetting front in equation (12) is proportional to the square root of time. Thus, the rate of the distance covered by the wetting front reduces gradually in time as shown in Figure 4a. Figure 4b shows how the time-dependent flow velocity decreases, which is particularly significant at the beginning. Equation (13) was used for the prediction of velocity over time. In Figure 4c, the velocity of the wetting front over the length of the geotextile is presented by using equation (14), indicating a considerable drop in velocity, as predicted. In Figure 4d, velocity was converted to flow using Darcy's law to quantify the number of liters being drained per day per feet by using equation (15).

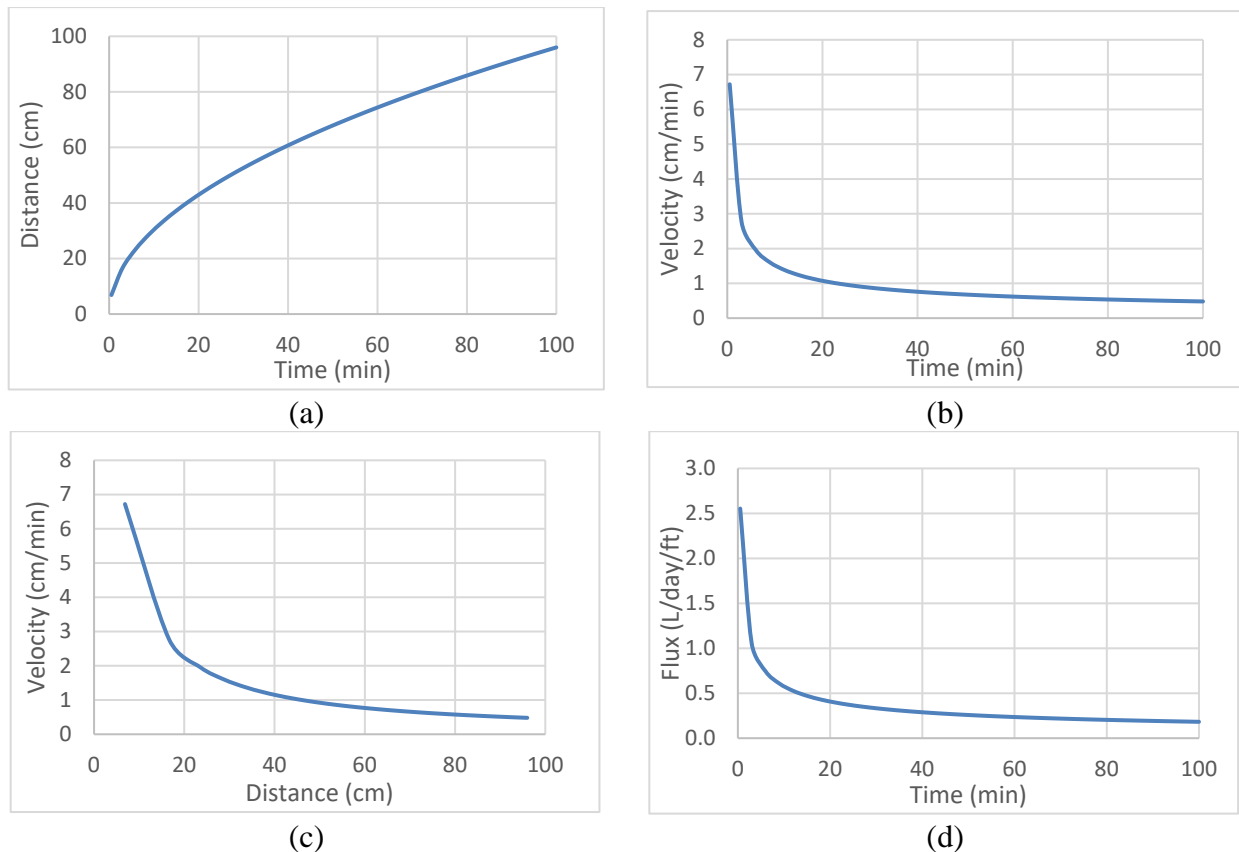


**Figure 4. Prediction of spontaneous horizontal flow in geotextiles with enhanced drainage capabilities: (a) distance versus time; (b) velocity versus time; (c) velocity versus distance; and (d) flux versus time.**



## EXPERIMENTAL RESULTS OF SPONTANEOUS HORIZONTAL CAPILLARY FLOW

To validate the theoretical prediction of flow, a series of horizontal drainage tests were conducted to quantify the spontaneous horizontal flow of geotextiles with enhanced drainage capabilities at the wetting front. Other researchers, such as Azevedo (2016) and Guo (2017), have also reported results for similar tests.

The materials used for the horizontal drainage tests conducted in this study include: a water reservoir; 20-cm-wide by 1-m-long geotextile with enhanced drainage capabilities; ruler; hygrometer; humidifier; UV light; water dye; test box, also referred to as “environmental box;” and stopwatch.

Testing involved placing an end of the geotextile with enhanced drainage capabilities inside the water reservoir, while leaving the opposite end exposed to the atmosphere. The geotextile was positioned horizontally throughout testing, as displayed in Figure 5a. Tests were carried out in a sealed environmental box in which the temperature and relative humidity were controlled to prevent evaporation of water from the open micro-channels of the wicking fibers. A humidifier was placed inside the environmental box to maintain a relative humidity close to 100%. Keeping a high relative humidity is a crucial part of this testing setup since evaporation could reduce considerably the velocity of the wetting front. Thus, this test under lower relative humidity might not be in good agreement with the theoretical analysis presented previously due to the assumption considered for the derivation of the flow equations (12), (13), (14) and (15). Finally, a yellow dye was added to the water in the reservoir to facilitate easy identification of the wetting front using UV lights, as pictured in Figure 5b. Time and wetted length were recorded throughout testing.

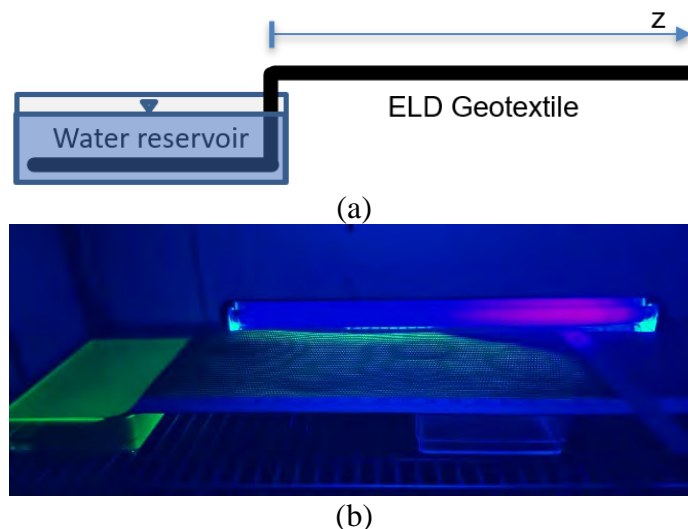


**Figure 5. Horizontal drainage test setup: (a) layout of test setup; and (b) image of advancing wetting front during testing.**

The results obtained from a series of five tests (repeats) performed under the same conditions are shown in Figure 6. Distance versus time is plotted in Figure 6a, showing the results of the 5 tests as well as the average values. It is revealed that the flow stopped after approximately 100 minutes. Figure 6b only shows the average data. It is observed a considerable decrease in velocity of the wetting front over time. Figure 6c presents the average velocity from the five tests performed in terms of wetted length. A significant decrease in velocity was observed along the initial 10 cm to 20 cm, beyond which the flow velocity continued decreasing, but at a much lower rate. In Figure 6d, the average velocity of the wetting front from the five tests was converted to water flow by estimating the cross-sectional area of the capillary tubes contained in the geotextile tested.

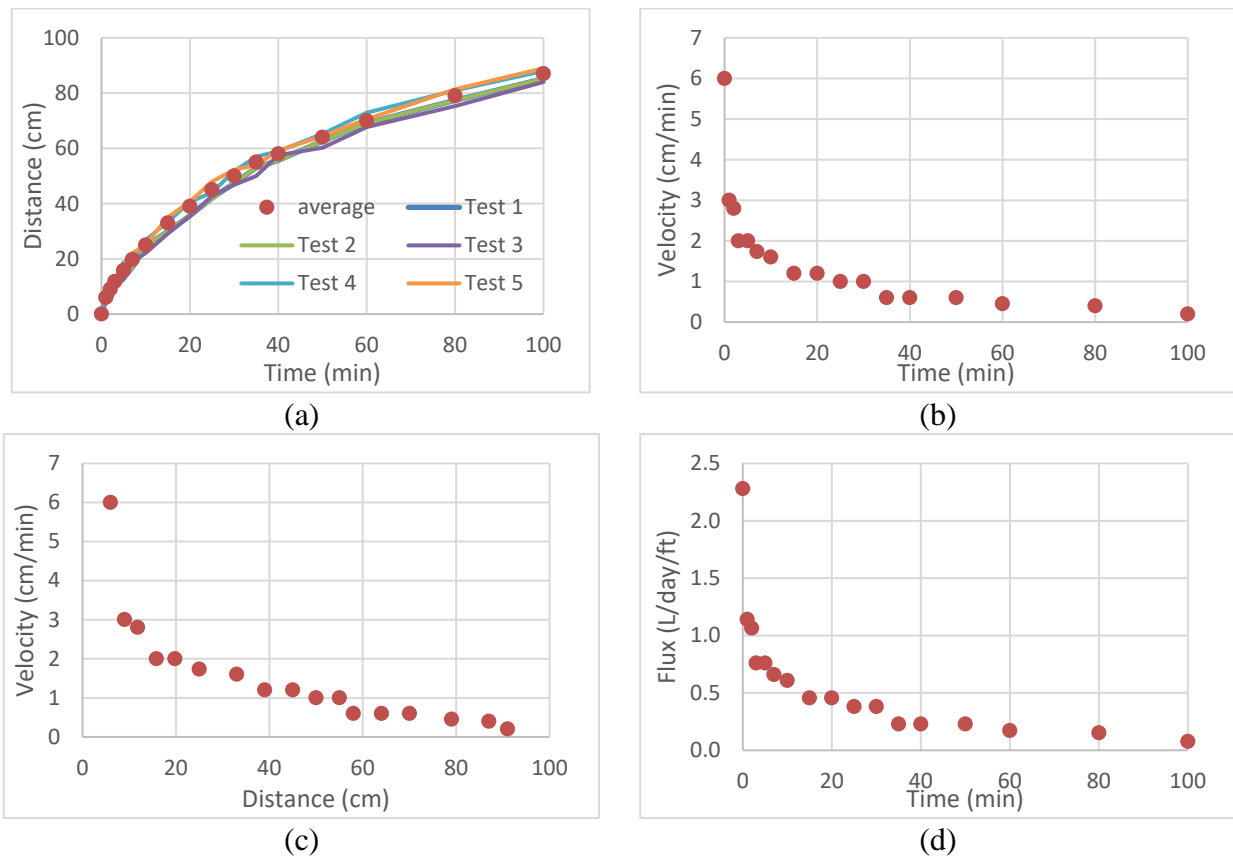


**Figure 6. Experimental results from horizontal drainage tests: (a) distance versus time; (b) velocity versus time; (c) velocity versus distance; and (d) flux versus time.**

### COMPARISON BETWEEN EXPERIMENTAL AND PREDICTED RESULTS

A comparison was made between the analytical predictions and experimental results. Data from both analyses analytical and average values of the experimental results are plotted together in Figure 7. Figure 7.a shows the plot of the distance over time of both analyses. The prediction seems to slightly overpredict the flow particularly after 60 minutes. Figure 7.b plots the velocity against time. In this case both analyses seem to be overlapped. Figure 7.c plots the velocity against distance. In this case overlapping results of both analyses are observed as well. Lastly, Figure 7.d shows the flux over time, presenting matching results from both theoretical and analytic analyses. Thus, the

theoretical model and the laboratory tests seemed to be in agreement with each other. It should be noted that the equivalent diameter adopted in the prediction of flow through the wicking fibers was obtained through back calculation using data from figure 6. However, once such diameter was established, the trends of the different variables (distance, velocity, flux) was adequately predicted by the model. The results showed that the simplified theoretical model assuming enclosed capillary tubes with a circular cross-sectional area accurately predicted flow through more complex, open micro-channels, such as wicking fibers under high relative humidity (>95%). Nevertheless, tests conducted at a lower relative humidity might require other theoretical models that consider evaporation rate and/or open cross-sectional areas.

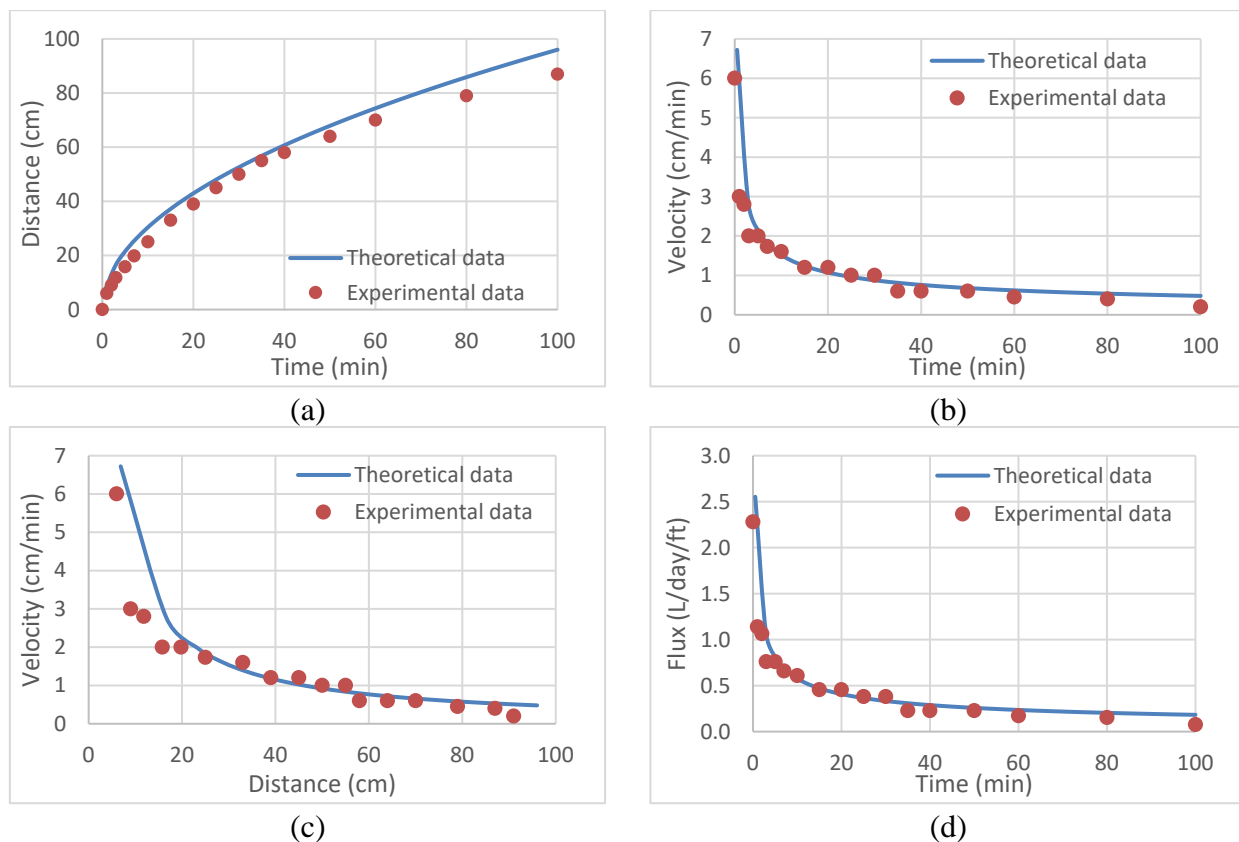


**Figure 7. Comparison of theoretical and experimental results: (a) distance versus time; (b) velocity versus time; (c) velocity versus distance; and (d) flux versus time.**

## CONCLUSION

The quantification of the lateral drainage provided by geotextiles with enhanced drainage capabilities can be challenging because results may vary depending on the laboratory conditions under which geotextiles with enhanced drainage capabilities are tested. This paper focused on the prediction of the spontaneous horizontal flow rate of a geotextile enhanced drainage capabilities in isolation. A theoretical prediction was derived based on Lucas-Washburn law and a series of horizontal drainage tests were conducted to validate the flow prediction. Good agreement was observed between the theoretical prediction of flow and experimental data under a high relative

humidity (>95%). However, for cases in which evaporation is likely, more complex flow predictions that consider evaporation rate and/or open micro-channels models might be needed to accurately predict spontaneous horizontal flow in geotextiles enhanced drainage capabilities.

## ACKNOWLEDGEMENTS

The authors gratefully acknowledged the financial support provided by TenCate Geosynthetics to this research.

## REFERENCES

- Azevedo, M. (2016), *Performance of Geotextiles with Enhanced Drainage.*, The University of Texas, Austin, Texas, USA.
- Berthier, J., and Brakke, K. A. (2012), *The physics of microdroplets.*, Scrivener Publishing LLC, Hoboken, New Jersey, USA.
- Berthier, J., Theberge, A. B., & Berthier, E. (2019), *Open-Channel Microfluidics Fundamentals and applications.*, Morgan and Claypool, Washington, Seattle, USA.
- Cohen, B., & Whitman, A. (1999), *Isaac Newton The Principia Mathematical principles of natural philosophy.*, The Regents of the University of California, Oakland, California, USA.
- De Gennes, P.-G., Brochard-Wyart, F., & Quere, D. (2002), *Capillarity and Wetting Phenomena: Drops, pearls, waves.*, Springer, Paris, Île-de-France, France.
- Guo, J. (2017), *Evaluation and design of wicking Geotextiles for Pavement Applications.*, University of Kansas, Lawrence, Kansas, USA.
- Lucas, R. (1918), Ueber das Zeitgesetz des Kapillaren Aufstiegs von Flüssigkeiten., *Colloid and Polymer Science*, 23,15-22.
- Washburn, E. W. (1921), The Dynamics of Capillary Flow. *Physical Review*, 17(3), 273-283.



# White Polyethylene Geomembrane: Forensic and Laboratory Evidence for Superior Durability

Boyd Ramsey<sup>1</sup> and Adam K. Maskal, P.E.<sup>2</sup>

<sup>1</sup>Boyd Ramsey Consulting, LLC, Houston, TX, USA; e-mail: [Boyd@Boydramseyconsulting.com](mailto:Boyd@Boydramseyconsulting.com)

<sup>2</sup>Solmax Geosynthetics, Visalia, CA, USA; e-mail: [amaskal@solmax.com](mailto:amaskal@solmax.com)

## ABSTRACT

White Polyethylene Geomembranes have been available in the market for over two decades and have been used broadly, often exposed (uncovered) in demanding and sensitive applications. The performance of these materials has far exceeded the initial (circa 1990's) expectations. There is increasing evidence that the durability and lifespan of a white geomembrane in an exposed application is longer, not only than projections, but perhaps even than for traditional black colored geomembranes of comparable composition. This paper presents data in support of that hypothesis and in fact, reaches the conclusion that in exposed application, white surfaced geomembrane is the material of choice, based on durability as well as other pertinent considerations. Data and evidence from forensic evaluations as well as laboratory testing for durability is presented and new estimates of lifespan are presented.

## INTRODUCTION

White Polyethylene Geomembranes have been available in the market for over two decades and have been used broadly, often exposed (uncovered) in demanding and sensitive applications. The performance of these materials has far exceeded the initial (circa 1990's) expectations. There is increasing evidence that the durability and lifespan of a white geomembrane in an exposed application is perhaps longer, not only than projections, but than that of traditional black colored geomembranes of comparable composition. This paper presents data in support of that hypothesis, and in fact reaches the conclusion that in exposed applications, white surfaced geomembrane is the material of choice, based on durability as well as other pertinent considerations. Data and evidence from forensic evaluations as well as laboratory testing for durability is presented and new estimates on lifespan are presented.

## FORENSIC EVALUATIONS

The successful performance of white geomembranes in the field has been well established. Cowlitz County, Washington (Thiel) is possibly the most complete forensic examination. However, the Polk County, Florida site (Roberts and separately, Ramsey) (green surfaced, with very similar stabilization) has also been extensively documented. The Palo Verde Nuclear Generating Station has been one of the largest consumers of white geomembrane as reported by Eichelberger. Samples from each of these sites, as well as others, have been included in this study. Further information on the performance of white geomembrane can be found in Rentz (2007) and other references. In general, white geomembrane materials present multiple benefits

as contrasted with traditional black geomembrane, these include improved damage detection, fewer and smaller wrinkles / less thermal expansion and contraction and expanded installation windows and improved safety and handling. Nearly all of these are due to the lower temperature of the white geomembrane that occurs as a result of sunlight reflection as compared to the exceptionally high absorption of solar energy of black materials.

The materials used in this examination came from various locations and climates around the world. **Table 1** lists the details of the samples being reported.

**Table 1. Sample Identification**

<b>Sample ID</b>	<b>Description</b>
<b>A</b>	Polk County, Florida, USA 1.5 mm exposed green landfill cap. Sample exposed outdoors for 21 years at Latitude 27° North tropical environment
<b>B</b>	Polk County, Florida, USA 1.5 mm exposed green landfill cap. Sample from original installation, but stored in a warehouse, aged 21 years but no UV/solar exposure
<b>C</b>	Toowoomba, Queensland, Australia. 1.0 mm white geomembrane from an exposed outdoor evaporation pond in service since 2012 at Latitude 27° South, warm and temperate environment
<b>D</b>	Cowlitz Country, Washington, USA 1.5 mm exposed white geomembrane from an exposed outdoor pond in service since 1993 at Latitude 46° North, Mild Mediterranean climate
<b>G</b>	Palo Verde Nuclear Generating Station, Phoenix AZ, USA 2.0 mm sample from 1999 installation, but stored in a warehouse, aged but no UV/solar exposure.
<b>J</b>	Commercial sample from 2020, 1.5 mm white geomembrane, stored in a warehouse, no UV/solar exposure
<b>K</b>	Commercial sample from 2020, 2.0 mm black geomembrane, stored in a warehouse, no UV/solar exposure
<b>M</b>	Commercial sample from 2013, 2.0 mm white conductive geomembrane, but stored in a warehouse, aged but no UV/solar exposure

## **SAMPLING GROUPINGS**

In the following graphs and presentation of data, the samples are delineated into three groups:

- Those materials that have been exposed in-service (A, 21 years C, 8 years and D, 25 years);
- Those materials that have aged, but have not been exposed in-service (B, 21 years G, 21 years M and H, 7 years); and
- Those materials that can be considered “new” – manufactured recently with no exposure in-service (J and K).

## **TEMPERATURE OF EXPOSED GEOMEMBRANE**

There is existing literature and studies on the temperature differentials between black and white geomembranes exposed to the environment. Koerner (G.) in "Temperature Behavior of Field Deployed HDPE Geomembranes," (addresses both the overall difference and the seasonality in the northern hemisphere at Latitude 40° North (G. Koerner, 1995). Rentz reports a temperature delta (Black vs. White geomembrane) of 22° C at the Queen's University Queen's University Environmental Liner Test Site II (QUELTS II) in August at Latitude 44° North (Rentz, 2007). Cadwallader reports a 25° temperature differential, presumably at Latitude 36° North (Cadwallader, 1993). Further, Cadwallader includes the assumption proven in this paper: "Advantages of maintain a lower geomembrane temperature are also evident in long term aging tests." Pelte (1994) reports the largest differential of 35° C at latitude 45° North. Pelte also conducted laboratory scale testing demonstrating greater differentials in the temperature response of black and white geomembranes, both polyethylene and polyvinylchloride.

The primary author also has significant field experience in evaluating the temperature of geomembranes that comes in the form of both personal observation and the recording of weld/seaming activity temperatures.

Taking this all under consideration, for the purposes of this evaluation a temperature differential of 25°C is used to estimate the temperature difference / behavior of white vs. black polyethylene geomembranes when exposed to the environment.

## **SPECIFICATION OF DURABILITY CRITERIA**

When the Geosynthetics Institute originally (June 1997) created the specification "GRI GM-13" consideration was given to durability. Similar to the other properties of the specification, multiple "successful" materials were tested, these values reported and a requirement was negotiated in relation to the performance of existing materials that were known to be functioning well. For durability considerations, this was agreed to be the retention of Oxidative Induction Time (OIT), proposed to represent the length of the "Stage A" of geosynthetic lifespan as reported by Hsuan and Koerner. The parties involved in the discussions were all participants in the geosynthetic and geomembrane industry, with manufacturers, design and quality engineers and major consumers all represented. This group agreed that the retention of OIT with the values enumerated within the specification should be acceptable. The long-term success and the broad global use of the specification proves this decision to be correct.

For High Pressure OIT, this value is a minimum initial HP-OIT of 400 minutes with the retention of HP-OIT of 80% of the initial value after oven aging at 85°C for 90 days. The specifics of this testing are included in ASTM specifications: ASTM D 5885 and D 5721 respectively. To comply with GM-13, a geomembrane material had to lose HP-OIT during Oven aging at 85° C a rate of less than 0.89 minutes/day over a 90-day period. This performance level has served the geomembrane industry well in the following decades and is the basis for comparison in this paper's evaluation.

## **LABORATORY EVALUATION PROGRAM**

The material sample listed above were subjected to Oven Aging in a modified fashion, generally as directed by GM-13 and ASTM 5721. The modification was a reduction in the oven temperature to reflect the difference in field temperatures as discussed above. The oven aging

was conducted at 60° C. The oven aging was conducted at the Geosynthetic Institute, Folsom, PA in the summer of 2021. Samples of the materials as initially received, and after 30, 60 and 90 days of oven aging were tested for HP-OIT. This testing was conducted at the Solmax laboratory in Rechlin, Germany. This laboratory is certified within the GAI-LAP (Geosynthetic Accreditation Institute-Laboratory Accreditation Program) to conduct this test as well as multiple other certifications.

There have been recent significant changes to the HP-OIT testing document published by ASTM (5885). These relate primarily to sample preparation and are not completely addressed here. However, it is important to understand how the data reported herein was generated. The samples tested here were tested in the “as-is” condition. That is, a section was taken from the entire thickness of the sample, weighted and tested for HP-OIT properties as it existed at that point. No grinding, homogenization, plaque preparation or other alteration of the samples occurred prior to testing.

Further to sample preparation and testing, it should be noted how the values reported were calculated. In multi-layer geomembrane materials, it is common for the different layers to be stabilized with different varieties of stabilizer, different concentrations of stabilizer, or both. In HP-OIT testing, this can manifest itself in results that contain “shoulders” as indicated in illustration one below. This contrasts with other results that are more indicative of **Figure 2**.

**Figure 1: HP-OIT v. Time Curve with Shoulder**

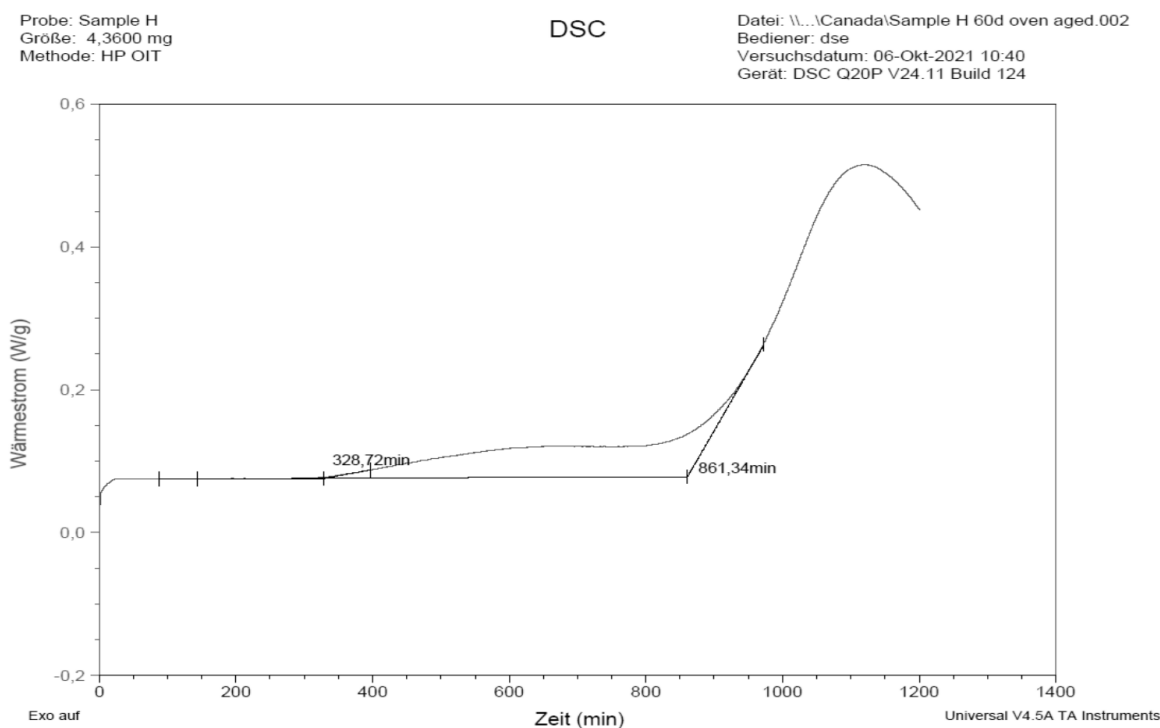
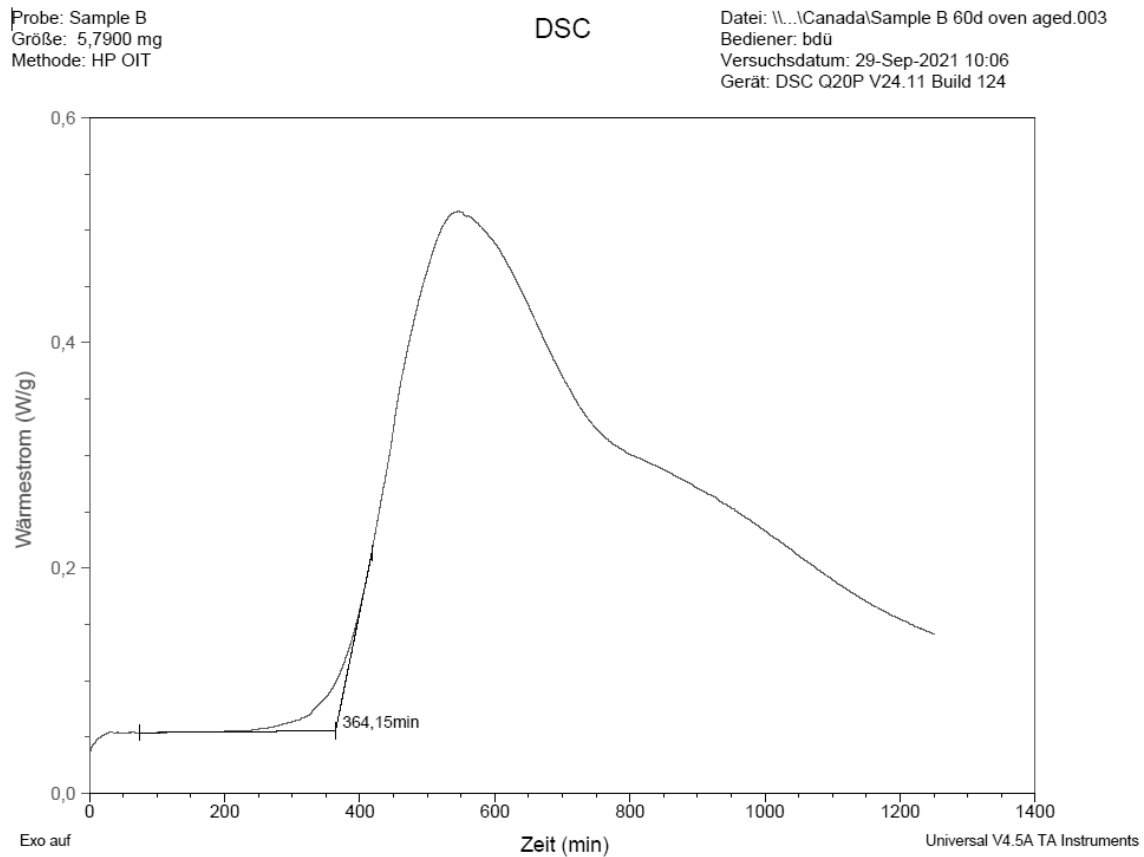




**Figure 2: HP-OIT v. Time Curve without Shoulder**



In this examination, small shoulders such as shown above in Illustration one were ignored and the much larger exothermic reaction demonstrated by the large steeply sloped curve to the right was used to calculate the HP-OIT for that sample. In some cases, retesting was done to validate results that appeared inconsistent or unexpected. In every case, no data points were discarded, and the values reported below are the results of one, or the average of two test results.

The author is sympathetic to the attempts to improve the reliability and repeatability of the HP-OIT test by requiring sample homogenization. Striving to reduce testing variation is a good thing. However, in this case, and generally, the benefit of testing the material in the condition and state in which it is actually used greatly outweighs the need to reduce variation. I would not endeavor to try to explain to a design engineer, owner, or other stakeholder that rather than simply taking a section of material and testing it, it was justifiable to significantly modify the material prior to testing.

## RESULTS

The results are reported below in two tables and three graphs: Illustration Three lists the numerical values for HP-OIT test results. Illustration Four lists these same results but in the format of a percentage of original OIT retained.

**Figure 3. HP-OIT Test Results**

Tested Values	T = zero days	T = 30 days	T = 60 days	T = 90 days	OIT loss (Min/day)
<b>A (green)</b>	110	108	107	97	0.14
<b>B (green)</b>	427	337	367	371	0.62
<b>C</b>	651	644	604	634	0.19
<b>D</b>	329	325	309	264	0.72
<b>G</b>	506	529	518	541	-
<b>H</b>	900	896	784	832	0.76
<b>J</b>	502	461	424	420	0.91
<b>K (black)</b>	1776	1771	1659	1756	0.22
<b>M</b>	520	551	506	519	0.01

**Figure 4. Percentage of HP-OIT Retained**

% retained	T = zero	T = 30 days	T = 60 days	T = 90 days
<b>A (green)</b>	100%	98%	97%	88%
<b>B (green)</b>	100%	79%	86%	87%
<b>C</b>	100%	99%	93%	97%
<b>D</b>	100%	99%	94%	80%
<b>G</b>	100%	105%	102%	107%
<b>H</b>	100%	100%	87%	92%
<b>J</b>	100%	92%	84%	84%
<b>K (black)</b>	100%	100%	93%	99%
<b>M</b>	100%	106%	97%	100%

These same results are presented graphically in **Figures 5, 6, and 7**. Here the results are grouped by sample type: **Figure 5** – materials exposed in-service, **Figure 6** - materials that have aged, with no exposure, and **Figure 7** – “new” – materials manufactured recently with no exposure.

**Figure 5. Exposed in-service Samples**

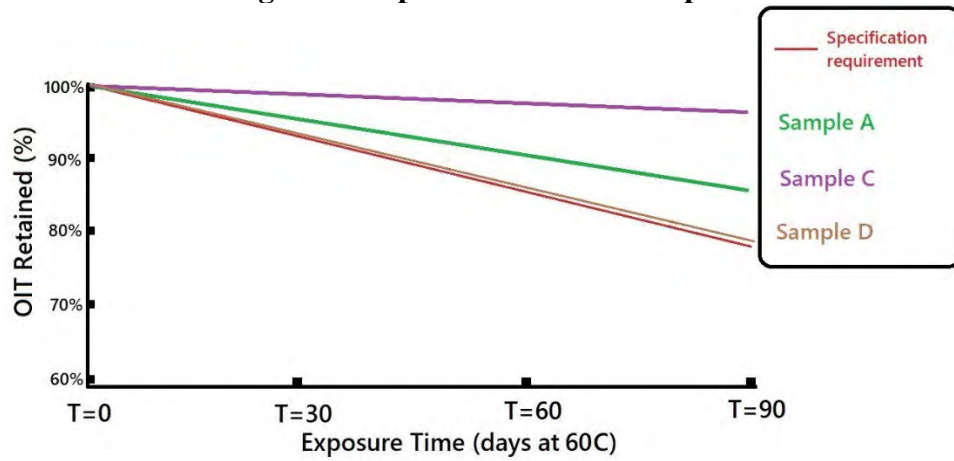


**Figure 6. Aged, not Exposed**

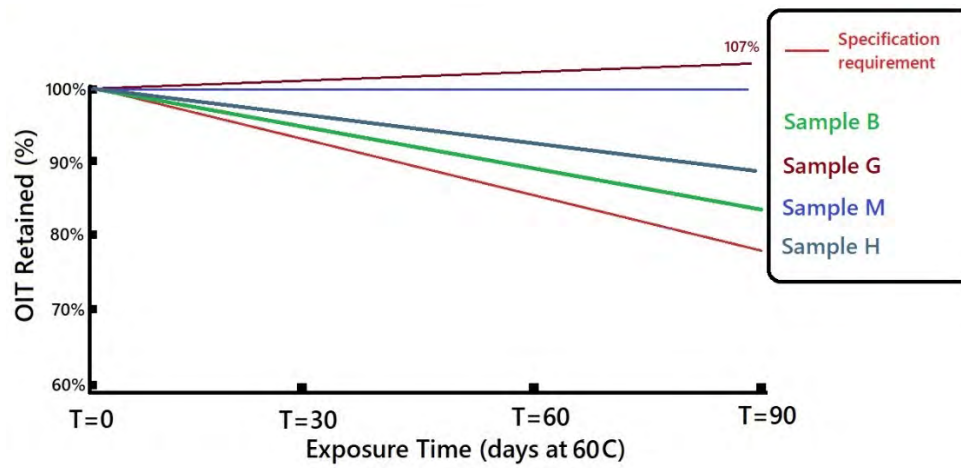
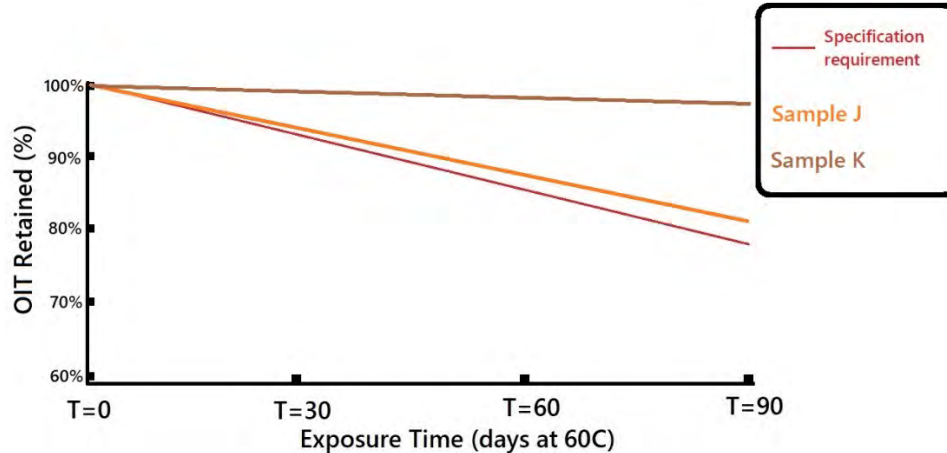


**Figure 7. “New” material, manufactured recently with no exposure.**



The result is that all materials tested exceed the specification requirement for HP-OIT retention albeit at a lower temperature. However, as lower daily temperature is clearly a feature of the non-black/white materials, the authors are confident that this is a clear, logical, and now demonstrated contributor to extended lifespan. This has been demonstrated across multiple locations, multiple materials and different applications. Exposed white surfaced polyethylene geomembrane materials should be expected to last longer than black surfaced materials in so far as the effects of temperature.

## **APPLICATION OF RESULTS TO CURRENT LIFESPAN PROJECTIONS**

In the Koerner (R.M.) Keynote lecture at the 2016 GeoAmericas event, held in Miami, Florida a detailed analysis and calculation was presented for the estimated lifespan of exposed polyethylene geomembranes. One of the metrics used to estimate lifespan, in addition to OIT, was the retention of physical properties, specifically tensile strength and tensile elongation. These properties were used to prepare (Koerner) figure 19C which lists the predicted lifespan of materials at a range of field temperatures. Using this data and the temperature ranges from the Koerner work and extending the results demonstrated in this paper, one can expect an additional 17 years of lifespan from white polyethylene geomembrane materials as compared with black in an exposed application.

Clearly this estimation comes with many caveats as there are multiple factors effecting lifespan. However, the results of testing of exposed forensic samples, field evaluations reported in literature, as well as the modeling and testing contained in this paper demonstrate consistently that white surface polyethylene geomembranes have lower temperatures in the field, and this results in improved lifespan and durability.

## **CONCLUSIONS**

What has been presented is a combination of forensic field evaluations, public literature information and in a new addition to the industry knowledge, the behavior of white surface



polyethylene geomembranes in retention of HP-OIT at a temperature that reflects field exposure temperatures. This data and information all imply and support the hypothesis that these materials will have a longer lifespan than that of the equivalent black geomembrane materials. Literature suggests that this improvement is approximately 17 years in duration of lifespan.

## ACKNOWLEDGEMENTS AND APPRECIATION

The author acknowledges and thanks Solmax, who funded this work, Dr. George Koerner and the Geosynthetic Institute who contributed to the testing, Rick Thiel who supplied samples and data and continues to share his knowledge and information with our industry and all of my professional colleagues who have assisted me over the years.

## REFERENCES

- ASTM D5721, “Standard Practice for Air-Oven Aging of Polyolefin Geomembranes”, American Society for Testing and Materials, West Conshohocken, Pennsylvania, USA.
- ASTM D5885, “Standard Test Method for Oxidative Induction Time of Polyolefin Geosynthetics by High-Pressure Differential Scanning Calorimetry”, American Society for Testing and Materials, West Conshohocken, Pennsylvania, USA.
- Cadwallader, M., Cranston, M., and Peggs, I. D. (1993). “White-surfaced HDPE geomembranes: Assessing their significance to liner design and installation.” Proc., Geosynthetics’ 93, Industrial Fabrics Association International, St. Paul, MN, 1065–1079.
- Case, Mark E., Koerner, George R., Koerner, Robert M., Hsuan, Yick (2010), Case History of a 16-Year Old Exposed HDPE Geomembrane Cover, Proceedings of 9th International Conference on Geosynthetics, Guarujá, Brazil
- Eichelberger, C., Hersh, G. and Pittawala, S. (2013, Oct.) “Geosynthetics: The solution for managing nuclear power generation water supply in an arid environment” *Geosynthetics Magazine*, Oct. 2013.
- Fischer, R., & Ketola, W. (1994). “Surface Temperatures of Materials in Exterior Exposures and Artificial Accelerated Tests”. *Materials Science*, DOI:[10.1520/STP18174S](https://doi.org/10.1520/STP18174S)
- Giroud, J.P. and Morel, N., (1992) “Analysis of Geomembrane Wrinkles” *Geotextiles and Geomembranes* Volume 11, Issue 3, 1992, Pages 255-276
- Gleason, M.H., Houlihan, M.F., and Palutis, J.R., “Exposed Geomembrane Cover Systems: Technology Summary,” Proceedings of the Sixth International Conference on Geosynthetics, Portland, Oregon, February, 2001, pp. 905-918.
- GRI - GM13 Standard Specification for “Test Methods, Test Properties and Testing Frequency for

High Density Polyethylene (HDPE) Smooth and Textured Geomembranes”, The Geosynthetic Institute, Folsom, PA, USA

Hsuan, Y.G., and Koerner, R.M. 1998. “Antioxidant depletion lifetime in high density polyethylene geomembranes”. *Journal of Geotechnical and Geoenvironmental Engineering*, ASCE, 124(6): 532–541. doi:10.1061/(ASCE)1090-0241

Ivy, N., (2002), HDPE geomembrane after 20 years of service, *GFR Magazine* June/July 2002

Jafari, N.H. et.al., (January 2014) “Service Life of HDPE Geomembranes Subjected to Elevated Temperatures”, *Journal of Hazardous, Toxic, and Radioactive Waste*, American Society of Civil Engineers. DOI: 10.1061/(ASCE)HZ.2153-5515.0000188

Koerner, G. R. and Koerner, R. M., "Temperature Behavior of Field Deployed HDPE Geomembranes," Proc. Geosynthetics '95, IFAI, St. Paul, MN, pp. 921-937.

Koerner, R. “Lifetime Predictions of Exposed Geotextiles and Geomembranes” Proceedings of GeoAmericas 2016 3rd Pan-American conference on Geosynthetics, Miami, FL USA

Koerner R. et.al. “GRI White Paper #6 on Geomembrane Lifetime Prediction: Unexposed and Exposed Conditions”, Geosynthetic Institute, Folsom, PA website: <http://www.geosynthetic-institute.org/> accessed September 4, 2020.

Koerner R. et.al. “GRI Report #44 Exposed Lifetime Predictions of 19-Different Geosynthetics in the Laboratory and in Phoenix, Arizona” Geosynthetic Institute, Folsom, PA website: <http://www.geosynthetic-institute.org/> accessed September 4, 2020.

Koerner, R. M., Koerner, G. R. and Hsuan, Y. G., “Lifetime Prediction of Exposed Geomembranes,” Proceedings of the GRI-18 Conference on “Geosynthetics Research & Development In-Progress” at GeoFrontiers, January 26, 2005, GII Publication, Folsom, PA.

Pelte, T., Pierson, P., and Gourc, J.P. (1994). “Thermal analysis of geomembranes exposed to solar radiation”. *Geosynthetics International*, 1(1): 21–44

Ramsey B., (2016, Sept.) “13-Year Study of Exposed, Green Geomembrane Cover”, *Geosynthetica.com*

Web reference: <https://www.geosynthetica.com/13-year-exposed-green-geomembrane/>  
Accessed November 15, 2021.

Rentz, A.K., et.al., (August 2007) “Comparison of Wrinkles in White and Black HDPE Geomembranes”, *Geosynthetics International*, Volume 14 Issue 4, , pp. 219-227

Roberts, M., Bonilla, V., Kelner, R., and Choate, A. (April 2005), “Exposed Geomembrane Liner Cap Takes on Three Hurricanes in Polk County, South Central Florida” 2005 March/April, *MSW Management*, pp. 72-77. Web reference:

[http://www.erosioncontrol.biz/MSW/Articles/The EGC Takes On Three Hurricanes in Polk County 1545.aspx](http://www.erosioncontrol.biz/MSW/Articles/The_EGC_Takes_On_Three_Hurricanes_in_Polk_County_1545.aspx)

- Rowe, R.K. et.al. "Ageing of HDPE geomembrane exposed to air, water and leachate at different temperatures" *Geotextiles and Geomembranes* vol. 27 (2009) pg.137–151.
- Rowe, R.K., and Ewais, A.M.R., "Ageing of exposed geomembranes at locations with different climatological conditions", *Canadian Geotechnical Journal*, 25 August 2014, <https://doi.org/10.1139/cgj-2014-0131>
- Suits, L.D. and Hsuan, G., (1992), Technical Note: Assessing the photo-degradation of geosynthetics by outdoor exposure and laboratory weatherometer", *Geotextiles and Geomembranes* 11 pp. 255-276.
- Take W.A. et.al., (2003) "Quantifying geomembrane wrinkles using aerial photography and digital image processing", *Geotextiles and Geomembranes* 21, 111–122.
- Take, W.A. et al, "Thermal exposure conditions for a composite liner with a black geomembrane exposed to solar radiation", *Geosynthetics International*, Volume 22 Issue 1, February 2015, pp. 93-109
- Tarnowski, C., and Baldauf, S. 2006. "Ageing resistance of HDPE-geomembranes - Evaluation of long-term behavior under consideration of project experiences". In *Geosynthetics*. Edited by J. Kuwano and J. Kosaki. Millpress, Rotterdam, N.L.D., pp. 359–362.
- Thiel R., (2019, Feb.) "A leachate pond geomembrane after 25 years of service", *Geosynthetics Magazine*, Feb, 2019.
- Thiel, R., Purdy, S. and Yazdani, R. (2003), "Case History of Exposed Geomembrane Cover for Bioreactor Landfill," Session D06, Proceedings of the Sardinia Conference, 2003.
- Thomas, R.W., and Ancelet, C.R.. (1993). "The effect of temperature, pressure and oven ageing on the high pressure oxidative induction time of different types of stabilizers. In the *Proceedings of the Geosynthetics '93 Conference*, IFAI, St.Paul, Minn. pp. 915–924.
- Yako, M. A., Koerner, G. R., Hsuan, Y. G. and Koerner, R. M. (2010), "Case History of a 20-Year Old Exposed HDPE Surface Impoundment Liner," 9th ICG, Brazil (on CD).

## **Contact Angle Determination of a Wicking Geotextile Composed of Both Hydrophilic and Hydrophobic Materials**

**Chuang Lin, Ph.D.,<sup>1</sup> Lei Zhou<sup>2</sup>, Feng Zhang, Ph.D.<sup>3\*</sup>, Decheng Feng, Ph.D.<sup>4</sup>, Jingying Chu<sup>5</sup>, and Zhiyuan Wang<sup>6</sup>**

<sup>1</sup>Harbin Institute of Technology, No.73 Huang He Street, Harbin, Heilongjiang Province, China, 150090; e-mail: linchuang@hit.edu.cn;

<sup>2</sup>Harbin Institute of Technology, No.73 Huang He Street, Harbin, Heilongjiang Province, China, 150090; e-mail: 120L050713@stu.hit.edu.cn;

<sup>3\*</sup>Harbin Institute of Technology, No.73 Huang He Street, Harbin, Heilongjiang Province, China, 150090; e-mail: zhangf@hit.edu.cn;

<sup>4</sup>Harbin Institute of Technology, No.73 Huang He Street, Harbin, Heilongjiang Province, China, 150090; e-mail: fengdecheng@hit.edu.cn;

<sup>5</sup>TenCate Industrial Zhuhai Co., Ltd., A 601 Nangang Road (West), Gaolan Port Economic Zone, Zhuhai, 519050 Address; e-mail: j.chu@tencategeo.com;

<sup>6</sup>TenCate Industrial Zhuhai Co., Ltd., A 601 Nangang Road (West), Gaolan Port Economic Zone, Zhuhai, 519050 Address; e-mail: ewang@solmax.com.

### **ABSTRACT**

Capillary break effect causes disruption of water migration between a woven geotextile and a base course within a road embankment. Excess water accumulates at the soil-geotextile interface, softens the base course and reduces the stiffness of a road embankment. A wicking geotextile, composed of polyethylene reinforcing yarns and wicking yarns, was a dual-functional woven geotextile designed for both drainage and reinforcement purposes. How to evaluate the wettability of such a composite material is a key question for a better understanding of the interactions between the wicking geotextile and the water. This study proposed a laboratory testing method to determine the contact angle of such a composite material. Based on the sessile drop test results, the contact angles of the PP yarn, the wicking yarn, and the wicking geotextile as an integrity were 95.5°, 0°, and 87.2°, respectively. Based on the Cassie model, the calculated contact angle for the wicking geotextile was 83.1°, indicating that the proposed testing technique was a proper method in determining the contact angle of a composite material.

### **INTRODUCTION**

Woven geotextiles are often used for confinement and reinforcement purposes in a roadway embankment due to its high tensile strength (Subaida, Chandrakaran, and sankar, 2009; Lee, Mannan, and Ibrahim, 2020). The embankment was normally under unsaturated conditions for most of the time during its service life. Numerous researchers observed excess water accumulation at the soil-geotextile interface due to capillary break effect (Pandey, Hossain, and Ahmed, 2021; Juan et al., 2022). Capillary break effect often occurred at the interface of two geomaterials under an unsaturated condition (Zornberg et al., 2017). The pores within a base course are smaller than those in a geotextile, resulting in a higher ability to hold water. Under the influence of rainfall infiltration and capillary action, the water content gradually increases with time for the base course adjacent to the soil-geotextile interface. As the water content increases, the stiffness of a base



course decreases and deteriorations, such as pumping and pot hole, are expected under cyclic traffic loadings.

Nowadays, a dual-functional wicking geotextile has the ability to laterally drain water out of a road embankment meanwhile to reinforce a road embankment. Figure 1a shows the configuration for the wicking geotextile. The prototype of the wicking geotextile is based on Mirafi® H2Ri manufactured by SOLMAX (previously TenCate Geosynthetics). The wicking geotextile is made of high modulus polypropylene (PP) yarns and wicking yarns (Figure 1b). Similar to traditional woven geotextiles, the PP yarns are designed for the reinforcement purpose. In comparison, the wicking yarns are composed of fibers with deep-grooved and continuous channels. The diameter of the fiber ranges from 30  $\mu\text{m}$  to 50  $\mu\text{m}$  and the opening of the deep-groove is 5  $\mu\text{m}$  to 12  $\mu\text{m}$ , respectively. The wicking yarn has a specific area of 3650  $\text{cm}^2/\text{g}$  and ensures a higher ability to absorb water from the adjacent soil under an unsaturated condition. The basic physical, hydraulic, and mechanical properties of the wicking geotextile are presented in Table 1. Both laboratory tests and field observations validated the efficiency of the wicking geotextile in dehydrating road embankments (Lin, Zhang, and Han, 2018; Guo, Han, and Zhang, 2021; Lin et al. 2022).

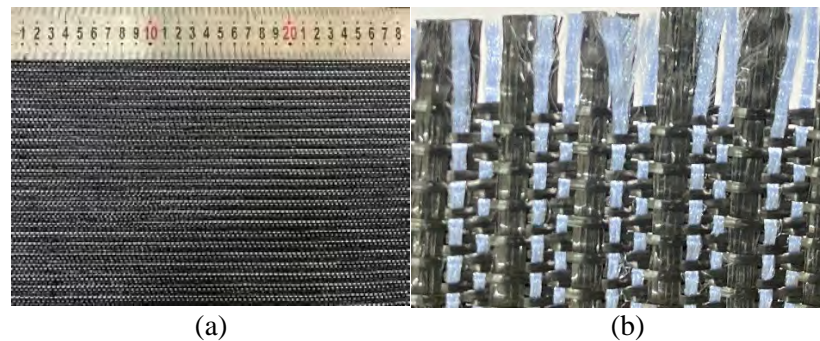


**Figure 1. Wicking geotextile: (a) configurations and (b) components**

**Table 1. Wicking geotextile physical properties**

Mechanical Properties	Unit	Average Roll Value
Tensile Modulus at 2% Strain (CD)	kN/m	15.8
Tensile Modulus at 2% Strain (MD)	kN/m	7
Permittivity	$\text{sec}^{-1}$	0.4
Flow Rate	$\text{l/min/m}^2$	1222
Pore Size ( $O_{50}$ )	$\mu\text{m}$	85
Pore Size ( $O_{95}$ )	$\mu\text{m}$	195
Apparent Opening Size (AOS)	mm	0.425
Wet Front Movement (24 minutes)	cm	15.2 (Vertical Direction)
Wet Front Movement (983 minutes) Zero Gradient	cm	186.2 (Horizontal Direction)

Since the wicking geotextile is a composite material that consists of a hydrophobic PP material and a hydrophilic wicking fiber, it is important to determine the wettability of the wicking geotextile in order to further evaluate the interactions between the geotextile and the water within soil pores under unsaturated conditions. The term wettability is extensively used to describe the spreading behavior of liquids over a solid membrane surface (Florence, A.T., 2006). Contact angle

is often used to characterize the wettability of a membrane or a composite. Contact angle is defined as the angle at which a liquid/vapor interface meets the solid surface (Koc, M. and Bulut, R., 2014). There were three major models to describe the contact angle of a geomaterial, including the Young model, the Wenzel model, and the Cassie model (Ismail et al., 2022). Young's model was often used to describe the contact angle between a liquid and an ideal surface which was atomically smooth, chemically homogeneous, nonreactive and rigid, as shown in Equation 1. However, in reality, the wicking geotextile has a rough surface and the Young model is not applicable for wicking geotextile. Wenzel (1949) argued that the roughness of the surface increased the actual contact surface of the solid-liquid phases (Figure 2b) and proposed an improved model accounting for the surface roughness, as expressed in Equation 2. The wicking geotextile is a composite material and two functional groups with different chemical heterogeneities for the PP and wicking yarns. Cassie model was proposed to describe the contact angle of a solid surface which was mosaics of different materials, as shown in Equation 3. Therefore, the Cassie model was used in this study to determine the contact angle of the wicking geotextile.

$$\cos \theta_Y = (\gamma_{SG} - \gamma_{SL}) / \gamma_{LG} \quad (1)$$

$$\cos \theta_W = r(\gamma_{SG} - \gamma_{SL}) / \gamma_{LG} = r \cos \theta_Y \quad (2)$$

$$\cos \theta_C = f_1 \cos \theta_1 + f_2 \cos \theta_2 \quad (3)$$

Where,  $\theta_Y$ ,  $\theta_W$ , and  $\theta_C$  are contact angles when using the Young, Wenzel, and Cassie model;  $\gamma_{SV}$ ,  $\gamma_{SL}$ ,  $\gamma_{LV}$ ,  $\gamma_{SG}$ , and  $\gamma_{LG}$  are the solid-vapor, solid-liquid, liquid-vapor, solid-gas, and liquid-gas interfacial tensions;  $r$  is the roughness factor, and is defined as the ratio of surface area to the geometric surface area ( $r \geq 1$ );  $\theta_1$  and  $\theta_2$  are the contact angle for the components of a composite material by considering a solid surface solely consisting of material 1 and of material 2, respectively; and  $f_1$  and  $f_2$  are the fractal surface areas for materials 1 and 2 ( $f_1 + f_2 = 1$ ), respectively.

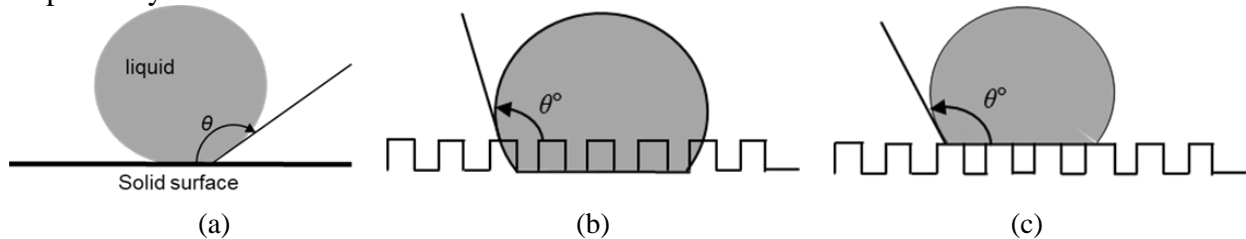


**Figure 2. Contact angle models: (a) Young model, (b) Wenzel model, and (c) Cassie model**

This study aims at determining the contact angle of the wicking geotextile composed of two different chemical heterogeneities. The sessile drop measurement technique is used to determine the contact angle of the PP yarns, the wicking yarns. The wetting process of the wicking geotextile is demonstrated and the contact angle of the wicking geotextile is determined using Cassie Model. Finally, the changes of contact angle with time are discussed for the wicking geotextile to demonstrate the influence of the wicking yarns on the wettability of the wicking geotextile.

## TEST METHOD AND PROCEDURE

A contact angle goniometer is used to determine the contact angle of the PP yarn, the wicking yarn, and the wicking geotextile as an integrity, respectively. Figure 3 shows the configurations and test

setup for the apparatus. The testing apparatus consists of a digital camera, a sample holder, a syringe holder, and a back light. A test sample is placed on top of the sample holder with a double layered sticker to ensure a relatively smooth and flat surface. A halogen lamp is placed at the right side of the testing apparatus to ensure a proper brightness for the image obtained from the camera. A micro-syringe is fastened on the syringe holder to control the volume of water applied on the test sample. Images of the drop in contact with the substrate test sample are captured by a digital camera at a time interval of 25 images per second.

Sessile drop testing technique is used to determine the contact angle of the PP yarn, the wicking yarn, and the wicking geotextile. The testing protocol follows the ASTM standard test method for surface wettability and absorbency of sheeted materials using an automated contact angle tester (ASTM D5725-99). The PP or the wicking yarn is fastened on the sample holder with two strips of electrical tape so that the water droplet can be directly placed on top of the yarns. Contact angle is measured by dispensing a water droplet of 2  $\mu\text{L}$  onto the surface of the test sample. The digital camera records the wetting process by capturing images at a rate of 25 images per second. Then, the captured images are analyzed using a computer with image processing software to obtain the contact angle of the water droplet. The change of contact angle with time is also recorded by generating the a 3-5 sec video using the captured images. The sessile drop test is performed for at least 10 times for each test sample and the test results are repeatable and reproducible.

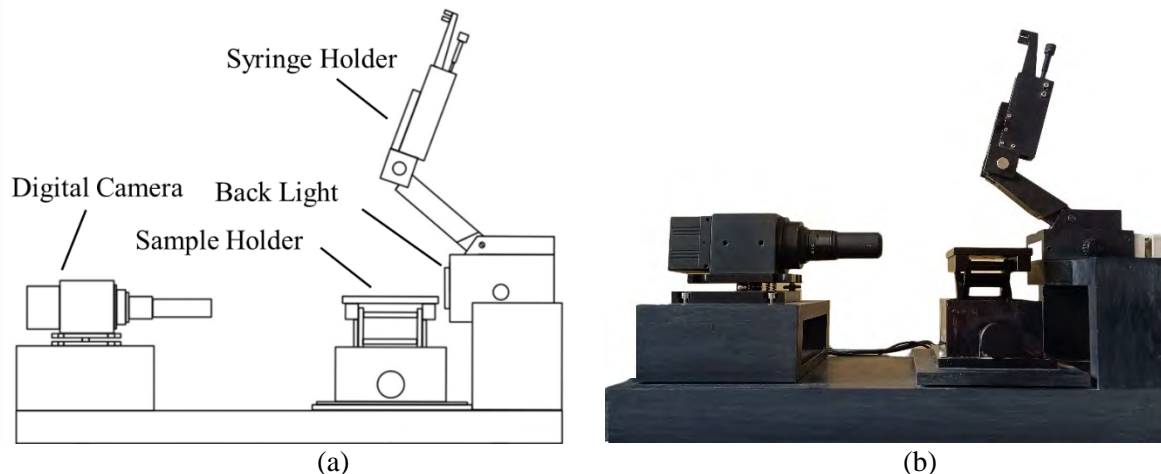


**Figure 3. Contact angle goniometer: (a) schematic plot, and (b) test setup**

## RESULTS AND DISCUSSIONS

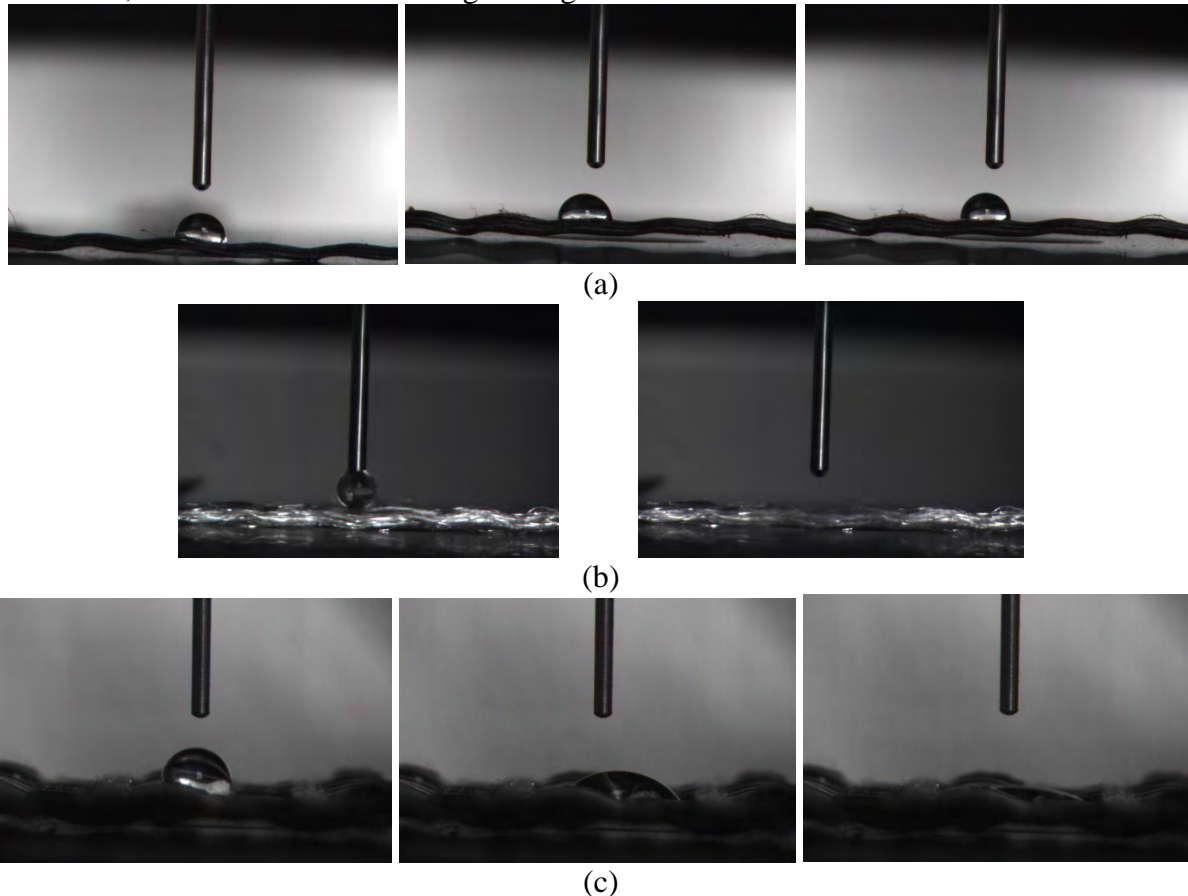
Wetting can be considered as a process of liquid-solid interface replacing gas-liquid and gas-solid interfaces. In comparison, spreading demonstrates a process of the solid-liquid interface replacing the gas-liquid interface meanwhile generating a new gas-liquid interface. In retrospect of Equations 1, if  $\gamma_{SL} - \gamma_{LG} < 0$ ,  $\cos \theta < 0$  and  $0^\circ < \theta < 90^\circ$ , indicates that the liquid can wet the surface of the solid and the surface of the solid is hydrophilic, and vice versa. Specifically, when  $\gamma_{SG} = \gamma_{SL} + \gamma_{LG}$ ,  $\cos \theta = 1$  and  $\theta = 0^\circ$ , means that the liquid can completely wet the solid surface, and the solid surface can be considered as a super-hydrophilic surface.

Figure 4 shows the sessile drop test results. Since the PP yarn is hydrophobic and the wicking yarn is hydrophilic, the wetting process of those two materials are expected to be different.

Figure 4a shows the shapes of the water droplet at 0s, 3s, and 5s during the wetting test of the PP yarn. The shapes of the water droplet do not change and the corresponding contact angles are  $96.7^\circ$ ,  $95.5^\circ$ , and  $96.3^\circ$ , respectively. This phenomenon indicates that for the PP yarns, the material is hydrophobic and the contact angle do not vary with time.

In contrast, Figure 4b shows the wetting process of the wicking yarn. The first image is captured before the water droplet is in contact with the wicking yarn. The shape of the droplet is spherical and the influence of gravity can be neglected. The second image shows the moment the water droplet is in contact with the wicking yarn and the water is laterally drained along the wicking yarn. Note that the time interval for taking the two images is  $1/25$  s and the water droplet is already laterally transported along the wicking yarn. This phenomenon indicates that water can completely spread over the fiber surface and the corresponding contact angle of the wicking yarn can be considered as  $0^\circ$ .

Figure 4c shows the wetting process of the wicking geotextile as an integrity. The first image shows the shape of the water droplet at the beginning of the sessile drop test and the corresponding contact angle is  $83.1^\circ$ . After that, as the water droplet is in contact with the hydrophilic wicking yarn, part of the water is laterally drained along the wicking yarn. The contact angle decreases to  $20.2^\circ$  at 1 s (second image in Figure 4c). As the wicking yarn continues to absorb water and to laterally transport water, the corresponding contact angle decreases to  $9^\circ$  at about 1.32s, as shown in the third image in Figure 4c.



**Figure 4. Wetting process: (a) PP yarn (hydrophobic), (b) wicking yarn (hydrophilic), and (c) wicking geotextile as an integrity**



Figure 5 further shows the changes of contact angles for the PP yarn, the wicking yarn, and the wicking geotextile as an integrity. For the PP yarn, the contact angle values ranges from 92° to 98°, with an average value of 95.5°. In contrast, the wicking yarn is super hydrophilic and the corresponding contact angle is 0°. As for the wicking geotextile, it is a composite material that consists of the PP yarn and the wicking yarn. The wettability of the wicking geotextile is expected to be in between of the PP and wicking yarns, and the test results also proves the authors' argument. The contact angle of the wicking geotextile is 87.2° at the beginning of the test, and quickly decreases to 20.1° at 1s, and further decreases to 9° at 1.3s.

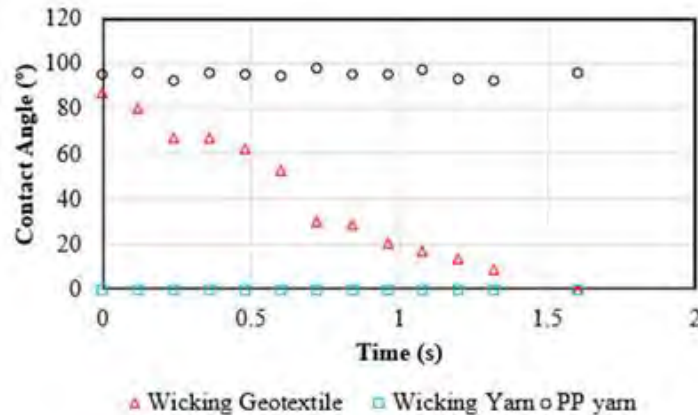


**Figure 5. Contact angles variations with time**

According to Cassie model, the contact angle of a composite material can be determined by using Equation 3. The fractal surface area for the PP yarn ( $f_1$ ) and the wicking yarn ( $f_2$ ) are 0.81 and 0.19, respectively. According to Figure 5, the corresponding contact angles,  $\theta_1$  and  $\theta_2$  are 95.5° and 0°, respectively. Therefore, the contact angle of the wicking geotextile is 83.1° based on Cassie model, which is consistent with the test results from the sessile drop test (87.2°).

## CONCLUSION

The wicking geotextile is composed of hydrophobic PP yarns and hydrophilic wicking yarns. How to evaluate the wettability of such a composite material is a key question for a better understanding of the interactions between the wicking geotextile and the water within the pores of a soil. This paper proposes a laboratory testing technique to determine the contact angle for the wicking geotextile based on Cassie model. Test results shows that the contact angles of the PP yarns and the wicking yarns are 95.5° and 0° respectively. Moreover, based on the sessile drop test, the contact angle of the wicking geotextile is 87.2° at the beginning of the test, decreases to 9° at 1.3s, and finally decreases to 0° at 1.5s. Last but not the least, the contact angle based on Cassie model is 83.1°, which is consistent with the value obtained from the sessile drop test.

## ACKNOWLEDGEMENTS

This study is sponsored by State Key Laboratory of Frozen Soil Engineering of China and the wicking geotextile is provided by TenCate Industrial Zhuhai Co., Ltd.

## REFERENCES

- Subaida, E.A., Chandrakaran, S., and Sankar, N. (2009). Laboratory performance of unpaved roads reinforced with woven coir geotextiles, *Geotextiles and Geomembranes*, 27(3), 204-210.
- Lee, S.L., Mannan, A.M., Ibrahim, H.W.W. (2020). Shear strength evaluation of composite pavement with geotextile as reinforcement at the interface, *Geotextiles and Geomembranes*, 48(3), 230-235.
- Guzman-Martinez, C.J., Farcia, F.E., and Vega-Posada A.C. (2022). Effects of hydro-mechanical material parameters on the capillary barrier of reinforced embankments, *Soils and Foundations*, 62(1), 101090.
- Zornberg, G.J., Azevedo, M., Sikkema, M., and Odgers, B. (2017). Geosynthetics with enhanced lateral drainage capabilities in roadway systems, *Transportation Geotechnics*, 12, 85-100.
- Pandey, P., Hossain, M.D.S., and Ahmed, A. (2021). Performance evaluation of modified moisture barrier in mitigating expansive soil associated pavement distresses, *Transportation Geotechnics*, 31, 100667.
- Lin, C., Zhang, X., and Han, J. (2018). Comprehensive material characterizations of pavement structure installed with wicking fabrics, *Journal of Materials in Civil Engineering*, 31(2), 04018372.
- Guo, J., Han, J., and Zhang, X. (2021). Experimental evaluation of wicking geotextile-stabilized aggregate bases over subgrade under rainfall simulation and cyclic loading. *Geotextiles and Geomembranes*, 49(6), 1550-1564.
- Lin, C., Zhang, X., Galinmoghdam, J., and Guo, Y. (2022). Working mechanism of a new wicking geotextile in roadway applications: a numerical study, *Geotextiles and Geomembranes*, 50, 323-336.
- Koc, M. and Bulut, R. (2014). Assessment of a sessile drop device and a new testing approach measuring contact angles on aggregates and asphalt binders, *Journal of Materials in Civil Engineering*, 26(3), 391-398.
- Florence, A.T. (2006). *Interfacial Forces in Aqueous Media*, 2<sup>nd</sup> ed., Taylor & Francis, Boca Raton, FL, USA.
- Ismail, F.M., Islam, A.M., Khorshidi, B., Tehrani-Bagha, A., and Sadrzadeh, M. (2022). Surface characterization of thin-film composite membranes using contact angle technique: review of quantification strategies and applications, *Advances in Colloid and Interface Science*, 299, 102524.
- Wenzel, R.N. (1949). Surface roughness and contact angle, *Journal of Physical and Colloid Chemistry*, 53, 1466-1497.
- ASTM D5725-99 (1999). Standard Test Method for Surface Wettability and Absorbency of Sheeted Materials using an Automated Contact Angle Tester, *ASTM International*, West Conshohocken, Pennsylvania, USA.

## Efficacy of Nonwoven Based Geosynthetic Drainage Product for Pore Pressure Reduction in Moderately Fine Soils or Tailings

I.R. Fleming, Ph.D., P.Eng.,<sup>1</sup> Michael G. Andree, B.E.,<sup>2</sup> and  
S. Fourmont<sup>3</sup>

<sup>1</sup>Civil Eng., Univ of Saskatchewan, Saskatoon, SK Canada S7N 5A9; [ian.fleming@usask.ca](mailto:ian.fleming@usask.ca)

<sup>2</sup>Civil Eng., Univ of Saskatchewan, Saskatoon, SK Canada S7N 5A9; [michael.andree@usask.ca](mailto:michael.andree@usask.ca)

<sup>3</sup>Afitex-Textel Geosynthetics, Boucherville, QC, Canada J4B 2X3; [sfourmont@afitextexel.com](mailto:sfourmont@afitextexel.com)

### ABSTRACT

A common challenge in geotechnical engineering is to reduce pore pressures in fine-grained soils or tailings and geosynthetic drainage may be proposed for such applications. Depending on the relative unsaturated permeability of soil and geotextile, a capillary break may develop, resulting in higher water content in the soil along with increased pore pressure (or lower suction) and consequent decrease in factor of safety against slope failure. While high (saturated) geotextile permeability may be desirable under some conditions, formation of a capillary break inhibits drainage and compromises overall performance of the soil/geosynthetic system. In this study, the water characteristic curve (GWCC) was measured for a common geocomposite drainage product. An unsaturated permeameter was used to measure permeability under limited matric suction. The applicability of the Fredlund-Xing equation to estimate unsaturated permeability from the GWCC was confirmed. A series of transient and steady-state experiments were carried out in a lab-scale physical model with two different silt-sized soils to confirm that the unsaturated behaviour of the soil/geosynthetic composite system could be predicted by independent laboratory measurements of the two materials. Finally, numerical simulations were conducted of the performance of the drainage product in reducing pore-pressures in an unsaturated embankment subject to rainfall.

### INTRODUCTION & BACKGROUND

The performance of a geosynthetic in any geotechnical engineering application depends on the resulting *soil-geosynthetic system*. In some cases, measurement of soil and geosynthetic properties separately is insufficient to enable the response of the composite system to be predicted. In the case of geosynthetic drainage, historical emphasis has been on saturated properties (i.e. standards for measurement of saturated permeability for in-plane or cross-plane directions). As is well established in geotechnical engineering, permeability (or hydraulic conductivity) soil is not a *value* (although the saturated conductivity  $k_{SAT}$  is), but rather a *function*, depending upon the degree of saturation, or more commonly expressed as a function of soil suction (Fredlund et al, 2012).

The soil-water characteristic curve (SWCC) is characterised by the following parameters (Fredlund et al, 2012):

- i. saturated water content (= porosity);
- ii. the air-entry value (AEV) for drying curves or the water-entry value (WEV) for wetting curves which is the suction at which air begins to enter the larger pores of a saturated soil or water enters the finest pores of a dry soil; and
- iii. the residual water content and residual suction.

The performance under field conditions of a drainage geosynthetic placed within fine or moderately fine-grained soil or soil-like materials (i.e. mine tailings) will therefore depend on the unsaturated permeability of the two (or more) materials *and their interaction*. The capillary barrier effect occurs when a finer material overlies a coarser material, and the system is subject to downward vertical flow. The capillary barrier effect has been extensively studied in the context of soil covers for mining waste by Nicholson et al (1989), Barbour (1990), Akindunni et al (1991), O'Kane et al (1998) Bussi re et al (2003) along with numerous others. Figure 1 shows the vertical distribution of pressure head and water content under steady state downward vertical flow through such a system (Barbour, 1990).

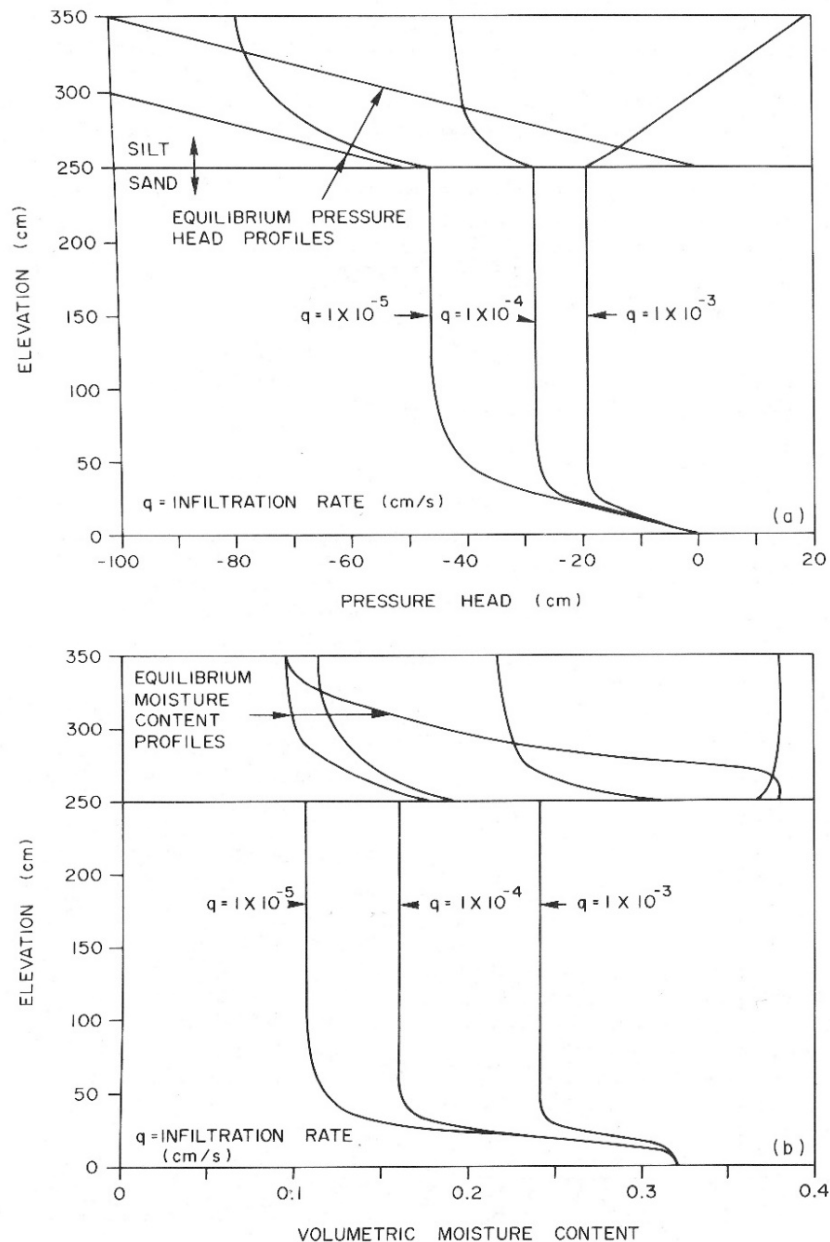


**Fig. 1. Profiles of pressure head and volumetric moisture content vs. elevation for silt over sand under constant infiltration rate. (from Barbour, 1990 used with author's permission)**



For geotextiles, work by Henry (1990 and 1995), Stormont and Morris (2000), and Henry and Holtz (2001) evaluated the use of geotextiles as moisture limiting barriers in unsaturated soils. Their work focused on the change in hydraulic behaviour of an unsaturated, layered soil system due to the inclusion of a nonwoven geotextile and concluded that a geotextile may be effective in mitigating upward moisture migration in unsaturated soils.

Numerous studies have been conducted to obtain the WCC of nonwoven geotextiles which are characterized by low AEW and desaturate at relatively low suctions compared to soils. Various testing methods have been used, and the literature shows general agreement between methods ranging from simple to complex. Stormont et al (1997) and Lafleur et al (2000) both performed hanging column tests on several nonwoven geotextiles along consecutive wetting and drying paths which demonstrated the difference between geotextile products, wet/dry hysteresis, and the impact of manufacturing surfactants. The WCC was unique for each geotextile product. Knight and Kotha (2001) measured the WCC of a nonwoven geotextile by controlling water outflow in a capillary pressure cell and compared the methodology to that of Stormont et al. (1997). The method allowed for control of the suction and thus volumetric water content of the specimen by precisely applying small increments of air pressure and suggest that that this method provides more detail in the curve in a fraction of the time of the hanging column method. Knight and Kotha (2001) repeated the test with one, three, and six geotextile samples stacked in the cell and found the WCC was unaffected.

In the Stormont et al (1997) study, when wetted a second time, the geotextile reached a reduced peak water content due to air entrapment from drying. Residual surfactants from manufacturing reduced the saturated water content of the geotextile. This is similar to the findings of Park & Fleming (2004) who showed the effect on the WCC of both the test method (hanging column and pressure plate) which suggested evaporation loss in a hanging test, even with the sample contained in a humid polyethylene tube and also confirmed the effect of pre-washing the sample to remove the lubricating oils used during needle-punching (Figure 3).

In addition to comparing geotextiles composed of polypropylene (PP) and polyester (PET), Stormont & Morris (2000) also considered the wetting behavior of the PET geotextile when modified with clay, silt and sand and found that it increased the WEV compared to the unmodified geotextile. Similarly, Bathurst et al. (2009) obtained a WRC for a nonwoven PP geotextile in a suction plate apparatus as part of a sand column infiltration study. Samples were tested in a new condition and a modified condition, which involved rubbing the sample with a wet kaolin paste. Excess kaolin was brushed off after drying. The tests were conducted along drying paths following by wetting paths and the authors noted the considerable difference between modified and new samples, with the saturated water content more closely resembling that of the kaolin.

McCartney and Znidarcic (2010) measured the WCC of a nonwoven geotextile using a permeameter with flexible walls. The approach is far more complex than those previously discussed, requiring a specially designed system and pump. The apparatus enabled application of higher confining pressure to their samples than is possible in a pressure plate cell. Previous students at the University of Saskatchewan (Park, 2005, Cunningham, 2018, Andree, 2021) have used a Tempe cell suction plate apparatus to measure drying WCCs of nonwoven geotextiles. The cell was modified to allow for confining pressure to be applied vertically through the cap as shown in Figure 2. Typical results are presented in Figure 4.

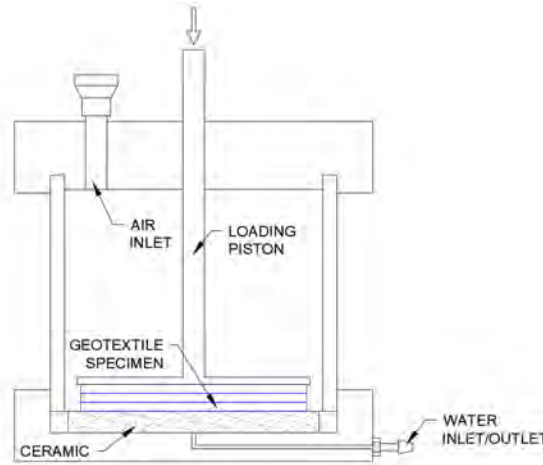


**Figure 2. Pressure cell apparatus used at Univ of Saskatchewan to measure WCC of nonwoven geotextile under varying normal stress.**

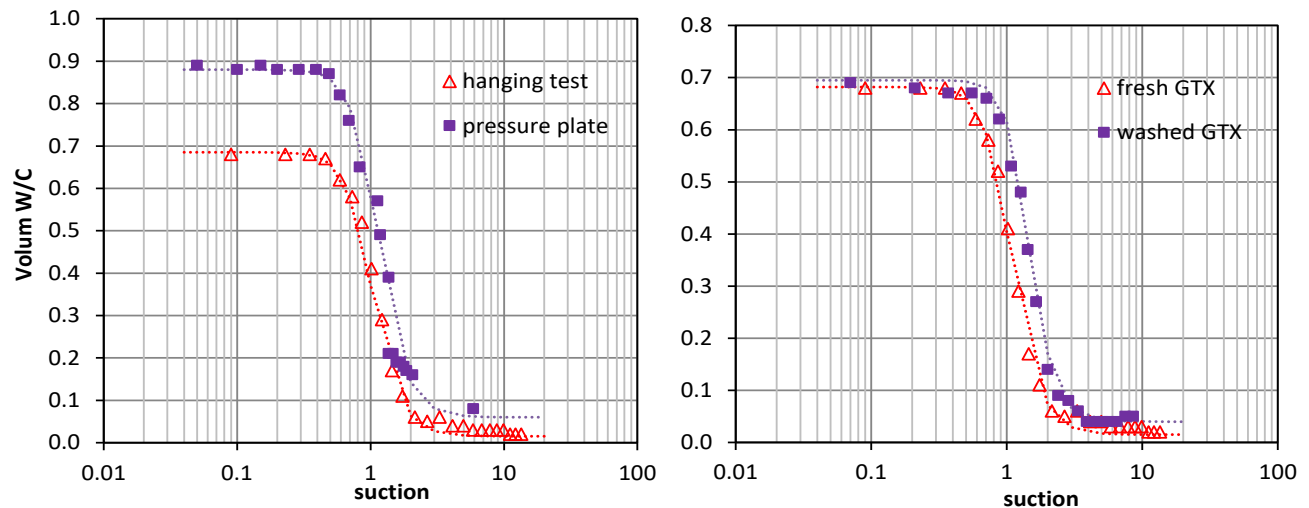


**Figure 3. Wetting and drying WCC for nonwoven geotextile and effect of washing the fabric (left) and effect on WCC of test method (right) From Park & Fleming, 2004.**

Determination of the unsaturated hydraulic conductivity of nonwoven geotextiles is a challenging undertaking at a single point of suction, let alone at a variety of suctions. For this reason the common practice is to use curve-fitting parameters based on the WCC to predict the hydraulic conductivity function of a material (e.g. van Genuchten 1980, Fredlund et al. 1994). On the other hand, Iryo and Rowe (2003) showed that the predicted K-functions based on WCC curve fitting parameters for geotextiles may not show good agreement with observed values, perhaps due to the different pore shapes for particle vs fibre based porous media.

This presents a challenge for application of geosynthetic drainage to finer grained soils or soil-like materials such as tailings as a capillary break will often develop (Park & Fleming, 2004). A number of additional studies have examined this, including Bathurst et al, (2009) who constructed a sand column, sand-new geotextile column, and sand-modified geotextile column where the geotextile was rubbed with a kaolin paste. Instead of applying water by infiltration, a 225 cm total head was applied at the top, and 20 cm at the bottom. The pore pressure at the wetting

front was observed with tensiometers. In the sand-only column there was no evidence of a capillary break, however, a capillary break formed in both geotextile columns. For the new geotextile, pressure above the geotextile reached 0.5 kPa. In the modified geotextile column, the influence of kaolin clogging increased the pressure above the geotextile to near 5 kPa. The degree of ponding suggests that the WCCs are not conservative as they do not accurately capture the soil-geotextile interaction. However, the application of a total head boundary rather than an infiltration boundary could be the cause of this high pressure, as similar studies did not exhibit pressures above 0 kPa.

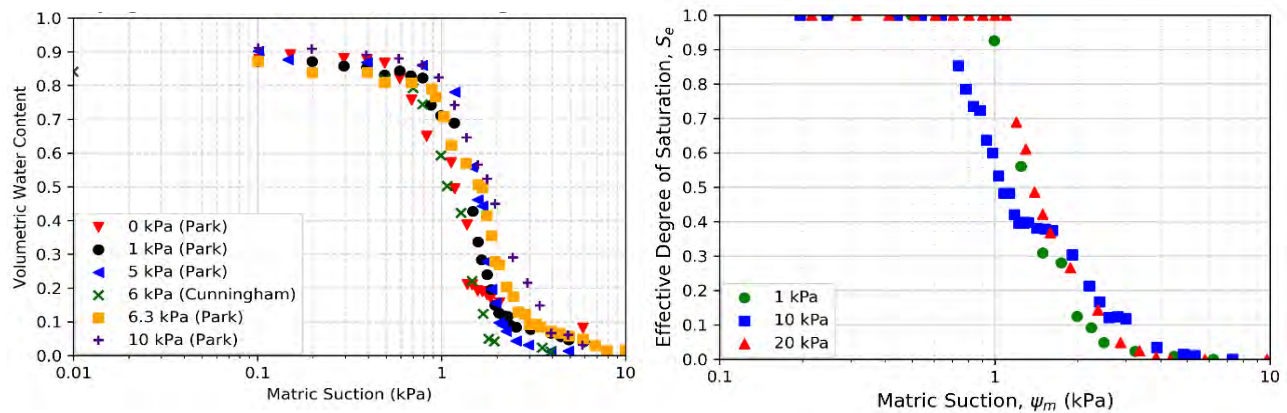


**Figure 4. Previous work at UofS showing effect of normal stress on WCC of nonwoven geotextiles (left, Park, 2005 & Cunningham, 2018; right Andree & Fleming, 2021).**

Portelinha and Zornberg (2017) constructed a nonwoven PET geotextile-reinforced wall with a clayey sand backfill. Backfill was compacted and five reinforcement layers were placed sloping toward a geocomposite drain and shotcrete facing. A simulated rainfall was applied from the top of the wall. Frequency Domain Reflectometry (FDR) was used to monitor water content at the midpoint above each geotextile layer and tensiometers were placed immediately over each geotextile. A large FDR array was placed in the topmost layer to evaluate the development of a capillary barrier. Once the rainfall was applied, no ponding was observed. As the infiltration front advanced, the volumetric water content reached an equilibrium of 0.31 compared to the initial 0.26. As the front reached the top geotextile layer, FDR sensors in the upper layer approached a saturated water content of 0.36, indicating that a capillary barrier was formed. This resulted in a 4 day delay for infiltration to reach each subsequent layer until suction reduced to breakthrough. In total, it took 30 days to reach the bottom of the wall. Piezometers at the geotextile-soil interface showed that pressure reached 0 kPa but did not rise above. Moisture sensors in the bottom four layers did not detect saturated water content at any point. The geotextiles were ineffective as drains until breakthrough of each capillary break occurred. In total, 25% of the water volume was diverted through the geotextiles. Wetting stains on the shotcrete facing indicated that most drainage occurred in the upper layers.

All of the above studies have clearly shown that under most conditions, the hydraulic properties of nonwoven geotextiles are similar to those of sands or fine gravels. This is not particularly surprising. While nonwoven geotextiles are not *coarse-grained*, the experimentally obtained WCCs do imply that they are *coarse-pored* and have a similar average pore size to sands and gravels (Zornberg et al. 2010).

## MATERIALS & METHODS

The current study was intended to evaluate the performance of a drainage geocomposite DrainTube© which incorporates small perforated corrugated mini-pipes placed in pockets between two layers of the 2 or-3 geotextile layers that are needle-punched together. First, the SWCC was measured for the various layers of nonwoven geotextile under various normal loads (Figure 4r). Subsequently, an in-plane unsaturated permeameter was designed and built so as to enable a range of normal (cross-plane) stress to be applied to a sample while in-plane flow is measured under a range of hydraulic gradients (Figure 5). This apparatus was loosely based on previous work (Stormont et al. 1998, Stormont & Morris, 2000) in which unsaturated in-plane geotextile transmissivity was directly measured.

Andree and Fleming (2021) described the apparatus and presented results for  $k(\psi)$  up to about 2 kPa of suction at which this particular nonwoven geotextile was at about 20% effective saturation. Significantly, it was found (Andree et al, 2022) that using the formulation of Fredlund et al (1994) to predict the  $k(\psi)$  unsaturated permeability function a better fit was found than had been possible using the formulation of van Genuchten (1980). This addresses a concern that had been raised by Iryo & Rowe (2003) that given that the methods to estimate  $k(\psi)$  from the WCC are based on experiments with soil (a particulate porous media), these same fitting parameters might not be adequate for fibre-based porous media such as nonwoven geotextiles. SWCC fitting parameters for all materials are included in Table 1.

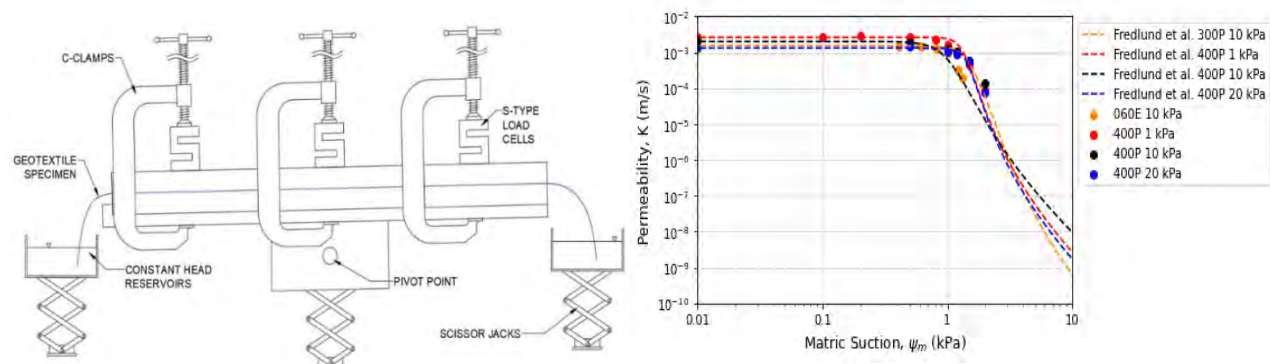


**Figure 5. Unsaturated permeameter for nonwoven geotextiles under normal stress.**

**Table 1. Fitting parameters for all materials used in this study.**

Material (Vertical Load)	van Genuchten		Fredlund and Xing (1994)		
	$a_{vg}$	$n_{vg}$	$a_{fx}$	$n_{fx}$	$m_{fx}$
Geotextile 1 (1 kPa)	1.28	5.71	1.19	7.79	1.46
Geotextile 1 (10 kPa)	0.98	3.22	0.86	4.45	1.21
Geotextile 1 (20 kPa)	1.39	6.36	1.27	8.56	1.40
Geotextile 2 (10 kPa)	1.42	5.31	1.43	5.23	2.15
Aluminum Oxide Grit	9.96	8.98	8.28	14.81	0.64
Sand	10.90	11.72	9.14	24.61	0.40

A lab-scale physical model was then constructed which incorporated a layer of the drainage geocomposite. Under various infiltration rates the capture rate of the geocomposite was measured at varying position and height above the water table. Electronic tensiometers (METER Terros 31)



were placed at various elevations above and below the geocomposite as shown in Figure 6. The mini-pipes in the drainage geocomposite were connected directly to small laboratory valves installed in the sidewall. Pinholes were also drilled through the sidewall to allow collection and quantification of the water flowing in the nonwoven between the mini-pipes.

The apparatus was filled with two different moderately fine-grained soil materials. One was a commercially available aluminum oxide (alox) grit that is commonly used for sandblasting. The second material was a rock crusher dust that was sieved to a particle size of 75-150 microns with some fines present. Both soils are classified by USCS as silty sands and have similar grain size distribution (GSD) and WCC as shown in Figure 7.

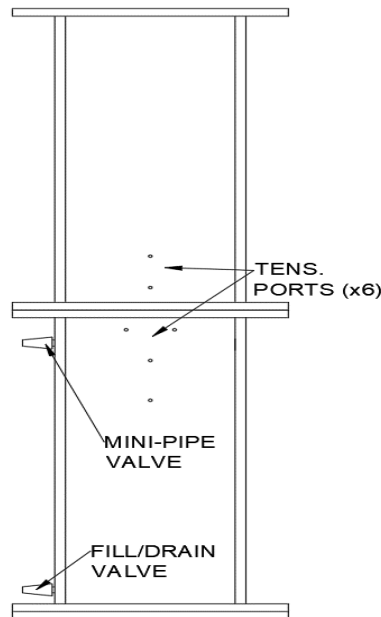


**Figure 6. Lab-scale physical model**

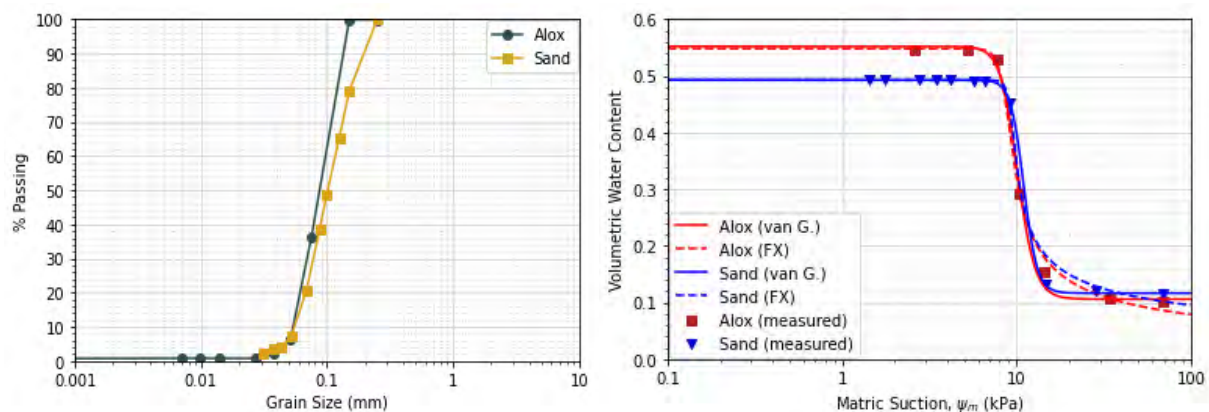


**Figure 7. Grain size distribution and SWCC for the two soils used in the lab scale model.**

## RESULTS & ANALYSES

The capture efficiency was found to be dependent chiefly on the infiltration rate and depth to the water table. As shown in Figure 8, the capture efficiency was higher when the water table is shallower. Interestingly, capture occurred with a water table at 220 mm below the geosynthetic in the sand but did not occur at similar conditions when applied over the alox grit.

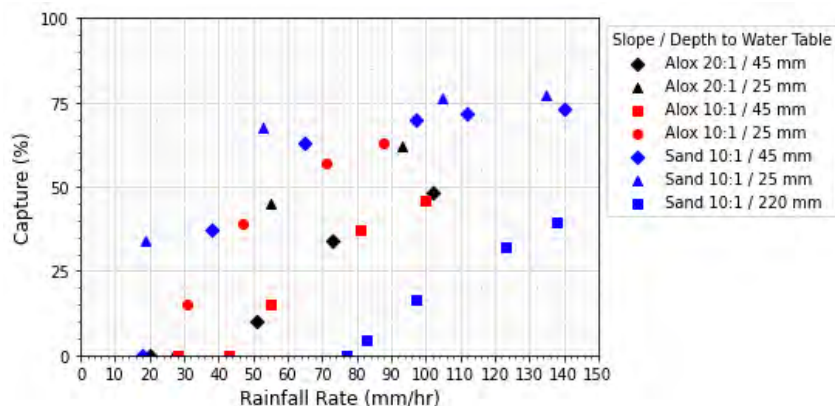


**Figure 8. Capture efficiency in the lab-scale physical model**

These results were then satisfactorily reproduced with a 3D saturated-unsaturated finite element simulation using GeoStudio SEEP3D using the same dimensions as the physical infiltration apparatus. A unique steady-state analysis was created for each rainfall rate and water table level that was experimentally tested. The geotextile was represented as a 3 mm thick prism with a 1 mm mesh. The soil near the geotextile was meshed similarly fine and became larger with distance from the geotextile. The mini-pipe was represented as a “seepage face” boundary condition, which requires the program to review the nodes along the boundary to check for positive pressures. If pressures are above 0 kPa, the node is set to a zero-pressure boundary condition. The downstream end of the geotextile was also represented by this condition.

Calibration was achieved simply by adjusting the saturated permeability of the geotextile, aloxx grit, and sand. The WCC’s were also slightly “softened” by changing the fitting parameters to smooth the sharp transition between saturated, desaturation, and residual states which enhances the solver’s ability to converge while not significantly altering the characteristics of the material

The lab-scale physical model demonstrated that the material properties and interaction in a composite soil-geosynthetic system may be characterised using laboratory-determined properties for the materials determined independently. In order to evaluate the anticipated performance of the drainage geocomposite under service conditions, transient 3D saturated-unsaturated seepage models were constructed in SEEP3D based on the 3 m tall embankment model by Iryo and Rowe (2005b). Analyses considered durations of several days to achieve a steady-state pressure condition. The model geometry and boundary conditions are shown in Figure 9.

The results shown in Figure 10 clearly show the development of a capillary barrier effect at the geosynthetic-soil interfaces with greater severity at the upper elevations, exceeding the base case pressure. The geosynthetic-only case provided little reduction in pressure head over the base case over the full profile, while the inclusion of mini-pipes provided relief of pore pressure, particularly between elevations 0 m and 0.75 m. It is also evident that a tighter spacing of mini-pipes provides a greater reduction in pressure head, particularly at the embankment toe.

Boundary	Boundary Condition	Notes
Lateral Extents, Back, Bottom	No-Flow	-
Top	Flux Rate (m/s)	Rainfall Rate
Slope Face	Flux Rate (m/s) with Seepage Face	Rainfall Rate (adjusted for slope)
Geotextile ends at Slope Face	Flux Rate (m/s) with Seepage Face	Rainfall Rate (adjusted for slope)
Mini-Pipe	Seepage Face	0 m upon review

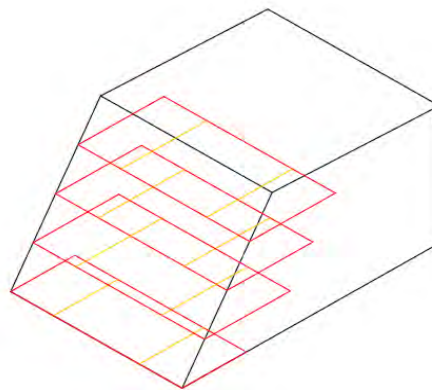
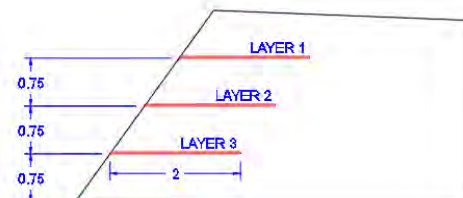
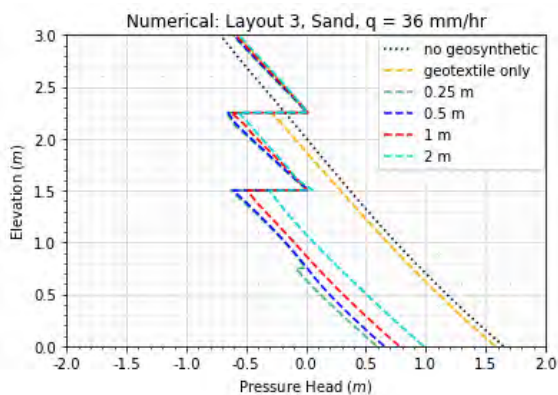
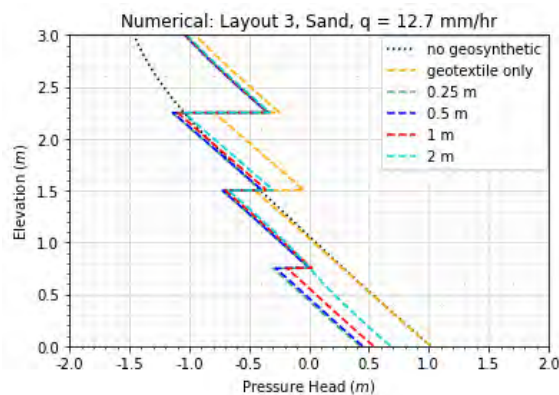


Figure 9. Numerical model setup for the 3 m embankment

Figure 10. Numerical model results for the 3 m embankment

## CONCLUSION



The work summarised in this paper has clearly demonstrated that the principles of unsaturated soil mechanics apply to fibre-based porous media just as they do to particulate porous media. The fitting parameters of Fredlund et al (1994) may be used to estimate  $k(\psi)$  with a good degree of fit to carefully-obtained experimental data (the fitting parameters of van Genuchten (1980) do not provide the same degree of fit and have no advantage in the authors' opinion).

Physical modelling showed that laboratory-determined WCC's (and consequently  $k(\psi)$  functions) obtained independently for the soil and geosynthetic materials can be used as inputs in saturated-unsaturated numerical seepage models to describe the performance of the soil-geosynthetic composite system (at least for these specific materials tested).

For the 3m embankment composed of silty sand, placement of a drainage geocomposite may introduce the capillary barrier effect.

In the case where nonwoven geotextile alone is used, numerical simulations suggested that pore pressures (or matric suction) would be unchanged in the lower 1.5 m of the structure and that suction would be decreased (i.e. higher water content) in the upper 1.5 metres, thus decreasing stability. Addition of the mini-pipes improved performance relative to the nonwoven alone, increasing suction in the lower 2.25 m – most of the embankment. – and thus increasing stability.

In general it may be concluded that for moderately fine materials, placement of geosynthetic drainage can be beneficial, but the designer must be careful to avoid certain combinations of material properties, geometry and hydraulic loading under which the capillary barrier effect can increase pore pressure and reduce stability.

In order to ensure success, the geotechnical engineer is well-advised to carry out proper laboratory characterisation of the unsaturated properties of the soils as well candidate geosynthetic materials. Properly conducted, numerical simulations of saturated-unsaturated flow can be used to evaluate variations in geometry, layer spacing etc to evaluate the response of the system and select design parameters for improved stability.

## REFERENCES

- Akindunni, F.F., Gillham, R.W., and Nicholson, R.V. 1991. Numerical simulations to investigate moisture-retention characteristics in the design of oxygen-limiting covers for reactive mine tailings. *Canadian Geotechnical Journal*, **28**, pp. 446-451.
- Andree, M.G. and Fleming, I.R., 2021. Unsaturated Characterization and Permeability of a Nonwoven Geotextile, *GeoNiagara 2021 74<sup>th</sup> Canadian Geotechnical Conference*
- Andree, M.G., Fleming, I.R., and Fourmont, S., 2022. A numerical study on the pressure-reducing ability of a nonwoven geotextile based drainage product in an unsaturated embankment subject to rainfall, *GeoCalgary 2022 75<sup>th</sup> Canadian Geotechnical Conference*.
- Barbour, S.L. 1990. Reduction of acid generation in mine tailings through the use of moisture-retaining cover layers as oxygen barriers. *Canadian Geotechnical Journal*, **27**, pp. 398-401.
- Bathurst, R.J., Siemens, G., and Ho, A.F. 2009. Experimental investigation of infiltration ponding in one-dimensional sand-geotextile columns. *Geosynthetics International*, **16**(3) pp. 158–172.
- Bussière, B., Aubertin, A., and Chapuis, R.P. 2003. The behaviour of inclined covers used as oxygen barriers. *Canadian Geotechnical Journal*, **40**, pp. 512-535.
- Cunningham, H. & Fleming, I.R. 2017 Analysis of flow through a defect in geomembrane in a large-scale constant head apparatus, *70th Canadian Geotechnical Conference, Ottawa*
- Fredlund, D.G., Rahardjo, H., and Fredlund, M.D., 2012. *Unsaturated Soil Mechanics in Engineering Practice*. Wiley Interscience., New York, NY, USA. ISBN: 9781118133590
- Fredlund, D.G., and Xing, A. 1994. Equations for the soil-water characteristic curve. *Canadian Geotechnical Journal*, **31**(4), pp.521-532.
- Fredlund, D.G., Xing, A., and Huang, S. 1994. Predicting the permeability function for unsaturated soils using the soil-water characteristic curve. *Canadian Geotechnical Journal*, **31**(4): 533–546.
- Iryo, T., and Rowe, R.K. 2003. On the hydraulic behavior of unsaturated nonwoven geotextiles. *Geotextiles and Geomembranes*, **21**(6): 381–404.
- Knight, M.A., and Kotha, S.M. 2001. Measurement of Geotextile-Water Characteristic Curves Using a Controlled Outflow Capillary Pressure Cell. *Geosynthetics International*, **8**: 271–282.
- Lafleur, J., Lebeau, M., Faure, Y.-H., Savard, Y., and Kehila, Y. 2000. Influence of Matric Suction on Drainage Performance of Polyester Geotextiles. *53rd Canadian Geotechnical Conference, Montréal, QC*.
- McCartney, J.S., and Znidarcic, D. 2010. Testing system for hydraulic properties of unsaturated nonwoven geotextiles. *Geosynthetics International*, **17**(5): 355–363.



- Meier, A., Fleming, I.R., Barbour, S.L., Ayres, B. and O’Kane, M. (2006). “Field Scale Trials of a Geosynthetic Capillary Break.” *59th Canadian Geotechnical Conf.*, Vancouver, pp160-165.
- Nicholson, R.V., Gillham, R.W., Cherry, J.A., and Reardon, E.J. 1989. Reduction of acid generation in mine tailings through the use of moisture-retaining cover layers as oxygen barriers. *Canadian Geotechnical Journal*, **26**, pp. 1-8.
- O’Kane, M., Wilson, G.W., Barbour, S.L., 1998. Instrumentation and monitoring of an engineered soil cover system for mine waste rock. *Canadian Geotechnical Journal*, **35**, pp. 828-846.
- Park, K.D. and Fleming, I.R. (2004). Determination of unsaturated properties of a nonwoven geotextile for use in a geocomposite capillary barrier. *57th Canadian Geotechnical Conference*, Québec, Session 5E pp36-43.
- Park, K.D. and I.R. Fleming, (2005). One-dimensional column testing for evaluation of a geosynthetic capillary break. *58th Can. Geotechnical Conference*, Saskatoon.
- Park, K.D. and Fleming, I.R. (2006). Evaluation of a geosynthetic capillary barrier. *Geotextiles and Geomembranes*, **24**(1), pp. 64-71.
- Portelinha, F.H.M., and Zornberg, J.G. 2017. Effect of infiltration on the performance of an unsaturated geotextile-reinforced soil wall. *Geotextiles and Geomembranes*, **45**(3), pp. 211–226.
- Stormont, J.C., Henry, K.S., and Evans, T.M. 1997. Water Retention Functions of Four Nonwoven Polypropylene Geotextiles. *Geosynthetics International*, **4**(6), pp. 661–672.
- Stormont, J.C., Evans, T.M., Stockton, T.B., and Ray, C. 1998. Unsaturated Hydraulic Properties of a Nonwoven Polypropylene Geotextile. *Joint Conference on the Environment, Waste-management Education and Research Consortium*. Albuquerque, NM. pp. 213–216.
- Stormont, J.C., and Morris, C.E. 2000. Characterization of Unsaturated Nonwoven Geotextiles. *Advances in Unsaturated Geotechnics*. ASCE, Reston, VA. pp. 153–164.
- van Genuchten, M.T. 1980. A Closed-form Equation for Predicting the Hydraulic Conductivity of Unsaturated Soils. *Soil Science Society of America Journal*, **44**(5), pp. 892–898.
- Zhang, X. & Belmont, N. 2011. Use of Wicking Fabric to Help Prevent Differential Settlements in Expansive Soil Embankments *GeoFrontiers 2011*, American Society of Civil Engineers
- Zornberg, J.G., Bouazza, A., and McCartney, J.S. 2010. Geosynthetic capillary barriers: Current state of knowledge. *Geosynthetics International*, **17**(5), pp. 273–300.
- Zornberg, J.G., Azevedo, M., Sikkema, M., and Odgers, B. (2017). Geosynthetics with Enhanced Lateral Drainage Capabilities in Roadway Systems. *Transportation Geotechnics*, **12**, pp. 85-100.

## Experimental Investigation on the Effect of Fines Content on the Drainage Performance of Wicking and Non-wicking Geotextiles

Javad Galinmoghadam<sup>1</sup>, Xiong Zhang, Ph.D., P.E.<sup>2</sup>, and  
Mahtab Delfanazari<sup>3</sup>

<sup>1</sup>Department of Civil, Architectural, and Environmental Engineering, Missouri University of Science and Technology, Rolla, MO, 65401; e-mail: [j.galinmoghadam@mst.edu](mailto:j.galinmoghadam@mst.edu)

<sup>2</sup>Department of Civil, Architectural, and Environmental Engineering, Missouri University of Science and Technology, Rolla, MO, 65401; e-mail: [zhangxi@mst.edu](mailto:zhangxi@mst.edu)

<sup>3</sup>Department of Civil, Architectural, and Environmental Engineering, Missouri University of Science and Technology, Rolla, MO, 65401; e-mail: [m.delfanazari@mst.edu](mailto:m.delfanazari@mst.edu)

### ABSTRACT

It is well known that soil engineering properties can be improved by reducing water content. The amount of improvement in soil properties is a function of soil type and the amount of water that has been removed from it. The amount of water that can be extracted from the soil varies with soil type and drainage system. For a specific drainage system, the soil type affects the amount of water available to the drainage system.

Many conventional drainage systems can only work under saturated to nearly saturated conditions. On the contrary, wicking geotextile has proven to be effective under both saturated and unsaturated conditions. Thus, it can extract more water from soils under similar conditions and provide more improvement in soil properties. Consequently, even if in-situ soil that is drained using conventional systems might not meet the design strength requirement, it could be suitable when it is used with the wicking geotextile as the drainage system. In this way, the quality requirement for soil can be reduced resulting in cost savings.

In this study, the drainage performance of a wicking geotextile was investigated in 5 different types of soils with fines content varying from 0 to 20% in a set of laboratory experiments. The drainage performance of the wicking geotextile was compared to the non-wicking geotextile with similar properties. For this purpose, a box filled with different soils was instrumented and the soil moisture content was continuously monitored. Results suggested that in soil having fines contents of less than 15%, wicking geotextile drained more water. However, at higher fines contents, the non-wicking geotextile drained more water from the soil.

### INTRODUCTION

The engineering properties of soil can be improved by decreasing its water content. An increase in soil moisture causes a reduction in soil stiffness and strength leading to damage and increasing the cost of repair and maintenance. While soil moisture can vary due to climatic and subsurface flow conditions, drainage systems are installed to control soil moisture.

Geotextiles have been used for many applications that are either directly or indirectly related to controlling soil moisture (Han, 2013, 2015; Zornberg, 2017). For instance, numerous studies have been conducted on the effect of using geotextile to mitigate fines migration and pumping issues in roads and railways (Al-Qadi et al., 2004; Alobaidi and Hoare, 1996, 1998; Kermani et al., 2018; Yang and Yu, 1989). Although in these studies, the filtration and separation

functions of the geotextiles were their focus, if soil moisture was controlled, fines migration would not happen and thus, there would be no need to use the geotextile separation and filtration functions. In cold regions, geotextiles have been used to minimize frost heave and thaw weakening by directly removing soil moisture (Al-Qadi et al., 2004; Ghazavi and Roustaei, 2013; Henry, 1990; Henry and Holtz, 2001; Kebria et al., 2022; Raymond et. al, 2000).

In recent years, a new type of wicking geotextile has been developed. Different from conventional geotextiles, the wicking geotextile was designed with polyethylene multifilament fibers for reinforcement and specially designed nylon wicking fibers with deep grooves for lateral drainage purposes (Lin et al, 2021a). Wicking geotextile can have drainage, filtration, separation, and reinforcing functions. Several studies have shown that the wicking geotextile effectively drains water under both saturated and unsaturated conditions for a variety of applications (Currey, 2016; Galinmoghadam et al., 2022; Guo et al., 2017; Lin et al., 2016, 2021b; Wang et al., 2017; Zhang and Presler, 2012; Zhang et al., 2014). The soil types in these studies vary from clay and silt to sand and gravel. Up to now, there is no information on the soil type in which, wicking geotextile can effectively drain water. This study aims to compare the drainage performance of the wicking geotextile in soils with different fines contents to obtain the limiting fines content for drainage application. To better compare the results, the drainage performance of the wicking geotextile was compared to a non-wicking geotextile with similar properties.

## MATERIALS AND METHOD

**Materials.** The soils used in this study were obtained by mixing different percentiles of sandy silt with clean sand. The sandy silt soil had a gravel, sand, and fines content of 0%, 49%, and 51%, respectively, and its group symbol was ML based on the unified soil classification system (USCS). The clean sand on the other hand had a gravel, sand, and fines content of 2%, 98% and 0%, respectively, and had a group symbol of SP based on USCS. These two soils were mixed at different percentiles to provide soil mixes with different fines contents of 5%, 10%, 15%, and 20%. Then the soils with 0%, 5%, 10%, 15%, and 20% fines content were used to investigate the drainage performance of wicking and non-wicking geotextiles. The particle size distribution of the ML and SP soils along with the different soil mixes are shown in Figure 1.

In this study, the drainage performance of a wicking geotextile (Mirafi ® H2Ri that will be referred to as WG hereafter) was studied when installed in soils with different fines content. For comparison purposes, a non-wicking geotextile (Mirafi ® RS580i that will be referred to as NWG hereafter), with similar properties to the WG was used in the same soil mixtures. The weaving pattern and the apparent opening size of both geotextiles are identical (AOS = 0.425 mm). Additionally, both geotextiles share the same reinforcing wrap and weft yarns. Their only difference is that in the NWG, the wicking warps were replaced by non-wicking yarns.

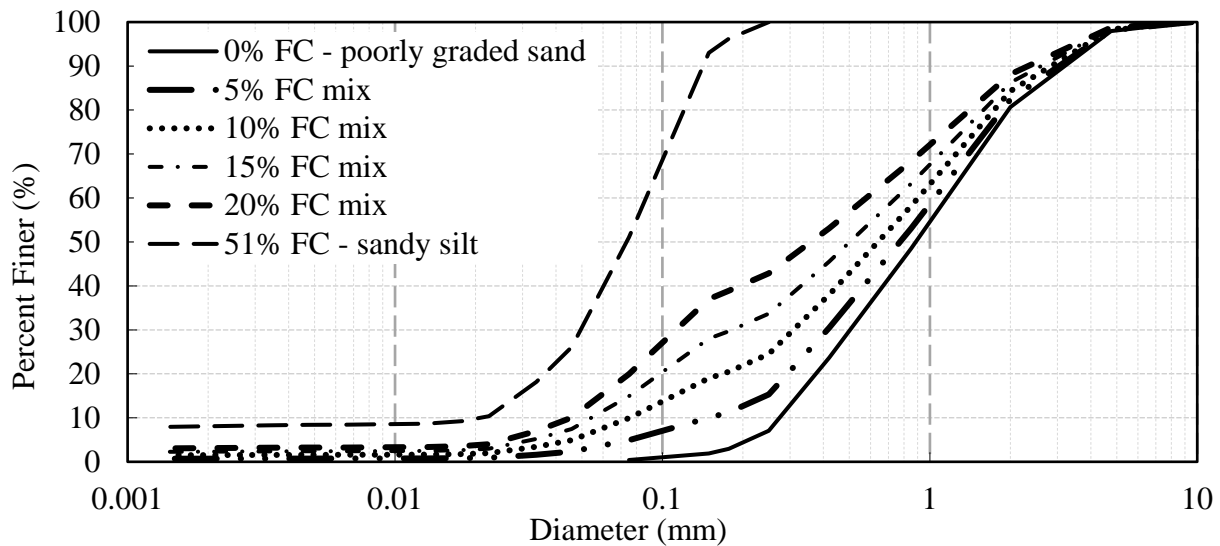


**Figure 1. Soil gradation curves of the different soil mixes.**

Figure 2a shows a picture of the WG used in this study and its schematic cross-section. As depicted in Figure 2a, WG has two different warps which are weaved by wefts. The reinforcing warp is made of polypropylene with high tensile strength. The unique properties of the WG come from its wicking warps that are woven at the top, middle, and bottom of the fabric cross-section. These warps give the WG great potential for maximizing capillary action and water transport through transmissivity in an unsaturated environment. Each wicking warp consists of 144 hydrophilic and hygroscopic nylon wicking fibers for drainage purposes. These fibers are highly hydrophilic with multichannel cross-sections, which have a high shape factor and a great number of channels per fiber (specific surface area =  $3650 \text{ cm}^2/\text{g}$ ). The weaving pattern of the WG allows it to absorb water from both the top and the bottom sides and transport it. If the end of the WG is exposed to the atmosphere, a large suction gradient is generated in the WG from its buried end in the soil to the exposed end. The suction gradient is the driving force that continuously transports water from the buried end of the WG yarns to the exposed end. At the exposed end of the WG, water will be vaporized into the surrounding atmosphere and gradually dries the soil. More information about the WG and its hydraulic properties can be found in (Lin et al., 2018, 2021b).

Figure 2b shows the picture and the schematics of the cross-section of the NWG. As mentioned earlier, the weaving pattern, reinforcing warp, and weft of the NWG are identical to those of WG. The only difference between the two geotextiles is that each wicking warp in WG is replaced by a single circular shape reinforcing warp in NWG.



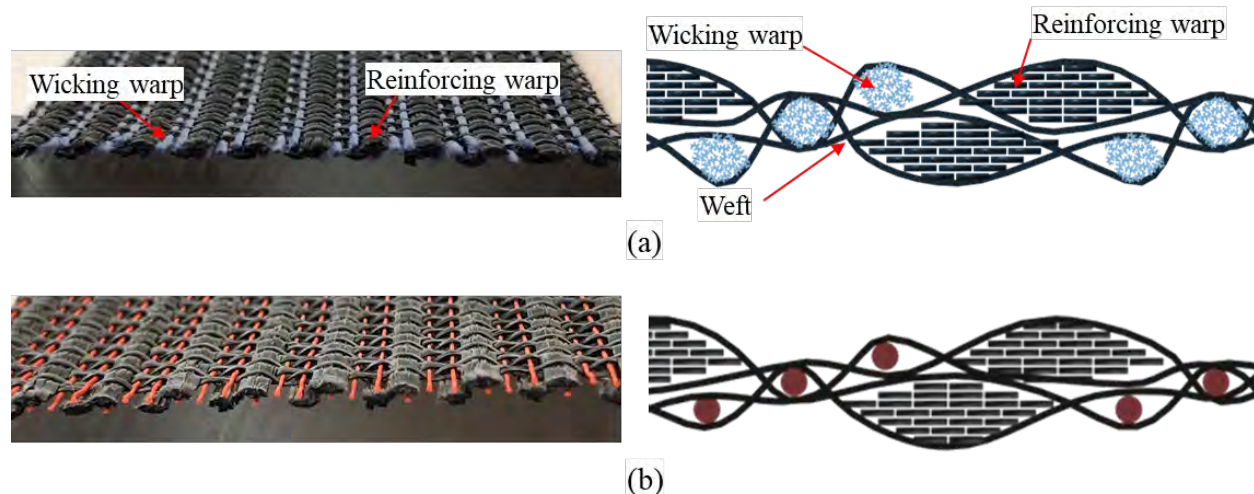


**Figure 2. (a) Wicking geotextile (WG) and (b) Non-wicking geotextile (NWG).**

**Experimental Details.** A series of small-scale box tests were conducted to study the drainage performance of the WG compared to NWG installed in different soil types. The configuration of the drainage tests is shown in Figure 3. The testing box had two separate transparent acrylic containers with an aluminum frame on each side which could simultaneously perform two tests. The testing container on each side has a dimension of 66 cm long by 20 cm wide by 60 cm high. As shown in Figure 3, the NWG is placed on the left side of the box and the WG is installed on the right side. Two valves were installed at the bottom of each side of the box in order to supply water to saturate the soil. A 2 mm-wide opening was located at a height of 10 cm on the sidewall of each container as an outlet for water to flow out of the system. To monitor the soil moisture during the tests, 11 moisture sensors were installed on each side of the testing box in four layers at depths of 9 cm, 12 cm, 24 cm, and 39 cm from the bottom of the box, respectively. The sensors work based on the dielectric constant to measure volumetric water content with a  $\pm 2\%$  accuracy for non-uniform soils and general field conditions. For this study however, each sensor was individually calibrated for the clean sand and sandy silt to achieve an accuracy of  $\pm 0.5\%$ . More details on test setup and instrumentation can be found in (Zhang and Galinmoghadam, 2020).

For each test, the soil mix was prepared first. Each container was filled with the soil mix at a dry unit weight of 17.5 to 18.3 kN/m<sup>3</sup> using 3 cm lifts until the height of the soil was 48 cm. During the placement of each lift, moisture sensors were also installed at their corresponding locations based on what is shown in Figure 3. When the soil height reached 10 cm, a 17 cm wide geotextile was placed on the soil and was extended outside the box for 20 cm through the 2 mm opening as shown in Figure 3. The space between the opening and the geotextile was then sealed to ensure that water would only drain through the geotextile. Consequently, water would move along the geotextile planes as a result of geotextile transmissivity. In other words, the transmissivity of the WG and NWG when installed in soils with different fines contents is directly compared.

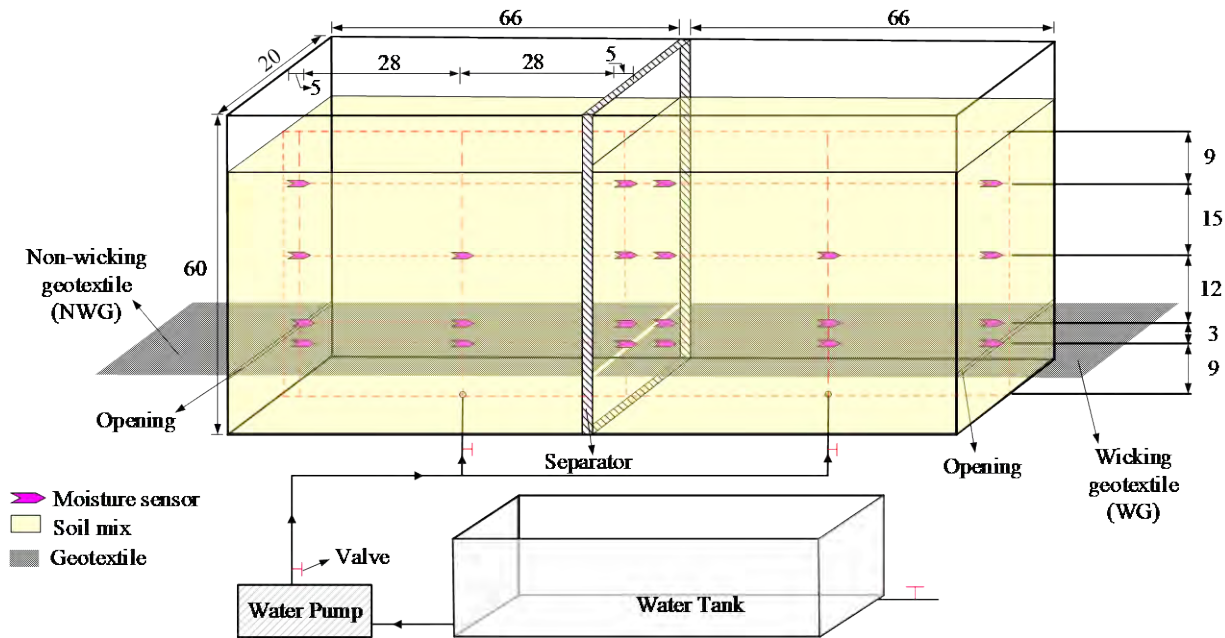


**Figure 3. Schematics of the box test setup.**

At the beginning of each test, the opening was completely sealed, and water was allowed through the inlet at a small flow rate to saturate the box without disturbing the soil. Water inflow continued until 1.5 cm of water ponded on the soil surface for at least 20 minutes. After the saturation process was completed, the inlet valves were closed, and the seal of the openings was removed allowing water to drain through the geotextiles. During the drainage, sensor data were obtained every 30 seconds for further analysis.

## ANALYSIS AND RESULTS

The volumetric water content readings from the sensors were used to plot contours of soil moisture at different times. The contours were plotted by linearly interpolating the volumetric water content at discrete sensor locations to obtain a continuous spatial distribution of soil moisture at each time during the tests. The difference between the water content when the saturation was finished and the water content at any time during the drainage is the amount of drained water. The contours of the remaining water content are integrated over the vertical plane of sensors and then divided by the total initial water content, to obtain the fraction of drained water.

Figure 4 shows the curves of the fraction of drained water at different times after the start of the drainage in all tested cases. The solid lines represent curves for the soils with WG and the dashed lines are the ones for NWG for different fines contents (FC in Figure 4). Right at the start of the drainage, all curves read zero since no water was drained yet. As time passed, water started to drain from soils through the extended geotextile at the opening of each side of the box. Most of the water was drained by the first day. And then, the rate of drainage reduced with time.

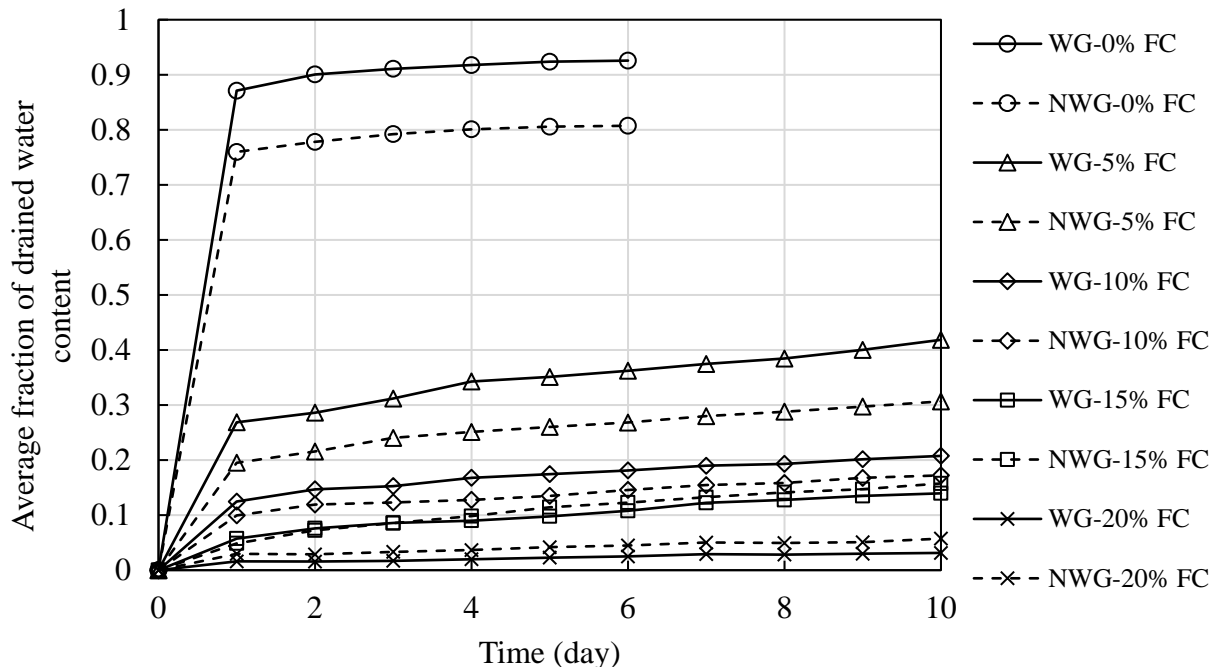


**Figure 4. Fraction of drained to initial water content during drainage.**

As can be observed in Figure 4, the fraction of drained water in clean sand was the highest in all soils. This is expected since the clean sand had larger voids accommodating water transport. In other words, the hydraulic conductivity of the clean sand compared to other soil mixes was higher. Additionally, when the fines content of the soil mix increased, the specific surface area of the soil increased, and thus, the soil's ability to hold water was higher. In summary, the increase in fines content of the soil reduced its hydraulic conductivity and increased the soil's water holding capacity. As a result, less water could be extracted under similar conditions.

For the clean sand with WG, more than 0.93 of the water was drained by day 6. For the same soil with NWG, the final accumulated fraction of drained water was 0.81. As a result, the performance of the WG was more than 12% better than that of NWG. When the fines content of the soil was increased to 5% (5% FC), the final fraction of drain water in WG and NWG cases dropped to 0.42 and 0.31 respectively. Additionally, the distribution of the drained water in time was more uniform as the fines content increased. In other words, less water was drained during the first day and more water was drained after that, compared to the soil with 0% FC. For the 10% FC soil mix, the fraction of the drained water for WG and NWG was 0.21 and 0.17, respectively. As can be seen, the fraction of drained water in WG exceeded the NWG only by 4%. In another study, WG was used in a base course soil with 10% fines content. It was found that the WG drained 4% more water compared to the soil without installation of the WG (Galinmoghdam and Zhang, 2020). Even though the soil used in this study is different from that of the full-scale field test, the reduction in moisture content by using WG agrees with it.

When the two geotextiles were tested in soil with 15% fines content, the fraction of drained water for WG and NWG cases were 0.14 and 0.16 respectively. In other words, the WG drained 2% less water than the NWG. Similarly, when the fines content of the soil increased to 20%, the fraction of drained water to the total initial water content was 6% and 3% in NWG and WG respectively.

Figure 5 shows the variation of the average fraction of drained water to total initial water content on day 6 along the depth of the soil. These curves were obtained by integrating contours of the fraction of drained water content along 3 cm height at different elevations for each test.

As can be seen in Figure 5, the amount of drained water increased at the higher elevation due to the gravitational potential of water. Similar to the results shown in Figure 4, Figure 5 shows that the average drained water fraction was reduced as the fines content increased. One key observation in Figure 5 is that the fraction of drained water suddenly increased at 10 cm height where the geotextiles were installed. In many cases, the jump in the fraction of drained water was higher in cases where the WG was installed compared to the ones where NWG was installed. This is due to the capillary effect in the wicking yarns which helped WG absorb more water from the adjacent soils and made the soil drier.

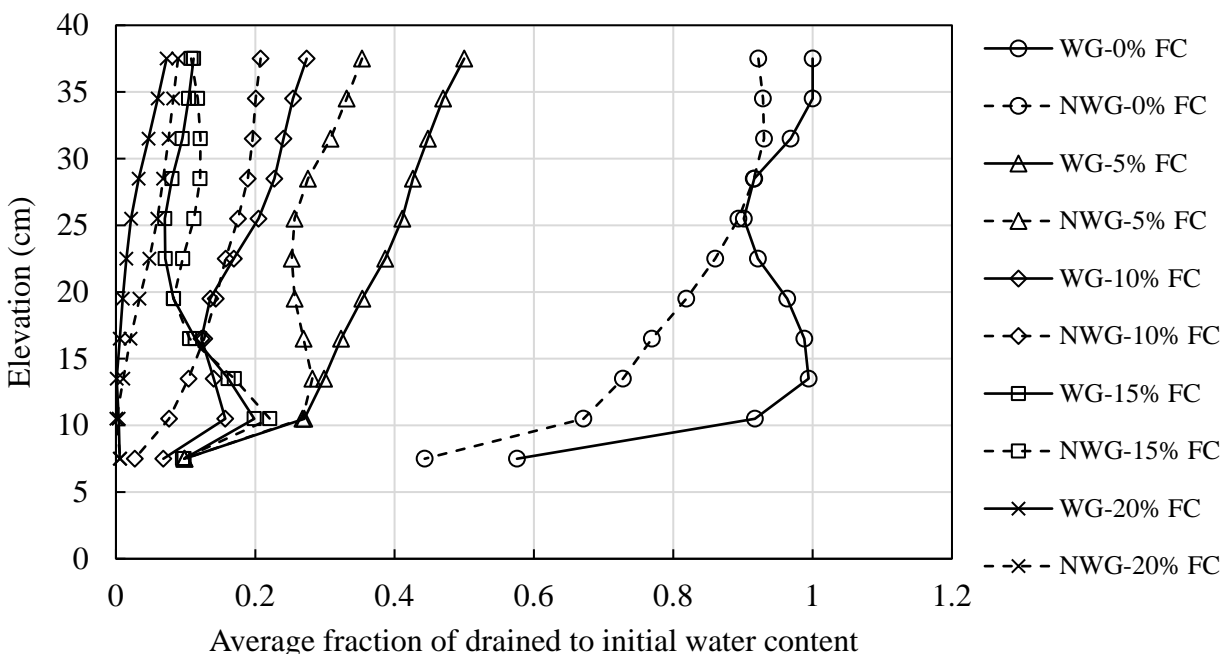


**Figure 5. Comparison of the average fraction of drained water at different heights of the soil for different soil and geotextile types on day 6.**

## CONCLUSION

Several small-scale box tests were conducted in order to compare the transmissivity of the wicking geotextile with non-wicking geotextile in soils with different fines contents. The wicking and non-wicking geotextiles shared the same weaving pattern, apparent opening size, reinforcing wraps, and wefts. Soils used in this study had fines contents of 0%, 5%, 10%, 15%, and 20%, and similar degrees of compaction. Results suggested that the total amount of drained water decreased as the fines content increased due to a reduction in hydraulic conductivity and an increase in soil water holding capacity. Additionally, as the fines content increased, the drop in the rate of drainage reduced as time passed. As a result, less water was drained at the early stages of the test. Up to soil fines content of 10%, the drainage performance of the wicking geotextile was better than the non-wicking geotextile. At 15% fines content, the two types of geotextiles drained nearly similar amount of water. When the fines content increased to 20%, the non-wicking geotextile drained



more water compared to the wicking geotextile. As a result, the limiting fines content for the wicking geotextile is concluded to be somewhere between 10% and 15%.

It should be noted that the conclusions are made based on 5 small-scale box tests. Although the results obtained in this research agree with the full-scale test in another study, more tests may be required to obtain conclusive results.

## REFERENCES

- Al-Qadi, I. L., Lahouar, S., Loulizi, A., Elseifi, M. A. and Wilkes, J. A. (2004). Effective approach to improve pavement drainage layers, *Journal of Transportation Engineering*, 130(5): 658–664.
- Alobaidi, I., and Hoare, D. J. (1998). The role of geotextile reinforcement in the control of pumping at the subgrade-subbase interface of highway pavements, *Geosynthetics International*, 5(6): 619–636. <https://doi.org/10.1680/gein.5.0138>
- Alobaidi, Imad. and Hoare, D. J. (1996). The development of pore water pressure at the subgrade-subbase interface of a highway pavement and its effect on pumping of fines, *Geotextiles and Geomembranes*, 14(2): 111–135. [https://doi.org/10.1016/0266-1144\(96\)84940-5](https://doi.org/10.1016/0266-1144(96)84940-5)
- Currey, J. (2016). *H2Ri Wicking Fabric Experimental Feature Final Report Dalton Highway MP 197-209 Rehabilitation, Technical report, Alaska DOTandPF, Project No. IM-DP-065-4(8)/61214*.
- Galinmoghadam, J., Liu, J., Zhang, X., Lin, C. and Guo, Y. (2022). Mitigating Pumping in Pavement Shoulder Using Wicking Geotextile: An Experimental Study, *Transportation Research Record: Journal of the Transportation Research Board*, 036119812210917. <https://doi.org/10.1177/03611981221091730>
- Galinmoghadam, J. and Zhang, X. (2020). Use of Wicking Fabric to Reduce Pavement Pumping, In *GeoCongress 2020* (Vol. 2020-Febru, pp. 630–639). Minneapolis, MN: American Society of Civil Engineers. <https://doi.org/10.1061/9780784482810.065>
- Ghazavi, M. and Roustaei, M. (2013). Freeze–thaw performance of clayey soil reinforced with geotextile layer, *Cold Regions Science and Technology*, 89, 22–29. <https://doi.org/10.1016/J.COLDREGIONS.2013.01.002>
- Guo, J., Wang, F., Zhang, X. and Han, J. (2017). Quantifying water removal rate of a wicking geotextile under controlled temperature and relative humidity, *Journal of Materials in Civil Engineering*, 29(1): 4016181.
- Han, J. (2013). Design of planar geosynthetic-improved unpaved and paved roads, In *Geotechnical Practice Publication* (pp. 31–41). Reston, VA: American Society of Civil Engineers. <https://doi.org/10.1061/9780784412817.003>
- Han, J. (2015). Principles and practice of ground improvement. John Wiley and Sons.
- Henry, K. S. (1990). *Laboratory investigation of the use of geotextiles to mitigate frost heave*, COLD REGIONS RESEARCH AND ENGINEERING LAB HANOVER NH.
- Henry, K. S. and Holtz, R. D. (2001). Geocomposite capillary barriers to reduce frost heave in soils, *Canadian Geotechnical Journal*, 38(4): 678–694. <https://doi.org/10.1139/t01-010>
- Kebria, M. M., Na, S. H. and Yu, F. (2022). An algorithmic framework for computational estimation of soil freezing characteristic curves, *International Journal for Numerical and Analytical Methods in Geomechanics*. <https://doi.org/10.1002/NAG.3356>
- Kermani, B., Xiao, M., Stoffels, S. M. and Qiu, T. (2018). Reduction of subgrade fines migration into subbase of flexible pavement using geotextile, *Geotextiles and Geomembranes*, 46(4):

- 377–383. <https://doi.org/10.1016/j.geotexmem.2018.03.006>
- Lin, C., Galinmoghadam, J., Han, J., Liu, J. and Zhang, X. (2021a). Quantifying and Incorporating the Benefits of Wicking Geotextile into Pavement Design, *Journal of Transportation Engineering, Part B: Pavements*, 147(3): 04021044. <https://doi.org/10.1061/JPEODX.0000300>
- Lin, C., Presler, W., Zhang, X., Jones, D. and Odgers, B. (2016). Long-Term Performance of Wicking Fabric in Alaskan Pavements, *Journal of Performance of Constructed Facilities*, 31(2): D4016005. [https://doi.org/10.1061/\(asce\)cf.1943-5509.0000936](https://doi.org/10.1061/(asce)cf.1943-5509.0000936)
- Lin, C., Zhang, X., Galinmoghadam, J. and Guo, Y. (2021b). Working mechanism of a new wicking geotextile in roadway applications: A numerical study, *Geotextiles and Geomembranes*. <https://doi.org/10.1016/J.GEOTEXMEM.2021.11.009>
- Lin, C., Zhang, X. and Han, J. (2018). Comprehensive Material Characterizations of Pavement Structure Installed with Wicking Fabrics, *Journal of Materials in Civil Engineering*, 31(2): 04018372. [https://doi.org/10.1061/\(asce\)mt.1943-5533.0002587](https://doi.org/10.1061/(asce)mt.1943-5533.0002587)
- Raymond, G., Bathurst, R. and Hajek, J. (2000). Evaluation and suggested improvements to highway edge drains incorporating geotextiles, *Geotextiles and Geomembranes*, 18(1): 23–45. [https://doi.org/10.1016/S0266-1144\(99\)00005-9](https://doi.org/10.1016/S0266-1144(99)00005-9)
- Wang, F., Han, J., Zhang, X. and Guo, J. (2017). Laboratory tests to evaluate effectiveness of wicking geotextile in soil moisture reduction, *Geotextiles and Geomembranes*, 45(1): 8–13.
- Yang, C. and Yu, X. (1989). Mud-pumping prevention of railway subgrade by using geotextile, In *Proceedings of the Tenth International Conference on Soil Mechanics and Foundation Engineering* (pp. 1693–1695).
- Zhang, X. and Galinmoghadam, J. (2020). Performance of Wicking Geotextile on Mitigating Water Pumping, *Issue on I-44 Highway*. No. CMR 20-003. Missouri Department of Transportation, Jefferson City, Missouri.
- Zhang, X. and Presler, W. (2012). *Use of H2Ri Wicking Fabric to Prevent Frost Boils in the Dalton Highway Beaver Slide Area, Alaska*. Alaska University Transportation Center, Alaska Department of Transportation and Public Facilities.
- Zhang, X., Presler, W., Li, L., Jones, D. and Odgers, B. (2014). Use of Wicking Fabric to Help Prevent Frost Boils in Alaskan Pavements, *Journal of Materials in Civil Engineering*, 26(4): 728–740. [https://doi.org/10.1061/\(asce\)mt.1943-5533.0000828](https://doi.org/10.1061/(asce)mt.1943-5533.0000828)
- Zornberg, J. G. (2017). Functions and applications of geosynthetics in roadways, *Procedia Engineering*, 189, 298–306.

## Hydrophobizing treatment in saline soil: conditions and mechanisms

Gege Huang, M.S.,<sup>1</sup> Hongjie Lin, Ph.D.<sup>2</sup>

<sup>1</sup>Sun Yat-sen University; e-mail: [huanggg3@mail2.sysu.edu.cn](mailto:huanggg3@mail2.sysu.edu.cn)

<sup>2</sup>Sun Yat-sen University; e-mail: [linhj33@mail.sysu.edu.cn](mailto:linhj33@mail.sysu.edu.cn)

### ABSTRACT

Saline soils exist in arid and semi-arid regions or in regions of hot climate and poor natural drainage. Constructions on saline soils are faced with challenges of large deformations and instability because of their poor engineering properties (weak water stability, water-induced collapsibility, etc.). Traditional soil stabilizers, such as limes and fly ash may be unsuitable to saline soils as they can aggravate salt crystallization-induced expansion. This paper proposes to use hydrophobic agents as stabilizers to improve the water stability of saline soils. Two widely-used hydrophobic agents (dichlorodimethylsilane and polydimethylsiloxane) and three potential ones (methanesiliconic acid sodium salt, triethoxy(octyl)silane and Tung oil) were tested. The soil water stability was quantified by water absorption test. Soil hydrophobicity, an important soil property referring to the effectiveness of hydrophobizing agents, was investigated by sessile drop method. The soil unconfined compressive strength (UCS) was also determined. Based on the result of these three tests, the feasibility and suitability of hydrophobic agents were discussed.

### INTRODUCTION

Saline soils are defined as the soil containing chlorine, sulfate or carbonate salts. Salts in the soils have high sinkability and salt expansion, which affect the engineering properties and consequently result in the volumetric instability of geotechnical constructions. For example, in the construction of pavement subgrades and subbases, collapsible and corrosive chlorine saline soils may drive the deformation of subgrade and the corrosion of concrete structures (Petrukhin, 1993; Wang & Chai, 2011). To mitigate the impact of saline soils, a number of stabilization methods have been proposed by researchers based on the aspect of its strength and volumetric stability. Li et al. (2012) are among the pioneers to test the feasibility of renewable materials combining traditional stabilizers (*e.g.*, limes) for saline soil improvement. Horpibulsuk et al. (2012) investigated the effectiveness and mechanisms of cement-based stabilization method in saline clayey soils.

The stabilization of saline soils develops in recent years, in which most work focused on the strength of saline soils, following a traditional idea that higher soil strength can improve the stability of geotechnical constructions. This is reasonable and practical in normal soils. For saline soils, however, this concept may witness a challenge since the disasters of construction on saline soil are majorly attributed to the migration and phase change of salts. For example, when sulfate soils are mixed with cement, the salt expansion can be greater and even exacerbate the disease of subgrade. Noticing the driving factors of volumetric instability of saline soils are soluble salts and water, removing soluble salts or inhibiting water migration in saline soils should also be considered as the measures. For the former way, some researchers have investigated potential stabilizers. For example, Cheng et al. (2017) has considered the application of Friedel's salt to strengthen the saline soils, which can potentially mitigate the deformation of constructions on saline soil areas. For the

latter one, this paper proposes to induce soil hydrophobicity in saline soil and therefore, the water infiltration can be prevented.

Soil hydrophobicity (or so-called soil water repellency) is a special soil property referring to the affinity of soils to water. Water can infiltrate into common soils as they are hydrophilic, while for hydrophobic soils, water droplets can bead up on the soil surface (Figure 1). In such soils, the migration of water can be dramatically inhibited. Of interest to geotechnical constructions in saline soil area, inducing soil hydrophobicity can mitigate the water-induced disasters by saline soils. Although a number of hydrophobizing methods have been proposed and tested in common soils such as clayey and silty mineral soils, sands or even agricultural soils (Bauters et al., 2000; Lin et al., 2019; Zhou et al., 2021), little work has been done on the feasibility of these hydrophobizing methods in saline soils. This paper aims to investigate the effectiveness of existing and potential hydrophobic agents in saline soils. Specific objectives are:

- (1) To compare the effectiveness of different hydrophobic agents in saline soils from the aspect of severity and stability of induced hydrophobicity;
- (2) To investigate the influence of hydrophobic agents on the engineering properties including soil strength and water stability;

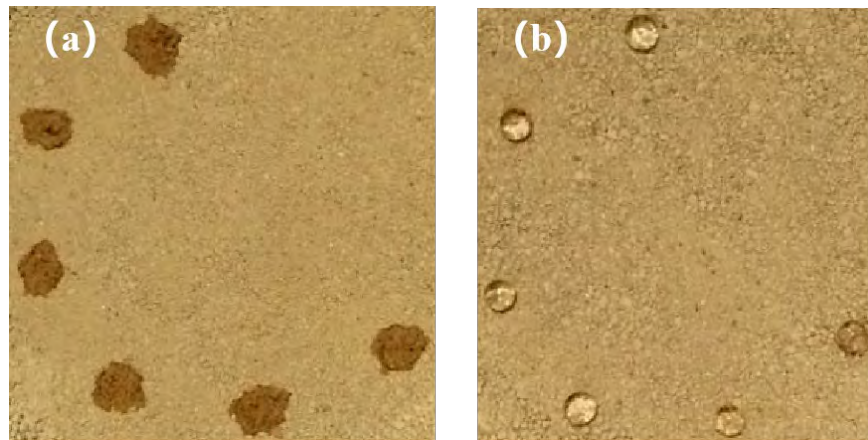


**Figure 1. Water droplets on (a) hydrophilic and (b) hydrophobic soils.**

## METHODOLOGY

### Materials

The saline soils used in this project were collected from Golmud, Qinghai in China. The soil properties, ion content and particle size distribution curves are shown in Table 1, Table 2 and Figure 2, respectively. The soils are classified as chloride saline sandy soils.

**Table 1. Soil properties of saline soils from Golmud, Qinghai, China**

Soil type	C <sub>u</sub>	C <sub>c</sub>	Chloride concentration (%)	Sulfate concentration (%)	Water content (%)	Specific gravity
Chloride saline soil	13.3	1.1	3.3±1.70	0.4±0.11	4.0~6.0	2.59



**Table 2. Ion content of the saline soils**

Ion species	Cl <sup>-</sup>	SO <sub>4</sub> <sup>2-</sup>	Na <sup>+</sup>	Ca <sup>2+</sup>	K <sup>+</sup>	Mg <sup>2+</sup>
Concentration (wt.%)	6.475	7.375	5.7125	1.405	0.2265	0.18075

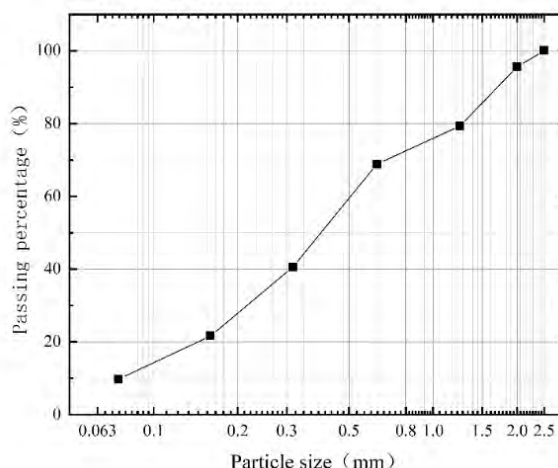


**Figure 2. Particle size distribution of the saline soils.**

Five different hydrophobic agents were tested in this project as shown in Table 3. Dichlorodimethylsilane (DCDMS) and Polydimethylsiloxane (PDMS) are two widely used hydrophobic agents. Their applications and mechanisms in hydrophobizing soils have been well investigated. After treatment of DCDMS, the methyl of DCDMS coating makes the soil hydrophobic. PDMS is composed of basic part A and curing agent B. The strong chemical bonding inherent and thermal stability provide PDMS the precondition to form hydrophobized coating of soil particles. Methanesiliconic acid sodium salt (MASS), Triethoxy(octyl)silane (TEOS) and Tung oil have some potentials in hydrophobizing soils, based on our previous works (Lin et al., 2019). Methanesiliconic acid sodium salt can generate silicone coatings on the soil particle surface by reacting with soil water and carbon dioxide in the air. TEOS as a hydrophobizing agent has been used in construction industries such as glass coating and hydrophobic concrete. It reacts with H<sub>2</sub>O to generate silicon resin which exhibits hydrophobicity. Tung oil as a traditional and sustainable waterproofing material has been proved to be cost-effective in common mineral soils. For each hydrophobic agent, 1.0, 3.0 and 5.0% of concentration by weight were used.

**Table 3. Hydrophobic agent property**

Hydrophobizing agents	Chemical formula or compounds	Form	Density (g/mL)	Commercial resource
Dichlorodimethylsilane	(CH <sub>3</sub> ) <sub>2</sub> SiCl <sub>2</sub>	liquid	1.07	Sigma-Aldrich
Polydimethylsiloxane	(C <sub>2</sub> H <sub>6</sub> OSi) <sub>n</sub>	liquid	0.97	Sigma-Aldrich
Methanesiliconic acid sodium salt	CH <sub>3</sub> SiO <sub>3</sub> Na	Solution (30%), Liquid	-	YuanYe Biotech
Triethoxy(octyl)silane	CH <sub>3</sub> (CH <sub>2</sub> ) <sub>7</sub> Si(OC <sub>2</sub> H <sub>5</sub> ) <sub>3</sub>	Liquid	0.88	Aladdin
Tung oil	Alpha-eleostearic acid Linoleic acid	Liquid	0.94	Acme

### Sessile drop test

In soil science, a widely-used method to measure contact angle is the sessile drop method given its reproducibility and quickness (Bachmann et al., 2000). The soil sample was fixed on a platform and a water droplet was placed on it through a syringe at a speed of 10  $\mu\text{l/s}$  (Figure 3). The shape of the water droplet on the surface of soil samples was recorded with contact angle measured automatically.

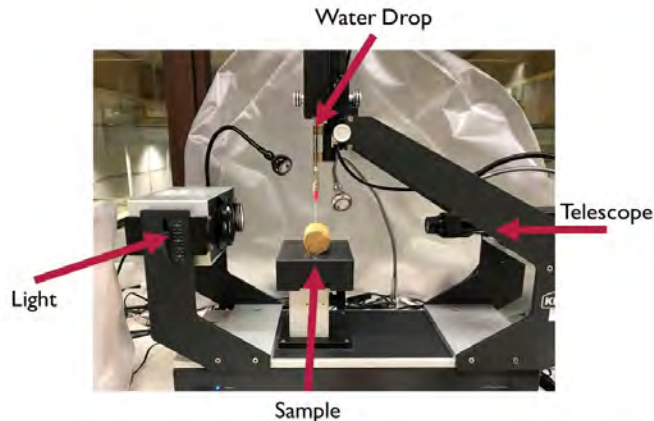


**Figure 3. Sessile drop method to measure the contact angle of treated soils.**

### Cyclic wetting-drying test

Untreated and treated soil samples were compacted in a mould (36.5 mm in diameter and 105.0 mm in height), following the method proposed by Sridharan & Sivapullaiah (2005) to the maximum density. After that, soil samples were oven dried at 105°C for 24 hours. The oven-dried samples were partially immersed in water and witness wetting-drying cycles. This wetting-drying test follows the standard of ASTM D-559 (1993). After each wetting-drying cycle, samples were collected, with the water content and volumetric change measured.

### Unconfined compression test

The unconfined compression test was performed to determine the unconfined compressive strength (UCS) of the soil at the maximum dry density. Soil samples which had been compacted in the mould were air-dried for one week before the test. The top and bottom surfaces of the sample were flat such that the force acting on the soil was uniformly distributed (Lin et al., 2017). The test was carried out by a compression machine (Tritech 50kN, Wykeham Fattance, United Kingdom) at a loading rate of 1mm/min of compression. For each type of soil, three samples were tested.

## PRELIMINARY RESULTS AND DISCUSSION

### Time-dependent soil hydrophobicity

The contact angle change of hydrophobized saline soils with 1.0% of hydrophobic agents was plotted in Figure 4. Within 24 hours of adding hydrophobic agents in saline soils, the soil hydrophobicity could be induced as the contact angle reached the peak. While for DCDMS, Tung

oil and PDMS-treated soils, the contact angle was unstable and witnessed a decrease after three days. TEOS- and MASS-treated saline soils had a stable contact angle within 14 days.

The chloride saline soils contained an amount of chloride and sulfate salts, with the pH greater than 10. For PDMS- and DMDCS-treated soils, the coatings are siloxane, which are degradable under extreme pH and the existence of kaolin clay. As for Tung oil coatings, it was reported that under alkaline conditions Tung oil can undergo hydrolysis. Therefore the contact angle decreased with time. While for MASS- and TEOS-induced soils, the coatings were durable with contact angle remaining at 113-115°.

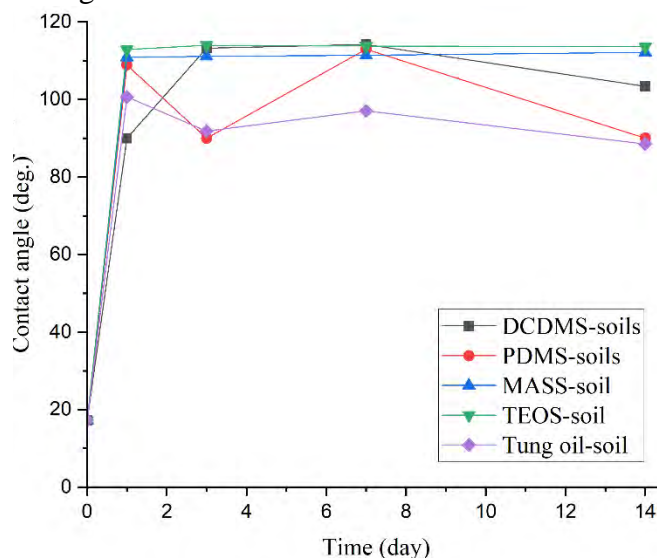


**Figure 4. Contact angle change of hydrophobized saline soils.**

If the soils were washed and oven-dried before the hydrophobizing treatment, i.e., the salts were removed firstly, the soil hydrophobicity induced by all types of hydrophobic agents was stable and durable as shown in Figure 5. This further support the aforementioned explanation that salts and extreme pH condition drives the degradation of some hydrophobic coatings.

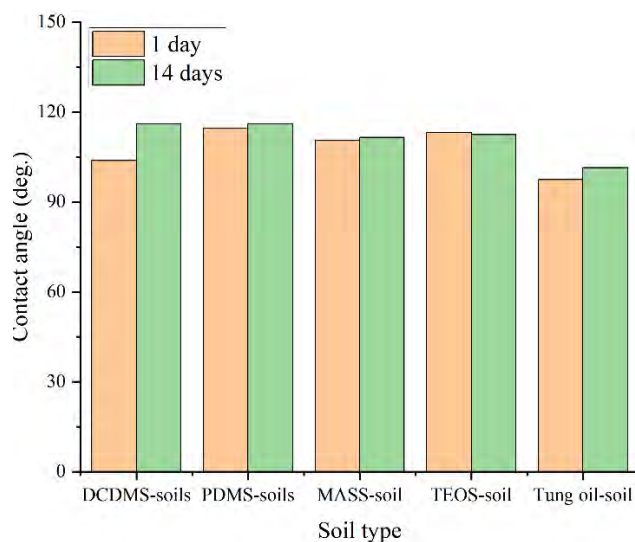


**Figure 5. Contact angle change of hydrophobized washed soils.**

## Volume change and collapsibility

All hydrophobic agents can enhance the durability of saline soils under wetting-drying cycles because of induced soil hydrophobicity. Figure 6 shows the volumetric change of soil samples treated by 1.0% of hydrophobic agents under wetting-drying cycles. For untreated (natural) saline soils, after four cycles the soil sample was collapsed. Hydrophobic soils can undergo more wetting-drying cycles: Tung oil-treated soils were collapsed until five wetting-drying cycles, and MASS-treated soils show the greatest durability in which the volume change is less than 10% after five cycles of wetting-drying. Noticing that the wetting-drying test is only to quickly quantify the volumetric stability and collapsibility of soils. For the engineering practice, it is proposed to carry out a soaked (wet) California bearing ratio (CBR) test.

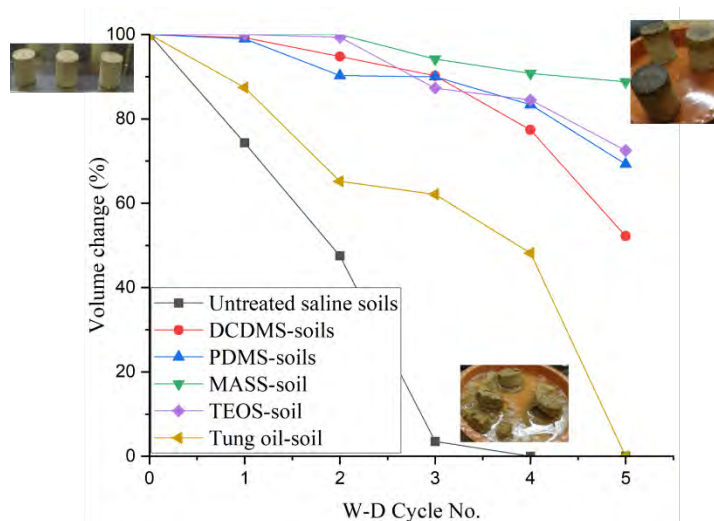


**Figure 6. Volumetric change of hydrophobized saline soils during wetting drying cycles.**

## Unconfined compressive strength

It is found that with an increase of hydrophobic agent concentrations, the strength of soils was firstly increased (Figure 7). For Tung oil-treated soils, the UCS was continuously enhanced with higher concentrations. While for DCDMS- and MASS-treated soils, the strength of soils had a peak at a concentration of 1~3%, and higher concentration (5%) resulted in a lower strength. The strength of Tung oil-treated soil is from the hardening of Tung oil (Lin et al., 2019). For DCDMS- and MASS-treated soils, the cohesion between soil particles was enhanced as the hydrophobic agents generate polymeric siloxanes coatings which can bond particles. While for a great amount of DCDMS or MASS, the generated siloxanes were then in a liquid form and could lubricate the soils.



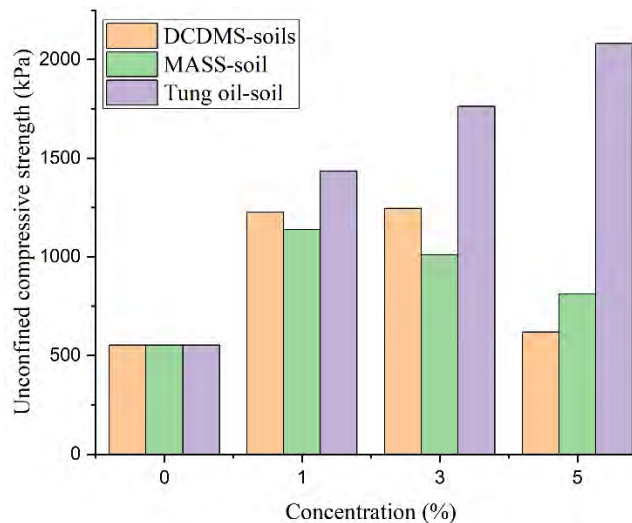


**Figure 7. Unconfined compressive strength of treated soils with different concentrations.**

## CONCLUSION

This project proposes a novel saline soil improvement method by hydrophobizing treatment, to inhibit the salt and water migration in soils and mitigate consequent disasters in engineering applications. The feasibility and suitability of five types of hydrophobic agents were demonstrated by three aspects: soil volumetric stability, soil hydrophobicity and soil strength, with corresponding tests conducted. The preliminary conclusions are as follows:

- (1) The soil hydrophobicity can be induced by all hydrophobic agents, but only Methanesiliconic acid sodium salt and Triethoxy(octyl)silane can produce a durable soil hydrophobicity.
- (2) The volumetric stability of saline soils was improved by hydrophobic agents because of the soil hydrophobicity which inhibit the water soaking.
- (3) The soil strength was enhanced by a proper concentration of hydrophobic agents (1~3%), while with greater concentration, soils might be weak.

This paper only takes a very first step on the hydrophobizing treatment in saline soils. Further study would be carried out to find out the mechanisms and optimize the hydrophobizing conditions.

## REFERENCE:

- Bachmann, J., Horton, R., Van Der Ploeg, R. R., & Woche, S. (2000). Modified Sessile Drop Method For Assessing Initial Soil–Water Contact Angle Of Sandy Soil. *Soil Science Society Of America Journal*, 64(2), 564-567.
- Bauters, T., Steenhuis, T. S., Dicarlo, D. A., Nieber, J. L., Dekker, L. W., Ritsema, C. J., Parlange, J., & Haverkamp, R. (2000). Physics Of Water Repellent Soils. *Journal Of Hydrology*, 231, 233-243.
- Cheng, Y., Li, Z., Huang, X., & Bai, X. (2017). Effect Of Friedel’S Salt On Strength Enhancement Of Stabilized Chloride Saline Soil. *Journal Of Central South University*, 24(4), 937-946.
- Horpibulsuk, S., Phojan, W., Suddeepong, A., Chinkulkijniwat, A., & Liu, M. D. (2012). Strength Development In Blended Cement Admixed Saline Clay. *Applied Clay Science*, 55, 44-52.

- Li, M., Chai, S. X., Zhang, H. Y., Du, H. P., & Wei, L. (2012). Feasibility Of Saline Soil Reinforced With Treated Wheat Straw And Lime. *Soils And Foundations*, 52(2), 228-238.
- Lin, H., Lourenço, S. D. N., Yao, T., Zhou, Z., Yeung, A. T., Hallett, P. D., Paton, G. I., Shih, K., Hau, B. C. H., & Cheuk, J. (2019). Imparting Water Repellency In Completely Decomposed Granite With Tung Oil. *Journal Of Cleaner Production*, 230, 1316-1328. [Http://Doi.Org/Https://Doi.Org/10.1016/J.Jclepro.2019.05.032](http://doi.org/https://doi.org/10.1016/j.jclepro.2019.05.032)
- Lin, H., Zheng, S., Lourenço, S. D., & Jaquin, P. (2017). Characterization Of Coarse Soils Derived From Igneous Rocks For Rammed Earth. *Engineering Geology*, 228, 137-145.
- Petrukhin, V. P. (1993). *Construction Of Structures On Saline Soils..* Aa Balkema.
- Sridharan, A., & Sivapullaiah, P. V. (2005). Mini Compaction Test Apparatus For Fine Grained Soils. *Astm Geotechnical Testing Journal*, 28(3), 7.
- Wang, P., & Chai, S. (2011). Laboratory And In-Situ Tests On Solidified Saline Soils For Highway Fillings. *Engineering Geology*, 19(3), 440-446.
- Zhou, Z., Kwan Leung, A., Akbar Karimzadeh, A., Hei Lau, C., & Li, K. W. (2021). Infiltration Through An Artificially Hydrophobized Silica Sand Barrier. *Journal Of Geotechnical And Geoenvironmental Engineering*, 147(6), 6021006.

## Investigation of Moisture Reduction in Sandy Soil using Geotextiles

Md. Wasif Zaman,<sup>1</sup> and Jie Han, Ph.D., P.E.<sup>2</sup>

<sup>1</sup>Department of Civil, Environmental, & Architectural Engineering, the University of Kansas;  
email: [mdwasif.zaman@ku.edu](mailto:mdwasif.zaman@ku.edu)

<sup>2</sup>Department of Civil, Environmental, & Architectural Engineering, the University of Kansas;  
email: [jiehan@ku.edu](mailto:jiehan@ku.edu)

### ABSTRACT

This study investigated the ability of two woven geotextiles to reduce moisture from a sandy soil with a high moisture content close to its field capacity: (i) wicking geotextile and (ii) non-wicking geotextile. Water was mixed with a river sand to create a moist soil close to its field-capacity ( $\omega=7.5\%$ ) and then it was compacted to a relative density of 75% inside a large direct shear steel box. A geotextile sheet longer than the steel box was placed in the middle so that moisture could transport out of the soil through the geotextile to the outside environment and then evaporated. Soil samples were collected from different locations inside the box after three and seven days to determine the variations of moisture contents. The test results show that the wicking geotextile could reduce the moisture content of the soil effectively inside the upper box after three days. After seven days, it was observed that the wicking geotextile also reduced the moisture content of the soil underneath the geotextile. The test results with the non-wicking geotextile show that the water trapped on the non-wicking geotextile due to its inability to absorb and transport water out of the soil.

### INTRODUCTION

The “Wicking” concept in performance apparel has been well known to the garment industry since the late 1950s to transport and evaporate body moisture out to the environment. Textile engineers and researchers have conducted many investigations on the properties and size/shape of pore structures of fibrous materials as summarized by Zaman et al. (2022a). Several studies indicated that wicking fibers can effectively absorb and transport liquid (Adler and Walsh 1984, Hsieh 1995, Rajagopalan et al. 2001, Nyoni and Brook 2006, Fangueiro et al. 2010, Chatterjee and Singh 2014). However, the quantity and transfer rate of liquid mostly depend on the fiber type, pore structure, internal surface, chemical treatment, and liquid property. Hsieh (1995) concluded that the geometrical configuration of the fibrous material controls the liquid travel distance. Nyoni and Brook (2006) reported that the penetration and retention of liquid in the fabric depended on the pore size, shape, and orientation. In their study, Yanilmaz and Kalaoğlu (2012) concluded that the greater wicking height happened in the fabrics having smaller capillary pores between yarns. In addition, Chatterjee and Singh (2014) concluded that macro-capillaries controlled short-term wicking while microcapillaries controlled long-term wicking in the fabric.

Removal of water (e.g., drainage) in an efficient and timely manner is necessary to increase the short-term and long-term performance of earth structures including slopes, walls, and roadways (Azevedo and Zornberg 2013, Lin et al. 2017, Lin and Zhang 2018, Guo et al. 2019). Traditional geotextiles made of synthetic permeable textile materials (e.g. polyester, polyamide, polypropylene, and polyethylene) are not effective in unsaturated soil conditions due to fiber

properties and pore structures (Koerner 2012). Both the traditional woven and non-woven geotextile fibers are unable to produce enough capillary force that allows them to absorb and transport moisture from soil particles under a certain saturation limit. Hence, the moisture that comes from precipitation, freeze-thaw, and capillary rise of the groundwater remains within base/subbase courses and subgrade and weakens the soils and induces distresses of roadways over time. To overcome this problem, a wicking geotextile containing special hydrophilic and hygroscopic nylon fibers with deep-grooved channels has been introduced to the market. This product has demonstrated its excellent moisture wicking ability (i.e., wicking drainage), especially under unsaturated soil conditions as compared with those commonly-used woven and non-woven geotextiles in several studies (Zhang et al. 2014, Guo et al. 2017, Wang et al. 2017, Zornberg et al. 2017, Lin and Zhang 2020, Biswas et al. 2021). Capillary water in the soil migrates towards the wicking geotextile due to the suction difference between the unsaturated soil and the wicking geotextile and finally evaporates into the air through the exposed portion of the geotextile to the environment (Zhang et al. 2014, Wang et al. 2017, Guo et al. 2017, Guo et al. 2019).

Several experimental studies reported that the presence of nylon fibers in the wicking geotextile enhanced the lateral drainage from unsaturated soils (Azevedo and Zornberg 2013, Guo et al. 2017, Lin and Zhang 2018, Hachem and Zornberg 2019, Lin et al. 2019). Wang et al. (2017) performed physical model tests showing that the wicking geotextile reduced more moisture from the soil that was adjacent to the geotextile. Lin and Zhang (2018) studied the drainage efficiency of the wicking geotextile placed in aggregates containing 14.5% fines where the geotextile worked at a slower wicking rate. Guo et al. (2019) performed laboratory soil column tests with the wicking geotextile to remove moisture from the aggregate base with 10% fines. They reported the effective wicking distance from the geotextile as approximately 200 mm in that specific type of aggregate material. Bai et al. (2021) studied the drainage performance of the wicking geotextile and found its effective drainage distance more than 50 mm above and below the geotextile. Lin et al. (2019) found that the wicking geotextile was able to remove approximately 2% of the water from the optimum value in the base course, which resulted in an increase in the resilient modulus approximately by two to three times. Guo et al. (2021) showed that the test section with the wicking geotextile produced the least permanent deformation because of the additional hydraulic stabilization provided by the wicking drainage. Lin et al. (2021) conducted a series of numerical simulations to quantify the working mechanism of the wicking geotextile and reported that wicking fibers removed water under light rainfalls while the wicking geotextile acted as a permeable geomaterial under heavy rainfalls.

The practical applications of the wicking geotextile have also been reported in several field studies. Lin et al. (2017) collected field data of the wicking geotextile buried in Alaskan pavements, showing that the wicking geotextile was able to reduce moisture contents of the soils in the pavements during thawing in Spring. Zornberg et al. (2017) presented several case histories and highlighted the drainage benefit of using the wicking geotextile over traditional geotextiles in unsaturated pavement sections. The wicking geotextile was also used in roadways to mitigate pavement pumping (Galinmoghdam and Zhang 2020, Galinmoghdam et al. 2022). Guzman et al. (2021) demonstrated the field performance of the wicking geotextile placed at the side slopes of the arctic highway embankments. They further observed enhanced drainage during the thawing season due to the presence of wicking fibers in the geotextile. Biswas et al. (2021) monitored the field performance of the wicking geotextile in the expansive subgrade soil and reported that the wicking geotextile was able to remove moisture within more than 0.3 m of the subgrade soils placed underneath the geotextile. They also reported the reduction in permanent deformations of



a road section constructed with the wicking geotextile. Liu et al. (2022) reported field monitoring data of the wicking geotextile constructed under a concrete pavement where the wicking geotextile removed more moisture from the aggregate base than the nonwoven geotextile. They also observed a decrease in the wicking performance due to the presence of smaller particles in the aggregate base.

The objective of this study was to investigate the moisture reduction ability of the wicking geotextile from a sandy soil prepared at approximately its field capacity condition. This paper compares the moisture reduction results between the wicking geotextile and the traditional woven geotextile.

## TEST MATERIALS AND METHODS

**Sand.** In this study, Kansas River sand was selected as a soil material. Table 1 lists the physical properties of the river sand, while Fig. 1 shows its grain size distribution. This river sand had round to sub-round particles and was classified as poorly-graded sand (SP) according to the Unified Soil Classification System (USCS). Water was mixed with the dry sand at a moisture content of 7.5% to simulate an unsaturated condition, which is considered approximately the field capacity of this type of soil. Wet sand was stored in a plastic container overnight. The next day the wet sand was mixed again thoroughly before being placed into a large direct shear box which had upper and lower boxes with the dimension of 100 mm high, 300 mm wide, and 300 mm long. The moisture contents of the prepared specimens ranged from 7.3% to 7.7%. The wet sand was placed into the lower shear box and then compacted to 75% relative density using a hand compactor that consisted of a square metal plate attached to a metal rod. A geotextile sheet of 500 mm long and 300 mm wide was then placed on top of the compacted sand in the lower box in such a way that 100 mm of the geotextile from the left and right side was exposed to the air. Fig. 2 shows the illustration of the test setup. More sand was then poured into the upper shear box and compacted to the same density. Moisture contents at different locations of the prepared specimen were measured after three and seven days. The relative humidity and temperature of the room were approximately 40% and 10°C, respectively.

**Table 1. Physical properties of river sand**

Soil type	D <sub>10</sub> (mm)	D <sub>30</sub> (mm)	D <sub>50</sub> (mm)	D <sub>60</sub> (mm)	C <sub>u</sub>	C <sub>c</sub>	G <sub>s</sub>	γ <sub>d,max</sub> (kN/m <sup>3</sup> )	γ <sub>d,min</sub> (kN/m <sup>3</sup> )
Sand	0.32	0.6	0.85	1	3.13	1.13	2.65	18.85	16.02

Note: D<sub>10</sub>=10% of particles finer than this size (effective particle size); D<sub>30</sub>=30% of particles finer than this size; D<sub>50</sub>=50% of particles finer than this size (mean particle size); D<sub>60</sub>=60% of particles finer than this size; C<sub>u</sub>=coefficient of uniformity; C<sub>c</sub>=coefficient of curvature; G<sub>s</sub>=specific gravity; γ<sub>d,max</sub>=maximum dry unit weight; and γ<sub>d,min</sub>=minimum dry unit weight

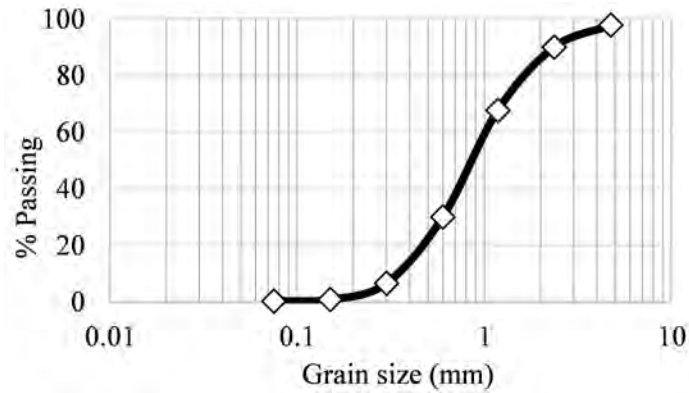


**Figure 1. Grain size distribution of river sand.**

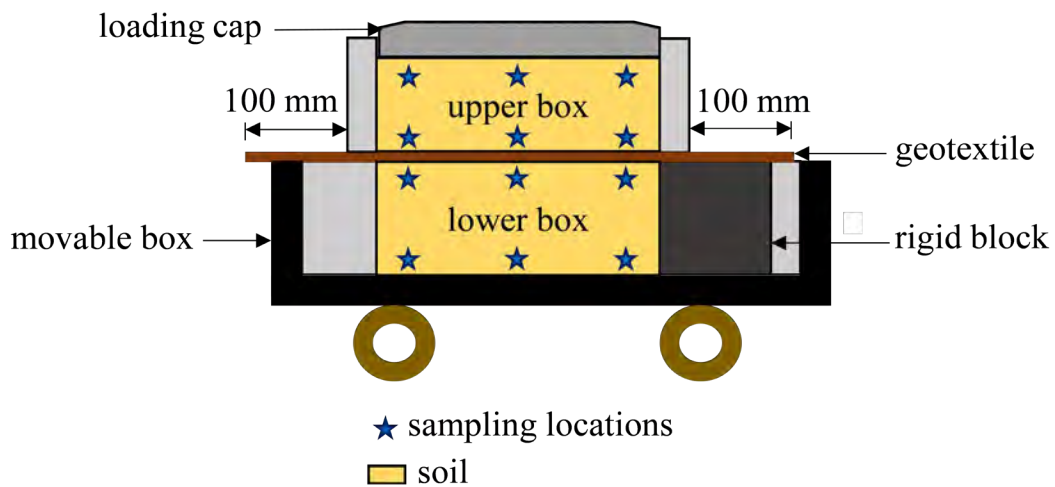


**Figure 2. Illustration of the test setup (figure is not drawn to scale).**

**Geotextile.** Two types of woven geotextile: (i) wicking (WW) and (ii) nonwicking (NWW), were used in the present study. Table 2 provides the properties of the geotextiles collected from the manufacturer. The unit mass of the geotextile specimen used in this study was measured according to the ASTM D5261 standard.

**Table 2. Properties of geotextile (provided by the manufacturer)**

Woven geotextile	Property	Unit	Value
Wicking (WW)	Apparent opening size	Mm	0.43
	Pore size (O <sub>50</sub> )	Microns	85
	Pore size (O <sub>95</sub> )	Microns	195
	Permittivity	sec <sup>-1</sup>	0.4
	Flow rate	l/min/m <sup>2</sup>	1222
	Thickness	Mm	1.24
	Unit mass	g/m <sup>2</sup>	497
	Specific gravity of fibers	-	0.96
	Porosity	%	58.6
	Tensile strength (2% strain, MD)	kN/m	7
	Tensile strength (2% strain, CD)	kN/m	15.8
	Wet front movement (vertical)	Mm	152
	Wet front movement (horizontal)	Mm	1862
Nonwicking (NWW)	Apparent opening size	Mm	0.60
	Permittivity	sec <sup>-1</sup>	0.4
	Flow rate	l/min/m <sup>2</sup>	1222
	Thickness	Mm	1.22
	Unit mass	g/m <sup>2</sup>	385
	Specific gravity of fibers	-	0.91
	Porosity	%	65.3
	Tensile strength (2% strain, MD)	kN/m	14
	Tensile strength (2% strain, CD)	kN/m	19.3
	Tensile Strength (ultimate)	kN/m	70

## TEST RESULTS AND DISCUSSION

A total of four specimens were prepared in the large direct shear test box with wet soil having a moisture content of approximately 7.5%. Two specimens were prepared with the wicking geotextile and kept for three and seven days, respectively. After three and seven days, the specimens were demolished to collect soil samples from different locations in the test box to determine the moisture contents. A similar procedure was followed to prepare other two tests with the nonwicking geotextile.

Figure 3 shows the moisture content distributions in the soil after three days along the depth of the test box. Figure 3a shows that the soil just above the wicking geotextile had approximately 5.2% moisture content after three days. Figure 3b shows that the soil just above the nonwicking geotextile had approximately 9.2% moisture content after three days. This comparison indicates that the wicking geotextile reduced the moisture content by approximately 30% whereas the nonwicking geotextile increased the moisture content by approximately 22% in the unsaturated soil placed just above the geotextile. The initial moisture content of the soil was approximately 7.5%. Zaman et al. (2022b) concluded that the wicking geotextile consisting of nylon fibers had a better wettability compared to the nonwicking geotextile made with polypropylene fibers. Therefore, moisture in the unsaturated soil can easily wet and enter the wicking geotextile's surface, followed by lateral movement in the deep groove channels.

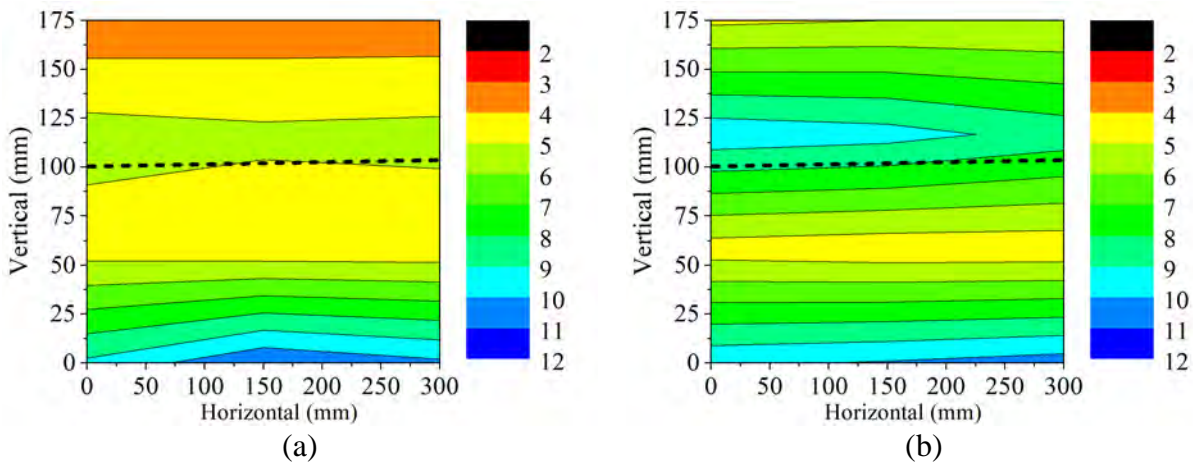


**Figure 3. Moisture content distributions (percentage) in the test box after three days: (a) wicking geotextile and (b) nonwicking geotextile (the dashed line represents the geotextile location).**

Figure 4 shows the moisture content distributions in the soil after seven days. It was observed that there was approximately 4.2% and 10% moisture in the soil placed just above the wicking (Fig. 4a) and nonwicking (Fig. 4b) geotextiles in the upper shear box, respectively. Seven days test results indicated that the wicking geotextile reduced moisture content approximately by 44% whereas the nonwicking geotextile increased the moisture content approximately by 33% in the soil placed just above the geotextile. In case of wicking geotextile, it was also observed that there was approximately 4.4% and 3.4% moisture in the soil placed just below the geotextile after three and seven days, respectively. It was evident that the wicking geotextile removed moisture over time from the soil placed underneath the geotextile in the lower shear box. Although, this study aimed to compare the moisture wicking ability of two woven geotextiles from the unsaturated soil, the results show that the wicking geotextile effectively removed the moisture up to the top surface of the soil in the upper box (i.e., 75 mm thick). The seven-day test results also indicate that the wicking geotextile could wick water out of the soil from a depth of approximately 75 mm below the geotextile. The wicking fibers were found effective to provide higher capillary suction against soil suction and gravity in the unsaturated soil. In the case of the nonwicking geotextile after seven days, more soil moisture traveled downward due to the gravity effect and accumulated on top of the geotextile surface. In other words, the nonwicking geotextile worked as a moisture barrier rather than removing the moisture.



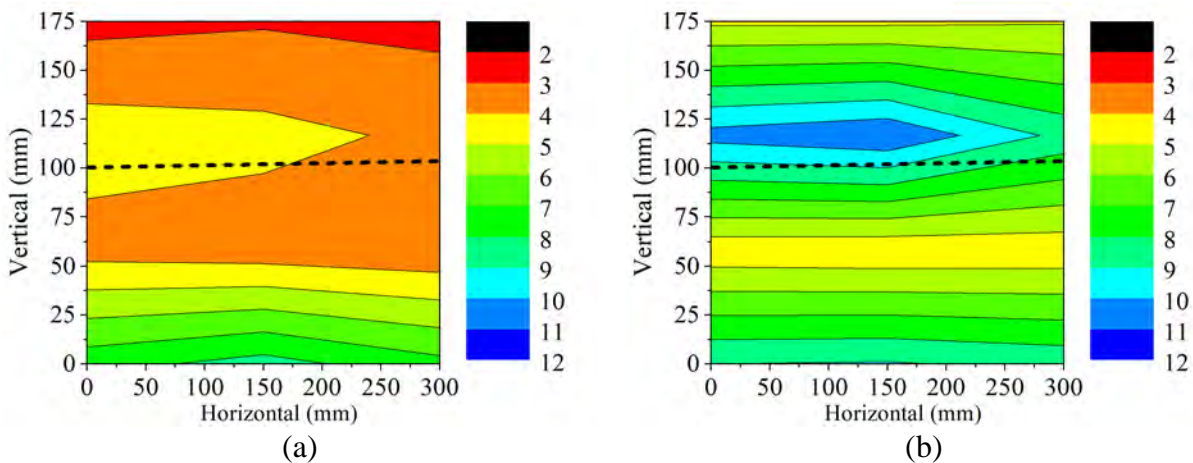
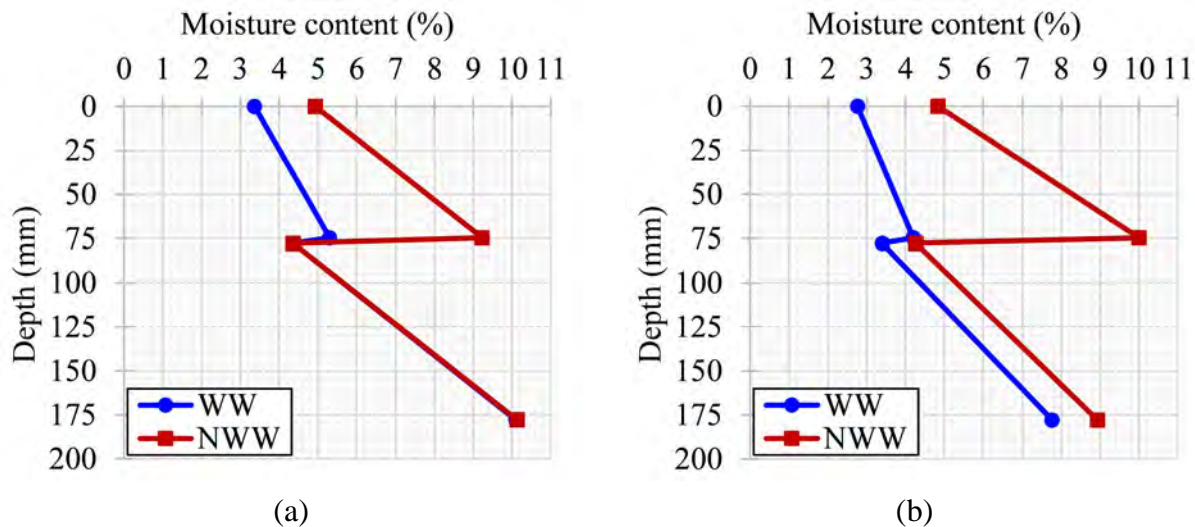


**Figure 4. Moisture content distributions (percentage) in the test box after seven days: (a) wicking geotextile, and (b) nonwicking geotextile (the dashed line represents the geotextile location).**

Figure 5 shows the average moisture content distribution of the soils along the depth of the test box. The geotextile was located at 75 mm. The three-day test results (Fig. 5a) show that the wicking geotextile effectively removed moisture from the soil contained in the upper shear box. On the other hand, moisture accumulated on the nonwicking geotextile's surface within the same time period. The seven-day test results (Fig. 5b) show that the wicking geotextile effectively removed moisture from the soil contained in the upper and lower shear boxes while more moisture accumulated on the nonwicking geotextile's surface due to the gravity effect and inability of the polypropylene fibers to wick water out to the air.



Note: WW=wicking woven geotextile; NWW=nonwicking woven geotextile

**Figure 5. Average moisture content in the soil after: (a) 3 days and (b) 7 days.**

## CONCLUSIONS

This study investigated and compared the wicking ability of two types of woven geotextiles in a river sand using a direct shear box. The sand was prepared at a moisture content close to its field capacity. The geotextile was placed between upper and lower boxes with a 100-mm exposure length on both sides. The evaporation tests were carried out for three and seven days. The moisture contents of the soils at different locations were measured after each test. Important findings from this study are summarized as follows:

- (1) The wicking geotextile reduced moisture content approximately by 30% and 44% from the unsaturated soil placed above the geotextile after three and seven days, respectively. However, moisture accumulated on the nonwicking geotextile's surface without being removed or transferred downward.
- (2) In addition to removing moisture from the soil placed above the geotextile, the wicking geotextile effectively wicked moisture out from the soil underneath the geotextile after seven days.
- (3) The test result indicated the influenced zone was 75 mm above and below the wicking geotextile. To accurately determine this influence distance, a test box with a greater height and depth is required. Also, a waiting period longer than seven days should be considered to quantify the maximum amount of moisture removed by the wicking geotextile.

## ACKNOWLEDGEMENTS

This study was sponsored by TenCate Geosynthetics Americas. Mr. John Lostumbo at TenCate Geosynthetics Americas provided technical guidance for this study. The first author received the GSI Fellowship from the Geosynthetic Institute and the Testing Innovation Fellowship from the Geosynthetic Institute (GSI), the North America chapter of the International Geosynthetic Society (IGS-NA), and ASTM's Committee D35 on Geosynthetics for part of this study.

## REFERENCES

- Adler, M. M., & Walsh, W. K. (1984). Mechanisms of transient moisture transport between fabrics. *Textile Research Journal*, 54(5), 334-343.
- ASTM D 5261. Standard Test Method for Measuring Mass per Unit Area of Geotextiles. *ASTM International*, West Conshohocken, PA, USA.
- Azevedo, M., & Zornberg, J. G. (2013). Capillary barrier dissipation by new wicking geotextile. *In Pan-American conference on unsaturated soils*, 20-2.
- Bai, M., Liu, Z., Zhang, S., Liu, F., Lu, L., & Zhang, J. (2021). Experimental study on the effect of fabric parameter on drainage performance of wicking geotextile. *Fibers and Polymers*, 22(7), 2044-2051.
- Biswas, N., Puppala, A. J., Khan, M. A., Congress, S. S. C., Banerjee, A., & Chakraborty, S. (2021). Evaluating the performance of wicking geotextile in providing drainage for flexible pavements built over expansive soils. *Transportation Research Record*, 2675(9), 208-221.
- Chatterjee, A., & Singh, P. (2014). Studies on wicking behaviour of polyester fabric. *Journal of Textiles*, 1-11.

- De Guzman, E. M. B., Alfaro, M. C., Doré, G., Arenson, L. U., & Piamsalee, A. (2021). Performance of highway embankments in the Arctic constructed under winter conditions. *Canadian Geotechnical Journal*, 58(5), 722-736.
- Fangueiro, R., Filgueiras, A., Soutinho, F., & Meidi, X. (2010). Wicking behavior and drying capability of functional knitted fabrics. *Textile Research Journal*, 80(15), 1522-1530.
- Galinmoghadam, J., Liu, J., Zhang, X., Lin, C., & Guo, Y. (2022). Mitigating Pumping in Pavement Shoulder Using Wicking Geotextile: An Experimental Study. *Transportation Research Record*, 03611981221091730.
- Guo, J., Wang, F., Zhang, X., & Han, J. (2017). Quantifying water removal rate of a wicking geotextile under controlled temperature and relative humidity. *Journal of Materials in Civil Engineering*, 29(1), 04016181.
- Guo, J., Han, J., Zhang, X., & Li, Z. (2019). Evaluation of moisture reduction in aggregate base by wicking geotextile using soil column tests. *Geotextiles and Geomembranes*, 47(3), 306-314.
- Guo, J., Han, J., Zhang, X., & Li, Z. (2021). Experimental evaluation of wicking geotextile-stabilized aggregate bases over subgrade under rainfall simulation and cyclic loading. *Geotextiles and Geomembranes*, 49(6), 1550-1564.
- Hachem, A. E., & Zornberg, J. G. (2019, March). Enhanced Lateral Drainage Geotextile to Mitigate the Effects of Moisture Migration from a High Water Table. In *Geo-Congress 2019*: ASCE, Reston, Virginia, USA, 27-234.
- Hsieh, Y. L. (1995). Liquid transport in fabric structures. *Textile Research Journal*, 65(5), 299-307.
- Koerner, R. M. (2012). *Designing with geosynthetics*, sixth edition, Xlibris Corporation.
- Lin, C., Presler, W., Zhang, X., Jones, D., & Odgers, B. (2017). Long-term performance of wicking fabric in Alaskan pavements. *Journal of Performance of Constructed Facilities*, 31(2), D4016005.
- Lin, C., & Zhang, X. (2018). A bio-wicking system to dehydrate road embankment. *Journal of Cleaner Production*, 196, 902-915.
- Lin, C., Zhang, X., & Han, J. (2019). Comprehensive material characterizations of pavement structure installed with wicking fabrics. *Journal of Materials in Civil Engineering*, 31(2), 04018372.
- Lin, C., & Zhang, X. (2020). Comparisons of Geotextile-Water Characteristic Curves for Wicking and Non-Wicking Geotextiles. In *Geo-Congress 2020*, ASCE, Reston, Virginia, USA, 629-636.
- Lin, C., Zhang, X., Galinmoghadam, J., & Guo, Y. (2022). Working mechanism of a new wicking geotextile in roadway applications: A numerical study. *Geotextiles and Geomembranes*, 50(2), 323-336.
- Liu, H., Han, J., Al-Naddaf, M., Parsons, R. L., & Kakrasul, J. I. (2022). Field monitoring of wicking geotextile to reduce soil moisture under a concrete pavement subjected to precipitations and temperature variations. *Geotextiles and Geomembranes*. <https://doi.org/10.1016/j.geotexmem.2022.07.001>
- Nyoni, A. B., & Brook, D. (2006). Wicking mechanisms in yarns-the key to fabric wicking performance. *Journal of the Textile Institute*, 97(2), 119-128.
- Rajagopalan, D., Aneja, A. P., & Marchal, J. M. (2001). Modeling capillary flow in complex geometries. *Textile Research Journal*, 71(9), 813-821.
- Wang, F., Han, J., Zhang, X., & Guo, J. (2017). Laboratory tests to evaluate effectiveness of wicking geotextile in soil moisture reduction. *Geotextiles and Geomembranes*, 45(1), 8-13.

- Yanilmaz, M., & Kalaoğlu, F. (2012). Investigation of wicking, wetting and drying properties of acrylic knitted fabrics. *Textile Research Journal*, 82(8), 820-831.
- Zaman, M. W., Han, J., & Zhang, X. (2022a). Technical Review of Development and Applications from Wicking Fabric to Wicking Geotextile. *In Geo-Congress 2022*, ASCE, Charlotte, North Carolina, USA, 587-596.
- Zaman, M. W., Han, J., & Zhang, X. (2022b). Evaluating wettability of geotextiles with contact angles. *Geotextiles and Geomembranes*, 50(4), 825-833.
- Zhang, X., Presler, W., Li, L., Jones, D., & Odgers, B. (2014). Use of wicking fabric to help prevent frost boils in Alaskan pavements. *Journal of Materials in Civil Engineering*, 26(4), 728-740.
- Zornberg, J. G., Azevedo, M., Sikkema, M., & Odgers, B. (2017). Geosynthetics with enhanced lateral drainage capabilities in roadway systems. *Transportation Geotechnics*, 12, 85-100.



## **Effect of tensile strength development in stabilisation geogrids on bearing capacity in pavements and railway application.**

**K. Zamara<sup>1</sup>, P. Mazurowski<sup>2</sup>, J. Kawalec<sup>3</sup>, and G. Fowmes<sup>4</sup>**

<sup>1</sup>Tensar International Ltd, Blackburn, United Kingdom

<sup>2</sup>Tensar Polska Sp. z o.o., Gdańsk, Poland

<sup>3</sup>Silesian University of Technology, Gliwice, Poland

<sup>4</sup>Warwick University, UK

### **ABSTRACT**

Improvement of aggregates bearing capacity by installation of stabilising geogrids is a common technique typically when reduction of the aggregate thickness or increase of bearing pressures within the given aggregate thickness is required on a project. The approach of using geogrids in all: pavements, railways and airfields applications to improve design life, increase bearing capacity, achieve construction programme gains or reduce total cost is common. However, the mechanisms involved in the process of stabilising aggregate layers by geogrid installation are still a point of argument between researchers, manufacturers and practitioners.

Pavements design methods incorporating stabilising geogrids are in many cases empirical or approximate based on limited research. Both pavement and geotechnical engineers address the effect of geogrid installation in the given structure by using an improvement factor, other similar coefficients, geogrids tensile strengths or adjusting soil/geogrid composite properties. However, these do not address the actual mechanisms that stabilisation geogrid introduces to the engineering system. Whilst recent ISO 10318-1:2015 defines geogrid stabilisation function by means of enhanced aggregate interlock and confinement, still many practitioners and manufacturers confuse it with reinforcement function described by means of tensile strength and product strain, that potentially have no or minimal effect on improving bearing capacity of a pavement or rail track.

Due to that common confusion observed in the industry the Authors of this paper decided to examine published literature, to establish what are typical measured values of reported tensile stress and strains developing in stabilising geogrids under a prescribed bearing pressure. This is important as monitoring results of geogrid installed in soils/aggregate has a major influence on geotechnical design philosophy and overall understanding of mechanism of bearing capacity improvement by stabilising geogrid.

**KEY WORDS:** Geogrids, strain sensors, stabilisation, tensile strain.

### **INTRODUCTION**

Improvement of surface bearing capacity by installation of stabilising geogrids within a pavement or rail structure is a common technique that limits construction costs by reduction of the aggregate thickness or increase of design life within the given aggregate thickness. The approach of using geogrids in all: pavements, railways and airfields applications to improve design life, increase bearing capacity, achieve construction programme gains or reduce total cost is common. However, the mechanisms involved in the process of stabilising aggregate layers by geogrid installation and improvement of surface bearing capacity are still a point of argument between researchers, manufacturers and practitioners.

Incorporation of geogrids within a pavement or rail structures contributes to reduced carbon footprint emissions, meaning reduced need for aggregate material or reduced maintenance

work required for the structure, therefore solutions incorporating geogrids became popular amongst local councils or road authorities worldwide for its sustainability goal.

This paper presents and evaluates research that investigated geogrids improvement effects on surface bearing capacity within pavements and railway track beds. This paper summarises the reported strain force and tensile strength recorded either through full scale experiments or scaled down laboratory experiments. Axial forces and corresponding strains developing within geogrids are an important aspect that allows to understand principal mechanisms that contribute to increased surface bearing capacity of a stabilized layer. The available site data or laboratory experiments are limited, however the trends of geogrid behaviors for both type of structures: pavements and railways are similar.

ISO 10318-1:2015 defines geogrid mechanical stabilisation function by means of aggregate interlock and confinement, as opposed to reinforcing function being correlated to geogrid tensile strength (e.g. in mechanically stabilised earth walls applications). Stabilisation historically has been researched and covered under reinforcing function of geogrids, however many studies (e.g. Haas 1988, Cook et al 2016) have distinguished in-between the two different reinforcement and stabilisation mechanisms.

## **STABILISATION GEOGRIDS IN FLEXIBLE PAVEMENTS**

Geogrids in pavement application can be installed as ground improvement technology, where the layer mechanically stabilized by geogrid reduces stresses transferred through the surface to the weak subgrade. Further they are often installed within the capping to reduce the thickness of this layer or extend the design life of this pavement. Geogrids also can be installed within pavement base for pavement optimization reducing significantly thickness of expensive layers of the pavement or extending pavement design life.

For all this installation locations geogrids through interlock and confinement create a stiffer layer of aggregate which enhances the angle of load distribution, allowing higher bearing pressures being imposed on the structure surface (e.g. Cook et al 2016). Figure 1 presents the principals of the interlock and confinement mechanisms that comprise an essence for the true geogrid stabilization mechanisms.

It was observed that typically strain measurement appears to be a by-product of studies focusing on global performance of a system, where focus would be rather on another aspect such total settlements and system deformation, rather than solely geogrid axial performance study in soil. However, in the last decades many researchers attempted to measure strains developing in geogrids in both laboratory and field experiments.

Table 1 and 2 summarise the relevant research and the main aspects of the reviewed studies. It is noticeable that very little published data exists where geogrids were monitored for strains development. The reported studies in majority include railway applications.

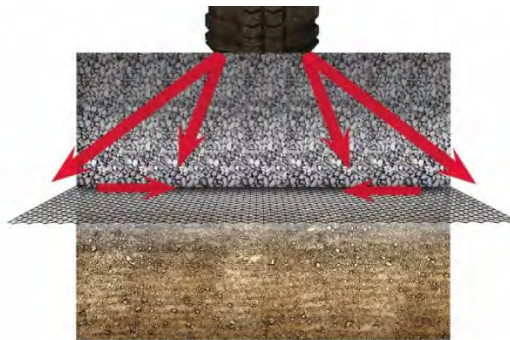


**Figure 1. Mechanism of geogrid support – stabilizing through interlock and confinement**

**Test results.** Even though geogrids in flexible bounded or unbounded pavements have been installed for decades, there is a scarce of information available on *in situ* geogrid performance in pavement applications. More data was published for railway applications, which implies that more research in that topic has been undertaken for railway industry.

Hass et al 1988 and Tang et al 2012 undertook a study that investigated geogrids strain development due to cyclic loading imposed by either a loaded plate or moving wheel simulator. Both were the laboratory studies.

Cyclic plate load test is by far the most popular and simple way of laboratory measurements. Hass et al 1988 reported up to 700 000 cycles of load where maximum strain reached 1.3%. Interestingly, this study also shows the gradual increase in strains where at 250 000 cycles 0.5% strain was not exceeded. Haas et al 1988 concluded that for the maximum geogrid performance within the flexible pavement structure, it should be positioned so the strains developing in the geogrid remain within 0.05 to 0.2% beneath the load center. In addition, the grid in its design life should not exceed 1 to 2% strain for the given allowable rut depths. According to Haas et al 1988 this allows the grid to work within elastic limits providing the aggregate with effective confinement and prolonging life of the pavement structure.

Tang et al 2012 used a more sophisticated equipment resembling more the actual mechanism of a wheel load for a pavement. A reduced scale model mobile load simulator (MMLS3) was used to investigate mechanically stabilized pavement performance. Pavement section was scaled to one-third of the full-scale test (40mm asphalt, 100mm base layer and subbase layers). Tang et al 2012 reported strains of 0.2% under the load of 2.7kN and 100 000 cycles. Maximum reported tensile strength was at 0.65kN. The study also concludes on reduced rate of deformation with time on the tested sections with geogrids, in comparison to control section without any geogrid.

The study of Ibrahim et al 2017 is unique, as it takes a product that is designed for reinforcement applications (e.g. retaining walls) and for typical membrane mechanisms (Figure 3) e.g. high tensile strength, and studies it against mechanical stabilization application. The research similarly to Haas et al 1988 undertook a laboratory investigation however a static plate load test was used here driven to very high stresses – up to 1MPa acting on 100mm dia loading plate. The results of tests with geogrid being installed at various depths within the granular fill were presented. The results show relatively low strains development within monitored geogrids and strains level changing as the geogrid is placed at different depths of the base course. Conditions resembling typical working conditions of geogrids strains of 0.4% were not reached. Interestingly strains of the base course layer was monitored at different levels with strains of the layer reaching 1.5% for geogrid located at the interface between asphalt concrete and base course.



**Figure 2. Mechanism of reinforcement – membrane effect.**

The above limited research shows that geogrid working conditions are well within geogrids elastic limits. The offered improvement of bearing capacity results from geogrid characteristics and interaction with the aggregate that is not reflected through geogrids ultimate tensile strength. The high-level aggregate stiffness created by installation of a geogrid forms a stiffer platform that transfer the loads from the wheel through to the surface and the subgrade using much larger area, than comparing with the aggregate without a geogrid. Enhanced reduction of the surface pressures, however, this occurs within very small strain levels in the geogrid.

Not all above research converted strains into tensile force, however still it is expected that at such a minimal developed strain level, tensile strength would remain within very low levels not exceeding few kN.

**Table 1. Summary of research incorporating strain measurement on geogrids in pavements**

References	Application	Results Maximum	Comment
Haas et al 1988	Flexible pavement	Max 1.3% @ 700 000 cycles  <0.5% @ 250 000 cycles	Laboratory. Cyclic plate load test in a box;  550kPa load (80psi), 700 000 loading cycles
Tang et al 2013	Flexible pavement	Max 0.2% Max 0.65kN/m	Reduced scaled accelerated pavement testing.  100,000 passes MMLS3 applying load of 2.7kN  The strain gauge had a backing material constructed from polyimide, and the measurement grid is made of a constantan alloy that can sustain strains up to 5%.
Ibrahim et al 2017	Flexible pavement	Max 0.4% at 826kPa for geogrid@150mm deep base course	Uniaxial grid being tested in a box using static plate load test loads up 1000kPa were imposed. Geogrid was tested at various heights in the box.

## STABILISATION GEOGRIDS IN RAILWAY

In railway track bed structures geogrids are typically installed within ballast or sub-ballast layers. Installations within ballast layers typically are solely to extend the periods between ballast tamping works. This is achieved by improved lateral confinement of the ballast by geogrid installation.

Installation of geogrids within sub-ballast layer aims at improving layers bearing capacity but also to limit vertical and horizontal deformation at the surface. Improvement of sub-ballast bearing capacity results in reduced stresses being transferred to the underlaying subgrades, what is response results in reduced deformations of the rail alignment. Again, in railway application the improved aggregate confinement creates a stiffer aggregate layer that enhances transfer of dynamic forces applied by the passing train to the underlaying subgrade.



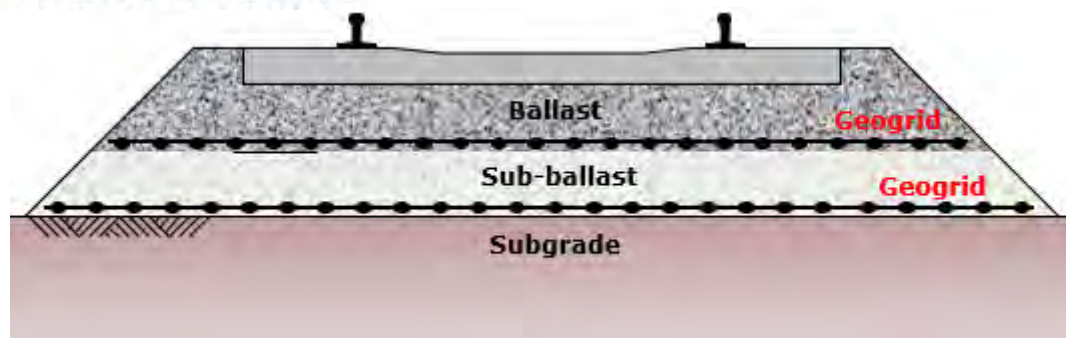


Figure 2. Geogrids in railway track bed engineering

**Test Results.** The published railway studies present a wide range of methodologies being utilized to investigate track bed performance. Horníček L and Rakowski Z 2019 undertook a laboratory study using a testing box and a cyclic plate load mechanism to measure settlement, where lateral pressures imposed on the box under dynamic load were measured. Up to 2 000 000 load cycles were applied to the sample. The project investigated railway tunnel applications hence the sample comprised ballast only or sub-ballast, both with interlayered geogrids. Strains were recorded using strand meters installed on the geogrid samples Horníček L and Rakowski Z 2019. This study recorded max strain developing in the geogrid to be 0.028%. No information on axial forces developing within geogrids were provided. Significant number of cycles allowed to show that within initial part the material undergoes still initial compaction whilst after 100 000 cycles only further 1mm deformation occurs.

Another study Anantanasakul et al 2012 reported a field trial where under a life railway line different types of instrumented geogrids were installed in the ballast and sub-ballast. This study recorded the highest cumulative strains ranged between 0.6% and 1.8%. This reflected plastic long term deformation, whilst elastic deformation reported that under an actual load of a traveling train strains were between 0.14 to 0.17%. This study also concluded with the effectiveness of geogrids improving as the subgrade stiffness was decreasing.

An interesting study on high speed railway was reported by Chen et al 2016, where load transfer platform with induced consolidation was monitored. Reported axial forces do not exceed 2 kN/m for construction stage of 2.7m high embankment. Further oscillation of  $\pm 0.2$  kN/m occurs along the geotextile during static load stage of 40kPa. When the 'consolidation' of soil is induced by forcing settlement of soil between the piles, increased tensile forces develop just 7 to 18kN/m for induced 35mm settlement between the piles. Locations of maximum tensile strength development are located on piles edge. Interestingly Chen et al 2016 compared the static case with theoretically derived tensile forces based on BS8006 or modified approach of BS8006. For the cases where the calculated settlement was not exceeding 30mm tensile force on the geogrid was overestimated by a factor of 2. With the increased deformation of the subgrade modified calculation methods were closer to the actual monitored values.

Lenart and Klompmaker 2010 published a study where during rail rehabilitation, monitoring instrumentation was installed on the geogrid that was used as sub-ballast and ballast stabilisation. The monitoring data covered five years of the rail operations. Strains in both directions: transverse and longitudinal were monitored. Monitoring instrumentation in form of strain gauges attached to geogrids and extensometers in soil were installed within the monitored sections. The reported maximum cumulative strains from strain gauges at sub-ballast level did not exceed value of 0.3-0.4%. it is worth noting that an initial high peak is recorded following installation and further plateau in the graph varying by  $\pm 0.1$ %. Similar results were presented for geogrid installed underneath a ballast.



**Table 1. Summary of research incorporating strain measurement on geogrids in pavements**

References	Application	Results Maximum	Comment
Anantanasakul et al 2012	Railway	Max cumulative strains between 0.6% to 1.8%  Transient strains induced by 30 tons axial load traveling at 40km/hr 0.14%-0.17%	Field trial. 90 days of monitoring $2.3 \times 10^5$ load cycles.  6 sections various grids monitored
Chen et al 2016	High speed rail embankment on load transfer platform	0.33kN/m @ static load of 40kPa 1.5kN/m @ subsoil soil settlement of 20mm at pile cap location	Load transfer platform test. Large scale laboratory test with 8 actuators. Static test with load varying from 4kPa to 40 kPa, then induced consolidation in soft soils, lastly dynamic load with speed of 324km/h
Hornicek & Rakowski 2019	Railway	Max strain 0.028%	Laboratory. Cyclic plate load test in a box;  Up to 100kN applied to 0.79m DIA plate;  Up to 2 000 000 loading cycles, tests run with 25, 50, 75 and 100kN load;
IGS 2019	Railway	Max strain 0.15% @ 21 kN load  Max strain 0.2% @ 31 kN load	Laboratory. Cyclic load of a single sleeper.  Load between 21kN (passenger train) to 31kN (freight train)  100 000 loading cycles
Lenart, S., Klomp maker, J. 2014.	Railway	Max strain recorded 0.4%	Site monitoring over a period of 5 years

## DESIGN IMPLICATIONS

Implementing stabilisation geogrids in a design either for pavements or for railway is not a straightforward task. The benefit of using geogrids to improve structures performance has been recognized for decades and has been recommend by Road and Rail Authorities across the world. However, the improvement effect varies depending on a geogrid manufacturer.

One of the latest developments in the field that attempts to quantify the geogrid effect and that resembles the true stabilising mechanisms of geogrids within the mechanically stabilized layer is presented by Lees 2017 and Lees and Clausen 2020. Research shows that the effect of the increased confinement that geogrid offers to stabilised soil diminishes with distance from the geogrid (Figure 3). The effect of geogrid is not constant across the stabilised layers. Hence, Lees 2017 choose to vary stabilised soil block strength parameters with distance from the geogrid (see Figure 4).

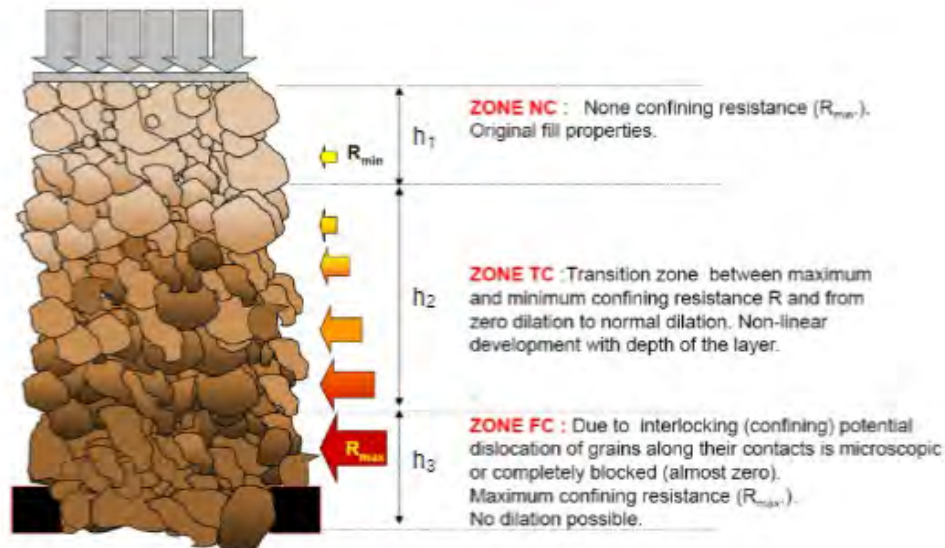


**Figure 3. Hypothetical zones of confining resistance (interlocking effect)**

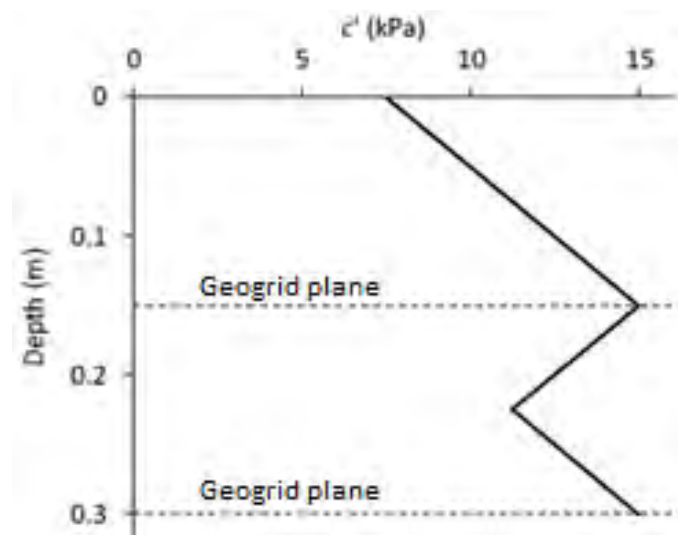


**Figure 4.  $c'$ -profile adopted for stabilised sandy gravel layer in FEA of plate load test (Lees 2017)**

## CONCLUSIONS

Measurement of the actual geogrids axial forces that develop in the product post installation, during its lifetime provides a valuable insight to the principal mechanism of the product support to the structure. The above review aims to provide the engineer with scientifically supported evidence demonstrating true stabilisation mechanisms that improves bearing capacity of aggregate layer mechanically stabilized by geogrids.

Mechanism involved in stabilisation application of geosynthetics differ from typical reinforcement mechanism where tensile strength and strains developed within the product are the design parameters. Stabilisation manifests itself by increased confinement and geogrid interlocking aggregate, where developed strains and tensile strength do not perform a critical role.

Even though much of research indicates that stabilizing geogrids to improve over all performance of the structures and increase surface bearing capacity, need to operate within

very little tensile strain (<0.5%), there is still much contradicting information in the literature and within the industry.

This paper presented a high-level review of the literature and available research to understand better the actual mechanisms involved in improved bearing capacity results of an aggregate mechanically stabilized by geogrids. The review addressed both flexible pavement and railway applications.

Typical values recorded by researches globally, focusing specifically on strains and axial tensile forces development were reported. The aim of this exercise was to examine the common argument around required magnitude of tensile strength within stabilising geogrid. The values recorded by various researchers worldwide range from 0.01% and exceed 1%. The higher values typically are associated with membrane effect developing in the geomembrane where reinforcement mechanisms are triggered, and higher deformations occur. Relatively low axial strain values correspond with relatively low axial tension values ranging in the reported data between. From the monitored deformation many studies demonstrated improved performance of the mechanically stabilized layer as opposed to un-stabilised control.

## REFERENCES

- Anantanasakul, P., Indraratna, B., Nimbalkar, S. S. & Neville, T. (2012). Field monitoring of performance of ballasted rail track with geosynthetic reinforcement. In G. A. Narsilio, A. Arulrajah & J. Kodikara (Eds.), 11th Australia - New Zealand Conference on Geomechanics: Ground Engineering in a Changing World (pp. 241-246). Australia: Engineers Australia.
- BS 8006-1:2010+A1:2016 *Code of practice for strengthened/reinforced soils and other fills*
- Chen RP, Wang YW, Ye XW, Bian XC and Dong XP 2016 *Tensile force of geogrids embedded in pile-supported reinforced embankment: A full-scale experimental study*. Geotextiles and Geomembranes 44 (2016) 157-169
- Cook, J., Dobie, M. and Blackman, D., 2016. *The Development of APT Methodology in the Application and Derivation of Geosynthetic Benefits in Roadway Design*. © Springer International Publishing Switzerland 2016 J.P. Aguiar-Moya et al. (eds.), The Roles of Accelerated Pavement Testing in Pavement Sustainability, DOI 10.1007/978-3-319-42797-3\_17
- Cook J and Horvat F 2014. Assessment of particle confinement within a mechanically stabilised layer. 10th International Conference on Geosynthetics, Berlin, Germany 21-25 September 2014.
- Horníček L and Rakowski Z 2019 *Mechanically Stabilized Granular Layers - An Effective Solution for Tunnel Projects*. In: Badr M., Lotfy A. (eds) Sustainable Tunneling and Underground Use. GeoMEast 2018. Sustainable Civil Infrastructures. Springer, Cham
- Haas R, Walls J and Carroll RG 1988 Geogrid Reinforcement of Granular Bases in Flexible Pavements; Transportation Research Record 1188
- IGS 2019. 10 – 13 November 2019, the IGS Technical Committee on Stabilization (TC-S), prof Bian of Zhejiang University presentation, Prague, Czech Republic.
- ISO 2015. Geosynthetics – Part 1: Terms and definitions 10318-1:2015. ISO/TC 221 Geosynthetics.
- Lees AS and Clausen J 2020. Strength envelope of granular soil stabilised by multiaxial geogrid in large triaxial tests. Canadian Geotechnical Journal 2020, 57 (3): 448-452.
- Lees AS 2017 Simulation of geogrid stabilisation by finite element analysis. Proceedings of the 19th Intern. Conf. on Soil Mechanics and Geotechnical Engineering, Seoul 2017

- Lenart, S., Klompmaker, J. 2014. *Geogrid reinforced railway embankment on soft soil – Experiences from 5 years of field monitoring*. 10<sup>th</sup> ICG Berlin 2014
- Rakowski, Z., Kawalec, J. 2009. Mechanically stabilized layers in road construction, not published printed conference presentation, XXVII. International Baltic Road Conference, August 2009, Riga (Latvia)
- Tang X, Stoffels S and Palomino AM 2013 Reinforcement Tensile Behavior Under Cyclic Moving Wheel Loads; Transportation Research Record Journal of the Transportation Research Board 2363(-1):113-121

## **Evaluation of Geosynthetic-reinforced Asphalt Milling Characteristics and Suitability as Pavement Base Course**

**Ashray Saxena<sup>1</sup>, Natalia S. Correia<sup>2</sup>, V. Vinay Kumar<sup>3</sup>, and Jorge G. Zornberg<sup>4</sup>**

<sup>1</sup>Department of Civil, Architectural and Environmental Engineering, University of Texas at Austin, Austin, Texas-78712, e-mail: [saxena\\_ashray@utexas.edu](mailto:saxena_ashray@utexas.edu)

<sup>2</sup>Federal University of Sao Carlos, Civil Engineering Department, Washington Luis Rd., km 235, Sao Carlos, Sao Paulo 13.565-905, Brazil, e-mail: [ncorreia@ufscar.br](mailto:ncorreia@ufscar.br)

<sup>3</sup>Department of Civil, Architectural and Environmental Engineering, University of Texas at Austin, Austin, Texas-78712, e-mail: [vinay.vasanth@utexas.edu](mailto:vinay.vasanth@utexas.edu)

<sup>4</sup>Department of Civil, Architectural and Environmental Engineering, University of Texas at Austin, Austin, Texas-78712, e-mail: [zornberg@mail.utexas.edu](mailto:zornberg@mail.utexas.edu)

### **ABSTRACT**

The use of reclaimed asphalt pavement (RAP) as roadway base course has provided both, environmental and economic benefits leading to sustainable pavement construction practices. Specifically, reuse of milled asphalt layers in pavement construction reduces the requirement of virgin aggregates (VA) and the associated cost. On the other hand, due to the possibility of milling asphalt layers that contain geosynthetic interlayers, studies have been carried out to understand the characteristic and behavior of RAP obtained from geosynthetic-reinforced asphalt, which is referred herein, as GRAP. The objective of this research is to investigate the suitability of reusing the GRAP as pavement base course. Accordingly, blends of 50% RAP and 50% VA base course material, and 50% GRAP and 50% VA were evaluated, as well as 100% VA. The laboratory evaluation of different blends included determination of particle size distribution, moisture-density relationship, coefficient of permeability, water absorption and bitumen content, and fragmentation value. Comparison of characteristics of different blends evaluated in this study suggest RAP containing geosynthetic fragments exhibited similar behavior compared to only RAP. Additionally, the results from this investigation indicate that both RAP and GRAP blends with VA exhibited adequate workability and properties, indicating their potential use as pavement base course material.

### **INTRODUCTION**

The practice of milling the pre-existing asphalt surfaces, either partially or completely prior to the placement of the hot mix asphalt (HMA) overlay is the most common and traditional flexible pavement rehabilitation technique. During the asphalt milling process, large quantities of material including asphalt that are analogous to an aggregate-sized particle are generated, which is known as recycled asphalt pavement (RAP). RAP has been used in infrastructure applications since 1930 (Texas Report 1272-1S, 1994) with the aim of reducing the use of non-renewable aggregates in the roadways. The use of RAP as an alternative material is certainly a sustainable construction, since the need of excavating or producing raw materials for construction, their handling, transportation and storage can be minimized, which in turn minimize the energy consumption and impact of construction activity on the environment.



The Federal Highway Administration (FHWA) estimated that 100.1 million tons of asphalt pavements are milled off each year during resurfacing and widening projects (Thakur and Han 2015). RAP is mostly used to produce new asphalt mix for the base courses, and as a replacement of granular material in base and subbase courses, as well as in the shoulders, parking lots, bicycle paths, gravel road rehabilitation, residential driveways, trench backfill, and embankments among others. The Texas Department of Transportation (TxDOT) promotes using RAP in many pavement management strategies, such as hot recycling for new asphalt surfaces, shoulder surfacing and extra widening of roadways. In addition, warm and cold recycling of RAP includes usage of RAP as base or sub-base aggregate and as a backfill in retaining walls. Recently, several developments in the incorporation of RAP bases for environmentally friendly roadway applications have been demonstrated. Hopp et al. (2015) opines that there is a potential for significant economic benefits if RAP is used in base and subbase applications, i.e., approximately 30% in material cost savings could be realized with a 50% replacement of virgin aggregates (VA) with the RAP. Numerous researchers (e.g., Highter et al. 1997; Bejarano 2001; Guthrie et al. 2007; Abdelrahman et al. 2010; Cosentino et al. 2012; Seferoglu et al. 2018; Plati and Cliatt 2019) conducted laboratory studies on suitability and evaluation of RAP as a roadway base material that included moisture-density characteristics, California Bearing Ratio (CBR), unconfined compressive strength (UCS), shear strength characteristics, and resilient modulus. Plati and Cliatt (2019) demonstrated that both 100% RAP and 50% RAP-50% VA blends produced modulus values similar to that of conventional (100% VA) blends. Overall, most of the studies suggest that RAP blended with VA and/or stabilized with chemical additives can be a potential roadway base. However, few studies have reported contradictory results regarding the RAP blends' mechanical behavior. While, it is important to note that the RAP behavior depends on multiple parameters including their particle size gradation, bitumen content of RAP and percentage of RAP mixture included in the blends (Seferoglu et al. 2018).

On the other hand, geosynthetic interlayers have been very widely installed within the asphalt layers mainly to minimize reflective cracking (Kumar and Saride 2017; Saride and Kumar 2019); minimize permanent deformations and strains (Correia and Zornberg 2016; Kumar et al. 2021a, 2022); and enhance fatigue performance (Kumar et al. 2021b) of asphalt pavements. However, such conditions may lead to the possibility of milling asphalt layers that may contain geosynthetic interlayers. Hence, experimental research studies on the topic of geosynthetic-reinforced asphalt milling need to be conducted to understand the characteristics and behavior of RAP obtained from milling such asphalt layers reinforced with geosynthetic interlayers. While this topic is quite new or rather very limited literature exists, it is important to note that with the growing trend of incorporating geosynthetics within the asphalt, there is a possibility for an increase in the occurrence of RAP that contains remnants of geosynthetic interlayers. The question of whether the geosynthetic-reinforced asphalt millings affect the engineering performance of an asphalt mix containing RAP with geosynthetic fibers has been raised by Gu et al. (2021). Furthermore, discussions of whether geosynthetic-reinforced asphalt is “millable”, whether geosynthetics tear apart or not during milling or if they interfere with the milling process have become more frequent concerns to the asphalt pavement community, while this is a rarely explored topic. However, Tran et al. (2012) did explore such a topic of milling the geosynthetic-reinforced asphalt layers. In addition, they compared properties of asphalt mixtures prepared using 30% RAP (without geosynthetics) and 30% RAP containing a geosynthetic reinforcement obtained from their study, separately. They reported that there were no significant variations between the two asphalt mixtures, in terms of their tensile strength characteristics, rutting performance, moisture damage,

and thermal cracking analysis. On the other hand, Gu et al. (2021) highlighted that a 30% RAP containing milled polypropylene fabric had excellent resistance against moisture damage, rutting and thermal cracking conditions. In addition, they reported that the performance of asphalt mixtures containing RAP with geosynthetic fibers were quite similar to that of a conventional asphalt mixture without any RAP.

In summary, the evaluation of millability and recyclability of geosynthetic-reinforced asphalt millings are very limited in number, which needs more attention. In this regard, this study aims at evaluating the characteristics of geosynthetic-reinforced asphalt millings, referred herein as GRAP, and their suitability as a roadway base. Specifically, different blends including VA, RAP, and GRAP have been evaluated under laboratory conditions, in this study. The evaluation includes determination of particle size gradation, moisture-density relationship, coefficient of permeability, water absorption, bitumen content and fragmentation value.

## MILLING AND SAMPLE COLLECTION

The geosynthetic-reinforced asphalt millings and the conventional RAP were collected from an ongoing rehabilitation project along US70/84 at Muleshoe, TX that required removal of asphalt layers completely and placing new asphalt layers. The pavement structure (see Fig. 1a) comprised of limestone granular base and subbase layers with a combined thickness of 300 mm and an asphalt layer with a total thickness of 110 mm that consisted of a 50 mm thick bottom layer and a 60 mm thick top layer with a paving fabric at their interface. A dense graded asphalt concrete referred as TY-C was adopted in both the top and bottom asphalt layers. Until 1995, the roadway had only 50 mm thick asphalt layer and during the pavement rehabilitation process in 1995, a paving fabric was installed prior to the placement and compaction of the 60 mm thick asphalt overlay. The paving fabric, used as stress relieving interlayer, was a polypropylene nonwoven geotextile. The milling operation comprised of two stages: first, milling the top 50 mm of the 110 mm thick asphalt layer to collect the RAP without any geosynthetic. Next, the remaining 60 mm thick asphalt layer comprising geosynthetic at a depth of 10 mm from the previously milled surface was milled to collect the GRAP samples. Figure 1 shows the roadway profile prior to the milling (see Fig. 1a) and the roadway profile after the milling operation (see Fig. 1b).

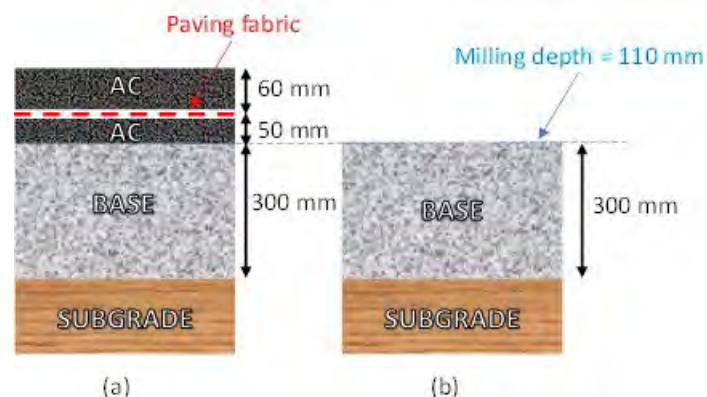


Fig. 1. Road profile: (a) before milling; (b) after milling.

The milling operation was completed using a cold milling machine and no detrimental effect was observed during the process of milling geosynthetic-reinforced asphalt. The

fibers/pieces of milled geosynthetic were evenly distributed in the RAP. Figure 2 shows the process of milling the asphalt with and without geosynthetic interlayer to collect the RAP and GRAP samples in this study. As shown in the figure, the asphalt was milled and loaded via conveyors onto the dump truck and then transported to the stockpile. Samples were then collected from the stockpiles for the laboratory evaluation conducted in this study. Figure 3 shows the GRAP mixture consisting of geosynthetic fibers/pieces, and it can be observed that the geosynthetic pieces have asphalt mastic glued around them, which maybe crushed to match the grain size gradation requirements.



Fig. 2 - Milling operations to collect RAP and GRAP samples at US70/84 (July 2022).



Fig. 3 – GRAP samples collected in this study.



## MATERIALS AND METHODS

### Reclaimed Asphalt Pavement (RAP)

Control RAP and GRAP samples collected from the stockpiles were completely dried out to identify the necessity of crushing them before their characterization. Crushing process was conducted in the laboratory using the modified Proctor compaction hammer that included repeatedly dropping 4.5 kg weight from a height of 450 mm for 100 times. Figure 4 presents the sample collected from stockpile (Fig. 4a), which is being crushed in the laboratory (Fig. 4b), and the crushed GRAP sample used for characterization (Fig. 4c). The crushed RAP and GRAP samples were sieved to determine their gradation curves as presented in Fig. 5. The sieve analysis helped to identify RAP particle sizes and whether GRAP required screening the geosynthetic fibers. As shown in the figure, the gradation curves for RAP and GRAP varied slightly due to the presence of geosynthetic pieces and the asphalt mastic around them, which eventually led to a coarser gradation for GRAP in comparison with RAP samples tested in this study.



Figure 4. (a) GRAP sample collected from the stockpile; (b) GRAP crushing in the laboratory; and (c) Crushed GRAP sample.

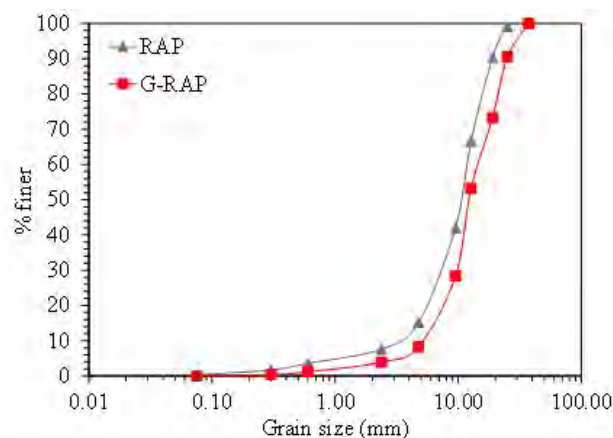


Figure 5. Particle size distribution curves of crushed RAP and GRAP.

During the sieve analysis of GRAP samples, fragments of geosynthetics were observed only up to 12.7 mm sieve and no traces were found thereafter, as shown in Figure 6. This condition maybe due to the reason that geosynthetic pieces were larger in size and additionally, the asphalt

mastic around them increased their size. On the other hand, based on the gradation curves of RAP and GRAP material, additional VA material was blended separately to match the gradation requirements of granular road base.

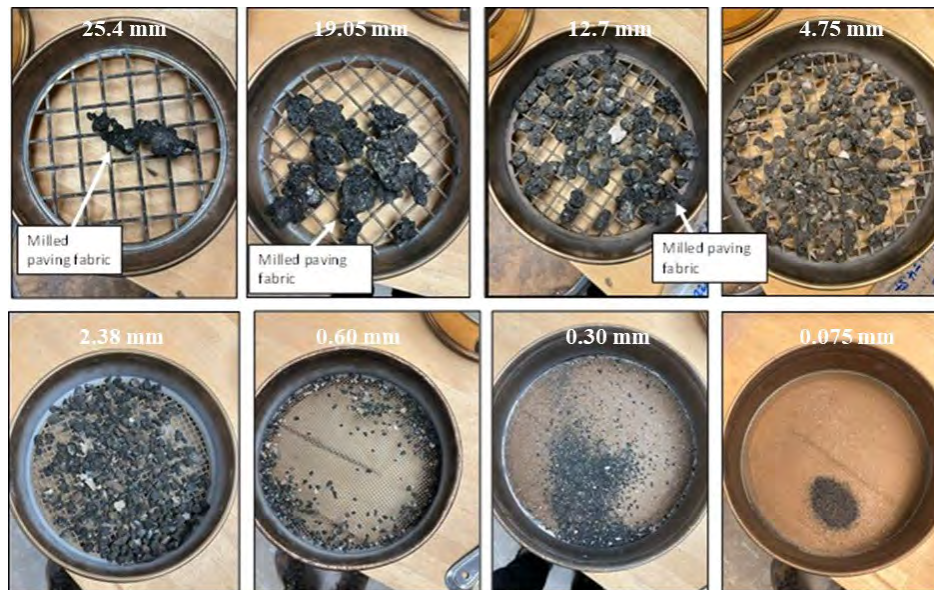


Figure 6. Overview of GRAP sieving and fragments of milled geosynthetic.

### Virgin aggregate-RAP mixtures

Three different blends including VA, GRAP and RAP were investigated in this study to evaluate their suitability as a roadway base (see Fig. 7). Specifically, 50%RAP-50%VA (Fig. 7c) and 50%GRAP-50%VA (Fig. 7b) blends were developed and characterized along with a 100% VA blend (Fig. 7a) for comparisons. The VA material adopted in this study mainly comprised limestone aggregates and was obtained from Marble Fall Quarry - Texas Material in Texas, per AASHTO requirements. The RAP-VA and GRAP-VA mixtures were blended to meet gradation specifications (TxDOT, 2014) and are referred herein as 50-50 RAP, 50-50 GRAP mixtures. Figure 8 shows that gradation curves for all the three different blends of materials investigated in this study along with the upper and lower gradation limits for a roadway base. As shown in the figure, the different blends investigated in this study satisfy the base course gradation requirements, per TxDOT: Item 341 (TxDOT, 2014).

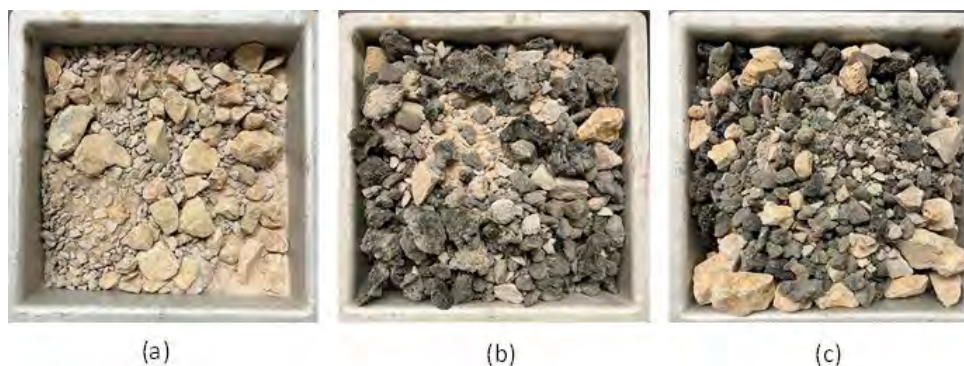


Figure 7. Investigated materials: (a) virgin aggregate; (b) 50-50 GRAP; (c) 50-50 RAP.



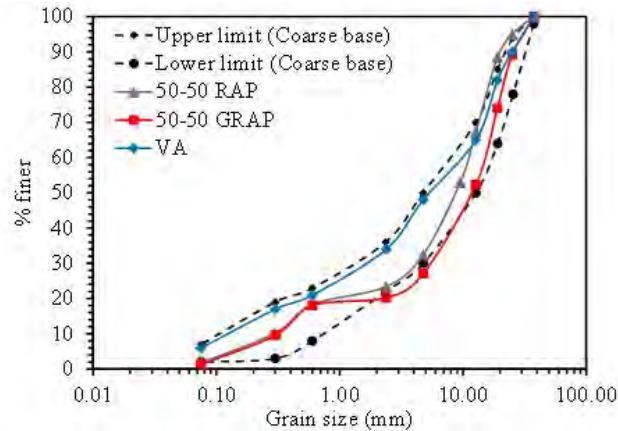


Figure 8. Investigated material gradation curves and coarse base limits.

## Testing Program

The testing program included characterizing the RAP-VA and GRAP-VA blends along with VA blends for comparison. The characterization included determining the moisture-density relation, permeability characteristics, water absorption and binder content in RAP and GRAP, and fragmentation test results. The moisture-density characteristics for VA, 50-50 RAP, and 50-50 GRAP blends were determined using modified Proctor tests, per AASHTO T 180. Specifically, a hammer of 4.5 kg was lifted and dropped from a height of 450 mm, to compact the material in five equal layers with about 56 impacts per layer.

Permeability characteristics of VA, 50-50 RAP and 50-50 GRAP blends were evaluated, per ASTM D2434. Consequently, a constant head permeability test method was chosen for determining the permeability coefficient using a cylindrical sample with 152 mm diameter and 254 mm height. Samples were compacted considering 100% degree of compaction. Figure 9 shows the different samples during the constant head permeability test: VA (Fig. 9a), 50-50 RAP (Fig. 9b) and 50-50 GRAP (Fig. 9c).

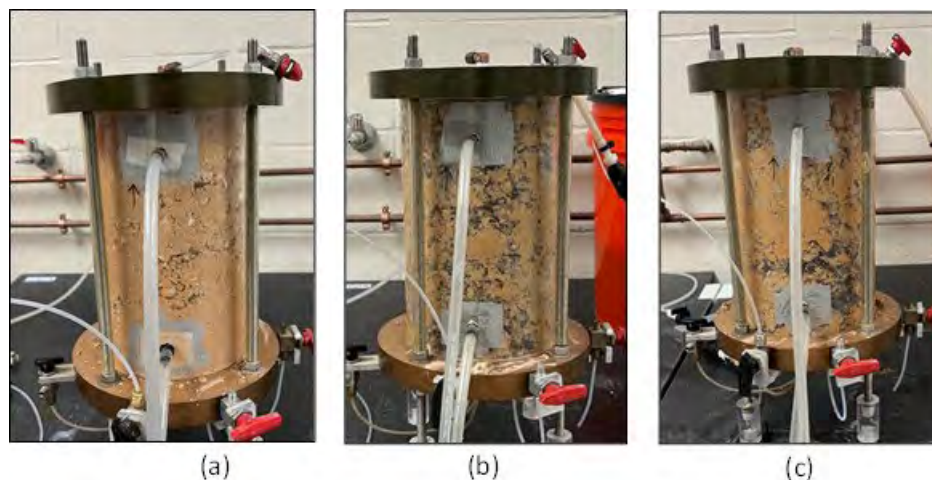


Figure 9. Permeability tests of investigated materials: (a) Virgin aggregate; (b) 50-50 RAP; (c) 50-50 GRAP.

Water absorption value presents the ability of an aggregate to absorb bitumen. In this study, water absorption tests were conducted on VA, 50-50 RAP and 50-50 GRAP blends, per AASHTO T85. Specifically, about 3 kgs of sample was measured and immersed in water for about 24 hours, removed after 24 hours and surface dried before measuring their weight again. Finally, the surface dried samples were completely dried in the oven and weighed again. On the other hand, bitumen extraction tests were conducted only on RAP and GRAP samples, per AASHTO T164. In the case of GRAP, pieces of large geosynthetics were manually removed to determine the binder content of the surrounding aggregate particles. Figure 10 shows the bitumen extraction test used in this study.



Figure 10. Bitumen extraction test.

The RAP samples evaluated in this study contained fragments of geosynthetic, hence the fragmentation test was conducted, per RILEM TC237-SIB technical committee recommendation (Tebaldi et al. 2019) to evaluate the influence of geosynthetic fragments on aggregate quality after impact and temperature variations. The fragmentation test was conducted using a modified Proctor setup (per ASTM D1557 and AASHTO T180) on a fractioned single size aggregate material that was subjected to a series of standard impact loads at various temperatures. The fragmentation test measures a particle's resistance to fragmentation after being subjected to a series of shocks from the impact of a steel mass (rammer) being dropped onto a constrained sample inside a cylindrical steel mold. The amount of material passing through a 1.6 mm sieve is then measured. As a result, the coefficient of fragmentation is defined as the ratio of the weight of the material passing through 1.6 mm sieve after impact and the weight of the material before impact. This test is recommended to be performed with aggregate material divided into four parts of 20/30, 14/20, 10/14 and 5/10 mm at three different temperatures (5°C, 20°C and 40°C). Prior to testing, the material must be stored in the oven for at least 4 hours. A standard rammer delivers 56 blows on each of the five layers in the modified Proctor compaction test. The percentage of the material passing through 1.6 mm control sieve is then calculated after aggregate material is subjected to impact loads. It should be noted that the control sieve used in this study is 1.7 mm, similar to that used by Guduru et al. (2022).

## RESULTS AND DISCUSSION

### Moisture-Density Characteristics

The modified Proctor compaction of VA blends resulted in an optimum moisture content (OMC) and maximum dry densities of 5.5% and 24.1 kN/m<sup>3</sup>, respectively. Similarly, the OMC and MDD

for the 50-50 RAP material was determined to be 5.0% and 22.1 kN/m<sup>3</sup>, respectively. While the OMC and MDD of 50-50 GRAP blends were determined to be 4.43% and 21.4 kN/m<sup>3</sup>, respectively. In the case of moisture content, it was found that the presence of RAP reduced the 50-50 RAP blend OMC by 0.5%. In the case of 50-50 GRAP, the reduction was 0.57% compared to 50-50 RAP blends. Thus, the presence of the geosynthetic did not significantly alter the moisture characteristic of the RAP-VA blend. While, the MDD for RAP blends was lower than that of VA. The same behavior was found by Guthrie et al. (2007) and Seferoglu et al. (2018), explained by the presence of bitumen surrounding the RAP aggregates, which inhibits compaction and reduces dry densities of RAP-VA blends. On the other hand, the presence of the geosynthetic in the RAP blends did not significantly influence the MDD characteristics compared to that of 50-50 RAP blends.

### **Permeability Characteristics**

The coefficient of permeability for VA blends were determined to be 0.24 cm/s and 0.234 cm/s from duplicated tests. While, the coefficient of permeability of 50-50 RAP and 50-50 GRAP blends were determined to be 0.598 cm/s and 1.17 cm/s, respectively. This is consistent with moisture-density characteristics results obtained in this study for RAP and GRAP blends. On the other hand, researchers (e.g., Mokwa and Peebles 2008; Gupta et al. 2009) reported that the permeability of RAP blends increased as the percentage of RAP material in the blend increased. While, a contradicting behavior was reported by Maher et al. (1997), MacGregor et al. (1999), and Seferoglu et al. (2018). Overall, the differences among different blends tested in this study may be due to the variations in virgin aggregate characteristics, milled RAP aggregate size and bitumen content. In the case of the presence of paving fabrics in the RAP, the coefficient of permeability was higher due to the higher bitumen content and geosynthetic pieces present in the RAP.

### **Water absorption and Bitumen content**

The water absorption values for VA, 50-50 RAP and 50-50 GRAP blends were respectively determined to be 2.82%, 2.06% and 2.51%. The water absorption value of 50-50 RAP blend was lower than the VA due to the aged binder coated on to the RAP material. On the other hand, the 50-50 GRAP blend was able to absorb more water than 50-50 RAP blend due to the presence of geosynthetic fragments. The bitumen content of RAP and GRAP samples were determined to be 4.92% and 5.87% respectively, by weight of aggregates. Similar results with 4.5% and 5.0% bitumen contents were obtained for RAP and GRAP samples by Gu et al. (2021) from their study. In addition, they reported that the geosynthetic interlayers absorbs substantial amount of tack based on their asphalt retention capacities, hence a higher binder content was determined in GRAP samples compared to that of RAP samples. On the other hand, Tran et al. (2012) reported the binder contents in RAP and GRAP samples tested in their study as 5.88% and 6.37%, respectively. The variations in the bitumen contents of RAP and GRAP samples among different research studies may be due to the tack coat type and the geosynthetic interlayer adopted.

### **Fragmentation test**

The fragmentation values for VA, RAP and GRAP blends tested at different temperatures are presented in Fig. 11. RAP and GRAP blends showed an increase in the fragmentation value with

decreasing test temperature. Similar behavior was observed by Guduru et al. (2022), which was attributed to the brittle behavior of bitumen at a lower temperature, i.e. at 5 °C, compared to other temperatures, which caused the finer agglomerated particles separated because of the repeated impact loading. In fact, the VA blends were not affected by temperature in comparison to the RAP blends. An interesting behavior was noticed in GRAP blends which was less affected by repeated impact loading and temperature compared to RAP blends. It is believed that the geosynthetic fragments may have contributed to more energy dissipation and less grain breakage.

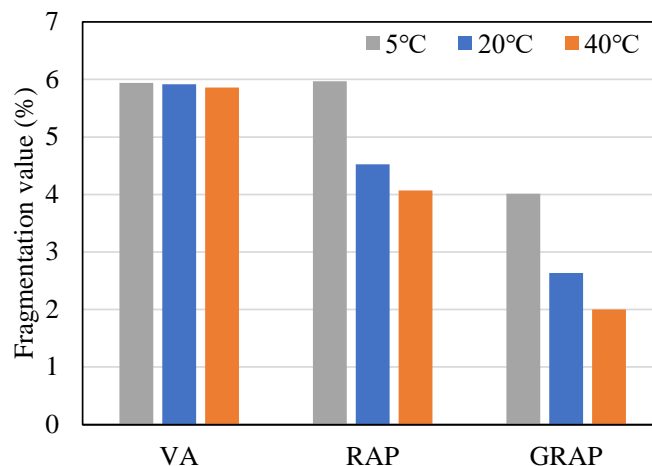


Figure 11. Fragmentation test results on VA, RAP and GRAP blends.

## CONCLUSIONS

This study presented characteristics and performance-related parameters and properties of a RAP that contains geosynthetic fibers, referred herein as GRAP, and the suitability of RAP blends with virgin aggregate as roadway base materials. An approach on the milling process of the geosynthetic-reinforced asphaltic layer was presented. The following conclusions were drawn from this investigation:

- The presence of geosynthetic in the asphaltic layers did not affect overall milling process reported in this study.
- The presence of the geosynthetic in the GRAP-VA blends did not significantly influence the moisture-density characteristics compared to that of RAP-VA blends tested in this study.
- Hydraulic permeability of different blends evaluated in this study were on the order of 0.24 cm/s, 0.598 cm/s, and 1.17 cm/s respectively, for VA, 50-50 RAP and 50-50 GRAP blends.
- The presence of geosynthetic fragments in the GRAP-VA blends has significantly influenced the permeability characteristics.
- The water absorption capacity of GRAP samples were higher than of the RAP samples evaluated in this study, due to the presence of geosynthetic fragments in the GRAP sample.
- The binder content of GRAP samples were higher (5.87%) than that of RAP samples (4.92%) evaluated in this study, due to the asphalt retention capacity of geosynthetic fragments in the GRAP sample.
- The fragmentation values of GRAP and RAP samples evaluated in this study, decreased with increasing temperature. In addition, GRAP sample was less affected by repeated



impact loading and temperature compared to that of RAP sample, due to the presence of geosynthetic fragments in the GRAP sample.

Overall, it can be inferred that behavior of RAP blends may differ depending on virgin aggregate characteristics, milled RAP aggregate size and bitumen content, as well as RAP percentage and compaction conditions.

## REFERENCES

- AASHTO T164 (2022). Standard Method of Test Quantitative Extraction of Asphalt Binder from Asphalt Mixtures. Washington, DC: American Association of State and Highway Transportation Officials
- AASHTO T180 (2022). Standard Method of Test for Moisture-Density Relations of Soils Using a 4.54-kg (10-lb) Rammer and a 457-mm (18-in.) Drop. Washington, DC: American Association of State and Highway Transportation Officials.
- AASHTO T85 (2022). Standard Method of Test for Specific Gravity and Absorption of Coarse Aggregate. Washington, DC: American Association of State and Highway Transportation Officials.
- Abdelrahman, M., Alam, T., and Zollars, J. (2010). Performance of High Recycled Asphalt Pavement (RAP) Content as Base Layer in Flexible Pavement. *The Journal of Solid Waste Technology and Management*, 36(3), 131-142.
- ASTM D1557 (2021). Standard Test Methods for Laboratory Compaction Characteristic of Soil using Modified Effort, *ASTM International*, West Conshohocken, PA, USA.
- ASTM D2434 (2022). Standard Test Methods for Measurement of Hydraulic Conductivity of Coarse-Grained Soils, *ASTM International*, West Conshohocken, PA, USA.
- Bejarano, M.O. (2001). Evaluation of Recycled Asphalt Concrete Materials as Aggregate Base. Technical Memorandum, University of California, Pavement Research Center, Richmond.
- Correia, N. S., and Zornberg, J. G. (2016). Mechanical Response of Flexible Pavements Enhanced with Geogrid-reinforced Asphalt Overlays. *Geosynthetics International*, 23(3), 183-193.
- Cosentino, P. J., Kalajian, E. H., Bleakley, A. M., Diouf, B. S., Misilo, T. J., Petersen, A.J., Krajcik, R. E., and Sajjadi, A. M. (2012). Improving the Properties of Reclaimed Asphalt Pavement for Roadway Base Applications (No. FL/DOT/BDK81 97702). Florida Institute of Technology. Civil Engineering Department.
- Gu, F., Andrews, D., and Marienfeld, M. (2021). Evaluation of Bond Strength, Permeability, and Recyclability of Geosynthetic Products. *Geosynthetics Conference*, 2021, 362-373.
- Guduru, G., Tavva, T. L., and Kuna, K. (2022). Estimation of Reclaimed Asphalt Pavement (RAP) Characteristics Using Simple Indicative Tests. *Road Materials and Pavement Design*, 23(4), 822-848.
- Gupta, S., Kang, D. H., and Ranaivoson, A. (2009). Hydraulic and Mechanical Properties of Recycled Materials, Report No. MN/RC 2009-32, Minnesota Department of Transportation, St. Paul, MN, USA, 2009.
- Guthrie, W. S., Cooley, D., and Eggett, D. L. (2007). Effects of Reclaimed Asphalt Pavement on Mechanical Properties of Base Materials. *Transportation Research Record*, 2005(1), 44-52.
- Highter, W. H., Clary, J. A., and DeGroot, D. J. (1997). Structural Numbers of Reclaimed Asphalt Pavement Base and Subbase Course Mixes, Report UMTC-97-03, vol. 111, University of Massachusetts Transportation Center, Amherst, MA, USA.



- Hopp, E. Stephen Lane, D., Michael Fitch G., and Shetty, S. (2015). Feasibility of Reclaimed Asphalt Pavement (RAP) Use as Road Base and Subbase Material. Project No.: RC00080, Final Report VCTIR 15-R6, Virginia Center for Transportation Innovation and Research, 2015.
- Kumar, V. V., and Saride, S. (2017). Evaluation of Flexural Fatigue Behavior of Two-Layered Asphalt Beams with Geosynthetic Interlayers Using Digital Image Correlation. Proceedings of the Transportation Research Board 96th Annual Meeting, Washington DC, USA, 8-12.
- Kumar, V. V., Saride, S., and Zornberg, J. G. (2021a). Mechanical Response of Full-Scale Geosynthetic-reinforced Asphalt Overlays Subjected to Repeated Loads. *Transport. Geotech*, 30, 100617. <https://doi.org/10.1016/j.trgeo.2021.100617>.
- Kumar, V. V., Saride, S., and Zornberg, J. G. (2021b). Fatigue Performance of Geosynthetic-reinforced Asphalt Layers. *Geosynth. Int.*, 28(6), 584-597. <https://doi.org/10.1680/jgein.21.00013>.
- Kumar, V. V., Roodi, G. H., Subramanian, S., and Zornberg, J. G. (2022). Influence of Asphalt Thickness on the Performance of Geosynthetic-reinforced asphalt: Full-scale Field Study. *Geotext. Geomembr*, 50(5), 1052-1059.
- MacGregor, J. A., Hight, W. H., and DeGroot, D. J. (1999). Structural Numbers for Reclaimed Asphalt Pavement Base and Subbase Course Mixes. *Transportation Research Record*, 1687(1), 22-28.
- Maher, M. H., Gucunski, N., and Papp Jr., W. J. (1997). Recycled Asphalt Pavement as a Base and Sub-Base Material. *ASTM Special Technical Publication*, 1275, 42-53.
- Mokwa, R. L., and Peebles, C. S. (2008). Strength, Stiffness, and Compressibility of RAP/Aggregate Blends. *Pavement Mechanics and Performance*, vol. 154, pp. 247-255.
- Plati, C. and Cliatt, B. (2019). A Sustainability Perspective for Unbound Reclaimed Asphalt Pavement (RAP) as a Pavement Base Material. *Sustainability*, 2019, 11(1), 78.
- Saride, S., and Kumar, V. V. (2019). Reflection Crack Assessment Using Digital Image Analysis. In: *Frontiers in Geotechnical Engineering, Developments in Geotechnical Engineering* (ed. G. M. Latha), Springer, Singapore, 139-156, [https://doi.org/10.1007/978-981-13-5871-5\\_8](https://doi.org/10.1007/978-981-13-5871-5_8).
- Seferoğlu, A. G., Seferoğlu, M., T., and Akpınar, M. V. (2018). Investigation of the Effect of Recycled Asphalt Pavement Material on Permeability and Bearing Capacity in the Base Layer. *Advances in Civil Engineering*, volume 2018, Article ID 2860213.
- Tebaldi, G., Dave, E., Falchetto, A. C., Hugener, M., Perraton, D., Grilli, A., Presti, D. L., Pasetto, M., Loizos, A., Jenkins, K., Apeagyei, A., Grenfell, J., and Bocci, M. (2019). Recommendation of RILEM TC237-SIB on Fragmentation Test for Recycled Asphalt. *Materials and Structures*, 52(82), 1-6.
- Texas Transportation Institute (1994). Texas Report 1272-1S - Summary Report: Routine maintenance uses for milled reclaimed asphalt pavement (RAP), <https://static.tti.tamu.edu/tti.tamu.edu/documents/1272-1S.pdf>
- Thakur, J. K., and Han, J. (2015). Recent Development of Recycled Asphalt Pavement (RAP) Bases Treated for Roadway Applications. *Transportation Infrastructure Geotechnology*, 2(2), 68-86.
- Tran, N. H., Julian, G., Taylor, A. J., Willis, R., and Hunt, D. (2012). Effect of Geosynthetic Material in Reclaimed Asphalt Pavement on Performance Properties of Asphalt Mixtures. *Transportation research record*, 2294(1), 26-33.
- TxDOT (2014). Standard Specifications for Construction and Maintenance of Highways, Streets, and Bridges. Texas Department of Transportation (TxDOT), Austin, Texas, USA.

## **Local Stiffness Enhancement by Multi-axial Geogrid Stabilization Evaluated Through Shear Wave Measurement**

**Mingu Kang<sup>1</sup>, Han Wang<sup>2</sup>, Issam I. A. Qamhia, Ph.D.<sup>3</sup>, Erol Tutumluer, Ph.D.<sup>4</sup>, and Mark H. Wayne, Ph.D., PE<sup>5</sup>**

<sup>1,2</sup> Department of Civil and Environmental Engineering, University of Illinois at Urbana-Champaign, 205 N. Mathews Ave., Urbana, Illinois 61801; e-mail: minguk2@illinois.edu.

<sup>3</sup>Department of Civil and Environmental Engineering, University of Illinois at Urbana-Champaign, 205 N. Mathews Ave., Urbana, Illinois 61801; e-mail: qamhia2@illinois.edu

<sup>4</sup>Department of Civil and Environmental Engineering, University of Illinois at Urbana-Champaign, 205 N. Mathews Ave., Urbana, Illinois 61801; e-mail: tutumlue@illinois.edu (Corresponding Author)

<sup>5</sup>Tensar International Corporation, e-mail: mwayne@tensarcorp.com

### **ABSTRACT**

Geogrids are commonly used in paved and unpaved roadways for unbound aggregate stabilization, which restrains the lateral movement of granular materials by means of geogrid-aggregate interaction. The effectiveness of geogrid stabilization highly depends on the relationship between geogrid aperture geometry and aggregate particle size and shape properties. The direct measurement and quantification of aggregate particle interlocking within the vicinity of the geogrid is the key to evaluating the effectiveness of geogrid stabilization. This paper presents an experimental study recently conducted to investigate multi-axial geogrid stabilized dense-graded aggregates through permanent deformation behavior and shear wave measurement. Repeated loading tests in a triaxial setup were conducted to characterize the permanent deformation behavior while shear wave transducers, also known as bender element (BE) sensors, were used to measure the shear wave velocity propagated through aggregates. The improved modulus of unbound aggregates within the vicinity of the geogrid was successfully quantified using BE sensors. The collective experimental results showed that the ratio of geogrid aperture size ( $S$ ) and median aggregate size ( $D_{50}$ ) serves as a good indicator of the effectiveness of geogrid stabilization for well-graded aggregate gradations. An optimum range between 2 to 3 for  $S/D_{50}$  ratio is recommended to achieve the maximum interlock and therefore most effectively stabilize dense-graded pavement base/subbase layers using geogrids.

### **INTRODUCTION**

Geogrids are very effective in stabilizing unbound aggregates used in pavement base or subbase layers. The main benefit can be realized either by reducing the base/subbase layer thickness or by extending the pavement life through an increase in rutting resistance (Zornberg et al., 2018). The stabilization of unbound aggregates relies upon certain interaction mechanisms, often referred to as the geogrid-aggregate interlock, where the lateral movement of aggregate particles is restrained

by geogrid ribs. The composite layer consisting of geogrid and stabilized aggregates is deemed to have a higher modulus, i.e., mechanical stabilization, and the modulus diminishes as the distance from the geogrid increases in lower confinement regions.

The effectiveness of stabilization depends on the properties of both geogrid and aggregates. On one hand, the stability and stiffness of geogrid ribs and junctions, as well as the aperture geometry, have an influence on the functionality of the geogrid to restrain the aggregate movements (Giroud et al., 2004). Numerous research studies have been conducted to study the effectiveness of stabilization in terms of various geogrid properties (Webster, 1993; Cancelli et al., 1999; Perkins, 1999; Berg et al., 2000; Abu-Farsakh et al., 2012). On the other hand, an appropriate relationship between geogrid aperture and strike-through aggregate particle size facilitates the degree of the interlocking. Brown et al. recommended that for a 50 mm (2-in.) nominal ballast size, a geogrid aperture size of 60 to 80 mm (2.36-in. to 3.15-in.) had to be selected for stabilization (Brown et al., 2007). Mulabdić et al. suggested that a ratio between aperture size and aggregate median diameter ( $D_{50}$ ) should range from 2 to 3 to achieve maximum stabilization (Minažek, 2010; Mulabdić et al., 2018). Federal Highway Administration (FHWA) documentation indicates the aperture size should be larger than  $D_{50}$  but smaller than two times the particle size corresponding to 85% passing by weight ( $D_{85}$ ) (Holtz et al., 2008).

A quantitative investigation of the mechanical stabilization has been the key to better understanding the influence of geosynthetics on the stiffening of the aggregate layers and how to characterize such a modulus distribution through mechanistic-empirical (ME) pavement design procedures. Over past three decades, many experimental studies have been conducted to collect data and help facilitate further establishment of interlock mechanisms (Perkins, 1999). Ferreria and Zornberg (2018) conducted large-scale pullout tests to document the interaction between geogrid and aggregate particles. Numerical modeling techniques, especially the discrete element method (DEM) was also utilized by many researchers to study the interlocking between geogrid and aggregate particles (Kwon et al., 2009; Qian et al., 2011; Qian et al., 2018). However, it has been historically difficult to characterize the stiffness enhancement of geogrid stabilized aggregates through direct measurement. Although various research efforts have shown that permanent deformation (i.e., rutting) reductions could be realized, the inclusion of geogrid didn't demonstrate obvious enhancement of resilient modulus, which is the main input property to characterize granular material load-deformation behavior in AASHTO's Pavement ME design method (Abu-Farsakh et al., 2012; Byun et al., 2019; Kang et al., 2020).

Bender element shear wave transducers have been used widely in geotechnical engineering to characterize the soil modulus through shear wave velocity measurement. Recent research efforts have demonstrated the viability of bender elements in accessing the small-strain modulus behavior of aggregates both in laboratory testing setup and field installation (Byun et al., 2019; Kang et al., 2020; Kang et al., 2021; Kang et al., 2022). The flexibility of bender elements in terms of installation (i.e., any location and orientation) provides the direct and quantitative evaluation of local stiffness enhancement, which is needed to investigate geogrid-aggregate interlocking. Using a modulus degradation curve, which links the elastic modulus at small strain (i.e., modulus measured through shear wave velocity) to the modulus at larger strain (i.e., resilient modulus), the utilization of bender elements can incorporate modulus enhancement into ME pavement design procedures, and meanwhile, function as a powerful tool for different geogrid evaluation and comparison (Sawangsuriya et al., 2006; Kang et al., 2022c).

This paper presents experimental results of a new multi-axial geogrid stabilizing dense-graded aggregates evaluated by means of permanent deformation testing and shear wave

measurements. The BE shear wave velocity measurements have shown that there is an increased stiffness zone in the geogrid vicinity or certain stiffening trends. Results of previous experiments using different aggregates and geogrids are also presented to compare and evaluate the effectiveness of stabilization through shear wave velocity measurement. The collective results from the different studies demonstrate that there is an optimum range for a geogrid aperture size (S) to  $D_{50}$  ratio ( $S/D_{50}$ ) to achieve the most effective modulus enhancement through interlocking.

## EXPERIMENTAL STUDY

**Material Properties.** A crushed limestone conforming to the Illinois Department of Transportation (IDOT) CA06 dense graded material gradation, often used for pavement base/subbase application in Illinois, was used to prepare test specimens in this study. The grain size distribution obtained following ASTM C136-06 procedure is shown in Figure 1. The material was well-graded with a maximum particle size of 25 mm (1-inch) and  $D_{50}$  as 6.0 mm (0.24-inch). The optimum moisture content (OMC) and the maximum dry density (MDD) were determined as 5.88% and  $23.01 \text{ kN/m}^3$  (146.5 pcf), respectively, according to ASTM D1557-12.

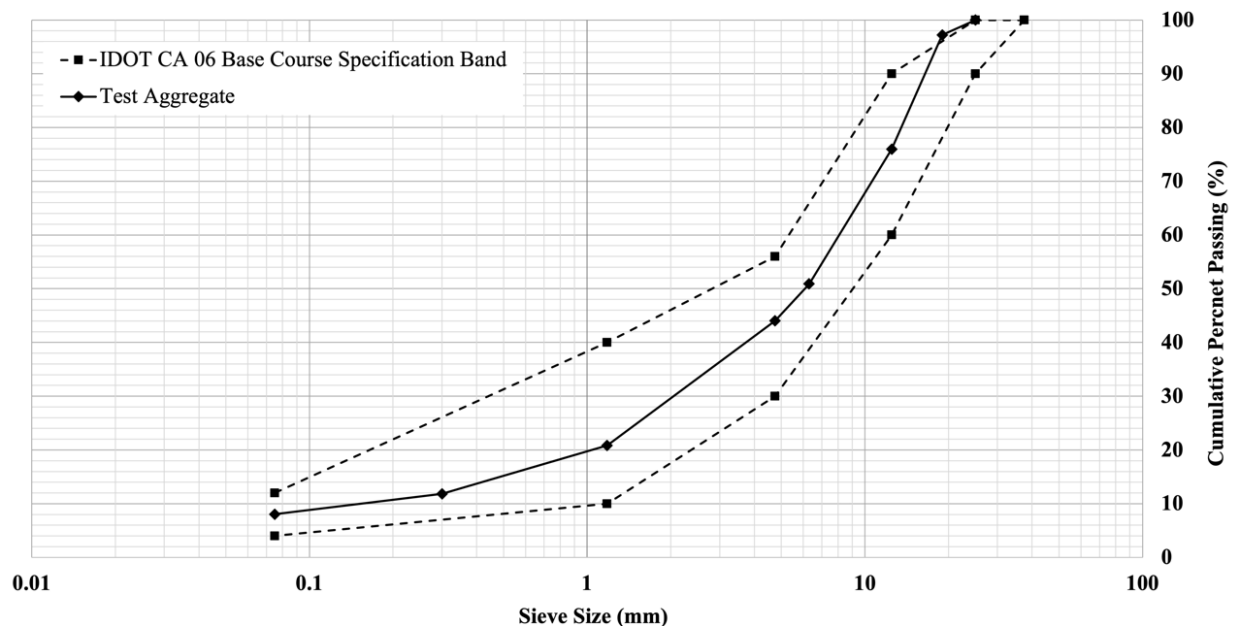


**Figure 1. Particle size distributions of dense-graded aggregate materials evaluated for geogrid stabilization in this study.**

**Multi-axial Geogrid.** The geogrid tested was manufactured from a coextruded, composite polymer sheet, which was then punched and oriented. The geogrid consists of continuous and non-continuous ribs forming three different aperture geometries including hexagons, trapezoids, and triangles. The detailed information on the geogrid is presented in Table 1.

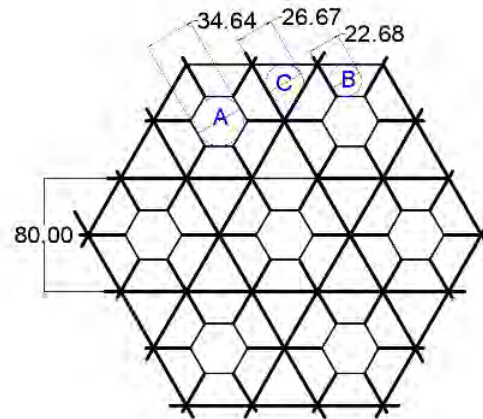
**Experimental Setup.** A repeated load triaxial testing apparatus accommodating the cylindrical specimens with a diameter of 15.2 cm (6-in.) and height of 30.5 cm (12-in.) was used in this study. The specimen was prepared in four lifts and 56 blows using the rammer were applied to each lift for the modified Proctor effort according to ASTM D1557-12. The average achieved dry density

is 20.49 kN/m<sup>3</sup> (130.43 pcf), which is lower than the MDD given the larger thickness compacted. For the stabilized specimen, the geogrid was placed at the mid-height of the specimen after the compaction of the second lift. Two internal linear variable differential transformers (LVDTs), positioned along the diameter of the specimen, were installed to measure the axial resilient and permanent deformations of the test specimen. The measurements from two LVDTs were averaged to represent the specimen's axial deformation considering possible misalignment or tilting. The vertical load level applied to the specimen was recorded through a load cell placed over the specimen. The confining pressure was applied using the compressed air inside an acrylic chamber.

**Table 1. Properties of geogrid tested.**

Index Property	Test Geogrid (GG)
Rib pitch, mm (in.)	80 (3.20) *
Diameter of largest inscribed circle, mm (in.)/weighted aperture area**	(A) Hexagon: 34.64 (1.36)/ 9.37% (B) Trapezoid: 22.68 (0.89)/ 40.63% (C) Triangle: 26.67 (1.05)/ 50.00%
Polymer type	polypropylene

Aperture Details  
(Showing largest inscribed circle)



\*Continuous parallel rib pitch

\*\*Aperture shapes included with geogrid coupons in triaxial testing

Six BE sensors working as three pairs, each fixed on a mount base, were attached to the membrane and embedded in the aggregate specimen. Each bender element sensor has the dimension of 20 mm×10 mm×0.6 mm (0.8-in. × 0.4-in. × 0.02-in., length × width × thickness). Within one pair, one bender element sensor works as a source to generate the shear wave and the other sensor works as a receiver for shear wave measurement. The three pairs of BE were installed at 2.5 cm (1-in.), 6.4 cm (2.5-in.), and 10.1 cm (4-in.), respectively, above the specimen mid-height to capture the modulus profile along the specimen upper half. To generate and measure the shear waves, an equipment setup consisting of a function generator, a filter-amplifier and an oscilloscope was utilized. A schematic drawing of the test setup is shown in Figure 2.

**Test Procedure.** Repeated load triaxial testing was performed to evaluate the permanent deformation behavior with and without geogrid. The test was conducted at a confining pressure of 103.4 kPa (15 psi) and the total of 10,000 load cycles with a deviator stress of 310.3 kPa (45 psi) were applied to the sample. Each load repetition consists of a haversine pulse with 0.1-s loading



and the 0.9-s rest period. The applied loads and the deformations were recorded throughout the test using load cell and two LVDTs, respectively.

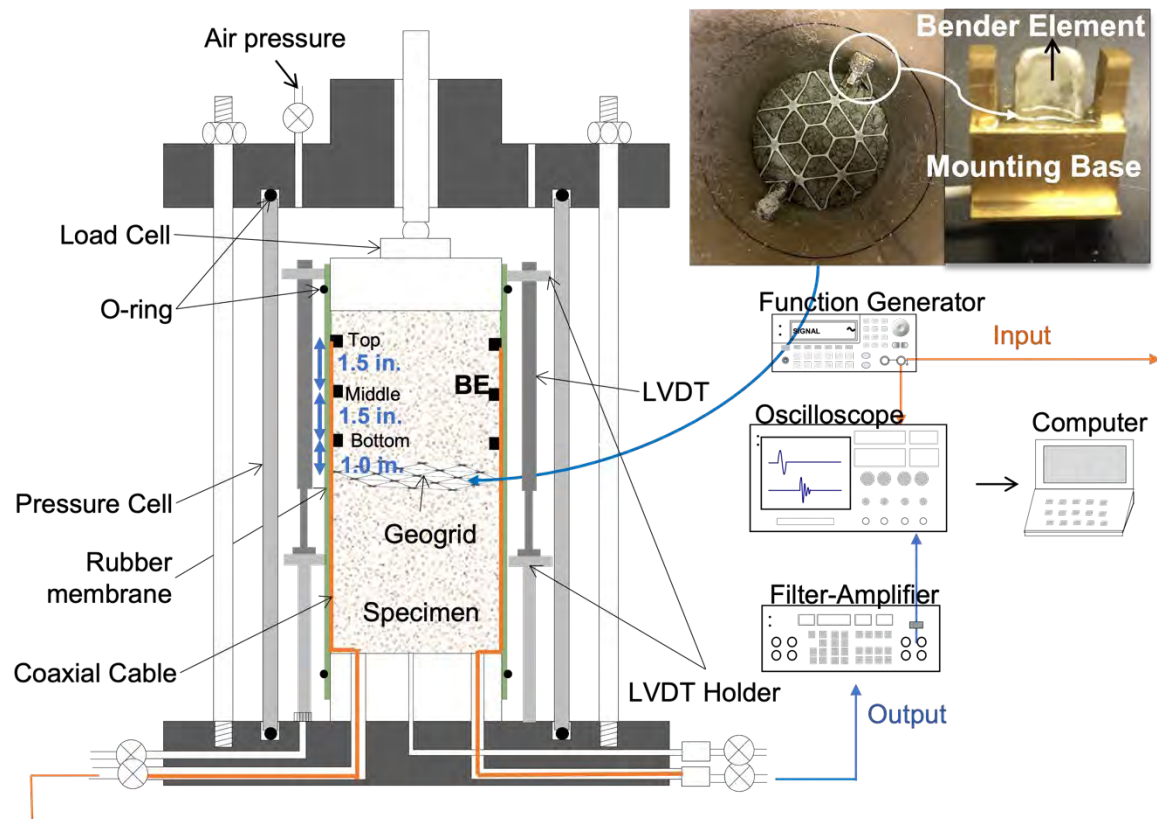


**Figure 2. Schematic drawings of the BE instrumentation and the repeated load triaxial test setups for the shear wave measurement system.**

In addition, shear wave signals from three pairs of BEs were collected before applying the repeated load pulses to determine the local stiffness of the sample at three different locations. A sinusoidal input signal with the resonant frequency of the aggregate material was provided for the source BE transducer to magnify the output signal (Clayton, 2011). The output signal detected by the receiver BE transducer was filtered by the bandpass filter and collected using the oscilloscope. In total 1,024 output signals were stacked and averaged for the clear output signal.

## EXPERIMENTAL RESULTS AND DISCUSSION

**Results from Permanent Deformation Test.** Figure 3 shows the permanent strain accumulation of the tested aggregate specimen with the multi-axial geogrid measured by averaging two LVDT readings during the repeated load triaxial test. The total accumulated strain of the sample was 0.6% after 10,000 load cycles. The permanent strain of the aggregate material is a function of the number of load repetitions and the stress state. The test results can be presented by the widely used phenomenological model proposed by Monismith et al. (1975) as follows:

$$\varepsilon_p = 0.00076N^{0.229} \quad (1)$$

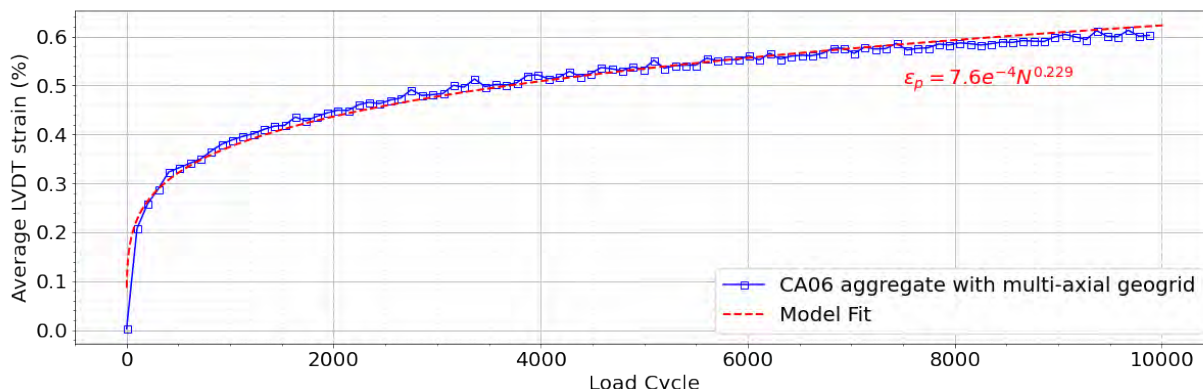


**Figure 3. Permanent strain accumulation throughout the 10,000 pulses.**

**Results from BE measurements.** The shear wave signals collected using three pairs of BE sensors are presented in Figure 4. The first arrival times are presented as red dots on the signals. Clearly, the first arrival times from three pairs of BEs are comparable for unstabilized aggregates [see Figure 4(a)], but the first arrival time is slower in the vicinity of the geogrid for geogrid stabilized aggregates [see Figure 4(b)]. Shear wave velocity ( $V_s$ ) is a function of the first arrival time of the signal as expressed in Equation 2.

$$V_s = \frac{L}{t_{tip-tip}} \quad (2)$$

where  $t_{tip-tip}$  is the first arrival time of the shear wave, and  $L$  is the distance between the BE pair.

Figure 5 shows the shear wave velocity profiles of the aggregate specimens with and without geogrid stabilization. The shear wave velocity of the unstabilized specimen was relatively constant throughout the specimen length. However, the shear wave velocity gradually increased from top to bottom, as it gets closer to the geogrid location. This increasing trend of shear wave velocity indicates a geogrid-stiffened zone created in specimen midheight, which has been reported by many researchers (Kwon et al., 2009; Byun et al., 2017; Byun et al. 2019; Kang et al., 2020; Kang et al. 2022a).

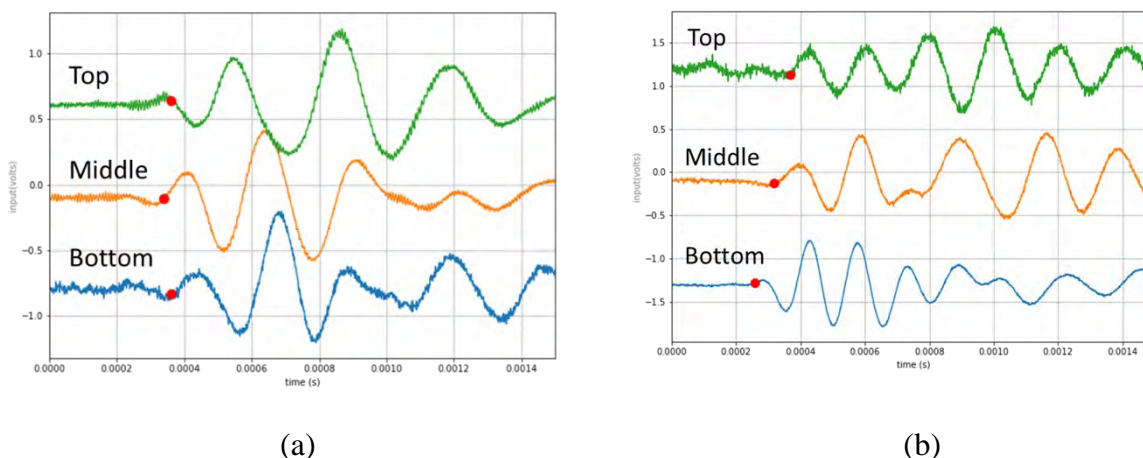


**Figure 4. Shear wave signals at 15 psi confinement: (a) without geogrid, and (b) with multi-axial geogrid.**

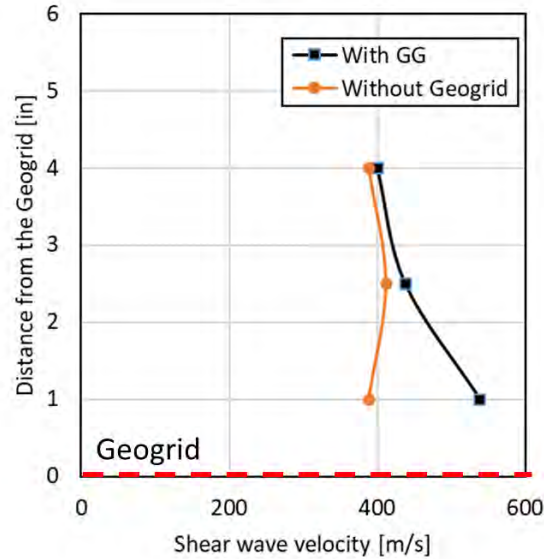


**Figure 5. Shear wave velocity profile with and without multi-axial geogrid (GG).**

The shear modulus of the aggregates can be computed from shear wave velocity and the aggregate density using Equation 3 (Santamarina et al., 2001).

$$G_{max} = \rho V_s^2 \quad (3)$$

where  $\rho$  is density of the specimen and  $G_{max}$  is a small strain shear modulus. In addition, the small-strain elastic modulus is a function of the shear modulus and Poisson's ratio, expressed in Equation 4.

$$E_{BE} = 2G_{max}(1 + \nu) \quad (4)$$

where  $E_{BE}$  is the small-strain elastic modulus from the BEs, and  $\nu$  is the Poisson's ratio of the aggregate material. Therefore, the small-strain elastic modulus can be derived from the shear wave velocity measurement using BE field sensors. A Poisson's ratio of 0.35 was assumed for the granular material in this study.

To quantify the effect of geogrid stabilization, the enhancement ratio, which is defined by modulus from the geogrid-stabilized specimen divided by the modulus from the unstabilized specimen, was proposed by Kang et al. (2020) as shown in Equation 5.

$$\text{Enhancement Ratio}_{E_{BE}} = \frac{E_{BE}(\text{stabilized})}{E_{BE}(\text{unstabilized})} \quad (5)$$

The enhancement ratios should be greater than one to indicate the benefit of geogrid stabilization and its effectiveness. To consider the local stiffening effect in vicinity of geogrid, shear wave velocity was obtained from the BE pair at the bottom location. The modulus enhancement ratio of the test aggregates with multi-axial geogrid (GG) was 1.92, which indicates that the modulus near the geogrid improved nearly twice when compared to the unstabilized specimen. Therefore, the multi-axial geogrid stabilization of the dense-graded aggregate material is shown to be effective in terms of the local stiffness improvement or stiffening.

**Effect of Geogrid Aperture Size to Median Aggregate Particle Size Ratio.** Multiple studies have been conducted at UIUC using BE pairs in the triaxial specimen setup described herein (Byun et al., 2017; Byun et al., 2019; Kang et al., 2020). To investigate the effectiveness of geogrid stabilization of dense-graded aggregate materials using different types of geogrids, a comparison of the enhancement ratio from this study and the previously reported test results was conducted. Figure 6 shows the particle size distribution of dense-graded aggregate materials from the previous studies and the tested aggregate material used in this study. The five aggregate materials conform to typical dense-graded aggregate gradation used for the unbound base layer of pavement, classified as A-1-a material according to the AASHTO soil classification standard.

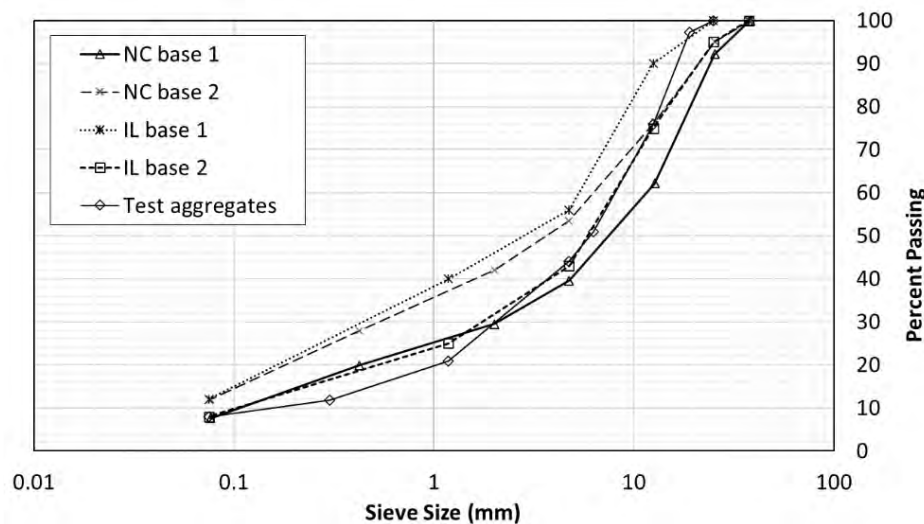


**Figure 6. Particle size distributions of dense-graded aggregate materials from the current and previous studies.**

**Table 3. Properties of geogrids evaluated for stabilization through UIUC research studies.**

Index Property	GG1	GG2	GG3
Rib pitch, mm (in.)	40 (1.57)	33 (1.30)	33 (1.30)
Diameter of largest inscribed circle, mm (in.)	23.1 (0.909)	19.1 (0.752)	33 (1.30)
Polymer type	polypropylene	polypropylene	polypropylene
Radial stiffness at low strain (kN/m @ 0.5% strain)	225	200	
Tensile strength at 2% strain (kN/m)			6

Aperture Details  
(Showing largest inscribed circle)

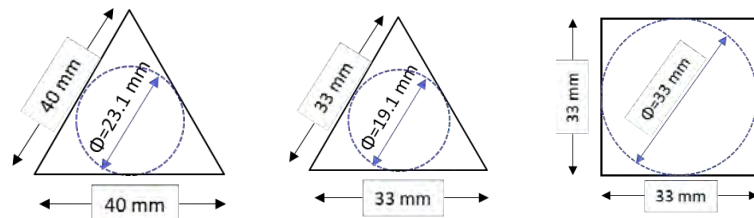




Table 3 summarizes the geogrid properties used in the previous studies. In total, three different types of punched and drawn geogrids with different aperture geometries, including triangular and square, were included in addition to multi-axial GG presented for comparison in this study. To accommodate the different aperture shapes, the size of the geogrid was defined based on the size of the largest inscribed circle in the aperture (S), which can be related to the largest aggregate sizes for the aperture strike-through controlling the interlocking mechanisms.

**Table 4. Geogrid and aggregate properties and modulus enhancement ratio.**

	Byun et al. (2017)	Byun et al. (2019)		Kang et al. (2020)				This study*
Material	NC base 2	NC base 1		IL base 2		IL base 1		Test Aggregate
OMC (%)	5.6	5.8		5.5		5.9		5.9
MDD (kN/m <sup>3</sup> )	24.3	22.7		22.59		22.84		23.01
D <sub>50</sub>	4	8.4		5.88		2.82		6.00
Geogrid	GG1	GG1	GG3	GG1	GG2	GG1	GG2	GG
Geogrid aperture size (S)	23.1	23.1	33	23.1	19.1	23.1	19.1	(A) 34.64 (B) 22.68 (C) 26.67
S / D <sub>50</sub>	5.78	2.75	3.93	3.93	3.25	8.19	6.77	(A) 5.77 (B) 3.78 (C) 4.45
Modulus Enhance. Ratio	1.48	4.13	2.85	1.15	3.51	1.69	1.53	1.92

\* (A) Hexagon, (B) Trapezoid, and (C) Triangle, as listed in Table 1.

Table 4 summarizes the aggregate material properties, geogrid properties, and amount of modulus enhancement achieved through stabilization using different aggregates and geogrids. The enhancement ratios were calculated based on the modulus improvement at a confining pressure of 103.42 kPa (15 psi) to consider the local stiffening effect in vicinity of geogrid. The modulus enhancement ratios determined at various geogrid aperture size to median aggregate grain size ratios (S/D<sub>50</sub>) are visualized in Figure 7. The ratio indicates that the most effective stabilization in terms of local stiffness was shown when the ratio is in 2 to 3 range. The effect of geogrid stabilization is closely related to the ratio between the geogrid aperture size to aggregate particle size (Holtz et al., 2008; Mehrjardi et al., 2017). In addition, Mulabdić et al. (2018) reported that the maximum soil-geogrid interaction intensity from the pullout test with biaxial geogrid was shown when the S/D<sub>50</sub> ratio ranges from 2 to 3. It is noted that for the multi-axial GG, there are three different aperture geometries with different sizes. The three apertures were labelled as A (i.e., hexagon), B (i.e., trapezoid) and C (i.e., triangle) as described in Table 1. To further investigate the stabilization effectiveness in terms of different aperture geometry and size, three S/D<sub>50</sub> ratios for GG were calculated for each aperture size as shown in Figure 7. Based on a weighted average, the predominant aperture area of the triangular is 50.0 % [see Table 1]. As shown in Figure 7, the

predominant aperture, based on a weighted average, show better agreement with the trend of modulus enhancement ratio in terms of the  $S/D_{50}$ .

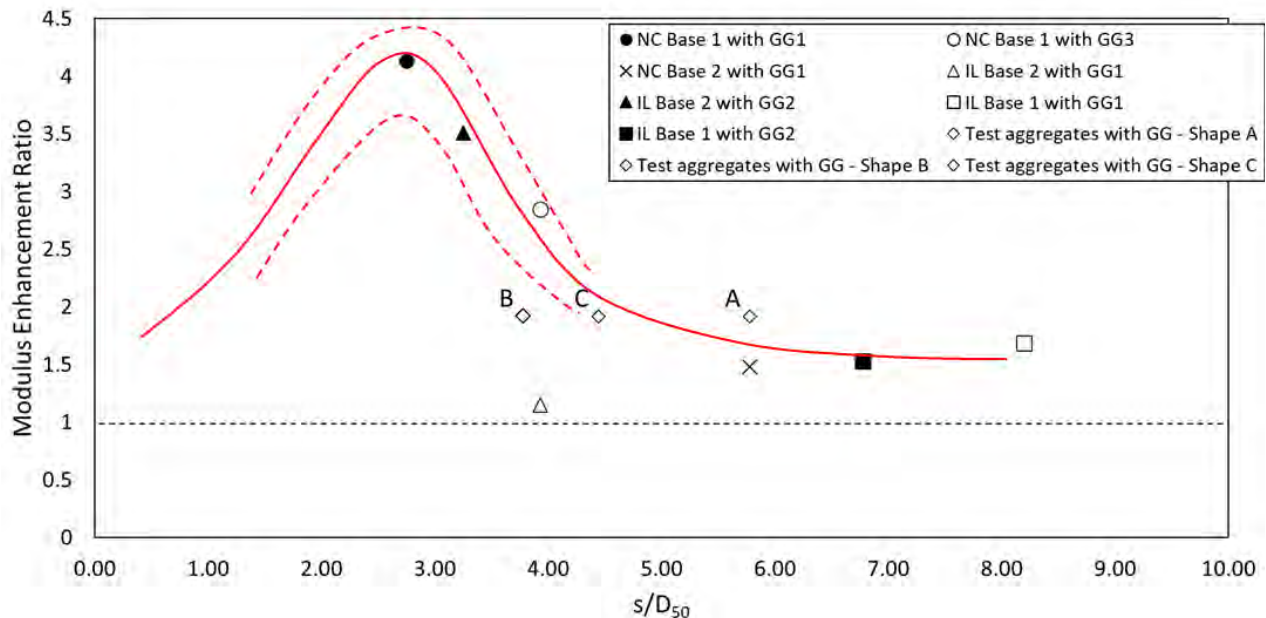


**Figure 7. Modulus enhancement ratios defined various geogrid aperture sizes and median aggregate grain sizes. The solid line shows a general trend of geogrid interaction intensity suggested by a data set. The dashed line indicates the influence of additional factors, i.e. geogrid type.**

## SUMMARY AND CONCLUSIONS

This paper presents research findings from an experimental evaluation of mechanically stabilized dense-graded aggregates using a new multi-axial geogrid by means of permanent deformation testing and shear wave measurement. A crushed limestone aggregate material following Illinois DOT CA06 dense-graded base gradation were used to prepare the specimen in this study. The multi-axial geogrid consists of continuous and non-continuous ribs forming three different aperture geometries including hexagons, trapezoids, and triangles. A cylindrical test specimen with a diameter of 15.2 cm (6-inch) and a height of 30.5 cm (12-inch) was prepared with and without geogrid for repeated load triaxial testing. The geogrid was installed at the mid-height in the mechanically stabilized specimen, and the three BE pairs were installed at three different heights above the mid-height. After collecting the shear wave signals at three different locations, a total of 10,000 load cycles were applied to the sample using a pulsed deviator stress of 310.3 kPa (45 psi). Finally, an enhancement ratio, defined as modulus from the geogrid-stabilized specimen divided by the modulus from the unstabilized specimen, was evaluated in the vicinity of the geogrid to quantify effectiveness of stabilization in terms of the local stiffness enhancement.

The BE measured shear wave velocity has shown that there is a stiffness zone in the geogrid proximity with a higher modulus. The modulus enhancement ratio achieved by multi-axial geogrid stabilization was 1.92, which indicates that the modulus near the geogrid was improved nearly twice when compared to the unstabilized specimen. Comparisons were made for the enhancement ratios achieved in previous study findings detailing modulus enhancement ratios achieved using

different aggregates and geogrids, especially focusing on the size ratio between geogrid aperture and aggregates. Based on the experimental study on four different geogrids and five different aggregate materials, there is an optimum range for geogrid aperture size (S) to  $D_{50}$  ratio ( $S/D_{50}$ ) from 2 to 3 to achieve the most effective modulus enhancement through interlocking. Further research on the geogrid aperture size to  $D_{50}$  ratio with additional types of geogrids and aggregates is suggested to confirm the optimum ratio presented herein.

## REFERENCES

- Abu-Farsakh, M., Souci, G., Voyiadjis, G. Z., & Chen, Q. (2012). Evaluation of factors affecting the performance of geogrid-reinforced granular base material using repeated load triaxial tests. *Journal of Materials in Civil Engineering*, 24(1), 72-83.
- ASTM C 136-06. Standard Test Method for Sieve Analysis of Fine and Coarse Aggregates, *ASTM International*, West Conshohocken, Pennsylvania, USA.
- ASTM D1557-12. Standard Test Methods for Laboratory Compaction Characteristics of Soil Using Modified Effort (56,000 ft-lbf/ft<sup>3</sup> (2,700 kN-m/m<sup>3</sup>)), *ASTM International*, West Conshohocken, Pennsylvania, USA.
- Berg, R. R., Christopher, B. R., and Perkins, S. W. (2000). Geosynthetic reinforcement of the aggregate base course of flexible pavement structures. *GMA white paper II, Geosynthetic Material Association*, Roseville, MN, 100.
- Brown, S. F., Kwan, J., & Thom, N. H. (2007). Identifying the key parameters that influence geogrid reinforcement of railway ballast. *geotextiles and geomembranes*, 25(6), 326-335.
- Byun, Y. H., & Tutumluer, E. (2017). Bender elements successfully quantified stiffness enhancement provided by geogrid-aggregate interlock. *Transportation Research Record*, 2656(1), 31-39.
- Byun, Y. H., Tutumluer, E., Feng, B., Kim, J. H., & Wayne, M. H. (2019). Horizontal stiffness evaluation of geogrid-stabilized aggregate using shear wave transducers. *Geotextiles and Geomembranes*, 47(2), 177-186.
- Cancelli, A., & Montanelli, F. (1999). In-ground test for geosynthetic reinforced flexible paved roads, *Geosynthetics '99: Specifying Geosynthetics and Developing Design Details*, IFAI, Boston, Massachusetts, U.S.A., Vol. 2, 863-878.
- Giroud, J. P., & Han, J. (2004). Design method for geogrid-reinforced unpaved roads. I. Development of design method. *Journal of Geotechnical and Geoenvironmental Engineering*, 130(8), 775-786.
- Clayton, C. R. I. (2011). Stiffness at small strain: research and practice. *Géotechnique*, 61(1), 5-37.
- Holtz, R.D., Christopher, B. R., and Berg, R. R. (2008). *FHWA-HNI-07-092: Geosynthetics Design & Construction Guidelines – Reference Manual*. United States. National Highway Institution. Federal Highway Administration. U.S. Department of Transportation. Washington, D.C.
- Kang, M., Kim, J. H., Qamhia, I. I., Tutumluer, E., & Wayne, M. H. (2020). Geogrid stabilization of unbound aggregates evaluated through bender element shear wave measurement in repeated load triaxial testing. *Transportation Research Record*, 2674(3), 113-125.
- Kang, M., Qamhia, I. I., Tutumluer, E., Flynn, M., Garg, N., & Villafane, W. (2022a). Near geogrid stiffness quantification in airport pavement base layers using bender element field sensor. In *Advances in Transportation Geotechnics IV* (pp. 703-715). Springer, Cham.

- Kang, M., Qamhia, I. I., Tutumluer, E., Garg, N., & Villafane, W. (2022b). Airport Pavement Stiffness Monitoring and Assessment of Mechanical Stabilization using Bender Element Field Sensor. *Transportation Research Record*, 03611981221084685.
- Kang, M., Qamhia, I. I., Tutumluer, E., Hong, W. T., & Tingle, J. S. (2021). Bender element field sensor for the measurement of pavement base and subbase stiffness characteristics. *Transportation Research Record*, 2675(8), 394-407.
- Kang, M., Wang, H., Qamhia, I. I., & Tutumluer, E. (2022c). Modulus Properties of Granular Materials at Various Strain Levels from Repeated Load Triaxial Testing with Bender Elements. In *Geo-Congress 2022*, p. 420-430.
- Kwon, J., & Tutumluer, E. (2009). Geogrid base reinforcement with aggregate interlock and modeling of associated stiffness enhancement in mechanistic pavement analysis. *Transportation research record*, 2116(1), 85-95.
- Mehrjardi, G. T., & Khazaei, M. (2017). Scale effect on the behaviour of geogrid-reinforced soil under repeated loads. *Geotextiles and Geomembranes*, 45(6), 603-615.
- Minažek, K. Model investigation of interaction of grid and soil, *PhD thesis*, University of Zagreb, Croatia, 2010.
- Monismith, C. L., Ogawa, N., & Freeme, C. R. (1975). Permanent deformation characteristics of subgrade soils due to repeated loading. *Transportation research record*, (537).
- Mulabdić, M., Minažek, K., and Kaluđer, J. (2018). Geogrids-what is important. In *Proceedings of the International Conference on Road and Rail Infrastructure CETRA*.
- Perkins, S. W. (1999). Geosynthetic reinforcement of flexible pavements: laboratory based pavement test sections (No. FHWA/MT-99-001/8138). Montana. Department of Transportation.
- Qian, Y., Tutumluer, E., & Huang, H. (2011). A validated discrete element modeling approach for studying geogrid-aggregate reinforcement mechanisms. In *Geo-Frontiers 2011: Advances in Geotechnical Engineering* (pp. 4653-4662).
- Qian, Y., Tutumluer, E., Mishra, D., & Kazmee, H. (2018). Effect of geogrid reinforcement on railroad ballast performance evaluated through triaxial testing and discrete element modeling. *Proceedings of the Institution of Civil Engineers: Ground Improvement*.
- Roodi, G. H., Zornberg, J. G., Aboelwafa, M. M., Phillips, J. R., Zheng, L., & Martinez, J. (2018). Soil-geosynthetic interaction test to develop specifications for geosynthetic-stabilized roadways (No. FHWA/TX-18/5-4829-03-1). University of Texas at Austin. Center for Transportation Research.
- Sawangsuriya, A., Bosscher, P. J., & Edil, T. B. (2006). Alternative testing techniques for modulus of pavement bases and subgrades. In *Geotechnical Applications for Transportation Infrastructure: Featuring the Marquette Interchange Project in Milwaukee, Wisconsin* (pp. 108-121).
- Santamarina, J.C., Klein, A., Fam, M.A. (2001). *Soils and Waves*, J. Wiley and Sons, Chichester, UK.
- Webster, S. L. (1993). Geogrid reinforced base courses for flexible pavements for light aircraft: test section construction, behavior under traffic, laboratory tests, and design criteria. *Technical Rep. GL-93-6*, U.S.Army Engrs. Waterways Experiment Station (USAE-WES), Vicksburg, MS, 86
- Zornberg, J. G., Roodi, G. H., Sankaranarayanan, S., and Hernandez-Urbe, L. A. Geosynthetics in roadways: Impact in sustainable development. *Keynote Lecture, ICG*, 2018. 16-21.



# **Role of Geosynthetics in Improving Freeze-thaw Resistance of Bases – a Literature Survey**

**Jiming Liu<sup>1</sup>, Cheng Lin<sup>1</sup>, Mian Huang<sup>1</sup>, and Sanat Pokharel<sup>2</sup>**

<sup>1</sup>University of Victoria, 3800 Finnerty Road, Victoria, British Columbia V8P 5C2, Canada; e-mail: chenglin918@uvic.ca

<sup>2</sup>Stratum Logics, 26550 Acheson Road, Acheson, AB T7X 6B2, Canada.

## **ABSTRACT**

Repetitive freeze-thaw (F-T) action is one of the leading factors responsible for road damage in seasonal frost regions. Geosynthetics have been widely applied to improve road longevity in cold regions; however, the beneficial effect of Geosynthetics in improving the F-T resistance of paved and unpaved roads is not well appreciated. This paper focuses on a comprehensive literature review of experimental investigations into the geosynthetics (e.g., geogrid, geotextile, and geocell) improved bases under seasonable F-T cycles. The reviewed experiments include element tests, model tests, and field trials. This paper specifically looks into the role of geosynthetics in the F-T resistance of bases and the underlying mechanisms. It is shown that geosynthetics are effective in reducing the frost heave and thaw settlement and improving the bearing pressure of the bases.

## **INTRODUCTION**

In seasonal frost regions, freeze-thaw (F-T) action is one of the leading factors responsible for road damage. This process repeatedly alters the void ratio and reconstitutes the base and subgrade soils, which can lead to a decrease in the strength and resilient modulus of soils and an increase in permeability of soils (Qi et al., 2006). In freeze seasons, the ground is frozen and heaved. The freeze-induced heave is in general attributed to the volumetric expansion of pore water and the formation of segregated ice lenses. The segregated ice lenses, are likely to be formed at a slow rate of decrease in temperature, and oriented parallel to the surface exposed to the freezing temperature (Andersland & Ladanyi, 2003). During this process, a freezing front forms and propagates downwards in soils, which accumulates water if the water supply in the vicinity is available by the cryogenic suction and capillary suction (Bing et al., 2015; Henry & Holtz, 2001). Figure 1(a) illustrates the formation of ice lenses with available water supply (Terzaghi, 1952). In comparison, the formation of segregated ice lenses plays a more critical role in heave than the water-to-ice volumetric expansion.

In thaw seasons, road sections including base and subgrade can consolidate and experience a remarkable decrease in strength and stiffness if the thawed water is trapped and the road is subjected to repeated traffic loads. Figure 1(b) shows a simplified model of thaw consolidation (Morgenstern and Nixon, 1971). The trapped water occurs as the downward drainage in the thawing soil is blocked by the underlying frozen soil layer. The increased water content increases the degree of saturation and pore pressure of the thawing soil layer if its permeability is low. This, therefore, reduces soils' stiffness and shear strength, lowers the bearing capacity of the road

sections, and is responsible for rutting, potholes, and other types of distress (Simonsen & Isacsson, 1999). Figure 2(a) illustrates that at the early stage of thawing when the thaw depth is shallow above the subgrade, pore pressure could build up in the base course, resulting in nonuniform deformation at road surface; when the thaw depth progresses deeper into the subgrade [Figure 2(b)], the weakening in the subgrade results in large deformation of road surface subjected to heavy traffic loading.

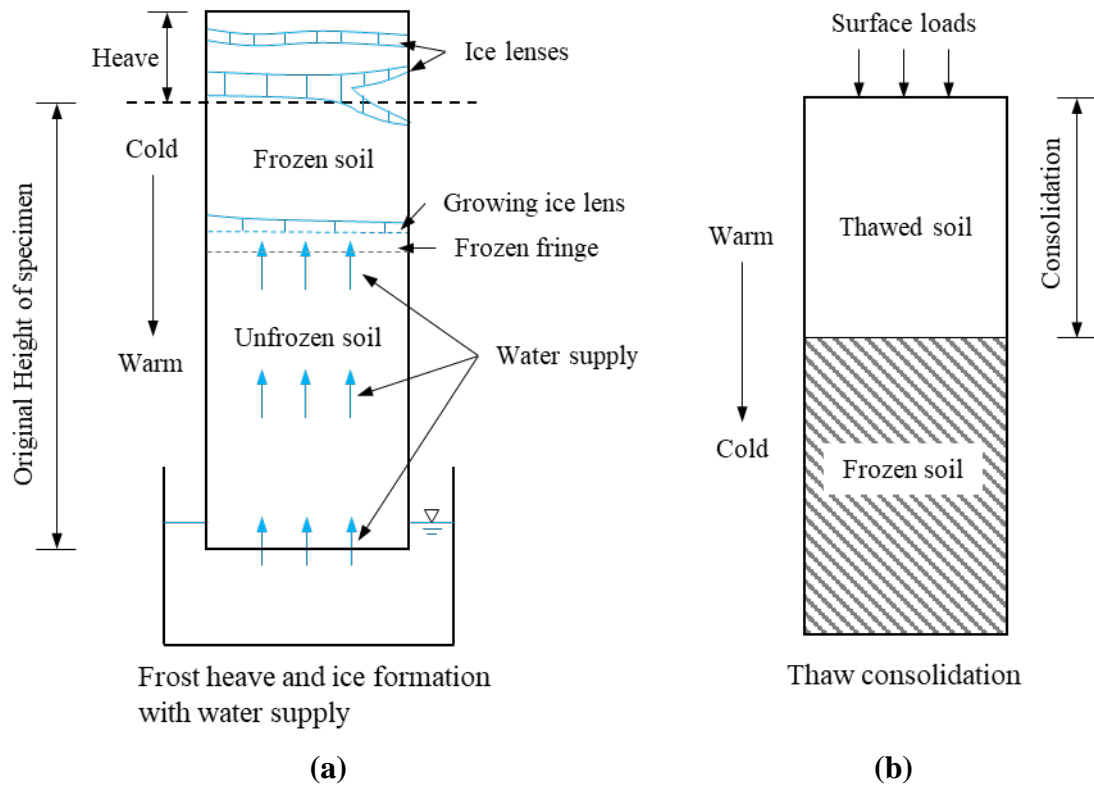


**Figure 1. Models of frost heave and thaw consolidation** [(a) and (b) are reproduced from Terzaghi (1951) and Morgenstern and Nixon (1971), respectively]

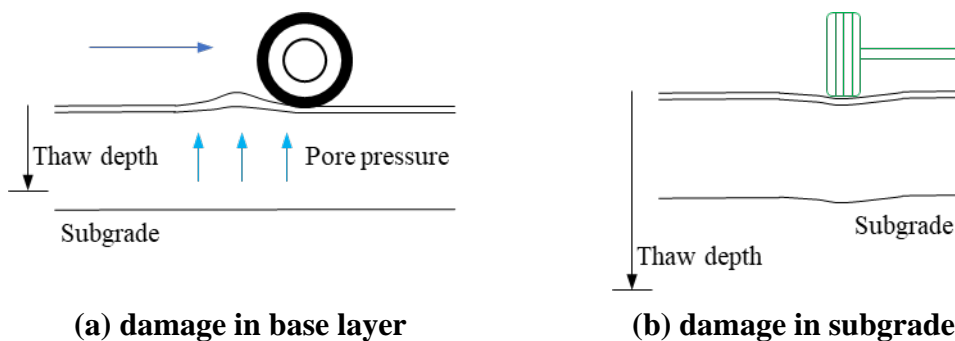


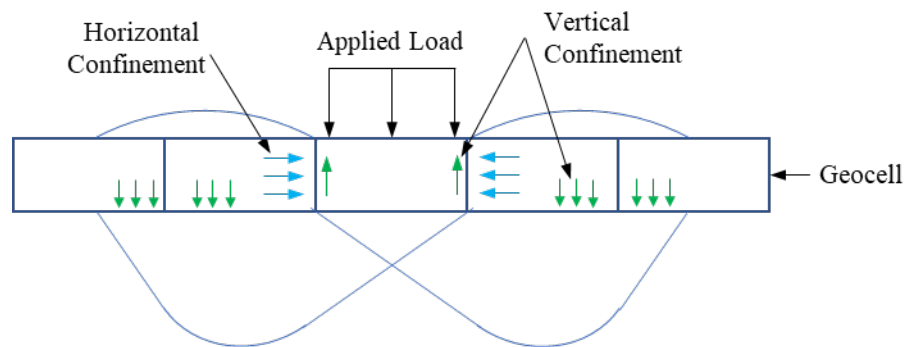
**Figure 2. Distress of base and subgrade during thawing** [modified from Simonsen and Isacsson (1999)]

**Functions of geosynthetics in roads.** Geosynthetics have been widely utilized in road construction as geosynthetics perform a number of functions that improve road performance and increase service life of roads. Giroud et al. (2021) have summarized functions of geosynthetics in roads as given Table 1 and illustrated in Figure 3.

**Table 1. Functions of Geosynthetics in roads**

Function	Description	Examples
Reinforcement	Increasing the strength or reducing the deformation of a material/system	<ul style="list-style-type: none"> <li>• Geogrid reinforced asphalt course</li> <li>• Geotextile that restraining subgrade heave/carrying load by tensioned membrane effect</li> </ul>
Stabilization	Forming a geosynthetic-soil composite material that is less deformable than the soil	<ul style="list-style-type: none"> <li>• Geocell confined soils</li> <li>• Geogrid interlocking with aggregate</li> </ul>
Stress-Relief Interlayer	A geotextile that minimizes stress concentration at the bottom of asphalt overlay in a paved road	/
Separation	preventing intermixing of two materials	Geotextile between subgrade and the overlying granular layer
Fluid Barrier	Preventing or minimizing the migration of fluids	<ul style="list-style-type: none"> <li>• Geomembrane</li> <li>• Geotextile impregnated with bitumen</li> </ul>
Drainage	Conveying a fluid driven by hydraulic gradient or by capillarity	<ul style="list-style-type: none"> <li>• Geotextile, geonet</li> <li>• Wicking geotextile</li> </ul>
Filtration	Allowing water to pass while retaining the soil through which water is flowing	Geotextile

Among the functions in roads in Table 1, those relevant to the mitigation of F-T damages are reinforcement, stabilization, fluid barrier, and drainage. This review is central on the mechanisms, pros and cons, design and construction considerations of these four functions of geosynthetics.



Typical stabilization with geocell

**(a) Stabilization**

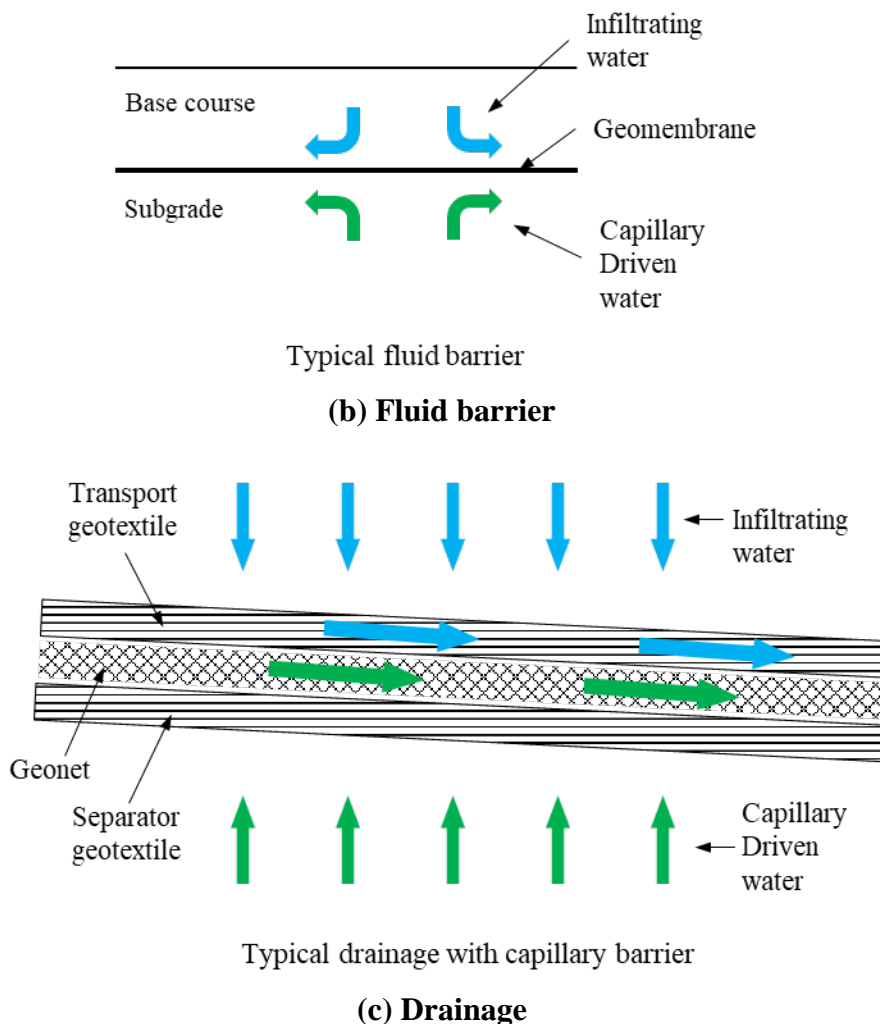


**Figure 3. Typical design of geosynthetics to perform desired functions** [(a) and (c) are reproduced from Pokharel (2010) and Henry and Stormont (2002), respectively]

**Geosynthetics in improving freeze-thaw resistance.** Occurrence of frost heave in roads is premised on three conditions: subfreezing temperature, water supply and migration, and presence of frost-susceptible soils, while thaw weakening is induced by buildup of water in road sections and repeated traffic loads. Thus, countermeasures are commonly devised in practice to control one or more of these influencing factors, which includes: (1) insulation against freezing, (2) modifying frost-susceptible soils, (3) cutting water supply, and (4) improving drainage condition. The functions of geosynthetics listed in Table 1 can be tied to these countermeasures. For example, addition of a layer of geocells and geogrids in the base or at the base-subgrade interface can stabilize frost-susceptible subgrade soils and reinforce the overlying base (Countermeasure 2). Geomembranes or geocomposites (geotextile, geonet, and geomembrane as will be discussed later) are used to cut water migration upward to the base course layer (Countermeasure 3). Wicking geotextiles or geocomposites (geotextiles wrapping aggregates or geonet) are utilized to improve drainage condition in roads by redirecting the water to road shoulders (Countermeasure 4). To the best of our knowledge, Geosynthetics have not been applied in practice to address the first countermeasure yet; however, geocomposite consisting of a geonet sandwiched between



nonwoven geotextiles has been conceptualized as an insulation layer and numerically analyzed for its efficacy (Ahmed and Islam 2020). Excluding Countermeasure 1, the rest three measures can be categorized into two methods: i.e., mechanical method (Countermeasure 2) and hydraulic method (Countermeasures 3 and 4). In the following sections, laboratory element/model tests and field trials to assess each method are reviewed and outcomes of the tests analyzed.

## MECHANICAL METHODS

Geogrids and geocells that perform stabilization/reinforcement functions are considered as a mechanical method to mitigate F-T damages. The lateral confinement of geogrids, and cellular confinement of geocells, are beneficial in reducing axial deformation and loss of strength and resilient modulus in both base and subgrade soils subjected to freeze-thaw cycles.

**Geogrids.** Limited research has been devoted to evaluating the effect of geogrids on reduction in freeze-thaw distress in roads. Table 2 synthesizes the limited studies in the literature.

**Table 2. Summary of research about geogrid in resisting freeze-thaw damage**

References	Specimen size (mm)*	Aperture size (mm)	Type of reinforcement	Type of tests	Effectiveness in resisting F-T damage***
Yang et al. (2021)	140(H) × 70(D)	1×1	multi-layer biaxial	element	• moderate to major
Zhao et al. (2020)	200(W) × 400(H)	35×35	multi-layer biaxial	element	• moderate to major
Alfaro and Pathak (2012)	450(L) × 420(W) × 520(H)	46×64	single-layer biaxial	model	• minor
Li et al. (2017)	Unpaved roads	25×33	single-layer biaxial alone single-layer biaxial +NG**	field	• no to minor • minor to moderate
Henry et al. (2005)	Unpaved roads	25×33	single-layer biaxial	field	• no

\*H= Height, D= Diameter, W= Width, L= Length, \*\* nonwoven geotextiles; \*\*\*rank scale: major, moderate, minor, no

Yang et al. (2021) performed dynamic triaxial tests (element scale) on geogrid reinforced expansive soil subjected to seven F-T cycles and two confining stresses (i.e., 10 kPa and 50 kPa). The specimens were reinforced with biaxial geogrids at depths of 35mm, 70mm, and 105mm below their top surface. It was found that after the prescribed F-T cycles, both unreinforced and reinforced specimens under 10 kPa confining stress expanded, but those under 50 kPa consolidated. Addition of geogrids helped reduce axial deformation caused by F-T cycles: i.e., a decrease in expansion by 54.2% and compression by 9.2%. Inclusion of geogrids increased the dynamic shear modulus and the damping ratio of the expansive soil.

Zhao et al. (2020) conducted a series of element-scale tests to evaluate various influencing factors on F-T responses of geogrid-reinforced silty clay. The influencing factors included water content, degree of compaction, reinforcement spacing (i.e., vertical spacing between two neighboring geogrid layers), number of F-T cycles, freezing temperature, and overburden pressure.

The results showed that initial water content, reinforcement spacing, and overburden pressure had most significant effects on the frost heave and thaw settlement of the soil specimens.

Alfaro and Pathak (2012) conducted model tests on geogrid-reinforced sandy silt subjected to F-T cycles under constant normal (20 kPa) and horizontal (14 kPa) stresses applied on the soil surface. Compared to the unreinforced soil, the geogrid-reinforced soil showed smaller the lateral displacement. The horizontal deformations of soil were cumulative, while the vertical deformations were scattering around zero and the magnitude was smaller than that in the horizontal direction. The authors also observed slippage at the soil-geogrid interface during thawing process.

Li et al. (2017) conducted field tests on a 3.2 km stretch of heavily used unpaved road in Iowa, USA to evaluate the efficacy of various measures to improve freeze-thaw resistance of unpaved roads. The measures included Macadam Stone Base layers, aggregate drainage column, stabilization with cement or bentonite, and geosynthetics reinforcement (biaxial geogrids, nonwoven geotextiles, and geocomposites placed between the aggregate base and the frost-susceptible subgrade). The outcome of each measure was assessed using elastic modulus by falling weight deflectometer (FWD) tests. It was found that geogrids could improve the modulus of road sections before F-T cycles. However, after thawing, the geogrid test sections showed a reduction in modulus, but remained stiffer than the control (or unimproved) sections. Addition of a separate nonwoven geotextile layer beneath the geogrid was able to slow down the modulus degradation after thawing, although it slightly reduced the enhancement from geogrid before F-T cycles. The geocomposites and aggregate column sections showed no noticeable improvement as compared to the control sections. But from the field observation, they were effective in preventing frost boils, benefited from improved surface drainage.

In summary, the past studies demonstrated that to mitigate F-T damage, a single layer of geogrid reinforcement was inadequate. Multi-layer geogrid reinforcement combined with a layer of separator (e.g., non-woven geotextiles) would enhance the F-T resistance of reinforced sections. Furthermore, most of research has focused on biaxial geogrids; however, no research is concerned about triaxial geogrids or multi-axial geogrids. Further research is warranted to advance the understanding of the effectiveness of (1) multi-layer geogrid reinforcement through the model and field tests, (2) other types of geogrids, and (3) geogrid reinforcement in different types of base and subgrade (i.e., different frost susceptibility).

**Geocells.** Li et al. (2021) performed splitting tests on geocell-reinforced asphalt mixture, after one F-T cycle. The geocell used is polypropylene geocell. The tensile strength of the asphalt increases by 12.5% with geocell reinforcement. After one F-T cycle, both reinforced and unreinforced asphalt experienced drop of the tensile strength. While the tensile strength of the geocell-reinforced specimens was 23.3% larger than that of the unreinforced. The residue tensile strength of reinforced specimens, before and after the F-T cycle, was close and larger than that of the unreinforced. The unreinforced asphalt specimens were found to have nearly zero residue tensile strength.

**Table 3. Summary of research about geocell in resisting freeze-thaw damage**

References	Specimen size (mm)*	Geocell Size (mm)*	Type of Geocell	Type of tests	Effectiveness in resisting F-T damage**
X. Li et al. (2021)	100(L) × 100(W) × 100(H)	200(H) 60×60(A)	single-layer Polypropylene	element	• moderate to major

Huang et al. (2021)	750(L) × 750(W) × 170(H)	150(H) 245×210(A)	single-layer nano-polymeric alloy (NPA)	model	• major
Henry et al. (2005)	Unpaved roads	101.6(H) 152.4(H)	Single-layer	field	• major
Pokharel et al. (2017)	Paved roads	150(H) 245×210(A)	single-layer nano-polymeric alloy (NPA)	field	• major

\*H= Height, W= Width, L= Length, A=Aperture. \*\*rank scale: major, moderate, minor, no

Huang et al. (2021) developed a model test apparatus that could perform F-T and plate load tests on soils. The F-T test and the plate load test were run in sequence not simultaneously. A special feature of this device is the use of aluminum material to fabricate the walls of the F-T box. It acted as a heat sink to reduce the heat exchange between the ambient and the soil, thus reducing the thickness of insulation. The results showed that geocells reduced both frost heave and thaw settlement of sand base, by 18% and 34%. After F-T cycles, the loss of stiffness and bearing capacity in plating loading tests was also suppressed, and these two properties of soil with geocell reinforcement were approximately 40% and 253% higher than those of the unreinforced. Note the bearing capacity in this paper was defined based on the largest measured value instead of the value at the maximum curvature.

Henry et al. (2005) ran a series of field tests on unpaved roads for two seasonal F-T cycles between 2001 and 2003 to evaluate different candidate remedies (Table 4) for unpaved roads against F-T damages in Vermont, USA. The subgrade soils at the project sites were mostly silty sand, often containing sufficient fine particles so that the subgrade was considered frost susceptible. The remedies involved in the test are listed in Table 4.

**Table 4. Summary of remedies in the field trial of unpaved roads**

Categories	Remedy	Description
Reinforcement	Geogrid	between base (0.3 m thick) and subgrade
	Geocell	In the aggregate base (0.3 m thick) and immediately above subgrade surface
Separator	Geotextile	between base (0.3 m thick) and subgrade
Draining	Drainage	Lower trench drain, and perforated PVC drainpipe underground, wrapped in geotextile and surrounded by crushed stone
	‘Geowrap’	Gravel layer (0.3 m thick) wrapped by geotextile
Capillary barrier	GCBD	Geosynthetic Capillary Barrier Drain, sloped 2-5% to cut vertical water flow and drainage to drainpipe, at a depth of 0.3 m below the road surface
Chemical stabilization	Cement Stabilization	6% Portland cement by weight added to a 0.3 m (12 in) thick road surface material, or 8% cement to an 0.2 m (8 in) thick surface layer

In the field tests, both test sections and control sections were 30 m (i.e., 100 feet) long. The remedies, which either permanently improved the strength of the top layers of the road or reduced the water content of the road, performed the best (higher bearing capacity and less rutting). Specifically, the cement stabilization and geocell reinforcement had significantly improved the strength of roads, with relatively high CBR values, as these two methods effectively improved the strength of the top layers of roads. It is noted that this study only collected two-year data, which might not reflect the long-term performance. According to the five-year monitoring of a paved

road section in Alberta, Canada by Pokharel et al. (2017), the geocell-reinforced base outperformed the cement-treated base after two to three years of operation, showing considerably less cracks of road surface for the geocell-reinforced section.

The GCBD (Geosynthetic Capillary Barrier Drain) and the ‘Geowrap’ (Gravel layer wrapped by geotextile) test sections showed noticeable performance improvement as well. Good drainage condition by these two methods helped the upper soil layers dry faster, thus, achieving a faster recovery from thaw weakening for the soils. In contrast, methods of geogrids, geotextiles, combined use of geogrid and geotextile, and drainage provided no significant benefit to the road during thaw seasons.

The past studies demonstrated that geocells are effective in mitigating F-T damage to base, subgrade, and asphalt pavement. The benefits of geocells include mitigating frost heave and thaw settlement through their “slab” like reinforcement to base course. A full understanding of geocell performance requires more advanced model scale tests that can incorporate consideration of different influencing factors such as different base/subgrade materials and conditions, different geocell materials, temperature gradient, water supply, traffic loading, etc. These are still not available and require further research efforts. Field tests and monitoring are still the most valuable approach and more tests of this kind are encouraged to advance the understanding of geocells’ role in mitigating F-T degradation to roads.

## HYDRAULIC METHODS

This section introduces hydraulic methods available in practice and literature to reduce F-T damages to roads. Most of the hydraulic approaches capitalize on drainage functions of geosynthetics such as wicking geotextiles or fluid barrier functions to block water migration with materials like geomembranes.

To improve the drainage in road sections, methods like wicking geotextiles, geotextiles wrapping aggregates, or geonets are often considered. This kind of methods helped reduce strength loss and frost heave and attain fast recovery from thaw weakening. As frost heave primarily results from segregated ice lenses, efforts have been dedicated to stopping the water supply driven by capillary action. A method of capillary barrier is invented for this purpose. As a matter of fact, the capillary barrier also evacuates water in addition to cutting its path from subgrade to base. That is, it can capture capillarity-driven water, stop it from crossing the barrier, and then convey it out of road structure. Thus, geosynthetics with high hydraulic conductivity or high hydraulic transmissivity are often chosen for capillary barrier, which include geotextiles, geonets, and wicking geotextiles.

Geomembranes can be used as a fluid barrier because of their extremely low hydraulic conductivity; however, they are less commonly used to cope with F-T issues than the forgoing materials that have drainage or both barrier and drainage functions. This is likely due to that geomembranes are unable to (1) provide reinforcement to base or (2) prevent water flow into base from the road surface.

**Table 5. Summary of research about hydraulic methods in resisting freeze-thaw damage**

References	Type of materials	Functions	Type of tests	Effectiveness in resisting F-T damage*
Ghazavi & Roustaei (2013)	Geotextile	Drainage	element	minor to moderate



Lai et al. (2012)	geotextile, crushed rock, geomembrane	Drainage, Fluid barrier	element and field	moderate to major
Henry & Holtz (2001)	geotextile, geonet	Drainage	element	major
Henry & Stormont (2002)	geotextile, geonet	Drainage	element and model	major
Henry et al. (2005)	geotextile, geonet	Drainage	field	major
	geotextile, granular	Drainage	field	major
Zhang et al. (2014)	wicking geotextile	Drainage	field	major

\*Rank scale: major, moderate, minor, no

**Drainage.** Drainage Ghazavi and Roustaei (2013) performed element-level experimental tests on nonwoven geotextile reinforced clayey soils subjected to a maximum of nine F-T cycles in a closed system. The tests involved unconsolidated undrained (UU) triaxial test and computerized tomography (CT) imaging. One layer of geotextile was placed in the middle height of specimens measuring 100 mm height and 50 mm diameter. It was observed that the geotextile provided a limited benefit to suppress the height change of the specimen but reduced the loss of undrained shear strength by approximately 30% after the F-T cycles.

Lai et al. (2012) designed and investigated a road embankment improved with both barrier and drainage functions. This improved section consisted of, from top to bottom, geotextiles, crushed rocks, and geomembranes. In the field trial, the improved section was placed under bituminous pavement and cement stabilized macadam layers, and above a coarse subgrade soil layer. The control section had the drainage and barrier layers replaced by the coarse soil. It is worth noting that the porous crushed-rock layer acted as an insulation layer due to its lower thermal conductivity besides the drainage layer. As such, the presence of this layer reduced the frost penetration depth of the embankment as well as water accumulated in the sections above it. The soil's water content below the geomembrane was smaller than above it, confirming the effectiveness of the barrier created by the geomembrane. During the freezing season, the improved section showed less vertical movement than the control section. This might benefit from the reduced frost penetration depth and improved drainage of the improved section.

**Capillary Barriers.** A typical capillary barrier consists of porous material with sufficient pore size and thickness. The requirement for barrier thickness is to ensure the potential capillary rise terminates within the barrier.

Henry and Holtz (2001) investigated the potential for a geocomposite as capillary barrier to mitigate frost heave. The geocomposite consisted of two geotextiles sandwiching a thick geonet, with soil fines placed in the geotextiles. The experiments were conducted on 150 mm high cylindrical soil specimens with the capillary barriers placed at 30 mm above the specimen bottom or 5 mm above the water level during freezing. This narrow distance between the capillary barrier and the water level was set because of the large pores of geonet used, and therefore the thickness of the barrier itself had exceeded the potential capillary rise. The test results had confirmed this as the moist geocomposite capillary barrier could remarkably reduce the frost heave if the water level is lower than the geocomposite. However, in some cases, the geocomposite failed to reduce the frost heave if soil's saturation was fast because rapid saturation could lead to the hydraulic contact between the freezing front and the water supply. This research recommended the capillary barriers to be tilted to help redirect the migrating water toward the roadside.

Drawing on the previous study (Henry and Holtz 2001), Henry and Stormont (2002) further developed a Geocomposite Capillary Barrier Drain (GCBD), which consisted of three layers: i.e., from top to bottom, transport layer (special-designed geotextile), capillary barrier (geonet), and separator (geotextile). The GCBD was designed to be installed between base and subgrade. The transport layer was set to increase unsaturated drainage and maintain an unsaturated state so a functional capillary barrier could be developed. The separator layer was used to protect the capillary barrier from intrusion of the underlying soils. The research used a thermally treated fiberglass geotextile to sandwich the geonet capillary barrier, for both transport and separator layers. This specially designed geotextile, featuring a remarkable water retention function and water transmissivity, was heavy, woven, and multifilament, with a mass unit area of  $2370 \text{ g/m}^2$ , a thickness of 3.2 mm., and an O95 size of 0.075 mm. Both laboratory level element and model tests were conducted, with infiltration performed on the specimens. The model tests were performed in a 6 m (Length)  $\times$  1.3 m (Width)  $\times$  1.2m (Height) box, where a pavement structure was formed, with asphalt pavement, base layer, the GCBD, subgrade layer, and a ditch drain. The results of the infiltration tests show that the GCBD was effective in limiting water changes in base and subgrade. And in their later field trial, the GCBD was built inside unpaved roads. The field trial results show that the geosynthetic capillary barrier drain (GCBD), as well as 'Geowrap', a geotextile-wrapped granular layer, contributed significant improvement and a fast recovery of strength to the road during the thaw seasons (Henry et al., 2005)

A geosynthetic named wicking geotextile was used as a capillary barrier in recent years. The horizontally installed wicking geotextiles use their high capillary suction to draw and redirect capillarity-driven water inside the road sections to the side of the road. This is a different method than the previous method that uses the porous material with low capillary suction and sufficient thickness to detain the rising water.

Zhang et al. (2014) reported a field trial using wicking geotextiles to mitigate frost boils in Alaska, USA. The field trial was located at a downhill slope with a gradient of 11%. It included an 18.3 m long test section of paved road, where the most 'soft spots' were observed before the field test. Two layers of wicking geotextiles were installed in the test section above the estimated water table, with one end exposed to the air at the road shoulder. Over the course of two-year tests, no frost boils or soft spots were observed. As the wicking geotextiles can drain out water inside the treated zone, they could reduce the frost heave as well as eliminate thaw weakening. Since the frost boils did not occur after treatment, the soils did not reach saturation in the test section. From the mapped water content contours during rainfall, two layers of wicking geotextiles provided an effective drainage condition for the road base.

Overall, effectiveness of methods such as geocomposite capillary barrier, wicking geotextiles, and geotextiles wrapping aggregates is confirmed by field trials in the past studies. However, field tests are still limited and cost prohibited. More advanced model tests that can consider both F-T and plate load tests will be useful in providing a comprehensive evaluation of these measures in roads with different subsurface and climate conditions.

## CONCLUSIONS

In this paper, experimental research on geosynthetics (geogrids, geocells, geotextiles, geomembranes, or geocomposites) in improving road base subjected to freeze-thaw cycles is reviewed and summarized. These geosynthetics could provide both mechanical and hydraulic benefits to road structures in mitigating the F-T damages. Mechanical improvement provides

reinforcement to base and stabilization to subgrade, which can resist the frost heave and thaw consolidation, and mitigate the loss of the strength and modulus of road base after F-T cycles. Multi-layer geogrid or single layer geocell can be an effective solution for the mechanical improvement. Hydraulic improvement alleviates F-T damages by intercepting water and redirecting it out of the road section, which thus prevents the formation of segregated ice lens during freezing and drains water trapped in the thawed section during thawing. The hydraulic methods frequently make uses of geosynthetics with high hydraulic conductivity, or high hydraulic transmissivity, which include geotextiles, geonets, and geocomposites that consist of geotextiles and geonets. In some cases, geomembranes are applied as a fluid barrier to cut off the water flow to prevent the formation of segregated ice lens or prevent intrusion of fines into the base.

In general, geosynthetics can be an effective solution for improving freeze-thaw resistance of road structures. A combination of different geosynthetics that address different mechanisms to mitigate freeze-thaw damages may be considered to optimize their effectiveness.

## REFERENCES

- Ahmed, A., & Islam, M. A. (2020). Effect of Using Geosynthetics in Mitigation of Freeze-Thaw through Numerical Analysis. In *Geo-Congress 2020: Geotechnical Earthquake Engineering and Special Topics*, ASCE, Minneapolis, MN, USA: 436-445
- Alfaro, M. C., & Pathak, Y. P. (2012). Laboratory performance of geogrid-reinforced soils subjected to freezing and thawing. *Geotechnical Testing Journal*, 35(5), 784-795.
- Andersland, O. B., & Ladanyi, B. (2003). *Frozen ground engineering*. John Wiley & Sons, Hoboken, NJ, USA.
- Bing, H., He, P., & Zhang, Y. (2015). Cyclic freeze-thaw as a mechanism for water and salt migration in soil. *Environmental Earth Sciences*, 74(1), 675-681.
- Ghazavi, M., & Roustaei, M. (2013). Freeze-thaw performance of clayey soil reinforced with geotextile layer. *Cold Regions Science and Technology*, 89, 22-29.
- Giroud, J. P., Han, J., Tutumluer, E., & Dobie, M. J. D. (2021). The use of geosynthetics in roads. *Geosynthetics International*. <https://doi.org/10.1680/jgein.21.00046>
- Henry, K. S., & Holtz, R. D. (2001). Geocomposite capillary barriers to reduce frost heave in soils. *Canadian Geotechnical Journal*, 38(4), 678-694.
- Henry, K. S., and Stormont, J. C. (2002). *Geocomposite barrier drain for limiting moisture changes in pavement subgrades and base courses*. Final Rep. for NCHRP-IDEA Project 68, The National Academies, Washington, DC, 24.
- Henry, K. S., Olson, J. P., Farrington, S. P., & Lens, J. (2005). *Improved Performance of Unpaved Roads During Spring Thaw*. Research Report, US Army Corps of Engineers, Engineer Research and Development Center.
- Huang, M., Lin, C., Pokharel, S. K., Tura, A., & Mukhopadhyaya, P. (2021). Model tests of freeze-thaw behavior of geocell-reinforced soils. *Geotextiles and Geomembranes*, 49(3), 669-687.
- Lai, Y., Zhang, S., & Yu, W. (2012). A new structure to control frost boiling and frost heave of embankments in cold regions. *Cold Regions Science and Technology*, 79-80, 53-66.
- Li, C., Vennapusa, P. K. R., Ashlock, J., & White, D. J. (2017). Mechanistic-based comparisons for freeze-thaw performance of stabilized unpaved roads. *Cold Regions Science and Technology*,

141, 97–108.

- Li, X., Zhu, Y., Su, T., Wang, X., & Zhang, X. (2021). Study on performance improvement of new geocell reinforced asphalt mixture. *Construction and Building Materials*, 273, 121693.
- Morgenstern, N. T., & Nixon, J. F. (1971). One-dimensional consolidation of thawing soils. *Canadian Geotechnical Journal*, 8(4), 558-565.
- Pokharel, S. K., Han, J., Leshchinsky, D., Parsons, R. L., & Halahmi, I. (2010). Investigation of factors influencing behavior of single geocell-reinforced bases under static loading. *Geotextiles and Geomembranes*, 28(6), 570-578.
- Pokharel, S., Norouzi, M., & Breault, M., (2017). New advances in novel polymeric alloy geocell-reinforced base course for paved roads. In *Proceedings of TAC 2017: Investing in Transportation: Building Canada's Economy–2017 Conference and Exhibition of the Transportation Association of Canada*, Ottawa, Ontario, Canada.
- Qi, J., Vermeer, P. A., & Cheng, G. (2006). A review of the influence of freeze-thaw cycles on soil geotechnical properties. *Permafrost and periglacial processes*, 17(3), 245-252.
- Simonsen, E., & Isacsson, U. (1999). Thaw weakening of pavement structures in cold regions. *Cold regions science and technology*, 29(2), 135-151.
- Terzaghi, K.(1952). Permafrost. *J. Boston Soc. Civ. Eng.* 39(1): 1–50. Also in *Contributions to Soil Mechanics 1941-1953*; Boston: Boston Society of Civil Engineers, pp. 319–68.
- Yang, Z., Liu, X., Zhang, L., Niu, F., Ling, X., Li, G., & Shi, W. (2021). Dynamic Behavior of Geosynthetic-Reinforced Expansive Soil under Freeze-Thaw Cycles. *Advances in Civil Engineering*, 2021.
- Zhang, X., Presler, W., Li, L., Jones, D., & Odgers, B. (2014). Use of Wicking Fabric to Help Prevent Frost Boils in Alaskan Pavements. *Journal of Materials in Civil Engineering*, 26(4), 728–740.
- Zhao, R., Zhang, S., He, J., Gao, W., Jin, D., & Xie, L. (2020). Experimental study on freezing and thawing deformation of geogrid-reinforced silty clay structure. *Bulletin of Engineering Geology and the Environment*, 79(6), 2883-2892.



## Role of High-Modulus Geogrids in Improving Base Layer Properties

**Krishneswar Ramineni, S.M. ASCE<sup>1</sup>; Anand J. Puppala, Ph.D., P.E., D.GE, F. ASCE, F. ICE<sup>2</sup>; Md Ashrafuzzaman Khan, Ph.D., P.E., A.M. ASCE<sup>3</sup>; Nripojoyoti Biswas, Ph.D., A.M. ASCE<sup>4</sup>; Prince Kumar, S.M. ASCE<sup>5</sup>**

<sup>1</sup>Zachry Dept. of Civil and Environmental Engineering, Texas A&M Univ., College Station, TX.

E-mail: [r.k@tamu.edu](mailto:r.k@tamu.edu)

<sup>2</sup>Zachry Dept. of Civil and Environmental Engineering, Texas A&M Univ., College Station, TX.

E-mail: [anandp@tamu.edu](mailto:anandp@tamu.edu)

<sup>3</sup>Texas A&M Transportation Institute, Bryan, TX.

E-mail: [m-khan@tti.tamu.edu](mailto:m-khan@tti.tamu.edu)

<sup>4</sup>Zachry Dept. of Civil and Environmental Engineering, Texas A&M Univ., College Station, TX.

E-mail: [nripojoyoti.biswas@tamu.edu](mailto:nripojoyoti.biswas@tamu.edu)

<sup>5</sup>Zachry Dept. of Civil and Environmental Engineering, Texas A&M Univ., College Station, TX.

E-mail: [prince.kumar@tamu.edu](mailto:prince.kumar@tamu.edu)

### ABSTRACT

The use of geogrids to improve pavement performance has been gaining popularity among transportation practitioners over the last few decades. However, limited studies are available on the performance of High-Modulus Geogrids (HMGs) placed at various depths in base layers. Furthermore, considering rapid construction and monitoring requirements, practitioners prefer rapid measurement of pavement layer stiffness based on non-destructive tests. To address some these research gaps, a series of laboratory studies were conducted by reinforcing base materials with HMGs placed at a different depth to study the influence of geogrid location on layer strength and stiffness. This study focused on evaluating the performance of unreinforced and geogrid-reinforced unbound base materials by performing California Bearing Ratio (CBR) tests, Light Weight Deflectometer (LWD), and Variable Energy Dynamic Cone Penetrometer (VE-DCP) studies. Correlations were developed between the CBR and other engineering tests based on the performance of the HMGs. Overall, it was observed that HMG reinforced composite sections showed significant improvement in stiffness and overall layer performance as compared to unreinforced section.

### INTRODUCTION

Over the past few decades, geosynthetic materials have been successfully used to improve the performance of pavement layers (Giroud and Han 2004a, Zornberg and Gupta 2009, Abu-Farsakh et al. 2016). A wide range of geosynthetics like geotextiles and geogrids are being used as reinforcements to resist tensile stress and increase the stiffness of pavement layers (Tingle and Jersey 2005, Zornberg 2017). Past researchers reported that the geogrids placed between the interface of base and subgrade layers improved the performance of pavement by offering lateral confinement, higher load distribution through the base layer, and tensioned membrane effect

(Kwon et al. 2005, Perkins et al. 2012, Abu-farsakh et al. 2016, Laziz Muhmood and Khudhur 2021, Saride et al. 2022). The application of geosynthetics also helped to improve the bearing capacity of the foundation system by resisting slippage and increasing the pullout resistance (Biswas and Ghosh 2018, 2019). Although there are several studies conducted with geogrid reinforced soil and bases, pavement failure can still occur with such reinforcement as there is limited knowledge regarding the engineering properties of the reinforced layer and the depth of optimum location of the reinforcement (Kamel et al. 2004). The improvement of the base layer stiffness of the reinforced section depends on the interlocking of the base aggregate material with the geogrid, which is also the function of the in-plane stiffness and stability modulus of the geogrid (Giroud and Han 2004b).

The inclusion of geosynthetic improved the overall stiffness of the pavement layer, as recorded from the California Bearing Ratio (CBR) studies (Duncan-Williams and Attoh-Okine 2008). Both the soaked and unsoaked CBR values for the geogrid reinforced section was evaluated by comparing the load-penetration curves obtained from the reinforced and unreinforced sections (Laziz Muhmood and Khudhur 2021). In the field, the CBR values of the base and subgrade layer can be determined from Dynamic Cone Penetration (DCP) and Variable Energy Dynamic Cone Penetration (VE-DCP). The VE-DCP tests can be conducted on the soil sample prepared within the CBR mold to determine the cone resistance along the depth of the sample (Gansonré et al. 2022).

The surface modulus of the base and subgrade layer can be determined based on the stress-strain curve generated under the impact load from the Lightweight Deflectometer (LWD) device (Senseney et al. 2012, Ebrahimi and Edil 2013, Grasmick et al. 2015). The estimated elastic moduli from LWD tests were used to validate the assumed design parameters in the Mechanistic-Empirical Design Guideline (Ebrahimi and Edil 2013, Kuttah 2021). The layer coefficients of the pavement layers were also correlated with the elastic modulus obtained from the LWD test (Ebrahimi and Edil 2013). The LWD tests conducted within the CBR mold could simulate the field loading condition as the stress paths and the effect of deviatoric stress influence were recorded to be similar for both cases (Kuttah 2021). However, limited studies are available to quantify the benefits of geogrid with LWDs.

The primary objectives of this study were to determine the optimum location of geogrid below the base layer and subsequently determine the effect of the High-Modulus Geogrids (HMGs) on the strength and stiffness of base layers considering CBR, VE-DCP, and LWD tests. The utilization of high moduli geogrid could provide better confinement and improve the long-term serviceability of the pavement layers. Additionally, the LWD and VE-DCP tests on geosynthetic reinforced composite sections will be useful to determine the overall layer performance and the vertical zone of influence of the reinforcement in pavement layers, respectively. The following section presents the materials used for the research study and the testing methods followed.

## **MATERIALS AND METHODS**

**Materials.** The crushed stone aggregates were collected from a local supplier and used as a base material in this study. Basic material characterization studies were performed in accordance with different ASTM standards (Table 1). Figure 1 shows the grain size distribution of base aggregates.

Based on the Unified Soil Classification system (USCS), the material was classified as well-graded gravel (GW).

**Table 1. Basic material characterization of base aggregates.**

Parameters	Standard	Values
Maximum dry unit weight ( $\text{kN/m}^3$ )	ASTM D698	19.0
Optimum Moisture Content (%)	ASTM D698	7.5
Gravel (%)	ASTM C136	51.7
Sand (%)	ASTM C136	46.3
$C_u, C_c$	ASTM C136	20, 1.3

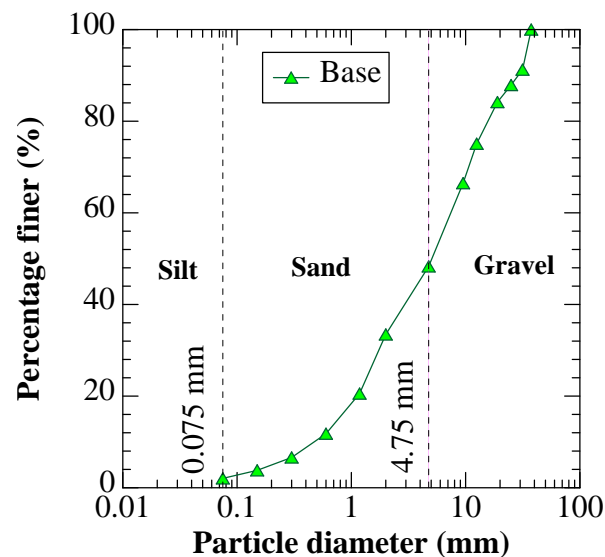


**Figure 1. Grain size distribution of base aggregates.**

Commercially available biaxial geogrids with high stiffness were used in this study. The punched and drawn biaxial geogrids were made of polypropylene. Three geogrids that were selected for this study have different strengths and stiffness, and the other material properties of each geogrid are presented in Table 2.

**Engineering Test Methods.** Oven-dried aggregates were mixed uniformly with the optimum water percentage (7.5% by dry unit weight) to prepare a homogeneous mixture. The homogeneous mixture was placed in four layers to a total target height ( $H$ ) of 114 mm in a CBR mold. Each layer was compacted to the height of 28.5 mm using static compaction. A single layer of geogrid was installed at a depth of 0.25 $H$ , 0.5 $H$ , and 0.75 $H$  from the loading surface to understand the effects of location on the performance. After studying the influence of geogrid location, different HMGs were placed at a depth of 0.25 $H$ , and the effects of stiffness on composite section performance were investigated. In addition to the reinforced sections, one unreinforced (UR) section was

prepared to understand the improvement with geogrids. The section performances were studied using three different engineering tests, including CBR, LWD, and VE-DCP tests (Figure 2).

**Table 2. High-Modulus Geogrids (HMGs) material properties.**

Parameters	HMG1	HMG2	HMG3
Aperture dimensions (mm)	25×33	36×36	33×33
Minimum rib thickness (mm)	1.30	1.50	2.30
Ultimate tensile strength (N)	1068	1008	1646
Aperture stability ( <i>j</i> ) (m-N/deg)	0.80	0.98	1.50

**California Bearing Ratio (CBR) tests.** The CBR test was performed using a universal testing machine on all different test sections. The CBR mold (Diameter, B = 150 mm) was placed under the loading piston, and a surcharge of 5 kg was added to the top of the soil. The test was performed at a strain rate of 1.3 mm/min, and the CBR values were calculated from load-penetration curves corresponding to 2.5 mm and 5 mm of penetrations.

**Light Weight Deflectometer (LWD) tests.** LWD is a portable non-destructive method to measure the elastic moduli of the pavement layers. In this study, a 10 kg standard weight was released from a drop height of 4 in. (100 mm) on a 150 mm diameter loading plate. The modulus of the tested sections was measured from the deflection and the stresses recorded by the LWD. The modulus was calculated using Equation 1 derived from the theory of elasticity for a cylinder of an elastic material with constrained lateral deflections (Schwartz et al. 2017).

$$E_{MOD} = \left(1 - \frac{2\mu^2}{1-\mu}\right) \times \frac{4H}{\pi D^2} \times \frac{F_{peak}}{\delta_{peak}} \quad (\text{Eq.1})$$

where  $E_{MOD}$  = Modulus of soil from LWD using proctor mold,

$\mu$  = Poisson's Ratio,

$F_{peak}$  = Maximum impact load,

$\delta_{peak}$  = deformation corresponding to the maximum load,

$H$  = height of the soil sample,

$D$  = diameter of the soil sample.

**Variable Energy Dynamic Cone Penetrometer (VE-DCP) tests.** The VE-DCP is a lightweight DCP that uses variable energy to drive the cone. The test was performed by driving the cone by hammering the rod at the other end using an anvil. The impact force from the hammer for each blow was measured by a strain gauge, and the depth of penetration was measured using a retractable belt. The tip resistance was calculated by using the depth of penetration and energy of the hammer blow. The mold diameter to the cone diameter ratio was 9.375 in this study, indicating a potential effect of the boundary conditions (Ampadu et al. 2017). However, as the primary objective of the study was to perform a relative study between different test sections, the effect of the confinement on absolute values was assumed to be uniform for all test configurations.



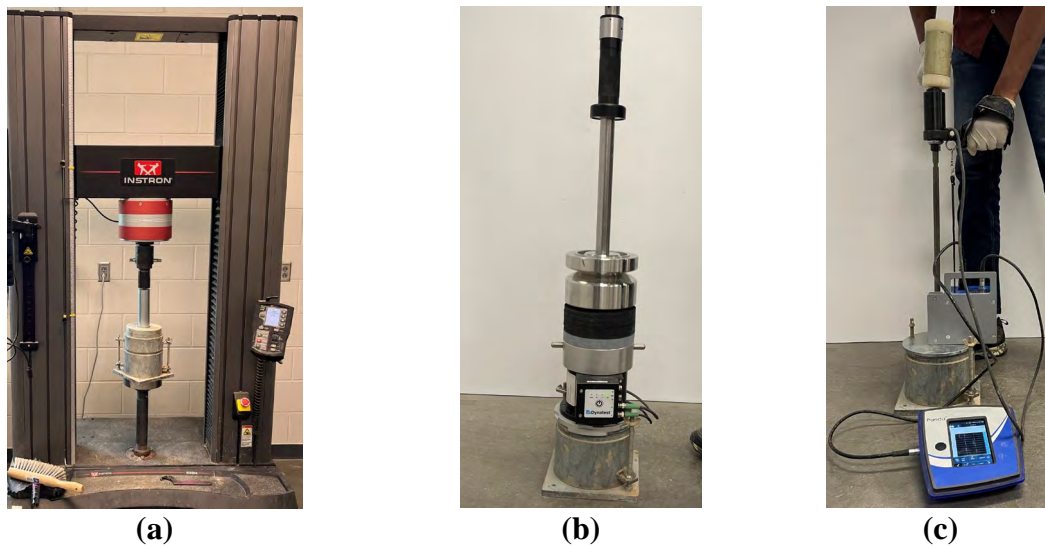


Figure 2. Engineering tests a) CBR b) LWD and c) VE-DCP.

## ANALYSES OF TEST RESULTS

The following section presents the outcome of the experimental studies using CBR, LWD and VE-DCP on the unreinforced and reinforced test setups.

**CBR Studies.** The results from the CBR tests are represented in Figures 3a and 3b and Tables 3 and 4. The stress vs. penetration curves is plotted for the different depths of the geogrid layer (HMG2) from the surface of the base layer (Figure 3). The inclusion of the geogrid layer affected the bearing capacity of the base layer. The load-penetration curves obtained from the CBR tests indicated that at the penetration depth of 12.5 mm, the load-bearing capacities for the UR, 0.75H, 0.50H, and 0.25H sections were approximately 1,600, 2,300, 2,850, and 4,400 kPa, respectively. For the reinforced sample, the reduction of depth of reinforcement from 0.75H to 0.25H helped to enhance the bearing capacity from 1.43 to 2.75 times as compared to the unreinforced section. Particle interlocking in the geogrid aperture and the tension membrane effect due to polyethylene material elasticity affected the soil bearing capacity. The maximum benefit of including soil reinforcement was observed when the location of the reinforced layer was approximately 0.25H from the surface. Further increase in depth resulted in lowering the bearing capacity of the reinforced layers.

The failure mechanism of the layer due to plunger movement could be considered similar to the classic bearing capacity failure of footings. The presence of the geogrids within the elastic triangular wedge below the plunger helped the reinforcement to resist the lateral movement of the radial shear zone and passive zone. The combined effects from the reduction in soil slippage due to particle interlocking and tensile strength of the geogrid improved the capacity. However, provision of reinforcement at lower depth, i.e., beyond the zone of influence below the plunger (approximately  $1.5-1.75D$ ,  $D$  = diameter of the plunger), has a marginal influence on layer capacity. The effects of the location of the HMG layers were also corroborated by the CBR values

(Table 3). The maximum CBR value was obtained for the reinforcement depth of 0.25H (at 5 mm penetration), eventually reduced with an increase in the depth of the geogrid layer.

The inclusion of geogrids with high aperture stability modulus at the same location (0.25H from the surface) affected the bearing capacity of the base layer (Figure 3b). The load-penetration curves obtained from the CBR tests also indicate that at the penetration of 12.5 mm, the corresponding load bearing capacities for the UR, HMG1, HMG2, and HMG3 sections are approximately 1,600, 2,800, 4,400, and 6,500 kPa, respectively. The change in geogrid stability modulus value ( $j$ -value) from 0.80 to 1.50 helped to enhance the bearing capacity by a factor of 1.75 to 4.06 compared to the unreinforced section.

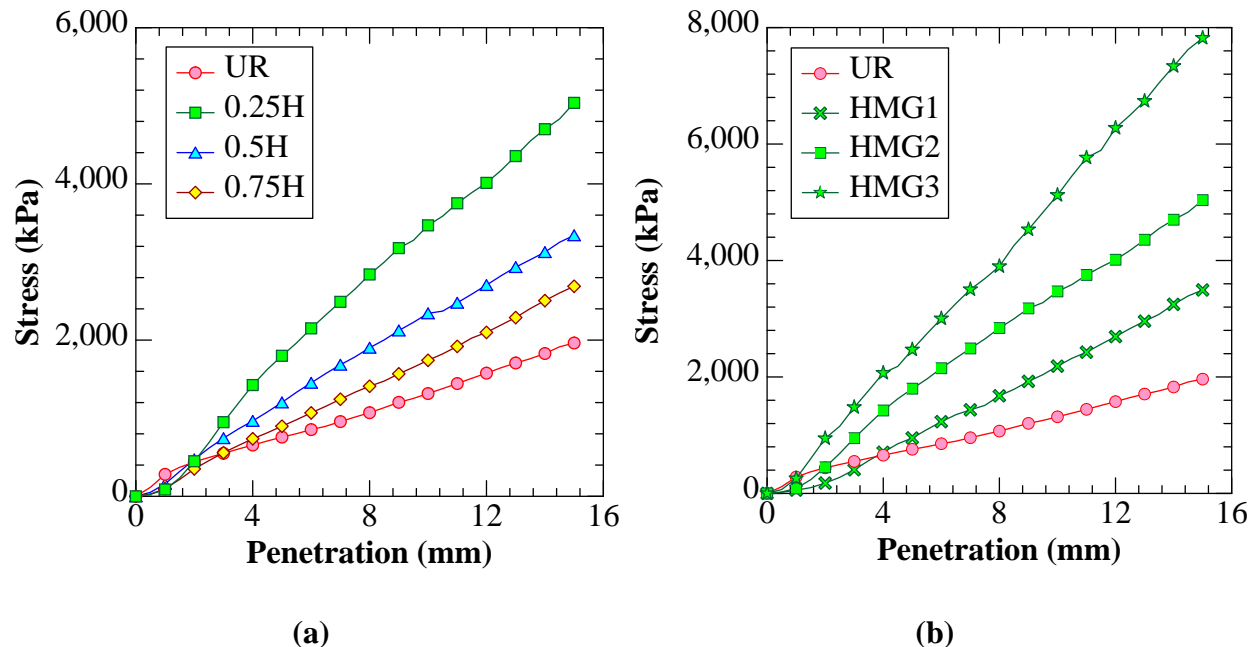


**Figure 3. Variation of stress with penetration values considering the a) Effects of the depth of geogrid (HMG2) location b) Effects of reinforcement moduli values for geogrids installed at 0.25H.**

High strengths from the planar materials resisted deformations from surface loads by providing higher restrain to the aggregates in the apertures and consequently improved the overall layer stiffness. The CBR value of the reinforced layers also showed an improvement with an increase in the moduli values of the geogrids (Table 4).

**Table 3. CBR values for HMG2 geogrid for different depths below the surface.**

CBR	UR	0.25H	0.5H	0.75H
2.5 mm penetration	7.2	17.1	10.7	8.3
5.0 mm penetration	7.3	20.7	12.8	9.5

**Table 4. CBR values for different HMGs at 0.25H.**

CBR	UR	HMG1	HMG2	HMG3
2.5 mm penetration	7.2	10.2	17.1	19.1
5 mm penetration	7.3	13.0	20.7	24.9

Therefore, from the CBR studies, it was observed that the application of geogrids with higher aperture stability modulus and at a depth of 0.25H has the maximum benefit in improving the capacity for the tested base material. This observation was further verified using the LWD test results in the next section.

**Light Weight Deflectometer (LWD) Studies.** Similar to the CBR results, the effects of the location of the reinforcement layer were evident from the moduli ( $E_{MOD}$ ) obtained from the LWD studies (Figure 4a). The maximum improvement in the modulus of the reinforced section was observed when the geogrid layer was installed at 0.25H from the surface. Furthermore, with further increase in reinforcement depth, the modulus values reduced, indicating a reduction in the reinforcing efficacy of the geogrid layer. The stiffness values corresponding to the reinforcement depth of 0.75H, 0.50H, and 0.25H were observed as 1.28, 1.45, and 1.71 times higher as compared to the unreinforced section. Figure 4b illustrates that a higher improvement in modulus could be realized by including geogrids with higher  $j$ -value, and subsequently corroborating the observations from the CBR studies. The stiffness values corresponding to the sections reinforced with HGM1, HGM2, and HGM3 were observed to be 1.62, 1.71, and 1.85 times higher as compared to the unreinforced section.

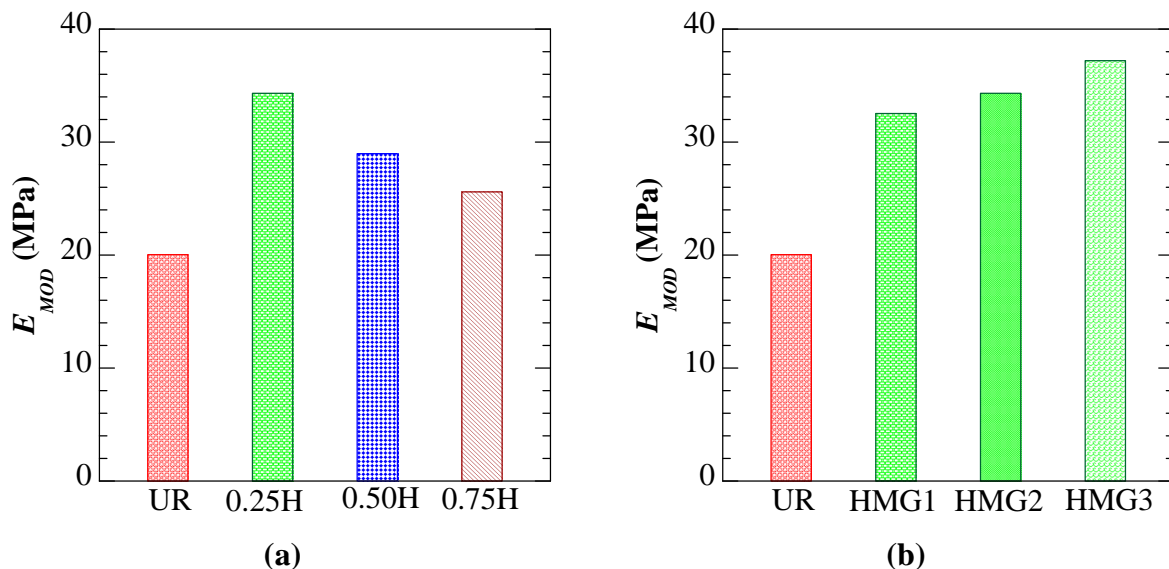


**Figure 4. Elastic moduli values of the sections considering the a) Effects of the depth of geogrid (HMG2) location b) Effects of reinforcement modulus values for geogrids installed at 0.25H.**

The CBR and the LWD studies provided some evidence of the overall improvement in the composite sections. The next analysis with VE-DCP provides further understanding of the reinforcement mechanism using the concept of the zone of influence of the HMG reinforcement in the base layer.

**VE-DCP Studies.** The results from the VE-DCP studies were used to understand the influence of soil reinforcement in different zones within the base layer. The composite section was divided into

three zones to understand the influence of geogrid layers (Figure 5a). The average tip resistance ( $q_r$ ) in the zones for unreinforced and reinforced sections is shown in Figure 5b. The application of HMGs had a significant influence between  $0.125H$  to  $0.375H$  or, in the region near the reinforcement location. An increase in geogrid stiffness had higher efficacy in restraining particle rearrangement, improved particle interlocking, and subsequently resulted in an improvement in layer stiffness. Both Zone 2 and 3 demonstrated an improvement in tip resistance or indirectly an improvement in packing density and stiffness with an increase in stiffness of the geogrids. However, the average tip resistance of Zone 1 was observed to be higher for low modulus geogrid, which subsequently degraded with an increase in geogrid stiffness. As the thickness of Zone 1 was marginal and located near the surface, the rigidity of the reinforcement layer probably interfered with the particle packing density during the compaction and resulted in lower tip resistance. However, a cumulative effect of three zones clearly indicated that the presence of HMGs significantly improved the overall layer performance.

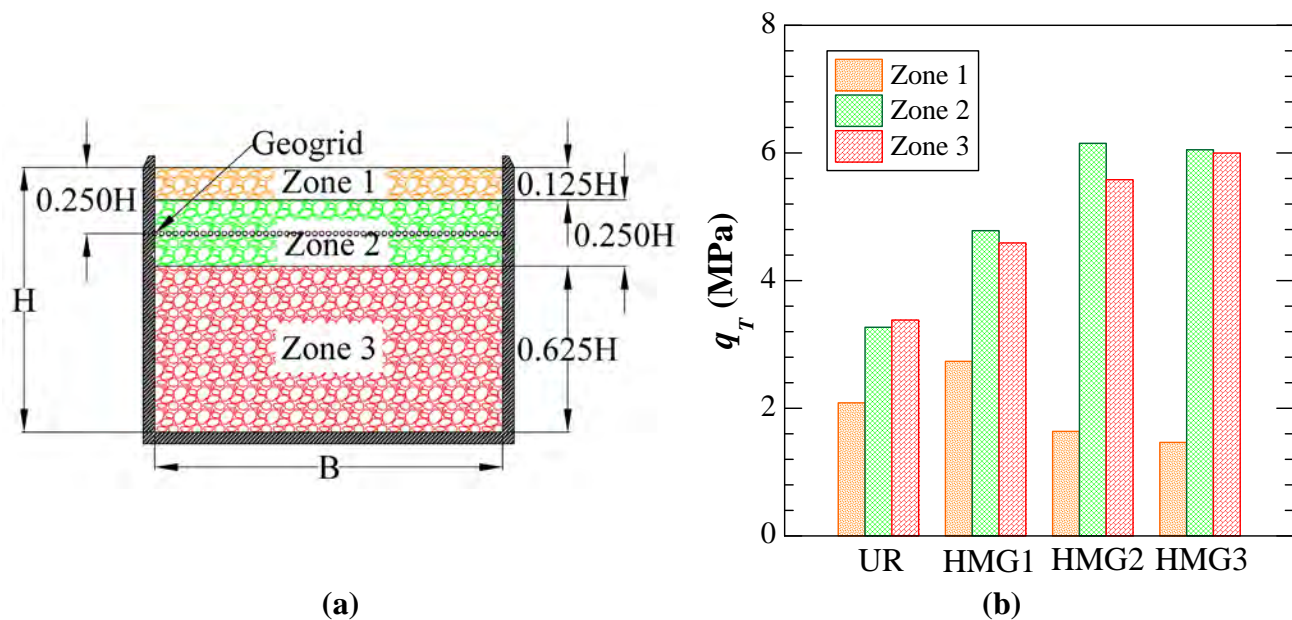


**Figure 5. Effects of HMGs on tip resistance a) Different zones of the composite section b) Average tip resistance in different zones in the test sections.**

**Correlations between CBR, LWD, and VE-DCP.** The following section presents some preliminary correlations between the CBR values and the other engineering test results. CBR, LWD, and VE-DCP studies illustrated that the capacity of the reinforced section was significantly dependent on the type and location of reinforcement in the base layer. Based on the experimental results first, the  $E_{MOD}$  of the sections obtained from LWD tests were correlated with CBR results for different HMGs at a depth of  $0.25H$  from the surface (Figure 6a). An exponential correlation was developed as shown in Equation 2,

$$CBR = 1.72e^{0.069E_{MOD}} \quad (\text{Eq. 2})$$

The  $R$ -squared value was predicted as 0.89, indicating a good fit. The experimental results indicated that the modulus values of the reinforcements directly affected the soil CBR and increased with an increase in the  $j$ -values of the HMGs. Similarly, the CBR values were correlated to the tip resistance ( $q_T$ ) of Zone 2 in the tested sections (Figure 6b). An exponential correlation was predicted with the goodness of fit value of 0.93, indicating a very good correlation (Equation 3).

$$CBR = 1.94e^{0.40q_T} \quad (\text{Eq. 3})$$

The ability of the HMGs to improve the soil interlocking in Zone 2 directly influenced the tip resistance near the reinforced layer zone and consequently improved the overall CBR values or stiffness of the base layer.

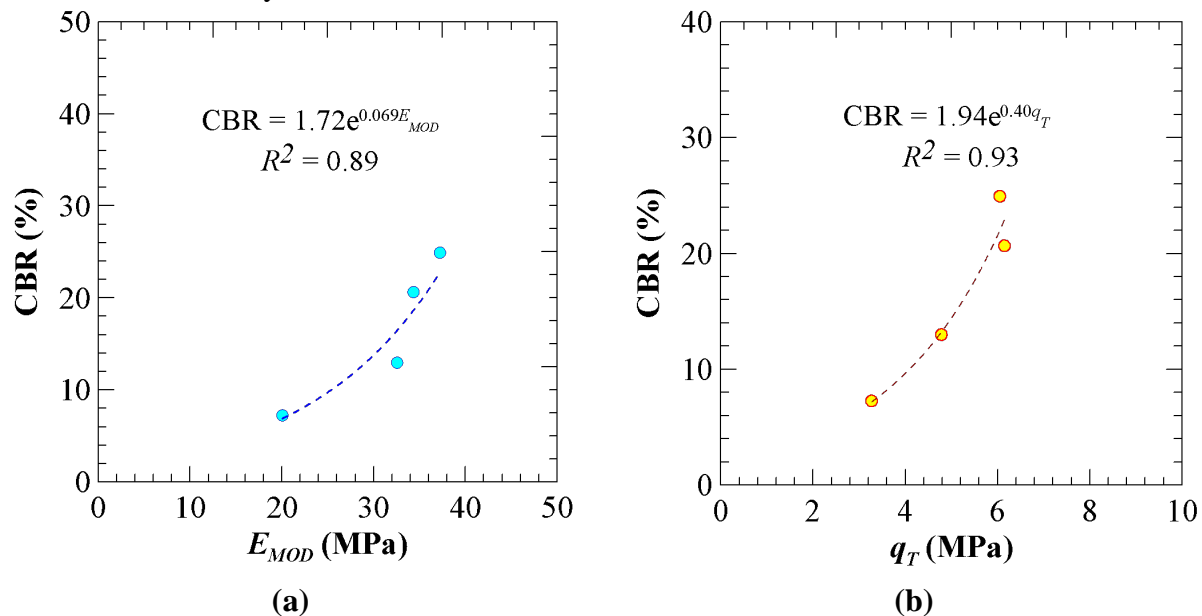


**Figure 6. Correlations between a) CBR and Elastic modulus of test sections b) CBR and tip resistances near geogrid layer (Zone 2).**

## CONCLUSIONS

This research study presents the effects of high-modulus geogrid on the performance of the base aggregate material in terms of stiffness obtained from DCP, VE-DCP, and LWD. The results obtained from the laboratory studies helped to determine the optimum location and strength of reinforcement required to obtain desirable performance. Some major findings from the current study are summarized as follows.

The location of geogrid reinforcement at a depth of approximately 0.25H (H = height of the sample) from the surface resulted in maximum load-bearing capacity. The change in geogrid stability modulus value ( $j$ -value) from 0.80 to 1.50 helped to enhance the bearing capacity by 1.75 to 4.06 times as compared to the unreinforced section. The composite modulus ( $E_{MOD}$ ) obtained from the LWD studies corroborated the optimum location of reinforcement to be 0.25H and maximum improvement was observed when the  $j$ -value was maximum.



The influence zone of reinforcement was verified with the VE-DCP test, which shows that maximum tip resistance was observed close to the reinforcement location. The reinforced section with HMG3 showed the highest tip resistance within the reinforced zone as the higher geogrid stability modulus restricted the rearrangement of aggregates and subsequently improved the particle interlocking. This study also provided some preliminary correlations between the CBR with the LWD modulus and tip resistance. Overall, the benefits of using HMGs were investigated using laboratory studies which could be potentially beneficial for the design of future pavements reinforced with such high-modulus geosynthetic products.

## ACKNOWLEDGEMENTS

This research was funded by Industrial Fabrics, Inc. (Mr. Jay Richardson, Mr. Cody Colvin, Mr. Keith Brooks, and Mr. Al Florez). The authors also acknowledge the support of the NSF Industry-University Cooperative Research Center (I/UCRC) program funded 'Center for Integration of Composites into Infrastructure (CICI)' site at TAMU (NSF PD: Dr. Prakash Balan; Award #2017796)

## REFERENCES

- Abu-Farsakh, M., Hanandeh, S., Mohammad, L., and Chen, Q. (2016). Performance of geosynthetic reinforced/stabilized paved roads built over soft soil under cyclic plate loads. *Geotextiles and Geomembranes*, 44(6): 845-853 doi.org/10.1016/j.geotextmem.2016.06.009
- Abu-farsakh, M.Y., Akond, I., and Chen, Q. (2016). Evaluating the performance of geosynthetic-reinforced unpaved roads using plate load tests. 8436. *Taylor & Francis*. doi:10.1080/10298436.2015.1031131.
- Ampadu, S. I. K., P. Ackah, F. O. Nimo, and F. Boadu. (2017). A laboratory study of horizontal confinement effect on the dynamic cone penetration index of a lateritic soil. *Transportation Geotechnics*, 10: 47–61. https://doi.org/10.1016/j.trgeo.2016.12.002.
- Biswas, N., and Ghosh, P. (2018). Interaction of adjacent strip footings on reinforced soil using upper-bound limit analysis. *Geosynthetics International*, 25(6): 599-611. Thomas Telford Ltd. doi: 10.1680/jgein.18.00020.
- Biswas, N., and Ghosh, P. (2019). Bearing capacity factors for isolated surface strip footing resting on multi-layered reinforced soil bed. *Indian Geotechnical Journal*, 49(1): 37–49. Springer India. doi:10.1007/s40098-017-0293-z.
- Duncan-Williams, E., and Attoh-Okine, N.O. (2008). Effect of geogrid in granular base strength - An experimental investigation. *Construction and Building Materials*, 22(11): 2180–2184. doi:10.1016/j.conbuildmat.2007.08.008.
- Ebrahimi, A., and Edil, T.B. (2013). Lightweight deflectometer for mechanistic quality control of base course materials. *Proceedings of the Institution of Civil Engineers: Geotechnical Engineering*, 166(5): 441–450. doi:10.1680/geng.11.00011.
- Gansonré, Y., Breul, P., Bacconnet, C., Benz, M., and Gourvès, R. (2022). Prediction of in-situ dry unit weight considering chamber boundary effects on lateritic soils using Panda® penetrometer. *International Journal of Geotechnical Engineering* 16(4): 408-414. doi.org/10.1080/19386362.2019.1698211
- Giroud, J.P., and Han, J. (2004a). Design method for geogrid-reinforced unpaved roads. II.

- Calibration and applications. *Journal of Geotechnical and Geoenvironmental Engineering*, 130(8): 787–797. doi:10.1061/(asce)1090-0241(2004)130:8(787).
- Giroud, J.P., and Han, J. (2004b). Design method for geogrid-reinforced unpaved roads. I. Development of design method. *Journal of Geotechnical and Geoenvironmental Engineering*, 130(8): 775–786. doi:10.1061/(asce)1090-0241(2004)130:8(775).
- Grasmick, J.G., Mooney, M.A., Senseney, C.T., Surdahl, R.W., and Voth, M. (2015). Comparison of multiple sensor deflection data from lightweight and falling weight deflectometer tests on layered soil. *Geotechnical Testing Journal*, 38(6): 851–863. doi:10.1520/GTJ20140172.
- Kamel, M.A., Chandra, S., and Kumar, P. (2004). Behaviour of subgrade soil reinforced with geogrid. *International Journal of Pavement Engineering*, 5(4): 201–209. doi:10.1080/1029843042000327122.
- Kuttah, D. (2021). Determining the resilient modulus of sandy subgrade using cyclic light weight deflectometer test. *Transportation Geotechnics*, 27(December 2020): 100482. Elsevier Ltd. doi:10.1016/j.trgeo.2020.100482.
- Kwon, J., Tutumluer, E., and Kim, M. (2005). Development of a mechanistic model for geosynthetic-reinforced flexible pavements. *Geosynthetics International* 12(6): 310–320. doi.org/10.1680/gein.2005.12.6.310
- Laziz Muhmood, A.A., and Khudhur, R.M. (2021). Using geotextile to reduce the required thickness of sub base layer of the road and improvement in CBR value. *Journal of Physics: Conference Series*, 1973(1). doi:10.1088/1742-6596/1973/1/012120.
- Perkins, S.W., Asce, M., Christopher, B.R., Asce, M., Lacina, B.A., Asce, M., and Klompmaker, J. (2012). Mechanistic-empirical modeling of geosynthetic-reinforced unpaved roads. *International Journal of Geomechanics* 12(4): 370–380. doi:10.1061/(ASCE)GM.1943-5622.0000184.
- Saride, S., Baadiga, R., Balunaini, U., and Madhira, M.R. (2022). Modulus improvement factor-based design coefficients for geogrid- and geocell-reinforced bases. *Journal of Transportation Engineering, Part B: Pavements*, 148(3): 1–14. doi:10.1061/jpeodx.0000380.
- Schwartz, C. W., Z. Afsharikia, and S. Khosravifar. (2017). *Standardizing lightweight deflectometer modulus measurements for compaction quality assurance*.
- Senseney, C.T., Krahenbuhl, R.A., and Mooney, M.A. (2012). Genetic algorithm to optimize layer parameters in Light Weight Deflectometer backcalculation. *International Journal of Geomechanics*, 13(4): 473–476. doi:10.1061/(asce)gm.1943-5622.0000222.
- Tingle, J.S., and Jersey, S.R. (2005). Cyclic plate load testing of geosynthetic-reinforced unbound aggregate roads. *Transportation Research Record*, (1936): 60–69. doi:10.3141/1936-08.
- Zornberg, J.G. 2017. Functions and applications of geosynthetics in roadways. *Procedia Engineering*, 189: 298–306. doi:10.1016/j.proeng.2017.05.048.
- Zornberg, J.G., and Gupta, R. (2009). Reinforcement of pavements over expansive clay subgrades. *Proceedings of the 17th International Conference on Soil Mechanics and Geotechnical Engineering: The Academia and Practice of Geotechnical Engineering*, 1: 765–768. doi:10.3233/978-1-60750-031-5-765.

## **25m<sup>3</sup> Geotextile Bags and Geotextile Tubes Used to Protect a 42” Pipeline Against Scouring, 30M Deep on the Seabed, Covenas, Colombia, S.a**

**Eng. Nicolas Ruiz R<sup>1</sup>, Eng. Mauricio Rendón G.,<sup>2</sup>**

<sup>1</sup>Solmax, Bogota, Colombia; e-mail: [nruiz@solmax.com](mailto:nruiz@solmax.com)

<sup>2</sup>Geosoluciones de Ingenieria SAS, Bogota, Colombia; e-mail: [gerencia@geomembranas.com.co](mailto:gerencia@geomembranas.com.co)

### **ABSTRACT**

The buoy that is part of the offshore terminal for tanker ships loading oil off the Colombian coastline is anchored to a submerged pipeline 42” in diameter that sits 30m deep over the seabed.

Underwater currents have caused localized scouring along the pipeline, creating voids underneath it and additional strain on the pipe. In providing a definitive solution, ECOPETROL, Colombia’s Oil Company and hence owner of this infrastructure, through its concessionary OCENSA, made it clear from the beginning that it should be paramount the loading of oil vessels would be the number one priority of the facility, therefore very specific windows of operation are open to install or build any solution.

With this restriction in mind, the project opted to fill onshore large Geotextile bags, 25m<sup>3</sup> in capacity each, that would be loaded onto a barge using a lifting harness made of polyester geogrid and a PVC coating. The geotextile bags would be lowered into position using a large crawler crane which would be fixed on to the barge and set into position with the help of deep-sea divers. With the bags in place, resting on each side of the pipeline, a geotextile tube would be installed in between the bags and under the pipeline and filled from the surface with a sand and water slurry to create an even surface.

The geotextile bags are fabricated from high strength polypropylene woven geotextile and are 5.0m long x 2.5m wide x 2.0m high and each has a filled capacity of 25m<sup>3</sup> and weighing in approximately 40 tons. Once the Geotextile bag and Geotextile tube are in position, a final Geotextile tube type-of -mattress would be placed overlapping the bags and the geotextile tube and filled with a sand slurry to fill in voids so that it can provide the support required to keep the submerged pipeline stable and in place. This geosynthetic system will provide a long-lasting solution for this scouring problem for good.

### **INTRODUCTION**

**Project Background.** The crude oil pipeline stretches from the south eastern plains in Colombia, in Cusiana and runs northwest to Covenas, on the Caribbean coast of Colombia, covering a total length of 850km on land and 12km underwater, lying on the bottom of the sea bed, 30m deep, where it connects to a manifold and valve system known as “TLU buoy” where super tanker ships are loaded, and the crude oil is exported or sent to the refinery in near-by Cartagena. Figure 1 – Project Location.

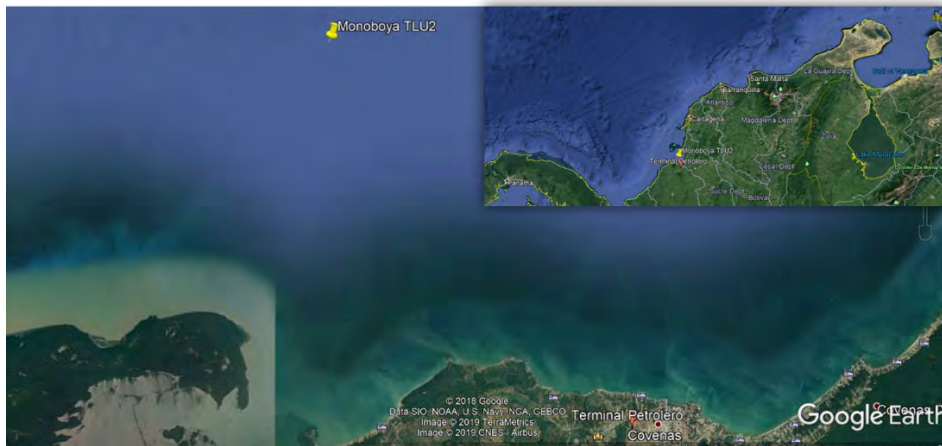


**Figure 1 – Project Location**

The submerged pipeline is 42" (1.06m) in diameter, it seats on the seabed and undergoes constant electronic monitoring and scuba diving supervision. Localized scouring along the pipeline has been detected in the past, mainly caused by underwater currents and several attempts to stop it have been made, with partial success.

An inquiry was brought to our attention on finding a way to solve this scouring problem for good and a solution utilizing a combination of geosynthetics was chose: large Geotextile bags units would be placed along each side of the pipeline; then, Geotextile Tubes and a Geotextile tube type-of-mattress would be installed. Figure 2 – Proposed Solution - 30m deep

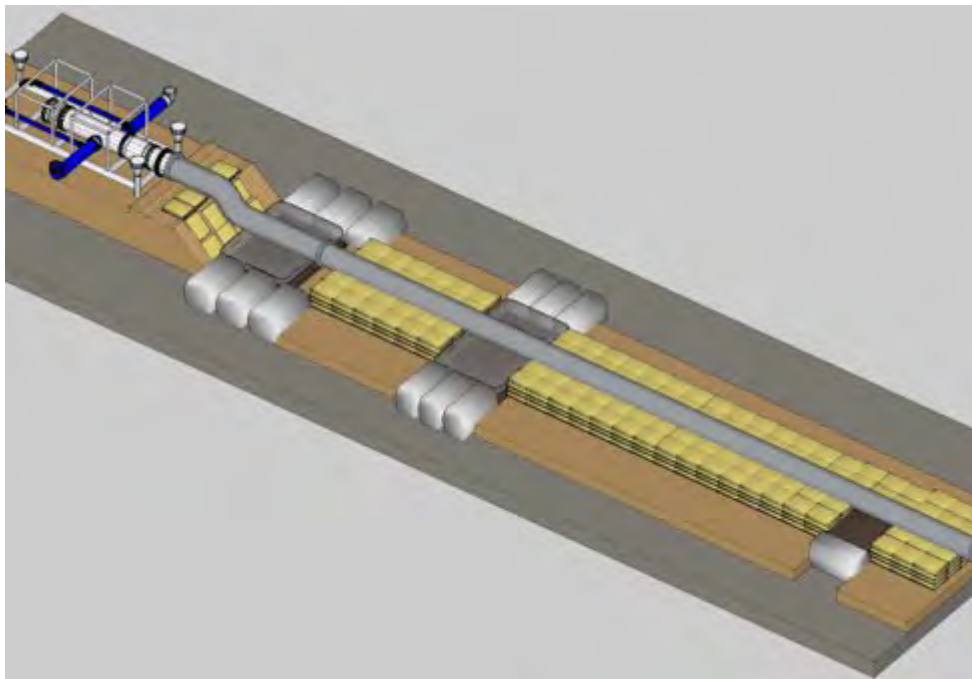


**Figure 2 – Proposed Solution - 30m deep**



**The Challenge.** One of the constraints to carry out the installation of the Geotextile Bags and geotextile tubes, was the time frame allowed to move near the buoy and carry out field maneuvers, as the priority of operation of the buoy consists in exporting crude oil, therefore any attempt to work around the site, would have to be done in between tankers approaching the buoy. Any schedule overrun, could mean thousands of dollars in liabilities.

To reduce such risk, it was decided to split the construction process into two phases: the first phase would be carried out onshore, with the deployment of the Geogrid Lifting Harness and the Geotextile bag units. Initially, these bags were designed with a capacity of  $35\text{m}^3$ , but it was later decided to bring them down to  $25\text{m}^3$ . The bags would be deployed over the geogrid lifting harness, filled and then loaded on to a barge. A total of 21 Geotextile bag units would be required for this project, containing over  $525\text{m}^3$  of coarse grain material.

Once the Geotextile bag units were lowered into position, all crane and additional vessels would no longer be required, thus reducing construction risks to manual deployment of the Geotextile tubes and mattresses.

## LABORATORY TESTS

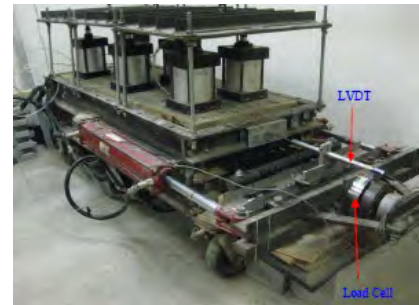
**Geogrid Pullout Testing.** To determine the Geogrid Lifting Harness Factors of Safety, we carried out Pullout tests, as per ASTM D 6706, using a  $400\text{kN/m}$  geogrid as pullout specimen overlying by a  $200\text{kN/m} \times 200\text{kN/m}$  geotextile sample, so as to simulate the behavior of the geogrid – geotextile bag system interaction.



Geogrid Setup



Geotextile Setup



Complete Test Setup

**Image 1 – Pullout Tests**

**Test Results: Apparent Friction Coefficient.** Pullout tests allowed us to determine the apparent coefficient of friction of Geogrid – Geotextile system, which would be used to calculate the geogrid's lifting harness factors of safety against rupture and pullout resistance, based on the geotextile bag's geometry and weight. These friction coefficients and the dimension of the geotextile bags were incorporated into the calculation of the factor of safety against pullout of the geogrid, which acts as a lifting harness.

## GEOBAG AND GEOTEXTILE TUBE DIMENSIONING

Several factors were taken into consideration for the design of the geotextile bag and Geotextile Tubes used on this project. Although geotechnical information was not made available, a recent



survey and bathymetric report were used to determine the fill height and capacity of all units, as shown on Figure 3 – Localized Scouring.

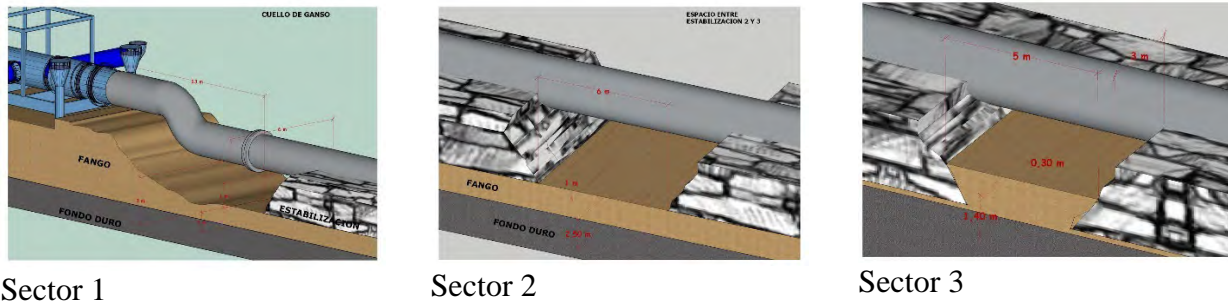


**Figure 3 – Localized Scouring**

Three sectors were identified that would require stabilization. As there was no geotechnical data, information provided by the diving team was used to determine the size of geotextile bags. A layer of fine grain material, approximately 1.2 to 1.5m in thickness was present. Therefore, geotextile bag units that would be placed along the side of each sector should be as heavy as possible so that they would sink through this layer and become stable reducing future settlements. Initially, geotextile bag units were designed to contain 35m<sup>3</sup> but were later reduced to 25m<sup>3</sup> each. Fabrication and lifting would have been possible; however, this decision was made in stake of risk management on behalf of the client. Final geotextile bag design was a unit made of a woven geotextile, 200kN/m x 200kN/m and 5.0m long, 2.5m wide and 2.0m high.

Proposed Solution by sector: Figures 4 to 6 show the proposed location of Geotextile bags, geotextile tubes and mattress around and under the submerged pipeline.

Sector 1. It included the use of 6units 25m<sup>3</sup> geotextile bags with 3 of the bags located on each side of the pipeline. It also incorporated 1 geotextile tube 12.2m in circumference, filled to a design height of 2.0m. This geotextile tube would contain aprox. 61.0m<sup>3</sup> of sand. Finally, the top geotextile tube would act as a mattress to support the pipeline, would have a design fill height of 1.0m or until it reached the bottom of the pipeline, which ever occurred first. This unit would be 9.14m in circumference and 15m long. Its purpose would be to rest over the geotextile bags and the geotextile tube as a support for the submerged pipeline. This unit would contain 54m<sup>3</sup> of pumped sand. The above is depicted on Figure 4 – Sector 1.

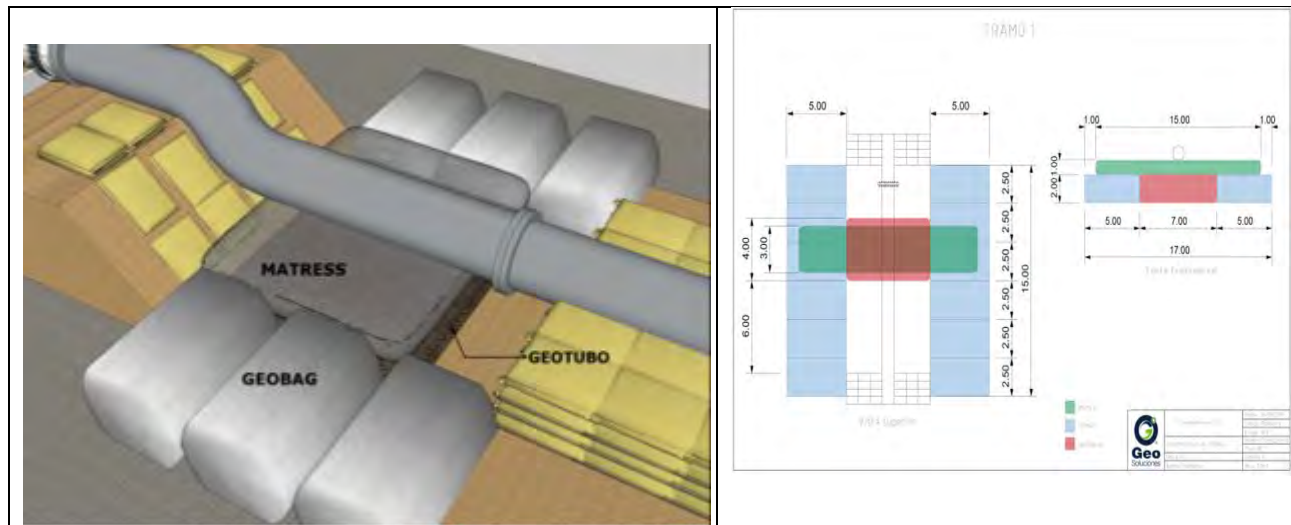


**Figure 4 – Sector 1**

Sector 2. It incorporated the use of 6 units 25m<sup>3</sup> geotextile bags with 3 of the bags located on each side of the pipeline. It also incorporated 1 geotextile tube 12.2m in circumference, filled to a design height of 2.0m. This geotextile tube would contain aprox. 61.0m<sup>3</sup> of sand. Finally, the top geotextile tube would act as a mattress to support the pipeline, would have a design fill height of 1.0m or until it reached the bottom of the pipeline, which ever occurred first. This unit would be 9.14m in circumference and 15m long. Its purpose would be to rest over the geotextile bags and the geotextile tube as a support for the submerged pipeline. This unit would contain 54m<sup>3</sup> of pumped sand. The above is depicted on Figure 5 – Sector 2.

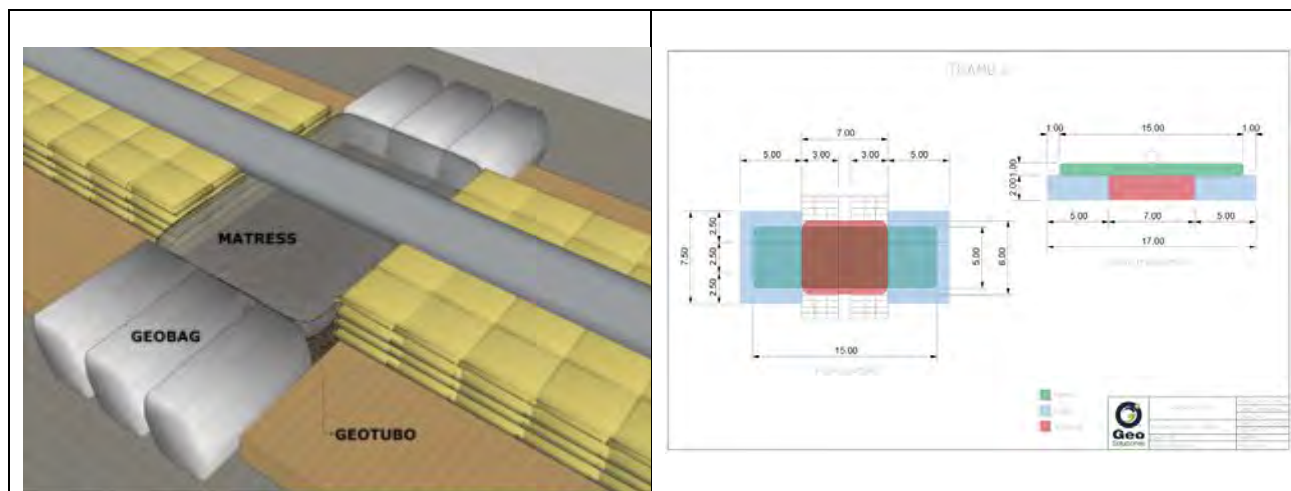


**Figure 5 – Sector 2.**

Sector 3. It included the use of 1 unit 25m<sup>3</sup> geotextile bag with 3 of the bags located on each side of the pipeline. It also incorporated 1 geotextile tube 12.2m in circumference, filled to a design height of 1.7m. This geotextile tube would contain aprox. 54.0m<sup>3</sup> of sand. Differently from Sectors 1 & 2, this one did not incorporate the use of a Geotextile tube to serve as a mattress because the pipeline had not fully eroded underneath, hence, the Geotextile tube was used to give support to the scoured section. The above is depicted on Figure 6 – Sector 3.

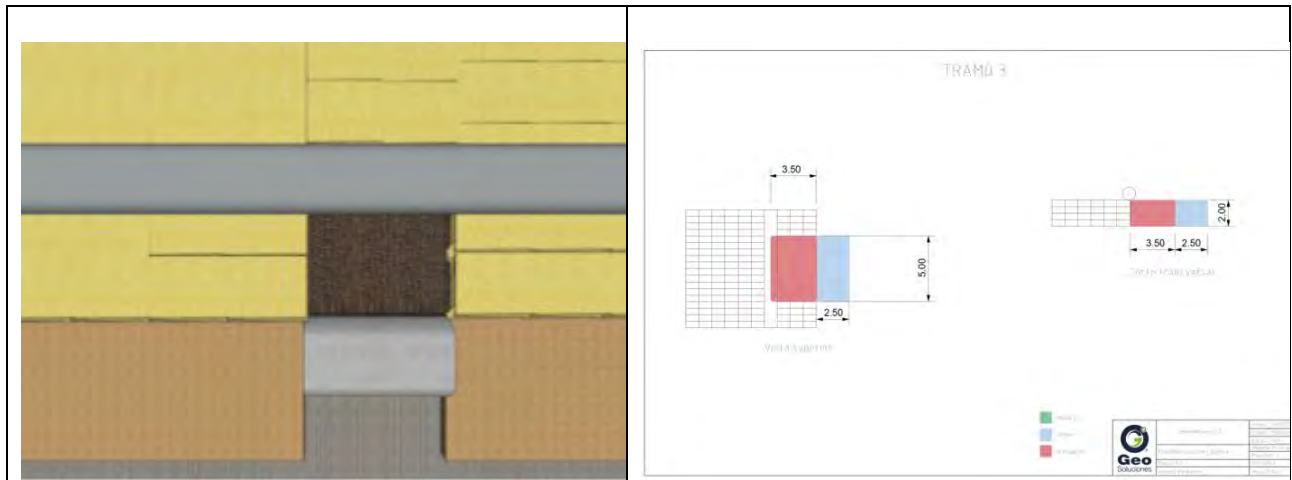


**Figure 6 – Sector 3**

Each geotextile was 30m lowered into position with the use of a crawler crane and the Geogrid lifting harness. Figure 7 – Geotextile bag Lifting Harness and Installation.



**Figure 7 – Geotextile Bag Lifting Harness and Installation**

Geotextile Tubes were designed with a fill height of 2.0m also, having Flat-Ends on each end so that they would snug fit between Geobag units. These Geotextile tubes were lowered and secured into position by divers and pumped from the surface using electric submersible pumps from a sand box located on board of the service tug. Figure 8 – Slurry Box

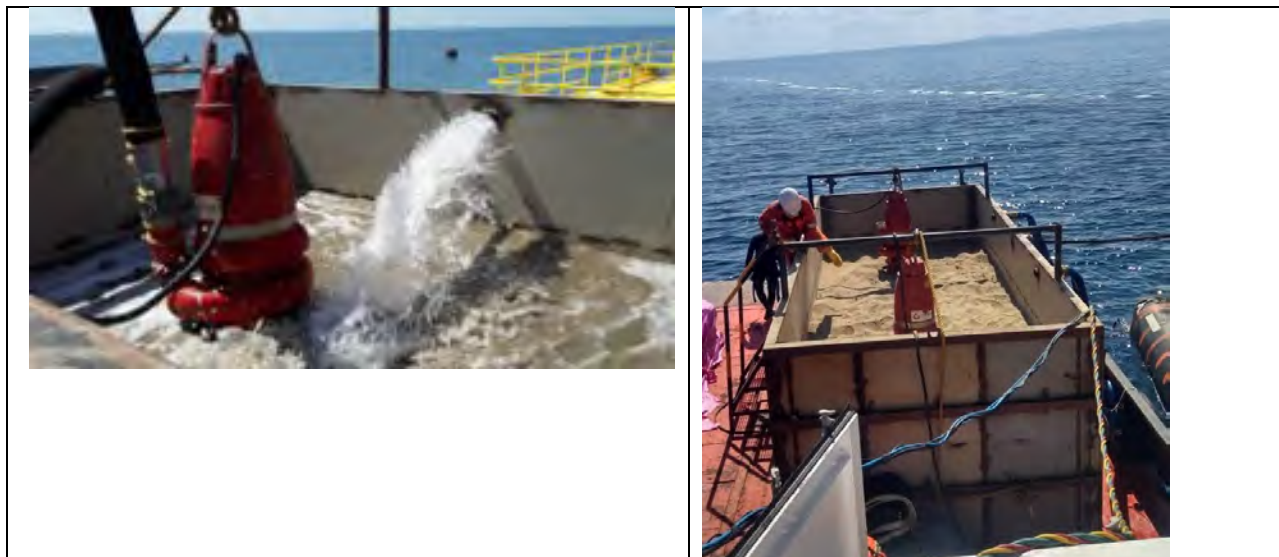


**Figure 8 – Slurry box**

## **RESULTS AND CONCLUSIONS**

The main purpose to eliminate or reduce the scouring and lack of soil underneath the submerged 42” diameter pipeline was achieved by the construction of a massive, yet flexible structure made of different geotextile elements, such as geotextile bags and geotextile tubes. Rather than utilizing rigid and expensive concrete forms, the use of these elements proved a technical yet economically feasible solution for this important problem. At no time, loading of oil vessels was interrupted by the construction of the submerged footing, which was one of the driving conditions of the construction solution.

All geotextile bags, Geotextile tubes and mattresses were installed successfully and have provided support to all scoured sections. Installing the Geotextile tubes on the seabed by divers proved difficult as time was limited during each dive, yet it was achieved. Also, pumping the sand slurry 30m to the bottom was accomplished successfully.

Project was completed in late 2019 and has performed as expected, to the point that it has been recognized by the ECOPETROL group, Colombia’s National Oil Company, as one of innovation.

## **REFERENCES**

- Ruiz, N., Geobags para la protección de la socavación en las esclusas de Gatún, Canal de Panamá, Geosynthetics 2017, Santiago, Chile, 2017
- Anmoba Solutions SAS, Análisis de cargas durante el bombeo de estabilización de lecho en oleoducto submarino, Bogota, 2019
- SGI Testing Services, LLC, TenCate Geosynthetics Geogrid Pullout Testing (ASTM D 6706), Georgia, 201166



## **Dredging Works and Geotextile Tube Applications for The Construction of Deep C Industrial Zones, Vietnam**

**Lum Kong Lim, P.E.,<sup>1</sup> Soon Hoe Chew, Ph.D.,<sup>2</sup>  
Jasper Verstreep,<sup>3</sup> and Jun Yuen Tan<sup>4</sup>**

<sup>1</sup>TenCate Geosynthetics Asia Sdn Bhd, 14, Jalan Sementa 27/91, Seksyen 27, 40400, Shah Alam, Selangor, Malaysia; e-mail: [lklim@solmax.com](mailto:lklim@solmax.com)

<sup>2</sup>National University of Singapore, Block E1A, #07-03, No. 1 Engineering Drive 2, Singapore, 117576; e-mail: [ceecsh@nus.edu.sg](mailto:ceecsh@nus.edu.sg)

<sup>3</sup>Independent Professional, 140, Jalan Kapar 27/89, Seksyen 27, 40400, Shah Alam, Malaysia; email: [jjv6490@stern.nyu.edu](mailto:jjv6490@stern.nyu.edu)

<sup>4</sup>TenCate Geosynthetics Asia Sdn Bhd, 14, Jalan Sementa 27/91, Seksyen 27, 40400, Shah Alam, Selangor, Malaysia; e-mail: [jytan@solmax.com](mailto:jytan@solmax.com)

### **ABSTRACT**

This paper discusses the use of geosystem containment solution which consists of geotextile tubes, high strength basal reinforcement and sand filled mattress as a containment dyke in an area with severe weather conditions and vulnerable to tropical storms and even typhoons. It is part of the construction of a land reclamation project, namely Deep C Industrial Zone in Lach Huyen, Vietnam. The Deep C Industrial Zone is located adjacent to the new Lach Huyen container port and is the biggest industrial zone development in Vietnam, comprising 3000ha of land divided into 5 separate industrial zones. The land reclamation was constructed in packages after the completion of the containment dyke. Design consideration, the construction techniques for filling the geotextile tubes, laying of high strength reinforcement and sand filled mattress will be discussed in this paper. A key requirement was that the fabric used to fabricate tubes are required to exhibit high resistance to UV degradation and weathering for long term exposure before final coverage with rock. The field data on the UV degradation of the geotextile tubes after 5 years will be highlighted. A total of 88,000m<sup>2</sup> of basal reinforcement and 19km of geotextile tube were installed in this project.

### **INTRODUCTION**

Deep C was established in year 1997 by a consortium of international investor lead by the Belgian company Rent-A-Port and the Vietnamese local governments. Since then, it had evolved to be one of the biggest industrial zone developers in Vietnam with a total of 5 industrial zones and about 3000ha of land for lease (Figures 1, 2 and 3). The design for the land reclamation required a containment dyke to be constructed as a perimeter bund wall to encompass the area to be reclaimed. The land reclamation for the peninsula of the so called 'Deep C II' in the Gulf of Tonkin, was constructed in packages after completion of the 'geotextile tube dyke' comprising of woven geotextile materials at the bottom, and stacked geotextile tubes with a sand filled mattress at the top in combination with backfilled sand.

The original consultant design of the containment dyke consists of conventional armor rocks bund wall (Figure 4) which is difficult to construct due to the soft underlying marine clay



with an undrained shear strength of 5 kPa for the first 6 – 9m and 10 kPa for the following 6 to 8m.



**Figure 1. Layout of Lach Huyen Bridge and Deep C Development.**



**Figure 2. Part of the Deep C II project, Vietnam.**



**Figure 3. Lach Huyen Bridge and Deep C II project, Vietnam.**

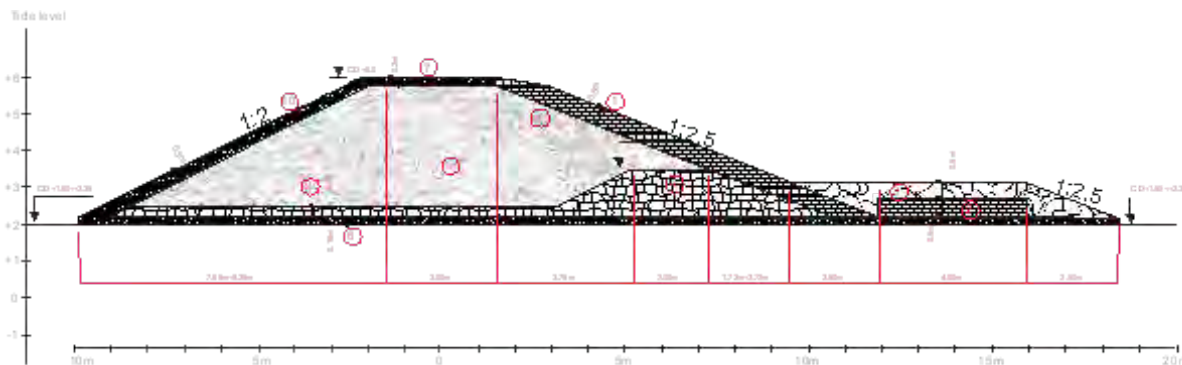


**Figure 4. Original design using conventional armor rocks system.**

The successful use of Geosystem containment dyke for the Lach Huyen bridge project which was adjacent to Deep C II prompted the project owner to evaluate their original design to a Geosystem containment dyke system (Figure 5). The construction of the Deep C II perimeter dyke was separated into three parcels; Parcel 1 in year 2015 (2.73km), Parcel 2 in year 2017 (3.16 km) and Parcel 3 to be carried out in year 2020 (3.1km) (Figure 6).

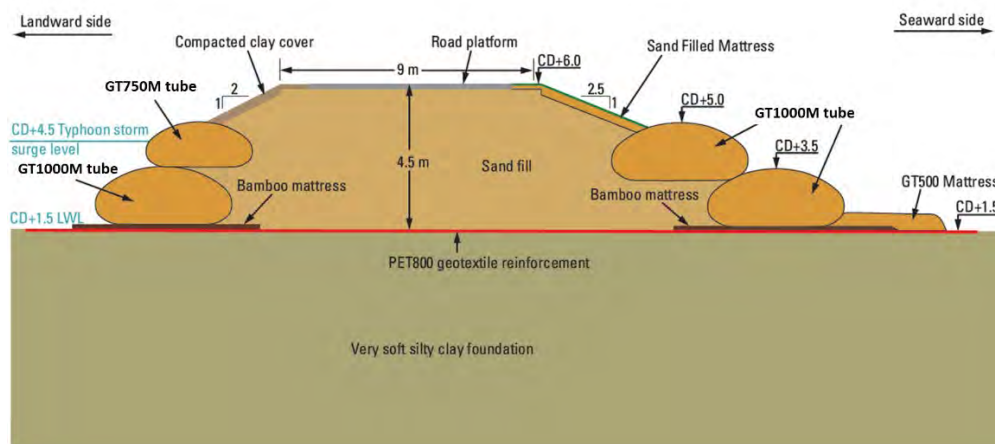


**Figure 5. Revised design using Geosystem containment dyke.**



**Figure 6. Deep C II was constructed in three different parcels.**

## SITE CONDITIONS

The subsoil in the area generally consists of very thick alluvial and marine clay deposits above a dense to very dense sand/gravel foundation. The soft clay layers have a low bearing capacity and excessive settlement characteristics. The first layer consists of very soft organic sandy silty clay with thickness of about 6 to 9 m and undrained shear strength of about 5 kN/m<sup>2</sup>. The second layer consists of soft to very soft clay with fine sand with thickness of about 6 to 8 m and undrained shear strength of about 10 kN/m<sup>2</sup>. Below that is an approximately 4.5 m layer of stiff to very stiff clay with gravel. The fourth layer generally consists of medium stiff clay (Figure 7).

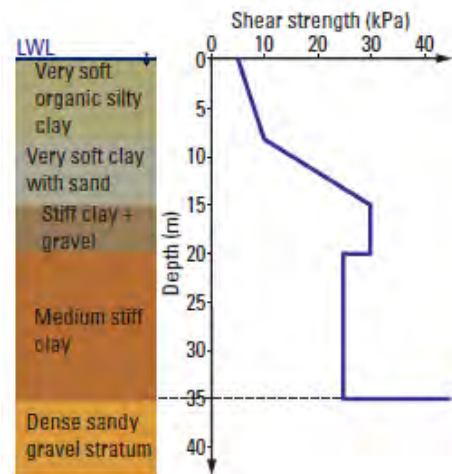
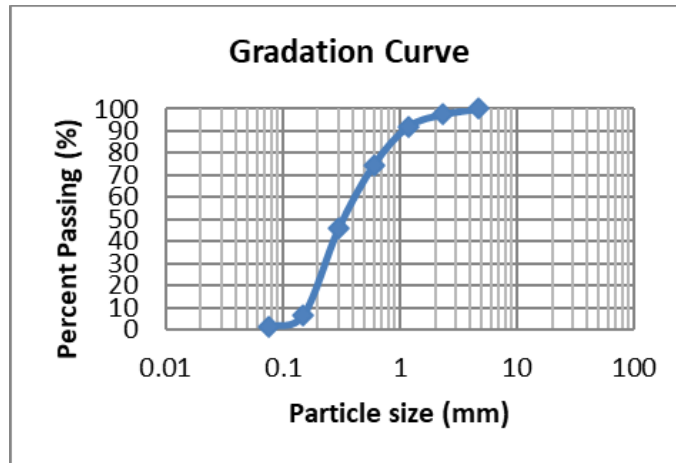


Figure 7. Underlying soil properties at project site.

## DESIGN AND STABILITY ANALYSIS

Conditions that influence the properties of the geotextile over time should be considered. The polymer used to manufacture geotextile tubes should be durable in biological, chemical environment and have ultraviolet (UV) light resistance. In the design analyses, a global factor of safety of 3.5 - 5 was applied for creep, construction damage, environmental damage, seam efficiency, etc. The geotextile tensile stresses of the tube during hydraulic filling were analyzed using Geotube® Simulator software program, which is a computer program developed by TenCate Geosynthetics North America. The required ultimate circumferential and axial tensile strength of the tube were determined to be 115 kN/m and 89 kN/m respectively. As the design life of the geotextile tube needs to be 5 years in tidal conditions, a woven polypropylene geotextile tube of circumference 12.6m with a tensile strength of 200 kN/m in both warp and weft directions and seam strength of 160 kN/m was supplied to the project. Exhumation of geotextile tube in Lach Huyen bridge after 5 years exposure in similar site conditions has shown a tensile strength retention of 50%.

The geotextile tube supplied was lined with a nonwoven geotextile inner liner filter as fine sand was used for the tube filling (Figure 8). The nonwoven geotextile filter was stitched to the woven fabric at an interval of 0.3m center to center. This stitching is critical to prevent the delamination of the nonwoven filter geotextile during the pumping operation (Figure 9).



**Figure 8. Gradation curve of the sand used for tube filling.**



**Figure 9. Geotextile tube with nonwoven filter inner liner.**

## **HIGH STRENGTH BASAL REINFORCEMENT AND SAND FILLED MATTRESS**

The external stability analysis was carried out by Slope/W software (by Geo-Slope International, Calgary, Canada) using Morgenstern-Price method. Morgenstern-Price method was used as it used the moment and force equilibrium in the computation of the factor of safety (F.S.) compared to Bishop Method which used only the force equilibrium in the F.S. computation (Geo-Slope International Ltd., 2012). From the external stability requirement to achieve a F.S. > 1.2, a layer of high strength basal reinforcement geotextile with ultimate tensile strength of 800 kN/m was required at the base of the geotextile tube. The sand filled mattress was designed according to CUR – 217 design guide and checked against tensile rupture and soil piping (Bezuijen, 2013). The sand filled mattress was designed to a filled thickness of 180 mm. The fabrics used for the sand filled mattress fabrication are made from composite coarse grain that allows soil entrapment, high UV resistance and vandalism resistance.



## CONSTRUCTION METHODOLOGY – SCOUR APRON

A layer of bamboo mattress was constructed at a grid formation of 0.7m x 0.7m and installed over the soft marine clay. The bamboo mattress allows construction trafficability and increases the bearing capacity of the soft underlying marine clay. A scour apron of 8.8m circumference was then installed over the bamboo mattress. The scour apron and bamboo mattress are pegged in position using bamboo pegs to ensure that it stays in position during high tide. The scour apron was then pumped to an inflated height of 0.5m with a width of 3.9m (Figure 10).



**Figure 10. Scour apron pumped to an inflated height of 0.5m.**

## CONSTRUCTION METHODOLOGY – GEOTEXTILE TUBE

The installation of the geotextile tube had to be properly planned and scheduled to the influence of daily tidal fluctuations. The geotextile tube installation was carried out during the low tide and secured to the timber mattress. A portable steel tank was used for mixing the sand and water to form the sand slurry (Figure 11). The pumping of sand slurry into the geotextile tube is carried out during low tide by inserting the discharge pipe into “filling ports” at one end of the tube while the other end “filling ports” is left open for water pressure relief. All other intermediate ports are closed. This filling operation is repeated until the whole tube attained the final filling height of 2m (Figure 12).

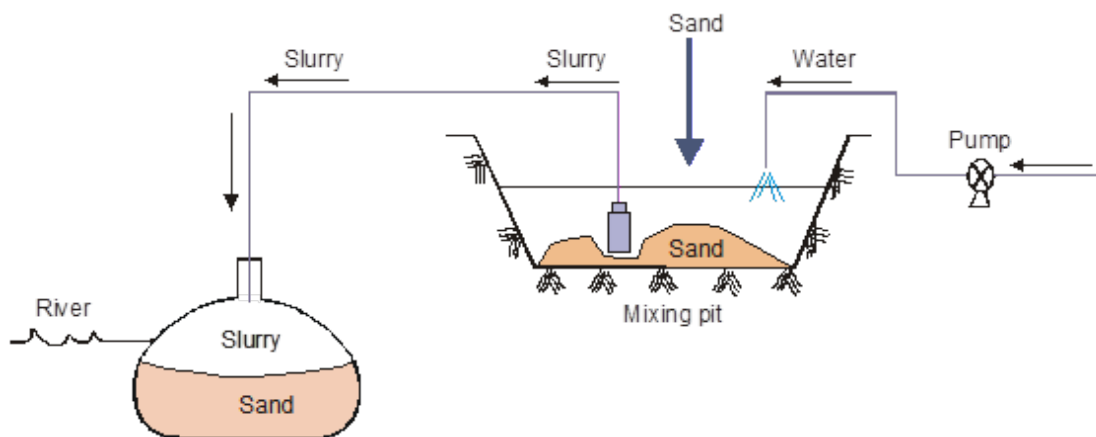


**Figure 11. Schematic of mixing tank and pump set unit.**





**Figure 12. Geotextile tube installation in progress.**

### **CONSTRUCTION METHODOLOGY – HIGH STRENGTH BASAL REINFORCEMENT**

The high strength basal reinforcement was supplied in roll width of 5 m and 100 m length. The roll was then cut to 25m length and stitched to form panels of 16 m x 25 m. The pre-stitched reinforcement fabric was then installed over the scour apron during the low tide and pegged into position using bamboo pegs at one meter spacing to prevent movement during sand backfilling operation (Figure 13).



**Figure 13. High strength basal reinforcement over bamboo mattress.**

### **CONSTRUCTION METHODOLOGY – SAND FILLED MATTRESS**

Special composite sand filled mattresses with coarse fiber surface were installed on the slopping ground above the crest of the geotextile tubes (Figure 14). The coarse fiber surface is designed to trap and hold the topsoil in place and allow the growth of vegetation on top. The sand filled mattresses were anchored into a trench at the crest. The vegetation establishment over the sand filled mattress was very rapid and most of the sand filled mattress are covered with vegetation after 9 months exposure (Figures 15, 16 and 17).



**Figure 14. Newly installed sand filled mattress at tube crest.**



**Figure 15. Sand filled mattress covered with vegetation after 9 months.**



**Figure 16. Vegetation growth over the sand filled mattress and geotextile tube.**





**Figure 17. Close up of sand filled mattress covered with vegetation.**

## **UV RESISTANCE**

The geotextile tubes will be exposed to UV for several years before subsequent reclamation covers the tubes. The UV radiation will cause bond breakage in the polymer leading to the loss of tensile strength over time. As such, the geotextile tubes used in this project have a retained strength of more than 90% after 500 hours of exposure in the Xenon Arc accelerated UV testing chamber, tested according to ASTM D4355.

To further understand the actual degradation of the geotextile tube exposed to the field condition, some geotextile samples are collected from an adjacent project site with the geotextile tubes installed for more than 5 years (Figure 18). The samples collected were then tested in an accredited laboratory to determine the retained tensile strength. Table 1 shows the retained tensile strength of the geotextile tube exposed for more than 5 years.



**Figure 18. Geotextile sample collected at an adjacent project site.**

**Table 1. Retained tensile strength after exposed for 5 years at site.**

Sample	Sample 1	Sample 2	Sample 3
Original tensile strength (MD)	200 kN/m	200 kN/m	200 kN/m
Retained tensile strength (MD)	135.1 kN/m	112.9 kN/m	114.5 kN/m
Percent strength retained (MD)	67.5%	56.5%	57.3%
Original tensile strength (CD)	200 kN/m	200 kN/m	200 kN/m
Retained tensile strength (CD)	163.8 kN/m	130.1 kN/m	147.6 kN/m
Percent strength retained (CD)	81.9%	65.1%	73.8%

Sample 1 is collected from the curve surface of the geotextile tube while samples 2 and 3 are collected from the top surface of the geotextile tube. It is observed that the samples located at the top surface exhibit lower retained strength, this indicates that the UV exposure is more severe at the top surface. Nevertheless, the minimum retained strength across the samples collected is around 56% and there is no loss of serviceability observed after 5 years of exposure.

## CONCLUSION

Geosystem containment dyke using a combination of geotextile tube, PET high strength basal reinforcement and sand filled mattress was successfully used in Parcel 1 and 2 of Deep C II project to replace conventional armor rocks revetment system. Filling of geotextile tubes with fine grain material was successfully done. The laying of high strength reinforcement geotextile and the sand mattresses along the slope were also completed. The system was found to perform satisfactorily, with the minimum retained strength, across the samples collected, of around 56% and there is no loss of serviceability observed after 5 years of exposure. Thus, it can be seen that the geosystem containment dyke is cost effective, environmentally friendly and reduce construction time. In total 19km of geotextile tube, 88,000m<sup>2</sup> of basal reinforcement and 46,000m<sup>2</sup> of sand filled mattress were successfully installed in this portion of the works.

## REFERENCES

- ASTM D4355. Standard Test Method for Deterioration of Geotextiles by Exposure to Light, Moisture, and Heat in a Xenon Arc-Type Apparatus, *ASTM International*, West Conshohocken, Pennsylvania, USA.
- Bezuijen, A. and Vastenburg, E.W. (2013). *Geosystems: Design Rules and Applications*, CRC/Balkema, Leiden, The Netherlands.
- Geo-Slope International Ltd. (2012). *Geostudio 2012*, Geo-Slope International Ltd., Calgary, Ab, Canada.

## **Investigation of Geotextile Integrity Subjected to Vertical Drains Installation**

**Soh Jun Ming,<sup>1</sup> Chew Soon Hoe, Ph.D.,<sup>2</sup> Tan Yeow Chong<sup>3</sup>, Audrey Yim<sup>4</sup>, Abel Quek<sup>5</sup>, Lim Dao Jing<sup>6</sup>, Kee Shanyin<sup>7</sup>**

<sup>1</sup> National University of Singapore, 21 Lower Kent Ridge Road, Singapore 119077; e-mail: ceesjm@nus.edu.sg

<sup>2</sup> National University of Singapore, 21 Lower Kent Ridge Road, Singapore 119077; e-mail: ceecsh@nus.edu.sg

<sup>3</sup> Housing & Development Board, 480 Lor 6 Toa Payoh, Singapore 310480; e-mail: tan\_yeow\_chong@hdb.gov.sg

<sup>4</sup> Housing & Development Board, 480 Lor 6 Toa Payoh, Singapore 310480; e-mail: audrey\_hm\_yim@hdb.gov.sg

<sup>5</sup> Housing & Development Board, 480 Lor 6 Toa Payoh, Singapore 310480; e-mail: quek\_jia\_wei@hdb.gov.sg

<sup>6</sup> Housing & Development Board, 480 Lor 6 Toa Payoh, Singapore 310480; e-mail: lim\_dao\_jing@hdb.gov.sg

<sup>7</sup> Housing & Development Board, 480 Lor 6 Toa Payoh, Singapore 310480; e-mail: kee\_shanyin@hdb.gov.sg

### **ABSTRACT**

Typically, sand dykes are used as coastal protection structures. An alternative to sand dykes is the use of geotextile tube bunds. For most coastal protection bunds, it is likely that there will be a layer of soft clay beneath the bund, and ground improvement of this layer is necessary. This may involve the installation of Prefabricated Vertical Drains (PVD) through the geotextile tube bund. Therefore, the geotextile material that makes up the bund should allow conventional PVD installation to penetrate through and maintain its integrity even after penetration. A laboratory test was developed to investigate the resistance of geotextiles to penetration by simulating action of penetration by PVD anchor plates on the geotextile. Two anchor plate designs were tested, a conventional design and a modified design. The applied load to penetrate the geotextile, and the types of tearing behavior were studied. The disturbance to the geotextile material around the penetrated area was also evaluated. Test results show that the anchor plate design is critical in ensuring effective penetration of the geotextile material, and at the same time minimize disturbance to the geotextile adjacent to the penetrated hole, preventing unintentional propagation of damage.

### **INTRODUCTION**

The use of geotextile tubes as an alternative to sand dykes in coastal protection applications has increasingly been explored. This is especially critical in areas that lack access to sand resources, or due to environmental considerations that sand mining should be avoided. Geotextile tubes have also been found to offer advantages, such as the method of installation being less damaging to environments, and the cheaper construction costs with the use of natural sand or clay infill materials as compared to many conventional structures that requires significant use of cement (e.g., concrete seawalls and breakwaters) (Heerten et al., 2000).



For most coastal protection structures, it is likely that there will be a layer of soft clay beneath the geotextile tube bund. As a result, ground improvement of the soft clay below is necessary. Ground improvement may involve the installation of Prefabricated Vertical Drains (PVD) through the geotextile tube bund, resulting in penetration through the geotextile material at localized spots. An illustration of a conventional PVD anchor plate design is shown in Figure 1. The anchor plate and mandrel forms two key components of PVD installation operations. However, this conventional anchor plate design, typically used for ground improvement process in soft clay, may not be suitable to penetrate the high strength geotextiles that are increasingly being used.

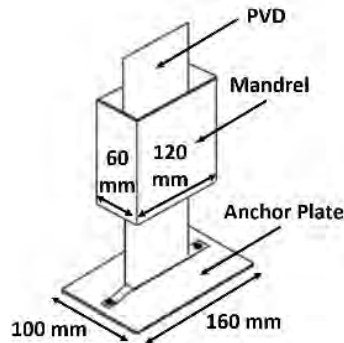


**Figure 1. Mandrel and Steel Anchor Plate for PVD installation (Trong et al., 2020)**

In addition, the geotextile must maintain its integrity after it has been penetrated. The penetration process should not result in enlarging or worsening of damage to geotextile material adjacent to the area of penetration.

A laboratory study was developed to investigate the force needed to penetrate the geotextile, simulating the penetrating action of PVD anchor plates on a geotextile body. Two different anchor plate designs were tested. The first is a conventional design typically used in soil improvement applications, the second is a modified design.

## METHODOLOGY

### Material Properties

A high strength polypropylene woven geotextile commonly used in the construction of geotextile tubes was tested. Its properties, expressed in Machine Direction (MD) and Cross Machine Direction (CD), are listed in Table 1.

**Table 1. Geotextile Properties**

Property	Standard	Unit	Value
Wide Width Tensile Strength (MD/CD)	ISO 10319	kN/m	130/130
Strain at Tensile Strength (MD/CD)	ISO 10319	%	10/10

## Testing Setup

A customized geotextile testing apparatus was designed and constructed at the National University of Singapore (NUS) geotechnical laboratory. The geotextile sample is fixed to a loading frame using a clamping ring that is kept in place with nut and bolts. The effective geotextile sample tested was a circular area measuring 1 m in diameter as illustrated in Figure 2. A hydraulic actuator was used to push the anchor plate setup downwards onto the geotextile sample until failure. The 3D design of the anchor plate used in this setup is shown in Figure 3.

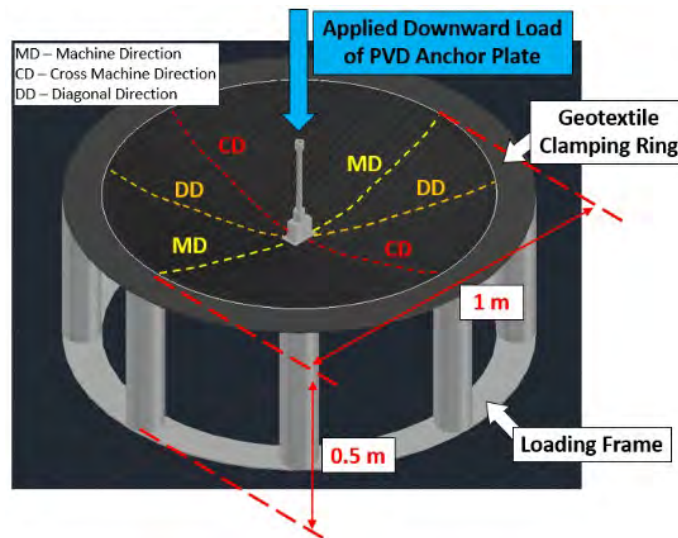


Figure 2. Illustration of Geotextile Testing Apparatus

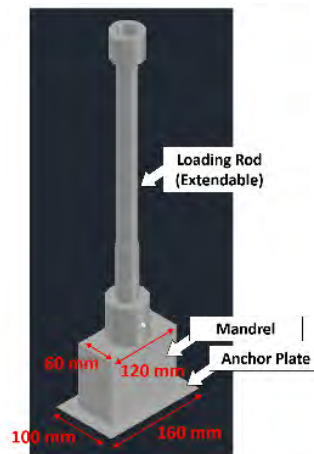
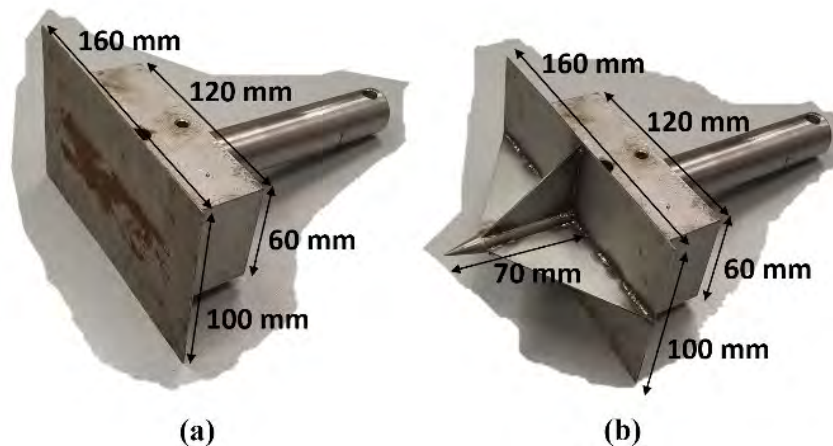


Figure 3. Illustration of anchor plate setup used in this study

Two PVD anchor plate designs were used. The first design tested was similar to conventional PVD anchor plate designs, measuring 160x100 mm and 1 mm thickness. A mandrel with base dimensions of 120x60 mm was attached to this anchor plate. The second design tested was a modified anchor plate with a sharpened pin measuring 10 mm in diameter and 70mm long protruding out from the bottom of the conventional anchor plate. Four additional stiffening plates were installed around the protruding pin at 90 degrees interval. The PVD anchor plate designs are shown in Figure 4.



**Figure 4. Design of (a) Conventional Anchor Plate; (b) Modified Anchor Plate**

### Instrumentation

The geotextile samples were extensively instrumented in the Machine Direction (MD), Cross Machine Direction (CD) and Diagonal Direction (DD). A total of 9 strain gauges were installed, 3 in each direction. Figure 5 illustrates the strain gauge positions and Figure 6 shows the completed setup. A load cell was also used to monitor the load acting on the geotextile sample during the penetration test. During the test, the length of the anchor plate was positioned along the Machine Direction of the geotextile.

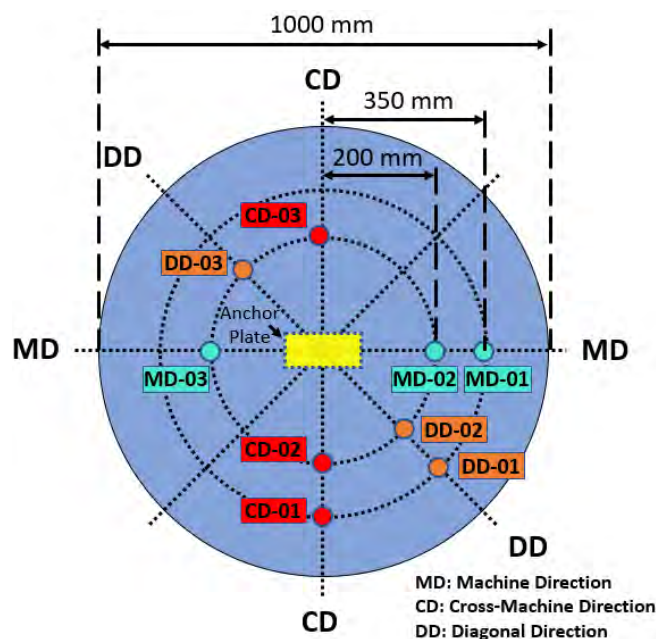


**Figure 5. Strain gauge arranged on geotextile sample**

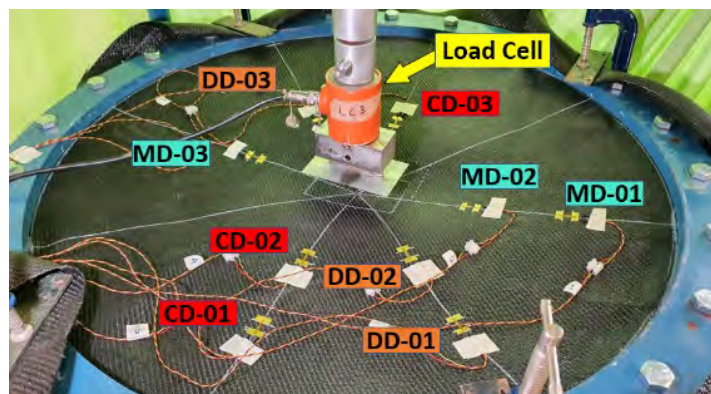


Figure 6. Completed test setup with strain gauges installed

## RESULTS & ANALYSIS

### Conventional PVD Anchor Plate

Figure 7 shows the anchor plate load cell and geotextile strain gauge readings from the penetration test with conventional anchor plate. The readings from the strain gauges were converted to load using the load-strain relationship of the geotextile. As the hydraulic actuator had an extension limit of 300 mm, the actuator had to be retracted when the limit was reached. The loading rod was then extended, and a second push was then conducted until the geotextile sample was fully penetrated.

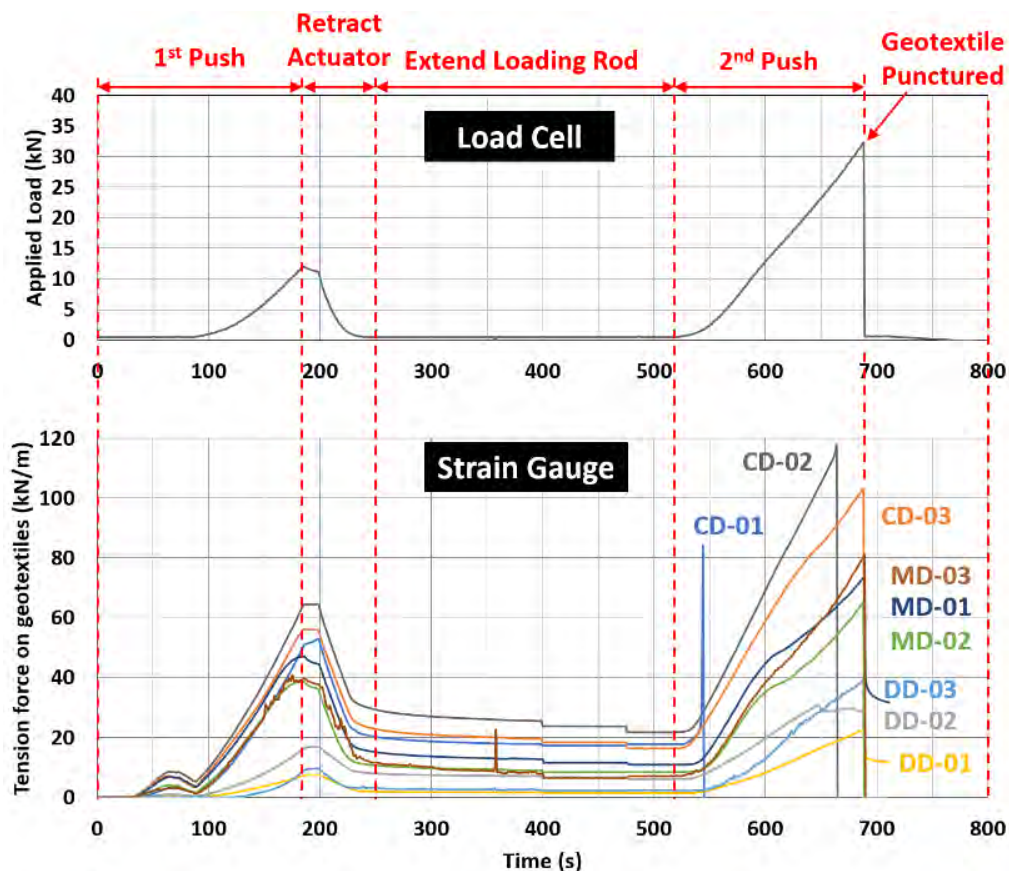


Figure 7. Results of Penetration Test using Conventional Anchor Plate



The results showed that there was good agreement between the readings from the load cell and strain gauges. When load was applied to the geotextile, there was a corresponding increase in the strain readings, suggesting that the vertical loading from the anchor plate was causing deformation of geotextile, resulting in tension force within the geotextile in all directions. The anchor plate penetrated through the geotextile at a maximum vertical load of 32 kN. The largest tension on the geotextile was developed in the Cross-Machine direction, at approximately 118 kN/m. It should be noted that this was quite close to the ultimate tensile strength of the geotextile, at 130 kN/m. This may be due to the flat design of the anchor plate, making it necessary to overcome the tension force in a large number of geotextile yarns, thus resulting in significant tension activated across the geotextile sample, similar to a wide width tensile condition.

Figure 7 also clearly shows that the geotextile direction yarns along CD direction experienced the largest tension (80-118 kN/m), and the yarns along MD experienced tensile force of around 60-80 kN/m, whereas the yarns along DD direction were about 20-40 kN/m. Hence, the yarns along CD direction would break first upon reaching its ultimate capacity of 130 kN/m. This was observed in the photo showing the failed yarns in Figure 9.

During the test, it was also observed that there was a significant “bounce back” effect immediately after the anchor plate had penetrated through the geotextile. This was due to the sudden drop from maximum to zero tension after the anchor plate had penetrated through the geotextile, creating a significant “bounce back” effect as the geotextile returned to its un-tensioned state. This effect also resulted in an immediate failure of all installed strain gauges.

Figure 8 shows the deformation of the geotextile sample (from below the sample) prior to the penetration of the flat anchor plate. The geotextile sample was largely intact, with minimal to no individual yarn failures observed. The post-penetration opening is shown in Figure 9. It can be seen that the area of tearing is largely confined to the area around the anchor plate, with a significant number of yarns torn along the Cross-Machine Direction (CD). These observations further support the finding that the flat design of the anchor plate has to overcome the tensile strength of a large number of yarns at the same time, and resulting in the geotextile sample experiencing large amounts of tension.

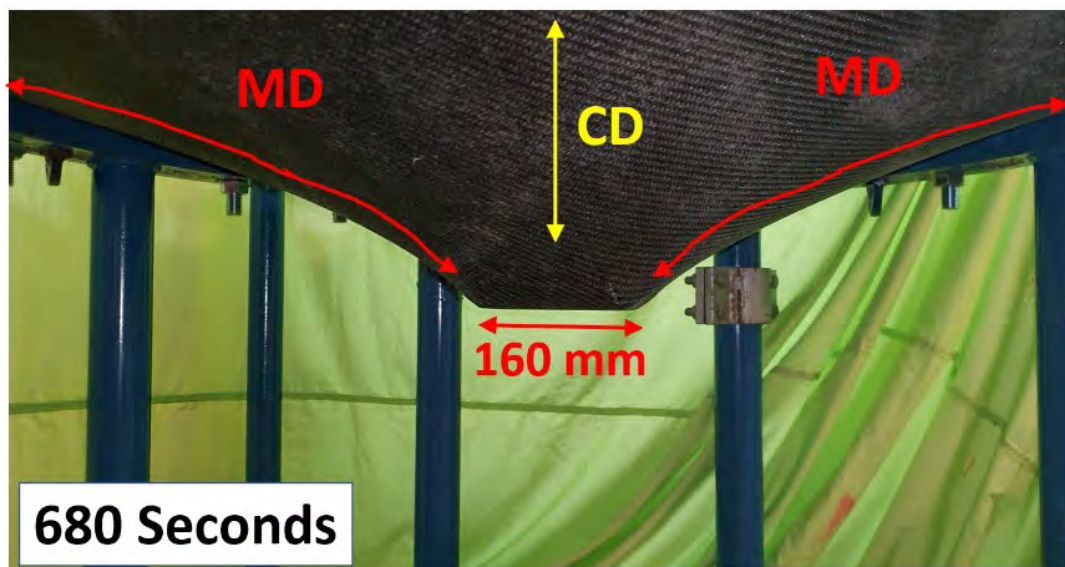


**Figure 8. Deformation of Geotextile Sample at 680 seconds**



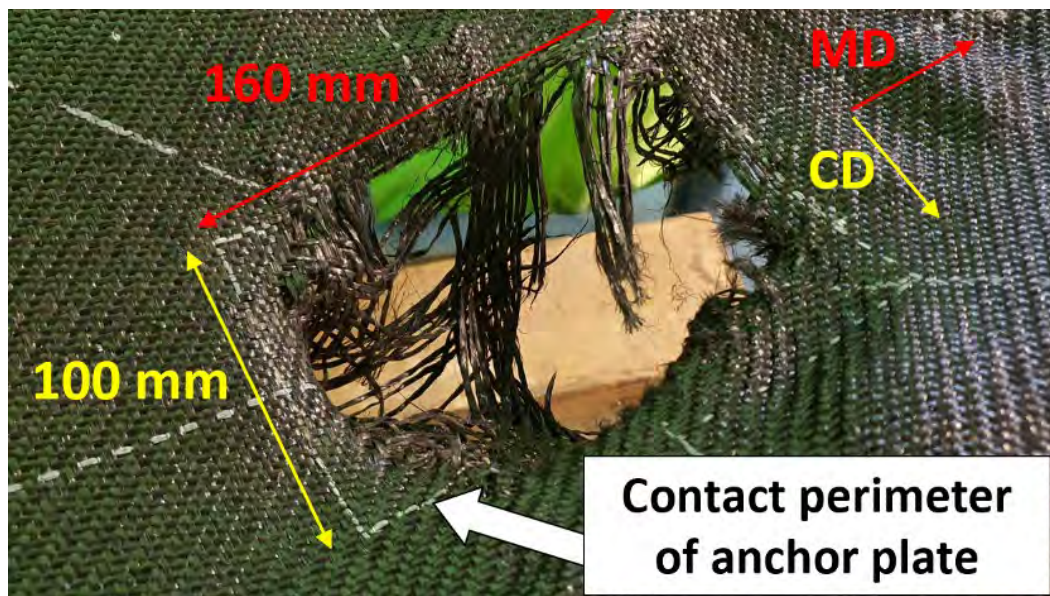


Figure 9. Post-Penetration Opening

### Modified PVD Anchor Plate

The second anchor plate design featured an additional sharpened shaft supported by 4 stiffening plates (see Figure 4). The results of the test are shown in Figure 10. Similar to the previous test with the conventional anchor plate design, the strain gauge readings showed good agreement with load cell readings. As the vertical load from the anchor plate increased, there was a corresponding increase in the strain gauge readings.

Due to the steeper angle of the reinforcement plates perpendicular to the direction of the yarns in MD direction, the tearing of the yarns in the MD direction occurred first between 0-60 seconds. This was shown by the erratic increase in MD load (which was likely due to the gradual tearing of individual yarns one after another) and the significantly higher tension force activated compared to readings in CD and DD directions strain gauges. Between 60-140 seconds (until failure), the strain gauges in CD directions registered higher tension load than the other directions, which means that the yarns in the CD direction were subjected to greater tension, while the yarns in the MD direction experienced some reduction in tensile force. The geotextile was successfully penetrated at 140 seconds, with a peak applied load of around 7.5 kN. This was significantly smaller than the peak vertical load of 32 kN observed with the test using conventional anchor plate.

It was also observed that all of the strain gauges were still functional after successful penetration was achieved. This suggests that there was much smaller disturbance to the geotextile around the area of penetration. The sample with modified anchor plate also failed in a shorter duration compared to the setup using the conventional anchor plate. Therefore, it was easier and faster to punch through the geotextile using modified anchor plate than the conventional one.

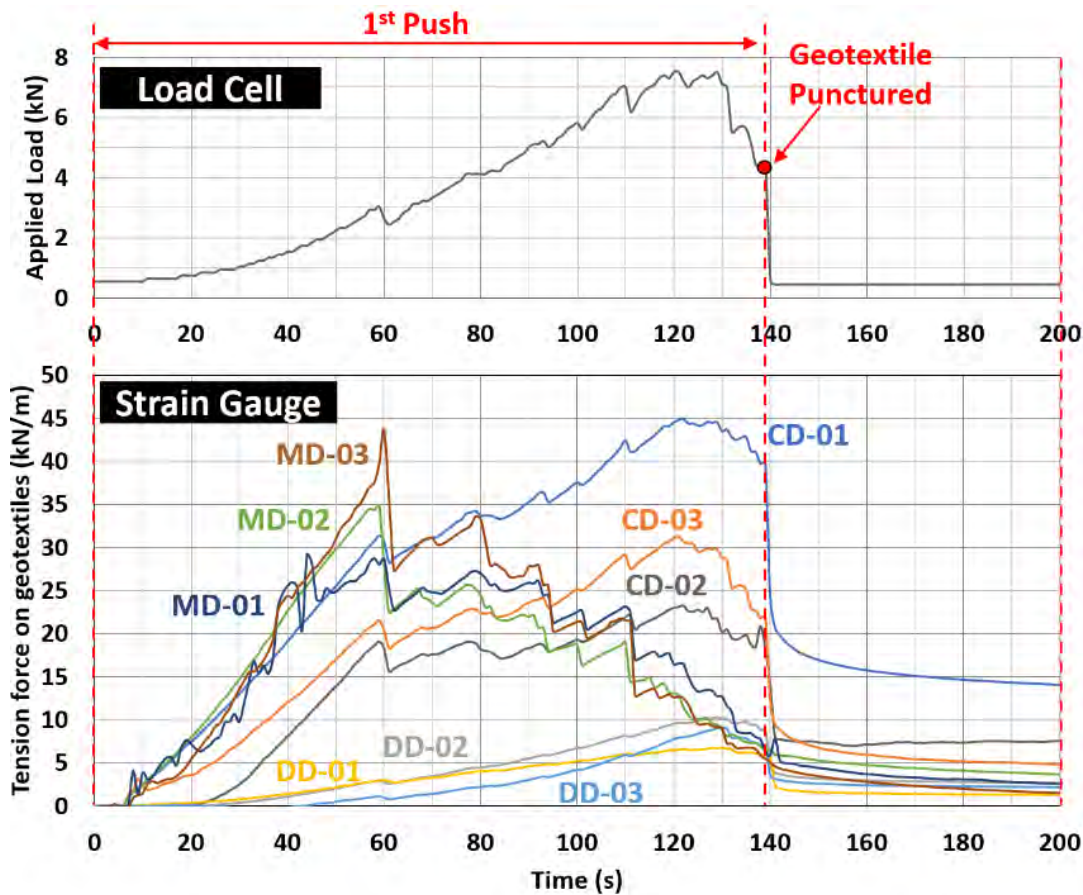


**Figure 10. Results of Penetration Test using Modified Anchor Plate**

Figure 11 shows the state of the geotextile sample at 60 seconds and at 135 seconds. The modified anchor plate successfully penetrated through the geotextile shortly after 135 seconds. In the early stage (60 seconds), the sharpened protrusion caused initial separation of yarns. Just prior to penetration (i.e., 60 seconds), it could be observed that the yarns in MD had mostly failed, but there were still yarns in CD that were still intact.

In addition, it could be observed from the post-penetration opening in Figure 12 that the tear area was much smaller than the area of the anchor plate. This was likely due to the tearing effect of the sharpened protrusion and stiffening plates, allowing the yarns to be gradually torn one by one. As a result, less tension was activated in the overall geotextile sample as compared to the penetration test by the conventional anchor plate.

Thus, these observations support the findings from the load cell and strain gauge results that with modified anchor plate, the yarns in MD direction were likely torn first before the yarns in CD direction.



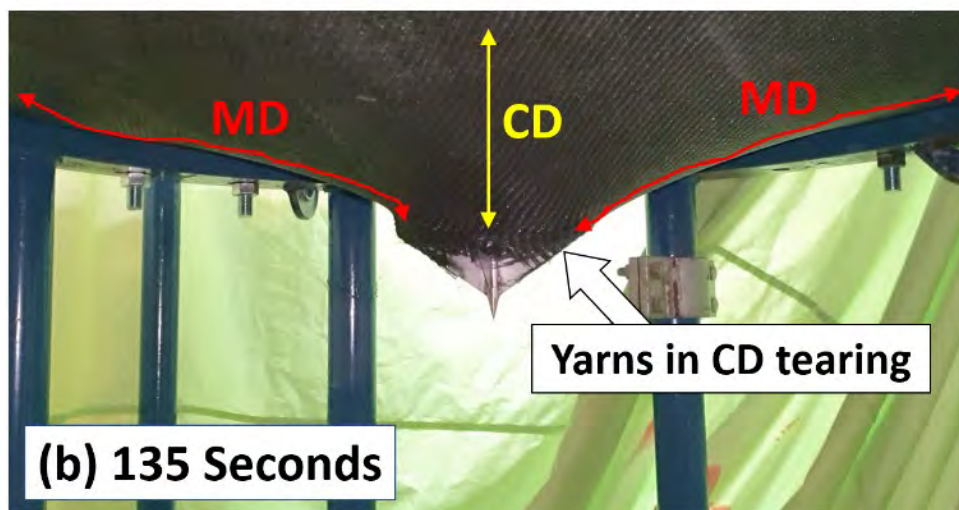
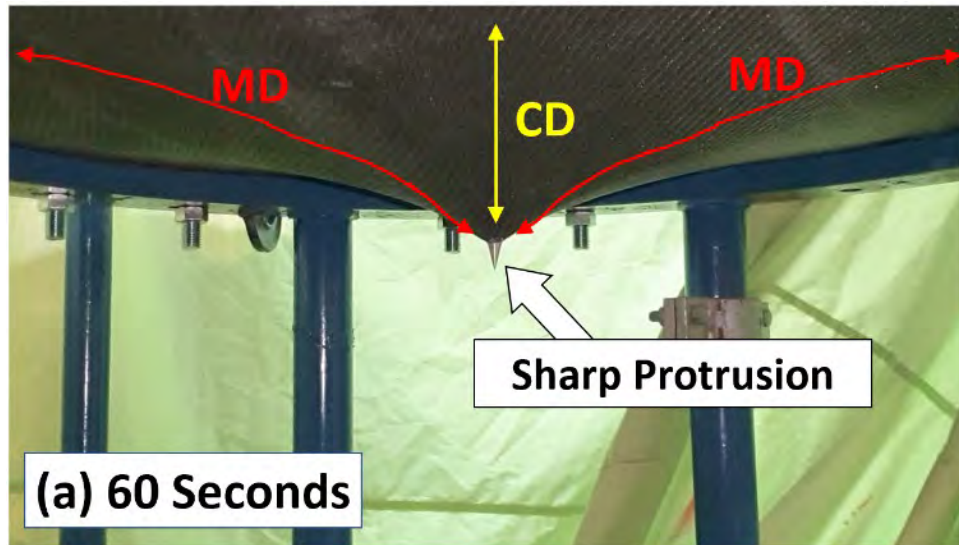


Figure 11. (a) Deformation at 60 seconds; (b) Deformation at 135 seconds

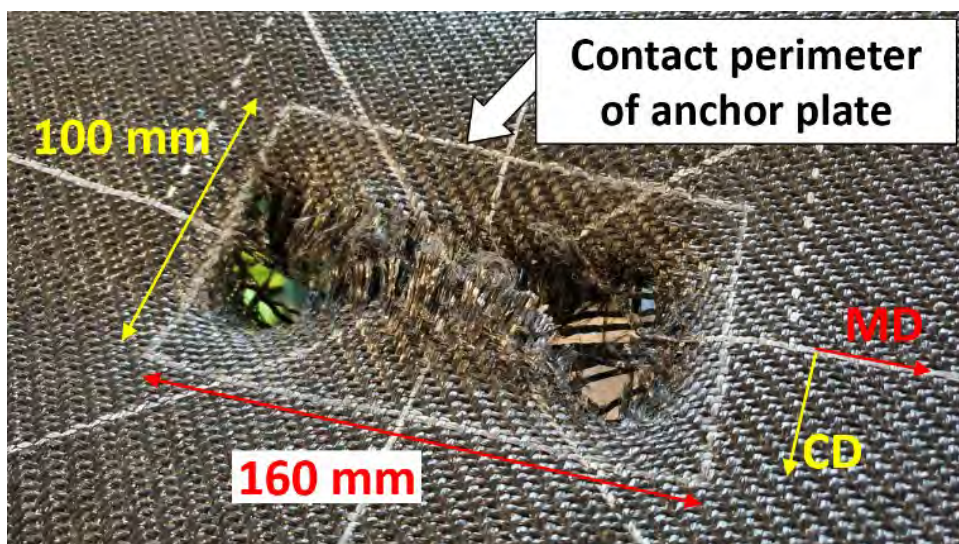


Figure 12. Post-Penetration Opening

## CONCLUSION

Based on the results from the penetration tests, there were several conclusions that could be made:

1. The modified anchor plate could penetrate the geotextile material with a smaller vertical load and in a shorter duration than the conventional anchor plate.
2. The modified anchor plate penetrated the geotextile material through gradual tearing of individual yarns, whereas the conventional plate design tore a large number of yarns at the same time. As a result, significantly larger amount of tension was experienced in the geotextile sample when conventional anchor plate was used.
3. As a result of larger tension activated, a significant “bounce back” effect was observed in the geotextile sample tested with the conventional anchor plate, resulting in significant disturbance to the geotextile around the area of penetration. This was not as significant when the modified anchor plate was used.

Therefore, for PVD to be able to penetrate through geotextile material effectively, it is recommended that a modified anchor plate design similar to what was used in this research be utilized.

## ACKNOWLEDGEMENTS

This research is supported by the National Research Foundation, Singapore, and Ministry of National Development, Singapore, under its Cities of Tomorrow R&D Programme (CoT Award No. CoT-V4-2019-4). Any opinions, findings, conclusions, or recommendations expressed in this material are those of the author(s) and do not reflect the views of National Research Foundation, Singapore, and Ministry of National Development, Singapore.

## REFERENCES

- Heerten, G., Jackson, A., Restall, S., Stelljes, K. (2000). Environmental Benefits of Sand Filled Geotextile Structures for Coastal Applications. *ISRM International Symposium*. Melbourne, Australia.
- Trong, N., Cuong, L.T., Lam, L.G., Phuoc, H.D., Nguyen, P. (2020). Solution for Partially Penetrated Vertical Drains with Anchor Plate. *Geotechnical Engineering Journal of the SEAGS & AGSSEA*. Vol 51(4).



## Use of Treated Soft Soil as Infill Material in Geotextile Tubes

**Chew Soon Hoe, Ph.D.,<sup>1</sup> Soh Jun Ming<sup>2</sup>, Tan Yeow Chong<sup>3</sup>, Audrey Yim<sup>4</sup>, Abel Quek<sup>5</sup>, Lim Dao Jing<sup>6</sup>, Kee Shanyin<sup>7</sup>**

<sup>1</sup> National University of Singapore, 21 Lower Kent Ridge Road, Singapore 119077; e-mail: ceecsh@nus.edu.sg

<sup>2</sup> National University of Singapore, 21 Lower Kent Ridge Road, Singapore 119077; e-mail: ceesjm@nus.edu.sg

<sup>3</sup> Housing & Development Board, 480 Lor 6 Toa Payoh, Singapore 310480; e-mail: tan\_yeow\_chong@hdb.gov.sg

<sup>4</sup> Housing & Development Board, 480 Lor 6 Toa Payoh, Singapore 310480; e-mail: audrey\_hm\_yim@hdb.gov.sg

<sup>5</sup> Housing & Development Board, 480 Lor 6 Toa Payoh, Singapore 310480; e-mail: quek\_jia\_wei@hdb.gov.sg

<sup>6</sup> Housing & Development Board, 480 Lor 6 Toa Payoh, Singapore 310480; e-mail: lim\_dao\_jing@hdb.gov.sg

<sup>7</sup> Housing & Development Board, 480 Lor 6 Toa Payoh, Singapore 310480; e-mail: kee\_shanyin@hdb.gov.sg

### ABSTRACT

Geotextile tubes, increasingly used in coastal protection structures, are typically infilled with sand to give the bund shape and stability. An alternative infill material are soft soils. During infilling of this soft soil, piping of fine-grained soil particles through the geotextile occurs, leading to wastage of material. The low strength of soft soil also affects the stability of the bund. This paper investigates the feasibility of using Cement Mixed Soils (CMS) as infill material in geotextile tubes, addressing the challenges of untreated soft soils. This is done through a series of laboratory tests to determine an optimal CMS mix, followed by a full-scale site trial using this mix. During the tube infilling process, the transition of “initial piping” to “no piping” was observed. Results from Unconfined Compressive Strength on cured CMS samples and post installation tests showed an increase in strength of infilled CMS over time. Strain gauges installed on the geotextile tubes, and readings from Shape Array Accelerometers showed only minor settlement of geotextile tube during the infilling process and when tubes were stacked on one another. Results show that CMS is a feasible alternative to sand as an infill material in geotextile tubes for coastal protection applications.

### INTRODUCTION

Lawson (2008) defines geotextile tubes as tubular containers that are formed in situ on land or in water. Geotextile tubes are used in a wide variety of applications. Utilizing its filtration characteristics, geotextile tubes can be used in sludge dewatering to encapsulate contaminated sediments or sludge (Lawson, 2008). Another increasingly common application of geotextile tubes today is in coastal protection, as an alternative to conventional structures (Siew et al., 2014) such as dykes, revetments, and breakwaters. Sand slurry is the preferred infill material for geotextile

tubes due to its ease of availability and fast consolidation characteristics. However, in regions where sand resources are limited, alternative materials such as soft soil can be explored.

The use of soft soil, however, comes with its own technical challenges. Due to the small particle size of soft soil, there will be excessive piping of the fine-grained material through the geotextile material during infilling. As a result, multiple infilling cycles are required before the target filled height can be reached (Chew et al., 2018). This is illustrated by Eng (2016), shown in Figure 1.

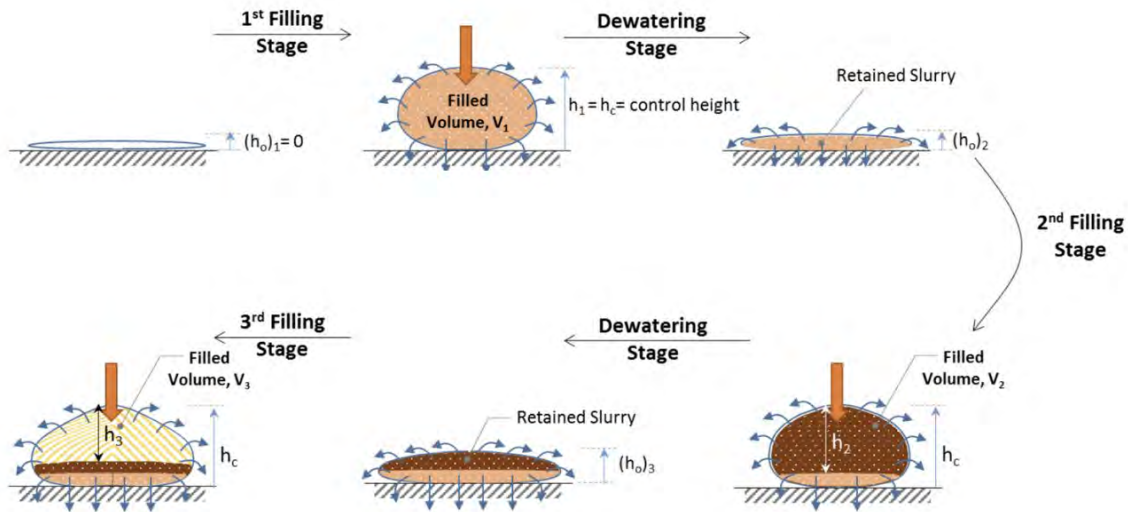


**Figure 1. Illustration of multiple filling cycles of geotextile bag with soft soil (Eng, 2016)**

In addition, the continued settlement of the infill soft soil over a long period will affect the stability of the geotextile tube structure (Shin and Oh, 2007). To tackle these issues, cement is added to soft soil to reduce piping and strengthen the soft soil. However, there has been limited studies done on the effectiveness of using Cement Mixed Soils (CMS) as an infill material for geotextile tubes, and if it could overcome the challenges associated with untreated soft soil.

To validate the effectiveness of using CMS in geotextile tubes, a field trial was conducted in Singapore, where six geotextile tubes were filled with CMS and lowered onto the seabed to form a bund shown in Figure 2. Extensive instrumentations were installed to monitor the behavior of CMS within geotextile tubes throughout the construction process.

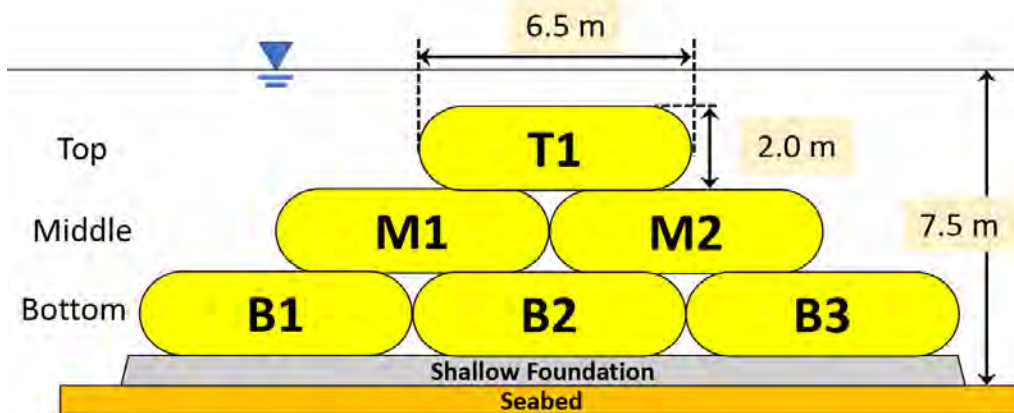


**Figure 2. Cross Section of Geotextile Tube Bund**

## MATERIALS AND EQUIPMENT

**Material and Construction Design.** In the site trial, the body of the geotextile tubes were made from high strength polypropylene geotextile. The properties are provided in Table 1, with the tensile strength presented in terms of Machine Direction (MD) and Cross Machine Direction (CD).

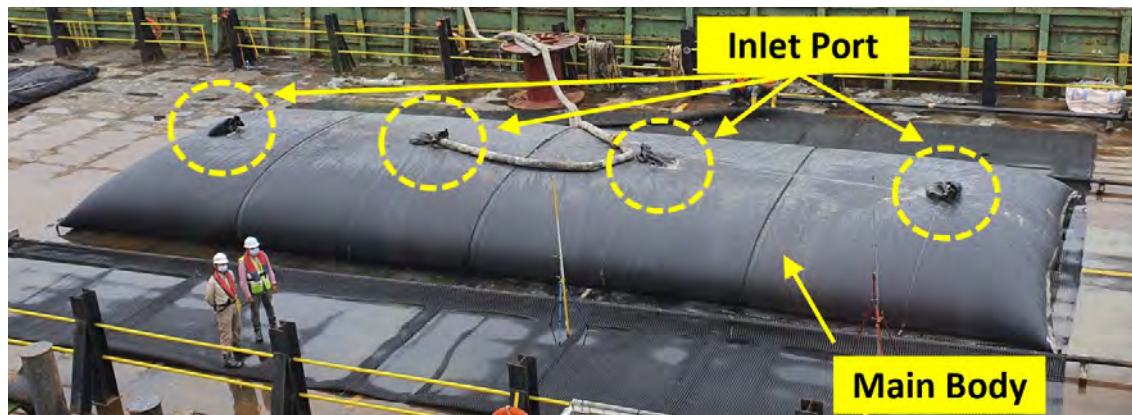
**Table 1. Properties of geotextile material used in trial**

Property	Standard	Unit	Value
Wide Width Tensile Strength (MD/CD)	ISO 10319	kN/m	200/200
Strain at Tensile Strength (MD/CD)	ISO 10319	%	12/10
Apparent Opening Size ( $O_{90}$ )	ISO 12956	mm	0.35





The geotextile tubes had lengths ranging between 20-22 m, and cross-sectional circumferences of 12.6m. The tubes were filled in a single pumping session until it was 2.0-2.2 m in height, and had a filled width of approximately 6.5m.

A picture of a geotextile tube undergoing infilling at site is shown in Figure 3. Once infilling was completed, the filled material was allowed to cure for 12 hours. The geotextile tube was then lowered onto the seabed using a high-capacity crane. The preparation process of the geotextile tubes prior to putting it onto the seabed is shown in Figure 4. The sequence of construction for the 6 geotextile tubes to form a bund is illustrated in Figure 5.

Three of the geotextile tubes were heavily instrumented with strain gauges, Total Pressure Cell (TPC) and Pore Pressure Transducers (PPT). The positions of the instrumentations are illustrated in Figure 6. Shape Accelerometer Array (SAA) were also installed at various locations to monitor the settlement of the geotextile tubes during the bund construction process as shown in Figure 7.



**Figure 3. Geotextile tube during infilling on a barge**

<p>1. Adding and mixing of Cement to soft soil</p>  <p>Duration: 1 hour</p>	<p>2. Infilling CMS material into tube</p>  <p>Duration: 2-3 hours</p>
<p>3. Self-weight consolidation and cementation</p>  <p>Duration: 12 hours</p>	<p>4. Lifting and lowering onto seabed</p>  <p>Duration: 2 hours</p>

**Figure 4. Preparation process of geotextile tube prior to sitting on the seabed**



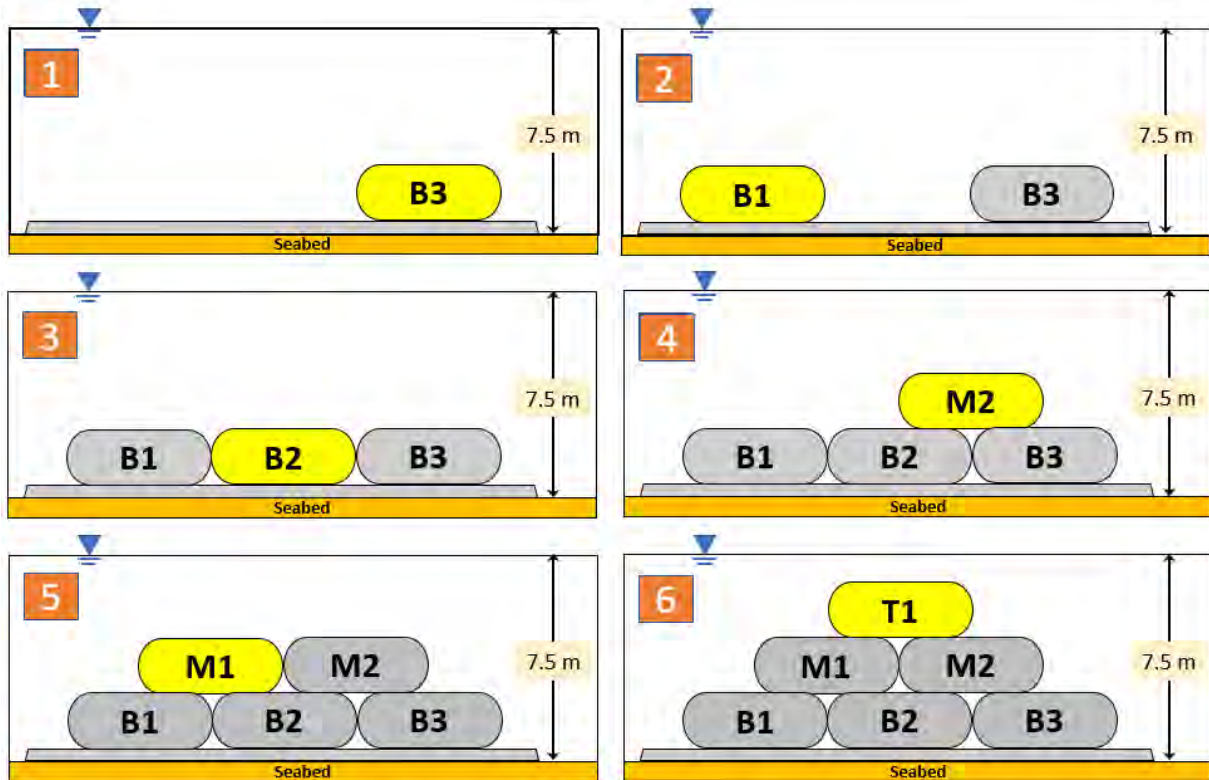


Figure 5. Construction sequence of geotextile tubes forming into a bund (Front View)

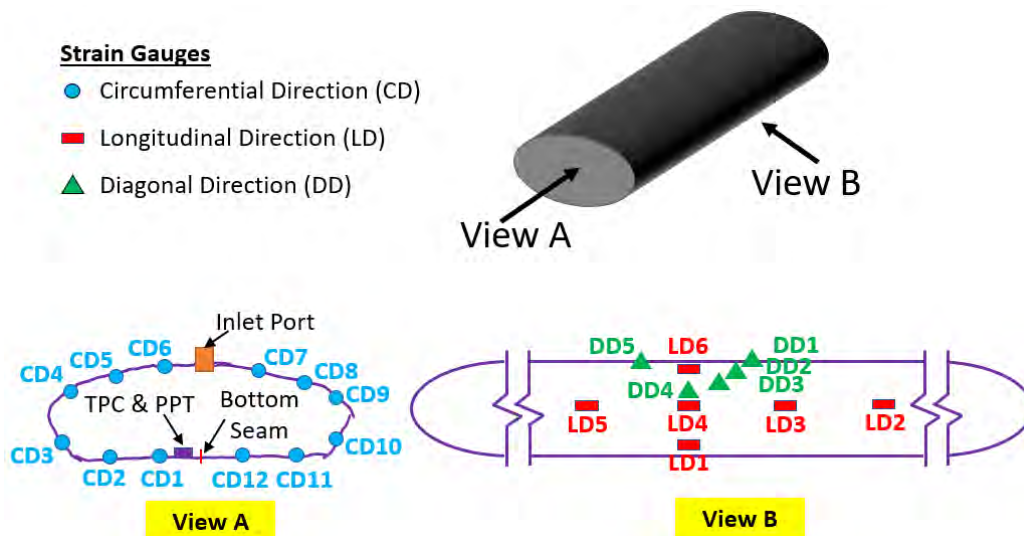
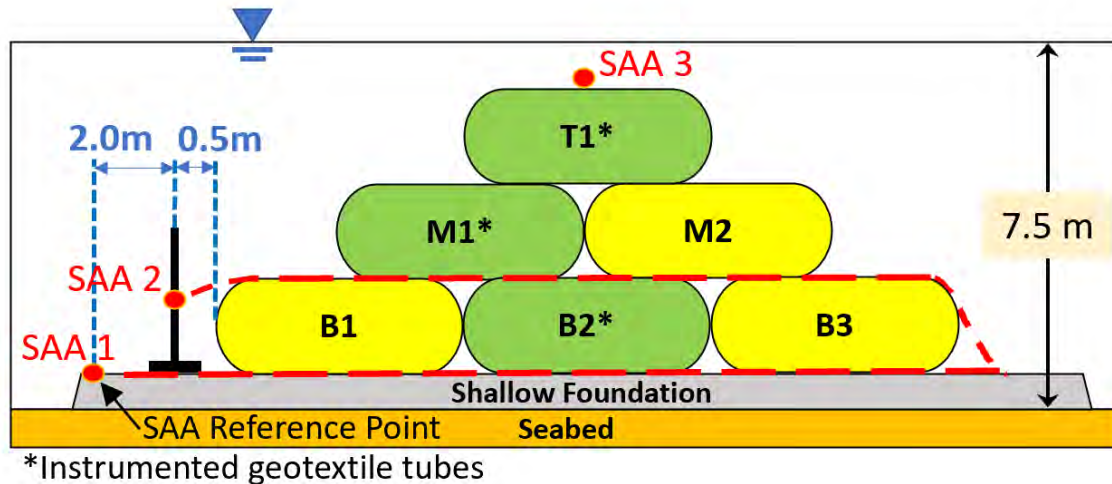


Figure 6. Geotextile tube instrumentation



**Figure 7. Positions of SAA for settlement measurement**

**Infill Material.** The soft soil used in the CMS was dredged on site, and comprised of previously dumped soil that originated from excavation activities from various land-based construction projects. The particle size distribution of the soil is shown in Figure 8. The soil consisted largely of silt, with small amounts of sand and clay present.

A target 28-day unconfined compressive strength design value of 60-100 kPa was determined for the geotextile tubes to ensure stability of the bund. Other factors such as a sufficiently high “flow” value (i.e., low viscosity value) for pumping, and a reduction factor between laboratory results and in-situ strength results were also considered. A cement content of 8% (by bulk unit weight of untreated soil) is used for the first two tubes B1 and B3, and 6% for the subsequent geotextile tubes.

The soil had an initial moisture content between 175-190%, and a bulk density of 1.30 g/cm<sup>3</sup> before mixing with cement. After addition of Ordinary Portland Cement (OPC), the bulk density of CMS was observed to be 1.34 - 1.36 g/cm<sup>3</sup>. For each geotextile tube, during infilling, samples from the CMS mix were collected and cured in seawater for 7 and 28-days in laboratory before its unconfined compressive strength (UCS) was tested.

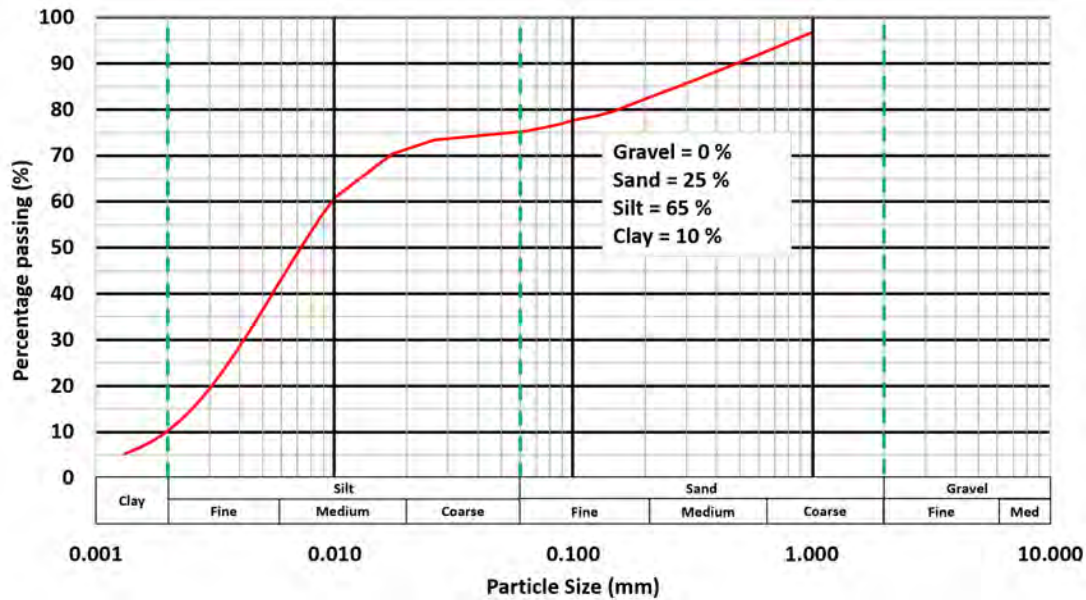


Figure 8. Particle size distribution of soft soil

## FIELD TRIAL RESULTS AND ANALYSIS

**Strength of CMS Material.** Figure 9 shows the UCS test results from samples taken during infilling, and then cured in seawater in laboratory. The 28-day UCS strength of samples from tubes B1 and B3 was found to be between 130-190 kPa. The subsequent tubes registered a 28-day UCS of 55-60 kPa.

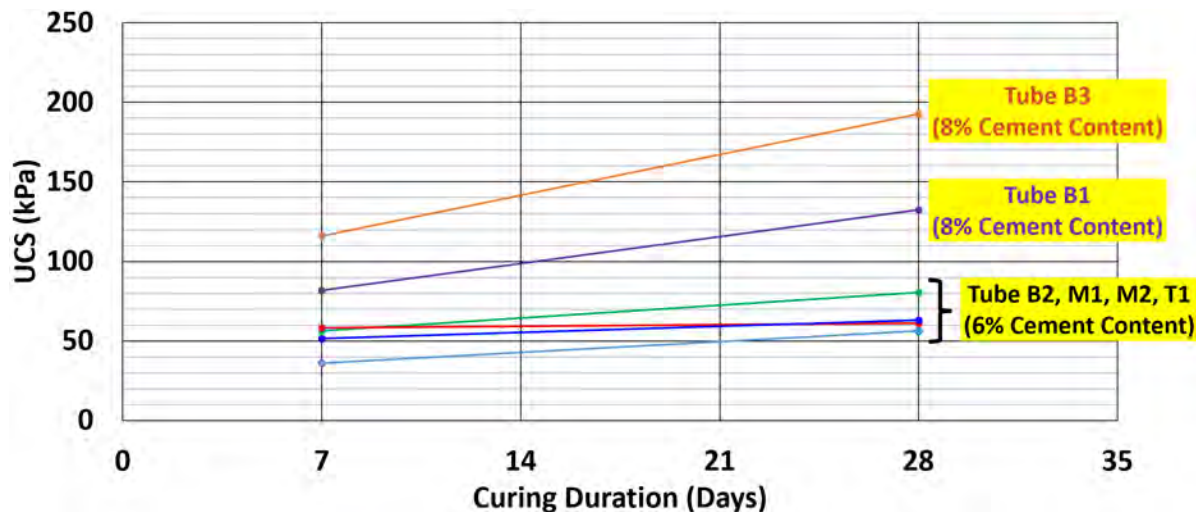
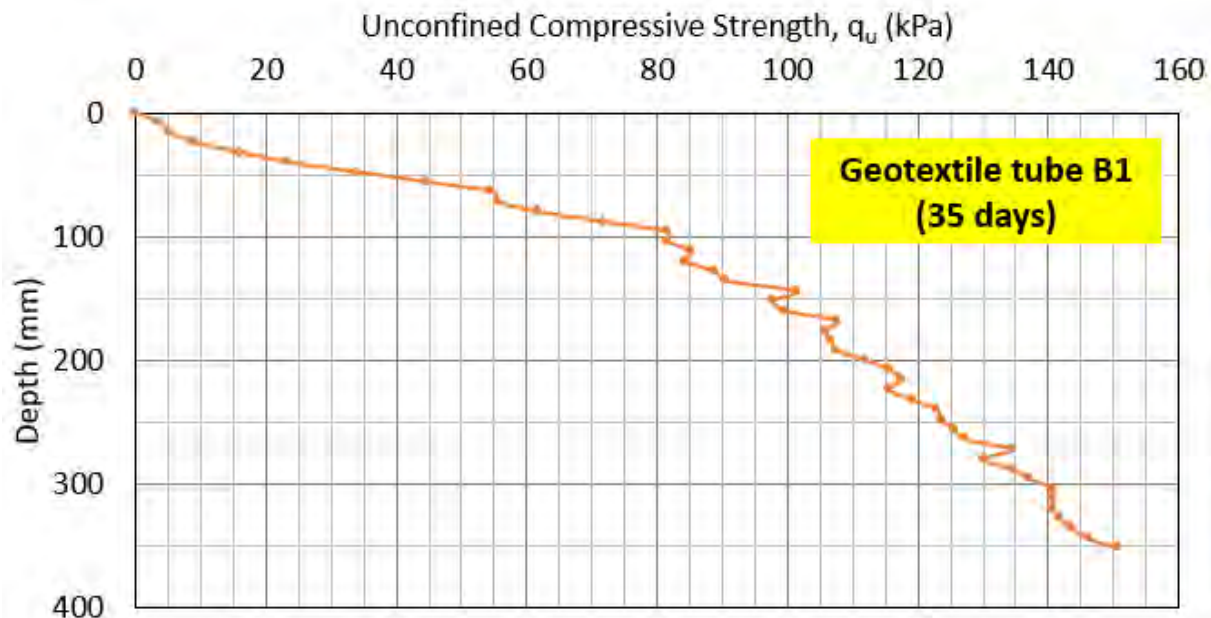


Figure 9. Infilling samples UCS results

A CPT test, using a custom-built Marine CPT, was also conducted on the bottom layer tube B1 35 days after it had been lowered onto the seabed. The CPT cone penetrated approximately 350 mm into the geotextile tube at a speed of 8 mm/s until it encountered some pieces of stone, which was likely from the soft soil material used. Correlation test was conducted to establish the conversion

from tip resistance  $q_c$  to UCS  $q_u$ . A  $q_c$ - $q_u$  correlation factor was applied to the CPT cone tip resistance to obtain the UCS value. Figure 10 shows the variation of UCS with depth in tube B1.

It was observed that the 35-day UCS strength of the in-situ CMS in tube B1 was slightly higher than the 28-day UCS strength of samples taken during infilling of tube B1. This may be due to the slightly longer curing duration (28 for lab value vs 35 days for in-situ value). Curing under confinement pressure with 7m water depth may have also contributed to the higher in-situ  $q_u$  strength of the infilled CMS in tube B1 (Bushra et al., 2013).



**Figure 10. Marine CPT readings (Tube B1)**

**Infilling Behavior of Geotextile Tube B2.** In analyzing the settlement behavior of CMS filled geotextile tubes, focus will be placed on tube B2 as it experienced the largest amount of loading due to its position within the bund. Figure 11 represents the strain gauge readings from geotextile tube B2 during the infilling period and the subsequent 12-hour monitoring period prior to lowering of the tube into water.

It was observed that the strain gauge readings increased gradually during infilling as the geotextile tube gradually took shape and the geotextile material experienced tension. Strain readings were at its highest once infilling ended and the tube reached the target filled height of 2.0-2.2 m. During the 12-hour monitoring period, a minor decrease in strain was registered (~0.2%) and the shape of the geotextile tube on-site was observed to remain relatively uniform and unchanged. A similar strain gauge behavior was observed for all 3 instrumented geotextile tubes (i.e., B2, M1 and T1).

Figure 12 shows the TPC readings for 3 instrumented tubes. There was an approximately 5 kPa drop in pressure reading over the 12-hour monitoring period for all three instrumented geotextile tubes, likely due to the dewatering of the infill material. This represents an 8-12% drop in the maximum TPC reading. In addition, minor piping of CMS slurry was observed only at the start of infilling period, and quickly stopped around 15-20 minutes. At the end of the project, the geotextile tube height was observed to reduce by about ~0.10m (5% of initial height) for all tubes



after the 12-hour monitoring period.

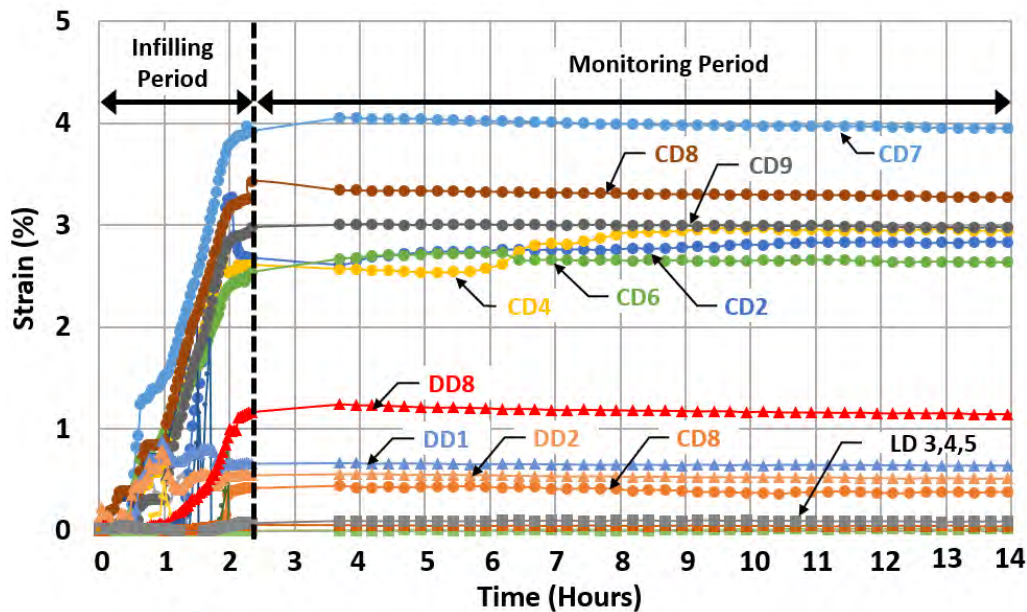


Figure 11. Strain gauge readings for tube B2 during 12-hour monitoring period

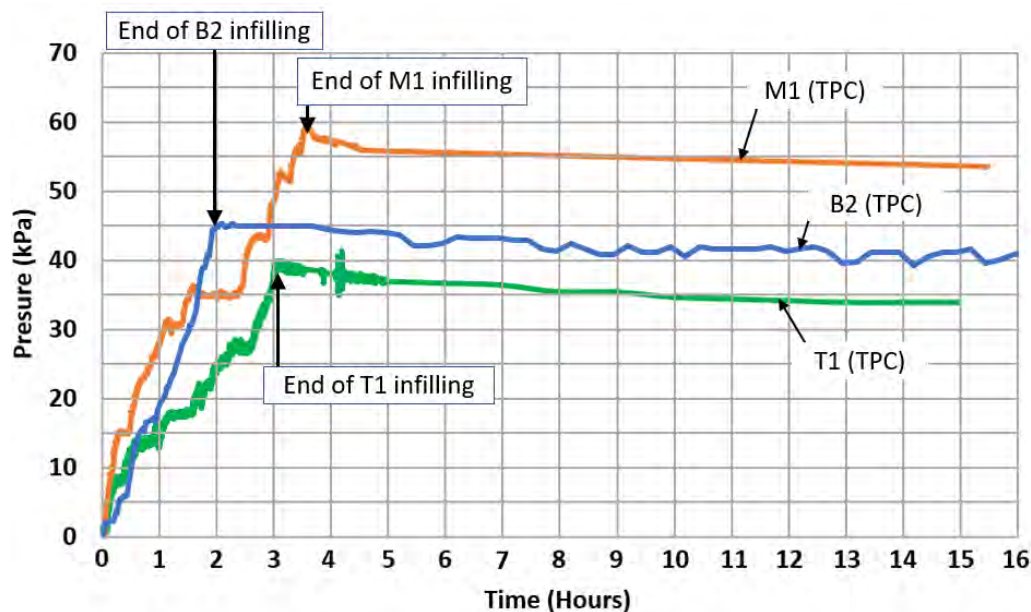
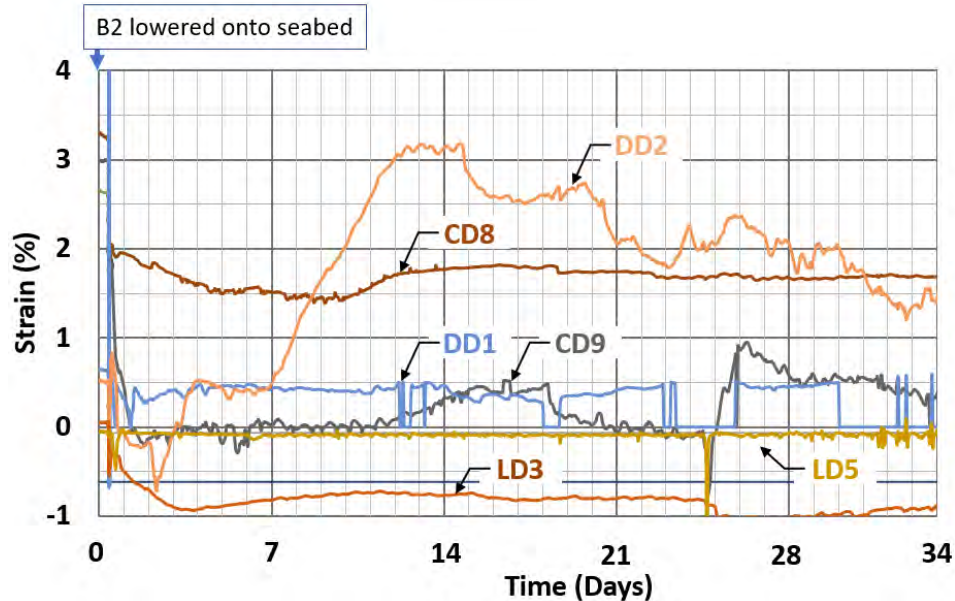


Figure 12. TPC Readings for B2, M1 and T1 during 12-hour monitoring period  
Submerged Curing and Consolidation of Geotextile Tube B2.

Figure 13 shows selected strain gauge readings after geotextile tube B2 was lowered onto the seabed and prior to the stacking of subsequent tubes (i.e., M1, M2 & T1) on top of B2. During this submersion period of 35 days, most strain gauge readings in all directions were relatively

constant (i.e., DD1, CD8, LD5, LD3) except DD2 and CD9, which suggested that the shape and height of the geotextile tube remained largely unchanged. Certain strain gauges (DD2) seemed to slowly increase and then decrease as the geotextile tube appeared to have been subjected to minor adjustments to its shape. Finally, analysis of Shape Accelerometer Array (SAA) data from SAA 1 and 2 found the settlement of geotextile tube B2 during this period to be approximately 0.02m.



**Figure 13. Strain gauge readings for B2 during submerged curing and consolidation  
Stacking of Geotextile Tubes onto Bottom Layer Geotextile Tubes.**

During the lowering and stacking operations of the middle and top layer geotextile tubes onto the bottom layer tube B2, strain gauge and the SAA readings are important in observing its deformation and settlement. Figure 14 shows selected strain gauge readings of geotextile tube B2 during the lowering of tubes M2, M1 and T1 on top of it. Strain gauges DD2 and CD9 experienced reduction in tension (at points A, B, C and D) and CD6 experienced increase in tension. This was likely due to the positions of these strain gauges on tube B2 that would be “stretched” or “compressed” when there is a tube stacked on top of it. LD5 strain readings remain relatively constant, suggesting that there was minimal deformation along the longitudinal length of the geotextile tube. Overall, changes in strain readings were quite small. This suggested that during the loading of middle and top layer geotextile tubes, the shape tube B2 remained largely uniform.

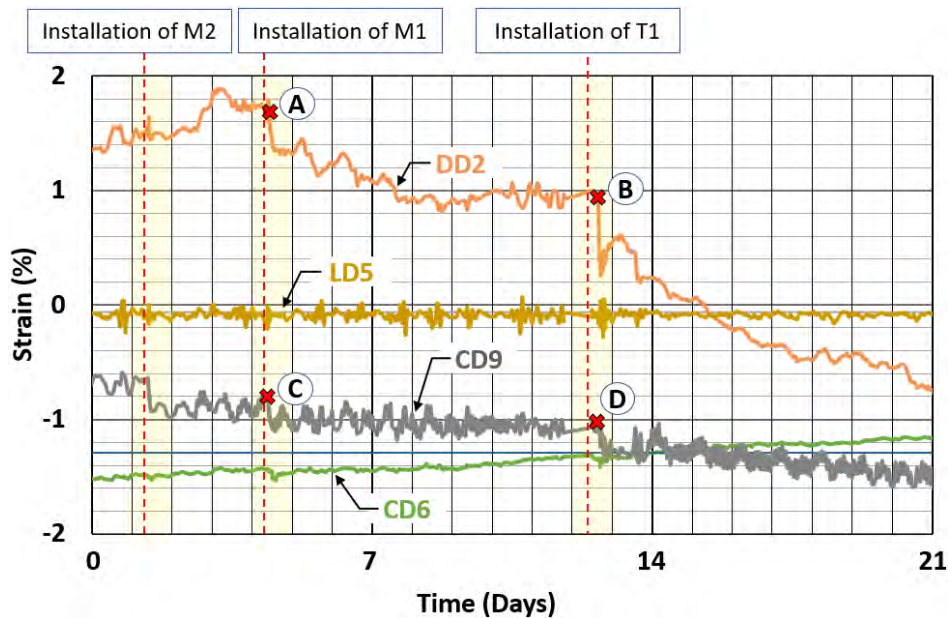


**Figure 14. Strain gauge readings for B2 during lowering of middle and top layer tubes**

Figure 15 shows their estimated positions on the seabed after all 3 geotextile tubes in the bottom layer have been lowered. CMS (at 6% cement content of untreated soft soil) was infilled in the spaces between the three geotextile tubes in preparation for the stacking of the next layer of geotextile tubes. The SAA could capture the settlement of the seabed soil due to the imposed load by the individual geotextile tubes. Minor settlement of 80-120mm was observed directly beneath the bottom layer tubes.

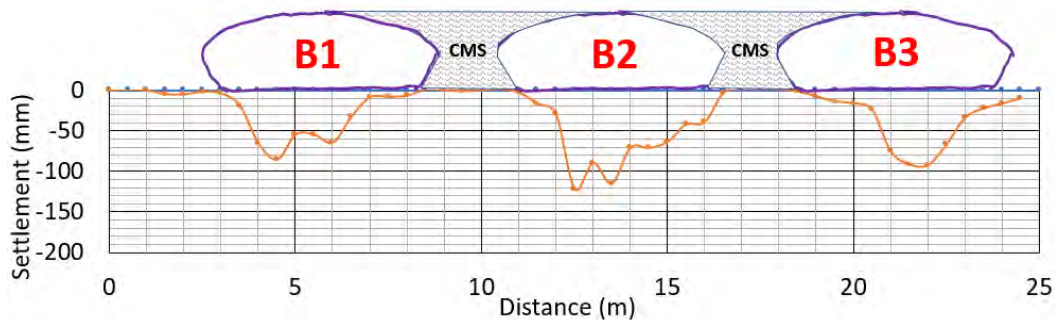


**Figure 15. Position of bottom layer geotextile tubes**

After the lowering of the bottom layer geotextile tubes (B1 to B3), tubes from the middle (M1 & M2) and top layer (T1) would be subsequently stacked on top of it. Using readings from SAA 1 and SAA 2, the settlement profile of the top surface of the bottom layer geotextile tubes when additional tubes were lowered and stacked onto it can be estimated and shown in Figure 16. It is noted that the 4th geotextile tube M2, was lowered 35 days after tube B2 was successfully lowered onto the seabed.



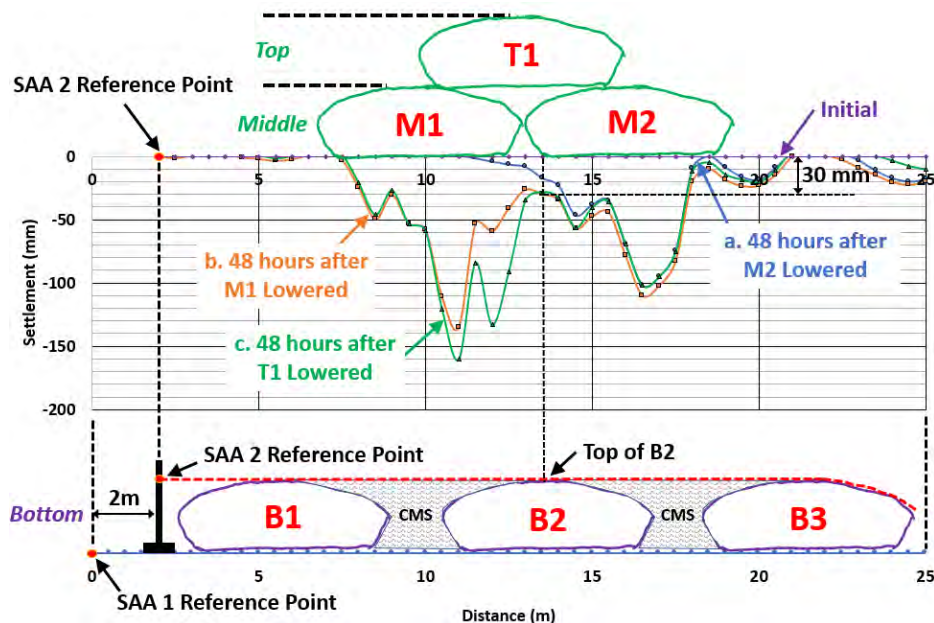


**Figure 16. Settlement profiles of bottom layer geotextile tubes with middle and top layer tubes stacked on top of it**

Figure 16 shows the settlement values at the top surface of the bottom layer tubes, and the relative positions of tubes after all 3 layers of geotextile tubes have been lowered successfully. The settlement readings shown are taken 48 hours after each middle and top layer geotextile tubes were lowered.

It can be seen that the height at the center of bottom layer tube B2 decreased by 30 mm after stacking of the middle layer tubes on top of it. The height of bottom layer tube B2 remained the same after the top layer tube T1 was stacked on top of the middle layer tubes M1 and M2. A larger settlement of 160 mm towards the left edge and 110 mm towards the right edge of tube B2 was observed, which may be due to the tubes from the middle layer tubes (M1 & M2) deforming slightly to conform to the gap of the bottom geotextile tubes.

Overall, from the initial infilling to the eventual stacking of two layers of geotextile tubes on top of bottom layer tubes, the total settlement of the crest of bottom geotextile tube B2 was approximately 0.15m (~8% of initial filled height), summarized in Table 2.

**Table 2. Summary of settlement of tube B2 throughout construction process**

Phase	Settlement of geotextile tube B2 (m)
1: Infilling and 12-hour monitoring period	0.10
2: Submerged cementation and consolidation	0.02
3: Stacking of middle and top layer geotextile tubes on top of bottom layer	0.03



## CONCLUSION

The lowering of six geotextile tubes filled with Cement Mixed Soils (CMS) to form a bund has been completed successfully. Analysis of results from strain gauges, total pressure cells and shape array accelerometers installed showed that there was only a minimal amount of settlement on bottom layer geotextile tube B2, which experiences the largest amount of vertical stress out of the six tubes. The CMS material was able to help minimize piping during infilling and maintain the shape of the geotextile tube. Therefore, CMS appears to be an effective infill material for use in geotextile tubes.

## ACKNOWLEDGEMENTS

This research is supported by the National Research Foundation, Singapore, and Ministry of National Development, Singapore, under its Cities of Tomorrow R&D Programme (CoT Award No. CoT-V4-2019-4). Any opinions, findings, conclusions, or recommendations expressed in this material are those of the author(s) and do not reflect the views of National Research Foundation, Singapore, and Ministry of National Development, Singapore.

The authors also gratefully acknowledge the assistance of numerous personnel and workers from Toa-Samsung Joint Venture and Geoharbour Co., Ltd for facilitating and supporting the site trial.

## REFERENCES

- Bushra, I., & Robinson, R. G. (2013). Shear Strength Behavior of Cement Treated Marine Clay. *International Journal of Geotechnical Engineering*, 455-466.
- Chew, S.H., Audrey Yim, H.M., Koh, J.W., Eng, Z.X., Chua, K.E., and Danette Tan, S.E. (2018). Performance of Pilot Test of Geotextile Filled with Lightly Cemented Clay. *Proceedings of the 11th International Conference on Geosynthetics*.
- Eng, Z. X. (2016). Experimental Studies on the Dewatering Process of Slurry Fine Grained Soils in Geotextile Tubes. A Thesis Submitted for the Degree of Doctor of Philosophy. Singapore.
- Lawson, C. R. (2008). Geotextile Containment for Hydraulic and Environmental Engineering. *Geosynthetics International*, 384-427.
- Siew, C. L., Roslan, H., Shervin, M., & Song, K.-I. (2014). Utilisation of Geotextile Tube for Sandy and Muddy Coastal Management. *The Scientific World Journal*.
- Shin, E.C., & Oh, Y.I. (2007). Coastal Erosion Prevention by Geotextile Tube Technology. *Geotextile and Geomembranes*, 25(4): 264-277.

## Effectively Utilizing a Nature-Based HPTRM Solution for Municipal Drainage Channels

Drew Loizeaux, P.E.,<sup>1</sup> Jared Hill, P.E.,<sup>2</sup> and  
Matt Patton, P.E.<sup>3</sup>

<sup>1</sup>Propex, 4019 Industry Drive, Chattanooga, TN; e-mail: [drew.loizeaux@propexglobal.com](mailto:drew.loizeaux@propexglobal.com)

<sup>2</sup>Propex, 4019 Industry Drive, Chattanooga, TN; e-mail: [jared.hill@propexglobal.com](mailto:jared.hill@propexglobal.com)

<sup>3</sup>Propex, 4019 Industry Drive, Chattanooga, TN; e-mail: [matt.patton@propexglobal.com](mailto:matt.patton@propexglobal.com)

### ABSTRACT

The Reinland Drain is a municipal drainage channel in South-Eastern Manitoba that receives flows from the entire Pembina Valley. It was originally built in 1966 on shifting sandy soil that has suffered from years of accelerated erosion. In 2010, a sheet piling drop structure reinforced with large rock riprap was installed. Later that year, erosional damage of the drain side slopes and around the structure occurred after a spring flood event. Following the damage in 2010, minor remediation was completed to stop the progressive erosion. In 2016, damage from significant flooding caused major failures to nearly two miles of the channel. Instead of installing more riprap, the town decided to find a longer-term solution to stabilize the eroded channel banks and prevent further loss. The project aimed to better dissipate water throughout the channel and protect area farmers from losing property. The project design included rock filled gabion mattress along the base of the channel, and approximately 45,000 square yards of ARMORMAX 75 Engineered Earth Armoring System (EEAS) installed on the slopes of the channel. This paper will show how the incorporation of the EEAS as a nature-based solution helped reduce the overall cost and environmental footprint of the project.

### INTRODUCTION

The Reinland drainage channel is located within the Rural Municipality (RM) of Stanley, about 10 miles south of the Town of Winkler, Manitoba. Constructed in 1966, it functioned to collect stormwater runoff from the adjacent farmland, draining into Buffalo Creek, which outlets into the Red River near the town of Saint Jean Baptiste. The soil in the area generally consists of fine sand and silt, making the channel more susceptible to erosion. Throughout the years, the channel experienced various levels of erosion due to storm events.

In 2016 the RM was completing some improvements to an upstream section of the channel and created a berm to divert water into a spillway. A series of significant rain event occurred in July of 2016, causing a rise in the water level within the spillway. On July 20<sup>th</sup>, the berm between the spillway and the drainage channel failed, causing the built-up water to flow back into the drainage channel and the erosion of the downstream section (See Figure 1). After an engineering evaluation, it was determined that the probable cause of the erosion was the elevated water levels, high water velocities, and erodible soils.



**Figure 1. Channel Erosion prior to remediation.**

When looking for the appropriate solution to the challenging erosion within the drainage channel, several options for remediation were considered. One option considered the removal and replacement of the erodible soils and the temporary protection of an Erosion Control Blanket (ECB) until vegetation could establish. While this solution may have been lower cost, it relied heavily on significant vegetation establishment, and as seen in the historical performance of the channel, the unreinforced vegetation that had been established did not provide sufficient protection.

Traditional, hard armoring solutions such as rock riprap and gabion mattresses were considered as well. While these hard armoring options are commonly used in various erosion control applications, there are significant challenges associated with their use. Both riprap and gabion mattresses are designed base of their rock size. The rock, whether confined within a gabion mattress or unconfined with riprap, needs to be heavy enough to stay in place during the storm event being evaluated. Higher velocities and shear stress require larger rock sizes and thicker rock layers. Larger rock sizes create larger void spaces between the rocks, which can lead to internal erosion that is not always identified quickly. Due to the manufacturing process and the inefficiency of transportation, rock riprap and gabion mattresses typically have both a high material cost and high carbon footprint.

There are times where hard armoring is the appropriate solution and there are times where hard armoring is the “that’s how we’ve always done it” solution. The RM and engineer of the Reinland Drainage Channel sought out a innovative solution to optimize the use of hard armoring by incorporating an Engineered Earth Armoring System (EEAS). The EEAS was selected to stabilize the channel banks because it offered cost savings as well as an environmental benefit over the hard armoring. The EEAS is composed of PYRAMAT 75 High Performance Turf



Reinforcement Mat (HPTRM) and Engineered Earth Anchors that work together to lock soil and vegetation in place and protect against hydraulic stresses for up to 75 years (See Figure 2).



**Figure 2. Engineered Earth Armoring Solution - HPTRM (Left) and Earth Anchor (Right).**

## DESIGN CONSIDERATIONS

When evaluating the Reinland Drainage Channel, the engineer of record considered the hydraulic flow conditions present for various flood events and the overall cost of the solution. The hydraulic design incorporated HEC-RAS modeling with flow return periods from 2 years up to 100 years. With each design flow, the maximum velocity, shear stress, and water surface elevation was calculated in order to choose the most appropriate solution in each scenario.

The drainage channel was modeled having 3.5 Horizontal to 1.0 Vertical (3.5H:1.0V) side slopes and a bottom width that varied along length of the channel. The design flow of 1,345 ft<sup>3</sup>/s for the 100-year flood event resulted in a maximum velocity of 5.8 ft/s and a maximum shear stress of 0.5 lb/ft<sup>2</sup>. In addition to the velocities and shear stresses generated, the 100-year flood event showed a maximum flow depth of 7.3 ft. The more frequent design flow of 170 ft<sup>3</sup>/s for the 2-year flood event resulted in a maximum velocity of 3.3 ft/s and a maximum shear stress of 0.2 lb/ft<sup>2</sup>. In addition to the velocities and shear stresses generated, the 2-year flood event showed a maximum flow depth of 3.1 ft. Due to the frequency of flood events and the somewhat constant water level in the bottom of the channel, it was determined that it would not be viable to maintain vegetation along the channel bottom. The solutions considered would then have to be able to provide adequate erosion control performance in a fully unvegetated state.

The first two options considered for channel protection looked at the use of either rock riprap or gabion mattresses as hard armoring. For the hydraulic evaluation of the hard armoring, Manitoba Infrastructure recommended the use of Hydraulic Engineering Circular No. 23 (HEC-23) from the Federal Highway Administration (FHWA). Based on the expected velocity, the design methodology within HEC-23, and with the riprap classifications utilized by Manitoba Transportation, a Class 350 riprap with a thickness of 16 inches was determined to meet the hydraulic requirements. Alternatively, based on the expected shear stress and design methodology a gabion mattress thickness of 9 inches was determined to meet the hydraulic requirements. The initial evaluation considered the use of hard armoring across the channel bottom and along the side slopes incorporating 2 ft of freeboard above the 100-year design high water level.

The final two options considered a combination of the previously considered hard armoring and the use of the Engineered Earth Armoring System (EEAS). The EEAS has been used in critical erosion control applications for over 20 years and has been successfully implemented by the U.S.



Army Corps of Engineers (USACE) in various regions and climates. The HPTRM component of the system helps retain soil and reinforce vegetation while the anchor component helps secure the HPTRM in place and reduce soil movement. When tested per ASTM D-6460 in a fully vegetated state with typical site conditions, the EEAS can resist shear stresses of up to 16 lb/ft<sup>2</sup> and velocities of up to 25 ft/s (See Figure 3). The HPTRM has a tensile strength of 4,000 lb/ft and a high resistance to degradation, allowing the system to resist any non-hydraulic stresses such as debris loading or maintenance vehicles for a design life of up to 75 years.



**Figure 3. Full Scale Testing per ASTM D-6460 – Vegetated HPTRM (Left) and during Flume Test (Right)**

The combined hard armoring and EEAS solution looked to optimize the use of both systems. The hard armoring along the channel bottom and up to the 2-year flood event would provide protection during the more frequent occurrences and would help control erosion even if vegetation did not establish along the bottom. The EEAS protecting the side slopes from the 2-year flood event up to 1-ft above the 100-year flood event would provide a vegetated solution with a reduced overall cost and environmental impact.

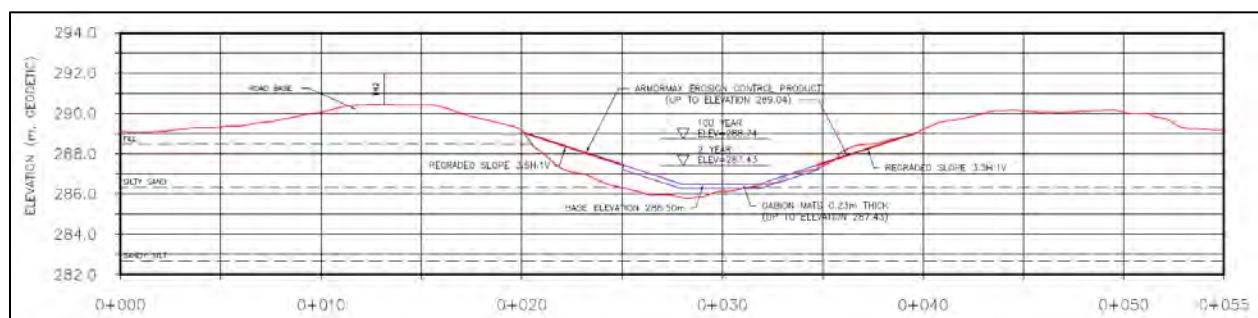


**Figure 4. Drainage Channel Cross-Section**

To further analyze the available options, a cost comparison was prepared to aid in determining the most appropriate solution. The installation estimate of the hard armoring included equipment mobilization and demobilization, regrading of existing soils, excavation of existing soils, installation of a separation fabric, and installation of either the rock riprap or the gabion mattress. The installation estimate of the EEAS included the installation of the EEAS as well as topsoil and revegetation efforts. The cost comparison shown in Table 1 aided in final selection of

the erosion control solution for within the drainage channel. Based on the hydraulic performance and the cost estimates, it was determined that the combination of the gabion mattress up to the 2-year flood event and the EEAS up to 1-ft above the 100-year flood event would provide the most optimized solution. The combination of gabion mattress with the EEAS was able to provide a 41% reduction in project cost over the initial rock riprap design alternative.

**Table 1. Cost Comparison for Alternatives Considered**

Alternative	Total Cost
Rock Riprap (100-Year Protection)	\$8,446,000
Gabion Mattress (100-Year Protection)	\$6,184,500
Rock Riprap (2-Year Protection) and EEAS (100-Year Protection)	\$6,032,000
Gabion Mattress (2-Year Protection) and EEAS (100-Year Protection)	\$4,964,000

## ENVIRONMENTAL BENEFITS

In addition to the performance and economic benefits shown, there were significant environmental benefits of incorporating the EEAS into the overall erosion control solution. Utilizing an EEAS provides an opportunity to remove pollutants from overland flow with the use of vegetation, deter burrowing animals, reduce the amount of construction machinery needed for installation and reduce traffic and emissions by improving shipping efficiencies. While often overlooked, these topics are crucial for the long-term success of erosion control projects.

Hard armor, such as rock riprap is a conventional solution to prevent soil erosion. However, the EPA states in “Storm Water Technology Fact Sheet - Turf Reinforcement Mats” (EPA-832-F-99-002, Sept. 1999) that while “these permanent measures can withstand great hydraulic forces, they are costly, and they do not provide the pollutant removal capabilities of vegetative systems”. The EPA has established the use of vegetation as a best management practice (BMP). Vegetation acts to slow water velocities, increasing sedimentation and filtration of heavy metals, and encourages infiltration of water back into the ground water table. Turf Reinforcement Mats (TRMs) and HPTRMs are also set as standard BMPs by the EPA to allow for the use of vegetated solutions where the hydraulic limits of unreinforced vegetation has been reached. The EPA further states that “TRMs provide a cooler substrate than traditional hard armor techniques, reducing water temperature increases that could otherwise impact aquatic life”.

The carbon footprint of a given solution can be simplified and broken down into manufacturing and shipping. The estimated carbon footprint for the EEAS described here, including HPTRM, Earth Anchors, and temporary securing pins is 3.8 kg CO<sub>2e</sub> per SM, from cradle to grave. For comparison, the manufacturing alone of rock riprap generates 36.6 kg CO<sub>2e</sub> per SM for a 16-inch thick section. In addition to manufacturing, the improved shipping efficiency of the EEAS can provide even further carbon footprint reduction. To provide 48,000 SY of EEAS it would require 4 trucks to ship from Ringgold, GA to Stanley, Manitoba, for a total of around 5,800 miles. Alternatively, the equivalent coverage of rock riprap would require 2,134 trucks traveling an assumed 90-mile transport distance, for a total of around 192,060 miles. By using the EEAS as an alternative to rock riprap, the transportation emissions, as well as additional costs of pavement wear, traffic congestion, noise pollution and crash potential was reduced by 97%.



## INSTALLATION AND PERFORMANCE

The installation of the gabion mattress along the channel bottom began in December of 2017. With the gabion mattress installed along the bottom, the EEAS installation began in January of 2018 along the channel side slopes, down to the toe of the slope. Due to the cold weather during the installation, the contractor elected to pre-drill the anchor locations through the frozen soil to improve the earth anchor installation rate (See Figure 5). Once the EEAS was installed, the gabion mattress would be completed up the side slopes, overlapping the EEAS up to the 2-year flood event (See Figure 6).



**Figure 5. Winter Installation of Gabion Mattress and EEAS (01/2018)**

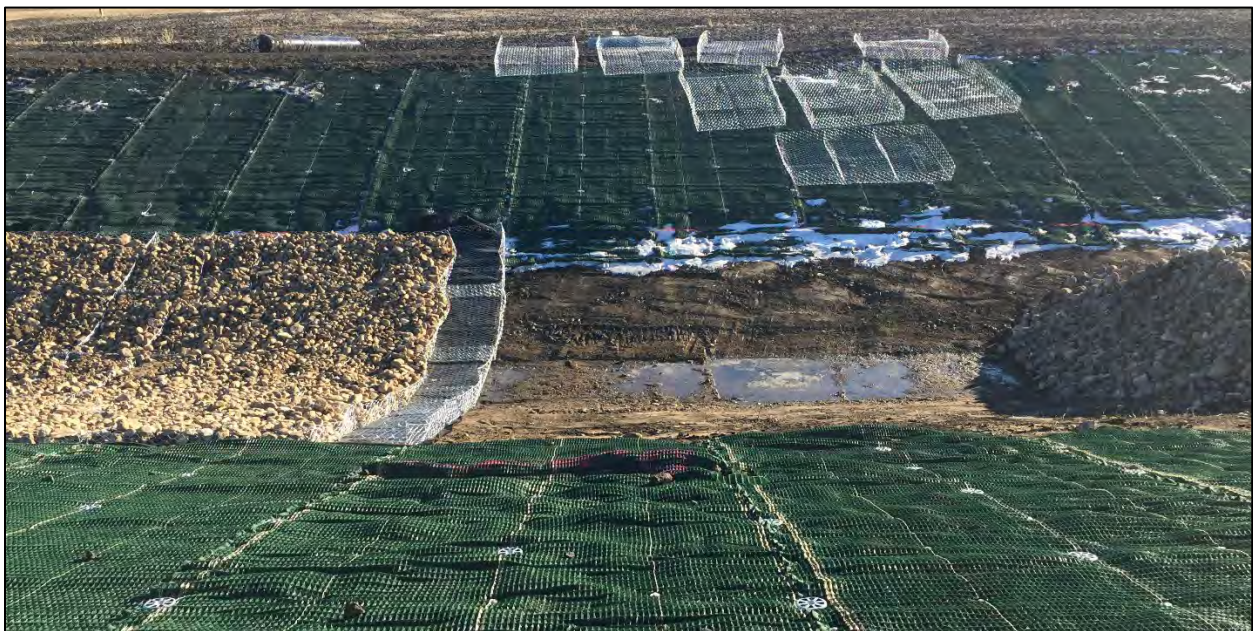


**Figure 6. Transition between Gabion Mattress and EEAS (02/2018)**



With the installation of both the gabion mattress and EEAS complete, the drainage channel began to be engaged from various precipitation events, providing performance even prior to vegetation establishment (See Figure 7). In June of 2018, during a more appropriate time for vegetation establishment, the EEAS was hydroseeded along the slope surface (See Figure 8).



**Figure 7. Performance Prior to Vegetation Establishment (05/2018)**



**Figure 8. Hydroseeded EEAS (06/2018 - Left) and Vegetation beginning to Establish (07/2018 – Right)**

In September of 2021, over 3.5 years since the original installation, the site was inspected to evaluate the vegetation establishment and overall performance of the EEAS. The site regularly



has standing water along the channel bottom and effectively uses the gabion mattresses to control erosion in these areas (See Figure 9). The vegetation establishment across the EEAS along the channel side slopes has proven extremely successful. The grasses and other native vegetation are able to be mowed somewhat frequently due to the high tensile strength and durability of the EEAS (See Figure 10).



**Figure 9. Continued Performance and Vegetation Establishment (09/2021)**



**Figure 10. Overall Channel and Mowing (09/2021)**

Recent storm events have put the erosion solutions within the drainage channel to the test. Figures 11 and 12 show a performance comparison of the gabion mattress and EEAS downstream



versus an unreinforced channel section upstream. The results of the unreinforced upstream section showed significant erosion along the channel bottom, causing erosion and geotechnical failures along the side slopes. With a stark contrast from the upstream section, the downstream channel section protected by the gabion mattress and reinforced by the EEAS is continuing to provide superior erosion control performance with a vegetated, nature-based solution.



**Figure 11. Gabion Mattress and EEAS Performing after storm event - Downstream Section (05/2022)**



**Figure 12. Unreinforced Section showing erosion and geotechnical failures after storm event - Upstream Section (05/2022)**

## CONCLUSION

Providing efficient solutions for erosion control has become increasingly challenging as projects are progressively more complex, balancing performance, cost, and environmental impact. Using the Engineered Earth Armoring Solution (EEAS) provides a nature-based solution that has a long history of performance, reduces cost versus conventional hard armoring, and improves the environment through efficiency and use of vegetation. The Reinland Drainage Channel successfully implemented the EEAS as part of their erosion control solution, reducing project costs by over \$3 million and reducing carbon emissions by over 2,300 tons.

## REFERENCES

- ASTM D 6460. Standard Test Method for Determination of Rolled Erosion Control Product (RECP) Performance in Protecting Earthen Channels from Stormwater-Induced Erosion, *ASTM International*, West Conshohocken, Pennsylvania, USA.
- Federal Highway Administration (FHWA), 2009. “Bridge Scour and Stream Instability Countermeasures: Experience, Selection, and Design Guidance,” Hydraulic Engineering Circular No. 23, Third Edition, FHWA-NHI-09-111 HEC-23.
- Hill, J (2020). The Environmental Benefits of High Performance Turf Reinforcement Mats, *Informed Infrastructure*, 34–39.
- Loizeaux, D (2018). Engineered Earth Armoring Solutions: An Alternative to Rock Riprap, *Informed Infrastructure*, 31–37.
- Patton, M (2020). Hydraulic Performance Benefits of Engineered Earth Anchors, *Informed Infrastructure*, 36–43.
- U.S. Environmental Protection Agency (USEPA), 1999. “Storm Water Technology Fact Sheet: Vegetated Swales,” EPA 832-F-99-006, Washington, D.C., USEPA Office of Water.
- U.S. Environmental Protection Agency (USEPA), 1999. “Storm Water Technology Fact Sheet: Turf reinforcement mats,” EPA 832-F-99-002, Washington, D.C., USEPA Office of Water.

## Hydraulic Roughness Testing of Geosynthetics

C. Joel Sprague, P.E.<sup>1</sup> and James E. Sprague, CPESC<sup>2</sup>

<sup>1</sup>TRI Environmental – South Carolina; e-mail: jsprague@tri-env.com

<sup>2</sup>TRI Environmental – South Carolina; e-mail: jesprague@tri-env.com

### ABSTRACT

Hydraulic roughness is the measure of the amount of frictional resistance water experiences when passing over land and through channels or pipes and depends on the characteristics of the conveying surface and, to a lesser extent, the characteristics of the flow. The Manning equation is an empirical equation that is commonly used to describe gravity flow in a conduit based on the conduit's geometry, slope, and surface friction expressed as Manning's Roughness Coefficient, or Manning's  $n$ . The Manning equation is an empirical equation because most pipes and channels flow under turbulent conditions, and we do not yet have a sufficient scientific understanding of turbulence to derive equations based on first principles. Thus, testing that reasonably simulates the range of flow and conduit conditions anticipated and back-calculating using Manning's equation is necessary to obtain an appropriate Manning's  $n$  for design of the hydraulic conveyance system. This paper focuses on describing different testing setups and procedures for geosynthetics in different applications and presents some typical test-derived Manning's  $n$  values.

### INTRODUCTION TO HYDRAULICS OF OPEN CHANNEL FLOW AND CONDUITS FLOWING PARTIALLY-FULL

Following is a very basic introduction to concepts and equations that apply to the design or analysis of open channels and conduits for culverts and storm drains.

Continuity and Velocity. The continuity equation is the statement of conservation of mass in fluid mechanics. For the special case of steady flow of an incompressible fluid, the following equation, known as the continuity equation, applies:

$$Q = A_1 V_1 = A_2 V_2 \quad \text{Equation 1.}$$

where:

- $Q$  = discharge (cfs or  $\text{m}^3/\text{s}$ )
- $A$  = flow cross-sectional area (sq. ft. or  $\text{m}^2$ )
- $V$  = mean cross-sectional velocity (fps or  $\text{m/s}$ , perpendicular to the flow area).
- The subscripts 1 and 2 refer to successive cross sections along the flow path.

As indicated by the Continuity Equation (Eq. 1), the average velocity in a channel cross-section, ( $V$ ) is the total discharge divided by the cross-sectional area of flow perpendicular to the cross-section.

Manning's Equation. Most channel analysis procedures use the following equation, known as Manning's Equation, for uniform flow as a basis for analysis:



$$V = (Z / n) R^{2/3} S^{1/2} \quad \text{Equation 2.}$$

where:

- V = Velocity in cfs or m<sup>3</sup>/sec
- Z = 1.486 for English measurement units, and 1.0 for metric
- n = Manning's roughness coefficient (a coefficient for quantifying the roughness characteristics of the channel or conduit)
- R = hydraulic radius (ft. or m) = A / WP
- WP = wetted perimeter of flow (the length of the channel boundary in direct contact with the water) (ft. or m)
- S = slope of the energy gradeline (ft./ft. or m/m) (For uniform, steady flow, S = channel slope, ft./ft. or m/m).

By combining Manning's Equation with the continuity equation, a variation on the Manning's Equation is derived for determining uniform flow capacity as shown in Equation 3.

$$Q = (Z / n) A R^{2/3} S^{1/2} \quad \text{Equation 3.}$$

## THE IMPORTANCE OF ROUGHNESS COEFFICIENTS

Open channels and partially-full conduits exhibit some resistance to water flow, and that resistance is referred to as roughness. All hydraulic conveyance formulas quantify roughness subjectively with a coefficient. In Manning's Equation, the roughness coefficient, or n-value, will range depending on the characteristics of the conduit or channel lining exposed to the flow.

Determination of a proper n-value is the most difficult and critical of the engineering judgments required when using the Manning's Equation. Suggested values for Manning's roughness coefficient ("n" values) for traditional materials can be found in published tables and charts that have been developed from testing and experience. An example of some typical Manning's roughness coefficients related to well known geosynthetics is shown in Table 1. Still, for newer materials, roughness coefficients will likely have to be determined by large-scale flow testing.

**Table 1. Typical Manning's Roughness Coefficients**

Facility	Lining		Hydraulic Roughness (Manning's n) Values	
			Minimum	Maximum
Conduits	Plastic Pipe	Smooth	0.011	0.015
	Smooth	Corrugated	0.018	0.030
Open Channel	Bare Soil	Unlined	0.020	0.023
	RECP Lined Soil	Straw Blanket	0.025	0.065
		Excelsior Blanket	0.028	0.066
		Turf Reinforcement Mat	0.021	0.036
	Grass Lined, < 8" flow	6" length	0.05	0.09
		12" length	0.09	0.18
	Grass Lined, > 8" flow	6" length	0.04	0.06
		12" length	0.07	0.12

Ref. ODOT Hydraulics Manual

## TESTING FOR HYDRAULIC ROUGHNESS ASSOCIATED WITH NEW MATERIALS

**Introduction to Hydraulic Roughness Testing.** Hydraulic roughness is a way to describe any resistance to flow, including friction losses, in conduits flowing partially full, such as culverts and storm sewers, or in open channels. As noted above, Manning's equation is commonly used to quantify the flow in these conduits and channels and the Manning's n-value is a measure of hydraulic resistance to flow and depends on the characteristics of the pipe or channel lining and, to a lesser extent, the characteristics of the flow. While many traditional materials have been tested and associated n-values are widely published (see Table 1), newer materials will have to be subjected to laboratory flow testing in order to accurately determine an material-specific Manning's n-value.

**Overview of Large-scale Test Setup and Procedures.** Typically, a long, straight test section is set up within a re-circulating flow system. The pipeline or channel test section runs between a head box and the receiving sump of the re-circulating water-supply system. A typical setup for a pipe system is shown in Figure 1. The pipe or channel has a constant, known slope. The head box typically accommodates a sharp-crested weir (V-notch for lower flows and rectangular for higher flows) to accurately introduce a known flow rate into the upstream end of the pipe or channel as shown in Figure 2. The discharge is determined from the water level upstream of the weir, measured with a water level data logger. The head box must be large enough to also serve as a stilling basin, with baffles separating the incoming pumped flow from the still water discharging over the weir and into the pipeline or channel. The pipeline or channel then discharges into a receiving sump as shown in Figure 3, and the sump outflow is re-circulated to the headbox. The slope of the test section should, ideally, simulate the anticipated application environment. For example, the pipe was tested on a 1%, typical of buried sewers, to avoid creating turbulent flow. Piezometric heads (water depths) were measured at six locations along the pipe using a manometer board as shown in Figure 4.

**Specific Test Procedure.** The test procedure is based on generally accepted hydraulic principles as expressed in Manning's equation. If the flow cross section is uniform, the slope and roughness of the pipe or channel are known, and the flow is moved by the force of gravity only, the rate of flow in the pipe or channel may be calculated using Manning's equation. In testing, the rate of flow is known, along with slope, and the area of flow is calculated from the measured depth of flow. The associated roughness coefficient (a.k.a. Manning roughness coefficient, "n") is then back-calculated using Manning's equation. In this testing, a range of flows is run representing different partially-full flows. Each flow produces an associated flow depth. Together, the flows and associated flow depths are used to establish the basic hydraulics, including the *Manning's n*, of the test setup. For each test (flow level) the data collected consisted of reading of the weir headwater level to the nearest mm and the manometer readings for the six piezometers to the nearest mm. These tests were run at multiple discharges with depths of uniform flow that ranged from less than 20% to more than 90% percent of the diameter. Figures 5 through 8 show the headbox and weirs used. Example results from testing PVC sewer pipe are shown in Table 2. The Manning's n data is plotted in Figure 9. Note that as flow depth goes up, the roughness goes down. This is typical of most channel lining materials.



**Figure 1. Re-circulating Flow Test Setup**



**Figure 2. V-notch Weir in Headbox**



**Figure 3. Sump Discharge is Pumped Back to Headbox**



**Figure 4. Monometer Board for Reading Piezometric Heads**

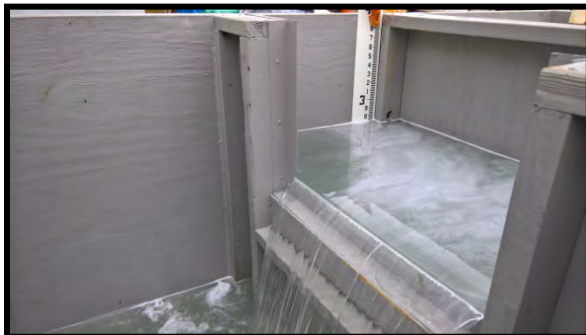


**Figure 5. Rectangular Weir used for High Flow Testing**



**Figure 6. 33° V-Notch Weir used for Lower Flow Testing**



**Figure 7. Headbox and Weir with attached Stillwell for HOBO logger**



**Figure 8. Example of Timed Catch to Verify Flow Rate**

**Table 2. Basic Pipeline Hydraulics**

Run #	Weir	Avg Depth (in.)	Pipe Dia. (ft)	y/D	Depth over Weir (ft)	Q (cfs)	Q (gpm)	Catch			Pipe Slope (ft/ft)	EGL / Friction Slope (ft/ft)	Manning n
								Avg Weight	Avg Time	Avg Q			
								lbs	sec	gpm			
1	33° V	0.38	0.65	0.049	0.152	0.007	3.0	4.21	9.88	3.1	-0.0093	-0.0092	0.0095
2	33° V	1.33	0.65	0.171	0.442	0.098	43.9	20.42	3.38	43.5	-0.0093	-0.0092	0.0092
3	33° V	1.86	0.65	0.239	0.582	0.195	87.4	21.89	1.80	87.5	-0.0093	-0.0092	0.0091
4	33° V	3.08	0.65	0.395	0.863	0.521	233.9	n/a	n/a	n/a	-0.0093	-0.0092	0.0089
5	2 ft Rect	1.20	0.65	0.154	0.052	0.079	35.3	n/a	n/a	n/a	-0.0093	-0.0092	0.0092
6	2 ft Rect	1.86	0.65	0.238	0.095	0.193	86.7	n/a	n/a	n/a	-0.0093	-0.0092	0.0091
7	2 ft Rect	3.05	0.65	0.391	0.182	0.508	227.9	n/a	n/a	n/a	-0.0093	-0.0092	0.0090
8	2 ft Rect	3.33	0.65	0.427	0.203	0.597	267.9	n/a	n/a	n/a	-0.0093	-0.0092	0.0090
9	2 ft Rect	4.03	0.65	0.517	0.256	0.841	377.4	n/a	n/a	n/a	-0.0093	-0.0092	0.0089
10	2 ft Rect	4.89	0.65	0.628	0.315	1.140	512.0	n/a	n/a	n/a	-0.0093	-0.0091	0.0089
11	2 ft Rect	6.03	0.65	0.773	0.381	1.507	676.4	n/a	n/a	n/a	-0.0093	-0.0093	0.0089
12	2 ft Rect	7.69	0.65	0.985	0.397	1.600	718.2	n/a	n/a	n/a	-0.0093	-0.0093	0.0093

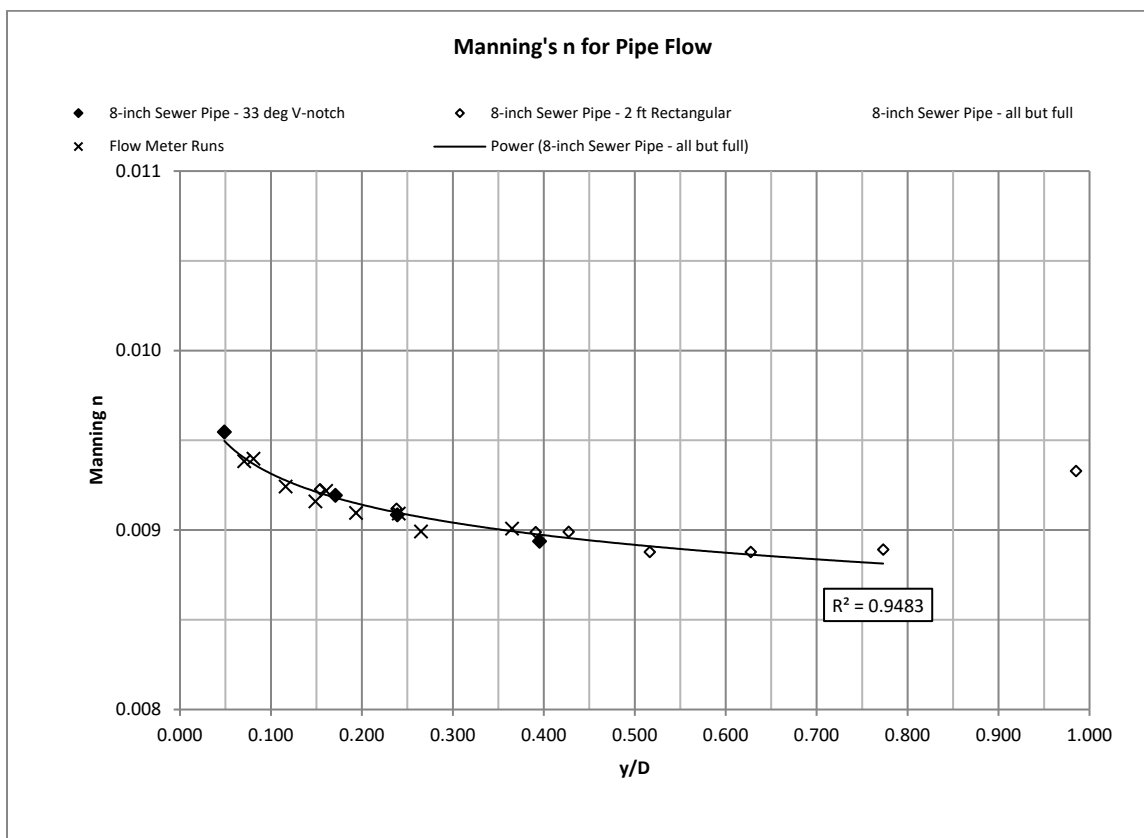


**Figure 9. Plot of Manning's n vs. Depth of Flow**

### The Effects of Nonuniform Liner Conditions

Typical Manning's n-values represent a continuous run of pipe or a continuous linear channel condition without joints or constrictions, leaving the designer to make judgments concerning the



affects these joints or constrictions might have on the design flow. While it is impractical to characterize all potential “restrictions” to flow that could be present, it is important for designers to have some sense of how much such restrictions may affect flow. To this end, testing was performed on two identical 12-inch dual wall corrugated pipelines, one with joints and the other without. The test setup followed the same protocol as outlined above. Figure 10 shows how the Manning n varies with the ratio y/D for the two pipes and confirms that, in this case, the joint design did not add flow restriction (increased roughness) to the pipeline.

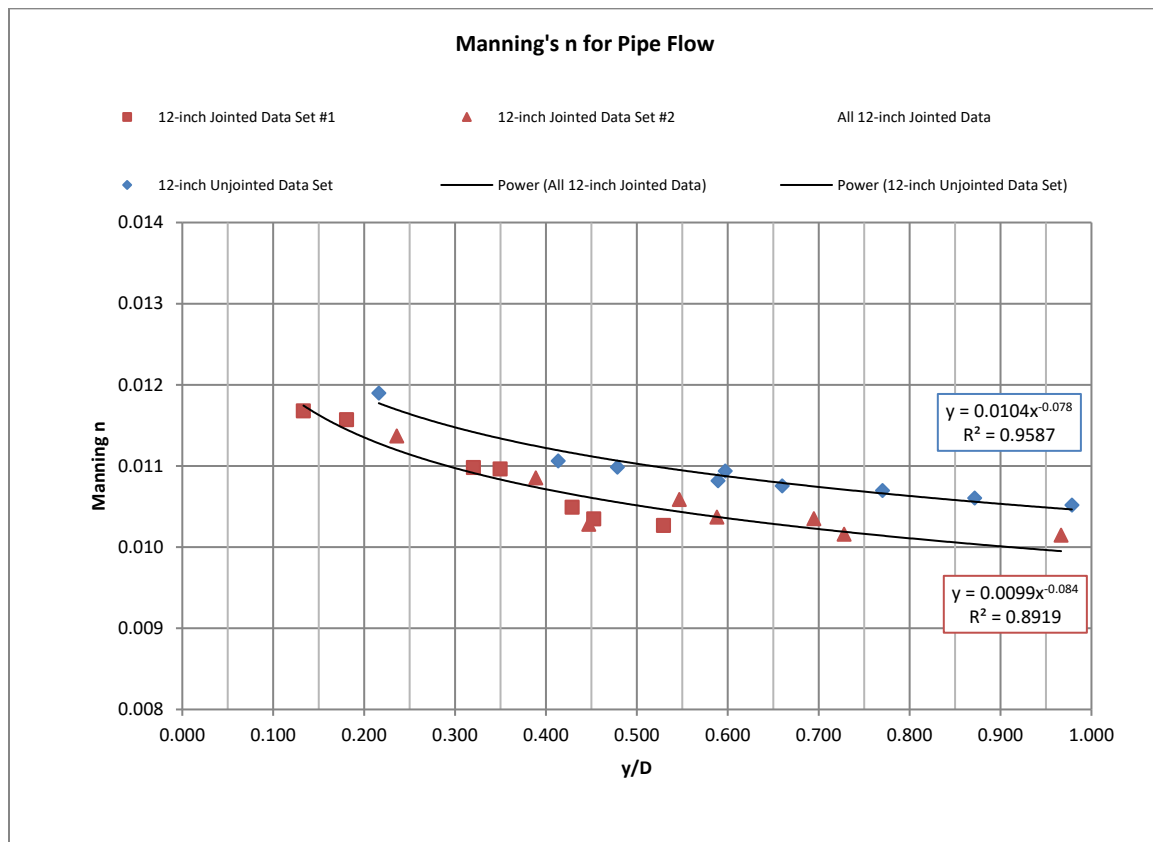


**Figure 10: Manning n values for 12-inch pipe**

## MANNING'S ROUGHNESS COEFFICIENT TESTING FOR VARIOUS PLANAR GEOSYNTHETIC SYSTEMS

Geosynthetics are frequently used in stormwater conveyance systems to protect against or even eliminate erosion. Turf reinforcement mats have been used for decades to create long-term erosion resistant channel linings. They are initially exposed to stormwater runoff in the unvegetated condition, but eventually become integrated with and reinforcement by a stand of vegetation. Both of these conditions have been studied (tested) extensively and there is a substantial body of information on associated Manning's n-values as shown in Table 1.

Still new geosynthetics, such as geosynthetic cementitious composite mats (GCCMs) and engineered geosynthetic turf systems have emerged as viable options for expansive steep slope and channel protection, and designers have required a better definition of the hydraulic roughness introduced by these systems.

**Geosynthetic Cementitious Composite Mats (GCCMs).** Testing was done to simulate concentrated runoff in a GCCM lined storm drainage channel. By measuring flow rate and associated flow depth, the resistance to flow, known as the Manning's Roughness Coefficient, can be determined for the tested material.

A trapezoidal channel with low slope provided an accurate hydraulic radius and the least turbulent flow for hydraulic testing in accordance with ASTM D6460. It should be noted that the flows were still somewhat turbulent as a result of normal irregularities in the product surface when installed. These slight, unavoidable irregularities produced slightly varying flow depths and velocities from cross-section to cross-section as would be expected in a normal channel and had a more pronounced affect on the roughness associated with lower flow depths. Prior to product testing, the channel was "calibrated" by lining it with polyethylene sheeting to create a very, very low friction condition to compare to. The Manning's  $n$  for this calibrated condition was 0.010. Pictures of the test setup are shown in Figures 11 – 16. The Manning's  $n$  values determined from testing are plotted in Figure 17. Once again, note that as the flow depth goes up, the roughness goes down.



**Figure 11. Trapezoidal Channel Prepared**



**Figure 12. Product Positioned for Deployment**



**Figure 13. Spraying Water to Hydrate Product**



**Figure 14. Upstream Sharp Crested Weir**



**Figure 15. Uniform Flow Introduced Over the Sharp Crested Weir**



**Figure 16. Depth Measurements used a Point Gauge**

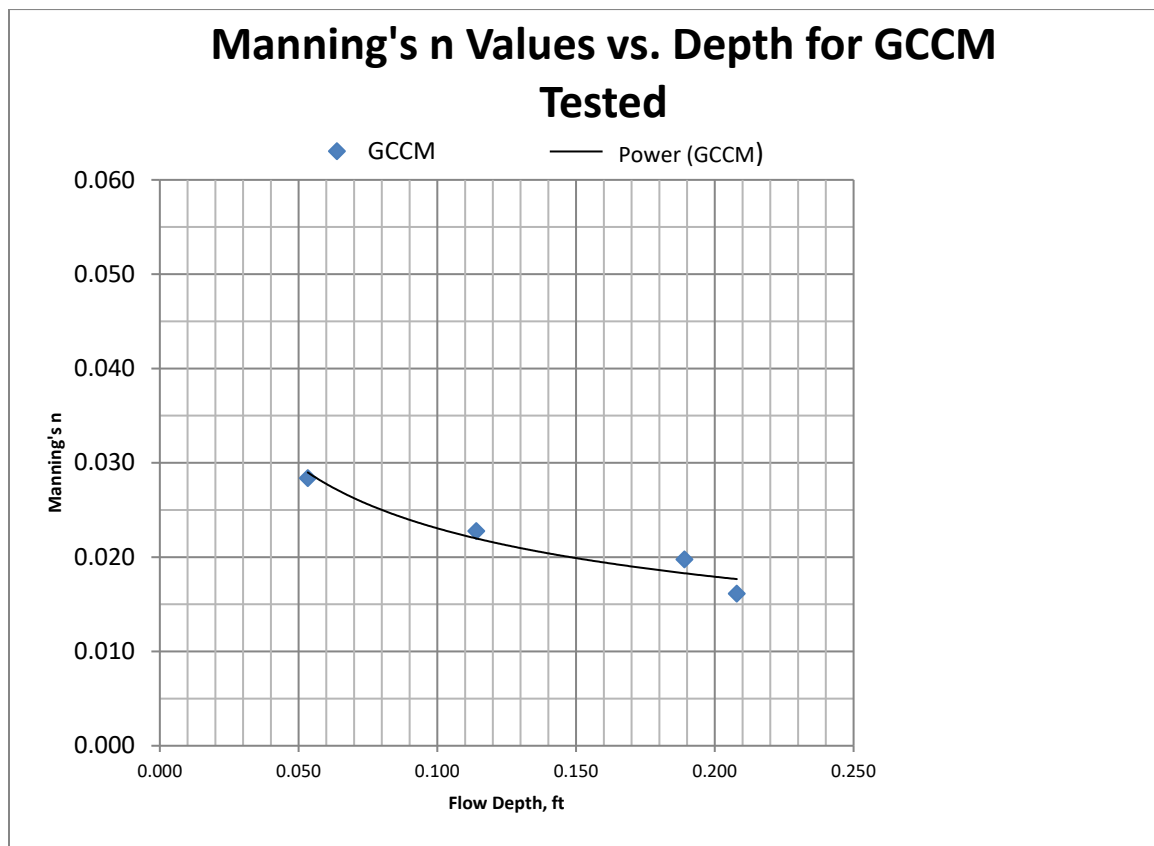


**Figure 17. Manning's n vs. Water Depth for Geosynthetic Turf in Channel Flow**

**Engineered Geosynthetic Turf System in Channels.** Testing was done to simulate concentrated runoff in a Geosynthetic Turf lined storm drainage channel. As described above, by measuring flow rate and associated flow depth, the Manning's Roughness Coefficient can be determined. Pictures of the test setup are shown in Figures 18 and 19. The Manning's n values determined from testing are plotted in Figure 20.



**Figure 18. Installation of Geosynthetic Turf System, including Ballast Media**



**Figure 19. Uniform Flow in Turf-lined Channel**

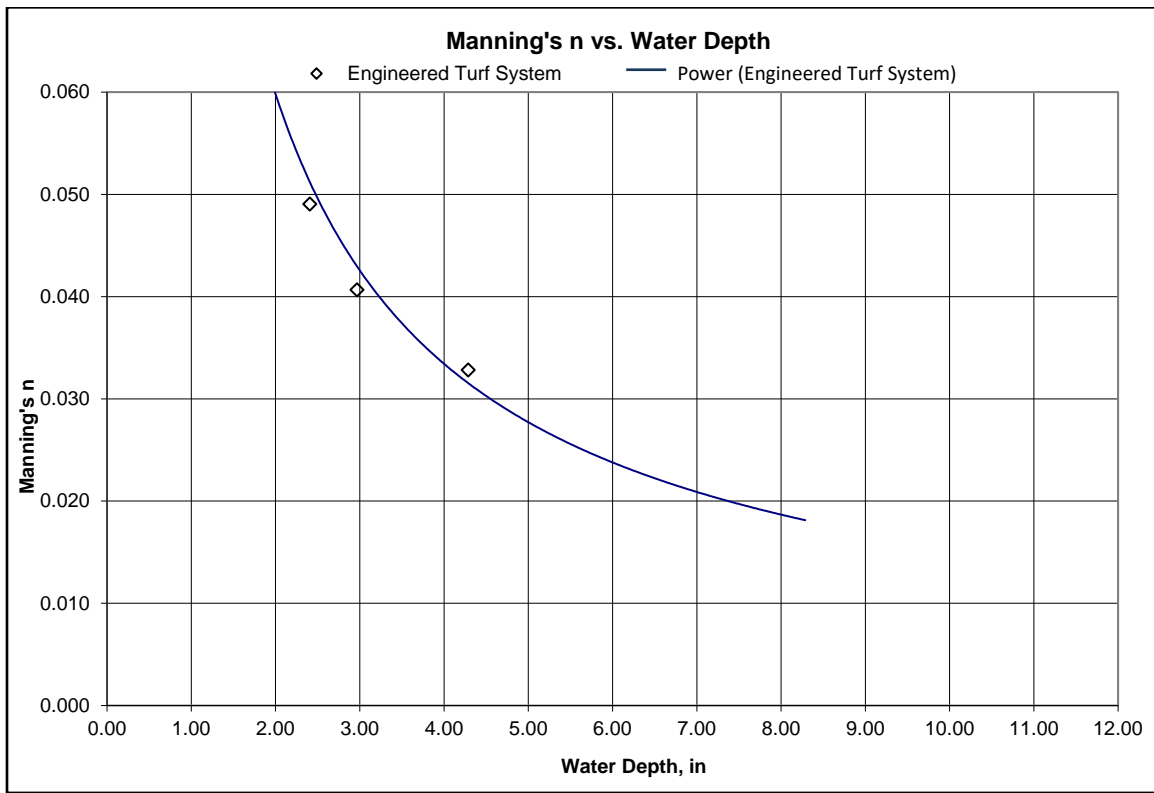


**Figure 20. Manning's n vs. Water Depth for Geosynthetic Turf in Channel Flow**

**Testing Geosynthetic Engineered Turf System on Steep Grades.** One of the advantages of geosynthetics is their ease of use and economy in applications where natural materials can be challenging or expensive to install. Steep slope applications, such as landfill caps, are a good example. Yet, to properly incorporate these materials into a stormwater drainage system, the flow conditions must be accurately simulated. To this end, a test setup was developed to expose a



geosynthetic engineered turf system in a steep (3:1) 2-ft wide flume with a smooth, impermeable bottom, and expose it to increasing flows while measuring the flow depth along the slope for each flow level. Then, using Manning's equation, the flow-specific roughness coefficient was back-calculated.

The impermeable flume bottom was outfitted with monometer ports along the slope length connected to a monometer board to facilitate the hydrostatic reading of flow depths. Depths were also measured manually using a depth gauge as a backup to corroborate the monometer readings. Additionally, the flow rate was measured using a weir once a steady-state flow condition was attained. Figure 21 shows the test setup used in the testing described herein.

The inclined slope was 10 ft long with 6 monometer ports at 1-ft spacing from station 2.5 ft to 7.5 ft. The 3-dimensional matting material was affixed to the slope using rigid metal angle iron and flat stock affixed with clamps at the top of the slope and along both edges. Water from the re-circulating pumping/piping system was delivered to a headbox at the top edge of the slope. Flow passed through and over the matting and discharged in the underlying 4 ft wide x 8 ft long weir box that incorporated a 2-ft rectangular sharp crested weir. The weir box discharged to a sump that ensured a stable head on the re-circulating flow system. The sump box measured 4 ft wide x 8 ft long.



**Figure 21. Steep Slope Test Apparatus Setup**

A 2400 gallon potable water reservoir system, comprised of eight 300 gallon “totes”, connected to the pump/pipe recirculation system through a 2 inch PVC header system. Two pump/pipe recirculation systems were used depending on the desired flow rate. One system was

comprised of 4-inch PVC pump inlet piping and 2 inch PVC pump outlet piping and a variable speed 3 hp pump. The other system was comprised of 8 inch PVC pump inlet piping and 4 inch layflat outlet piping and a variable speed 15 hp pump. The recirculation systems were able to maintain constant flows through the headbox, weir box and sump system at a wide range of flow rates.

Figure 22 presents a summary of the test results graphically, showing Manning's n versus flow rate and flow depth for both the tested product and the smooth surface-only condition.

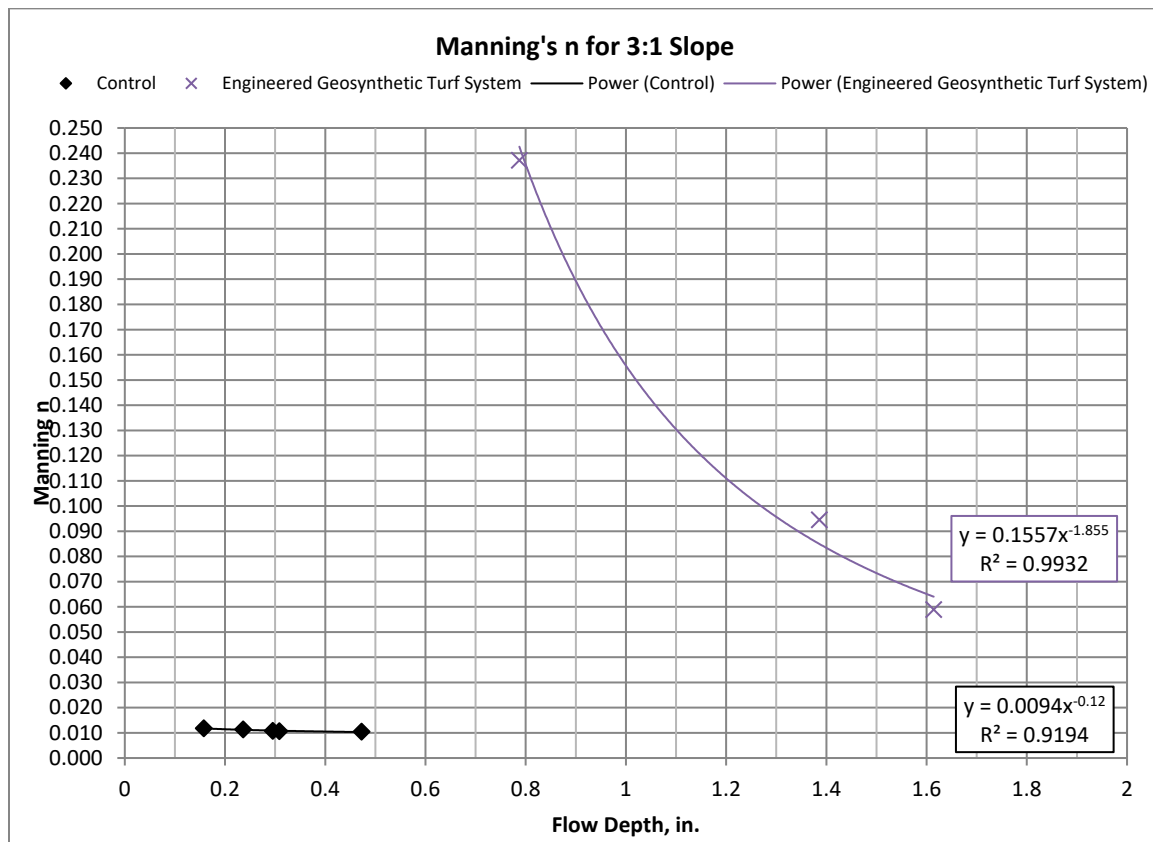


**Figure 22. Manning's Roughness Coefficient, n, vs. Flow Depth**

## CONCLUSIONS

Hydraulic roughness is the measure of the amount of frictional resistance water experiences when passing through open channels or pipelines. This frictional resistance depends on the characteristics of the conveying surface and, to a lesser extent, the characteristics of the flow and, is empirically determined from testing. When back-calculated using values from testing in the Manning equation, the frictional resistance is referred to as Manning's Roughness Coefficient, or Manning's n.

The Manning equation is for simulating water flows in channels and culverts where the water is open to the atmosphere, i.e. not flowing under pressure. It is an empirical equation derived from curve fitting to observed test data. It is an empirical equation because most pipes and channels flow under turbulent conditions, and we do not yet have a sufficient scientific understanding of turbulence to derive equations based on first principles. Thus, testing that reasonably simulates

the flow and conduit conditions anticipated is necessary to obtain an appropriate Manning's  $n$  for design of the hydraulic conveyance system.

This paper has described different setups and procedures for testing geosynthetics, including plastic pipe, in different applications and has presented some typical test-derived Manning's  $n$  values. In all cases, by measuring flow rate and associated flow depth in testing, the resistance to flow - Manning's  $n$  - was determined for each tested material by back-calculating using Manning's equation. It was shown that in all cases Manning's  $n$  varies with flow depth, thus it is necessary to test each setup over a range of flow rates.

## **REFERENCES**

Ohio Department of Transportation (2014), "ODOT Hydraulics Manual"

## **Installation of Geotextile Tubes as Perimeter Bund in Mega-reclamation Project at Penang, Malaysia**

**Chew Soon Hoe, Ph.D.,<sup>1</sup> Soh Jun Ming<sup>2</sup>,  
Lim Lum Kong<sup>3</sup>, Tan Jun Yuen<sup>4</sup>, Siew Kok Hau<sup>5</sup>, Ang Cheng Poh, Albert<sup>6</sup>**

<sup>1</sup> National University of Singapore, 21 Lower Kent Ridge Road, Singapore 119077; e-mail: ceeesh@nus.edu.sg

<sup>2</sup> National University of Singapore, 21 Lower Kent Ridge Road, Singapore 119077; e-mail: ceeshjm@nus.edu.sg

<sup>3</sup> TenCate Geosynthetics Asia, 14 Jalan Sementa 27/91, Seksyen 27, Selangor 40400; email: lklim@solmax.com

<sup>4</sup> TenCate Geosynthetics Asia, 14 Jalan Sementa 27/91, Seksyen 27, Selangor 40400; email: jytan@solmax.com

<sup>5</sup> TenCate Geosynthetics Asia, 14 Jalan Sementa 27/91, Seksyen 27, Selangor 40400; email: khsiew@solmax.com

<sup>6</sup> Gateway Structure Sdn Bhd, No 42, Level 1, Jalan MR 1/3, Taman M-Residensi, Selangor 48020; email: info@gssb.com.my

### **ABSTRACT**

Seri Tanjung Pinang (STP) Reclamation project is a mega reclamation project at Penang, Malaysia. Geotextile tubes were infilled with sand up to 2.3m filled height and installed in 4 layers onto the seabed with -6 to -10 mCD to form the 1.6km containment bund wall. To minimize the use of divers and maximize installation efficiency, an innovative method of installation was developed. Two triangular shaped end spreaders were fabricated to lower empty geotextile tubes onto the seabed. This method of installation was found to be cost-effective, fast, and safe. Testing of the full-scale pumping inlet port was carried out at National University of Singapore to simulate the possible mode of failure during infilling process. Stability checks such as sand tightness and wave stability checks were done. Total suspended solid (TSS) level in the vicinity of the geotextile tube bund were measured throughout the infilling operation to ensure Environment Impact Assessment requirement compliance. It was found that the TSS level reduced rapidly with distance and time after infilling of geotextile tubes has started. At the time of this paper submission, the contractor has successfully installed about 4km of the 13km of geotextile tubes designed for this project.

### **INTRODUCTION**

Seri Tanjung Pinang is a seafront development on the northeast coast of Penang Island, Malaysia. This development project consisted of two land reclamation phases, where Phase 1 (STP1) reclamation work was completed in year 2005, and Phase 2 (STP2) reclamation work commenced in year 2016. Sand filling and soil treatment was the designated reclamation method used to reclaim STP1, and STP2 continued to adopt this reclamation method.

Prior to reclaiming the land for STP2 development, a perimeter bund must be established not only to comply with the environmental requirement but also to protect the sand fill against current and wave attack. STP2 perimeter bund consists of geotextile tubes as the bund core, with a primary and secondary rock armor as outer protection layer for the geotextile tube. The rock



armor layers are to protect the geotextile tubes from getting punctured by ocean debris or sharp objects and as a UV protection barrier to prolong the geotextile tube core lifetime. A schematic drawing of the perimeter bund is shown below in Figure 1.

In this paper, a new installation method will be presented. Material tests, stability checks and environmental assessment of Total Suspended Solids (TSS) will also be discussed.

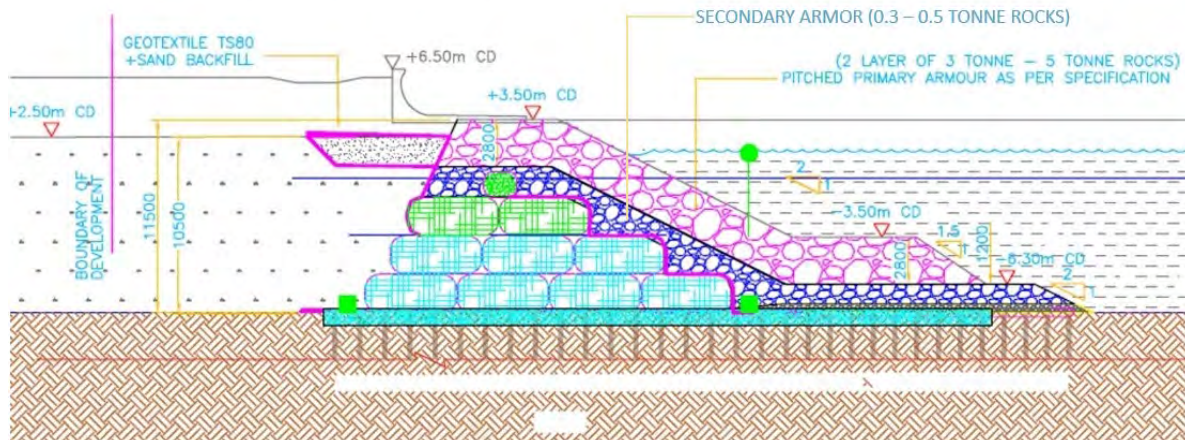


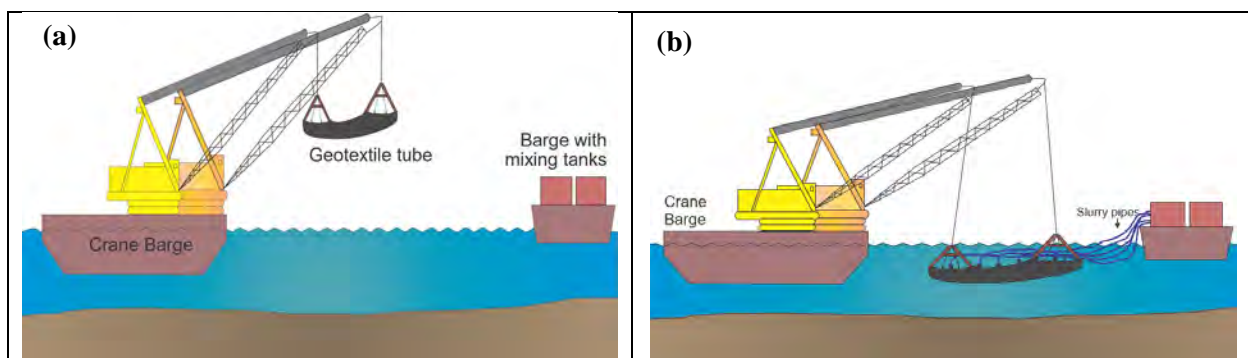
**Figure 1. Schematic Cross Section of Perimeter Bund**

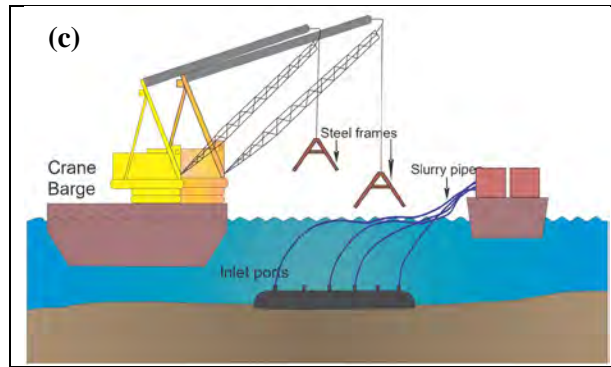
## INSTALLATION METHOD

An innovative installation method was developed to install the geotextile tubes in this project. Two triangular shaped end spreaders (steel frame) were fabricated, holding the two ends of the 50 m long geotextile tube, and lowered using two cranes on a flat bottom barge.

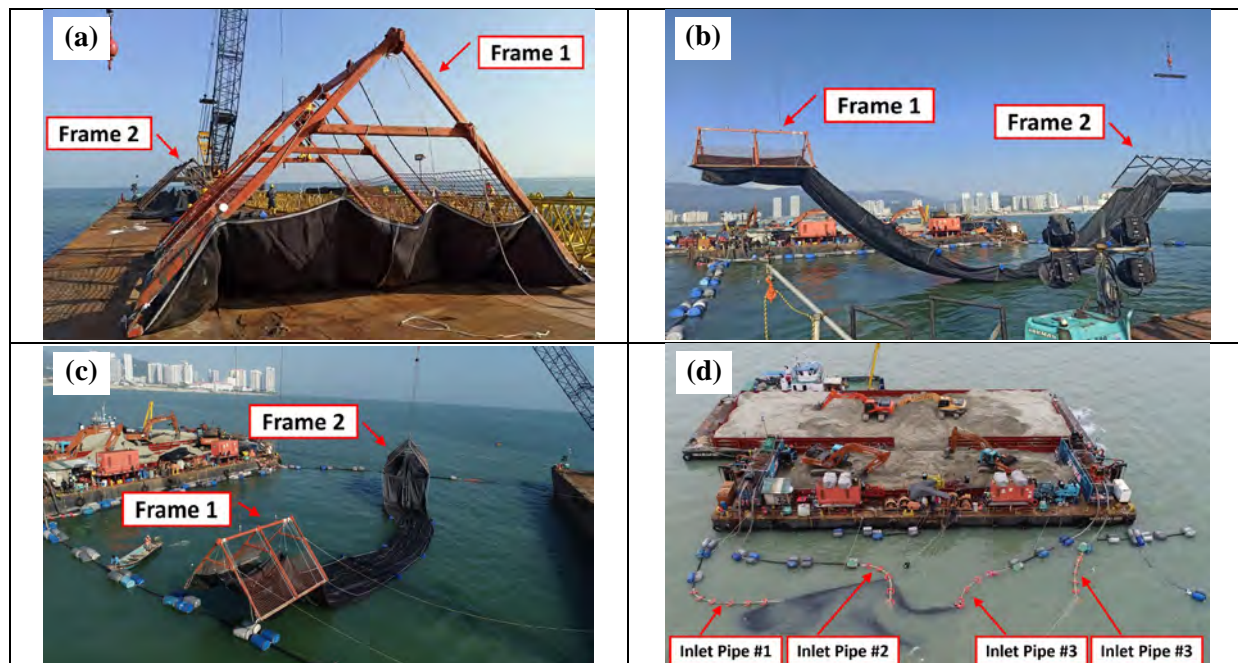
Figure 2 shows a simplified illustration of the construction process. The weight of the sand during infilling helps to weigh and thus lower the geotextile tube down to the desired position on the seabed. Once the geotextile tubes are at their desired position on the seabed, the steel frames are retrieved. This method of installation was found to be cost-effective, fast, and safe.

Figure 3 shows the site photos of the installation process of geotextile tubes, in which: (a) Loops at the both ends of the tube are each tied to a steel frame; (b) Geotextile tube is lifted up at two ends, using the triangular steel frames; (c) Geotextile tube is lowered into position; (d) Four (4) numbers of inlet slurry pipes are attached to the inlet ports on the geotextile tube, and sand slurry is pumped into the geotextile tube through all 4 inlet ports simultaneously while it is fully submerged in water.





**Figure 2. Illustration of the Installation Process of Geotextile Tubes on Site. (a) Lowering of empty geotextile tubes; (b) Connection of the inlet ports to the sand slurry pumps and lowered onto seabed; (c) Retrieval of steel frames after infilled with sand slurry on the seabed.**



**Figure 3. Installation Process of the Geotextile Tubes on Site (Site Pictures)**

## MATERIAL TESTS

**Geotextile Strength.** The geotextile material used for geotextile tube fabrication have to sustain the loads generated during the filling process and throughout its service life. This is most critical during the infilling process, as tension is generated from the stretching of the geotextile as sand slurry is infilled. Subsequently, the tension forces will reduce due to the compaction and densification of fill materials and its change from fully fluid state to solid state upon the completion of filling (Yee, 2016). Table 1 shows the specifications of the geotextile tube material used in this project.

**Table 1. Specification of geotextile material used in geotextile tube**

Properties	Test Method	Value
Wide width tensile strength (MD)	ISO 10319	> 200 kN/m
Wide width tensile strength (CD)	ISO 10319	> 200 kN/m
Elongation at tensile strength (MD)	ISO 10319	< 12 %
Elongation at tensile strength (CD)	ISO 10319	< 10 %
CBR puncture strength	ISO 12236	> 22 kN
Drop cone perforation diameter	ISO 13433	< 7 mm
Abrasion resistance	ASTM D4886	80 % retained strength
UV resistance (500 hours)	ASTM D4355	90 % retained strength
Pore size (O <sub>90</sub> )	ISO 12956	< 0.35 mm
Water permeability (Q <sub>50</sub> )	ISO 11058	> 20l m <sup>2</sup> /s
Seam strength (CD)	ISO 10321	> 170 kN/m

The geotextile tubes used in this project are fabricated from multiple panels of geotextiles using circumferential seaming method. As such, the circumferential tension will be imposed on the Machine Direction (MD) of the geotextile, and axial tension along the length of the geotextile tube will be imposed on the Cross-Machine Direction (CD) of the geotextile as well as the seam along the circumference of the geotextile tube. Special equipment was used for the circumferential seaming of the geotextile tube to achieve a high seam efficiency of 85%.

Several commercial software is available in the market to calculate the tension generated in the geotextile tube during filling, such as GeoCoPS, SOFTWIN, TubeWin© and Geotube® Simulator. In this project, TubeWin© geotextile tube analysis software is used to determine the tension generated in the geotextile material and predict the dimension of the fully filled geotextile tube under fully submerged conditions. The circumference of the geotextile tube used was 15.7m with a filled height of 2.3m. The unfactored hoop stress generated on the tube fabric in the MD direction is 13.68 kN/m and 10.8 kN/m in the CD Direction. Table 2 summarizes the results obtained from the analysis. The geotextile material specifications are able to meet the predicted stresses experienced during installation.

**Table 2. Summary of analysis results**

Parameter	Units	Predicted Value	Material Specs.
Machine Direction (MD)	kN/m	13.68	200
Cross Machine Direction (CD)	kN/m	10.80	200
Seam Strength	kN/m	10.80	170
Inlet Port Strength	kN/m	13.68	27.4*
Total width of the geotextile tube	m	6.733	-
Base contact width of the geotextile tube	m	5.605	-
Volume	m <sup>3</sup> /m	13.282	-

\* Value obtained from test discussed in Section 3.2



It is noted that there is a factor of safety of two for the inlet port strength, which is sufficient for the pumping operations in the initial stages of the construction. The factor of safety for the geotextile material (i.e., MD, CD direction and seam strength) is significantly higher as these are important for long term durability of the geotextile tube.

**Inlet Port Strength.** The inlet port is a critical component of the geotextile tube, especially during the infilling process. Tearing of the inlet port sleeve geotextile during infilling will lead to leakage of infill material, resulting in wastage of material and environment damage. A custom-designed testing apparatus was built in the National University of Singapore (NUS) Geotechnical Lab to investigate the strength of a full-scale inlet port sleeve, illustrated in Figure 4. The geotextile body is fixed to a circular frame using clamps, and the sleeve is fixed around a hanging steel drum. A hydraulic piston pushes down on the steel rod connected to the steel drum until tearing of the sample is observed.

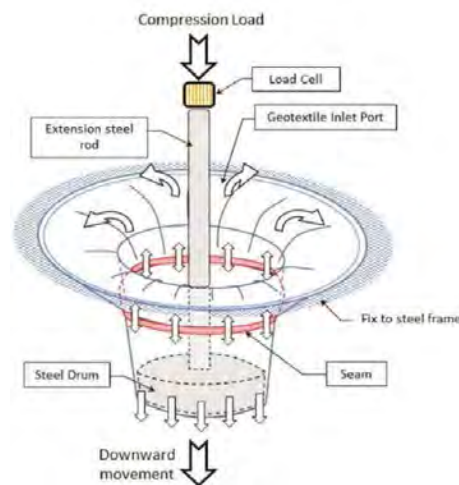
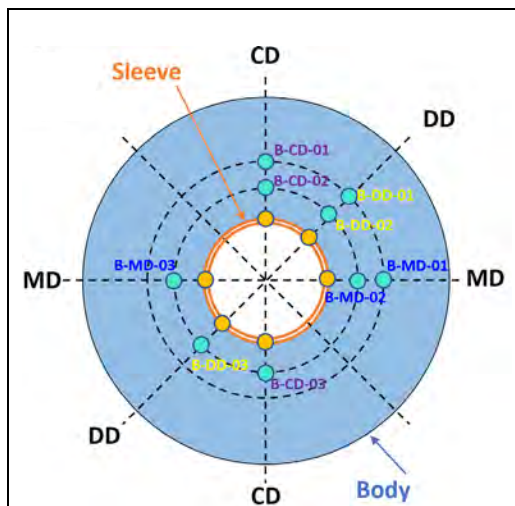


**Figure 4. Illustration of Inlet Port Strength Test Apparatus in NUS**

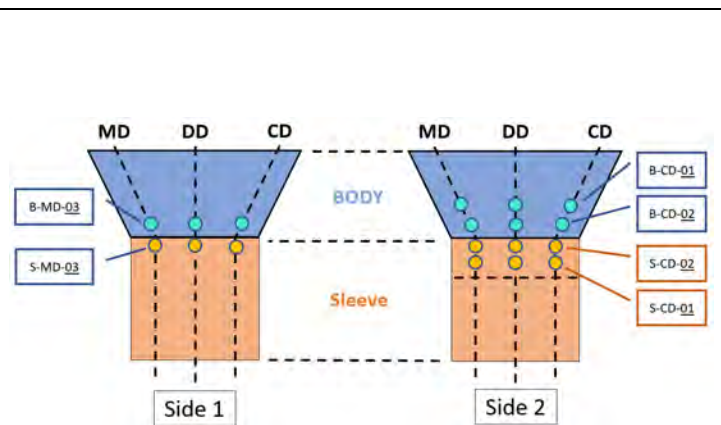
There are two main sections of the inlet port. The geotextile sleeve (where the slurry pipe is attached) and the main geotextile body. The sleeve is seamed to the main body using a 6-lap seam design. Figure 5 and 6 shows the strain gauge setup on the body and sleeve sections of the inlet port sample respectively. A total of 18 strain gauges are installed on the inlet port sample in various direction (9 each on the body and sleeve).

Figure 7 shows the results of the inlet port strength test. Two separate pushes by the hydraulic piston are required (second time with an extension rod) due to its limited pushing length. Results show good agreement in the trend of readings between the load cell and strain gauges. As load is applied, tension in both sleeve and body geotextile increases.





**Figure 5. Strain gauge positions on inlet port body (Plan View)**



**Figure 6. Strain gauge positions on inlet port sleeve (Side View)**

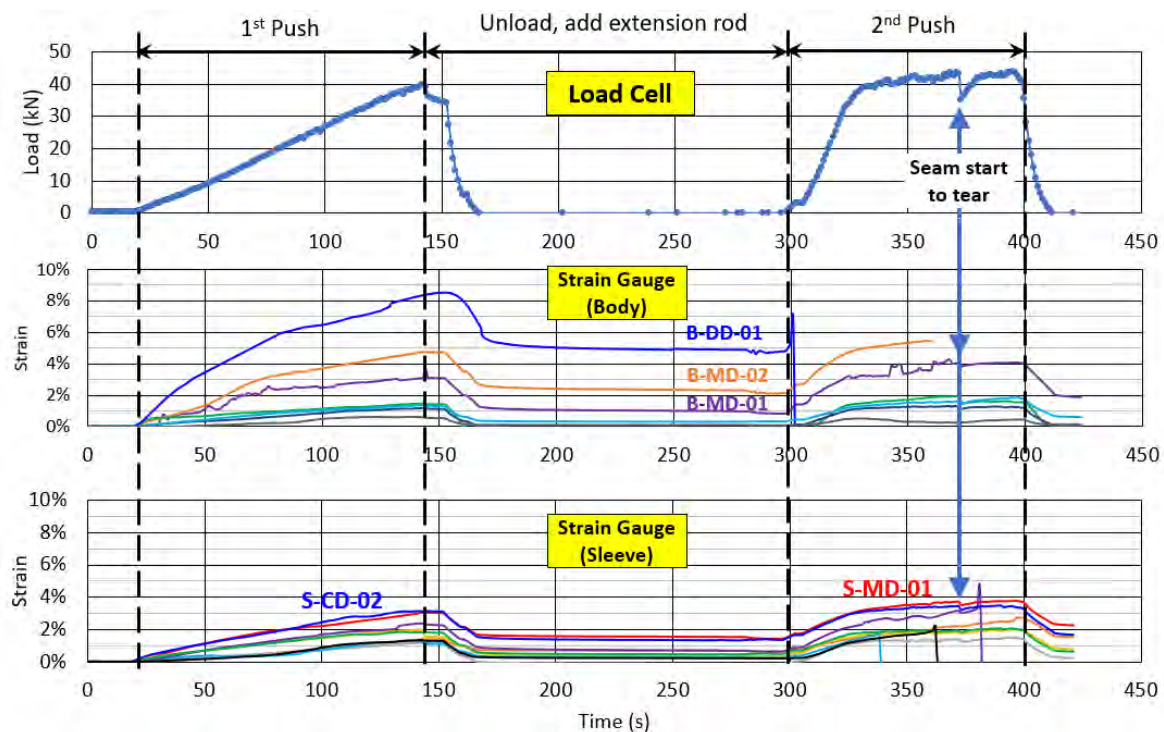


**Figure 7. Load cell and strain gauge readings**

The maximum strain registered is approximately 8% in the diagonal direction. From material testing, it was shown that in the diagonal direction the geotextile can take a maximum strain of ~20% before failure. Thus, the strain readings of the geotextile are well below their specified strain at maximum tensile load in all directions (MD, CD & DD). This is confirmed from observations

during the test, where failure occurred not in the geotextile fabric itself, but due to tearing of the seam connection. A maximum load of 43 kN or 27.4 kN/m (based on circumference of inlet port) was reached before the seam between sleeve and body geotextile starts to tear. During actual geotextile tube infilling works on site, this inlet port strength appears to be sufficient as there was no observed tearing of the inlet port section during infilling operations.

## STABILITY AND ENVIRONMENTAL CHECKS

**Sand Retention vs Geotextile Opening.** Geotextile tubes are often made from woven polypropylene geotextile with small opening size and high permeability to ensure the retention of sand in the geotextile tubes and fast discharge of water during the filling process. During the infilling process, some initial loss of sand is expected due to the dynamic load generated from the hydraulic filling process. However, it is important to ensure that there is no sand loss over time, especially throughout the service life of the structure. Excessive loss of sand over time will lead to the deformation of the geotextile tubes, which will subsequently result in the loss of service or damage to the structure founded on top of the tubes structure. Table 3 shows the recommended sand retention criteria proposed by Bezuijen and Vastenburg (2013).

**Table 3. Recommended sand retention criteria (Bezuijen and Vastenburg, 2013)**

Hydraulic load	Requirement 1	Requirement 2
Stationary load (current)	$O_{90} < 5D_{10}\sqrt{C_u}$	$O_{90} < 2D_{90}$
Dynamic load (wave attack)	$O_{90} < 1.5D_{10}\sqrt{C_u}$	$O_{90} < D_{90}$

$O_{90}$  = pore size of the geotextile tubes

$D_{10}$  = sieve size through which 10% fraction of the sand material passes

$D_{60}$  = sieve size through which 60% fraction of the sand material passes

$D_{90}$  = sieve size through which 90% fraction of the sand material passes

$C_u$  = uniformity coefficient of the sand ( $D_{60} / D_{10}$ )

Figure 8 shows the particle size distribution curve of the sand materials used for the filling of geotextile tubes. As the geotextile tubes used to form the core of the perimeter bund in the project are subjected to wave attack, the sand retention criteria will be checked against dynamic load conditions. Table 4 summarizes the result of the sand retention criteria, where the results show that the  $O_{90} = 0.35$  mm of the chosen geotextile material is sufficient to prevent piping of sand material from the geotextile tube.

**Wave Stability.** The project area is located at the north of Penang Straits. As this area is subjected to frequent wave attack, the geotextile tubes are required to withstand the hydraulic forces exerted by the waves. Bezuijen and Vastenburg (2013) recommended the use of the following for an initial approximation on the stability of geotextile tubes against wave attack:

$$\frac{H_s}{\Delta_t \cdot D_k} \leq 1.0$$

where:

$H_s$  = significant wave height (in m)

$\Delta_t$  = relative buoyant density of the geotextile tube

$D_k$  = effective thickness of the geotextile tube (in m)

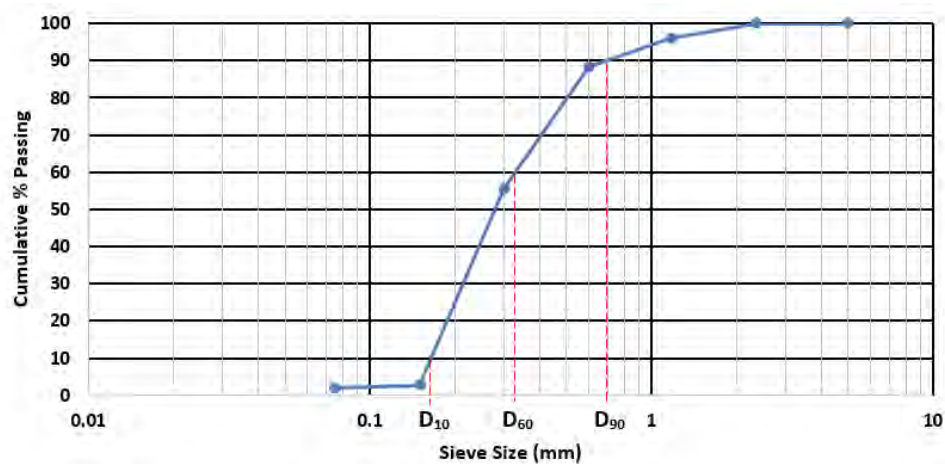


**Figure 8. Particle size distribution curve for the sand fill**

**Table 4. Sand retention check**

$O_{90}$	0.35mm
$D_{10}$	0.17mm
$D_{60}$	0.33mm
$D_{90}$	0.70mm
$C_u$	1.94
Dynamic Load (Wave Attack) Check	
Requirement 1	$O_{90} < 1.5D_{10}\sqrt{C_u}$ $0.35mm < 0.36mm$
Requirement 2	$O_{90} < D_{90}$ $0.35mm < 0.70mm$

For geotextile tubes placed perpendicular to the direction of the wave attack, the effective thickness ( $D_k$ ) is taken as the width of the filled geotextile tube. On the other hand, for geotextile tube placed parallel to the direction of the wave attack, the effective thickness is taken as the length of the tube

if the length is less than 2 times its filled width, else the effective thickness shall be taken as 2 times its filled width. Since the geotextile tube length is much larger than its width, the critical condition is when  $D_k$  = width of filled geotextile tubes.

The relative buoyant density ( $\Delta_t$ ) of the geotextile tube can be calculated using the following equation:

$$\Delta_t = \frac{\rho_s - \rho_w}{\rho_w}$$

where:

$\rho_s$  = density of the sand filled in the geotextile tube (approximate 1900 kg/m<sup>3</sup>)

$\rho_w$  = density of water (approximately 1030 kg/m<sup>3</sup> for seawater)

Sand filled geotextile tubes placing in a seawater environment result in a relative buoyant density of 0.84. The project utilized geotextile tubes with 15.7m circumference and a filled height of 2.3m. Hydraulically filling of sand into the geotextile tube to the designed height results in a filled tube width of approximately 6.7m. With the design wave height ( $H_s$ ) of 2.5m at the project site and taking the tube's width of 6.7m as the effective thickness ( $D_k$ ) results in the following:

$$\frac{H_s}{\Delta_t \cdot D_k} = 0.44 < 1.0$$

This check satisfies the condition in which the geotextile tube design for the project is stable against the design wave height of 2.5m.

**Total Suspended Solids (TSS) Analysis.** In reclamation projects, it is required that turbidity arising from construction activities be controlled and limited within the site area. Silt curtains are often deployed surrounding the site boundary to limit the dispersion of sediment out of the project site. As the geotextile tubes are filled with sand through hydraulic filling, it is of interest to understand the contribution of the geotextile tube filling activities to the turbidity of the surrounding water.

Turbidity is measured in terms of the concentration of total suspended solid (TSS) in mg/L. Several locations along the length of the geotextile tube have been identified for the collection of the water samples for the measurement of TSS (see Figure 9) during the filling of geotextile tube of 50.5m length. Three sample points (A, B & C) are located at 1m away from the edge of tube while another three sample points (D, E & F) located at 31m away from the edge of tube. The water samples are collected from all 6 sample points at 5 different times, which are before filling of the tube (Set 1), 15 minutes after filling of the tube (Set 2), 1 hour after filling of the tube (Set 2), after filling stop (Set 4), and 24 hours after completion of filling (Set 5). The water samples collected are then sent to the laboratory for the measurement of TSS, the results are presented in Figure 10.



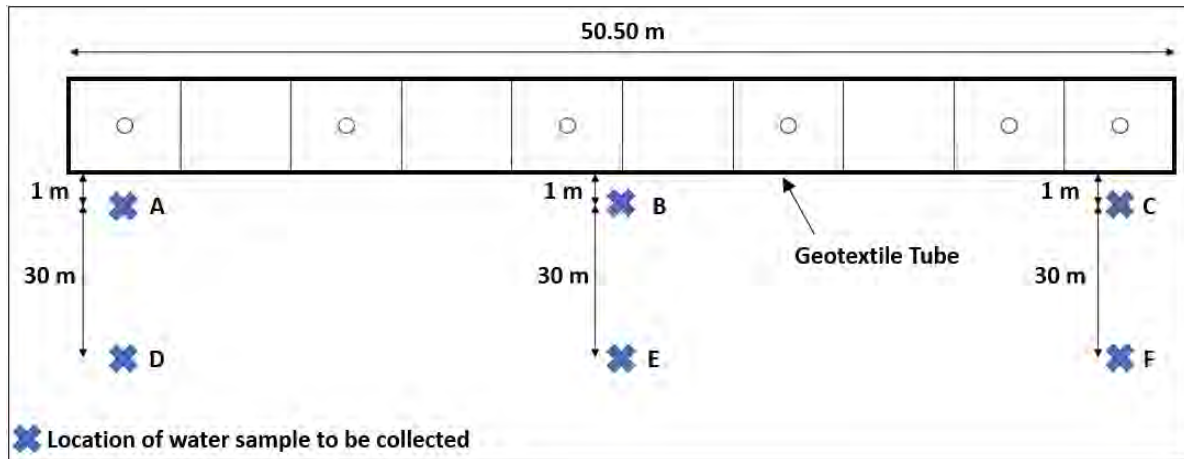


**Figure 9. Water sample collection plan for TSS analysis (Plan View)**

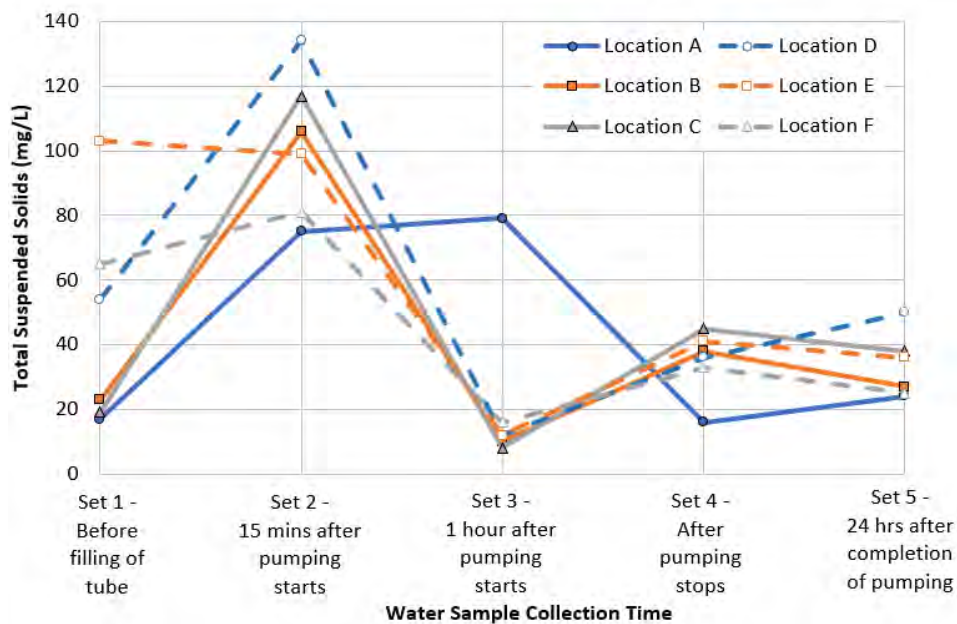


**Figure 10. Total suspended solid (TSS) at different collection time**

Set 1 (before filling) and Set 5 (24hrs after completion of filling) TSS results are used to represent the water quality at the site when there are no filling activities. From the results, it is observed that there is a significant increase in TSS value at 15 minutes after the filling started (Set 2). During the initial filling stage, it is expected that some fines will be washed out of the geotextile tube due to the dynamic loading from the hydraulic filling of sand. However, the water samples collected 1 hour after the filling started (Set 3) show that the TSS result dropped to below 20 mg/L except for the water sample collected at location A. This is likely because sand accumulation inside the geotextile tube over time forms a natural filter layer around the circumference of the tube that reduces the piping out of fines through the geotextile material.

The results also indicate that the TSS at 31 m away from the geotextile tube may not be lower than the TSS at 1 m away from the tubes at some locations (e.g., location D vs location A).

This is possible due to wave action during to the infilling stage.

In summary, the amount of TSS in the area around the geotextile tube may go up to 80-140 mg/L at about 15 min – 1 hour after the start of infilling operation. However, the TSS stabilized to about 20-50 mg/L when the infilling operations stop which is basically the original condition. Thus, throughout the filling process of the geotextile tube, the TSS of the surrounding water is kept at a relatively low concentration except during the initial filling stage.

## CONCLUSION

This paper introduces a new installation method for submerged, sand slurry filled geotextile tubes. It was found that the new method is cost efficient, fast and safe. In preparation for the construction project, preparatory tests and checks were also done on the material and stability. Material strength of the geotextiles and the inlet port design were found to be sufficient for the requirements of the site. Stability checks also show that the geotextile pore size and geotextile tube design satisfy the design criteria. Site monitoring of total suspended solids show that the largest amount of observed TSS is within the first 15 minutes to 1 hour of infilling, after which it drops to the pre-filling levels and remains stable.

## REFERENCES

- Bezuijen, A. and Vastenburg, E. (2013). *Geosystem: Design Rules and Applications*, CRC Press, Boca Raton, Florida, United States.
- Yee, T.W. (2016). Geotextile Filters and Containment Systems for Riverbank and Coastal Erosion Protection in Asia, 6th Asian Regional Conference on Geosynthetics - Geosynthetics for Infrastructure Development, New Delhi, India.

## Shoreline Protection in Kerala Coastline (India) and Use of Geosynthetics

**T. G. Antony Balan, Ph.D., P.E.<sup>1</sup>**

<sup>1</sup> Central Water Commission, India and Karunya University, Coimbatore, India; D-8,  
Kutralam Nagar Extn, Kovaipudur Post Office, Coimbatore 641042; e-mail:  
thadicaran@hotmail.com.

### ABSTRACT

India has a long coastline of 7516.6 km spread along the nine maritime States and four Union Territories, out of which 5422.60 km is that of the country's mainland. The coastline of Kerala State is 569.70 km, out of which 480 km is protected by constructed seawalls, mainly by that of the rubble mount type seawalls. The efficacy of seawalls in protecting life and property of the coastal regions of Kerala which has high population density and oversees economic activities of high value is well documented. The programme of construction of these seawalls in Kerala started in 1962 and was in good progress for over two decades, but later the enthusiasm tapered off. Many of these structures need renovation / remodelling now. In this paper, some recently executed (pilot) projects of geosynthetic-tubes and geosynthetic-bags in coastal protection works are presented with photographs from actual locations. The paper discusses some of the issues encountered while proposing seawalls using geosynthetic-tubes as a substitute to rubble-mount seawalls.

**Key Words:** Coastal Protection, the Malabar Coastline, Seawalls, Groynes, Geosynthetic Bags, Geosynthetic Tubes.

### INTRODUCTION

India has a long coastline of 7516.6 km spread along the nine maritime States and four Union Territories, out of which 5422.60 km coastline is that of the country's mainland. The coastline of Kerala State is 569.70 km, out of which 480 km is protected by constructed-seawalls (mainly by that of the rubble-mount type seawalls). The coastal region of Kerala (also known as Malabar Coast) has high population density and oversees economic activities of high value. The efficacy of seawalls in protecting life and property of this region is well documented. The programme of construction of these seawalls in Kerala started in 1962 (with the III<sup>rd</sup> Five Year Plan of India) and had been in good progress for over two decades, but later the enthusiasm tapered off. Many of these structures need renovation / remodelling now.

The mainland coastline in India is unintended and generally emergent. The West Coast is exposed with heavy surf and rocky shores while the East Coast is relatively low lying with exclusive alluvial plains, shelving and beaches, lagoons, deltas and marshes. Thus, Indian Coast is very diverse in its geomorphic features. **Figure 1** is a map titled Coastline of India and Coastal Plains of India (sourced from [www.pmfiias.com](http://www.pmfiias.com)) and depicts the extent of these alluvial plains. Indian coast is endowed with a wide range of coastal ecosystems like mangroves, coral reefs, sea grasses, salt marshes, sand dunes, estuaries etc., which are generally characterised by distinct biotic and abiotic properties and processes.

The landform features of Kerala, one of the southern-most states of India, comprise of highlands slopping down from the Western Ghats, midlands made up of undulating hills and valleys and lowlands or the coastal areas made up of river deltas, backwaters (lagoons) and the shore of Arabian Sea. The coastal-belt of Kerala consists of narrow longitudinal barrier strip of low-lying land, sandwiched between the Arabian Sea and continuous chain of lagoons and



Figure 1. Coastline of India | Coastal Plains of India  
(Source: [www.pmfias.com](http://www.pmfias.com))

backwaters with river outlets at several points. The width of this strip is even less than a few hundred meters at many places. The state has as many as 41 rivers flowing west into the Arabian Sea. But, since many of them drain into backwaters (lagoons) before entering the sea, the sea is deprived of the much-required nutrient-rich sediment material. Geologically, the coast is made up of recent sediments consisting alluvial deposits yet to reach equilibrium conditions. The foreshore is steep with slopes varying from 1:5 to 1:10. As a result, during rough seas and high waves, large quantities of beach material are eroded.

The state has the maximum concentration of population in the coastal areas. **Figure 2** is an aerial photograph of Neerkunnam Reach, Alappuzha District, Kerala (Photograph: April 2018). The density of the population that live here in the coastal-belt and the proximity to the beach is visible in the photograph. The specific feature of interest in the picture to this paper is the 100m long geosynthetic-tube structure built as a pilot project at Neerkunnam (for protecting the area from sea-erosion) which is functioning well.

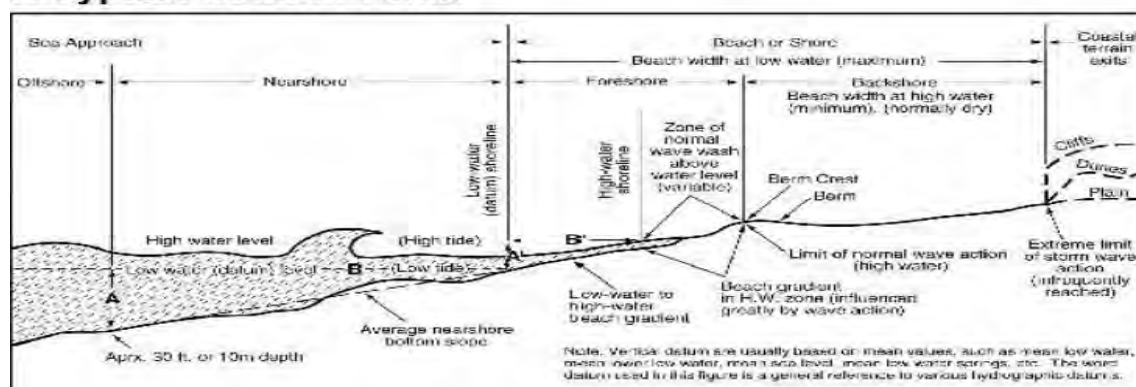


Figure 2. Aerial Photograph of Coastal Reach at Neerkunnam, Alappuzha District, Kerala (Photograph: April 2018) . (Source: KIIDC 2018)



Coastal area encompasses both the land-side and the sea-side. Generally, the areas in the coastal zone are mostly made up of sediment-material of the land brought by the rivers and deposited at the point where the river outfall into the shallow waters of the sea, the movement of these sediments are further caused through the near-shore activity of the sea by wave action and littoral-drift. Sandbars and shoals are also shaped and reshaped by the same activity of the sea. **Figure-3** is a “Visual definition of terms describing a typical beach profile” sourced from internet, explaining the technical terminology associated with coastal engineering. An authentic definition sketch is available as Figure 1-1 at page 2 of the “The Shore Protection Manual” by US Army Corps (1984). The coastal processes that occur at on both the seaside and the landside of the coast mentioned above are depicted in the figure.

### A Typical Beach Profile



**Figure 3. Visual Definition Sketch of a Typical Beach Profile**  
(Source: Internet & US Army Corps (1984))

The coastal processes are dynamic in nature. The coastal processes both offshore and onshore are predominantly dictated by the location specific dynamics of the sea waves and the sediment characteristics. The seaside is constantly acted upon by action by rain, wind, waves and tides, and periodically by cyclones and monsoons, and also occasionally by tsunami and earthquakes. Wave determines the composition and geometry of beaches, since wave interact with human, shore-structures and off-shore structures, safe design of these structures depends to a large extent on the selected wave characteristics. The structural stability criteria are often stated in terms of extreme environmental conditions (wave heights, periods, water levels, astronomical tides, storm surges, tsunamis, and winds).

The shoreline is constantly affected by the littoral-drift and sediment movement along the shore depending on the predominant wind and wave directions. The sea in the coastal areas require a certain amount of beach material (sand) to be held in suspension all the time, to contain the kinetic energy of the waves at any given point of time. During the monsoon months, the sea is generally turbulent, and the high energy of the waves keep the sediment in suspension. The shoreline needs to supply required additional amount of sand as and when the kinetic energy of the sea is high. During the non-monsoon months, the wave energy is low, and the sea recedes adding fresh additional width to existing beaches. Beaches form the first line of defence against the waves and are constantly moving on-shore, offshore and along-shore (littoral-drift). The shoreline behaviour is very complex and difficult to understand, and it cannot be expressed by equations because many of the processes are site-specific.

Information on beach profile is essential in designing structural modifications, such as, seawalls, revetments, and breakwaters both connected and detached. Many researchers have developed equations that can represent many beach profiles expressing the water depth ( $h$ ) at a point as a function of the distance of the point offshore. Longshore sediment transport ( $Q$ )

is the volumetric rate of sand movements parallel to the shoreline. Much longshore transport occurs in the surf zone and is caused by approach of wave at an angle to the shoreline. Longshore sediment transport ( $Q$ ) is assumed to depend on the longshore component of wave energy flux ( $P_{ls}$ ). Threshold of sand movement by waves action has been investigated by a number of researchers and have given various empirical expressions. ‘Modified Shield’s Diagram’ depicts the works of various researchers in this field. Wave forces act on fixed coastal and offshore structures; the forces may be classified as due to non-breaking waves, breaking waves, broken waves. Fixed coastal structures include (a) wall-type structures such as seawalls, bulkheads, revetments, and certain type of breakwaters, and (b) rubble structures such as breakwaters, groynes, and revetments. For more detailed information on the topic, one may refer to Figures 84-5 to 84-8 of J. B. Herbich (2004), namely: Chapter on “Shallow Water and Deep-Water Engineering”, Section XIII of “The Engineering Handbook” Edited by Richard C. Dorf (Editor-in-Chief).

## COASTAL PROTECTION WORKS

Coastal protection works that were implemented in Kerala over the last few decades can be grouped into three categories: Hard measures, immediate measures, and soft measures. The protection works such as Rubble-mount Seawalls and Groynes are of a permanent nature (those with 50 years designed service-life) and fall in the category of hard measures. By Public Works Department of State Government (PWD) nomenclature, those measures with 5 to 20 year as designed service-life, such as: jute-bags, geo-textiles, geosynthetic-bags and geosynthetic-tubes, are the immediate / temporary measures, and are taken up to cover the gestation period while awaiting planning, financing and implementing more long-term solutions. After the Tsunami (2004), there were clamour for also considering side-by-side the soft solutions such as: Bio-shield, Sand Nourishment, Coastal Regulation Zoning (as per 1991 Act), Mangrove Forests *etc.* Out of these solutions, we are discussing in this paper, only three measures that were recently implemented by the Kerala Irrigation Infrastructure Development Corporation, a Government of Kerala Undertaking (KIIDC) and the Irrigation Department of Government of Kerala (KID), namely, the traditional rubble-mount seawalls, the geosynthetic-tubes and the geotextile bags,

**Rubble-Mount Seawalls (with Tetrapod as Armour Layer).** The Central Water and Power Engineering Research Station, Pune (CWPRS) is a premier organization under the Ministry of Water Resources, River Development & Ganga Rejuvenation (MoWR, RD & GR) and has been leaders in the coastal engineering discipline since long. In the 1960’s, when Kerala implemented coastal protection using rubble-mount seawalls on a large-scale (480 km out of a coastline of 569.70 km), the typical design profile of seawall--suitable for Kerala coast beach-profile--was specifically developed by CWPRS after physical modelling in their laboratory at Pune, and this profile was extensively used. The experience of past six decades show that the designs were robust and a standing testimony to the expertise of CWPRS in the field. For rubble mounted breakwaters, the weight of the individual stones in the armour layer is the primary criterion for the design. The ability of the construction agency to handle such large-stones in the work-spot has been the limiting factor in the choice of the protection measure adopted at a given location. Kerala falls in the equatorial regions (Latitude:  $8^{\circ} 17' N$  --  $12^{\circ} 45' N$ ) where the tidal variation is small (Mean High Water Level is only + EL 1.20 m (MSL). The CWPRS designs (1960s) of seawalls provided a Crest Height up-to + EL 2.50 m (MSL). The gradual rise of mean-sea-level (MSL) globally has necessitated re-evaluation of the Seawall Crest Height (now) to +4.00 m (MSL) for effective protection of the habitat behind the seawalls.

Advances in mathematical modelling has now made such headways in simulating and modelling physical processes that it has rendered physical modelling of coastal processes a thing of the past. CWPRS, Indian Institute of Technology, Madras (IITM), and National Institute for Ocean Technology (NIOT), all have robust expertise in modelling coastal processes using computational models, in various aspects of the phenomenon. **Figure 4** shows the typical cross section for a sea wall designed by IITM for the CP 1028 to CP 1032 Reach of NEERKUNNAM Coast in ALAPPUZHA (Kerala). The typical seawall as per design consists of the following components: (1) a geofabric filter layer at the bottom, (2) a layer with 10-50 kg stones (intermediate size stones), (3) a layer with 150-200 kg stones (large size stones), and (4) on the top an armour layer of stones of specified design size or of concrete tetrapod of design weight or size. A typical seawall design has (a) the main body of the seawall (b) a launching apron on the seaside, and (c) a drainage channel on the landside. The design parameters are: (1) Top of Armour Layer (EL) = +6m, (2) Existing Beach Profile (EL) = +3m, (3) Mean Highwater Level (EL) = +1.2m, (4) Launching Apron Crest (EL) = +0.0m, Weight of Armour Unit (**W**) as per Hudson's Formula  $\frac{\rho g H^3}{K_s \Delta^2 \cot a} = 2 \text{ T}$ .

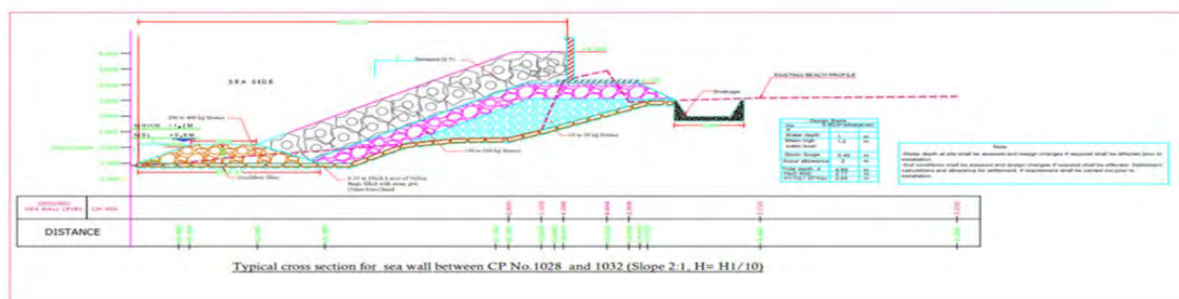


**Figure 4. A Typical Cross Section of Rubble-Mount Seawall With 2T Tetrapod as Armour Layer. Designs By IITM 2021. (Source: KIIDC 2021)**

The Chellanam Reach of the coast has been under severe attack by the sea in recent years (2018-2022). **Figure 5** is a photograph--taken on 30.11.2022 during author's visit to the site--of a portion of the reach where a rubble -mount sea wall is currently under reconstruction and reformation as per the IITM design. The seawall is provided with an armour layer of concrete-tetrapod of 2T weight. Of specific interest to the IGS Forum, is the specifications of the geofabric filter layer provided in design (see Figure 4) at the bottom of the seawall. The specifications in the contract document is reproduced here "...Providing filter of sea wall with woven fabric filter GWT-26-130 weight not less than 130gm/m<sup>2</sup> pore size (mm) less than 0.075 with and overlap of 30cm at all joints stitched together pulled up into folds uniformly and sufficiently in both direction for avoiding extension..."





**Figure 5. A Rubble-Mount Seawall with Concrete Tetrapod as Armour Layer Reach Under Construction at Challam Coast (Nov 2022). (Source: KID 2022)**

**Geosynthetic Tubes.** Geotextile tubes are basically containment systems in tubular forms filled with locally available sand which are formed in-situ on land or in water to protect shore and marine environments. It is in tubular shape made of geo-textile and is generally filled with sand or dredged material. These tubes are generally about 1 m to 3 m in diameter, though they can be customised to any size depending on their application. Today geotextile tubes ranging in diameters from 1.5 m to 5.0 m are used in many coastal and flood protection applications.

Ganga Flood Control Commission, Patna (September 2016), a Government of India organization under the Ministry of Water Resource, River Development & Ganga Rejuvenation (GFCC), had come out with a publication “Guidelines for Use of Geotextiles/ Geotextile bag/ Geotextile tubes in construction of Flood Management Works” (GFCC 2016). **Figure 6** is a “Typical Design Layout of Geo-Tube Structure” from that reference wherein a 3-tier structure using 6 geo-tubes are used.



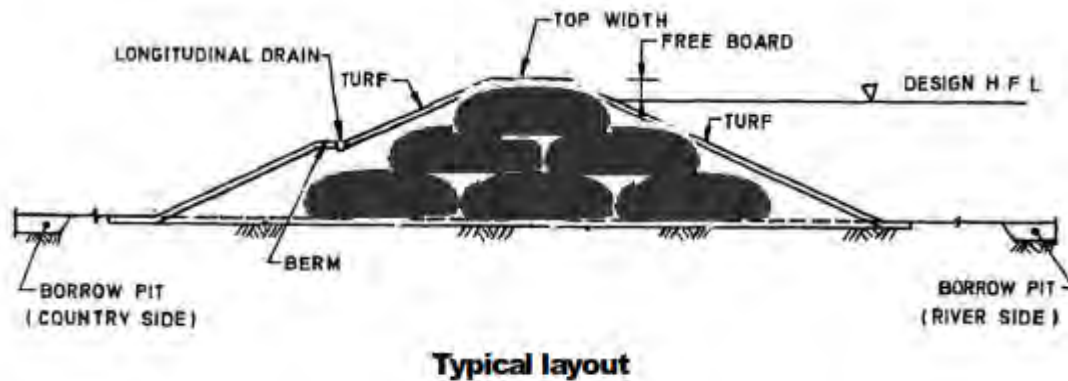
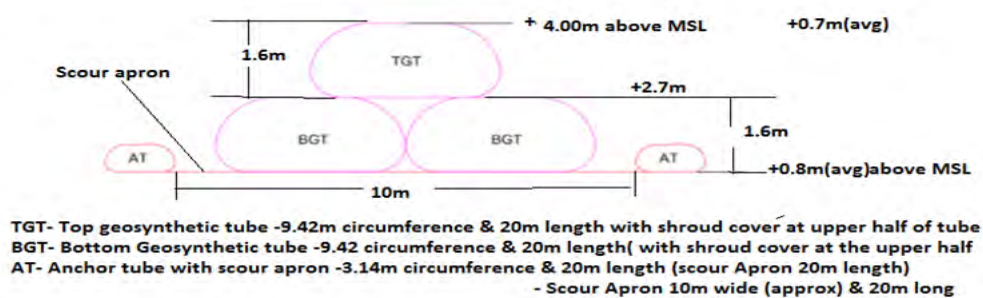
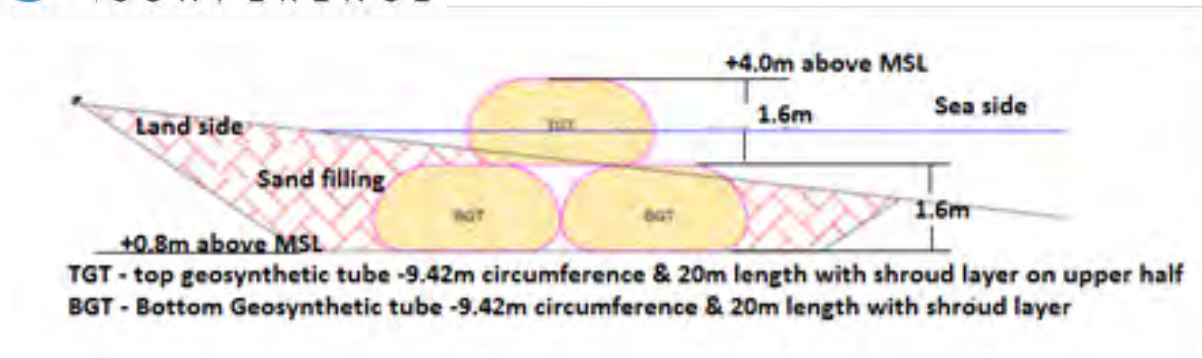


**Figure 6. Typical Layout of Geotextile Tube Structure for Groynes.**  
(Source: GFCC 2016)

Proposals for Construction of Groyne-Field in Ambalapuzha of Alapuzha District, Kerala (Chainage 77.300km to 82.740km) were taken up in 2016, as a permanent solution to the persistent coastal erosion problems of Ambalapuzha Coast. The designers (IITM) proposed construction of a “groynes-field” consisting of 30 groynes of varying lengths (5 X 20 M, 7 X 30 M, 9 X 40 M, 9 X 50 M) using rubble-stones covering 5400 M of coastline. KIIDC, the implementing agency, drawing inspiration and guidance from the GFCC Guidelines (2016), proposed the use of Geosynthetic-Tubes in place of the rubble-stones; and, utilizing the IIM designs of seawalls, prepared a proposal/ detailed project report for consideration under Kerala Infrastructure Finance Bank a Government of Kerala Undertaking KIFB) funded projects. **Figures 7 & 8** are the typical layouts of coastal protection structures comprising of groynes (Figure 7) and seawalls (Figure 8) to be built using geosynthetic tubes as envisaged in this project. The crest height is EL + 4.0m (above MSL). This is a 2-tier 3-geosynthetic tube structure (with an additional anchor-tube of smaller diameter on the seaside to replace the launching apron in the conventional CWPRS seawall design profile for Kerala Coast.



**Figures 7. Typical Layout of Coastal Protection Structures Using Geotextile Tubes for Groynes, at Proposed Project at Ambalapuzha Reach. (Source: KIIDC 2018)**



**Figures 8. Typical Layout of Coastal Protection Structures Using Geotextile Tubes for Seawalls. Proposed Project at Ambalapuzha Reach. (Source: KIIDC 2018)**

The geotextile tubes in the main formation are of +9.42 M circumference and 20 m in length with shroud cover at upper half of tube. The smaller anchor tubes are with +3.14 M circumference and 20 m in length. The geotextile tubes when placed in the formation shown in the Figures 7 & 8, form a 3.2 M high embankment (i.e., 1.6 M / layer). The geotextile specifications (as given at Sections 8.3 to 8.5 of the Guidelines (p64-68)) cover the following properties: (1) Geotextile tube strength requirements, (2) Drainage requirements, (3) Environmental considerations, and (4) Construability requirements. The 3m diameter and 20m long geotextile has mechanical properties (Warp/Weft) as 80/70 KN/m and hydraulic properties as 18 l/m<sup>2</sup>/s permeability. The Indian Standard (IS) and American Standard (ASTM) Codes are also given in the Guidelines (p 65).

Two examples of implementing geosynthetic-tubes as pilot projects for coastal protection (2018-22) could be identified in informal discussions with KIIDC and KID officials. **Figures 9 & 10** are photographs of coastal protection works involving these geosynthetic-tubes executed by KID and KIIDC. Figure 9 is recent photograph of geosynthetic tubes at Vypeen Reach. Figure 10 as well as the areal-photograph at Figure 2 introduced earlier, covers the Neerkunnam Beach, Alappuzha, which was a pilot project to test-out the efficacy of geosynthetic-tubes in the coastal settings.



**Figure 9. Geosynthetic Tubes as Seawalls for Coastal Protection, at Vypeen Reach. (Source: KID)**



**Figure 10. Geosynthetic Tubes as Seawalls for Coastal Protection, Pilot project at Neerkunnam Beach, Alappuzha (2018). (Source: KIIDC)**

**Geotextile Bags.** Sand filled in Jute Bags have been used by local communities in protection works against the fury of river/sea for centuries now. This is an immediate measure that the people in the locality resort to in case of sudden attack of sea in a vulnerable area of the beach. The measure is highly labour intensive, and a lot of volunteering work is contributed by calamity affected people themselves. No high technological skills are required. The measure may protect the valuable structures immediately behind, such as dwelling-houses or essential road communications. The protection may last for one season after which it may be strengthened periodically for the sinking of the walls.

Apart from the construction of rubble mount seawalls for permanent protection from sea erosion, KID, the mandated agency in Kerala State, also resort to use of geotextile bags as a coastal protection measure of immediate nature in vulnerable areas. Of-late, the Jute-Bags are replaced by more durable and larger capacity ‘Geotextile Bags’ made of geosynthetic material, a manufactured industrial product. The Geo-Bags (2m X 1m X 0.35m) when filled with beach sand, become sandbags of 1.8m X 0.8m X 0.30m) overall dimensions. For filling 100 m of the wall, 522.72 m<sup>3</sup> beach sand is required for erecting a 4m wide X 1.2m high wall. The bags are stacked in “Flemish Bond” pattern to form the wall. **Figure 11** shows photographs of coastal protection works done by Irrigation Department (KID) using geotextile bags as temporary protection during 2018-2021 in the Vypeen to Kannamaly Reach of the Kerala Coast (2021-2022). KID has been implementing geotextile bags as immediate (means temporary) measure and seawalls as permanent (means long-term) measure.

**Figure 11. Two Photographs of Geotextile Bags as Temporary Coastal Protection Works. (Source: KID 2021-22)**





Strategies aimed at protecting coastal areas of high value economic activity are vastly different from those coastal areas with negligible or no economic activity. While important coastal infrastructure / facilities (such as: harbours and ports, rail-terminals, land stretches that has national highways, communication lines and pipelines, urban centres and urban residential housing) are secured with (permanent) protection by seawalls / groynes (crest level +6m MSL); and rural habitats are protected by seawalls / geosynthetic-tubes (crest level +4m MSL); the general coastline---tourist beaches, mangrove forests and river estuaries---can be left undisturbed for natural processes to shape and reshape the shoreline. Also, the geomorphological features of the coastline greatly influence the type of (human) engineering interventions on nature.

For the purpose of discussion on strategies, a number of factors play a predominant role. These are: [\*] Importance of the facility protected, [\*] Risk to human life and property, [\*] Cost and serviceability of protection measures, [\*] Geomorphology of the coastline, [\*] Demographic features, [\*] Fund availability (one-time/budget-support), [\*] Legal framework and right to property, [\*] Technological capability of the executing agency, [\*] Support services availability (PMA/ Designs/ Modelling facilities/ PRA), [\*] Regulatory Acts and Environmental Regulations in force, [\*] Law and order situation, [\*] Beneficiary interest and perceptions about the efficacy of protection, and, [\*] The polity: democratic/authoritarian. Some of the author's observations and recommendations borne out of his experience are also included in the last part of discussions.

**Infrastructure.** Coastal areas that have high economic value need a higher level of protection against coastal erosion. Institutions (such as: Port Authorities, National Highway Authorities, *etc.*) that plan, construct and manage such facilities, are generally **well-funded**, and can support a higher level of protection to the infrastructure (seawall/groynes with higher crest levels).

**PWD Jurisdiction.** The Public Works Departments of the maritime states (PWD) are generally mandated with overall coastline management. Generally, the shorelines under PWD jurisdiction exclude areas that are owned and managed by the high-economic-value infrastructure-agencies mentioned previously. The coastlines that are managed by PWD are those of tourist beaches or those areas where the fishermen community are active. In the PWD nomenclature, those structures that last 50 years (service-life) are 'permanent structures' and those that last 20 years and less are classified as 'temporary structures'. Seawalls and groynes built of rubble-mount, concrete tetrapods are considered as permanent structures, whereas seawalls and groynes built of geosynthetic material such as: geo-bags, geo-textiles, and geotextile tubes are considered as temporary structures, because of the manufacturer performance guarantees of 20 years for these industrial products. The temporary walls built of geotextile-bags are expected to last only 1-5 seasons. Thus, bulk of the shoreline is mandated to be protected by the PWD with their project-funding made available through regular annual budget-support.

**Demographic features and risk to human life.** Since the coastal area in Kerela supports high population density, and residential properties almost touch the built-seawalls, periodical and seasonal erosion of the coastline is a major issue that touch the day-to-day life and economic activity of the people living in the coastal belt. Ever-since the 1960's when rubble-mount seawalls were constructed at public cost along the Kerala Coast, the general-public felt an increased sense of security and constructed permanent dwelling units--in place of their



temporary shelters as homesteads--much closer to the shoreline and almost touching the seawalls.

**CRZ.** As per the Coastal Regulation Zoning, (CRZ Act 1991), new construction and dwelling units are not permitted in the CRZ. The present way-of-life in the coastal belt is to live in individual homes built in their own homesteads. The population that resides close to the shoreline or the seawall may have to be relocated to safer places at public cost.

**Perceptions (Beneficiary / PWD).** The local population always crave for permanent solution to their problem, without resorting to re-location. They believe that the seawall along-with a series of groynes will give them a permanent protection to their land and property, whereas all other solutions are those that will give them only relief of a temporary nature or at best for a few seasons or for a few years. Generally, PWD prefer to choose a material or a method of construction that can withstand vandalism to a large extent. Both these perceptions are non-conducive to large-scale use of geosynthetic tubes supported coastal protection structures. Scientific studies and greater thrust at public education can change these perceptions to a large extent, in future.

**Existing network of seawalls.** The existing network of seawalls undertaken in the 1960's had few deficiencies. [1] In many stretches, there were gaps left in continuity of the seawalls, some deliberately for fishermen to land their ships/boats and some inadvertently due to funding uncertainties and construction phasing. These 'fishing-gaps' have been a source of shoreline changes due to entry of sea into these areas in its eroding phase. [2] The geotextile filter layer at the bottom of these seawalls shown in the design profiles, is non-existent in many reaches and this results in sinking of the seawall with passage of time. [3] The drainage network on the landside of the seawall and connecting it to proper drainage routes for evacuating the salt-water out to the sea in many cases is either non-existent /unserviceable or omitted when the project was originally taken up. These deficiencies need to be rectified when renovations of these seawalls are taken up.

**Law and Order.** Encroachment for private gain and vandalism of public property for no gain, both result in loss of public wealth and early deterioration of the built infrastructure. Vandalism affects both rubble-mount seawalls and geotextile tubes. In the case of rubble-mount and stone-crates seawalls, it is the theft of the stones from the walls. In the case of the geotextile tubes, it is the piercing of the synthetic lining material. Vandalism particularly affects geosynthetic-tubes, because if no timely repairs are affected, the damage progressively increases resulting in the failure of the structure. If there are sufficient disincentives from the legal and administrative machinery to such encroachments, this evil can be contained to a large extent.

In conclusion, author recommends use of geosynthetic tubes to manage the shoreline either in the form of seawalls (parallel to the beach) or groynes (at an angle to the beach) that are properly planned and executed. The author also recommends the site-specific study of coastal processes using computer models, before taking up protection works or deciding on the choice of type of protection.

An overview of the recent coastal protection activities in State of Kerala in India is presented. Even though 480 km out of 569.70 km of the coastline was protected by constructed-seawalls since the 3<sup>rd</sup> Five-Year-Plan of India (1962), many of these structures need renovation now. Also, due to global warming and resulting change in the mean-sea-level (MSL), the coastal protection works have now to be reworked by raising the crest level of seawalls from EL +2.5M (MSL) to +4.0 M (MSL). The paper presents three recent examples of coastal protection structures using concrete-tetrapod, geotextile-bags and few pilot projects of geotextile tubes; and advocates, increased use of geosynthetics for the future works. The author strongly advocates the use of computational models for simulating / predicting coastal processes and for accessing the efficacy of proposed measures, before embarking on their implementation. Also, the author strongly advocates restructuring the land-use in the CRZ to improve the multidimensional indices of living standards of fishermen community whose livelihood is closely associated with the coastal area, and at the same time, the interventions in the form of engineering works are carried out in right earnest (in letter and spirit) with the best professional knowledge available.

## REFERENCES

- GFCC. (2016). Ganga Flood Control Commission, Patna. “Guidelines for Use of Geotextiles/ Geotextile bag/ Geotextile Tubes in Construction of Flood Management Works”. A Government of India organization under the Ministry of Water Resource, River Development & Ganga Rejuvenation.
- Herbich., J. B. (2004). Chapter on “Shallow Water and Deep Water Engineering”, Section XIII “*The Engineering Handbook*” by Richard C. Dorf (Editor-in-Chief).
- Internet Sources: [www.pmfias.com](http://www.pmfias.com)
- KID. (2021). Kerala Irrigation Department. Information Brochure. “Temporary protection work using Geo-Bag (a) at Pazhangad in Edavanakkad and (b) at Chellanam Beach.”
- KIIDC. (2018). “Detailed Project Report on Construction of Groyne Field in Ambalapuzha of Alapuzha District, Kerala (Chainage 77.300km to 82.740km)”.
- Thadicionar, Antony Balan T. G., Dr. (2005). Chief Engineer, Cauvery and Southern Rivers Organization, Central Water Commission, Coimbatore, India. “Recent Tsunami impact on peninsular India coastline and performance of coastal protection works”. Invited Lecture. Presented at CBIP, New Delhi.
- Thadicionar, Antony Balan, T. G., Dr. (2011). Tsunami impact and coastal protection works, Presented at National Seminar on “*Tsunami Resistant Structures and its Design in Steel and Concrete*” Sponsored by Ministry of Earth Sciences, held on 28-29 December 2011 at Sri Krishna College of Technology, Kovaipudur, Coimbatore, India.
- US Army Corps. (1984). “*Shore Protection Manual*”.

**NOTATIONS**

<b>CWC :</b>	Central Water Commission
<b>CWPRS :</b>	Central Water and Power Research Station
<b>EL :</b>	Elevation (MSL)
<b>GFCC :</b>	Ganga Flood Control Commission
<b>GOI :</b>	Government of India
<b>IITM :</b>	Indian Institute of Technology, Madras
<b>KID :</b>	Irrigation Department of Government of Kerala
<b>KIFB :</b>	Kerala Infrastructure Finance Bank (Government of Kerala Undertaking).
<b>KIIDC :</b>	Kerala Irrigation Infrastructure Development Corporation, (Govt of Kerala)
<b>MoWR,RD&amp;GR:</b>	Ministry of Water Resources, River Development and Ganga Rejuvenation
<b>MSL :</b>	Mean Sea Level
<b>NIOT :</b>	National Institute for Ocean Technology, Goa
<b>PWD :</b>	Public Works Department of State Government

## Emerging Uses of Geosynthetic Floating Covers in the Energy Sector

Alex Gersch,<sup>1</sup>

<sup>1</sup>Layfield Australia, Glenelg North, SA, Australia; e-mail: [alex.gersch@layfieldgroup.com](mailto:alex.gersch@layfieldgroup.com)

### ABSTRACT

There are emerging applications in the energy sector, adapting geosynthetic floating cover technology for various renewable energy processes, including generation, storage and saving functions. Climate change has seen a significant focus on renewable energy generation and storage, carbon emission reduction, conserving water resources, and reducing the environmental impact of the energy industry. Water utilities have significant experience with floating covers in reducing the energy required in water treatment and to capture biogas at wastewater treatment plants. Utilities are now combining floating cover and photovoltaic solar power knowledge to transition to become energy generators rather than energy consumers. Large scale energy storage applications are now emerging using heated and chilled liquid storages, with insulated floating covers. This thermal energy is being used to generate electricity through an Organic Rankin Cycle engine or to provide direct heating. Trends are also changing in the oil and gas industry and floating covers are increasingly being used by the industry to reduce energy consumption and to protect water and the environment. This paper discusses the current applications, current developments, and future trends.

### INTRODUCTION

Geosynthetic floating cover technology has been accepted by water utilities throughout the world as an economical solution to protect the quality of potable water since the late 1960's (Gersch, 2019). In the 1980's the technology was adapted for odor control on wastewater impoundments. The odor control cover technology was then adapted very quickly to accommodate the capture of biogas, which was seen as a waste product and disposed of in flares. As global climate studies gave a better understanding of the atmospheric warming effect of methane, the biogas cover was adapted to suit re-use of the biogas in boilers and electrical co-generation plants.

Climate change has seen more severe weather events. Longer, more severe droughts have been occurring in both northern and southern hemispheres and are generating more demand for covers to conserve water, particularly in the energy sector. Water conservation in the traditional energy sector has come under scrutiny and the use floating covers for evaporation control are becoming more widespread. The same influence of climate change has also driven more severe storms, particularly in equatorial regions. Rainwater can become contaminated in process water storages and can affect water chemistry of the process water and an increase in demand for rain collection covers has again been witnessed in the energy sector, particularly in sub-tropical and tropical regions. During reviews of available areas for installation of photo voltaic solar panel installations, water storages have been identified as ideal locations with large, unshaded areas, often located close to electrical transmission networks, and often located adjacent high energy intensity industries. With Government and Corporate focus on achieving net zero carbon emissions, the investment in renewable energy generation globally has increased, and floating



solar has become increasingly adopted where existing land usage limits available alternative options. Emerging renewable energy technologies using large scale thermal energy storage will see the adaption of floating cover technology once again. The timeline of adoption of floating covers in various applications can be seen in Figure 1.

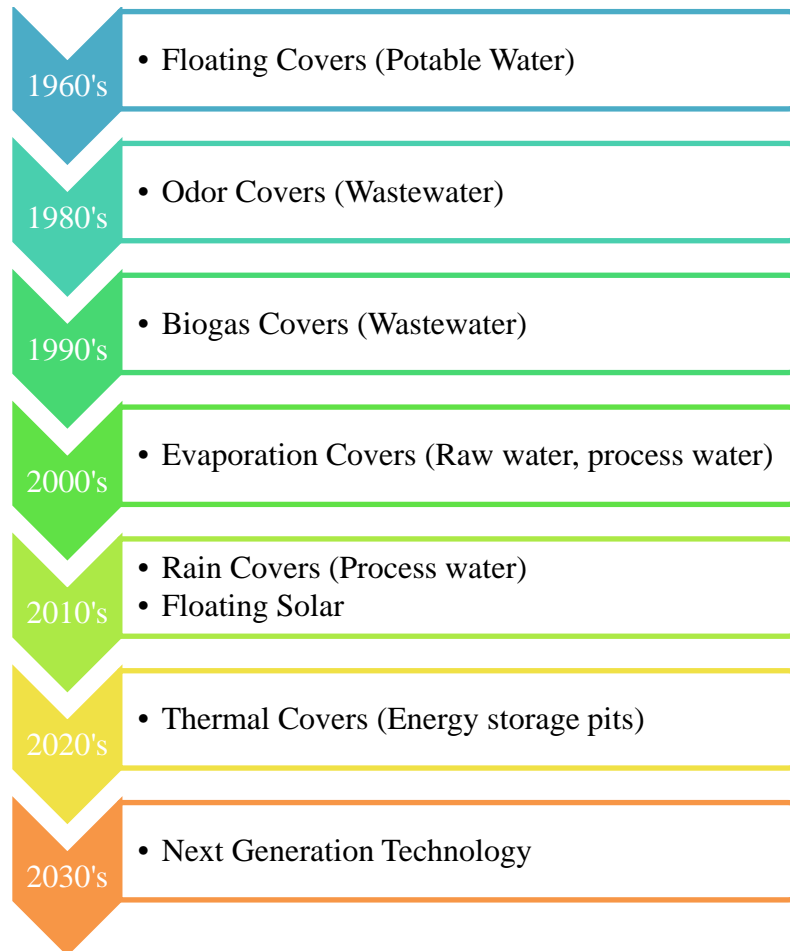


**Figure 1. Geosynthetic Floating Cover Adoption Timeline.**

## DISCUSSION

### Potable Water Covers:

The use of floating covers by water utilities has demonstrated the capacity to protect potable water from contamination, reduce chemical dosing of disinfectants, reduce water losses and therefore reducing pumping costs (Barry, 2007) (Spang, Manzor, and Loge, 2020). The use of floating covers in this sector is widely accepted and there is no need to discuss this application in this paper any further.

### Wastewater (Biogas) Covers:

Biogas is generally a mixture of methane, carbon dioxide and small quantities of other gases produced by anaerobic digestion of organic matter in an oxygen-free environment (FGI, 2022). The precise composition of biogas depends on the digestion process and the type of feedstock.

The potential for biogas production has been recognized for many years, however, it has been seen more as a bi-product of treating waste water rather than a resource. The capture of biogas from anaerobic lagoons at wastewater treatment plants has generally been used to appease neighboring communities by reduce obnoxious odors. It should be noted that biogas from municipal solid waste landfills have been managed in a similar way. An investigation by the International Energy Agency found of the potential 570 million tons of oil equivalent biogas generated globally, only 6% was being captured and used, leaving a huge potential resource yet to be exploited (International Energy Agency, 2020). Methane released into the atmosphere is 28 to 36 times more potent a greenhouse gas than carbon dioxide, absorbing much more energy while it exists in the atmosphere (International Energy Agency, 2021). As a result, Local, State and Federal Governments in various countries have enacted a mixture of incentives and regulatory requirements to promote the capture and beneficial re-use of biogas, either to provide heat energy for industrial applications or in electrical co-generation plants. An early adopter has been Melbourne Water at the Western Treatment Plant, processing unscreened raw municipal effluent using biological anaerobic and aerobic treatment processes. The two large anerobic lagoons are covered with geomembrane covers and captured methane is used to generate 70,000 megawatt hours of renewable electricity annually, making the treatment plant self-sufficient with excess power exported to the energy grid (refer Figure 2.). There are now numerous examples where wastewater treatment plants use biogas to power a substantial percentage of their electricity, heating, and cooling requirements on a smaller scale. Methane is now being seen as an energy source, rather than a waste bi-product, with even waste water channels now being covered to capture fugitive biogas emissions (refer Figure 3.).



**Figure 2. HDPE Floating cover on the anaerobic section of a wastewater treatment lagoon capturing biogas and eliminating odors. An energy company has an offtake agreement with the municipal water authority to use the gas to generate electricity. Victoria, Australia. (Image: Melbourne Water, 2021)**



**Figure 3. CSPE Floating cover on a channel at a Wastewater Treatment Plant capturing biogas and to eliminate odors. South Australia.**  
(Image: Google Earth 2018)

### Evaporation Covers:

In many locations around the world, annual evaporation rates are significantly higher than rainfall, for example, the majority of central Australia has annual evaporation rates over 3000mm while annual rainfall is in the vicinity of only 150mm (Australian Bureau of Meteorology, 2022), making evaporation losses a major factor in water supply. Average evaporation rates for oil and gas regions in Australia and North America are shown in Table 1. Evaporation losses exacerbate water license competition, higher water extraction costs, increased pumping energy requirements and increased likelihood of long-term environmental impact on ground water. Analysis of energy intensity for water sourcing, conveyancing, treatment and distribution by water companies average 610 kWh/million liters in a municipal setting (Young, 2015). Any savings in water use therefore result in meaningful energy savings.

**Table 1. Average Evaporation Rates for Oil & Gas regions in Australia and North America**

<b>Month</b>	<b>Moomba, South Australia (Australia) monthly (mm)</b>	<b>Roma, Queensland (Australia) monthly (mm)</b>	<b>Texas Water Development Board (USA) monthly (mm)</b>	<b>San Joaquin District, California (USA) monthly (mm)</b>
January	492.9	319.3	68.6	41.15
February	403.2	240.8	84.6	33.53
March	387.5	241.8	141.7	142.24
April	252	186	182.6	134.87
May	161.2	136.4	190.5	194.82
June	111	96	227.8	299.72
July	120.9	108.5	235.7	257.05
August	170.5	142.6	212.9	268.73
September	246	210	165.9	153.16
October	328.6	266.6	132.1	106.68
November	396	276	98.0	74.68
December	474.3	300.7	74.9	29.72
<b>ANNUAL TOTAL</b>	<b>3544.1</b>	<b>2524.7</b>	<b>1815.3</b>	<b>1736.3</b>

There is an emerging trend of using floating covers to conserve the water resource to eliminate losses due to evaporation, particularly in the exploration of oil and gas reserves, due to the direct cost of sourcing and supplying water, and to improve resource companies' environmental stewardship during exploration and development activities. Oil and gas companies have started to modify the use and operation of their infrastructure to move away from short term temporary uncovered storages at rig sites to more centralized medium term covered storages supplying water across larger distances to a network of drill sites (Fraser and Killian 2015). These storages tend to be in service for shorter durations than municipal water storages and are typically designed with budgetary considerations as per the example shown in Figure 4.



**Figure 4. 0.75mm proprietary polyolefin floating cover on a coal seam gas raw water storage to eliminate evaporation, reducing water supply and pumping costs. Texas, USA. (Image: Layfield Group)**

In addition to the adoption of floating covers in the more traditional energy industry, with global focus on renewable energy and storage, pumped hydro storages are increasingly being seen as a feasible method of achieving large energy storage, however in areas with net evaporation loss climates, evaporation covers are also being evaluated. The major challenge to be overcome in these types of applications will be the very high flow rates and volume changes and the associated hydraulic forces on the underside of the covers.

### **Rain Covers:**

A novel use of floating covers is emerging in the traditional Oil & Gas energy sector in sub-tropical and tropic equatorial regions. Typically, process water ponds in this sector of the energy industry contain traces of hydrocarbons, salts and other contaminants that require treatment. To reduce the water inventory requiring treatment, energy companies are installing rain covers prior



to the onset of the wet season, preventing rainfall from intermingling with the process water. The rainwater is discharged through stormwater infrastructure, and at the commencement of the dry season, the geosynthetic covers are removed. Due to the seasonal nature, the covers tend to be less complex fabricated from lighter weight geomembranes and have been adapted for earthen pits and tanks (refer Figure 5. and Figure 6.) The use of rain covers also maintains the water chemistry of the process water in applications where the chemistry is critical.



**Figure 5. 0.75mm proprietary polyolefin rain cover on a coal seam gas frac storage to eliminate rainfall intermingling with stored fracking liquid.**  
NT, Australia. (Image: MPC, 2018)



**Figure 6. 1.00mm proprietary polyolefin floating cover on syngas process water to eliminate odors and rainfall ingress.**  
Qld, Australia. (Image: A. Gersch, 2015)

### **Floating solar:**

Floating covers and pontoons are also being adapted to carry photovoltaic solar panels. This adaption has been a relatively simple process as it has simply merged two existing technologies, and while there are some additional capital costs over stand-alone technology there are several very distinct advantages with floating solar.

1. Floating solar utilizes existing open space and does not require allocation of land which would normally be used for other purposes.
2. Ponds and lagoons are generally very open and no shading from vegetation occurs on the PV modules.
3. There is no vegetation management required, typical of ground mounted solar PV installations.
4. The micro-climate over a large mass of water is cooler and therefore the P.V. modules operate at higher efficiency than roof mounted or ground mounted P.V. modules.
5. Many water storages are associated with energy intensive industries with high energy demand e.g. water treatment plants, and the power generated can either be used in these plants, or exported into the electricity network.

Open water floating solar (P.V. modules mounted on a network of pontoons) has been the most popular to date with over 250 installations in over 30 countries globally (refer Figures 7. and 8.). Many water users and water utilities are turning to this technology in their effort to achieve carbon neutral goals (Climate Action, 2017) and as cost efficiencies are being achieved through the widespread adoption of solar generation, capital costs have come down dramatically (PV Magazine USA, 2020).



**Figure 7. Open water floating solar (CN)**  
(Image: Climate Action, 2017)



**Figure 8. Open water floating solar (CN)**  
(Image: PV Magazine USA, 2020)

### **Insulated covers:**

Insulate covers are being used as a cost-effective way of reducing heat loss in open lagoons or tanks to either maintain biologic activity and as a very efficient way of storing excess energy. Biological wastewater treatment processes slow down with colder temperatures, and this can cause significant problems in cold climates. Insulated covers have been installed on waste water lagoons to reduce temperature loss and maintain biological activity through the winter months.

An emerging technology is to store excess energy in thermal pits by heating water up to 90°C. The hot water is then used at a later time, either as a direct heat source for industrial or municipal applications (AalborgCSP, 2019). To efficiently store the water, heavily insulated covers are required to maintain the energy in storage pits. This requires the use of specialized high temperature polyolefin materials suitable for continuous operating temperatures above 80 deg C, and chemically resistant to the corrosion inhibitors and disinfectants typically used in these types of application.

A unique application of this technology is currently being adapted in Australia, essentially using the thermal pits as a heat battery for thermal hydroelectric power generation. During daylight hours a mirror array focusses sunlight on high efficiency photovoltaic cells generating electricity. The PV cells are water cooled with the heat generated being stored in a large thermal pit, while electricity generated by the PV cells is either dispatched into the electricity grid or used to chill water in a second thermal pit. During periods of low solar irradiance or at night, the thermal energy differential from the hot and cold pits is used to generate dispatchable electricity using an organic Rankine cycle engine. Thermal Hydro is a low cost, large scale, long duration energy storage system. The system relies heavily on geosynthetic geomembrane materials capable of withstanding hot (or cold) continuous operating conditions, high UV exposure on the top surface of the covers, and incorporating substantial thermal insulation properties (Fairhead and Pece, 2022).





**Figure 9. Bi-modal HDPE insulated floating cover on a thermal pit storing hot water for power generation using a thermally driven Organic Rankine Cycle (ORC) engine. Victoria, Australia.**  
(Image: Raygen, 2021).



**Figure 10. Insulated floating cover on a hot water thermal pit. Marstal, Denmark.**  
(Image: AalborgCSP, 2019).

## CONCLUSION

While floating covers have been used for the last five decades in protection of water and the environment, there has been significant growth in the adoption of floating cover technology in various energy applications, both in the traditional energy sector and with emerging energy generators. While fossil fuel consumption is expected to decline as the world transitions to renewable energy sources, the oil and gas industry is embracing floating covers to reduce the carbon footprint associated with exploration and extraction and to improve their environmental stewardship. The biogas industry has also embraced floating covers to capture and store biogas. The IEA estimates the industry is set to grow 40% over the period to 2040 as every region around

the world has significant scope to produce biogas and/or biomethane, with the largest opportunities being across the Asia Pacific region. With a global focus in achieving net zero carbon emissions by 2050, the use of renewable energy has created new opportunities for floating covers, demonstrated by the adoption of floating solar installations and more recently the use of thermal energy pits to store heated and chilled water. It is the authors opinion that more floating cover applications will emerge in the coming decade as new technologies are developed requiring large scale liquid storage facilities.

## REFERENCES

- AalborgCSP, (2019). *Pit Thermal Energy Storage for Increased Efficiency and Flexibility*.  
<https://www.aalborgcsp.com/>
- Australian Bureau of Meteorology, (2022). *Climate Averages*,  
<http://www.bom.gov.au/climate/averages/tables>
- Climate Action, (2017). *China breaks ground on the world's largest floating solar plant*.  
<https://www.climateaction.org/news>
- Barry, J. (2007). *Energy and Water Efficiency in Municipal Water Supply and Wastewater Treatment*, Alliance to Save Energy, Washington, D.C. USA.
- Fairhead, G., Pece, D., (2022). *Design Challenges of a Geomembrane Lined and Covered Hot Water Thermal Storage*, ACIGS, QLD, Australia.
- FGI, (2022). *Guideline for Positive Pressure Biogas Cover Systems*, Fabricated Geomembrane Institute, University of Illinois, Urbana, Champaign, Urbana, Illinois, USA
- Fraser, B., and Killian B (2015) *Emerging Applications for Evaporation Control Covers*, Geosynthetics 2015, Portland, OR, USA
- Gersch, A., (2019). A History of Geomembrane Floating Covers in Australia *Geosynthetics '19*, IFAI, Houston, TX, USA, 1150.
- International Energy Agency, (2020). *Outlook for biogas and biomethane: Prospects for organic growth*, <https://www.iea.org/reports>
- International Energy Agency, (2021). *Methane and climate change*,  
<https://www.iea.org/reports/methane-tracker-2021/methane-and-climate-change>
- PV Magazine USA, (2020). *Floating solar nearing price parity with land-based US solar*.  
<https://www.pv-magazine.com/2020/10/07>  
<https://raygen.com/technology>
- Spang, E., Manzor, S., and Loge, F., (2020). *The cost-effectiveness of energy savings through water conservation: a utility-scale assessment*. IOP Publishing, Temple Circus, Temple Way, Bristol, UK.
- Young, R. (2015). *A Survey of Energy Use in Water Companies*, ACEEE



# **Feasibility Evaluation of Lightweight Aggregate to Improve Performance of Load Transfer Platforms in Geosynthetic-reinforced Embankments**

**Yu-qiu Ye<sup>1</sup>, Jie Han, Ph.D., P.E., F. ASCE,<sup>2</sup> and Rui Rui, Ph.D.<sup>3</sup>**

<sup>1</sup>Dept. of Civil, Environmental, and Architectural Engineering, the University of Kansas, 1530 West 15th St., Lawrence, KS 66045, corresponding author. E-mail: [yuqiu@ku.edu](mailto:yuqiu@ku.edu)

<sup>2</sup>Dept. of Civil, Environmental, and Architectural Engineering, the University of Kansas, 1530 West 15th St., Lawrence, KS 66045. E-mail: [jiehan@ku.edu](mailto:jiehan@ku.edu)

<sup>3</sup>School of Civil Engineering and Architecture, Wuhan University of Technology, 122 Luoshi Rd., Wuhan 430070. E-mail: [r.rui@whut.edu.cn](mailto:r.rui@whut.edu.cn)

## **ABSTRACT**

Lightweight aggregate has unique characteristics of light self-weight, high friction angle, and good interaction with geosynthetics, and may be used as a fill material in load transfer platforms (LTP) in embankments over soft soils. This study included three plane-strain trapdoor tests to evaluate the feasibility of using lightweight aggregate to improve the performance of load transfer platforms in embankments. These model tests consisted of trapdoor movement and loading stages to investigate the mobilization and degradation of soil arching. The localized surface footing loading was applied using a hydraulic jack. The vertical pressures on the trapdoor and the stationary support were measured using earth pressure cells and the settlement of the footing was measured using a displacement transducer. Test results showed that soil arching mobilized with the settlement of the trapdoor and degraded with the footing loading. The geosynthetic reinforcement hindered the degradation of soil arching and improved the bearing capacity of the embankment under footing loading. Lightweight aggregate had favorable soil arching behavior and low vertical pressures on the trapdoor and the stationary support; therefore, it is proved to be a good alternative material for load transfer platforms in embankments.

## **INTRODUCTION**

Soil arching is a common phenomenon in many geotechnical applications, such as retaining walls (Handy 1985; Rui et al. 2019; Lai et al. 2022), pile-supported embankments (Nunez et al. 2013; Chen et al. 2016; Eskişar et al. 2018), and tunnels (Zou et al. 2019; Long et al. 2020). Terzaghi (1943) defined the soil arching effect as a load transfer between a yielding portion and adjoining stationary portions (also called supports) under or within a fill, and involves a redistribution of stresses in the fill. Soil arching occurs as a result of differential settlement between a stiff structure and its surrounding soil. The general belief is that the soil arching effect is a key load transfer mechanism for the above-mentioned geotechnical applications and has been increasingly investigated using model tests and numerical

simulations in recent years.

Trapdoor test is an effective and efficient method to study the soil arching effect. To investigate the mobilization and degradation of soil arching, Terzaghi (1943), Dewoolkar et al. (2007), Iglesia et al. (2014), and Al-Naddaf et al. (2019) conducted a series of two-dimensional (2D) plane-strain single-trapdoor tests, Chen et al. (2008), Bhandari (2010), and Rui et al. (2018) performed 2D plane-strain multiple-trapdoor tests, and Bao (2020) conducted 3D discrete element method (DEM)-simulated trapdoor tests. Van Eekelen et al. (2012) adopted a foam cushion to simulate the soft soil in the trapdoor test, while Al-Naddaf et al. (2019) utilized springs to simulate the soft soil. Model test results from Iglesia et al. (2014) showed the progressive development of soil arching changed from a curved arch, a triangular arch, to a rectangular arch with the displacement of the trapdoor. Rui et al. (2018) revealed three deformation patterns (e.g., triangular expanding pattern, tower-shaped development pattern, and equal settlement pattern) for unreinforced pile-supported embankments and two deformation patterns (e.g., concentric ellipse pattern and equal settlement-concentric arches pattern) for geosynthetic-reinforced pile-supported embankments. Many model test results showed that the vertical pressures on the trapdoor decreased to a lowest value with the settlement of the trapdoor and then either maintained the lowest value or slowly increased with an increase of settlement. To better describe the mobilization and degradation of soil arching, Iglesia et al. (2014) proposed a ground reaction curve and Han et al. (2017) later simplified this ground reaction curve into three straight segments.

Lightweight aggregate has been increasingly used as fill materials in geotechnical and transportation applications due to its low self-weight and high shear strength. Meles et al. (2014) used lightweight aggregate as a fill material for highway embankments and Saride et al. (2010) used lightweight aggregate to control the embankment settlement.

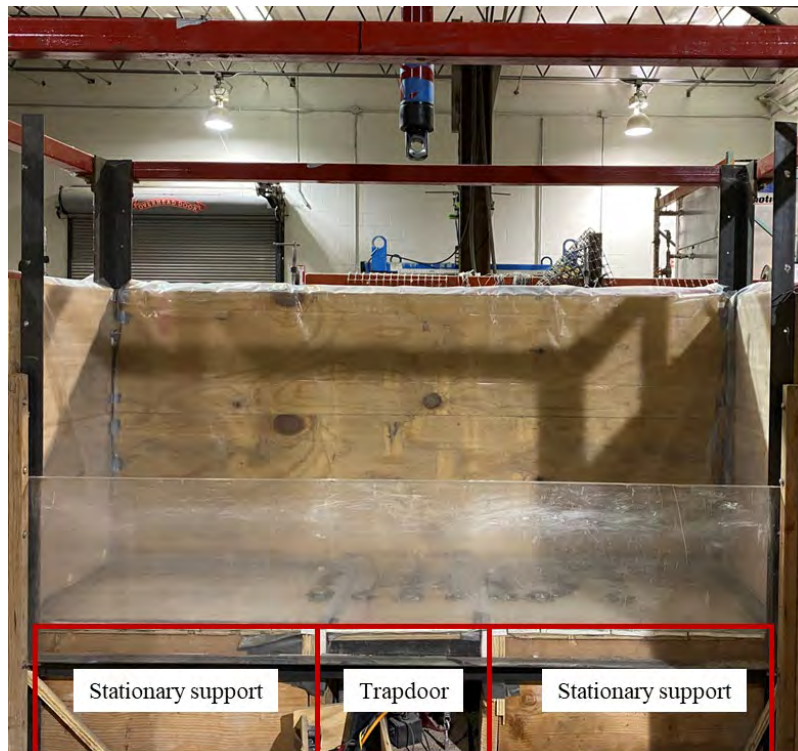
To evaluate the feasibility of lightweight aggregate in load transfer platforms and the benefits of the geosynthetic reinforcement in pile-supported embankments, this study included three plane-strain trapdoor tests to investigate the mobilization and degradation of soil arching after fill placement and under static footing loading and the effect of a single layer of geotextile reinforcement.

## MODEL TESTS

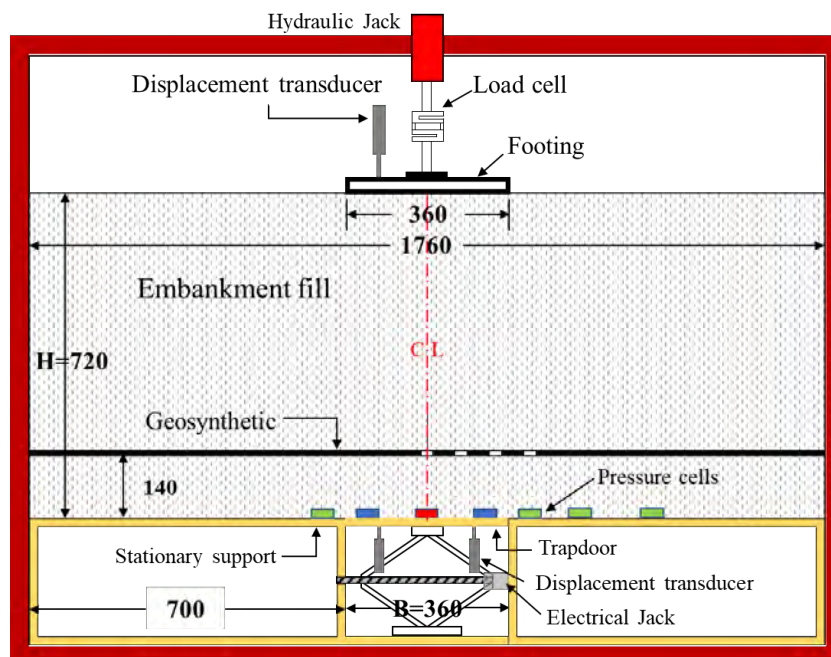
**Test setup.** Figure 1 shows the plan view of the trapdoor test box. The trapdoor test box was designed to have an inner size of 1.76 m long, 0.46 m wide, and 1.5 m high. This box was composed of three sides of plywood panels and one side of Plexiglas panel to allow the visual observation of soil deformations during the test. The three sides of plywood panels were covered by a layer of plastic sheet to reduce the friction from the box side walls. The trapdoor had a width of 0.36 m and a length of 0.46 m, and was placed in the center of the

test box and between two stationary supports. The settlement of a subsoil was simulated by the downward movement of the trapdoor, which was mounted on and controlled by an electrical jack. The distance from the edge of the trapdoor to the box sidewall was 0.7 m, which is approximately twice the width of the trapdoor. This study applied footing loading on the surface of the embankment fill using a hydraulic jack attached to a rigid steel footing. The steel footing had the same dimension as the trapdoor (i.e., 0.36 m wide and 0.46 m long) and was installed above the center of the trapdoor.

**Material Properties.** This study adopted lightweight aggregate and Kansas River sand as regular granular embankment fills in the trapdoor tests. Figure 2 shows the photo of Kansas River sand and lightweight aggregate. Figure 3 shows the particle size distributions for the lightweight aggregate and the Kansas River sand based on sieve analysis tests. The lightweight aggregate had coefficients of uniformity ( $C_u$ ) and curvature ( $C_c$ ) of 7.45 and 1.01, respectively. The Kansas River sand had coefficients of uniformity ( $C_u$ ) and curvature ( $C_c$ ) of 3.18 and 0.99, respectively. This lightweight aggregate is classified as well-graded gravel according to the Unified Soil Classification System (USCS) (ASTM 2011). The lightweight aggregate had a maximum density of  $776 \text{ kg/m}^3$  and a minimum density of  $640 \text{ kg/m}^3$ , respectively, while the Kansas River sand had a maximum density of  $1885 \text{ kg/m}^3$  and a minimum density of  $1602 \text{ kg/m}^3$ , respectively, determined with ASTM D4254 (ASTM 2014b) and ASTM D4253 (ASTM 2014a). During the placement of the embankment fill, the lightweight aggregate and the Kansas River sand were poured and compacted at a targeted relative density of 75%. The compacted lightweight aggregate at this relative density had a unit weight of  $7.4 \text{ kN/m}^3$  and a peak friction angle of  $45^\circ$  based on direct shear tests. The compacted Kansas River sand at this relative density had a unit weight of  $18.0 \text{ kN/m}^3$  and a peak friction angle of  $37^\circ$  based on direct shear tests. One layer of nonwoven geotextile with the size of 1.76 m long and 0.46 m wide was used as reinforcement. Table 1 shows the material properties of the nonwoven geotextile. It should be pointed out that nonwoven geotextiles are typically not used as reinforcement due to their low strengths. In this study, a low-strength geotextile is preferred for reduced-scale model tests considering scale factors; therefore, the non-woven geotextile was selected.



(a)



(b)

**Figure 1.** Trapdoor test box: (a) photo; and (b) schematic (unit: mm)





**Figure 2.** Embankment fill: (a) Kansas River sand; and (b) lightweight aggregate

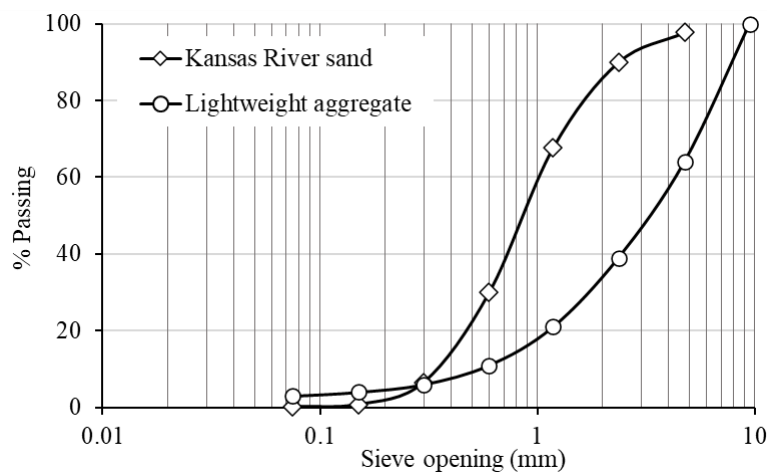


**Figure 3.** Particle size distribution.

**Table 1.** Material properties of nonwoven geotextile (Tencate 2014).

Property	Unit	value
Tensile strength @ 2% strain	kN/m	4.1 (MD) × 6.6 (XMD)
Tensile strength @ 5% strain	kN/m	8.5 (MD) × 13.4 (XMD)
Ultimate tensile strength	kN/m	25 (MD) × 33 (XMD)
Unit mass	g/m <sup>2</sup>	119
Unit mass	N	400
Grab elongation	%	50
Trapezoid tear	N	156
Puncture	N	245
Mullen burst	KN/m <sup>2</sup>	1276

Note: MD = machine direction and XMD = cross-machine direction.

**Instrumentation.** This study used seven earth pressure cells to measure the vertical earth pressures on the trapdoor and the stationary support during each test. Figure 4 shows the installation of earth pressure cells. One earth pressure cell (designated as TC) was installed along the centerline of the trapdoor and four earth pressure cells (designated as TE and SE) were installed symmetrically about the centerline of the trapdoor at distances of 130 and 230 mm, respectively. To investigate the influence area of the soil arching effect, two earth pressure cells (designated as S1 and S2) were placed at distances of 360 and 550 mm from the centerline of the trapdoor. Each pressure cell had an outside diameter of 50 mm, a sensing-surface diameter of 46 mm, a thickness of 11.3 mm, and a maximum capacity of 200 kPa. This study utilized three displacement transducers to monitor the displacements of the trapdoor and the footing with a measuring capacity of 50 mm. Two displacement transducers were placed under and along the diagonal line of the trapdoor and one displacement transducer was placed above the footing.

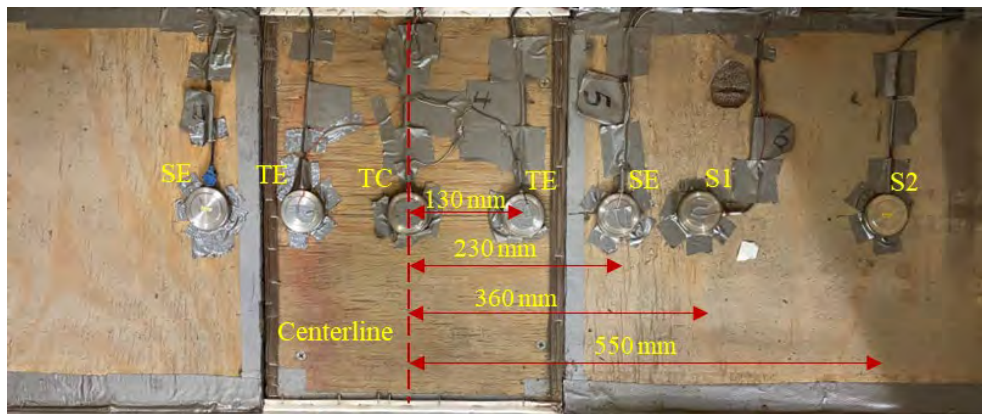


**Figure 4.** Layout of earth pressure cells.

**Test procedure.** Based on the mass-volume control method, the embankment fill was placed in seven lifts and each lift had a thickness of 100 mm except for the top lift with a thickness of 120 mm. After the placement of each lift, the soil was compacted using the manually-held steel compactor to achieve a relative density of 75%. In the reinforced trapdoor test, one layer of nonwoven geotextile was installed at a height of 140 mm and was free at its edges. When the box was filled up to a height of 720 mm, the trapdoor test was conducted by slowly lowering the trapdoor at a speed of 0.02 mm/s. The trapdoor stopped moving at each 1-mm displacement increment for a period of 2 minutes to ensure the earth pressure cell readings were stable and the deformations were measured until the trapdoor reached a settlement of 35 mm. After the trapdoor stage, footing loading was applied on the surface of embankment

fill using the hydraulic jack at an increment of approximately 7 kPa, during which the trapdoor was held in place. The loading stage ended when the measured pressure on the center of the trapdoor exceeded the pressure on the stationary supports or the footing load reached a relatively large value (e.g., 120 kPa) to protect the trapdoor box from damage. Table 2 shows the test program.

**Table 2.** Test program.

Test No.	Embankment type	Backfill type
T1	Unreinforced	Kansas River sand
T2	Unreinforced	Lightweight aggregate
T3	Reinforced	Lightweight aggregate

## TEST RESULTS

**Overburden stress.** This study measured the vertical pressures during the placement of the embankment fill. Figure 5 shows the vertical pressures on the trapdoor and the stationary part in the reinforced test T2, in which TE and SE represent the average value of two measured vertical pressures. The measured vertical pressures show a linear increase and well matched the theoretical overburden stress ( $\gamma H$ ,  $\gamma$  is fill unit weight and  $H$  is fill height), indicating that the friction effect from the box side walls is negligible.

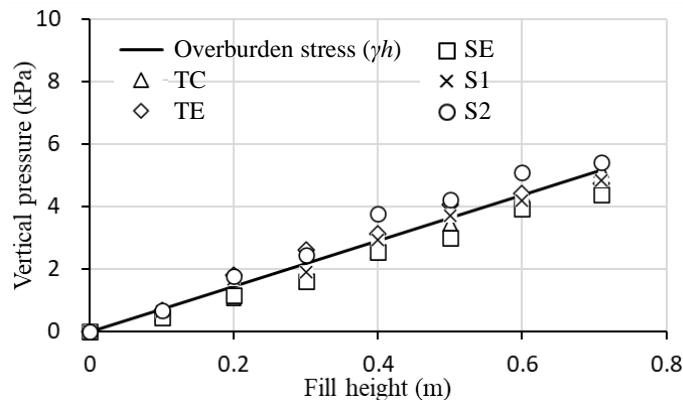
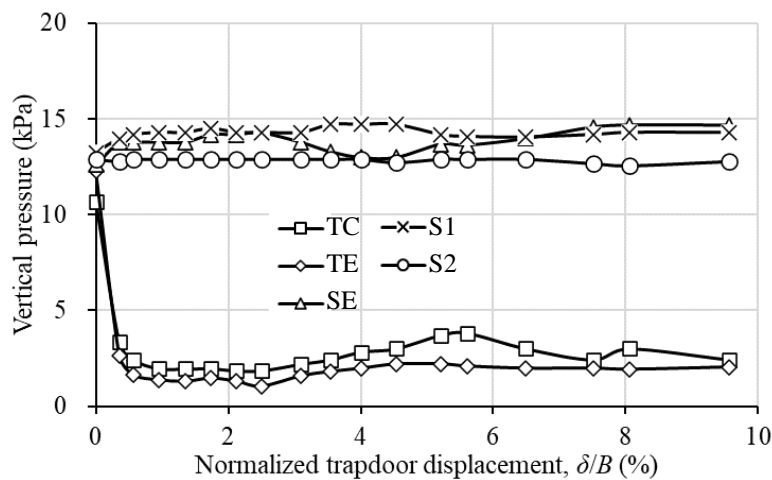


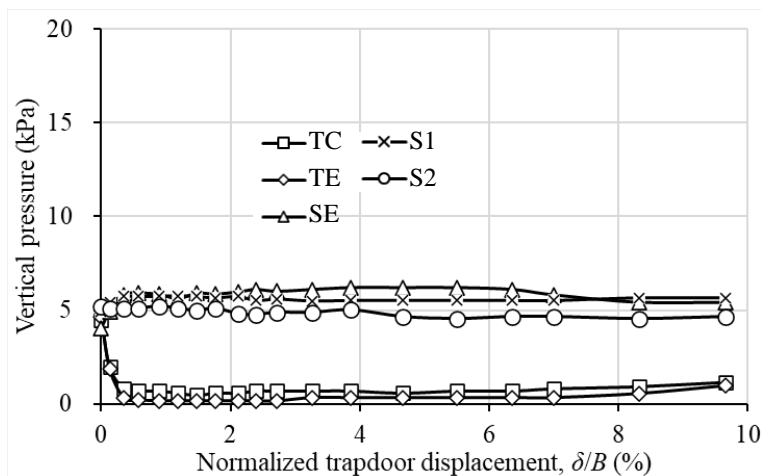
**Figure 5.** Measured and theoretical vertical pressures on the trapdoor and the stationary support.

**Development of soil arching.** Figure 6 shows the measured vertical pressures on the trapdoor and the stationary supports versus the normalized trapdoor displacement ( $\delta/B$ , the ratio of the trapdoor displacement  $\delta$  to the width of the trapdoor  $B$ ). The measured vertical pressures on the trapdoor decreased

with the trapdoor displacement to a lowest value and then either maintained around the lowest value or slowly increased with an increase of trapdoor displacement, while the vertical pressures on the stationary support increased to a peak value with the trapdoor displacement and then either maintained around the peak value or slowly decreased. The trapdoor displacement value for the vertical pressures on the trapdoor to reach the lowest value was approximately 2 mm ( $\delta/B = 0.5\%$ ), which was consistent with that found by Al-Naddaf (2019). Tests T2 and T3 had lower vertical pressures on the trapdoor and stationary support than those on test T1, indicating that the use of lightweight aggregate as a load transfer platform material could effectively reduce the vertical pressure. In addition, the measured pressure on S2 was lower than those on S1 and SE. This phenomenon showed that the soil arching effect decreased as the distance from the trapdoor increased.



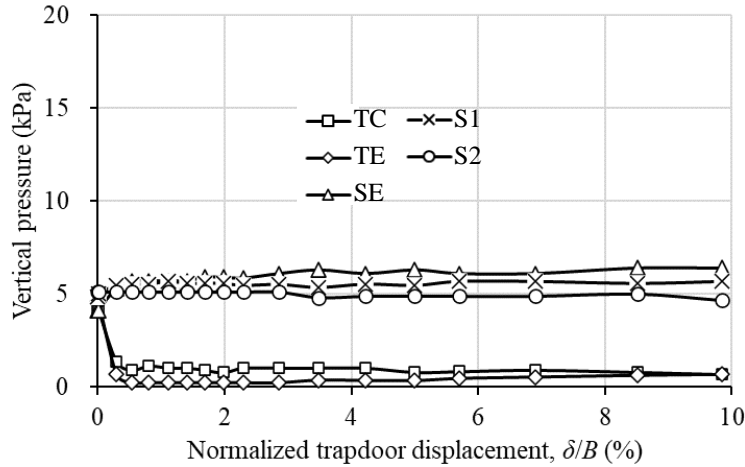
(a) T1



(b) T2

**Figure 6.** The measured vertical pressures versus the normalized trapdoor displacement  
(To be continued)





(c) T3

**Figure 6.** The measured vertical pressures versus the normalized trapdoor displacement  
(Continued)

Soil Arching Ratio (SAR) is defined as the ratio of the average vertical pressure above the yielding base ( $\sigma_v$ ) to the overburden pressures ( $\gamma H$ ) plus the uniform surcharge ( $q$ ). The soil arching ratio has been commonly used to represent the development of soil arching. For example, the lower SAR value indicates the greater soil arching. Figure 7 shows the variations of the soil arching ratio versus the normalized trapdoor displacement. Test T1 had a higher SAR value than tests T2 and T3, indicating that the lightweight aggregate had more soil arching effect than the Kansas River sand. In addition, the degradation of soil arching occurred at  $\delta/B = 2\%$  to  $3\%$  for test T1 and  $\delta/B = 5\%$  to  $7\%$  for tests T2 and T3. In other words, the Kansas River sand embankment fill had an earlier degradation than the lightweight aggregate.

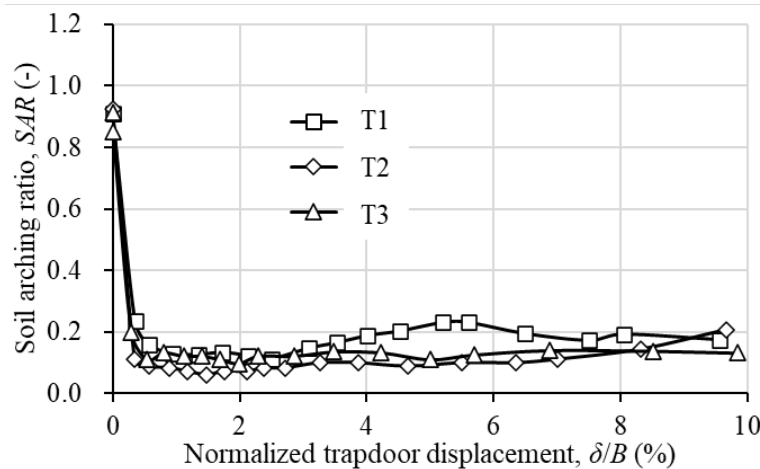
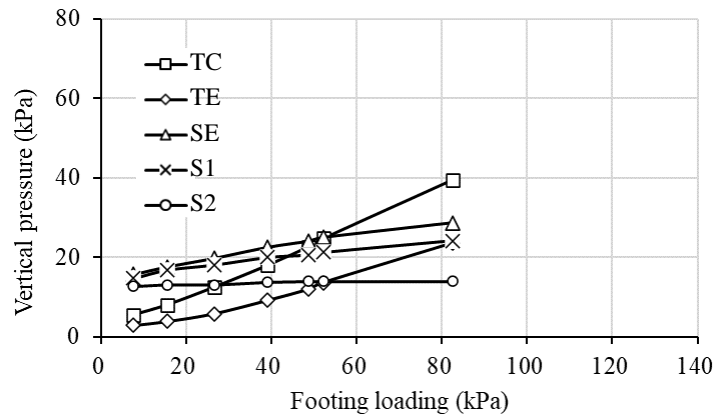
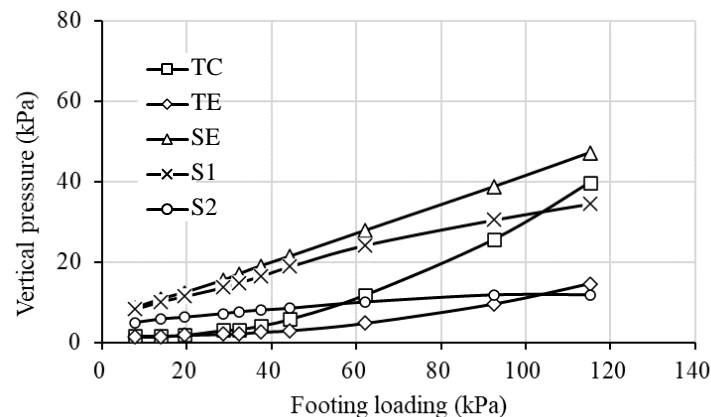


**Figure 7.** Variations of soil arching ratio versus the normalized trapdoor displacement.

**Effects of footing loading.** Figure 8 shows the variations of the measured vertical pressures versus the footing loading. In general, the measured vertical pressures on the center of the trapdoor (TC) showed the fastest increase with the footing loading. The measured vertical pressures on the edge of the stationary support (SE) showed a relatively slow increase as compared with those on the center of the trapdoor (TC). When the footing loading increased from 7 to 80 kPa, the measured vertical pressures on S2 in Test T1 maintained stable, while the measured vertical pressures on S2 in Test T2 and T3 showed a slight increase. This phenomenon indicated that the influence zone of the footing loading in the lightweight aggregate embankment was larger than in the Kansas River sand. The measured vertical pressures on TC exceeded the vertical pressures on the S1 at the footing loading of 50, 105, and 125 kPa for tests T1, T2, and T3, respectively. Soil arching in the lightweight aggregate had less degradation than in the Kansas River sand under footing loading and the installation of the nonwoven geotextile hindered the degradation.

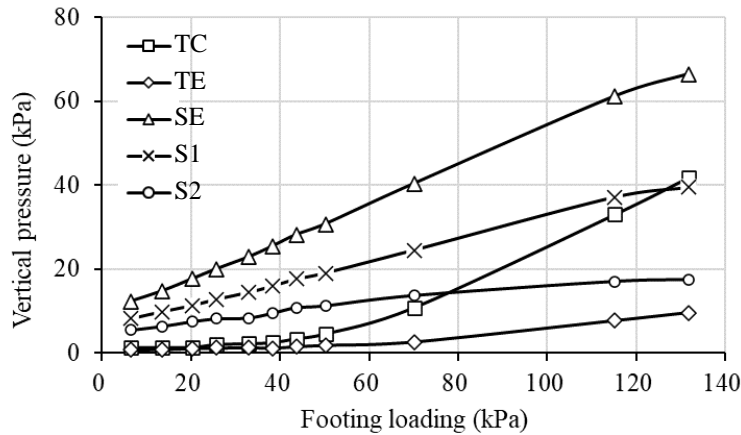


(a) T1



(b) T2

**Figure 8.** Variations of the measured vertical pressures versus the footing loading (To be continued)



(c) T3

**Figure 8.** Variations of the measured vertical pressures versus the footing loading  
(Continued)

Figure 9 shows the footing settlement curve under footing loading. Reinforced test T3 had a lower footing settlement at the same loading level as compared with unreinforced tests T1 and T2. The figure shows that the lightweight aggregate had a higher bearing capacity than the Kansas River sand and the installation of the geotextile increased the bearing capacity of the lightweight aggregate.

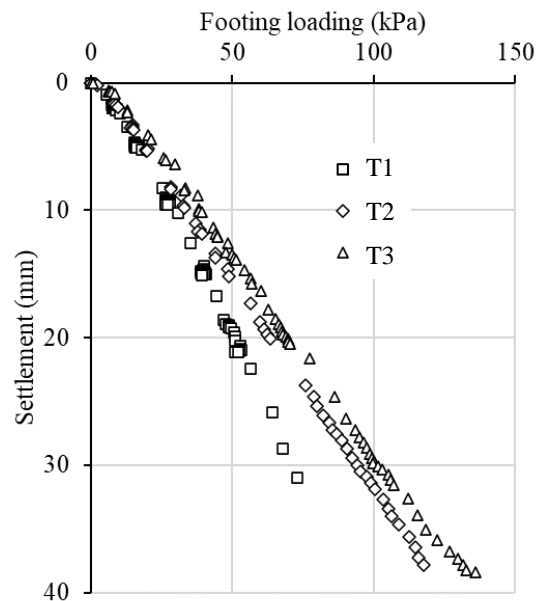


**Figure 9.** Load-settlement curve.

## CONCLUSIONS

This study included three model tests under a plane-strain condition to evaluate the feasibility of using a lightweight aggregate to improve the performance of load transfer platforms in embankments. The test box with a trapdoor was used to simulate the settlement of the subsoil between two stationary supports. In one of the tests, a nonwoven geotextile was used to reinforce the embankment. Based on the test results, the following conclusions can be drawn:

- (1) The lightweight aggregate embankment fill had lower vertical pressures acting on the trapdoor and resulted in more soil arching effect than the Kansas River sand.
- (2) The geotextile hindered the degradation of soil arching and increased the bearing capacity under footing loading.
- (3) The reinforced lightweight aggregate is a good alternative material for load transfer platforms at the bottom of the embankment.

## ACKNOWLEDGEMENT

The first author would like to acknowledge the John Ries Scholarship received from the Expanded Shale, Clay and Slate Institute (ESCSI) for this lightweight aggregate study. The lightweight aggregate used for the trapdoor test was donated by Arcosa Lightweight. The authors appreciate Mr. Jack Moore, Marketing & Technical Manager – Southern Region at Arcosa Lightweight for his support.

## REFERENCES

- Al-Naddaf, M., Han, J., Xu, C., Jawad, S., and Abdulrasool, G. (2019). Experimental investigation of soil arching mobilization and degradation under localized surface loading, *Journal of Geotechnical and Geoenvironmental Engineering*, 145(12), 04019114.
- Bao, N., Wei, J., Chen, J. F., and Wei, P. (2020). 2D and 3D discrete numerical modelling of soil arching. *Journal of Zhejiang University-SCIENCE A*, 21(5): 350-365.
- Bhandari, A. (2010). Micromechanical analysis of geosynthetic-soil interaction under cyclic loading. Ph.D. dissertation, Department of Civil, Environmental, and Architectural Engineering, the University of Kansas.
- Chen, R. P., Wang, Y. W., Ye, X. W., Bian, X. C., and Dong, X. P. (2016). Tensile force of geogrids embedded in pile-supported reinforced embankment: A full-scale experimental study, *Geotextiles and Geomembranes*, 44(2):157-169.
- Dewoolkar, M. M., Santichaiant, K., and Ko, H. Y. (2007). Centrifuge modeling of granular soil response over active circular trapdoors, *Soils and Foundations*, 47(5): 931-945.
- Eskişar, T., Otani, J., and Hironaka, J. (2012). Visualization of soil arching on reinforced embankment with rigid pile foundation using X-ray CT, *Geotextiles and Geomembranes*, 32: 44-54.
- Handy, R. L. (1985). The arch in soil arching. *Journal of Geotechnical Engineering*, 111(3): 302-318.



- Han, J., Wang, F., Al-Naddaf, M., and Xu, C. (2017). Progressive development of two-dimensional soil arching with displacement, *International Journal of Geomechanics*, 17(12): 04017112.
- Iglesia, G., Einstein, H., and Whitman, R. (2014). Investigation of Soil Arching with Centrifuge Tests, *Journal of Geotechnical and Geoenvironmental Engineering*, 140(2): 04013005.
- Lai, F., Yang, D., Liu, S., Zhang, H., and Cheng, Y. (2022). Towards an improved analytical framework to estimate active earth pressure in narrow  $c-\phi$  soils behind rotating walls about the base, *Computers and Geotechnics*, 141: 104544.
- Long, Y. Y., and Tan, Y. (2020). Soil arching due to leaking of tunnel buried in water-rich sand. *Tunnelling and Underground Space Technology*, 95: 103158.
- Meles, D., Bayat, A., Hussien Shafiee, M., Nassiri, S., and Gul, M. (2014). Investigation of tire derived aggregate as a fill material for highway embankment, *International Journal of Geotechnical Engineering*, 8(2): 182-190.
- Nunez, M. A., Briançon, L., and Dias, D. C. F. S. (2013). Analyses of a pile-supported embankment over soft clay: Full-scale experiment, analytical and numerical approaches, *Engineering Geology*, 153, 53-67.
- Rui, R., Han, J., Van Eekelen, S. J. M., and Wan, Y. (2019). Experimental investigation of soil-arching development in unreinforced and geosynthetic-reinforced pile-supported embankments. *Journal of Geotechnical and Geoenvironmental Engineering*, 145(1): 04018103.
- Rui, R., Ye, Y. Q., Han, J., Zhang, L., and Zhai, Y. X. (2020). Experimental and theoretical investigations on active earth pressure distributions behind rigid retaining walls with narrow backfill under a translational mode, *International Journal of Geomechanics*, 20(10): 04020178.
- Saride, S., Puppala, A. J., Williammee, R., and Sirigiripet, S. K. (2010). Use of lightweight ECS as a fill material to control approach embankment settlements. *Journal of Materials in Civil Engineering*, 22(6): 607-617.
- Tencate. (2014). *Mirafi MPV400 production specification*. Pendergrass, GA: Tencate Geosynthetics Americas.
- Terzaghi, K. (1943). *Theoretical Soil Mechanics*. John Wiley & Sons, New York, NY, USA.
- Van Eekelen, S. J., Bezuijen, A., Lodder, H. J., and van Tol, E. A. (2012). Model experiments on piled embankments. Part I, *Geotextiles and Geomembranes*, 32: 69-81.
- Chen, Y. M., Wei-Ping, C., and Ren-Peng, C. (2008). An experimental investigation of soil arching within basal reinforced and unreinforced piled embankments. *Geotextiles and geomembranes*, 26(2): 164-174.
- Zou, J., Chen, G., and Qian, Z. (2019). Tunnel face stability in cohesion-frictional soils considering the soil arching effect by improved failure models, *Computers and Geotechnics*, 106: 1-17.

## Geogrid-reinforced Timber Pile Supported Modular Block Retaining Wall

Mickey L. Snider<sup>1</sup>, P.E.

<sup>1</sup>Wang Engineering, Inc., 1145 N. Main St. Lombard, IL 60148; [msnider@wangeng.com](mailto:msnider@wangeng.com)

### ABSTRACT

Replacement of the Burlington Northern and Santa Fe (BNSF) rail line over Interstate 294 in Western Springs, Illinois required the construction of a shoo-fly bridge and embankment to maintain a minimum of three tracks in service. Shoo-fly construction pushed the 8-meter-tall (25 foot) rail embankment south and adjacent to local roads that could not be closed for the duration of construction; a 6-meter-tall temporary retaining wall would be required along the right-of-way. The subsurface investigation through the area indicated the presence of a buried wetland filled with organic silty loam and fibrous peat overlying soft, organic-rich silty clay and soft, non-organic clay with total thickness of up to 8 meters (27 feet). Due to high loads, greater than 100 meters (350 feet) of bent piers and bridge structure were the initial track concept. Recently completed projects in the area, however, had shown a more cost-effective alternative of placing modular-type retaining walls over a 90 cm (3 feet) thick aggregate platform reinforced with two layers of biaxial geogrid and supported on timber piles up to 15-meters (48 feet) long. The timber piles were driven 1.8 meters (6 foot) on-square center into competent underlying glacial till and granular outwash and designed to provide 3 cm (1 to 1.5 inch) settlement for pile loads up to 672 kN (151 kips). Post-construction monitoring was performed via inclinometers and nested piezometers to measure lateral soil deformations and pore pressures induced below the load transfer platform. The monitoring showed lateral foundation soil movement of 5 cm (2 inches) and induced pore pressures of less than 3 kPa (0.5 psi). The load transfer platform was successful in supporting boring the vertical wall loading and the overall global stability of the wall.

### INTRODUCTION

The collar counties surrounding Cook County and the City of Chicago occasionally encounter peat and muck, deposited in kettle bogs formed following the Wisconsin Glaciation. These deposits are often revealed during investigations in support of roadways and infrastructure projects. For many years, the typical response to encountering these materials has been either large-scale removal of the material or construction of land bridges consisting of tightly spaced, buried concrete pile bents with reinforced-concrete slab decks and deep, steel pilings. The traditional solutions to construction through these poor soil conditions are costly to state and county agencies in both immediate construction dollars, as well as long-term maintenance.

In Western Cook County, Illinois, the Illinois State Toll Highway Authority (ISTHA) has begun a major reconstruction of Interstate 294, also known as the Central Tri-State Tollway. Replacement of the cross-bridges has been a primary component of the reconstruction with few presenting as many challenges as the reconstruction of the Burlington Northern and Santa Fe (BNSF) Rail bridge in Western Springs. The rail bridge was required to maintain 3 active tracks at all times. A 3-track shoo-fly bridge would be constructed immediately to the south of the existing bridge and would require the eastern approach embankment to widen and push south by almost 30 meters (90 feet) at the toe. Beginning 300 meters (1000 feet) east of the bridge, the

approach embankment runs parallel to Burlington Avenue, a municipal roadway and the only access point to a major public park; this roadway was also required to stay open. A 90-meter (300-foot) long temporary modular block retaining wall was proposed immediately adjacent to Burlington Avenue to support the shoo-fly track widening.

The subsurface investigation of the southeast approach embankment revealed peat and soft, organic silts with thicknesses of greater than 8 meters (27 feet) in some areas. Initial concepts revolved around designing a temporary bridge structure. However, after discussion with ISHTA and BNSF, the modular wall option was preferred and a geogrid-reinforced, timber pile-supported wall foundation system was developed as an alternative.

Locally, pile-supported embankments have been used sparingly, but with increasing frequency, by both the Illinois Department of Transportation (IDOT), as well as the Cook County Department of Highways. This scenario would see the concept adapted for modular wall and mechanically-stabilized earth (MSE) retaining systems. The embankment systems have traditionally resulted in significant cost savings for the letting agencies; the hope at the BNSF over I-294 was that a similar cost savings could be realized.

## **SITE CONDITIONS AND GEOLOGY**

The site lies approximately 15 miles southwest of the Chicago Loop at the limit between the Valparaiso and Tinley Morainic Systems. A *Site Location Map* is shown as Figure 1. The site lies at the limit between the Valparaiso and Tinley Moraines in a slight depression or basin fill area (Bretz 1955). The youngest natural soils within the basin fill consist of weak, compressible clay and silt of moderate to high organic content and muck. The compressible soils reach 8 meters (27 feet) in thickness and extends approximately 1,500 meters (5,000 feet) along the rail alignment on each side of Flag Creek, which represents the major drainage feature in the area. The basin fill has been removed in a number of select areas during development of the I-294 corridor; however, weak and compressible soils remain largely in areas along the length of the BNSF corridor beneath and adjacent to the embankment that is close to 100 years old.

The base of the rail embankment along Burlington Avenue sits at an elevation of about 196 to 197 meters (645 to 647 feet) and is relatively flat. The embankment is about 7 to 8 meters (20 to 25 feet) tall with a pre-construction rail tie elevation of about 204 meters (670 feet).

The post-glacial peat, muck, and other organic soils deposits, informally known as Grayslake Peat, fill in kettle holes between moraines. The Valparaiso Morainic System was formed during the Wisconsin Episode of glaciation. Silty and clayey diamictos of the Wadsworth Formation make up the Palatine Moraine and underlie most of the surrounding area. The Wadsworth Formation consists of relatively homogeneous and massive, gray till, with clay to silty clay matrix, a high content of black shale clasts, and silt and sand lenses. In western Cook County the Wadsworth Formation averages about 18 meters thick (Hansel and Johnson 1996). At depth, the Wadsworth Formation rests on top of the Lemont Formation, which consists of a silt-rich diamicton easily recognized on boring logs due to its higher blow count values and lower moisture contents than the overlying Wadsworth diamicton.



**Figure 1. Site Location Map; BNSF Railroad over Interstate 294**

## **SOIL AND GROUNDWATER CONDITIONS**

The subsurface conditions along the proposed temporary modular wall were investigated by advancing 7 SPT borings (Figure 2) to depths up to 15 meters (50 feet) below grade, pushing undisturbed Shelby tubes, performing in-situ pressuremeter testing, and installing a groundwater monitoring piezometer. Below the existing pavement structure along Burlington Avenue, the investigation encountered (A) man-made ground (fill); (B) upper organic silt loam and peat; (C) lower organic silt loam and clay; (D) soft to medium stiff silty clay loam; and (E) medium dense to dense sand and sandy gravel.





**Figure 2. Boring Location Plan with Proposed Modular Wall Footprint**

The units showed lateral continuity across the length of the proposed wall. The clayey fill material, placed to support the pavement structure of Burlington Road, is a consistent 5 to 6 feet thick, while the upper organic material and peat are present with consistent thickness in all but two of the borings. The exception is the lower organic, which drives deeper in Boring RWB-34 than in other borings across the length of the wall, as can be seen in the soil profile (Figure 3).

The upper organic unit presents as black and dark brown silty loam and generally non-fibrous peat with thickness between 1.5 and 3.0 meters. The material is comprised heavily of silt and sand-sized fractions with Liquid ( $L_L$ ) and plastic ( $P_L$ ) limits measuring 124 and 82%, respectively. Natural water contents measured 110% to as high as 270%, and organic content by loss-on-ignition (LOI) was 22 to 30%. Liquidity indices of the upper organic are well in excess of 1.0, and occasionally 2.0.

A one-dimensional consolidation test was performed on a Shelby tube sample of this unit from boring SAB-18. The compressibility coefficient ( $cc$ ) measures 2.32 with an initial void ratio ( $e_o$ ) of 3.6 for a sample with a moisture content of 151%, which is about the average moisture measured within this unit. The coefficient of consolidation ( $cv$ ) at loading levels for 100 to 200 kPa (2,000 to 4,000 psf) were very slow, about 0.01 square feet per day or less.

At elevations of 193 feet, the organic silty loam and peat is underlain by the lower organic deposit consisting of lower moisture organic silty clay loam. The silty clay loam has moisture content values from about 40 to 70% which are very close to the measured  $L_L$  values of 57 to 74%. The  $P_L$  values were measured at 27 to 30% and the  $L_I$  is about 0.7 to 1.0, or close to the liquid state.

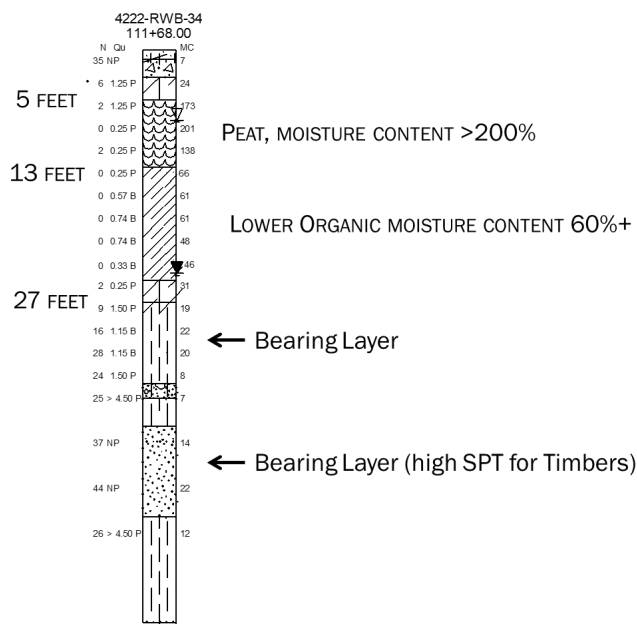


**Figure 3. Subsurface Soil Profile**

Laboratory strength values of the lower organic were measured by unconfined, UU, and CU testing methods. The  $S_u$  values within this unit measure about 50 kPa; the moisture content and compressibility, however, is significantly lower than the upper organic silty loam. Oedometer testing performed on two samples of this unit measured  $c_c$  values of 0.42 to 0.82 for initial void ratios of 1.2 to 1.8. The compressibility shows good correlation to both the natural moisture content and initial void ratio of the material. The  $c_v$  values remain extremely low, showing about 0.05 square feet per day.

At depths of about 6 meters (20 feet) and elevations of 192 to 189 meters (630 to 620 feet), the borings encountered a layer of soft to medium stiff, gray silty clay loam with higher strength and noticeably lower moisture content than the upper and lower organic deposits. Laboratory strength testing by unconfined compressive strength show  $S_u$  values closer to 182 kPa (600 psf) with corresponding moisture content values of 35 to 48%. Unlike the organic layers, this material is much more discontinuous across the site; where it was encountered it has a maximum thickness of only 1.5 to 2.1 meters (5 to 7 feet).

Deeper foundation soils across the site consisted of stiff to very stiff clays with  $S_u$  values of 62 to 163 kPa (1,300 to 3,400 psf) and dense sand with SPT N-values generally greater than 40 blows per 0.3 meters (foot).

Groundwater levels along the length of the proposed wall were monitored in an observation well (4222-RWB-34-PZ). The well is screened within the upper organic deposit between about 1.8 and 3.0 meters (6 to 10 feet) below the Burlington Avenue pavement elevation. Hydrostatic groundwater was measured at an average elevation of 195 meters (640 feet), shown in Figure 4, or only 0.9 to 1.2 meters (3 to 4 feet) below the existing grade. Considering the groundwater levels in the immediately vicinity of the site, precipitation and surface runoff are the only sources of groundwater recharge.

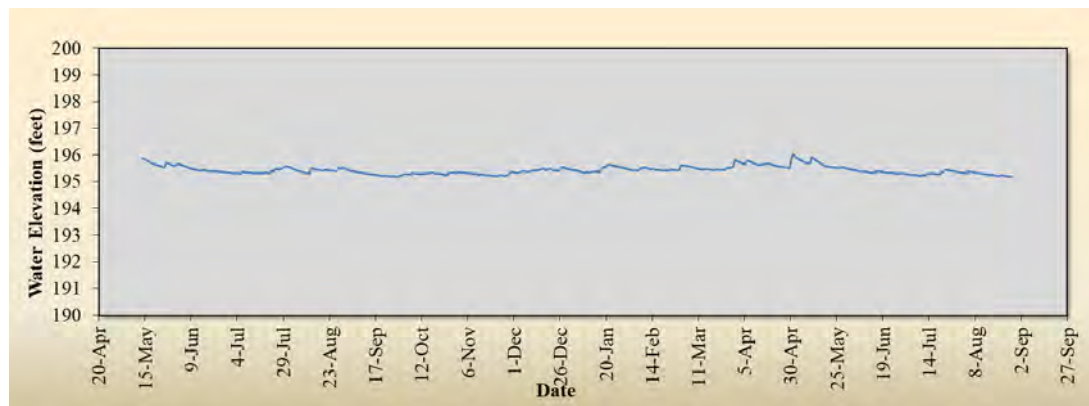


**Figure 4. Groundwater Monitoring Data**

## PILE AND GEOSYNTHETIC SUPPORT DESIGN

The proposed temporary wall, slated to be a modular-type wall, was designed at a bit higher than 6 meters (19 feet) and would transfer an ultimate bearing pressure of around 220 kPa (4,600 psf) due to the required 3-track design. It was clear the in-situ soil profile would be incapable of providing adequate bearing capacity, even considering only the service dead load of 100 kPa (2,100 psf). Considering the required depth of embedment for the wall, excavation would take the leveling pad vertically through the fill and essentially to the top of the upper organic deposit; there would be no fill or ‘crust’ to provide load transfer from the soft and compressible deposits over to more rigid elements. Furthermore, to provide meaningful cost savings, the foundation support would need to be provided via ground improvement or inexpensive timber piling. Aggregate columns in this case would have insufficient lateral confinement and rigid inclusions were required to have extremely close and impractical spacing. Based on price and availability the timber piling was the clear, economical choice for deep foundation support, but they would also need to be capable of handling the high loading from the railroad and an innovative way of transferring load to the piles needed to be developed.

The geometry of the piling was designed to support both the wall loading for 5.5-meter (18-foot) long wall stems, as well as to provide global stability for the embankment up and behind the wall. The final pile layout included two rows of large-diameter timber piles immediately beneath the wall, spaced at 6-feet on-center and capped with 3-foot square concrete caps for an ( $s-a$ )/ $a$  ratio of 1. The loads in the piles were determined based on the tributary area and were calculated at nominal required bearing values of 1032 kN (232 kips) with corresponding factored loads of 672 kN (151 kips). The system then included four additional rows of smaller-diameter piles up into the embankment, designed for 480 kN (108 kips), to provide global stability support.

Previous research (Rui et al 2019) suggested an unreinforced piled-embankment system with this geometry and  $H/(s-a)$  ratio would provide a Stress Reduction Ratio (SSR) of around 0.4, a stress recovery rate of about 0.3, and uniform settlement at the top of the embankment. Some evaluation methods for determination of arching in piled embankments tend to under-predict the loads transferred to the piles, however, so an SSR closer to 0.2 or 0.3 was anticipated, particularly considering the relatively large height of the fill (Van Eekelen et al 2013).

In most locations beneath the wall the upper organic soil unit would be exposed immediately beneath the excavation performed for placement of the pile caps. The reinforcement design evaluations were performed employing methods published by Filz and Smith (2006) via

the Virginia Transportation Research Council (VTRC). Dozens of software iterations were performed using the Geobridge 1.2 workbook, with the results compared against the expected SSR and resulting tension in the geogrid. Ultimately, the design converged on two layers of biaxial geogrid with a combined stiffness requirement of 440 kN per meter (30,000 lbs per foot) and allowable reinforcement strength of 12 to 18 kN per meter (800 to 1,200 lbs per foot) at 2% strain after reductions.

Polymeric geogrid load behavior that is both time and strain dependent (McGown et al 2004). The calculated ultimate, applied load on the wall included three tracks of live rail loading equivalent to about 35% of the total calculated load. The strain induced in the geogrid mobilizes primarily, however, from the longer-term service dead load of the wall and embankment, even though the tensile strength was required to meet the ultimate load. The loading was also only scheduled to be in service for approximately 14 to 16 months. Therefore, taking time and dead load into account the geogrid was designed to act with a stiffness at only 2% strain, as opposed to a higher stiffness at 5% strain. Post-construction settlement was estimated at about 30 centimeters. The two layers of biaxial grid were installed 1.3 cm (6 inches) apart, with the bottom layer 1.3 cm above the top of the pile caps. The total load transfer platform aggregate thickness was 90 cm (3 feet) of Illinois Department of Transportation (IDOT) gradation CA-6 stone.

## PERFORMANCE MONITORING

The timber support piles were to be driven through organic deposits and verified with the Washington State Department of Transportation (WSDOT) dynamic formula, in accordance with the IDOT (2012) standard. Due to the uncertainty of pile verification, both with the use of timber piling as well as driving through peat and organics, the capacity of the piles was verified by dynamic Pile Driving Analyzer (PDA) to assist in establishing site-specific driving criteria and ensure adequate axial capacity. The piles were proposed to terminate at 39 to 40 feet with 232 kips of nominal capacity; the PDA testing showed an average nominal capacity of 205 kips at depths of 38 to 48 feet. The reciprocal factor of safety for the piling was calculated at 2.3 for the service loading and approximately 1.35 to 1.4 for the extreme, 3-track loading.

The overall effectiveness of the geogrid system was evaluated by inclusion of nested, 690 kPa (100 psi) maximum pressures piezometers, installed below and between the pile caps, to measure increases in pore pressure beneath the load transfer system, and an inclinometer installed within Burlington Avenue to monitor potential bulging and lateral load transfer within the organic materials. The upper piezometer was installed at a depth of 2.1 meters (7 feet) below the base of the leveling pad with upper organic soil unit 2 and the second piezometer was installed at 5.2 meters (17 feet) below pad elevation within the organic silty soil unit 3. The inclinometer was positioned about 8 feet from the face of the wall and extended from the surface of Burlington Avenue to a depth of 14 meters (46 feet), locked into the underlying sand unit 4. Schematics of the monitoring placements are illustrated in Figure 5.



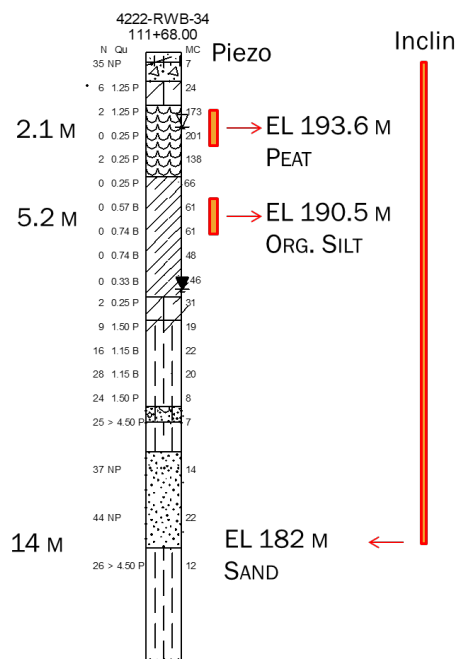


**Figure 5. BNSF Modular Wall Monitoring Device Geometry**

Construction of the wall began in late May 2020 and took approximately 1 week to complete. The piezometers and inclinometer were installed two weeks prior to wall placement to allow for grout set-up and for initial, baseline pore pressure values to be established. Placement of the bottom row of modular block units on May 30 (Figure 6) resulted in a maximum pore pressure increase of only 1.4 kPa (0.2 psi), showing a significant shedding of load over the piles via the geogrid. The second row of blocks placed on June 1<sup>st</sup> (Figure 6) barely registered 0.7 kPa (0.1 psi) during placement and by the time the final row of blocks was placed on June 3<sup>rd</sup> (Figure 6) the ground had actually achieved a state of pore pressure lower than the initial condition. For the remainder of construction, the maximum increase in pore pressure occurred during driving of the stability piles behind the wall, where pore pressures reached approximately 3.0 kPa (0.4 psi).

The inclinometer set approximately 8 feet from the front face of the wall deformed slowly, but consistently to a deformation of approximately 2.5 cm (1 inch) at a point 4 months after the completion of wall construction (Figure 7). The deformation had slowed considerably about 2 weeks following the completion of the wall, but again was accelerated in late June through late July by driving of the support piling behind the wall.

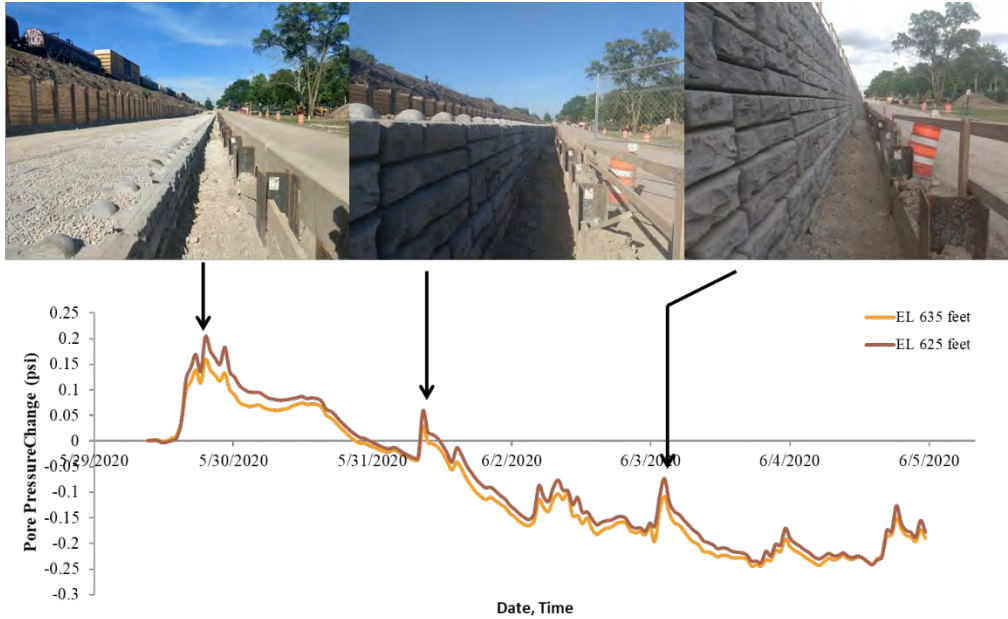


**Figure 6. Pore Pressure Response during Wall Construction**

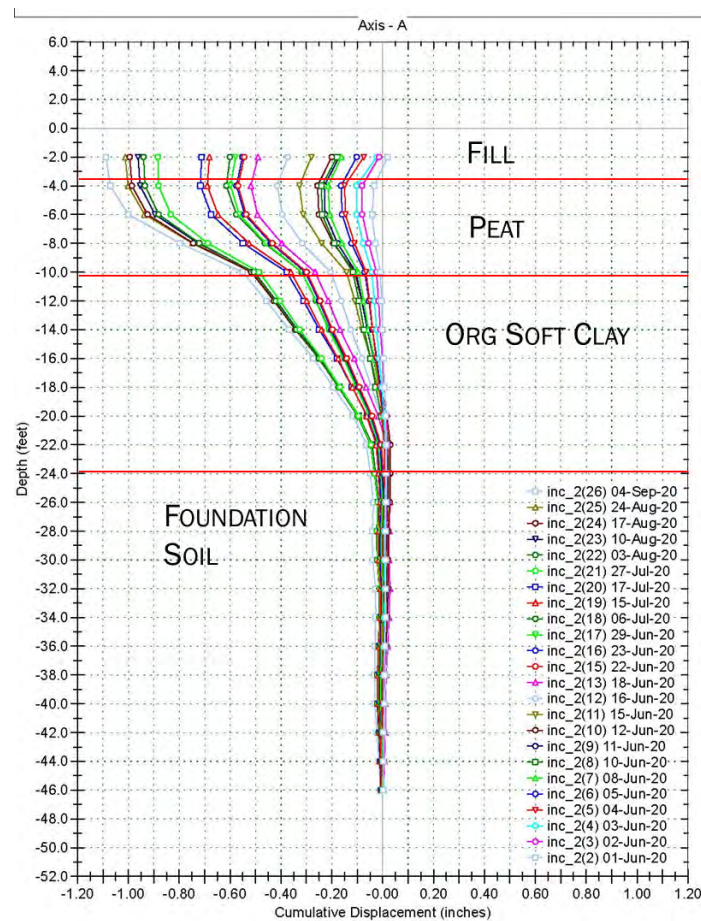


**Figure 7. Post-Construction Inclinerometer Deformations**

## CONCLUDING REMARKS

Pile- or column-supported walls are a cost effective alternative to deep foundation solutions on sites that contain deposits of peat and soft, organic soils. Even with relatively high expected loads, the load transfer platform system with multiple rows of geosynthetic over relatively cost-effective timber piling supported a 5.8 meter wall while allowing less than 2 kPa of excess pore pressure within the underlying highly deformable deposits. Lateral movements of the wall over its service life were ultimately less than 5 cm. Greater pore pressure and lateral movement were recorded as a result of additional pile driving behind the wall than that of the vertical wall load itself. As of this writing, the wall has been deconstructed, the shoo-fly tracks removed, and the new BNSF Bridge over Interstate 294 is in full operation.

## ACKNOWLEDGEMENTS

The authors greatly acknowledge the support and cooperation of the Illinois State Toll Highway Authority as well as our client Gannett Fleming, Inc.

## REFERENCES

- AASHTO (2012) "LRFD Bridge Design Specifications" *American Association of State Highway and Transportation Officials*. Washington, D.C.
- British Standard BS8006-1 (2010) "Code of Practice for Strengthened/Reinforced Soils and Other Fills" p. 250.
- Collin, J. (2007) "U. S. State-of-Practice for the Design of Geosynthetic Reinforced Load Transfer Platform in Column Supported Embankments" *Geo-Denver 2007 Congress: New Peaks in Geotechnics: Denver, USA*.
- Collin, J.G., Han, J., and Huang, J. (2005) "Geosynthetic reinforced column support embankment design guidelines" *The North America Geosynthetics Society Conference*.
- Filz, G.M., and Smith, M.E. (2006) "Design of Bridging Layers in Geosynthetic-Reinforced, Column-Supported Embankments." *Charlottesville, Virginia Transportation Research Council*.
- Gauding, G., Couwenberg, J., and Joosten, H. (2006) "Peat accumulation in kettle holes: bottom up or top down" *Mires and Peat*, v. 1, p. 1-16.
- Hansel, A.K., and Johnson, W.H. (1996) "Wedron and Mason Groups: Lithostratigraphic Reclassification of the Wisconsin Episode, Lake Michigan Lobe Area, ISGS Bulletin 104." *Champaign, Illinois State Geological Survey*, p 116
- IDOT (2012) "Standard Specifications for Road and Bridge Construction." *Illinois Department of Transportation*
- McGown, A, Kupec, J, Heerten, G, and Voskamp, W. (2004) "Current Approaches to the Determination of the Design Stiffness and Strength of Polymeric Biaxial Geogrids"
- Rui, R., Han, J., Van Eekelen, S., and Wan, Y. (2018) "Experimental Investigation of Soil-Archng Development in Unreinforced and Geosynthetic-Reinforced Pile-Supported Embankments." *Journal of Geotechnical and Geoenvironmental Engineering*, Vol. 145(1)
- Sloan, J., Filz, G., and Collin, J. (2012) "Task 10 Report. Column-Supported Embankments: Field Tests and Design Recommendations." *Strategic Highway Research Program, Project SHRP2 R02*, Washington, D.C., Transportation Research Board of the National Academies.

- Van Eekelen, S., Jansen, H., Van Duijnen, P., De Kant, M., Van Dalen, J., Brugman, M., Van Der Stoel, A., and Peters, M. (2010) "The Dutch design guideline for piled embankments." *9th International Conference on Geosynthetics*, Guarujá, Brazil, p. 1911-1916.
- Van Eekelen, S.J.M., Bezuijen, A., and Van Tol, A. (2013) "An Analytical Model for Arching in Piled Embankments." *Geotextiles and Geomembranes*, v. 39, p. 78-102.



## **Polymeric Alloy Geocell Reinforced Design for a Heavily Loaded Gravel Pad with Restricted Fill Thickness**

**Arghya Chatterjee, M.Sc., P.Eng.,<sup>1</sup> Sanat Pokharel, Ph.D., P.Eng.,<sup>2</sup> and Marc Breault.<sup>3</sup>**

<sup>1</sup>Sr. Project Engineer, Stratum Logics, Acheson, Canada; arghya.chatterjee@stratumlogics.com

<sup>2</sup>Principal Engineer, Stratum Logics, Acheson, Canada; sanat.pokharel@stratumlogics.com

<sup>3</sup>President, Paradox Access Solution, Acheson, Canada; marc@paradoxaccess.com

### **ABSTRACT**

Pipelines conveying oil and gas often cross thick organic deposits requiring compressor stations to be built on the weak water-bearing subgrade. Strict environmental restrictions do not allow the removal of underlying organics. This restriction compounded with the associated cost of removal, hauling out, and bringing in a huge amount of virgin aggregate for construction, pose a threat to the overall sustainability of the project. This paper highlights a qualitative approach to selecting the best geosynthetic reinforcement option. The technique was implemented on a compressor pad in Blainville, Canada. The design was optimized for heavy construction loads (multiple 65 Metric Ton compressors) and associated traffic loads on top of a saturated, weak, organic subgrade. Additional geotechnical challenges of fill thickness restrictions and the environmental requirement not to disturb the subgrade were resolved by maximizing the reduction of stress transferred to the existing subgrade and minimizing total fill with better confinement, using novel polymeric alloy (NPA) geocells. Compared to the hypothetical expectations from a conventional design method, the NPA geocell reduced fill volume by 54%, reduced surface settlement by 52.5%, and allowed 63% of the gravel to be replaced with cheaper sand.

### **INTRODUCTION**

Demand for infrastructure development on marginal lands is growing faster than ever. Many of these marginal lands are in environmentally sensitive areas where infrastructure development impacts the environment causing sustainability to get prerogative over other factors.

In Canada, peatland covers about 1.3 million km<sup>2</sup> or about 13% of the available surface area (MacFarlane, 1969). Infrastructure development over peatland requires a reliable soil improvement method to improve the load-bearing capacity of the weak subgrade soil. Strict environmental restrictions significantly increase the difficulty of strengthening weak subgrade soils. It may not always be possible to completely mitigate the environmental footprint, but it can be significantly minimized by utilizing the available geosynthetic soil reinforcement technology. Sustainable development in these areas is centered on using less quantity of scarce virgin aggregate and possibly complete avoidance of the removal and replacement of thick organic native soil. The effectiveness of high-strength novel polymeric alloy (NPA) geocell was studied in the past by several authors. Norouzi et al. (2017) and Pokharel et al. (2019) demonstrated the effectiveness of using NPA geocells for soil reinforcement and reducing environmental footprint. Multiple successful examples of building on top of organic soil without subgrade removal were reported by Shenouda et al. (2021). Yei et al. (2021) summarized the methods for the development of roads on muskeg land. However, all these studies came short in explaining a mechanical approach to

selecting the best possible soil reinforcement solution for given specific project demands. Ramesh et al. (2011), using digital image correlation, identified some properties of geocell influencing the area of load distribution. Hegde and Sitharam (2017) reported that for a softer subgrade, the tensile strength of the geocell material has a more pronounced influence than the surface roughness of the geocell. Thus, it was important not to neglect the strength of reinforcing material for the current study.

The current project under discussion is a 230m x 250m compressor pad with a linked 50m x 25m valve pad (**Figure 1**) located in Blainville, Quebec, Canada. This time-sensitive project was a valuable addition to Quebec's infrastructure. The selection of location was based on existing pipelines and their valve orientation. The specific location presented multiple challenges such as the requirement to build a new access road, environmental permits, geotechnical considerations, and seismic considerations. Despite all the limitations, it was necessary to build a station pad that could support the mobilization of multiple 65 Metric Ton compressor and transformer loads.

This paper discusses an innovative methodology for ground improvement using polymeric alloy geocell reinforcement at the granular subbase and base layers. The reinforcement methodology made the project feasible and had positive impacts on social, economic, and environmental aspects. Discussions are also focused on reinforcement interaction mechanisms and the suitability of the selected option. This study develops a generalized approach for selecting the most suitable reinforcement method specific to design conditions. The approach was implemented on a full-scale project with great success. The results of this design approach met all the design expectations and exceeded the demands of the project. The performance of the pad observed over more than two years has been excellent.

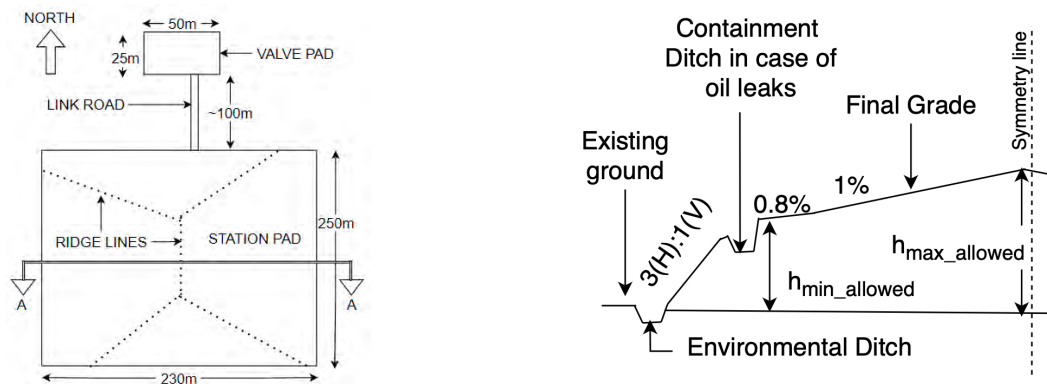


**Figure 1. The layout of pad layout**

**Design Challenges.** Geotechnical challenges, environmental restrictions, and minimum load support requirements were three major challenges to the feasibility of the project discussed here.

### 1. Geotechnical challenges

- **Presence of peat at the surface** – Top 1m to 2.5m was observed to be organic peat. Building infrastructure on top usually demands the removal of the entire organic layer.
- **Weak soil profile for the depth of 32m**– Multiple boreholes showed undrained shear strength of around 19kPa, at depths depth between 3m to 6m below existing ground. This was the critical value for design.
- **Pre-consolidation limits** – Samples collected from 3m to 4.5m depth below existing ground showed pre-consolidation pressure of 62kPa. This limited the maximum thickness

of fill that could be added to avoid extremely large settlements or applying pre-loading. The geotechnical report limited the maximum grade raise to 2.1m of gravel fill.

- **Seismic zone** – A thick deposit of soft to medium clay was present to a depth exceeding 30m. As per the National Building Code of Canada, this soil type is defined as Class F. A site-specific assessment showed the peak of the response spectrum to be 0.55\*g. This presented the potential for liquefaction of the soil.
- **Presence of groundwater on the surface** – It is almost impossible to compact granular infill on top of the saturated soft organic subgrade. This would add to the risk of liquefaction if unconfined/unreinforced sand was used as infill in addition to the potential for a long-term settlement of the soft clay layers to a depth of more than 30m.
- **Settlement expected** – Based on the geotechnical report for the applied load not exceeding the pre-consolidation pressure an average short-term settlement of 0.8m was expected on the top subgrade layers with compression of organics and an additional 75mm due to the long-term clay layer settlement. This short-term settlement would demand additional fill to maintain the minimum grade elevation for 1 in 10 years water level. Also, this short-term settlement increases the quantity of fill material.

## 2. Environmental limitations

- **Restriction to remove saturated existing organics** – There was no permission for hauling out subgrade material. Also, a temporary workspace had to be preserved and returned to its original natural state after use (reclaim land).
- **The limited window for construction** – As the job site was near a residential neighborhood, disruption to the municipal road from material hauling was to be kept to a minimum. Based on total construction days allowed, there was roughly a 4-month window for entire earthwork completion, most of which was through the winter months.

## 3. Load support requirement

Though the thickness of the embankment structure was limited based on the maximum allowable dead load, there was no opportunity to reduce the live loads. **Table 1** shows the critical loads for which the pad was designed. Other non-critical loads were a 65 MT picker on wheels, a pallet load of equipment parts (140kPa for 1m<sup>2</sup> area), a storage container (2.5m x 12m @31MT), concrete barriers, etc.

**Table 1: Design loads**

#	Load description	Pressure on the final grade (unfactored)	Load area
S1	Typical, loaded highway trucks on wheels	750 kPa	0.03 m <sup>2</sup>
S2	Compressors on Jack and slide mat	190 kPa	3.35 m <sup>2</sup>
S3	110T outrigger crane on crane mats	125 kPa	14.7 m <sup>2</sup>

Short term loadings (**Table 1**) were not expected to impact pre-consolidation limits. Geotechnical reports had indicated that maximum seven-day overloading (applied pressure beyond pre-consolidation pressure) would be required to trigger significant settlement. However, static

long-term loading, such as storage containers and concrete barriers, limits the maximum dead load that can be applied without causing an unacceptable level of consolidation settlement. Thus, for those loads, the maximum fill was restricted in the geotechnical report to 1.8m. Since the pre-consolidation limits are spot data on specific boreholes, there is always the risk of an area having localized low pre-consolidation limits. Thus, a margin of safety of around 10% was used on maximum static long-term loads. Areas, where fill height exceeded 1.8m, were demarcated in drawings as areas not suitable for staging loads. Snow load was considered as part of dead weight affecting total allowable fill height.

The maximum allowable fill thickness,  $h_{max-allowed}$  (**Figure 1**), was limited to 2.1m by the geotechnical engineer (excluding the 0.8m expected immediate compression settlement of top organic layers). Since the surface grading design of the pad demanded a minimum 1% positive slope for drainage, the maximum fill at the edges was limited to 1.1m ( $h_{min-acceptable}$  in **Figure 1**). The slope was reduced to 0.8% along the edges (maximum of 20m from the free edge), for achieving the minimum grade elevation for the 1 in 10 years event (**Figure 1**). This zone is along the fence line and is not expected to carry any loads stated in **Table 1**.

## METHODOLOGY

Given that the depth of settlement sensitive to weak soil was at least 32m to the bedrock, the project was in an environmentally sensitive area, and the limited construction window, the conventional ground improvement methods would not have been possible. Electric methods, chemical methods, and stone columns would not have been viable options. Cost, schedule, and the potential for huge settlement of the underlying soft strata ruled out the pre-loading option as well. Light fill using geofabric was also investigated. However, as this compressor pad was being built to handle oil and gas having a potential risk of hydrocarbon leaks, the geofabric option was also dropped. Thus, building an embankment for load support with limited reinforced fill height to create a strong granular structure without removing subgrade was the best available option.

**Understanding soil reinforcement.** Unlike steel and concrete with uniform material properties across the industry, reinforcing soil with geosynthetics demands unique designs. A generalized approach for using geosynthetics has yet to be formulated due to the complexity of characterizing soil reinforcement. However, based on the known mechanisms of stress distribution within reinforced soil, an attempt is being made to theoretically and qualitatively assess the ideal reinforcement.

Failure of soil at any depth can happen either from particles themselves degrading or from relative movement of the particles with respect to one another (**Figure 2**). Unlike the strong chemical bond in concrete, the strength of soil depends on the mechanical interaction between particles and the strength of the particle itself. Interparticle interaction depends on the fundamental friction property of the material, the arrangement of particle geometry, and the surrounding conditions (**Figure 2**). For this study degradation of particles is assumed to be negligible.

The purpose of reinforcement is to improve the bulk properties, particularly layer modulus. Reinforcing soil cannot change particle geometry and the arrangement of particles. However, it can improve the boundary conditions and thus improve inter-particle interaction. Also, owing to the reinforcing material's higher strength properties (like elastic stiffness) as compared to the surrounding particle system, it can share the stress transferred from the soil. The extent of strength sharing depends on the interaction between particles and the reinforcement. This reinforcement-



particle interaction depends on the geometry of the particles, the geometry of reinforcement (affecting parameters like total contact area), the interface friction between reinforcement and particles, and particle confinement. Reinforcement improves soil bulk properties (as summarized in **Figure 3**) by sharing stress (due to reinforcement-particle interaction) and by improving particle confinement (which in turn improves stress sharing).

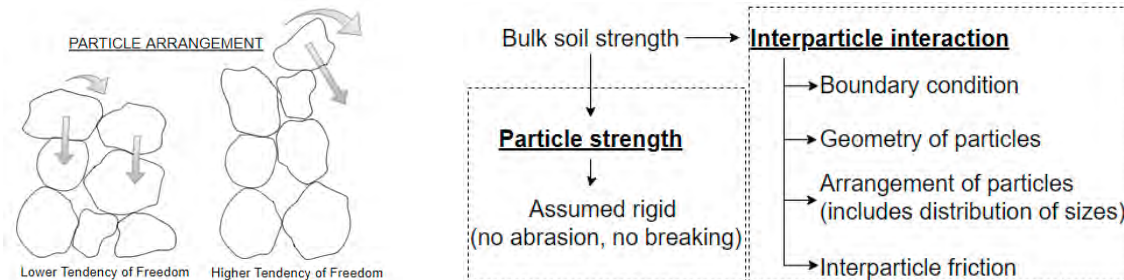


**Figure 2. Particle interaction leading to the bulk properties**

To understand the most suitable reinforcement, the existing set of challenges required assessment. For example, with sand having a low friction angle, and less natural inter-particle interaction due to its particle shape lacking interlocking properties, the confinement aspect of reinforcement is the most important. Stress sharing for sand is expected to be better as the total area of contact between the reinforcement and particle is expected to be more. However, if the reinforcement does not provide enough confinement, then its high-strength material properties may not be optimally utilized through stress sharing. Alternatively, in well-graded fractured particles with good interlocking characteristics, confinement is natural. Stress sharing would depend on particle size to reinforcement opening size and the boundary support depends on the material properties of the reinforcement (such as yield strength with the total amount of reinforcement per unit volume of particle system).

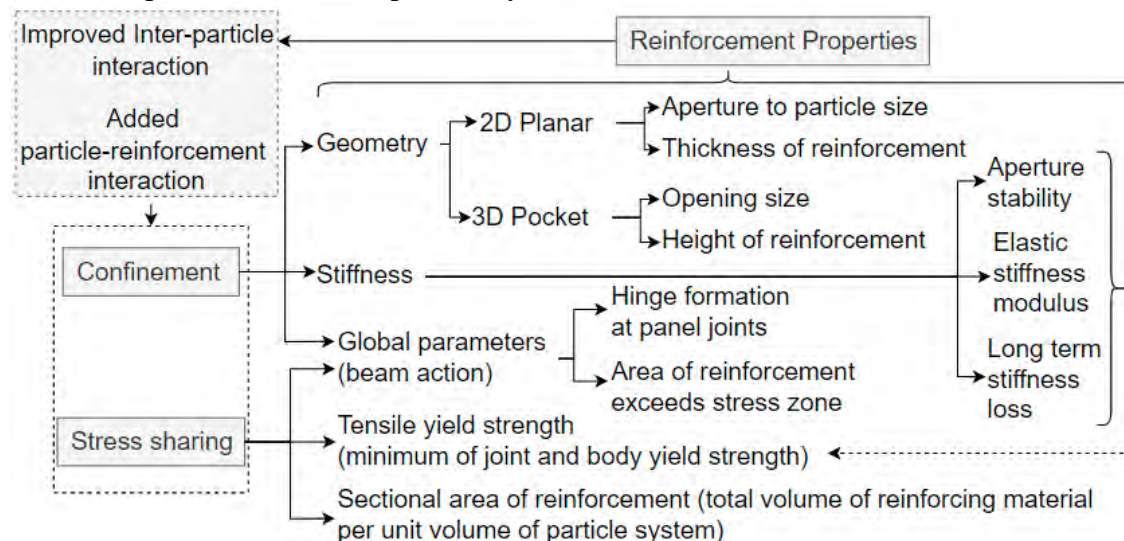


**Figure 3. Properties contributing to the reinforcement of soil**

Due to wall height and planar geosynthetic at the base, the three-dimensional pocket geometry of the geocell provides better confinement than planar reinforcement alone (**Figure 4**), particularly when the particles of granular fill are not interlocking. Even a stronger reinforcement with high yield strength may not necessarily perform better if the particles can move with respect

to the reinforcement. If the reinforcement is not stiff enough (has a low elastic modulus), then it may allow for shape adjustment within the cross-section of the reinforcement (the wall of 3D reinforcement can bow if there is a lateral pressure difference on either side of the reinforcement wall or the aperture of 2D reinforcement may increase) allowing space for particle movement (confinement loss), thus, minimizing the stress sharing by reinforcement. It should be noted that loss of elastic stiffness over time or with load frequency shall have the same effect as confinement loss (**Figure 5**). The three-dimensional geometric confinement improves further with a layer of geosynthetics below, creating pocket geometry for vertical confinement.

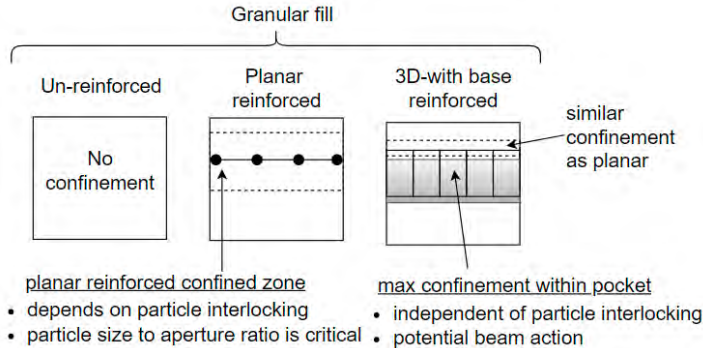


**Figure 4. Various confinement on reinforcement geometry**

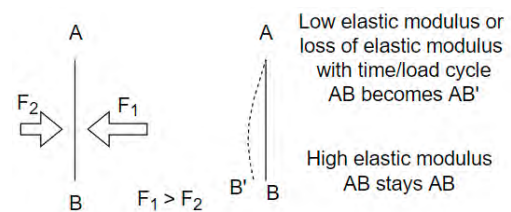


**Figure 5. Confinement loss with wall bowing**

The maximum strength contribution of reinforcement ( $F_R$ ) can be calculated based on **Equation-1**, where,  $F_y$  = Yield Strength,  $n$  = Number of panels per unit length, and  $A_r$  = effect area of each panel (perforations excluded). A loss factor  $\Phi$ , varying between 0 to 1, can be used to account for confinement loss and incomplete interaction between particles with reinforcement.

$$F_R = \Phi * F_y * n * A_r \quad \text{(Equation 1)}$$

Within the three-dimensional pocket geometry, if the confinement is 100% (all particles within the pocket are rigidly locked in position), then the reinforced soil can potentially behave like a beam. Reinforcement wall height ( $h_r$ ) is the expected depth of the beam for the second moment of inertia ( $I_R$ ) calculation. Beam action not only bridges local soft spots but also, maximizes the stress distribution over a wider area (**Figure 8**) and thus, reduces the vertical propagation of stress. It must be noted that if the reinforcement panels are not rigidly connected creating a unibody panel, or there are other conditions leading to the development of hinge-like behavior, then the advantage of beam action may not be applicable.

**Figure 6** shows the aspects relevant to the current project that led to the selection of specific reinforcement choices. Long-term behavior of the material plays an eminent role in performance and maintenance, particularly with the high load frequency of construction vehicles. Thakur et al. (2013) showed the creep advantage of using novel polymeric geocell (NPA). Creep resistance is an outcome of reinforcement holding material and geometric properties over time (with large load cycles).

To build on the soft subgrade Amarnath et al. (2015) showed the performance of 3D pocket geometry on the soft clay subgrade. Compaction and workability are big challenges when the subgrade is not strong enough to support compaction equipment. Yet, achieving a minimum of 92% modified proctor density (at +/-2% of optimum moisture) for sand was necessary to avoid

possible liquefaction risk. With sand, the lack of interlocking capability demanded 3D pocket confinement. Also, the beam action (with each reinforcement panel being rigidly connected) was necessary for workability on the saturated soft subgrade (**Figure 12**).

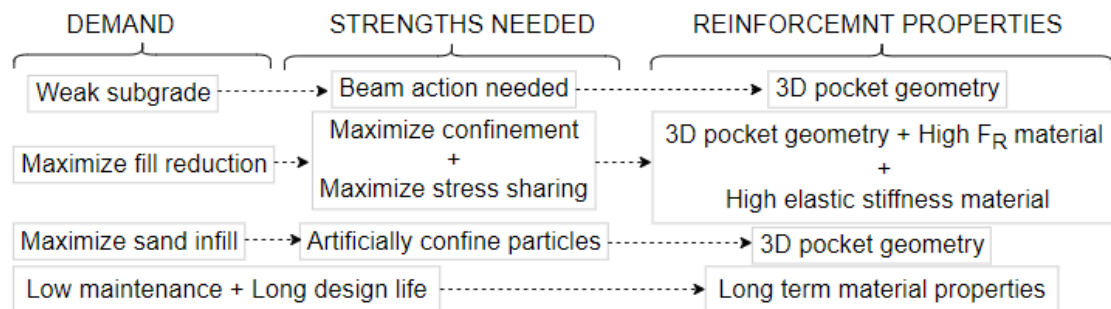


**Figure 6. Selection parameters for reinforcement**

To limit fill height, it was necessary to maximize the reinforcement effect with multiple layers of 3D reinforcement. Available 3D reinforcement with maximum elastic stiffness modulus and maximum  $F_R$  (**Equation 1**) would best serve the purpose. After a detailed study of available options, Type C and Type D NPA geocell with properties stated in **Table 2**, were selected for the current design. In addition to that proven to be a sustainable solution (Norouzi et al. 2017), NPA Geocell reinforcement was chosen.

**Table 2: Properties of NPA geocell selected**

Characteristics	Type C	Type D
Wide-width strength at yield	19 kN/m	22 kN/m
Coefficient of soil-cell friction efficiency	0.95	0.95
Long term plastic deformation at 65°C (load 6.6 kN/m)	<3.0%	<3.0%
Dynamic (elastic stiffness) modulus at +30°C	>775 MPa	>800 MPa

The Han and Pokharel design method (Pokharel, 2010 and Han, 2015) for unpaved road design was used to design the geocell-reinforced structural gravel layers for rutting criteria. This method was validated for road design in different subgrade conditions in Canada by Pokharel et al. (2015), Yui et al. (2019), and Shenouda et al. (2021). This method determines the base course thickness required for the design loads (**Table 1**), effectively reducing bearing pressure for reinforced granular fill, and thus increasing bearing capacity-based subgrade strength. For the given saturated peat subgrade CBR was calculated to be within 0.5% to 0.8%. **Figure 7** shows the typical design section with 3 layers of NPA geocell. 1200N non-woven geotextile was used directly on top of the existing subgrade which not only added to the pocket geometry but also acted as a separation layer. The performance of the design depended on the long-term creep resistance of the pocket geometry. The 800N woven geotextile (**Figure 7**) was checked for potential failures from local stress within the pocket. For the top layer Type D was used as that layer had the exposure to maximum fatigue. For the remaining two bottom layers Type C was found to be optimal.

The middle layer was originally designed with MG112 (sand) (BNQ 2560 -114/2014). However, it was changed as other trades of construction (pipe installation, piles, etc.) had to start

operating prior to the completion of the top layer. Though that was structurally safe, local yielding under the loaded tires with a shorter turning radius invited the risk of equipment getting stuck in the sand and/or damaging the geocell layer. Thus, the middle layer was replaced with gravel.

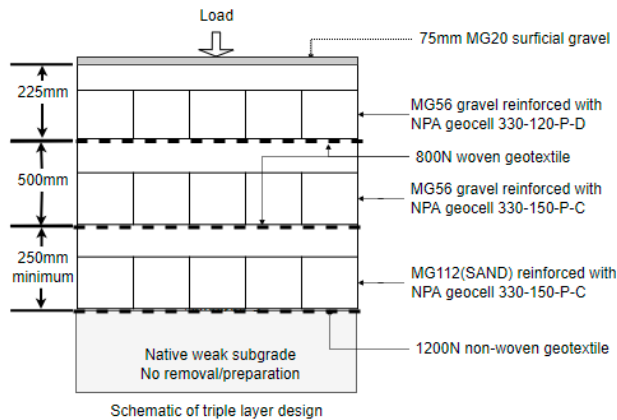


Figure 7. Typical reinforced layer design

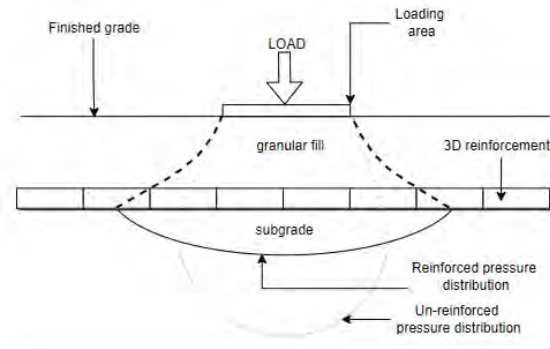


Figure 8. Schematic effect of increasing granular layer stiffness

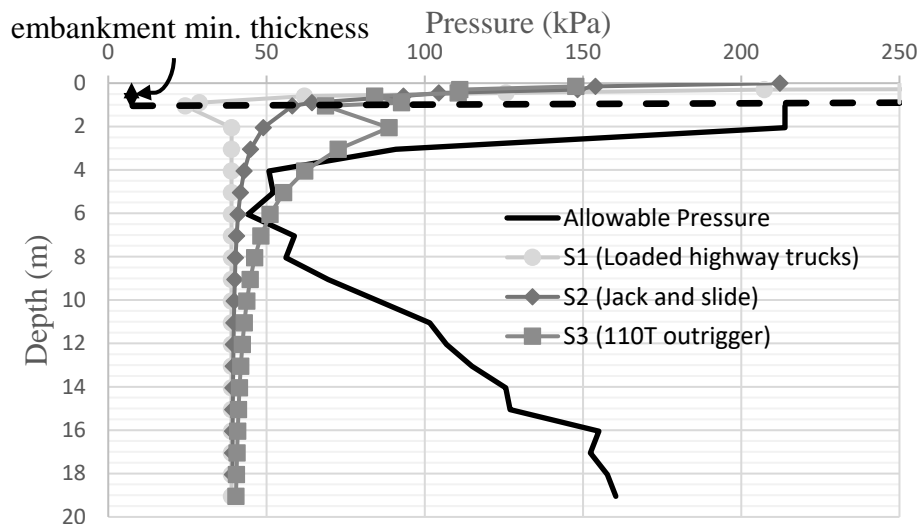


Figure 9. Stress profile with depth for various loads

For the weak clay underneath, it was observed that design failure may not happen at subgrade elevation, rather it can be triggered at depths between 4m to 8m. Thus, the design was adjusted for safe operations at the weakest zones of the soil column (**Figure 9**). Since the allowable pressure is approximate spot data, with a factor of safety 3, pressure distribution from critical loads (**Table 1**) at around 4m depth in **Figure 9** was considered acceptable (within 10% of the average allowable pressure envelope).

**Maintenance plan and winter compaction.** For the given construction schedule, it was necessary to build the pad through the winter months. Due to the confinement from geocell pockets, it was deemed acceptable to compact unfrozen granular fill in sub-zero air temperatures. However, it was recommended that the bottom layer of the geocell (at least 2 lifts of 300mm total) for the entire



pad shall be completed before the ground freezes. This was necessary for the initial settlement of peat. Heating and hoarding were not required.

With winter construction and other trades running with the intent to continue their operation while the reinforced granular layers were being built, a maintenance plan was necessary. Peak loads (**Table 1**) were not allowed until all three design layers were complete. However, after the second layer of geocell with a minimum 75mm gravel cover was in place, conventional highway truck loads were allowed under the strict observation of the site engineer. Maintenance recommendations stated that rutting exceeding 50mm, needed surface grading. Adding 50mm granular fill on the surface and compacting was recommended for ruts extending over large areas or to maintain the grade for positive drainage. With deeper rutting, it was recommended to stop loading that area further, until material up to subgrade elevation is excavated and rebuilt to design specifications (including stitching new geocell with surrounding geocell layers). Some amount of surface maintenance (grading and re-compaction of the surface) was also expected during the first seasonal thawing. No axle load limits during the thawing season were deemed necessary.

## RESULTS AND DISCUSSION

The geocell-reinforced design made the project feasible and attained high standards of sustainability. A reduction in fill has a major impact on all sustainability parameters in any earthworks project. Less infill material and no subgrade removal reduced the number of trucks on the road. Compared to a hypothetical unreinforced section, the total reduction of infill volume was almost 54% and a 100% elimination of subgrade removal. This equated to roughly 9,800 fewer truck loads (at 30 metric tons per truck) hauling in material and 3,100 trucks hauling out the peat. Based on a typical US haul truck producing 161.8gm of CO<sub>2</sub> per ton-mile (based on the Green Fright Handbook by Jason M., et al. (2015)), that's a total saving from trucks alone of 739MT of CO<sub>2</sub> for the environment. This includes virgin material extraction and hauling required.

Fewer trucks on municipal roads mean less traffic volume for the local community and less damage on municipal roads. Selected NPA geocell, with high dynamic elastic modulus, do not deteriorate material properties significantly with high load frequency. Due to this property, there are low strains within the reinforcing material and less confinement loss over time. This adds to the low maintenance cost.

For the compressor station pad and the valve pad, necessary compaction in the first lift (225mm thick sand fill on top of the subgrade with NPA geocell) was achieved. Using 3 layers of NPA geocell, meant all the loads could pass failure conditions within the given fill limit. The minimum fill necessary at edges was 1.05m and allowed was 1.1m. This was made possible because of stiffer layers distributing stress over a wider area (**Figure 8**). The design could successfully achieve and exceed all the limitations posed by geotechnical and environmental reports (**Figure 10**).

The settlement was checked at multiple locations with the placement of plates on top of the existing ground prior to the placement of any fill and an extension projecting out for periodic survey measurements. Observed settlement at no point exceeded 380mm, where the expected settlement from the geotechnical report was 800mm. This was possible because of reduced stress on the subgrade. The reduction of 52.5% of settlement which led to further fill reduction had a significant impact on total cost savings. Less fill means less virgin material extraction from the quarry.

Avoiding heating and hoarding through winter accelerated the construction process and added to cost savings. Not limiting axle load during the first thawing season did not lead to any noticeable failure. This also added to the ease of the accelerated construction schedule. Some occasional surface maintenance (around once every 3 or 4 weeks) and maintenance (grading) during the first thawing period were necessary. The original maintenance plan expected maintenance of local areas every 2 to 6 weeks depending on load frequency and the total thickness of the structure. At no point was excavation or rebuilding necessary. Maintenance efforts did not involve any excavation or interfere with the construction execution plan and schedule. Reclaiming land for temporary staging areas was an easy recovery as the organic layer was well preserved under the non-woven geotextile separation.

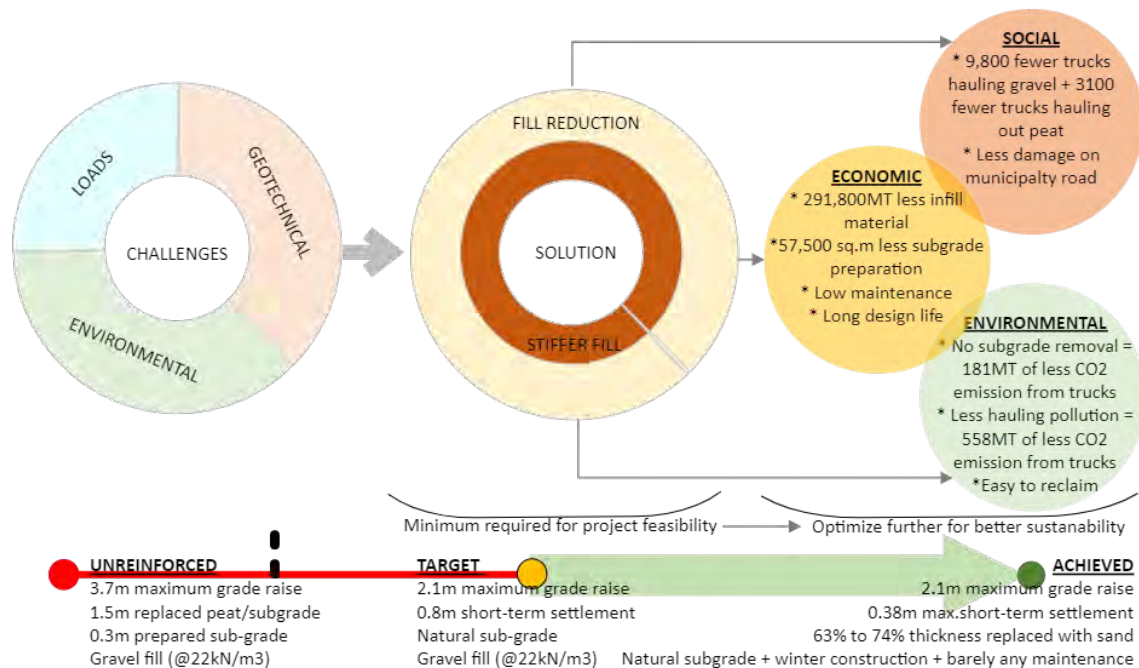


**Figure 10. Target and achieved design summary**

The subgrade condition where construction started is shown in **Figure 11**. Work progressed smoothly through the winter months (**Figure 12** and **Figure 13**). **Figure 14** and **Figure 15** show operation and crane loading on top of the pad. Visual inspection after 18 months from completion of construction showed no rutting or local settlement areas disrupting smooth surface drainage (**Figure 16**).



**Figure 11. Existing subgrade condition and bottom layer of geocell**





**Figure 12. Progress of 3 layers of geocell through winter**

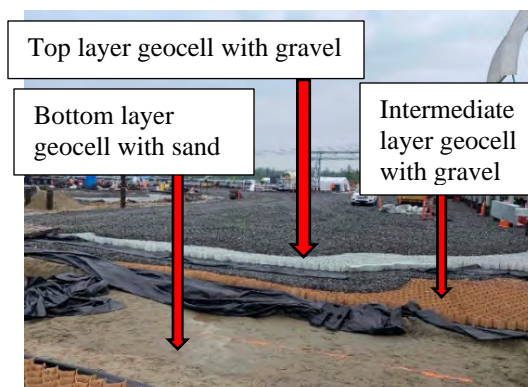


**Figure 13. Top layer geocell being built**



**Figure 14. Operation in progress**



**Figure 15. Crane lifting**



**Figure 16. Pad surface after 18 months of operation**

## CONCLUSION

Through this paper, an attempt has been made to qualitatively assess the right soil reinforcing product based on specific design challenges/requirements. It also highlights how the right ground improvement design can convert an almost unfeasible project into a sustainable solution. NPA geocell as the choice of reinforcement with high elastic modulus and yield strength played a major role in the successful execution of the project. One of the major aspects of sustainability, cost

savings, was achieved by reducing the hauling (eliminating around 12,900 hauling truck trips). That, along with maximizing infill reduction (around 43% reduced fill thickness), maximizing the use of locally available cheaper infill (up to 74% thickness of infill was replaced by sand), and eliminating the subgrade removal, helped reduce the environmental impact. Additionally, the reduction in the number of truck trips helped reduce the safety and societal impacts.

There is the future scope of research on developing calibrated mathematical tools for optimizing the selection and design of the most suitable soil reinforcement.

## REFERENCE

- Giroud, J.P. and Han, J. (2004), Design method for geogrid-reinforced unpaved roads, I: Development of design method, *Journal of Geotechnical and Geoenvironmental Engineering*, 130(8): 775–786.
- Han, J. (2015), *Principles and Practice of Ground Improvement*, John Wiley & Sons, Inc., Hoboken, NJ, USA.
- Pokharel, S. K. (2010), *Experimental Study on Geocell-Reinforced Bases under Static and Dynamic Loading*, Civil, Environmental, and Architectural Engineering Department, University of Kansas, Kansas, USA.
- MacFarlane, I. C. (1969), *Muskeg Engineering Handbook*. University of Toronto Press, Toronto, Ontario, Canada.
- Norouzi, M., Pokharel, S.K., Breault, M., & Breault, D. (2017), Innovative Solution for Sustainable Road Construction, *Leadership in Sustainable Infrastructure*, CSCE, Vancouver, Canada, 085:1-10.
- Pokharel, S.K., Yui, T.Y., Breault, M., Norouzi, M. (2019), High Strength Geocell and Geogrid Hybrid Reinforcement for Compressor Station Gravel Pad on Very Soft Subgrade, *Geosynthetics 2019*, IFAI, Houston, TX
- Yui, T., Pokharel S., Ali M., and Breault M. (2021), Unpaved Access Road Utilizing Polymeric Geocell Reinforcement over High Water Bearing Muskeg, *Geosynthetics 2021*, IFAI, Roseville, MN, USA, 1: 606-617
- Norouzi, M., Pokharel, S.K., Breault, M., & Breault, D. (2019), Geocell-Reinforced Pavement Structure State of Practice in Canada, *Innovation in geotechnical and materials engineering*, TAC-ITS Canada Joint Conference, Halifax, Canada.
- Thakur J.K., Han, J., Parsons R.L. (2013), Creep behavior of geocell-reinforced recycled asphalt pavement (RAP) bases, *ASCE Journal of Materials in Civil Engineering*, 25(10), 1533-1542.
- Amarnath M. Hegde, T.G. Sitharam. (2015), Effect of infill materials on the performance of geocell reinforced soft clay beds, *Geomechanics and Geoengineering*. 10:3, 163-173, DOI: 10.1080/17486025.2014.921334
- Jason M, Elena C, Marcelo N, Christina W (2015), *The Green Freight Handbook*, Published by environmental defense fund, New York, NY, USA.
- BNQ 2560 -114/2014 Bureau de Normalisation du Quebec (Travaux de genie civil – Granulats)
- Ramesh G., Swetha K., Nithin S., Rajagopal K. (2021), Assessment of load distribution mechanism in geocell reinforced foundation beds using Digital Imaging Correlation Techniques, *Transportation Geotechnics*, Vol. 31, 100664, ISSN 2214-3912.
- Hegde A, Sitharam T.G. (2017), Experiment and 3D-numerical studies on soft clay bed reinforced with different types of cellular confinement systems, *Transportation Geotechnics*, Vol. 10, pp 73-84, ISSN 2214-3912.



## Decentralized Stormwater Runoff Treatment with Active Geocomposites

Trevor M. Walker, P.E.,<sup>1</sup> Stefan Niewerth, Ph.D.,<sup>2</sup>

<sup>1</sup>HUESKER Inc., 3701 Arco Corporate Drive, Suite 525, Charlotte, NC, 28273; e-mail: [twalker@HUESKER.com](mailto:twalker@HUESKER.com)

<sup>2</sup>HUESKER Synthetic GmbH, Fabrikstrasse 13-15, 48712 Gescher, Germany; e-mail: [niewerth@HUESKER.de](mailto:niewerth@HUESKER.de)

### ABSTRACT

A research project is underway which is exploring contamination reduction through the use of sustainable drainage systems. Geotextiles were evaluated in the laboratory for their ability to retain total suspended solids in stormwater runoff from roadways. In the subsequent phase, tests were conducted using active geocomposite materials installed within road drainage areas to determine their pollutant retention in the field. Various geotextile and soil combinations were installed adjacent to the road and water samples were taken from collection tanks. The field trial has been running for about seven months. This paper will elaborate on the background of sustainable drainage systems, the lab and field test procedures, and discussion of their results.

### INTRODUCTION

Stormwater runoff from paved streets consists of a variety of pollutants and total suspended solids (TSS). Hydrocarbons, microplastics, and metals/metalloids are prominent substances that contribute to pollution within the road runoff. In order to reduce the amount of contamination entering stormwater sewers, sustainable drainage systems (SuDS) are being explored.

Sustainable drainage systems (SuDS) are a stormwater management strategy that utilizes natural occurring hydrological and biophysical processes of more ecofriendly systems to treat and transport stormwater. This is in contrast or a supplement to the more conventional approach of pipes and concrete structures that serve only to transport the runoff to a treatment facility (Chen 2021). Examples of SuDS include rainwater harvesting systems, green roofs, infiltration systems, swales, bioretention systems, permeable pavements, attenuation storage tanks, detention basins, and wetlands (Chen 2021). The system being evaluated in a current research project, and that will be discussed herein, is a drainage area constructed adjacent to the roadway that provides preliminary treatment of the stormwater runoff. The primary technology behind the decentralized treatment is the active geocomposite material installed within the drainage layers. The reason for using the word “decentralized” is that the drainage cross-section, which includes the active geocomposite and overlying fill material, provides a layer of water treatment prior to the runoff arriving at a treatment facility where typically the comprehensive methods of water treatment are “centralized”.

### SYSTEM COMPONENTS

The main component in the treatment system defined here is an oil-absorbing active geocomposite mat. This is a three-layer composite consisting of two black protective geotextiles (300 g/m<sup>2</sup> PP non-woven) sandwiching a white oil-absorbent layer (200 g/m<sup>2</sup> PP non-woven) and is displayed

in Figure 1. The three components are needle-punched over their entire surface and are thus friction-locked. The product has a standard width of 2.2 m and a length of 40 m.



**Figure 1. Picture of active geocomposite mat used in this study.**

The active geocomposite is a certified oil binder, with entry in the GÖC eV list (Association of Manufacturers of Tested Oil & Chemical Binding Agents). Due to its material structure, it is not only suitable for the absorption of oils and other fuels and lubricants, but also for the filtration of TSS. This ability essentially results from the average product thickness of 6 mm and the average O-90 value of 45  $\mu\text{m}$ . These product properties ensure that the fine particles are retained, but that the system still has a permeability of  $k > 1.0 \text{ E-}06 \text{ m/s}$  after a pollutant load of more than 200g Millisil W4 was subjected to a 7 cm diameter sample. This corresponds to a classification as "permeable" according to DIN 18130-1 (Laboratory tests for determining the coefficient of permeability of soil) even after many years with a pollutant load on a heavily trafficked road. Basically, it is stated that the active geocomposite complies with all specifications for a geotextile according to the German guideline Technical Terms of Delivery for Geosynthetics in Earthworks for Road Construction (TL Geok E-StB Tech 2019).

To protect the active geocomposite against mechanical impacts and UV radiation, a topsoil must be installed as a second component above the geotextile. In the field tests, a bulk material mixture with a comparatively high proportion of coarse grains was selected as the topsoil in accordance with the German Guidelines for the Design, Construction and Maintenance of Green Pavements (FLL 2018). In the FLL 2018, the material is referred to as "gravel turf" and is defined as a "mixture that is particularly suitable for vegetation and has a high load-bearing capacity". The grain-size distribution of the bulk material mixture is displayed in Figure 2. The combination of the active geocomposite and the vegetated fill mixture leads to the high TSS retention rates and thus constitutes the required system components. *Illustration 2 shows distribution with log scale.*

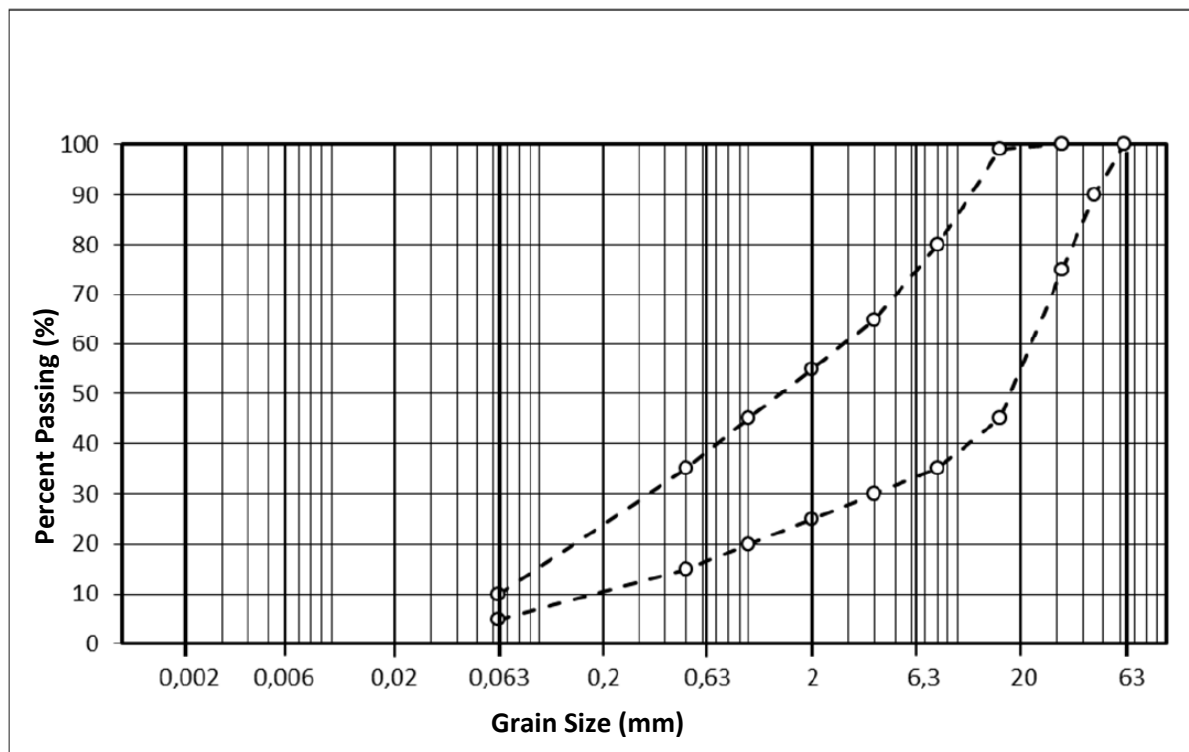
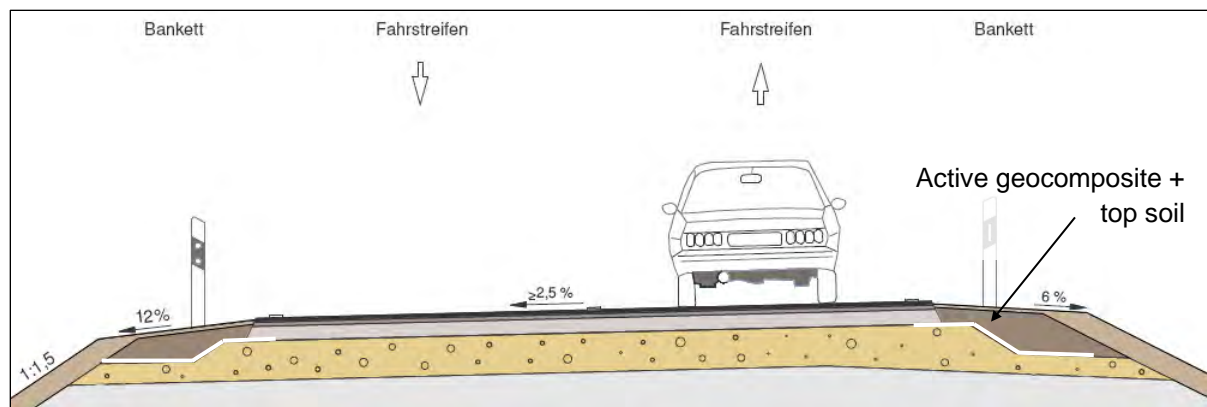


Figure 2. Grading curve range for the bulk material mixture.

## SYSTEM STRUCTURE

A major advantage of the system is the simple installation, either on new road constructions or existing roads. The system structure requires approximately 1.50 m of space in the shoulder area of a road. This is possible with almost all standard cross-sections according to the applicable guidelines for the construction of roads.

**New road construction.** Along with a new road construction, the active geocomposite is laid in the edge area of the road with a width of 0.20 m to 0.50 m under the asphalt structure. After the base layer has been compacted, the composite is rolled out accordingly and then overlaid with the asphalt structure. In this way, the filter mat is friction-locked to the road body. Due to the product width of 2.20 m, the active geocomposite is installed in the soil over a width of up to 2.00 m in the roadbed area. This width, in connection with the permeable bulk material mixture, is sufficient to filter the runoff water of the road body. Whether or not the system will be installed on the uphill side of the road must be determined on a case-by-case basis, since most of the runoff will migrate downgradient. A cross-section of the roadway section incorporating the treatment system is displayed in Figure 3.



**Figure 3. Cross-section of new roadway with active geocomposite and topsoil system.**

**etrofitting existing roads.** When retrofitting existing roads, the active geocomposite cannot be laid under the existing surface or binder course. Instead, it should be somehow anchored to these layers. Simple nail systems, e.g. with nails, are suitable for this purpose. A design recommendation to create a fixed connection of the geocomposite to the existing road would need to be provided.

## DESCRIPTION OF LABORATORY AND FIELD TESTS

In order to prove the effectiveness of the system consisting of the active geocomposite and a bulk material mixture for the decentralised treatment of precipitation runoff, an extensive measurement program was carried out in the field as well as in the laboratory. Here, the focus was on the test procedures of the DIBt (German Institute of construction techniques) for the discharge of precipitation runoff into the soil-groundwater system. In the DIBt test regulations, a defined retention of 92% Millisil W4 is required in the laboratory test. This refers to 80% retention of TSS smaller 63 microns. In addition, the DIBt procedure requires a further test for the retention of heavy metals (copper and zinc) and chlorinated hydrocarbons (CHCs).

Within the framework of the research project, the retention of various nonwovens as well as active geocomposites against TSS (in the field) and Millisil W4 (in the laboratory) was investigated. The tests were carried out by the project partner Münster University of Applied Science and are shown in Figure 4. The tests were based on the tests developed by DIBt for the approval of filter systems. Based on the test procedure, a defined amount of Millisil W4 was applied to the nonwovens and the retention was calculated with the help of a weight determination. To achieve this, the weight of the unloaded test specimen and the weight of the Millisil load were measured. After filtering through the loaded water, the test specimens were dried and the difference in weights before and after filtration were determined. The calculations showed that the active geocomposite (AS 200 in Figure 4) has a uniform retention of TSS in all three-test series, which is 95.41% on average, which exceeds the 92% retention limit value defined by DIBt.



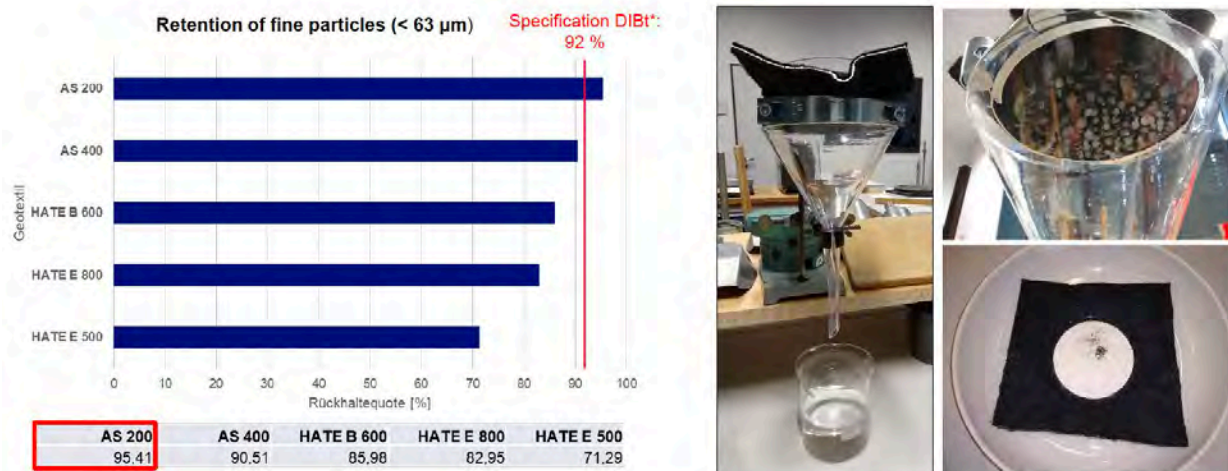


**Figure 4. Laboratory tests retention rates Millisil W4 at Münster University of Applied Sciences.**

In the next step of the research project, five test fields were set up with different geotextile/soil combinations to treat the runoff. The primary constituents of the fields were as follows: Field 1 consisted of only soil, Field 2 consisted of soil overlying a geocomposite made with recycled material, Field 3 consisted of soil overlying an active geocomposite impregnated with granular activated carbon (GAC), Field 4 consisted of soil overlying two geocomposites containing the oil absorbent and GAC, and Field 5 consisted of soil overlying the oil absorbing geocomposite. These layers were placed within a sealed box having a gentle slope, where the runoff would infiltrate downward through the layers and into a gutter linked to specific sampling points within manhole.

During the field trials, water samples were regularly taken from collection tanks connected to the test fields. Water samples were tested for TSS, metals, and polycyclic aromatic hydrocarbons (PAH). Daily precipitation was also measured during field testing. As per the laboratory tests, the best performance in the field was shown with the active geocomposite AS 200. As a reference for determining the retention rate, a gutter was installed directly next to the test fields. This was where the unfiltered and untreated road runoff was collected. The water that seeped through the test fields was collected in collection tanks, which were emptied after each sampling. Areas of the test fields are pictured in Figure 5.



**Figure 5. Photos of the test fields in Münster (Busso-Peus Straße).**

The left-hand side of Figure 6 displays the TSS retention percentages for the active geocomposite and topsoil treatment system located in Field 5 for 16 filtered runoff water samples. The right-hand side displays the quantitative measurements of the TSS from both Field 5 and from the unfiltered runoff, which is designated as the blind test field. The retention percentages were calculated using the absolute values from the measured TSS concentrations from the Field 5 and unfiltered collection areas.

Test series	TSS Retention with Tektoseal Active AS 200 + top soil [%]
E-1	96,58
E-2	97,90
E-3	98,82
E-4	91,36
E-5	99,70
E-6	93,46
E-7	89,98
E-8	83,11
E-9	97,02
E-10	97,64
E-11	(113,88)
E-12	99,25
E-13	98,48
E-14	95,29
E-15	98,92
E-16	(100,35)
<b>Average:</b>	<b>95,53 (excl. Values in brackets)</b>

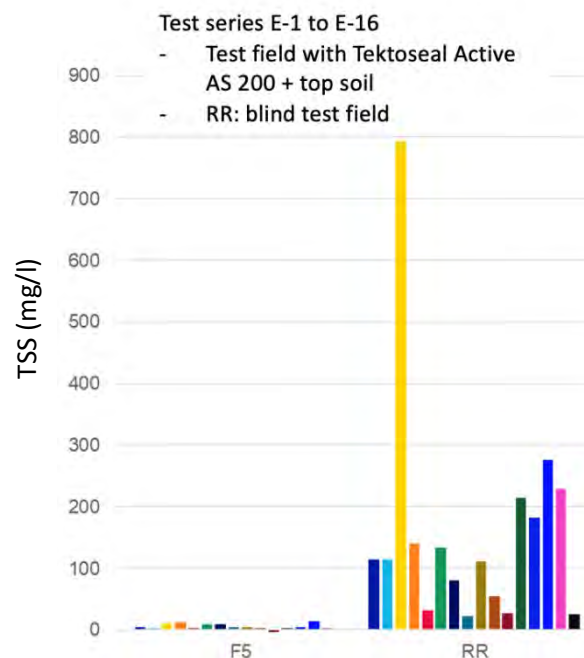


**Figure 6. TSS load results of the treated runoff from field 5 and untreated runoff area.**

In addition to the TSS evaluation, analyses for various pollutants within the stormwater were also regularly carried out by an independent laboratory in Münster. For lead, copper and zinc, the system resulted in an average reduction according to Table 1 below.

**Table 1: Removal of heavy metals from leachate**

Metal	Unfiltered street runoff in gutter [mg/l].	Test field with Active Geocomposite AS and bulk mixture [mg/l].	Percentage Retention
<b>Lead (Pb)</b>	0,007	< 0,001	<b>86%</b>
<b>Copper (Cu)</b>	0,028	0,005	<b>81%</b>
<b>Zinc (Zn)</b>	0,111	0,023	<b>80%</b>

So far, no hydrocarbons have been detected in the leachate. In principle, however, the removal of hydrocarbons by the treatment system will occur, since the core of the filter mat consists of an oil-absorbing non-woven, and this is the original intended use of the active geocomposite. Contaminants with mineral oils will be stored long-term within its inner structure. Other laboratory tests outside this scope have demonstrated that the geocomposite can remove more than 99% of hydrocarbons contained in an emulsified mixture. The scope of research does not include investigating biodegradation of the sorbed oil over time.

## CONCLUSION

Sustainable drainage systems are continuing to develop into important infrastructure features that reduce the stress on the environment and water treatment facilities. Their ability to reduce contaminant concentration in stormwater runoff prior to the water reaching the treatment facility is a prominent feature of these systems. The study described herein proves that stormwater runoff can be pre-treated very effectively through the use of an active geocomposite and overlying fill material in drainage areas. TSS and metals were significantly reduced through the use of this system. Therefore, the combination of the lab tests and field performance of the decentralized stormwater treatment system make a strong case for the system's implementation on a larger scale.

## REFERENCES

- DIN 18130-1, *Soil - investigation and testing; Determination of the coefficient of water permeability - Part 1: Laboratory tests*, Beuth publishing DIN, 1998-05.
- FLL, (2018), *Guidelines for the design, construction and maintenance of vegetated pavements*, Research organization for landscaping and landscape architecture.
- Season S. Chen, Daniel C.W. Tsang, Mingjing He, Yuqing Sun, Leslie S.Y. Lau, Richard W.M. Leung, Edwin S.C. Lau, Deyi Hou, An Liu, Sanjay Mohanty, (2021), Designing sustainable drainage systems in subtropical cities: Challenges and opportunities, *Journal of Cleaner Production*, Volume 280, Part 2, 2021, 124418, ISSN 0959-6526.
- TL Geok E-StB, (2019) *Technical delivery conditions for geosynthetics in earthworks for road construction*, FGSV, ISBN: 978-3-86446-249-8.

## Evolution in Geosynthetics Starts with Utilizing Data Technology

Gregory Pignataro<sup>1</sup> and Evan Bao<sup>2</sup>

<sup>1</sup> COMANCO, Plant City, FL; e-mail: gpignataro@comanco.com

<sup>2</sup> COMANCO, Plant City, FL; e-mail: ebao@comanco.com

### ABSTRACT

This paper focuses on the automation of the geosynthetics installation QA/QC process by way of software integration in the field data entry and office data management. Technology is essential to the advancement of geosynthetic installations, especially data application. In its most basic form, data application is a means of gathering, storing, and utilizing information more easily than its predecessor(s). If implemented appropriately, data application technology improves process efficiency. Users and downstream stakeholders of process improvements can then capitalize by delivering quicker, higher-quality, more economical products. The geosynthetics industry is lagging in the area of data application. From a feasibility perspective and assessing practical implementation opportunities, many workflows widely used for tracking geosynthetic installations and its associated means and methods are antiquated and, furthermore, lack reliable authenticity verification. The current accountability requirements require a robust catalog of information reporting to substantiate this important environmental construction practice. The combination of room to evolve in practice and existing data requirements make the geosynthetics industry an ideal suitor for this technology integration. While advancements in materials manufacturing, welding equipment, and post-installation leak surveys already contribute to progress, there is a lack of universally accepted information infrastructure to aggregate all facets of an installation. Software automation create a cyclical geosynthetics ecosystem that benefits the industry as a whole.

### INTRODUCTION

The QA/QC process is the logical starting point for the automation of the QA/QC process as it performs three key functions when automated

First, it improves physical field quality assurance (QA), which produces geosynthetics installations with greater focus on assuring that the services meet the regulatory requirements of each project rather than just collecting data.

Second, automation expedites the review and reporting quality control (QC) by built-in analysis algorithms.

Third, automation creates a centralized database that leverages past installation and supplements of the experience with different materials in geosynthetics projects throughout the industry (Ramsey 2019).

These general principles will be examined more in-depth and evolve in the following paragraphs. The cyclical nature of improved QA/QC is illustrated in Figure 1 below.



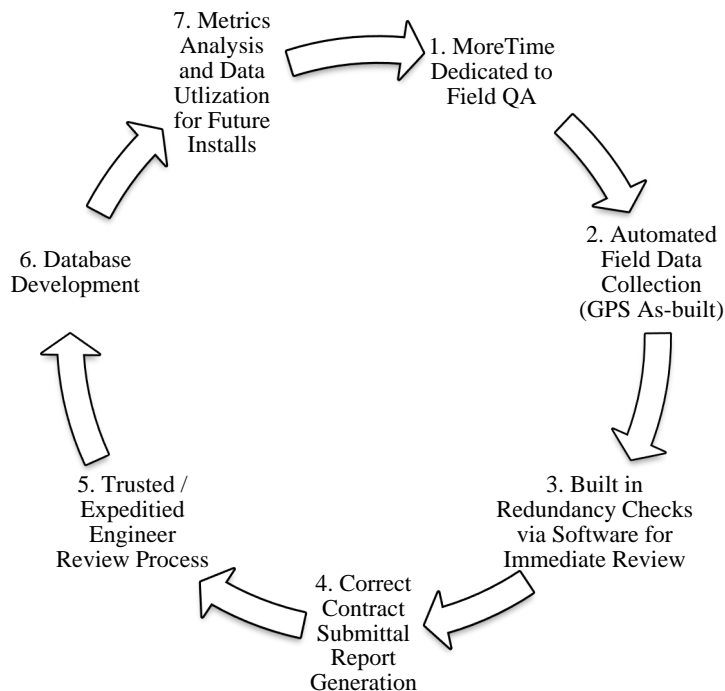


**Figure 1. Automated QA/QC Software Process**

## **AUTOMATED FIELD DATA COLLECTION**

Geosynthetics by nature (i.e., typical industry specifications derived from GSI and ASTM Standards) require a large amount of redundancy when it comes to proper deployment and seaming. These practices must be performed meticulously (QA) and then documented (QC). Typically, these duties are completed by an installer's individual QA/QC technician and verified by an on-site 3<sup>rd</sup> party owner representative (CQA). There are more specifications within a geosynthetic system regarding subgrade conditions, cover soil placements, and more. The focus of this paper is the data associated with geosynthetics deployment and seaming. However, there are boundless opportunities to integrate the ancillary components (subgrade condition, cover soil placement, etc.) of a geosynthetics installation system when a software infrastructure has been established.

Currently, the industry handwrites QA/QC documentation. This is hard to comprehend in 2022 considering the magnitude of legitimate QA needed for this craft and associated documentation required on a per-acre basis by installer QA/QC technician and 3<sup>rd</sup> Party CQA (Koerner 2012). There are two main identifiable liabilities with this current practice. The first is that it takes significant time and manpower for document upkeep, such as as-built drawings panel placements, roll number, roll deployment, trial welds, destructive sample testing, seam information, and repair information. The real value from a QA/QC Technician and 3<sup>rd</sup> party CQA is within the QA portion. Their roles should lean heavily on physical inspection of the geosynthetic installation for quality workmanship, not necessarily just the documentation (Toepfer 2016). The documentation can be perfect, but if the systems fail due to improper workmanship that went unaddressed during construction because QA efforts were limited due to the QC effort, project stakeholders are still at risk. The second is that manual documentation

allows for greater chance of human error and information fabrication/manipulation. Conforming QA/QC data collection and increasing the speed of data collection and analysis for the day-to-day field documentation will directly enhance the quality of geosynthetic installations.

Based on these observed areas of improvement to means and methods, automation must be applied to each section of required QC to address data collection speed and reliability. This automation begins with as-built generation. Hand sketched, scaled drawings that include all pertinent panel information are extremely labor-intensive to complete, and information can easily be missed. If information is missed during the as-built phase, ripple effects on seam and repair info will also go unnoticed. An existing step in the right direction is the seldom-seen “GPS As-built” specification requirement. Anyone with GPS equipment can shoot points at each panel intersection and grade break. Once that is completed in the field, the points file can eventually become a GPS coordinated as-built once they are connected by a program such as AutoCAD or similar. However, to populate this “GPS As-built,” a reference hand drawing is likely needed for location reference. This includes panel numbering, roll assignment, repair and destruct locations, and terminations. Therefore, simple “GPS As-built” within these limited parameters does not address speed but addresses reliable future use. With no speed improvement, QA/QC technicians cannot shift that time allocation to physical QA, which is the more valuable time commitment.

A more encompassing improvement to the As-built portion of QA/QC, and in turn, other downstream information collection practices, would be universal use of “*automated* GPS As-built” generation. Computer software can automatically generate the linework, panel, repair, and destruct numbering and termination call-outs without handwriting or using another software to connect the dots and annotate manually. By merely assigning attributes to the GPS points, the software algorithm creates physical lines and other panel information. This allows field techs to quickly see the as-built evolve in the field to address any missing information or shots in real-time. This approach allows for more time inspecting the seams, assessing changing in-situ conditions, examining proper heat seal and grinding techniques, all of which are directly tied to improving the installation quality. Finally, with a software platform, these field documents can also be uploaded via cloud technology, so office personnel or clients may see this information in real-time. This functionality can be used as another set of eyes for checking information, specification adherence, real installed quantity verification, material

## **BUILT IN RECORD KEEPING AND REAL-TIME CQA**

Remembering automated GPS as-built is the foundation for an improved system; the abundance of metadata within the as-built can be used to populate the other QC specification requirements. The software knows every panel intersection, the locations of every repair and destruct, terminations, panel placement square footage reports, seam and repair information. This native ‘knowledge’ is used to automatically generate the QA/QC result as a result. This automation makes sure that every piece of info on the repair and seam reports is in line with what is on the as-built and, most importantly, within project specification. Currently, the typical process is to walk the liner physically, hand draw the as-built, then once again walk the liner to populate every line of seam control and repair reporting on their separate respective report sheets. Using a field tablet or similar technology, automated GPS as-built offers the opportunity to shoot points and attribute those points once. Welding and testing information can then be filled in on the already generated lines. Automation eliminates the need to collect the same information multiple times and eliminates paper recordkeeping.

To further improve efficiency, it is essential to acknowledge that some information does need to be “filled in,” requiring the tech to read the information on the liner itself. These parameters are set up prior to the job so that he/she is not repeatedly writing the same information, once again saving time. These “fill in” areas on the seam and repair reports are replaced with dropdowns accompanied by other pre-set conditions. One example of those pre-set conditions is air test information input. With software, the technician will utilize a pre-set drop down for the initial start time only, and the end time will automatically populate based on job specification, typically five minutes later. See the example screenshot below in Figure 2.

timesheet ... timesheet ... timesheet ... (2)

Seam Control Form for Job: 072010278 Layer: Cell 4 Material: Primary

32662 Total LF of Welding To Date Combined  
66 Number of Destructs Needed

Extrusion LF Weld Total To Date: 16  
Fusion LF Weld Total To Date: 32646

Test Types:  
VA - Vacuum LA - Lance  
AP - Air Pressure SP - Spark

Air Pressure Hold Time: 5 Min. Allowable Air Pressure Loss: 2 PSI Destruct Spacing: 500.0 Ft.

Seam Sort: 1 2 Date Weld Date: Operator: Machine: Mach. Sp: Mach. Tp: Pre. Tp: Test Date: Test Type: Copy

Weld Date	Seam #	S Len	Weld Time	Operator	Mach. Num	M. Sp	M. Tp	P. Tp	Test Date	T. Type	AT Time In	PSI In	AT Time Out	PSI Out	Loss	Res.	Save
06/11/2	100/EX-L	22	01:00 PM	Angel Rodriguez	WE-A106	8	850		06/11/2	AP	04:52 PM	30	04:57 PM	30	0	P	S
06/10/2	101/102	38	08:42 AM	Francisco M	ET-A064	9	850		06/10/2	AP	11:35 AM	30	11:40 AM	30	0	P	S
06/10/2	101/102	356	08:45 AM	Francisco M	ET-A071	9	850		06/10/2	AP	11:35 AM	30	11:50 AM	30	0	P	S
06/11/2	101/EX-L	22	11:38 AM	Angel Rodri	WE-A105	8	850		06/11/2	AP	04:50 PM	30	04:55 PM	30	0	P	S
06/10/2	102/103	38	09:01 AM	Charles Mon	WE-A113	9	850		06/10/2	AP	11:44 AM	30	11:49 AM	30	0	P	S
06/10/2	102/103	310	09:04 AM	Charles Mon	WE-A117	9	850		06/10/2	AP	11:45 AM	30	11:50 AM	30	0	P	S
06/11/2	102/EX-L	22	11:35 AM	Angel Rodri	WE-A106	8	850		06/11/2	AP	04:50 PM	30	04:55 PM	30	0	P	S
06/11/2	103/EX-L	22	11:32 AM	Angel Rodri	WE-A106	8	850		06/11/2	AP	04:32 PM	30	04:37 PM	30	0	P	S
06/11/2	104/EX-L	22	11:29 AM	Angel Rodri	WE-A106	8	850		06/11/2	AP	04:32 PM	30	04:37 PM	30	0	P	S
06/11/2	105/EX-L	22	11:26 AM	Angel Rodri	WE-A106	8	850		06/11/2	AP	04:31 PM	30	04:36 PM	30	0	P	S
06/11/2	106/EX-L	22	11:23 AM	Angel Rodri	WE-A106	8	850		06/11/2	AP	04:31 PM	30	04:36 PM	30	0	P	S
06/11/2	107/EX-L	22	11:20 AM	Angel Rodri	WE-A106	8	850		06/11/2	AP	04:30 PM	30	04:35 PM	30	0	P	S
06/11/2	108/EX-L	22	11:17 AM	Angel Rodri	WE-A106	8	850		06/11/2	AP	04:30 PM	30	04:35 PM	30	0	P	S
06/11/2	109/EX-L	22	11:14 AM	Angel Rodri	WE-A106	8	850		06/11/2	AP	04:15 PM	30	04:20 PM	30	0	P	S
06/11/2	110/EX-L	22	11:11 AM	Angel Rodri	WE-A106	8	850		06/11/2	AP	04:15 PM	30	04:20 PM	30	0	P	S
06/10/2	111/112	16	01:09 PM	Charles Mon	WE-A113	9	850		06/10/2	AP	03:50 PM	30	03:55 PM	30	0	P	S
06/10/2	111/112	189	01:10 PM	Charles Mon	WE-A113	9	850		06/10/2	AP	03:50 PM	30	03:55 PM	30	0	P	S
06/11/2	111/EX-L	21	11:08 AM	Angel Rodri	WE-A106	8	850		06/11/2	AP	04:15 PM	30	04:20 PM	30	0	P	S
06/11/2	112/EX-L	7	11:08 AM	Angel Rodri	WE-A106	8	850		06/11/2	AP	04:15 PM	30	04:20 PM	30	0	P	S

Template Evolution in

**Figure 2. Populated Seam Control Example**  
**Hundreds of lines auto populated from automated GPS as-built**

Currently, the industry relies on thorough contractor QA/QC technicians, persistent site CQA's, and post-project data review by engineers to capture all this information. But do we really know the QC data submittals are correct per project specification during and at the completion of the project? Initiating redundant software assistance benefits owner representative CQA as well. To some extent, the software can do the job of a CQA from a documentation standpoint by cross-referencing all of this data with the appropriate previously defined specification. For example, when a line of seam control or repair reporting is completed, a check function automatically makes sure the information is in line with the appropriate pre-weld information. This real-time inspection principle provides unique advantages in terms of speed of work and reassurances to the CQA team that everything is completed and documented, prior to being covered by a subsequent layer in the lining system. If incorrect or missing data is

identified, it may be too late to confirm or verify the information because another layer may cover the materials in question.

It is important to recognize that other solutions have been developed with similar features; specifically, Glen Toepfer's Supertek and Geo-X's 'Geo-Q' platforms.

## **REPORT GENERATION**

Foundational improvements to QA/QC field means and methods have made the physical data collection faster, less strenuous, and more authentic for field personnel. It has also been recognized that automated QA/QC software integration provides real-time project updates via a cloud platform for other stakeholders in geosynthetic installation projects to monitor progress.

Because all parties within the field setting are working more effectively, the final phase of an install relating to submittals is now more easily developed. Again, comparing to the current state of practices, multiple sheets of paper or, at best, excel documents typically need to be compiled, put into a clean format, and printed in a legible manner for professional submission. This process requires an additional meticulous individual (usually a corporate QA/QC Engineer or similar) by the installation contractor to make sure every piece of info is accounted for. Once submitted, this process must be essentially repeated by the project's engineer of record. QA/QC software provides solutions to this sequence of events.

By having a centralized program, users may "print" submittals upon completion. Furthermore, as examined previously, the process of checking accuracy is an on-going effort within the software. Therefore, once the final panel, seam, repair, or other is documented with automated GPS as-built and ran through QA/QC software, the reports can be trusted for accuracy. This process substantially decreases the time allocation needed for report review and submission post-installation. On a per 20-acre basis, this type of systematic field approach results in an 80%-time reduction requirement by the installation QA/QC engineer compiling the final submittal. Conservatively, a 20-acre installation's final package, including as-built drawing, can be completed in an 8-hour workday.

## **DATA BASE DEVELOPMENT AND LEVERAGING**

At the completion of a geosynthetics installation, contractors and engineers are left with a vast amount of data and information. Previously, this info would not be used post project completion. At most, installers keep track of their destructive test failure rate as a general industry parameter to track a company's quality. But there is much more in-depth analysis that can be made with a metrics analysis tool. Some parameters which are valuable for installers, engineers, and owners include:

- Field Pre-weld Pass/Fail Rate
- Field Destruct Pass/Fail Rate
- Laboratory Destruct Pass/Fail Rate
- Linear Feet Welded – Extrusion
- Linear Feet Welded – Fusion
- Square Foot Deployed
- Repairs by Type (How many repairs are caused by burning out, losing laps, etc.)
- Waste Percentages (how well a company utilizes material)



All of which can then be filtered by:

- Date Range (time of year)
- Material
- Welding Technician
- Welding Equipment Used
- Superintendent
- Job Site
- Client
- Design Engineer

A combination of these metrics provides far more comprehensive picture of a project's success above and beyond simple Pass/Fail percentages.

The climate of our generation is data-driven. Every industry in the world is optimizing data collection to be able to leverage its operating efficiency. Accurate, centralized data management software benefits installers, engineers, owners, manufacturers, and other stakeholders in the geosynthetics industry. Up until now, tangible improvements to field and reporting under the QA/QC umbrella have been addressed. But in addition to these baseline improvements, there are more widespread advantages downstream that can recirculate to an improved next project.

Some examples include targeted internal training by installers if trends are seen with specific employees not performing well or a specific material is continually underperforming. Legitimate résumé generation during pre-construction submittals for owners and engineers. Other miscellaneous data optimization examples include reductions in billing conflicts (Geo-X 2020) and advantages going into prospect cell or cover construction projects. Tie-in points are known for the existing cell or covered area; cut and fill plans are easily and accurately adopted from a known boundary previously established from the as-built GPS locations.

While advancements in materials manufacturing (better additives, taped seams, conductive backed materials), welding equipment (data acquisition fusion welders), post-install leak detection (leak integrity testing), and existing “justified quality management systems” (Koerner 2012) are already contributing greatly to the advancement of geosynthetics, a QA/QC software platform is needed to substantiate and document the effectiveness of these tangential advances. Show how these other stewards of the industry improved failure rates. Record the data that informed the material selection process for the right application. Right now, these metrics are stored within the heads of those who performed on these specific projects. The data application democratizes the information for rapid decision making, promoting time devoted to the most important aspect of the project, construction of a quality installation that best serves its intended purpose.

## CONCLUSION

The roadblock for universal acceptance of QA/QC software use seems to be that the industry, built around the regulatory agencies that govern permittance of a lined facility's use, does not require efficient authenticity like other industries. Furthermore, any previous attempts to fill the gaps within the current process did not approach the remedy holistically. To truly improve the

work flow of a geosynthetic lined system, and final product, the solution must start in the field, seamlessly translate to office reporting, and produce a robust, leverageable data warehouse to be used for continued improvements. This cyclical model results in cost savings for multiple stakeholders involved in a venture utilizing this technology.

## REFERENCES

- Koerner, K.M. & Koerner, G., (2012), *Need for and Justification of Quality Management Systems for Successful Geosynthetic Performance* [White Paper]. Geosynthetic Institute. <https://geosynthetic-institute.org/papers/paper26.pdf>
- Ltd, Geo-X (Pty). "QA/QC Management System." *GeoX*, 2020, [geo-x.co.za/qaqc-management system/](https://geo-x.co.za/qaqc-management-system/).
- Ramsey, B. (2019). Improvements and Advances in Construction Quality Assurance for Geosynthetics, *17th African Regional Conference on Soil Mechanics and Geotechnical*, Boyd Ramsey Consulting LLC, Houston, Texas, USA: 1-9.
- Toepfer, Glen. Interview by Chris Kelsey. *An Insurance Policy for Geosynthetic Installations*, 21 Jan. 2016, <https://www.geosynthetica.com/cqas-insurance-policy-geosynthetic-installations/>.

## **New Geotextile Quarry By-Product Geocomposite System for Permanent Road Foundation**

Syed Faizan Husain,<sup>1</sup> Taeyun Kong,<sup>2</sup>  
Erol Tutumluer, Ph.D.<sup>3</sup>, Mark Marienfeld, P.E.<sup>4</sup>, and Issam I.A. Qamhia, Ph.D.<sup>5</sup>

<sup>1</sup>University of Illinois at Urbana Champaign; e-mail: sfh3@illinois.edu

<sup>2</sup>University of Illinois at Urbana Champaign; e-mail: taeyunk2@illinois.edu

<sup>3</sup>University of Illinois at Urbana Champaign; e-mail: tutumlue@illinois.edu

<sup>4</sup>TreadMark, PO Box 461, Williamston, SC 29697; e-mail: mark.marienfeld@gmail.com

<sup>5</sup>University of Illinois at Urbana Champaign; e-mail: qamhia2@illinois.edu

### **ABSTRACT**

This paper reports on the preliminary investigation into a new geocomposite system (GCS) consisting of a typical coarse sand sized quarry by-product (QB) aggregate material sandwiched between two nonwoven geotextiles intended for pavement layer separation, stabilization, and drainage applications. First, results from standard direct shear strength testing are presented to evaluate the shear strength of QB. Then, the interface shear strength is evaluated using a modified form of direct shear strength test setup. These results are used to model an interface bond between QB and nonwoven geotextile in an axisymmetric finite element model to solve for critical pavement responses, such as vertical stress/strain on top of subgrade, and assess improvement provided by the geocomposite. Next, permittivity values are reported for the proposed geocomposite using a bench-scale constant head permeameter. Finally, a variable energy dynamic cone penetrometer device, known as PANDA, is used to characterize the cone resistance of the proposed GCS in bench scale specimens. The results indicate that the new geocomposite system functions as an appropriate pavement structural layer to provide separation, stabilization, and enhanced drainage. Sustainability benefits include construction cost savings, use of waste materials, lightweight construction, conservation of preferred construction materials, and creation of a permanent road foundation.

### **INTRODUCTION**

Geosynthetics are known to enhance pavement performance and increase service life of the pavement structure by stabilizing unbound granular materials, providing separation between pavement layers, filtration of subgrade fines while facilitating drainage, and many other functions. This paper introduces a new GCS which includes in the design crushed aggregate waste by-products sandwiched between nonwoven geotextiles.

Quarry by-products (QB) are coarse sand sized waste aggregates produced during the manufacturing process of crushed aggregate in stone quarries. In the state of Illinois, more than 950,000 short US tons of QB is generated as excess every year (Tutumluer et al., 2015; LaHucik et al., 2016; Qamhia, 2019). The interaction between the granular material and geosynthetics primarily controls the stability and is considered an important design criterion. Previous research studies (Frost et al., 2002; Dove et al., 2006) have generated substantial published results on the interactions between fine grained clayey soils and geotextiles since geosynthetic clay liners (GCLs) are extensively used in waste containment facilities. However, evaluation of sand-geotextile interaction has been the subject of relatively few research efforts (Haeri et al., 2000; Tuna and Altun, 2012) with substantially different research approaches and experimental designs. Specifically, there have been limited studies focused on the base, subbase, or subgrade geomaterial

layer interactions with geotextiles in relation to overall structural performance of pavements. While the interface shear strength measured using the monotonically loaded direct shear test device may not be an accurate representation of the small-strain cyclic response expected in a pavement system, it can help approximate surface-to-surface bond behavior between granular base/subbase and geotextile layers within numerical analysis research domain.

Pumping of subgrade fines into base and localized punching of base layer aggregate into the subgrade is referred to as pavement layer intermixing. Layer separation and drainage are two of the key aspects in pavement design and performance. Improper interface separation between layers can lead to intermixing of aggregate and subgrade material (Qamhia and Tutumluer, 2021). Aggregate penetration and subgrade fines erosion become inevitable under high hydrodynamic pressure environments often caused by moving vehicles on a road surface and this eventually results in a loss of support and development of premature pavement distress. In addition, improper design of drainage can lead to development of pumping issues and development of ice lenses during the winter season from entrapped water in the pavement structure. In this study, preliminary experimental and numerical assessments of a new geotextile and quarry by-product geocomposite system (referred as GCS hereafter) are presented. The proposed GCS is constructed by sandwiching a mechanically compacted layer of QB between two layers of nonwoven geotextiles. The overall concept of the new GCS and its pavement application are illustrated in Figure 1. In addition to mechanical stabilization effects, geotextile layers within the proposed GCS are expected to function as separation barriers between base and quarry by-products, base, and subgrade, and QB and subgrade while enhancing both the vertical permittivity (cross-plane drainage) and lateral transmissivity characteristics of the overall pavement structure. Implementation of the proposed GCS can, therefore, provide an effective permanent road foundation.

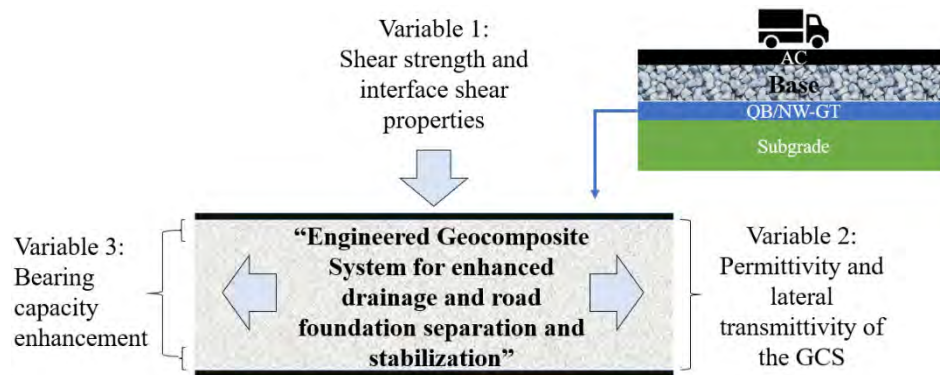


**Figure 1: Proposed geotextile and quarry by-product (QB) geocomposite system (GCS)**

## OBJECTIVE AND SCOPE

This paper describes an experimental research study conducted at the Illinois Center for Transportation with the objective to evaluate the shear strength, permeability, and bearing capacity improvement of the new GCS. The shear strength characteristics and the interface friction angle between nonwoven geotextile (NW-GT) and QB are evaluated using direct shear strength (DSS) tests and used later as inputs into a finite element (FE) model. The GCS is installed between base and subgrade in a pavement system and the FE model is used to solve for critical pavement responses, for example, vertical stress/strain on top of subgrade. A bench scale constant head permeameter was fabricated to evaluate the permittivity of the new GCS. Further, in order to



examine the bearing capacity improvements with the new GCS, a variable-energy dynamic cone penetrometer was utilized. The outcome of the study demonstrates the suitability and effectiveness of the new GCS towards improved flexible pavement system performance.

## MATERIALS STUDIED

**Unbound Granular Materials.** Figures 2 and 3 present the sieve analysis and moisture-density test results performed on QB and dense-graded basecourse aggregate, designated by Illinois DOT as CA06, materials following the ASTM C136-06 and ASTM D698-12, respectively. The QB material is primarily uniform sand, classified as poorly graded sand (SP) based on the Unified Soil Classification System, and A-1-a soil according to the AASHTO soil classification system. The average fineness modulus (FM) for QB, which is an index number that represents the mean size of the particle in soil sample, was calculated as 5.46, and this value indicates that the average aggregate size is in between No. 16 (1.18 mm) and No. 8 (2.36 mm) sieve sizes. The moisture-density properties, i.e., maximum dry density and optimum moisture content values, for the QB material were determined by conducting standard Proctor compaction tests using a 4-in. mold following ASTM D698-12. As shown in **Figure 3**, the optimum moisture content (OMC) of the QB sample was determined to be 11.7% and the corresponding maximum dry density ( $\gamma_{dmax}$ ) was found to be 116.1 pcf (18.24 kN/m<sup>3</sup>). These values were used for sample preparation in the experimental program.

**Nonwoven Geotextile.** Geotextiles are woven or needle punched (nonwoven) planar layers that are used for providing stabilization, confinement, separation, and drainage in geotechnical systems. Nonwoven geotextiles are generally mechanically interlaced polypropylene fiber yarns that have a higher permittivity and greater elongation potential compared to woven geotextiles. Generally, geotextiles are used as a separation layer in pavement structures to prevent intermixing of subgrade soils and base course materials. The nonwoven geotextile used in this study had an average grab tensile strength of 240 lbs. (1067.5 N), grab tensile elongation of 70% by ASTM D4632, and an apparent opening size (AOS) of 0.0070 in. (No. 80 US standard sieve opening) by ASTM D4751.

## SHEAR STRENGTH TESTS

To determine the shear strength properties of the QB material and to ascertain interface friction, direct shear tests were performed in accordance with ASTM D3080-04 and ASTM D6243-20. The tests were performed under three normal stress conditions of 10 psi (68.95 kPa), 15 psi (103.42 kPa), and 20 psi (137.90 kPa). As per standard test procedure, at least three hours of standing time was allowed between preparation and testing to ensure uniform moisture distribution. Considering in-service pavement foundations are subjected to cyclical water infiltration, the GCS was evaluated under two test conditions: dry and submerged. The dry condition in this context refers to the state where the QB is compacted at OMC and the test is conducted without immersing the specimen in a water bath. On the other hand, the submerged conditions indicate that the specimen is compacted at OMC and is submerged in a water bath for the duration of the test. For the interface shear test, following modifications were made to the shear box assembly: a 4 in. by 4 in. (100 mm by 100 mm) wooden block was wrapped with the nonwoven geotextile as shown in **Figure 4 (a) and (b)**. The top shear box was then filled with the QB to examine the interaction between NW-GT and QB. Note that the geotextile used was discarded after each test and replaced with a new one to minimize the effects of surface damage and particle embedment during testing. The direct shear

test equipment used in this study has vertical and horizontal displacement transducers. The rate of horizontal displacement was set to be 0.005 in. per minute (0.127 mm per minute), small enough to eliminate strain rate effects, for all interface friction tests, and the deformation results were collected at every 0.005 in. of travel. Each test was performed until the specimen started showing dilative behavior as shown in **Figure 5**, which is considered as a typical failure criterion for loose sands and interfacial strength tests (Haeri et al., 2000).

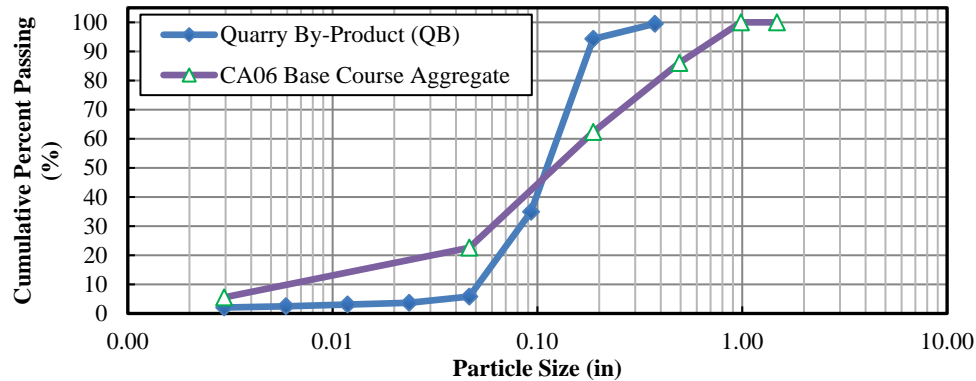


**Figure 2: Gradations of QB and CA06 materials used in the study (ASTM C136-06)**

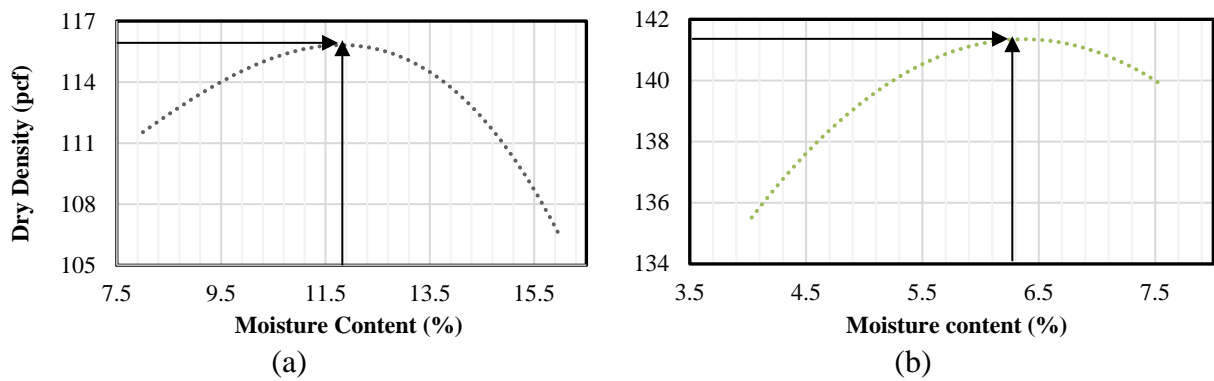


**Figure 3: Moisture density curves for (a) QB and (b) CA06 materials (ASTM D698-12)**

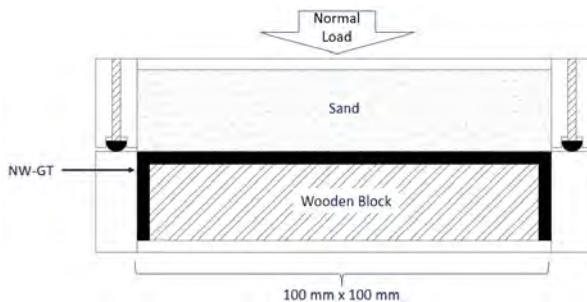


**Figure 4 (a): Interface shear strength experimental test setup**

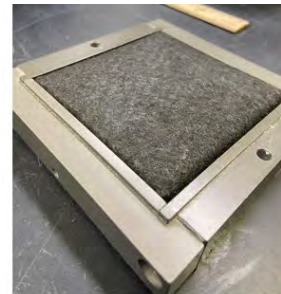


**Figure 4 (b): Modified bottom shear box**

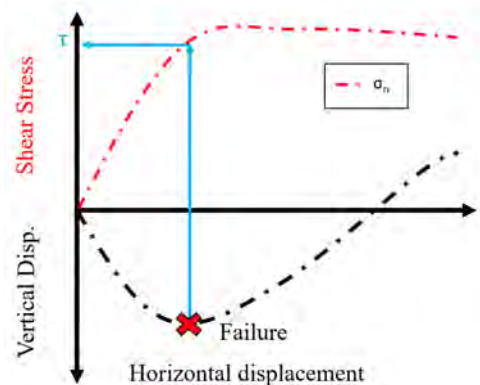
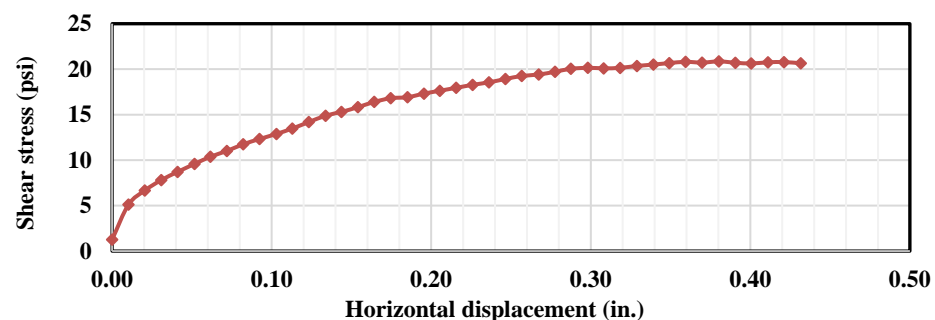
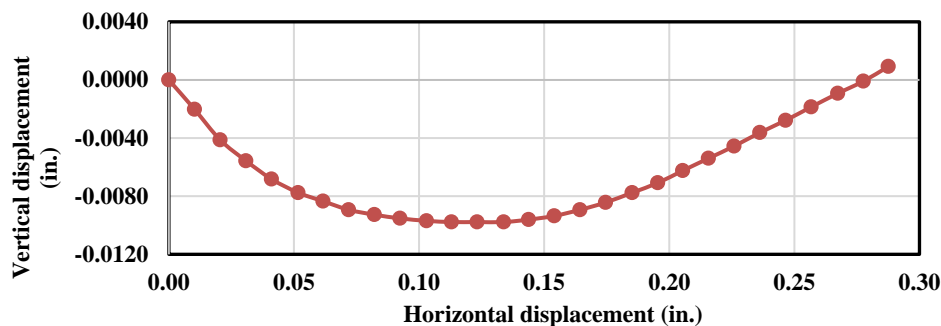


Figure 5: Typical direct shear test results in loose sands

**Shear Strength Test Results.** The typical results from DSS tests on QB sand, compacted at the OMC of 11.7% and tested in dry condition, are shown in **Figure 6 (a) and (b)**. As expected, results show contractive behavior before dilation at which point failure conditions are said to have been reached. Similar trends, i.e., loose sand behavior, was observed for specimens tested under submerged conditions. Computed internal friction angles ( $\phi$ ) are given in **Figure 7**. It was assumed that for unconfined compression conditions no shear resistance would be observed in the specimens indicating a zero cohesion for sandy QB. The dry specimen exhibited an internal friction angle of  $45.1^\circ$ . As expected, internal friction angle decreased to  $42.5^\circ$  when the QB specimen was fully submerged in the water. The influence of this reduction on pavement performance was evaluated using FE analysis to be presented in a later section.

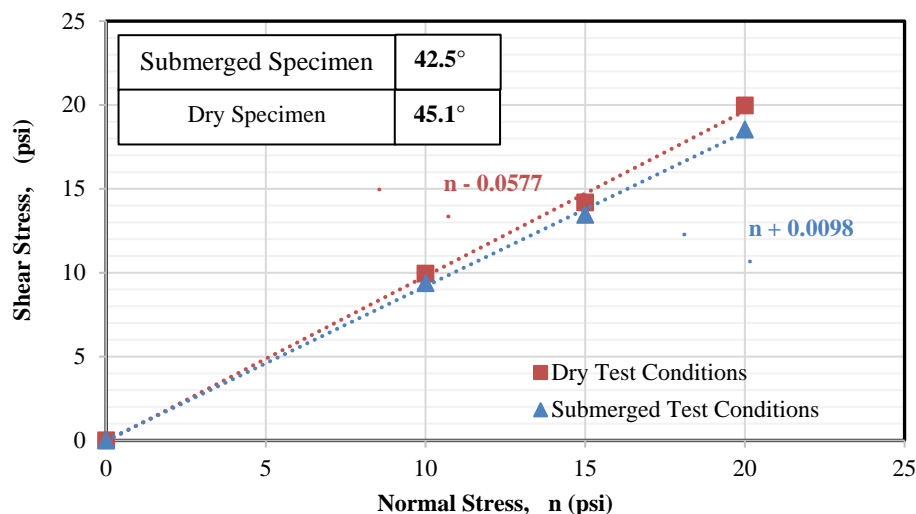


(a)



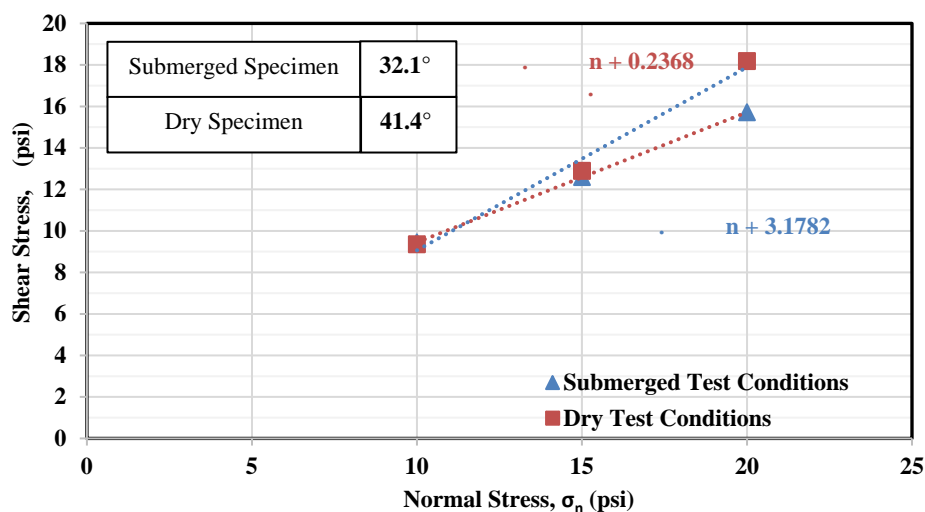
(b)

Figure 6: Direct shear test results on dry specimen tested at 15 psi normal stress



**Figure 7: Internal friction angles determined for QB in dry and submerged conditions**

**Interface Friction Angle.** The computed interface friction angle values between the two NW-GT and QB materials are given in **Figure 8**. The results confirm the findings from literature (Haeri et al., 2000; Tuna and Altun, 2012) that there exists no well-defined ultimate failure point in case of sand geotextile interaction. It should be noted that unlike internal shear strength determination using DSS test, some interface shear resistance will be offered even under unconfined conditions ( $\sigma_n = 0$  psi). This is due to entanglement between nonwoven geotextile fibers and QB. Appreciable differences in interface friction angles were observed between dry (41.4°) and submerged (32.1°) specimens. Again, computed interface friction angle for the submerged case was found to be lower than that obtained from the dry case. Previous research (Portelinha and Zornberg, 2017) on mechanically stabilized earthen walls has shown that, if allowed to laterally drain, the presence of a nonwoven geotextile can prevent the fully submerged/fully saturated interface condition from occurring. This enhancement should be beneficial in roads as well.



**Figure 8: Computed interface friction angles between nonwoven geotextile and QB**



## PAVEMENT FINITE ELEMENT MODEL

An axisymmetric finite element model of a conventional flexible pavement was developed for layered pavement response analysis and evaluation of the new GCS as a pavement structural layer. Experimental findings were used as Mohr-Coulomb material property inputs to model the QB layer. This was done to ensure accurate shear response in the modeling process. NW-GT on the top and bottom of the GCS were modelled as finite thickness elastic elements and a general penalty friction contact was assigned between the QB and NW-GT. The pavement layers of asphalt concrete (AC) unbound granular base, and subgrade were all modelled as linear elastic materials for a simple layered elastic analysis. The pavement structure is composed of 4 in. (100 mm) of AC layer underlain by 6 in. and 12 in. thick unbound granular base layer options. The thickness of the QB layer was kept constant at 4 in. (100 mm) as in the test model. The subgrade thickness was assumed to extend to a depth of 6 ft 6 in. (2,000 mm). The pavement geometry for test specimen analysis is shown in **Figure 9**.

Academic version of ABAQUS software was used to perform all finite element simulations. A uniform circular tire pressure of 90 psi (620.5 kPa) was applied over an area of 6 in. (150 mm) in radius. Critical vertical stress and deformation responses were recorded at subgrade level below the proposed GCS layer to evaluate the extent of stabilization and reduction in base layer thickness requirements. FEM material input parameters based on experimental results and assumptions described in the previous sections are listed in **Table 1**. Input values for geotextile layers were adopted from literature (Pedroso et al., 2006). Note that the present study adopts an unconfined modulus value for geotextile. Previous research studies (McGown et al., 1986, Boyle et al., 1996) reported that confined modulus values of geotextiles could be one to four times higher than the unconfined modulus. This is because nonwoven geotextiles may fail by unraveling in a grab tensile test, but the unraveling is stopped forcing the fibers to break in the confined, in-road service conditions.

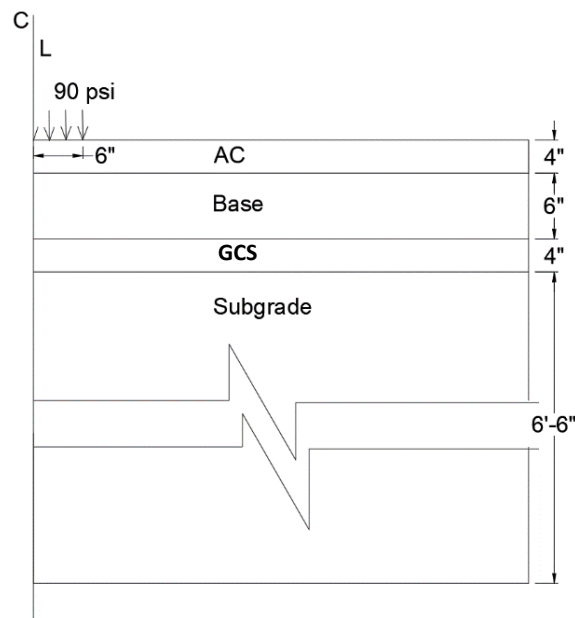


**Figure 9: Pavement geometry as modelled in ABAQUS FE analysis**

Critical pavement responses from the FE analyses are presented in **Table 2**. The results indicate that use of GCS can help reduce base layer thickness requirement while reducing the critical pavement response at the top of subgrade and bottom of the AC layer. The GCS with 6 in. of base course exhibits a top of asphalt concrete rutting on par with a 12-in. thick base layer. A previous study (Finn et al., 1986) reported on fatigue evaluations using tensile strain at the bottom of asphalt concrete layer as follows:

$$\log(N_f) = 16.664 - 3.291 \log\left(\frac{\varepsilon_t}{10^{-6}}\right) - 0.854 \log(E) \quad (1)$$

where  $N_f$  is the number of load applications for the development of 10% fatigue cracking in the wheel path,  $\varepsilon_t$  is the horizontal tensile strain at the bottom of asphalt concrete, and  $E$  is the modulus of AC. Note that the new GCS was found to reduce bottom of the AC strain value that can potentially enhance fatigue life of the pavement.

**Table 1. FE Analysis Material Inputs**

Material	Modulus of Elasticity		Poisson's Ratio
	psi	MPa	
Asphalt concrete	400,000	2757.9	0.35
Base Layer	30,000	206.84	0.38
Subgrade	10,000	68.947	0.45
Nonwoven Geotextile	52,213	360	0.41
<b>QB Material Tested</b>	<b>Dry Test Condition</b>		<b>Submerged Test Condition</b>
Internal Friction Angle (°)	45.07		42.47
Interface Friction Angle (°)	41.43		32.09

**Table 2. Conventional Flexible Pavement FE Analysis Results**

DESCRIPTION	TOP OF SUBGRADE				BOTTOM OF AC	TOP OF AC	
	Vertical Stress		Vertical Def.		Horizontal Strain (µstrains)	Vertical Def.	
	psi	kPa	in.	mm		in.	mm
12" Base	11.50	79.3	0.017	0.44	302	0.025	0.64
6" Base	19.30	133.1	0.024	0.61	314	0.030	0.76
4" GCS/6" Base	10.73	73.9	0.016	0.41	306	0.026	0.66

## BENCH SCALE HYDRAULIC CONDUCTIVITY TESTS

Cylindrical barrels, as shown in **Figure 10**, were fitted with piezometers and sloping bottom for conducting bench scale permittivity testing of the new GCS. The cylindrical barrel was measured to be 23 in. in internal diameter and 34 in. in height. Holes were drilled on the side at the level of 1 in. below and above the geotextiles for attaching piezometers to measure the hydraulic head loss and a hole was drilled in the center of the base to collect outflow. Outflow was measured using an effluent collection container and discharge was measured for every 10 liters of outflow. The cylindrical tank was placed on two wooden planks measuring about 10 in. above the ground surface to allow for placing the effluent collection container. To prevent the movement of water around

the GCS, the sides of the geotextiles were sealed using two layers of waterproof duct tape. The permittivity is defined as the ratio of hydraulic conductivity to the thickness of the GCS and can be calculated using the following equation (Williams and Abouzakhm, 1988).

$$P = \frac{Q}{HA} \quad (2)$$

In the formula, “Q” is the average rate of discharge (made constant at  $9.72 \times 10^{-3}$  cu. ft. per s), “H” is the head difference between the piezometers (observed as 0.82 in.), and “A” is the cross-sectional area of the drainage path (0.67 sq. ft.). Using the equation, the average permittivity of the GCS was computed as  $2.15 \times 10^{-1} \text{ s}^{-1}$ .

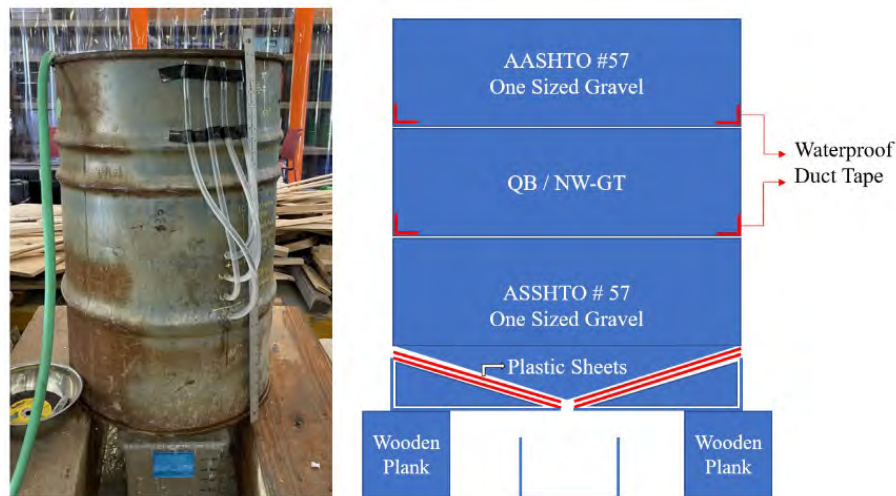


**Figure 10: Cross-sectional view of cylindrical tank used for permittivity testing**

## DYNAMIC CONE PENETROMETER TESTING

To assess the base course compaction and bearing capacity, a variable energy dynamic cone penetrometer known as PANDA developed by Sol Solutions was utilized. The distinctive feature of this device is that the penetration is carried out by means of manually driving the cone tip using a hammer. The variable penetration energy is measured using a calibrated strain gauge attached on top of the anvil. The data from depth measurement and load magnitude with each blow are then displayed on a handheld data storage unit. For this study, a retractable cone tip of 2 in<sup>2</sup> projected area was attached to the end of a 3 ft-long penetrometer rod. Two bench scale models as shown in **Figure 11 (a) and (b)** were prepared inside cylindrical barrels and DCP soundings were performed. The two models investigated are as follows. First, a 10-in. thick control specimen of CA-06 base layer aggregates was prepared. The second specimen was prepared by compacting 6 in. of CA-06 base layer aggregate and 4 in. of QB in the GCS sandwiched between two nonwoven geotextiles. The compacted density of CA06 material was observed to be similar in both control (127 pcf) and test (125 pcf) specimens, while the relative compaction efficiency achieved in the 4 in. thick QB was found to be 87%. A 3-in. thick geofoam with known strength property of California Bearing Ratio (CBR) of 5 was used as a substitute for subgrade in preparation of all specimens. Additionally, all specimens were compacted at their respective OMC values with the same compaction effort.

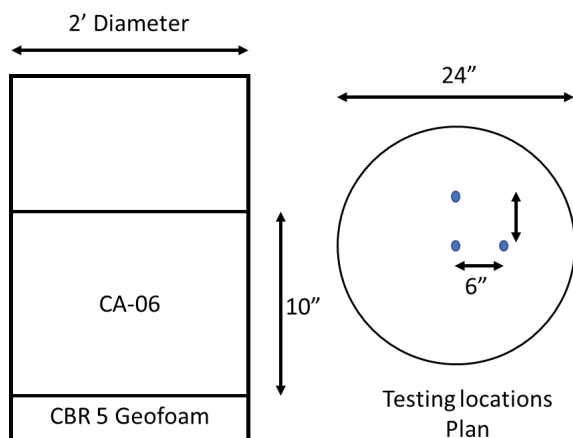


**Figure 11(a): Control specimen testing plan**

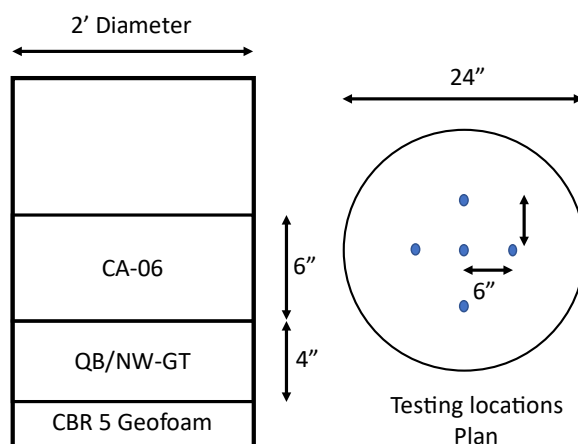


**Figure 11(b): Test specimen testing plan**

The cone tip resistance profiles for the control and test specimens are summarized in **Figure 12**. At the level of GCS installation, the test specimen offered an average cone tip resistance between 1056 psi (7280.86 kPa) and 1519 psi (10473.14 kPa). Within the same depth range, the cone tip resistance in the control specimen varied between 813 psi (5605.44 kPa) and 1143 psi (7880.71 kPa).

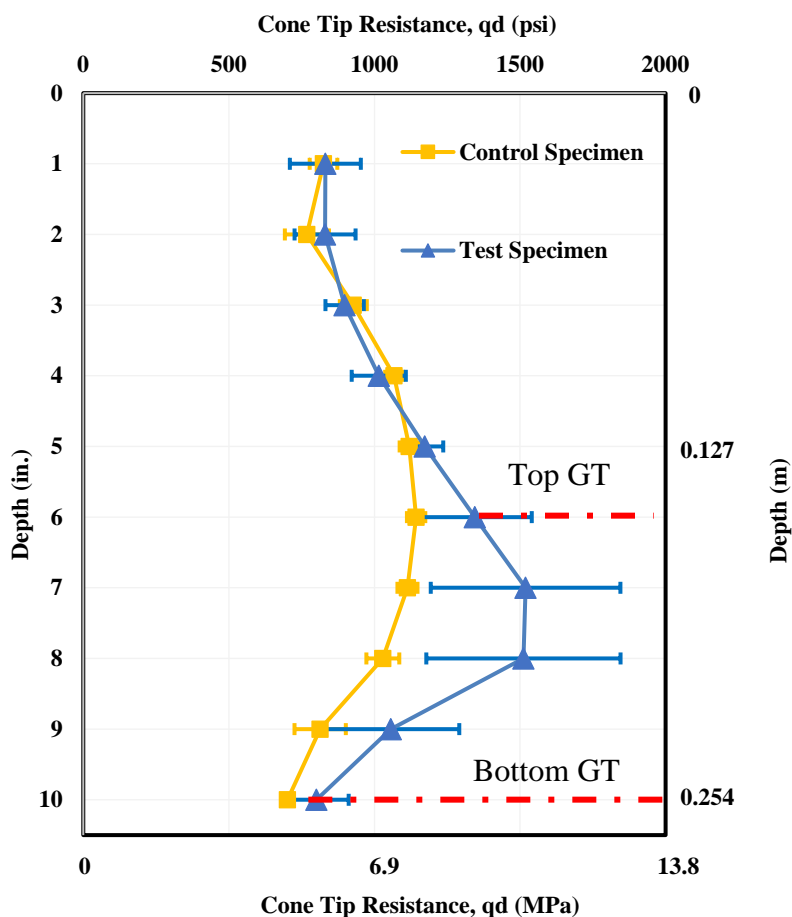


**Figure 12: Cone tip resistance values compared between control and GCS test specimens.**



The GCS specimen exhibits higher resistance to penetration due to the presence of two geotextile layers. Therefore, the DCP test results can be interpreted that a higher penetration resistance is encountered at the level of GCS installation leading to an enhanced bearing capacity compared to the dense graded base course granular material.

## CONCLUSIONS AND RECOMMENDATIONS

This study reported on preliminary experimental and numerical assessments of a newly proposed geocomposite system (GCS) made by sandwiching two nonwoven geotextiles with a quarry by-product (QB) layer in the middle. The new GCS is intended as a pavement structural layer to enable a permanent road foundation by providing separation, stabilization, and drainage. The results from the experimental program reveal that the GCS provides for high drainage potential in the road foundation while maintaining its structural layer strength and integrity. The numerical analysis results reinforced the latter physical experimental findings and provided an insight into the in-service performance of the GCS. The proposed GCS is expected to provide large-scale utilization of quarry aggregate waste without additional processing thus serving toward a sustainable pavement application. The cost benefit of using this GCS in road foundations is related to the potential for using less of the premium aggregate base, less over excavation costs, minimal cost of the geotextiles, more of lighter weight QB materials, and the minimal cost and local availability of quarry by-products or sand. Specific experimental findings, study conclusions and future recommendations are as follows:

1. The pavement analysis results indicated that 4 in. of QB sandwiched between the two layers of nonwoven geotextiles and overlain by 6 in. basecourse aggregate would result in critical pavement responses on top of subgrade, i.e., vertical stress and deformation, comparable to those of a 12-in. thick base layer.
2. The permittivity of the proposed GCS was found to be  $0.215 \text{ s}^{-1}$ .
3. The dynamic cone penetrometer soundings revealed that a bench scale test specimen prepared using the GCS and unbound granular material offers an enhanced cone tip resistance compared to a control specimen prepared exclusively using granular base material.
4. While the bench scale experimental test results and associated numerical analyses presented in this study provide for an encouraging outlook of the proposed GCS, more research is needed to evaluate the full-scale performance of the GCS in flexible and rigid pavement systems before implementation in field.
5. Further studies evaluating the resilient response at varying test conditions and subjected to repeated freezing and thawing cycles are needed to ensure durability of the GCS.
6. The pavement benefits of the lateral transmissivity of the GCS needs verification.
7. The zone of stabilization influence achieved by different nonwoven geotextiles and different sand sized and shaped materials inside the GCS sandwich needs to be optimized.
8. Multiple GCS layers and methods of placement need to be investigated.

## REFERENCES

ASTM C136-06. Standard Test Method for Sieve Analysis of Fine and Coarse Aggregates, *ASTM International*, West Conshohocken, Pennsylvania, USA.

- ASTM D698-12. Standard Test Methods for Laboratory Compaction Characteristics of Soil Using Standard Effort (12,400 ft-lbf/ft<sup>3</sup> (600 kN-m/m<sup>3</sup>)), *ASTM International*, West Conshohocken, Pennsylvania, USA.
- ASTM D4632. Standard Test Method for Grab Breaking Load and Elongation of Geotextiles, *ASTM International*, West Conshohocken, Pennsylvania, USA.
- ASTM D4751. Standard Test Methods for Determining Apparent Opening Size of a Geotextile. *ASTM International*, West Conshohocken, Pennsylvania, USA.
- Dove, J. E., Bents, D. D., Wang, J., & Gao, B. (2006). Particle-scale surface interactions of non-dilative interface systems. *Geotextiles and Geomembranes*, 24(3), 156-168
- Finn, F., Saraf, C. L., Kulkarni, R., Nair, K., Smith, W., & Abdullah, A. (1986). *Development of pavement structural subsystems* (No. 291).
- Frost, J. D., Evans, T. M., Hebeler, G. L., & Giroud, J. P. (2002, September). Influence of wear mechanisms on geosynthetic interface strengths. In *Geosynthetics: State of The Art-Recent Developments. Proceedings of The Seventh International Conference on Geosynthetics*, 7<sup>th</sup> ICG, held on 22-27 September 2002, Nice, France. Volume 4.
- Haeri, S. M., Noorzad, R., & Oskoorouchi, A. M. (2000). Effect of geotextile reinforcement on the mechanical behavior of sand. *Geotextiles and Geomembranes*, 18(6), 385-402.
- LaHucik, J., Schmidt, S., Tutumluer, E., & Roesler, J. (2016). Cement-treated bases containing reclaimed asphalt pavement, quarry by-products, and fibers. *Transportation Research Record*, 2580(1), 10-17.
- McGown, A., Andrawes, K.Z. and Kabir, M.H., 1982, "Load-Extension Testing of Geotextiles Confined In Soil", *Proceedings of the Second International Conference on Geotextiles*, IFAI, Vol. 3, Las Vegas, Nevada, USA, August 1982, pp. 793-798.
- Boyle, S. R., Gallagher, M., & Holtz, R. D. (1996). Influence of strain rate, specimen length and confinement on measured geotextile properties. *Geosynthetics International*, 3(2), 205-225.
- Pedroso, E. O., Bueno, B. D. S., Benjamim, C. V. D. S., & Zornberg, J. G. (2006). Field monitoring and numerical prediction of the response of a non-woven geotextile-reinforced wall. In *Proceedings of the 8th International Conference on Geosynthetics*, Yokohama, Japan (Vol. 3, pp. 1129-1132).
- Portelinha, F. H. M., & Zornberg, J. G. (2017). Effect of infiltration on the performance of an unsaturated geotextile-reinforced soil wall. *Geotextiles and Geomembranes*, 45(3), 211-226.
- Propex Operating Company. (2011). *Product Data Geotex 801*. Chattanooga: Propex Operating Company
- Qamhia, I. I. (2019). *Sustainable pavement applications utilizing quarry by-products and recycled/nontraditional aggregate materials* (Doctoral dissertation, University of Illinois at Urbana-Champaign).
- Qamhia, I. I., & Tutumluer, E. (2021). *Evaluation of Geosynthetics Use in Pavement Foundation Layers and Their Effects on Design Methods*. Illinois Center for Transportation/Illinois Department of Transportation.
- Tuna, S. C., & Altun, S. (2012). Mechanical behavior of sand-geotextile interface. *Scientia Iranica*, 19(4), 1044-1051.
- Tutumluer, E., Ozer, H., Hou, W., & Mwumvaneza, V. (2015). *Sustainable aggregates production: green applications for aggregate by-products* (No. FHWA-ICT-15-012). Illinois Center for Transportation.
- Williams, N. D., & Abouzakhm, M. A. (1989). Evaluation of geotextile/soil filtration characteristics using the hydraulic conductivity ratio analysis. *Geotextiles and Geomembranes*, 8(1), 1-26.

## **Simplified Model for Analysis of Piled Embankment Considering Multi-Interaction Arching and Subsoil Consolidation**

**Tuan A. Pham** <sup>1,2</sup>, and **Daniel Dias** <sup>3,4</sup>

<sup>1</sup>Department of Geotechnical Engineering, Heriot-Watt University, Edinburgh, Scotland, UK

<sup>2</sup>Department of Civil Engineering, The University of Tokyo, Hongo-Bunkyo, Tokyo, Japan ;  
e-mail: [ta.pham@hw.ac.uk](mailto:ta.pham@hw.ac.uk)

<sup>3</sup>Laboratory 3SR, Grenoble Alpes University, CNRS UMR 5521, Grenoble, France

<sup>4</sup>AFITEXINOV Group, 15 Rue Louis Blériot, 28300 Champhol, France; e-mail:  
[d.dias69@gmail.com](mailto:d.dias69@gmail.com)

### **ABSTRACT**

The focus of this paper is to present a multi-interaction model under a simplified form for calculating load transfer to piles and geosynthetic strain of piled embankment. The multi-interaction model is established from the integrated load transfer mechanism and interaction between linked elements of a geosynthetic-reinforced and pile-supported embankment, including fill soils, geosynthetic, platform, subsoil, and pile. The proposed method is the results of the combination of the tensioned membrane theory for geosynthetics, soil arching theory for fill soils, friction interaction model, and subsoil support, thereby providing a more suitable design approach that enables a realistic and suitable approximation of the bearing behavior of the structured composite, and believed to be a useful tool for engineers in designing the soil-geosynthetic system. The proposed method can apply for both cohesive and non-cohesive fill soils. Using this method, the influence of subsoil consolidation degree, ultimate bearing capacity of subsoil, friction, fill soil cohesion, and platform on behavior and deformation of the piled embankment are investigated. The result of the proposed method is compared to the field measurement and two design standards to study its validity. The results showed a good agreement between the proposed method with measured data and better than that of existing design models.

*Keywords: piled embankment, geosynthetic, analytical model, interaction, soil arching, membrane action, subsoil, consolidation.*

### **INTRODUCTION**

A geosynthetic-reinforced and pile-supported (GRPS) technique was widely developed in recent years to address issues with bearing capacity and deformation. With this technique, the pile components are arranged in a predictable configuration and driven through the soft soil to a lower load-bearing stratum. One or more layers of geosynthetic reinforcement are positioned above the pile head. By using the soil arching and geosynthetic membrane effect, this integrated method minimizes the fill load transferred to soft ground and maximizes the load transferred to stiff piles. The GRPS systems have shown to perform well in terms of both bearing capacity and serviceability in a variety of applications, particularly for highway, railway, and road embankments (Hoppe and Hite, 2006; Filz and Smith, 2006; Lee et al., 2019; Van Eekelen and Han, 2020; Pham and Dias, 2021a; Pham and Dias, 2021b; Pham, 2021).

There are existing several simplified calculation procedures, which allow for dimensioning of the geosynthetic reinforcement (NGG, 2005; BS8006, 2010; EBGeo, 2011; Iglesia et al., 2014; Van Eekelen et al., 2014; Pham et al., 2022). However, there is currently no analytical method that can precisely characterize the complicated behavior of the system embankment - geosynthetic - piles - subsoil, though. Therefore, when predicting loads transferred to the piles, geosynthetic, and subsurface for the same embankment, various techniques yield different results (Pham, 2019; Pham, 2020 a, b; Pham and Dias, 2022). The primary author will attest that any people named as coauthors have seen the final version of the paper and agreed to its submission for publication.

This study's main objective is to develop an integrated method for analyzing pile-supported and geosynthetic-reinforced embankments. The proposed method is based on the theory of multiple interactions between related soil-structure elements, allowing for a realistic and appropriate approximation of the bearing behavior of the structural composite. To determine the approach's validity, the results from the present method were compared to those from other design methods.

## ANALYSIS OF LOAD TRANSFER MECHANISM

The settlement between piles is greater than that on the tops of piles due to the piles' higher stiffness in comparison to the soft subsoil, which causes geosynthetic reinforcement to deflect. The geosynthetic is stretched because of the geosynthetic deflection, which also causes the fill soil's stresses to be redistributed. The mass of the embankment between the pile caps tends to shift downward as a result of geosynthetic deflects, but this movement is in part prevented by shear resistance in the fill above the pile caps. By shifting loads onto stiffer parts and reducing stresses on soft subsoil, the stress equilibrium situation is created. This load transfer mechanism is termed the “soil arching effect” (Pham 2020 a, c). Meanwhile, the stretching of the geosynthetic material mobilizes a portion of its strength, and tensile forces are generated that called “tensioned membrane effect”.

The issue at hand involves a complicated relationship between the pile, soil, and geosynthetic. The problem can be substantially simplified, however, if the soil response (arching) is uncoupled from the geosynthetic response (tensioned membrane). Consequently, a two-step process is employed. First, the arching theory is used to examine the soil layer behavior. This stage applies pressure to the piles' tops and the soft soil between them (Figure 1a). Second, the relationship between the pressure on the geosynthetic, the tension within the geosynthetic, and the deflection of the geosynthetic is established using the tensioned membrane theory. The second phase involves externally loading the geosynthetic reinforcement with vertical tension (Figure 1b). Considering this, the following sections describe a computation method that combines these two load transfer mechanisms.



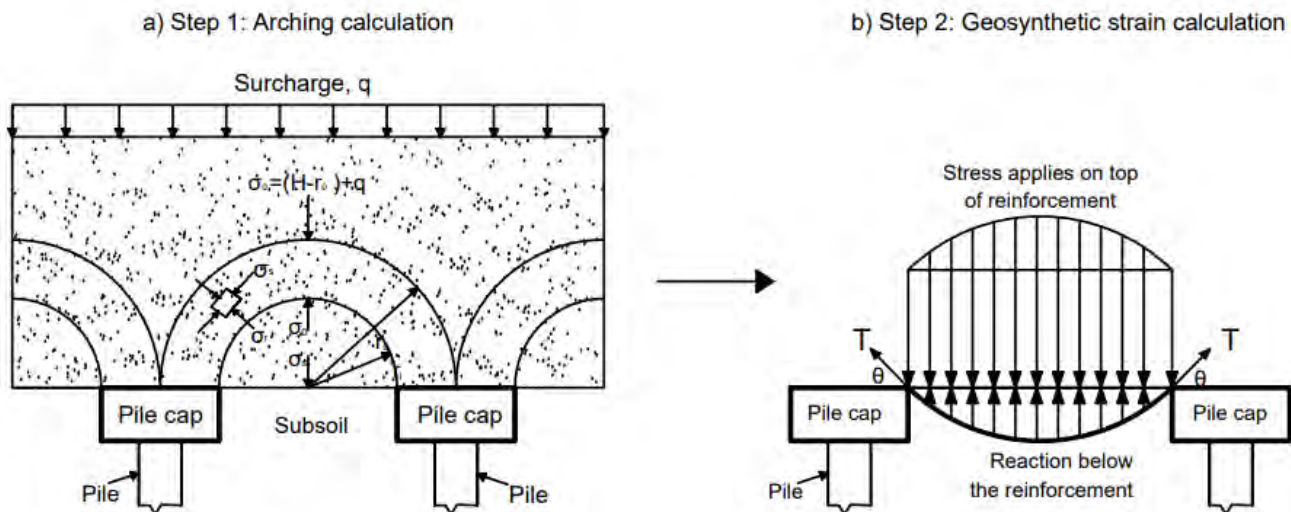


Figure 1. Two-step design procedure for GRPS embankment design

## SIMPLIFIED SOIL-STRUCTURE INTERACTION MODEL

In this section, an integrated approach is presented with considering the multi-interaction theory between linked soil-structure elements. Several following various phenomena are combined into the proposed method: 1) arching theory in fill soil layers, ii) tensioned membrane theory for geosynthetic, iii) frictional interaction along the interface of geosynthetic-soil, iv) platform-geosynthetic-subsoil interaction model, v) subsoil consolidation, and vi) nonlinear behavior model for subsoil. The proposed method is expected to provide a more comprehensive design approach that enables a realistic and suitable approximation of the bearing behavior of the GRPS embankment.

An inherent assumption in this uncoupled two-step approach is that the soil deformation required to generate the soil arch is compatible with the tensile strain required to mobilize the geosynthetic tension. Also, the geosynthetic reinforcement is homogenous, isotropic, and is in tension only.

**Soil arching in piled embankment.** In the first step, arching theory is used to compute the stress re-distribution in the embankment. The fill soil layer develops arching as a result of the subsoil settling. Due to the weight of the embankment soils and surcharge, some of the applied stress is subsequently communicated laterally. As a result, the normal stress transmitted to the area of the geosynthetic and subsoil between piles is less than the typical vertical stress.

The analysis presented here is based on the “multi-arching theory” (Fig. 2) in granular soil and similar to the analysis presented by Kempfert et al. (2004) as well as adopted into EBGeo (2011). The main refinement in the present analysis is the inclusion of the fill soil cohesion, critical height, and the uniform surcharge on the embankment fill. As for the cohesion of the fill soil, it is assumed that the stress state in the arch is uniform around the semicircle and that the limit state occurs in the entire arch, which gives tangential stress:

$$\sigma_{\theta} = \sigma_z \cdot K_p + K_c \cdot c \quad (1)$$

Here,  $K_p$  is passive earth pressure coefficient,  $c$  is cohesion of embankment soils, and  $K_c$  is cohesion coefficient.

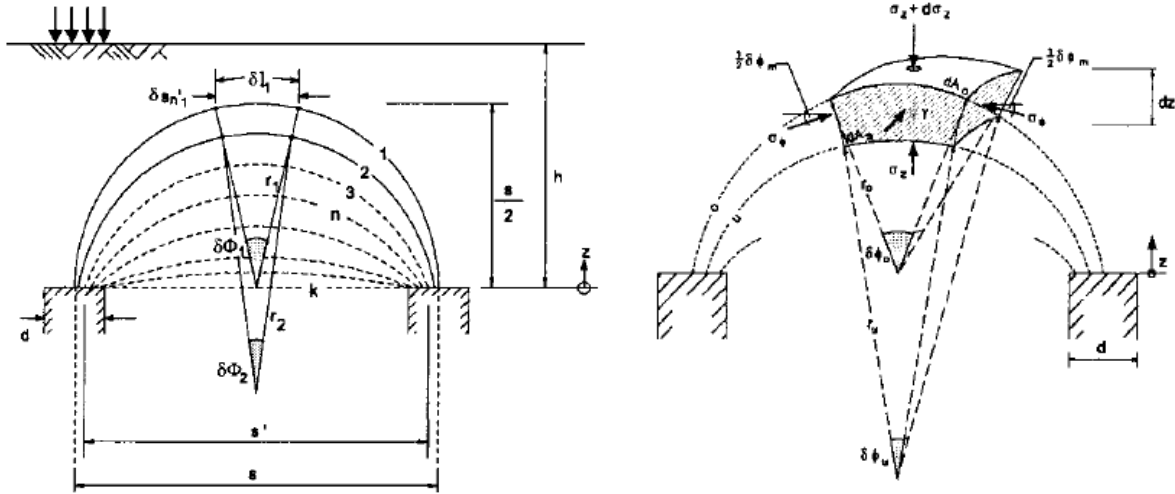


**Figure 2. Multi-Arch model (after Kempfert et al., 2004)**

The critical height,  $H_{crit}$  is included into proposed method to consider the influence of embankment height on arching mobilization. At a low embankment height, the shear resistance in the embankment fill is not large enough to develop the arching and reduce the pressure applied onto the foundation soil or the geosynthetic. With the increase in the height of the embankment, more shear resistance accumulates for enhancing the development of soil arching. However, the soil above critical height is not mobilized for arching.

The vertical equilibrium of the crown element is:

$$-\sigma_z \cdot dA_u + (\sigma_z + d\sigma_z) \cdot dA_0 - 4\sigma_\phi \cdot dA_s \cdot \sin(\delta\phi_m/2) + \gamma dV = 0 \quad (2)$$

The solution of the equation (2) gives the vertical stress acting on the geosynthetic and subsoil directly by arching effect:

$$\sigma_s^a = \lambda_1^X \cdot \left( \gamma + \frac{q}{H} \right) \cdot \left[ H \cdot (\lambda_1 + H_{crit}^2 \cdot 2)^X + H_{crit} \cdot \left( \left( \lambda_1 + \frac{H_{crit}^2 \cdot 2}{4} \right)^{-X} - (\lambda_1 + H_{crit}^2 \cdot 2)^{-X} \right) \right] - \lambda_1^X \cdot c \cdot K_c \quad (3)$$

Where

$$X = \frac{\sqrt{2}}{2} \cdot \frac{a \cdot (K_p - 1)}{\lambda_2 \cdot s}; \quad \lambda_1 = \frac{(s-a)^2}{4}; \quad \lambda_2 = \frac{s^2 + 2 \cdot a \cdot s - a^2}{2 \cdot s^2};$$

$$K_p = \tan^2 \left( 45^\circ + \frac{\varphi}{2} \right); \quad K_c = \frac{\cos \varphi}{1 - \sin \varphi}$$

Where,  $a$  is width of square pile cap,  $s$  is center-to-center-pile spacing,  $\gamma$  is unit weight of fill soils,  $H$  is embankment height,  $H_{crit}$  is critical height.

**Geosynthetic-subsoil interaction model.** As a second step, the vertical stress by arching,  $\sigma_s^a$ , is applied to the geosynthetic reinforcement as external loading. In all cases, a possible upwards counter-pressure  $\sigma_{up}$  from the partially soft subsoil between piles is assumed, which reduces the tension in reinforcement, is still a matter of discussion and safety philosophy, as shown in Figure 3. Equation (3) had to be developed to reflect this interaction.

$$\sigma_{GR} = \sigma_s^a - \sigma_{up} \quad (4)$$

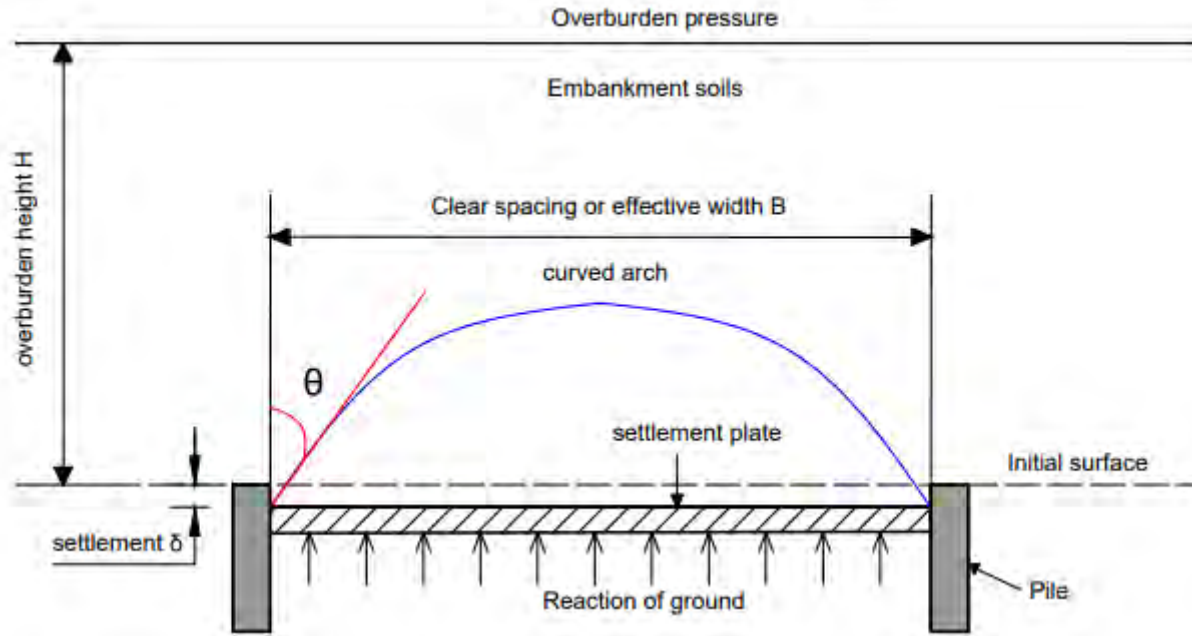


**Figure 3. Subgrade reaction model**

A concept to take into account the supporting soft soils in a deformation-related way is introduced by using a modulus of subgrade reaction  $K_s$ . The non-linear behavior model of the subsoil is introduced here to reflect the subgrade reaction curve (Kondner, 1963; Pham, 2020b; Pham, 2022). The consolidation effect of soft subsoil is applied in the proposed model. The pressure deflection relation at any point is given by the following expressions:

$$\sigma_{up} = \frac{y \cdot K_s}{U[1 + y \cdot K_s / q_{su}]} \quad (5)$$

Where,  $\sigma_{up}$  is the upward counter-pressure of subsoil,  $y$  is the maximum geosynthetic deflection,  $U$  is the consolidation degree of subsoil at any given time,  $K_s$  is subgrade reaction modulus of subsoil.

**Tensioned membrane theory of geosynthetic.** The deformed shape of geosynthetic is assumed to be circular (Pham, 2020 a). According to the tensioned membrane theory, the tension in a geosynthetic is determined by the following equation:

$$T = \sigma_{GR} \cdot \Omega \cdot (s - a) \quad (6)$$

in which,  $\Omega$  = a dimensionless factor. The dimensionless factor  $\Omega$  is defined as follows

$$\Omega = \frac{1}{4} \left[ \frac{2y}{s-a} + \frac{s-a}{2y} \right] \quad (7)$$

Replacing Equations (6) into (5), results in the tension of a geosynthetic being calculated as follows:

$$T = \frac{1}{4} (\sigma_s^a - \sigma_{up}) \left[ 2y + \frac{(s-a)^2}{2y} \right] \quad (8)$$

**Friction interaction analysis.** Pham (2019) and Pham et al. (2021) conducted the numerical analysis to investigate the interaction between subsoil-geosynthetic-platform, and have found that a great amount of skin friction is mobilized along with geosynthetic-soils interfaces. Therefore, the tension in the geosynthetic is considered as a function of two strain components, one due to the load and the other due to the skin friction. Thus, mathematically

$$T = T_\varepsilon + T_f \quad (9)$$

where  $T$  is maximum tension in geosynthetic,  $T_\varepsilon$  is the tension component induced by stretching of geosynthetic, and  $T_f$  is the tension component induced by skin friction.

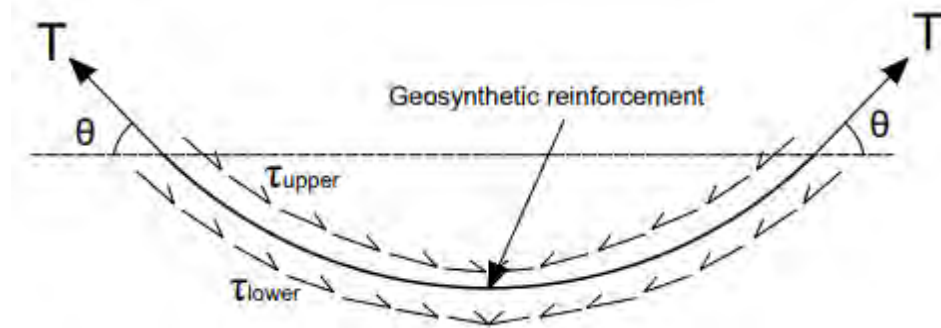


**Figure 4. Soil-geosynthetic friction interaction analysis**

To consider the friction characteristics mobilized along with interfaces, the shear strength parameters of soils is multiplied with an interaction coefficient between the reinforcement material and the proposed soil. The total shear stresses,  $\tau$ , is a result of skin friction along the upper and lower sides of the soil-geosynthetic interfaces (Figure 4) is expressed as follows:

$$\tau = \tau_{upper} + \tau_{lower} = 0.85(\alpha_p \tan \phi_p \cdot \sigma_s^a + \alpha_s \tan \phi_s \cdot \sigma_{up} + K_c \cdot c_s) \quad (10)$$

where  $\phi_p$  and  $\phi_s$  = friction angle of soils at the upper side and lower side of the interface respectively,  $c_s$  = total cohesion of soil at upper and lower sides of interfaces,  $\alpha$  = interaction coefficient between geosynthetic-soils. Value  $\alpha_p$  varies within 0.65 to 0.85 while value  $\alpha_s$  varies from 0.60 to 0.75

The tension in geosynthetic induced by skin friction along interfaces is calculated by:

$$T_f = \tau(s - a)/4 = \frac{0.85}{4} \cdot (\alpha_p \tan \phi_p \cdot \sigma_s^a + \alpha_s \tan \phi_s \cdot \sigma_{up} + K_c \cdot c_s) \cdot (s - a) \quad (11)$$

**Geosynthetic deformation model.** It is assumed that, in the considered cross-section, the deflected geosynthetic has the shape of a smooth curve that can be described as an arc of a circle. It is pre-assumed that the geosynthetic strain is uniformly distributed in the considered cross-section. In the case of a circular curve, the expression for strain was given by Giroud (1990). This expression is:

$$\varepsilon = \frac{\theta}{\sin \theta} - 1 \quad (12)$$

where  $\theta$  is deflected angle and is a function of  $y/s'$ , defined as follows:

$$\sin \theta = \frac{2}{\frac{2y}{s-a} + \frac{s-a}{2y}} \quad (13)$$



Equation (13) can be expressed as follows:

$$\sin \theta = \frac{4y/(s-a)}{1+4(y/(s-a))^2} \quad (14)$$

If  $y/(s-a)$  is small, a classical approximation gives the following:

$$\sin \theta \approx 4y/s' - 16(y/s')^3 \quad (15)$$

Hence, the following truncated series expansion can be used:

$$\theta = \sin^{-1}(\sin \theta) \approx \sin \theta + (\sin \theta)^3/6 \quad (16)$$

Combining Equations (14) and (15) gives the following:

$$\theta \approx (4y/s') - 16(y/s')^3 + (1/4)(4y/s')^3 \quad (17)$$

Replacing Equations (14) and (17) back into (12) yields the following:

$$\varepsilon = \frac{4y/s'}{4y/s' - 16(y/s')^3} - 1 = \frac{1+4(y/s')^2}{1-16(y/s')^4} - 1 \quad (18)$$

Using a classical approximation, this becomes the following:

$$\varepsilon \approx \frac{8}{3} \cdot \left( \frac{y}{s-a} \right)^2 \quad (19)$$

The tension in the geosynthetic induced by arching load is:

$$T_\varepsilon \approx \frac{8}{3} \cdot \left( \frac{y}{s-a} \right)^2 \cdot J_{GR} \quad (20)$$

Substitute Equations (19) and (10) back into (9) gives the maximum total tension in geosynthetic:

$$T = \frac{8}{3} \cdot \left( \frac{y}{s-a} \right)^2 \cdot J_{GR} + \frac{0.85}{4} \cdot (\alpha_p \tan \varphi_p \cdot \sigma_s^a + \alpha_s \tan \varphi_s \cdot \sigma_{up} + K_c \cdot c_s) \cdot (s-a) \quad (21)$$

**3.6 Solution of typical design problems.** The typical design problems of GRPS embankment is entirely solved by combining Equations (8) and (21). The following fourth-order equation is obtained.

$$\beta_1 y^4 + \beta_2 y^3 + \beta_3 y^2 + \beta_4 y + \beta_5 = 0 \quad (22)$$

where

$$\beta_1 = 21.33 J_{GR} U K_s;$$

$$\beta_2 = 21.33 J_{GR} U q_{su} - 4 U K_s \sigma_s^a (s-a)^2 + 4 K_s q_{su} (s-a)^2; \quad \beta_3 = 1.7 \alpha_p \tan \varphi_p \sigma_s^a U K_s (s-a)^3 + 1.7 \alpha_s \tan \varphi_s K_s q_{su} (s-a)^3 + 1.7 U K_s K_c c_s (s-a)^3 - 4 \sigma_s^a U q_{su} (s-a)^2; \quad \beta_4 = 1.7 \alpha_p \tan \varphi_p \sigma_s^a U q_{su} (s-a)^3 + 1.7 U q_{su} K_c c_s (s-a)^3 + K_s q_{su} (s-a)^4 - \sigma_s^a U K_s (s-a)^4;$$

$$\beta_5 = -\sigma_s^a U q_{su} (s-a)^4.$$

It should be noted that  $\sigma_s^a$ , is estimated by using Eq. (3). Substitute value of maximum geosynthetic deflection back into Eqs. (8) or (21) to find the maximum tension in geosynthetic. The performance of the load transfer mechanism is assessed through the term of efficacy that defined as the percentage by weight of the embankment soils and surcharge carried by the pile caps.

$$E = E_a + E_m \quad (23)$$

The efficacy component,  $E_a$ , which defined as the proportion of embankment load distributed directly on the pile cap by arching effect is:

$$E_a = 1 - \frac{\sigma_s^a \cdot A_s}{(\gamma H + q) \cdot A} \quad (24)$$

The efficacy component,  $E_m$ , which defined as the proportion of embankment load transferred onto the pile cap by tensioned membrane effect of geosynthetic:

$$E_m = \frac{\gamma/(s-a)}{1+4(\gamma/(s-a))^2} \cdot \frac{32aT}{(\gamma H + q) \cdot A} \quad (25)$$

In this study, the strain calculation of GR is presented for 2D configuration with some simplifications. The maximum differential settlement is determined at the mid-point of pile spacing. To find geosynthetic strain for 3D configuration, the pile spacing ( $s-a$ ) in calculation coefficients of Equation (22) should be replaced by diagonal,  $s_d = (s-a)\sqrt{2}$ .

## VALIATION OF PROPOSED METHOD

The proposed method is validated by using a well-documented case study of a geogrid-reinforced and piled supported highway embankment with a low area improvement ratio (Liu et al., 2007). The embankment was 120 m in length, 5.6 m in height, and 35 m in width at its crown. 1 to 1.5 H to 1 V was the side slope. The primary component of the fill material was powdered fuel ash, which had an average unit weight of 18.5 kN/m<sup>3</sup>, a cohesiveness of 10 kPa, and a friction angle of 30°. In order to create a square pattern, the annular concrete piles were spaced three times their diameter, or 3 m, from the centres of the adjacent piles. The pile cap covering percentage over the entire foundation area, or the area ratio, was 8.7%. To create a 0.5 m thick composite-reinforced bearing layer, a layer of biaxial polypropylene grid TGG90-90 was sandwiched between two layers of 0.25 m thick gravel. The geogrid has a tensile strength of 90 kN/m in both the longitudinal and transverse directions, and an 8% maximum permissible tensile strain. In around 55 days, the embankment was built up to a height of 5.6 m.

A summary of input parameters for calculation as follows: Embankment -  $H = 5.6$  m,  $\gamma = 18.5$  kN/m<sup>3</sup>,  $\phi = 42^\circ$ ,  $c = 10$  kPa; Pile -  $a = 1.0$  m,  $s = 3.0$  m; Subsoil -  $U = 0.92$ ,  $K_s = 550$  kPa/m,  $q_{su} = 550$  kPa; Geosynthetic -  $J_{GR} = 1180$  kN/m; Interfaces -  $\phi_p = 40^\circ$ ,  $\phi_s = 10^\circ$ ,  $c_s = 20$  kPa; Interaction coefficients -  $p = 0.8$ ,  $s = 0.6$ ; No surcharge load. The results are presented in terms of the maximum deflection and tension in the geosynthetic because they are of more interest to geotechnical engineers for design purposes.

**Table 1. Comparison of results from analytical solutions and field measurements**

	Proposed method	EBGE O (2011)	BS8006 (2010)	Nordic Guideline (2004)	Geogrid Bridge Filz et al. (2019)	Japanese PWRC (2001)	Field measurement
Total efficacy, E (%)	61.1	55.6	58.0	60.5	81.8	41.0	62.57

Maximum tension in geosynthetic, T (kN/m)	20.7	46.33	285.8	83.6	79.1	-	19.97
Maximum geosynthetic deflection, y (mm)	90.1	97.0	60.0	327.96	317.0	172.1	72.0

It is noted that the proposed method provides a better agreement with the measured results than EBGeo and BS8006 for all three comparison terms, particularly for the maximum geosynthetic deflection and tensile force (Table 1). The BS8006 method gives the highly conservative values for the tension in the geosynthetic but under-predicts the maximum GR deflection. This is due to that a constant strain is assumed to calculate geosynthetic deflection. The EBGeo method over-predicts significantly the maximum tension in geosynthetic. Other remaining methods highly over-predict the strain and deflection of geosynthetic (Figure 6)

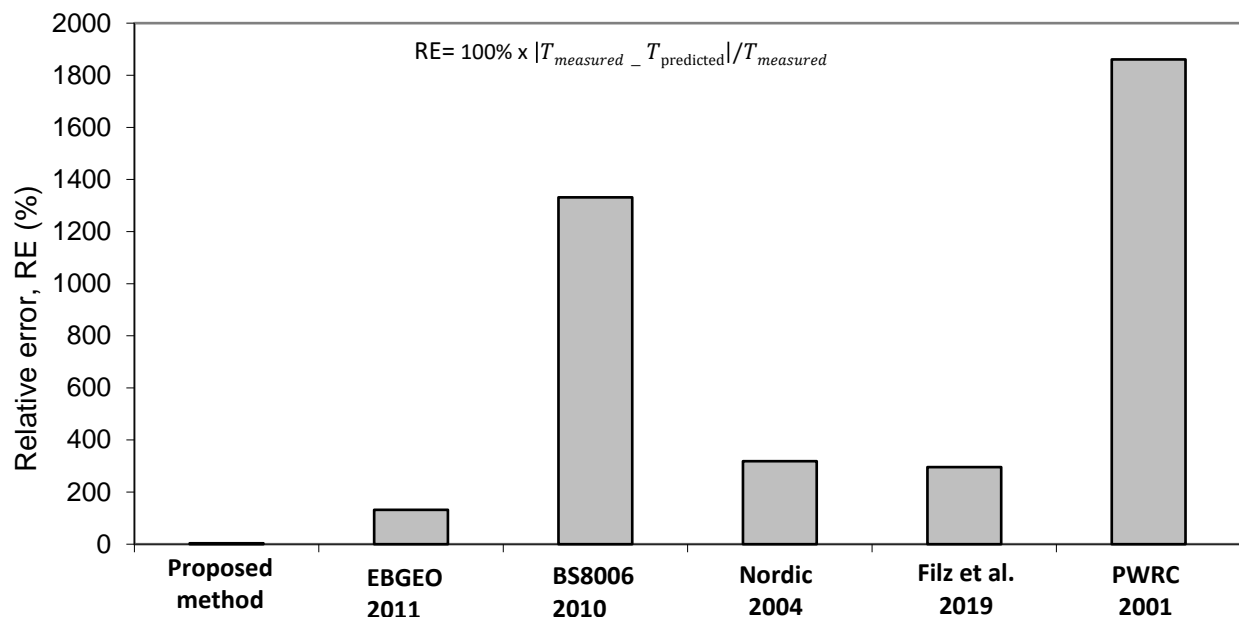


**Figure 6. Relative error of methods in predicting tension in geosynthetic**

## CONCLUSIONS

This study examined the load-deflection behavior of a GRPS embankment using a multi-interaction model presented in a closed-form. The integrated load transfer mechanism between related elements such as fill soils, geosynthetic, platforms, subsoils, and piles form the basis of the multi-interaction model. The proposed method is believed to be a useful tool for engineers in the design of the soil-geosynthetic system since it offers a realistic and appropriate approximation of the bearing behavior of the structured composite.

Both cohesive and non-cohesive soil pile embankments can use the suggested approach. This method is used to evaluate the effects of friction, fill soil cohesion, platform, subsoil consolidation degree, and subsurface ultimate bearing capacity on the behavior and deformation of the piled

embankment. The result of the proposed method is compared to the field measurement and five design methods to study its validity. The comparison results showed a good agreement between the proposed method with measured data and generally better than the design standards of EBGeo and BS8006 and other design methods.

To investigate the validity of the suggested method, the result is compared to measurements collected in the field and five different design approaches. The comparative results revealed that the proposed method and measured data agreed well, and that it performed typically better than existing design standards and methods like BS8006 and EBGeo.

## REFERENCES

- BS8006-1, BSI (2010). Code of practice for strengthened/reinforced soils and other fills. BSI, London, UK.
- EBGeo (2011). Recommendations for Design and Analysis of Earth Structures Using Geosynthetic Reinforcements, EBGeo, German Geotechnical Society, Auflage, German, vol. 2.
- Filz, G. M., & Smith, M. E. (2006). *Design of bridging layers in geosynthetic-reinforced, column-supported embankments*. Virginia Center for Transportation Innovation and Research.
- Giroud, J. P., Bonaparte, R., Beech, J. F. & Gross, B. A. (1990). Design of soil layer-geosynthetic systems overlying voids. *Geotextiles and Geomembranes*, 9, No. 1, 11–50.
- Hoppe, E. J., & Hite, S. L. (2006). *Performance of a pile-supported embankment* (No. FHWA/VTRC 06-R36). Virginia Transportation Research Council.
- Iglesia, G. R., Einstein, H. H., & Whitman, R. V. (2014). Investigation of soil arching with centrifuge tests. *Journal of Geotechnical and Geoenvironmental engineering*, 140(2), 04013005.
- Kempfert, H. G., Göbel, C., Alexiew, D. & Heitz, C. (2004). German recommendations for reinforced embankments on pile-similar elements. In EuroGeo3-Third European Geosynthetics Conference, Geotechnical Engineering with Geosynthetics, Deutsche Gesellschaft für Geotechnik, Munich, Germany, pp. 279–284.
- Kondner, R. L. (1963). Hyperbolic stress-strain response: cohesive soils. *Journal of the Soil Mechanics and Foundations Division*, 89(1), 115-144.
- Lee, T., Lee, S. H., Lee, I. W., & Jung, Y. H. (2019). Quantitative performance evaluation of GRPE: a full-scale modeling approach. *Geosynthetics International*, 1-6.
- Liu, H. L., Ng, C. W., & Fei, K. (2007). Performance of a geogrid-reinforced and pile-supported highway embankment over soft clay: case study. *Journal of Geotechnical and Geoenvironmental Engineering*, 133(12), 1483-1493.
- NGG - Nordic Geosynthetic Group (2005). Nordic Guidelines for Reinforced Soils and Fills.
- Pham, T. A. (2019). Analysis of soil-foundation-structure interaction to load transfer mechanism in reinforced piled embankments. *Aust Geomech J*, 54(1), 85-100.
- Pham, T. A. (2020a). Load-deformation of piled embankments considering geosynthetic membrane effect and interface friction. *Geosynthetics International*, 27(3), 275-300. <https://doi.org/10.1680/jgein.19.00030>
- Pham, T. A. (2020b). Analysis of geosynthetic-reinforced pile-supported embankment with soil-structure interaction models. *Computers and Geotechnics*, 121, 103438. <https://doi.org/10.1016/j.compgeo.2020.103438>



- Pham, T. A. (2020c). Behaviour of piled embankment with multi-interaction arching model. *Géotechnique Letters*, 10(4), 582-588. <https://doi.org/10.1680/jgele.20.00084>
- Pham, T. A. (2021). Design and analysis of geosynthetic-reinforced and floating column-supported embankments. *International Journal of Geotechnical Engineering*, 1-17. <https://doi.org/10.1080/19386362.2021.1997209>
- Pham, T. A., Tran, Q. A., Villard, P., & Dias, D. (2021). Geosynthetic-reinforced pile-supported embankments— 3D discrete numerical analyses of the interaction and mobilization mechanisms. *Engineering Structures*, 242, 112337. <https://doi.org/10.1016/j.engstruct.2021.112337>
- Pham, T. A., & Dias, D. (2021a). Comparison and evaluation of analytical models for the design of geosynthetic-reinforced and pile-supported embankments. *Geotextiles and Geomembranes*, 49(3), 528-549. <https://doi.org/10.1016/j.geotexmem.2020.11.001>
- Pham, T. A., & Dias, D. (2021b). 3D numerical study of the performance of geosynthetic-reinforced and pile-supported embankments. *Soils and Foundations*, 61(5), 1319-1342. <https://doi.org/10.1016/j.sandf.2021.07.002>
- Pham, T. A., Wijesuriya, K., & Dias, D. (2022). Analytical model for the design of piled embankments considering cohesive soils. *Geosynthetics International*, 1-45. <https://doi.org/10.1680/jgein.21.00034>
- Pham, T. A., & Dias, D. (2022). A simplified model for the analysis of piled embankments considering arching and subsoil consolidation. *Geotextiles and Geomembranes*. <https://doi.org/10.1016/j.geotexmem.2021.12.003>
- Pham, T. A. (2022). Micromechanical-Based Shear Strength Equation Considering the Stress-State Effect for Unsaturated Soils. *International Journal of Geomechanics*, 22(9), 06022022.
- Van Eekelen, S. J. M., & Han, J. (2020). Geosynthetic-reinforced pile-supported embankments: state of the art. *Geosynthetics International*, 27(2), 112-141. <https://doi.org/10.1680/jgein.20.00005>

## **Environmental, Social, and Governance (ESG) Offerings of an Engineered Turf Final Cover System**

**Rutuparna Joshi, P.E.,<sup>1</sup>**

<sup>1</sup>Watershed Geosynthetics, LLC, 11400 Atlantis Place, Suite 200, Alpharetta, GA 30144; e-mail: [rjoshi@watershedgeo.com](mailto:rjoshi@watershedgeo.com)

### **ABSTRACT**

Use of an engineered turf cover (ETC), an alternative final cover, provides various environmental benefits including saving valuable soil and land resources, avoiding impacts associated with borrow areas, conservation of water, improved water quality, and significantly lower carbon emissions when compared to traditional covers (Joshi, 2022a). Reductions and avoidances in carbon emissions are realized when using an ETC. Select quantifications for reduction and avoidances in carbon emissions are included. In conjunction with the environmental benefits, several positive social benefits that can be realized as a result of using geosynthetics are discussed. Further, when using an ETC, opportunities exist for beneficial reuse of lands including development of solar energy. A discussion on development solar energy on landfills and impoundments and opportunities for community engagements are presented. A variety of governance aspects and priorities exist for private and public entities (e.g., resilience, risk, predictability). While governance aspects may be organizations-specific and subjective, some common themes may be drawn. Offerings from the use of an ETC as they relate to such common themes are discussed.

### **INTRODUCTION**

**Engineered Turf Cover and Solar System.** Modern engineered landfills have been traditionally closed using soil-only and soil-geosynthetic covers. Use of an engineered turf cover (ETC) as an alternative final cover system has steadily increased over the past decade for closure of municipal solid waste (MSW) landfills, industrial waste landfills, hazardous waste sites, coal combustion residual (CCR) units, and other waste impoundments. An ETC may consist of a geomembrane, an engineered turf, and an infill material (Figure 1 shows an example ETC). The geomembrane serves as a hydraulic barrier, the engineered turf covers and protects the geomembrane from (UV) radiation exposure and wind uplift, and the sand infill provides additional wind ballast, UV protection of the turf, and improves trafficability. An ETC provides for a preferred foundation for development of solar farms on top of landfills and impoundments. An example solar system consisting of friction strips, mounting rails, and photovoltaic (PV) panels that can be directly installed on top of an ETC is shown in Figure 2.

**Environmental, Social, and Governance (ESG) aspects and ETC.** In recent times, organizations including owners of waste containment facilities across multiple industries (e.g., solid-waste, utilities, manufacturing, mining) have placed significant focus on environmental,

social, and governance (ESG) aspects. Organizations are increasingly looking for enhancement of ESG factors and reduction of ESG risks. Many businesses are steering towards decarbonization of their infrastructure and application of sustainability principles across their supply chains. Organizations seek carbon free or less carbon intensive solutions and those that align with their ESG goals. An ETC provides one such solution for final covers on waste containment facilities.

In evaluating ESG aspects and risks, a comparative analysis of the alternatives is necessary. For the subject of this paper, the engineering feature in question is final cover system for landfills and waste containment facilities. A discussion of the ESG aspects and risks is presented by drawing a comparison between conventional final covers including a soil cover component and ETCs.

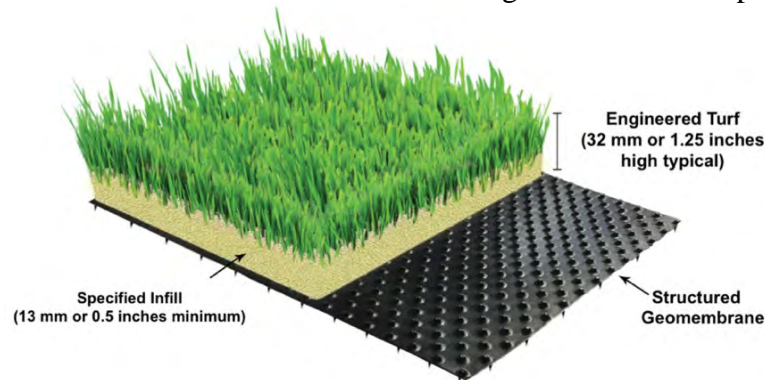


**Figure 1. Example engineered turf cover system.**

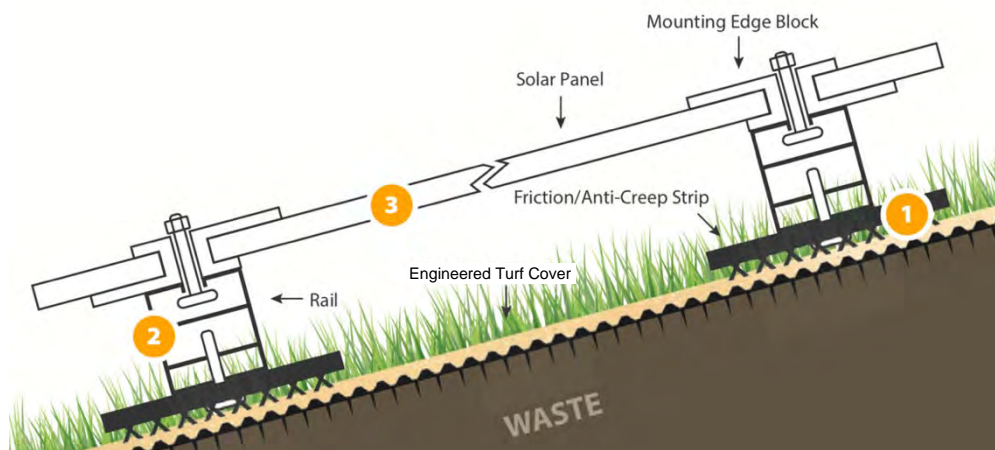


**Figure 2. Example solar power generation system.**

## ENVIRONMENTAL ASPECTS

ETC final cover system replaces the vegetative soil and protective soil layers of a conventional final cover system, typically 2 feet in thickness, thereby significantly reducing the soil and earthwork necessary for construction as compared to traditional soil covers. Obtaining soils and construction materials necessitates various environmental impacts. These negative impacts can be drastically reduced or eliminated when using ETC.

Various environmental benefits are realized in using an ETC, including the following:

- Drastic reduction in carbon emissions

- Avoidance of negative impacts to land and soil resources
- Avoidance of deforestation and land use change
- Avoidance of land disturbance
- Avoidance of potential loss of topsoil
- Reduction in construction materials (soils and geosynthetics) required for closure
- Water conservation
- Additional carbon sequestration.

In assessing environmental aspects, life cycle analysis (LCA) and carbon emissions of the alternatives need to be considered. Carbon emissions have been studied and detailed quantifications have been documented in companion studies as described below. For the purpose of this paper, select environmental benefits from the aforementioned list are illustrated further.

**Drastic Reduction in Carbon Emissions.** Detailed studies evaluating carbon emissions of multiple final cover systems have been performed. Joshi 2022a includes a comparison of carbon emissions for final cover systems on industrial waste landfills. Joshi 2022b includes a comparison of carbon emissions for final cover systems on Coal Combustion Residual (CCR) Units. Both studies include production, transportation, and construction emissions. Joshi 2022b includes quantification of select post-closure emissions. Joshi 2022a includes detailed quantification of carbon emissions for a traditional soil-only cover and an ETC. Based on Joshi 2022a and Joshi 2022b, it is observed that approximately 65% to 75% reduction in carbon emissions is achieved when using an ETC. Readers are referred to these studies for further details.

**Avoidance of Deforestation and Land Use Change.** Soils for traditional covers are obtained from borrow areas. Use of ETC reduces the required footprint of borrow areas. It is noted that borrow areas may also be used to provide soils for other purposes of site operations. For instance, in landfilling operations, borrow areas may be used for obtaining soils for daily covers and structural fill for access roads. Therefore, borrow areas may not be eliminated; however, the required footprint can be reduced. Depending on the condition of the prospective borrow area, potential deforestation and land use change are avoided. This helps in preserving soil and land resources and corresponding carbon sequestration.

To evaluate deforestation and land use change, permitted borrow areas in the State of Georgia were studied. The Georgia Environmental Protection Division's Surface Mining Unit issues Surface Mining Permits which are generally used for permitting borrow areas. More than 20 permitted borrow areas near landfill sites were reviewed. Thirteen borrow areas with permitted footprint of more than 20 acres were selected. Land Classification and land use change for the borrow areas pre- and post-development were studied using GIS data portals of various counties (e.g., Chatham County, Georgia; Bibb County, Georgia). Further, Google Earth Pro was used to review historic aerial imagery of the borrow areas and verify the pre- and post-development land use. Based on the review, it was observed that more than 75% of the borrow areas were forested pre-development.

Figure 3a shows a forested landscape and Figure 3b shows a borrow area with forested landscape in the background. Land use change is evidently seen in Figure 3b. Per data developed by the U.S. Department of Agriculture (USDA) Forest Service for the U.S. Environmental Protection Agency (EPA), the carbon stock density (i.e., carbon sequestration) of U.S. forests in 2019 was 200 metric tons of carbon per hectare (or 81 metric tons of carbon per acre) (EPA, 2022a). This equates to 733 metric tons of CO<sub>2</sub> equivalents per hectare or 297 metric tons of CO<sub>2</sub> equivalents per acre (MT CO<sub>2</sub> e/acre). Further, the average annual sequestration of carbon per area



was 0.57 metric tons C/hectare/year which equates to 0.84 MT CO<sub>2</sub> e/acre/year sequestered annually by one acre of an average U.S. forest (EPA, 2022a).

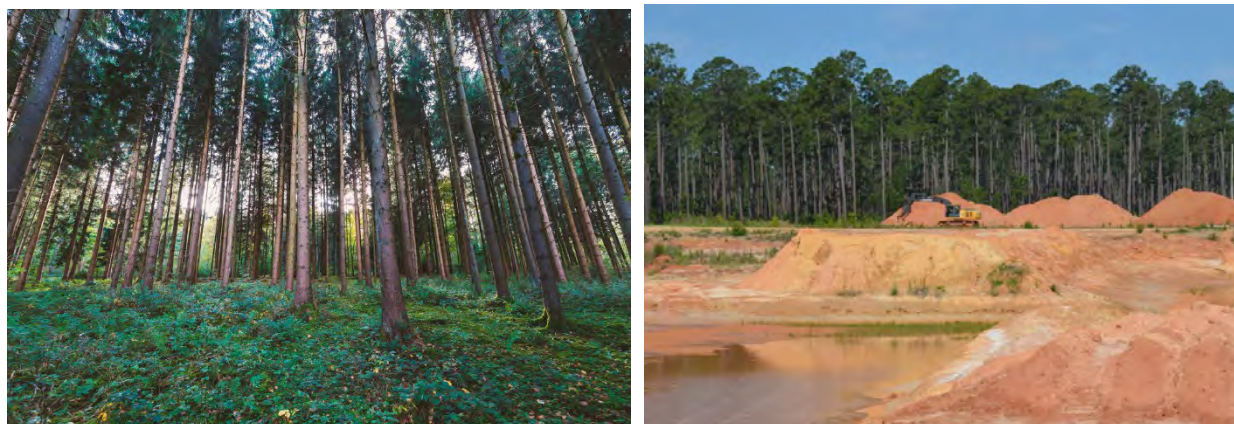


**Figure 3. (a) Forest landscape (Unsplash, 2021); (b) Borrow area (U.S. Army, 2021).**

With this in view, avoidance of one acre of deforestation for a borrow area, for example, equates to preservation of 297 MT CO<sub>2</sub> e emissions and an additional annual carbon sequestration of 0.84 MT CO<sub>2</sub> e. Assuming a 10-acre borrow area is needed for a 100-acre landfill with a 2-ft thick traditional soil cover, avoidance of 10 acres of deforestation when using ETC equates to 2,970 MT CO<sub>2</sub> e emissions and an additional annual carbon sequestration of 8.4 MT CO<sub>2</sub> e.

**Avoidance of Land Disturbance and Associated Impacts.** In addition to the negative impacts of deforestation and land use change, land disturbing activities further exacerbate impacts to the environment. The exposed bare soil areas are highly susceptible to erosion from wind and water. This results in accelerated erosion of the exposed soil areas. There are no roots to bind and stabilize the soil and no cover that can absorb the energy of rain and slow the velocity of runoff. For instance, the expected erosion rates at construction sites are 45 tons/acre/year in contrast to 1 ton/acre/year for forest land and 5 tons/acre/year for farmland (GSWCC, 2019). Erosion further leads to sedimentation, a process by which eroded material is transported from a subject area and deposited downstream. There are several negative impacts of sedimentation including the following:

- Deterioration of water quality
- Increased likelihood of flooding
- Impacts to aquatic life, wildlife, and habitat

It is noted that sedimentation, which mostly results from land disturbance, is the #1 non-point source pollutant (GSWCC, 2019) and contributor to poor water quality discharge. An example of water quality deterioration is shown in Figure 4. Other pollutants such as petroleum may leak from the equipment being used in the borrow areas. Further, land disturbance and excavation activities may have an impact on the local groundwater. In using an ETC, land disturbance to obtain borrow soil is avoided or considerably reduced thereby avoiding the associated detrimental impacts.



**Figure 4. Example of water quality deterioration (GSWCC, 2019)**

**Conservation of Water.** Water conservation can be realized during and post-construction when using an ETC. For instance, in some cases traditional soil cover is required to comprise of a compacted clay layer. Compaction of a clay layer in multiple lifts necessitates moisture conditioning of the clay to achieve certain hydraulic conductivity requirement. Use of multiple water trucks is necessitated for moisture conditioning. For instance, an estimated four (4) 5000-gallon water trucks are needed for 3% moisture conditioning of an 18-inch-thick clay layer over just one acre. Further, earthwork at project sites necessitate use of dust suppression measures, which are primarily performed using multiple full-time water trucks. With an ETC installation, use of dust suppression water trucks can be dramatically reduced. After the construction, use of water for irrigation and other operations and maintenance purposes is not needed either.

## **SOCIAL ASPECTS**

**Renewable Energy and Positive Social Impact.** Landfills, industrial waste containment areas, and other impaired lands can be beneficially repurposed with installation of solar power generation systems. Solar systems have been successfully installed on impaired lands and landfills. ETCs can provide a foundation for solar systems without having detrimental impacts on the landfill final cover systems or engineered covers on waste containment areas. Solar energy generated provides a clean source of energy to owners.

The energy can be used for facility operations and strategies may be developed to make the facility operations carbon neutral. For instance, a solar energy array on a Superfund landfill site in Hopewell Township, Pennsylvania is used to power the groundwater cleanup process. Additional energy can be distributed to a local community, provided to a local industry, or be put into the grid via an interconnect. For instance, Township Council of Old Bridge, New Jersey, recently approved a redevelopment plan to construct a solar field at the 130-acre Global Landfill site which will be used to power 400 local homes and reduce resident's utility bills by 20% (Reed, 2022, Loyer, 2022). Such generation and distribution of clean energy provides positive social impact.

**Community Engagement.** Public and private entities seek community engagement. Development of solar energy on waste containment facilities and otherwise impaired lands provide owners an opportunity to engage the community. Environmental education events can be organized to engage the public on innovative use of closed landfills and generation of clean energy. The benefits in



terms of public perception toward a more sustainable source of energy, though not quantifiable at present, are nevertheless significant (Alexander 2010).

**Avoidance of Community Impacts.** The necessitation and environmental impacts of borrow areas were discussed briefly in the preceding section. For conventional final cover systems where soil is obtained from off-site borrow areas, the soil needs to be transported to the project site or application area, which leads to on-road truck traffic. On-road truck traffic impacts the surrounding communities and local air quality. Especially, for landfills located in major metropolitan and urban areas, presence of on-site borrow areas is scarce and community impacts due to use of trucks hauling dirt can be significant. Further, even for sites with on-site borrow areas, off-road dump trucks are needed for transporting materials, generally on unpaved roads, thereby generating dust.

Figure 5 shows a schematic contrasting the equipment, material, and trips required just for transportation of materials for construction of 1-acre of a 2-ft-thick soil cover v. 1-acre of an ETC cover. Assuming an on-site borrow area, the soil cover necessitates about 160 truckloads of a 40-ton articulated dump truck whereas an ETC requires less than one truckload each for the geomembrane and the engineered turf, and five truckloads of sand. When a project uses an off-site borrow area, 1-acre of a 2-ft-thick soil cover is estimated to require an additional 265 on-road dump trucks.



**Figure 5. Schematic for transportation of construction materials: Soil cover v. ETC.**

**Health and Safety.** It is noted that the construction time for an ETC cover is generally less than that for soil covers (especially, with permeability requirements) and soil-geosynthetic covers. Weather delays tend to have a significant impact on construction of soil covers. In relative terms, lesser number of construction hours (employee and contractor work hours) are necessary for ETCs. Consequently, the likelihood of health and safety incidents may also be reduced.

As described previously, the number of truck trips for transporting soil materials is almost eliminated when using ETCs. This avoids potential health and safety incidents on the community roads, as also avoids potential health and safety impacts to truck drivers and surrounding

communities. The number of hours for truck trips and handling of soil on site are drastically reduced. Consequently, the likelihood of health and safety incidents may also be reduced.

**Water Quality.** Use of the engineered turf cover provides immense water quality improvement during and after construction. For instance, as seen in Figure 6, the quality of stormwater runoff from the engineered turf cover area is much less turbid than that from a soil cover area at the same landfill site. Water quality improvements benefit local creeks, streams, and water bodies downstream of the landfills and thereby benefiting the local environment and community.

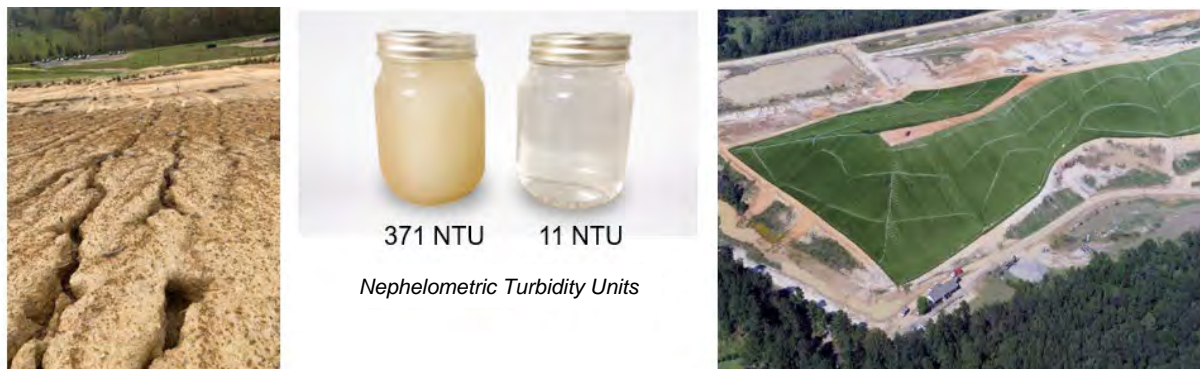


**Figure 6. Comparison of stormwater runoff quality of soil cover and ETC areas.**

## GOVERNANCE ASPECTS

A variety of governance aspects and priorities exist for private and public entities. Governance aspects and priorities may differ between different industries as also between organizations within the same industry. While governance aspects of entities may be subjective, some common themes can be drawn. A few commonly observed governance themes are identified, and closure options are viewed through the lens of these themes.

**Minimization of Risk.** Risk management is an undoubted component of organizational growth and development. Organizations seek minimization of risk to their businesses. From a waste containment facility standpoint, owners will naturally seek civil and environmental infrastructure solutions that are risk averse. One of the main concerns with final cover systems is erosion. Soil covers are susceptible to erosion and regulations have therefore required designing erosion control layer and use of erosion control measures. The main drawbacks to a surficial layer of soil are problems in initiating vegetative growth and vulnerability to wind or water erosion if the vegetative growth is not suitably thick (Koerner and Daniel, 1997) (See Figure 7a). These drawbacks, and hence risks, do not exist for an ETC.

In addition, with final cover systems constructed with soil covers, there is a likelihood of sloughing and sliding of cover soils underlain by geosynthetics or natural soil liners – also referred to as veneer slope instability. Veneer slope instability concerns do not exist with an ETC as there is no soil to fail (see Figure 7b). Adoption of ETC, from this standpoint, minimizes owner's risk during the post-closure period.





**Figure 7. (a) Poor vegetation and erosion gullies on traditional soil cover (b) Veneer slope failure of traditional soil cover (Maier, 2012).**

**Reliability and Predictability.** Organizations seek reliability and predictability. The post-closure care (PCC) costs at landfills and waste containment facilities are significantly reduced when using ETCs as compared to traditional final cover systems. For instance, there is no mowing to be performed, the stormwater ponds do not need to be cleaned as often, and there are no slope sloughing or veneer slides to be repaired. PCC costs are minimal and predictable, thus enabling owners to plan accordingly. The materials used for ETC are consistent as against soils from borrow areas (as would be the case with other geosynthetics applications), thereby providing infrastructure reliability across multiple sites for a given organization.

**Resiliency.** More than 3,000 acres of ETC have been installed on sites located in a wide assortment of climatic conditions. Some ETC installations have experienced significant or even historic weather events. Case studies and performance of the ETC installations with respect to various extreme weather conditions including tropical storms and hurricanes, strong winds, freezing temperatures, UV radiation, lightning and fire have been documented in Zhu et al. (2020) and Zhu (2021). Owners seek resilient infrastructure. As evidenced from field evaluations, ETC installations provide robust performance while maintaining operational continuity and minimizing site costs.

**Liability to Asset.** RE-powering America's Land is an US EPA (EPA, 2022b) initiative which encourages development of solar energy on current and formerly contaminated lands, landfills, and mine sites when such development is aligned with the community's vision. Use of ETC along with solar energy generation allows organizations to align with US EPA initiatives. Further, an impaired piece of land can be converted into a productive asset.

## **SUMMARY AND CONCLUSION**

Multiple environmental, social, and governance benefits can be realized in using ETCs. Carbon emissions associated with ETCs are about 65% to 75% less than that of the alternatives (Joshi 2022a and Joshi 2022b). Select environmental benefits discussed in the paper include preservation of land and soil resources, avoidance of deforestation and land use change, avoidance of land

disturbance, and conservation of water. Social benefits of using ETCs include avoidance of community impacts, increased health and safety of employees and the public, better water quality, opportunity for development of solar energy, community engagement, and positive social impact on the local community. Some governance aspects that the use of ETC enhances are minimization of risks, reliability and predictability, resiliency, and conversion of liability to an asset. In summary, an ETC solution offers values that align very well with environmental, social, and governance aspects of multiple public and private organizations.

## REFERENCES

- Alexander, T. (2010). Solar energy landfill caps, *Waste Advantage Magazine*, June, 28–32.
- Bibb County, Geographical Information System (GIS) portal. (2022).  
<https://qpublic.schneidercorp.com/Application.aspx?AppID=702&LayerID=11410&PageTypeID=1&PageID=0>, Accessed May 31, 2022.
- Chatham County, Geographical Information System (GIS) portal. (2022).  
<https://qpublic.schneidercorp.com/Application.aspx?AppID=1094&LayerID=27085&PageTypeID=1&PageID=10978>, Accessed May 31, 2022.
- Georgia Soil and Water Conservation Commission (GSWCC) (2019). Level II: Introduction to Design, Level II Final Notebook, May 2-3.
- Google Earth Pro 7.3.4.8642. (2022). Current and historical imagery of multiple borrow area locations in Georgia, USA, Accessed in May 2022.
- Joshi R. (2022a). A True Green Cover for Industrial Waste Landfills, *Pulping, Engineering, Environmental, Recycling and Sustainability (PEERS) Conference*, Providence, Rhode Island, October 30 - November 2, 2022.
- Joshi R. (2022b). Relative Sustainability of Engineered Turf Alternative Final Cover System for CCR Units, *World of Coal Ash Conference (WOCA) Conference*, Covington, Kentucky, May 16 - 19, 2022. Presented on 17 May 2022 in Session H2 - *CCP's and Sustainable Construction*.
- Koerner, Robert M., and David E. Daniel. (1997). *Final covers for solid waste landfills and abandoned dumps*, New York: ASCE Press.
- Loyer, S. (2022). Old Bridge landfill-to-solar farm redevelopment could slash local energy bills, *MyCentralJersey.com*, July 29.
- Maier, T. (2012). How Steep Is Too Steep? Design and Construction of Final Cover Systems, *Georgia SWANA Fall Conference*, Young Harris, GA, October 17, 2012.
- Reed, J. (2022). From Superfund to Solar: Repurposing Old Landfills, *MSW Management*, August 2.
- Unsplash. (2021). <https://unsplash.com/photos/qQYmavu2heI>, Accessed August 5, 2021
- U.S. Army,  
<https://home.army.mil/stewart/index.php/about/Garrison/DPW/environmental/prevention-and-compliance/borrow-pits>, Accessed August 5, 2021.
- U.S. EPA. (2022a). Greenhouse Gases Equivalencies Calculator - Calculations and References, <https://www.epa.gov/energy/greenhouse-gases-equivalencies-calculator-calculations-and-references>, Accessed on August 8, 2022.
- U.S. EPA. (2022b). <https://www.epa.gov/re-powering>, Accessed August 5, 2022.
- Zhu. M. (2021). Geotechnical and Wind Performance of Engineered Turf Landfill Cover, *Geo-Extreme 2021*, ASCE GSP 328, Savannah, GA, USA.

Zhu, M., Cooley, B., Ayers, M. (2020). Case Studies of Extreme Weather Performance of Engineered Turf Final Cover System, *Geosynthetics 2020*, IFAI, North Charleston, SC, USA.

## Hydraulic Conductivity of Bentonite-Polymer Composite Geosynthetic Clay Liners Under Elevated Temperature and Extreme pH

Sarah A Gustitus-Graham, EI, PhD<sup>1</sup> and Craig H Benson, PhD, PE, NAE<sup>2</sup>

<sup>1</sup>Geosyntec Consultants, Inc., 12802 Tampa Oaks Blvd, Suite 151, Tampa, FL 336317; e-mail: sgustitusgraham@geosyntec.com

<sup>2</sup>Wisconsin Distinguished Professor Emeritus, Geological Engineering, University of Wisconsin-Madison, Madison, WI 53706 USA, chbenson@wisc.edu

### ABSTRACT

Two BPC-GCLs containing proprietary polymers were permeated with aggressive solutions at 20 °C and 60 °C. BPC-GCLs were also statically exposed to elevated temperature (i.e., batch aged) in permeant solutions at 60 °C for periods of 15, 30, 60 and 120 days, after which they were permeated at 20 °C. BPC-GCLs permeated at 60 °C maintained similar or lower hydraulic conductivity than those permeated at 20 °C. The comparable hydraulic conductivities are attributed to minimal differences in swell index of the NaB component, flow stress of the polymer component, and polymer retention at 20 and 60 °C. The batch aged BPC-GCLs maintained low hydraulic conductivity ( $<10^{-10}$  m/s) as long as they retained sufficient polymer to clog pore spaces. The BPC-GCL sample that retained the least polymer (2.0 g polymer/kg BPC) during the exposure period had a significantly higher hydraulic conductivity ( $2.9 \times 10^{-7}$  m/s). There were no distinct relationships between hydraulic conductivity and batch aging time, flow stress of the polymer gels, or polymer loading for batch aged samples with hydraulic conductivities  $<10^{-10}$  m/s.

### INTRODUCTION

Bentonite-polymer composite geosynthetic clay liners (BPC-GCLs) can maintain low hydraulic conductivity to liquids that are too aggressive for conventional sodium bentonite (NaB) GCLs (e.g., liquids from mining waste and mineral beneficiation, coal combustion residuals, low level radioactive waste, incinerator ash) (Ashwamy et al., 2002; Athanassopoulos et al., 2015; Tian et al., 2016; Tian and Benson, 2018; Chen et al., 2019). The polymer hydrogel in BPC-GCLs fills larger pore spaces, resulting in flow paths that are finer and more tortuous than those in a NaB-GCLs (Scalia et al., 2014; Chen et al., 2019; Tian et al., 2019). However, if the polymer is eluted from the pores or the polymer structure is altered or degraded, larger and less tortuous flow paths can develop, and BPC-GCLs may become more permeable (Tian et al., 2019).

Wastes that require BPC-GCLs may exhibit elevated temperatures (Klein et al., 2001; Koerner and Koerner, 2006; Yeşiller et al., 2015). Mining waste temperatures have been reported as high as 65 °C and MSW incinerator ash temperatures as high as 87 °C (Yeşiller et al., 2015). Elevated temperatures in the waste can result in elevated temperatures at the liner. For example, Klein et al. (2001) reported that when waste temperatures reached as high as 70 °C in a MSW incinerator ash landfill, liner temperatures could reach 46 °C.

Hydraulic conductivity of NaB-GCLs may increase by an order of magnitude or more as the temperature increases from 20 to 60 °C (Ishimori and Katsumi, 2012; Ozhan, 2018). Ishimori and Katsumi (2012) report that a NaB-GCL had a higher intrinsic permeability and higher hydraulic conductivity at 60 °C than at 20 °C, despite that bentonite swelling increases with



increasing temperature (Mitchell and Soga 2005). Ozhan (2018) reports that the hydraulic conductivity of BPC-GCLs permeated with  $\text{MgCl}_2$  solutions increases with temperature.

Elevated temperatures may alter the viscoelastic properties of polymer gels in BPC-GCLs, affecting hydraulic conductivity. For example, the storage modulus, loss modulus, and flow stress, which define the viscous and elastic characteristics of a polymer hydrogel, depend on temperature and polymer structure (Young and Lovell, 2011). Flow stress of a polymer is the viscoelastic property that defines the transition between elastic (solid-like) and viscous (liquid-like) behavior in hydrogels. Gustitus and Benson (2020) indicate that polymers with lower flow stress (less resistance to flow) may be more prone to elution, which results in higher hydraulic conductivity.

In this study, the hydraulic conductivity of two commercially available BPC-GCLs to acidic and alkaline solutions were evaluated at 20 °C and 60 °C. Viscoelastic properties of the hydrated polymer component of each BPC were also evaluated at 20 °C and 60 °C.

## MATERIALS AND METHODS

Two commercially available BPC-GCLs were used in this study. BPC-GCL-P1, containing polymer P1, is designed for use with alkaline (high pH) solutions. BPC-GCL-P2, containing polymer P2, is designed for use with acidic (low pH) solutions. P1 and P2 are cross-linked polymers. Both BPC-GCLs contain nonwoven upper and lower geotextiles bonded by needlepunching. Average polymer loading was 65 g polymer/kg BPC for BPC-GCL-P1 and 60 g polymer/kg BPC for BPC-GCL-P2.

High and low pH solutions meeting the criteria in EN 14030 were used as permeant liquids (EN 14030:2001). The acidic solution was comprised of 25 mM  $\text{H}_2\text{SO}_4$ , 1 mM  $\text{FeSO}_4$ , and 1 mM  $\text{Fe}_2(\text{SO}_4)_3$ . The alkaline solution was a saturated solution of  $\text{Ca}(\text{OH})_2$  (2.5 g/L). EC and pH of the solutions are in Table 1.

**Table 1. pH and EC of permeating solutions.**

Solution	pH	EC (mS/cm)
Alkaline	12.4	8.8
Acidic	1.8	14.0

Hydraulic conductivity testing on each BPC-GCL was conducted in a flexible-wall permeameter using the falling headwater constant tailwater method in accordance with ASTM D6766. The average effective stress was 29 kPa and the average hydraulic gradient was 115. No backpressure was used to preclude geochemical changes that would not occur at natural porewater pressures. Unless otherwise specified, tests were carried out at room temperature (approximately 20 °C and not exceeding 24 °C).

Flexible-wall permeameters were modified for hydraulic conductivity testing at elevated temperatures up to 60 °C (Figure 1). A flexible heating cord was attached to the bottom plate around the circumference of the sample. A thermocouple was used to monitor the temperature of the cell water directly above the sample, which was regulated by a temperature controller connected to the thermocouple. The entire permeameter is encased in insulation to reduce heat loss and promote isothermal conditions. Testing indicated that the temperature of the GCL in the permeameter is within 1 °C of the cell water temperature, and the cell water temperature is

maintained within 1 °C of the set-point up to 60 °C. The uniform heating of the BPC-GCL in the permeameter is slightly different than would occur in the field, where heat is transferred vertically across the BPC-GCL. However, BPC-GCLs typically are 7-10 mm thick; therefore, the temperature differential across the GCL would be negligible in the field.

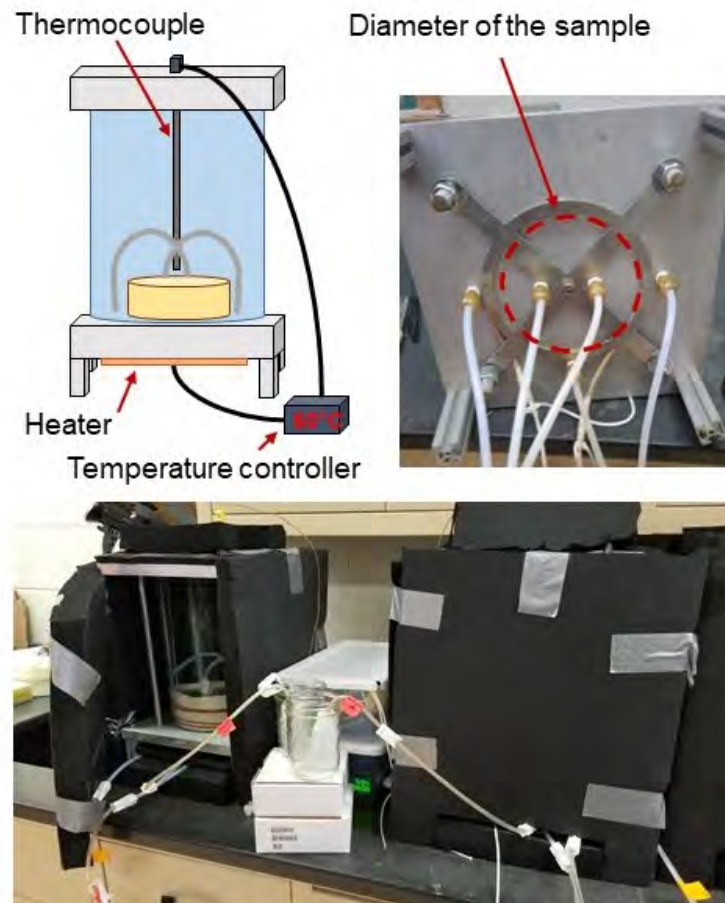


**Figure 1. Elevated temperature permeameters used for measuring hydraulic conductivity at 60 °C.**

BPC-GCL samples were batch aged in the permeant solutions for periods of 15, 30, 60 and 120 days to assess the effects of temperature while minimizing the concurrent effects of polymer elution that occur during permeation. Batch aging was conducted in hydration cells (Figure 2) submerged in glass-coated steel pots. The top and bottom plates of the hydration cells were perforated with 3-mm-diameter holes that allow solution to contact the sample. The permeant solution was refreshed every 15 d.

BPC-GCL samples in the hydration cells had a diameter of 230 mm and the plates could be set up to 18 mm apart. Spacing between the plates was set to 12 mm to constrain swelling of the BPC-GCL. A 5- $\mu$ m polypropylene filter and a nonwoven geotextile were placed between the plates and the BPC-GCL to promote even hydration (geotextile) and minimize polymer elution (filter).

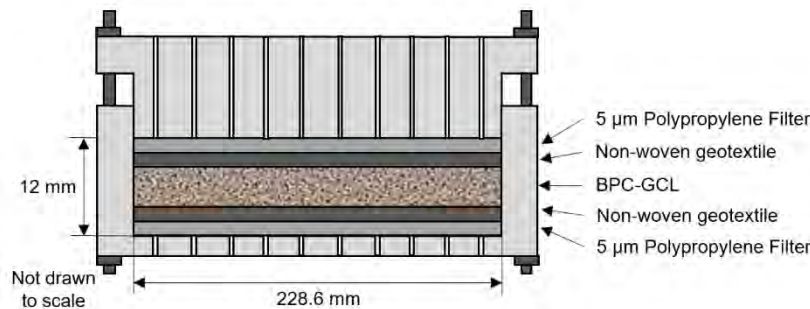


**Figure 2. Hydration cell used for batch aging of GCLs.**

Polymers P1 and P2 hydrated with the permeant solutions were batch aged at 60 °C in air-tight glass containers with minimal headspace for periods of 15, 30, 60, 90, 120 and 180 days. A unique sample was used for each condition so that the containers remained sealed until termination of the batch aging period. The gels were hydrated at a moisture content of 500% to represent the in-situ gel moisture content in the BPC-GCLs. Although the in-situ moisture content of the gel in the BPC-GCLs is not known, the gels hydrated at 500% moisture content appeared visually and tactilely similar to gels in the pore space of hydrated BPC-GCL samples.

Flow stress of the polymer gels was determined by conducting shear-strain-amplitude sweeps with controlled-shear deformation using a parallel plate rheometer (Anton Paar MCR 302, Austria) following the method in Gustitus and Benson (2020). Amplitude sweeps were completed over a range of 1-10,000% shear strain using a 25-mm-diameter sand-blasted parallel plate. Storage modulus and loss modulus were measured, and flow stress was computed as the stress when the storage modulus became less than the loss modulus. Tests were carried out at 20°C for all batch aged gels, and at 20, 40, and 60°C for unaged gels. Duplicate measurements were averaged to determine flow stress.

Swell index was measured in general accordance with ASTM D5890, except the BPC was ground to 100% passing the US No. 40 mesh sieve and 65% passing the US No. 60 mesh sieve. A coarser grind was used to reduce the effect of grinding on the polymer. Scalia et al. (2019) demonstrate that swell indices of bentonite ground to pass a No. 40 sieve are similar to those for bentonite ground to pass a No. 200 sieve. Duplicate measurements were averaged to determine the swell index.

Two sections (25 mm x 25 mm) of each BPC-GCL were sampled to assess polymer loading following the method in Gustitus et al. (2020). Samples were removed post-permeation for continuously permeated samples, and post-batch aging for batch aged samples, which are still being permeated. Polymer loading decreased over the course of 180 days for both batch aged BPC-GCLs as a result of elution into the batch aging solution.

## RESULTS

### *HYDRAULIC CONDUCTIVITY*

A summary of the hydraulic conductivities is in Table 2, including the duration of the test.

**Table 2. Hydraulic conductivities of GCLs for different test conditions.**

BPC-GCL	Solution	Condition	Hydraulic Conductivity (m/s)	Duration of Permeation (days)	
BPC-GCL-P1	Alkaline	No batch aging, 20°C permeation temperature	6.2 x10 <sup>-12</sup>	579	
		No batch aging, 60°C permeation temperature	4.3 x10 <sup>-12</sup>	180	
		Batch aged at 60 °C, 20° C permeation temperature	15 days	3.5 x10 <sup>-12</sup>	501
			30 days	1.0 x10 <sup>-11</sup>	414
			60 days	1.6 x10 <sup>-11</sup>	341
			120 days	1.2 x10 <sup>-11</sup>	310
			180 days	2.0 x10 <sup>-11</sup>	101
BPC-GCL-P2	Acidic	No batch aging, 20°C permeation temperature	1.1 x10 <sup>-10</sup>	299	
		No batch aging, 60°C permeation temperature	7.5 x10 <sup>-12</sup>	432	
		Batch aged at 60 °C, 20° C permeation temperature	15 days	1.6 x10 <sup>-11</sup>	624
			30 days	4.4 x10 <sup>-11</sup>	395
			60 days	2.9 x10 <sup>-11</sup>	342
			120 days	7.5 x10 <sup>-12</sup>	298
			180 days	2.9 x10 <sup>-7</sup>	< 1

BPC-GCL-P1 permeated at 20 °C (no batch aging) had a hydraulic conductivity of  $6.2 \times 10^{-12}$  m/s, and was relatively constant over the duration of the test (579 days). BPC-GCL-P1 permeated at 60 °C had a hydraulic conductivity of  $4.3 \times 10^{-12}$  m/s. The hydraulic conductivity of this GCL varied between  $2.1 \times 10^{-13}$  m/s and  $1.4 \times 10^{-11}$  m/s over the test duration (180 days) with no systematic trend. Hydraulic conductivities of the GCLs batch aged for 15 to 180 days range from  $3.5 \times 10^{-12}$  m/s (batch aged for 15 days, permeated for 501 days) to  $2.0 \times 10^{-11}$  m/s (batch aged for 180 days, permeated for 101 days).

BPC-GCL-P2 permeated at 20 °C (no batch aging) had a hydraulic conductivity of  $1.1 \times 10^{-10}$  m/s. The hydraulic conductivity of this sample initially was  $9.4 \times 10^{-10}$  m/s, and dipped to as low as was  $2.4 \times 10^{-12}$  m/s before increasing later in the test. BPC-GCL-P2 permeated at 60 °C had a hydraulic conductivity of  $7.5 \times 10^{-12}$  m/s, and remained relatively constant over the test duration of the test (432 days). Hydraulic conductivities of the GCLs batch aged for 15 to 120 days ranged from  $7.5 \times 10^{-12}$  m/s (batch aged for 120 days, permeated for 298 days) to  $4.4 \times 10^{-11}$  m/s (batch aged 30 days, permeated 395 days). The hydraulic conductivity of the GCL batch aged for 180 days was  $2.9 \times 10^{-7}$  m/s, which is the highest of any BPCs that were tested by three orders of magnitude.

### FLOW STRESS

Flow stress of the gels at temperatures ranging from 20 to 60 °C with no prior exposure to elevated temperature is shown in Figure 3. Flow stress of the P1-gel decreases from 1405 Pa at 20 °C to 1144 Pa at 40 °C, then increases to 1327 Pa at 60 °C. The flow stress of the P2-gel is consistently



lower than that of the P1-gel, and decreases from 1328 Pa at 20 °C to 824 Pa at 40 °C, and is relatively constant thereafter (793 Pa at 60°C).

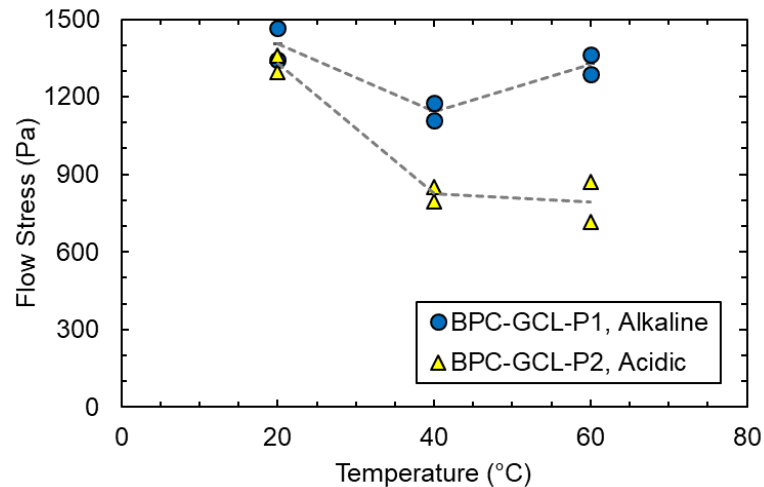


**Figure 3. Flow stress of polymer gels as a function of temperature.**

Flow stress of batch aged P1 and P2 gels as a function of exposure time is shown in Figure 4. Flow stress of the P1 gel was relatively consistent through 60 days, peaked at 90 days, then systematically decreased until it approached a liquid state (flow stress = 0) at 180 days. In the initial condition, the P1 gel was comprised of individual hydrated granules approximately 1 mm in diameter (Figure 5A). This condition was maintained through 60 days of aging (Figure 5B). After 90 days of elevated temperature, the granules adhered strongly to each other (Figure 5C). After 180 days, the gel was a uniform viscoelastic gel with a consistency of raw honey (Figure 5D).

In contrast to the P1 gel, flow stress of the P2 gel remained relatively constant over the 180-day period. The P2 gel was comprised of individual hydrated granules with a diameter of approximately 1 mm throughout the 180-day period of elevated temperature (Figure 6). However, the color of the P2 gel changed slightly from clear to a light brown tint as the gel aged.

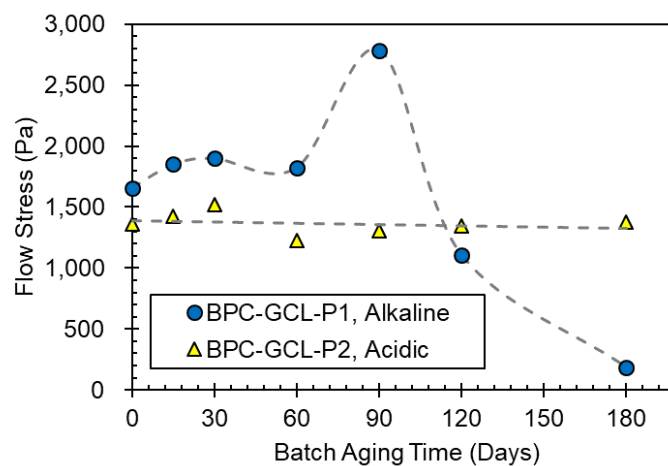


**Figure 4. Flow stress of gels P1 and P2 batch-aged at 60 °C as a function of time, when tested at 20 °C.**

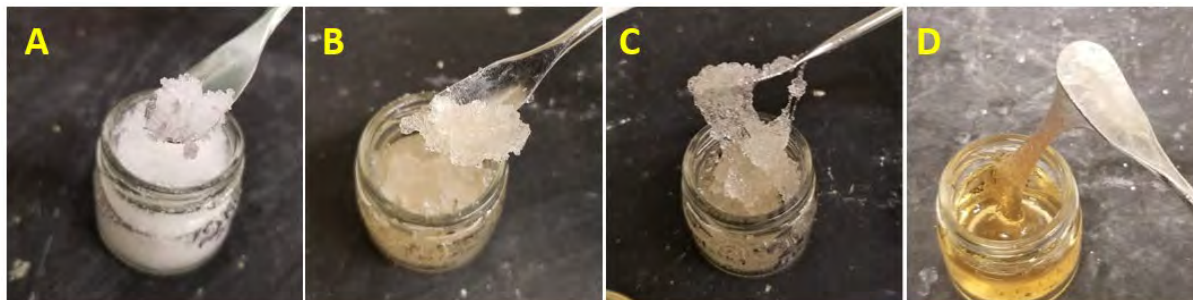


**Figure 5. Hydrated P1 polymer gels: (A) unaged and batch aged at 60 °C for (B) 60 days, (C) 90 days, and (D) 180 days.**

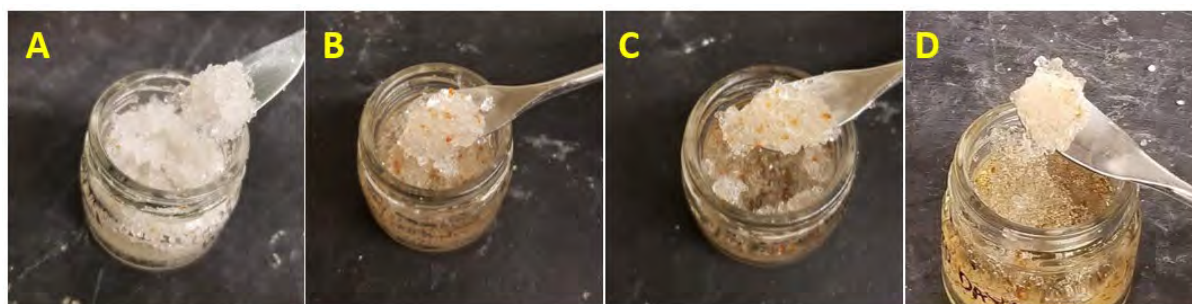


**Figure 6. Hydrated P2 polymer gels: (A) unaged and batch aged at 60 °C for (B) 60 days, (C) 90 days, (D) 180 days.**

#### *SWELL INDEX*

Swell index of the base bentonite and the BPCs in the permeant solutions is shown in Figure 7. Swell index of the base bentonite and both BPCs increases slightly with increasing temperature, with greater sensitivity to temperature in the alkaline solution than the acidic solution. The greater sensitivity to temperature in the alkaline solution may be attributed to the decreasing solubility of  $\text{Ca}(\text{OH})_2$  with increasing temperature.

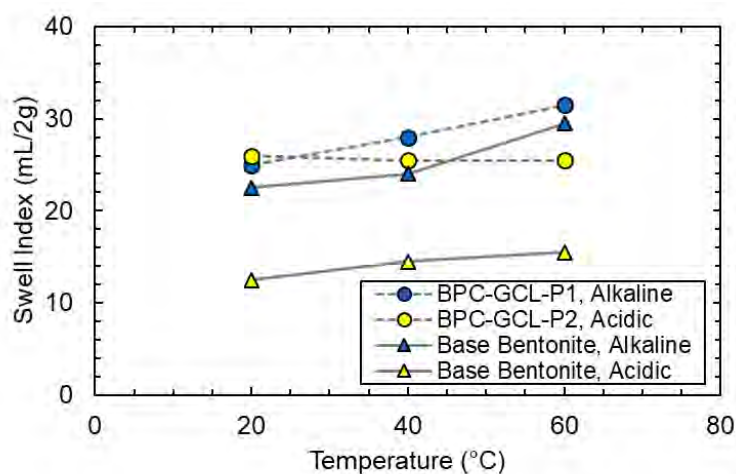


**Figure 7. Swell index of base bentonite, BPC-P1, and BPC-P2 as a function of temperature.**

Polymer loading of each BPC-GCL is shown in Figure 8. Two sections (25 mm x 25 mm) of each BPC-GCL were sampled to assess polymer loading. Samples were removed post-permeation for continuously permeated samples, and post-batch aging for batch aged samples. Polymer loading decreased over the 180-day period for both batch aged BPC-GCLs, most likely due to elution. Elution of polymers from BPC-GCLs has been observed in other studies, and has been attributed to physical processes (e.g., seepage forces) and/or chemical processes (e.g., contraction of polymer chains in response to high ionic strength solutions) (Tian et al., 2016 and 2017).

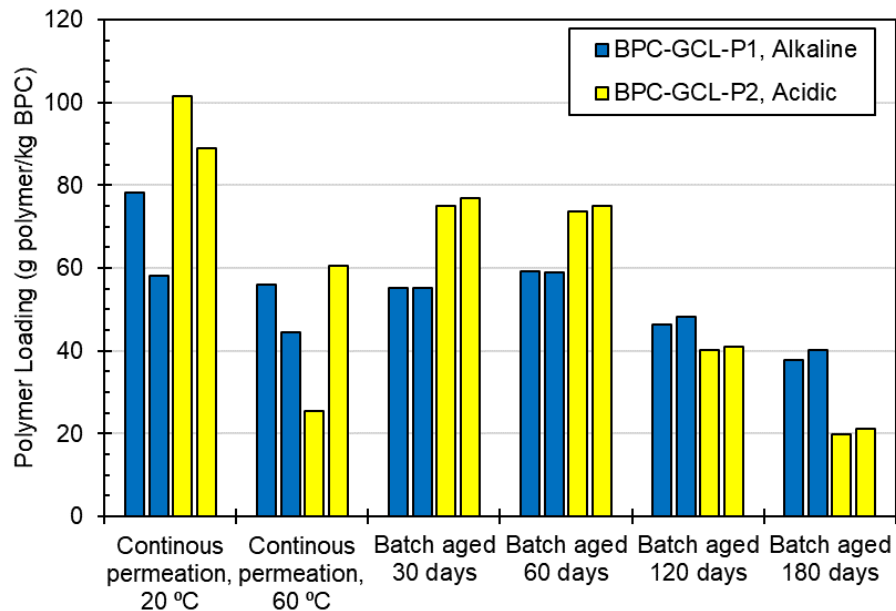


**Figure 8. Polymer loading remaining in continuously permeated BPC-GCLs (at test termination) and batch aged BPC-GCLs (after batch aging and prior to permeation).**

## DISCUSSION

The hydraulic conductivities of all BPC-GCL-P1 samples permeated with the alkaline solution were within one order of magnitude of each other, regardless of continuous permeation temperature (20 or 60 °C) or batch aging time (0 to 180 days; Table 2). This is consistent with the negligible difference in the flow stress of the P1 hydrated polymer gel at 20 and 60 °C. That is, the tendency of the P1-gel to elute was similar at 20 and 60 °C. The swell index of the BPC is also 29% higher at 60 °C than at 20 °C, which should promote lower hydraulic conductivity. Similar conditions should be expected for temperatures between 20 and 40 °C.

The hydraulic conductivity of BPC-GCL-P2 permeated with acidic solution at 20 °C (no external aging) is higher than the hydraulic conductivity of BPC-GCL-P2 continuously permeated at 60 °C or batch aged at 60 °C for up to 120 days. Additionally, hydraulic conductivity of BPC-GCL-P2 at 20 °C increased slowly, whereas the hydraulic conductivity of BPC-GCL-P2 permeated at 60 °C remained relatively constant. The observed decrease in flow stress from 20 to 60 °C was expected to result in increased in polymer elution, and therefore an increase in hydraulic conductivity; however, the opposite occurred for BPC-GCL-P2, which retained higher polymer loading in the sample permeated at 20 °C. A concurrent modest increase in swell index for the elevated temperature sample is unlikely to account for the lower hydraulic conductivity at 60 °C.

Therefore, additional change(s) to the bentonite or polymer may be occurring that are not accounted for in these experiments.

There are no distinct relationships between hydraulic conductivity of batch aged samples and batch aging time (Figure 9), flow stress (Figure 10), or polymer loading (Figure 11). The lack of correspondence is consistent with the minimal differences in hydraulic conductivity between most of the test specimens. The exception is BPC-GCL-P2 aged in acidic solution for 180 days, which had the highest hydraulic conductivity by approximately four orders of magnitude ( $2.9 \times 10^{-7}$  m/s). This specimen had the lowest polymer loading (2.0 g polymer/kg BPC) of any of the specimens tested, and permeation with rhodamine dye revealed that flow was occurring through one 20-mm-wide section of the hydrated BPC. The low polymer loading and the presence of a dye-stained flow path indicate that polymer elution occurred during batch aging, and the pore space between the bentonite granules was no longer clogged by polymer, at least in the vicinity of the flow path.

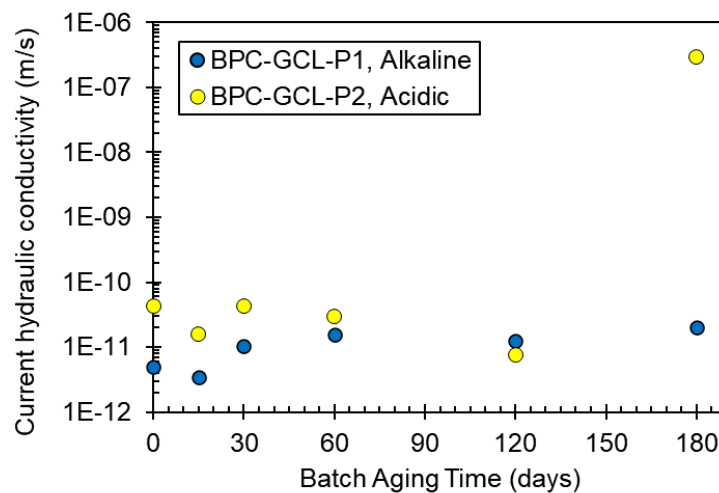


**Figure 9. Hydraulic conductivity of batch-aged BPC-GCLs vs. batch aging time at 60 °C.**

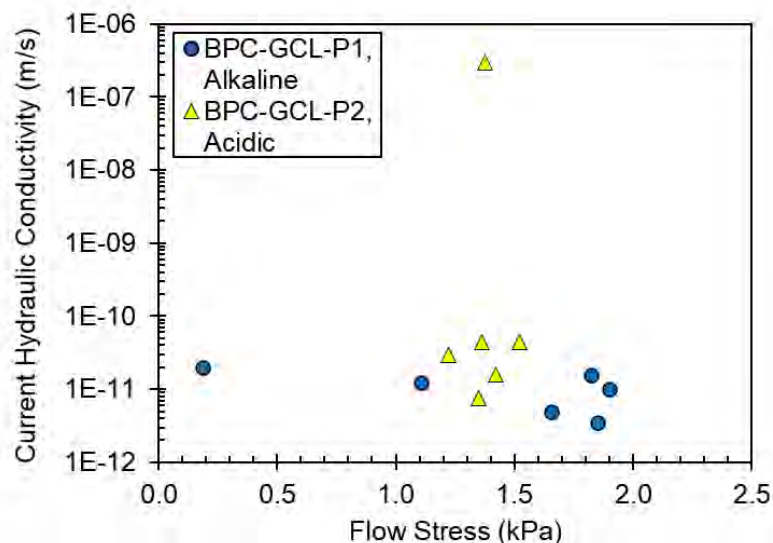




**Figure 10. Hydraulic conductivity of batch-aged BPC-GCLs versus flow stress of the corresponding polymer gel at 20 °C.**

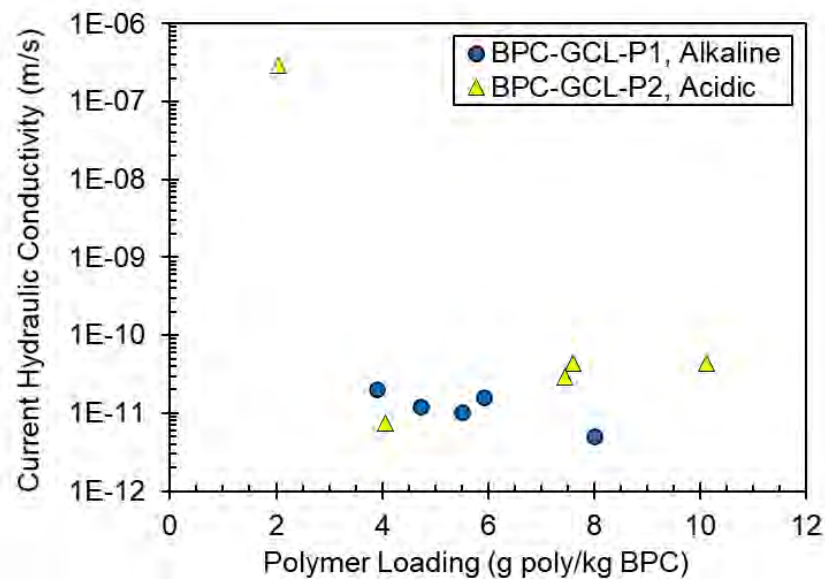


**Figure 11. Hydraulic conductivity of batch aged BPC-GCLs versus polymer loading of the BPC-GCL after batch aging at 60 °C.**

## CONCLUSIONS

The effect of elevated temperature on the hydraulic conductivity of two BPC-GCLs containing difference proprietary polymers was assessed by continuous permeation at 20 and 60 °C and batch aging at 60 °C. The flow stress of the polymer gels and the swell index of the of base bentonite and BPCs was also measured as a function of temperature.

All but one of the BPC-GCLs exposed to elevated temperatures during permeation or batch aging maintained hydraulic conductivity below  $1 \times 10^{-10}$  m/s. The exception was a BPC-GCL exposed to batch aging in the acidic solution for 180 d. For this specimen, sufficient polymer was eluted to form a preferential flow path. These findings suggest that these BPC GCLs are likely to continue to maintain low hydraulic conductivity even at high temperatures. However, if field conditions promote polymer elution, the polymer loading may diminish sufficiently for the hydraulic conductivity to increase appreciably.

The hydraulic conductivity of the BPC-GCLs permeated at 60 °C was comparable to or lower than the hydraulic conductivity of those permeated at 20 °C for the GCL-solution pairs tested. BPC-GCLs batch aged for periods of up to 120 days all had comparable hydraulic conductivity, regardless of changes in polymer loading or flow stress of the polymer gels. Only BPC-GCL-P2 aged for 180 days in acidic solution had a significantly higher hydraulic conductivity, which is attributed to greater polymer elution during batch aging compared to the other batch aged samples. The effects of elevated temperatures may be dependent on the polymer and solution chemistry, and therefore testing of site-specific leachates with site-specific BPC-GCLs should be performed to understand the potential impacts of elevated temperatures.

## ACKNOWLEDGMENTS

This study was supported by CETCO, the US Department of Energy's Consortium for Risk Evaluation with Stakeholder Participation (CRESP) III through Cooperative Agreement No. DE-FC01-06EW07053, the Environmental Research and Education Foundation through a fellowship to the first author, and the Jefferson Scholars Foundation at University of Virginia. Materials for the study were provided by CETCO.

## REFERENCES

- Ashmawy, A K, El-Hajji, D, Sotelo, N, and Muhammad, N (2002). Hydraulic performance of untreated and polymer-treated bentonite in inorganic landfill leachates. *Clay. Clay Miner.*, **50**(5), 546–52.
- ASTM D5890-19. Standard test method for swell index of clay mineral component of geosynthetic clay liners. West Conshohocken, PA, ASTM International, 2019.
- ASTM D6766-20. Standard test method for evaluation of hydraulic properties of geosynthetic clay liners permeated with potentially incompatible aqueous solutions. West Conshohocken, PA, ASTM International, 2020.
- Athanassopoulos, C, Benson, C H, Donovan, M, and Chen, J (2015). Hydraulic conductivity of a polymer - modified GCL permeated with high - pH solutions. *Geosynthetics 2015*, Industrial Fabrics Association International, St. Paul, MN, 181–6.
- Chen, J, Salihoglu, H, Benson, C H, and Likos, W J (2019). Hydraulic conductivity of bentonite-polymer geosynthetic clay liners to coal combustion product leachates. *J. Geotech. Geoenviron.*, **145**(9), 04019038.
- EN 14030:2001 (2001). Geotextiles and geotextile-related products – screening test method for determining the resistance to acid and alkaline liquids. Brussels, Belgium; European Committee for Standardization, 44(5), 1448-1466.
- Gustitus, S A and Benson, C H (2020). Assessing polymer elution and hydraulic conductivity of bentonite-polymer composite geosynthetic clay liners permeated with aggressive solutions. *Proc. of 4<sup>th</sup> Pan American Conference on Geosynthetics*, Rio De Janeiro.
- Gustitus, S. A., Nguyen, D., Chen, J., and Benson, C. H. (2020). Quantifying Polymer Loading in Bentonite-Polymer Composites Using Loss on Ignition and Total Carbon Analyses. *Geotechnical Testing Journal*, In Press.
- Ishimori, H, and Katsumi, T (2012). Temperature effects on the swelling capacity and barrier performance of geosynthetic clay liners permeated with sodium chloride solutions. *Geotext. Geomembrane*, **33**, 25–33.
- Klein, R, Baumann, T, Kahapka, E, and Niessner, R (2001). Temperature development in a modern municipal solid waste incineration (MSWI) bottom ash landfill with regard to sustainable waste management. *J. Hazard. Mater.*, **83**(3), 265–80.
- Koerner, G R, and Koerner, R M (2006). Long-term temperature monitoring of geomembranes at dry and wet landfills. *Geotext. Geomembrane*, **24**(1), 72–77.
- Mitchell, J K, and Soga, K (2005). *Fundamentals of Soil Behavior* (3rd Edition). John Wiley & Sons.
- Ozhan, H O (2018). Hydraulic capability of polymer-treated GCLs in saline solutions at elevated temperatures. *Appl. Clay Sci.*, **161**, 364–73.
- Scalia, J, Benson, C H, Bohnhoff, G L, Edil, T B, and Shackelford, C D (2014). Long-term hydraulic conductivity of a bentonite-polymer composite permeated with aggressive inorganic solutions. *J. Geotech. Geoenviron.*, **140**(3), 04013025.

- Scalia, J, Benson, C H, and Finnegan, M (2019). Alternate procedures for swell index testing of granular bentonite from GCLs. *Geotech. Test. J.*, **42**(5), 1169-84.
- Tian, K, Benson, C H, and Likos, W J (2016). Hydraulic conductivity of geosynthetic clay liners to low-level radioactive waste leachate. *J. Geotech. Geoenviron.*, **142**(8), 04013037.
- Tian, K., Benson, C. H., and Likos, W. J. (2017). Effect of an anion ratio on the hydraulic conductivity of a bentonite-polymer geosynthetic clay liner. *Geotechnical Frontiers 2017*, 180–189.
- Tian, K, and Benson, C H (2018). Containing bauxite liquor using bentonite-polymer composite geosynthetic clay liners. *Proc. 8th Intl. Conference on Environmental Geotechnics*, Springer Nature, Singapore, L. Zhan et al. (Eds.), 672–8.
- Tian, K, Likos, W, and Benson, C H (2019). Polymer elution and hydraulic conductivity of bentonite–polymer composite geosynthetic clay liners. *J. Geotech. Geoenviron.*, **145**(10), 04019071.
- Yeşiller, N, Hanson, J L, and Yee, E H (2015). Waste heat generation: a comprehensive review. *Waste Manage.*, **42**, 166–79.
- Young, R J, and Lovell, P A (2011). *Introduction to Polymers* (3<sup>rd</sup> Edition). CRC Press.

## **Practical Aspects of Exposed Geomembrane Cap (EGC) Design and Construction**

**James Walker, P.E.<sup>1</sup>**

<sup>1</sup>Tetra Tech, 39395 W. Twelve Mile Rd., Farmington Hills, MI 48331; 810-610-0778;  
[jim.walker@tetrattech.com](mailto:jim.walker@tetrattech.com)

### **ABSTRACT**

The design and construction of exposed geomembrane covers (EGCs) involves multiple interrelated components to achieve a successful project. These include selection of geomembrane, subgrade preparation, gas collection, stormwater modifications for increased surface runoff, anchoring of the EGC to prevent wind uplift. Post-construction operation and maintenance activity considerations are also important to consider. Design manuals are not readily available specific for EGCs. This paper provides background and experience for such installations from a number of completed EGC projects.

### **INTRODUCTION**

EGCs are often used to help manage a variety of concerns at landfills including:

1. Odor control
2. Reduction of leachate generation and management
3. Improvement in gas collection
4. Control of erosion and improved stormwater runoff quality
5. Enhancement for slope stability
6. Serve as intermediate cover or interim final cover to allow for future airspace recovery





## **Figure 1 – Typical EGC Installation**

The successful installation and performance of an EGC requires a number of upfront planning considerations involving current and future planned waste operations. Budget concerns, future disposal plans, gas collection system activities, access roads, future phased development, stormwater management and other considerations may limit the area where an EGC is warranted. Once an area is selected for an EGC, project management activities need to establish the budget, preparation work (subgrade, slope grading, gas system updates, stormwater management), how the project will be contracted, materials procured, over what period the cost will be amortized, project schedule, regulatory notifications and approvals and CQA requirements established.

### **EGC MATERIALS**

A variety of materials and material thicknesses have been installed for temporary EGCs at landfills. The material selection is based on the intended purpose, budget, availability, O&M and intended life. Specific elements to consider are tensile strength for wind uplift and downdrag, anticipated settlement, VOC permeability, abrasion resistance, vehicle loading, ease of installation and compatibility with other materials. EGC materials often include LLDPE, HDPE, EVOC and PVC geosynthetic materials ranging in thickness from 12mils to 60mils in both the standard black and green colors. Design considerations for selection of the EGC include the following:

- Design life
- Tensile & puncture strengths
- Elongation properties
- Extent of wrinkles development
- Abrasion resistance
- Availability
- Aesthetics
- Cost
- Repair effort

### **SERVICE LIFE**

While the service life of a typical exposed geomembrane has been demonstrated as being robust, other less predictable conditions mostly affect the service life of an EGC. Experience has shown that service life is dictated not by degradation but by stress from settlement, expansion / contraction, stone and gas piping and O&M traffic abrasion, wind, ice and seaming construction. One major influence is the extent of extrusion seams due to the potential detrimental effects of high heat differential between the seamed and unseamed material. Reinforced geomembranes have shown to perform better than unreinforced long term due to the reduced expansion and contraction stress on the material.

### **SUBGRADE PREPARATION FOR INSTALLATION**

Subgrade considerations are important to consider in order to assure a smooth installation. Is waste regrading needed initially - either to achieve preferred slopes or for drainage? Is the current surface adequate as a foundation for the geomembrane or does it need to be enhanced to

remove or cover vegetation, stones or protruding trash, fill in rills such as those shown in Figure 2, or regrade to eliminate flat area? Existing benches and diversion berms need to be evaluated as part of the stormwater design and the subgrade modified accordingly. Areas prone to potential seeps should be mitigated to prevent pooling under the geomembrane. If additional soil is needed for subgrade preparation, project cost and duration will increase therefore this should be assessed early on in the design of an EGC to meet project goals.



**Figure 2 – Erosion Rills In Need Of Grading For An EGC Subgrade Preparation**

The EGC will need to be integrated with the landfill gas collection and control system (GCCS). GCCS components have been placed both below and above EGCs and there are pros and cons to each. This may also include access to and protection for gas condensate and leachate forcemain piping. Piping above grade provides easy access for O & M activities, especially if significant settlement is expected but is subject to breakage or reverse grade from downdrag and harmful impacts if leaks occur. In addition, odor impacts from leaks are easier to locate and repair. Piping below grade is not readily accessible for repairs but not susceptible to environmental impacts if leaks do occur.

In addition to the landfill's GCCS, undercap gas collection should be considered to control uplift of the EGC. This is often done by installation of flat drains as shown in Figure 3.



**Figure 3 – Installation of EGC Undercap Flat Drains for Gas Control**

## **ANCHORAGE**

Anchorage of the EGC is necessary to prevent uplift from wind and gas pressure as well as movement up and down the slope. Anchorage alternatives include, undercap and edge of cap soil anchor trenches as shown in Figures 4 and 5, overlying reinforced geotextile windscreen shown in Figure 6, overlying roads (with protection against puncture) shown in Figure 7 and platypus anchors shown in Figure 8. There are pros and cons to each type of anchorage. Undercap soil anchor trenches involve staged construction of earthworks and geosynthetics which requires close coordination. In addition, anchor trenches may interfere with undercap drainage for seepage control, buried gas piping or expose odorous waste during construction. Above cap roads on the other hand may interfere with stormwater management and landfill gas collection piping – but may be helpful for O&M activities. Above cap reinforced geotextile windscreens are popular due to the ease and quickness of construction and aesthetic appeal.





**Figure 4 – EGC Anchor Trench Construction**



**Figure 5 – Placement of an EGC in Prepared Anchor Trenches**





**Figure 6 – Installation of a Reinforced Geotextile Windscreen for EGC Anchorage**



**Figure 7 – Roads Overlying an EGC Used for Anchorage and O & M Access Activities**



**Figure 8 – Platypus Soil Anchors Being Installed to Anchor an EGC**

It is often beneficial to weld the EGC to the baseliner for control of odor and leachate. This work can be expensive, time consuming and challenging if significant soil cover exists as shown in Figure 9 and or access is limited.



**Figure 9 – Welding of EGC to Baseliner at Perimeter of a Landfill**



## **STORMWATER MANAGEMENT**

Stormwater management must be considered for EGCs and often requires significant upgrading. The expected runoff may increase by three or four times for peak flow and total runoff as compared to a vegetated interim cover. This requires evaluation of diversion berms, channels, downslope drainage components, culverts and stormwater management ponds to determine what components are adequate and what need to be upgraded. As part of the evaluation and upgrade, the decision of whether or not the stormwater runoff will be managed by interim diversion berms, benches or channels on slopes, or sheet flow is necessary. Benches are beneficial for O&M activities, however there is a greater potential for unsupported bridging of the geomembrane which can be a significant safety hazard for personnel walking on the slope for O&M tasks. One area that requires close attention for erosion protection is at the bottom toe of slope where the high velocity sheet flow dissipates to channel flow. To mitigate the potential for erosion at the toe, it is often necessary to install riprap, a geosynthetic erosion control mat or in some cases compost has been used as a successful stabilizer.

Sometimes for active disposal operations, it is necessary to maintain active access roads across a slope being lined with an EGC. This requires design, construction access and scheduling of the EGC to maintain active operations with minimal interruption.

## **INTERGRATED DESIGN**

The design of an EGC must be an integrated design incorporating the above elements to assure a successful project. Following determination of the service life, selection of the geomembrane and anchorage and establishment of subgrade preparation requirements, an EGC site plan such as the plan shown in Figure 10 should be prepared. The plan in Figure 10 shows the existing and proposed grades, perimeter and internal anchor trench locations, undercap gas and seepage collection and stormwater controls. The undercap gas and seepage controls have been designed with considering the locations of the internal anchor trenches. The perimeter edge of the EGC has been designed with a sloping diversion berm / anchor trench to manage concentrated stormwater and direct it to downslope pipes.

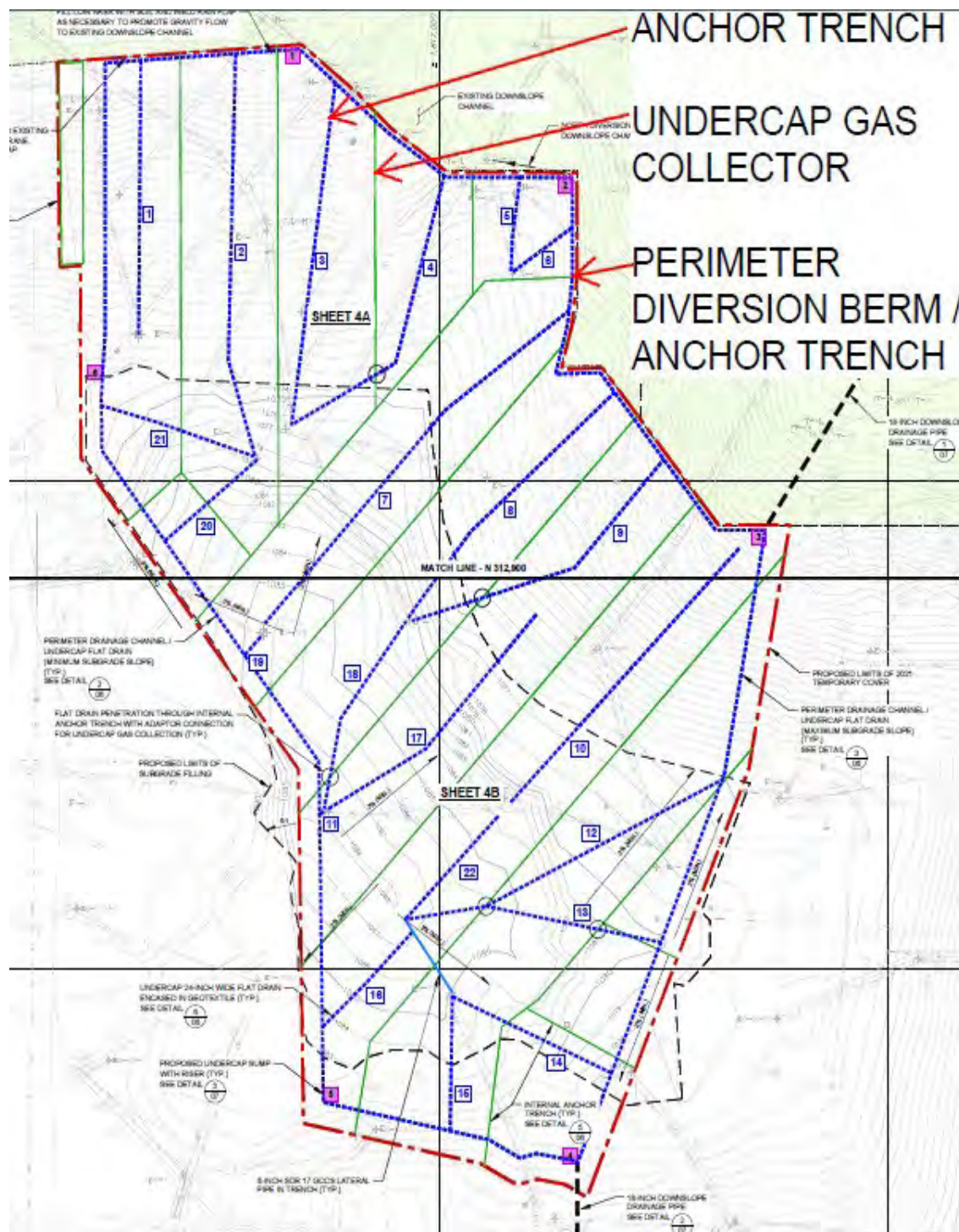


**Figure 10 – Example of an Integrated EGC Site Plan Design**



## EGC COSTS

Based on experience with EGC projects in the last three years, costs for design and installation typically range from \$60,000 per acre to \$80,000 per acre without major stormwater, GCCS or subgrade fill work, but can range up to \$200,000 per acre for a double-layered turf/geomembrane cap. Per acre costs for the EGC project shown in Figure 10 were approximately \$ 78,000 per acre and a breakdown of the cost is shown in Figure 11.

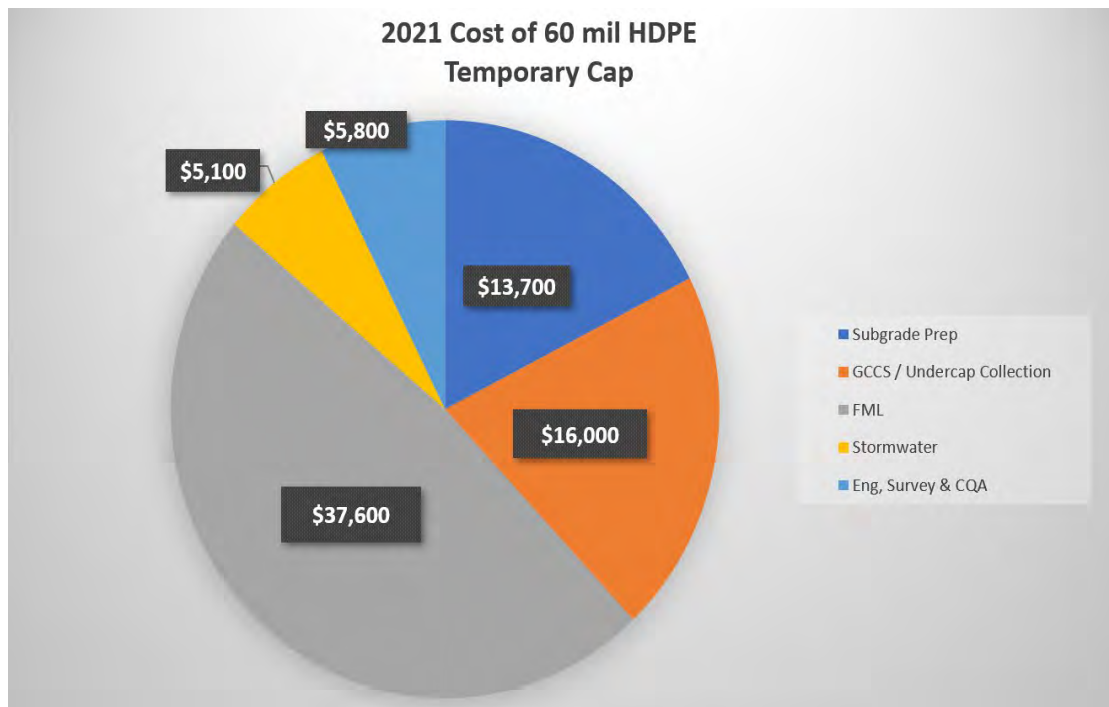


**Figure 11 – Per Acre Cost Breakdown for an EGC**

## O & M CONSIDERATIONS

Once an EGC is installed, planning and budget should be considered for O&M activities which may include the following:

1. Access for GCCS O&M and replacement wells
2. Repair of holes and tears from stones and excessive stress from settlement, gas uplift, gas wells and piping, O&M activities and animal damage
3. Repair of above-cap piping leakage
4. Regrading due to nonuniform settlement and ponding
5. Repair of erosion from increased stormwater runoff

## SUMMARY

EGCs have proven to be tremendous benefit for numerous facilities faced with a variety of operational challenges. Optimal benefits from an EGC requires careful planning, design and installation of multiple interrelated components to achieve the intended goals for the cost and effort extended.

## Remediation of a former quarry and permanent containment of buried toxic materials

Stephan Fourmont<sup>1</sup>, Louise Chaput, P.E.<sup>2</sup>, Kevin Randall, M.Sc.<sup>3</sup>

<sup>1</sup>Afitex-Textel, Quebec Canada; [sfourmont@afitextexel.com](mailto:sfourmont@afitextexel.com)

<sup>2</sup>WSP, Quebec Canada; [louise.chaput@wsp.com](mailto:louise.chaput@wsp.com)

<sup>3</sup>Sanexen, Quebec Canada; [krandall@sanexen.com](mailto:krandall@sanexen.com)

### ABSTRACT

The site of the former Landreville quarry, owned by Les Carrières Rive-Sud Inc. (CRS), was used for stone extraction, and crushing operations until 1992 and was the scene of illegal dumping of toxic waste. A remediation plan for the quarry was approved by the Ministry of the Environment of Quebec in 2015, and work began in the spring of 2018. The remediation work consists of containing the toxic materials buried in a portion of the quarry and backfilling a part of the flooded area of the CRS site to secure the wall of the former dump. This required approximately 2.5 million cubic meters (3,300,000 yd<sup>3</sup>) of clean soil and coarse materials (concrete, brick, and rock) to be imported to the site. The final cover system includes a geomembrane, a drainage geocomposite for rainwater drainage and mechanical protection, and a drainage geocomposite for gas collection. The CRS site remediation plan also includes gas treatment and groundwater quality monitoring. This paper presents the various technical requirements for the site remediation and explains how the different geosynthetics selected and implemented were able to meet the project expectations.

### PROJECT BACKGROUND

The rehabilitation project of the former Landreville quarry is part of a process initiated in 2004 to definitively solve the problem that the current site represents for the health and safety of the public as well as for the environment. The project is located in Boucherville, QC, Canada (Figure 1).



**Figure 1. Project location (source: Plan de réhabilitation, Juillet 2012)**

The objectives of the project are as follows:

- Secure the site for the purpose of protecting public health and safety.
- Establish a mechanism to control emissions that degrade the environmental conditions of the surrounding area.
- Substantial reduction of meteoric water infiltration on the top of the old dump.
- Containment and capture of biogas to prevent its migration out of the former quarry.
- If required, the capture and treatment of groundwater contaminated by the former landfill.

The materials present at the decommissioned disposal site consist of a matrix of fill (clayey silt and clay) and residual materials (demolition materials, foundry residues and other debris). Lenses of decomposing putrescible material have been observed. The height of the material can reach 20 m (66 ft). The following mitigation measures are in place to meet the project objectives:

- Backfilling and reprofiling of the former landfill waste with a 16 m (52 ft) maximum thick layer of low contaminated material.
- Installation of a liner/drainage system over the landfill area to capture and discharge biogas produced under this new liner and to limit water infiltration from the surface.
- Installation of a biogas collection trench around the perimeter of the landfill.
- Installation of a groundwater pumping well in the area of the landfill and treatment of the pumped water before discharge (if required).
- Construction of a mound on top of the geosynthetic cover to a maximum height of 25 m (82 ft).

The mound to be built on top of the final cover is part of a large landscape project that will convert the site into a public municipal park. It will be built gradually for 7 years. It will occupy the entire area of the former quarry, including the dump area. Its maximum projected elevation is 54 m (177 ft) for a total volume of approximately 2,200,000 m<sup>3</sup> (2,877,000 yd<sup>3</sup>). The soil imported to the site contains low levels of contamination. The disposal of this soil allows the project to be financed as the generators of the imported soil pay to disposal fees to the regulated site. The installation of the geosynthetic cover at the early stages allowed the implementation of mitigation measures for the biogas generated by the site to be accelerated.

The surface area of the geosynthetic liner/drainage cover is 85,000 m<sup>2</sup> (915,000 sf). The mound involves loads of soil deposited on the geosynthetics that are much higher than most final geosynthetic covers. A typical facility has up to 1m (3ft) of soil. This increased height has impacted the design and the choice of the geosynthetics material used.

## **FINAL COVER REQUIREMENTS**

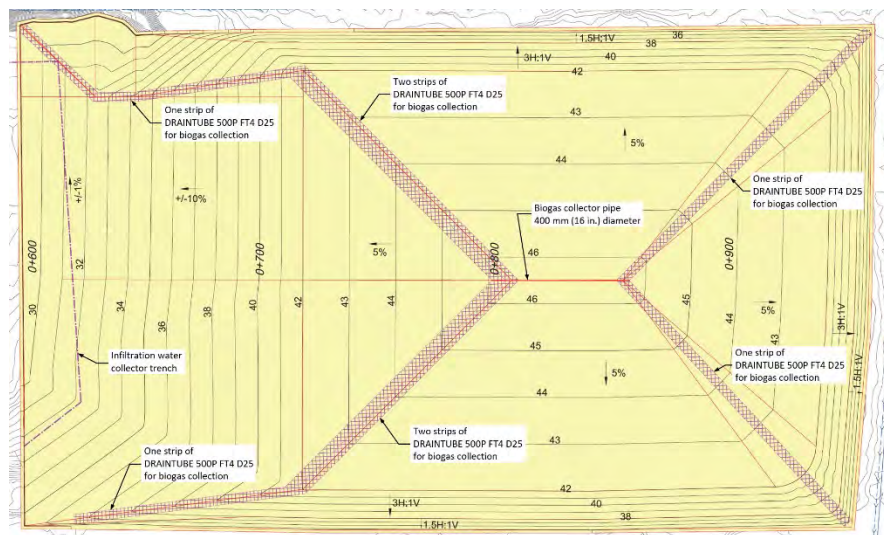
The final cover of the site was designed to limit the entry of surface water into the waste. This prevents additional water from leaching into the waste and allows for collection of biogas produced by the waste. These factors will prevent any risk to the health of the public since the site will be rehabilitated into a public municipal park, including a 45,000 m<sup>3</sup> (59,000 yd<sup>3</sup>) lake filled with underground and runoff water.



The design of the final cover of the site had to meet several technical constraints to ensure its long-term watertightness and to meet the expectation of a renowned municipal park. These include:

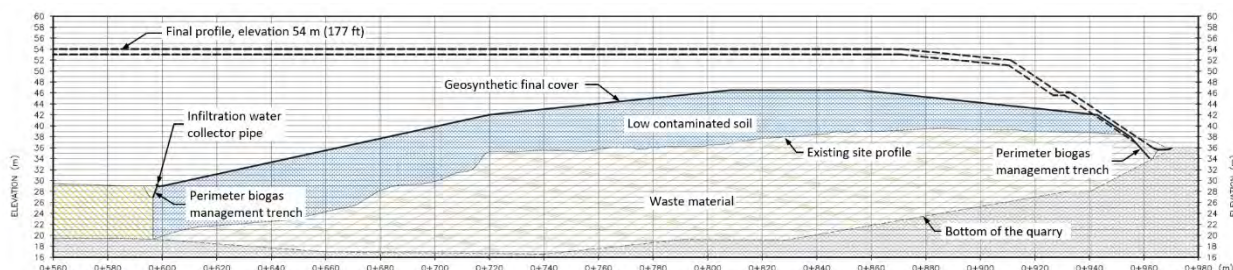
- Final soil covers sustainable for mature vegetation and recreational activity.
- A northern slope length up to 160 m (525 ft) facing the lake with 3 separated steps to enjoy the scenery (Montreal's skyline from south shore).
- Water quality in the lake sustainable for aquatic activity, excluding swimming.
- Strong measures to prevent growth of invasive species on the newly rehabilitated site.

Figure 2 shows a plan view of the cover prior to the installation of the liner/drainage system. The dome has slopes of 5 to 10% and the sides have slopes of 33 and 66%. The stability of the cover on the 66% slopes is not a long-term concern because this area has been designed as a 2 m (6-1/2 ft) deep perimeter drainage trench that will be completely filled.



**Figure 2. Plan view of the cover prior to the installation of the liner/drainage system (source: Demande de modification de l'approbation du plan de réhabilitation, 2020)**

Figure 3 shows a cross section of the southern part of the final cover. The final elevation of the site at the end of the project can be seen.



**Figure 3. Cross section of the final cover (source: Demande de modification de l'approbation du plan de réhabilitation, 2020)**

The typical cross-section designed for the final geosynthetic cover is shown in Figure 4 and is comprised from bottom to top with:

- A multi-linear drainage geocomposite for biogas collection.
- An LDPE waterproofing geomembrane that is 1.5 mm thick.
- A multi-linear drainage geocomposite for rainwater collection and protection of the geomembrane.

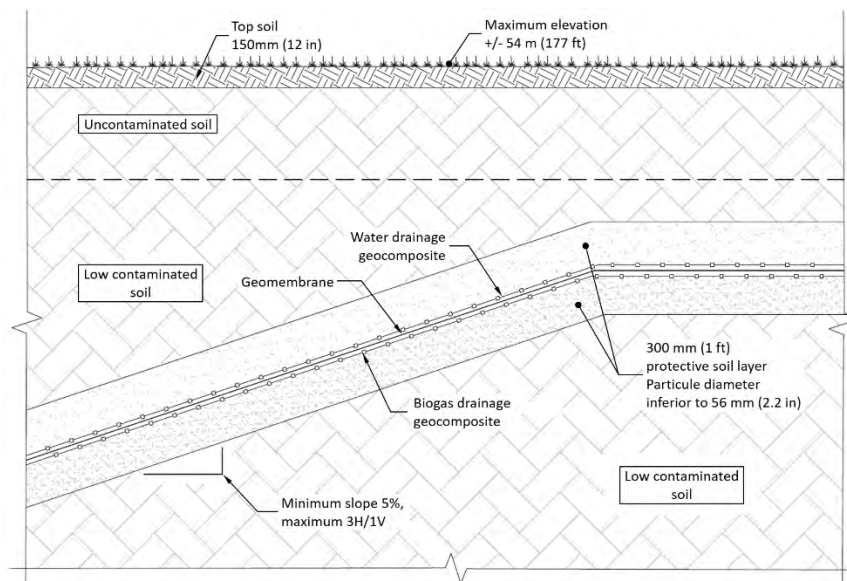


**Figure 4. Detail of the final cover composition (source: Demande de modification de l’approbation du plan de réhabilitation, 2020)**

## GAS COLLECTION

The biogas generation rate was estimated to be  $0.0086 \text{ m}^3/\text{hr}/\text{m}^2$  ( $4.70 \times 10^{-4} \text{ scfm}/\text{ft}^2$ ) using the model developed by the EPA. It was determined using a conservative approach, assuming that all of the stored material is putrescible, and that degradation of the waste began in 1979 (more than 10 years after placement). This low rate does not require an active biogas capture system.

The geocomposite for the gas collection is a multi-linear drainage geocomposite (as defined by ASTM D4439) Drintube type. It is composed of two needle-punched non-woven geotextile layers incorporating corrugated and perforated polypropylene mini-pipes of 25 mm (1 in) diameter. The mini-pipes are spaced 2 m (80 in) apart across the width of the product.

The product is connected at the end to a solid header pipe using mechanical connectors. This system allows each mini-pipe of the geocomposite to be connected directly to the main header, thus reducing pressure losses. The depression (negative pressure) in the geocomposite under the geomembrane and thus the collection of gas is optimized. The collection of the biogas is based on a passive system but has been designed and implemented to be connected to an active vacuum system in the event that the biogas migrates off-site after construction.

Figure 5 shows a typical cross section of the geocomposite/collector connection. This mechanical connection also limits the risk of movement of the geocomposite in relation to the collector, should settlement occur during the final refilling of the cover.

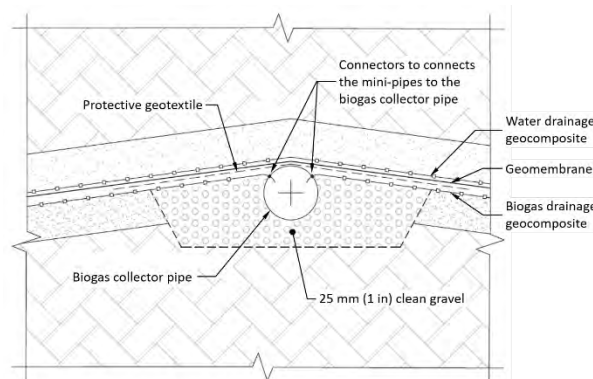


**Figure 5. Connection detail of the multi-linear drainage geocomposite to the header pipe (source: Demande de modification de l’approbation du plan de réhabilitation, 2020)**

The drainage geocomposite collects the biogas from the entire cover and drains it to the header pipe with a stable drainage capacity, even under high loads (after the construction of the mound on the geosynthetics cover). Indeed, whatever the hydraulic gradient, the geocomposite shows a stable transmissivity under loads up to 2,400 kPa (50,000 psf), when confined between a geomembrane and a sand layer.

In addition, the creep resistance of the geocomposite was also tested to ensure that, even under high load, the product will not exhibit a loss of drainage capacity over time. Figure 6 shows the transmissivity of the product measured for loads between 24 kPa (500 psf) and 2,400 kPa (50,000 psf) with several gradients, and presents the variation with time of the transmissivity of the geocomposite under 2,400 kPa (50,000 psf) for 1,000 hours.

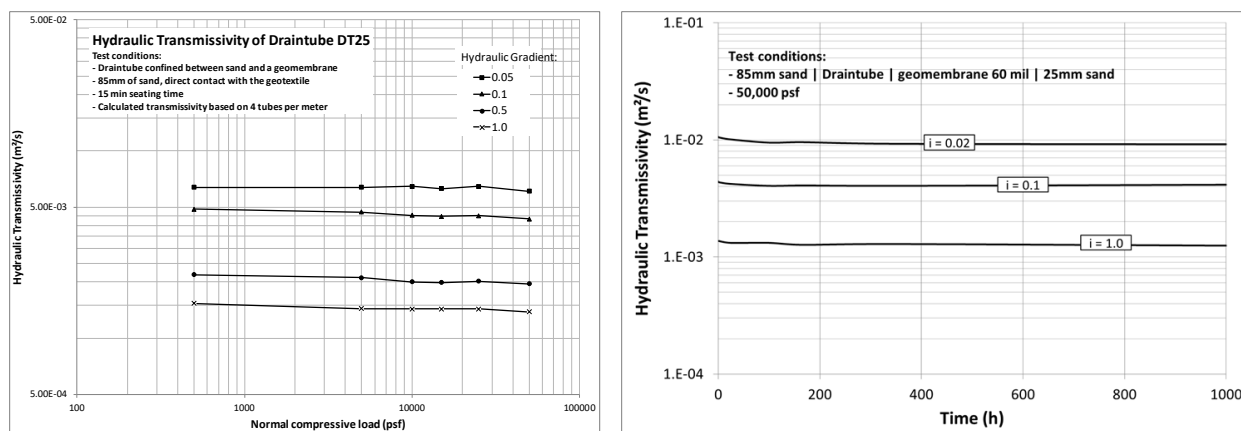


**Figure 6. Hydraulic transmissivity of the multi-linear drainage geocomposite for several loads, and over of the time**

The results presented above confirm that when confined, normal load does not have any significant effect on the transmissivity of the multi-linear geocomposite up to 2,400 kPa (50,000 psf). It also did not experience any change in transmissivity over the 1,000 hours under that load.

This resistance to creep in compression is specific to this multi-linear geocomposite. It is documented by Saunier et al. (2010) and in the ASTM D7931 Standard Guide for specifying drainage geocomposites.

## WATERPROOFING

The waterproofing geomembrane installed over the gas drainage geocomposite is a textured low-density polyethylene (LDPE) geomembrane with a minimum thickness of 1.5 mm (60 mils) in compliance with GRI GM17.

The geomembrane has two main functions. It helps to limit water getting into the contaminated soils of the landfill (limiting the risk of waste leaching) and also prevents gas from diffusing into the topsoil, allowing for efficient collection by the multi-linear drainage geocomposite.

Substantial differential settlements are not anticipated in the geosynthetics, given the age of the waste. In addition, the large layer of uncontaminated soil on the old waste before the geosynthetics are installed limits the phenomenon of localized settlement that could have significantly stressed the geomembrane during reloading. Moreover, the LDPE geomembrane has a better behavior towards potential deformations than a HDPE membrane.

## RAINFALL WATER DRAINAGE

The main functions of the drainage layer placed directly on the geomembrane are to drain the infiltrated rainwater and to mechanically protect the geomembrane against puncture by the upper soil layers.

The purpose of the drainage of infiltrated rainwater is to reduce the hydraulic head on the geomembrane and to stabilize the upper soil layer by preventing it from becoming saturated. The performance of the filtration and drainage system must be maintained over the long-term and under heavy loads, since the overlying soil will be up to 25 m (82 ft) thick in some places, which equates to a stress of 450 kPa (9,400 psf).

The rainwater drainage geocomposite is a multi-linear drainage geocomposite DRAINTUBE type. It is composed of two needle-punched non-woven geotextile layers incorporating 25 mm (1 in) diameter corrugated and perforated polypropylene mini-pipes. The mini-pipes are spaced 1 m (40 in) apart across the width of the product. The product is preferably installed with the mini-pipes in the direction of the slope. It is connected at the toe to a collection trench (Figure 7).

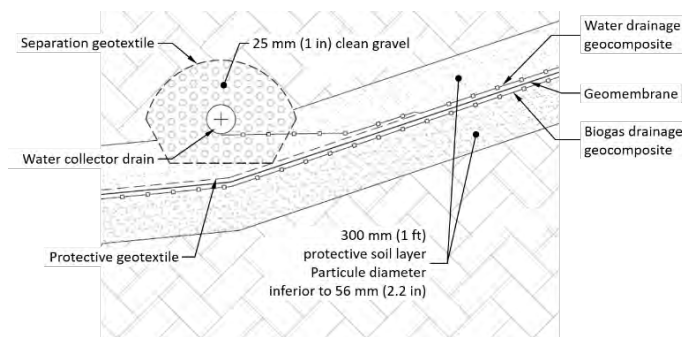


**Figure 7. Connection detail of the drainage geocomposite to the collector trench (source: Demande de modification de l’approbation du plan de réhabilitation, 2020)**

As explained in the previous paragraph, the multi-linear geocomposite is not sensitive to creep in compression when confined, which allows it to maintain its hydraulic characteristics under high loads. It has a transmissivity of  $1 \times 10^{-3} \text{ m}^2/\text{s}$ , measured at a hydraulic gradient of 0.1, confined



under 480 kPa (10,000 psf) between a geomembrane and a layer of sand, for 100 hours. The geocomposite was sized to drain a flow of  $1 \times 10^{-6}$  m/s ( $1.45 \times 10^{-3}$  gpm/ft<sup>2</sup>).

The multi-linear geocomposite also protects the geomembrane against puncture by the overlying soil. Its CBR puncture strength is greater than 3,200 N (719 lb). The backfill in contact is a 300 mm (1 ft) layer of granular soil with particle diameters less than 56 mm (2.2 in).

## CONSTRUCTION WORK

The installation of the geosynthetics was optimized and adapted in order to meet the constraints related to the earthwork and the treatment of specific points, in particular the decontamination of areas identified during the reprofiling of the cover, prior to the installation work as shown in Figure 8.



**Figure 8. Soil surface conditions before the installation of the geosynthetics**

Figure 9 shows the unrolling of the multi-linear geocomposite for gas collection. Once in place, it is longitudinally welded continuously with the hot wedge welder (the same one used to weld the geomembrane) to avoid any displacement during the installation of the geomembrane above it. Sand bags are also used at the edge of the rolls.



**Figure 9. Installation of the multi-linear geocomposite for gas collection**

The mechanical connection of the mini-pipes of the geocomposite to the main header is shown in Figure 10. The upper geotextile of the multi-linear geocomposite is then put back in place to protect the connections.



**Figure 10. Mechanical connection of the geocomposite mini-pipes to the main header**

The geomembrane is unrolled on the drainage geocomposite and welded using the double-welding method (Figure 11).





**Figure 11. Installation of the geomembrane on the geocomposite**

The drainage geocomposite for infiltrated rainwater removal is installed on the geomembrane (figure 12). It is also longitudinally welded continuously with the hot wedge welder to avoid any displacement during the backfilling process.



**Figure 12. Infiltrated rainwater drainage geocomposite**

It is backfilled as the work progresses, with the tracked construction equipment travelling on a thick layer of soil to prevent any damage to the geosynthetics (Figure 13).



**Figure 13. Backfilling**

Finally, a general view of the site during construction of the geosynthetic final cover is shown in Figure 14.



**Figure 14. General view of the final cover construction**

## CONCLUSION

The construction of an impermeable final cover on the toxic waste is an essential part of the overall remediation project of the former quarry that will ultimately become a renowned municipal public park. The impermeable final cover that includes drainage layers for rainwater and gas collection prevents the rainwater to infiltrate the toxic material and the gas from dissipating on the site.



The use of geosynthetics materials has reduced the need for importing granular drainage media from outside of the site. More specifically the use of multi-linear drainage geocomposites maintained the required drainage capacity for gas collection and water drainage after the final cover was buried under a maximum of 26 m (85 ft) of soil material and increased the weathertight performance of the cover by protecting the geomembrane from mechanical puncture and controlling the hydraulic heads (water and gas) on its overall surface.

The large amount of earthwork on the site in conjunction with the construction of the final cover over an area of 85,000 m<sup>2</sup> (915,000 sf) required strong cooperation between the different stakeholders (general contractors, geosynthetics installers, engineering firms, etc.) which has been the case during the overall direction of the project.

## REFERENCES

ASTM D4439. Standard Terminology for Geosynthetics, *American Society for Testing and Materials*, West Conshohocken, PA, USA

ASTM D4716. Standard Test Method for Determining the (In-plane) Flow Rate per Unit Width and Hydraulic Transmissivity of a Geosynthetic Using a Constant Head, *American Society for Testing and Materials*, West Conshohocken, PA, USA

ASTM D7931. Standard Guide for Specifying Drainage Geocomposites, *American Society for Testing and Materials*, West Conshohocken, PA, USA

Saunier, P., Ragen, W. and Blond, E. (2010). Assessment of the resistance of drain tube planar drainage geocomposites to high compressive loads. 9th International Conference on *Geosynthetics*, Guarujá, Brazil, Vol3

## High Performance Geomembranes in Aggressive Mining Applications

Alex Gersch<sup>1</sup>

<sup>1</sup>Layfield Australia, Glenelg North, SA, Australia; e-mail: [alex.gersch@layfieldgroup.com](mailto:alex.gersch@layfieldgroup.com)

### ABSTRACT

Operating conditions associated with mining activities can generally be classified as aggressive environments. Liquor retention ponds, evaporation ponds and tailings dams are some of the mining applications which require geosynthetic liners with specific mechanical and chemical compatibility properties, which are usually the focus of owners and designers when assessing suitable geomembrane materials. Previous project specifications have often been adopted without consideration of the lessons learnt in previous long term mining applications. Additionally, the impact of environmental ambient conditions can be overlooked or given second order priority during the assessment process. This paper discusses the approach taken by an Australian project team to select a suitable geomembrane material for use in a critical evaporation pond application containing a very acidic liquor with very high UV exposure combined with very high maximum ambient temperatures exceeding 40 deg C. The project team underwent an extensive testing protocol to better determine how a combination of factors influenced the material assessment process and final material selection.

### BACKGROUND

To support ongoing mining operations, a significant mining company in Australia required additional evaporation pond capacity. Located in a region of Australia subject to very high solar irradiance, regularly exceeding 28MJ/m<sup>2</sup> per day, and subsequently very high UV exposure and very high maximum ambient temperatures in excess of 40 deg C not commonly experienced at other mining locations globally (refer Appendix A, Table 4. Average Climate Statistics for the Site). The mine facility, which has been operational for over 30 years, uses evaporation ponds to manage acidic liquor decanted from the tailing's retention and storage facility. The liquor has an average pH of 0.79 and, as can be anticipated in such an application, is high in metallic oxides and chlorides.

The existing tailings and evaporation ponds were lined with GRI GM13 compliant high density polyethylene geomembranes; however, the mining client had experienced some variability in the performance of HDPE geomembranes in the same applications at this particular site. Despite advances in polyolefin additive packages over previous decades, the client had witnessed unexpected material degradation with HDPE liners in more recent evaporation ponds. The evidence from site was supported by numerous studies on the degradation of polyolefin materials when exposed to higher temperature operating conditions (Bhartu 2015). When other mine sites with similar operations were referenced, it was realized these reference sites in North and South America did not experience the same level of solar exposure (refer Figure 1.) (Solargis, 2022).

As part of their internal assessment process, the client instigated an assessment of the performance of the geomembrane materials installed in the existing evaporation ponds. Samples were exhumed from various positions in the existing evaporation pond to analyze the effect of the liquor and environmental conditions. The results would be used to determine the testing and selection criteria of the geomembrane for the new facility, and ultimately, the material type.

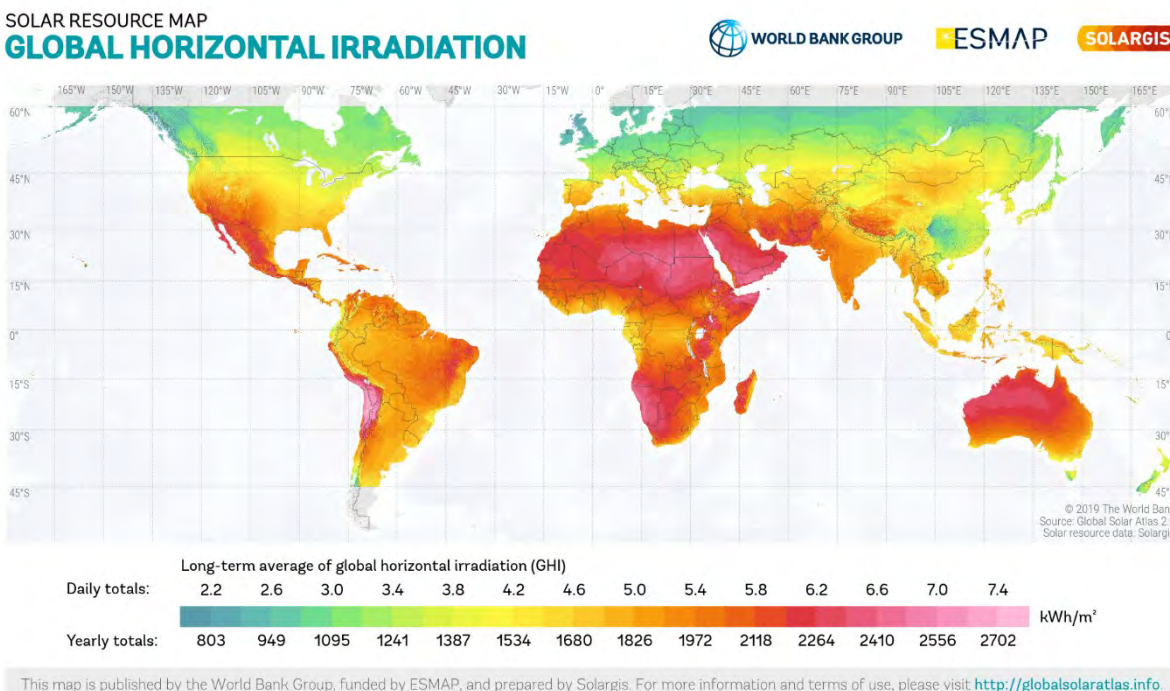


**Figure 1. Solar Exposure & Australia's higher exposure than North & South America**

## METHODOLOGY

Geomembrane samples were taken from various locations in the existing evaporation pond to analyze the effect of the acidic liquor and environmental conditions. Samples were taken from the floor area which was continuously exposed to acidic liquor and sediment containing high concentrations of metallic oxides and chlorides, from the sloped batter walls in the intermediate wet/dry zone, and from the anchor trench where the liner was not exposed to liquor or ambient environmental conditions.

The exhumed geomembrane samples were then tested by an independent laboratory experienced in geomembrane testing, to determine the remaining ultra-violet (UV) stabilizers and antioxidant (AO) package. Results were then analyzed using Arrhenius mathematical modelling to estimating remaining life expectancy based on depletion rates of the AO and UV stabilization packages. The testing revealed the acidic liquor was not the primary source of degradation and provided some level of protection from climate related degradation processes, whereas areas above the liquid line exhibited significant reductions in AO and UV stabilization packages (refer Table 1.). The estimated service life of the geomembrane on the batter slopes exposed to the "splash zone" was less than half that of that predicted for the geomembrane section on the floor that was continuously exposed only to the acidic liquor. A significant

reduction in the antioxidant package was also observed in the HDPE geomembrane material exhumed from the anchor trench that had not been exposed to either the acidic liquor or UV. This finding was completely unexpected. It was theorized this could be due to the heat soak of the earthen embankment during summer months, potentially reaching temperatures of 35 deg C.

**Table 1. Existing geomembrane remaining AO/UV stabilizers and estimated life expectancy**

	<b>a) Floor Sample</b>	<b>b) Wall Sample</b>	<b>c) Anchor Trench</b>
Exposure	Continuously exposed to acidic liquor.	Fully exposed at the intermediate wet/dry zone.	No exposure to liquor or environmental conditions.
Remaining AO package.	63%	13%	50%
Remaining UV stabilizers	75%	32%	67%
Estimated residual life remaining.	12 years	2 years	6 years
Total estimated service life	22 years	9 years	16 years

As a result, the client initiated a comprehensive material selection process to evaluate potential materials during the design phase of the new evaporation pond, commencing with an expression of interest for supply of suitable materials. The evaluation included high performance and regular high density (HDPE) and medium density (MDPE) polyethylene's, polyvinyl chlorides (PVC), ethylene interpolymers (EIA), bituminous (BGM) and geosynthetic clay (GCL) liner materials. After receiving submissions from manufacturers and suppliers, a desktop review was undertaken by the client subsequently reducing the number of potential materials from eight to four.

## SELECTION CRITERIA

When the expression of interest was requested, Layfield (the Manufacturer) conducted a formal review of the Client's test results, the application, the location and associated environmental factors of the existing HDPE liner material. The main degradation mechanisms in the application were identified as UV exposure, high geomembrane surface temperatures and chemical exposure to very acidic liquid with the splash zone of the liner being exposed to all three degradation mechanisms.

An analysis matrix was subsequently completed by the Manufacturer to determine the most appropriate material. HeatGard, a raised temperature HDPE (PE-RT) geomembrane produced from a bi-modal polyethylene resin having the highest ranking. This PE-RT resin is a proprietary formulation polymerized using a dual gas phase reactor to produce a HDPE resin with unique properties. During development of the geomembrane, the resin Manufacturer and the geomembrane Manufacturer worked together closely to produce a formulation incorporating a significant antioxidant and UV stabilization package, specifically suitable for exposed applications in aggressive environments.



**UV Resistance.** UV Resistance is achieved in the geomembrane with a substantial UV stabilization package developed specifically for exposed geomembrane applications. In addition, the carbon black loading of 2-3% provides an impenetrable surface to UV light eliminating concurrent sub-surface degradation of the material. The Manufacturer's UV testing of 1600hrs in accordance with ASTM D7238 has shown an exceptionally high 99% retention of high-pressure oxidation induction time (HP-OIT) results to ASTM D5885.

**Geomembrane Surface Temperatures.** It is well known that surface temperatures of exposed black geomembranes significantly exceed ambient temperatures when exposed to solar radiation. The mine site is known to receive extremely high solar radiation levels, averaging in excess of  $28\text{MJ/m}^2/\text{day}$  in summer months. Temperatures on black geomembranes in similar regions in Australia have been recorded at:

Shaded conditions (Ambient): 50 deg C.

Exposed to direct solar radiation: 80 deg C.

Exposed to direct & reflected solar radiation: 123 deg C.

In this application it was assumed that the liner would not be exposed to any reflected incidence and therefore maximum temperatures were expected to reach 80 deg C. At this temperature, the antioxidant package in standard grade HDPE geomembranes would deplete rapidly (Abdelaal and Rowe, 2014) and as experienced by the client in existing storages on site. Oven aging testing and Arrhenius modelling undertaken by the Manufacturer was able to predict anti-oxidant depletion rates at the temperatures expected to be experienced by the geomembrane liner at the mine site, as shown in Figure 2. (Mills and Beaumier, 2017).

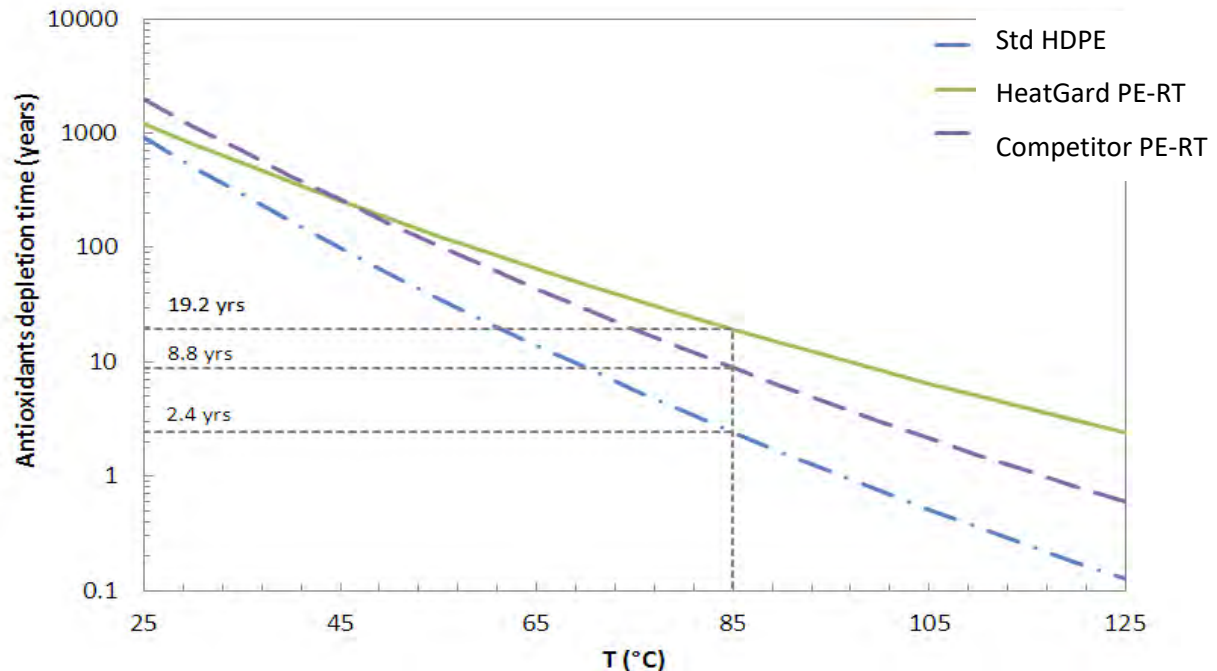


**Figure 2. – Arrhenius modelling of antioxidant depletion rates at elevated temperatures.**

**Chemical Resistance – Acid.** The geomembrane proposed by the Manufacturer has very high resistance up to 30% sulfuric acid at 60 deg C, – well above the expected liquor temperature and maximum recorded 5% sulfuric acid present in the existing storage. There was further evidence

from the existing storages that polyethylene has the necessary chemical resistance to the contained liquid.

The antioxidant package used in the geomembrane has significant resistance to hydrolysis. Many of the antioxidant packages used in standard geomembrane resins contain a phenolic antioxidant with an ester, which suffers attack by acidic liquids. The antioxidant package used in the selected geomembrane contains a dendrimeric structure that does not suffer from hydrolysis.

## **MATERIAL TESTING**

The client engaged a specialist engineering consulting company to evaluate the suggest geomembrane materials and determine a suitable testing regime to evaluate the short listed materials, and once a material was selected, to provide manufacturing quality assurance. After an initial desktop review, four candidate geomembranes were shortlisted. A specialist polymer testing laboratory was engaged to undertake a significant testing regime. In addition to the standard test criteria set out in GRI GM13 additional testing was used to simulate accelerated in-service conditions (Folwell, Gassner, and Phillips, 2021). This testing focused on the primary degradation mechanisms of chemical attack from the acidic liquor, and UV exposure with high temperatures.

The client provided sufficient liquor solution to the test laboratory to undertake 90 day immersion testing in accordance with ASTM D5322 and ASTM D5747 to replicate the expected chemical exposure. Samples of virgin geomembrane, fusion welded geomembrane and extrusion welded geomembrane were all immersion tested at 55 deg C, 70 deg C and 85 deg C and material performance was evaluated using Arrhenius modelling of OIT depletion rates to estimate the service life of the geomembrane.

Reduction in tensile results can potentially give an early indication of any performance issues with the geomembrane's chemical resistance properties after immersion testing. Tensile tests were undertaken on virgin samples to create a base line and after immersion for 30, 60 and 90 days in accordance with ASTM D6693.

Stress crack resistance of HDPE geomembranes is also critical in the long-term performance of the material. Notched Constant Tensile Load (NTCL) SCR testing was undertaken in accordance with ASTM 5397 on virgin geomembrane samples prior to immersion and after immersion for 30, 60 and 90 days at 55 deg C.

90-day Oven Aging in accordance with ASTM D5721 and UV exposure for 1600 hours in accordance with ASTM D7238 was also undertaken to assess the geomembrane performance with respect to degradation above the waterline on the exposed slopes of the storage.

Oven aged samples were subjected to both standard and high-pressure oxidative induction time testing in accordance with ASTM D3895 and ASTM D5885. Virgin samples were initially tested to determine a baseline performance and samples removed at 30, 60 and 90 days to assess the degradation rate of the oxidation induction time.

At the conclusion of the testing the high performance PE-RT geomembrane was selected as the most suitable material due to it's very low reduction in OIT and HP-OIT performance after immersion testing, oven aging and UV exposure and due to it's very high NTCL stress crack resistance.

## MANUFACTURING REQUIREMENTS

In addition to standard, in-house quality assurance testing and monitoring in accordance with GRI GM13, the client required specific material performance properties to be tested with a higher frequency, and for testing to be duplicated at an independent test laboratory to corroborate the in-house test results (refer Table 2. & 3.). As some of these tests are of significant duration, index type test results were signed off to allow the geomembrane material to be shipped while the endurance properties were still undergoing testing. The material was then signed off and accepted for installation after the endurance testing was completed for each batch. Completing the shipping and endurance testing concurrently truncated the material supply lead times significantly.

**Table 2. Index properties tested by manufacture and independent test laboratory.**

Property	Test Method	Manufacturers Laboratory	Independent Laboratory
Thickness	ASTM D5199	Per Roll	Per Roll
Tensile Properties Strength at break Elongation at break Strength at Yield Elongation at yield	ASTM D6693	Per 5 Rolls	Per 5 Rolls
Tear Resistance	ASTM D1004		
Puncture Resistance	ASTM D5397		
Carbon Black Content	ASTM D1603		
Carbon Black Dispersion	ASTM D5596		
Density	ASTM D1505		
MFI	ASTM D1238		

**Table 3. Endurance properties tested by manufacture and independent test laboratory.**

Property	Test Method		Manufacturers Laboratory	Independent Laboratory
Oxidative Induction Time Standard OIT <b>AND</b> High Pressure OIT	ASTM D3895 ASTM D5885		Per resin batch or per 60 rolls	Per resin batch or per 60 rolls
NCTL Stress Crack Resistance	ASTM D5397	1000 hrs		
UV Resistance High Pressure OIT retained	ASTM D7238 ASTM D5885	1600 hrs		
Oven Aging at 85 deg C Standard OIT	ASTM D5721 ASTM D3895	90 days		
Oven Aging at 85 deg C High Pressure OIT	ASTM D5721 ASTM D5885	90 days		

For additional quality assurance, the client required the geomembrane manufacturing process to be witnessed by an independent quality audit team. This was facilitated by the manufacturer in close collaboration with the client, engineering consultant and auditing company.

## CONCLUSIONS

Many mining sites are located in aggressive environments and the affect on geomembrane materials is exacerbated by mineral extraction processes often producing liquors with extremely low acidity or very high alkalinity. When specifying materials, Engineers need to consider the significant influence of environmental factors as well as consider the chemical compatibility of the proposed materials. Samples taken from an existing geomembrane lined storage on site clearly demonstrated the impact of environmental factors exceeded the impact of exposure to very acidic liquor.

Undertaking a thorough materials evaluation process prior to materials specification has clearly identified the benefits of using a high performance PE-RT geomembrane in this application. With this knowledge the client could proceed with construction with a high level of confidence that the material performance would exceed the expected life of the storage. It also demonstrated the benefit of open collaboration between the client, engineering consultant and geomembrane manufacturer during the evaluation and manufacturing phases, leading to the successful completion of the project (refer Figure 3.).



**Figure 3. The completed storage facility in operation.**

## REFERENCES

- Abdelaal, F.B., Rowe, R.K., (2014). Effect of high temperatures on antioxidant depletion from different HDPE geomembranes,.
- Bhartu, V.G., (2015). Degradation of Mechanical Properties of Geotextiles and Geomembranes Exposed to Outdoor Solar Radiation under Various Exposure Conditions—Part I: Results of UV-Degradation. *Journal of Geological Resource and Engineering* 4 (2015) 173-184 doi:10.17265/2328-2193/2015.04.002, India.
- Bureau of Meteorology, (2022). Climate statistics for Australian locations. <http://www.bom.gov.au/climate/averages/tables.shtml>
- Folwell, J., Gassner, F., Phillips, G., (2021). Accelerated Aging Testing of Geomembranes for Tailings Liquor. *Mine Waste and Tailings 2021*, Brisbane, Queensland, Australia.



- Mills, A. and Beaumier, D. (2017). *Long-term Performance of HDPE Geomembranes Exposed to High Service Temperature*, IFAI Geo17, USA
- Mills, A., Fraser, B. and Beaumier, D. (2019). *Long-term Performance of HDPE Geomembranes Exposed to a High Temperature Brine Solution*, IFAI Geo19, USA.
- Solargis, (2022). Solar resource maps of World, <https://solargis.com/maps-and-gis-data/download/world>
- Peggs, I., (2003). *Geomembrane Liner Durability: Contributing Factors and The Status Quo*. UK IGS 2003, England.

## APPENDIX A - Average Site Climate Statistics

**Table 4. Average Climate Statistics for the Site.**

Statistic Element	Jan	Feb	Mar	Apr	May	Jun	Jul	Aug	Sep	Oct	Nov	Dec	Annual
Mean maximum temperature (Degrees C)	37	35.6	32.2	27.3	22.3	18.5	18.7	20.8	25.3	28.6	32.1	34.7	27.8
Highest temperature (Degrees C)	48.5	46.8	43.2	40	33	27	29	34.6	39	42	47.4	47.4	48.5
Lowest maximum temperature (Degrees C)	17.5	18.9	18.5	17.3	13	12	11	9.8	16	14.9	17.9	22	9.8
Decile 1 maximum temperature (Degrees C)	30	28.6	25.5	22	18.1	15.6	15.2	17	19.4	22	25.3	28	
Decile 9 maximum temperature (Degrees C)	43.5	42	38.8	33	27	21.8	23	25.5	32	36.6	39	41.8	
Mean number of days >= 30 Degrees C	27.6	23.7	21.3	8.5	0.8	0	0	0.5	6.2	12.3	19.2	24.8	144.9
Mean number of days >= 35 Degrees C	20.3	16	9.7	1.3	0	0	0	0	1.1	4.7	9.4	15	77.5
Mean number of days >= 40 Degrees C	10.1	6.1	1.4	0	0	0	0	0	0	0.3	2.4	5.5	25.8
Mean minimum temperature (Degrees C)	21.2	20.1	17.2	12.8	8.2	5.1	4.3	5.6	9.3	12.8	16.4	19	12.7
Lowest temperature (Degrees C)	11.5	11	5	1	-3	-6	-5	-4	-1.1	2.2	6	8	-6
Highest minimum temperature (Degrees C)	33	33.7	28.5	24	19	15.5	14.8	18.5	25	26.2	30	32.8	33.7
Decile 1 minimum temperature (Degrees C)	16	15	12	7.2	3	-0.4	-0.8	0.2	4	7	11.2	14	
Decile 9 minimum temperature (Degrees C)	27	26	22.7	18.6	14	11	9	11.1	15.1	19.1	22.9	25	
Decile 1 monthly rainfall (mm)	0.3	0	0	0.2	0.4	0.8	0.4	0	0	0	0.1	1.1	52.3
Decile 5 (median) monthly rainfall (mm)	4.1	6.6	2.5	4.2	9.3	4.9	2	4.9	5	5.5	10	10.2	132.6
Decile 9 monthly rainfall (mm)	43.8	44.8	23.2	37	18.2	45	17.7	25	28.2	32	35.2	35.8	230.6
Highest daily rainfall (mm) for years	52	61.6	36.2	86	17	45	13	17.4	24.6	41	40	48.8	86
Mean number of days of rain for years	3.2	2.8	2.6	3.3	3.3	4.2	3.3	3.8	4	3.8	4	4.2	42.5
Mean daily wind run (km)	424	396	353	296	276	264	289	325	379	396	405	415	352
Maximum wind gust speed (km/h)	94	76	94	70	81	74	70	74	93	91	109	93	109
Mean daily solar exposure (MJ/(m*m))	28.6	26	22.2	17.1	13.1	11.2	12.2	15.4	19.8	23.9	26.7	28.4	20.4

## **Initial Stress Condition and the Hydraulic Conductivity of BPC Geosynthetic Clay Liners for Acidic Heap Leach Solutions**

**Craig H. Benson<sup>1</sup>, Yu Tan<sup>2</sup>, Jimmy Youngblood<sup>3</sup>, and Sabrina L. Bradshaw<sup>4</sup>**

<sup>1</sup>Geological Engineering, University of Wisconsin-Madison, Madison, Wisconsin, 53706, USA; chbenson@wisc.edu

<sup>2</sup>Geological Engineering, University of Wisconsin-Madison, Madison, Wisconsin, 53706, USA; ytan84@wisc.edu

<sup>3</sup>Solmax Inc., 19103 Gundle Road, Houston, Texas, 77073, USA; jyoungblood@solmax.com

<sup>4</sup>Geological Engineering, University of Wisconsin-Madison, Madison, Wisconsin, 53706, USA; sbradshaw@wisc.edu

### **ABSTRACT**

Four commercially available bentonite-polymer composite (BPC) geosynthetic clay liners (GCLs) and one conventional sodium bentonite (NaB) GCL were permeated with a synthetic copper heap leach solution. The BPCs were comprised of granular NaB dry-blended with granular proprietary polymers. The NaB GCL was comprised of the same bentonite as the BPCs. Tests were conducted under two different stress scenarios. In the low stress scenario, testing began at low initial confining stress (20 kPa), followed by a ramp up to 600 kPa. The high stress scenario began with a higher initial confining stress (200 kPa) simulating a 10-m-thick layer of ore rapidly placed on the pad, followed by the same ramp up to 600 kPa. Permeation with the copper heap leach solution adversely affected the NaB GCL, with the hydraulic conductivity exceeding  $10^{-9}$  m/s for all but one case. The BPC GCLs had much lower hydraulic conductivities ( $< 9.1 \times 10^{-11}$  m/s). Hydraulic conductivity of the BPC GCLs varied with type of polymer and decreased modestly as the effective stress was ramped up. The BPC GCLs permeated with higher initial stress had lower hydraulic conductivity compared to those initially permeated at low initial stress, indicating that high initial stress affords protection for BPC GCLs.

### **INTRODUCTION**

Geosynthetic clay liners (GCL) are used in lining systems for heap leach facilities to collect leach solution draining from the ore. Conventional GCLs are comprised of a thin layer of sodium (Na) bentonite granules sandwiched between two geotextiles that are bonded together by needlepunching or stitching. To achieve low hydraulic conductivity, the bentonite granules must swell sufficiently during hydration to fill the intergranular pores (Fig. 1a) and seal off the needlepunching fiber bundles. If swelling is insufficient to fill the intergranular pores (Fig. 1b) and seal off the bundles, the GCL will have high hydraulic conductivity. The hydraulic conductivity of GCLs with Na bentonite can range six orders of magnitude or more depending on how much the bentonite granules swell (Jo et al. 2001, Kolstad et al. 2004).

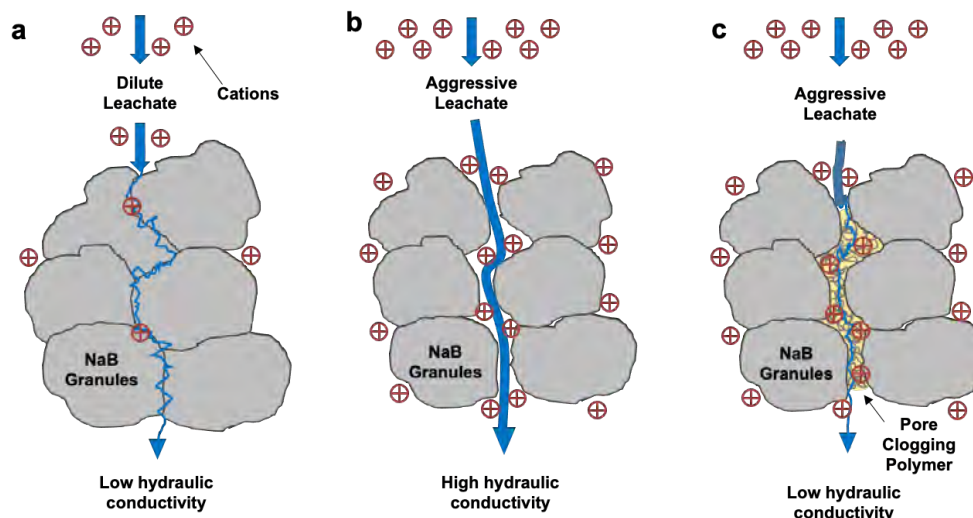


Figure 1: Swelling of Na bentonite granules in conventional GCL closes intergranular pores to yield low hydraulic conductivity (a), suppressed swell of granules by aggressive leachate leaves intergranular pores open yielding high hydraulic conductivity (b), and polymer gel in BPC clogs intergranular pores yielding low hydraulic conductivity (c).

The swelling of bentonite is highly sensitive to the geochemistry of the solution to be contained. Solutions with higher ionic strength, a preponderance of polyvalent cations (charge of +2 or higher), or extreme pH, often referred to as “aggressive solutions,” suppress bentonite swelling, resulting in a GCL with hydraulic conductivity that may be too high for the barrier application of interest (Jo et al. 2001, Kolstad et al. 2004, Scalia and Benson 2016). In such cases, a GCL containing a bentonite-polymer composite (BPC) can be suitable (Scalia and Benson 2016, Tian et al. 2019, Chen et al. 2019, Norris et al. 2022, Tan et al. 2022). BPC GCLs contain a mixture of bentonite and polymer granules. When the BPC hydrates, the granules form a gel that clogs intergranular pores in the hydrated bentonite, resulting in narrow and tortuous flow paths and low hydraulic conductivity (Fig. 1c). The low hydraulic conductivity persists provided the hydrated polymer remains in the intergranular pores and retains a gel structure. However, the rheology of polymer gels is sensitive to the geochemistry of the hydrating solution, and some gels are eluted from the intergranular pore space. If elution is significant, the hydraulic conductivity of a BPC GCL can increase significantly (Scalia and Benson 2016, Tian et al. 2019, Norris et al. 2022).

In this study, four commercially available BPCs and one conventional Na bentonite (NaB) GCL were hydrated and permeated with a synthetic copper heap leach solution that had low pH and contained predominantly divalent cations. The NaB GCL and the BPCs were provided by the manufacturer. The BPCs were comprised of granular Na bentonite dry-blended with granular polymer. Each BPC had a unique polymer. The NaB GCL was comprised of the same bentonite used in the BPCs. Polymers used in the BPCs and the polymer loading are proprietary to the GCL manufacturer and were not divulged to the investigators. Tests were conducted under different loading conditions representing different overburden pressures in the heap leach facility. Findings from these tests are described in this paper.



## MATERIALS

**Geosynthetic Clay Liners.** The NaB GCL provided by the manufacturer consisted of 4.8 kg/m<sup>2</sup> of granular bentonite sandwiched between a nonwoven geotextile and a woven-nonwoven composite geotextile bonded by needlepunching. The composite geotextile consists of a woven slit film geotextile bonded to a nonwoven geotextile, with the slit film geotextile internal to the GCL. Mock BPC GCLs simulating a commercial GCL were prepared by placing 5 kg/m<sup>2</sup> of BPC comprised of dry blended NaB and granular polymer between the same geotextiles used for the NaB GCL. The mock GCLs were not needlepunched.

**Synthetic Copper Heap Leach Solution.** A typical copper heap leach solution was identified using data on the geochemistry of five copper heap leach solutions reported by Ghazizadeh et al. (2018). The geochemistry of these solutions was described in terms of the two master variables affecting the hydraulic conductivity of NaB GCLs, ionic strength (I):

$$I = \sum_{i=1}^n C_i z_i^2 \quad (1)$$

and RMD:

$$RMD = \frac{M_M}{\sqrt{M_D}} \quad (2)$$

where  $C_i$  is the concentration of the  $i^{\text{th}}$  ionic species in the solution,  $z_i$  is the valence of the  $i^{\text{th}}$  species,  $M_M$  is the total molarity of monovalent cations in solution, and  $M_D$  is the total molarity of polyvalent cations in solution (Kolstad et al. 2004). RMD represents the relative abundance of monovalent and polyvalent cations. A recipe was created to represent the median concentration of the copper heap leach solutions reported in Ghazizadeh et al. (2018), with  $I = 689$  mM and  $RMD = 0.020 \text{ M}^{0.5}$  (Table 1). The recipe was checked for charge balance and over-saturation using Visual MINTEQ. The solution was titrated with sulfuric acid to achieve pH 2.2. The final solution had an electrical conductivity (EC) of 200 mS/m and an anion ratio ( $A_r$  = molar ratio of chloride to sulfate) of 0.59.

Table 1. Recipe for synthetic copper heap leach solution.

Constituent	Concentration (g/L)
Al <sub>2</sub> (SO <sub>4</sub> ) <sub>3</sub> -18H <sub>2</sub> O	9.62
CaCl <sub>2</sub>	1.46
CuCl <sub>2</sub>	0.18
KCl	0.13
MgCl <sub>2</sub> -6H <sub>2</sub> O	5.05
MgSO <sub>4</sub>	8.77
MnSO <sub>4</sub> -H <sub>2</sub> O	1.16

## METHODS

**Swell Index and Active Water Content.** Swell index (SI) and active water content (AWC) tests were conducted on the NaB (SI only) and the BPC (SI and AWC) using the copper heap leach solution for hydration. Swell index tests were conducted in accordance with ASTM D5890 and

the procedures in Tan et al. (2022). The NaB and BPCs were ground in a motorized grinder (Retsch RM 200, Haan, Germany) until 100% of the particles passed the No. 100 sieve and a minimum of 65% passed the No. 200 sieve. Two grams of ground and dry NaB or BPC were gradually added to a graduated cylinder containing 90 mL of copper heap leach solution. The cylinder was filled to 100 mL after the bentonite was added. The swell volume at 24 hr was recorded as the swell index.

Active water content (AWC) tests were conducted following the methods in Geng et al. (2022). BPCs were placed in 50-mL centrifuge tubes along with the copper heap leach solution at a 1:10 solid-to-liquid ratio. The tubes were tumbled end-over-end for 48 h at 30 RPM, and then centrifuged at 10,000 RPM for 20 min in a Beckman Allegra 25R centrifuge (Beckman Coulter, Palo Alto, California) with a centripetal acceleration of 25,000 g. The solution separated from the BPC mixture during centrifugation was spiked with Rhodamine dye to identify the interface between the solution and the hydrated polymer gel and strongly bonded bentonite. Water content of the hydrated polymer gel and strongly bonded bentonite was measured at 105 °C using ASTM D2216 and reported as active water content.

**Hydraulic Conductivity.** The GCLs were hydrated and permeated with the synthetic heap leach solution in flexible-wall permeameters in general accordance with the procedures described in ASTM D6766. The test setup was very similar to setups illustrated schematically in ASTM D6766. The test specimens had a diameter of 150-mm and were placed in the permeameters between two heavy nonwoven geotextiles used to spread flow uniformly across the surface of the specimen. NaB GCL specimens were trimmed from a GCL roll using a sharp razor knife, with deionized (DI) water applied around the edge to prevent loss of bentonite during trimming. Mock GCLs were prepared from the BPCs and geotextiles, as described previously. All GCL specimens were oriented in the permeameter with the nonwoven geotextile on the influent side and the composite geotextile on the effluent side of the GCL. The woven slit-film geotextile in the composite was on the interior face of the effluent side of the GCL. To prevent sidewall leakage, a layer of paste was smeared around the periphery of the test specimen, and a thin wedge of paste was placed along the periphery of the effluent surface of the GCL before the specimen was sealed with the flexible membrane. The paste was prepared with NaB or BPC and DI water. O-rings were used to seal the membrane to the pedestals.

Cell pressure was applied using tap water via a pressure panel board employing compressed air and an air-over-water interface to provide the desired cell pressure. The influent was contained in a burette and the outflow was collected in a 50-mL polyethylene container. The influent burette and the effluent container were both vented in a manner that maintained atmospheric pressure while minimizing evaporation. No backpressure was used to preclude unintended geochemical alterations associated with elevated pressure (i.e., Le Chatelier's principle). Flow was oriented in the downward direction to simulate the field scenario. The specimens were hydrated with the heap leach solution for 48 hr with the cell pressure and influent head applied and the effluent valve closed (no hydraulic gradient). Permeation commenced after 48 hr of hydration by gradually opening the effluent valve. Checks for sidewall leakage were made on specimens having much higher hydraulic conductivity than anticipated. The permeant solution was spiked with rhodamine WT dye, which stains preferential flow paths bright magenta. None of the tests were found to have sidewall leakage.

Tests were conducted under two different stress scenarios: low and high initial confining stress. In the low initial stress (LS) scenario, testing began at low initial confining stress (20 kPa) simulating a thin layer of ore on the heap leach pad, followed by a ramp up to 600 kPa in seven

increments (20 kPa to 50, 100, 200, 300, 400, 500, and 600 kPa) representing increasing ore thickness. The high initial stress (HS) scenario began with a higher initial confining stress (200 kPa) simulating a 10-m-thick layer of ore rapidly placed on the pad, followed by the same ramp up to as much as 600 kPa. The two scenarios were evaluated to determine if higher stress prior to contact with permeant solution provides additional protection of the GCL from adverse chemical interactions. In all cases, tests were required to reach the hydraulic and chemical termination criteria in D6766 before the stress was incremented to the next level. Hydraulic equilibrium was defined as steady flow and inflow equal to outflow per the criteria in D6766. Chemical equilibrium was defined as EC of the effluent within 10% of the EC of the influent per the EC criteria in D6766. Several of the tests are still being conducted. The most recent data at the time this paper was prepared are reported herein.

## RESULTS

A typical response of the NaB and BPC GCLs to permeation with the copper heap leach solution is shown in Fig. 2 for the first test at low initial stress test (20 kPa) with the NaB and BPC GCLs. The hydraulic conductivity declines gradually as the bentonite swells (NaB GCL) and the polymer gel clogs pores (BPC GCL). An equilibrium hydraulic conductivity is reached in about 4 PVF for the NaB GCL and 2.0 PVF for the BPC GCL.

Hydraulic conductivities of the NaB and BPC GCLs are summarized in Tables 2 and 3 and are shown as a function of effective stress in Fig. 3. Hydraulic conductivities of the GCLs tested at low initial confining stress (LS) are shown in Fig. 3 with solid symbols. Hydraulic conductivities of GCLs with high initial confining stress (HS) are shown in Fig. 3 with open symbols.

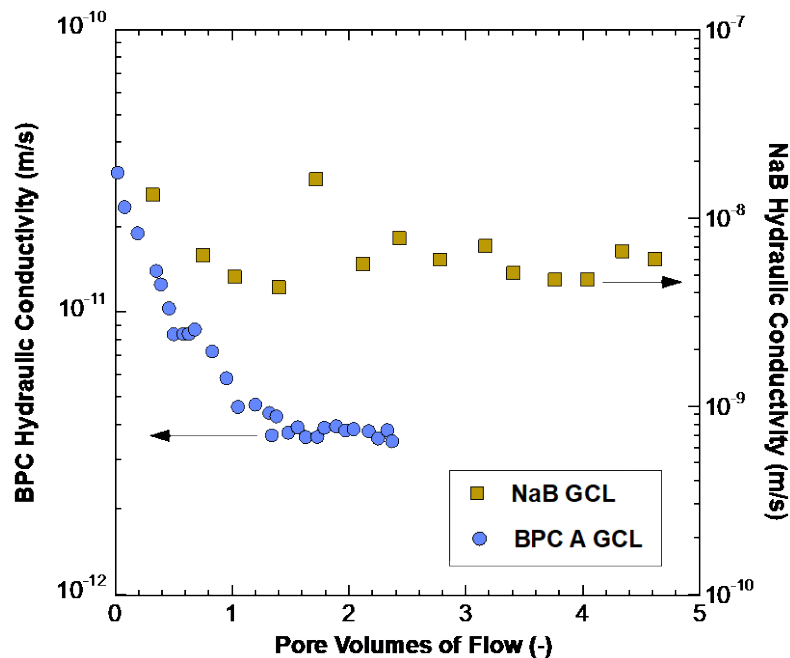


Figure 2: Typical response of NaB and BPC GCLs to permeation with copper heap leach solution. Tests conducted at 20 kPa effective stress with low initial stress.

Table 2. Summary of hydraulic conductivity test conditions and outcomes for tests conducted with low initial stress (20 kPa).

GCL	Stress During Permeation (kPa)	Pore Volumes of Flow	Test Duration (d)	Hydraulic Conductivity (m/s)
NaB	20	4.25	28.0	$5.4 \times 10^{-9}$
	50	4.88	78.1	$5.7 \times 10^{-9}$
	100	4.83	55.1	$6.4 \times 10^{-9}$
	200	5.94	22.8	$5.7 \times 10^{-9}$
	300	9.29	33.1	$4.6 \times 10^{-9}$
	400	2.15	4.4	$3.6 \times 10^{-9}$
	500	2.59	16.0	$2.7 \times 10^{-9}$
	600	1.51	3.9	$2.1 \times 10^{-9}$
BPC A	20	2.57	182.7	$3.8 \times 10^{-12}$
	50	0.73	75.6	$4.8 \times 10^{-12}$
	100	0.44	47.4	$4.2 \times 10^{-12}$
	200	0.56	50.8	$3.8 \times 10^{-12}$
	300	0.19	41.0	$1.9 \times 10^{-12}$
	400	0.23	26.8	$3.1 \times 10^{-12}$
	500	0.55	78.0	$3.4 \times 10^{-12}$
	600	0.34	36.0	$3.2 \times 10^{-12}$
BPC B	20	3.19	182.2	$3.9 \times 10^{-12}$
	50	0.54	53.7	$3.7 \times 10^{-12}$
	100	0.92	71.0	$4.4 \times 10^{-12}$
	200	0.62	50.8	$4.4 \times 10^{-12}$
	300	0.21	41.0	$2.6 \times 10^{-12}$
	400	0.16	25.2	$2.3 \times 10^{-12}$
	500	0.55	78.0	$3.4 \times 10^{-12}$
	600	0.36	36.0	$3.4 \times 10^{-12}$
BPC C	20	5.85	70.8	$3.7 \times 10^{-11}$
	50	7.07	83.9	$6.2 \times 10^{-12}$
	100	5.14	54.2	$6.1 \times 10^{-11}$
	200	5.59	22.7	$4.6 \times 10^{-11}$
	300	7.63	83.1	$1.5 \times 10^{-11}$
	400	1.28	15.9	$1.0 \times 10^{-11}$
	500	1.06	41.0	$7.4 \times 10^{-12}$
	600	4.32	123.2	$6.1 \times 10^{-12}$
BPC D	20	2.81	169.3	$2.1 \times 10^{-11}$
	50	3.47	75.6	$4.3 \times 10^{-11}$
	100	2.54	48.3	$3.0 \times 10^{-11}$
	200	4.48	50.8	$5.9 \times 10^{-12}$
	300	1.91	41.0	$4.8 \times 10^{-11}$
	400	1.21	26.8	$1.9 \times 10^{-11}$
	500	1.77	72.3	$1.5 \times 10^{-11}$
	600	0.73	36.0	$1.2 \times 10^{-11}$



Table 3. Summary of hydraulic conductivity test conditions and outcomes for tests conducted with high initial stress (200 kPa).

GCL	Stress During Permeation (kPa)	Pore Volumes of Flow	Test Duration (d)	Hydraulic Conductivity (m/s)
NaB	200	7.04	171.2	$6.7 \times 10^{-10}$
	300	10.3	68.1	$2.0 \times 10^{-9}$
	400	1.27	4.4	$1.8 \times 10^{-9}$
	500	3.58	17.0	$3.2 \times 10^{-9}$
BPC A	600	2.25	3.9	$2.5 \times 10^{-9}$
	300	0.19	141.0	$7.3 \times 10^{-13}$
	400	0.07	26.8	$8.3 \times 10^{-13}$
	500	0.19	116.2	$6.3 \times 10^{-13}$
BPC B	200	0.75	240.4	$1.0 \times 10^{-12}$
	300	0.33	148.0	$1.3 \times 10^{-12}$
	400	0.33	126.0	$1.0 \times 10^{-12}$
BPC C	200	0.95	240.4	$2.4 \times 10^{-12}$
	300	0.69	151.2	$2.4 \times 10^{-12}$
	400	0.15	26.8	$1.9 \times 10^{-12}$
	500	0.51	116.2	$1.8 \times 10^{-12}$
BPC D	200	1.26	240.4	$2.5 \times 10^{-12}$
	300	0.86	151.2	$3.3 \times 10^{-12}$
	400	0.20	26.8	$2.6 \times 10^{-12}$
	500	0.76	116.2	$2.6 \times 10^{-12}$

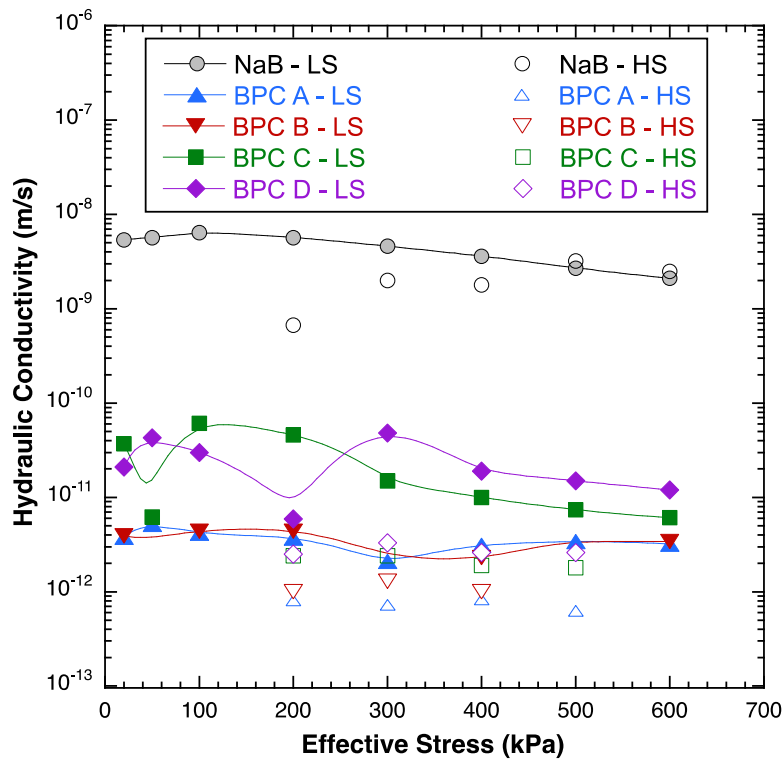


Figure 3: Hydraulic conductivity of GCLs to copper heap leach solution as a function of effective stress (LS = low initial stress = 20 kPa, HS = high initial stress = 200 kPa).

**Hydraulic Conductivity of NaB GCLs.** The NaB GCL had hydraulic conductivity exceeding  $10^{-9}$  m/s for all tests conducted with low initial stress, and for all but the first increment (200 kPa) for tests with high initial stress, indicating that the aggressive copper heap leach solution suppresses swelling of the NaB granules and closure of intergranular pores (Tables 2 and 3, Fig. 3). The high hydraulic conductivity of the NaB GCL to the copper heap leach solution is consistent with the SI of the NaB, which is 9.1 mL/2g when hydrated in the copper heap leach solution and 34.9 mL/2g when hydrated in DI water. Hydraulic conductivities of the NaB GCL to the copper heap leach solution generally are too high for the GCL to be effective, indicating that liners for copper heap leach facilities require GCLs that are more chemically resistant.

Hydraulic conductivity of the NaB GCL tested at low initial stress increased slightly (1.2x) as the confining stress increased from the initial 20 kPa up to 50 kPa and then up to 100 kPa, which was unexpected. The hydraulic conductivity then decreased monotonically and gradually with increasing confining stress (Fig. 3). The unexpected modest increase in hydraulic conductivity as the stress increased from 20 kPa suggests that the NaB GCL was not in geochemical equilibrium when the stress was increased, despite meeting the termination criteria in D6766. The increase in hydraulic conductivity at higher effective stress also corresponds to additional permeation, suggesting that slow rate-limited cation exchange between the solution and NaB may have been occurring, as reported in Jo et al. (2004, 2005, 2006). This effect was more significant for NaB GCLs with high initial stress, with the hydraulic conductivity increasing 4.7x as the effective stress was incremented upward from 200 kPa to 500 kPa, and only decreasing modestly as the stress was increased from 500 to 600 kPa. Moreover, any benefits of the initial high effective stress were ameliorated as the stress increased, with the NaB GCLs with low and high initial stress having essentially the same hydraulic conductivity at 500 kPa and at 600 kPa.

**Hydraulic Conductivity of BPC GCLs.** Hydraulic conductivity of the BPC GCLs is also shown in Fig. 3 as a function of effective stress for low and high initial stress (solid and open symbols). Much lower hydraulic conductivities ( $10^{-13}$  to  $10^{-10}$  m/s) were obtained with the BPC GCLs than the NaB GCL ( $10^{-10}$  to  $10^{-8}$  m/s), indicating that BPC GCLs can be more effective in liners for aggressive copper heap leach solutions.

For low initial confining stress, hydraulic conductivity of the BPC GCLs increases modestly (< 2x) as the confining stress is increased from 20 kPa up to as much as 100 kPa, and then decreases nearly monotonically with increasing confining stress. As with the NaB GCLs, the unexpected increase in hydraulic conductivity between 20 kPa and 100 kPa suggests that the GCLs were not in geochemical equilibrium, despite meeting the termination criteria in D6766 before the stress was increased. As the stress is increased further, the hydraulic conductivity diminishes gradually, with a reduction of at most 10-fold from the highest to low hydraulic conductivity. This suggests that the pore space is only changing modestly with increasing stress, and that the primary mechanisms contributing to low hydraulic conductivity (bentonite swelling and pore clogging by polymer) were established at the lowest stress.

BPC GCLs C and D exhibited unusual dips in hydraulic conductivity at 50 kPa (BPC C) and 200 kPa (BPC D), followed by increases in hydraulic conductivity at the next increment in stress. This may indicate that the polymer is being re-distributed in the pore space when the stress is increased, that pores not filled with polymer at lower stress are closed as the stress increases, and/or polymer elution is occurring intermittently.

**Effect of Elevated Initial Stress.** Hydraulic conductivities obtained from the low and high initial stress tests are compared in Fig. 4. Hydraulic conductivities of the BPC GCLs with high initial stress were approximately 2 to 20-fold lower than BPC GCLs with low initial stress, with 5-fold lower being typical. The BPC GCLs with high initial stress had very low hydraulic conductivity, less than  $3.3 \times 10^{-12}$  m/s. The BPC GCLs with high initial stress also were nearly insensitive to the effective stress (Fig. 3), with similar hydraulic conductivities obtained for stresses from 200 to 500 kPa. This suggests that larger pores are closed by the initial higher stress, providing some protection against higher hydraulic conductivities. Similar benefit was not realized for the NaB GCL, which had similar hydraulic conductivity for tests with low and high initial stress, except for the test at 200 kPa.

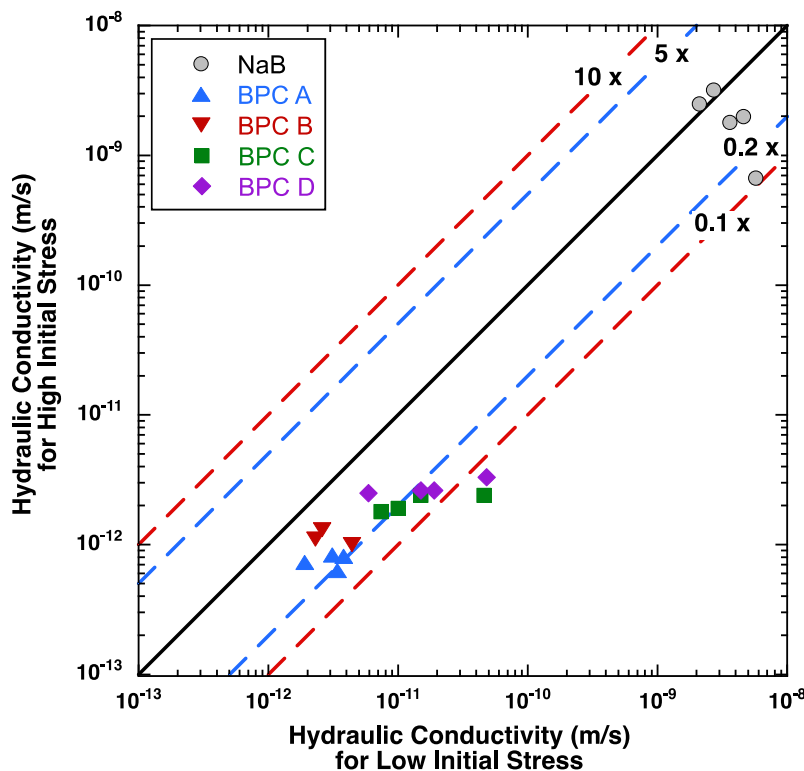


Figure 4: Hydraulic conductivity of NaB GCLs and BPC GCLs for tests conducted at high initial stress (200 kPa) vs. low initial stress (20 kPa).

**Efficacy of Swell Index and Active Water Content.** Efficacy of SI and AWC as indicators of the hydraulic conductivity of the NaB and BPC GCLs to the copper heap leach solution is shown in Fig. 5 using data from the low initial stress tests at 20 kPa along with data reported in Tan et al. (2022) (solid black circles). The data from the tests in this study are consistent with the data reported in Tan et al. (2022). The lowest hydraulic conductivities are realized for the highest SI and AWC, but neither index is effective in discriminating between less permeable and more permeable BPC GCLs. More study is needed to identify indicator tests that are effective predictors of the hydraulic conductivity of BPC GCLs.

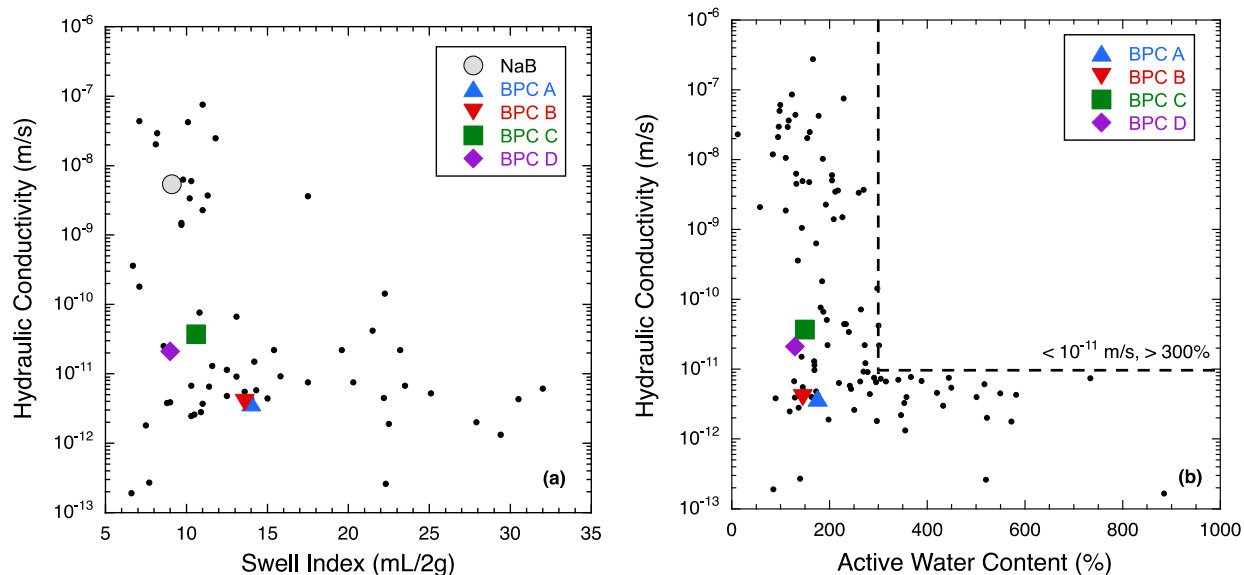


Figure 5: Hydraulic conductivity of GCLs vs. swell index (a) and active water content (b) for NaB or BPC GCLs hydrated in copper heap leach solution. Small solid black symbols from Tan et al. (2022).

## SUMMARY AND CONCLUSIONS

The hydraulic conductivity of geosynthetic clay liners (GCLs) containing commercially available bentonite-polymer composites (BPCs) or sodium bentonite (NaB) was evaluated using a synthetic copper heap leach solution as the permeant liquid. The BPCs were comprised of granular NaB dry-blended with granular polymer. Each GCL had a unique polymer, with the polymer used in each BPC and the polymer loading proprietary to the manufacturer. The NaB GCL was comprised of the same bentonite as used in the BPCs.

The tests were conducted on NaB GCL specimens trimmed from a test roll provided by the manufacturer and on mock BPC GCL specimens prepared from the BPCs and geotextiles provided by the manufacturer. Tests were conducted under two different stress scenarios: low and high initial confining stress. In the low stress scenario, testing began at low initial confining stress (20 kPa) simulating a thin layer of ore on the heap leach pad, followed by a ramp up to as much 600 kPa in seven increments representing increasing ore thickness. The higher stress scenario began with a higher initial confining stress (200 kPa) simulating a 10-m-thick layer of ore rapidly placed on the pad, followed by the same ramp up to as much as 600 kPa. The two scenarios were evaluated to determine if higher stress prior to contact with solution protects the GCL from adverse chemical interactions.

Permeation with the copper heap leach solution adversely affected the Na-bentonite GCL, with the hydraulic conductivity exceeding  $10^{-9}$  m/s for all but one case (200 kPa stress under high initial stress condition). The BPC GCLs had much lower hydraulic conductivities ( $< 9 \times 10^{-11}$  m/s), indicating that BPC GCLs can be more effective than NaB GCLs as liners for copper heap leach pads. The BPC GCLs permeated with higher initial stress had lower hydraulic conductivity at comparable stress compared to those initially permeated at low initial stress, indicating that high initial stress affords protection for BPC GCLs against excessive hydraulic conductivity. Similar protection was not realized for the NaB GCL. None of the BPC GCLs were needlepunched, and



different hydraulic conductivities might have been obtained with needlepunching. Future studies should address the effect of needlepunching on the hydraulic conductivity of BPC GCLs.

Hydraulic conductivity of the BPC GCLs varied between polymers, indicating that efficacy of a BPC GCL for containing leach solutions depends on the polymer employed. Hydraulic conductivity of the BPC GCLs decreased only modestly with increasing effective stress, indicating that the BPC GCLs had very small and tortuous pore spaces. Given that the hydraulic conductivity of the BPCs GCLs varied with polymer type, site specific testing is recommended. Other factors in the field might also affect BPC GCLs, which would also be addressed with site-specific testing.

Swell index (SI) and active water content (AWC) were evaluated as indices of hydraulic conductivity of the BPC GCLs. Data from the tests in this study were consistent with SI and AWC data from past studies on BPC GCLs, but neither index was an effective indicator of hydraulic conductivity of the BPCs. Additional study is needed to identify an appropriate index test for the hydraulic conductivity of BPC GCLs.

## ACKNOWLEDGEMENT

Financial support for this study was provided by Solmax Inc. The findings reported herein are those solely of the authors and may not represent the perspectives or policies of Solmax Inc.

## REFERENCES

- Chen, J., Salihoglu, H., Benson, C., Likos, W. and Edil, T. (2019). Hydraulic Conductivity of Bentonite–Polymer Composite Geosynthetic Clay Liners Permeated with Coal Combustion Product Leachates. *J. of Geotech. Geoenviron. Eng.*, 145, 04019038.
- Geng, W., Salihoglu, H., Likos, W. and Benson, C. (2022). Index Tests for Geosynthetic Clay Liners Containing Bentonite-Polymer Composites, *Environmental Geotechnics*, in press.
- Ghazizadeh, S., Bareither, C., Scalia, J. and Shackelford, C. (2018). Synthetic Mining Solutions for Laboratory Testing of Geosynthetic Clay Liners, *J. Geotech. Geoenviron. Eng.*, 2018, 144(10), 06018011.
- Jo, H., Katsumi, T., Benson, C. and Edil, T. (2001). Hydraulic Conductivity and Swelling of Non-Prehydrated GCLs Permeated with Single Species Salt Solutions, *J. of Geotech. Geoenviron. Eng.*, 127(7), 557-567.
- Jo, H., Benson, C. and Edil, T. (2004). Hydraulic Conductivity and Cation Exchange in Non-Prehydrated and Prehydrated Bentonite Permeated with Weak Inorganic Salt Solutions, *Clays and Clay Minerals*, 52(6), 661-679.
- Jo, H., Benson, C., Lee, J., Shackelford, C. and Edil, T. (2005). Long-Term Hydraulic Conductivity of a Non-Prehydrated Geosynthetic Clay Liner Permeated with Inorganic Salt Solutions, *J. Geotech. Geoenvironmental Eng.*, 131(4), 405-417.
- Jo, H., Benson, C. and Edil, T. (2006). Rate-Limited Cation Exchange in Thin Bentonitic Barrier Layers, *Canadian Geotech. J.*, 43, 370-391.
- Kolstad, D., Benson, C. and Edil, T. (2004). Hydraulic Conductivity and Swell of Nonprehydrated GCLs Permeated with Multispecies Inorganic Solutions, *J. Geotech. Geoenviron. Eng.*, 130(12), 1236-1249.
- Norris, A., Aghazamani, N., Scalia, J. and Shackelford C. (2022). Hydraulic Performance of Geosynthetic Clay Liners Comprising Anionic Polymer–Enhanced Bentonites, *J. Geotech. Geoenviron. Eng.*, 148, 04022039.

- Scalia, J. and Benson, C. (2016). Polymer Fouling and Hydraulic Conductivity of Mixtures of Sodium Bentonite and a Bentonite-Polymer Composite, *J. Geotech. Geoenvironmental Eng.*, 142, 04016112.
- Tan, Y., Chen, J., Bradshaw, S. and Benson, C. (2022). Screening Bentonite-Polymer Composite Geosynthetic Clay Liners Using Swell Index and Active Water Content, *Geotextiles and Geomembranes*, in review.
- Tian, K., Likos, W. and Benson C. (2019), Polymer Elution and Hydraulic Conductivity of Bentonite–Polymer Composite Geosynthetic Clay Liners, *J. Geotech. Geoenvironmental Eng.*, 145, 04019071.

## **Sustainable Practices with Geosynthetics in Mining: Review of Select Case Studies**

**José Pablo George, M.S., CPESC-IT<sup>1</sup>, and Michael Dickey, P.E.<sup>2</sup>**

<sup>1</sup>Reynolds Presto Products/Presto Geosystems/USA, International Manager; e-mail:

[JosePablo.George@PrestoGeo.com](mailto:JosePablo.George@PrestoGeo.com)

<sup>2</sup>Reynolds Presto Products/Presto Geosystems/USA, Director; e-mail:

[Michael.Dickey@PrestoGeo.com](mailto:Michael.Dickey@PrestoGeo.com)

### **ABSTRACT**

The mining industry faces unique challenges to improve production output while navigating environmental, social, and governance (ESG) issues. When it comes to sustainable development, operation, and closure, the industry faces myriad challenges—such as poor soil conditions, weak subgrades, and other geotechnical challenges that can complicate efforts to meet ESG goals.

In this regard, some of the more common geotechnical challenges that sites must contend with include constructing and maintaining heavy-duty haul roads, stabilizing and protecting slopes, tailings management, and site reclamation. Compared to conventional methods, integrating geosynthetics into designs can help achieve a more sustainable approach to overcome these geotechnical challenges.

Geosynthetics can be used in mine closure and reclamation design to improve resilience of closed facilities against extreme weather events and provide valuable protection against the long-term effects of climate change. This article discusses case studies demonstrating how geosynthetics have been successfully used at mining sites to facilitate sustainable practices that improve performance, reduce operational costs, improve long-term resilience, and reduce overall emissions.

### **INTRODUCTION**

Incorporating geosynthetics into mine site designs, throughout operation, and in closure planning can provide structural resiliency and reduced maintenance while helping transition to sustainable best practices.

Geosynthetics can benefit the construction of haul roads that will be used not only during active mining operations, but also during the closure and post-closure phases. This technology can improve bearing capacity and eliminate excessive rutting, reduce material quantities needed for construction, and in many cases, allow for beneficial reuse of certain onsite materials, such as waste rock, overburden, or granular tailings, thereby reducing costs and emissions associated

with handling and transporting conventional aggregate materials. This savings is especially important with inflation-related cost increases and supply-chain interruptions and shortages.



**Figure 1. Energy dissipaters incorporated as part of a concrete-filled geocell mine channel, Peru**

In establishing permanent stormwater collection and conveyance systems for post-closure planning, specialized geosynthetic products such as geocells can provide protection on oversteepened slopes, provide resistance against sliding, and protect against erosion on surfaces otherwise too steep to support vegetation. They can also be customized to handle severe hydraulic conditions beyond the capabilities of many other channel lining alternatives such as the system shown in **Figure 1**. The case studies presented herein illustrate just a small sliver of the potential applications for which geosynthetics might be used in closure and post-closure activities. It is in the interest of the mining industry to continue to explore practical and innovative uses of geosynthetic products during closure planning, and previous project successes suggest there is a place for geosynthetics in helping mining companies transition to sustainable practices and develop resilient design strategies for long-term post-closure care and reclamation.

This article discusses two case studies demonstrating how geosynthetics have been successfully used at mining sites to facilitate sustainable practices that improve performance, reduce operational costs, improve long-term resilience, and reduce demands on natural resources.

The first case study summarizes geosynthetics used for channel armoring, highlighting their resilience when facing record storm events, and compares them to other channel lining solutions.

The second case study examines stabilization of a haul road and highlights how geosynthetics were used to reduce the overall cross-section thickness while improving long-term operational performance.

## **CASE STUDY 1**

**Channel armoring... Mine Closure Channel, Guatemala: geocells and non-woven geotextile integrated into strategy for long-term stormwater management at closed mine.**



Geosynthetics can be incorporated to handle high-flow stormwater in remote locations, and their long-term resiliency makes them ideal for mine closure applications where environmental restrictions hold sites to consistent and permanent high performance, yet site access often only allows for occasional monitoring post-closure. Expanded durability standards are especially important with increased frequency of record storm events, and if either seismic activity or differential settlement is expected. As our case study will discuss, this mine site in Guatemala experienced record storms and strong seismic activity, and the geosynthetically enhanced channel armoring delivered consistent performance that stood up to the challenges.

A remote mine site in Guatemala was planning for closure, and their channels had anticipated hydraulic flow of 425 cubic feet per second (cfs), and a 16.86 feet per second (f/s) velocity over a length of over 1,300 feet. There was a rapids included in the channel, and the client wanted to allow for excavator entry as needed for future cleanout. The mine site was originally considering an 8-inch reinforced, poured concrete channel, and looked to optimize design while maintaining a trapezoidal channel formation. While design calculations supported a 4-inch system to allow excavator support, the mine site preferred a 6-inch depth for additional factor of safety. This was still 2 inches thinner than originally budgeted, so it already offered considerable savings in concrete costs.

The design included a nonwoven geotextile as separation layer, 6-inch geocells with polypropylene tendons and load transfer system, and 4,000-psi concrete. The geosynthetics included in the design allowed for a resilient and fully armored, seamless channel without the need for expansion joints and the potential failure zones seen with traditional poured channels. The channel is in its third year of performance without incident, even with record storm events and strong seismic activity.

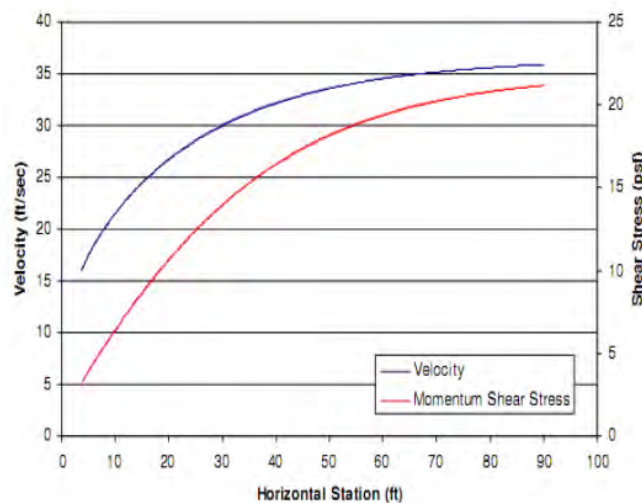


**Figure 2. Hydraulic conditions during 114.5 cfs geocell channel testing at CSU**

**Comparison of channel lining options.** High-performing geocells have been rigorously tested for channel armoring, allowing stability at severe hydraulic conditions and sheer stresses, with a thin cross-section. Colorado State University's Engineering Research Center ran hydraulic testing for a number of channel lining materials, including geocell concrete channels. At the conclusion of the test matrix, which included severe hydraulic conditions, it was determined that the performance threshold for the 3-inch geocell with concrete infill had not been exceeded for

the highest flows capable of being delivered to the test flume (Colorado State University, 2009) **Figures 2 and 3.**

This included flow velocities of around 35.7 ft/s and shear stresses of 20.9 pounds per square foot (psf). Performance threshold was defined as the point at which deformation, soil loss, or loss of intimate contact with the embankment sub-grade occurred. Testing discharges corresponded to quantifiable overtopping flow depths.

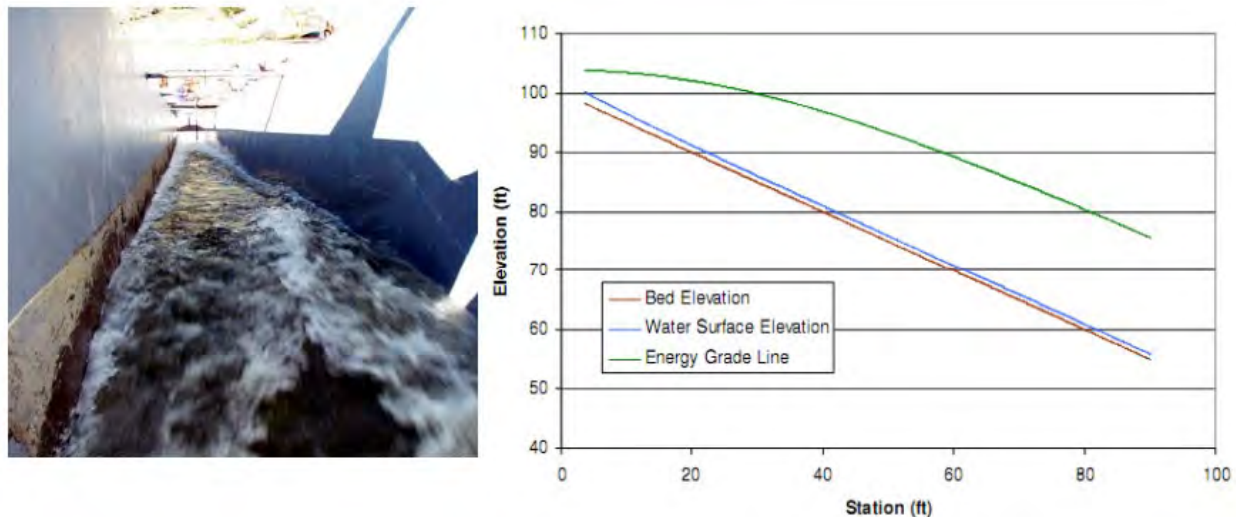


**Figure 3. hydraulic testing of geocell channels at Colorado State University**

Geocells with concrete infill have the long-term resilience and economy to be considered a best practice and is considered among the solutions with “highest long-term performance results” from the U.S. Bureau of Reclamation’s 10-year canal lining study (SWS, 2014).

**Table 1** provides a comparison of allowable velocities and shear stresses for various channel lining alternatives.

**Table 1. Channel Lining Comparison of Allowable velocity and shear stress**

Boundary type	Allowable Velocity (ft/s)	Allowable shear stress (psf)	Relative cost
Straw with net	1-3	0.45	\$
Coconut fiber with net	3-4	2.25	\$-\$\$
Fully vegetated	8-21	8	\$-\$\$
Gabions	1-19	10	\$\$\$-\$\$\$\$
Concrete	18 and greater	12.5	\$\$\$-\$\$\$\$
Geocells with concrete	Greater than 35	Greater than 20	\$\$\$-\$\$\$\$

(United States Department of Agriculture, 2007)

## CASE STUDY 2

**load support application: geocells and high-strength woven geotextile integrated into heavy duty haul road at active mine, Suriname.** This case study discusses how geosynthetics were incorporated into the design of a haul road at an active mine, with heavy loading over soft subgrade, and local scarcity of quality angular aggregates. The prepared subgrade strength exhibited a California Bearing Ratio (CBR) value of 2.5%, consisting of saprolite and clay. Anticipated loading included Cat 785 haul trucks (275-ton vehicles) and the haul road useful design life of 10 years at 250 movements per day. Surface loading calculated to be 151,750 pounds (lbs), with surface contact pressure 101 pounds per square inch (psi), and 55% of the total 550,000 lbs weight on the rear axle of the haul trucks. Sticky clay soils and tropical rains made the road impassable with every storm event, and adequate aggregate materials for standard construction solutions were not to be found nearby.

The mine engineers were looking at wheel load-based cover estimates for the haul road, as suggested in **Figure 4** and standard design guidelines (Tannent, et al 2001). The CAT 785D loading, with less than 3% subgrade strength suggested total cover around 1.5 meters (4.9 feet) thick.

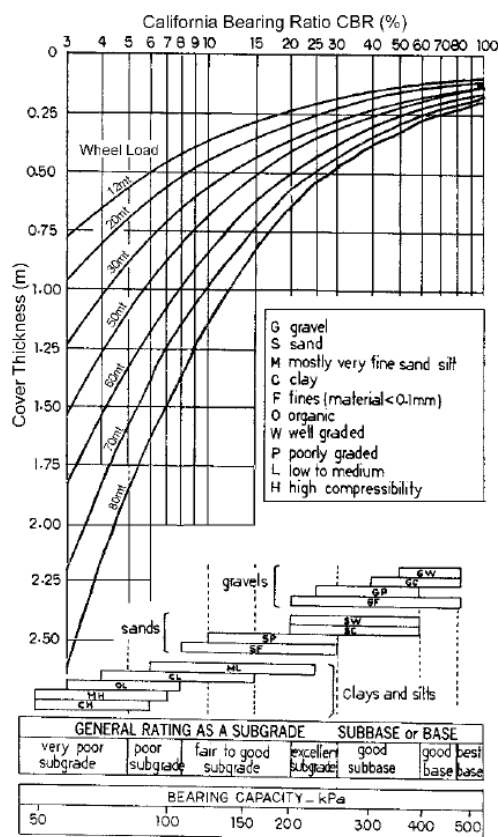


**Figure 4. wheel load-based cover estimates for haul roads**

Geocells offered a value engineering solution, with just one layer of 6-inch geocells being able to support the heavy haul truck loading over soft subgrades and reduce total thickness to 30 inches. Geocells dramatically increase the shear resistance of the infill, which allows the use of lower-quality fill to carry concentrated loads that would otherwise require crushed aggregate to

prevent localized, near-surface shear failure. Per client preferences, a 4,800 pounds per foot (lbs/ft) woven geotextile was followed by compacted, locally available coarse river sand, known as small miners residue, and geocells.

The results of the geocell installation offered great reduction in the total cross-section needed, reducing it by 35% with coarse sand wear surface, and by 50% with aggregate wear surface. The **estimated savings in construction costs** are around \$100,000 per mile. Since installation, there has been **a reduction in road maintenance costs of over 65%**. There are no down times due to rain events, and there have not been any deep ruts observed since installation. There is less vehicle maintenance, and less fuel required. Better productivity and operational costs, safer site conditions, and the expansion opened before the scheduled date, and under budget.

When used as intended, geosynthetics are engineered solutions that enhance soil properties and reduce demands placed on natural resources. However, it is important that the product be properly formulated for long-term stability, so as to preclude any potential release of chemicals or microplastics into the environment in the future. In the case of the Surname project, product quality requirements included an expanded set of durability parameters including resistance to oxidation (per EN ISO 13438, with estimated durability greater than 50 years), resistance to weathering (per EN 12224, with exposure to weathering conditions more intense than naturally occurring conditions), and Environmental Stress Crack Resistance of over 5,000 hours (per ASTM D1693), all to ensure the long-term stability in the environment. (ASTM and ISO, 2022).

**Comparison of Haul Road Alternatives.** Stable mining access and haul roads deliver faster cycle times, with less rolling resistance, less expenses needed for fuel and tires, and less structure required. Traditional cross-sections require frequent maintenance and high-quality aggregates. If high-quality, angular aggregates are readily available on site, a geogrid can offer structural benefits to the haul road. Quality geogrids and aggregates interlock to create a mechanically stabilized layer to help distribute loading and increase bearing capacity, controlling movement in the areas interacting with the geogrid layer. If properly sized aggregates with high friction angles are not available, other geosynthetic options such as geocells or a combination of geocells and geotextiles can offer a value engineering solution to meet project objectives.



**Figure 5. side-by-side testing of HDPE geocells and aluminum geocells at the Waterways Experiment Station, Vicksburg, MS, circa 1979**



Geocells have been used for load support and foundation applications worldwide for more than 40 years. The early applications of geocells consisted primarily of stabilized, expedient sand roads for military vehicles, using sand as the geocell infill, as in **Figure 5**. In the early 1990s, the U.S. Army deployed over 6 million square feet of geocells to stabilize the shifting desert sands and provide mobility for troops and military vehicles. By utilizing the principle of soil confinement to enhance soil strength, geocellular confinement turns sand into a load-supporting composite structure that can support heavy vehicle loading under repeated load cycles.

The use of on-site salvaged material as geocell infill, such as sand or other granular material, can provide a value-engineering approach compared to traditional methods, while reducing cross-section thickness and the associated excavation and material costs, and increasing installation speed. **Figure 6** provides a comparison of four structurally equivalent unpaved road sections over a weak subgrade with CBR value of 0.5%, illustrating relative differences in section thicknesses, emissions, and general costs.



**Figure 6. Load support cost-benefit comparison (Presto Geosystems 2022)**

**Figure 6 from left to right:** Traditional cross-section of unconfined aggregates; Aggregates with geogrid and high-strength woven geotextile at subgrade; 6-inch geocell with 2 to 3 inches of aggregate wear surface, aggregate infill, and woven geotextile at subgrade; 6-inch geocell with 2 to 3 inches of aggregate wear surface, on-site salvaged material (OSM), and woven geotextile at subgrade. All subgrade strength values of 0.5% CBR. As shown, the use of locally available sand or low-quality waste rock as infill for geocells can offer considerable savings in construction costs accompanied by an overall reduction in emissions, reducing the total section thickness to only 15 inches, and limiting aggregate use to just the wearing course.

## RESULTS AND DISCUSSION

In the foregoing sections, two case studies were presented that provided examples where geosynthetic products were successfully used at mining sites in support of sustainable practices. In each case, sustainable practices were generally evaluated within the context of four possible benefits, including: 1) reductions in demands on natural resources; 2) improvements in long-term resilience; 3) improved performance; and 4) reduced operational costs. A summary of the findings from each case study is provided in **Table 2**.

**Table 2 Summary of Sustainable Practices, Case Studies 1 and 2**

Sustainable Practice	Case Study 1: Mine Closure Channel, Guatemala	Case Study 2: Mine Haul Road, Suriname
Reduction in demand on natural resources	Overall volume of concrete needed for channel lining reduced by 25%; required formwork was minimal	Overall volume of aggregates / fill for road construction reduced by 50%; overall reduction in construction emissions
Improvement in long-term resilience	Resilience against major storms; capability to withstand flow velocities over 35 ft/s and shear stresses over 20 psf; long-term post-closure protection of storm water management systems	Reduction in excessive rutting following storm events; significant decrease in road maintenance and repair due to stabilized road base
Performance improvements	Relatively easy to configure / customize to fit specific site needs; energy dissipaters can be incorporated to withstand extreme flow conditions	Smooth / stable access road; reduced rolling resistance; improved fuel efficiency; reduction in truck emissions
Reduction in operational costs	Reduced failure risk and post-closure costs associated with repair / maintenance of storm water management, collection, and conveyance systems	65% reduction in road maintenance costs; overall reduction in wear on haul trucks

## CONCLUSION

Comprehensive mine planning and associated infrastructure design can help make effective use of capital while reducing risk and mitigating environmental impact. The mining industry faces unique challenges to improve production output while navigating environmental, social, and governance (ESG) issues. When it comes to sustainable development, operation, and closure of mines, the industry faces myriad challenges—not the least of which are poor soil conditions, weak subgrades, and other geotechnical challenges that can complicate miners' efforts to meet ESG goals. Mine sites must realize safe, productive, and reliable operations while optimizing return on investment. Geosynthetics can offer technical and economic advantages to mine operations, whilst helping sites transition towards a higher degree of sustainability.

In this regard, geosynthetics are an essential ingredient to sustainable mining, and can be invaluable as mine operators contend with geotechnical challenges such as constructing and maintaining heavy-duty haul roads, stabilizing and protecting slopes, tailings management, and site reclamation. Compared to conventional methods, integrating geosynthetics into designs can help achieve a more sustainable approach to overcome many of these geotechnical challenges. On the other hand, purposeful insertion of non-biodegradable substances into the environment as a method to **increase sustainability** may sound counterintuitive; however, it is important to distinguish **responsible** use of engineered materials designed for long-term performance in the environment from that of single-use plastics that have received the brunt of growing anti-plastic sentiment in recent times. When used as intended, geosynthetics are engineered solutions that enhance soil properties and reduce demands placed on natural resources and can therefore be considered best management practice for mine sites in support of achieving ESG goals. It is understood then, that geosynthetic products must also be properly formulated for long-term stability in the environment, so as to preclude release of chemicals or microplastics into the environment. This can be accounted in the design phase by incorporating strict product quality requirements into project specifications and enforcing quality requirements during construction.

## ACKNOWLEDGEMENTS

We extend deepest gratitude to Steve Webster at the Waterways Experiment Station and Gary Bach from Presto Products Company, for their pioneering efforts in the late 1970s in devising a method to weld polyethylene strips to form the cellular structure that became geocell technology.

A version of this article was previously published in *Planning for Closure* 2022.

## REFERENCES

Colorado State University, Engineering Research Center (2009) *Hydraulic Testing and Data Report for GEOWEB 30v with Concrete*, research summary courtesy Presto Geosystems, viewed 01 September 2022, and available <https://2y2qpw2op3o93ygu164frm9z->

[wpengine.netdna-ssl.com/wp-content/uploads/2016/10/GWCH-Geoweb-Concrete-Infill-CSU-Research-Summary.pdf](http://wpengine.netdna-ssl.com/wp-content/uploads/2016/10/GWCH-Geoweb-Concrete-Infill-CSU-Research-Summary.pdf)

Mine Haul Road in Suriname (2022), Presto Geosystems, case study viewed 01 September 2022, and available [https://www.prestogeo.com/case\\_studies/suriname-mining-haul-road/](https://www.prestogeo.com/case_studies/suriname-mining-haul-road/)

Presto Geosystems, (2022), *Cost-Benefit Comparison* graphic shared with the authors courtesy of Presto Geosystems, brand names and details removed for this article's publication. Shared as Figure 1.

Presto Geosystems, (2022), The History of Geocells, article viewed 01 September 2022, and available <https://www.prestogeo.com/blog/the-history-of-geocells/>

SWS, Storm Water Solutions, (25 August 2014), *Geocell Systems Help Rehabilitate Canals*, article viewed 01 September 2022, and available <https://www.estormwater.com/erosion-control/article/10982513/geocell-systems-help-rehabilitate-canals>

Tannant, Dwayne D. and Regensburg, Bruce, (2001), Guidelines for Mine Haul Road Design, viewed 01 September 2022, and available <https://open.library.ubc.ca/media/download/pdf/52383/1.0102562/1>

United States Department of Agriculture, Natural Resources Conservation Service, (2007) *Part 654 Stream Restoration Design, National Engineering Handbook, Chapter 8, Threshold Channel Design*, (viewed 01 September 2022 and available <https://directives.sc.egov.usda.gov/OpenNonWebContent.aspx?content=17784.wba> as a link directly to Chapter 8). Table 8-11 "Allowable velocity and shear stress for selected lining materials" referenced from 8-37.



## Effect of Spread Footing Loads on Stability of Geosynthetic-Reinforced Retaining Walls

S. Mustapha Rahmaninezhad, Ph.D.,<sup>1,2</sup> Thang Pham, Ph.D., P.E.,<sup>3</sup> Thuy Vu, Ph.D.,<sup>4</sup> Ashley Alanis,<sup>5</sup> and Alfonso A. Soto, P.E., D.GE.<sup>6</sup>

<sup>1</sup>Department of Civil Engineering, University of Texas Rio Grande Valley, One West University Blvd, Brownsville, TX 78520, USA.; e-mail: [m.rahmaninezhad@utrgv.edu](mailto:m.rahmaninezhad@utrgv.edu)

<sup>2</sup>Geotechnical Department, Terracon Consulting Inc., 1506 Mid Cities Dr, Pharr, TX 78577, USA; e-mail: [srahmaninezhad@terracon.com](mailto:srahmaninezhad@terracon.com)

<sup>3</sup>Department of Civil Engineering, University of Texas Rio Grande Valley, 1201 W University Dr, Edinburg, TX 78539, USA; e-mail: [thang.pham@utrgv.edu](mailto:thang.pham@utrgv.edu)

<sup>4</sup>Department of Civil Engineering, University of Texas Rio Grande Valley, 1201 W University Dr, Edinburg, TX 78539, USA; e-mail: [thuy.vu@utrgv.edu](mailto:thuy.vu@utrgv.edu)

<sup>5</sup>Geotechnical Department, Terracon Consulting Inc., 1506 Mid Cities Dr, Pharr, TX 78577, USA; e-mail: [ashley.alanis@terracon.com](mailto:ashley.alanis@terracon.com)

<sup>6</sup>Geotechnical Department, Terracon Consulting Inc., 1506 Mid Cities Dr, Pharr, TX 78577, USA; e-mail: [alfonso.soto@terracon.com](mailto:alfonso.soto@terracon.com)

### ABSTRACT

In the past two decades, geosynthetic-reinforced retaining (GRR) walls have been used as bridge abutments to retain soils and directly support bridge superstructures (such as girders) and traffic loads. In this construction method, the bridge superstructure rests on a spread footing on top of the GRR walls. The additional vertical pressures induced by the spread footing loads increase the pullout resistance of the geosynthetics at the front or rear of the GRR walls, which improve the internal stability. On the other hand, by increasing the induced stresses by spread footing, the compound stability of GRR walls may decrease. Limited studies have been conducted to investigate this complex and nonintuitive stability concern. The objective of this study is to investigate the effect of the spread footing loads on the internal and compound stability of GRR walls with modular block facing. The limit equilibrium (i.e., the Bishop modified method) in the ReSSA program was used to determine the possible slip surfaces and their corresponding factors of safety (*FS*) of the GRR walls subjected to spread footing loads. Parametric and analytical studies were carried out to determine how increasing the spread footing load affects the location of the possible slip surfaces and their corresponding *FS*. The results showed that the *FS* of a 5-m-tall GRR wall subjected to an example optimum spread footing load was approximately 1.5% higher than that wall without spread footing (i.e., negligible). However, by increasing the spread footing load from the optimum load to the failure load, the *FS* decreased by approximately 83%.

### INTRODUCTION

In recent years, geosynthetic-reinforced retaining (GRR) walls have been employed as bridge abutments to retain soils and directly support spread footings on the top of GRR walls (instead of using traditional deep foundations) (Helwany et al., 2003; Lee and Wu, 2004; Zheng Xu et al., 2018; Hatami and Doger 2021; Rahmaninezhad and Han, 2021). The main advantages of

supporting spread footings directly on the top of the GRR walls (as compared with using the deep foundation option) are to reduce the overall cost and construction time of a project and minimize bumps at the end of bridge decks (Rahmaninezhad, 2019). Usually, these bumps occur due to a differential settlement between pile-supported abutments and approach slabs.

According to the FHWA design guideline (Berg et al., 2009) for GRR walls, the tensile force in geosynthetic reinforcement is computed based on the lateral earth pressure ( $\sigma_h$ ) and the tributary area of this pressure. The FHWA guideline proposes the following equation for the GRR walls subjected to spread footing loads to calculate the lateral earth pressure at each level.

$$\sigma_h = K_a (\gamma Z + \Delta\sigma_v) + \Delta\sigma_h \quad \text{Eq. 1}$$

where  $K$  is coefficient of the lateral pressure;  $\gamma Z$  is vertical pressure due to the overburden pressure; and  $\Delta\sigma_v$  and  $\Delta\sigma_h$  are the vertical (normal) and horizontal (shear) pressures induced by the spread footing loads. **Figure 1** shows the distribution of vertical pressure induced by footing loads on top of the GRR wall at a 2:1 (vertical to horizontal) pyramidal distribution pattern.

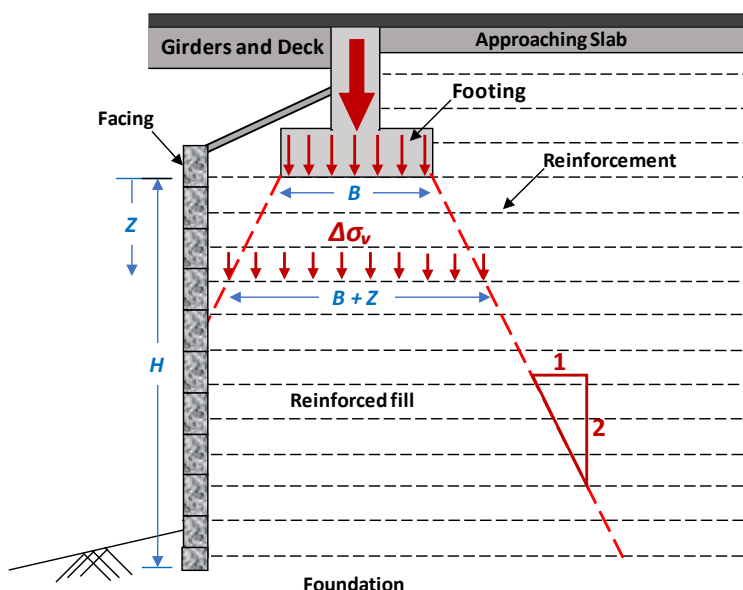


**Figure 1. 2:1 Pyramidal distribution adopted in FHWA design guideline (modified from Berg et al., 2009)**

In the GRR walls, the reinforced fill is divided into active and stable zones by a failure surface (location of maximum tensile force lines). The active zone tends to slide down (under its self-weight and surcharge on top of the wall), while the anchored reinforcements in the stable zone stabilize the active zone (Han, 2015). Based on the FHWA guideline (Berg et al., 2009), there is a bi-linear failure surface (to calculate the internal stability of the walls) starting from the outer edge of the spread footing and developing through the reinforced fill into the toe of the wall, as shown in **Figure 2**. In GRR walls, if the sum of the width of the spread footing ( $B$ ) and the offset distance ( $d$ ) is greater than  $H \times \tan(45^\circ - \phi/2)$  where  $\phi$  is the peak soil friction angle, the location of the critical failure surface needs to be modified to extend to the back edge of the spread footing.

Limit Equilibrium (LE) methods are the most commonly used method to evaluate the global and compound stability of GRR walls (Han, 2015; Han 2021). Han and Leshchinsky (2004

and 2010) and Leshchinsky and Han (2004) proved that numerical and LE methods generally resulted in similar outcomes when they are used to analyze GRR walls. Xiao et al. (2016) demonstrated that the failure surface estimated using the LE method has an agreement with observed failure surfaces in the GRR walls under footing loads in a plane strain condition.

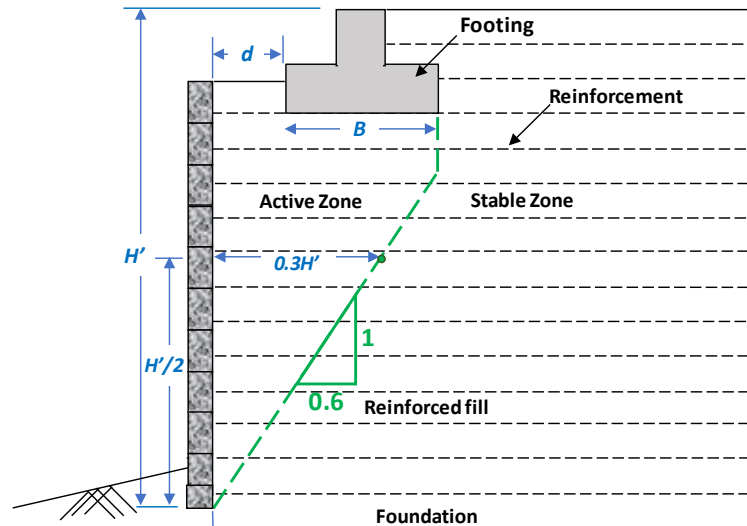


**Figure 2. Potential failure surface (modified from Berg et al., 2009)**

Xie et al. (2019) proposed a LE approach to calculate the bearing capacity of strip footings on the GRR walls. Rahmaninezhad and Han (2021) found an exponential relationship between the calculated factor of safety using LE method and the maximum lateral facing deflection of the GRR walls under footing loading. Rahmaninezhad et al. (2020 and 2021) used LE analysis to investigate the effect of the embedment depth, width, and the offset distance of the spread footing on the possible failure surfaces pattern and the compound stability of GRR walls with modular block facing.

The objective of this study is to find the impact of the magnitude of spread footing load on the internal and compound stability of GRR walls. The LE method incorporated in the ReSSA software Version 3.0, developed by the ADAMA Engineering, Inc. (2008), was used to determine the possible slip surfaces and the corresponding factors of safety (*FS*) of GRR walls subjected to different magnitudes of spread footing loads using Bishop's simplified method (Bishop, 1955). Parametric and analytical studies were conducted to determine an optimum spread footing load that generates the maximum *FS*. In this study, other aspects of GRR wall stability (such as internal stability, sliding, and overturning) were not considered for evaluation.

## INTERNAL AND COMPOUND STABILITY

**Limit Equilibrium (LE) Methods.** LE methods have been commonly used to analyze the stability of the GRR walls (Xiao et al., 2016; Song et al., 2017; Gaudio et al., 2018; Hung et al., 2020). Bishop's simplified method (Bishop, 1955) and Spencer's method (Spencer, 1981) are two prevalent methods for LE analysis. Bishop's simplified method assumes a circular failure surface. However, a two-part or three-part wedge failure is used in Spencer's method. Rahmaninezhad (2019) showed that the failure surface calculated using Bishop's simplified method has a better

agreement with observed failure surfaces in GRR walls under footing loads as compared with Spencer's method.

**Internal Stability.** Internal stability analysis assumes the failure surface passes through the reinforced fill. The geosynthetic reinforcement is considered to provide tensile resistance against the movement of the active zone. The three different internal failure modes in GRR walls are tensile rupture, pullout from the stable zone, and pullout from the face (as shown in **Figure 3**). The horizontal ( $\Delta\sigma_h$ ) and vertical ( $\Delta\sigma_v$ ) pressures induced by the spread footing loads (on top of GRR walls) may increase the tensile force and the pullout resistance, respectively. In GRR walls subjected to footing loads, the maximum tensile force ( $T_{max}$ ) and pullout resistance ( $T_{pullout}$ ) of geosynthetic reinforcement can be estimated using the following equations:

$$T_{max} = K_r (\sigma_v + \Delta\sigma_v) S_v \quad \text{Eq. 2}$$

$$T_{pullout} = 2F^* \alpha (\sigma_v + \Delta\sigma_v) L_a R_c \quad \text{Eq. 3}$$

Where  $\sigma_v$  is vertical pressure;  $F^*$  is pullout resistance (or friction-bearing-interaction);  $\alpha$  is a scale effect correction factor;  $\sigma_z$  is normal pressure applied on the geosynthetic;  $\Delta\sigma_v$  is pressure induced by the spread footing load;  $L_a$  is anchorage length of the geosynthetic reinforcement; and  $R_c$  is percent coverage of the geosynthetic area in the running length of the wall.

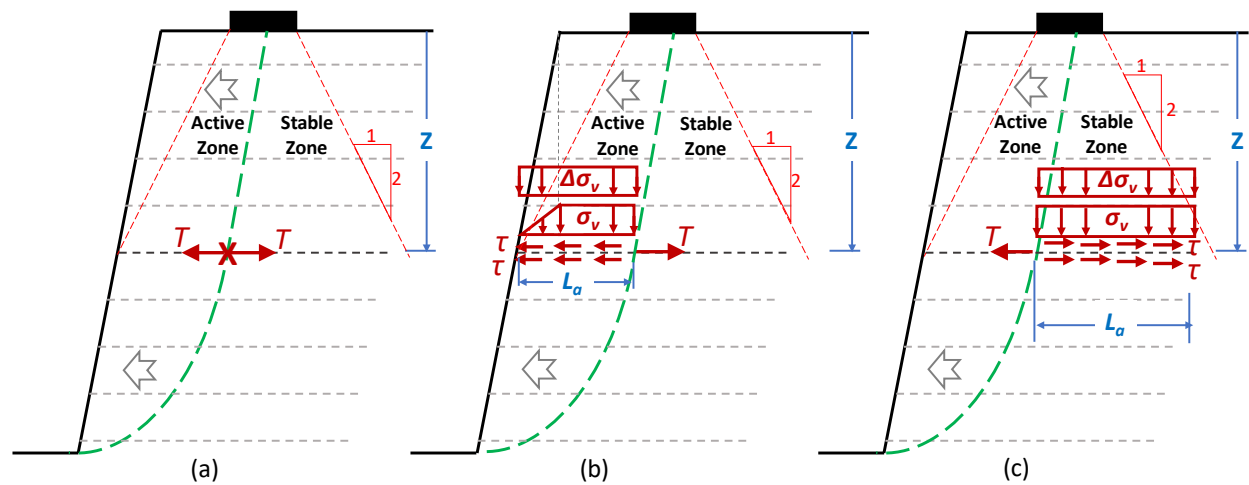


**Figure 3. Internal failure: (a) rupture, (b) front pullout, and (c) rear pullout (modified from Han and Leshchinsky, 2006).**

**Compound Stability.** The compound stability is usually determined utilizing rotational or wedge analyses using LE programs (e.g., ReSSA) to evaluate potential failure surfaces. The FHWA design guideline strongly suggests that the compound failures should be considered for GRR walls with complex conditions such as walls subjected to footing loads (Berg et al., 2009).

**Factors of Safety (FS).** The FS for GRR walls is defined in terms of shear stress, shear force, and moment, as follows (Han, 2015):



$$FS = \frac{\text{Shear Strength}}{\text{Shear Stress}} \quad \text{Eq. 4}$$

$$FS = \frac{\text{Resisting Force}}{\text{Driving Force}} \quad \text{Eq. 5}$$

$$FS = \frac{\text{Resisting Moment (provided by soil and reinforcement)}}{\text{Driving Moment}} \quad \text{Eq. 6}$$

## PARAMETRIC STUDY

**Modeling.** The geometry and material properties of the example walls used in this study are shown in **Figure 4**. The model walls have a height ( $H+h$ ) of 5.8 m. The embedment depth of the footing ( $h$ ) was 1.2 m. In these walls, the foundation soil was assumed to have high shear strength. This assumption prevented any possible failure in the foundation soil below the GRR wall. The length of reinforcement layers increased linearly from the bottom with a 1:1 slope toward the top of the walls. The vertical spacing ( $S_v$ ) between reinforcement layers was 0.4 m. The offset distance between the back of the wall facing and the front edge of the footing ( $d$ ) and the magnitude of the footing pressure ( $q$ ) induced by spread footing load ( $P$ ) varied. In this parametric study, one parameter was changed from the baseline case while all others were constant.

Xiao et al. (2016) and Rahmaninezhad (2019) suggested calibrating the cohesion of the interface between the geogrid and the blocks by the mechanical or frictional connection mode with the test data. In this study, the interface cohesion ( $c_f$ ) was determined as 75 kPa for the walls with block facing with mechanical connection. Also, the interface friction angle ( $\phi_f$ ) between blocks was determined as 44°.

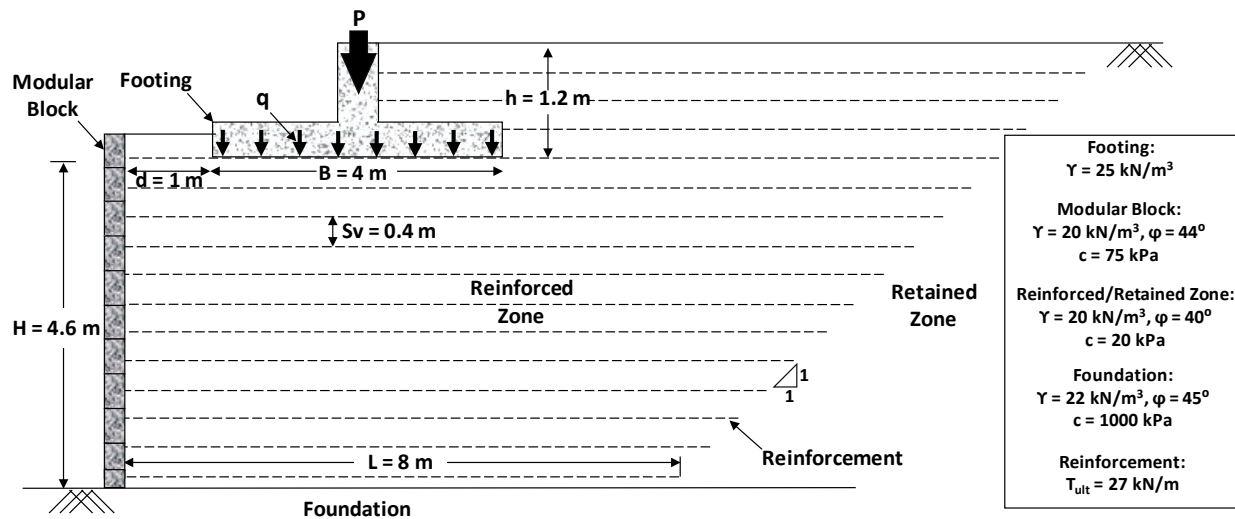


**Figure 4. Dimensions and material properties of the example wall**

**Results.** The possible failure surface and the corresponding  $FS$  of GRR walls under spread footing pressure were determined using Bishop's simplified method. However, this approach does not consider the footing pressure-induced confining stress effect on the soil and reinforcement resistance. **Figure 5** shows the locations and shapes of potential failure surfaces within GRR walls at different magnitude of the footing pressure ( $q$ ). **Figure 5** indicates that when  $q$  was 40 kPa or less, the walls generated a deep failure mechanism using the Bishop's simplified method. In these

walls, the failure surfaces began from the retained zone and developed into the reinforced zone towards the wall facing toe.

When  $q$  was 45 kPa or greater, the failure surface using Bishop's simplified method was shallower than for walls with  $q = 40$  kPa or less. In these walls, the possible failure surface passed from the footing and developed into the reinforced zone towards the wall facing toe. The footing with a greater  $q$  resulted in a slightly shallower failure zone than those with a smaller  $q$ , as shown in **Figure 5**. For example, when  $q$  was 45 kPa, the failure surface passed from beyond the far end of the footing and developed into the reinforced zone towards the walls facing toe. However, when  $q$  was 45 kPa, the failure surface passed from the center of the footing and developed into the reinforced zone towards the wall facing toe.

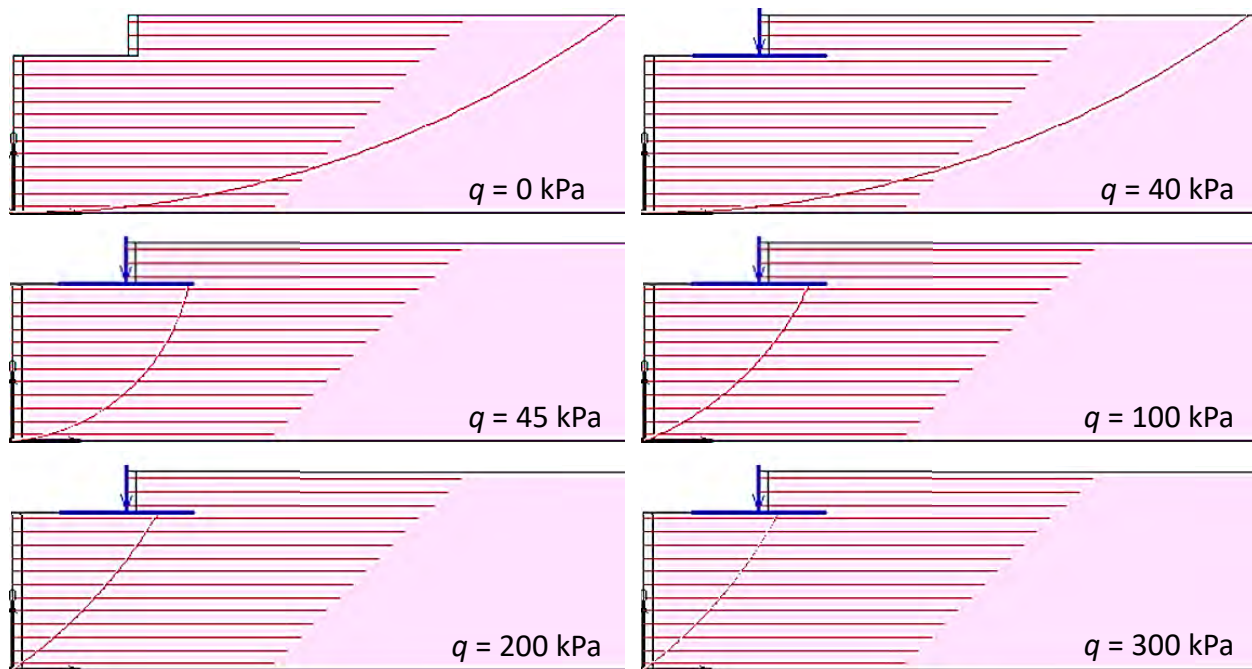


**Figure 5. Locations and shapes of potential failure surface**

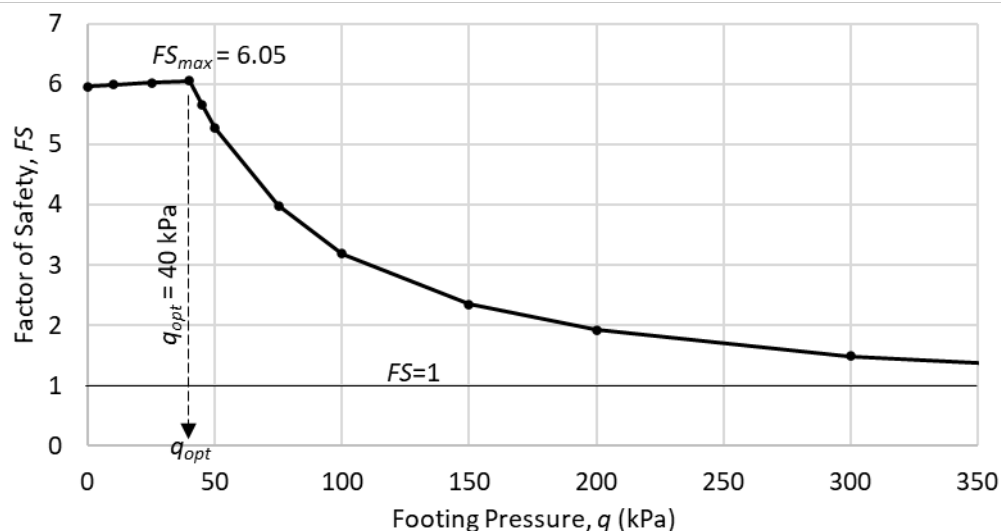


**Figure 6. Calculated factor of safety ( $FS$ ) versus footing pressure ( $q$ )**

**Figure 6** presents the calculated  $FS$  of GRR walls (using Bishop's simplified method) versus  $q$ . The results indicate that, with increasing  $q$  from 0 to 40 kPa, the  $FS$  slightly increased from about 5.9 to 6.1. Then, with increasing  $q$  (greater than 40 kPa), the  $FS$  significantly decreased. For instance, when the magnitude of  $q$  was 50, 100, 200, and 300 kPa, the corresponding  $FS$  values were 5.3, 3.2, 1.9, and 1.4, respectively. In this case, 40 kPa can be considered as an optimum spread footing pressure ( $q_{opt}$ ) that resulted in the highest  $FS$ .

## CONCLUSION

The effect of the magnitude of spread footing pressure ( $q$ ) on the stability of GRR walls was investigated in this parametric study. The Limit Equilibrium (LE) program, ReSSA version 3.0, developed by ADAMA Engineering, Inc., was employed to determine the potential failure surfaces and calculate the factors of safety ( $FS$ ) using Bishop's simplified method. From this parametric study, the following conclusions can be made:

1. When  $q$  was low, the failure surfaces, using Bishop's simplified method, began from the retained zone and developed into the reinforced zone towards the wall facing toe.
2. Under a large magnitude of  $q$ , failure surfaces began from behind the footing and developed into the reinforced zone towards the wall facing toe.
3. Generally, the walls with lower magnitude of  $q$  had a deeper failure surface comparing with those with higher  $q$ , using Bishop's simplified method.
4. When a GRR wall is subjected to a low magnitude of  $q$ , the  $FS$  is slightly higher than the wall without footing pressure.
5. Increasing  $q$  to a larger magnitude, the  $FS$  decreased significantly.
6. The LE approach used in this study considers only force and moment equilibrium and did not consider the stress level in the reinforced and retained soils or the loading effects on their behavior. The authors will conduct additional studies using a numerical method approach to verify the results of this study and to evaluate the stress-deformation behavior of the GRR walls under footing loads.

## REFERENCES

- ADAMA Engineering, Inc, (2008). ReSSA Software Version 3.0 Newark, Delaware, USA.
- Berg, R., Christopher, B., and Samtani, N. (2009). *Design and construction of mechanically stabilized earth walls and reinforced soil slopes, vols. 1 & 2*. Report No: FHWA-NHI-10-024. FHWA, U.S. Department of Transportation.
- Bishop, A.W. (1955). The use of the slip circle in the stability analysis of slopes. *Geotechnique* 5, 7–17.
- Gaudio, D., Masini, L. and Rampello, S., (2018). A performance-based approach to design reinforced-earth retaining walls. *Geotextiles and Geomembranes*, 46(4), 470-485.
- Han, J. (2015). *Principles and practice of ground improvement*, John Wiley & Sons.
- Han, J. (2021). Limit equilibrium analysis and design of geosynthetic-reinforced fill walls under special conditions. *Indian Geotechnical Journal*, 51(1), 50-62.

- Han, J. and Leshchinsky, D. (2004). Limit equilibrium and continuum mechanics-based numerical methods for analyzing stability of MSE walls. In *17<sup>th</sup> ASCE Engineering Mechanics Conference*, 13-16.
- Han, J. and Leshchinsky, D. (2010). Analysis of back-to-back mechanically stabilized earth walls. *Geotextiles and Geomembranes*, 28(3), 262-267.
- Hatami, K., and Doger, R. (2021). Load-bearing performance of model GRS bridge abutments with different facing and reinforcement spacing configurations. *Geotextiles and Geomembranes*, 49(5), 1139-1148.
- Helwany, S.M., Wu, J.T. and Froessl, B. (2003). GRS bridge abutments—an effective means to alleviate bridge approach settlement. *Geotextiles and Geomembranes*, 21(3), 177-196.
- Hung, W.Y., Yang, K.H., Nguyen, T.S. and Pham, T.N.P. (2020). Performance of geosynthetic-reinforced soil walls at failure. *Journal of GeoEngineering*, 15(1), 13-29.
- Lee, K.Z., and Wu, J.T. (2004). A synthesis of case histories on GRS bridge-supporting structures with flexible facing. *Geotextiles and Geomembranes* 22 (4), 181-204.
- Leshchinsky, D. and Han, J. (2004). Geosynthetic reinforced multitiered walls. *Journal of Geotechnical and Geoenvironmental Engineering*, 130(12), 1225-1235.
- Rahmaninezhad, S. M. (2019). *Geosynthetic-reinforced retaining walls with flexible facing subjected to footing loading*, Doctoral dissertation, University of Kansas.
- Rahmaninezhad, S.M. and Han, J. (2021). Lateral facing deflections of geosynthetic-reinforced retaining walls under footing loading. *Transportation Geotechnics*, 30, p.100594.
- Rahmaninezhad, S.M., Han, J., and Al-Naddaf, M., (2020). Limit equilibrium analysis of geosynthetic-reinforced retaining walls subjected to footing loading. *Geo-Congress 2020: Engineering, Monitoring, and Management of Geotechnical Infrastructure*. 464-471.
- Rahmaninezhad, S.M., Han, J., Al-Naddaf, M., and Mamaghani, J. (2021). Limit equilibrium analysis of geosynthetic-reinforced retaining wall-supported footings. *Geosynthetic Conference 2021 Proceedings*. 691-701.
- Song, F., Liu, H., Chai, H. and Chen, J. (2017). Stability analysis of geocell-reinforced retaining walls. *Geosynthetics International*, 24(5), 442-450.
- Xiao, C., Han, J. and Zhang, Z. (2016). Experimental study on performance of geosynthetic-reinforced soil model walls on rigid foundations subjected to static footing loading. *Geotextiles and Geomembranes*, 44(1), 81-94.
- Xie, Y., Leshchinsky, B., and Han, J. (2019). Evaluation of bearing capacity on geosynthetic-reinforced soil structures considering multiple failure mechanisms. *Journal of Geotechnical and Geoenvironmental Engineering*, 145(9), p.04019040.
- Xu, P., Hatami, K., Bao, J. and Li, T. (2020). Bearing capacity and failure mechanisms of two-tiered reinforced soil retaining walls under footing load. *Computers and Geotechnics*, 128, p.103833.
- Zheng, Y., Fox, P. J., and McCartney, J. S. (2018). Numerical simulation of deformation and failure behavior of geosynthetic reinforced soil bridge abutments. *Journal of Geotechnical and Geoenvironmental Engineering*, 144(7), 04018037-04018037.



# Migrating from the Simplified Method to the Stiffness Method for Internal Stability Design of MSE walls

Richard J. Bathurst<sup>1</sup> and Tony M. Allen<sup>2</sup>

<sup>1</sup>GeoEngineering Centre at Queen's-RMC, Kingston, Canada; e-mail: [bathurst-r@rmc.ca](mailto:bathurst-r@rmc.ca)

<sup>2</sup>WSDOT (retired), Olympia, WA, USA; e-mail: [tonyallen1957@gmail.com](mailto:tonyallen1957@gmail.com)

## ABSTRACT

In the most recent edition of the AASHTO LRFD Bridge Design Specifications published in 2020, the Stiffness Method is specified for the internal stability design of geosynthetic MSE walls. A key feature of this approach is the use of the creep-reduced tensile stiffness of the reinforcement as a key parameter to compute the magnitude of reinforcement loads under operational conditions. This is a paradigm shift from the Simplified Method which is based on the strength of the soil. The paper describes the essential features of the Stiffness Method. The resulting margins of safety when tensile strength and pullout limit states are just satisfied in LRFD using the Simplified and Stiffness Methods are also compared probabilistically.

## INTRODUCTION

The Stiffness Method is specified in the current edition of the AASHTO LRFD Bridge Design Specifications (AASHTO 2020) for the calculation of reinforcement loads under operational conditions for internal stability design limit states of geosynthetic mechanically stabilized earth (MSE) walls. This is a paradigm shift from the Simplified Method that appears in earlier editions of the AASHTO specifications (i.e., AASHTO 2017). The Simplified Method computes loads based on the soil peak friction angle for geosynthetic MSE walls. The signature feature of the Stiffness Method, as the name implies, is the stiffness of the reinforcement. This approach recognizes that it is the stiffness of the reinforcement and not the strength of the soil that has the dominant influence on the magnitude of the maximum tensile load in each reinforcement layer under operational conditions.

## PRELIMINARIES

The AASHTO code adopts a load and resistance factor design (LRFD) approach in which limit states for a single load case are expressed as:

$$\phi R_n - \gamma_Q Q_n \geq 0 \quad (1)$$

Here,  $R_n$  and  $Q_n$  are nominal resistance and load values, and  $\phi$  and  $\gamma_Q$  are corresponding resistance and load factors, respectively. The expectation in LRFD is  $\phi \geq 1$  and  $\gamma_Q \geq 1$ . Figure 1 shows the limit states that are associated with the internal stability design of geosynthetic MSE walls. The wall geometry in this figure is purposely simple to focus attention on the main differences using the two methods. With the exception of the soil failure limit state, all limit states appear in both the Simplified and Stiffness Methods. The second major difference between the methods is the calculation of the maximum tensile load in a reinforcement layer denoted as  $T_{max}$ .

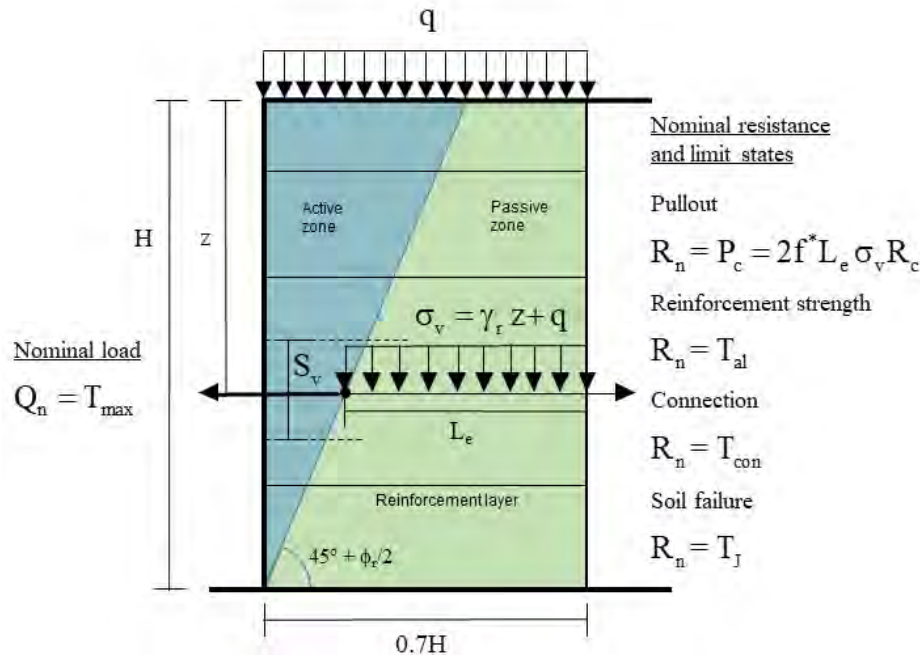


**Figure 1. Geometry and limit states for geosynthetic MSE wall.**  $Q_n$  = nominal reinforcement tensile load (e.g., kN/m),  $R_n$  = nominal resistance (e.g., kN/m),  $T_{max}$  = maximum tensile load,  $P_c$  = pullout capacity (e.g., kN/m),  $f^*$  = dimensionless interface shear coefficient,  $L_e$  = reinforcement layer length in passive zone,  $R_c$  = coverage ratio due to discontinuous reinforcement roll placement within a layer,  $T_{al}$  = allowable or long-term tensile load,  $T_{con}$  = connection capacity between reinforcement and wall facing, and  $T_j$  = tensile load corresponding to soil failure. Other parameters are described in the text.

In the Simplified Method,  $T_{max}$  is computed as:

$$T_{max} = S_v K_r \sigma_v = S_v K_r (\gamma_r z + q) \quad (2)$$

where,  $S_v$  = the contributory area (vertical) spacing between reinforcement layers,  $K_r$  = equivalent coefficient of lateral earth pressure =  $K_a = (1 - \sin \phi_r) / (1 + \sin \phi_r)$  where  $\phi_r$  is the peak friction angle of the reinforced soil,  $\sigma_v = \gamma_r z + q$  where  $\gamma_r$  is the unit weight of the reinforced soil,  $q$  = uniform surcharge pressure, and  $z$  is the depth of the reinforcement layer below the crest of the wall. The calculation of  $T_{max}$  using the Stiffness Method is:

$$T_{max} = S_v [\gamma_r H D_{tmax} + (H_{ref}/H) \gamma_r S] K_{avh} \Phi_{fb} \Phi_g \Phi_{fs} \Phi_{local} \Phi_c \quad (3)$$

Here,  $H$  = height of the wall,  $D_{tmax}$  = dimensionless load distribution factor,  $H_{ref}$  = reference uniform surcharge height = 6 m,  $S$  = height of equivalent uniform surcharge with soil unit weight  $\gamma_r$  where  $q = \gamma_r \times S$ ,  $K_{avh}$  = equivalent horizontal component of active earth pressure accounting for wall batter and back slope angle (=  $K_a$  for the geometry in Figure 1), and the remaining  $\Phi$  terms are influence factors described shortly.

The Stiffness Method was developed to replace the Simplified Method used for both steel reinforced and geosynthetic reinforced MSE walls. In this paper, the focus is on geosynthetic MSE

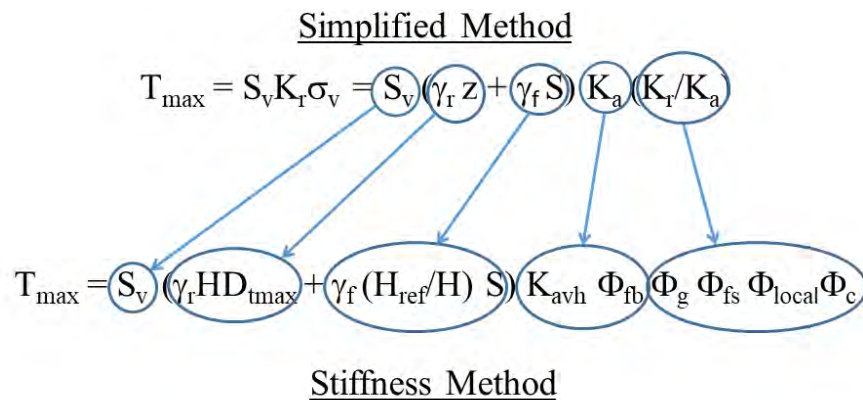


**Figure 2. Equivalency between Simplified Method and Stiffness Method (after Allen and Bathurst 2015).**

walls. The connection between the two methods is illustrated in Figure 2. The first term is the contributory spacing ( $S_v$ ) which remains the same for both methods.

**Dimensionless load distribution factor ( $D_{\max}$ ).** Comparison of the distribution of the maximum measured tensile loads in full-scale field and laboratory walls under operational (serviceability) conditions was shown to follow a trapezoidal distribution with depth below the crest of the wall. This is different from the distribution which increases linearly with depth for walls with uniform spaced layers of reinforcement using the Simplified Method (Allen et al. 2003). The linear distribution is a consequence of classical active earth pressure theory. In fact, the incremental construction of MSE walls and soil compaction result in loads that are typically much less than those assumed using classical active earth pressure theory (i.e., Equation 2). In order to simply the trapezoidal distribution that appeared in the first versions of the Stiffness Method (Allen et al. 2003; Bathurst et al. 2005), the distribution of maximum loads was assumed to follow a bi-linear distribution. This change also helps to discourage a compound failure mechanism from passing through the heel of the reinforced zone.

Figure 3 shows the computed distribution of maximum tensile loads for a simple unsurcharged vertical wrapped-face wall of  $H = 6$  m. Input parameters for this simple scenario are found in the figure caption and legend and are explained later in the paper. The distribution of  $T_{\max}$  using the Stiffness Method can be seen to follow a bi-linear distribution which increases from left to right as the stiffness  $J$  of the reinforcement increases. The bilinear distribution is also a function of wall height. The Simplified Method gives a single linear distribution independent of the reinforcement stiffness. At shallow depths and for the stiffest reinforcement cases there is reasonable agreement between the two methods for this flexible wrapped-face wall example. However, as the depth of the layer increases further below the top of the wall and the stiffness of the reinforcement decreases, the Stiffness Method predicts smaller loads. The corresponding maximum reinforcement strains ( $\epsilon_{\max}$ ) in the wall are also shown in the figure.

**Uniform surcharge.** In the Simplified Method the magnitude of  $T_{\max}$  will increase linearly with increases in uniform surcharge pressure  $q = \gamma_f \times S$  (Equation 2). Measurements from instrumented walls showed that in fact the influence of the surcharge pressure is greater for short walls of 6 m

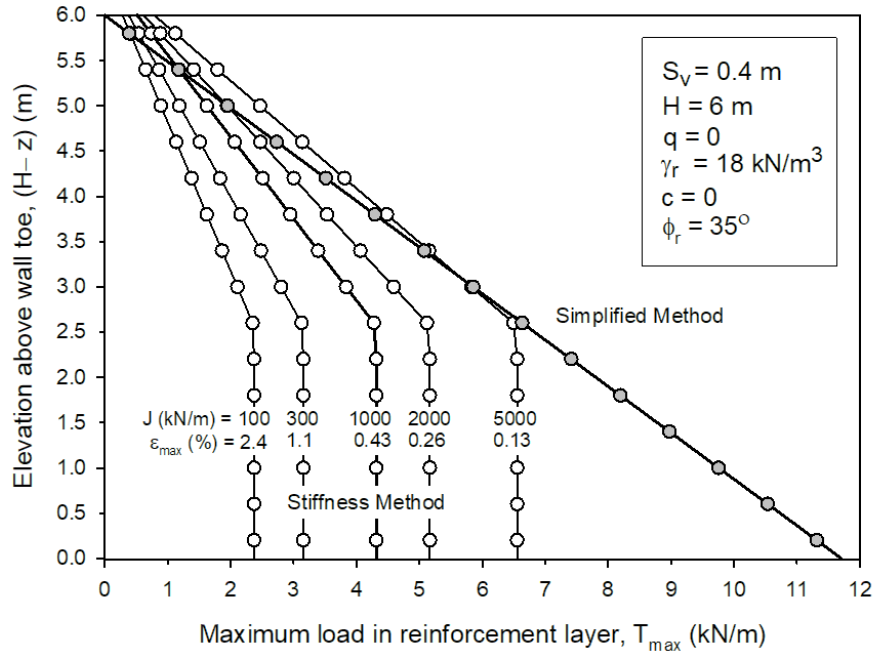


**Figure 3. Distribution and magnitude of maximum tensile loads ( $T_{\max}$ ) in 6 m-high wrapped-face wall.**  $\omega = 0$ ,  $S = 0$ ,  $\Phi_{fb} = \Phi_{fs} = \Phi_{local} = \Phi_c = 1$ .

or less. The magnitude of  $\gamma_f \times S$  in Equation 3 is adjusted using the multiplier  $H_{ref}/H$  where  $H_{ref} = 6$  m for walls of 6 m height or greater, and  $H_{ref}/H = 1$  for shorter walls.

**Facing batter.** As the facing batter angle ( $\omega$ ) from the vertical increases, the loads in the reinforcement layers will decrease, but not as rapidly as predicted using Coulomb theory. This effect is captured by the non-dimensional facing batter factor  $\Phi_{fb}$  which is 1 for vertical-faced walls and decreases with increasing batter angle measured from the vertical. The influence of the batter angle is coupled with  $K_{avh}$  which is the horizontal component of the active earth pressure coefficient  $K_a$ . For vertical or near-vertical walls (e.g., facing angle  $\omega \leq 10^\circ$ ),  $\Phi_{fb}$  can be taken as 1 with little practical error.

**Reinforcement stiffness.** The influence of reinforcement stiffness is contained in the global stiffness factor  $\Phi_g$  which is expressed as:

$$\alpha = \left( \frac{S_{global}}{p_a} \right) \quad (4)$$

where,  $\alpha = 0.16$  and  $\beta = 0.26$  are constants that have been determined by model calibration with tensile loads deduced from instrumented walls, and  $p_a = 101$  kPa (atmospheric pressure) used to make the equation non-dimensional.  $S_{global}$  is the global reinforcement stiffness computed as:



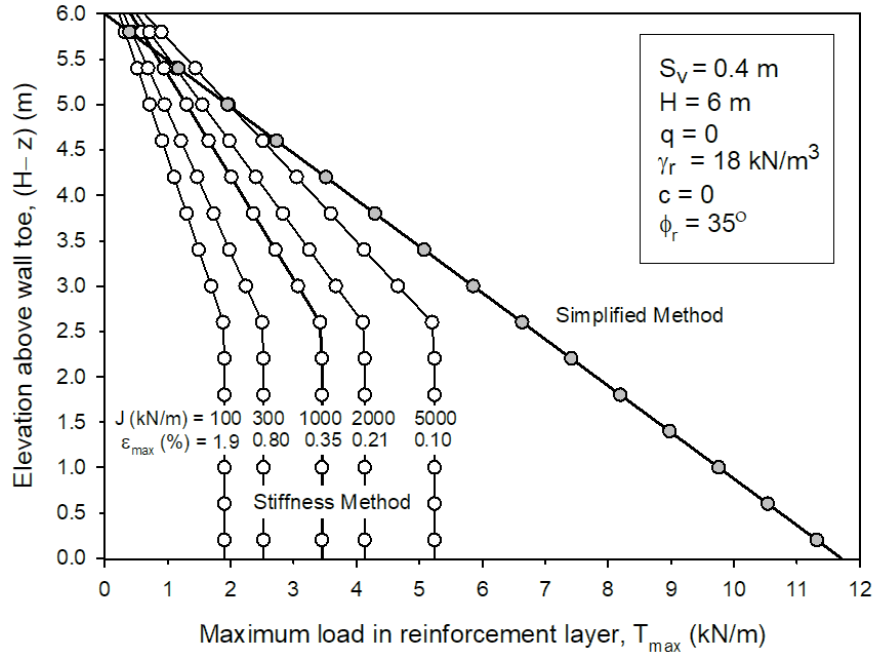


**Figure 4. Distribution and magnitude of maximum tensile loads in 6 m-high block-face wall.**  $\omega = 0$ ,  $S = 0$ ,  $\Phi_{fs} = 0.80$ ,  $\Phi_{fb} = \Phi_{local} = \Phi_c = 1$ .

$$S_{global} = \frac{J_{ave}}{(H/n)} = \frac{\sum_{i=1}^n J_i}{H} \quad (5)$$

Here,  $J_{ave}$  is the average stiffness of all  $n$  layers in the wall, and  $J_i$  = layer stiffness. The latter is taken at a strain of 2% and an isochronous time of 1000 h (i.e.,  $J(\epsilon = 2\%, t = 1000 \text{ h})$ ). The 1000-h time was selected because it was found to be a typical time for wall construction and creep strains were typically complete. Most well-constructed walls with demonstrated good performance have shown maximum strains of 1% or less. Geogrid and geotextile reinforcement products have stiffness values in the range of about 100 to 5000 kN/m (Allen and Bathurst 2019; Bathurst and Naftchali 2021). A typical value is about 1000 kN/m. As noted earlier in Figure 3, the reinforcement loads increase as stiffness increases. This behavior cannot be predicted using the Simplified Method.

The magnitude of maximum reinforcement loads can be influenced by local changes in spacing and reinforcement type (i.e., different stiffness  $J_i$ ). This scenario is addressed by the local stiffness factor which has a default value  $\Phi_{local} = 1$  corresponding to the case when all layers are equally spaced and have the same stiffness.

**Facing stiffness.** Thus far the results presented have focused on the simple case of a MSE wall with a wrapped-face configuration which is very flexible. Most walls are constructed with a hard facing and these structural facings can assist to carry lateral earth pressures and thus reduce the maximum tensile reinforcement loads that would otherwise be carried by the reinforcement layers. The facing stiffness factor  $\Phi_{fs}$  appears in the Stiffness Method formulation to account for the contribution of the facing and has a value  $\Phi_{fs} = 1$ . For the wrapped-face wall in the example so far,  $\Phi_{fs} = 1$ . Nevertheless, for tall walls with (say)  $H > 10 \text{ m}$  and a thin concrete panel face construction,

the wall can behave like a flexible MSE wall and thus  $\Phi_{fs} = 1$ . The reader is directed to the cited papers and AASHTO (2020) for details. A typical value for the facing stiffness factor of a modular block-faced wall is 0.80. Figure 4 repeats the previous maximum reinforcement load calculations with this value. Comparison of Figure 4 with Figure 3 shows that the effect of the hard facing is to reduce the maximum tensile loads in each layer.

**Soil cohesion.** A permanent and consistent cohesive strength component ( $c > 0$ ) in the reinforced soil backfill will reduce the earth pressure that would otherwise be carried by a purely frictional soil. The cohesion factor  $\Phi_c$  ranges from 0 to 1 with the value of 1 corresponding to the no-cohesion case ( $c = 0$ ). It is important to emphasize that  $\Phi_c < 1$  values can only be used if the  $c$ - $\phi$  soil has significant true cohesion due to clay content and defined by plasticity index  $PI > 6$ , and this cohesion will persist over the lifetime of the structure. This definition thus excludes the case of a transient apparent cohesion due to matric suction for partially saturated granular soils as well as  $c$ - $\phi$  soils that could soften/weaken over time due to moisture or deformation.

Returning to the original wrapped-face wall case and assuming  $c = 5$  kPa gives  $\Phi_c = 0.5$ . The influence of this true cohesion on maximum reinforcement loads is clear when Figure 5 is compared to Figure 3. The Simplified Method ignores any cohesive strength component in a  $c$ - $\phi$  soil even if present; thus the  $T_{max}$  curve remains unchanged from the previous examples. For design using the Stiffness Method, a conservative assumption is to ignore true cohesion when available. Current practice in North America specifications for MSE walls is to use “select” granular fill and to ignore any cohesive soil strength component. However, in other countries such high quality materials may not be available or may be cost-prohibitive. This was the primary motivation to include the cohesion factor starting with an earlier version of the Stiffness Method (Miyata and Bathurst 2007).

**Soil failure limit state.** Another unique feature of the Stiffness Method is the soil failure limit state which is used to ensure that the reinforced soil zone remains at a working stress condition consistent with operational conditions. This limit state does not appear in the Simplified Method which is a fully force-based design approach. For the assumption of working stress conditions to be valid, the soil must not fail (i.e., develop a contiguous failure mechanism through the reinforced soil zone). Of course it is not practically possible to include this requirement directly in the Stiffness Method. However, Allen and Bathurst (2002) compared reinforcement strains in instrumented geosynthetic MSE walls that exhibited poor performance (e.g., excessive wall deformations, sustained creep deformations in the reinforcement, and cracking and slumping of the reinforced soil mass) and those that did not. They found that if average geosynthetic reinforcement strains remained below  $\epsilon_{max} = 2.5\%$  to  $3\%$ , then working stress conditions could be assumed to exist. Numerical modelling reported by Bathurst and Naftchali (2022) for geosynthetic MSE walls has also demonstrated this link between maximum tensile strain and working stress conditions. In AASHTO (2020) an additional margin of safety on the above strain values was adopted by specifying  $2\%$  for stiff-faced walls and  $2.5\%$  for flexible face walls. Figures 3-5 show that these criteria are not exceeded even for the example walls constructed with a very low-stiffness geosynthetic reinforcement. The experience of the writers is that most geosynthetic MSE walls constructed with granular backfills meeting AASHTO (2020) specifications exhibit strains less

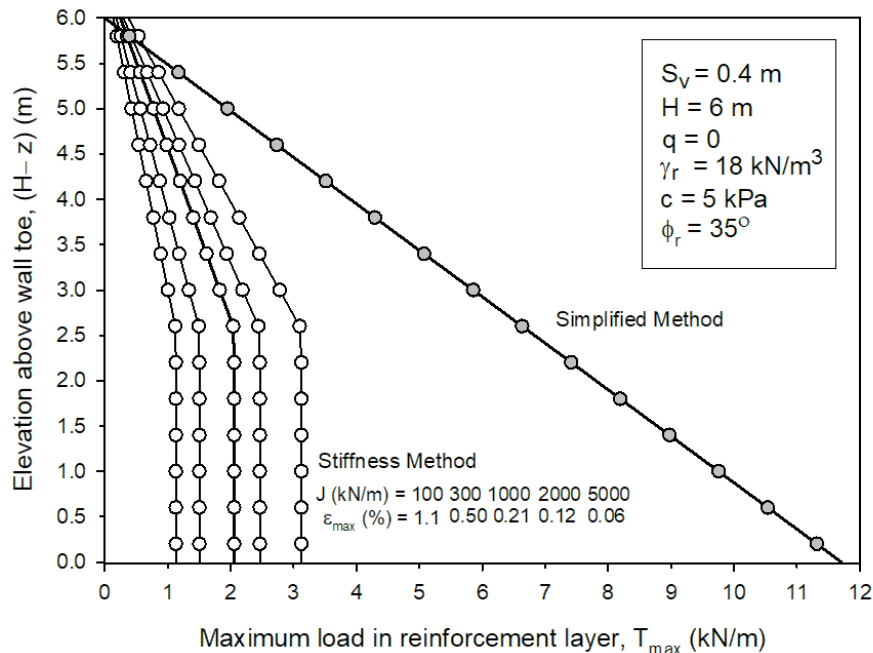


**Figure 5. Distribution and magnitude of maximum tensile loads in 6 m-high wrapped-face wall with  $c = 5$  kPa.  $\omega = 0$ ,  $S = 0$ ,  $\Phi_{fs} = 0.80$ ,  $\Phi_{fb} = \Phi_{local} = 1$ ,  $\Phi_c = 0.5$ .**

than 1%. Nevertheless, the soil failure limit state is most often the most critical internal limit state for design of the four limit states shown in Figure 1.

## MARGINS OF SAFETY

Thus far the Simplified Method has been shown (at least visually) in the examples to be generally excessively conservative (on average) with respect to predicted reinforcement loads. The method can be seen to encourage stronger and stiffer geosynthetic reinforcement in the bottom half of the wall than is required using the Stiffness Method. A more informative appreciation of the differences in design outcomes is to examine the margins of safety in a probabilistic framework using back-calculated reliability index ( $\beta$ ) values.

Table 1 shows a summary of bias statistics for reinforcement (tensile) strength and pullout limit states first introduced in Figure 1. Bias is defined as the ratio of an observed (or measured) value divided by the predicted value. Load bias values were computed by dividing measured values from instrumented walls by the predicted values for the same reinforcement layer using the Simplified Method and the Stiffness Method. The two resistance models are for pullout and reinforcement (tensile) strength. The pullout model is expressed as:

$$P_c = 2f^*L_c\sigma_vR_c \quad (6)$$

The parameters have been previously defined in the caption to Figure 1 and related text. Pullout model bias values were computed by dividing measured pullout capacities from conventional laboratory pullout tests by the predicted values using Equation 6. In the analyses to follow, the

tensile strength of the geosynthetic reinforcement is taken as the long-term tensile strength ( $T_{al}$ ) computed as:

$$T_{al} = \frac{T_{ult} \times R_c}{RF} = \frac{T_{ult} \times R_c}{RF_{ID} RF_{CR} RF_D} \quad (7)$$

where,  $T_{ult}$  = reference ultimate tensile strength. Parameter RF is the combined reduction factor that accounts for loss of strength over the design life of the reinforcement due to installation damage ( $RF_{ID}$ ), creep ( $RF_{CR}$ ) and degradation (durability) mechanisms ( $RF_D$ ). The resistance bias for this limit state is taken as the measured strength divided by the nominal value which is slightly lower consistent with minimum average roll values (MARV)  $T_{ult}$  strengths used for design. The coefficient of variation (COV) of bias values is very small because these are engineered materials.

A model with mean bias greater than 1, or less than 1, demonstrates that the model under-predicts or over-predicts observed values *on average*, respectively. The COV of bias values is a further quantitative measure of the accuracy of the model. Finally, bias dependency is quantified by Pearson's correlation coefficient ( $\rho$ ). The larger the magnitude of  $\rho$  the greater the change in bias value (or model accuracy) with changes in magnitude of predicted nominal value. As mean bias approaches 1, COV approaches 0 and the correlation coefficient approaches 0, the better the model. Based on these criteria it can be seen in Table 1 that the Stiffness Method load model (LM2) is a more accurate model than the Simplified Method (LM1).

Using the bias statistics in Table 1, the magnitude of the actual reliability index ( $\beta$ ) can be computed for tensile strength and pullout limit states using the following equation:

$$\beta = A + B \times \ln(F_n) \quad (8)$$

where, A and B are collections of bias statistics described above and uncertainty in choice of nominal values  $Q_n$  and  $R_n$  at time of design ( $COV_{Q_n}$  and  $COV_{R_n}$ ) (e.g., see Bathurst and Allen 2021). The equation shows that  $\beta$  varies log-linearly with the magnitude of the nominal factor of safety  $F_n = R_n/Q_n$ . This equation provides a quantitative link between deterministic allowable stress design (ASD) (factor-of-safety approach) and modern concepts of reliability-based design.

Results of calculations using Equation 8 are shown in Figures 6a and 6b for the tensile strength limit state using the Simplified Method (LM1) and Stiffness Method (LM2), respectively, for the load side ( $Q_n$ ), and the long-term tensile strength (TM) for the resistance side ( $R_n$ ) (Equation 7). Figures 6c and 6d show calculation outcomes with the same load side equations but with the AASHTO pullout equation (Equation 6) for the resistance side. The calculations assume uncertainty in the estimate of nominal load values and nominal pullout values taken as  $COV_{Q_n} = COV_{R_n} = 0, 0.1, 0.2$  and  $0.3$ . The non-zero values correspond to the concept of high, typical and low levels of understanding at time of design that are used in Canadian foundation engineering practice (Fenton et al. 2014). A value of  $COV_{R_n} = 0$  for the tensile strength nominal value since all uncertainty in its value is captured by the COV of the bias. Curves with values of  $COV_{Q_n} = COV_{R_n} = 0$  can be understood to correspond to current practice in the US where the concept of level of understanding is not used in any formal way. Calculation outcomes using the Stiffness Method (load model LM2) show that for the same  $F_n$  value,  $\beta$  values decrease in the order of  $COV = 0, 0.1, 0.2$  and  $0.3$ . This may be expected since margins of safety in probabilistic terms can be expected to decrease as uncertainty in the magnitude of nominal load value increases. The opposite



**Table 1. Summary of bias statistics and bias dependency values for load and resistance models for geogrid reinforced soil walls constructed with granular soil**

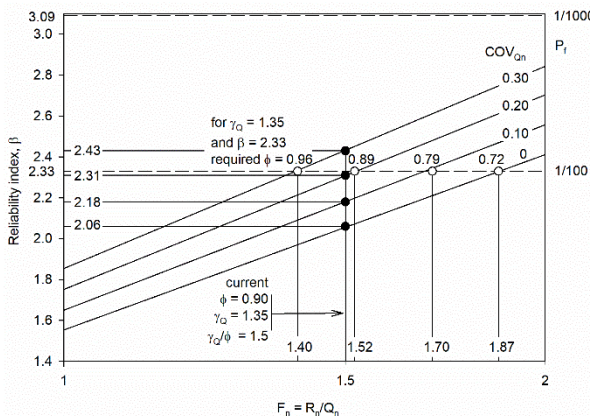
Model	Reference	Model equation	Number of data points, n	Mean of bias	COV of bias	Bias dependency $\rho$	Original data source
Load model LM1	AASHTO (2017)	2	96	0.43	0.95	-0.41	Allen and Bathurst (2015)
Load model LM2	AASHTO (2020)	3	96	1.00	0.28	0	Allen and Bathurst (2015)
Pullout model PM1	AASHTO (2017, 2020)	6	318	2.23	0.55	-0.46	Huang and Bathurst (2009)
Tensile strength TM	AASHTO (2017, 2020)	7	N/A	1.10	0.10	0	Bathurst and Miyata (2015) Miyata and Bathurst (2015) Miyata et al. (2014) Bathurst et al. (2011, 2012)

trend is observed when the poorer Simplified Method (load model LM1) is used. This counter-intuitive outcome is a result of the large negative bias dependency for this model (Table 1). This is an unfortunate outcome of using a poor load model for reliability-based design, and for LRFD calibration as discussed later.

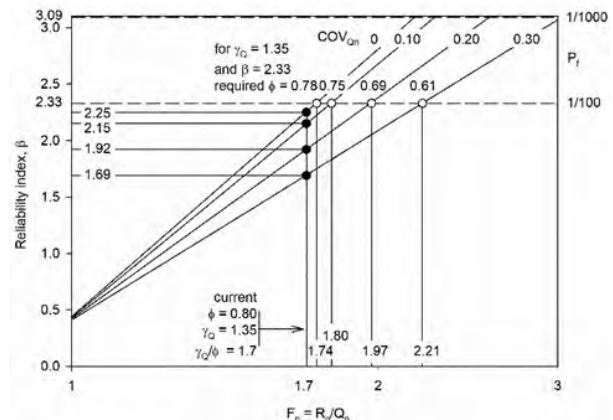
Also shown in Figure 6 are  $\beta$  values of 2.33 and 3.09 corresponding to probabilities of failure of the limit state of 1/100 and 1/1000. For internal stability limit states for MSE walls, the recommended target probability of failure is 1/100 (Allen et al. 2005). This may appear to be very high but the multiple reinforcement layers in MSE walls make these systems highly strength redundant; i.e., if one layer fails, the other layers can compensate.

For reliability-based design the curves in Figure 6 can be used directly. The internal design of the MSE wall can be adjusted by changing nominal load ( $Q_n$ ) and nominal resistance ( $R_n$ ) values so that  $F_n = R_n/Q_n$  gives a value  $\beta \geq 2.33$ . LRFD design can be understood to be reliability-based design with additional constraints imposed by specified load and resistance factors ( $\gamma_Q$  and  $\phi$ ). Specifically, a limit state (Equation 1) is just satisfied when  $F_n = R_n/Q_n = \gamma_Q/\phi$ . In AASHTO (2017, 2020) the load factor for dead load due to soil self-weight is  $\gamma_{P-EV} = \gamma_Q = 1.35$ . For the Simplified Method (AASHTO 2017),  $\phi = 0.90$  for both limit states; therefore  $F_n = 1.5$ . For the Stiffness Method (AASHTO 2020), the resistance factor is  $\phi = 0.80$  and  $0.70$  for tensile strength and pullout limit states, respectively; therefore,  $F_n = 1.7$  and  $1.9$  when these limit state functions are just satisfied. Values of  $F_n$  matching specified load and resistance factors are labelled “current” on each of the plots in Figure 6. The black closed symbols show the actual reliability index values using the assumed COV values for nominal load and resistance values for each limit state. Values falling below  $\beta = 2.33$  mean that using the current specified load and resistance factors is non-conservative (unsafe) if the limit state is just satisfied. Conversely, those values falling above  $\beta = 2.33$  have additional margins of safety and are thus conservative (safe) for design. The open circles show the

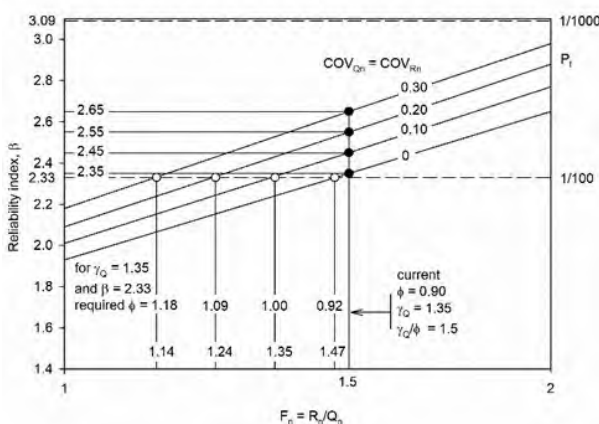
values of  $F_n$  that are required to just satisfy  $\beta = 2.33$  and the corresponding resistance factors assuming  $\gamma_Q = 1.35$ . The resistance factors for the Stiffness Method in AASHTO (2020) were calibrated assuming  $COV = 0$  for nominal load and nominal resistance terms ( $COV_{Qn} = COV_{Rn} = 0$ ) (Allen and Bathurst 2015; Bathurst et al. 2019). For this case, required values and current values are within 0.05 of specified values which is the round-off accuracy recommended for LRFD calibration (Allen et al. 2005). Using the Simplified Method requires  $\phi = 0.72$  (say 0.70) for the tensile strength limit state. For the pullout limit state the current specified value of  $\phi = 0.90$  is acceptably close to the computed value of  $\phi = 0.92$ . If calibration is carried out assuming a typical  $COV$  value for load and resistance terms and the Simplified Method, then the current resistance factor for the tensile strength limit state is acceptable (computed  $\phi = 0.89$  versus specified value of 0.90). However, for the same  $COV_{Qn} = 0.2$  (typical level of understanding) and the pullout limit state, the required value is  $\phi = 1.09 > 1.00$ . There is no theoretical reason why a resistance factor cannot be greater than 1, but code convention is that  $\phi < 1$ . This constraint highlights the unintended consequences of a load model that is excessively conservative when carrying out LRFD calibration.



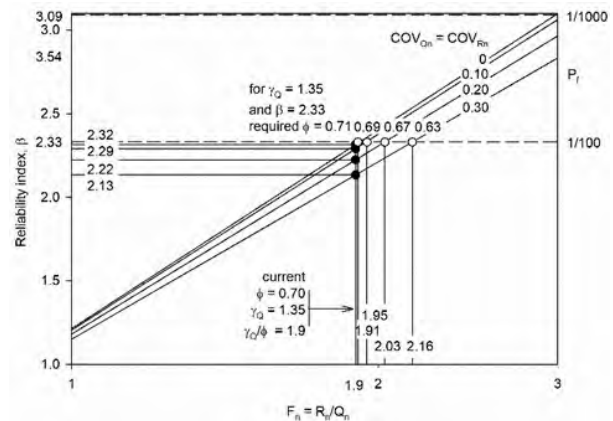
a) LM1-TM (AASHTO 2017)  
 $\gamma_Q = 1.35$ ,  $\phi = 0.90$ ,  $\gamma_Q / \phi = 1.5$



b) LM2-TM (AASHTO 2020)  
 $\gamma_Q = 1.35$ ,  $\phi = 0.80$ ,  $\gamma_Q / \phi = 1.7$



c) LM1-PM1 (AASHTO 2017)  
 $\gamma_Q = 1.35$ ,  $\phi = 0.90$ ,  $\gamma_Q / \phi = 1.5$



d) LM2-PM1 (AASHTO 2020)  
 $\gamma_Q = 1.35$ ,  $\phi = 0.70$ ,  $\gamma_Q / \phi = 1.9$

**Figure 6. Reliability index versus ratio of nominal resistance to nominal load.**

## CONCLUSIONS

This paper has demonstrated some of the major differences between the calculation of maximum loads in geosynthetic MSE walls using the current Stiffness Method in AASHTO (2020) and the Simplified Method that appears in earlier editions. The paper also demonstrates the true margins of safety to just satisfy tensile strength and pullout limit states using both tensile load models. The reader is directed to the papers by Allen and Bathurst (2015, 2018, 2019) for further details on how to use the Stiffness Method and its development.

## REFERENCES

- Allen, T.M. and Bathurst, R.J. (2002). Soil reinforcement loads in geosynthetic walls at working stress conditions. *Geosynthetics International*, 9(5-6): 525-566.
- Allen, T.M. and Bathurst, R.J. (2015). An improved simplified method for prediction of loads in reinforced soil walls. *ASCE Journal of Geotechnical and Geoenvironmental Engineering*, 141(11): 04015049.
- Allen, T.M. and Bathurst, R.J. (2018). Application of the Simplified Stiffness Method to design of reinforced soil walls. *ASCE Journal of Geotechnical and Geoenvironmental Engineering*, 144(5): 04018024.
- Allen, T.M. and Bathurst, R.J. (2019). Geosynthetic reinforcement stiffness characterization for MSE wall design. *Geosynthetics International*, 26(6): 592-610.
- Allen, T.M., Bathurst, R.J., Walters, D.L., Holtz, R.D. and Lee, W.F. (2003). A new working stress method for prediction of reinforcement loads in geosynthetic walls. *Canadian Geotechnical Journal*, 40(5): 976-994.
- Allen, T.M., Nowak, A.S. and Bathurst, R.J. (2005). Calibration to Determine Load and Resistance Factors for Geotechnical and Structural Design, Transportation Research Board Circular E-C079, Washington, DC, 93 p.
- AASHTO. (2017). *LRFD Bridge Design Specifications*, 8th Ed., American Association of State Highway and Transportation Officials (AASHTO), Washington, DC, USA.
- AASHTO. (2020). *LRFD Bridge Design Specifications*, 9th Ed., American Association of State Highway and Transportation Officials (AASHTO) Washington, DC, USA.
- Bathurst, R.J. and Allen, T.M. (2021). Reliability assessment of internal stability limit states for two as-built geosynthetic MSE walls. *ISSMGE International Journal of Geoengineering Case Histories*, 6(4): 67-84.
- Bathurst, R.J., Allen, T.M., Lin, P. and Bozorgzadeh, N. (2019). LRFD calibration of internal limit states for geogrid MSE walls. *ASCE Journal of Geotechnical and Geoenvironmental Engineering*, 145(11):04019087.
- Bathurst, R.J., Allen, T.M. and Walters, D.L. (2005). Reinforcement loads in geosynthetic walls and the case for a new working stress design method. *Geotextiles and Geomembranes*, 23(4): 287-322.
- Bathurst, R.J., Huang, B. and Allen, T.M. (2011). Analysis of installation damage tests for LRFD calibration of reinforced soil structures. *Geotextiles and Geomembranes*, 29(3): 323-334.
- Bathurst, R.J., Huang, B. and Allen, T.M. (2012). Interpretation of laboratory creep testing for reliability-based analysis and load and resistance factor design (LRFD) calibration. *Geosynthetics International*, 19(1): 39-53.

- Bathurst, R.J. and Miyata, Y. (2015). Reliability-based analysis of combined installation damage and creep for the tensile rupture limit state of geogrid reinforcement in Japan. *Soils and Foundations*, 55(2): 437-446.
- Bathurst, R.J. and Naftchali, F.M. (2021). Geosynthetic reinforcement stiffness for analytical and numerical modelling of reinforced soil structures. *Geotextiles and Geomembranes*, 49: 921-940.
- Bathurst, R.J. and Naftchali, F.M. (2022). Response to discussion by S.H. Mirmoradi and M. Ehrlich on “Geosynthetic reinforcement stiffness for analytical and numerical modelling of reinforced soil structures” by R.J. Bathurst and F.M. Naftchali, *Geotextiles and Geomembranes*, 49 (2021) 921-940.
- Fenton, G.A., Naghibi, F., Dundas, D., Bathurst, R.J. and Griffiths, D.V. (2016). Reliability-based geotechnical design in the 2014 Canadian Highway Bridge Design Code. *Canadian Geotechnical Journal*, 53(2): 236-251.
- Huang, B. and Bathurst, R.J. (2009). Evaluation of soil-geogrid pullout models using a statistical approach. *ASTM Geotechnical Testing Journal*, 32(6): 489-504.
- Miyata, Y. and Bathurst, R.J. (2007). Development of K-stiffness method for geosynthetic reinforced soil walls constructed with c- $\phi$  soils. *Canadian Geotechnical Journal*, 44(12): 1391-1416.
- Miyata, Y. and Bathurst, R.J. (2015). Reliability analysis of geogrid installation damage test data in Japan. *Soils and Foundations*, 55(2): 393-403.
- Miyata, Y., Bathurst, R.J. and Allen, T.M. (2014). Reliability analysis of geogrid creep data in Japan. *Soils and Foundations*, 54(4): 608-620.



## **New Closed-Form Analytical Solutions for Total Reinforcement Force in a GRS Retaining Wall at the Limit State**

**Patrick J. Fox, Ph.D., P.E., D.GE, F.ASCE<sup>1</sup>**

<sup>1</sup>Department of Civil and Environmental Engineering, Pennsylvania State University, University Park, PA 16802; e-mail: pjf14@psu.edu

### **ABSTRACT**

This paper presents a summary of new closed-form analytical solutions, developed by Fox (2022b), for the critical failure plane angle and maximum total reinforcement force in a geosynthetic-reinforced soil (GRS) retaining wall at the ultimate limit state. The solutions are obtained from a general force equilibrium analysis of a triangular soil wedge and can accommodate variable wedge geometry, pore pressure, shear strength parameters, reinforcement force inclination, surcharge stress, applied loads, pseudostatic seismic coefficients, and toe reaction forces. The soil wedge and facing column are treated as a combined block with a vertical load factor to account for soil downdrag on the back of the column. Predicted trends are similar and reinforcement force magnitudes are generally less than values obtained using Rankine and Coulomb earth pressure theories. The solutions are derived and then demonstrated using a numerical example.

### **INTRODUCTION**

Traditionally, internal stability analysis for geosynthetic-reinforced soil (GRS) retaining walls has been conducted using the tied-back wedge method, in which reinforcement loads are calculated from Rankine, Coulomb, or Mononobe-Okabe active earth pressure theory, or modifications thereof, and the contributory area for each layer. For walls with equal reinforcement vertical spacing, this method yields reinforcement loads that increase linearly with depth. The NCMA (2010) design method and AASHTO (2020) Simplified Method are examples of this approach. Based on a study of GRS retaining wall case histories, Allen et al. (2002) concluded that reinforcement loads calculated using tied-back wedge methods generally were overly conservative. This led to the development of the K-Stiffness Method (Allen et al. 2003; Bathurst et al. 2008) and subsequent Simplified Stiffness Method (Allen and Bathurst 2015; 2018; AASHTO 2020), which are empirical methods to calculate reinforcement loads for GRS retaining walls under working stress (i.e., operational) conditions.

The relative merits of these approaches have been debated in the literature. Tied-back wedge methods emphasize strength in the conventional manner but fail to consider component stiffness and provide conservative estimates of reinforcement loads. A key limitation is that classical lateral earth pressure theory does not account for the presence of reinforcement. Reinforcement forces change the equilibrium condition for the soil failure wedge and thus alter the effective normal force and critical angle for the internal failure plane. Tied-back wedge methods also ignore horizontal and vertical reaction forces at the toe of the wall (e.g., Bathurst et al. 2000; Huang et al. 2010; Mirmoradi and Ehrlich 2017; Zhang et al. 2019), which explains, in part, why predicted reinforcement loads often are substantially conservative, especially toward the bottom of the wall. Conversely, the Simplified Stiffness Method emphasizes stiffness, which is



Corresponding forces for an effective stress stability analysis are based on total weights and boundary pore pressures. The facing column has weight  $W_f$  and the soil wedge has weight  $W_s = 0.5\gamma LL_w \sin(\beta - \theta)$ , where  $\gamma$  is the average total soil unit weight within the wedge. Pseudostatic seismic coefficients  $k_h$  and  $k_v$  can be specified in the horizontal and vertical directions, respectively, and act uniformly on the facing and wedge. Including separate pseudostatic seismic coefficients  $k_{qh}$  and  $k_{qv}$ , the uniform surcharge yields a resultant horizontal force  $Q_{qh} = k_{qh}qL_t \cos \alpha$  and resultant vertical force  $Q_{qv} = (1 - k_{qv})qL_t \cos \alpha$ . Applied forces  $Q_h$  and  $Q_v$  also can be specified in the horizontal and vertical directions. These forces are constant and can include pseudostatic multipliers. The soil on the base failure plane carries effective normal force  $N'$ , pore pressure force  $U = uL$ , total normal force  $N = N' + U$ , and shear force  $S = c' + N' \tan \phi'$ , where  $u$  is the average pore pressure on the plane and  $c'$  and  $\phi'$  are soil effective stress strength parameters. This plane also carries a total reinforcement tensile force  $T_t$  at angle  $\rho$ , measured counterclockwise from horizontal, which is the sum contribution from all reinforcement elements acting on  $\overline{AC}$ . The reinforcement force is primarily intended to represent geosynthetic reinforcement layers (e.g., geogrids), but also can represent other mechanical stabilization elements (e.g., soil nails, FHWA 2015) that allow the soil wedge to achieve an active failure condition. The leveling pad at the toe of the wall carries horizontal reaction force  $R_h$  and vertical reaction force  $R_v$ . For wrapped-face GRS walls,  $R_h = R_v = 0$ . All force values are per unit width in the third dimension and positive for the directions indicated in Fig. 1(b).

The vertical toe reaction force is defined as  $R_v = mW_f$ , where  $m$  is a vertical load factor (Damians et al. 2013) and  $W_f$  corresponds to the full facing column height without reduction for hinge height (Bathurst et al. 2001; NCMA 2010). The vertical load factor reflects force transmitted to the back of the column due to relative shear displacement of the backfill soil. A vertical pseudostatic seismic coefficient may be applied to  $W_f$  to calculate  $R_v$ , depending on the desired level of conservatism. Also assuming full mobilization of shear strength at the leveling pad, the horizontal toe reaction force is defined as  $R_h = C_{lp} + R_v \tan \phi_{lp}$ , where  $C_{lp}$  is the interface adhesion force and  $\phi_{lp}$  is the interface friction angle for the top or bottom surface of the leveling pad, whichever yields lower shear resistance. This Mohr-Coulomb relationship for  $R_h$  is based on experimental measurements (Bathurst and Simac 1993; Hatami and Bathurst 2005).

Equilibrium is considered for the facing column and reinforced soil wedge taken as a combined block, similar to free body diagrams presented by Bathurst and Simac (1991) and Leshchinsky (2009). This circumvents the need to characterize lateral earth pressures and reinforcement connection forces at the facing, which are affected by soil downdrag and the local construction process and are difficult to predict (Bathurst et al. 2001). As such, forces on the block sum to zero in both the horizontal ( $x$ ) and vertical ( $z$ ) directions,

$$-k_h(W_s + W_f) - Q_h - Q_{qh} - (N' + U)\sin \theta + S \cos \theta + T_t \cos \rho + R_h = 0 \quad (1)$$

$$-(1 - k_v)(W_s + W_f) - Q_v - Q_{qv} + (N' + U)\cos \theta + S \sin \theta + T_t \sin \rho + R_v = 0 \quad (2)$$

which yields the effective normal force on the base failure plane and total reinforcement force,

$$N' = \frac{\left\{ \begin{aligned} &(-k_h W_f - Q_h + R_h + T_i \cos \rho)(\tan \theta - \tan \alpha) + H(c' - u \tan \theta)(1 - \tan \alpha \cot \beta) \\ &- [k_{qh} qH + 0.5k_h \gamma H^2 (1 - \tan \alpha \cot \beta)](1 - \tan \theta \cot \beta) \end{aligned} \right\}}{(\sin \theta - \cos \theta \tan \alpha)(\tan \theta - \tan \phi')} \quad (3)$$

$$T_i = \frac{C_1 \sin^2 \theta + C_2 \sin \theta \cos \theta + C_3 \cos^2 \theta + C_4}{C_5 \sin^2 \theta + C_6 \sin \theta \cos \theta + C_7 \cos^2 \theta} \quad (4)$$

where,

$$C_1 = (-Q_h + R_h) \tan \phi' - Q_v + R_v + qH \cot \beta (k_{qh} \tan \phi' + 1 - k_{qv}) - [W_f - 0.5\gamma H^2 \cot \beta (1 - \tan \alpha \cot \beta)](k_h \tan \phi' + 1 - k_v) \quad (5)$$

$$C_2 = (-k_h W_f - Q_h + R_h)(1 - \tan \alpha \tan \phi') + [(1 - k_v)W_f + Q_v - R_v](\tan \alpha + \tan \phi') - qH [k_{qh}(\tan \phi' - \cot \beta) + (1 - k_{qv})(1 + \tan \phi' \cot \beta)] - 0.5\gamma H^2 (1 - \tan \alpha \cot \beta) [k_h(\tan \phi' - \cot \beta) + (1 - k_v)(1 + \tan \phi' \cot \beta)] \quad (6)$$

$$C_3 = [Q_h - R_h - (Q_v - R_v) \tan \phi'] \tan \alpha - qH [k_{qh} - (1 - k_{qv}) \tan \phi'] + [W_f \tan \alpha - 0.5\gamma H^2 (1 - \tan \alpha \cot \beta)] [k_h - (1 - k_v) \tan \phi'] \quad (7)$$

$$C_4 = H(c' - u \tan \phi')(1 - \tan \alpha \cot \beta) \quad (8)$$

$$C_5 = -\sin \rho - \cos \rho \tan \phi' \quad (9)$$

$$C_6 = \sin \rho (\tan \alpha + \tan \phi') - \cos \rho (1 - \tan \alpha \tan \phi') \quad (10)$$

$$C_7 = \tan \alpha (-\sin \rho \tan \phi' + \cos \rho) \quad (11)$$

The critical angle  $\theta_{cr}$  for base failure plane corresponds to the maximum  $T_i$  and can be determined analytically. The derivative of Eq. (4) is taken with respect to  $\theta$  and the numerator is set equal to zero, yielding the quadratic equation  $C_8 \tan^2 \theta_{cr} + 2C_9 \tan \theta_{cr} + C_{10} = 0$  and solution,

$$\theta_{cr} = \tan^{-1} \left( \frac{-C_9 - \sqrt{C_9^2 - C_8 C_{10}}}{C_8} \right) \quad (12)$$

where,

$$C_8 = C_1 C_6 - C_2 C_5 + C_4 C_6 \quad (13)$$

$$C_9 = C_1 C_7 - C_3 C_5 - C_4 C_5 + C_4 C_7 \quad (14)$$

$$C_{10} = C_2 C_7 - C_3 C_6 - C_4 C_6 \quad (15)$$



Applicable values of parameters yield  $C_9^2 \geq C_8 C_{10}$  and thus a non-negative term under the radical sign in Eq. (12) and real value for  $\theta_{cr}$ . Parameters may vary with  $\theta$  and need to be adjusted once  $\theta_{cr}$  is obtained, and  $\theta_{cr}$  recalculated. Once  $\theta_{cr}$  is determined, corresponding values of  $S$ ,  $N'$ , and  $T_i$  are obtained with  $\theta = \theta_{cr}$  and a check of the solution is made using Eqs. (1) and (2). Fox (2022b) performed verification checks of the foregoing solutions and showed exact agreement with existing analytical solutions for simplified conditions, including Rankine, Coulomb, and Mononobe-Okabe theories, and good agreement with experimental data from a large-scale GRS retaining wall test conducted by Bathurst and Benjamin (1990).

## NUMERICAL EXAMPLE

A GRS retaining wall consists of a modular block (segmental) facing column, an unreinforced concrete leveling pad, and backfill soil with horizontal reinforcement layers. Based on data provided by Hatami and Bathurst (2005), the facing is assumed to have a weight of 6.6 kN/m per meter of wall height. The leveling pad shearing surface has no adhesion ( $C_{ip} = 0$ ) and interface friction angle  $\phi_{ip} = 36^\circ$  (Yu et al. 2016). The backfill soil consists of clean sand ( $\gamma = 19 \text{ kN/m}^3$ ,  $c' = 0$ ,  $\phi' = 42^\circ$ ) with a horizontal top surface ( $\alpha = 0$ ) and no pore pressure ( $u = 0$ ). The reinforcement force is assumed to align with the original direction of the reinforcement ( $\rho = 0$ ).

The effect of base failure plane angle  $\theta$  on system forces for vertical and battered walls is shown in Fig. 2. The facing column has height  $H = 8 \text{ m}$ , which gives  $W_f = 52.8 \text{ kN/m}$ , and the backfill soil exerts no downdrag on the facing ( $m = 1$ ). The vertical wall is first considered ( $\beta = 90^\circ$ ). With increasing  $\theta$ , the horizontal toe force  $R_h = 38.4 \text{ kN/m}$  and vertical toe force  $R_v = 52.8 \text{ kN/m}$  are constant, and the soil wedge weight  $W_s$  and effective normal force on the base failure plane  $N'$  decrease nonlinearly as the wedge becomes progressively smaller. The total reinforcement tensile force required to support the active soil wedge forms a concave-down relationship with a maximum value of  $T_i = 82.1 \text{ kN/m}$  at critical angle  $\theta_{cr} = 66.0^\circ$ . This value of  $\theta_{cr}$  also is given by Eq. (12). For comparison, Rankine earth pressure theory, which forms the basis of the AASHTO (2020) Simplified Method, yields the same critical angle ( $66.0^\circ$ ) and a required total reinforcement force (i.e., total lateral earth force) of  $T_i = 120.5 \text{ kN/m}$ . Thus, the reinforcement force given by the current analysis is equal to that from Rankine theory less the horizontal toe force (i.e.,  $120.5 \text{ kN/m} - 38.4 \text{ kN/m} = 82.1 \text{ kN/m}$ ); however, this straightforward subtraction relationship does not hold for general conditions (e.g.,  $m \neq 1$ ,  $\rho \neq 0$ ). Coulomb earth pressure theory, which forms the basis of the NCMA (2010) design method, gives  $\theta_{cr} = 63.1^\circ$  and  $T_i = 98.8 \text{ kN/m}$ , where the total reinforcement force corresponds to the horizontal component of lateral earth force and a wall interface friction angle  $\phi'_w = 2\phi'/3 = 28^\circ$ , as recommended by NCMA (2010). Compared to Rankine and Coulomb, the current analysis yields reductions in  $T_i$  of 32% and 17%, respectively, for the vertical wall. If a small apparent cohesion  $c' = 2 \text{ kPa}$  is included to account for nominal moisture in the backfill soil (e.g., Hatami and Bathurst 2005;

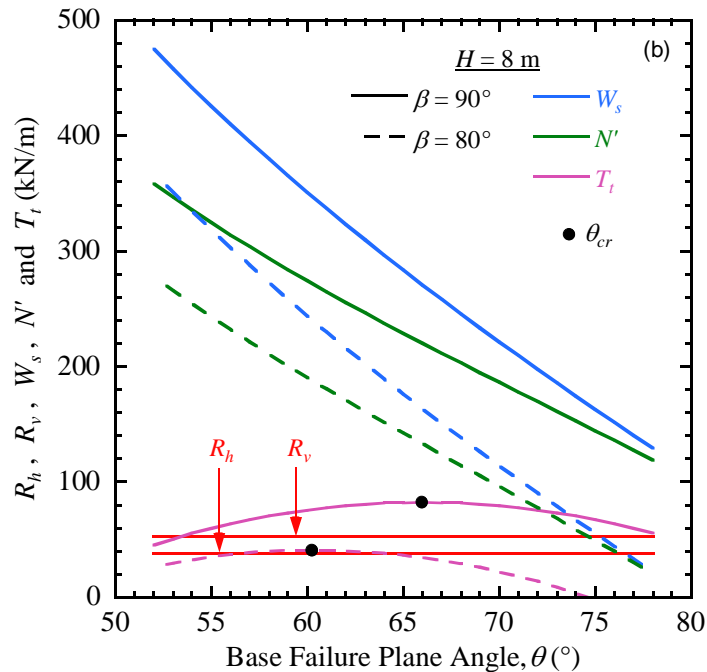


**Figure 2. Wedge forces with varying base failure plane angle.**

Zheng et al. 2017), the current analysis gives the same  $\theta_{cr} = 66.0^\circ$  and lower  $T_i = 67.9$  kN/m. The reduction in  $T_i$  is significant (17%) and, as discussed by Vahedifard et al. (2014), highlights the important effect of even a small amount cohesion, true or apparent, on the results.

Fig. 2 also presents corresponding values for the same GRS retaining wall with  $\beta = 80^\circ$  (i.e.,  $\omega = 10^\circ$ ). The results show similar trends, with  $R_h$  and  $R_v$  unchanged and smaller values for the other forces. In this case, the current analysis gives  $\theta_{cr} = 60.3^\circ$  and  $T_i = 40.9$  kN/m. The  $10^\circ$  batter has a large effect and yields a 50% reduction in the maximum  $T_i$ . For this case, Coulomb earth pressure theory gives  $\theta_{cr} = 59.2^\circ$  and  $T_i = 71.8$  kN/m for the battered wall. Thus, the current analysis, when compared to Coulomb, yields a reduction in  $T_i$  of 43% for the battered wall, which is a substantially larger percentage reduction than for the vertical wall case.

The effect of wall height  $H$  is illustrated in Fig. 3 for a vertical GRS wall. Fig. 3(a) presents results for leveling pad interface friction angle  $\phi_{lp} = 26^\circ, 36^\circ$ , and  $46^\circ$  and vertical load factor  $m = 1$ . Values of  $W_f$  and  $R_v (= W_f)$  increase linearly from 6.6 to 85.8 kN/m as  $H$  increases from 1 m to 13 m. The horizontal toe force  $R_h$  also increases linearly, with the highest values corresponding to  $\phi_{lp} = 46^\circ$ . Under these conditions, the critical angle of the base failure plane is constant ( $\theta_{cr} = 66.0^\circ$ ) and the effective normal force  $N'$  is independent of  $\phi_{lp}$  and increases nonlinearly with  $H$ . Total reinforcement force  $T_i$  also increases nonlinearly, with the

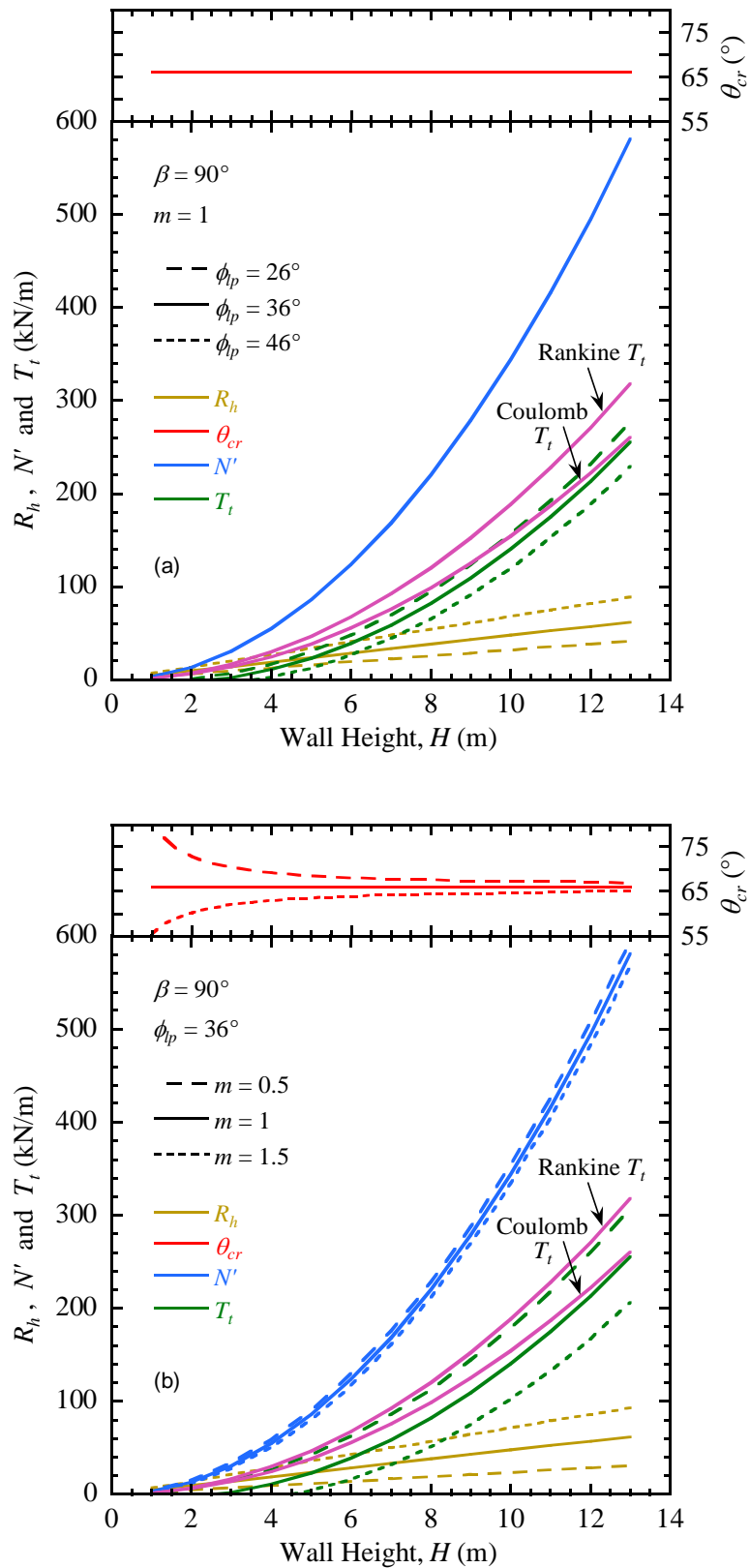


Figure 3. Wedge forces with varying wall height for varying: (a)  $\phi_{ip}$ , and (b)  $m$ .

highest values obtained for the lowest  $R_h$  (i.e.,  $\phi_{lp} = 26^\circ$ ). Corresponding values of  $T_t$  from Rankine theory and Coulomb theory follow a similar trend, with Coulomb values lower than Rankine values by 18% and generally higher than values obtained from the current analysis, especially for lower wall heights. Fig. 3(b) presents additional results for  $\phi_{lp} = 36^\circ$  and  $m = 0.5$ , 1, and 1.5.  $W_f$  values are unchanged and  $R_h$  and  $R_v$  both increase linearly with  $m$  and  $H$ . Under these conditions,  $\theta_{cr} = 66^\circ$  for  $m = 1$  as in Fig. 3(a) but varies with  $H$  for  $m \neq 1$ . This variability of  $\theta_{cr}$  diminishes with increasing wall height and produces small variations in  $N'$ . Values of  $T_t$  display a stronger dependency on  $m$  and are largest for  $m = 0.5$ , which again corresponds to the lowest  $R_h$ . Rankine  $T_t$  values are slightly higher than the values obtained for  $m = 0.5$ , whereas Coulomb values are in closer agreement with the current analysis for  $m = 1$  and higher walls. In both figures, the reinforcement force at the ultimate limit state diminishes to zero for low-height walls (e.g.,  $H = 2.5$  m for  $m = 1$  and  $\phi_{lp} = 36^\circ$ ), which highlights the criticality of specified toe forces in the current method. The trends in Fig. 3 are consistent with the general expectation that the relative contribution of toe resistance is a function of wall height and, as wall height increases, the percentage of total restoring force carried by the toe decreases (Bathurst et al. 2001; Leshchinsky 2007; Mirmoradi and Ehrlich 2017). A more detailed analysis of this example is provided by Fox (2022b).

For GRS walls having a facing column, a key input parameter for the current analysis is the vertical load factor  $m$  that accounts for soil downdrag on the back of the column and defines the vertical reaction force at the toe of the wall, where  $m = 1$  indicates a vertical force on the leveling pad equal to the self-weight of the column. Based on additional information not presented here, Fox (2022b) reported that measurements from published research studies consistently yield  $m \geq 1$  and often  $m > 1.5$ , indicating soil downdrag forces of significant magnitude in most cases. Also, Coulomb earth pressure theory provided a good estimate of  $m$  for several large-scale GRS retaining wall tests. Analysis of the single combined block also avoids the need to solve higher-order polynomial equations associated with multi-wedge methods (Fox 2021a,b; 2022c) and, as such, the solutions can be expressed in closed form and are more convenient for routine use. The planar failure surface assumption may be compromised with the application of concentrated loads such as a spread footing for bridge support (Zheng et al. 2018) and, under such conditions, viewed as a first approximation.

## CONCLUSION

This paper presents new closed-form analytical solutions, developed by Fox (2022b), for the critical failure plane angle and corresponding maximum total reinforcement force away from the facing for a GRS retaining wall, as obtained from a general force equilibrium analysis of a triangular soil wedge at the active limit state. The solutions do not require a specialized numerical code or procedure and can accommodate variable wedge geometry, pore pressure, shear strength parameters, reinforcement force inclination, surcharge stress, applied loads, pseudostatic seismic coefficients, and reaction forces at the toe. The soil wedge and facing column are treated as a combined block with a vertical load factor to account for soil downdrag on the back of the column. Predicted trends are similar and reinforcement force magnitudes are generally less than values



obtained using Rankine and Coulomb theories. Corresponding solutions for an unreinforced soil retaining wall are presented by Fox (2022a).

## REFERENCES

- AASHTO (2020). *LRFD Bridge Design Specifications, 9<sup>th</sup> Edition*, American Association of State Highway and Transportation Officials, Washington, DC, 1912 p.
- Allen, T. M., and Bathurst, R. J. (2015). Improved simplified method for prediction of loads in reinforced soil walls, *Journal of Geotechnical and Geoenvironmental Engineering*, 141(11): 04015049.
- Allen, T. M., and Bathurst, R. J. (2018). Application of the simplified stiffness method to design of reinforced soil walls, *Journal of Geotechnical and Geoenvironmental Engineering*, 144(5): 04018024.
- Allen, T. M., Bathurst, R. J., and Berg, R. R. (2002). Global level of safety and performance of geosynthetic walls: An historical perspective, *Geosynthetics International*, 9(5-6): 395-450.
- Allen, T. M., Bathurst, R. J., Holtz, R. D., Walters, D., and Lee, W. F. (2003). A new working stress method for prediction of reinforcement loads in geosynthetic walls, *Canadian Geotechnical Journal*, 40(5): 976-994.
- Bathurst, R. J., and Benjamin, D. J. (1990). Failure of a geogrid-reinforced soil wall, *Transportation Research Record 1288*, Transportation Research Board, Washington, DC, 109-116.
- Bathurst, R. J., and Simac, M. R. (1991). Review of three instrumented geogrid reinforced soil retaining walls, *Geosynthetics: Design and Performance*, 6th Annual Symposium, Vancouver Geotechnical Society, Vancouver, BC, 15 p.
- Bathurst, R. J., and Simac, M. R. (1993). Laboratory testing of modular unit-geogrid facing connections, STP 1190, *Geosynthetic Soil Reinforcement Testing Procedures*, S. C. J. Cheng, ed., ASTM International, 32-48.
- Bathurst, R. J., Walters, D., Vlachopoulos, N., Burgess, P., and Allen, T. M. (2000). Full scale testing of geosynthetic reinforced walls, *Proceedings, GeoDenver 2000*, GSP 103, ASCE, 201-217.
- Bathurst, R. J., Walters, D. L., Hatami, K., and Allen, T. M. (2001). Full-scale performance testing and numerical modelling of reinforced soil walls, *4th International Symposium on Earth Reinforcement*, IS Kyushu 2001, A.A. Balkema, Fukuoka, Japan, (2): 777-799.
- Bathurst, R. J., Miyata, Y., Nernheim, A., and Allen, A. M. (2008). Refinement of K-Stiffness Method for geosynthetic-reinforced soil walls, *Geosynthetics International*, 15(4): 269-295.
- Damians, I. P., Bathurst, R. J., Josa, A., Lloret, A., and Albuquerque, P. J. R. (2013). Vertical-facing loads in steel-reinforced soil walls, *Journal of Geotechnical and Geoenvironmental Engineering*, Vol. 139, No. 9, 1419-1432.
- FHWA (2009). *Design and construction of mechanically stabilized earth walls and reinforce soil slopes – Volume 1*, Publication No. FHWA-NHI-10-024, Federal Highway Administration, Washington, DC.
- FHWA (2015). *Soil Nail Walls – Reference Manual*, Geotechnical Engineering Circular No. 7, Publication No. FHWA-NHI-14-007, Federal Highway Administration, Washington, DC.
- Fox, P. J. (2021a). Analytical solutions for general two-wedge stability, *Journal of Geotechnical and Geoenvironmental Engineering*, 147(8): 04021075.

- Fox, P. J. (2021b). Analytical solutions for three-wedge stability with vertical wedge interfaces, *International Journal of Geomechanics*, 21(10): 04021194.
- Fox, P. J. (2022a). Analytical solutions for active lateral earth force, *Journal of Geotechnical and Geoenvironmental Engineering*, 148(6): 06022005.
- Fox, P. J. (2022b). Analytical solutions for internal stability of a geosynthetic-reinforced soil retaining wall at the limit state, *Journal of Geotechnical and Geoenvironmental Engineering*, 148(10): 04022076.
- Fox, P. J. (2022c). Analytical solutions for general three-wedge stability, *International Journal of Geomechanics*, 22(12): 04022219.
- Hatami, K., and Bathurst, R. J. (2005). Development and verification of a numerical model for the analysis of geosynthetic-reinforced soil segmental walls under working stress conditions, *Canadian Geotechnical Journal*, 42(4): 1066-1085.
- Huang, B., Bathurst, R. J., Hatami, K., and Allen, T. M. (2010). Influence of toe restraint on reinforced soil segmental walls, *Canadian Geotechnical Journal*, 47(8): 885-904.
- Leshchinsky, D. (2007). Discussion of: "The influence of facing stiffness on the performance of two geosynthetic reinforced soil retaining walls." by R. J. Bathurst, N. Vlachopoulos, D. L. Walters, P. G. Burgess, and T. M. Allen. *Canadian Geotechnical Journal*, 44(12): 1479-1482.
- Leshchinsky, D. (2009). On global equilibrium in design of geosynthetic reinforced walls, *Journal of Geotechnical and Geoenvironmental Engineering*, 135(3): 309-315.
- Leshchinsky, D., and Vahedifard, F. (2012). Impact of toe resistance in reinforced masonry block walls: Design dilemma, *Journal of Geotechnical and Geoenvironmental Engineering*, 138(2): 236-240.
- Mirmoradi, S. H., and Ehrlich, M. (2017). Effects of facing, reinforcement stiffness, toe resistance, and height on reinforced walls, *Geotextiles and Geomembranes*, 45(1): 67-76.
- Mirmoradi, S. H., Ehrlich, M., and Dieguez, C. (2016). Evaluation of the combined effect of toe resistance and facing inclination on the behavior of GRS walls, *Geotextiles and Geomembranes*, 44(3): 287-294.
- NCMA (2010). *Design Manual for Segmental Retaining Walls, 3<sup>rd</sup> Edition*, National Concrete Masonry Association, Herndon, VA, 284 p.
- Vahedifard, F., Leshchinsky, B. A., Sehat, S., and Leshchinsky, D. (2014). Impact of cohesion on seismic design of geosynthetic-reinforced earth structures, *Journal of Geotechnical and Geoenvironmental Engineering*, 140(6): 04014016-1.
- Yu, Y., Bathurst, R. J., and Allen, T. M. (2016). Numerical modeling of the SR-18 geogrid reinforced modular block retaining walls, *Journal of Geotechnical and Geoenvironmental Engineering*, Vol. 142, No. 5: 04016003.
- Zhang, W., Chen, J.-F., and Yu, Y. (2019). Influence of toe restraint conditions on performance of geosynthetic-reinforced soil retaining walls using centrifuge model tests, *Geotextiles and Geomembranes*, 47(5): 653-661.
- Zheng, Y., Sander, A. C., Rong, W., Fox, P. J., Shing, P. B., and McCartney, J. S. (2017). Shaking table test of a half-scale geosynthetic-reinforced soil bridge abutment, *Geotechnical Testing Journal*, 41(1): GTJ20160268.
- Zheng, Y., Fox, P. J., and McCartney, J. S. (2018). Numerical simulation of deformation and failure behavior of geosynthetic reinforced soil bridge abutments, *Journal of Geotechnical and Geoenvironmental Engineering*, 144(7): 04018037.

## **Applications of Geosynthetics for Building Passive Protective Structures against Rockfall, Debris Flows and Snow Avalanches**

**Stéphane Lambert, Ph.D.,<sup>1</sup> Maddalena Marchelli, Ph.D.,<sup>2</sup> and Reza Mohamadi, P.E.,<sup>3</sup>  
Ragavendra Pavan, M.V., B.Tech, PGDBM,<sup>4</sup> and Pietro Rimoldi, P.E.<sup>5</sup>**

<sup>1</sup>INRAE, ETNA, 38000 Grenoble, France; e-mail: [stephane.lambert@inrae.fr](mailto:stephane.lambert@inrae.fr)

<sup>2</sup>DIATI, Politecnico di Torino, Italy; e-mail: [maddalena.marchelli@polito.it](mailto:maddalena.marchelli@polito.it)

<sup>3</sup>Engineered Asset Upkeep, North Vancouver, BC- Canada; e-mail: [Rmohamadi@eaupkeep.ca](mailto:Rmohamadi@eaupkeep.ca)

<sup>4</sup>Strata Geosystems (I) Pvt Ltd, Mumbai, India; e-mail: [pavan.ragav@gmail.com](mailto:pavan.ragav@gmail.com)

<sup>5</sup>Eng. Pietro Rimoldi, Milano, Italy; e-mail: [pietro.rimoldi@gmail.com](mailto:pietro.rimoldi@gmail.com)

### **ABSTRACT**

This paper addresses the use of geosynthetics for building structures such as embankments, dams and mounds with the aim of intercepting, deviating and containing rockfall, snow avalanches and debris flows. In this paper some real cases are presented to illustrate the variety in structure designs and functions. Advantages in using geosynthetics for these structures are discussed. Some design considerations that are specific to these applications are raised, with a particular focus on the dynamic loading.

### **INTRODUCTION**

Inhabited areas, transport corridors and other infrastructure types in mountain and hilly zones are often threatened by rapid gravity driven natural hazards such as rockfall, debris flows and snow avalanches. These phenomena initiate up on the slope, propagate downward along a path mainly defined by the topography and progressively stop with decreasing gradient. Any element at risk, that is to say on the hazard propagation path, may be damaged or destroyed as a result of the large volume and/or velocity of the moving mass. The protection of the elements at risk may be based on active techniques, aiming at preventing the hazard initiation and on passive ones which aim is to deviate, slow down or stop the rockfall, debris flows or snow avalanches before they reach the critical areas.

Passive protection structures have been used for centuries, employing conventional materials such as earth, concrete, rip-rap and steel structural components. With the advent of geosynthetics, new design alternative with increasing complexity have been developed and implemented from the middle of the 80's. Examples of such structures are presented in the following, considering the three types of natural hazards for illustrating the variety in designs and functions. The cases are described from the available literature. Then, the advantages in using geosynthetics for reinforcing the passive protection structures are mentioned. Some specific difficulties with the designing such structures are also discussed.

### **ROCKFALL PROTECTION**

This application is the oldest and most widespread one among passive protection structures. Reinforced embankments and bunds may be used to arrest rock blocks with kinetic energies

ranging from 1 to 50 000 kJ, as well as rockslides. A ditch is most often associated to the embankment to collect the fallen material. In some rare cases, structures aim at deviating the rock block. Two out of the many available references describing real rockfall protection embankments are discussed as follows.

**Varzo, Italy.** The need for protecting the Simplon road against 15 000 kJ in kinetic energy rockfall motivated the construction of a huge embankment close to Varzo, Italy (Rimoldi et al., 2008). The embankment is 20 m in height and 600 m long (Figure 1). The choice of a reinforced embankment with 70° steep faces was imposed by the available space and the steepness of the mountain slope. The reinforcement layer consisted a heavy duty woven polypropylene geogrids, with a 3 mm mesh and a 340 kN/m tensile strength. Many other technical consideration were included in the design of the embankment.



**Figure 1. Huge rockfall protection embankment protecting the Simplon road, in Varzo, Italy (Rimoldi et al., 2008).**



**Figure 2. Rockfall protection embankment along the Trans-Canada highway. General view and cross-section (adapted from Simons et al., 2010).**

**Hells gate rapids, B. C., Canada.** In order to protect a portion of the Trans-Canada Highway, a 8m high and 96 m long rockfall protection embankment was built using a double sided reinforced soil structure (Simmons et al., 2010). The facings consist of gabions (Figure 2). The same hexagonal wire mesh as that used for the gabions is used as reinforcement tail. The structure is



designed to withstand a maximum rockfall impact energy of 10,000kJ maximum and it accounts for the limited space constraint.



**Figure 3. Avalanche control facility in Neskaupstaður, Iceland.**



**Figure 4. Snow avalanche deflecting dam in Belle-Plagne, France (Coulon and Bruhier, 2006).**

## SNOW AVALANCHE PROTECTION

The control of snow avalanche run out has motivated the construction of impressive reinforced structures. Geosynthetics allow building four types of passive structures forming an obstacle on avalanche paths. First, guiding walls prevent from excessive lateral expansion of snow avalanches towards settlements. Second, deflecting dams aim at deviating avalanches towards areas with no elements at risk. Third, mounds –or cone, splitters, wedge- may be used to break down the avalanche velocity. Last, dams may be used to contain the snow avalanche. These structures are rather massive, with an elevation defined based on the avalanche characteristics and are either placed normal or transversally to the avalanche propagation direction.

Similarly as for rockfall protection embankments, geosynthetics allow building structures with a greater height and steeper slope while keeping the structure total volume acceptable and with a steeper face opposed to the avalanche.

**Neskaupstaður, Iceland.** Since 2002, the village of Neskaupstaður, Iceland, is protected by 13 breaking mounds, 10 m in height, placed upstream a catching dam 400 m in length and 17 m in

height (see Figure 3). These structures are reinforced with strips, with a well graded rock as fill, and the face is  $76^\circ$  steep and made from galvanized steel facing. The strips consist of closely packed high tenacity polyethylene terephthalate (PET) fibers encased in a low density polyethylene (LDPE) sheath (Halifax et al., 2016).

Thereafter, nine large facilities with different designs have been built in Iceland, providing a rather exhaustive experience for the use of geosynthetics in snow avalanche protective structures (Indriðason and Hákonardóttir, 2019).

**Belle-Plagne, France.** In order to protect the ski resort, a snow avalanche deflecting dam was built on a  $50^\circ$  steep slope up hill the resort (Figure 4). This wall consists of two superimposed reinforced structures, with maximum heights of 8.5 and 4.3 m respectively. Reinforcement consists of geogrids made from polyester. The local slope material was used as fill which fine content induced constraints for the construction phase.

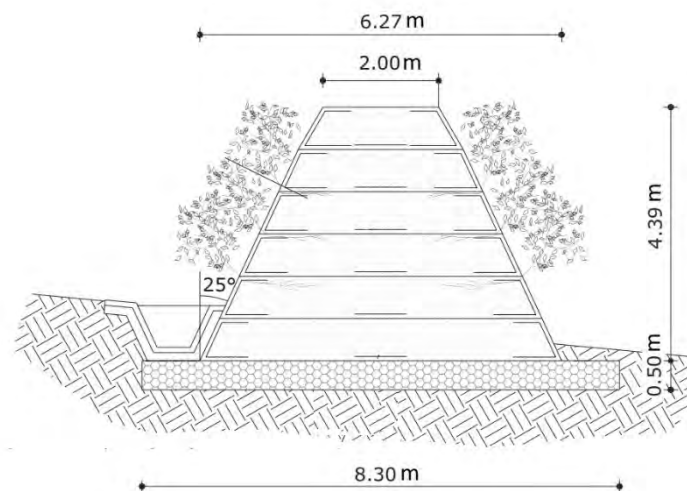


**Figure 5. Cross section of a debris flows catchment wall (adapted from Di Pietro and Tinti, 2008).**

## DEBRIS FLOWS PROTECTION

The use of reinforced structures for building debris flows protection structures is limited up to now. Only a few cases of such applications of geosynthetics are reported in the literature.

**Miseregne, Italy.** In order to protect the village of Miseregne, Val d'Aoste, Italy, a debris flow catchment basin was created by building a reinforced earth wall 4.39 m in height, 6.27 and 2 m in width at the top and base respectively (Figure 5)(Di Pietro and Tinti, 2008). The  $65^\circ$  inclined faces were vegetated. The wall was built perpendicular to the incoming flow, with a large opening to let the water through. In addition, the wall was built on a gabion foundation to insure progressive drainage of the stored debris flow material. Similar structures were also used for deflecting debris flows (Di Pietro and Tinti, 2008).

**Whistler, B.C., Canada.** In view of protecting Whistler against damaging effects of large debris flows, a ground reinforced structure (GRS) was used as abutment for a debris flow barrier (Figure

6). It has two function; first, to serve as support for the steel arch forming the barrier and, second, to contain the debris flow material (Strouth et al., 2012). This abutment is in particular designed to withstand the load transferred by the steel archs and that result from the interception of the debris flow by the barrier. A high - strength woven polypropylene geotextile was used as reinforcement. The fill is a well graded crushed granular material. The GRS is protected against erosion and impact by a 1-m thick facing made of cobbles that is grouted and contained by a welded wire covered with shotcrete.

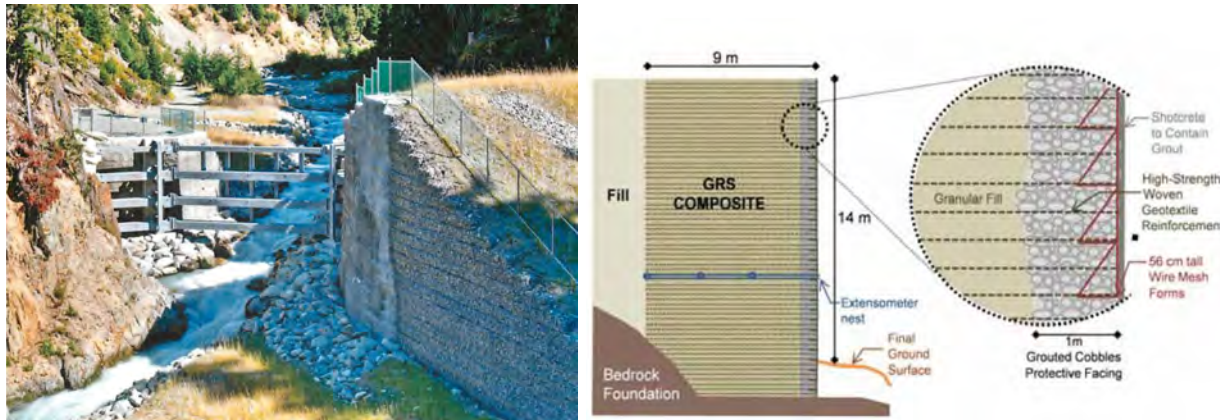


**Figure 6. Debris flow barrier which abutment is reinforced with geosynthetics. General view and cross-section (Strouth et al., 2012).**

## ADVANTAGES OVER OTHER SOLUTIONS

Various benefits results from the use of geosynthetics in these applications, in particular by comparison with structures made of compacted earth or concrete.

First, geosynthetics allow building tall structures, up to 25m in height in some cases. In such applications, the structure height is indeed a key input parameter for the structure design as it relates to its capacity in containing the avalanche, rockslide or debris flow volume or in intercepting bouncing rock blocks.

Second, the face of reinforced structure exposed to the natural event may be given a high inclination, up to 90°. This prevents from any spring board effect, associated with low inclinations and resulting in structure passing over by the moving volume to intercept.

Geosynthetics improve the structure internal stability with respect to the natural-event-induced loading. This was clearly demonstrated for rockfall protection (Blovisky et al., 2004; Peila et al., 2007). For this specific application, geosynthetics in fact distribute the loads along the structure longitudinal axis, from the impacted area.

As a corollary, these structures may be given a high height-to-width ratio, for meeting space constraints associated with some specific contexts (Simmons et al., 2010) or for limiting the structure mass in case the structure is built on a close-to-instability natural slope (Grimod and Segor, 2014). Also, slender structures allows saving fill material (Mannsbart, 2002).

Reinforced structures can conveniently be equipped with specific facings. The aim may be to meet aesthetic constraints (vegetated facing even if steep, rocky appearance...) (Bygness 2007, di Pietri and Tinti, 2008). Also, specific facings may improve the structure impact strength, for example creating a cushion or sacrificial layer made from crushable material, recycled tires... (Simmons et al., 2010; Lambert and Bourrier, 2013; Strouth et al., 2012). In addition, facings prevent reinforcement layers from ageing by atmospheric agents.

Last and not least, structures reinforced with geosynthetics generally constitutes, all in all, cost-effective alternative to conventional material and structures (Mannsbart, 2002; Strouth et al., 2012).

## **SPECIFIC DESIGN ISSUES**

Almost all reinforced structures mitigating gravity driven natural hazards consist of massive structures in elevation with respect to the soil. As such, most of the design principles detailed in the various recommendations and standards for mechanically stabilized earth (MSE) wall apply. This in particular concerns the structure global stability, overturning, base sliding, and bearing capacity. Nevertheless, the design of these protective structures requires also addressing some very specific facets. Some of these are detailed in the following.

**Loading related issues.** Rockfall, snow avalanches and debris flows exert very specific loadings on the lateral faces of passive protection structures. This loading is either localized in the case of rockfall and distributed, but not uniform, in the case of snow avalanches and debris flows. The typical loading orientation is along the horizontal axis in the latter cases and is inclined by an angle ranging from 0 to 50° in the former. Last, and not least, the hazard induced loadings vary with time and last between a few tens of milliseconds in the former case to a few seconds in the latter ones. These loadings are thus very specific and confront designers with uncommon issues relating to the actual whole structure response with time.

The first issue relates to the loading area and orientation. Figure 7 illustrates the case where the upper part of a reinforced breaking mound slipped along a geosynthetic layer due to an excessive lateral loading by an avalanche. To some extent, a similar observation can be made from Figure 8 where the structure face opposite to the impact by a projectile evidences differential sliding from one layer to the other. Both these observations relate to the fact that the loading is applied on the faces of the structure with an orientation close to that of reinforcement layers. Limited work to improve the design of the structure with respect to such lateral loading has been done up to now (Blovisky, 20004; Yang et al., 2016; Cuomo et al., 2020 ; Korini et al., 2021).





**Figure 7. Avalanche breaking mound after completion (left) and after partial destruction (right). Location: Taconnaz, France. (J.M. Tacnet, INRAE).**

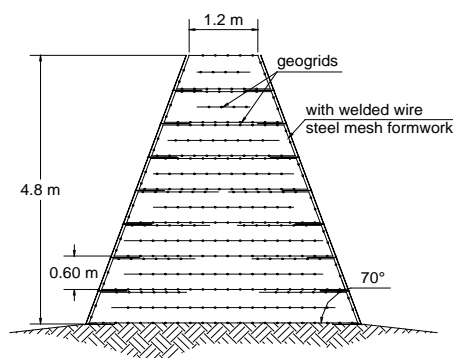


**Figure 8. Rockfall protection embankment after impact evidencing relative displacement between soil layers associated with horizontal reinforcement (from Peila et al., 2007).**

The definition of the proper loading to consider for the design is also an issue. Some recommendations exist for computing the loading applied on a structure by a rock block, a snow avalanche or a debris flow based on its velocity and mass (or unit mass) in particular (e.g. Barbolini et al, 2009; ONR, 2013; GEO, 2015). Nevertheless, structure design approaches consisting in considering a pseudo-static loading that is equivalent to this loading may not be relevant. This is particularly true for rockfall protection structures due to the very short impact duration. The difficulty concerns the equivalent loading to consider, the maximum value being not necessarily relevant for a loading which amplitude strongly varies with time. In addition, the response of the whole structure to such rapid loadings depends on mechanisms that are not accounted for by pseudo-static approaches (Lambert and Bourrier, 2013). In this context, employing numerical tools to model the actual response of these structures seems to be more satisfactory. Numerical modeling could be useful to extend design capabilities if enough data from full-scale tests and performance monitoring, report and analysis is available. Time and very specific skills are required for the numerical models to be reliable.

**Site specific constraints.** Gravity driven hazards passive protection structures are often built in environments characterized by steep and potentially unstable slopes, space constraints or poor quality of the onsite soil. The on-site soils often contain medium to large granular materials, with

angular shapes. Soil characteristics at the toe of mountain slopes may be extremely variable with space. Their fine content and water content may be high.

As for the global stability issue, the problem relates to the mass of structures built on steep slopes. This issue mainly concerns rockfall protection embankments built on slopes and the solution consists in building a structure with a high height-to-width ratio (Rimoldi et al., 2008). For the same reason, the ditch that is generally associated to the embankment may be suppressed (Grimod and Segor, 2014).

The on-site soil characteristics may pose various problems during the design and construction phases. General requirements for soil backfill characteristics when in contact with geosynthetics may not be met. The grain size distribution may require on-site sorting to eliminate large quantities of granular materials that are not suitable to reinforcement layers due to their size and angular shape (Rimoldi et al., 2008). This process requires space, which may constitute a constraint in narrow valleys for example.

Site specific testing of onsite materials should include shear properties, enabling the design of required reinforcement strengths and length. In addition, high water content and high fine content may pose a problem during compaction, for its feasibility, and for the structure stability. The poor quality of the onsite soil may also pose a foundation problem, in terms of bearing capacity, requiring geotechnical investigations.

Last, the interaction of the structure with other natural events occurring on slopes should be considered. For example, long embankments may constitute an obstacle to precipitation run-off with dramatic consequences in some cases (Jaecklin, 2006). Specific and efficient drainage systems are thus necessary uphill the structure. In the same spirit, openings through the structure may be required to let torrential flow through, if any.

## CONCLUSION

The use of geosynthetics for building passive protective structures against rockfall, debris flows and snow avalanches now benefits from a significant experience. The most frequent application concerns rockfall protection embankments. The review of the available literature reveals that geosynthetics allows tackling with a wide variety of constraints, in particular associated with the site characteristics and the function of the structure. Passive protective structures reinforced with geosynthetic appear extremely versatile, and present technical and cost advantages over conventional solutions. However, their design and building requires accounting for some constraints that are specific to the sites where that are built, as well as for the specific loading resulting from the interaction with debris flows, snow avalanches and rockfall.

## REFERENCES

Barbolini, M. and Domaas, U. and Faug, T. and Gauer, P. and Hakonardottir, K.M. et al.. *The design of avalanche protection dams Recent practical and theoretical developments*. EUROPEAN COMMISSION, 212 p., 2009, Climate Change and Environmental Risks, 978-92-79-08885-8.

- Blovsky, S. (2004). Model tests on protective barriers against rockfall. *15th European Young Geotechnical Engineers Conference*, Dublin, Ireland: 11-14
- Bygness, R. (2007). Using geosynthetics for avalanche protection in northern Iceland, *Geosynthetics*, 25(5): 16-20.
- Coulon, E. and Bruhier, J. (2006). Les merlons renforcés de protection. *Rencontres géosynthétiques*, Montpellier, France. June 2006 : 373-380
- Cuomo, S., Moretti, S., Frigo, L. and Aversa, S. (2020). Deformation mechanisms of deformable geosynthetics-reinforced barriers (DGRB) impacted by debris avalanches. *Bulletin of Engineering Geology and the Environment*, 79, 659–672
- Di Pietro, P. and Tinti, M. (2008). Remedial works against debris flows after the 2000 floods in Valle d'Aosta. *Interpreavent*. Vol. 1. Dornbirn, Vorarlberg, Austria. Vol. 1
- GEO (2015). Geotechnical Engineering Office. *Assessment of landslide debris impact velocity for design of debris resisting barriers*, GEO Technical Guidance Note No. 44. Geotechnical Engineering Office, the HKSAR Government; 2015. p. 4.
- Grimod, A. and Segor, V. (2014). Reinforced soil rockfall embankment to absorb high energy impacts along the regional road SR 507 Aymavilles-Cogne, Aosta (Italy); *GeoRegina 2014* september 28-october.
- Halifax, D. J., Freitag, N. and Sankey, J.E. (2016). Design and construction of a reinforced soil avalanche barrier at Neskaupstaður. *17th Nordic Geotechnical Meeting*, Reykjavik, May 25-28: 931-940
- Indriaoason, J. S. and Hákonardóttir, K. M. (2019). Experience and evaluation of reinforced soil systems in catching dams in Iceland 1998–2017. *International Symposium on Mitigative Measures against Snow Avalanches and Other Rapid Gravity Mass Flows*:137-140
- Jaecklin, F., 2006. Innovative design for repairing Gondo mudslide by 20 m high geogrid wall. *8th International Conference on Geosynthetics*, Ozaka, Japan: 1223–1228.
- Korini, O., Bost, M., Rajot, J.-P., Bennani, Y. and Freitag, N. (2021). The influence of geosynthetics design on the behavior of reinforced soil embankments subjected to rockfall impacts. *Engineering Geology*, (286).
- Lambert, S. and Bourrier, F. (2013). Design of rockfall protection embankments: A review, *Engineering Geology*, (154):77 – 88.
- Mannsbart, G. (2002). Geosynthetic reinforced protection structures in mountainous regions – examples of safe and cost-effective alternatives to conventional structures. *7th international conference on Geosynthetics*, Nice, France: 299–301
- ONR (2013) *ONR 24810: Technical Rock-Fall Protection – Terms, Actions, Design and Construction, Inspection and Maintenance*. Austrian Standard Institute.
- Peila, D., Oggeri, C., and Castiglia, C. (2007). Ground reinforced embankments for rockfall protection: design and evaluation of full scale tests, *Landslides*, 4: 255–265.
- Rimoldi, P., Lorzio, R., Pettinau, D., Rocallo, C. and Secci, R. (2008). Impressive Reinforced Soil Structures in Italy. *1st Pan American Geosynthetics Conference*, Cancun, Mexico: 789-798.
- Simons, M., Pollak, S. and Peirone, B. (2010). Design and construction of a high energy rockfall embankment on the Trans-Canada Highway. *Geo2010*, Calgary, Canada: 80-85.
- Strouth, A., Pritchard, M., Roche, D. and Vanbuskirk (2012). Geosynthetic reinforced soil walls for debris barrier in Whistler, B.C. *Geosynthetics*. Vol. 30. N. 4.

- Tissières, P., 1999. Ditches and reinforced ditches against falling rocks. *Joint Japan-Swiss Scientific Seminar on Impact Load by Rock Fall and Design of Protection Structures*, Kanazawa, Japan: 65–68.
- Yang, K.-H., Wu, J. T.H., Chen, R.-H. and Chen, Y.-S. (2016). Lateral bearing capacity and failure mode of geosynthetic-reinforced soil barriers subject to lateral loadings, *Geotextiles and Geomembranes*, 44(6): 799-812.



## **Design of True Abutments of Mechanically Stabilized Soil Walls under high seismicity in Guatemala City.**

**Alberto José Pérez Zarco. MSc.<sup>1</sup>**

<sup>1</sup> Ingnova Guatemala, [jperezarco@gmail.com](mailto:jperezarco@gmail.com)

### **ABSTRACT**

The use of mechanically stabilized soil retaining structures has had a great boom in recent years in Guatemala, especially as road structures. One of its most specialized and less used is a true abutment in bridges, where geometry and loads must be analyzed with special attention. These abutments work as a gravity wall, where the geosynthetic reinforcement creates together with the backfill soil a monolithic block. The integrity of this block is guaranteed by the internal stability of the structure, but due to the high loads, it is necessary to perform a global stability analysis also.

For the internal analysis, the tensile strength, pull-out strength and slip resistance of the geogrid are verified, as well as the strength of the geogrid-block connection are checked in case of wall with segmental blocks as a facade.

The AGIES NSE 5.3-2018 design guideline mentions the use of FHWA NHI-00-043 for the design of this type of structures. This standard guideline suggests a special approach for the design of true abutments and was the one used to perform design in the Guatemala City.

This paper provides the design of the true abutments of the "Paso a Desnivel Bárcenas", for a bridge of 43 meters free span, being the longest bridge with true abutments with segmental block facade.

### **INTRODUCTION**

Mechanically stabilized soil walls, hereinafter referred to as MSME, are retaining structures widely used throughout the world and in the last 20 years they have had a great boom in Guatemala. Most of these walls have been used in residential works, but their use in road infrastructure works is growing every day.

They are very reliable structures that have shown very good performance under extreme earthquake loads, as in the February 2010 earthquake in the Maule region of Chile, where these types of structures did not show any damage or significant displacements (FHWA, 2011). This is very important if we take into account the high seismic hazard with a Peak Ground Acceleration (PGA) used for the design of 0.44g.

Guatemala is located in the Pacific "Ring of Fire", at the junction of three main tectonic plates, which makes it a country with a high seismic hazard, steep topography and particular hydrology.

These structures have been widely used around the world as simple infill retaining walls to support structures or roads. The increased use and acceptance of the system has been driven by a number of factors, including cost savings, aesthetics, simple and fast construction techniques, good seismic performance, and the ability to tolerate differential settlement without structural problems. They can be divided into two main categories; those stabilized with inextensible reinforcements

such as steel bars or strips and those stabilized with geosynthetics. In the abutments of the "Barcenas Overpass", extensible reinforcements consisted HDPE high density polyethylene geogrids.

Among the more complex or specialized uses of this type of structure are true abutments, a system where the bridge header girder is loaded directly on the mechanically stabilized soil wall. This is a relatively new application in Guatemala, where the stresses applied to the reinforcement and the soil are mobilized to much higher levels compared to simple restrained MSME. One of the first and most important true abutments with geosynthetic reinforcement constructed in the United States is the Founders / Meadows bearing of Colorado State Highway 86 over U.S. Interstate 25 in Denver, Colorado, completed in 1999 showing very good performance (Abu-Hejleh, et al. 2003).

Compared to systems that involve the use of deep foundations such as piles to support bridge structures, the use of MSME has the potential to alleviate the "bridge out-strike" problem caused by differential settlement between the bridge abutment and the approach roadway (Wang, et al. 2002)

Currently in Guatemala there is no specific regulation for the design of this type of structures, but within the structural safety regulations of the Guatemalan Association of Structural and Seismic Engineering AGIES NSE 5.3-2018 mentions the use of the design manual of the Federal Highway Administration of the United States of America (FHWA NHI-00-043). For the road works in the country, the specifications for the design of bridges of the American Association of State Highway and Transportation Officials, (AASHTO) standards, are used (Pérez 2019).

The MSME design for the overpass was carried out from July to October 2021. This design included the construction of 618 square meters of MSME approach ramps and 527 square meters of MSME true abutments, located at km 22.5 of highway CA-09 South in the Municipality of Villa Nueva, Guatemala. The purpose of the overpass was to create a safe and efficient return to the CA-09 South.

## SEISMICITY

Earthquakes are relatively frequent occurrences in Guatemala. The country lies in a major fault zone known as the Motagua and Chixoy-Polochic fault complex, which cuts across Guatemala and forms the tectonic boundary between the Caribbean plate and the North American plate. In addition, along Guatemala's western coast line, the Cocos plate pushes against the Caribbean plate, forming a subduction zone known as the Middle America Trench located approximately 50 km off Guatemala's Pacific coast. This subduction zone led to the formation of the Central America Volcanic Arc and is an important source of offshore earthquakes. Both these major tectonic processes have generated deformations within the Caribbean plate and produced secondary fault zones, like the Mixco, Jalpatagua, and Santa Catarina Pinula faults. This dynamic between the plates has forged over millions of years the volcanic chain we know today, as well as the "Cuchumatanes" and "Las Minas" mountains (Pérez 2002).

According to the Structural and Seismic Engineering AGIES macro-seismicity map, for the city of Guatemala where the project site is located, a peak ground acceleration (PGA) of 0.44g needed to be considered. (see Figure 1).

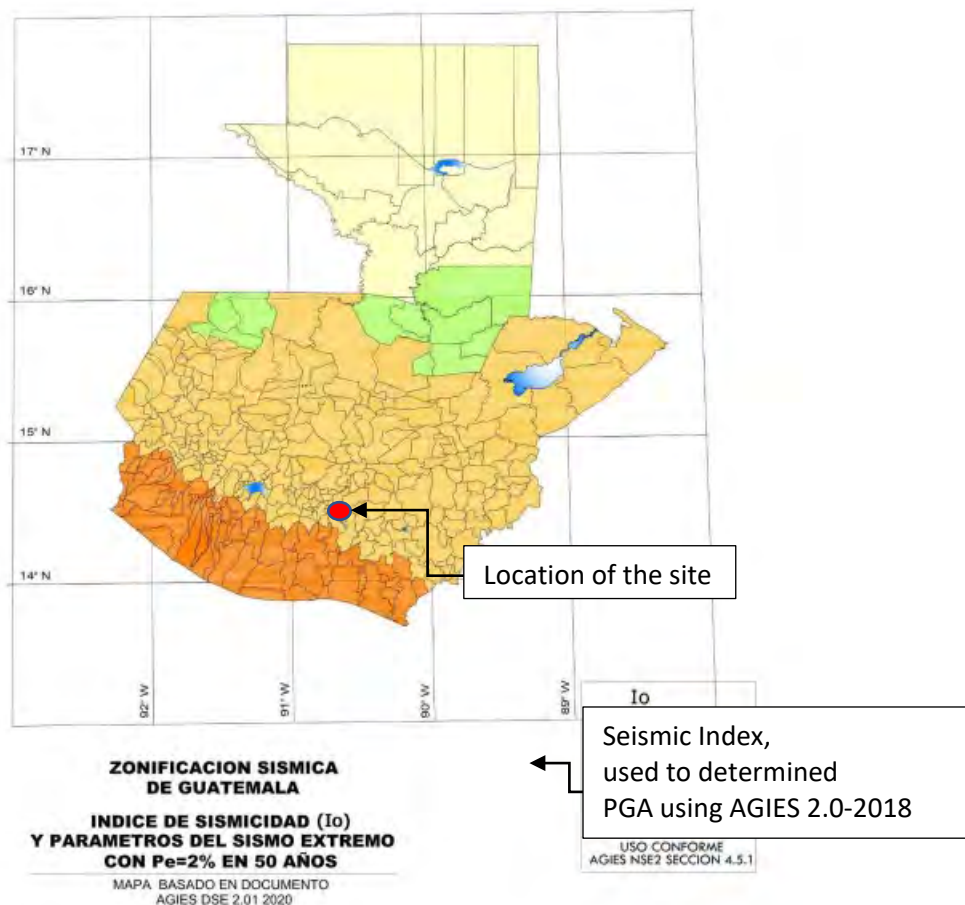


**Figure 1. Seismic Zone Map and location of the project**

## DESIGN AND CONSTRUCTION OF TRUE ABUTMENTS MSME

Originally the project contemplated a deep foundation system using drilled reinforced concrete piles. Due to the time and economic savings, it was decided to change the substructure to a mechanically stabilized soil system, where only 80 centimeters soil need to be excavated to build the MSME (see Figure 2).

The design of true MSME abutments is based on the same premises and structural concepts as any MSME, but in this case they qualify as complex walls and it is recommended to comply with certain guidelines well established in the specialized literature, such as the FHWA and AASHTO standards.

As for any other MSME retaining structure, the design should include two main controls: external stability and internal stability. The external stability controls consist of the sliding, bearing capacity and overturning checks, and follow the same principle as in a gravity retaining wall or MSME design. External stability provides the geometry of the geogrid reinforced "block", i.e. the length of the geogrid reinforcement. The mass of the reinforced soil block provides the restraining

force to slide with the thrust force coming from the active wedge in the retained soil. The bearing capacity must also be checked.



**Figure 2. Excavation for the MSME**

Internal stability comprises two fundamental checks: failure due to rupture and failure due to geogrid pullout or bond check. Internal stability provides the geogrid strength and spacing required for a stable structure to ensure a monolithically functioning block. Interaction factors are used for slippage and pullout and are derived from extensive testing between geogrids and various types of fills.

Depending on the international standard used to carry out the design of reinforced soil walls, internal stability can be carried out based on two different principles: the 2-part wedge design method and the 1-part wedge design method or also called "Tie Back". The 2-part wedge design method for geosynthetic reinforcement materials is mainly used in Germany (EBGEO) and Australia (AS4678).

The "Tie Back" or 1-part design method is mainly used in the UK, USA and Hong Kong. Both methods check the internal stability of the reinforced soil block, i.e. checking for geogrid pullout failure as well as failure against geogrid rupture, but considering different failure models. Both methods also check the sliding along the base of the entire reinforced soil block and the bearing capacity using the Meyerhof pressure distribution (Doulala-Rigby and Pérez 2019). Specifically for the design of this wall, the "Tie Back" method was used using the Mechanically Stabilized Earth Walls Program MSEW 3.0 from Adama Engineering, Inc.



In the case of true abutments, attention should be paid to the guidelines and recommendations proposed by the FHWA in their documents Publication NHI-10-024 and Publication NHI-00-043, this wall was designed according to these recommendations as follows:

- All loads that would be applied to the abutment were considered to estimate the pressure that would be transferred to the reinforced soil and not to exceed the service load of 200kPa and the ultimate load of 335kPa. The overloads considered were a live load of 248kN/m and a dead load of 184kN/m (both service loads), for which a footing width of 2.85 meters was established.

- The distance from the interior face of the facade and the footing was defined at 1.20 meters, and the distance from the exterior face of the facade and the center of the Beam Seat at 2.78 meters (see figure 3).

- An external stability analysis was performed to determine the geometry of the geosynthetic reinforcement, verifying the sliding, eccentricity, overturning and bearing capacity, checking the following safety factors (see table 1):

**Table 1 External Stability**

	Static F. S.	Seismic F. S.
Bearing capacity	2.50	1.875
Sliding on base	1.50	1.125
Overturning	2.00	1.50
Eccentricity	<L/6	<L/3

- An internal stability analysis was then carried out to determine the required length and strength of each reinforcement layer, its vertical spacing and connection strength, complying with the required safety factors (see Table 2).

**Table 2 Internal Stability**

	Static F. S.	Seismic F. S.
Geogrid Strength	1.50	1.125
Geogrid Pullout	1.50	1.125
Connection Strength	1.50	1.10
Sliding on geogrid	1.50	1.125

- The required strength of the connection was verified using the reduction factors  $CR_{ult}$  and  $CR_{cr}$ , which were established based on laboratory tests according to ASTM D6638, for short and long term.

- The global (general) and composite stability of the walls was verified with a limit equilibrium analysis, using Bishop's simplified method, complying with the following factors of safety (see table 3):

**Table 3 Global and Composite Stability**

	Static F. S.	Seismic F. S.
Global and composite stability	1.50	1.10

The following guidelines were also considered:

- The footing does not exceed the distance limited by the expected failure line of  $H \tan (45^\circ - \phi/2)$ .
- The layout and amount of reinforcement was extended to 50% of the total height of the wall up to the "fins" or sidewalls.
- Once external, internal, composite and global stability are satisfied, the design is transferred to construction drawings such as sections, plans, elevations and any other project specific details.

The results of the design show us that the geogrids length is up to 90% of the wall height (see figure 4), and geogrids with an LTDS strength of 57.2kN/m spaced between 60cm and 20cm are required to resist the applied stresses.

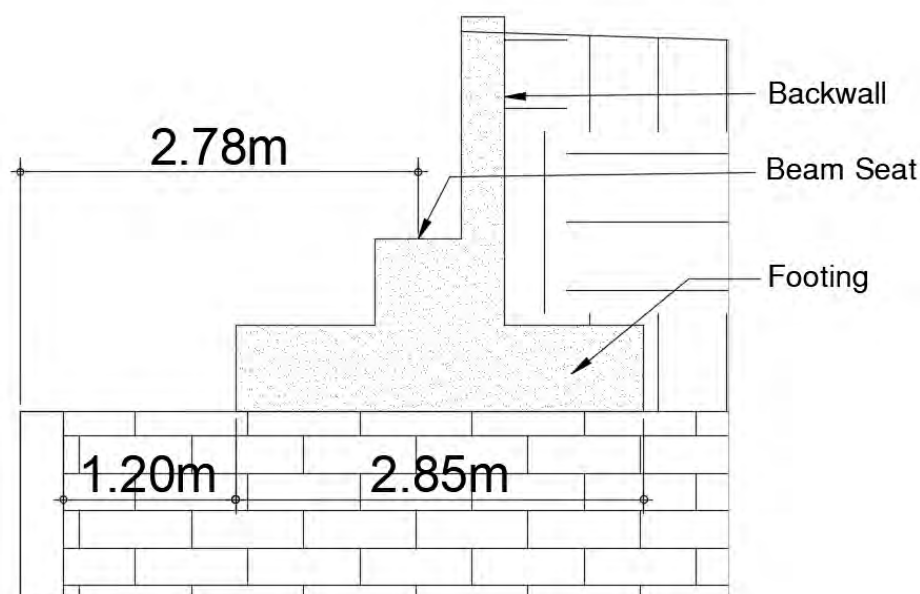


**Figure 3. Abutment Diagram**

The soil parameters were established according to the soil tests in lab. The retained and reinforced soil was a silty sand with an internal friction angle of  $36^\circ$  and a density of  $15.50\text{kN/m}^3$  and water content of 14%. In the MSMEs cohesion is disregarded for the design, but as a reference the soil cohesion is 26kPa. These parameters were obtained from a sample remolded and compacted to 90% of the Modified Proctor according to AASHTO T-180. According to the soil study, the foundation soil had the following properties: internal friction angle of  $29^\circ$ , cohesion  $25\text{kN/m}^2$  and density of  $14\text{kN/m}^3$  (De León 2019).

The abutments were constructed with a segmental facade of concrete blocks with compressive strength of  $100\text{kg/cm}^2$  (see Figure 5). In addition, used uniaxial geogrids characterized by long, thin openings and ribs formed by HDPE high density polyethylene, stretched in one direction during fabrication to produce a geogrid with significantly higher strength in the machine direction. These were placed perpendicular to the wall and secured to whatever cladding was chosen with the appropriate technique and connection. In this case interlocking connection with gravel in a segmental block façade was used. Geogrids with an ultimate strength of up to  $144\text{kN/m}$  were used for this project. The reinforcement of the abutment area was extended more than 50% of its height towards the sidewalls, until changing to the reinforcement of the ramps.

The reinforced backfill was placed in layers of 150mm to 300mm (max.) compacted, generally up to 90% of the AASHTO T-180 Modified Proctor, but in this case, it was up to 95% to decrease the possibility of deformation in the facade and improve the seismic behavior of the system (Xu, et al. 2020).

The length of the geogrids in the zone of contact with the natural soil was 90% of the total height of the abutment, while the upper zone, closer to the footing was the one with the highest stresses, so it was the most reinforced zone having geogrids distributed vertically every 20 centimeters (see Figure 4).

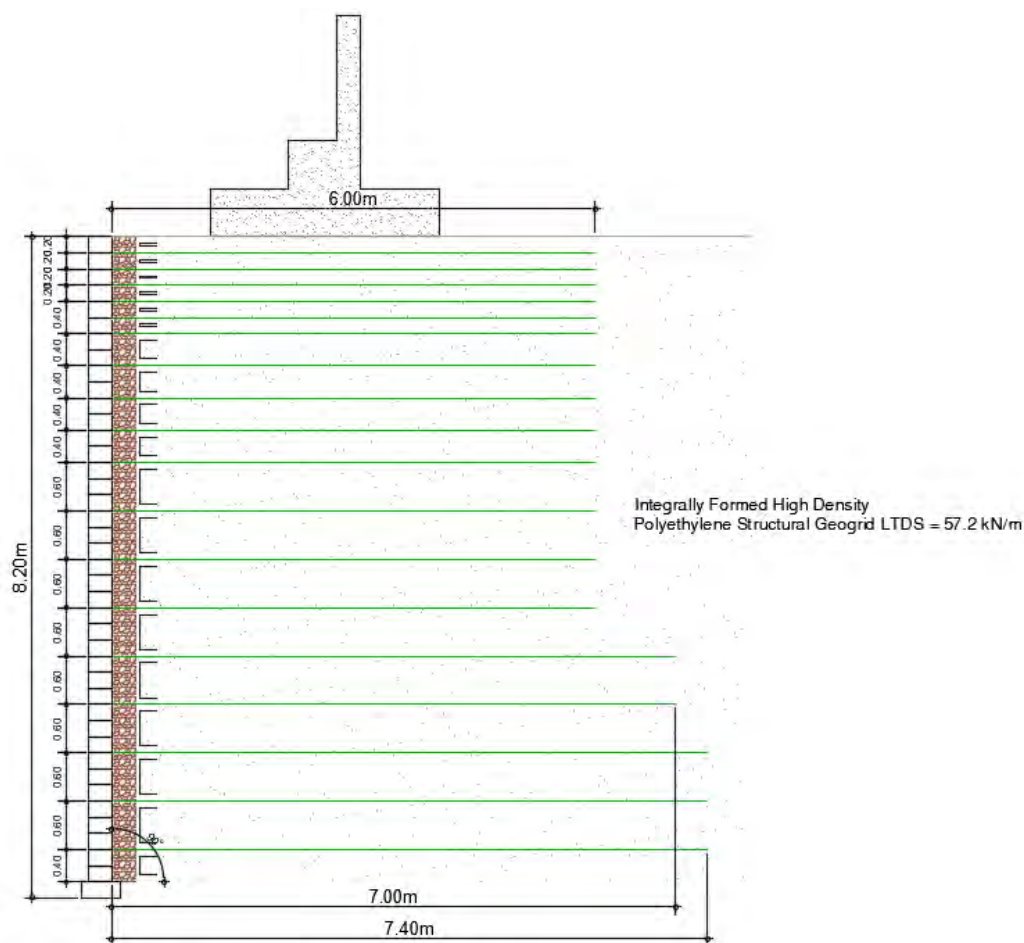


**Figure 4: MSME section of the true abutment**

The block-geogrid connection and the tensile strength were the two reviews that governed the design for internal stability, while the sliding review governed the design for external stability.

During the construction of the abutments, topographic controls were carried out to monitor possible displacements and/or settlements, and none were recorded throughout the project.



**Figure 5: Abutment in service**

## CONCLUSIONS

The increase in the use of MSME in residential and infrastructure works is due, among other reasons, to its ease of construction, structural efficiency, great performance in earthquakes, reduction in execution time, economic savings, aesthetics, and elimination of the bridge exit blow.

The design of the true MSME abutment system follows the same methodologies as a normal MSME, but with some special guidelines to be taken into account, paying attention to the overloads and geometries of the header beams, their location with respect to the wall face and performing global and composite stability analyses, among others.

The abutments of the Barcenas Overpass met the specifications established by the AGIES NSE-2018 standards that apply to the case and follows the recommendations of the FHWA in its Publication NHI-00-043.

The tensile strength and the block-geogrid connection governed the design in the area near the header beam so the geogrid density increased, while the embedment length in the low areas of the MSME was determinant to resist the sliding so it reached 100% of the total height of the wall.

The use of the MSME system in the construction of the abutments reduced the execution time of the project by about 20%, brought economic savings and its behavior has been as expected since its design. It has not presented deformations or settlements.

## BIBLIOGRAPHY

AASHTO, 2012. *LRFD Bridge Design Specifications*.

Abu-Hejleh. N, Zornberg. J, Elias. V, and Watcharamonthein. J, 2003. Design assessment of the Founders/Meadows GRS Abutment structure. *TRB 2003 Annual Meeting*



- AGIES, 2018. *Normas Estructurales de Diseño y Construcción Recomendadas para la República de Guatemala, 2018*. NR-1 Bases Generales de Diseño, Construcción. NR-2.1 Estudios geotécnicos y NR-5.3 Obras de retención.
- De León, W. 2019 *Informe de Estudio de Suelos, Paso a Desnivel Bárcenas*.
- Doulala-Rigby, C. Pérez, A. 2019. 40 años de estructuras de suelo reforzadas con geomalla de polietileno de alta densidad (HDPE). *XVI Panamerican Conference on Soil Mechanics and Geotechnical Engineering*
- FHWA, 2001. Publication NHI-00-043, *Mechanically Stabilized Earth Walls and Reinforced Soil Slopes Design and Construction Guidelines*.
- FHWA, 2009. Publication NHI-10-024, *Design and Construction of Mechanically Stabilized Earth Walls and Reinforced Soil Slopes – Volume I*
- FHWA, 2011. Publication No. FHWA-HRT-11-030, *Postearthquake Reconnaissance Report on Transportation Infrastructure Impact of the February 27, 2010, Offshore Maule Earthquake in Chile*.
- Pérez, A. 2002. *Propuesta de Modificación de la Escala de Intensidades Modificada de Mercalli para Guatemala*. Trabajo de graduación Maestría Ingeniera Estructural. Universidad del Valle de Guatemala.
- Pérez, A. 2019 Factores de conexión en Muros de Suelo Mecánicamente Estabilizado (MSME) con fachada de bloques modulares. *Primer Congreso Nacional de Ingeniería Sísmica y Geotécnica, Guatemala 2019*.
- Wang, T. & Abu-Hejleh, Naser & Watcharamonthein, J. & Zornberg, Jorge. 2002. Monitored Displacements of Unique Geosynthetic-Reinforced Soil Bridge Abutments. *Geosynthetics International*. 9. 71-95. 10.1680/gein.9.0211.
- Xu, P. Hatami, K. Jiang, G. 2020. Shaking table study of the influence of facing on reinforced soil wall connection loads. *Geosynthetics International* 2020, 27, No.4

## **Embankment Reinforcement using the World's Strongest Geogrid – Florianopolis Ring Road, Brazil**

**Andrade, E.,<sup>1</sup> Rodriguez, C., MSCE,<sup>2</sup> Ojaruega, V., MSCE,<sup>3</sup> Carmo, C., Ph.D,<sup>4</sup> and  
Santana, L.<sup>5</sup>**

<sup>1</sup>HUESKER Ltda.; e-mail: [emilia@huesker.com.br](mailto:emilia@huesker.com.br)

<sup>2</sup>HUESKER Inc.; e-mail: [crodriguez@huesker.com](mailto:crodriguez@huesker.com)

<sup>3</sup>HUESKER Inc.; e-mail: [vojaruega@huesker.com](mailto:vojaruega@huesker.com)

<sup>4</sup>HUESKER Ltda.; e-mail: [cassio@huesker.com.br](mailto:cassio@huesker.com.br)

<sup>5</sup>HUESKER Ltda.; e-mail: [leonardo.santana@huesker.com.br](mailto:leonardo.santana@huesker.com.br)

### **ABSTRACT**

Since 2015, a variant road was built for the relief of urban traffic in the south-eastern section of federal road BR 101, more precisely in Florianópolis, which is the capital city of Santa Catarina, Brazil. With a length of 4,828 km (3000 miles), BR-101 is a major Brazilian highway that runs from the city of Touros in the north to São José do Norte in the south in Brazil. In constructing this road, very challenging slope stability problems associated with very soft soils, which contained peat and turf were faced. Very high-strength geogrids were required to ensure the sliding stability of the slopes in the most critical section at a length of about 15 km and up to 12 m in height. This paper describes the design, installation, and, most importantly, characteristics of the slope stabilization using a very high ultimate strength polyester geogrid (1750 kN/m); so far, the highest strength geogrid used for this purpose known by the authors of this paper.

### **INTRODUCTION**

The Ring Road of the Metropolitan Region of Florianópolis is a major part of the Brazilian road infrastructure. Due to the high complexity of the soil conditions in the region and the 50 km highway, several technical and construction challenges had to be overcome.

The aim of constructing this variant road was to create an expressway that would avoid the metropolitan region of Florianópolis. In this way, providing an alternative route to the BR-101 traffic, avoiding the metropolitan region and allowing for more efficient urban mobility. Construction of the Florianópolis Ring Road began in 2014, is currently ongoing, and is expected to be completed in 2023.

The project is divided into several sections, and the pedological conditions of each section imposed different needs to the project. The most critical section in which the high-strength geogrids were used was the South Section, located in the municipality of Palhoças/SC, (Figure 1).

The 15 km long segment goes over rugged terrains and therefore required the construction of several tunnels as well as embankment with heights ranging up to 12 m in order to achieve the design required alignment for the variant. The geology in this section can be characterized by two domains: the crystalline domain, which consists of predominantly igneous and metamorphic rocks of the crystalline basement, and the sedimentary domain, where sediment deposition occurs mainly by marine fluvial processes. This second domain goes from station 226+900 on alignment to the BR-101 intersection. The high-strength geogrids were used on several segments and bridge

abutments due to the presence of thick layers of soft soils, to ensure the geotechnical stability of the embankments. In addition, woven polypropylene geotextiles were needed to provide separation and reinforcement for working platforms.

For the stabilization of the embankments in this area, geogrids of different strengths were specified, with tensile strengths ranging from 350 kN/m (24,000 lbs/ft) to 1750 kN/m (120,000 lbs/ft).

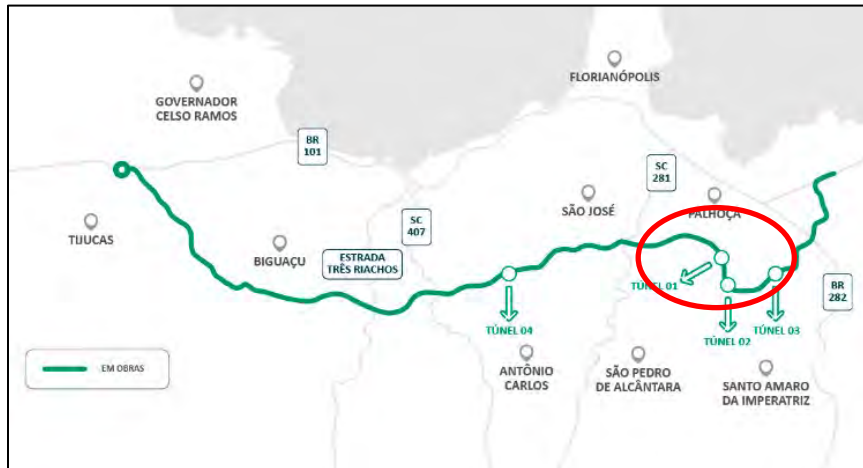


**Figure 1: Extents of the Florianopolis Ring Road**

The selected profile for design purposes is summarized in Figure 2. The results obtained from the SPT indicate that the upper 20 meters of natural terrain (terreno natural) is very soft.

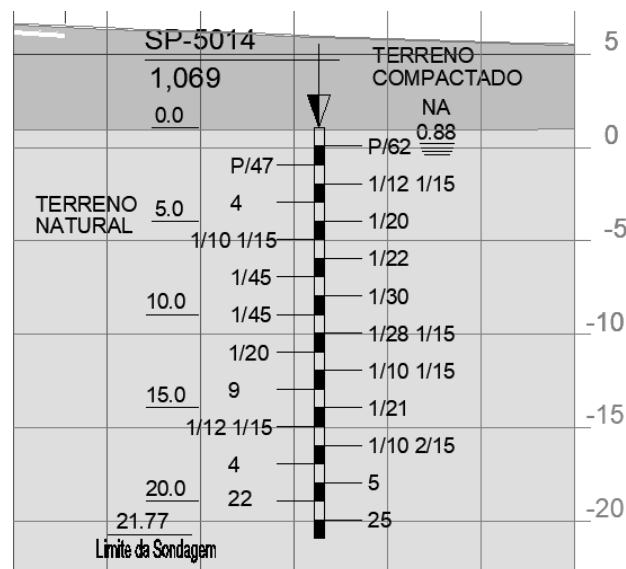


**Figure 2: Standard Penetration Test (SPT) on the Florianopolis Ring Road area, South Section.**

## TENSILE STRENGTH OF THE REINFORCEMENT FOR EMBANKMENTS ON SOFT SOILS

The soft soil present in this area is characterized by deep layers and low bearing capacity, and one of the solutions adopted was the use of geogrids to reinforce the embankments, where the geosynthetic acts as a passive reinforcement.

The foundation soils, when moving horizontally under the weight of the embankment, induce deformations in the geosynthetic, mobilizing a resistant traction force, restricting the displacement of the soil layers, and bringing the set to equilibrium.

The design strength of geosynthetic reinforcement was based on the strength available at the end of the design life (TCR), also known as the long-term design strength (LTDS). Especially when geosynthetic reinforcements are subject to creep strain. This strength was determined from isochronous load/strain (creep) curves, as shown in Figure 3.

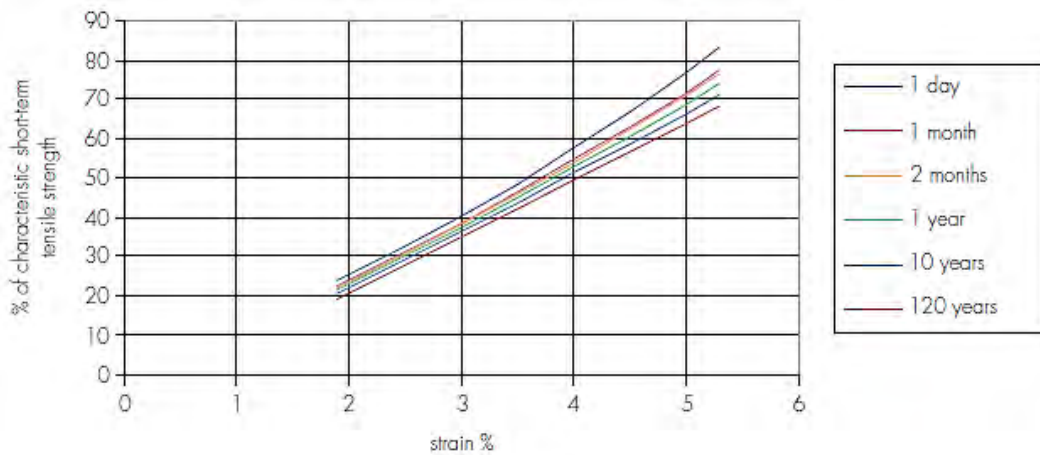


**Figure 3. Example of a stress/strain isochronous curves graph for a typical polyester geogrid.**

The design tensile strength of the geosynthetic reinforcement for Ultimate Limit State (ULS)  $T_{D(ULS)}$  is given by:

$$T_{D(ULS)} = \frac{T_{CR}}{f_m} = \frac{T_{char}}{f_m \times RF_{CR}} = \frac{T_{char}}{RF_{ID} \times RF_W \times RF_{CH} \times f_s \times RF_{CR}}$$

Where:

$T_{CR}$  : tensile creep rupture strength for the appropriate design life and temperature of the reinforcement.

$T_{char}$  : characteristic ultimate strength or nominal strength of the reinforcement.

$f_m$ : material safety factor to allow for the strength reducing effects of installation damage, weathering, chemical and other environmental effects and to allow for the extrapolation



of data required to establish the reduction factors.

$RF_{ID}$ : reduction factor for installation damage.

$RF_W$ : reduction factor for weathering, including exposure to ultra violet light.

$RF_{CH}$ : reduction factor for chemical/environmental effects.

$f_s$ : factor of safety for the extrapolation of data.

Other reduction factors or additional factors of safety could be applied to estimate the design tensile strength, according to local standards and recommendations. Usually, the data sheets provided by the manufacturers only include the typical values of the characteristic ultimate strength or the nominal strength ( $T_{char}$ ) of the reinforcement. However, the reduction factors should also be requested from the product manufacturer for design purposes as they are material-specific for each product and manufacturer.

These reduction factors should be certified by an independent board or agency, otherwise, general conservative values proposed by various literature such as the Geosynthetic Research Institute; GRI Standard Practice GG4(b), should be adopted.

## SPECIFICATION OF THE GEOSYNTHETIC REINFORCEMENT FOR THE BR – 101

The cloverleaf road that connects BR-101 to the Florianópolis Ring Road was constructed on very thick soft soils and varying embankment heights, requiring precise specification of different geosynthetic reinforcements strength to ensure an optimized solution for slope stabilization.

This Ultimate Limit State design results recommended different geogrids reinforced segments, with nominal tensile strengths between 350 kN/m (24,000 lbs/ft) and 1,750 kN/m (120,000 lbs/ft) totaling 150,000 m<sup>2</sup> of geogrids for reinforcement, of which 3,600 m<sup>2</sup> were specified with a resistance of 1,750 kN/m the highest strength ever recorded by the authors for polyester geogrids.

As shown in the cross section on Figure 4, geosynthetic drains and temporary surcharge were necessary to accelerate the settlements expected with the construction of embankments on soft soil layers 20 m (66 ft) deep.

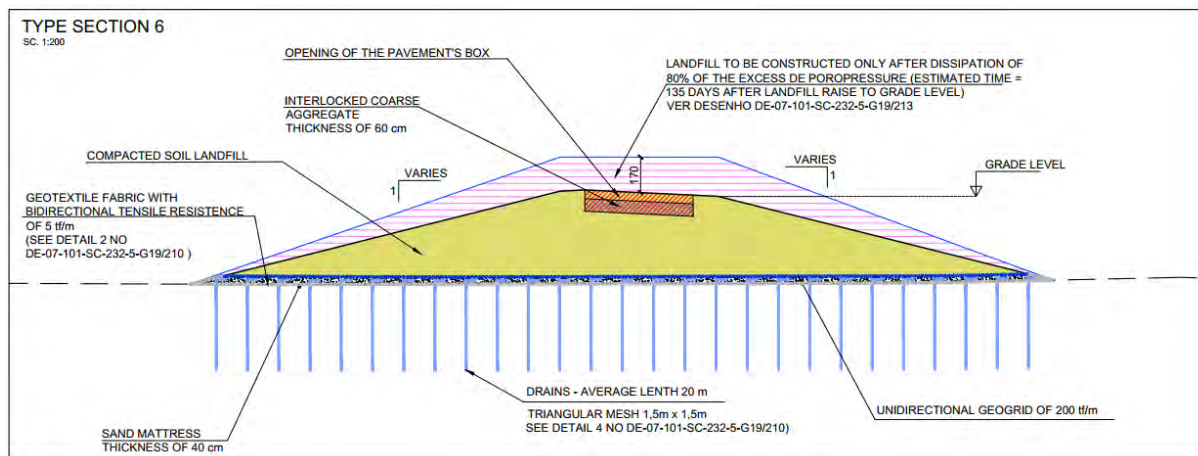


**Figure 4 – Cross section of the reinforced embankment**

An important technical study carried out to optimize the geogrids was related to the reduction factors provided by the designer. Initially, the projects indicated a value of 2.0 for the total reduction factor (TRF) of the geogrids, based on literature (FHWA, 2015).

However, the polyester geogrids fabricated by the manufacturer have British Board of Agreement (BBA 13/H197 - 2014) certified reduction factors. These reduction factors were obtained by extensive testing carried out on samples from various batches of geogrids, resulting in individual partial factor of safety values, which reflect better long-term performance for geogrids.

With these product-specific values and for a design lifespan of 60 years, a new, optimized global reduction factor  $FR_{global}$  of 1.74 was adopted using the following partial Reduction Factors:

*Reduction factor for fluency (60 years):  $FR_f = 1.50$ ;*

*Reduction factor for mechanical damage (60 years):  $FR_{dm} = 1.05$  for installation in sand or gravel;*

*Reduction factor for chemical and environmental damage (60 years):  $FR_{ch} = 1.03$ , for  $4 \leq pH \leq 9$ ; Safety factor by extrapolation of creep data (60 years):  $\gamma = 1.07$ , for  $4 \leq pH \leq 9$ .*

Table 1 presents the equivalence of the nominal tensile strengths originally indicated in the design and the values adopted for the supply of geogrids, manufacturer geogrids (GT), using the reduction factors certified by BBA.

**Table 1 – Comparison between tensile strength specified in the design and the proposed geogrids, considering certified reduction factors for the proposed geogrid line.**

Specified Tensile Strength (kN/m)	Total Reduction Factor used in the design	Design Tensile Strength (kN/m)	Strength Calculated with the proposed geogrid specific reduction factors (BBA 13/H197) - 60 years	Proposed geogrid tensile strength specification (kN/m)
2000	2	1000	1736	1750
1200	2	600	1041	1100
800	2	400	694	700
600	2	300	521	550
400	2	200	347	350

## GEOGRIDS SUPPLY AND CONSTRUCTION

Upon completion of the optimization studies for the reduction factors of the geosynthetic reinforcements and approval of the new specifications, customized reinforcement geogrids, specifically for each reinforced section of the highway were produced.

The unprecedented production of the 1750 kN/m geogrid, made of polyester at the manufacturer's plant, located in Germany, was carried out under conditions specifically determined to achieve the mechanical properties required by this project.

During production, quality control tests were a point of attention to ensure the design strength of the geogrid, as measuring the magnitude of tensile strength this high was not easy using conventional laboratory equipment.

The tests were carried out in the factory's internal laboratory, using high-capacity equipment to obtain accurate measurements of strain and resistance until rupture. These QA/QC tests are guaranteed by laboratory and equipment certification provided by Dakks (national accreditation body of the Federal Republic of Germany), which ensures that testing standards are strictly followed, in accordance with accreditation criteria. Figure 5 shows results obtained from five different tests, as it could be observed in terms of strain and strength, all the curves show similar performance. In all five tests (F-max), minimum resistance of 1700 kN/m @ 9% deformation.

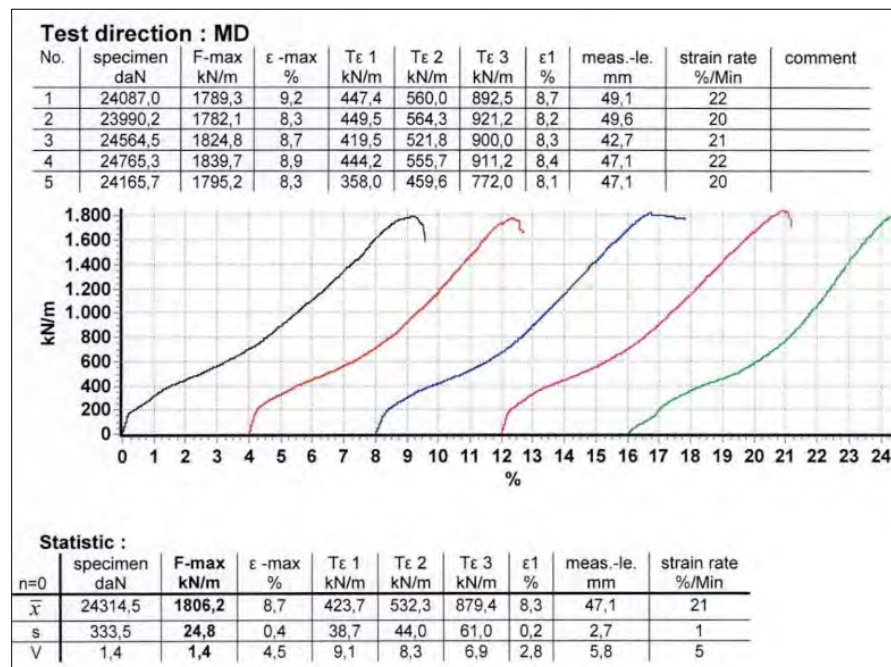


**Figure 5 – Tensile Strength test report for the 1750 kN/m geogrid.**

In addition to the specific physical and mechanical properties, the geogrid panels were produced in precise dimensions according to the paneling study developed for each section of the reinforced embankment segment, thereby reducing wastes from excess leftovers and overlaps. In red, Figure 6 shows a segment reinforced with the 1750 kN/m geogrid. Different colors in figure 6, represents other geogrids with different strengths used in this project.

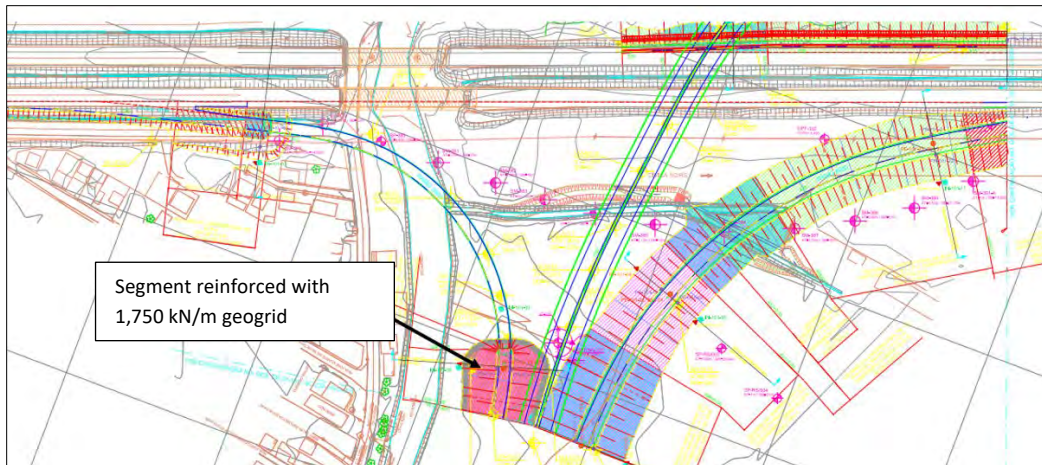


**Figure 6 – Segments of the project with geogrids of varying tensile strengths**

The installation of geosynthetics in the south section of the Florianópolis Ring Road began in August 2021, after the completion of the working platforms and installation of geosynthetic drains in areas with extremely soft soils. Figure 7 shows a general view of the embankments during construction.



**Figure 7 – Construction of embankments along the Florianópolis Ring Road**

The simplicity of installation of geosynthetics reinforcement and the production of custom-made panels in exact dimensions for each section of the embankment helped facilitate and accelerate the construction process, allowing for earlier completion of this portion of the project before the commencement of the rainy season in the region. This easy and quick installation helped contribute to delivery deadlines which was met according to the project schedule.

The photos in Figure 8 show the installation details of the geogrid in the project, such as overlap details and installation direction of the geogrid.





**Figure 8 – Installation of the 1750 kN/m Geogrid**

The revision of the specifications based on certificates of reduction factors for each specific product was a fundamental step in reducing costs and ensuring the most effective solution in the stabilization of slopes, maintaining the performance required when compared with the original design.

## CONCLUSIONS

This case history shows how large projects with special needs can benefit from detailed studies and from developed customized materials and solutions when specially designed to maximize the benefits offered by geosynthetic reinforcement solutions while minimizing waste of material and overkills in their design.

The slope stability analysis indicated that the configuration of the embankments along the Florianopolis will remain stable for static and earthquake conditions.

Customizing geosynthetics would optimize the time of installation by up to 30 %, which in turn might help reduce the time of the embankment construction.

## REFERENCES:

BS 8006-1: 2010 *Code of practice for strengthened/reinforced soils and other fills*  
BBA Technical Approvals for Construction. *Agrément Certificate 05/4266* – Product sheet 2

FHWA. (2015, Feb). *Federal Highway Administration Research and Technology*. Retrieved from Coordinating, Developing, and Delivering Highway Transportation Innovations: <https://www.fhwa.dot.gov/publications/research/infrastructure/bridge/14094/007.cfm>

## **Impact of Primary Geogrids Spacing and Secondary Geogrids on Geosynthetic Reinforced Soil-Integrated bridge Systems (GRS-IBS) and Lateral Earth Pressure.**

**Bahia S El Refai<sup>1</sup> and Dr. Patrick J Naughton, Ph.D.,<sup>2</sup>**

<sup>1</sup>Atlantic Technological University Sligo, Ireland; e-mail: bahia.elrefai@research.atu.ie

<sup>2</sup>Atlantic Technological University Sligo, Ireland; e-mail: patrick.naughton@atu.ie

### **ABSTRACT**

Geosynthetic Reinforced Soil – Integrated Bridge Systems (GRS-IBS) involve supporting a bridge deck directly on top of a reinforced soil structure without the need for piles or bridge bearings. In this study, Plaxis 2D was used to investigate the response of a GRS-IBS abutment to typical bridge loads. Four models were investigated consisting of the application of a constant vertical load and horizontal load. The horizontal load was applied in a cyclic manner, both towards and away from the abutment to replicate the effect of temperature variation on the structure. The analysis found that the spacing between the primary and secondary geogrids layers was an important factor in controlling wall displacement, vertical stress, settlement of the base of the bank seat and the lateral earth pressure. Decreasing spacing between the primary geogrid layers reduced wall deformations, peak vertical stress, settlement under the bank seat and the lateral earth pressure, while removing the secondary geogrid layers increased the wall deformations, peak vertical stress, settlement under the bank seat. The prediction of the earth pressure coefficient within the retained fill under phased loading showed good agreement with the predicted behavior in Plaxis 2D and that suggested by BS 8006-1 (2016) and Bathurst et al. (2008).

### **INTRODUCTION**

Bridges are an essential component in modern infrastructure to provide passage over an obstacle. Bridges, in their simplest design, consist of two abutments, one on either side of the obstacle, supporting the bridge deck spanning over the obstacle. Moreover, in conventional bridges, expansion joints and bearing are traditionally installed between the bridge deck and the supporting abutments to accommodate the relative movement and prevent the development of stresses generated by temperature between the superstructure and the abutment, Figure 1. These expansion joints require permanent maintenance due to damage from de-icing salts leaking through the deck joints in the superstructure components. This issue leads to corrosion and immobilization of the joints and bearing that represent a major element of conventional bridges, repair, and maintenance costs.

Given the problems with conventional bridges containing joints and bearings, the concept of physically and structurally connecting the superstructure and abutment to create an integral bridge have become very popular, Figure 2(a), Carder & Card (1997). For integral bridges the problems associated with joints and bearings are avoided. However, because of the integral connection between the superstructure and the abutment, the abutments are forced to move away from the soil they retain when the temperature decreases (in winter) and the superstructure contracts and move towards the soil when the temperature rises and the superstructure expands (in summer), Figure 2(b), Horvath (2000).

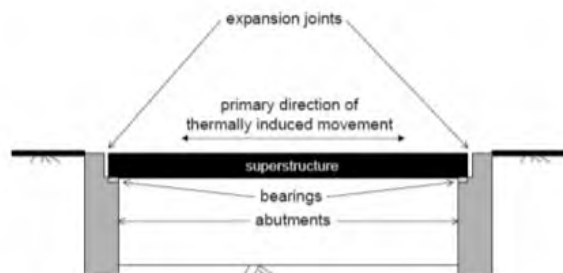


**Figure 1. Schematic of conventional bridge, after Horvath (2000).**

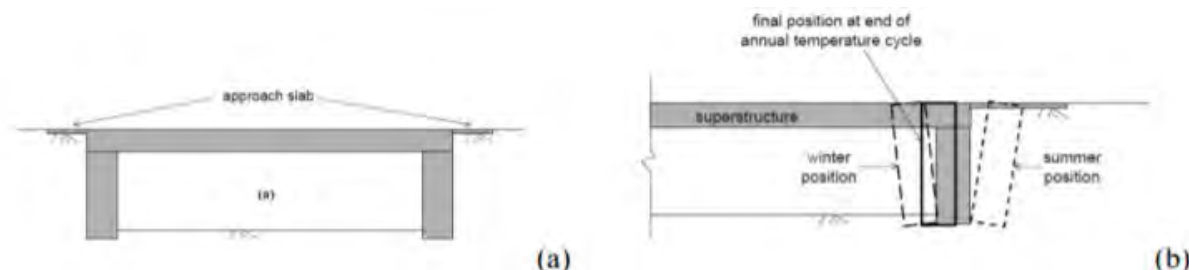


**Figure 1. Schematic of (a) integral bridge, (b) movement of abutment, after Horvath (2000).**

A solution evolved for an economical and faster way to construct a system that blend geosynthetic reinforced soil system (GRS) supporting a bridge superstructure without any joints. The Geosynthetic Reinforced Soil – Integral Bridge System (GRS-IBS), Figure 3, uses alternating layers of compacted granular fill with layers of geotextile reinforcements alternating layers of compacted granular fill with layers of geotextile reinforcement, rather than relying on a conventional bridge support system beneath the bridge (Adams et al. 2011).

## AIMS AND OBJECTIVES

This project investigates the mechanisms of action in integral bridges with reinforced soil abutments and how this affects the overall design of these systems. GRS-IBS systems have many cost and construction time advantages over conventional bridge systems. It is important to review some of the perceived issues with GRS-IBS system with respect to its long-term performance.

The FHWA design methodology for GRS-IBS (Adams & Nicks 2018) assumes a semi-empirical approach to design. Furthermore, many studies (Abu-Farsakh et al. 2017, 2018) have strongly argued that the method adopted by the FHWA (Adams & Nicks 2018), is a conservative approach and outlined that the failure modes of a GRS-IBS system are not appropriately addressed in that method. Abu-Farsakh et al. (2018) also argued that the failure envelopes outlined within BS 8006-1 (2016) failed to cover the true failure patterns within a GRS-IBS system. It is important to match a common design procedure and partial factors in determining the overall required forces and to determine an appropriate method of long-term design strength.

Garnier-Villarreal et al. (2014) showed that the GRS-IBS when designed using the FHWA design methodology (Adams & Nicks 2018) is working properly deformation wise, but they highlighted issues related to temperature changes and environmental conditions that seems to influence the behaviour of the structure. They suggest that the design should focus on seasonal influence and the need to collect more data to better understand the behavior of the system.



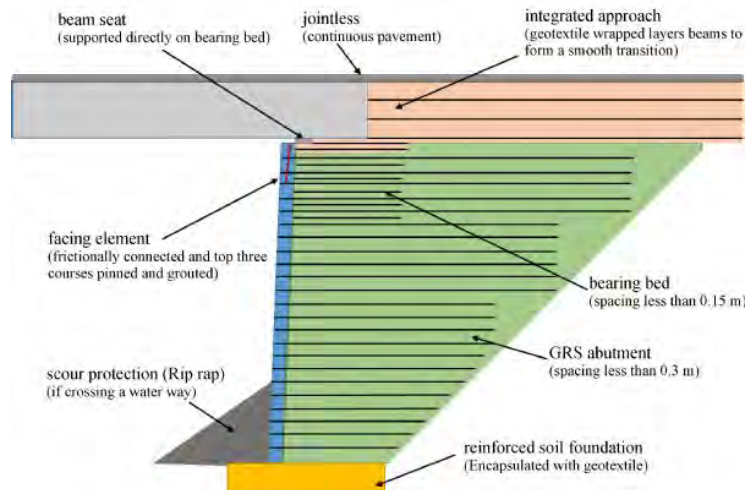


**Figure 2. Section View of GRS-IBS System**

Since GRS-IBS system are monolithic bridges, it is important to understand the impact of the integral arrangement on the soil mass with respect to deformation, stresses, and strains. Moreover, the diversity in design approach, in addition, to the lack of data concerning the long-term performance, it is unclear how these systems will perform over their design life, which is typically 100 years.

The core aims and objectives of this study were to:

- 1- Develop and validate a numerical model in Plaxis 2D that can capture the response of an instrumented GRS wall and a GRS-IBS system
- 2- To develop a numerical model, to better understand the behaviour of the GRS-IBS system under vertical and horizontal loads.
- 3- To conduct a numerical parametric study of integral bridges with reinforced soil abutments to identify the pertinent parameters including the spacing between primary geogrids and importance of secondary geogrids.

## METHODOLOGY

The methodology developed in this study consisted of a two-stage numerical analysis. The first stage involved the use of finite element analysis code Plaxis 2D to replicate the documented behavior of a full-scale geosynthetic reinforced soil (GRS) retaining wall reported on by Hatami & Bathurst, (2005), and a GRS-IBS system reported by Abu-Hejleh et al. (2000b). The second stage was to analysis the behavior of GRS-IBS systems, which consisted of reinforced fill, segmental facing blocks and geogrid reinforcement members.

### *Validation Model*

Numerical modelling was successfully used to investigate a range of parameters that influence the behaviour of GRS (Hatami & Bathurst, 2005 and Zheng & Fox, 2017). In this study Plaxis 2D was validated against two studies. The first study consisted of a full scale GRS wall (Hatami & Bathurst 2005). Both the predicted horizontal displacement of the wall and the predicted axial strain in the reinforcement from this study were found to be in good agreement with the reported values,

Figures 4 & 5. This validation model was previously discussed in detail by El Refai & Naughton (2022).

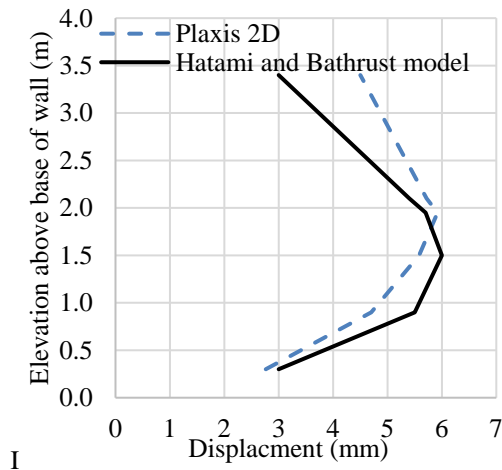


**Figure 4. Predicted wall face displacement from this study & Hatami & Bathurst.**

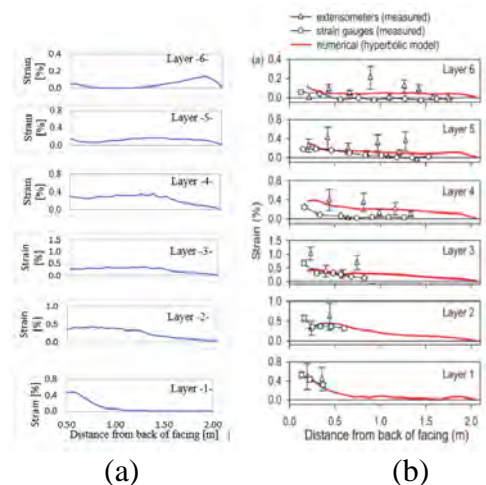


**Figure 5. Predicted axial strain from (a) this study and (b) Hatami & Bathurst.**

The second study consisted of a fully instrumented GRS-IBS bridge abutment reported by Abu-Hejleh et al. (2000). The predicted displacement value of the horizontal facing from this study showed good agreement with the reported measured values after the construction of the structure and the placement of the bridge abutment at Section 400 and Section 800, Figure 6. This validation model was previously discussed in detail by El Refai & Naughton (2022).

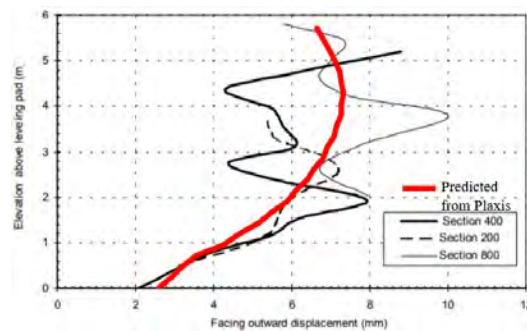


**Figure 6. Comparison of facing displacement after the construction of the structure from this study with those reported by Abu-Hejleh et al.**

### *Parametric Study Methodology*

In this study a parametric variation examined the influence of the length and vertical spacing of the primary geogrids and the length of additional secondary geogrid layers installed near the top of the wall on the performance of GRS-IBS. The structural geometry of each abutment was determined using the current FHWA guidance for GRS (Elias et al., 1997). A base line model was examined at a reinforcement length of 7m and a reinforcement vertical spacing of 0.6m, Figure 4. The model geometry was based on a 6 m high segmental wall with a vertical face. The vertical boundary in the model was 15m behind the end of the reinforcement layers. The concrete facing blocks were 0.15 m in height and 0.3 m wide. The blocks were arranged in 40 vertical blocks

supported on a steel plate. The wall supported an abutment bank seat 2 m wide, and 1.4 m deep located at different distances from the back of the facing block. The blocks, bank seat and back fill soil properties assigned in the models are presented in Table 1. An interface was created between the blocks, and the blocks and soil, Table 2. The stiffness, EA, of the geogrid reinforcement was 1500kN/m, corresponding to a short term strength of approximately 150kN/m for a polyester geogrid.

**Table 1. Model parameters for the backfill and facing blocks used in the Plaxis 2D analysis.**

Material	$\gamma$ (kN/m <sup>3</sup> )	$E_{50}^{ref}$ (MPa)	$E_{oed}^{ref}$ (MPa)	$E_{ur}^{ref}$ (MPa)	$c$ (kPa)	$p$ (°)	$\psi$ (°)
Backfill	22	50	28	100	0.15	1	44
Facing block	16	100	-	-	0.15	-	-

**Table 2. Backfill – facing block and facing block – facing block interface properties used in the Plaxis 2D model.**

Interface	E (MPa)	c (kPa)	$p$ (°)	$\psi$ (°)	$k_n$ (MN/m <sup>3</sup> )	$K_s$ (MN/m <sup>3</sup> )
Backfill–facing block	50	0	44	11	100	1
Facing block–facing block	100	46	57	0	1000	40

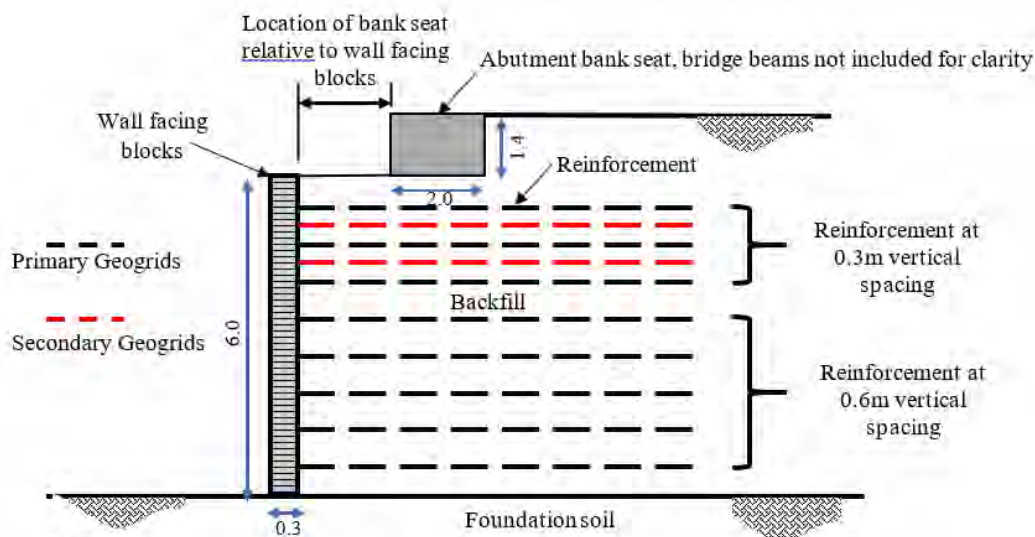


**Figure 7. Parametric Model geometry.**

The bank seat was supported by a fixed anchor plate at the top of the bank seat representing the bridge beams and was required to restrain the abutment from unconditional outward movement when the bridge loading was activated in the model. The axial stiffness of this fixed anchor plate was 16MN/m, which was selected to limit the horizontal displacement of the bridge beams to 1cm. Without this anchor the GRS wall would have no restraint to horizontal displacement.

The parametric model main geometry, boundary conditions, soil parameters, blocks parameters, interfaces between soil-block and interface between block-block were the same in all models.

A total of 4 finite element models were chosen to investigate the influence of varying geometric properties. These parameters were selected as they replicated the typical geometry and material characteristics used in practice for this type of wall construction. Table 3 outlines the parameters varied within Plaxis 2D as part of this parametric analysis. Four parametric models (Models PS-0 to PS-3) were analyzed to assess the impact of the spacing between the primary geogrids (PS-1 and PS-2), and the removal of the secondary geogrids (PS-3). All other parameters remained constant during the parametric variation.

**Table 2. Geometry changed in parametric Models**

Model	Abutment Width (m)	Length of primary geogrid (m)	Spacing between primary geogrid layers (m)	Number of secondary geogrid layer	Length of secondary geogrid (m)
PS-0	2.0	7	0.6	2	4.8
PS-1	2.0	7	0.3	2	4.8
PS-2	2.0	7	0.45	2	4.8
PS-3	2.0	7	0.6	x	x

### *Calculation of the bridge loads*

The vertical and horizontal loads used in this analysis are shown in Table 4, and were determined from the analysis of a single lane bridge deck, 15m long, supported on a 2m wide and 1.4m high bank seat using the Load Model 1 (LM1) model in BS EN 1991-1-1 (2002) and were previously discussed by El Refai & Naughton (2022). The Vertical and horizontal load from the self-weight, variable traffic loads and LM1 are the net value of the resultant force acting on the abutment in the direction of the body.

The LM1 model is for tandem axle and general uniformly distributed case in accordance with the design standard for traffic loads on bridges. BS EN 1991-1-1 (2002) was used to calculate the vertical traffic loads on the bridge. The shrinkage, creep, temperature and braking force loads were calculated EN 1992-2 (2005) for Irish conditions consisting of a temperature of 25°C, an ambient temperature of 15°C and a relative humidity of the ambient environment of 70%.

**Table 4. Magnitude of loads used in the analysis.**

Load	Self-weight	Variable traffic load	Traffic load LM1	Shrinkage	Creep	Temperature	Braking force
Vertical (kN)	185.3	31	72	0	0	0	4.3
Horizontal(kN)	123.4	36.6	10.5	-100	-44.2	±73.5	±23

### *Construction of the model*

The structure was constructed in stages within Plaxis 2D, with an analysis undertaken at each stage. The stages used in this study consisted of 10 phases and the pattern of the phases are:

- Phase 1: The first construction phase consisted of modelling the backfill, geogrid and facing blocks without the abutment bank seat or bridge loadings.



- Phase 2: The second construction phase involved adding the abutment bank seat and backfill immediately behind the bank seat. The analysis of this stage modelled the impact of the self-weight of the bank seat and bridge beams only.
- Phase 3: The third phase involved applying the vertical load of the bridge own weight at rest without any passing traffic to the bank seat.
- Phase 4: The fourth phase involved the application of the horizontal load coming from the shrinkage and creep of concrete, which was applied towards the bridge abutment.
- Phase 5: The fifth phase involved the application of the horizontal load from the temperature, both towards (inward) the bridge abutment.
- Phase 6 (phase n): The sixth phase involved the application of the vertical and horizontal load from all applied loads at rest.
- Phase 7 (phase n+1): The seventh phase involved the application of the vertical and horizontal load from all applied traffic loads.

## RESULTS

### *Total wall displacement*

The pattern of total wall displacement during all phases for the four models investigated (PS-0 to PS-3) were similar. Figure 8 presents the total wall face displacement for Model PS-0. The magnitude of predicted total wall displacement changed with the geometrical parameters, Table 4. Phase 9 showed the highest deformation at the top (19 mm) and at the mid-height of the wall (31 mm) due to the increased load from the traffic passing over the bridge. The location of maximum wall displacement remained at the mid height of the wall in models PS-0 and PS-4. However, in models PS-1 and PS-2 the location of the maximum deformation moved 0.2m upwards. This was attributed to a reduction in the spacing between the primary geogrids from 0.6m to 0.45m and 0.3m respectively.

In models PS-1 and PS-2 the wall displacement decreased when the vertical spacing between the primary geogrids reduced from 0.6m (PS-0) to 0.3m (PS-1) and the to 0.45m (PS-2) respectively. Models PS-0 and PS-3, where the secondary geogrids were removed from the model, showed an increase in wall displacement of 3 mm at the top of the wall but no significant change occurred at the mid height of the wall, Table 5.

### *Settlement of the abutment bank seat*

The pattern of the settlement under the bank seat was similar in all models, Models PS-0 to PS-3. Application of the vertical bridge loads to the bank seat, Phase 3, resulted in rotation of the bank seat away from the abutment, resulting in greater vertical settlement at the front of the bank seat (Point B), Figure 9. This rotation was permanent and was not altered by the subsequent application of horizontal loads in later phases, Figure 9.

The maximum settlement under the bank seat in the four models was under the bottom rear corner of the bank seat and tended to reach its minimum under the front corner of the bank seat (Models PS-0 – PS-3), Table 6.

In models PS-0, PS-2 and PS-3, the rear and front settlement of the bank seat decreased when the vertical spacing between the primary geogrids was reduced from 0.6 m (PS-0) to 0.3 m (PS-1) and 0.45 m (PS-2). Where in PS-2 the settlement decreased by 4 mm at the bottom rear and

3 mm at the bottom front, where in PS-3 the settlement decreased by 2 mm at the bottom rear corner and 1 mm at the bottom front corner, Table 6.

In models PS-0 and PS-3, where the secondary geogrids are removed from the model, a slight increase of 1 mm in settlement at both the bottom rear and bottom front corners was observed.

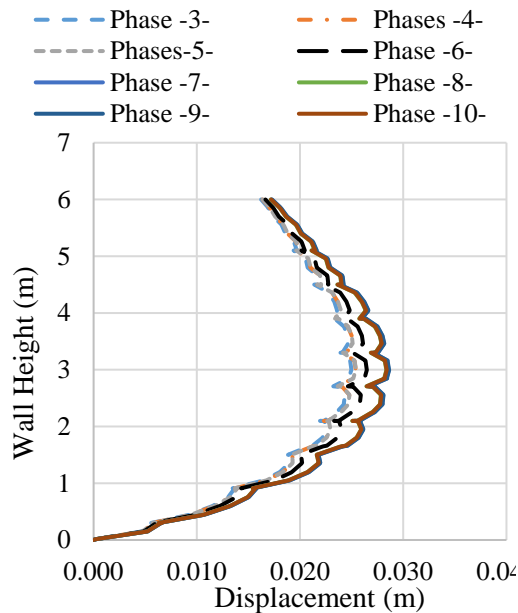


**Figure 8. Typical wall displacement shape, Model PS-0.**

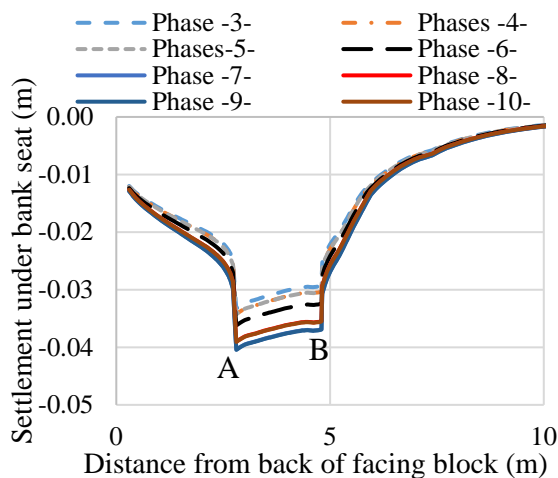


**Figure 9. Typical wall displacement shape, Model PS-0.**

**Table 5. Wall displacement summary.**

Model	Max. Wall Displacement (m)	Location of Max. Wall Displacement (m)	Top Wall Displacement (m)
PS-0	0.028	3.00	0.017
PS-1	0.021	3.15	0.014
PS-2	0.025	3.20	0.015
PS-3	0.029	3.00	0.020

**Table 6. Settlement of the abutment bank seat in all models.**

Model	A (at bottom rear corner of bank seat)	B (at bottom front corner of bank seat)
PS-0	-0.041	-0.037
PS-1	-0.037	-0.034
PS-2	-0.039	-0.036
PS-3	-0.042	-0.038

### ***Vertical stresses under the abutment bankseat***

The maximum vertical stresses under the bank seat occurred under the bottom front corner of the bank seat in all models. The vertical stress reached a minimum midway under the bankseat, Figure

10. The stress at the bottom front and bottom rear corners was similar to the vertical settlement of the bank seat (Models PS-0 – PS-3).

In models PS-0, PS-1 and PS-2, the vertical stresses under the rear and front corners of the bank seat decreased when the spacing between the primary geogrids was reduced from 0.6 m (PS-0) to 0.3 m (PS-1) and 0.45 m (PS-2). In PS-1 the vertical stresses decreased slightly, however in PS-2 the vertical stresses largely remained the same, Table 7. However, when the secondary geogrids were removed Models PS-0 and PS-3, a slight increase of 7% at both the bottom rear and bottom front corners occurred, Figure 7. and remained the vertical stresses under the front rear remained the same, Table 7.

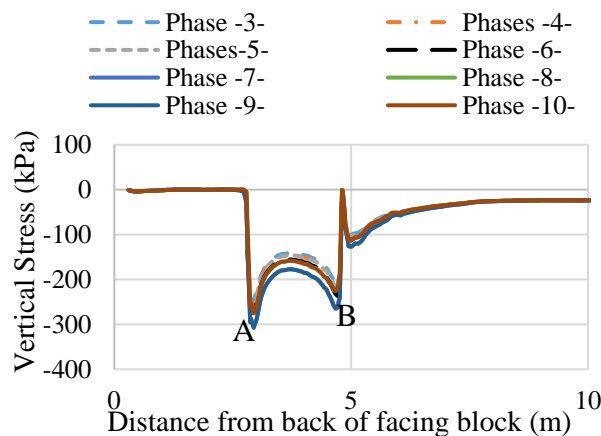


**Figure 10. Vertical stress distribution under the bank seat, Model PS-0.**

**Table 7. Vertical stresses under the bank seat in all models.**

Model	A (at bottom front corner of bank seat)	B (at bottom rear corner of bank seat)
PS-0	307.93	264.51
PS-1	294.60	229.49
PS-2	303.73	273.35
PS-3	258.58	263.77

### *Lateral Earth Pressure*

The lateral earth pressure at the top of the wall is affected by the axial tensile stiffness of the geogrids (BS 8006-1, 2016). BS 8006-1 (2016) identifies that where inextensible reinforcement is used, lateral earth pressures approximate to the at rest earth pressure condition and therefore the wall should be designed in accordance with the Coherent Gravity Method. Inextensible reinforcement are reinforcement materials that deform less than the surrounding soil at failure such as the metallic reinforcement (Elias et al. 2001).

Additionally, BS 8006-1 (2016) also specifies that unless otherwise shown by field measurements, active earth pressures may be assumed to act in walls with extensible reinforcement. Therefore, where extensible reinforcement is used, these walls should be designed using the Tieback Wedge Method. Extensible reinforcement are materials that deform as much as the surrounding soil such as geosynthetic reinforcement (Elias et al. 1997).

The K-stiffness method was developed by Bathurst et al. (2008) and uses stress to compute the reinforcement loads for the internal stability of GRS walls under service conditions. The K-stiffness method uses the at rest coefficient of earth pressure equations to determine the earth pressure coefficient. However, this does not infer an at rest state of stress. It is simply a convenient index value for use in the calculations.

The FHWA assume that the lateral earth pressure is independent of the wall height, surcharge or bridge loads due to the reinforcement restraining the lateral deformation of the soil

immediately above and below. The validity of this assumption is strongly dependent on the reinforcement spacing, (Adams et al. 2011).

In this study the earth pressure coefficient, defined as the ratio of predicted horizontal to vertical stress, was determined at two locations in model PS-0. Location A was a vertical line directly beneath the mid width of the bank seat, while Location B was directly behind the wall facing, Figure 11. Figures 12 and 13 present the lateral earth pressure at those two locations.

The lateral earth pressure at cross section A, Figure 12, showed the magnitude of the earth pressure coefficient tending toward the at rest value at the top and bottom of the wall. Over the mid-height of the wall the coefficient tended towards the active earth pressure coefficient.

However, the lateral earth pressure at cross section B, Figure 13, approached the active value where the geogrid was located, due of the lateral restraints caused by the geogrids above and below. Therefore, the lateral earth pressure acting on the facing block wall will be the “Bin Pressure” between two adjacent geogrids layer, which is practically independent of the wall height and affected by the spacing between the two geogrids (Wu 2001).

In addition, the lateral earth pressure at cross section B, showed that the value fluctuated around the value of active earth pressure coefficient (0.3), which shows a good agreement with BS 8006-1 (2016), where the active earth pressure maybe be assumed to act along the wall when using extensible reinforcement. Also, the data showed good agreement with the FHWA, with the lateral earth pressure independent of the wall height, loads magnitude, but strongly dependent on the geogrid spacing.

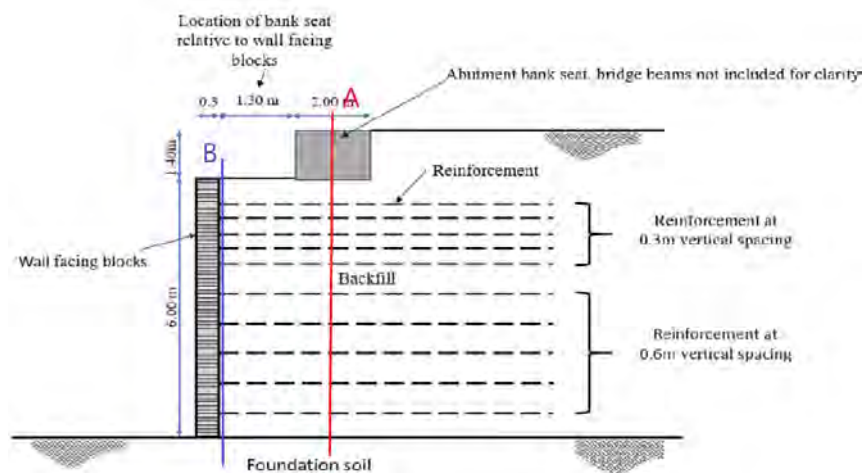


**Figure 11. Cross section location**

## CONCLUSIONS

Reducing the vertical spacing between primary geogrids from 0.6m to 0.3m and 0.45m (Models PS-0, PS-1 and PS-2), resulted in a slight decrease in the wall deformation and also affected the location of the maximum deformation, occurring higher up the face of the wall. This reduction in wall deformation at smaller vertical geogrid spacing correspondent to a parallel decrease in the settlement at the front and rear bottom corners of the bank seat. The rotation effect of the bank seat also decreased. However, this change did not impact the vertical stresses under the bank seat that remained almost the same.



Removing the secondary geogrids increased the wall deformation at the top of the wall and remained the same at the bottom of the wall. However, it did not impact the settlement of the backseat but did lead to a more uniform distribution of vertical stress directly beneath the bank seat, Models PS-0 and PS-3.

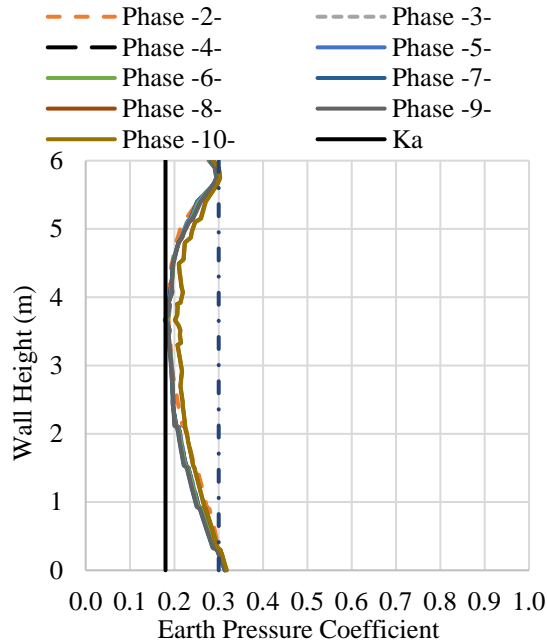


**Figure 12. Earth Pressure Coefficient Section A, Model PS-0**

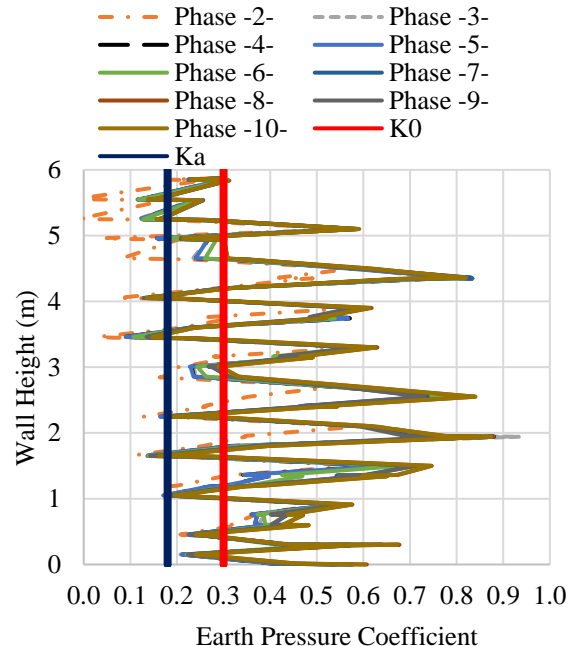


**Figure 13. Earth Pressure Coefficient at Cross Section B-Model PS-0**

The prediction of the earth pressure coefficient within the retained fill under phased loading was also shown a good agreement with that suggested by BS 8006-1 (2016) and Bathurst et al. (2008). The K-Stiffness method proposed by Bathurst et al. (2008) was shown to provide a reasonable estimate of the earth pressure coefficient under loading conditions. The behaviour of the earth pressure coefficient during phased loading conditions was found to be independent of applied vertical and horizontal loads from the bridge abutment. The magnitude of the earth pressure coefficient showed good agreement with the FHWA (Elias et al., 1997), with the lateral earth pressure independent of the wall height, and magnitude of load, while strongly dependent on the geogrid spacing (Wu, 2001).

Some recommendations should be taken into account for future design, it is very important to consider the spacing between geogrids to reduce the wall deformation and the bank seat settlement. Decreasing the spacing between primary geogrids displayed an over better response of the system than just adding secondary geogrids at the top of the wall. This study also showed that decreasing the vertical spacing between geogrids caused the earth pressure coefficient to approach the magnitude of the at rest lateral earth pressure coefficient. However, this does not necessary infer an at rest state of stress exists in the structure.

## REFERENCES

Abu-Hejleh, N., Wang, T., & Zornberg, J. G. (2000). Performance of geosynthetic-reinforced

- walls supporting bridge and approaching roadway structures. *In Advances in transportation and geoenvironmental systems using geosynthetics* (pp. 218-243).
- Abu-Farsakh, M., Ardah, A., & Voyiadjis, G. (2018). 3D Finite element analysis of the geosynthetic reinforced soil-integrated bridge system (GRS-IBS) under different loading conditions. *Transportation Geotechnics*, 15, 70-83.
- Adams, M., & Nicks, J. (2018). *Design and construction guidelines for geosynthetic reinforced soil abutments and integrated bridge systems* (No. FHWA-HRT-17-080). United States. Federal Highway Administration.
- Adams, M., Nicks, J., Stabile, T., Wu, J. T., Schlatter, W., & Hartmann, J. (2011). *Geosynthetic reinforced soil integrated bridge system, synthesis report* (No. FHWA-HRT-11-027). United States. Federal Highway Administration.
- Ardah, A., Abu-Farsakh, M. and Voyiadjis, G. (2017). Numerical evaluation of the performance of a Geosynthetic Reinforced Soil-Integrated Bridge System (GRS-IBS) under different loading conditions. *Geotextiles and geomembranes*, 45(6), pp.558-569.
- Bathurst, R. J., Miyata, Y., Nernheim, A., & Allen, A. M. (2008). Refinement of K-stiffness method for geosynthetic-reinforced soil walls. *Geosynthetics International*, 15(4), 269-295.
- BS 8006-1:2010+A1 (2016), *Code of practice for strengthened/reinforced soils and other fills*. British Standard Institution, London.
- BS EN 1991-1-1:2002. (2002). "BS EN 1991-1-1:2002 - Eurocode 1: Actions on Structures - Part 1-1: General Actions - Densities, Self-Weight, Imposed Loads for Buildings." *Eurocode 1* 2(2005):35 Table A.4.
- Carder, D. R., & Card, G. B. (1997). Innovative structural backfills to integral bridge abutments. *TRL REPORT* 290.
- Christopher, B. R., & Elias, V. (1997). *Mechanically Stabilized Earth Walls and Reinforced Soil Slopes Design and Construction Guidelines* (No. FHWA-SA-96-071). United States. Federal Highway Administration.
- CEN. (2005). EN 1992-2: 2005. Eurocode 2-Design of concrete structures. Part 2: Concrete bridges: Design and detailing rules.
- EL Refai B., and Naughton P. (2022). "Numerical Analysis of Stress Concentration around Bridge Bank Seat in Geosynthetic Reinforced Soil – Integrated Bridge Systems (GRS-IBS)," *EuroGeo7*, Poland, no. 2022.
- Garnier-Villarreal, M., Fratta, D., & Oliva, M. (2014). Evaluation of the Deformation of a Geosynthetic-Reinforced Soil Bridge Abutment. In *Geo-Congress 2014: Geo-characterization and Modeling for Sustainability* (pp. 4191-4202).
- Hatami, K., & Bathurst, R. J. (2005). Development and verification of a numerical model for the analysis of geosynthetic-reinforced soil segmental walls under working stress conditions. *Canadian Geotechnical Journal*, 42(4), 1066-1085.
- Horvath, J. S. (2000). Integral-abutment bridges: problems and innovative solutions using EPS geofoam and other geosynthetics. *Res. Rpt. No. CE/GE-00*, 2.
- Wu, J. T. (2001). *Revising the AASHTO guidelines for design and construction of GRS walls* (No. CIOT-D1D-R-2001-16). United States. Federal Highway Administration.
- Zheng, Y., & Fox, P. J. (2017). Numerical investigation of the geosynthetic reinforced soil-integrated bridge system under static loading. *Journal of Geotechnical and Geoenvironmental Engineering*, 143(6), 04017008.